



HAL
open science

Habilitation à Diriger des Recherches L'autophagie sélective au coeur de la physiopathologie

Flavie Strappazzon

► **To cite this version:**

Flavie Strappazzon. Habilitation à Diriger des Recherches L'autophagie sélective au coeur de la physiopathologie. Life Sciences [q-bio]. Université Claude Bernard Lyon 1, 2023. tel-04239017

HAL Id: tel-04239017

<https://hal.science/tel-04239017v1>

Submitted on 12 Oct 2023

HAL is a multi-disciplinary open access archive for the deposit and dissemination of scientific research documents, whether they are published or not. The documents may come from teaching and research institutions in France or abroad, or from public or private research centers.

L'archive ouverte pluridisciplinaire **HAL**, est destinée au dépôt et à la diffusion de documents scientifiques de niveau recherche, publiés ou non, émanant des établissements d'enseignement et de recherche français ou étrangers, des laboratoires publics ou privés.

Université Claude Bernard  Lyon 1

Habilitation à Diriger des Recherches

L'autophagie sélective au cœur de la physiopathologie

Flavie STRAPPAZZON
Chargée de Recherche, CNRS
Institut NeuroMyogène, INMG
Equipe Métabolisme Energetique et Développement Neuronal
(CNRS UMR 5310 - INSERM U1217 - Université de Lyon)

à soutenir le 11 Janvier 2023

Membres du Jury :

Monsieur Alain BUISSON
Madame Audrey ESCLATINE
Monsieur Mathias FAURE
Monsieur David BLUM
Monsieur Patrice CODOGNO
Madame Carole KRETZ

Rapporteur
Rapporteur
Rapporteur
Examineur
Examineur
Examineur

TABLE DES MATIERES

Curriculum Vitae	p2
Education-Expérience professionnelle.....	p2
Affiliations scientifiques.....	p4
Activités éditoriales et évaluations de demande de financements	p4
Evaluations de PhD.....	p4
Management scientifique.....	p4
Activités d'enseignement.....	p6
Présentations orales.....	p6
Vulgarisations scientifiques.....	p7
Animations scientifiques.....	p8
Financements.....	p8
Prix et récompenses	p9
Publications.....	p10
Bref résumé du parcours scientifique.....	p15
Résumé des études de recherche précédentes	p16
<u>Post-doctorat #1</u> : Study of the role of transglutaminase 2 protein (TG2) in the autophagy process (2008-2010).....	p16
<u>Post-doctorat #2</u> : Study of the molecular mechanisms underlying the function of AMBRA1 in autophagy (2010-2014).....	p17
<u>Projet effectué en tant que "Principal Investigator"</u> (dans la laboratoire dirigé par Prof F Cecconi) (2014-2017).....	p19
Responsable de laboratoire "Cellular and Molecular Neurosciences" (2018 –2021) "Study of mitophagy in physiopathological contexts".....	p22
Projets en cours	p25
Projet en cours N°1: A natural variant of the autophagic receptor NDP52 as a possible target for novel treatments in Alzheimer's disease (2021-2022).....	p26
Projet en cours N°2: Dissecting the role of mitophagy in breast cancer therapy resistance (2020-2025).....	p35
Projets proposés	p55
Projet proposé N°1: NDP52, a protein that protects against Alzheimer's.....	p56
Projet proposé N°2: Local modulation of mitophagy and refinement of cortical connectivity during axonal development.....	p64
Projet proposé N°3: Selective autophagy and skeletal striated muscle: identification of novel molecular mechanisms involved in myotonic dystrophy type 1 (DM1).....	p80
ANNEXES	p87

CURRICULUM VITAE

Flavie Strappazon

Née à Chambéry, (France) le 16-02-1981

Nationalité: Française

Deux enfants

PhD en Biologie Cellulaire

e-mail: flavie.strappazon@univ-lyon1.fr

EDUCATION-EXPERIENCE PROFESSIONNELLE

2022-aujourd'hui:

- Position permanente CRCN-CNRS au PNMG (Physiopathologie Génétique du Neurone et du Muscle) –Institut Neuromyogène (INMG), Lyon (France). Equipe dirigée par le Dr Courchet “Métabolisme énergétique et développement neuronal”.

2020- aujourd'hui:

- Principal Investigator (PI) du projet “*My First AIRC*” (Fondation italienne pour lutter contre le cancer). IRCCS Fondazione Santa Lucia, Rome, Italie “***Dissecting the role of mitophagy in breast cancer therapy resistance***”

2020-2021:

- PI du projet “AGYR2020” (Association italienne pour lutter contre la maladie d'Alzheimer). IRCCS Fondazione Santa Lucia, Rome, Italie “***Studying a natural variant of the autophagy receptor NDP52 as a possible target for novel treatments in Alzheimer's disease***”

Group leader d'un groupe composé de deux post-doctorands et un étudiant en master II.

2018-2020:

- PI du projet “*Roche per la Ricerca 2017*” (Prix en Neurosciences, Roche). Fondazione Santa Lucia, Rome, Italie “***Preventing Neurodegeneration in Multiple Sclerosis disease by activating mitophagy***”

Group leader d'un groupe composé d'un post-doctorand et deux étudiants en master II.

+ Collaborateur sur un projet financé par le Ministère italien de la santé “Giovani Ricercatori, under 40 years old”. “***Identification of new molecular targets promoting bone-marrow pre-metastatic niche in neuroblastoma***”

2014-2017:

- PI du projet “Giovani Ricercatori”, Financé par le ministère italien de la santé d’une durée de 3 ans, IRCCS Santa Lucia (lab. Prof Cecconi), Rome, Italie. **“Recovery of neuronal Parkinson’s disease neuronal functionality by modulation of Ambra1, a novel primer of mitophagy”**

2015-2016:

- PI du projet “Trampoline” financé par l’AFM-Telethon français, 1 an, IRCCS Santa Lucia (Lab. Prof Cecconi), Rome, Italie. **“Recovery of a dystrophic phenotype by modulation of Ambra1, a novel primer of mitophagy”**

2010-2014:

- Post-doctorande
Laboratoire dirigé par le Prof. F. Cecconi, IRCCS Santa Lucia, Rome, Italie (Contrats provenant de l’Université de Rome) « **Study of the role of Ambra1 at the mitochondria.**”

2008-2010:

- Post-doctorande (Marie Curie)
Laboratoire dirigé par le Prof. Mauro Piacentini, Université de Tor Vergata, Rome, Italie « **Study of the autophagic role of Transglutaminase 2 in vivo** »

2004-2007:

- PhD en Biologie Cellulaire
Laboratoire dirigé par le Prof. Sadoul, INSERM U108, Grenoble, France « **Role of Alix and its partners Alg-2 and Pyk2 in neuronal death**”
Mention Honorable avec félicitations du jury

2004:

- Master II en Biologie Cellulaire, Université de Grenoble, France.
Laboratoire dirigé par le Prof. Sadoul, INSERM U108, Grenoble, France « **Study of the role of Alix in cell death induced by U.V**»

2002-2003:

- Master I en Biologie Cellulaire et Physiologie, Université de Grenoble, France

1999-2001:

- Licence en Biologie Cellulaire et Physiologie, Université de Grenoble, France

1999:

- Baccalauréat scientifique, France.

AFFILIATIONS A DES ASSOCIATIONS SCIENTIFIQUES

- 2022:** Membre du bureau du Club Francophone de l'Autophagie (CFATG)
- 2019-2022:** Membre de deux associations: Associazione Italiana di NeuroImmunologia (AINI) et "Women in Autophagy Network" (WIA).
- 2011-2014 :** Membre du Club Francophone de l'Autophagie, France

ACTIVITIES EDITORIALES ET EVALUATION SCIENTIFIQUES

EDITEUR: Journal Cell Death and Diseases (Groupe Nature).

PEER REVIEW: Membre reviewers du journal Aging Neuroscience et Cells + reviewer pour différents journaux comme Autophagy J, Cell Death and Differentiation J, Nature Communications J, Molecular and Cellular Oncology J, Frontiers in Neurosciences J, BBA J etc...

J'ai participé à plusieurs évaluations de demandes de financement en collaboration avec le Prof Cecconi : projets **AIRC** (Italian association for cancer research) et projets **KBVU** (Danish Cancer Society).

EXAMINATIONS de PhD

Octobre 2019 (Italie) : Examineur du PhD d'Elena MARCHESAN (Université de Padoue) «Calcineurin regulates Parkin-translocation to mitochondria and mitophagy ». PhD dirigé par le Prof Luca Scorrano.

Décembre 2020 (Italie) : Rapporteur de la thèse de Silvia Sorrentino, Université de Rome « Cattolica del Sacro Cuore ». PhD dirigé par Dr MT Viscomi.

Octobre 2021 (France) : Examineur du PhD d'Emma GUILBAUD (Université Cote d'Azur) « *Nouvelles altérations métaboliques des cancers bronchiques non à petites cellules- Role de l'efflux du cholestérol et de la mitophagie* ». PhD co-dirigé par le Dr Laurent YVAN-CHARVET et le Dr. Stoyan IVANOV.

Octobre 2020-2022 (France) : Membre du comité de suivi de thèse de Caroline LIENARD. Thèse intitulée « Mécanismes et thérapies pour les maladies neuromusculaires » (Université de Montpellier, école doctorale ED168 + Université de Lyon, école doctorale BMIC). PhD dirigé par le Dr P Bomont.

MANAGEMENT SCIENTIFIQUE

A ce jour j'ai encadré 3 post-doctorands, 8 étudiants en Master II et co-encadré 1 PhD avec le Prof Cecconi.

Management scientifique passé:

Nom	Université	Formation	% d'encadrement	Dates	Publications
Matteo Vietri-Rudan	Tor Vergata, Rome	Master II	Co-encadrement avec le Prof Cecconi	Oct 2011-Oct 2012	1
Beatrice Biferali	Tor Vergata, Rome	Master II	Co-encadrement avec le Prof Cecconi	Oct 2013-Oct 2014	/
Anthea Di Rita	Tor Vergata, Rome	Master II + PhD	Co-encadrement avec le Prof Cecconi	Oct 2014-Oct 2018	10
Serena Verna	Tor Vergata, Rome	Master II	100% encadrement	Oct 2015-Oct 2016	/
Francesca Orrecchio	Tor Vergata, Rome	Master II	100% encadrement	Oct 2016-Oct 2017	/
Anthea Di Rita	Tor Vergata, Rome	Post-doctorante	100% encadrement	Déc 2018-Déc 2017	10
Teresa Maiorino	Santa Lucia Foundation	Bourse Post-Master II	100% encadrement	Dec 2019-Dec 2020	2
Krenare Bruqi	Tor Vergata, Rome	Master II	100% encadrement	Oct 2019-Mar 2020	1
Anna Mattioni	Santa Lucia Foundation	Post-doctorante	100% encadrement	Fév 2021-Fév 2022	1 en préparation
Francesco Naso	Santa Lucia Foundation	Post-doctorant	100% encadrement	Mar 2021-Mar 2022	1 en préparation

Management scientifique en cours:

Name	University	Formation	% of mentoring	Dates	Publications
Valentina Fraiese	Sapienza, Rome	Master II	100% encadrement	Sept 2021- Oct 2022	/
Anna Mattioni	Santa Lucia Foundation	Post-doctorante	100% encadrement	Fév 2022-Fév 2023	1 en preparation
Francesco Naso	Santa Lucia Foundation	Post-doctorant	100% encadrement	Mar 2022-Mar 2023	1 en preparation

ACTIVITES D'ENSEIGNEMENT

2004-2007 : Licence 2, Travaux pratiques de Neuro-anatomie/Physiologie et Neurobiologie Cellulaire. Université de Grenoble I, Joseph Fourier, sous la supervision du Dr Hemming et du Dr Torch (enseignement total : 8hrs/an).

2013-2022 : Licence 2, Cours magistraux de Biologie du Développement et de différenciation cellulaire (Responsable du cours: Prof. F Cecconi). Université de Rome, Tor Vergata (Italie) (6h/an).

2016-2019 : Créateur et Responsable de l'unité « Mitochondrial physiopathologies » pour les étudiants en Master II en Biologie Cellulaire et Moléculaire (cours optionnel). Université de Rome, Tor Vergata (Italie) (16 hrs /an).

2022 : Intervention dans le cours "Aging and Cell Death" pour des étudiants en Master II « Génétique de la cellule et pathologies ». Responsable C Kretz, Université Lyon 1 (2 hrs).

Total enseignement: 176 hrs.

PRESENTATIONS ORALES

Juin 2022: Présentation orale au 10th CFATG (Club Francophone de l'Autophagie), Besançon, France

Octobre 2021: Séminaire portant sur la mitophagie et les maladies neurodégénératives à l'université de Rome, Sapienza (Italie), invitée par le Dr. Guargualini

Septembre 2020: Webminar portant sur la mitophagie et les maladies neurodégénératives à l'institut NeuroMyoGene (Lyon, France), invitée par le Dr. Courchet

Mai 2019: Présentation orale au meeting international XXVIII AINI (Associazione Italiana Neuroimmunologia), Camogli, Italie.

Mars 2016: Présentation orale (Short talk) au meeting International "Gordon Research Conference" "From the Basics in the Signalling and Molecular Aspect of Autophagy to the Identification of Therapeutic Targets", Californie, USA.

Octobre 2015: Présentation orale (short talk) au meeting "European Cell Death Organization (ECDO)" "Death pathways and beyond", Genève, Suisse.

Novembre 2015: Séminaire au département de Biologie de l'université de Rome, Tor Vergata (invitée par le Prof Cecconi).

Avril 2014: Présentation orale au meeting International Gordon "Autophagy in stress, development and disease", Italie.

2006-aujourd'hui: Plus de 10 présentations de posters effectuées en tant que doctorante et post-doctorante à des meetings internationaux dans le domaine de la mort cellulaire et de l'autophagie (Canada, Japon, USA, etc.).

VULGARISATION SCIENTIFIQUE

2022 : Intervention au festival de l'orientation des lycéens de Bologne (Italie) pour favoriser l'insertion des femmes dans le domaine scientifique (Evènement intitulé : *A tutto STEAM ! Protagoniste al femminile oltre gli stereotipi di genere*)

2021 : Interview pour le journal "Sesta Stagione" afin d'expliquer au grand public (incluant les patients Alzheimer) mon projet financé par l'AirAlzh (Rome, Italie).

2021 : Présentation orale à la journée internationale « Alzheimer's Day » organisée pour le grand public, incluant les patients Alzheimer ou leurs familles (Cesenatico, Juin 2021, Italie).

2019 : Interview pour l'association "Bellunesi nel mondo"(Italie du Nord) afin d'expliquer e ma carrière professionnelle au grand public (<https://www.bellunesinelmondo.it/133-storie-dalla-community-di-bellunoradici-net-flavie-strappazon/>)

2018 : Interview en directe à la Radio Cusano (Rome, 22 Février) afin d'expliquer au grand public mon projet "Roche per la Ricerca" et ma carrière de jeune chercheuse (moins de 40 ans) (<https://www.tag24.it/201516-201516>)

2018 : Interview aux journalistes d'ADNKronos afin d'expliquer au grand public mes recherches (https://www.adnkronos.com/salute/2018/02/21/dalla-francia-all-italia-caccia-dei-segreti-della-sclerosi-multipla_I8HcoWYOvVQBQcdbqldXeM.html)

2018 : Interview au journal "Scienze e Medicina" Aquila (Italy) afin d'expliquer au grand public mes travaux de recherches publiés dans le journal Nature Communication (<https://www.improntalaquila.com/2018/09/14/sanita-scoperte-tre-nuove-molecole-che-controllano-neurodegenerazioni-e-tumori>)

2018 : Interview à l'Université de Rome Tor Vergata afin d'expliquer mes recherches « ROCHE »
(https://web.uniroma2.it/module/name/Content/action/showpage/content_id/52359)

2018 : Interview au prestigieux journal italien de nouvelles "La Repubblica" afin d'expliquer mes recherches financées par la ROCHE au grand public (<https://www.centronutrizionecarrozzo.it/sclerosi-multipla-si-testa-un-nuovo-modo-per-combatterla/>)

ANIMATIONS SCIENTIFIQUES

2022: Chairwomen au 10th Scientific Days of Autophagy (CFATG10), Besançon, France.

2015: Membre du comité d'organisation du meeting "EMBO conference on Autophagy" (Chairs: Francesco Cecconi, co-chair: Marja Jaatela), Sardègne, Italie.

2011: Membre du comité d'organisation du meeting "European Cell Death Organisation" meeting on Apoptosis (Chairs: Francesco Cecconi, Mauro Piacentini), Rome, Italie.

FINANCEMENTS

n=7 (comme PI ou Collaborateur) pour un total de 1 830 000 euros depuis 2014

+ 1 financement en cours de demande à l'association France Alzheimer

2021-2026 **Consortium "MYONEURALP2"**

- ❖ Fonds de l'AFM-Téléthon (France)
- ❖ 90 000 euros/an pendant 5 ans
- ❖ Titre du projet: Dysregulation of skeletal muscle homeostasis in neuromuscular disorders

2020- 2025 **Principal Investigator, "My First AIRC"**

- ❖ Fonds de l'AIRC (Foundation for Cancer Research in Italy)
- ❖ 500 000 euros
- ❖ Titre du projet: Dissecting the role of mitophagy in breast cancer therapy resistance.

2020- 2021 **Principal Investigator, Airalzh-Grant-for-Young-Researchers**

- ❖ Fonds de l'association Airalzh (Italian Association for Alzheimer's Research)
- ❖ 35 000 euros/ 1 an

2014: Bourse de voyage **CFATG** (Club Francophone de l'Autophagie) afin de participer au meeting Gordon "Autophagy in stress, development and disease" (Lucca, Italie) (450 euros).

2014: Prix de la meilleure présentation orale au meeting Gordon "Autophagy in stress, development and disease" (400 euros).

2017: Prix en Neurosciences "**Roche per la Ricerca 2017**" (100 000 euros),

2021: Ma post-doctorande (A. Mattioni) a obtenu un prix/invitation provenant de l'association "**Women in Autophagy**" afin de participer au meeting **Tau Consortium**.

2022: Ma post-doctorande (A. Mattioni) a obtenu un **Travel Grant EMBO** afin de participer au meeting EMBO **Autophagy in brain health and diseases**.

2022: Mon post-doctorant (F. Naso) a obtenu un **Travel Grant de la part du CFATG** afin de participer au meeting **10th Scientific Days of Autophagy (CFATG10)** à **Besançon, France**.

Metrics/Publications

Researcher ID /Publon: [ABB-6775-2020](#)

ORCID ID : 0000-0003-0285-7449

H-index (Scopus)= 20

Articles= 38 dont n=11 en tant qu'auteur principal (first, last or co-last author)

Citations totales=2348

ARTICLES DE RECHERCHE

Gambarotto L, Metti S, Chrisam M, Cerqua C, Sabatelli P, Armani A, Zanon C, Spizzotin M, Castagnaro S, **Strappazzon F**, Grumati P, Cescon M, Braghetta P, Trevisson E, Cecconi F, Bonaldo P. Ambra1 deficiency impairs mitophagy in skeletal muscle. J Cachexia Sarcopenia Muscle. 2022 May 20. IF: 12,91

Di Rita A, Angelini DF, Maiorino T, Caputo V, Cascella R, Kumar M, Tiberti M, Lambrugh M, Wesch N, Löhr F, Dötsch V, Carinci M, D'Acunzo P, Chiurchiù V, Papaleo E, Rogov VV, Giardina E, Battistini L, **Strappazzon F**. Characterization of a natural variant of human NDP52 and its functional consequences on mitophagy. Cell Death Differ. 2021 Aug;28(8):2499-2516. IF: 15,8

Di Rita A, Angelini DF, Maiorino T, Campoli G, Cascella R, Kumar M, Tiberti M, Lambrugh M, Wesch N, Löhr F, Dötsch V, Carinci M, D'Acunzo P, Chiurchiù V, Papaleo E, Rogov VV, Giardina E, Battistini L and **Strappazzon F**. Characterization of a natural variant of human NDP52 and its functional consequences on mitophagy. Cell Death Differ. 2021 Aug;28(8):2499-2516. IF: 15,8

Di Rita A, Maiorino T, Bruqi K, Pulcrano S, Bellenchi GC and **Strappazzon F*** . miR-218 inhibits mitochondrial clearance by targeting PRKN E3 Ubiquitin ligase. Int J Mol Sci. 2020 Jan 5;21(1). *Last and corresponding author IF: 5,9

Strappazzon F*, Di Rita A, Peschiaroli A, Melino G and Cecconi F*. HUWE1 controls MCL1 stability to unleash AMBRA1-induced mitophagy, Cell Death and Diff, 2019 Aug 21.

* Co-corresponding author IF: 15,8

Di Rita A, Peschiaroli A, Gruber J, Dötsch V, Nygaard M, Lambrugh M, Papaleo E, Dengjel J, El Alaoui S, Rogov V, **Strappazzon F*** and Cecconi F*. The E3 ubiquitin ligase HUWE1 promotes PINK1/PARKIN-independent mitophagy by regulating AMBRA1 activation, through IKK α . Nat Comm, 2018 Sep 14;9(1):3755. * co-last and co-corresponding author IF: 14,9

Di Rita A, D'Acunzo P, **Strappazzon F*** and Cecconi F* AMBRA1-mediated mitophagy counteracts oxidative stress and apoptosis induced by neurotoxicity in human neuroblastoma SHSY5Y cells. Frontiers in Cellular Neuroscience 2018 Apr 18;12:92. * co-last and cocorresponding author IF: 4,5

Antonelli M, **Strappazzon F**, Arisi I, Brandi R, D'Onofrio M, Sambucci M, Manic G, Vitale I, Barilà D, Stagni V. ATM kinase sustains breast cancer stem-like cells by promoting ATG4C expression and autophagy. Oncotarget. 2017 Mar 28;8(13):21692-21709. IF: 3,3

Strappazzon F*, Di Rita A, Cianfanelli V, D'Orazio M, Nazio F, Fimia GM, Cecconi F*. Prosurvival AMBRA1 turns into a proapoptotic BH3-like protein during mitochondrial apoptosis. Autophagy. 2016 Jun 2;12(6):963-75. * co-corresponding author IF: 16

D'Acunzo P, **Strappazzon F**, Caruana I, Meneghetti G, Di Rita A, Simula L, Weber G, Del Bufalo F, Dalla Valle L, Campello S, Locatelli F, Cecconi F. Inducing mitophagy reversibly by an optogenetic bimodular system. Nat Comm. 2019 Apr 4;10(1):1533. IF: 14,9

Becher J, Simula L, Volpe E, Procaccini C, La Rocca C, D'Acunzo P, Cianfanelli V, **Strappazzon F**, Caruana I, Nazio F, Weber G, Gigantino V, Botti G, Ciccocanti F, Borsellino G, Campello S, Mandolesi G, De Bardi M, Fimia GM, D'Amelio M, Ruffini F, Furlan R, Centonze D, Martino G, Braghetta P, Chrisam M, Bonaldo P, Matarese G, Locatelli F, Battistini L, Cecconi F. AMBRA1 Controls Regulatory T-Cell Differentiation and Homeostasis Upstream of the FOXO3-FOXP3 Axis. Dev Cell. 2018 Dec 3;47(5):592-607.e6. IF: 10

Capizzi M, **Strappazzon F**, Cianfanelli V, Papaleo E, Cecconi F. MIR7-3HG, a MYC-dependent modulator of cell proliferation, inhibits autophagy by a regulatory loop involving AMBRA1. Autophagy. 2017 Mar 4;13(3):554-566. IF: 16

Nazio F, Carinci M, Valacca C, Bielli P, Strappazzon F, Antonioli M, Ciccocanti F, Rodolfo C, Campello S, Fimia GM, Sette C, Bonaldo P, Cecconi F. Fine-tuning of ULK1 mRNA and protein levels is required for autophagy oscillation. J Cell Biol. 2016 Dec 19;215(6):841-856. IF: 10,5

Schiavi A, Maglioni S, Palikaras K, Shaik A, **Strappazzon F**, Brinkmann V, Torgovnick A, Castelein N, De Henau S, Braeckman BP, Cecconi F, Tavernarakis N, Ventura N. Iron-Starvation-Induced Mitophagy Mediates Lifespan Extension upon Mitochondrial Stress in C. elegans. Curr Biol. 2015 Jul 20;25(14):1810-22. IF: 10,8

Strappazzon F, Nazio F, Corrado M, Cianfanelli V, Romagnoli A, Fimia GM, Campello S,

Nardacci R, Piacentini M, Campanella M, Cecconi F. AMBRA1 is able to induce mitophagy via LC3 binding, regardless of PARKIN and p62/SQSTM1. *Cell Death Differ.* 2015 Mar;22(3):419-32. [IF:15,8](#)

Nazio F, **Strappazzon F**, Antonioli M, Bielli P, Cianfanelli V, Bordi M, Gretzmeier C, Dengjel J, Piacentini M, Fimia GM, Cecconi F. mTOR inhibits autophagy by controlling ULK1 ubiquitylation, self-association and function through AMBRA1 and TRAF6. *Nat Cell Biol.* 2013 Apr;15(4):406-16. [IF: 28,8](#)

D'Eletto M, Farrace MG, Rossin F, **Strappazzon F**, Giacomo GD, Cecconi F, Melino G, Sepe S, Moreno S, Fimia GM, Falasca L, Nardacci R, Piacentini M. Type 2 transglutaminase is involved in the autophagy-dependent clearance of ubiquitinated proteins. *Cell Death Differ.* 2012 Jul;19(7):1228-38. [IF: 15,8](#)

Strappazzon F, Vietri-Rudan M, Campello S, Nazio F, Florenzano F, Fimia GM, Piacentini M, Levine B, Cecconi F. Mitochondrial BCL-2 inhibits AMBRA1-induced autophagy. *EMBO J.* 2011 Apr 6;30(7):1195-208. [IF: 11,5](#)

Strappazzon F, Torch S, Chatellard-Causse C, Petiot A, Thibert C, Blot B, Verna JM, Sadoul R. Alix is involved in caspase 9 activation during calcium-induced apoptosis. *Biochem Biophys Res Commun.* 2010 Jun 18;397(1):64-9. [IF: 3,5](#)

Mahul-Mellier AL, **Strappazzon F**, Petiot A, Chatellard-Causse C, Torch S, Blot B, Freeman K, Kuhn L, Garin J, Verna JM, Fraboulet S, Sadoul R. Alix and ALG-2 are involved in tumor necrosis factor receptor 1-induced cell death. *J Biol Chem.* 2008 Dec 12;283(50):34954-65. [IF: 5,1](#)

Petiot A, **Strappazzon F**, Chatellard-Causse C, Blot B, Torch S, Verna JM, Sadoul R. Alix differs from ESCRT proteins in the control of autophagy. *Biochem Biophys Res Commun.* 2008 Oct 10;375(1):63-8. [IF: 3,5](#)

Mabrouk K, Ram N, Boisseau S, **Strappazzon F**, Rehaïm A, Sadoul R, Darbon H, Ronjat M, De Waard M. Critical amino acid residues of maurocalcine involved in pharmacology, lipid interaction and cell penetration. *Biochim Biophys Acta.* 2007 Oct;1768(10):2528-40. [IF: 3,6](#)

Strappazzon F, Torch S, Trioulier Y, Blot B, Sadoul R, Verna JM. Survival response-linked Pyk2 activation during potassium depletion-induced apoptosis of cerebellar granule neurons. *Mol Cell Neurosci.* 2007 Mar;34(3):355-65. [IF: 4,3](#)

REVUES

Di Rita A and **Strappazzon F**. A protective variant of the autophagy receptor CALCOCO2/NDP52 in Multiple Sclerosis (MS). *Autophagy* vol. 17,6 (2021): 1565-1567. [IF: 16](#)

DJ Klionsky et al., Guidelines for the Use and Interpretation of Assays for Monitoring Autophagy (4th edition). *Autophagy.* 2021;17(1):1-382. [IF: 16](#)

Strappazzon F. A global view of the miRNA-mitophagy connexion. *Prog Mol Biol Transl*

Sci. 2020;172:37-54. [IF:3,6](#)

Schiavi A*, **Strappazzon F***, Ventura, N. Mitophagy and iron: two actors sharing the stage in age-associated neuronal pathologies. *Mechanisms of Ageing and Development*, 2020, 188, 111252. *[co-first author IF: 5,4](#)

Di Rita A, **Strappazzon F**. Mitophagy could fight Parkinson's disease through antioxidant action. *Reviews in the Neurosciences*, 2019 - [degruyter.com](#)

Di Rita A, **Strappazzon F**. AMBRA1, a Novel BH3-Like Protein: New Insights Into the AMBRA1-BCL2-Family Proteins Relationship. *Int Rev Cell Mol Biol* . 2017;330:85-113. [IF: 6,2](#)

Cianfanelli V*, De Zio D*, Di Bartolomeo S*, Nazio F*, **Strappazzon F***, Cecconi F. Ambra1 at a glance. *J Cell Sci*. 2015 Jun 1;128(11):2003-8. * [co-first author \(equal contribution\) IF:5,2](#)

Strappazzon F*, Cecconi F*. AMBRA1-induced mitophagy: A new mechanism to cope with cancer? *Mol Cell Oncol* . 2015 Feb 25;2(2):e975647. * [co-corresponding author IF: 1,2](#)

Strappazzon F* and Cecconi F. The multifaceted mitochondrion: An attractive candidate for therapeutic strategies. *Pharmacol Res* . 2015 Sep;99:425-33. *[corresponding author IF: 7,6](#)

Campello S, **Strappazzon F**, Cecconi F. Mitochondrial dismissal in mammals, from protein degradation to mitophagy. *Biochim Biophys Acta*. 2014 Apr;1837(4):451-60. [IF: 3,6](#)

Strappazzon F, Campello S, Cecconi F. Non-apoptotic roles for death-related molecules: when mitochondria chose cell fate. *Exp Cell Res*. 2012 Jul 1;318(11):1309-15. [IF: 3,5](#)

Mahul-Mellier AL, **Strappazzon F**, Chatellard-Causse C, Blot B, Béal D, Torch S, Hemming F, Petiot A, Verna JM, Fraboulet S, Sadoul R. Alix and ALG-2 make a link between endosomes and neuronal death. *Biochem Soc Trans*. 2009 Feb;37(Pt 1):200-3. [IF: 6,5](#)

Chapitre de livres

Strappazzon F. A global view of the MiRNA-Mitophagy Connexion. Chapter 3 of the Book « Progress in Molecular Biology and Translational Science »; Special Issue « Autophagy in Health and Disease », 2020, 172, pp. 37-54.

Di Rita A, **Strappazzon F**. Chapter in the academic book « Oxidative Stress and Dietary Antioxidants in Neurological Diseases » edited by Colin Martin and Victor Preedy, 06-2020.

Ferraro E, Fuoco C, **Strappazzon F** and Cecconi F. Chapter 2 of the Book “Apoptosome” Edited by M D’Amelio and F Cecconi: Apoptosome structure and regulation Springer Science 2010.

BRIEF PROFESSIONAL CAREER SUMMARY

During my PhD, I worked at identifying the molecular mechanisms underlying neuronal cell death (laboratory directed by Prof. Sadoul INSERM U108, Grenoble). **This PhD was financed by a French government PhD scholarship.** After graduation, in 2008, I moved to Italy as a **post-doctoral ITN Marie-Curie Fellow** hosted by Prof. Piacentini (University of Rome). I worked on the molecular mechanisms involved in the assembly of protein aggregates, as well as their clearance by autophagy. Afterward, in 2010, as a second post-doctoral training, I joined the laboratory of Prof Cecconi, a leading expert in autophagy (Rome, Italy). My main researches focused on selective autophagy of mitochondria, i.e. mitophagy. I next evolved as a **Principal Investigator (PI)** in the laboratory of Prof Cecconi. In 2018 I became **head of laboratory** at Santa Lucia Foundation in Rome but without permanent position. Since 2022, I have a permanent position as a **CRCN CNRS** in the team “Métabolisme énergétique et développement neuronal” directed by J. Courchet at Physiopathologie Génétique du Neurone et du Muscle (PNMG) –Institut Neuromyogène (INMG), Lyon (France).

SUMMARY OF PREVIOUS RESEARCHES

Graduate studies (2004-2007): “***Characterization of the mechanisms of action of Alix and its partners Alg-2 and Pyk2 in neuronal survival and death***”

The pro-apoptotic protein Alix controls some aspects of cell death, particularly neuronal apoptosis induced by various stimuli. Alix implication in cell death signalling requires its interaction with its partner Alg-2 (apoptosis-linked gene-2), a regulator of calcium-induced apoptosis following endoplasmic reticulum (ER) stress. The work I have conducted has focused on defining the molecular mechanisms underlying the pro-apoptotic function of the Alix/Alg-2 couple upon apoptosis triggered by defects of calcium homeostasis. My work has established that the Alix/Alg-2 couple interacts in a calcium-dependent manner and promotes initiator caspase 9 activation triggering apoptotic cascade (see Strappazon et al., 2010, BBRC). I also studied the implication of the Alix/Alg-2 couple in death receptor induced apoptosis and showed that TNF1 induced apoptosis in neurons requires the recruitment of caspase 8 within macromolecular platform of activation which triggers

downstream effector caspase activation and cell death (see Mahul-Mellier et al., 2008, JBC). The altered neuronal activity resulting from epileptic seizures can lead to excitotoxic neuronal death, thus further worsening the disease. One classical model to study neuronal cell death *in vitro* is the apoptosis of cerebellar granular neurons (CGN) induced by potassium depletion. In this context, I studied the role of the tyrosine kinase Pyk2 as a putative negative regulator of the Alix/Alg-2 couple. My results provide evidence that the inactivation of Pyk2 by expressing a dominant-negative mutant in CGN overcomes the trophic effect of depolarization, and that increasing Pyk2 activity by overexpressing wild-type Pyk2 prevents CGN apoptosis induced by the suppression of membrane depolarization. We demonstrated that Pyk2 is an important downstream component of the Ca²⁺/CaM mediated survival cascade leading to AKT signalling activation in CGN (see Strappazon et al., 2007, Mol Cell Neurosc.). This cascade is important for developing-cerebellar granule cells in the external granule cell layer to cease proliferation and begin migration to the internal granule cell layer. **Thus, these results enriched our understanding of the putative dynamics of cerebellar neuronal development.**

Alix is known to bind to two protein members of the so-called Endosomal Sorting Complex Required for Transport (ESCRT), which facilitates membrane fission events during multivesicular endosome formation. Because ESCRT proteins were shown to be implicated in autophagy, a process involved in bulk degradation of cytoplasmic constituents in lysosomes, which can also participate in cell death, we investigated whether Alix could be involved in autophagy. We did not find any effect of this protein in the autophagic process (see Petiot et al., 2008 BBRC).

These results suggested that the capacity of several mutants of Alix to modulate cell death does not relate to their capacity to modulate autophagy. Furthermore, they demonstrated that the role of Alix is different from that of classical ESCRT proteins.

In total, my PhD work led to the publication of two articles as first author in *Mol and Cell Neuroscience* and *Biochem Biophys Res Commun* journals; two articles as second author in *J Biol Chem* and *Biophys Res Commun* journals and one review as second author in *Biochem Soc Trans* journal (see PDF bellow).



Contents lists available at ScienceDirect

Biochemical and Biophysical Research Communications

journal homepage: www.elsevier.com/locate/ybbrc

Alix is involved in caspase 9 activation during calcium-induced apoptosis

Flavie Strappazon¹, Sakina Torch, Christine Chatellard-Causse, Anne Petiot, Chantal Thibert, Béatrice Blot, Jean-Marc Verna², Rémy Sadoul^{*}

Inserm, U836, Team 2, Grenoble F-38000, France
 Université Joseph Fourier, Grenoble F-38000, France

ARTICLE INFO

Article history:

Received 9 May 2010

Available online 21 May 2010

Keywords:

ALG-2
 Apoptosis
 Cell death
 Cerebellar granule neurons
 Endoplasmic reticulum
 Thapsigargin

ABSTRACT

The cytoplasmic protein Alix/AIP1 (ALG-2 interacting protein X) is involved in cell death through mechanisms which remain unclear but require its binding partner ALG-2 (apoptosis-linked gene-2). The latter was defined as a regulator of calcium-induced apoptosis following endoplasmic reticulum (ER) stress. We show here that Alix is also a critical component of caspase 9 activation and apoptosis triggered by calcium. Indeed, expression of Alix dominant-negative mutants or downregulation of Alix afford significant protection against cytosolic calcium elevation following thapsigargin (Tg) treatment. The function of Alix in this paradigm requires its interaction with ALG-2. In addition, we demonstrate that caspase 9 activation is necessary for apoptosis induced by Tg and that this activation is impaired by knocking down Alix. Altogether, our findings identify, for the first time, Alix as a crucial mediator of Ca²⁺ induced caspase 9 activation.

© 2010 Elsevier Inc. All rights reserved.

1. Introduction

Calcium plays a central role in regulating a variety of cellular responses, notably in neurons. In particular, it is now well established that alteration in intracellular calcium homeostasis is a common feature of many apoptotic processes, which are associated with local elevations of cytosolic Ca²⁺ released from endoplasmic reticulum (ER) stores [1–5]. Although cytosolic Ca²⁺ elevation induces caspase 9 activation as a necessary step for apoptosis, the way of activation of the caspase remains dubious. In particular, it is still unclear whether caspase 9 activation requires Apaf-1 or occurs in a separate ER based complex [6–8]. Using Apaf-1 ^{−/−} cells, Rao et al. defined the apoptosis-linked gene-2 (ALG-2), a calcium-binding protein belonging to the penta-EF hand protein family, as a regulator of ER stress-induced death involving Ca²⁺ [8]. Indeed, knock-down of ALG-2 reduced cell death due to thapsigargin (Tg), which

Abbreviations: ALG-2, apoptosis-linked gene-2; Alix, ALG-2 interacting protein X; Apaf-1, apoptotic protease activating factor-1; BHK, baby hamster kidney; DIV, days *in vitro*; ER, endoplasmic reticulum; RFP, red fluorescent protein; Tg, thapsigargin.

^{*} Corresponding author. Address: Grenoble Institut des Neurosciences, Bâtiment Edmond J. Safra des Neurosciences, Chemin Fortuné Ferrini, Site Santé, 38706 La Tronche cédex, France.

E-mail address: remy.sadoul@ujf-grenoble.fr (R. Sadoul).

¹ Present address: Laboratory of Molecular Neuroembryology, IRCCS Fondazione Santa Lucia, Via del Fosso di Fiorano 64/65, 00143 Rome, Italy.

² Present address: Service des Ressources Humaines, Délégation Alpes, CNRS – BP 166, 38042 Grenoble, France.

elevates cytosolic calcium by blocking the ER Ca²⁺-ATPase. They went on to suggest that ALG-2 is part of a high molecular weight complex containing caspases 9 and 12 and that knocking down ALG-2 inhibits Tg-induced caspase 9 activation.

Ca²⁺ binding to ALG-2 induces a conformational change which allows it to interact with several proteins [9,10], among which the multifunctional adaptor protein Alix/AIP1 [11,12]. Alix is a cytosolic protein which interacts with proteins involved in deforming membranes during various processes including endocytosis, endosomal sorting, virus budding and cytokinesis [13,14]. Up-regulation of Alix expression *in vivo* correlates with calcium-induced cell death, as observed in degenerating neurons of the rat hippocampus undergoing epileptic seizures [15]. We also found that over-expression of the full length protein (Alix-wt) in cultured neurons was sufficient to activate caspases and thereby apoptosis. In contrast expression of the C-terminal half of the protein encompassing the ALG-2 binding site blocked neuronal death both *in vivo* and *in vitro* [16,17]. The pro- and anti-apoptotic functions of Alix-wt and Alix-CT, respectively, were tightly dependent on their capacity to bind to ALG-2. Expression of Alix lacking its ALG-2 binding site could block naturally occurring death of motoneurons during development of the chick embryo [18,19]. Given the fact that ALG-2 needs to bind Ca²⁺ in order to interact with Alix, these observations suggest that ALG-2 and Alix cooperate in transducing Ca²⁺-regulated signals during cell death. Here we report that knock-down of Alix protects cells from Tg-induced cell death which is mediated by caspase 9. Furthermore, we show that Alix

expression is required for caspase 9 activation induced by calcium elevation. These results suggest that Alix and ALG-2 act upstream of caspase 9 activation following cytosolic calcium elevation.

2. Material and methods

2.1. Constructs and antibodies

Polyclonal anti-Alix was previously described [16], rabbit anti-Flag (Sigma), monoclonal anti-HA (Cell Signaling), monoclonal anti-actin (Chemicon), alexa-488 conjugated goat anti-rabbit and alexa-488 conjugated goat anti-mouse (Molecular Probes), peroxidase-conjugated goat anti-mouse and peroxidase goat anti-rabbit (Jackson). Alix expression plasmids have been described previously [20]. pcDNA3 vectors coding for dominant-negative mutants of procaspase 8 (C360A) and 9 mutants (C287A) were a kind gift of P. Mehlen (Lyon).

2.2. Cell cultures

Primary cultures of cerebellar granule cells (CGN) were prepared from 6-day-old S/IOPS NMRI mice (Charles River Laboratories), as described previously [16]. Dissociated neurons were plated in Dulbecco's modified Eagle's medium (DMEM, Invitrogen) containing 25 mM KCl (K25 medium) supplemented with 10% fetal bovine serum. After 4 DIV, the medium was replaced with serum-free K25. Twenty-four hours later, thapsigargin (Invitrogen) (200 nM in 0.01% DMSO) or DMSO alone were added to K25 medium. Baby hamster kidney cells (BHK-21) were used as described previously [21]. Cells were treated with 1 μ M Tg 24 h after plating.

2.3. Cell transfections

Transient transfection of cultured CGN was performed using the calcium phosphate co-precipitation method as previously described [16]. BHK-21 cells were grown at 37 °C in Glasgow MEM (GMEM) supplemented with 5% fetal calf serum. Transient transfections of BHK-21 cells were performed using JetPEI (PolyPlus Transfection).

2.4. Establishment of an Alix-deficient BHK-21 cell line

An shRNA was cloned downstream of the human H1 promoter in the pSuperGFP vector (Oligoengine, Seattle, WA, USA). Forward and reverse sequences for the Alix shRNA construct were: 5'-GATCCCCGCGCTGGTGAAGTTCATCTTCAAGAGAGATGAACCTCACCAGCGCTTTTGGAAA-3' and 5'-AGCTTTTCCAAAAGCCGCTGGTGAAGTTCATCTCTTGAAGATGAACCTCACCAGCGCGGG-3', respectively. The synthetic oligonucleotides were synthesised by Invitrogen. The annealed oligonucleotides were ligated into the BglII–HindIII site of the pSuperGFP vector.

BHK-21 cells were transfected with pSuper–*Sh* Alix or pSuper vectors as control by using JetSi transfection (Polyplus tranfection). Cells were selected by adding G418 (800 μ g/ml) to the culture medium. After 15 days, clones were isolated and screened by Western blot analysis for the best reduction in Alix expression. Permanent cell lines (pSuper/*Sh* Alix and control) were maintained with G418 (800 μ g/ml).

2.5. Determination of cell viability

MTT assay. The tetrazolium salt MTT [3-(4,5-dimethyl-2-thiazolyl)-2,5-diphenyl-2H-tetrazoliumbromide] (Sigma) was added to cell cultures (1 mg/ml) and incubated for 30 min at 37 °C. Cells were then lysed in DMSO. Formazan production by living cells was assessed by measuring absorbance at 540 nm.

Hoechst staining. Cultures were fixed in 4% paraformaldehyde in PBS for 20 min at 4 °C and stained with the bisbenzimidazole (Hoechst 33342, Sigma; 4 μ g/ml) in PBS for 20 min at room temperature. Cells were washed three times with PBS, mounted in Mowiol (Calbiochem) and observed under an Axiovert microscope (Zeiss) connected to a CDD camera. For each condition, random images were captured and analyzed. Cell viability was then scored on the basis of nuclear morphology: cells containing condensed or fragmented nuclei were counted as dying or dead cells.

2.6. Determination of caspase 9 activation in cells

Caspase 9 Detection kit (Calbiochem) uses the fluorescent marker red LEHD-fmk which enters living cells and binds irreversibly to activated caspase 9. After 24 h treatment with 1 μ M Tg or vehicle (DMSO), cells were incubated for 1 h at 37 °C with the fluorescent marker according to the supplier's instructions and observed under an Axiovert microscope (Zeiss).

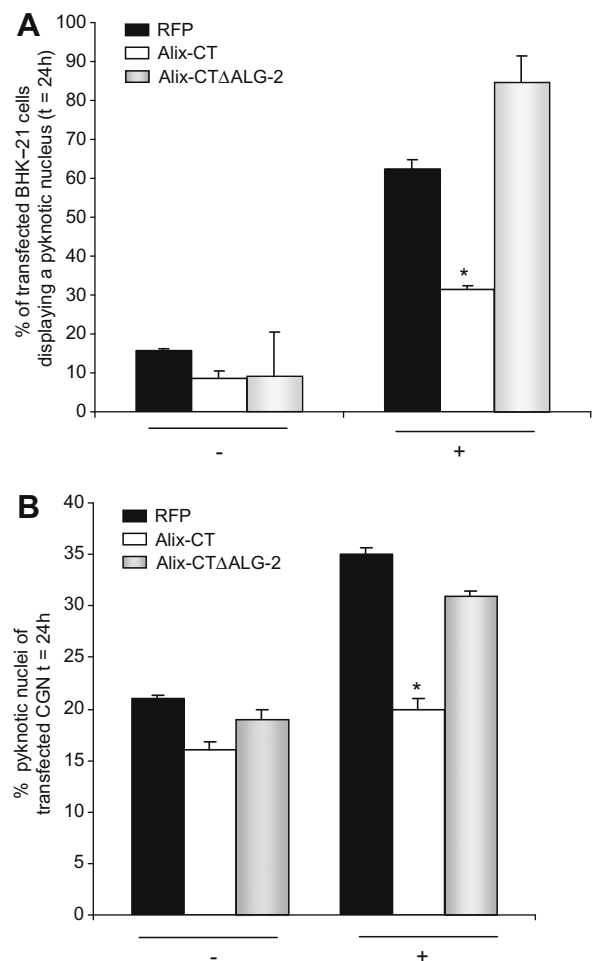


Fig. 1. Ectopic expression of the C-terminal half of Alix delays cell death of BHK-21 cells and CGN induced by an ER stress. BHK-21 cells grown for 24 h (A) or cerebellar granule neurons (CGN) cultured for 4 days (B) were transfected with vectors encoding either Flag-Alix-CT, Flag-Alix-CT Δ ALG-2 or RFP. One day later, cells were treated with Tg (1 μ M (a) 200 nM (B)) or vehicle (0.01% DMSO) for 24 h. Transfected cells were revealed using an anti-Flag antibody and cells with condensed/fragmented nuclei were scored as pyknotic. Results are expressed as the percentage of transfected cells displaying pyknotic nuclei. Values are given as a percentage (\pm SD) of cell death and statistical analysis was performed by analysis of variance (one-way ANOVA followed by Scheffe's post hoc test). * P < 0.05 versus RFP control.

2.7. Immunofluorescence

Cells were fixed in 4% paraformaldehyde in PBS for 10 min at 37 °C. After permeabilization and blocking with 3% goat pre-immune serum (Invitrogen), cells were incubated at room temperature with primary antibodies (monoclonal anti-HA: 1/100, polyclonal anti-Flag: 1/500) then with Alexa Fluor-conjugated secondary anti-mouse antibody (1/1000) or anti-rabbit antibody (1/1000) (Invitrogen). Cells were rinsed with PBS, and stained with Hoechst 33342 before examination.

2.8. Western blot analysis

Cells were washed twice with PBS before harvesting with lysis buffer (50 mM Tris-HCl, pH 7.4, 150 mM NaCl, 0.5% DOC (sodium deoxycholate), 1% NP40, 0.1% SDS (sodium dodecyl sulfate), 1 mM Na₃VO₄, 50 mM NaF, 10 mM β-glycerophosphate and 2× protease inhibitor cocktail (Complete™, Boehringer). Cell extracts were centrifuged at 15,000g for 15 min at 4 °C and 20 μg protein was separated by SDS-PAGE and transferred onto nylon membranes (Immobilon-P, Millipore). After incubation with the membranes primary antibodies were revealed using peroxidase-coupled secondary antibodies and the SuperSignal detection method (Pierce).

3. Results

3.1. Alix C-terminal half protects BHK-21 cells and cerebellar neurons from thapsigargin-induced cytotoxicity

We first used BHK-21 cells to analyze the effect of the C-terminal half of Alix (Alix-CT) on apoptosis following a Ca²⁺ increase due

to Tg treatment. 24 h after transfection, BHK-21 cells were treated with 1 μM Tg and viability estimated after a further 24 h culture period. Sixty percent of control RFP-expressing cells exhibited altered nuclear morphology indicative of apoptosis whereas 15% were dead or dying in untreated control cultures (Fig. 1A). In contrast, only 30% of Alix-CT-expressing cells died following the same treatment. Remarkably, Alix-CT deleted of its ALG-2-binding domain (Alix-CTΔALG-2) did not afford any protective effect against Tg-induced apoptosis (Fig. 1A).

Similar experiments using cerebellar granule neurons (CGN) gave comparable results. Indeed, while a 24 h incubation with 200 nM Tg increased death of RFP transfected CGN by 36%, the number of Alix-CT-expressing neurons showing a condensed or fragmented nucleus did not significantly differ from that of untreated cultures (Fig. 1B). Deletion of the ALG-2 binding site on Alix-CT abrogated its capacity to rescue neurons. Our findings indicate that expression of a dominant-negative form of Alix counteracts the deleterious effect of Tg in a way which depends on its capacity to interact with ALG-2.

3.2. Alix depletion reduces thapsigargin-induced cell death

To reinforce our suggestion of a possible role of Alix in mediating ER stress apoptosis, we established a BHK-21 cell line in which we down regulated Alix expression using a pSuper vector coding for a short hairpin RNA against Alix (*Sh* Alix). As illustrated in Fig. 2A, Alix content was reduced by at least 90% in cells stably expressing *Sh* Alix compared to control cells expressing an empty P-Super (*Sh* control). Exposure to 1 μM Tg did not significantly alter Alix expression in *Sh* control or *Sh* Alix cells (Fig. 2A). Using the MTT assay, we observed a time-dependent reduction in metabolic

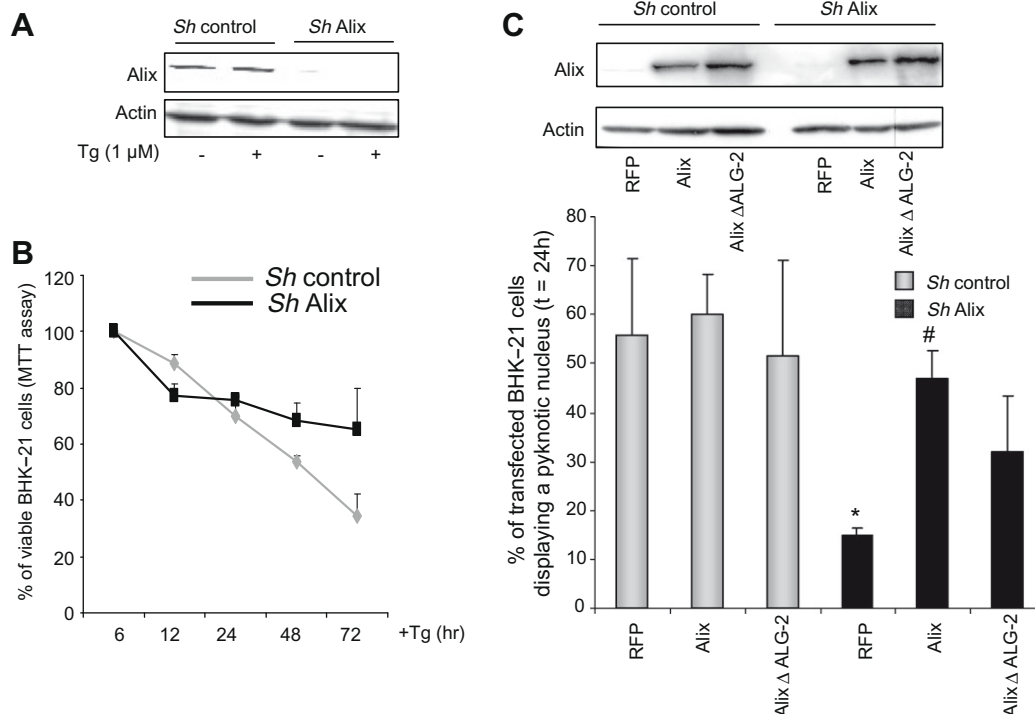


Fig. 2. Reduction of Alix expression protects BHK-21 cells from Tg cytotoxicity. (A) Western blot analysis of Alix expression in *Sh* control or *Sh* Alix BHK-21 cells with or without Tg for 24 h. (B) *Sh* control or *Sh* Alix BHK-21 cells were treated with 1 μM Tg and the percentage of viable cells was estimated at various time intervals using the MTT assay. Results are expressed as a percentage of the metabolic activity at $t = 0$ in Tg-treated cultures relative to DMSO-treated-control cultures. Each point represents the mean \pm SD of triplicate wells from three independent experiments. (C) Alix expression restores sensitivity of *Sh* Alix cells to Tg cytotoxicity. *Sh* control or *Sh* Alix BHK-21 cells were transfected with a vector coding either for Flag-Alix, Flag-AlixΔALG-2 or RFP. Upper panel: WB analysis of cell extracts of *Sh* control and *Sh* Alix cells using an anti-Flag antibody demonstrating expression of Alix and AlixΔALG-2 in transfected cells. Bottom panel: 24 h after transfection, cells were exposed to Tg (1 μM) during 24 h and then immunostained with an anti-Flag antibody. Cells were counted in 10 random fields in two or three different wells and condensed/fragmented nuclei were scored as pyknotic. Results are expressed as the percentage of transfected cells displaying a pyknotic nucleus. Data are means \pm SD of three independent experiments. Statistical analysis was performed by analysis of variance (one-way ANOVA followed by Scheffe's post hoc test). * $P < 0.05$ versus RFP-overexpressing *Sh* Alix cells. # $P < 0.05$ versus *Sh* control.

activity of *Sh* control cells following Tg treatment reaching 70% at 72 h (Fig. 2B). In contrast, after an initial limited decline, MTT metabolism remained constant over until the end of the experiment in *Sh* Alix cells. These findings suggest that Alix-depleted cells are less sensitive to Tg cytotoxicity. To confirm this, cell viability was estimated using Hoechst nuclear staining 24 h after addition of Tg. After Tg treatment about 55% of *Sh* control cells exhibited condensed or fragmented nuclei, while only 15% of *Sh* Alix cells showed these apoptotic features (Fig. 2C). Therefore, reducing Alix expression greatly improves the survival of BHK-21 cells exposed to Tg.

To strengthen our finding, we restored Alix expression in *Sh* Alix BHK-21 cells using an expression vector coding for the protein (Fig. 2C, upper panel). Even though, Alix over-expression did not affect the sensitivity of *Sh* control cells towards Tg, it almost completely restored Tg-induced death in *Sh* Alix cells (Fig. 2C). In contrast, RFP expression did not influence viability in either *Sh* control or *Sh* Alix cells. This observation, together with the fact that Alix- Δ ALG-2 did not significantly restore Tg-induced cell death indicates that Alix mediates apoptosis following cytosolic Ca^{2+} elevation and that this activity requires its capacity to bind to ALG-2.

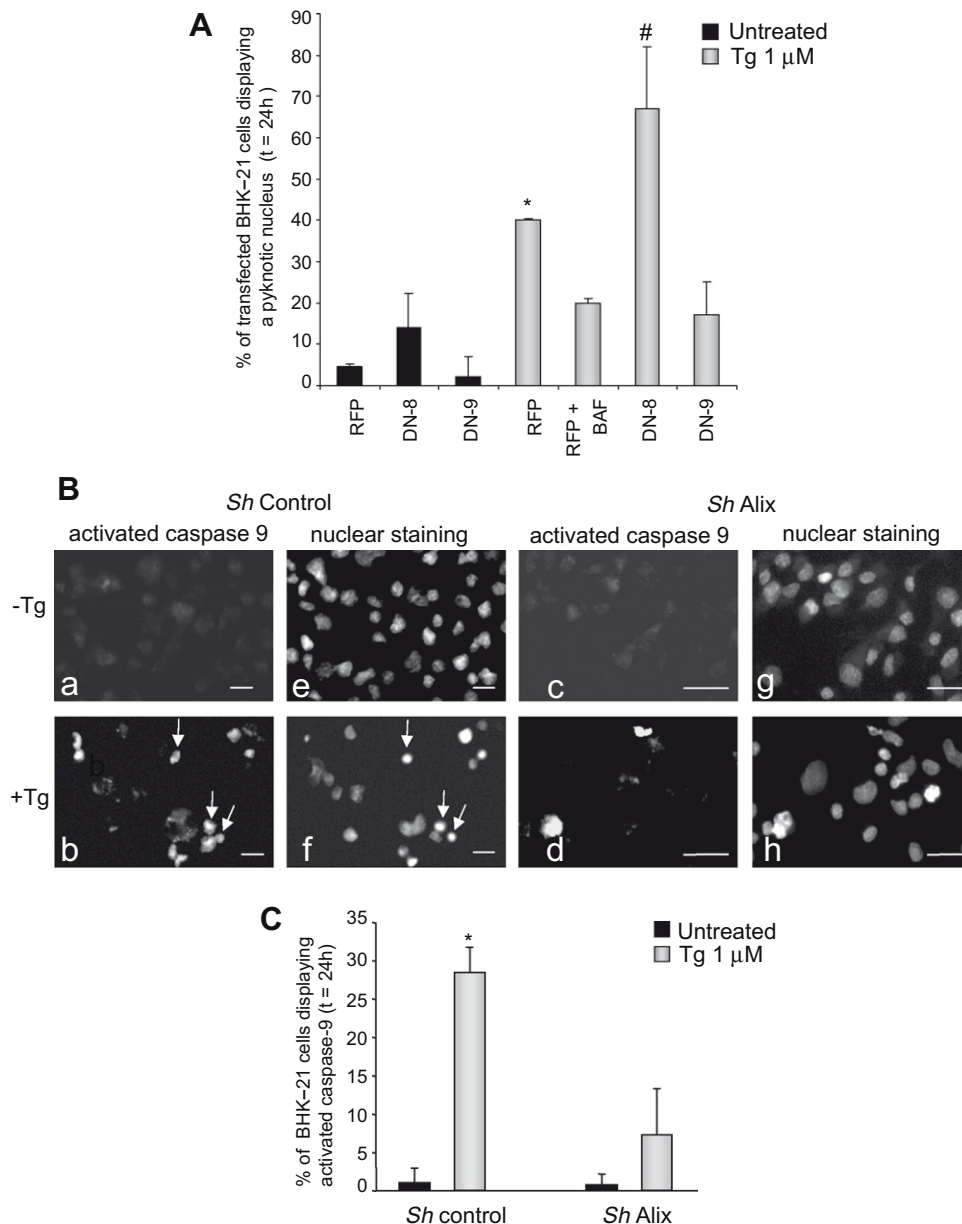


Fig. 3. Reduction of Alix expression impedes caspase 9 activation following Tg treatment in BHK-21 cells. (A) Expression of DN-caspase 9 protects cells from Tg-induced apoptosis. BHK-21 cells were transfected with vectors coding for RFP or dominant-negative forms of either caspase 8-HA or caspase 9-HA. Twenty-four hours later, cells were treated with 1 μ M Tg, 24 h. RFP transfected cells were treated or not with 100 μ M pan-caspase inhibitor BAF (Boc-aspartyl (OMe)-fluoromethylketone; Bio-Rad). Cells were then immunostained using a monoclonal anti-HA antibody and nuclei stained with Hoechst. Ten random fields from two or three different wells were counted and condensed/fragmented nuclei were scored as pyknotic. Results are expressed as the percentage of transfected cells displaying pyknotic nuclei. Data represent means \pm SD of three independent experiments. Statistical analysis was performed by analysis of variance (one-way ANOVA followed by Scheffe's post hoc test). * $P < 0.05$ versus DN-caspase 8 overexpressing BHK-21 cells (treated with DMSO). (B,C) Caspase 9 activation following Tg treatment requires Alix expression. *Sh* control or *Sh* Alix BHK-21 cells were treated with 1 μ M Tg or with DMSO vehicle. After 24 h cells were labeled for activated caspase 9 (red LETD-fmk) and stained with Hoechst. (B) Representative fields. Arrows indicate cells with pyknotic nuclei displaying activated caspase 9. (C) Quantification of cells displaying activated caspase 9. Results are expressed as the percentage of cells displaying activated caspases 9 could be observed between *Sh* Alix cells with or without Tg ($p = 0.14$).

3.3. Caspase 9 activation is required for Tg-induced apoptosis

Since Alix over-expression is sufficient to activate caspases in CGN [16], we hypothesized that Alix downregulation might affect activation of apical caspases following Tg treatment. Because some reports involved caspase 8 [22] and caspase 9 [7,23] in ER stress, we first determined which of these two caspases initiates Tg-induced death in BHK-21 cells. For this, we tested the effects on cell survival of catalytically dead mutants (DN-caspases) of caspases 8 and 9 which inhibit activation of their relevant endogenous counterparts. Twenty-four hours after transfection, BHK-21 cells were treated with 1 μ M Tg and further grown for 24 h (Fig. 3A). This treatment robustly increased the number of apoptotic cells among control cultures expressing RFP. Tg-induced apoptosis was significantly reduced by DN-caspase 9 expression as did the pan-caspase inhibitor BAF. In contrast expression of DN-caspase 8 did not afford protection but even significantly sensitized cells to Tg. Thus, activation of caspase 9 seems to be necessary for BHK-21 apoptosis induced by Tg.

3.4. Alix is involved in caspase 9 activation required for thapsigargin-induced apoptosis

We then tested the relationship between Alix and caspase 9 activation following Tg. Using a caspase 9 detection kit, activated caspase 9 could not be detected in either *Sh* control or *Sh* Alix cells (Fig. 3B). However, following a 24 h exposure to Tg, caspase 9 activation could be detected in 30% of *Sh* control cells. Most of these cells displayed condensed or fragmented nuclei typical of apoptosis. In sharp contrast, the number of cells containing activated caspase 9 did not increase significantly after Tg treatment in cells in which Alix was knocked down (Fig. 3C). This demonstrates that Alix is required for caspase 9 activation following Tg treatment.

4. Discussion

Alix controls some aspects of cell death, particularly neuronal apoptosis induced by various stimuli [15–17,24]. Here, we provide the first evidence for a role of Alix in mediating caspase 9 activation and apoptosis involving alteration in Ca^{2+} homeostasis. Expression of a dominant-negative form of Alix (Alix-CT) protects CGN and BHK-21 cells against apoptosis induced by Tg, which blocks the sarcoendoplasmic reticulum Ca^{2+} -ATPase (SERCA). Deletion of the ALG-2 binding site on Alix-CT abolished the capacity of the mutant to block cell death. Consistent with this, Alix knock-down in BHK-21 cells protected these cells against Tg whereas complementation with wt Alix (wild-type Alix) restored their susceptibility to Tg in a way depending on its capacity to bind ALG-2. Finally, we also show that Alix is necessary for caspase 9 activation, a process necessary for induction of apoptosis induced by Tg.

Our finding that, in BHK cells, caspase 9 is instrumental for apoptosis induced by cytosolic elevation is in good agreement with several reports showing that cells derived from caspase 9 knock-out animals or in which caspase 9 activation was blocked, are protected against death induced by alteration in ER calcium homeostasis [6–8]. More disputed is the way of activation of caspase 9, which was demonstrated to be both dependent and independent of the intrinsic/Apaf-1 pathway [6,8]. Rao et al. demonstrated that ALG-2 co-immunoprecipitates with vectorially expressed caspases 9 and 12. They also showed that knock-down of ALG-2 inhibits activation of procaspase 9 and suggested that activation by Tg stress features an Apaf-1-independent pathway that requires, among others, ATP, calcium, ALG-2, caspase 9, caspase 12 and additional factors present in microsomes [8]. Several studies have now shown that, in various situations and several types of cells [25], caspase 12 is not critical

for the ER stress-induced apoptotic cascade [6,22,23,26]. Our present results demonstrate that, like ALG-2, Alix expression is necessary for caspase 9 activation induced by Tg.

Another link between the ER and ALG-2 had been demonstrated by Draeby et al. [27] who reported that ALG-2 interacts with the ER-localized scotin protein which is a proapoptotic-p53-inducible protein. Noteworthy is that deletion of the PRD C-terminal region of scotin containing the ALG-2 binding site, abolished the ER localization and proapoptotic function of the protein. Furthermore, ALG-2 is temporarily and Ca^{2+} -dependently recruited by Sec31 of Cop-II at ER exit sites [28–30]. Alix also translocates to ER exit sites in response to a rise in cytoplasmic Ca^{2+} suggesting a possible function of the protein in this compartment [30]. In line with this, we have previously reported that Alix-CT expressed in HEK-293 cells concentrates on tubular vesicular structures stained with an antibody recognizing ER resident proteins bearing KDEL [20]. Thus, Alix and ALG-2 localization is compatible with a scenario in which changes in ER Ca^{2+} homeostasis induce the Ca^{2+} -dependent recruitment by ALG-2 of Alix and additional proteins required for the building of a platform allowing activation of caspase 9.

Acknowledgments

This study was partly supported by the Institut National de la Santé et de la Recherche Médicale (Inserm), the Université Joseph Fourier and by funds from the Association Française contre les Myopathies, the Association pour la recherche sur le cancer (ARC), the Association pour la Recherche sur la Sclérose Latérale Amyotrophique (ARS) and the Région Rhône-Alpes. F. Strappazzon is the recipient of a grant from the Ministère de l'Éducation Nationale, de l'Enseignement Supérieur et de la Recherche. The authors gratefully acknowledge P. Mehlen for caspase constructs, F.J. Hemming for revising the English manuscript, A.L. Mahul and S. Fraboulet for valuable suggestions throughout this work.

References

- [1] M.J. Berridge, M.D. Bootman, P. Lipp, Calcium – a life and death signal, *Nature* 395 (1998) 645–648.
- [2] M.J. Berridge, P. Lipp, M.D. Bootman, Signal transduction. The calcium entry pas de deux, *Science* 287 (2000) 1604–1605.
- [3] L.K. Nutt, A. Pataer, J. Pahler, B. Fang, J. Roth, D.J. McConkey, S.G. Swisher, Bax and Bak promote apoptosis by modulating endoplasmic reticular and mitochondrial Ca^{2+} stores, *J. Biol. Chem.* 277 (2002) 9219–9225.
- [4] B. Tombal, S.R. Denmeade, J.M. Gillis, J.T. Isaacs, A supramicromolar elevation of intracellular free calcium ($[Ca^{2+}]_i$) is consistently required to induce the execution phase of apoptosis, *Cell Death Differ.* 9 (2002) 561–573.
- [5] R. Rizzuto, P. Pinton, D. Ferrari, M. Chami, G. Szabadkai, P.J. Magalhaes, F. Di Virgilio, T. Pozzan, Calcium and apoptosis: facts and hypotheses, *Oncogene* 22 (2003) 8619–8627.
- [6] F. Di Sano, E. Ferraro, R. Tufi, T. Achsel, M. Piacentini, F. Cecconi, Endoplasmic reticulum stress induces apoptosis by an apoptosome-dependent but caspase 12-independent mechanism, *J. Biol. Chem.* 281 (2006) 2693–2700.
- [7] A. Masud, A. Mohapatra, S.A. Lakhani, A. Ferrandino, R. Hakem, R.A. Flavell, Endoplasmic reticulum stress-induced death of mouse embryonic fibroblasts requires the intrinsic pathway of apoptosis, *J. Biol. Chem.* 282 (2007) 14132–14139.
- [8] R.V. Rao, K.S. Poksay, S. Castro-Oregon, B. Schilling, G. del Rio, B.W. Gibson, H.M. Ellerby, D.E. Bredesen, R.H. Row, R.H. Row, Molecular components of a cell death pathway activated by endoplasmic reticulum stress, *J. Biol. Chem.* 279 (2004) 177–187.
- [9] H. Suzuki, M. Kawasaki, T. Inuzuka, M. Okumura, T. Kakiuchi, H. Shibata, S. Wakatsuki, M. Maki, Structural basis for Ca^{2+} -dependent formation of ALG-2/Alix peptide complex: Ca^{2+} /EF3-driven arginine switch mechanism, *Structure* 16 (2008) 1562–1573.
- [10] K. Katoh, H. Shibata, H. Suzuki, A. Nara, K. Ishidoh, E. Kominami, T. Yoshimori, M. Maki, The ALG-2-interacting protein Alix associates with CHMP4b, a human homologue of yeast Snf7 that is involved in multivesicular body sorting, *J. Biol. Chem.* 278 (2003) 39104–39113.
- [11] M. Missotten, A. Nichols, K. Rieger, R. Sadoul, Alix, a novel mouse protein undergoing calcium-dependent interaction with the apoptosis-linked-gene 2 (ALG-2) protein, *Cell Death Differ.* 6 (1999) 124–129.
- [12] P. Vito, L. Pellegrini, C. Guiet, L. D'Adamio, Cloning of AIP1, a novel protein that associates with the apoptosis-linked gene ALG-2 in a Ca^{2+} -dependent reaction, *J. Biol. Chem.* 274 (1999) 1533–1540.

- [13] R. Sadoul, Do Alix and ALG-2 really control endosomes for better or for worse, *Biol. Cell* 98 (2006) 69–77.
- [14] G. Odorizzi, The multiple personalities of Alix, *J. Cell Sci.* 119 (2006) 3025–3032.
- [15] F.J. Hemming, S. Fraboulet, B. Blot, R. Sadoul, Early increase of apoptosis-linked gene-2 interacting protein X in areas of kainate-induced neurodegeneration, *Neuroscience* 123 (2004) 887–895.
- [16] Y. Trioulier, S. Torch, B. Blot, N. Cristina, C. Chatellard-Causse, J.M. Verna, R. Sadoul, Alix, a protein regulating endosomal trafficking, is involved in neuronal death, *J. Biol. Chem.* 279 (2004) 2046–2052.
- [17] A.L. Mahul-Mellier, F.J. Hemming, B. Blot, S. Fraboulet, R. Sadoul, Alix, making a link between apoptosis-linked gene-2, the endosomal sorting complexes required for transport, and neuronal death in vivo, *J. Neurosci.* 26 (2006) 542–549.
- [18] A.L. Mahul-Mellier, F. Strappazzon, A. Petiot, C. Chatellard-Causse, S. Torch, B. Blot, K. Freeman, L. Kuhn, J. Garin, J.M. Verna, S. Fraboulet, R. Sadoul, F.J. Hemming, Alix and ALG-2 are involved in tumor necrosis factor receptor 1-induced cell death, *J. Biol. Chem.* 283 (2008) 34954–34965.
- [19] A.L. Mahul-Mellier, F. Strappazzon, C. Chatellard-Causse, B. Blot, D. Beal, S. Torch, F. Hemming, A. Petiot, J.M. Verna, S. Fraboulet, R. Sadoul, Alix and ALG-2 make a link between endosomes and neuronal death, *Biochem. Soc. Trans.* 37 (2009) 200–203.
- [20] C. Chatellard-Causse, B. Blot, N. Cristina, S. Torch, M. Missotten, R. Sadoul, Alix (ALG-2-interacting protein X), a protein involved in apoptosis, binds to endophilins and induces cytoplasmic vacuolization, *J. Biol. Chem.* 277 (2002) 29108–29115.
- [21] T. Tuomikoski, M.A. Felix, M. Doree, J. Gruenberg, Inhibition of endocytic vesicle fusion in vitro by the cell-cycle control protein kinase cdc2, *Nature* 342 (1989) 942–945.
- [22] A. Jimbo, E. Fujita, Y. Kouroku, J. Ohnishi, N. Inohara, K. Kuida, K. Sakamaki, S. Yonehara, T. Momoi, ER stress induces caspase-8 activation, stimulating cytochrome c release and caspase-9 activation, *Exp. Cell Res.* 283 (2003) 156–166.
- [23] E.A. Obeng, L.H. Boise, Caspase-12 and caspase-4 are not required for caspase-dependent endoplasmic reticulum stress-induced apoptosis, *J. Biol. Chem.* 280 (2005) 29578–29587.
- [24] D. Blum, F.J. Hemming, M.C. Galas, S. Torch, L. Cuvelier, S.N. Schiffmann, R. Sadoul, Increased Alix (apoptosis-linked gene-2 interacting protein X) immunoreactivity in the degenerating striatum of rats chronically treated by 3-nitropropionic acid, *Neurosci. Lett.* 368 (2004) 309–313.
- [25] Y. Kosuge, T. Sakikubo, K. Ishige, Y. Ito, Comparative study of endoplasmic reticulum stress-induced neuronal death in rat cultured hippocampal and cerebellar granule neurons, *Neurochem. Int.* 49 (2006) 285–293.
- [26] H. Shiraishi, H. Okamoto, A. Yoshimura, H. Yoshida, ER stress-induced apoptosis and caspase-12 activation occurs downstream of mitochondrial apoptosis involving Apaf-1, *J. Cell Sci.* 119 (2006) 3958–3966.
- [27] I. Draeby, Y.L. Woods, J.M. la Cour, J. Mollerup, J.C. Bourdon, M.W. Berchtold, The calcium binding protein ALG-2 binds and stabilizes Scotin, a p53-inducible gene product localized at the endoplasmic reticulum membrane, *Arch. Biochem. Biophys.* 467 (2007) 87–94.
- [28] J.M. la Cour, J. Mollerup, M.W. Berchtold, ALG-2 oscillates in subcellular localization, untemporally with calcium oscillations, *Biochem. Biophys. Res. Commun.* 353 (2007) 1063–1067.
- [29] H. Shibata, H. Suzuki, H. Yoshida, M. Maki, ALG-2 directly binds Sec31A and localizes at endoplasmic reticulum exit sites in a Ca²⁺-dependent manner, *Biochem. Biophys. Res. Commun.* 353 (2007) 756–763.
- [30] A. Yamasaki, K. Tani, A. Yamamoto, N. Kitamura, M. Komada, The Ca²⁺-binding protein ALG-2 is recruited to endoplasmic reticulum exit sites by Sec31A and stabilizes the localization of Sec31A, *Mol. Biol. Cell* 17 (2006) 4876–4887.

Alix and ALG-2 Are Involved in Tumor Necrosis Factor Receptor 1-induced Cell Death*

Received for publication, April 24, 2008, and in revised form, October 1, 2008. Published, JBC Papers in Press, October 20, 2008, DOI 10.1074/jbc.M803140200

Anne-Laure Mahul-Mellier^{†§1}, Flavie Strappazon^{†§2}, Anne Petiot^{†§}, Christine Chatellard-Causse^{†§}, Sakina Torch^{†§}, Béatrice Blot^{†§}, Kimberley Freeman^{†§}, Loriane Kuhn^{§||}, Jérôme Garin^{||}, Jean-Marc Verna^{†§}, Sandrine Fraboulet^{†§3}, and Rémy Sadoul^{†§4}

From [†]INSERM, U836, Equipe 2, Neurodégénérescence et Plasticité, Grenoble F-38042, France, ^{||}Commissariat à l'Énergie Atomique, Département des Sciences du Vivant Laboratoire d'Etude de la Dynamique des Protéomes, Grenoble F-38054, France, ^{||}INSERM, U880, Grenoble F-38054, France, and the [§]Université Joseph Fourier, Grenoble Institut des Neurosciences, Grenoble F-38042, France

Alix/AIP1 regulates cell death in a way involving interactions with the calcium-binding protein ALG-2 and with proteins of ESCRT (endosomal sorting complex required for transport). Using mass spectrometry we identified caspase-8 among proteins co-immunoprecipitating with Alix in dying neurons. We next demonstrated that Alix and ALG-2 interact with pro-caspase-8 and that Alix forms a complex with the TNF α receptor-1 (TNF-R1), depending on its capacity to bind ESCRT proteins. Thus, Alix and ALG-2 may allow the recruitment of pro-caspase-8 onto endosomes containing TNF-R1, a step thought to be necessary for activation of the apical caspase. In line with this, expression of Alix deleted of its ALG-2-binding site (Alix Δ ALG-2) significantly reduced TNF-R1-induced cell death, without affecting endocytosis of the receptor. In a more physiological setting, we found that programmed cell death of motoneurons, which can be inhibited by Alix Δ ALG-2, is regulated by TNF-R1. Taken together, these results highlight Alix and ALG-2 as new actors of the TNF-R1 pathway.

Endocytosis of cell surface receptors has long been described as an effective way of switching off extracellularly induced signals. Endocytosed activated receptors traffic through early endosomes and are sorted into intraluminal vesicles accumulating inside endosomes known as multivesicular bodies (MVBs).⁵ These MVBs fuse with lysosomes where the receptors meet their end by acid hydrolysis (1).

In some cases however, such as for neurotrophin-bound Trk receptors, activated receptors continue signaling inside endosomes (2). Also, in the case of death receptors, Schütze and co-workers (3) showed that endocytosis of TNF-R1, which occurs after binding to TNF α , is a necessary step for activation of caspases and consequently apoptosis. They found that the apical pro-caspase-8 is recruited and thereby activated on the surface of multivesicular endosomes containing activated TNF-R1.

Biogenesis of MVBs is under tight control by a set of proteins, making the so-called ESCRT-0 to -III (endosomal sorting complex required for transport), which sequentially associate on the cytosolic surface of endosomes (4). A partner of ESCRT proteins, which also regulates the making of MVBs, is the protein Alix/AIP1, first characterized as an interactor of the calcium-binding protein ALG-2 (apoptosis-linked gene-2) (5–7). Enveloped viruses, like human immunodeficiency virus, type 1, use Alix to recruit the ESCRT machinery to deform membranes and allow fission during viral budding (8, 9). Furthermore, two recent reports have claimed that Alix together with ESCRT proteins might also be involved in the abscission stage of cytokinesis (10, 11).

Besides Tsg101 and CHMP-4B of ESCRT-I and -III, respectively, Alix interacts with lysobisphosphatidic acid, a phospholipid involved in intraluminal vesiculation of endosomes (12), and with regulators of endocytosis (CIN85 and endophilins) (13, 14). However, the precise role of Alix on endosomes remains largely unclear because neither we nor other laboratories have found any striking effect of Alix on endocytosis and degradation of EGF or transferrin receptors (15, 16).

We and others have gathered evidence that Alix plays a role in cell death. In particular, expression of a mutant lacking the N-terminal part (Alix-CT) blocks death of HeLa cells induced by serum starvation (7) and of cerebellar neurons deprived of potassium (17). In this latter paradigm, Alix-CT, whose protecting activity was strictly correlated with its capacity to bind ALG-2, accumulated inside cytoplasmic aggregates together with ALG-2 and caspases. We also demonstrated, using elec-

* This work was supported in part by INSERM, the University Joseph Fourier, and grants from the Association Française contre les Myopathies, the Association pour la Recherche sur la Sclérose Latérale Amyotrophique, and the Association pour la Recherche contre le Cancer. The costs of publication of this article were defrayed in part by the payment of page charges. This article must therefore be hereby marked "advertisement" in accordance with 18 U.S.C. Section 1734 solely to indicate this fact.

¹ Supported by a fellowship from the Association Française contre les Myopathies. Present address: Imperial College London, Experimental Medicine & Toxicology, London W120NN, UK.

² Present address: European Center for Brain Research, Santa Lucia Foundation, Molecular Neuroembryology Unit, 00143 Rome, Italy.

³ To whom correspondence may be addressed: MRC Functional Genetic Unit, University of Oxford, Dept. of Physiology Anatomy and Genetics, OX1 3QX Oxford, UK. Tel.: 44-1865-282-273; E-mail: sandrine.fraboulet@dpag.ox.ac.uk.

⁴ To whom correspondence may be addressed: Grenoble Institute of Neuroscience, Chemin Fortuné Ferrini, BP 170, F-38042 Grenoble, France. Tel.: 33-456-52-05-44; E-mail: remy.sadoul@ujf-grenoble.fr.

⁵ The abbreviations used are: MVB, multivesicular body; DD, death domain; DED, death effector domain; HH, Hamburger-Hamilton; TNF, tumor necrosis

factor; TNF-R1, TNF receptor 1; TUNEL, terminal transferase dUTP nick end labeling; HA, hemagglutinin; wt, wild type; RIPA, radioimmune precipitation assay; MALDI-TOF, matrix-assisted laser desorption ionization time-of-flight; TBS, Tris-buffered saline; PBS, phosphate-buffered saline; MTN, motoneurons; DISC, death-inducing signaling complex; CaRIPA, RIPA buffer containing 1 mM CaCl₂; IP, immunoprecipitation; FADD, Fas-associated protein with death domain.

troporation in the chick embryo, that Alix mutants block programmed cell death of motoneurons during normal development, depending on binding to ALG-2 and ESCRT-I and -III. Our interpretation of these results is that some truncated forms of Alix behave as dominant negative mutants, blocking the formation of an ALG-2-Alix-ESCRT complex necessary for cell death (18). Therefore the Alix-ALG-2 complex could make a link between endosomes and a signaling or an execution step of neuronal death (19).

We have undertaken the present study to characterize this link and found that Alix and ALG-2 form a complex with endocytosed TNF-R1 and pro-caspase-8. The physiological relevance of these interactions was revealed by the demonstration that several Alix mutants inhibit TNF-R1-induced cell death both *in vitro* and *in vivo*.

EXPERIMENTAL PROCEDURES

Reagents and Antibodies—Human recombinant TNF α -FLAG was from Alexis Biochemicals (Covalab). Mouse monoclonal anti-hemagglutinin (HA) antibody was from Cell Signaling (Ozyme); polyclonal antibodies against Myc, TNF-R1, and FADD were from Santa Cruz Biotechnology; polyclonal antibodies against LAMP1 and EEA1 were from AbCam; anti-FLAG monoclonal (M1 and M2) and polyclonal antibodies were from Sigma-Aldrich; GM130 and monoclonal anti-AIP1/Alix were from BD Transduction; anti-ALG-2 was from Swant; HSP70 mitochondria was from Affinity Bioreagents (Ozyme); anti-caspase 8 was from Biovision (Clinisciences); horseradish peroxidase-conjugated goat anti-mouse and anti-rabbit Alexa⁵⁹⁴ antibody were from Jackson Laboratories; and biotinylated goat anti-rabbit antibody was from Vector Laboratories.

DNA Constructs—For expression in the chick embryo, human TNF-R1 (wt or mutants), a catalytically dead version of human pro-caspase-8 (mutation C360A), and baculovirus p35 were inserted into the pCAGGS expression vector (a gift of Tsuyoshi Momose, Nara Institute of Science and Technology). Mammalian expression vectors coding for DN-caspase-8-HA-tagged and p35 were a gift of P. Mehlen (INSERM, Lyon, France). Those coding for wt or mutated human TNF-R1 were kind gifts from W. Schneider-Brachert (University of Regensburg, Regensburg, Germany). Mutated ALG-2 Δ EF^{1,3} was a gift of M. Maki (Nagoya University, Nagoya, Japan).

In Ovo Electroporation—Fertilized Isa Brown eggs (Société Française de Production Avicole, St. Marcellin, France) were electroporated at Hamburger-Hamilton (HH) stage 16. Plasmid DNA was electroporated as described in Ref. 18.

Histological Analysis—Chick embryos were collected 48 h after electroporation processed and cryo-sectioned as described previously in Ref. 18.

Immunohistochemistry and Immunofluorescence—Frozen sections were incubated with polyclonal anti-TNF-R1 or monoclonal anti-HA antibodies, diluted to 1/100 in Tris-buffered saline containing 1% GS, 0.02% saponine (TBSS) for 12–24 h at 4 °C. The sections were rinsed in TBSS and treated with a secondary anti-rabbit Alexa⁵⁹⁴ antibody or a biotinylated goat anti-rabbit secondary antibody, amplified using the ABC kit (Vector Laboratories) and revealed with 3,3'-diaminobenzidine and nickel intensification. The sections were rinsed in

TBS, incubated 30 min at 37 °C in Hoechst 33342, 2 μ g/ml (Sigma, France) before mounting in Mowiol (Calbiochem, France).

Terminal Deoxynucleotidyl Transferase-mediated dUTP-Biotin Nick End Labeling (TUNEL) Method—TUNEL analysis was performed using an *in situ* cell death detection kit (Roche Applied Science). Fluorescent positive cells were counted in every third section. Twelve sections/embryo were counted.

Reverse Transcription-PCR—RNA were extracted from whole chick embryo using TRIzol reagent (Invitrogen). cDNAs were synthesized with Moloney murine leukemia virus reverse transcriptase (Promega) and controlled with glyceraldehyde-3-phosphate dehydrogenase. TNF-R1 expression was further analyzed by amplification of a 695-nt fragment with the following oligonucleotides: 5'-GATACTGTGTGTG-GCTGT-3' and 5'-CGTAAATGTCGATGCTCC-3' based on the chick TNF-R1 homologue (*Gallus gallus* accession number AJ720473).

Cell Culture and Transfection—HEK-293 cells were maintained in Dulbecco's modified Eagle's medium (Invitrogen) containing 10% fetal bovine serum (Invitrogen), 2 mM glutamine, 10 μ g/ml streptomycin, and 10 units/ml penicillin. BHK-21 cells were maintained in Glasgow minimum essential medium (Invitrogen) containing 5% fetal bovine serum, 2.6 g/liter tryptose phosphate broth, 2 mM glutamine, 10 μ g/ml streptomycin, and 10 units/ml penicillin. HEK 293 or BHK-21 cells were transfected using JetPEI (Ozyme).

Alix Knockdown in BHK Cells—The Alix small hairpin RNA was cloned downstream of the human H1 promoter in the vector pSuperGFP (Oligoengine). The sequences of the synthetic oligonucleotides (Invitrogen) used for Alix small hairpin RNA construct were the following: 5'-GATCCCCGCCGCTGGTG-AAGTTCATCTTCAAGAGAGATGAACTTCACCAGCGGCTTTTTGGAAA-3' and 5'-AGCTTTTCCAAAAAGTTCA-TCCAGCAGACTTACTCTCTTGAAGTAAGTCTGCTGG-ATGAACGGG-3'. Annealed oligonucleotides were ligated into the BglII cleavage site within the pSuperGFP vector linearized with the same restriction enzymes.

BHK cells were transfected with pSuper/shAlix plasmid or pSuperGFP vector for control using the JetSi transfection reagent (Polyplus Transfection). Transfected cells were selected using 800 μ g/ml of G418. After 15 days, the clones were isolated and selected for the best reduction in Alix expression. Cells (pSuper/shAlix and control) were grown in the presence of 800 μ g/ml of G418.

Mass Spectrometry and Protein Identification—Cultures of mouse cerebellar granule neurons were prepared as described previously (17) and cultured in basal medium Eagle containing 25 mM potassium. The medium was changed for basal medium Eagle containing 5 mM potassium, and the cells were lysed 4 h later in RIPA buffer (150 mM NaCl, 50 mM Tris, pH 8.0, 1% Nonidet P-40, 0.5% deoxycholate, 0.1% SDS containing a protease inhibitor mixture (Roche Applied Science). Immunoprecipitations were performed using polyclonal anti-Alix antibody and protein G-coupled Sepharose beads. After separation by SDS-PAGE, discrete bands were excised from the Coomassie Blue-stained gel. In-gel digestion was performed as previously described (20). Gel pieces were then sequentially extracted with 5% (v/v) formic acid solution, 50%

Alix and ALG-2 in TNF-R1-induced Cell Death

acetonitrile, 5% (v/v) formic acid, and acetonitrile. After drying, the tryptic peptides were resuspended in 0.5% aqueous trifluoroacetic acid. For MALDI-TOF mass spectrometry analyses, a 0.5- μ l aliquot of peptide mixture was mixed with 0.5 μ l of matrix solution (cyano-4-hydroxycinnamic acid at half-saturation in 60% acetonitrile, 0.1% trifluoroacetic acid (v/v)). The resulting solution was spotted on a MALDI-TOF target plate, dried, and rinsed with 2 μ l of 0.1% trifluoroacetic acid. Peptide mixtures were then analyzed with a MALDI-TOF mass spectrometer (Autoflex, Bruker Daltonik, Germany) in reflector/delayed extraction mode over a mass range of 0–4200 Da. The spectra were annotated (XMass software), and the peptide mass fingerprints obtained were finally submitted to data base searches against the Swissprot Trembl data base with an intranet 1.9 version of MASCOT software.

Immunoprecipitation and Western Blotting—Twenty-four hours after transfection, HEK-293 or BHK-21 cells were lysed in RIPA buffer. The cell lysates were cleared by a 14,000 \times g centrifugation for 15 min and incubated overnight at 4 °C with anti-FLAG monoclonal M2 antibody. Immune complexes were precipitated with protein G-Sepharose (Amersham Biosciences), and the beads were washed with RIPA buffer. Immunoprecipitated proteins were separated by 10% SDS-PAGE and transferred onto a polyvinylidene difluoride membrane (Millipore). The membranes were blocked with 5% milk in TBS containing 0.1% Tween and incubated with the appropriate antibodies. The bands were revealed using the ECL detection reagent (Perbio).

In the case of immunoprecipitation between endogenous Alix and TNF-R1, HeLa cells were lysed in RIPA buffer. The cell lysates were cleared by a 14,000 \times g centrifugation for 15 min followed by two incubations of 30 min with protein G-Sepharose beads. The cell lysates containing 5 mg of total proteins were incubated for 1 h at 4 °C with the polyclonal antibody against TNF-R1. Immune complexes were precipitated with protein G-Sepharose (Amersham Biosciences), and the beads were washed with RIPA buffer. Immunoprecipitated proteins were separated by 8% SDS-PAGE and treated as described above. Alix was detected using the monoclonal anti-AIP1/Alix from BD Transduction Laboratories.

Quantification of Cell Death Induced by TNF-R1—Twenty hours after transfection, HEK-293 were washed in PBS, pH 7.4, and fixed in 4% paraformaldehyde for 20 min at 4 °C. The cells were stained with polyclonal anti-TNF-R1 antibody (1/100) and anti-rabbit Alexa⁵⁹⁴ antibody (1/500). The cells were rinsed in TBS, incubated for 30 min at 37 °C in 2 μ g/ml Hoechst 33342 (Sigma), and mounted in Mowiol. Cell viability was scored on the basis of nuclear morphology, with condensed or fragmented nuclei being counted as dead.

In some cases, tetrazolium salt 3-(4,5-dimethylthiazol-2-yl)-2,5-diphenyltetrazolium bromide (Sigma) was added to cells at a final concentration of 1 mg/ml and incubated for 30 min at 37 °C. Dimethyl sulfoxide was used to dissolve the formazan product, and absorbance was measured in each well at 540 nm, using a measure at 630 nm as reference, in a Biotek EL_x-800 microplate reader (Mandel Scientific Inc.).

TNF α Internalization—BHK cells co-expressing TNF-R1 and the indicated proteins were incubated for 1 h at 4 °C with 1 ng of ¹²⁵I-labeled human recombinant TNF α (specific activity,

2160 kBq/ μ g) (PerkinElmer Life Sciences). The cells were then incubated at 37 °C to allow endocytosis for the indicated times. The amount of intracellular ¹²⁵I-TNF receptor complexes formed at 37 °C was estimated after washing cells for 5 min in cold acetic acid buffer (200 mM acetic acid, 500 mM NaCl, pH 2.5). After two washes in PBS, the cells were lysed in RIPA buffer. Total amount of cell-associated ¹²⁵I-TNF α was determined on cells, washed only with PBS, instead of the acetic acid buffer. The amount of internalized (pH 2.5 resistant) ¹²⁵I-TNF was calculated as a percentage of ¹²⁵I-TNF bound at pH 7.4.

Magnetic Isolation of Endosomes Containing TNF-R1 Bound to TNF α —HEK 293 cells transfected with TNF-R1 and Alix-Myc were incubated in a total volume of 1 ml of cold D-PBS (0.9 mM CaCl₂, 0.493 mM MgCl₂, 2.67 mM KCl, 1.47 mM KH₂PO₄, 138 mM NaCl, 8 mM Na₂HPO₄) containing 3% bovine serum albumin, 100 ng/ml TNF α -FLAG, and 10 μ g/ml anti-FLAG monoclonal M1 for 1 h at 4 °C. They were then washed twice in cold D-PBS and incubated for 1 h at 4 °C in 1 ml of cold D-PBS containing 50 μ l of protein G microbeads (μ MACS Protein G Microbeads, MACS Molecular, Miltenyi Biotec). The cells were then washed twice in cold D-PBS and incubated in Dulbecco's modified Eagle's medium containing 10% SVF and kept at 4 °C or incubated for 30 min at 37 °C. Removal of surface-bound M1 antibody was achieved by washing the cells three times for 5 min in cold PBS containing 1 mM EDTA. A post-nuclear supernatant was prepared in 8% sucrose supplemented in 3 mM imidazole, pH 7.4, and 2 \times protease inhibitor mixture. The magnetic immune complex was passed over a column placed in the magnetic field of a MACS Separator. The labeled TNF α receptor was retained within the column, whereas unbound material was washed away with 8% sucrose, 3 mM imidazole, pH 7.4. The magnetic fractions were collected by removing the column from the magnetic field and analyzed by SDS-PAGE and Western blotting. Solubilization of endosomes was performed using a solution of 8% sucrose, 3 mM imidazole, pH 7.4, containing 0.5% Triton X-100.

RESULTS

Alix Interacts with Pro-caspase-8 through ALG-2—To understand how Alix might control cell death, we first characterized some of the proteins interacting with it during apoptosis. For this, we used cerebellar granule cells, which survive in absence of serum when cultured in high extracellular potassium (25 mM) but undergo apoptosis soon after they are incubated in a medium containing normal extracellular potassium concentrations (5 mM). We previously observed that expression of Alix-CT blocks caspase activation in neurons deprived of potassium (17). We used a polyclonal anti-Alix antibody to immunoprecipitate the endogenous protein from cell lysates made from neurons incubated for 4 h in 5 mM potassium. Using peptide mass fingerprinting (see "Experimental Procedures"), we found caspase-8 among the proteins co-immunoprecipitated with Alix, suggesting that the protease may physically associate with Alix. We further showed that in BHK-21 cells, FLAG-tagged Alix (FLAG-Alix) and an HA-tagged, catalytically inactive version of pro-caspase-8 (HA-DN-pro-caspase-8) (Fig. 1) co-immunoprecipitated. This demonstrates that the two proteins exist in a complex and that activity of the caspase

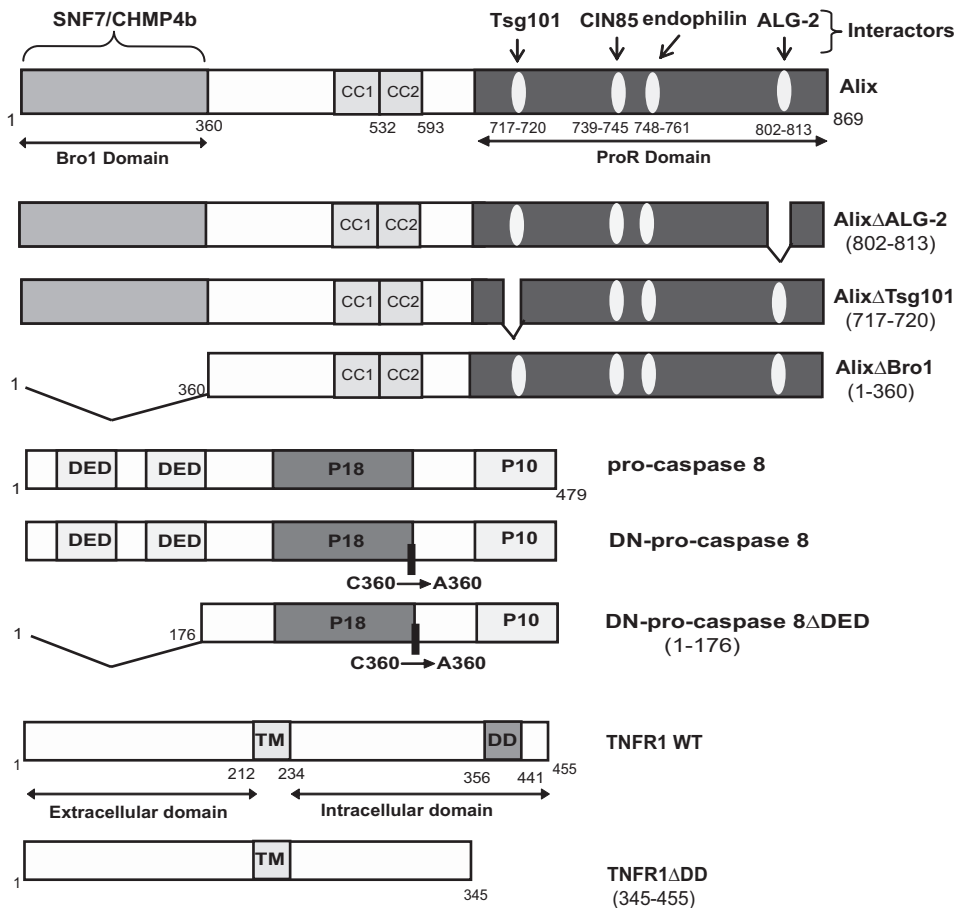


FIGURE 1. Schematic representation of Alix pro-caspase-8 and TNF-R1 and their mutants used throughout this study.

is not required for this interaction (Fig. 2A). Furthermore, deletion of the prodomain of pro-caspase-8 containing the two death effector domains (DEDs) abolished the capacity of the caspase to interact with Alix (Fig. 2B). The addition of 1 mM Ca²⁺ in the lysates strikingly enhanced the amount of Alix co-immunoprecipitating with pro-caspase-8 (Fig. 2A), and we detected endogenous ALG-2 in immunoprecipitates containing overexpressed Alix and pro-caspase-8 (Fig. 2C). This prompted us to test a potential interaction of pro-caspase-8 with ALG-2, whose binding to Alix depends on calcium. In the case where ALG-2 was co-expressed with DN-pro-caspase-8, ALG-2 co-immunoprecipitated with the caspase in presence of 1 mM CaCl₂ (Fig. 3A). Here again, this interaction required the pro-domain of the caspase (Fig. 3B). FLAG-Alix deleted of the sequence ⁸⁰²PPYPTYPGYPGY⁸¹³ necessary for the binding of ALG-2 (17) (AlixΔALG-2) (Fig. 1) did not immunoprecipitate with DN-pro-caspase-8 (Fig. 3C). On the other hand, ALG-2 could be co-immunoprecipitated with DN-pro-caspase-8 equally well from lysates of wt BHK cells or from cells in which Alix expression had been down-regulated using a pSuper vector coding for an small hairpin RNA against Alix, indicating that ALG-2 can interact with pro-caspase-8 independently of Alix (Fig. 3D).

Alix Immunoprecipitates with TNF-R1 Independently of ALG-2—The demonstration that TNF-R1 needs endocytosis to recruit pro-caspase-8 prompted us to test whether Alix and

ALG-2 act as adaptors bringing pro-caspase-8 into close vicinity of endosomes containing TNF-R1. First, we examined whether Alix and ALG-2 can form a complex with TNF-R1.

These experiments were performed in HEK 293 cells transiently transfected with expression vectors coding for TNF-R1 and Alix. As reported (21), TNF-R1 overexpression was sufficient to induce apoptosis, even in the absence of TNFα. Western blot analysis of Alix or TNF-R1 immunoprecipitates (Fig. 4A and not shown) revealed the presence of TNF-R1 and Alix, respectively, suggesting the existence of a complex containing both proteins. We further proved the existence of such a complex by showing that endogenously expressed Alix is pulled down with endogenous TNF-R1 immunoprecipitated from HeLa cells (Fig. 4B). In HEK 293 cells, TNF-R1 mutant deleted of the death domain (TNF-R1ΔDD) (Fig. 1) did not co-immunoprecipitate with Alix, indicating that the interaction depends on the integrity of this region (Fig. 4C). AlixΔALG-2, which does not inter-

act with pro-caspase-8, was capable of co-immunoprecipitating with TNF-R1 (Fig. 4C). This underscores the fact that binding of Alix to a TNF-R1 complex is independent of ALG-2 and of pro-caspase-8. Interestingly, Alix mutants lacking the Bro1 domain, required for interaction with CHMP-4B, or four amino acids necessary for binding to Tsg101, were not capable of co-immunoprecipitating with TNF-R1 (Fig. 4D). Thus, co-immunoprecipitation of Alix with TNF-R1 requires its ability to bind ESCRT proteins.

ALG-2 Immunoprecipitates with TNF-R1 in a Way That Tightly Depends on Its Capacity to Bind Calcium—We next asked whether ALG-2 can associate to TNF-R1. Lysates from HEK 293 cells co-transfected with FLAG-ALG-2 and wild type TNF-R1 expression vectors were immunoprecipitated with anti-FLAG (Fig. 5A) or with anti-TNF-R1 antibodies (not shown). In both cases, Western blots revealed co-immunoprecipitation of TNF-R1 with ALG-2. Furthermore, endogenous Alix was detected in the ALG-2 immunoprecipitates containing TNF-R1 (Fig. 5A).

We also used a mutated form of ALG-2, ALG-2ΔEF^{1,3}, harboring point mutations in the first and third EF hands, which abolish its capacity to bind calcium. In accordance to published observations (22), this calcium binding-deficient ALG-2 did not co-immunoprecipitate with Alix (Fig. 5B, panel a). ALG-2ΔEF^{1,3} was also unable to interact with TNF-R1, stressing the fact that ALG-2 must be able to bind Ca²⁺ to co-immunopre-

Alix and ALG-2 in TNF-R1-induced Cell Death

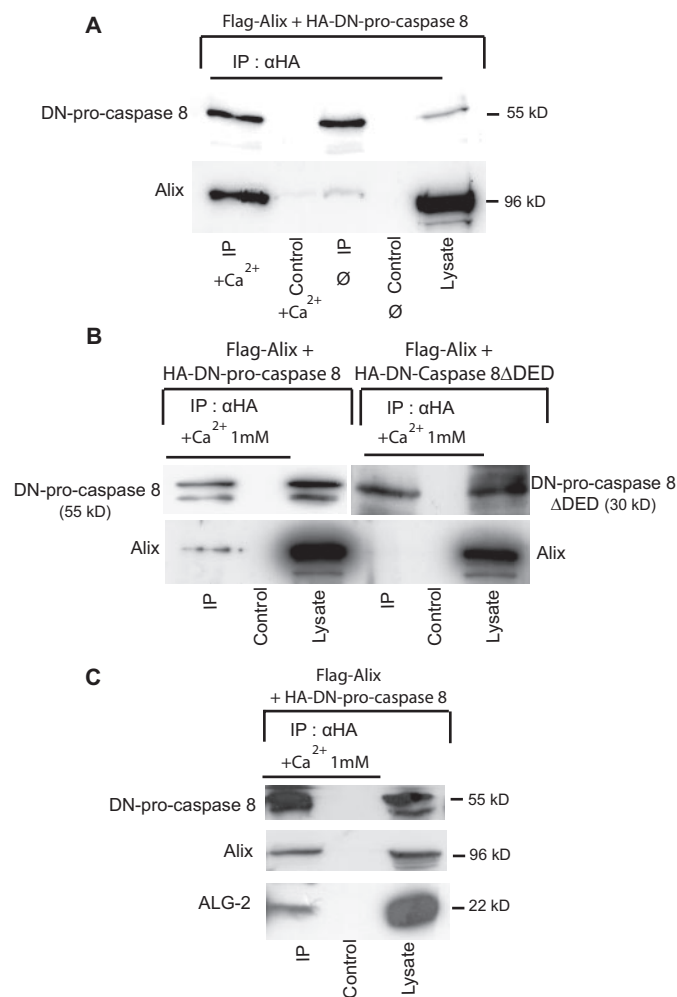


FIGURE 2. Alix co-immunoprecipitates with DN-pro-caspase-8. *A*, Alix/pro-caspase-8 co-IP requires calcium. BHK cells co-expressing FLAG-Alix and HA-DN-pro-caspase-8 were lysed and immunoprecipitated with anti-HA antibody in RIPA buffer supplemented or not with 1 mM CaCl₂. Immunoprecipitates were blotted and analyzed with polyclonal antibodies against Alix (*lower panel*) and against HA (*upper panel*). *B*, co-IP of Alix with DN-pro-caspase-8 requires the pro-domain of the zymogen. BHK cells co-expressing FLAG-Alix together with HA-DN-pro-caspase-8 or HA-DN-caspase-8-ΔDED were lysed and immunoprecipitated with anti-HA in RIPA buffer containing 1 mM CaCl₂ (CaRIPA) and analyzed as in *A*. *C*, endogenous ALG-2 is detected in pro-caspase-8/Alix co-immunoprecipitates. BHK cells co-expressing FLAG-Alix together with HA-DN-pro-caspase-8 were lysed and immunoprecipitated as in *B*; immunoprecipitates were analyzed by Western blot with polyclonal anti-HA, anti-ALG-2, and anti-FLAG antibodies (from *top* to *bottom*).

cipitate with TNF-R1 (Fig. 5*B*, *panel b*). These results show that even though formation of a complex containing TNF-R1/Alix does not necessitate interaction with ALG-2, the latter bound to calcium can associate with it, possibly by binding to Alix.

Alix Is Associated with TNF-R1 Receptosomes—Our observation that deletion of ESCRT-interacting domains from Alix impairs its capacity to bind to TNF-R1-containing complexes could suggest that interaction of the protein with the TNF-R1 complex occurs on endosomes. To examine this possibility, we used magnetic beads coupled to protein G to immunoprecipitate TNFα containing endosomes, a method modified from that published by Schütze and co-workers (3); FLAG-tagged TNFα was applied to HEK 293 cells overexpressing TNF-R1 at 4 °C in presence of M1, an anti-FLAG antibody binding only in pres-

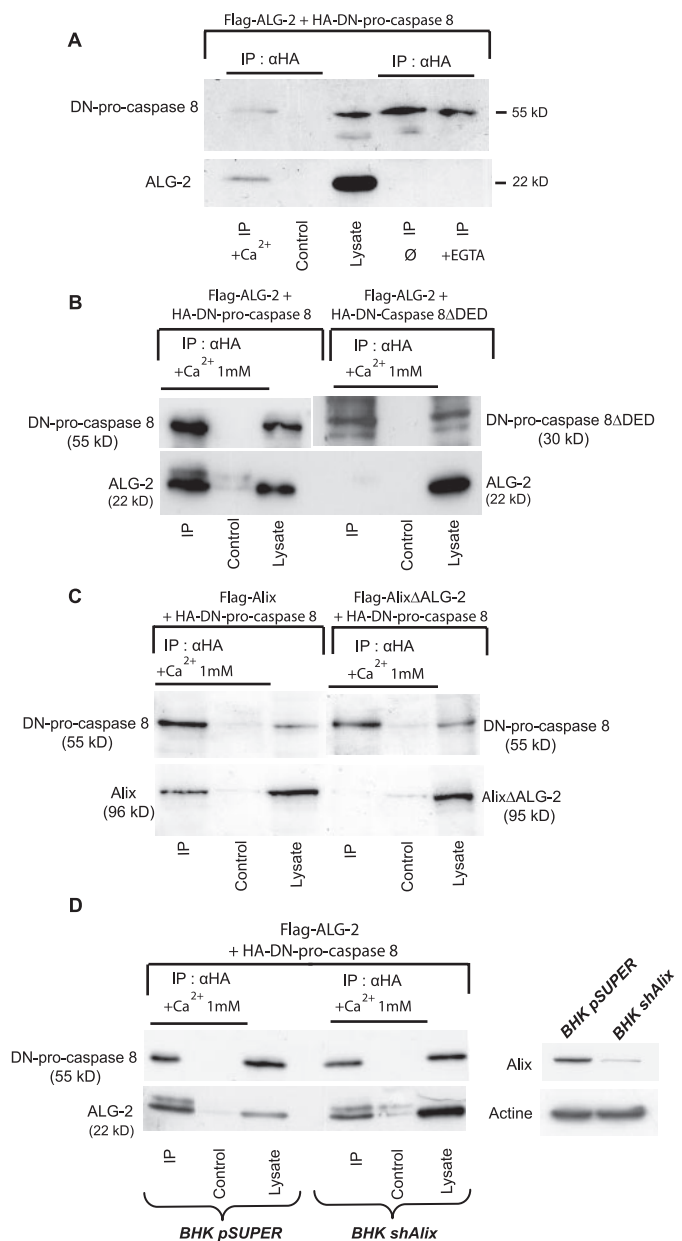


FIGURE 3. ALG-2 co-immunoprecipitates with DN-pro-caspase-8. *A*, ALG-2/pro-caspase-8 co-IP requires calcium. BHK cells co-expressing FLAG-ALG-2 and HA-DN-pro-caspase-8 were lysed and immunoprecipitated with anti-HA in RIPA buffer (∅) or RIPA buffer containing either 3 mM EGTA or 1 mM CaCl₂. Immunoprecipitates were analyzed using polyclonal antibodies against HA (*upper panel*) and FLAG (*lower panel*). *B*, co-IP of ALG-2 with DN-pro-caspase-8 requires the pro-domain of the zymogen. BHK cells co-expressing FLAG-ALG-2 together with HA-DN-pro-caspase-8 or HA-DN-caspase-8-ΔDED were lysed and immunoprecipitated with anti-HA in CaRIPA and analyzed as in *A*. *C*, co-IP of Alix with DN-pro-caspase-8 requires its ALG-2 binding domain. BHK cells were co-transfected with either FLAG-Alix WT or FLAG-AlixΔALG-2 and HA-DN-pro-caspase-8. IP with anti-HA antibody were performed in CaRIPA. Immunoprecipitates were analyzed by Western blot using polyclonal antibodies against HA (*upper panel*) and Alix (*lower panel*). *D*, ALG-2 co-immunoprecipitates with DN-pro-caspase-8 in cells depleted of Alix. BHK cells expressing shAlix to down-regulate expression of the protein were transfected with FLAG-ALG-2 and HA-DN-pro-caspase-8 lysed in CaRIPA and immunoprecipitated with an anti-HA antibody. Immunoprecipitates were analyzed by Western blot using anti-FLAG (*lower panel*) and HA polyclonal antibodies (*upper panel*). *Right inset*, Western blot analysis of lysates using a polyclonal antibody anti-Alix and a monoclonal anti-actin shows the decrease of endogenous Alix expression in BHK shAlix cells.

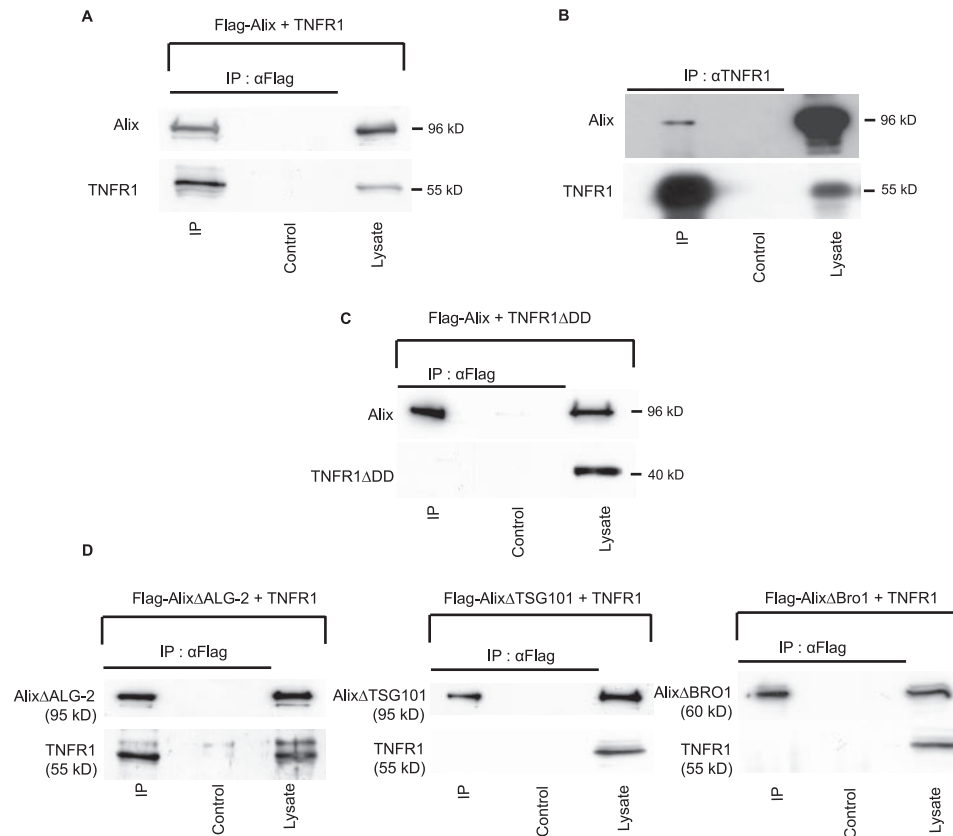


FIGURE 4. Alix co-immunoprecipitates with TNF-R1. *A*, Co-IP of overexpressed Alix and TNF-R1. RIPA lysates of HEK 293 cells co-expressing FLAG-Alix and TNF-R1 were immunoprecipitated with anti-FLAG antibodies and blots probed with anti-Alix (upper panel) and anti-TNF-R1 (lower panel). *B*, co-IP of endogenous Alix and TNF-R1. RIPA lysates of HeLa cells were immunoprecipitated using a polyclonal anti-TNF-R1. The IP was analyzed by Western blot using a monoclonal antibody against human Alix. *C*, co-IP of Alix with TNF-R1 requires the death domain of the receptor. RIPA lysates of HEK 293 cells co-expressing FLAG-Alix and TNF-R1 deleted from its death domain (TNF-R1 Δ DD) were immunoprecipitated with anti-FLAG or with anti-TNF-R1, and blots were probed with the appropriate polyclonal antibodies as in *A*. *D*, co-immunoprecipitation of Alix with TNF-R1 requires its binding site to Tsg101 and Bro1 but not to ALG-2. Cells co-expressing TNF-R1 and either FLAG-Alix Δ Tsg101, FLAG-Alix Δ Bro1, or FLAG-Alix Δ ALG-2 were solubilized in RIPA buffer, and total lysates were immunoprecipitated with anti-FLAG; Western blots were probed with the appropriate polyclonal antibodies as in *A* and *C*.

ence of calcium. The cells were incubated at 37 °C for 30 min to allow endocytosis and then treated briefly with EDTA to remove surface-bound antibody. The resulting immunoisolated membrane fractions contained TNF-R1, two markers of endosomes, EEA1 and Lamp-1, but neither the mitochondrial marker HSP70, nor *cis*-Golgi marker GM130, stressing the endosomal origin of these fractions (Fig. 6A). None of the proteins tested could be detected in magnetic particles recovered from cells left at 4 °C and treated with EDTA (Fig. 6A, lanes 0), thus demonstrating the efficiency of the washing procedure for removing the M1 anti-FLAG antibody from TNF α bound to TNF-R1 remaining on the cell surface.

Triton X-100 solubilization of the endosomal membranes, witnessed by the loss of EEA1 and Lamp-1 labeling, left intact TNF-R1, Alix, ALG-2, pro-caspase-8, and FADD immunoreactivity (Fig. 6B). This result indicates that these proteins interact within complexes containing endocytosed TNF-R1 bound to TNF α .

Alix Δ ALG-2 Protects HEK 293 Cells from TNF-R1-induced Cell Death without Affecting Internalization of the Receptor—HEK 293 cells die soon after transfection with an expression

vector coding for TNF-R1 but not with one encoding TNF-R1 Δ DD (Fig. 7A, panel a). Blocking clathrin-dependent endocytosis by a dominant negative mutant of dynamin 2a significantly reduced TNF-R1-induced cell death (Fig. 7A, panel a). Alix Δ ALG-2, which interacts with TNF-R1 but not with pro-caspase-8, inhibited cell death induced by TNF-R1, estimated by Hoechst nuclear staining (Fig. 7A, panel b) and 3-(4,5-dimethylthiazol-2-yl)-2,5-diphenyltetrazolium bromide assay (Fig. 7B). Alix-wt or Alix Δ TSG101, which cannot interact with TNF-R1, did not protect against TNF-R1-induced cell death (Fig. 7A, panel b).

Using ¹²⁵I-radiolabeled TNF α , we found no difference in TNF α internalization between TNF-R1 overexpressing cells co-transfected with control plasmid, Alix, or Alix Δ ALG-2, whereas internalization was abolished by co-transfection with a dominant negative mutant of dynamin 2a (Fig. 7C). These results indicate that the protective effect of Alix Δ ALG-2 is not due to blockade of receptor internalization.

Alix Δ ALG-2 Blocks Cell Death of Cervical Motoneurons, Which Is Regulated by TNF-R1—We finally tested whether the participation of Alix and ALG-2 in the TNF-R1

death pathway demonstrated *in vitro* may also apply *in vivo*. For this we searched whether programmed cell death of cervical motoneurons (MTN) in the chick embryo, which is efficiently blocked by expression of Alix Δ ALG-2 (18), depends on TNF-R1. Reverse transcription-PCR analysis revealed expression of the TNF-R1 mRNA in whole chick embryo extracts from HH stage 16 to HH stage 27 (Fig. 8A). We next used a polyclonal antibody, raised against the extracellular part of human TNF-R1, which we verified to recognize the chick counterpart (40.5% identity on the 222 extracellular amino acids). Indeed, the antibody revealed bands at the expected 55 kDa in blots prepared from chick fibroblasts (DF1 cell line) and chick embryo extracts (Fig. 8B). Immunostaining revealed expression of TNF-R1 in the dermomyotome but not in the neural tube of HH stage 16 chick embryo. Labeling of the ventral-most part of the ventral horn and of MTN axons growing out of the tube was detected at HH stages 21 and 24 (Fig. 8, C and D) and decreased at HH stage 27 (not shown). Taken together, these results show that TNF-R1 is transiently expressed in MTN during a short period corresponding to that of programmed cell death. In comparison, Alix is expressed in the same areas of the neural tube but

Alix and ALG-2 in TNF-R1-induced Cell Death

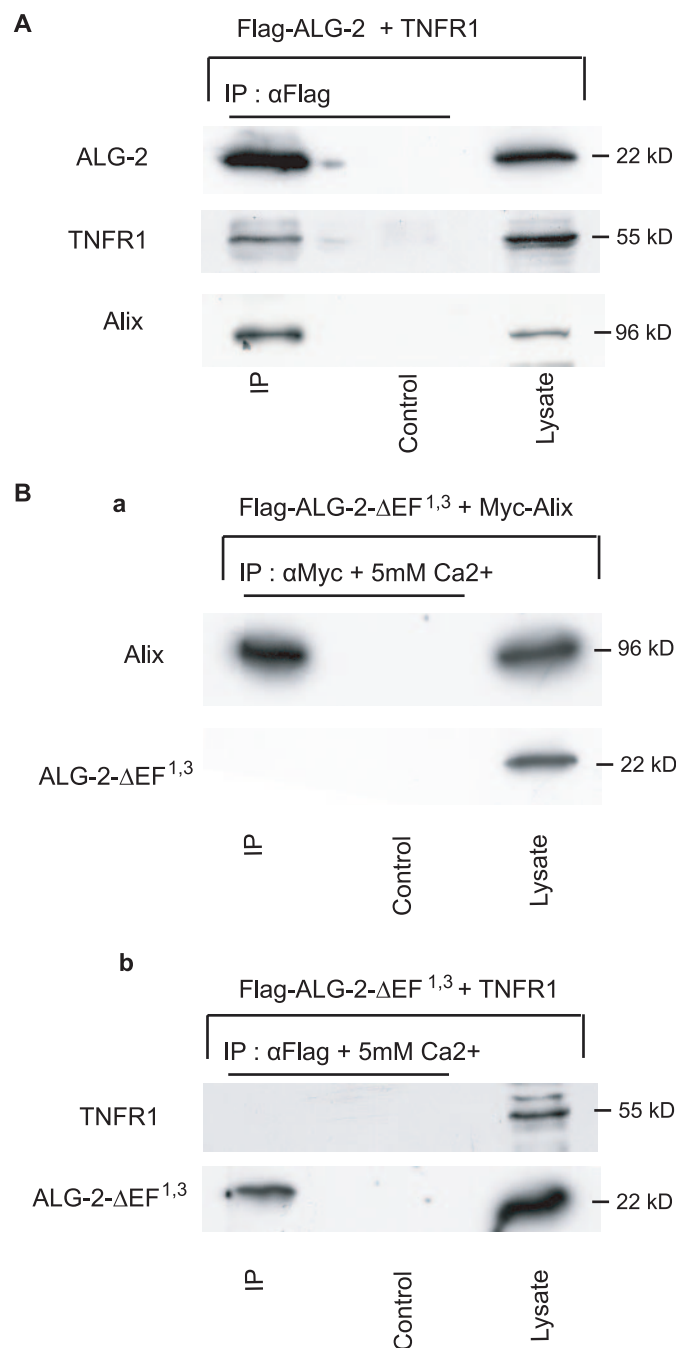


FIGURE 5. ALG-2 co-IP with TNF-R1 requires its capacity to bind calcium. A, ALG-2 co-IP with TNF-R1 and Alix. HEK293 cells were co-transfected with FLAG-ALG-2 and TNF-R1. RIPA cell lysates were immunoprecipitated with anti-FLAG or with anti-TNF-R1, and blots were probed with the appropriate antibodies. The bottom panel shows the presence of endogenous Alix within the immunoprecipitates as revealed with an anti-Alix antibody. B, calcium binding-deficient ALG-2 mutant does not co-IP with Alix (panel a) or with TNF-R1 (panel b). HEK293 cells co-expressing FLAG-Alix (panel a) or TNF-R1 (panel b) together with FLAG-ALG-2ΔEF^{1,3}, a point mutant unable to bind Ca²⁺, were solubilized and immunoprecipitated in CaRIPA; Western blots were probed with the appropriate polyclonal antibodies.

appearing earlier (HH stage 16) and for longer during development (23).

We first tested the involvement of caspase-8 during death of MTN, using electroporation of the chick neural tube. This technique allows expression of the protein of interest in one

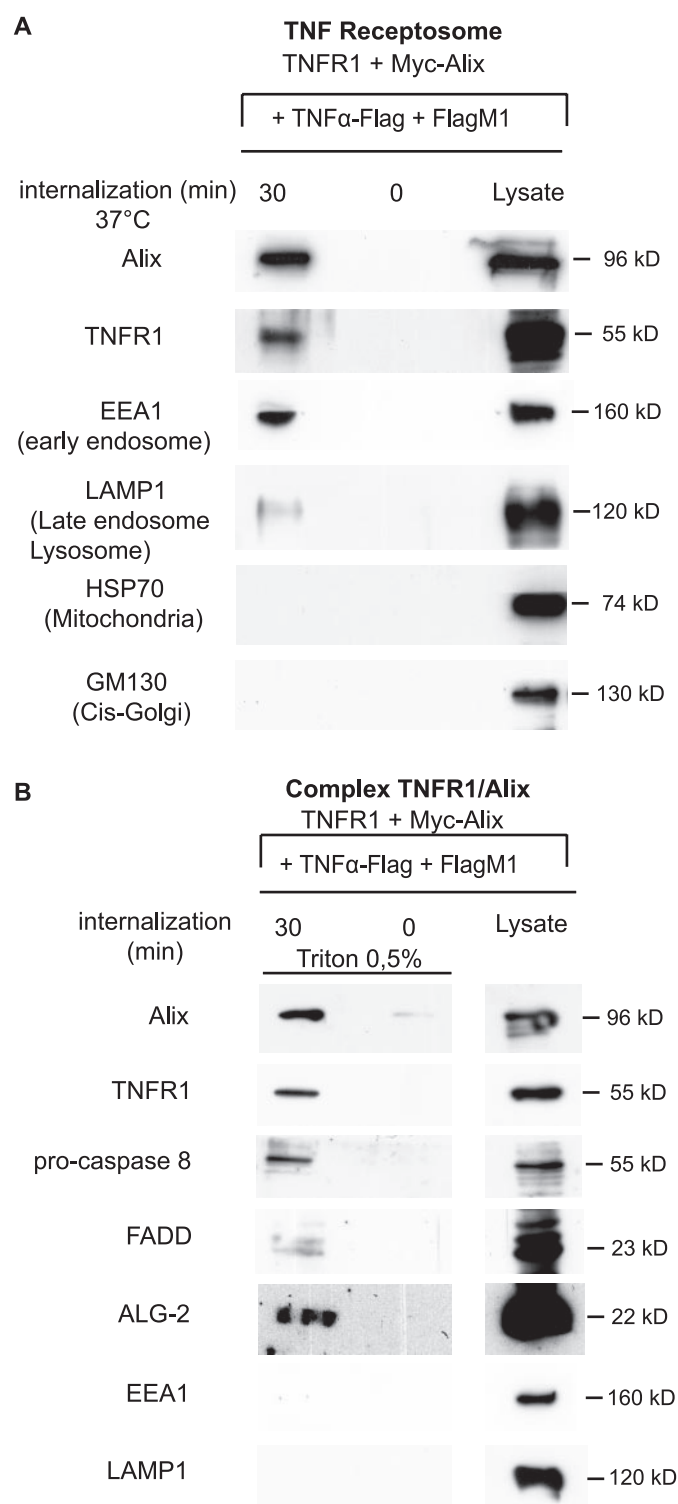


FIGURE 6. Alix and ALG-2 are present with pro-caspase-8 and FADD on TNF receptors. A, Western blot analysis of FLAG-TNFα containing endosomes prepared from HEK 293, over-expressing TNF-R1 and Myc-Alix. Lane 0, cells maintained at 4°C were washed with EDTA prior to endosome preparation. Lane 30, cells incubated for 30 min at 37°C to induce endocytosis of TNFα bound to TNF-R1 before lysis. Magnet-isolated endosomes were run on SDS-PAGE and immunoblotted to reveal the presence of EEA1 (early endosomes), LAMP1 (late endosomes and lysosomes), GM130 (cis-Golgi), or HSP70 (mitochondria). B, solubilization of TNF-R1 receptors leaves intact a complex containing Alix, ALG-2, FADD, and pro-caspase-8. TNF-R1 receptors prepared as in A were solubilized on the affinity column using 0.5% Triton X-100 and analyzed by Western blotting using the appropriate antibodies. The lack of EEA1 and LAMP1 confirms membrane solubilization of TNF receptors.

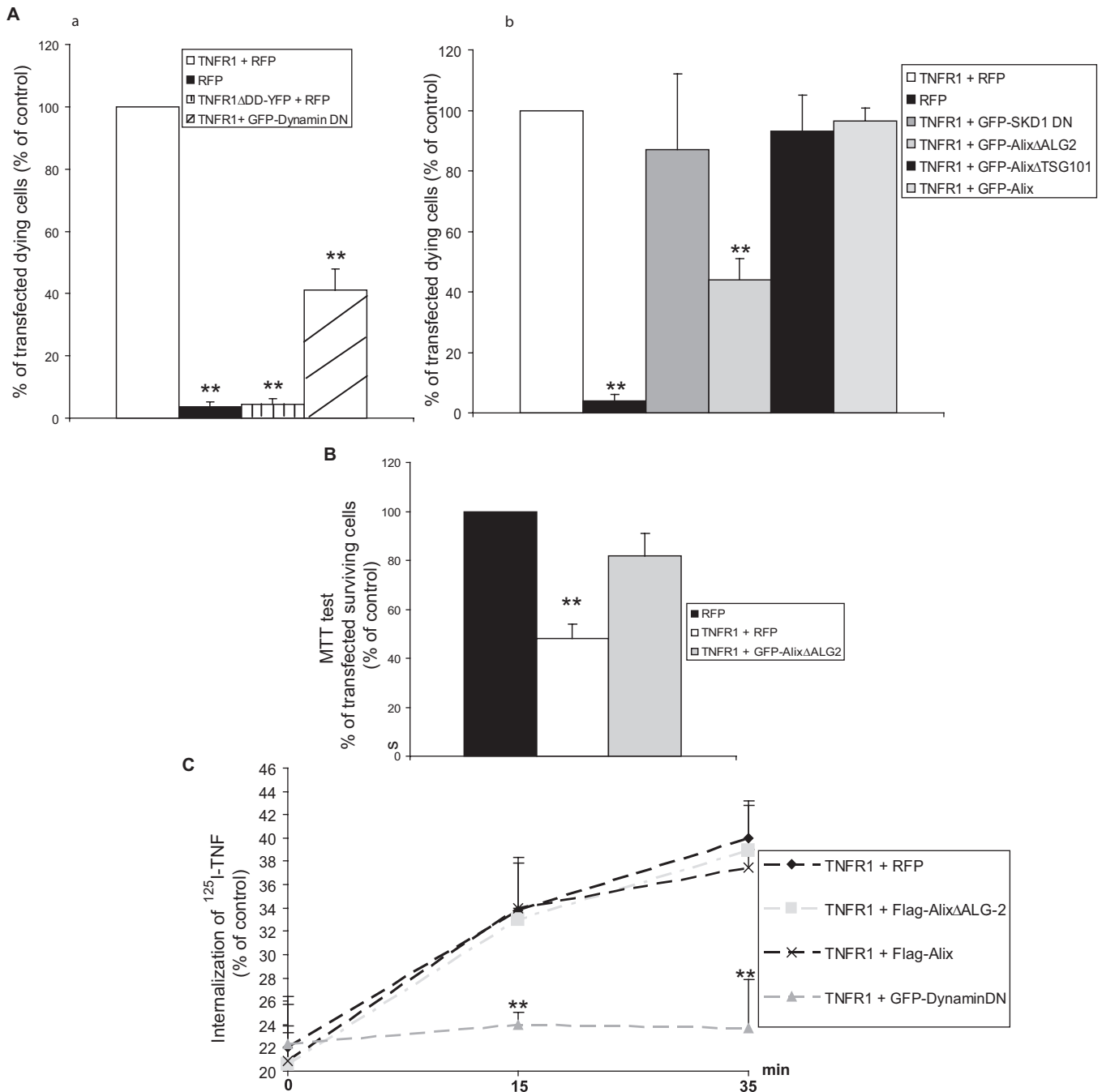


FIGURE 7. Alix Δ ALG-2 protects HEK293 cells from TNF-R1-induced cell death without impairing internalization of the receptor. *A*, TNF-R1 overexpression triggers apoptosis, which is inhibited by Alix Δ ALG-2 but not by Alix Δ Tsg101 or SKD1 DN. *Panels a and b*, HEK 293 cells transfected with expression vectors coding for RFP or TNF-R1 and the indicated proteins. Viability was scored on the basis of nuclear morphology; cells with condensed or fragmented nuclei were counted as dead. The values are the means \pm S.D. of dying cells from three independent experiments. **, *t* test, $p < 0.001$. *B*, 3-(4,5-dimethylthiazol-2-yl)-2,5-diphenyltetrazolium bromide metabolic colorimetric test confirms the protective effect of Alix Δ ALG-2. Each value represents the mean \pm S.D. of triplicate wells from three independent experiments. **, *t* test, $p < 0.001$. *C*, TNF-R1/TNF α internalization is impaired by a dominant negative form of dynamin but not by Alix or Alix Δ ALG-2. TNF-R1 internalization was analyzed using [125 I]TNF α in TNF-R1 expressing cells. Each point represents the mean \pm S.D. of triplicate wells from three independent experiments. **, *t* test, $p < 0.001$.

half of the embryo, the other half being left intact for comparison. p35, a baculovirus protein inhibiting most caspases (24), was electroporated into the cervical neural tube of HH stage 16 embryos, which were sacrificed 48 h later (Fig. 9*A*, *panel a*). Comparison between transfected and non transfected ventral horns of the same embryo revealed a reduction by half of the number of TUNEL positive neurons in the p35 expressing ventral horn (Fig. 9, *A*, *panel b*, and *B*). Using the

same technique, we found that expression of DN-procaspase-8 (Fig. 9, *A*, *panels c and d*, and *B*) also reduced the number of dying neurons to a similar degree as Alix Δ ALG-2 (18). This indicates a role of Alix/ALG-2 and of the death receptor-regulated apical caspase-8 in MTN programmed cell death during development.

Overexpression of human wild type TNF-R1 is sufficient, like Alix overexpression, to induce massive apoptosis throughout

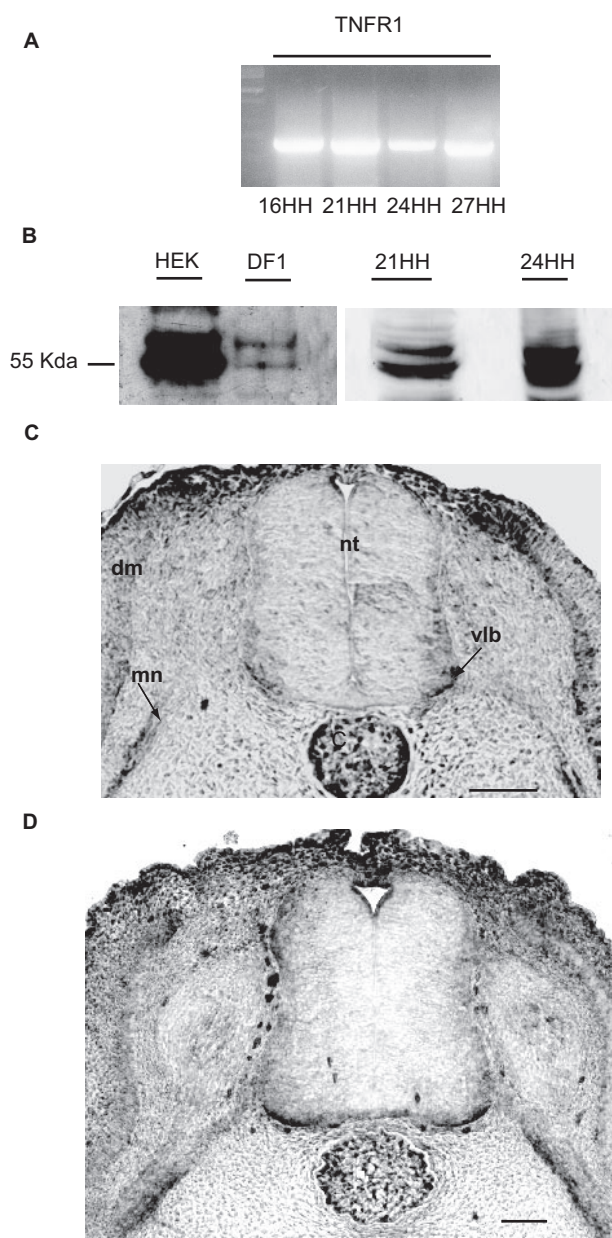


FIGURE 8. TNF-R1 is expressed during chick neural tube development. A, reverse transcription-PCR analysis shows gene expression in whole extracts from chick embryos from HH stage 16 to HH stage 27. B, polyclonal anti-TNF-R1 recognizes a main band at 55 kDa in HEK cells and a doublet with the lower band corresponding to 55 kDa in DF1 chick fibroblasts. A similar pattern is observed in chick embryo extracts (21HH, 24HH). C and D, cross-sections of HH stage 21 (C) or 24 (D) chick embryo neural tubes immunostained with polyclonal anti-TNF-R1. Scale bar, 50 μ m. C, cord; dm, dermomyotome; mn, motoneuron axons; nt, neural tube; vlb, ventro-lateral border.

the neural tube (data not shown). On the contrary, expression of TNF-R1 Δ DD halved the number of TUNEL-positive nuclei in the ventral part of the tube (Fig. 9, A, panels e and f, and B). This, together with our demonstration that the endogenous receptor is expressed at the time of programmed cell death, indicates that activation of TNF-R1 regulates the death of cervical motoneurons. Taken together, these *in vivo* data strongly suggest that Alix Δ ALG-2 blocks programmed cell death by interfering with TNF-R1 death signaling.

DISCUSSION

We previously showed that overexpressed Alix is sufficient to activate caspases and apoptosis and that this activity requires binding to ALG-2. On the contrary, expression of the C-terminal half of Alix blocked apoptosis depending on its capacity to bind ALG-2, suggesting that it acts by titrating out ALG-2 (17, 18). Interestingly, this truncated form of Alix accumulates in cytoplasmic inclusions, which also contain ALG-2 and activated caspases (17). Rao *et al.* (25) have shown that ALG-2 is necessary for caspase activation following an abnormal rise in cytosolic calcium. Their observations suggested that ALG-2 belongs to a complex allowing caspase-9 activation following cytosolic calcium elevation because of a stress to the reticulum. Our present results demonstrate that ALG-2 can also form a complex with pro-caspase-8, independently of Alix, and that this requires the prodomain of the zymogen but not the catalytic activity of the protease.

Historically, caspase-8 was described as an initiator caspase activated by members of the TNF-R1 family of death receptors stimulating the extrinsic pathway of apoptosis (26). These latter recruit, through an 80-amino acid-long death domain (DD), other DD-containing cytoplasmic proteins that participate in the formation of the death-inducing signaling complex (DISC) recruiting and activating pro-caspase-8 or 10. We observed that the DD of TNF-R1 is mandatory for the interaction with Alix and therefore with the Alix/ALG-2 complex. The TNF α ligand is known to induce, via the intracellular domain of the receptor, the rapid formation of complex I made of the adaptor TRADD, the protein kinase RIP1, and the signal transducer TRAF2. This complex signals cell survival through c-Jun N-terminal kinase (JNK) and I κ B kinase, the latter activating transcription factor NF κ B, whose targets can mediate cell survival. Complex I can dissociate from the receptor and, together with the adaptor protein FADD, recruit and activate pro-caspase-8 (27). Schütze and co-workers (3) introduced a twist to this model when they published convincing data showing that aggregation of TRADD, FADD, and caspase-8 can occur on TNF-R1 but that this is critically dependent on receptor endocytosis. In line with this, we observed that blocking clathrin-dependent endocytosis significantly inhibited apoptosis induced by TNF-R1. In their model, Schneider-Brachert *et al.* (3) claim that TNF-R1-containing endosomes would establish the platform on which the DISC may form. Because Alix can bind TNF-R1 on one side and ALG-2, which can interact with caspase-8, on the other, it may act as an adaptor for recruiting pro-caspase-8 on the surface of TNF-R1-containing endosomes. In favor of this model, we found that binding of Alix to TNF-R1 is totally abolished upon deletion of its binding domains to CHMP-4B and Tsg-101 of ESCRT-III and ESCRT-I, respectively, suggesting that stabilization of Alix binding to the TNF-R1 complex occurs through interactions with these endosomal proteins. Furthermore we could identify TNF-R1, Alix, ALG-2, caspase-8, and FADD within a common, Triton X-100-resistant complex in endosomal fractions containing TNF α bound to its endocytosed receptor. Thus, Alix Δ ALG-2 may block death induced by TNF-R1 by impairing the recruitment of pro-caspase-8 onto surface of TNF-R1-containing endosomes. The protecting

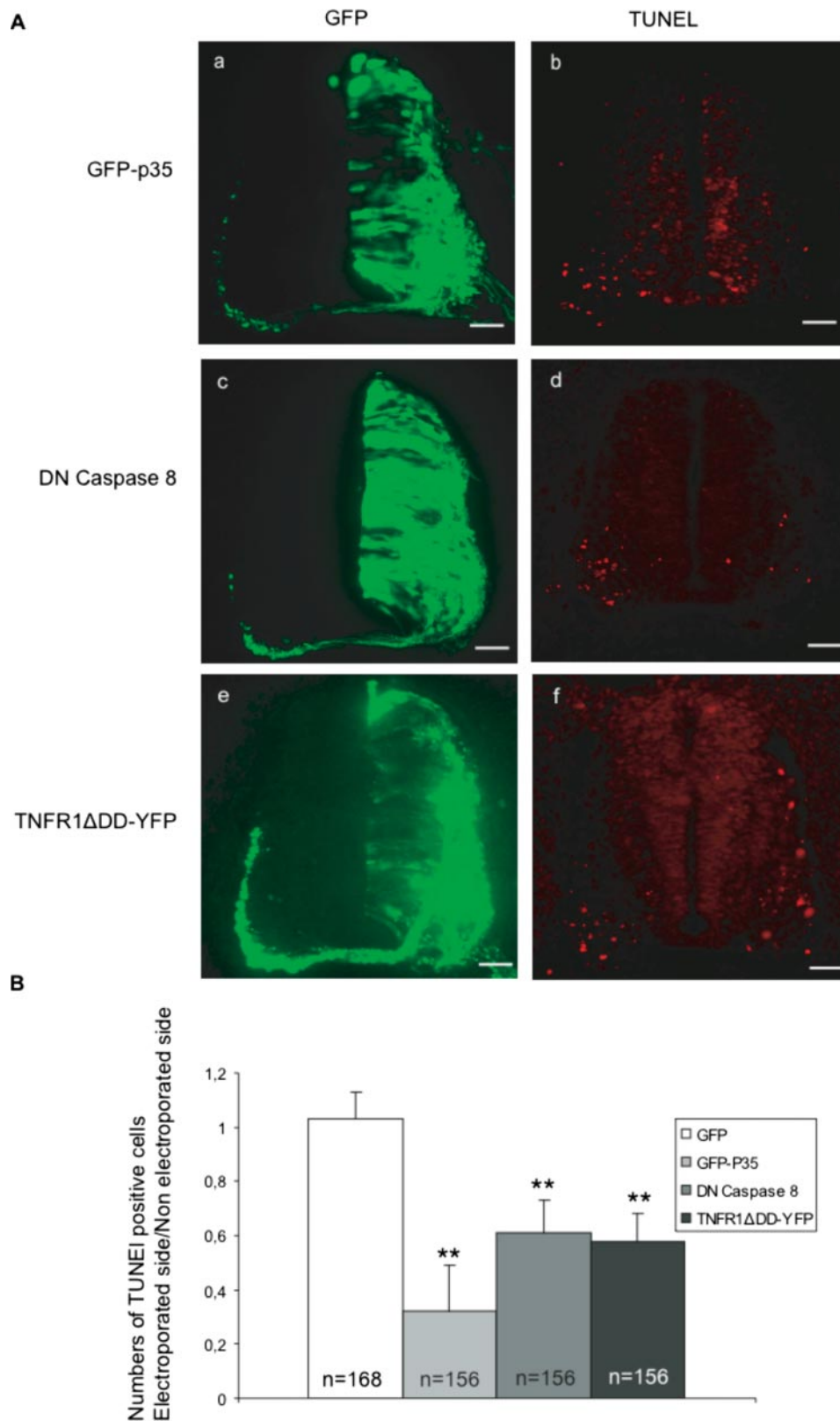


FIGURE 9. TNF-R1 is involved in early cell death of cervical motoneurons. *A*, cross-sections of HH stage 24 chick embryo neural tubes electroporated with pCAGGS expression vectors coding for: GFP-p35 (*panels a and b*), DN-pro-caspase-8 (*panels c and d*), TNFR1ΔDD-YFP (*panels e and f*). *Panels a, c, and e*, GFP expression 48 h after electroporation. *Panels b, d, and f*, TUNEL labeling of adjacent sections. Scale bar, 50 μm. *B*, ratio of TUNEL-positive cells in the electroporated versus nonelectroporated side of the neural tube. The mean numbers ± S.D. of TUNEL-positive cells in the neural tube of electroporated embryos, *n* = number of sections analyzed; 12 sections/embryo were counted. **, *t* test, *p* < 0.001.

effect of AlixΔALG-2 is not simply due to blocking of endocytosis of the activated receptor, because the latter process is not influenced by the mutant. Nor is it due to an impairment of the degradation of the receptor inside lysosomes because the dead version of the ATPase SKD-1, which leads to gross abnormalities in multivesicular endosomes (28), had no protecting activity against TNF-R1.

We have tested the effect of Alix/ALG-2 down-regulation on HeLa cells treated with 100 ng/ml of TNFα and 1 mg/ml cycloheximide and on Jurkat cells in which the NFκB survival pathway is inhibited by knockdown of the IKK Nemo (a kind gift of O. Micheau, Dijon, France; data not shown).

Down-regulation of Alix or ALG-2 did not afford statistically significant protection against TNF-R1-induced cell death in either case. The apparent discrepancy between these small interfering RNA results and those using mutant expressions might have two explanations: 1) Alix down-regulation was never complete, being reduced by 90% at best, and ALG-2 extinction never attained more than 50%. Thus, the remaining Alix and ALG-2 might be sufficient for recruiting and activating caspase-8. 2) In the absence of Alix/ALG-2, other proteins might allow the recruitment of the caspase onto TNF-R1-containing endosomes. A similar argument could be offered to explain why down-regulating FADD has no protective effect on TNF-R1-induced cell death (29). The fact that FADD is still widely accepted as being essential for TNF-R1-induced cell death, even after the very solid demonstration of Jin and El-Deiry, begs caution in the use of small interfering RNAs in the field of caspase activation.

We strengthened the notion of a role of Alix/ALG-2 in regulating TNF-R1-induced cell death, by demonstrating that programmed cell death of chick cervical MTN, which we had previously found to be inhibited by AlixΔALG-2 (18), is

Alix and ALG-2 in TNF-R1-induced Cell Death

driven by TNF-R1. Among death receptors of the TNF-R family, P75^{NGFR}, Fas, and TNF-R1 (30) have been postulated to play an active role during MTN developmental death. Sedel *et al.* (31) have shown that death of an embryonic day 12–13 rat MTN is regulated by TNF α and that death of mouse MTN is significantly reduced in double knock-out for TNF α and TNF-R1. In the chick embryo, TNF α was detected by immunohistochemistry from HH stage 18 (embryonic day 3) with a peak at HH stage 24–25 (embryonic day 4.5–5) (32), and we found that TNF-R1 is transiently expressed during programmed cell death of cervical MTN with a pattern reminiscent of that of Alix. The TNF-R1 pathway seems to be instrumental in controlling death of the MTN during this developmental period; indeed expression of TNF-R1 Δ DD or DN-procaspase-8, which both act as dominant negative mutants of the cognate proteins, reduced apoptosis of the MTN as much as the pan-caspase inhibitor p35. The fact that Alix Δ ALG-2 confers a similar protection of the same MTN (18) strongly suggests that this protection is due to a modification of the TNF-R1 pathway *in ovo*. It is here noteworthy that CIN85, another interactor of Alix, has been reported to be involved in TNF-R1 signaling (33), and we have observed that deletion of the CIN85-binding site impairs the death blocking activity of the C-terminal half of Alix in chick MTN.⁶

de Gassart *et al.* (34) have reported caspase activity in exosomes that correspond to intraluminal vesicles of MVBs and are enriched in Alix. Exosomes also bear TNF-R1, indicating that the receptor is a cargo of the intraluminal vesicles, but without its interactors TRADD, RIP, and TRAF2 (35). It may therefore be speculated that Alix and ALG-2, which accompany and get entrapped into vesicles budding inside MVBs, could pull TNF-R1 and caspase-8 inside endosomes. This would efficiently isolate the activated caspase from its cytosolic substrates and lead to its rapid degradation inside lysosomes fusing with MVBs. Thus, one reason for why activation of pro-caspase-8 in the vicinity of Alix and ALG-2 occurs on the surface of endosomes containing TNF-R1 is that it may allow a potent control to rapidly tune down caspase-8 activity.

Because ALG-2 binding to Alix is strictly calcium-dependent, our results also beg the question of the relationship between cytosolic calcium and TNF-R1. The present literature remains controversial about the role of cytosolic calcium in TNF α -induced cell death. Some investigators have failed to find evidence for a TNF α -induced calcium response in U937 monocytes (36) or in KYM-1 and HeLa cells overexpressing the TNF receptor (37). In contrast, Bellomo *et al.* (38) and Kong *et al.* (39) found an increase in intracellular calcium using BT-20 and L929 cells, respectively. More recently, Draper *et al.* (40) found a sustained rise in cytosolic calcium following cycloheximide/TNF α treatment of C3HA fibroblast cells. Fas, which also requires endocytosis for caspase-8 activation, has been shown to induce calcium release from internal stores. It is also noteworthy that endosomes are known to contain high concentrations of calcium and calcium leakage from endosomes regulates their maturation (41). Thus, a rise in calcium in the close

vicinity of endosomes might allow ALG-2 to bind to Alix and recruit caspase-8 on the surface of endosomes. This is even more relevant considering that Fas-mediated apoptosis requires calcium release from the endoplasmic reticulum (42), and we will now test whether Fas-mediated cell death also involves Alix/ALG-2 during activation of caspase-8. We will also need to examine whether the interaction of ALG-2 and Alix to pro-caspase-8 and TNF-R1, respectively, is direct or through proteins of the DISC. Interactions within this complex are homophilic between DD or DED. We showed that the DD of TNF-R1 and the DED containing pro-domain of pro-caspase 8 are obligatory for binding to Alix and ALG-2, respectively, and that FADD is present in the Alix/ALG-2/pro-caspase-8 complex. Because apparently, neither Alix nor ALG-2 contain death adaptor domains, we now need to characterize the new module that allows their interaction to the DISC.

Acknowledgments—We thank Patrick Mehlen, Wulf Schneider-Brachert, and Masatoshi Maki for reagents; Yves Goldberg, Karim Sadoul, and Fiona Hemming for critical reading of the manuscript and numerous suggestions throughout this work; Gilles Bodon for help with the receptorosome experiment; and Thomas Mellier for patience.

REFERENCES

1. van der Goot, F. G., and Gruenberg, J. (2006) *Trends Cell Biol.* **16**, 514–521
2. Barker, P. A., Hussain, N. K., and McPherson, P. S. (2002) *Trends Neurosci.* **25**, 379–381
3. Schneider-Brachert, W., Tchikov, V., Neumeyer, J., Jakob, M., Winoto-Morbach, S., Held-Feindt, J., Heinrich, M., Merkel, O., Ehrenschwender, M., Adam, D., Mentlein, R., Kabelitz, D., and Schütze, S. (2004) *Immunity* **21**, 415–428
4. Williams, R. L., and Urbe, S. (2007) *Nat. Rev. Mol. Cell. Biol.* **8**, 355–368
5. Missotten, M., Nichols, A., Rieger, K., and Sadoul, R. (1999) *Cell Death Differ.* **6**, 124–129
6. Vito, P., Lacana, E., and D'Adamio, L. (1996) *Science* **271**, 521–525
7. Vito, P., Pellegrini, L., Guet, C., and D'Adamio, L. (1999) *J. Biol. Chem.* **274**, 1533–1540
8. Strack, B., Calistri, A., Craig, S., Popova, E., and Gottlinger, H. G. (2003) *Cell* **114**, 689–699
9. von Schwedler, U. K., Stuchell, M., Muller, B., Ward, D. M., Chung, H. Y., Morita, E., Wang, H. E., Davis, T., He, G. P., Cimbara, D. M., Scott, A., Krausslich, H. G., Kaplan, J., Morham, S. G., and Sundquist, W. I. (2003) *Cell* **114**, 701–713
10. Carlton, J. G., and Martin-Serrano, J. (2007) *Science* **316**, 1908–1912
11. Morita, E., Sandrin, V., Chung, H. Y., Morham, S. G., Gygi, S. P., Rodesch, C. K., and Sundquist, W. I. (2007) *EMBO J.* **13**, 13
12. Matsuo, H., Chevallier, J., Mayran, N., Le Blanc, I., Ferguson, C., Faure, J., Blanc, N. S., Matile, S., Dubochet, J., Sadoul, R., Parton, R. G., Vilbois, F., and Gruenberg, J. (2004) *Science* **303**, 531–534
13. Chatellard-Causse, C., Blot, B., Cristina, N., Torch, S., Missotten, M., and Sadoul, R. (2002) *J. Biol. Chem.* **277**, 29108–29115
14. Chen, B., Borinstein, S. C., Gillis, J., Sykes, V. W., and Bogler, O. (2000) *J. Biol. Chem.* **275**, 19275–19281
15. Cabezas, A., Bache, K. G., Brech, A., and Stenmark, H. (2005) *J. Cell Sci.* **118**, 2625–2635
16. Schmidt, M. H., Hoeller, D., Yu, J., Furnari, F. B., Cavenee, W. K., Dikic, I., and Bogler, O. (2004) *Mol. Cell. Biol.* **24**, 8981–8993
17. Trioulier, Y., Torch, S., Blot, B., Cristina, N., Chatellard-Causse, C., Verna, J. M., and Sadoul, R. (2004) *J. Biol. Chem.* **279**, 2046–2052
18. Mahul-Mellier, A.-L., Hemming, F. J., Blot, B., Fraboulet, S., and Sadoul, R. (2006) *J. Neurosci.* **26**, 542–549
19. Sadoul, R. (2006) *Biol. Cell* **98**, 69–77
20. Ferro, M., Seigneurin-Berny, D., Rolland, N., Chapel, A., Salvi, D., Garin, J.,

⁶ A.-L. Mahul-Mellier, unpublished observation.

- and Joyard, J. (2000) *Electrophoresis* **21**, 3517–3526
21. Todd, I., Radford, P. M., Draper-Morgan, K. A., McIntosh, R., Bainbridge, S., Dickinson, P., Jamhawi, L., Sansaridis, M., Huggins, M. L., Tighe, P. J., and Powell, R. J. (2004) *Immunology* **113**, 65–79
 22. Shibata, H., Yamada, K., Mizuno, T., Yorikawa, C., Takahashi, H., Satoh, H., Kitaura, Y., and Maki, M. (2004) *J. Biochem. (Tokyo)* **135**, 117–128
 23. Fraboulet, S., Hemming, F. J., Mahul, A. L., Cristina, N., and Sadoul, R. (2003) *Gene Expr. Patterns* **3**, 139–142
 24. Bump, N. J., Hackett, M., Hugunin, M., Seshagiri, S., Brady, K., Chen, P., Ferez, C., Franklin, S., Ghayur, T., Li, P., Licari, P., Mankovich, J., Shi, L., Greenberg, A. H., Miller, L. K., and Wong, W. W. (1995) *Science* **269**, 1885–1888
 25. Rao, R. V., Poksay, K. S., Castro-Obregon, S., Schilling, B., Row, R. H., del Rio, G., Gibson, B. W., Ellerby, H. M., and Bredesen, D. E. (2004) *J. Biol. Chem.* **279**, 177–187
 26. Muzio, M., Chinnaiyan, A. M., Kischkel, F. C., O'Rourke, K., Shevchenko, A., Ni, J., Scaffidi, C., Bretz, J. D., Zhang, M., Gentz, R., Mann, M., Kramer, P. H., Peter, M. E., and Dixit, V. M. (1996) *Cell* **85**, 817–827
 27. Micheau, O., and Tschopp, J. (2003) *Cell* **114**, 181–190
 28. Fujita, H., Yamanaka, M., Imamura, K., Tanaka, Y., Nara, A., Yoshimori, T., Yokota, S., and Himeno, M. (2003) *J. Cell Sci.* **116**, 401–414
 29. Jin, Z., and El-Deiry, W. S. (2006) *Mol. Cell. Biol.* **26**, 8136–8148
 30. Raoul, C., Pettmann, B., and Henderson, C. E. (2000) *Curr. Opin. Neurobiol.* **10**, 111–117
 31. Sedel, F., Bechade, C., Vyas, S., and Triller, A. (2004) *J. Neurosci.* **24**, 2236–2246
 32. Wride, M. A., and Sanders, E. J. (1995) *Anat. Embryol. (Berl.)* **191**, 1–10
 33. Narita, T., Nishimura, T., Yoshizaki, K., and Taniyama, T. (2005) *Exp. Cell Res.* **304**, 256–264
 34. de Gassart, A., Geminard, C., Fevrier, B., Raposo, G., and Vidal, M. (2003) *Blood* **102**, 4336–4344
 35. Hawari, F. I., Rouhani, F. N., Cui, X., Yu, Z. X., Buckley, C., Kaler, M., and Levine, S. J. (2004) *Proc. Natl. Acad. Sci. U. S. A.* **101**, 1297–1302
 36. Hasegawa, Y., and Bonavida, B. (1989) *J. Immunol.* **142**, 2670–2676
 37. McFarlane, S. M., Anderson, H. M., Tucker, S. J., Jupp, O. J., and MacEwan, D. J. (2000) *Mol. Cell Biochem.* **211**, 19–26
 38. Bellomo, G., Perotti, M., Taddei, F., Mirabelli, F., Finardi, G., Nicotera, P., and Orrenius, S. (1992) *Cancer Res.* **52**, 1342–1346
 39. Kong, S. K., Fung, K. P., Choy, Y. M., and Lee, C. Y. (1997) *Oncology* **54**, 55–62
 40. Draper, D. W., Harris, V. G., Culver, C. A., and Laster, S. M. (2004) *J. Immunol.* **172**, 2416–2423
 41. Saito, M., Hanson, P. I., and Schlesinger, P. (2007) *J. Biol. Chem.* **282**, 27327–27333
 42. Wozniak, A. L., Wang, X., Stieren, E. S., Scarbrough, S. G., Elferink, C. J., and Boehning, D. (2006) *J. Cell Biol.* **175**, 709–714

Alix and ALG-2 Are Involved in Tumor Necrosis Factor Receptor 1-induced Cell Death

Anne-Laure Mahul-Mellier, Flavie Strappazzon, Anne Petiot, Christine Chatellard-Causse, Sakina Torch, Béatrice Blot, Kimberley Freeman, Loriane Kuhn, Jérôme Garin, Jean-Marc Verna, Sandrine Fraboulet and Rémy Sadoul

J. Biol. Chem. 2008, 283:34954-34965.

doi: 10.1074/jbc.M803140200 originally published online October 20, 2008

Access the most updated version of this article at doi: [10.1074/jbc.M803140200](https://doi.org/10.1074/jbc.M803140200)

Alerts:

- [When this article is cited](#)
- [When a correction for this article is posted](#)

[Click here](#) to choose from all of JBC's e-mail alerts

This article cites 42 references, 22 of which can be accessed free at <http://www.jbc.org/content/283/50/34954.full.html#ref-list-1>

Survival response-linked Pyk2 activation during potassium depletion-induced apoptosis of cerebellar granule neurons

Flavie Strappazon,^{a,b} Sakina Torch,^{a,b} Yaël Trioulier,^c Béatrice Blot,^{a,b}
Rémy Sadoul,^{a,b} and Jean-Marc Verna^{a,b,*}

^aInstitut National de la Santé et de la Recherche Médicale (INSERM), Laboratoire Neurodégénérescence et Plasticité, EMI108, France

^bUniversité Joseph Fourier, Grenoble I, F-38043 Grenoble, France

^cURA CEA-CNRS 2210, Service Hospitalier Frédéric Joliot, DRM, DSV, CEA, F-91401 Orsay cedex, France

Received 31 May 2006; revised 27 October 2006; accepted 14 November 2006
Available online 22 December 2006

Numerous extracellular stimuli trigger *trans*-autophosphorylation at Tyr⁴⁰² of Pyk2, inducing its activation. Pyk2 is a key mediator of several signaling pathways and has been implicated in apoptosis induced by specific stress signals. We investigated whether Pyk2 participates in cerebellar granule neuron (CGN) apoptosis induced by the suppression of membrane depolarization. We demonstrate that shifting CGN cultures from 25 mM to 5 mM KCl-containing medium induces an early, transient 70% increase in phosphorylated Tyr⁴⁰² and Tyr⁵⁸⁰ Pyk2 levels that is triggered by Ca²⁺ released from intracellular stores and mediated by calmodulin (CaM). Overexpression of Pyk2 increases CGN survival after 24 h by 70% compared to the control, thus suggesting that Pyk2 is involved in an anti-apoptotic response to K⁺ lowering. Furthermore, we show that CGN grown in K25 medium exhibit detectable CaM-dependent Pyk2 activity. When silencing Pyk2 activity by expressing a dominant-negative form, only 40% of the transfected neurons were alive 24 h after transfection when compared to the control. Overall, the present findings demonstrate for the first time that Pyk2 is a critical mediator of CGN survival.

© 2006 Elsevier Inc. All rights reserved.

Keywords: Cerebellar granule neurons; Apoptosis; Pyk2; Membrane depolarization; Calmodulin; Potassium depletion

Introduction

The 110-kDa nonreceptor tyrosine kinase Pyk2, also known as RAFTK (Avraham et al., 1995), CAK-β (Sasaki et al., 1995), pp125^{FAK2} (Herzog et al., 1996) or CADTK (Yu et al., 1996), is a member of the focal adhesion kinase (FAK) family. Pyk2 is activated by a variety of extracellular stimuli, including stress signals, such as TNFα, UV light or dexamethasone (Avraham et al., 2000; Chauhan et al., 1999; Pandey et al., 1999b; Tokiwa et al., 1996; Xiong and Parsons, 1997; Yu et al., 1996) and stimuli that elevate the cytoplasmic free Ca²⁺ concentration and/or activate protein kinase C (PKC) (Girault et al., 1999; Guo et al., 2004; Huang et al., 2001; Lev et al., 1995; Siciliano et al., 1996; Yu et al., 1996). Pyk2 activation in response to a rise in intracellular [Ca²⁺] can also be mediated by calmodulin (CaM) or CaM-dependent kinase II (CaMKII) (Della Rocca et al., 1997; Ginnan and Singer, 2002; Heidinger et al., 2002; Zwick et al., 1999). Upon stimulation, Pyk2 undergoes *trans*-autophosphorylation at Tyr⁴⁰², which induces its activation (Dikic et al., 1996). Pyk2 then recruits and activates Src family kinases that in turn further phosphorylate Pyk2 at three other tyrosine residues (Tyr⁵⁷⁹, Tyr⁵⁸⁰ and Tyr⁸⁸¹), phosphorylation at Tyr⁵⁷⁹ and Tyr⁵⁸⁰ being required for full activation of Pyk2 (Avraham et al., 2000; Dikic et al., 1996; Li et al., 1999; Park et al., 2004). Pyk2 is implicated as an upstream activator kinase in several intracellular signaling cascades (Avraham et al., 2000 for review), such as the p42/p44 ERK MAPK (Blaukat et al., 1999; Dikic et al., 1996; Lev et al., 1995), p38 MAPK (Pandey et al., 1999a; Tian et al., 2000) and JNK pathways (Blaukat et al., 1999; Tokiwa et al., 1996; Yu et al., 1996). Besides its kinase function, Pyk2 also acts as a scaffold protein and is associated in many cell types with various proteins, including PDK1 and phospholipase D2 (Avraham et al., 2000; Banno et al., 2005; Taniyama et al., 2003).

The ability of Pyk2 to be activated in response to a great variety of stimuli places it as a central player in the regulation of several distinct cellular processes (Andreev et al., 1999; Avraham et al., 2000; Girault et al., 1999; Lev et al., 1995; Li et al., 1999; Yu et al.,

Abbreviations: CAK-β, cell-adhesion kinase-β; CADTK, calcium-dependent tyrosine kinase; CaM, Ca²⁺/calmodulin; CaMKII, Ca²⁺ CaM-dependent kinase II; FAK, focal adhesion kinase; JNK, c-Jun N-terminal kinase; MAPK, mitogen-activated protein kinase; PKC, protein kinase C; PI3-K, phosphoinositide 3-kinase; Pyk2, proline-rich tyrosine kinase 2; RAFTK, related adhesion focal tyrosine kinase.

* Corresponding author. Inserm, E108, Pavillon de Neurologie, CHU Grenoble, BP 217, F-38049 Grenoble cedex 9, France. Fax: +33 476765822.

E-mail address: Jean-Marc.Verna@ujf-grenoble.fr (J.-M. Verna).

Available online on ScienceDirect (www.sciencedirect.com).

1996). In particular, it has been shown that, depending on the context, Pyk2 signaling can be involved in either cell survival or apoptosis. Thus, Pyk2 has been shown to mediate the trophic response of the murine line D1 to IL-7 (Benbernou et al., 2000), the antiapoptotic effect of endothelin-1 in cultured rat cardiomyocytes (Ogata et al., 2003) or the anoikis resistance of lung tumor cells (Wei et al., 2004). The first evidence of a pro-apoptotic function of Pyk2 came from the observation that its overexpression in rat and mouse fibroblasts leads to apoptotic cell death (Xiong and Parsons, 1997). Subsequently, the role of Pyk2 as a mediator of apoptotic signaling was reported in several death paradigms (Avdi et al., 2001; Nakagawa-Yagi et al., 2001; Pandey et al., 1999a,b; Ueda et al., 2000). For example, dexamethasone-induced apoptosis in multiple myeloma cells was shown to be associated with Pyk2 activation; in addition, overexpression of wild-type Pyk2 in these cells induces apoptosis, while expression of a kinase inactive form of Pyk2 blocked dexamethasone-induced apoptosis (Chauhan et al., 1999). More recently, it was shown that a high level of chronic Pyk2 activation promotes apoptotic signaling in cardiomyocytes (Melendez et al., 2004).

Pyk2 is highly expressed in brain where it plays crucial roles through, in particular, calcium-dependent signaling cascades (Avraham et al., 1995; Girault et al., 1999; Sasaki et al., 1995; Xiong and Mei, 2003). Thus, membrane depolarization increases tyrosine phosphorylation of Pyk2 in PC12 cell line and hippocampal slices (Corvol et al., 2005; Derkinderen et al., 1998; Lev et al., 1995; Park et al., 2000a; Siciliano et al., 1996). Activation of Pyk2 and its interaction with Src kinases lead to the formation of multiple molecular complexes that regulate several neuronal processes, such as neurite outgrowth, synaptic plasticity and differentiation (Avraham et al., 2000; Girault et al., 1999; Huang et al., 2001; Ivankovic-Dikic et al., 2000; Park et al., 2000b; Xiong and Mei, 2003). By contrast, the putative involvement of Pyk2 in neuronal survival or in response to stress is much less documented (Banno et al., 2005; Girault et al., 1999). To address this issue we investigated whether Pyk2 is involved in cerebellar granule neurons (CGN) apoptosis induced by suppression of trophic support. Cerebellar granule neurons (CGN) can survive in vitro in a high potassium (25 mM KCl) concentration in the absence of serum or growth factors, a condition supposed to mimic electrical activity through membrane depolarization, but die when shifted to the physiological K^+ concentration (5 mM KCl) (D'Mello et al., 1993; Gallo et al., 1987; Trioulier et al., 2004). Our results show that Pyk2 kinase activity is stimulated following induction of apoptosis and demonstrate that the overexpression of wild-type Pyk2 blocks, or at least delays, apoptosis induced by lowering K^+ . In line with a prosurvival function of Pyk2 in CGN, we found that the silencing of Pyk2 activity by expressing a dominant-negative form leads to the extensive death of CGN grown under depolarizing conditions. Altogether these findings thus demonstrate for the first time that Pyk2 is a critical mediator of CGN survival.

Results

K^+ depletion-induced apoptosis is characterized by an early, transient increase in Pyk2 activity and prevented by Pyk2 overexpression

CGN can be maintained for several days in vitro in a medium containing 25 mM KCl (K25 medium) in the absence of serum

or growth factors (Gallo et al., 1987). Reducing KCl concentration to 5 mM (K5 medium) triggers their apoptosis. As depicted in Fig. 1A, cell viability, assessed by MTT assay, is already significantly reduced to about 70% of the control 6 h after K^+ depletion and, 18 h later, approximately 30% of the neurons are still alive relative to K25 control cultures. Pyk2 autophosphorylation at Tyr⁴⁰² is considered to be a fundamental step in its activation since 70% of its tyrosine kinase activity is reported to be related to autophosphorylation (Li et al., 1999). We thus examined Pyk2 phosphorylation status by immunoblotting with an antibody that selectively recognizes Tyr⁴⁰²-phosphorylated Pyk2. Pyk2 is autophosphorylated in CGN grown in K25 medium, as evidenced by the presence of a clear phospho-Tyr⁴⁰² immunoreactive band at 116 kDa (Fig. 1B). When CGN were shifted to K5 medium, the level of phospho-Tyr⁴⁰² Pyk2 increased, peaking at 2h; at this time, phospho-Tyr⁴⁰² Pyk2/total Pyk2 ratio was about 70% greater than that recorded at the time of K^+ depletion ($t=0$; Fig. 1B). Phospho-Tyr⁴⁰² Pyk2 content then returned within 4 h to the control ($t=0$) level. A similar enhancement of Pyk2 phosphorylation at Tyr⁵⁸⁰ was evidenced using a specific anti-phospho-Tyr⁵⁸⁰ Pyk2 antibody (Fig. 1C), thus indicating that K^+ depletion-induced Pyk2 autophosphorylation promotes full, Src-mediated, Pyk2 activation and activity.

These results demonstrate for the first time that induction of CGN apoptosis by lowering extracellular potassium induces an early and transient enhancement of Pyk2 activation. This suggests that a transitory hyperactivity of the enzyme takes place during the early phase of K^+ depletion-induced apoptosis, at a time when no substantial cell death is observed.

To gain insights into the functional significance of Pyk2 activation in response to potassium depletion, neurons were transfected with wild-type Pyk2 and, 24 h later, deprived of K^+ (Fig. 2). It should be mentioned that several previous reports have demonstrated that overexpression of Pyk2 leads to its spontaneous activation and tyrosine phosphorylation (Melendez et al., 2004; Meyer et al., 2004; Tokiwa et al., 1996). At the end of the experiment, cellular viability was then determined by cell counting as described in Experimental methods. As depicted in Fig. 2, expression of wild-type Pyk2 markedly reduced apoptosis; indeed, the number of living wild-type Pyk2-overexpressing neurons 24 h following K^+ depletion was about 70% greater than that of RFP control transfectants. Thus, exogenously expressed wild-type Pyk2 is sufficient to enhance CGN survival following K^+ depletion. The protective effect of Pyk2 overexpression suggests that the increase in Pyk2 activity observed when CGN are deprived of the depolarizing level of extracellular KCl is a defense response aimed at protecting cells from stress.

Calmodulin mediates the Ca^{2+} -dependent enhancement of Pyk2 activity following K^+ depletion

We next attempted to identify some of the upstream events leading to low K^+ -induced Pyk2 activation in our model. Activity-dependent survival in many neuronal systems is thought to be mediated by a sustained rise of cytosolic free Ca^{2+} , resulting from a Ca^{2+} influx through voltage-gated calcium channels (Gallo et al., 1987; Franklin and Johnson, 1992). Although K^+ depletion has been associated with an immediate and permanent decrease in the levels of free intracellular calcium due to the closure of voltage

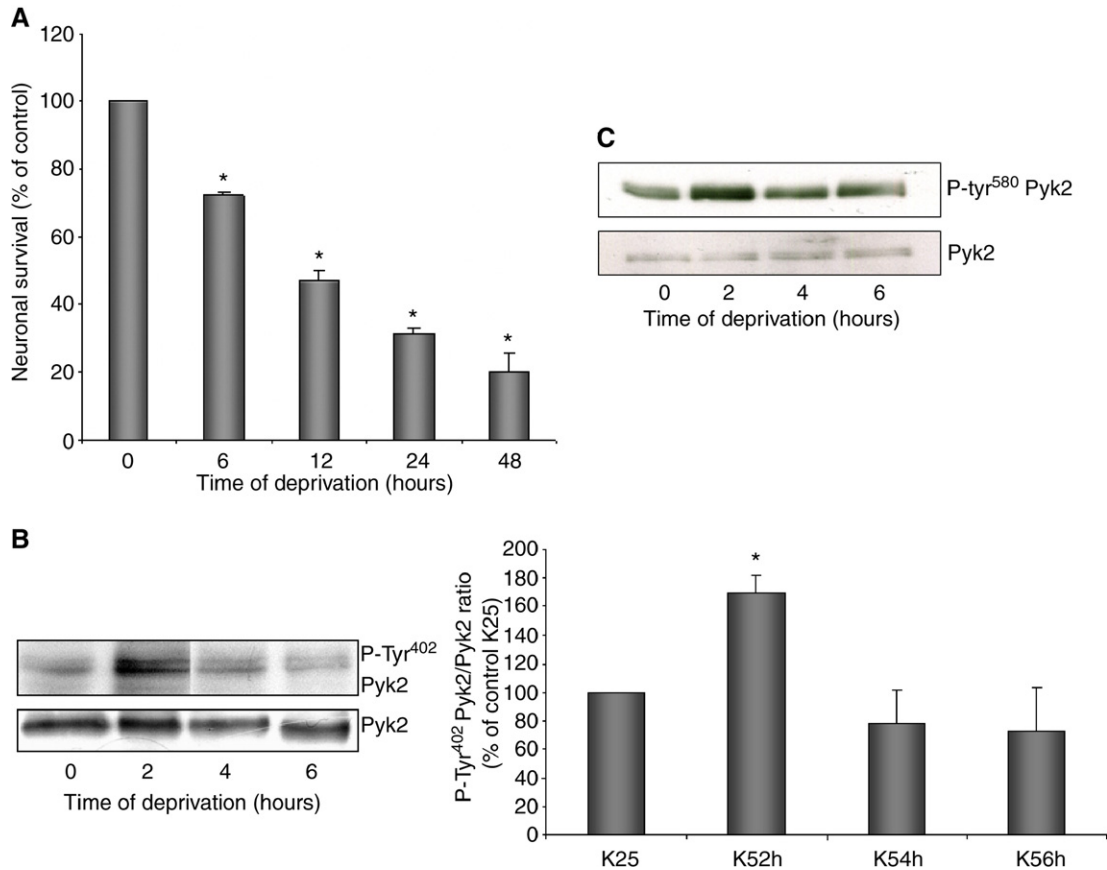


Fig. 1. Potassium depletion induces apoptosis of CGN which is accompanied by an early increase in Pyk2 activation. (A) After 5 DIV, CGN cultures were switched from K25 to K5 medium. The percentage of viable neurons was estimated at various time intervals using MTT assay. Results are expressed as a percentage of viable neurons (\pm SD) in potassium-deprived cultures relative to control K25 cultures. Each point value represents the mean \pm SD of triplicate wells from three independent experiments. Statistical analysis was performed by analysis of variance (one-way ANOVA followed by Scheffe's post hoc test). * P < 0.05 versus control at the time of medium shift ($t=0$). (B) After the indicated intervals, the neurons were lysed and Pyk2 autophosphorylation was assessed by means of immunoblotting with phospho-Tyr⁴⁰² Pyk2 antibody or Pyk2 antibody. Left panel: Results depict a representative experiment. Right panel: Densitometric analysis of phospho-Tyr⁴⁰² Pyk2 levels. Immunoblot signals were quantified and the phospho-Tyr⁴⁰² Pyk2/Pyk2 ratio calculated. The phosphorylation was normalized as a percentage of the basal level of control. Values are the means \pm SD of three experiments performed in triplicate. Statistical analysis was performed by analysis of variance (one-way ANOVA followed by Scheffe's post hoc test). * P < 0.05 versus control at the time of medium shift ($t=0$). (C) Following autophosphorylation, complete Pyk2 activation is achieved through the binding of Src and the phosphorylation of Pyk2 on Tyr^{579/580}. To demonstrate full Pyk2 activation, CGN were lysed at the indicated times and expression levels were assessed by immunoblotting with a specific phospho-Tyr⁵⁸⁰ Pyk2 antibody and Pyk2 antibody.

operated Ca²⁺ channels (Carboni and Wojcik, 1988; Courtney et al., 1990), we hypothesized that localized Ca²⁺ transients triggered in response to K⁺ lowering could be responsible for the increase in Pyk2 autophosphorylation. To test this possibility, CGN were shifted to K5 medium supplemented with either 10 μ M BAPTA-AM or 3 mM EGTA in order to chelate intracellular or extracellular Ca²⁺, respectively. The results (Fig. 3) show that blocking intracellular Ca²⁺ availability with BAPTA-AM abolished K⁺ depletion-induced Pyk2 autophosphorylation; indeed, the cellular content in phospho-Tyr⁴⁰² Pyk2 seen 2 h after K⁺ lowering in the presence of the drug was significantly reduced when compared to that of CGN grown in K5 medium alone and was similar to that found in CGN cultured in depolarizing K25 medium. In contrast, adding 3 mM EGTA to the K5 medium did not impact on the level of phospho-Tyr⁴⁰² Pyk2, demonstrating that increased Pyk2 activity following K⁺ depletion is not linked to entry of extracellular Ca²⁺. Thus, following K⁺ depletion, Pyk2

undergoes transient hyperactivation in response to a rise in cytosolic Ca²⁺ coming from intracellular stores.

Since calmodulin (CaM) is a major effector of Ca²⁺ signaling and mediates Pyk2 activity in several instances, we next evaluated its potential contribution to Pyk2 autophosphorylation induced by K⁺ depletion. To this end, CGN cultures were exposed to W13, an extensively used specific CaM antagonist, and W12, its less active structural analog as control (Hidaka and Tanaka, 1983). We observed that W13, but not W12, abrogated the increase in cellular levels of the Tyr⁴⁰²-phosphorylated form of Pyk2 associated with K⁺ depletion (Fig. 4), thus mimicking the effect of BAPTA-AM on Pyk2 phosphorylation (Fig. 3). The observed inhibitory effect is thus specific for CaM since it was not observed in the presence of W12. These findings implicate CaM as key mediator of the Ca²⁺-dependent increase in Pyk2 activity associated with K⁺ lowering.

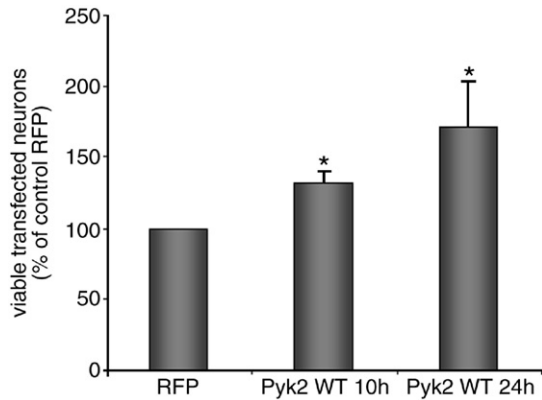


Fig. 2. Overexpression of Pyk2 protects CGN from death induced by potassium withdrawal. After 4 DIV, CGN were transfected with an expression vector coding for RFP or wild-type Pyk2 (Pyk2 WT). One day later, cultures were deprived of potassium (K5 medium) and grown for 10 h or 24 h. Cultures were then labeled with anti-Myc antibody and Hoechst dye. The transfected neurons showing condensed or fragmented nuclei (Hoechst staining) were scored as dying, and the percentage of transfected viable neurons was determined at 10 h and 24 h. Values are given for each time point after normalization with respect to RFP transfected control. For each condition, a total of 200–400 transfected neurons per construct were counted in 10 random fields in two or three different wells from 3 independent experiments. Statistical analysis was performed by analysis of variance (one-way ANOVA followed by Scheffe's post hoc test). * $P < 0.05$ versus control RFP-expressing neurons.

Pyk2 activity is involved in CGN survival induced by membrane depolarization

The above results prompted us to investigate whether Pyk2 could mediate the survival-promoting Ca^{2+} /CaM signaling pathway. To clarify this point, Pyk2 activity was selectively inhibited by expressing a dominant-negative form of Pyk2 (Pyk2 K457A) that is mutated in the Mg^{2+} -ATP-binding site residue (K457A) abolishing tyrosine kinase activity and tyrosine autophosphoryla-

tion (Li et al., 1999). The results show that the expression of the dominant-negative form of Pyk2 reduces membrane-depolarization-induced CGN survival compared to that of CGN transfected with either wild-type Pyk2 or an RFP-containing vector as control (Fig. 5). Thus, 48 h after transfection, only about 40% of Pyk2 K457A-expressing neurons were still alive. The death induced by the expression of Pyk2 K457A is apoptotic in nature, as attested by the presence of the nuclear morphological hallmarks of apoptosis and caspase activity (Fig. 5). Thus, the inactivation of Pyk2 kinase activity counteracts the trophic support provided by membrane depolarization leading to CGN apoptosis.

We then investigated whether Pyk2 activity in these culture conditions is also dependent upon CaM as well. As depicted in Fig. 6, treatment of 5-day CGN cultures with 30 μM W13 for 5 h led to a significant 40% decrease in phospho-Tyr⁴⁰² Pyk2 content when compared to untreated or W12-exposed neurons. These results thus indicate that active CaM is required for Tyr⁴⁰² autophosphorylation of Pyk2 under depolarizing conditions. During the course of this study, we noticed that the treatment of K25 cultures with W13 (30 μM) dramatically reduced CGN viability. Thus only 25% cells survived after a 14-hour exposure to W13 compared to cultures grown in K25 medium with or without W12 (Fig. 7A). This is consistent with the earlier report of Gallo et al. (1987) showing that calmodulin inhibitors (1 μM trifluoperazine or calmidazolium) blocked the beneficial effect of K^+ -induced depolarization on cerebellar granule cells. It must be pointed out that exposure to W13 also greatly increased neuronal death due to potassium depletion (Fig. 7A), suggesting that survival mechanisms involving CaM are still operating, at least during the early phase of the apoptotic cascade. The survival-promoting effects of depolarization on CGN have been shown to require the activity of Akt (Miller et al., 1997; Shimoke et al., 1999). By measuring the cellular content in phospho-Ser⁴⁷³ Akt and total Akt using specific antibodies, we found that a 5 h exposure to 30 μM W13 reduced the cellular level of phospho-Ser⁴⁷³ by 60% compared to untreated cultures (Fig. 7B); by contrast, W12 had no impact on this phosphorylation which remained essentially the same as in control K25 cultures. These results indicate that CaM is an upstream

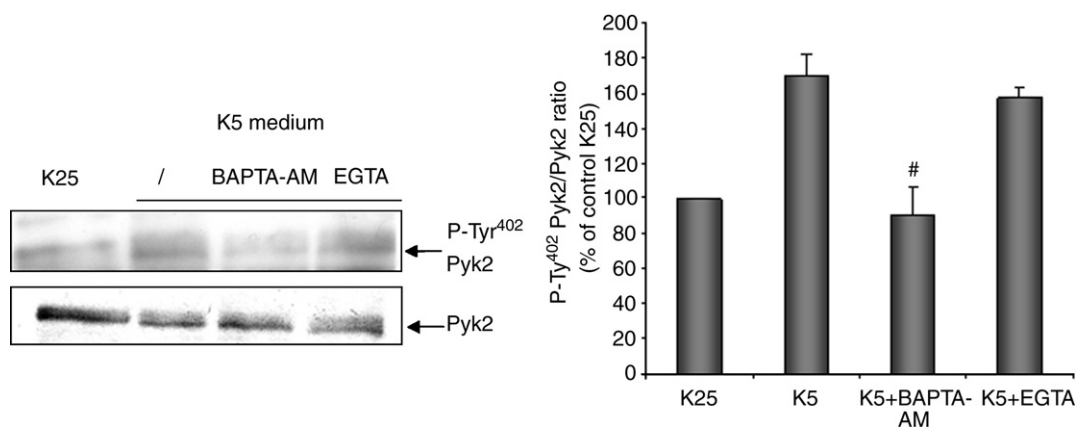


Fig. 3. Intracellular Ca^{2+} dependency of K^+ depletion-induced increase in Pyk2 autophosphorylation. After 5 DIV, CGN cultures were switched from K25 to K5 medium, with or without BAPTA-AM (10 μM) or EGTA (3 mM) and further grown for 2 h. Pyk2 autophosphorylation was assessed by immunoblotting with phospho-Tyr⁴⁰² Pyk2 antibody or Pyk2 antibody. Left panel: A representative experiment is shown. Right panel: Densitometric analysis of phospho-Tyr⁴⁰² Pyk2 levels. Immunoblot signals were quantified and the phospho-Tyr⁴⁰² Pyk2/Pyk2 ratio calculated. The phosphorylation was normalized as a percentage of the basal level of control. Values are the means \pm SD of three experiments performed in triplicate. Statistical analysis was performed by analysis of variance (one-way ANOVA followed by Scheffe's post hoc test). # $P < 0.05$ versus K5 cultures.

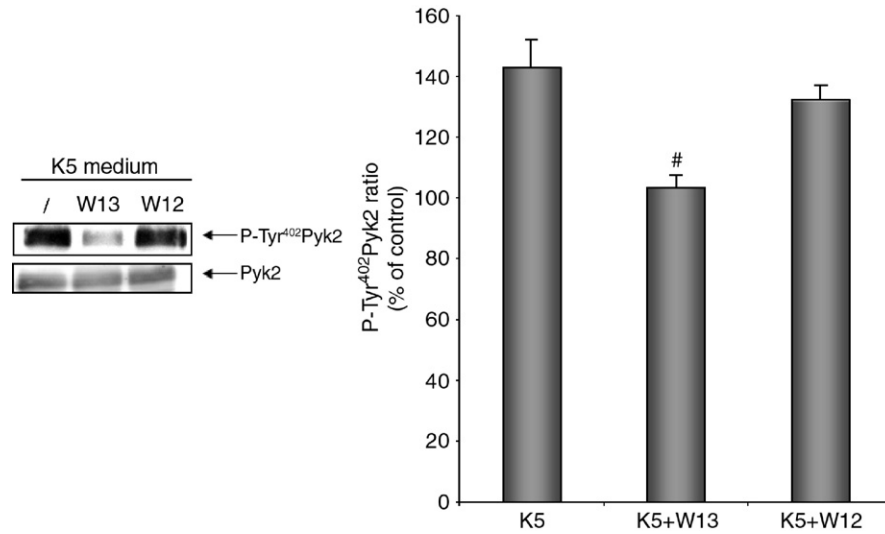


Fig. 4. CaM mediates the Ca²⁺-dependent increase in Pyk2 autophosphorylation following K⁺ depletion. After 5 DIV, K5 cultures, with or without the CaM specific inhibitor W13 (30 μM) or its inactive analog W12 (30 μM), were grown for 2 h. Pyk2 autophosphorylation was assessed by immunoblotting with phospho-Tyr⁴⁰² Pyk2 antibody or Pyk2 antibody. Left panel: A representative experiment is shown. Right panel: Densitometric analysis of phospho-Tyr⁴⁰² Pyk2 levels. Immunoblot signals were quantified and the phospho-Tyr⁴⁰² Pyk2/Pyk2 ratio calculated. The phosphorylation was normalized as a percentage of the basal level of control. The increase in phosphorylation was normalized to the basal level recorded in K25 medium and expressed as a percentage. Values are the means ± SD of three experiments performed in triplicate. Statistical analysis was performed by analysis of variance (one-way ANOVA followed by Scheffe's post hoc test). [#]*P* < 0.05 versus control K5 cultures.

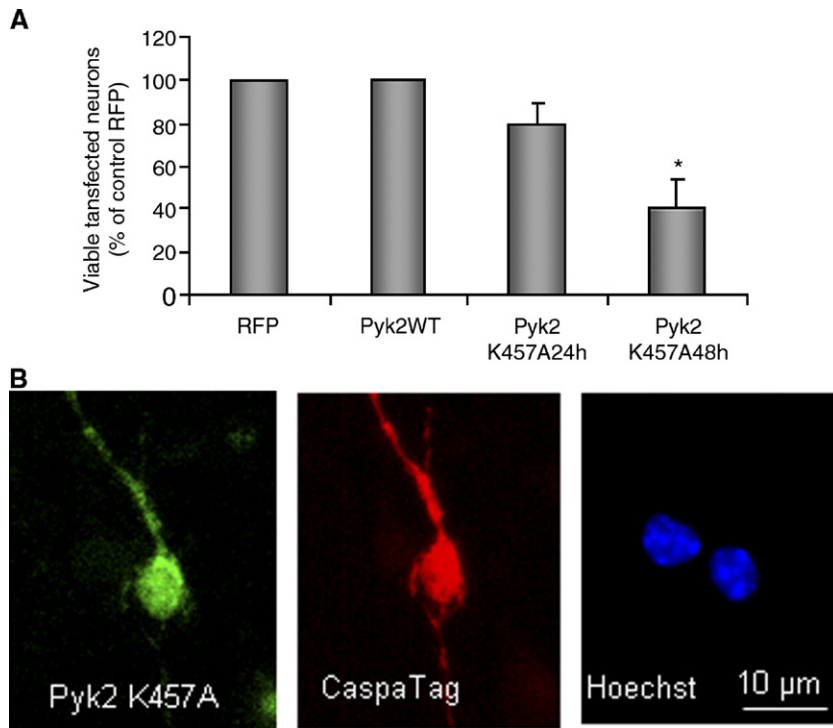


Fig. 5. Pyk2 K457A expression induces death of CGN cultured in K25 medium. After 4 DIV, CGN were transfected with an expression vector coding for either wild-type Pyk2 (Pyk2 WT), a dominant-negative mutant of Pyk2 (Pyk2 K457A) or an RFP control vector. One day later, cultures were kept in K25 medium and grown for 24 h. Cultures were then labeled with an anti-Myc antibody, CaspaTagTM to detect active caspases, and Hoechst dye. The transfected neurons showing condensed or fragmented nuclei (Hoechst staining) were scored as dying, and the percentage of viable transfected neurons was determined at 24 h and 48 h. Values are given for each time point with respect to the RFP control vector. For each condition, a total of 200–400 transfected neurons per construct were counted in 10 random fields in two or three different wells from 3 independent experiments. Statistical analysis was performed by analysis of variance (one-way ANOVA followed by Scheffe's post hoc test). ^{*}*P* < 0.05 versus control Pyk2 WT-expressing neurons. The bottom panel shows a Pyk2 K457A-expressing neuron triple-stained for Pyk2 K457A (red; revealed with anti-myc), activated caspases (green; CaspaTagTM) and nuclear morphology (blue; Hoechst staining). No caspase activity is detected in the adjacent, untransfected neuron. Scale bar: 10 μm.

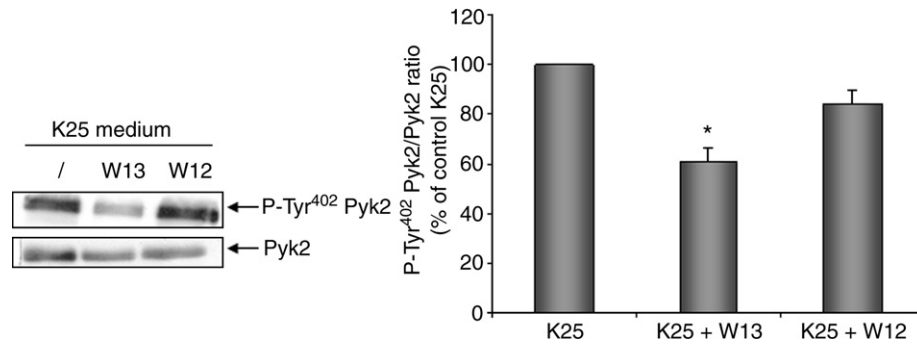


Fig. 6. CaM mediates Pyk2 autophosphorylation in K25 medium. After 5 DIV, K25 cultures, with or without the CaM specific inhibitor W13 (30 μ M) or its inactive analog W12 (30 μ M), were grown for 5 h. Pyk2 autophosphorylation was assessed by immunoblotting with phospho-Tyr⁴⁰² Pyk2 antibody or Pyk2 antibody. Left panel: A representative experiment is shown. Right panel: Densitometric analysis of phospho-Tyr⁴⁰² Pyk2 levels. Immunoblot signals were quantified and the phospho-Tyr⁴⁰² Pyk2/Pyk2 ratio calculated. The phosphorylation was normalized as a percentage of the basal level recorded in K25 medium. Values are the means \pm SD of three experiments performed in triplicate. Statistical analysis was performed by analysis of variance (one-way ANOVA followed by Scheffe's post hoc test). * P <0.05 versus control K25 cultures.

activator of Akt. We then wondered whether the regulation of Akt by CaM could be mediated through Pyk2. To this end, CGN were transfected with either Pyk2 WT, as control, or Pyk2 K457A, then further grown under depolarizing conditions for 24 h followed by immunolabeling with an anti-phospho-Ser⁴⁷³ Akt antibody (Fig. 7C). While Pyk2 WT-transfected neurons contain detectable levels of phospho-Ser⁴⁷³ Akt, those expressing Pyk2 K457A exhibited little or no activated Akt. Hence, these results strongly support the idea that Pyk2 lies upstream of Akt activation. In agreement with this statement, in contrast to untransfected neurons, Akt is still activated in neurons expressing Pyk2 WT after 24 h in non-depolarizing K5 medium (data not shown).

Altogether these results confirm previous results showing that depolarization-induced CGN survival critically relies on calmodulin-dependent processes. They demonstrate for the first time that Pyk2 is an important downstream component of the Ca²⁺/CaM-mediated survival cascade involved in the activation of Akt signaling.

Discussion

During the postnatal development of cerebellum, electrical activity promotes the calcium-dependent survival of neurons that have made appropriate synaptic connections. Depolarization by K⁺ of primary cultures of postnatal CGN induces Ca²⁺ influx through activation of L-type voltage-gated Ca²⁺ channels (Koike et al., 1989). These cultures provide a well-established model system to mimic the functional innervation of postmigratory granule cells in vivo (Gallo et al., 1987). Exposing CGN to serum-free medium containing a physiological concentration of KCl abrogates electrical-induced neuroprotection and triggers apoptosis (D'Mello et al., 1993). For years, this system has been extensively used as a model to investigate the intracellular signaling pathways underlying either activity-dependent survival or apoptosis. However, although several studies have revealed that in various neuronal systems depolarization-induced [Ca²⁺]_i increase activates the nonreceptor protein kinase Pyk2 (Derkinderen et al., 1996; Lev et al., 1995; Siciliano et al., 1996; Zwick et al., 1999), to date very little attention has been paid to whether and how this activity could regulate survival and death of post-mitotic neurons. The results of the present study provide, to our knowledge, the first evidence that

Pyk2 is critically involved in depolarization-induced survival of CGN. This conclusion comes mainly from two observations. Firstly, the inactivation of Pyk2 by expressing a dominant-negative mutant overcomes the trophic effect of depolarization, and, secondly, increasing Pyk2 activity by overexpressing wild-type Pyk2 prevents CGN apoptosis induced by the suppression of membrane depolarization.

In line with previous reports, Pyk2 was found to be phosphorylated at Tyr⁴⁰², its major autophosphorylation site, and Tyr⁵⁸⁰ in CGN maintained in 25 mM KCl-containing medium, indicative of a basal, constitutive Pyk2 activity in these conditions. Moreover, we observed that the pharmacological blockade of CaM activity, but not that of PKC (data not shown), a well known activator of Pyk2 in neurons (Lev et al., 1995; Siciliano et al., 1996; Yu et al., 1996), inhibits Pyk2 phosphorylation at Tyr⁴⁰² thus suggesting that CaM is the main upstream regulator of Ca²⁺-induced Pyk2 activation.

The mechanism of Pyk2 activation by CaM remains to be elucidated. CaMKII, a CaM-dependent kinase, might participate in Ca²⁺-dependent Pyk2 activation in neuronal cells (Zwick et al., 1999; Guo et al., 2004); however, we have some evidence indicating that Pyk2 phosphorylation remains unchanged in the presence of KN62, an inhibitor of CaM Kinase. Furthermore, during the course of this study, we noticed that the specific CaM inhibitor W13 (Soler et al., 1998) significantly prevented the trophic effect of K⁺-induced depolarization. Several distinct groups have already made similar observations (Gallo et al., 1987; Hack et al., 1993; Boutillier et al., 1999), although, in these studies, CaM was inhibited with trifluoperazine and/or calmidazolium which are known to also block voltage-dependent Ca²⁺ channels thus preventing calcium entry (Doroshenko et al., 1988; Franklin et al., 1995; Greenberg et al., 1987). However, our findings definitely establish that CaM plays a pivotal role in depolarization-promoted survival of CGN. CaMKIV, another downstream CaM effector, appears to be important for CGN survival via membrane depolarization (See et al., 2001). That Pyk2 might be a target of this kinase is worth considering and deserves further study.

CaM has been shown to regulate the activity of Akt (Lafon-Cazal et al., 2002), a well known pivotal mediator of CGN survival (Miller et al., 1997; Shimoke et al., 1999). In agreement, we found that W13 significantly reduced the Akt phosphorylation on Ser⁴⁷³.

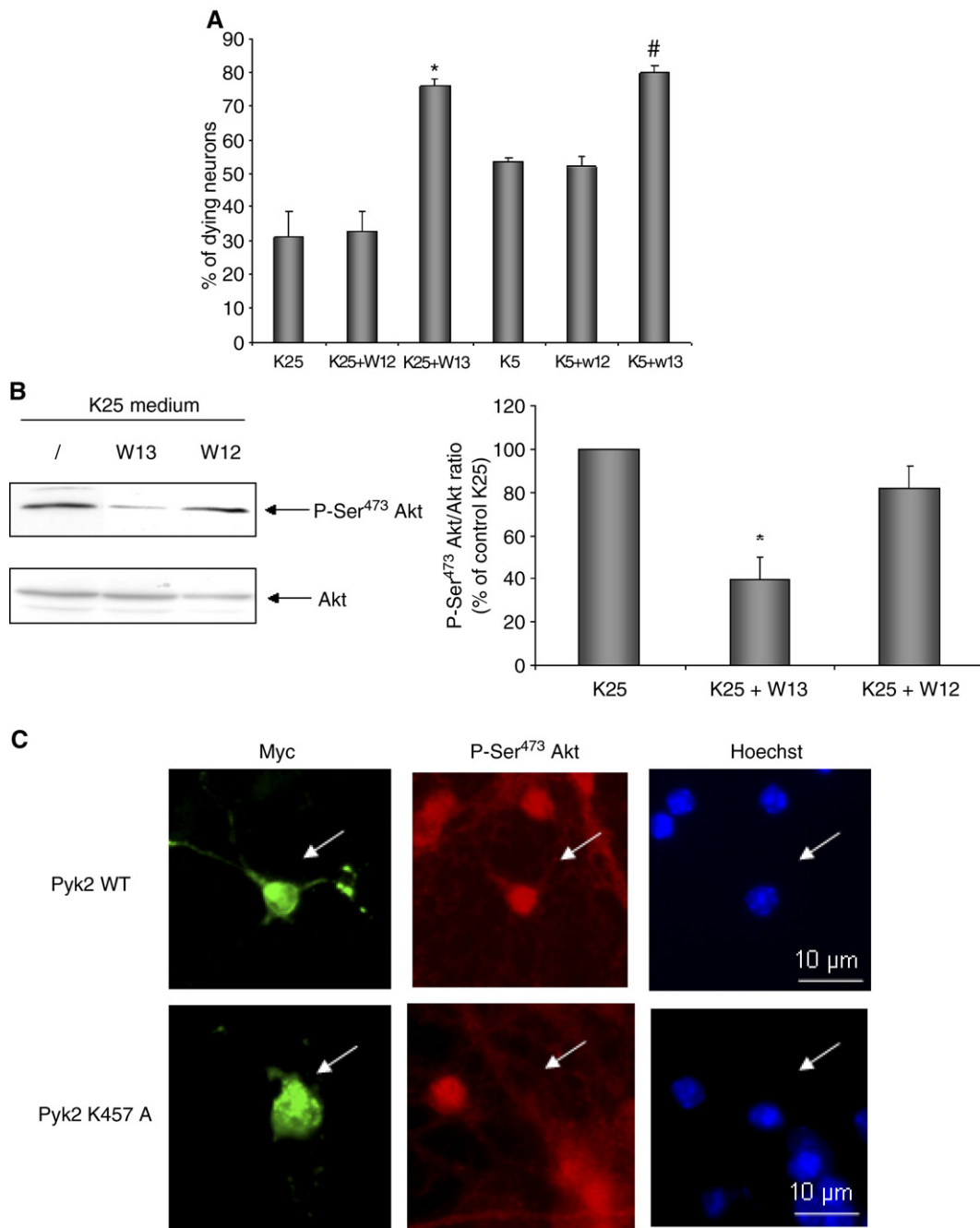


Fig. 7. CaM, through Pyk2, promotes Akt survival signaling cascade induced by membrane depolarization. (A) Effect of CaM inhibition on CGN viability. After 5 DIV, CGN cultures were switched from K25 to K5 medium with or without W13 (30 μ M) or W12 (30 μ M). Cell viability was determined 14 h after K⁺ depletion using the cell counting. Results are expressed as a percentage of dying neurons (\pm SD). Each point value represents the mean \pm SD of triplicate wells from three independent experiments. Statistical analysis was performed by analysis of variance (one-way ANOVA followed by Scheffe's post hoc test). * P <0.05 versus control K25 cultures or # P <0.05 versus control K5 cultures. No statistical difference was found between neurons grown in either medium containing W12 and their respective controls. (B) CaM inhibition strongly reduces Akt activity. After 5 DIV, K25 medium cultures were treated for 5 h with 30 μ M of either W13 or W12. Akt activity was evaluated by determining the cellular content in phospho-Ser⁴⁷³ Akt assessed by means of immunoblotting with phospho-Ser⁴⁷³ Akt antibody or Akt antibody. Left panel: A representative experiment is shown. Right panel: Densitometric analysis of phospho-Tyr⁴⁰² Pyk2 levels. Immunoblots were quantified by equalizing phospho-Ser⁴⁷³ Akt band intensity to the total Akt. The increase in phosphorylation was normalized to the basal level recorded in K25 medium and expressed as a percentage. Values are the means \pm SD of three experiments performed in triplicate. Statistical analysis was performed by analysis of variance (one-way ANOVA followed by Scheffe's post hoc test). * P <0.05 versus K25 cultures. (C) After 4 DIV, CGN were transfected with an expression vector coding for either wild-type Pyk2 (Pyk2 WT) or a dominant-negative mutant of Pyk2 (Pyk2 K457A) then grown for 24 h in K25 medium. Neurons were then fixed and labeled with anti-Myc antibody, anti-phospho-Ser⁴⁷³ Akt antibody and Hoechst. Immunofluorescence microscopy. Scale bar: 10 μ M.

In addition, experiments dealing with the expression of wild-type or dominant-negative forms of Pyk2 followed by immunocytochemical determination of Akt activity provided evidence for a putative functional link between Pyk2 and Akt activities. CaM thus appears to promote depolarization-induced CGN survival at least partly through a signaling cascade involving Pyk2 and Akt. It is well established that Akt is a direct target of phosphatidylinositol 3-kinase (PI3K) and that activation of PI3K-dependent 3-phosphoinositide-dependent protein kinase 1 (PDK1) is important for Akt activity in cells (Franke et al., 2003). Interestingly, Pyk2 was found to associate with and activate PI3K as well as Akt in various experimental situations (Banno et al., 2005; Koziak et al., 2001; Rocic et al., 2001; Rumsey et al., 2001; Sayed et al., 2000; Shi and Kehrl, 2001). In addition, Pyk2 was recently shown to physically interact with and mediate the phosphorylation of PDK1 (Taniyama et al., 2003).

In conclusion, our findings demonstrate that, at least in our culture system, Pyk2 is a key component of a Ca^{2+} /CaM-dependent signaling cascade leading to Akt activation and CGN survival induced by depolarizing conditions. The issue now is to identify the molecular mechanisms underlying the activation of Pyk2 by CaM as well as that of Akt by Pyk2.

Reducing the K^+ concentration to 5 mM leads to apoptosis of cerebellar neurons. We showed that a transient Ca^{2+} and CaM-dependent increase in Tyr⁴⁰²-phosphorylated Pyk2 levels occurs during the early phase of the death cascade. Moreover, the chelation of intracellular Ca^{2+} with BAPTA-AM abolishes this increase, while EGTA does not affect it. This indicates that Pyk2 activation following K^+ depletion is mediated through intracellular Ca^{2+} rather than by K^+ depletion-induced influx from extracellular Ca^{2+} . Pyk2 can be activated by agents that promote increase in $[\text{Ca}^{2+}]_i$ through Ca^{2+} release from intracellular stores: For example, Yu et al. (1996) have shown that exposure to the endoplasmic reticulum (ER) stressor thapsigargin, an ER Ca^{2+} -ATPase inhibitor, leads to Pyk2 activation through Ca^{2+} mobilization from intracellular stores. As K^+ depletion may trigger ER stress (Desagher et al., 2005), it is therefore possible that the transient $[\text{Ca}^{2+}]_i$ increase due to the K^+ depletion-induced Ca^{2+} release from ER stores initiates Pyk2 autophosphorylation. Moreover, we found that treatment of K5-grown CGN with W13 specifically abolishes the increase in Pyk2 autophosphorylation and substantially potentiates low- K^+ -induced death. These findings support the possibility that K^+ depletion triggers a transient Ca^{2+} release from intracellular stores which, through CaM, activates a survival response involving Pyk2. In agreement with this proposition, we present the first demonstration that, when overexpressed, Pyk2 protects CGN from cell death induced by suppression of membrane depolarization.

Several studies have evidenced, in non-neuronal as well as neuroblastoma cells, an activation of Pyk2 in response to stress signals, such as TNF α , UV light, dexamethasone, acrylamide or colchicine (Chauhan et al., 1999; Nakagawa-Yagi et al., 2001; Tokiwa et al., 1996), and, in these cases, Pyk2 induction is required for the death cascade (Chauhan et al., 1999; Xiong and Parsons, 1997). Moreover, overexpression of Pyk2 in fibroblasts has been found to induce apoptosis (Melendez et al., 2004; Xiong and Parsons, 1997), which can be prevented by FIP200 (FAK family kinase-interacting protein of 200 kDa), an endogenous inhibitor of Pyk2 (Ueda et al., 2000). In line with the results of the present study, there is however recent evidence that survival pathways can also be activated by stress and that,

in this context, Pyk2 activation can mediate stress-induced survival pathways (Banno et al., 2005; Dougherty et al., 2004; Wei et al., 2004). Thus, the function of Pyk2 during cell death may differ depending on the initiating stimulus and/or the cellular context. Concerning CGN, our experiments allow us to speculate that the enhancement of Pyk2 activity in response to K^+ depletion represents a failed effort to preserve cell viability. Pyk2 has been recently shown to associate with Alix/AIP1 (Schmidt et al., 2005), a protein involved, through its binding to Alg-2 (Missotten et al., 1999; Vito et al., 1999), in K^+ depletion-induced CGN apoptosis (Trioulier et al., 2004). Moreover, we have some recent evidence that Pyk2 phosphorylates Alix and this may regulate Alix/Alg-2 interaction (Strappazzon et al., in preparation). It is therefore possible that Pyk2 may exert, at least in part, its anti-apoptotic function through the inhibition of Alix/Alg-2 binding.

In conclusion, the present study provides evidence for a key role of Pyk2 in mediating the Ca^{2+} /CaM-dependent signaling cascade brought on by membrane depolarization in CGN. It furthermore underlines the putative involvement of Pyk2 activity in a cell response, likely triggered by compensatory Ca^{2+} mobilization from intracellular stores, aimed at handling the cellular stress originating from the suppression of membrane depolarization-induced Ca^{2+} influx.

Experimental methods

Reagents or chemicals and antibodies

Polyclonal antibodies were purchased from Cell Signaling Technology (rabbit anti-phospho-Tyr⁴⁰² Pyk2, Akt, phospho-Ser⁴⁷³ Akt antibodies), Upstate (rabbit anti-Pyk2 antibody) and Biosource (phospho-Tyr⁵⁸⁰ Pyk2). Mouse anti-Myc was from Santa Cruz Biotechnology. BAPTA-AM, W13 and W12 were from Calbiochem and EGTA from Sigma.

Cell culture media

All culture media were based on Dulbecco's modified Eagle's medium (DMEM, Invitrogen) containing 10 unit/ml penicillin, 10 $\mu\text{g}/\text{ml}$ streptomycin, 2 mM L-glutamine and 10 mM HEPES (K5 medium). KCl was added to a final concentration of 25 mM (K25 medium) and, at the beginning of the culture, supplemented with 10% fetal bovine serum (K25+S medium).

Primary neuronal cultures

Primary cultures of CGN were prepared from 6-day-old S/IOPS NMRI mice (Charles River Laboratories), as described previously (Gallo et al., 1987; Miller and Johnson, 1996), with some modifications (Trioulier et al., 2004). The cerebella were removed, cleared of their meninges, and cut into 1-mm pieces. They were then incubated at 37 °C for 10 min in 0.25% trypsin-EDTA (Invitrogen) in DMEM. Trypsin was inactivated with an equal volume of K25+S medium and 3000 units/ml DNase I (Sigma) and cerebella were dissociated by triturating with flame-polished Pasteur pipettes in DMEM containing trypsin inhibitor and 300 units/ml DNase I. Dissociated cells were centrifuged for 5 min at 500 \times g and the pellet was resuspended in fresh K25+S medium. Cells were then plated onto poly-D-lysine (10 $\mu\text{g}/\text{ml}$, Sigma) precoated 60-mm dishes and multiwell plates at a density of 3×10^5 cells/cm². Cultures were grown in K25+S medium in a humidified incubator with 5% CO₂/95% air at 37 °C. Cytosine- β -D-arabinoside (10 μM , Sigma) was added after 1 day in vitro (DIV) to prevent the growth of non-neuronal cells. After 4 DIV, K25+S medium was replaced with serum-free K25 medium to eliminate the 20% of cells dying within a few hours after serum removal (Miller and Johnson, 1996; Trioulier et al., 2004). Twenty-four hours later, cells were changed to K5

medium (induction of apoptosis) or maintained in K25 medium (control cultures). The various drugs used in this study were added at the time of switching cultures to K5 medium.

Determination of cell viability

Neuronal survival was estimated using either the MTT assay or by cell counting. The tetrazolium salt MTT [3-(4,5-dimethyl-2-thiazolyl)-2-5-diphenyl-2H tetrazolium bromide] (Sigma) was added to CGN cultures at a final concentration of 1 mg/ml and incubation of the cultures was continued for a further 30 min at 37 °C. Removing the culture medium and adding an equal volume of dimethyl sulfoxide to lyse cells and dissolve colored formazan terminated the reaction. The absorbance of each well at 540 nm, against 630 nm as reference, was determined using a Biotek EL_x-800 microplate reader (Mandel Scientific Inc.).

In other cases, at the end of the culture, cells were fixed in 4% paraformaldehyde in PBS for 10 min at 37 °C then stained with the DNA dye bisbenzimidazole (Hoechst 33342; 4 µg/ml; Sigma) in PBS for 20 min at room temperature. Cells were washed three times with PBS then mounted in Mowiol (Calbiochem) and observed under an Axiovert microscope (Zeiss) connected to a CDD camera. For each condition, random images were captured and analyzed using Metamorph™ software (Universal Imaging Corp.). Cell viability was scored on the basis of nuclear morphology, condensed or fragmented nuclei were taken to indicate cell death.

Quantification of CGN death with either method produced very comparable results.

Transfection of CGN

Plasmids containing either rat wild-type Pyk2 (bank access number: U69109) or a dominant-negative, kinase-dead Pyk2 mutant (K457A) cDNAs were generously donated by Dr. J.-A. Girault (Inserm U536, Institut du Fer à Moulin, Paris, France) and Red Fluorescent Protein (RFP) encoding vector was a gift from Dr. R.Y. Tsien (UCSD, Ca., USA). cDNAs were subcloned into pCI-MYC expression vector (Promega).

Transient transfection of cultured CGN was performed using the calcium phosphate coprecipitation method as previously described (Trioulier et al., 2004). The DNA/calcium phosphate precipitate was prepared and allowed to form for 25–30 min at room temperature before addition to the cultures. Eight micrograms of total plasmid DNA per 1.5×10^6 cells was used. After transfection, the cells were washed three times with DMEM. They were then returned to the 5% CO₂ incubator at 37 °C in K25 medium and cultured for the indicated time or switched to K5 medium 24 h later. At the end of the culture, cells were fixed and immunostained for Myc to identify transfected neurons. To assess the effect of Pyk2 overexpression, transfected neurons were scored blind as healthy or apoptotic according to nuclear morphology visualized with the DNA dye bisbenzimidazole (Hoechst 33342) as described above.

Immunofluorescence

CGN seeded on poly-D-lysine-coated coverslips were transfected and grown for 24 h then fixed in 4% paraformaldehyde in PBS for 10 min at 37 °C. After permeabilization and blocking, neurons were incubated at room temperature with primary anti-Pyk2, anti-Myc or anti-phospho-Ser⁴⁷³ Akt antibodies (1/100) then with Alexa Fluor-conjugated secondary anti-rabbit antibody (1/1000) (Dako; Denmark), for 3 h, 1 h or overnight respectively. Neuronal cultures were rinsed with PBS then stained with DNA dye bisbenzimidazole (Hoechst 33342) and coverslips were mounted using Mowiol.

Detection of active caspases

CaspaTag™ fluorescein caspase (VAD) activity kit (Chemicon) allows the detection of active caspases (caspase-1–9) in living cells through the use of a carboxyfluorescein-labeled fluoromethylketone pan-caspase inhibitor

(fam-VAD-fmk). This probe enters the cell and binds irreversibly to activated caspases. After 24 h in either K25 or K5 medium, CGN were incubated for 1 h at 37 °C with fam-VAD-fmk in accordance with the supplier's instructions and visualized under an epifluorescence microscope.

Western blot analysis

CGN were washed twice with PBS before being harvested with lysis buffer (20 mM Tris pH 7.2, 1 mM EGTA, 1 mM EDTA, 1 mM DTT, 0.27 M sucrose, 1% Triton X-100, 0.05% NP40, 1 mM Na₃VO₄, 50 mM NaF, 10 mM β-glycerophosphate and 2× protease inhibitor cocktail (Complete™, Boehringer)). Cell extracts were centrifuged at 15,000×g for 15 min at 4 °C and supernatants were stored at –80 °C. Protein concentrations were determined with BCA Protein Assay (Pierce). Proteins (20 µg) were separated by SDS-PAGE and transferred onto nylon membranes (Immobilon-P, Millipore). Membranes were incubated overnight at 4 °C with primary antibodies diluted 1/1000 in 5% BSA in TBS containing 0.1% Tween 20. Incubation with secondary peroxidase-coupled anti-rabbit IgG diluted 1/5000 was performed at room temperature for 45 min, and then antigens were revealed using SuperSignal detection method (Pierce). Levels of phospho-Tyr⁴⁰² Pyk2, phospho-Ser⁴⁷³ Akt as well as amounts of Pyk2 and Akt proteins were quantified by scanning the autoradiograms and measuring relative optical density with Metamorph™ software. Each band was normalized to the total Pyk2 or Akt level in the respective sample.

Acknowledgments

This study was partly supported by the Institut National de la Santé et de la Recherche Médicale, the University Joseph Fourier and by funds from the Association Française contre les Myopathies and Région Rhône-Alpes. Flavie Strappazzon is the recipient of a grant from the Ministère de l'Éducation Nationale, de l'Enseignement Supérieur et de la Recherche. We gratefully acknowledge Dr. F.J. Hemming for revising the English manuscript.

References

- Andreev, J., Simon, J.P., Sabatini, D.D., Kam, J., Plowman, G., Randazzo, P.A., Schlessinger, J., 1999. Identification of a new Pyk2 target protein with Arf-GAP activity. *Mol. Cell. Biol.* 19, 2338–2350.
- Avdi, N.J., Nick, J.A., Whitlock, B.B., Billstrom, M.A., Henson, P.M., Johnson, G.L., Worthen, G.S., 2001. Tumor necrosis factor-α activation of the c-Jun N-terminal kinase pathway in human neutrophils. Integrin involvement in a pathway leading from cytoplasmic tyrosine kinases apoptosis. *J. Biol. Chem.* 276, 2189–2199.
- Avraham, S., London, R., Fu, Y., Ota, S., Hiregowdara, D., Li, J., Jiang, S., Pasztor, L.M., White, R.A., Groopman, J.E., et al., 1995. Identification and characterization of a novel related adhesion focal tyrosine kinase (RAFTK) from megakaryocytes and brain. *J. Biol. Chem.* 270, 27742–27751.
- Avraham, H., Park, S.Y., Schinkmann, K., Avraham, S., 2000. RAFTK/Pyk2-mediated cellular signalling. *Cell Signalling* 12, 123–133.
- Banno, Y., Ohguchi, K., Matsumoto, N., Koda, M., Ueda, M., Hara, A., Dikic, I., Nozawa, Y., 2005. Implication of phospholipase D2 in oxidant-induced phosphoinositide 3-kinase signaling via Pyk2 activation in PC12 cells. *J. Biol. Chem.* 280, 16319–16324.
- Benbernou, N., Muegge, K., Durum, S.K., 2000. Interleukin (IL)-7 induces rapid activation of Pyk2, which is bound to Janus kinase 1 and IL-7Rα. *J. Biol. Chem.* 275, 7060–7065.
- Blaukat, A., Ivankovic-Dikic, I., Gronroos, E., Dolfi, F., Tokiwa, G., Vuori, K., Dikic, I., 1999. Adaptor proteins Grb2 and Crk couple Pyk2 with activation of specific mitogen-activated protein kinase cascades. *J. Biol. Chem.* 274, 14893–14901.
- Boutillier, A.L., Kienlen-Campard, P., Loeffler, J.P., 1999. Depolarization

- regulates cyclin D1 degradation and neuronal apoptosis: a hypothesis about the role of the ubiquitin/proteasome signalling pathway. *Eur. J. Neurosci.* 11, 441–448.
- Carboni, E., Wojcik, W.J., 1988. Dihydropyridine binding sites regulate calcium influx through specific voltage-sensitive calcium channels in cerebellar granule cells. *J. Neurochem.* 50, 1279–1286.
- Chauhan, D., Hideshima, T., Pandey, P., Treon, S., Teoh, G., Raje, N., Rosen, S., Krett, N., Husson, H., Avraham, S., Kharbanda, S., Anderson, K.C., 1999. RAFTK/PYK2-dependent and -independent apoptosis in multiple myeloma cells. *Oncogene* 18, 6733–6740.
- Corvol, J.C., Valjent, E., Toutant, M., Enslin, H., Irinopoulou, T., Lev, S., Herve, D., Girault, J.A., 2005. Depolarization activates ERK and proline-rich tyrosine kinase 2 (PYK2) independently in different cellular compartments in hippocampal slices. *J. Biol. Chem.* 280, 660–668.
- Courtney, M.J., Lambert, J.J., Nicholls, D.G., 1990. The interactions between plasma membrane depolarization and glutamate receptor activation in the regulation of cytoplasmic free calcium in cultured cerebellar granule cells. *J. Neurosci.* 10, 3873–3879.
- Della Rocca, G.J., van Biesen, T., Daaka, Y., Luttrell, D.K., Luttrell, L.M., Lefkowitz, R.J., 1997. Ras-dependent mitogen-activated protein kinase activation by G protein-coupled receptors. Convergence of Gi- and Gq-mediated pathways on calcium/calmodulin, Pyk2, and Src kinase. *J. Biol. Chem.* 272, 19125–19132.
- Derkinderen, P., Toutant, M., Burgaya, F., Le Bert, M., Siciliano, J.C., de Franciscis, V., Gelman, M., Girault, J.A., 1996. Regulation of a neuronal form of focal adhesion kinase by anandamide. *Science* 273, 1719–1722.
- Derkinderen, P., Siciliano, J., Toutant, M., Girault, J.A., 1998. Differential regulation of FAK+ and PYK2/Cakbeta, two related tyrosine kinases, in rat hippocampal slices: effects of LPA, carbachol, depolarization and hyperosmolarity. *Eur. J. Neurosci.* 10, 1667–1675.
- Desagher, S., Severac, D., Lipkin, A., Bernis, C., Ritchie, W., Le Digarcher, A., Journot, L., 2005. Genes regulated in neurons undergoing transcription-dependent apoptosis belong to signaling pathways rather than the apoptotic machinery. *J. Biol. Chem.* 280, 5693–5702.
- Dikic, I., Tokiwa, G., Lev, S., Courtneidge, S.A., Schlessinger, J., 1996. A role for Pyk2 and Src in linking G-protein-coupled receptors with MAP kinase activation. *Nature* 383, 547–550.
- D'Mello, S.R., Galli, C., Ciotti, T., Calissano, P., 1993. Induction of apoptosis in cerebellar granule neurons by low potassium: inhibition of death by insulin-like growth factor I and cAMP. *Proc. Natl. Acad. Sci. U. S. A.* 90, 10989–10993.
- Doroshenko, P.A., Kostyuk, P.G., Luk'yanetz, E.A., 1988. Modulation of calcium current by calmodulin antagonists. *Neuroscience* 27, 1073–1080.
- Dougherty, C.J., Kubasiak, L.A., Frazier, D.P., Li, H., Xiong, W.C., Bishopric, N.H., Webster, K.A., 2004. Mitochondrial signals initiate the activation of c-Jun N-terminal kinase (JNK) by hypoxia-reoxygenation. *FASEB J.* 18, 1060–1070.
- Franke, T.F., Hornik, C.P., Segev, L., Shostak, G.A., Sugimoto, C., 2003. PI3K/Akt and apoptosis: size matters. *Oncogene* 22, 8983–8998.
- Franklin, J.L., Johnson Jr., E.M., 1992. Suppression of programmed neuronal death by sustained elevation of cytoplasmic calcium. *Trends Neurosci.* 15, 501–508.
- Franklin, J.L., Sanz-Rodriguez, C., Juhasz, A., Deckwerth, T.L., Johnson Jr., E.M., 1995. Chronic depolarization prevents programmed death of sympathetic neurons in vitro but does not support growth: requirement for Ca²⁺ influx but not Trk activation. *J. Neurosci.* 15, 643–664.
- Gallo, V., Kingsbury, A., Balazs, R., Jorgensen, O.S., 1987. The role of depolarization in the survival and differentiation of cerebellar granule cells in culture. *J. Neurosci.* 7, 2203–2213.
- Ginnan, R., Singer, H.A., 2002. CaM kinase II-dependent activation of tyrosine kinases and ERK1/2 in vascular smooth muscle. *Am. J. Physiol.: Cell Physiol.* 282, C754–C761.
- Girault, J.A., Costa, A., Derkinderen, P., Studler, J.M., Toutant, M., 1999. FAK and PYK2/CAKbeta in the nervous system: a link between neuronal activity, plasticity and survival? *Trends Neurosci.* 22, 257–263.
- Greenberg, D.A., Carpenter, C.L., Messing, R.O., 1987. Interaction of calmodulin inhibitors and protein kinase C inhibitors with voltage-dependent calcium channels. *Brain Res.* 404, 401–404.
- Guo, J., Meng, F., Fu, X., Song, B., Yan, X., Zhang, G., 2004. N-methyl-D-aspartate receptor and L-type voltage-gated Ca²⁺ channel activation mediate proline-rich tyrosine kinase 2 phosphorylation during cerebral ischemia in rats. *Neurosci. Lett.* 355, 177–180.
- Hack, N., Hidaka, H., Wakefield, M.J., Balazs, R., 1993. Promotion of granule cell survival by high K⁺ or excitatory amino acid treatment and Ca²⁺/calmodulin-dependent protein kinase activity. *Neuroscience* 57, 9–20.
- Heidinger, V., Manzerra, P., Wang, X.Q., Strasser, U., Yu, S.P., Choi, D.W., Behrens, M.M., 2002. Metabotropic glutamate receptor 1-induced upregulation of NMDA receptor current: mediation through the Pyk2/Src-family kinase pathway in cortical neurons. *J. Neurosci.* 22, 5452–5461.
- Herzog, H., Nicholl, J., Hort, Y.J., Sutherland, G.R., Shine, J., 1996. Molecular cloning and assignment of FAK2, a novel human focal adhesion kinase, to 8p11.2–p22 by nonisotopic in situ hybridization. *Genomics* 32, 484–486.
- Hidaka, H., Tanaka, T., 1983. Naphthalenesulfonamides as calmodulin antagonists. *Methods Enzymol.* 102, 185–194.
- Huang, Y., Lu, W., Ali, D.W., Pelkey, K.A., Pitcher, G.M., Lu, Y.M., Aoto, H., Roder, J.C., Sasaki, T., Salter, M.W., MacDonald, J.F., 2001. CAKbeta/Pyk2 kinase is a signaling link for induction of long-term potentiation in CA1 hippocampus. *Neuron* 29, 485–496.
- Ivankovic-Dikic, I., Gronroos, E., Blaukat, A., Barth, B.U., Dikic, I., 2000. Pyk2 and FAK regulate neurite outgrowth induced by growth factors and integrins. *Nat. Cell Biol.* 2, 574–581.
- Koike, T., Martin, D.P., Johnson Jr., E.M., 1989. Role of Ca²⁺ channels in the ability of membrane depolarization to prevent neuronal death induced by trophic-factor deprivation: evidence that levels of internal Ca²⁺ determine nerve growth factor dependence of sympathetic ganglion cells. *Proc. Natl. Acad. Sci. U. S. A.* 86, 6421–6425.
- Kozlaci, K., Kaczmarek, E., Park, S.Y., Fu, Y., Avraham, S., Avraham, H., 2001. RAFTK/Pyk2 involvement in platelet activation is mediated by phosphoinositide 3-kinase. *Br. J. Haematol.* 114, 134–140.
- Lafon-Cazal, M., Perez, V., Bockaert, J., Marin, P., 2002. Akt mediates the anti-apoptotic effect of NMDA but not that induced by potassium depolarization in cultured cerebellar granule cells. *Eur. J. Neurosci.* 16, 575–583.
- Lev, S., Moreno, H., Martinez, R., Canoll, P., Peles, E., Musacchio, J.M., Plowman, G.D., Rudy, B., Schlessinger, J., 1995. Protein tyrosine kinase PYK2 involved in Ca²⁺-induced regulation of ion channel and MAP kinase functions. *Nature* 376, 737–745.
- Li, X., Dy, R.C., Cance, W.G., Graves, L.M., Earp, H.S., 1999. Interactions between two cytoskeleton-associated tyrosine kinases: calcium-dependent tyrosine kinase and focal adhesion tyrosine kinase. *J. Biol. Chem.* 274, 8917–8924.
- Melendez, J., Turner, C., Avraham, H., Steinberg, S.F., Schaefer, E., Sussman, M.A., 2004. Cardiomyocyte apoptosis triggered by RAFTK/pyk2 via Src kinase is antagonized by paxillin. *J. Biol. Chem.* 279, 53516–53523.
- Meyer, A.N., Gastwirt, R.F., Schlaepfer, D.D., Donoghue, D.J., 2004. The cytoplasmic tyrosine kinase Pyk2 as a novel effector of fibroblast growth factor receptor 3 activation. *J. Biol. Chem.* 279, 28450–28457.
- Miller, T.M., Johnson Jr., E.M., 1996. Metabolic and genetic analyses of apoptosis in potassium/serum-deprived rat cerebellar granule cells. *J. Neurosci.* 16, 7487–7495.
- Miller, T.M., Tansey, M.G., Johnson Jr., E.M., Creedon, D.J., 1997. Inhibition of phosphatidylinositol 3-kinase activity blocks depolarization- and insulin-like growth factor I-mediated survival of cerebellar granule cells. *J. Biol. Chem.* 272, 9847–9853.
- Missotten, M., Nichols, A., Rieger, K., Sadoul, R., 1999. Alix, a novel mouse protein undergoing calcium-dependent interaction with the apoptosis-linked gene 2 (ALG-2) protein. *Cell Death Differ.* 6, 124–129.

- Nakagawa-Yagi, Y., Choi, D.K., Ogane, N., Shimada, S., Seya, M., Momoi, T., Ito, T., Sakaki, Y., 2001. Discovery of a novel compound: insight into mechanisms for acrylamide-induced axonopathy and colchicine-induced apoptotic neuronal cell death. *Brain Res.* 909, 8–19.
- Ogata, Y., Takahashi, M., Ueno, S., Takeuchi, K., Okada, T., Mano, H., Ookawara, S., Ozawa, K., Berk, B.C., Ikeda, U., Shimada, K., Kobayashi, E., 2003. Antiapoptotic effect of endothelin-1 in rat cardiomyocytes in vitro. *Hypertension* 41, 1156–1163.
- Pandey, P., Avraham, S., Kumar, S., Nakazawa, A., Place, A., Ghanem, L., Rana, A., Kumar, V., Majumder, P.K., Avraham, H., Davis, R.J., Kharbanda, S., 1999a. Activation of p38 mitogen-activated protein kinase by PYK2/related adhesion focal tyrosine kinase-dependent mechanism. *J. Biol. Chem.* 274, 10140–10144.
- Pandey, P., Avraham, S., Place, A., Kumar, V., Majumder, P.K., Cheng, K., Nakazawa, A., Saxena, S., Kharbanda, S., 1999b. Bcl-xL blocks activation of related adhesion focal tyrosine kinase/proline-rich tyrosine kinase 2 and stress-activated protein kinase/c-Jun N-terminal protein kinase in the cellular response to methylmethane sulfonate. *J. Biol. Chem.* 274, 8618–8623.
- Park, J.H., Park, J.K., Bac, K.W., Park, H.T., 2000a. Protein kinase A activity is required for depolarization-induced proline-rich tyrosine kinase 2 and mitogen-activated protein kinase activation in PC12 cells. *Neurosci. Lett.* 290, 25–28.
- Park, S.Y., Avraham, H., Avraham, S., 2000b. Characterization of the tyrosine kinases RAFTK/Pyk2 and FAK in nerve growth factor-induced neuronal differentiation. *J. Biol. Chem.* 275, 19768–19777.
- Park, S.Y., Avraham, H.K., Avraham, S., 2004. RAFTK/Pyk2 activation is mediated by *trans*-acting autophosphorylation in a Src-independent manner. *J. Biol. Chem.* 279, 33315–33322.
- Rocic, P., Govindarajan, G., Sabri, A., Lucchesi, Rocic, P., Govindarajan, G., Sabri, A., Lucchesi, P.A., 2001. A role for PYK2 in regulation of ERK1/2 MAP kinases and PI 3-kinase by ANG II in vascular smooth muscle. *Am. J. Physiol. Cell Physiol.* 268, C90–C99.
- Rumsey, L.M., Teague, R.M., Benedict, S.H., Chan, M.A., 2001. MIP-1 α induces activation of phosphatidylinositol-3 kinase that associates with Pyk-2 and is necessary for B-cell migration. *Exp. Cell Res.* 268, 77–83.
- Sasaki, H., Nagura, K., Ishino, M., Tobioka, H., Kotani, K., Sasaki, T., 1995. Cloning and characterization of cell adhesion kinase beta, a novel protein-tyrosine kinase of the focal adhesion kinase subfamily. *J. Biol. Chem.* 270, 21206–21219.
- Sayed, M.R., Sheid, M.P., Stevens, C.M., Duronio, V., 2000. Thrombin-stimulated phosphatidylinositol 3-kinase activity in platelets is associated with activation of PYK2 tyrosine kinase: activation of both enzymes is aggregation independent. *J. Cell. Physiol.* 183, 314–320.
- Schmidt, M.H., Dikic, I., Bogler, O., 2005. Src phosphorylation of Alix/AIP1 modulates its interaction with binding partners and antagonizes its activities. *J. Biol. Chem.* 280, 3414–3425.
- See, V., Boutillier, A.L., Bito, H., Loeffler, J.P., 2001. Calcium/calmodulin-dependent protein kinase type IV (CaMKIV) inhibits apoptosis induced by potassium deprivation in cerebellar granule neurons. *FASEB J.* 15, 134–144.
- Shi, C.S., Kehrl, J.H., 2001. PYK2 links G(q)alpha and G(13)alpha signaling to NF-kappa B activation. *J. Biol. Chem.* 276, 31845–31850.
- Shimoke, K., Yamagishi, S., Yamada, M., Ikeuchi, T., Hatanaka, H., 1999. Inhibition of phosphatidylinositol 3-kinase activity elevates c-Jun N-terminal kinase activity in apoptosis of cultured cerebellar granule neurons. *Brain Res. Dev. Brain Res.* 112, 245–253.
- Siciliano, J.C., Toutant, M., Derkinderen, P., Sasaki, T., Girault, J.A., 1996. Differential regulation of proline-rich tyrosine kinase 2/cell adhesion kinase beta (PYK2/CAKbeta) and pp125(FAK) by glutamate and depolarization in rat hippocampus. *J. Biol. Chem.* 271, 28942–28946.
- Soler, R.M., Egea, J., Mintenig, G.M., Sanz-Rodriguez, C., Iglesias, M., Comella, J.X., 1998. Calmodulin is involved in membrane depolarization-mediated survival of motoneurons by phosphatidylinositol-3 kinase- and MAPK-independent pathways. *J. Neurosci.* 18, 1230–1239.
- Taniyama, Y., Weber, D.S., Rocic, P., Hilenski, L., Akers, M.L., Park, J., Hemmings, B.A., Alexander, R.W., Griendling, K.K., 2003. Pyk2- and Src-dependent tyrosine phosphorylation of PDK1 regulates focal adhesions. *Mol. Cell. Biol.* 23, 8019–8029.
- Tian, D., Litvak, V., Lev, S., 2000. Cerebral ischemia and seizures induce tyrosine phosphorylation of PYK2 in neurons and microglial cells. *J. Neurosci.* 20, 6478–6487.
- Tokiwa, G., Dikic, I., Lev, S., Schlessinger, J., 1996. Activation of Pyk2 by stress signals and coupling with JNK signaling pathway. *Science* 273, 792–794.
- Trioulier, Y., Torch, S., Blot, B., Cristina, N., Chatellard-Cause, C., Verna, J.M., Sadoul, R., 2004. Alix, a protein regulating endosomal trafficking, is involved in neuronal death. *J. Biol. Chem.* 279, 2046–2052.
- Ueda, H., Abbi, S., Zheng, C., Guan, J.L., 2000. Suppression of Pyk2 kinase and cellular activities by FIP200. *J. Cell Biol.* 149, 423–430.
- Vito, P., Pellegrini, L., Guiet, C., D'Adamio, L., 1999. Cloning of AIP1, a novel protein that associates with the apoptosis-linked gene ALG-2 in a Ca²⁺-dependent reaction. *J. Biol. Chem.* 274, 1533–1540.
- Wei, L., Yang, Y., Zhang, X., Yu, Q., 2004. Altered regulation of Src upon cell detachment protects human lung adenocarcinoma cells from anoikis. *Oncogene* 23, 9052–9061.
- Xiong, W.C., Mei, L., 2003. Roles of FAK family kinases in nervous system. *Front. Biosci.* 8, s676–s682.
- Xiong, W., Parsons, J.T., 1997. Induction of apoptosis after expression of PYK2, a tyrosine kinase structurally related to focal adhesion kinase. *J. Cell Biol.* 139, 529–539.
- Yu, H., Li, X., Marchetto, G.S., Dy, R., Hunter, D., Calvo, B., Dawson, T.L., Wilm, M., Anderegg, R.J., Graves, L.M., Earp, H.S., 1996. Activation of a novel calcium-dependent protein-tyrosine kinase. Correlation with c-Jun N-terminal kinase but not mitogen-activated protein kinase activation. *J. Biol. Chem.* 271, 29993–29998.
- Zwick, E., Wallasch, C., Daub, H., Ullrich, A., 1999. Distinct calcium-dependent pathways of epidermal growth factor receptor transactivation and PYK2 tyrosine phosphorylation in PC12 cells. *J. Biol. Chem.* 274, 20989–20996.



Alix differs from ESCRT proteins in the control of autophagy

Anne Petiot^{a,b}, Flavie Strappazon^{a,b,1}, Christine Chatellard-Cause^{a,b}, Béatrice Blot^{a,b}, Sakina Torch^{a,b}, Jean-Marc Verna^{a,b,2}, Rémy Sadoul^{a,b,*}

^aINSERM U836, Grenoble Institute of Neuroscience, F-38042 Grenoble, France

^bUniversité Joseph Fourier, Grenoble Institute of Neurosciences (GIN), F-38042 Grenoble, France

ARTICLE INFO

Article history:

Received 3 July 2008

Available online 3 August 2008

Keywords:

Alix
Autophagy
ESCRT
Endocytosis
MVB

ABSTRACT

Alix/AIP1 is a cytosolic protein that regulates cell death through mechanisms that remain unclear. Alix binds to two protein members of the so-called Endosomal Sorting Complex Required for Transport (ESCRT), which facilitates membrane fission events during multivesicular endosome formation, enveloped virus budding and cytokinesis. Alix itself has been suggested to participate in these cellular events and is thus often considered to function in the ESCRT pathway. ESCRT proteins were recently implicated in autophagy, a process involved in bulk degradation of cytoplasmic constituents in lysosomes, which can also participate in cell death. In this study, we shown that, unlike ESCRT proteins, Alix is not involved in autophagy. These results strongly suggest that the capacity of several mutants of Alix to block both caspase-dependent and independent cell death does not relate to their capacity to modulate autophagy. Furthermore, they reinforce the conclusion of other studies demonstrating that the role of Alix is different from that of classical ESCRT proteins.

© 2008 Elsevier Inc. All rights reserved.

Alix/AIP1 is a cytoplasmic protein which was first characterised as a partner of ALG-2 [1,2], a small Ca²⁺ binding protein involved in apoptosis [3]. Alix overexpression, *in vivo* as well as *in vitro*, is sufficient to activate caspases and thereby neuronal death, while some deletion mutants of the protein block both caspase-dependent and independent neuronal death [4,5]. Alix is a known partner of ESCRT proteins [6,7] (endosomal sorting complexes required for transport), which are central elements for the making of multivesicular bodies (MVBs), late endosome intermediates containing intraluminal vesicles (ILVs) that collect receptors and other membrane proteins endocytosed from the cell surface [8].

Alix interacts with two proteins of the ESCRT complex, Tsg101 [6] and CHMP-4B [7], lysobisphosphatidic acid (LBPA), a phospholipid involved in intraluminal vesiculation of endosomes [9], as well as with other regulators of endocytosis (endophilins [10]

and CIN85 [11]). Like ESCRT proteins, Alix is also required for the budding of enveloped viruses [12] and for the abscission reactions that complete mammalian cell division [13,14]. Even if Alix has been proposed to regulate membrane budding and abscission in MVBs, its precise role remains largely unclear as neither we nor other laboratories have found any striking effect of the protein on endocytosis and degradation of EGF receptors (J. Faure and coll, unpublished observations, [15–18]).

Macroautophagy, hereafter referred to as autophagy, is the major pathway for degradation of long-lived proteins and the only known pathway for elimination of organelles. Depending on the stimulus, autophagy leads to cellular destruction or, on the contrary, to survival by supplying nutrients from cell material degradation [19,20]. Formation of double-membrane vacuoles, referred to as autophagosomes, allows the engulfment of material which is then degraded in lysosomes. In higher eukaryotes, autophagosomes first fuse with endosomes, thereby giving rise to amphisomes which in turn fuse with lysosomes [21]. This may explain why proteins involved in the biogenesis of endosomes, like ESCRTs [22], the ATPase SKD1 [23], the small GTPases Rab7 [24] and Rab5 [25], and Hrs [26], all have an effect on the maturation of autophagosomes. Given the fact that Alix is somehow involved in cell death which is associated with autophagy, we have challenged the hypothesis that it may control autophagy in a similar way to ESCRT proteins. Surprisingly, we could not find any effect of Alix mutants or of Alix knock-down on several aspects of autophagy induced by amino acid depletion, thereby strongly suggesting that

Abbreviations: ALG-2, apoptosis linked gene-2; Alix, ALG-2 interacting protein X; ESCRT, endosomal sorting complex required for transport; GFP, green fluorescent protein; Hrs, hepatocyte growth factor regulated tyrosine kinase substrate; ILV, intraluminal vesicles; LC3, microtubule-associated protein 1 light chain 3; MVB, multivesicular body; Vps, vacuolar protein sorting.

* Corresponding author. Address: INSERM U836, Grenoble Institute of Neuroscience, F-38042 Grenoble, France. Fax: +33 4 56 52 05 54.

E-mail address: remy.sadoul@ujf-grenoble.fr (R. Sadoul).

¹ Present address: Laboratory of Molecular Neuroembryology, IRCCS Fondazione Santa Lucia, Via del Fosso di Fiorano 64/65, 00143 Rome, Italy.

² Present address: Service des Ressources Humaines, Délégation Alpes, CNRS - BP 166, 38042 Grenoble, France.

Alix does not directly participate in this process and therefore differs from classical ESCRT proteins.

Experimental procedures

Plasmids. Expression plasmids encoding GFP-SKD1(E235Q), GFP-LC3 (pEGFP LC3), and RFP-LC3 were kindly provided by T. Yoshimori (National Institute of Genetics, Mishima, Japan). Alix and Alix mutants expression vectors have been described in Chatellard-Causse et al., 2002 [10].

Construction of Alix sh RNA. For silencing Alix expression, a DNA insert encoding an RNA hairpin was cloned downstream of the human H1 promoter in the pSuperGFP vector (Oligoengine, Seattle, WA, USA). Forward and reverse sequences for the Alix shRNA construct were: 5'-GATCCCGCCGCTGGTGAAGTTCATCTCAAGAGAGA TGAACCTCACCAGCGCTTTTGGAAA-3' and 5'-AGCTTTTCCAAAA AGCCGCTGGTGAAGTTCATCTCTTGAAGATGAACTTACCAGCGGC GGG-3', respectively (Invitrogen). The annealed oligonucleotides were ligated into the BglIII–HindIII cleavage site within the pSuperGFP vector.

Cells culture and antibodies. Baby Hamster Kidney cells (BHK-21) were used as described in Ref. [27]. Rabbit anti-Alix as been previously described [10], mouse anti-Tsg101 was from Abcam, mouse anti-actin was from Chemicon, mouse anti Flag was from Sigma–

Aldrich, mouse anti-GFP was from Clontec and rabbit anti-LC3 was a kind gift from Priault M., (IBGC, UMR 5095, Bordeaux).

pSuper expressing BHK-21 cells. BHK-21 cells were transfected with pSuper/shAlix plasmid or pSuperGFP vector as control by using JetSi transfection (Polyplus tranfection). Transfected cells were selected by adding G418 (800 µg/ml) to the culture medium. After 15 days, clones were isolated and screened for the best reduction in Alix expression. Permanent cell lines (pSuper/shAlix and control) were maintained with G418 (800 µg/ml).

Transient cell transfections of BHK-21 cells. Plasmids encoding the different constructions were transfected using the JetPEI method. Cells were used 36 h following transfection.

Determination of cell viability. Cells were stained with Hoechst 33342 as described previously [4]. Cell viability was scored on the basis of nuclear morphology; condensed or fragmented nuclei were taken to indicate cell death.

In some cases, MTT (tetrazolium salt, 3-(4,5-dimethylthiazol-2-yl)-2,5-diphenyl tetrazolium bromide, 0.5 mg/ml) was added to cells and incubated for 30 min in the dark at 37 °C. The cells were rinsed and dissolved in 500 µl DMSO per well. Absorbance was measured at 540 nm.

Immunofluorescence. BHK-21 cells grown on glass coverslips were fixed in 4% paraformaldehyde in PBS for 20 min at 4 °C, permeabilized with 0.02% saponin, and immunostained as described in [4]. The primary antibody was revealed with anti-IgG coupled

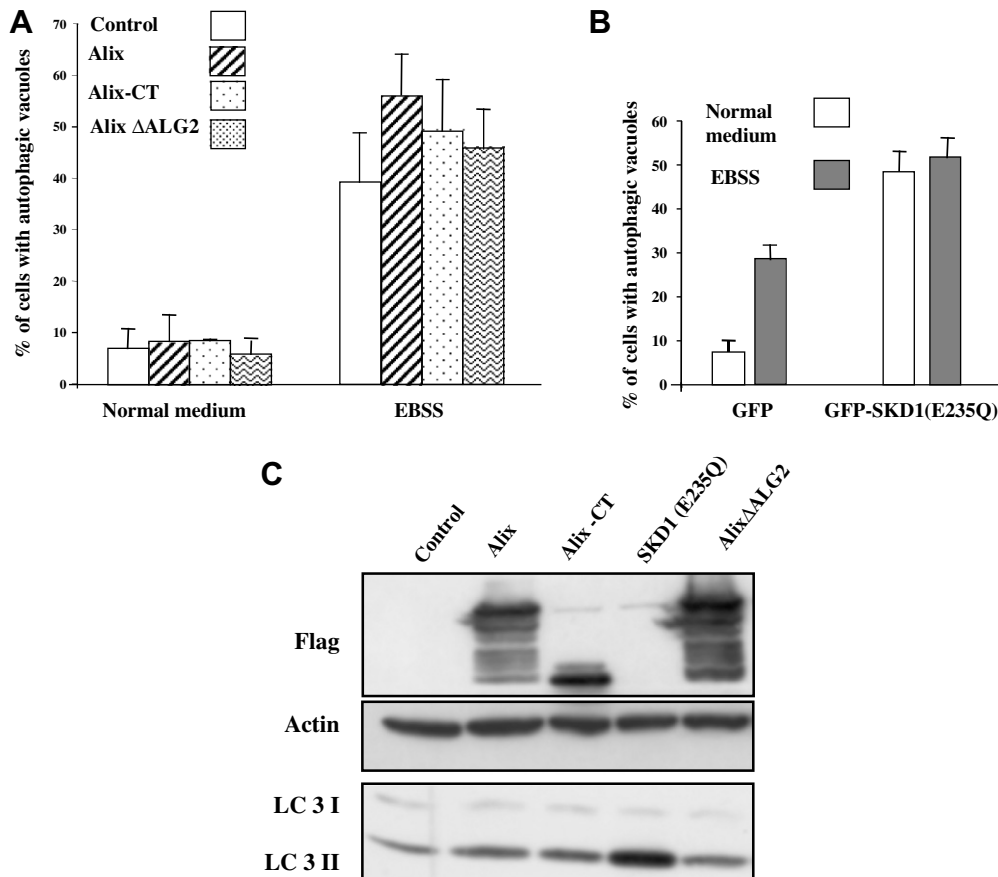


Fig. 1. Alix expression is not associated with the formation of autophagic vacuoles in BHK cells. (A) BHK cells were co-transfected with LC3-GFP and Flag tagged Alix plasmids. Cells were incubated for 4 h in normal medium or medium depleted of amino acids (EBSS condition) before labelling with a monoclonal anti-FLAG antibody. The percentage of autophagic cells represents the ratio between the number of cells expressing an autophagic pattern (vesicular labelling of LC3-GFP) and the total number of transfected cells. For each experiment, 200–300 transfected cells were counted per condition in 10 random fields in each of three different wells. Each experiment was performed three times. (B) BHK cells were co-transfected with LC3-RFP and GFP or GFP-SKD1(E235Q) plasmids. The percentage of autophagic cells was calculated as described above. (C) BHK cells transfected with different plasmids and incubated 4 h in normal or medium depleted of amino acids (EBSS). Conversion of LC3-I to LC3-II was analysed by immunoblotting using an anti-LC3 antibody. FLAG antibody was used to visualise expression of different Alix proteins. GFP-SKD1(E235Q) expression was visualized using an anti-GFP antibody (not shown). This Western blot is representative of three independent experiments.

to fluorochrome Alexa 594 or Alexa 488 (Molecular Probes). Image analysis was performed using Metamorph™ software (Universal Imaging Corp.).

Western blot analysis. Western blot analysis were performed as described [10].

Measurement of the degradation of long-lived proteins. Protein degradation was determined as previously described in Ref. [28]. Briefly, cells were incubated for 18 h at 37 °C with 0.2 μ Ci/ml L-[¹⁴C] valine. After three washes with PBS, cells were incubated 1 h in fresh medium supplemented with 10 mM cold valine. Autophagic degradation was induced by incubating cells in EBSS medium (lacking amino acids and foetal calf serum) supplemented with 10 mM cold valine throughout the chase period (4 h). Following the 4 h chase, proteins of the media and of the cell cultures were precipitated with trichloroacetic acid (10% at 4 °C). Radioactivity was determined by liquid scintillation counting. Percentage of protein degradation represents the ratio of acid-soluble radioactivity recovered from both cells and medium to the radioactivity contained in the precipitated proteins from both cells and medium.

Statistical analysis. Statistical analysis was performed using Student's *t* test. *p* < 0.05 was considered statistically significant.

Results

Alix is not involved in the making of autophagic vacuoles

In BHK-21 cells, like in many others, autophagy can be induced by depleting amino acids from the culture medium. The first steps

of autophagy were recorded by using the microtubule-associated protein-1 light chain 3 (LC3) to label autophagic membranes to which it binds selectively throughout the process of autophagy. As expected, the percentage of cells transfected with LC3-GFP displaying a vacuolar staining was less than 10% under normal conditions and rose to nearly 40%, 4 h after amino acid depletion (Fig. 1A). We tested the effect of expressing Alix or Alix mutants on autophagosomes: Alix-CT, which binds to Tsg101 of ESCRT-I but lacks the N terminal binding domain to SNF7/CHMP-4B of ESCRT-III, is thought to inhibit the ESCRT pathway. Alix Δ ALG-2 lacks the ALG-2 binding site and is capable of blocking cell death *in vivo*. None of the overexpressed Alix proteins impaired cell viability (data not shown). In normal or amino acid-depleted cultures, none of the Alix proteins changed significantly the number of cells with vacuolated LC3-GFP staining (Fig. 1A). In contrast, a significant increase in the number of vacuoles stained with LC3-RFP was observed in normal or amino acid-depleted cells transfected with an ATPase dead version of SKD1 (SKD1(E235Q)), (Fig. 1B). This mutant impairs the dissociation of the ESCRT complex from endosomes and thereby MVB formation. Furthermore, the level of the 16 kD lipidated, autophagosome-bound form of LC3 (LC3-II), detected by Western blot analysis, was visibly increased compared to the 18 kD cytosolic form in cells expressing SKD1(E235Q). In contrast, there was no change in the level of LC3-II in cells expressing wt. or mutated Alix, cultured in normal (not shown) or amino acid-depleted medium (Fig. 1C). The LC3-I band is almost undetectable probably because it is less sensitive to detection with the antibody used or because it is more labile than LC3-II in BHK cells.

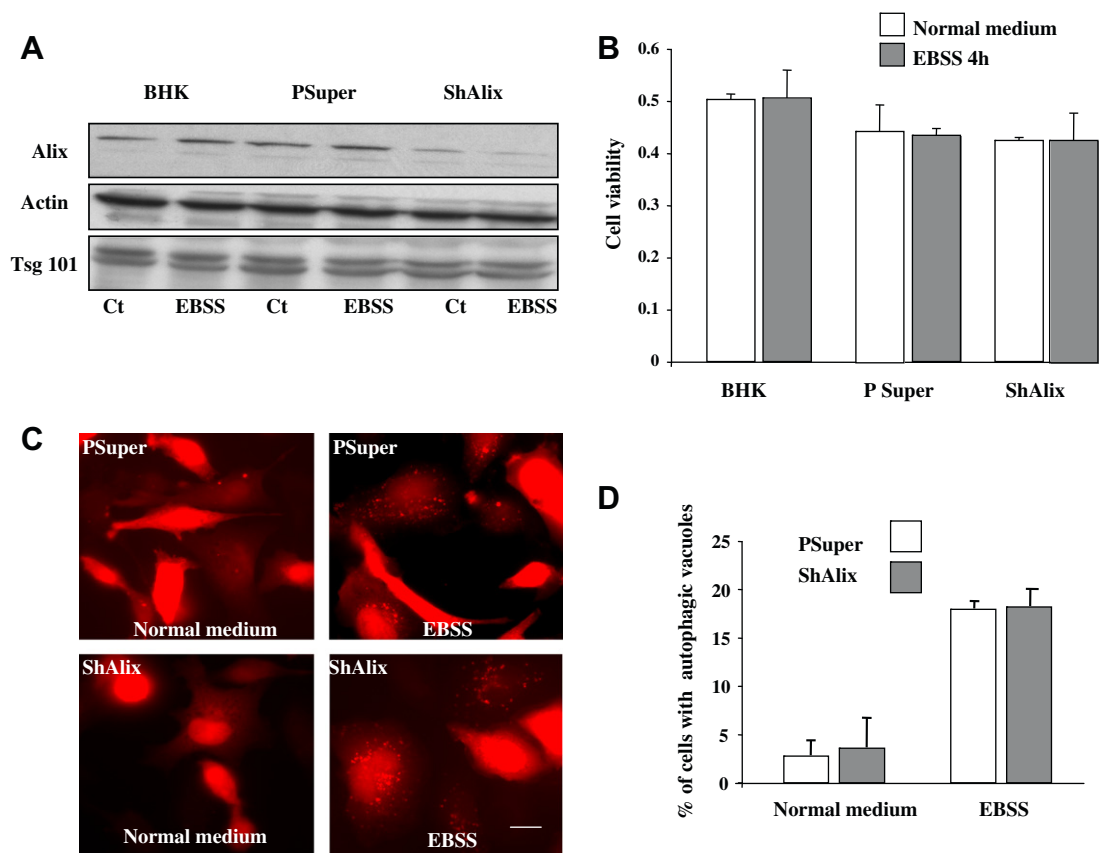


Fig. 2. Autophagy is not disturbed in Alix-depleted BHK cells. (A) Cells from BHK-21 cell lines expressing PSuper or a PSuper coding for an ShRNA against Alix (Sh Alix) were analysed by Western blotting using anti-Alix, anti-Tsg101 and anti-actin antibodies. (B) MTT test on PSuper and shAlix cells incubated in normal or EBSS conditions. (C) PSuper and shAlix cells were transfected with LC3-RFP and incubated for 4 h in normal medium or medium depleted of amino acids (EBSS). Bars: 5 μ m. (D) Number of cells containing LC3-RFP labelled vacuoles estimated in PSuper and shAlix transfected cells. The values reported are those of 200–300 transfected cells counted in three independent experiments.

We next tested whether downregulation of Alix expression could affect autophagy. For this, we used a BHK-21 cell line transfected with a pSuper plasmid expressing shRNA targeted to Alix. Alix expression was reduced by about 70%, whereas expression of actin or Tsg101 remained unchanged (Fig. 2A). As estimated by MTT, downregulation of Alix expression did not affect cell survival in any culture condition (Fig. 2B). The number of cells with vacuolar LC3-RFP staining was equivalent in cells with reduced Alix expression and in controls. This was true in both normal or in amino acid-depleted medium (Fig. 2C and D). Moreover, there was no significant difference in the levels of LC3-II, detected by Western blot analysis of pSuper and shAlix cells (data not shown). Taken together, these observations strongly suggest that unlike ESCRT proteins, Alix is not necessary for the formation of autophagic vacuoles.

Alix does not colocalise with autophagic vacuoles

Because endocytic proteins can be found on autophagosomal membranes [24–26], the localisation of overexpressed FLAG-Alix protein was studied in LC3-GFP transfected cells in normal or in amino acid-depleted medium. As illustrated in Fig. 3A, Alix did not colocalise with LC3-GFP, suggesting that Alix is not present in the autophagosome compartment. Alix-CT both formed and

delimited, spherical structures surrounding large ubiquitinated protein aggregates resembling those seen in ESCRT depleted cells ([10,22] and Chatellard-Cause, unpublished data). In contrast with this latter situation where it colocalized around the aggregates, LC3-GFP was never localised on Alix-CT induced spherical structures (Fig. 3B). ESCRT depletion and Alix-CT expression therefore induce the formation of morphologically similar, but distinct compartments.

Alix is not involved in autophagic protein degradation

We went on testing the effect of Alix on protein degradation. For this we quantified the percentage of acid-soluble radioactivity recovered from BHK-21 cells metabolically labelled with [¹⁴C] valine; it was almost doubled after cells were switched from DMEM to EBSS (Fig. 4A and B). This increase partly reflects autophagic degradation induced by amino acid-deprivation since the percentage of soluble [¹⁴C] was reduced by about 30% in cells cultured in EBSS containing LY294002, a phosphatidylinositol 3-kinase inhibitor known to block autophagic degradation [29]. Transient overexpression of SKD1(E235Q) significantly reduced autophagic degradation, whereas Alix or Alix-CT expression had no significant effect. Furthermore, the use of shAlix BHK cells, did not reveal any detectable effect of Alix downregulation on the level of autophagic

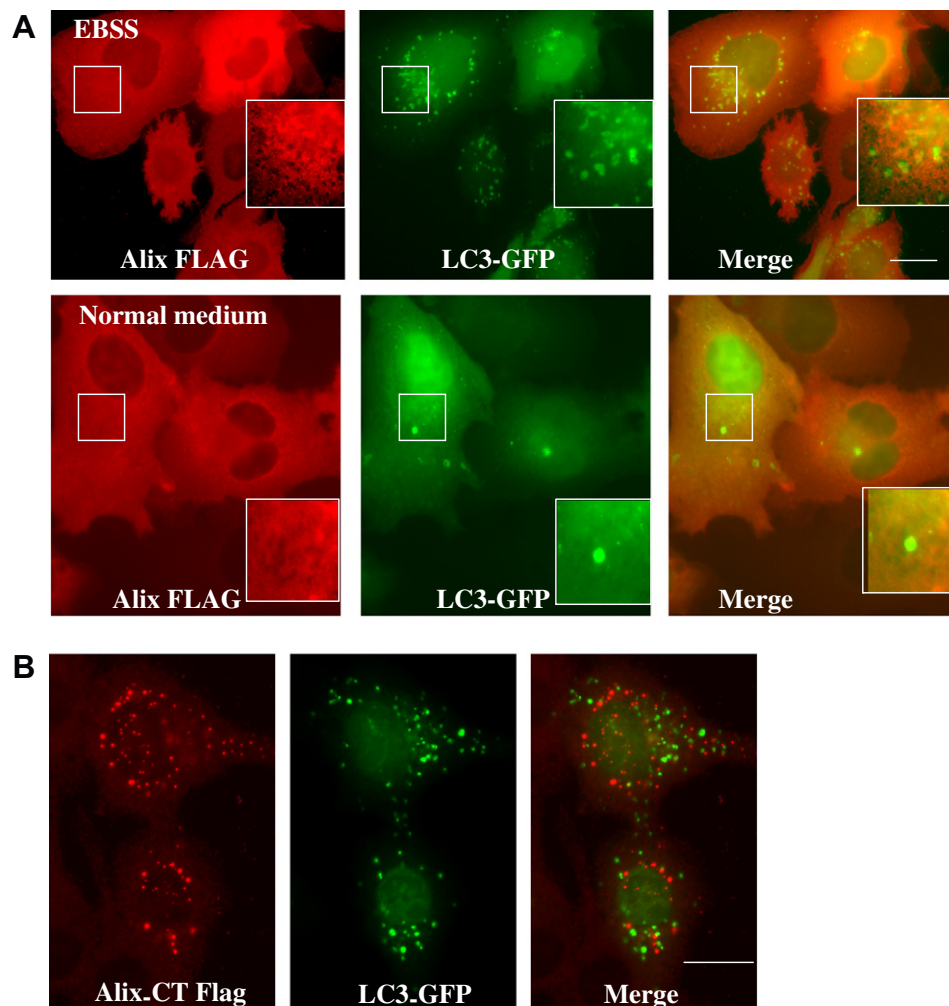


Fig. 3. Alix is not localised on autophagic vacuoles. (A) BHK cells were co-transfected with LC3-GFP and FLAG Alix, before 4 h incubation in normal medium or depleted amino acid medium (EBSS). Cells were then fixed and labelled with a monoclonal anti-FLAG antibody. (B) BHK cells were co-transfected with FLAG Alix-CT, before 4 h incubation in depleted amino acid medium (EBSS). Cells were then fixed and labelled with a monoclonal anti-FLAG antibody. Bars: (A) 5 μ m; (B) 2.5 μ m.

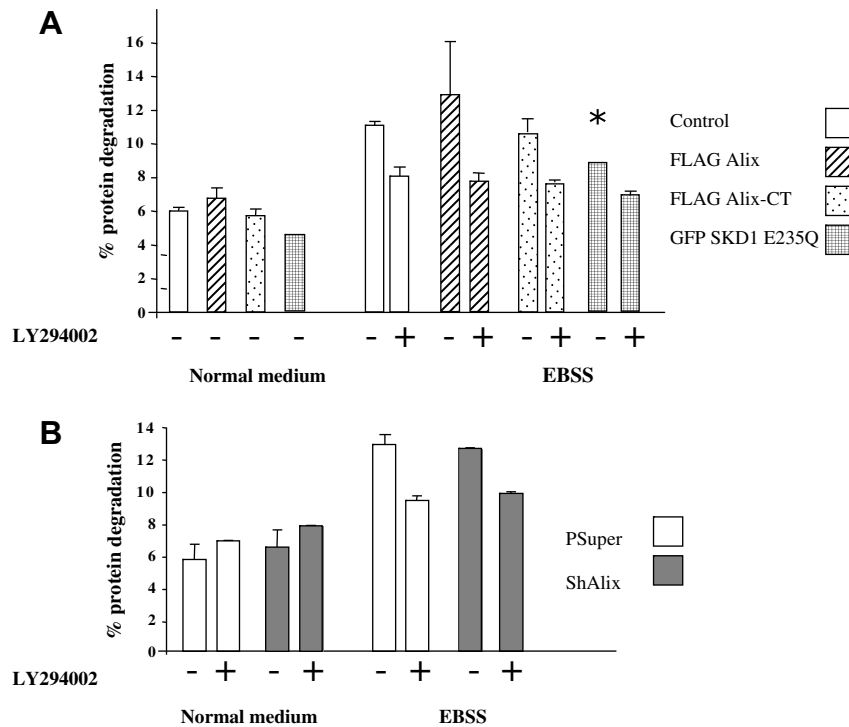


Fig. 4. Alix is not involved in autophagic protein degradation. The rate of [14 C] valine-labelled long-lived protein degradation, in normal or in a medium depleted on amino acids (EBSS), was measured in BHK cells expressing Flag tagged Alix proteins (A) or in PSuper shAlix cells (B). LY 294002 was used 4 h at 10 μ M. Data are expressed as the percentage of cellular protein degradation during the 4 h chase period. The values reported are the means of three determinations \pm SD. *test, $p < 0.05$.

protein degradation (Fig. 4B). Taken together, these results suggest that Alix is not involved in autophagic degradation due to amino acid depletion in BHK-21 cells.

Discussion

Here, we show that Alix downregulation or expression of Alix-CT does not impair autophagy as monitored by LC3 relocalisation or protein degradation, thus challenging the hypothesis that Alix acts as an ESCRT protein in the making of MVBs. ESCRT complexes (0-III) bind sequentially on the cytosolic surface of endosomes where they control the sorting of cargoes and budding of intraluminal vesicles [30]. Activity of the ATPase Vps4/SKD1 allows the dissociation of ESCRT-III complexes from the endosome limiting membrane. Expression of a dominant negative form of the ATPase, SKD1(E235Q), leads to abnormal MVBs [23] and produces accumulation of LC3 in *Drosophila* [22] and in starved HeLa cells [23]. In this latter case, Nara et al. also observed an increase LC3-II, in parallel to partial inhibition of protein degradation [23]; our present study reports similar results using BHK-21 cells. In higher eukaryotes, autophagosomes fuse with endosomal compartments to make amphisomes, which in turn fuse with lysosomes to form autolysosomes [31]. Autophagosomes and amphisomes, but not autolysosomes, form in ESCRT depleted HeLa cells, explaining the increase in the number of LC3 decorated vacuoles [32]. Such an increase was not seen after downregulation of Alix or expression of Alix-CT, which is thought to disorganize the ESCRT pathway by binding to ESCRT-I but not to ESCRT-III. Cells depleted of Tsg101 of ESCRT-I and Vps24 of ESCRT-III, accumulate large ubiquitin positive aggregates which concentrate LC3, a phenomenon probably reflecting their incapacity to eliminate polyubiquitinated proteins [32]. Alix-CT induces the formation of vacuoles containing ubiquitinated aggregates (C. Chatellard-Cause, unpublished) which differ from those detected in ESCRT depleted cells since they did not recruit LC3-GFP.

Our results demonstrating that Alix has no central role in the maturation of autophagosomes seem puzzling in view of its proposed role in the making of MVBs. Alix provides a link between different effectors of intraluminal vesicle budding through binding to proteins of both ESCRT-I [6] and ESCRT-III [7], and to lysobisphosphatidic acid (LBPA), a cone shaped lipid implicated in inward vesiculation [9]. The hypothesis of Alix playing a role in MVB genesis stems from its homology with a yeast protein, Bro-1p, which is required for the sorting of mono-ubiquitinated transmembrane proteins into intraluminal vesicles of MVBs [33]. In *Caenorhabditis elegans* ALX-1 is needed for proper MVB and late endosome function and thereby required for the degradation of membrane proteins [34]. Using electron microscopy, we have reported that Alix downregulation in HeLa cells impairs the budding of intraluminal vesicles inside endosomes [9]. However, contradicting this observation several reports showed that Alix seems to play no role in EGF receptor degradation, a process known to require ESCRT proteins [15–18]. Instead, Doyotte et al. found that sorting of EGF-R and genesis of MVBs require the Alix-related tyrosine phosphatase HD-PTP/PTN23 suggesting that some of the functions attributed to Alix, might in fact be due to HD-PTP [16]. Thus our study demonstrating that neither Alix knock-down nor expression of Alix-CT affect maturation of autophagosomes suggests once more that Alix plays a role clearly distinct from that of ESCRT proteins. Furthermore, our observations demonstrate that the potency of Alix mutants to block cell death *in vivo* and *in vitro* cannot simply be explained by a role of the protein in controlling autophagy, known to be involved in several aspects of cell death.

Acknowledgments

The authors thank Fiona Hemming for critical reading of the manuscript and all members of the lab for numerous suggestions throughout this work. This work was supported by Inserm, the University Joseph Fourier, and grants from the Association

Alix and ALG-2 make a link between endosomes and neuronal death

Anne-Laure Mahul-Mellier¹, Flavie Strappazzon², Christine Chatellard-Causse, Béatrice Blot, David Béal, Sakina Torch, Fiona Hemming, Anne Petiot, Jean-Marc Verna, Sandrine Fraboulet³ and Rémy Sadoul⁴

INSERM, U836, Equipe 2, Neurodégénérescence et Plasticité, Grenoble, F-38042, France, and Université Joseph Fourier, Grenoble Institut des Neurosciences, Grenoble, F-38042, France

Abstract

Alix [ALG-2 (apoptosis-linked gene 2)-interacting protein X] is a ubiquitous adaptor protein first described for its capacity to bind to the calcium-binding protein, ALG-2. Alix regulates neuronal death in ways involving interactions with ALG-2 and with proteins of the ESCRT (endosomal sorting complex required for transport). Even though all Alix interactors characterized to date are involved in endosomal trafficking, the genuine function of the protein in this process remains unclear. We have demonstrated recently that Alix and ALG-2 form in the presence of calcium, a complex with apical caspases and with the endocytosed death receptor TNFR1 (tumour necrosis factor α receptor 1), thus suggesting a molecular coupling between endosomes and the cell death machinery.

Introduction

Numerous observations suggest that, in several neurodegenerative diseases, including ALS (amyotrophic lateral sclerosis), AD (Alzheimer's disease) and Niemann–Pick disease, affected neurons display an early impairment in the endosomal system. For example, in AD brains, endosome abnormalities appear in neurons long before amyloid plaque and neurofibrillary tangle formation [1]. The endosomal system is composed of a series of intracellular compartments within which endocytosed molecules traffic. Most of the endocytosed proteins return to the membrane, while some meant for degradation are selectively entrapped in vesicles budding from the membrane into the lumen of endosomes. This process leads to the formation of endosome intermediates called MVBs (multivesicular bodies), filled with intraluminal vesicles; these and their cargoes will be hydrolysed after fusion of the MVBs with lysosomes [2]. One sorting signal used for the trafficking through MVBs is the mono-ubiquitination of cytosolic parts of transmembrane receptors, which occurs after their activation at the cell surface. Once inside endosomes, ubiquitinated cytoplasmic domains pointing out into the cytosol trigger the sequential building of the ESCRTs (endosomal sorting complexes required for transport) on to the endosomal membrane. CHMPs (charged multivesicular body

proteins) of ESCRT-III associate to form a lattice entrapping transmembrane proteins and which is necessary for endosomal membrane vesiculation [3]. Another actor of the vesicle budding inside endosomes might be the protein Alix [ALG-2 (apoptosis-linked gene 2)-interacting protein X]/AIP1 (actin-interacting protein 1), which binds to both ESCRT-I and ESCRT-III, as well as to LBPA (lysobisphosphatidic acid), a lipid facilitating the budding of vesicles inside MVBs [4].

An important hint that MVB abnormalities lead to neurodegenerative diseases came from the discovery that Niemann–Pick type C disease is linked to mutations inducing abnormal accumulation of unesterified cholesterol in MVBs and the concomitant death of neurons [5]. More recently, Reid et al. [6] found that the spastin protein encoded by *SPAST*, mutations of which were known to cause degeneration of cortical motoneurons in hereditary spastic paraplegia, interacts with CHMP1B of ESCRT-III. Mutations of the ESCRT-III subunit CHMP2B have also been reported to be linked with cases of FTD (frontotemporal dementia), the second most common cause of presenile dementia, characterized by a severe cortical atrophy, and with non-SOD1 (superoxide dismutase 1) ALS, associated with degeneration of motor neurons [7,8]. These genetic data fit with the morphological data to suggest that endosomal function is central to neurodegenerative pathologies. The connection between endosomal dysfunction and neurodegeneration means that certain trafficking and/or processing events taking place in endosomes are critically important for neuronal homeostasis. One possibility is that molecular interactions within endosomes control the initiation of a neuronal death programme. The adaptor protein Alix seems to mediate interactions of this type.

Alix ESCRTs endosomes

We first characterized Alix while searching for proteins capable of binding the calcium-binding protein ALG-2 [9]. At that time, the aim of our research was the definition of

Key words: apoptosis, calcium, caspase, endosomal sorting complex required for transport (ESCRT), neuron, tumour necrosis factor α receptor 1 (TNFR1).

Abbreviations used: AD, Alzheimer's disease; ALG-2, apoptosis-linked gene-2; Alix, ALG-2-interacting protein X; Alix-CT, C-terminal half of Alix; ALS, amyotrophic lateral sclerosis; BHK, baby-hamster kidney; CHMP, charged multivesicular body protein; ESCRT, endosomal sorting complex required for transport; LBPA, lysobisphosphatidic acid; MVB, multivesicular body; TNFR1, TNF α receptor 1.

¹Present address: Experimental Medicine and Toxicology, Imperial College London, London W12 0NN, U.K.

²Present address: European Center for Brain Research, Santa Lucia Foundation, Molecular Neuroembryology Unit, 00143 Rome, Italy

³Present address: MRC Functional Genetic Unit, Department of Physiology, Anatomy and Genetics, University of Oxford, Oxford OX1 3QX, U.K.

⁴To whom correspondence should be addressed (email remy.sadoul@ujf-grenoble.fr).

molecules involved in death induced by intracellular calcium, and our interest for ALG-2 began as it was reported to be required for T-cell apoptosis [10]. Alix is a 90 kDa cytosolic protein with no enzymatic signature, but with a long proline-rich C-terminal region, which binds ALG-2 only when the latter is complexed to calcium. Other Alix interactors have a demonstrated role in endocytosis: CIN85 (Cbl-interacting protein of 85 kDa)/SETA [SH3 (Src homology 3) domain-containing gene expressed in tumorigenic astrocytes]/Ruk (regulator of ubiquitous kinase), first involved in endocytosis of ubiquitinated tyrosine kinase receptors [11]; endophilins A, regulating clathrin-dependent endocytosis of surface receptors [12]; Tsg101 (tumour susceptibility gene 101) and SNF7/CHMP4B, members of ESCRT-I and -III respectively [13,14]; and LBPA, a phospholipid which is highly concentrated inside MVBs and may promote intraluminal vesiculation of endosomes [15]. Alix might orchestrate the deformation and fission of lipid bilayers since it was described as being involved in the budding of vesicles inside MVBs [15,16] and the abscission reactions that complete mammalian cell division [17]. The role played by the protein in deforming membranes was recognized as central by enveloped viruses, which recruit it in order to bud off membranes [18]. Surprisingly, however, neither we nor other laboratory groups have found any significant effect of Alix on endocytosis and degradation of EGF (epidermal growth factor) or transferrin receptors in mammalian cells [19]; thus the final consequence of Alix activity in MVBs remains largely unclear.

Alix links endosomes to neuronal death

One hint that Alix is involved in neuronal death comes from our observations of its up-regulation in rat-degenerating neurons of the striatum in a model of Huntington's disease [20] or of the hippocampus during epileptic seizures. In this latter case, neuronal death is known to occur because of calcium entering through glutamate receptors and is accompanied by a massive up-regulation of endocytosis and of autophagy [21]. Alix up-regulation could be a cause of neurodegeneration, since its overexpression by transfection was sufficient to activate caspases and induce death of post-mitotic cerebellar granule neurons. On the other hand, expression in these cultured neurons of the Alix C-terminal half (Alix-CT) of the protein, which acts as a dominant-negative mutant, blocked death induced by potassium deprivation. Both the pro- and anti-apoptotic effects of Alix and Alix-CT respectively required the integrity of the ALG-2-binding site, suggesting that the calcium-dependent interaction of ALG-2 with Alix is instrumental in controlling neuronal death [22]. We need here to emphasize that the cerebellar neurons used in these experiments were post-mitotic and therefore that the effects seen on apoptosis cannot be due to the role of Alix in cytokinesis. Furthermore, the neurons were cultured in the absence of serum and of exogenous factors and only survive because of chronic depolarization obtained by high extracellular potassium concentrations. This rules out that, in this paradigm, Alix mutants act on cell death by modifying

endosomal trafficking of trophic receptors. We went on to test whether Alix/ALG-2 might play a role in cell death in a more physiological setting, which is the programmed cell death occurring naturally during development of the chick embryo. Using electroporation, we found that expression of some mutants of Alix blocked death of motor neurons during normal development. This blocking effect was tightly dependent on binding to both ALG-2 and ESCRT-I and -III. Our interpretation of these results is that some truncated forms of Alix behave as dominant-negative mutants inhibiting the formation of an ALG-2–Alix–ESCRT complex necessary for cell death [23]. Therefore the Alix–ALG-2 complex could make a link between endosomes and a signalling, or an execution step of neuronal death [4].

Alix–ALG-2: a new caspase-activating platform bound to ESCRT?

Using immunoprecipitations coupled to MS, we found that, in dying cerebellar neurons, Alix associates in a complex containing the apical caspase 8. We have reproduced the formation of this complex in BHK (baby-hamster kidney) cells and shown that it is tightly dependent on calcium and on the capacity of Alix to interact with ALG-2 [24]. Another apical caspase, caspase 9, also co-immunoprecipitated with Alix and ALG-2, whereas execution caspases 3 and 7 did not. Caspases are synthesized as zymogens, and activation occurs through caspase proteolytic cleavage. Intrinsic and extrinsic pathways of apoptosis led to the recruitment of apical caspases on to multimeric complexes, inducing proximity and thereby autocatalytic activation of the zymogens. Activated apical caspases in turn cleave and thereby activate execution caspases, which dismantle the cell undergoing apoptosis. We therefore hypothesize that Alix functions as a scaffold allowing autocatalytic activation of caspase 8 and 9 and that the build-up of the complex is controlled by calcium binding to ALG-2. In agreement with this, expression of Alix-CT or knockdown of Alix protected BHK cells from death induced by thapsigargin, which elevates cytosolic calcium by blocking the sarcoplasmic/endoplasmic reticulum Ca^{2+} -ATPase (F. Strappazzon, S. Torch, C. Chatellard-Causse, A. Petiot, B. Blot, J.-M. Verna and R. Sadoul, unpublished work).

Our results, together with the tight relationship of Alix with endosomes, suggest a coupling of apical caspases to these latter organelles. A possible understanding of this unexpected link came from the work of Schneider-Brachert et al. [25] who reported that, in lymphocytes, activation of caspase 8 by TNFR1 (tumour necrosis factor α receptor 1) occurs only after the receptor has been endocytosed and passed on to MVBs. This finding has introduced the notion of death-inducing signalling endosomes [25]. We recently demonstrated that Alix binds to endocytosed TNFR1, whereas ALG-2 binds to pro-caspase 8 [24]. In the presence of calcium, the complex made by Alix and ALG-2 contains both pro-caspase 8 and TNFR1 and might thus be instrumental in adapting the caspase zymogen on to TNFR1-containing receptors. The physiological relevance of these interactions was given by

the observation that expression of Alix Δ ALG-2, which interacts with TNFR1, but not with caspase 8, blocks TNFR1-induced cell death without interfering with endocytosis of the receptor. Furthermore, we observed that the same mutant blocked programmed cell death of developing motor neurons in the chick embryo, which is controlled by TNFR1 [24].

Alix controls caspases . . . and what else?

Even though the idea of an Alix–ALG-2 complex allowing activation of apical caspases on the surface of endosomes is appealing, it cannot entirely explain the mechanisms by which Alix mutants block neuronal death. Indeed, we found that expression of P35, a baculovirus pan-caspase inhibitor, delays, but does not block, death of motor neurons *in vivo*, in contrast with Alix mutants which allow long-term survival of the same neurons [24]. This is in good agreement with numerous publications that have reported that, in most cases, inhibiting or knocking out caspases only blocks nuclear destruction, but does not allow neuronal survival. Thus neuronal death is the sum of caspase-dependent mechanisms involved in the dismantling of the nucleus and of caspase-independent mechanisms allowing destruction of the cytoplasm. The capacity of Alix mutants to block cell death both *in vivo* and *in vitro* suggests that the protein drives both caspase-dependent and -independent processes.

Caspase-independent mechanisms are ill-defined, but the presence of autophagic vacuoles in dying cells in which caspases are inhibited, or in certain neurons dying during development and in adult central nervous system, has led several authors to postulate that macro-autophagy is a caspase-independent mechanism contributing to cell destruction [26,27]. Macro-autophagy, hereafter referred to as autophagy, is the major pathway for degradation of long-lived proteins and the only known pathway for elimination of organelles. This process begins with the formation of double-membrane vacuoles, referred to as autophagosomes, which engulf cytoplasmic material. Autophagosomes fuse with endosomes, thereby giving rise to amphisomes, which in turn fuse with lysosomes [28]. Several proteins involved in the biogenesis of MVBs, among which the ATPase SKD1 (suppressor of K⁺ transport defect 1), as well as the three ESCRTs, modulate autophagy [29,30]. With this in mind, we have challenged the hypothesis that Alix might drive caspase-independent cell death by controlling autophagy. Using cerebellar granule neurons, we found that Alix-induced cell death is accompanied by a drastic increase in the number of autophagosomes, whereas expression of Alix-CT reduced the formation of autophagosomes in dying neurons. However, in cell lines whose viability is not influenced by Alix, overexpression or down-regulation of the protein had no effect on autophagosomes or autophagic protein degradation induced by amino acid depletion [31]. These results show that, in non-dying cells, Alix does not participate directly in autophagy, and reinforce the conclusion of other studies demonstrating that its role differs from that of classical ESCRT proteins. Thus, even though Alix's role in apoptosis seems to be due to a control of

caspase activation by both calcium and endosomes, its role in controlling caspase-independent processes remains obscure.

Funding

This work was supported in part by Inserm, the University Joseph Fourier, grants from the Association Française contre les Myopathies [grant number MNM 2007], the Association pour la Recherche sur la Sclérose Latérale Amyotrophique [grant number 060711] and the Association pour la Recherche contre le Cancer [grant number 4948]. A.-L.M.-M. was supported by a fellowship from the Association Française contre les Myopathies.

References

- Nixon, R.A. (2005) Endosome function and dysfunction in Alzheimer's disease and other neurodegenerative diseases. *Neurobiol. Aging* **26**, 373–382
- Gruenberg, J. and Stenmark, H. (2004) The biogenesis of multivesicular endosomes. *Nat. Rev. Mol. Cell Biol.* **5**, 317–323
- Williams, R.L. and Urbé, S. (2007) The emerging shape of the ESCRT machinery. *Nat. Rev. Mol. Cell Biol.* **8**, 355–368
- Sadoul, R. (2006) Do Alix and ALG-2 really control endosomes for better or for worse? *Biol. Cell* **98**, 69–77
- Nixon, R.A. (2004) Niemann–Pick Type C disease and Alzheimer's disease: the APP–endosome connection fattens up. *Am. J. Pathol.* **164**, 757–761
- Reid, E., Connell, J., Edwards, T.L., Duley, S., Brown, S.E. and Sanderson, C.M. (2005) The hereditary spastic paraplegia protein spastin interacts with the ESCRT-III complex-associated endosomal protein CHMP1B. *Hum. Mol. Genet.* **14**, 19–38
- Skibinski, G., Parkinson, N.J., Brown, J.M., Chakrabarti, L., Lloyd, S.L., Hummerich, H., Nielsen, J.E., Hodges, J.R., Spillantini, M.G., Thusgaard, T. et al. (2005) Mutations in the endosomal ESCRTIII-complex subunit CHMP2B in frontotemporal dementia. *Nat. Genet.* **37**, 806–808
- Parkinson, N., Ince, P.G., Smith, M.O., Highley, R., Skibinski, G., Andersen, P.M., Morrison, K.E., Pall, H.S., Hardiman, O., Collinge, J. et al. (2006) ALS phenotypes with mutations in CHMP2B (charged multivesicular body protein 2B). *Neurology* **67**, 1074–1077
- Missotten, M., Nichols, A., Rieger, K. and Sadoul, R. (1999) Alix, a novel mouse protein undergoing calcium-dependent interaction with the apoptosis-linked-gene 2 (ALG-2) protein. *Cell Death Differ.* **6**, 124–129
- Vito, P., Lacana, E. and D'Adamio, L. (1996) Interfering with apoptosis: Ca²⁺-binding protein ALG-2 and Alzheimer's disease gene ALG-3. *Science* **271**, 521–525
- Chen, B., Borinstein, S.C., Gillis, J., Sykes, V.W. and Bogler, O. (2000) The glioma-associated protein SETA interacts with AIP1/Alix and ALG-2 and modulates apoptosis in astrocytes. *J. Biol. Chem.* **275**, 19275–19281
- Chatellard-Causse, C., Blot, B., Cristina, N., Torch, S., Missotten, M. and Sadoul, R. (2002) Alix (ALG-2-interacting protein X), a protein involved in apoptosis, binds to endophilins and induces cytoplasmic vacuolization. *J. Biol. Chem.* **277**, 29108–29115
- von Schwedler, U.K., Stuchell, M., Muller, B., Ward, D.M., Chung, H.Y., Morita, E., Wang, H.E., Davis, T., He, G.P., Cimbora, D.M. et al. (2003) The protein network of HIV budding. *Cell* **114**, 701–713
- Strack, B., Calistri, A., Craig, S., Popova, E. and Gottlinger, H.G. (2003) AIP1/ALIX is a binding partner for HIV-1 p6 and EIAV p9 functioning in virus budding. *Cell* **114**, 689–699
- Matsuo, H., Chevallier, J., Mayran, N., Le Blanc, I., Ferguson, C., Faure, J., Blanc, N.S., Matile, S., Dubochet, J., Sadoul, R. et al. (2004) Role of LBPA and Alix in multivesicular liposome formation and endosome organization. *Science* **303**, 531–534
- Le Blanc, I., Luyet, P.P., Pons, V., Ferguson, C., Emans, N., Petiot, A., Mayran, N., Demareux, N., Faure, J., Sadoul, R. et al. (2005) Endosome-to-cytosol transport of viral nucleocapsids. *Nat. Cell Biol.* **7**, 653–664
- Carlton, J.G. and Martin-Serrano, J. (2007) Parallels between cytokinesis and retroviral budding: a role for the ESCRT machinery. *Science* **316**, 1908–1912

- 18 Odorizzi, G. (2006) The multiple personalities of Alix. *J. Cell Sci.* **119**, 3025–3032
- 19 Cabezas, A., Bache, K.G., Brech, A. and Stenmark, H. (2005) Alix regulates cortical actin and the spatial distribution of endosomes. *J. Cell Sci.* **118**, 2625–2635
- 20 Blum, D., Hemming, F.J., Galas, M.C., Torch, S., Cuvelier, L., Schiffmann, S.N. and Sadoul, R. (2004) Increased Alix (apoptosis-linked gene-2 interacting protein X) immunoreactivity in the degenerating striatum of rats chronically treated by 3-nitropropionic acid. *Neurosci. Lett.* **368**, 309–313
- 21 Hemming, F.J., Fraboulet, S., Blot, B. and Sadoul, R. (2004) Early increase of apoptosis-linked gene-2 interacting protein X in areas of kainate-induced neurodegeneration. *Neuroscience* **123**, 887–895
- 22 Trioulier, Y., Torch, S., Blot, B., Cristina, N., Chatellard-Causse, C., Verna, J.M. and Sadoul, R. (2004) Alix, a protein regulating endosomal trafficking, is involved in neuronal death. *J. Biol. Chem.* **279**, 2046–2052
- 23 Mahul-Mellier, A.-L., Hemming, F.J., Blot, B., Fraboulet, S. and Sadoul, R. (2006) Alix, making a link between ALG-2, the ESCRT complex and neuronal death *in vivo*. *J. Neurosci.* **26**, 542–549
- 24 Mahul-Mellier, A.L., Strappazon, F., Petiot, A., Chatellard-Causse, C., Torch, S., Blot, B., Freeman, K., Kuhn, L., Garin, J., Verna, J.-M. et al. (2008) Alix and ALG-2 are involved in tumor necrosis factor receptor 1-induced cell death. *J. Biol. Chem.* **283**, 34954–34965
- 25 Schneider-Brachert, W., Tchikov, V., Neumeier, J., Jakob, M., Winoto-Morbach, S., Held-Feindt, J., Heinrich, M., Merkel, O., Ehrenschwender, M., Adam, D. et al. (2004) Compartmentalization of TNF receptor 1 signaling: internalized TNF receptors as death signaling vesicles. *Immunity* **21**, 415–428
- 26 Clarke, P.G. (1990) Developmental cell death: morphological diversity and multiple mechanisms. *Anat. Embryol.* **181**, 195–213
- 27 Baehrecke, E.H. (2005) Autophagy: dual roles in life and death? *Nat. Rev. Mol. Cell Biol.* **6**, 505–510
- 28 Codogno, P. and Meijer, A.J. (2005) Autophagy and signaling: their role in cell survival and cell death. *Cell Death Differ.* **12** (Suppl. 2), 1509–1518
- 29 Nara, A., Mizushima, N., Yamamoto, A., Kabeya, Y., Ohsumi, Y. and Yoshimori, T. (2002) SKD1 AAA ATPase-dependent endosomal transport is involved in autolysosome formation. *Cell Struct. Funct.* **27**, 29–37
- 30 Rusten, T.E. and Simonsen, A. (2008) ESCRT functions in autophagy and associated disease. *Cell Cycle* **7**, 1166–1172
- 31 Petiot, A., Strappazon, F., Chatellard-Causse, C., Blot, B., Torch, S., Verna, J.-M. and Sadoul, R. (2008) Alix differs from ESCRT proteins in the control of autophagy. *Biochem. Biophys. Res. Commun.* **375**, 63–68

Received 6 November 2008
doi:10.1042/BST0370200

Post-doctoral training #1: Study of the role of transglutaminase 2 protein (TG2) in the autophagy process (2008-2010). Laboratory of Mauro Piacentini at the University of Rome, Tor Vergata (Marie Curie post-doctoral fellow).

During my PhD, I discovered the interesting field of autophagy, which was in full expansion at this time. I thus decided to perform a post-doctoral training in this field. To this end, I moved to Italy in 2008, to start my first post-doctoral training in the laboratory of Prof. Piacentini, expert in cell death and autophagy (University of Rome). Although the main function of autophagy is to provide nutrients for vital cellular functions during fasting and other forms of stress, it was more recently shown to selectively eliminate unwanted, potentially harmful cytosolic material, such as damaged mitochondria or protein aggregates. Autophagy consists in the formation of a double-membrane structure that sequesters cytosolic contents into large autophagic vesicles to form the autophagosomes. Autophagosomes subsequently fuse to lysosomes, where their contents are degraded. At the beginning of my post-doctoral training, the molecular mechanisms regulating the specific recognition and elimination of the aggregates by autophagy were just starting to be identified. Several studies had shown that Transglutaminase 2 (TG2), a multifunctional protein, is involved in the pathogenic mechanisms responsible for a number of human degenerative diseases characterized by the accumulation of protein aggregates in affected brains, such as Alzheimer's, Parkinson's and Huntington's disease. When I joined the laboratory, the team of Prof Piacentini was discovering that TG2 was involved in autophagosome maturation *in vitro*. Starting from these premises we decided to analyze the role of TG2 in autophagy *in vivo*. We observed a marked accumulation of ubiquitinated proteins in the absence of TG2 *in vivo*. We have also shown that the activation of TG2 transamidating activity is increased by autophagy induction. We therefore proposed that the activated enzyme may catalyze the misfolded protein crosslinking, leading to the formation of small aggregates and subsequently large aggregates. The formation of these ubiquitinated inclusions is next recognized by cargo proteins and uploaded inside the autophagosomes. **This work has been published in *Cell Death and Differentiation* journal and shed light on the possible involvement of the enzyme in the degenerative disorders involving the formation of aggregates and their clearance by autophagy** (see D'Eletto et al. 2012 *Cell Death and Diff*).

Post-doctoral training #2: Study of the molecular mechanisms underlying the function of AMBRA1 in autophagy (2010-2014). Laboratory of Francesco Cecconi at Santa Lucia Foundation (Rome).

At the time I did my first postdoc, it was not fully understood how the autophagy process was controlled but the team of Prof Piacentini in collaboration with the team of Prof Cecconi (Santa Lucia Foundation, Rome) highlighted the protein AMBRA1 (Activating Molecule in BECN-1 regulated Autophagy) as a novel positive regulator of autophagy in mammals. However, very little was known about the mechanisms of action of AMBRA1 in autophagy, therefore I took the opportunity to join the laboratory of Pr Cecconi (who discovered *AMBRA1* gene), in order to participate in studies dedicated to a better understanding of the molecular mechanisms underlying the function of AMBRA1.

Firstly, I revealed a previously unknown interaction between AMBRA1 and Bcl-2 at the mitochondrial outer membrane (MOM). In response to nutrient withdrawal, this interaction is dissociated, and AMBRA1 associates with BECLIN 1 at the endoplasmic reticulum (ER) to stimulate autophagy by promoting autophagosome formation. Bcl-2 can thus inhibit the initiation of autophagy by binding BECLIN 1 at the ER, as well as at mitochondrial membranes preventing AMBRA1 binding to BECLIN 1. **This work provides important novel insight into the importance of subcellular location on the activity of autophagy proteins and the crosstalk between autophagy and apoptosis involving Bcl2** (See Strappazzon et al. 2010, *EMBO*).

Autophagy-mediated degradation of mitochondria (hereafter mitophagy) is a pivotal quality control mechanism in cellular homeostasis. During this process, mitochondria are delivered to autophagosomes by *mitophagic receptors* that link their cargo to an adapter protein, LC3 (Microtubule-associated protein 1A/1B-light chain 3). When mitophagy is induced, the PTEN-induced putative kinase 1 (PINK1) is stabilized at the mitochondria, where it recruits the E3 Ubiquitin ligase PARKIN. In addition to the PINK1/PARKIN pathway, *mitophagy receptors* can also regulate mitophagy. They possess a consensus sequence (the LIR, LC3-Interacting region) that allows LC3 binding for selective autophagy. Primed by the fact that I discovered that a small pool of AMBRA1 was localized to the mitochondria (Strappazzon et al., 2010 *EMBO*), I decided to investigate a putative role of AMBRA1 in mitophagy. To this end, I generated “AMBRA1-ActA”, an organelle-targeted mutant of AMBRA1 (see Strappazzon et al. 2014 *Cell Death and Diff.*). Our data indicate that AMBRA1 is a LIR-containing protein that regulates both PARKIN-

dependent and -independent mitophagy. **For a long time, PINK1/PARKIN-dependent mitophagy pathway was one of the most common mitophagy described in mammals. With this work, we shed new light on the regulation of mitochondrial quality control and homeostasis in mammalian cells, by demonstrating a novel AMBRA1-dependent pathway of mitophagy.**

I also participated, as a second author, to an important study advancing our understanding of how two systems that regulate autophagy, ULK1 and BECLIN 1, come together (Nazio et al. 2012 *Nat Cell Biol*). Indeed, following mTOR (mammalian target of rapamycin) inhibition, autophagy is primed by the ULK1 and the BECLIN-1-Vps34-AMBRA1 complexes. Although several regulative steps have been described along this pathway, few targets of mTOR were known, and the cross-talk between ULK1 and BECLIN 1 complexes was not fully understood. We showed that under non-autophagic conditions, mTOR inhibits AMBRA1 by phosphorylation, whereas on autophagy induction, AMBRA1 is dephosphorylated. In this condition, AMBRA1 favours ULK1 stabilization, self-association and function. As ULK1 has been shown to activate AMBRA1 by phosphorylation, this work suggests that the proposed pathway may act as a positive regulation loop, which may be targeted in human disorders linked to impaired autophagy.

Finally, as a second author, I participated to another important study showing that the MicroRNA MIR7-3HG, a MYC-dependent modulator of cell proliferation, inhibits autophagy by a direct regulatory loop involving AMBRA1 (see Capizzi et al. 2016 *Autophagy*).

In total, this post-doctoral work leads to the publication of **two articles as first author** in *EMBO and Cell Death and Differentiation journals*; **two articles as second author** in *Nature Cell Biology and Autophagy J*, and two reviews **as first and second author** (see articles below).

Type 2 transglutaminase is involved in the autophagy-dependent clearance of ubiquitinated proteins

M D'Eletto^{1,6}, MG Farrace^{1,6}, F Rossin¹, F Strappazon², G Di Giacomo¹, F Cecconi^{1,2}, G Melino³, S Sepe⁴, S Moreno⁴, GM Fimia⁵, L Falasca⁵, R Nardacci⁵ and M Piacentini^{*1,5}

Eukaryotic cells are equipped with an efficient quality control system to selectively eliminate misfolded and damaged proteins, and organelles. Abnormal polypeptides that escape from proteasome-dependent degradation and aggregate in the cytosol can be transported via microtubules to inclusion bodies called 'aggresomes', where misfolded proteins are confined and degraded by autophagy. Here, we show that Type 2 transglutaminase (TG2) knockout mice display impaired autophagy and accumulate ubiquitinated protein aggregates upon starvation. Furthermore, p62-dependent peroxisome degradation is also impaired in the absence of TG2. We also demonstrate that, under cellular stressful conditions, TG2 physically interacts with p62 and they are localized in cytosolic protein aggregates, which are then recruited into autophagosomes, where TG2 is degraded. Interestingly, the enzyme's crosslinking activity is activated during autophagy and its inhibition leads to the accumulation of ubiquitinated proteins. Taken together, these data indicate that the TG2 transamidating activity has an important role in the assembly of protein aggregates, as well as in the clearance of damaged organelles by macroautophagy.

Cell Death and Differentiation (2012) 19, 1228–1238; doi:10.1038/cdd.2012.2; published online 10 February 2012

Misfolded proteins are a constant byproduct of eukaryotic cell metabolism resulting from genetic mutations, inappropriate posttranslational protein modifications, and environmental stress. It has been proposed that up to 30% of newly synthesized proteins are not properly folded.¹ These non-functional misfolded proteins are prone to form aggregates that can interfere with normal cellular functions inducing cellular stress, which can ultimately lead to cell death. Thus, the efficient management of misfolded proteins and their aggregates is essential for cellular viability, and thus cells have evolved several interconnected pathways to limit their accumulation.² This system of protein quality control acts at multiple levels, trying to re-establish the proper tertiary structure of unfolded or misfolded proteins via molecular chaperones, and eventually promoting the degradation of those aberrant proteins that fail to refold.² In fact, the misfolded proteins are recognized and poly-ubiquitinated by specific ubiquitin E3 ligases and this posttranslational modification targets them to proteasome degradation, which constitutes a critical part of the cytoprotective protein quality control machinery.^{3,4} Defects in the ubiquitin–proteasome machinery lead to the accumulation of misfolded proteins and aggregates under the specific form of 'aggresomes', a pathological condition commonly found in many degenerative diseases.² Recent findings suggest that the formation of aggresomes is an attempt to prevent the intracellular toxicity derived from

protein aggregates before they are actively removed by autophagy.⁵ In fact, once aggregated, misfolded proteins cannot be degraded efficiently by proteasome as they cannot pass through the narrow structures of the proteasome.⁶

Autophagy was initially described as a cellular response to nutrient deprivation by which cells are able to 'self-digest' part of their own cytoplasm to recycle essential macromolecules for survival.⁷ In the most characterized form of autophagy, macroautophagy, starvation induces a double-membrane structure that sequesters cytosolic contents (including mitochondria, peroxisomes, and ribosomes) into large autophagic vesicles to form the autophagosomes. Autophagosomes subsequently fuse to lysosomes, where their contents are degraded by hydrolytic enzymes.⁸ This feature makes autophagy an ideal way to remove protein aggregates that cannot be processed by proteasomes. The molecular mechanisms regulating the specific recognition and elimination of the aggresomes by autophagy have just recently begun to be uncovered.

This process requires autophagy cargo proteins, such as p62/SQSTM1 and NBR1, which bind ubiquitinated proteins via UBA domains, and interact with LC3 via their LIR domain.⁹ Therefore, at least two modifications, ubiquitination and oligomer formation, have been proposed to serve as *cis*-acting signals to promote selective autophagy.

¹Department of Biology, University of Rome 'Tor Vergata', Rome, Italy; ²Laboratory of Molecular Neuroembriology, IRCCS Fondazione Santa Lucia, Rome, Italy; ³Department of Experimental Medicine and Biochemical Sciences, Biochemistry IDI-IRCCS Laboratory, University of Rome 'Tor Vergata', Rome, Italy; ⁴Department of Biology-LIME, University of Rome 'Roma Tre', Rome, Italy and ⁵National Institute for Infectious Diseases IRCCS 'L. Spallanzani', Rome, Italy

*Corresponding author: M Piacentini, Department of Biology, University of Rome 'Tor Vergata', Rome 00173, Italy. Tel: +39 6 72594234; Fax: +39 6 72594222; E-mail: mauro.piacentini@uniroma2.it

⁶These authors contributed equally to this work.

Keywords: autophagy; MG132; p62; transglutaminase 2; ubiquitinated proteins

Abbreviations: TG2, Type 2 transglutaminase; Starv, starvation; CQ, chloroquine; 2-DG, 2-deoxy-D-glucose; Rap, rapamycin; MG132, Z-Leu-Leu-Leu-al; VCP, valosin-containing protein; PMP70, peroxisomal membrane protein; HD, Huntington's disease; MEFs, mouse embryonic fibroblast

Received 07.10.11; revised 05.12.11; accepted 21.12.11; Edited by RA Knight; published online 10.2.12

Type 2 transglutaminase (TG2) is a multifunctional protein that is capable of carrying a large number of biochemical functions. In the presence of high calcium levels, TG2 catalyzes a vast array of protein posttranslational modifications, including protein–protein crosslinking, incorporation of primary amines into proteins, as well as glutamine deamination. In addition, TG2 might also act as a G-protein, coupling various receptors to phospholipase C (PLC δ 1).¹⁰ This activity is inhibited by Ca²⁺, which then acts as a switch between the two main biochemical functions of the enzyme.¹⁰ Under physiological conditions, the low cytosolic Ca²⁺ concentration does not allow the enzyme to act as a transamidating agent.¹¹ However, catalytically inactive TG2 can perform other functions; for example, TG2 can associate with integrins to activate signaling pathways contributing to increase cell survival.¹⁰ If the stress or cellular damage is too severe, the Ca²⁺-dependent activation of TG2 crosslinking activity has an important role in the induction of apoptosis.¹²

Several studies show that TG2 is involved in the pathogenic mechanisms responsible for a number of human degenerative diseases characterized by the accumulation of protein aggregates in affected brains, such as Alzheimer's disease (AD), Parkinson's disease (PD), Huntington's disease (HD), and in liver diseases (Mallory bodies).^{13,14} We have recently shown that TG2 is involved in autophagosome maturation.^{15,16} Starting from these premises we decided to analyze the role of TG2 in autophagy and shed light on the possible involvement of the enzyme in the degenerative disorders involving the formation of aggresomes and their clearance by autophagy.

Results

Loss of TG2 leads to a defective autophagic response in the liver and heart upon starvation. In order to get an insight into TG2's role in the autophagic process, we decided to investigate the effect of its ablation *in vivo* by producing a transgenic mouse line lacking TG2 and expressing GFP-LC3, which is widely used as an *in vivo* marker for autophagic vesicles. The newly developed transgenic mouse line shows no abnormality and reproduces normally.

Liver: Considering the importance of autophagy in the liver upon starvation, we decided to start our analysis by examining this organ.¹⁷ In both TG2^{+/+} GFP-LC3- or TG2^{-/-} GFP-LC3-fed mice, GFP-LC3 signals were found to diffuse in the cytoplasm with few punctate dots (Figures 1a and c). Following 48 h of starvation (Starv), the number of GFP-LC3 dots increased in both mouse strains, indicating the expected induction of autophagy. However, in the TG2^{-/-} mice, the accumulation of the dots was significantly higher than in TG2^{+/+} mice (Figures 1b and d), suggesting that, in the absence of TG2, more autophagosomes are formed and/or less autophagosomes are degraded by fusing with lysosomes. The quantification of GFP-LC3-positive dots confirmed the increase of these structures after starvation (Figure 1e), with a significant difference in their number in livers of TG2^{-/-} mice compared with the TG2^{+/+} mice. These results are in agreement with the impairment of autophagosome maturation observed *in vitro* in cells lacking TG2.¹⁵

Heart: It is well known that heart muscle shows major changes during starvation; in fact, the number and size of

autophagosomes increased drastically after 48 h of fasting.¹⁷ Therefore, we decided to compare autophagy levels also in cardiac muscles of TG2^{+/+} GFP-LC3 with those of TG2^{-/-} GFP-LC3 mice following 48 h of starvation. As illustrated in Figures (1f–i), the increase in GFP-LC3-positive structures was more accentuated in TG2^{-/-} mice compared with the TG2^{+/+} mice. The quantification of the GFP-LC3 dots evidenced a drastic difference between the levels of autophagy induced in TG2^{+/+} mice compared with TG2^{-/-} mice (Figure 1j) similarly to those described above for the liver.

TG2 is degraded during autophagy. On the basis of the above-reported *in vivo* findings, we decided to further address the role of TG2 in autophagy. To this aim, we analyzed the TG2 protein level in mouse liver after 24–48 h of starvation. Interestingly, we observed a progressive significant decrease (up to 70% at 48 h) in the total protein levels compared with normally fed animals (Figure 2a). To verify whether this phenomenon could be due to the enzyme degradation into autophagolysosomes, we treated the starved animals with chloroquine (CQ), which is known to block the acidification of lysosomes, thus preventing the last stages of autophagy. The results reported in Figure 2b indicate that TG2 is rescued from degradation when the lysosomal activity is partially reduced by CQ. In order to verify whether the degradation of TG2 was a general autophagy-dependent event, we induced autophagy in 2fTGH cells, a human cell line expressing high TG2 levels, by several agents, that is, starvation, 2-deoxy-D-glucose (2-DG) and rapamycin (Rap) (Figure 2c). In the presence of all tested autophagy stimuli we observed a significant decrease of TG2 protein levels, which was comparable to that of p62, an autophagy-cargo protein degraded inside autophagolysosomes (unpublished observations). Prompted by this result, we investigated whether TG2 was detectable inside autophagosomes, by analyzing its co-localization with LC3 upon autophagy induction. The immunofluorescence analysis carried out in 2fTGH-GFP-LC3 cells reported in Figures 3a and b shows that the two proteins co-localize in punctate vesicular structures upon starvation. In keeping with this finding, ultrastructural analysis showed the presence of TG2 immuno-gold positive particles inside double-membrane autophagosomes (Figures 3c and d). To confirm the autophagosomal nature of these structures, we co-immunostained the same sections for p62, which showed the same localization (Figure 3d).

TG2 is present in protein aggregates containing p62. Several reports have suggested that TG2 has a role in the formation of ubiquitinated protein aggregates found in diseases affecting both the brain and the liver.¹⁸ These TG2-related aggregates contain poly-ubiquitinated proteins and therefore are likely to be bound by p62, via its UBA domain.⁹ In order to verify whether TG2 can physically interact with the cargo proteins mediating the delivery of ubiquitinated proteins to autophagosomes, we analyzed by immunoprecipitation the interaction of the enzyme with p62, NBR1 and the valosin-containing protein (VCP), which are essential elements able to convey ubiquitinated substrates into the autophagosomes.¹⁹ To this aim, we

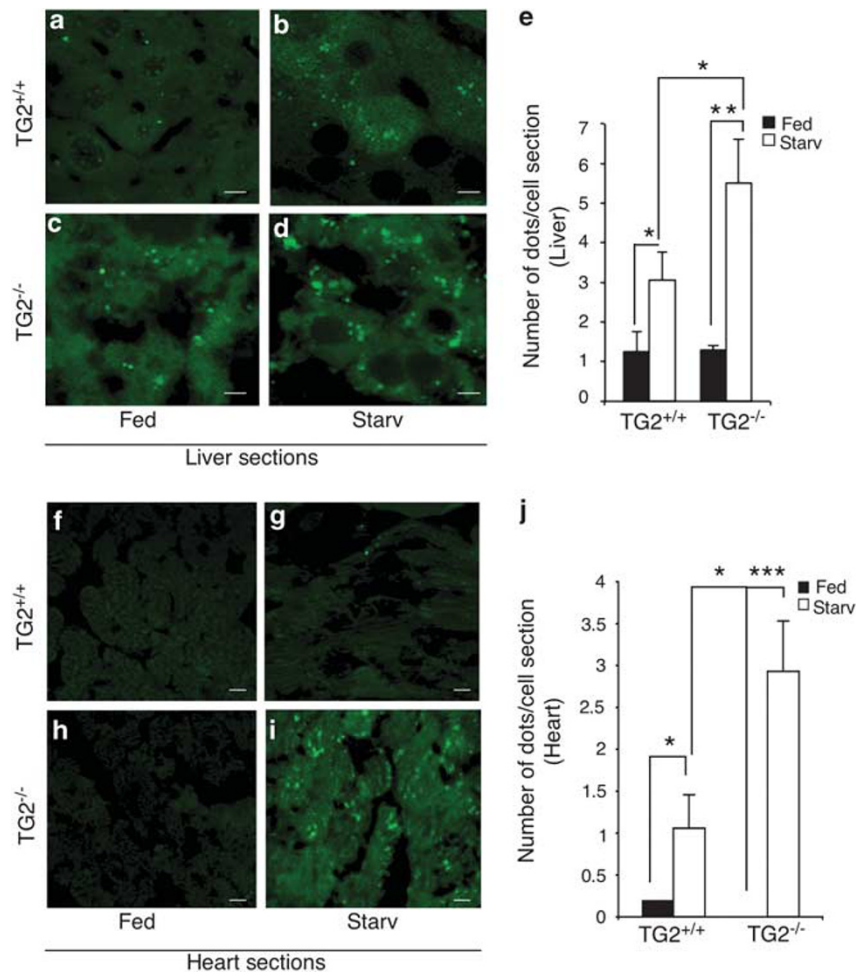


Figure 1 Effect of starvation on liver and heart autophagy in TG2^{+/+} GFP-LC3 or TG2^{-/-} GFP-LC3 mice. (a and b) Liver samples from TG2^{+/+} GFP-LC3 transgenic mice before (a) and after 48 h of starvation (b) were analyzed by fluorescence microscopy. (c and d) Liver samples from TG2^{-/-} GFP-LC3 transgenic mice before (c) and after 48 h of starvation (d) were analyzed by fluorescence microscopy. Scale bar, 8 μ m. (e) Quantitative analysis of the formation of GFP-LC3 dots following autophagy-induction. The number of dots was counted in five independent fields of three independent mice. Results are expressed as the mean \pm S.D. Statistical analysis was performed by analysis of variance ($^*P < 0.05$). (f and g) Heart samples from TG2^{+/+} GFP-LC3 transgenic mice before (f) and after 48 h of starvation (g) were analyzed by fluorescence microscopy. (h and i) Heart samples from TG2^{-/-} GFP-LC3 transgenic mice before (h) and after 48 h of starvation (i) were analyzed by fluorescence microscopy. Scale bar, 3 μ m. (j) Quantitative analysis of the formation of GFP-LC3 dots following autophagy-induction. The number of dots was counted in five independent fields of three independent mice. Results are expressed as the mean \pm S.D. Statistical analysis was performed by analysis of variance ($^*P < 0.05$, $^{**}P < 0.001$, $^{***}P < 0.0001$)

used 2fTGH cells, HEK293 cells in which the TG2 expression is undetectable, and HEK293^{TG2}, in which the wild-type enzyme was stably ectopically expressed (Supplementary Figure S1A). The results indicate that TG2 is part of a protein complex containing p62 (Figures 4a and b) and NBR1 (Supplementary Figure S1B), while the interaction with VCP (Figures 4a and b) and LC3 (unpublished observations) was not detected. Interestingly, in both cell lines the interaction between TG2 and p62 was largely increased upon the inhibition of the proteasome by MG132, which is known to determine the accumulation of ubiquitinated protein aggregates (Figure 7f).²⁰ In order to clarify whether TG2 cooperates with the cargo proteins in the clearance of ubiquitinated proteins, we analyzed TG2 transamidating activity in 2fTGH cells upon starvation. To this aim, we used the 5-(biotinamido)pentylamine incorporation method to verify the enzyme's transamidating activity *in vivo* under the employed experimental conditions.

Intracellular TG2 is known to be largely inactive under normal physiological settings, but it is activated under stressful conditions, which lead to the accumulation of free calcium in the cytoplasm.¹¹ Interestingly, we detected an increased labeling of TG2 substrate proteins already upon autophagy induction, but the amine incorporation was dramatically increased when autophagy induction was associated with the proteasome inhibition (Figure 4c).

The blockade of proteasomal degradation is known to determine a stressful cellular condition leading to the formation of 'aggresomes' containing ubiquitinated proteins.²⁰ To determine whether, under these conditions, TG2 and p62 co-localize on the aggresomes, we carried out the analysis of their ultrastructural localization in starved cells treated with MG132. The data reported in Figure 5 indicate that the enzyme is specifically localized in protein aggregates of various sizes. Interestingly, the co-localization with p62 is observed only in protein aggregates, which display a large

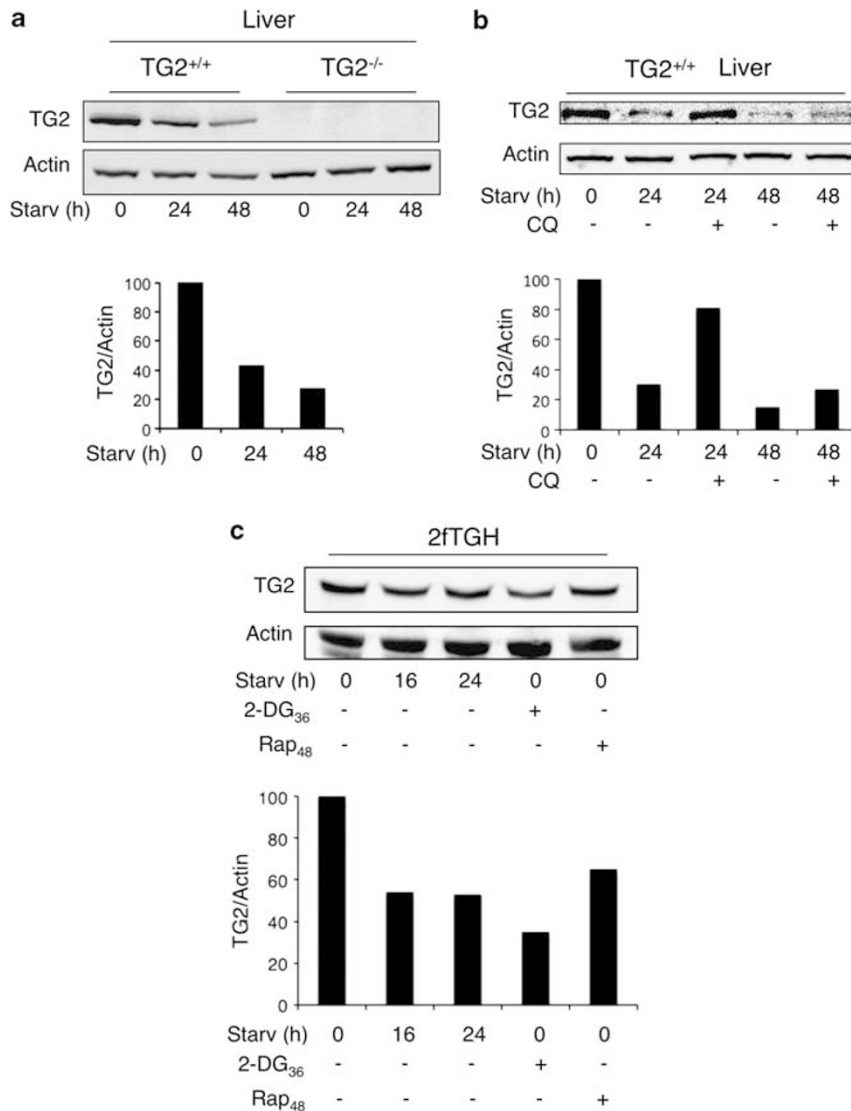


Figure 2 TG2 is degraded by autophagy. (a, upper panel) Immunoblot analysis of TG2 in liver tissues from TG2^{+/+} and TG2^{-/-} mice, before and after 24 and 48 h of starvation. Actin was used as loading control. (a, lower panel) Densitometric analysis of blots (quantification of TG2 bands normalized to actin levels). (b, upper panel) Immunoblot analysis of TG2 in liver tissues from TG2^{+/+} mice, before and after 24 and 48 h of starvation in the presence or not of CQ. For the autophagy inhibition the CQ was administered in the drinking water during the whole starvation time. Actin was used as loading control for immunoblot. (b, lower panel) Densitometric analysis of blots (quantification of TG2 bands normalized to actin levels). TG2 expression is reduced following autophagy induction and is rescued from degradation when the lysosomal activity is blocked by CQ. (c, upper panel) Western blot analysis of TG2 in 2fTGH cells subjected to different treatments to induce autophagy (see Materials and Methods). Actin was used as loading control for immunoblot. (c, lower panel) Densitometric analysis of blots (quantification of TG2 bands normalized to actin levels)

size, thus suggesting that TG2 could be recruited on small protein aggregates and participates to form larger complexes where p62 is later recruited. Furthermore, the immunofluorescence co-localization analysis of p62 and TG2, in cells treated with MG132, confirmed the presence of both proteins in the aggresomes (Supplementary Figure S2).

TG2 is involved in pexophagy. Considering that p62-dependent autophagy of ubiquitinated proteins has been shown to have a key role also in the clearance of damaged and hyper-accumulated organelles, such as mitochondria and peroxisomes, we decided to verify whether the above-described defect in TG2-mediated autophagy could be reflected in an abnormal homeostatic control of these

organelles.¹⁹ In fact, ubiquitination of peroxisomal proteins in mammalian cells is sufficient to cause their p62-mediated turnover by targeting these organelles to autophagosomes and lysosomes.²¹

We took advantage of a well-established pharmacological protocol of peroxisomal induction and subsequent removal in liver rodents.^{22,23} Peroxisomes are known to increase in their number and size, in response to a class of chemically unrelated substances, called peroxisome proliferators; when their administration is discontinued, the liver peroxisomal population rapidly decreases and readily returns to the pre-proliferation status due to autophagy-mediated clearance.^{21,24} We chose a model of inducing peroxisomal proliferation by dietary administration of ciprofibrate. Excess liver

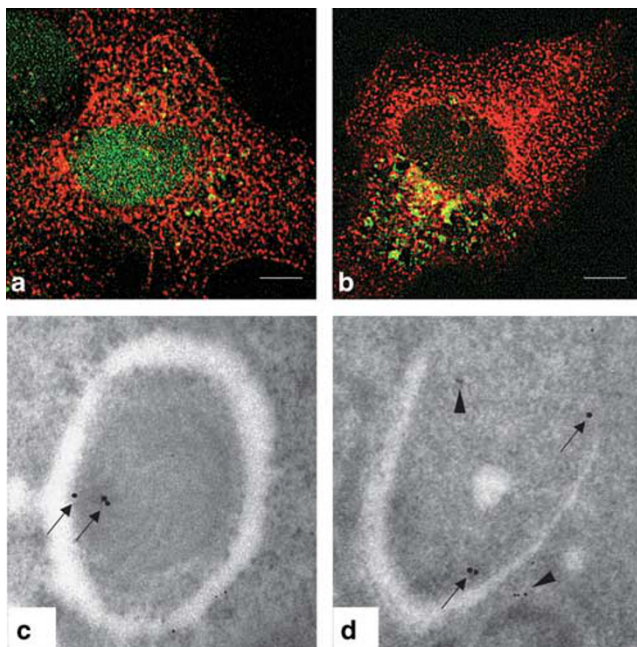


Figure 3 TG2 colocalizes with LC3 in the autophagosomes. (a and b) Immunofluorescence microscopy analysis of 2fTGH-GFP-LC3 cells undergoing autophagy. Cells expressing GFP-LC3 protein were cultured in complete medium (a) or subjected to starvation (b) in EBSS for 16 h, stained with an anti-TG2 antibody and analyzed by microscopy. Green dots represent autophagosomes, red dots TG2 protein, and yellow dots sites of overlap of GFP-LC3 with TG2. Scale bar, 6 μ m. (c and d) Immuno-gold analysis in human 2fTGH cells double-labeled against TG2 (15-nm gold particles) and p62 (5-nm gold particles). The colloidal gold particles, indicating the presence of TG2 (arrows) and p62 (arrowheads), were detected in typical autophagosome-like structures. Original magnification: \times 85 000

peroxisomes are normally degraded within a week, but this rapid removal is impaired in autophagy-deficient liver.²⁵

Morphological and molecular data indicated effectiveness of the treatment on both TG2^{-/-} and TG2^{+/+} mouse liver (Figure 6). Remarkable peroxisomal proliferation was demonstrated by increased number of catalase-positive organelles, as detected by transmission electron microscopy, immediately after ciprofibrate treatment (T0; Figures 6a and b). Consistently, the levels of the 70-kDa peroxisomal membrane protein (PMP70) were significantly higher in treated animals than in controls (Figure 6e). At later stages (T7), the size of peroxisomal population returned to normal values in the TG2^{+/+} liver, as assessed by PMP70 western blot analysis (Figure 6e), while in the hepatocytes of TG2^{-/-} mice, numerous peroxisomes were still present, as detected by ultrastructural (Figures 6c and d) and western blot analyses (Figure 6e). Though often found inside autophagic vacuoles, these organelles displayed normal morphological features, including homogeneous catalase cytochemical activity, and electron-dense cores (Figure 6d). These hallmarks, indicating intactness of the organelles in the knockout liver, were paralleled by intense PMP70 immunoreactivity, significantly higher than in TG2^{+/+} samples (Figure 6e).

Consistent with morphological data, immunoblot results using the autophagic marker LC3 II (Figure 6f) showed dramatic induction of the autophagic program in TG2^{+/+} liver, soon after suspension of ciprofibrate *in vivo* administration (T0).

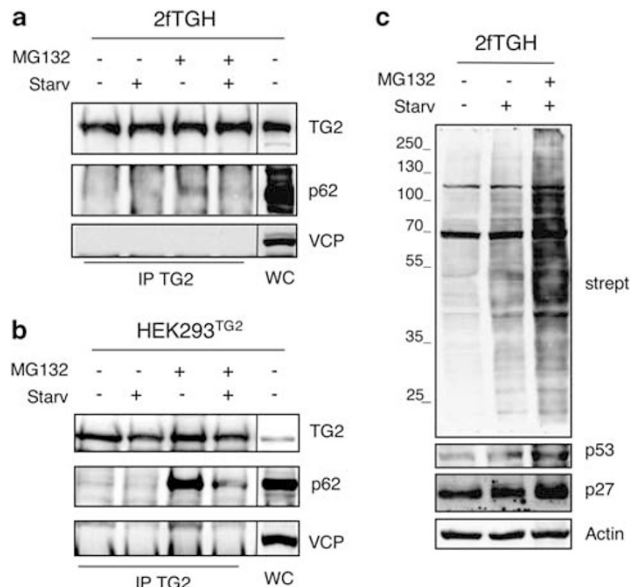


Figure 4 TG2 interacts with autophagy-related cargo proteins. (a) Western blot analysis of TG2, p62 and VCP proteins in human 2fTGH cells subjected to immunoprecipitation for TG2. After 4 h of treatment as indicated, cells were lysed and proteins were immunoprecipitated using anti-TG2 antibody (see Materials and Methods). Immuno- and co-immunoprecipitated proteins were separated by SDS-PAGE and immunoblotted using the indicated antibodies. WC, whole cell lysate, was used as protein control. (b) Western blot analysis of TG2, p62 and VCP proteins in HEK293^{TG2} cells stably transfected with TG2 protein, subjected to immunoprecipitation for TG2. After 2 h of treatment as indicated, cells were lysed and proteins were immunoprecipitated using anti-TG2 antibody. Immuno- and co-immunoprecipitated proteins were separated by SDS-PAGE and immunoblotted using the indicated antibodies. WC, whole cell lysate, was used as protein control. (c) Representative blot of the TG-catalyzed incorporation of 5-(biotinamido)pentylamine into proteins in 2fTGH cell line. Cells were labelled with 5-(biotinamido)pentylamine and treated as indicated for 4 h. After separation by SDS-PAGE, biotinylated proteins were revealed with HRP-conjugated streptavidin. p53 and p27 proteins were used as a control for monitoring proteasome inhibition, and actin was used as loading control

Later on, LC3 levels returned rapidly to control values (T7). By contrast, LC3 levels in TG2^{-/-} liver were unchanged at T0, and raised in the first week after treatment, indicating, together with the increased level of PMP70, a much slower clearance of peroxisomes due to an impaired autophagy flux.

Interestingly, autophagy serves to degrade intracellular lipid stores in murine liver through a process that has been termed 'macrolipophagy'.²⁶ Histological examination of paraffin sections stained either by hematoxylin and eosin (H&E) or by Sudan Black, as well as ultrastructural analysis, demonstrates lipid accumulation in TG2^{-/-} mouse liver after ciprofibrate treatment (Supplementary Figure S3), further confirming the impairment of autophagy in the presence of a defect in TG2 transamidating activity.

Impaired clearance of ubiquitinated protein aggregates in the absence of TG2 transamidating activity. Based on the above-described results, we decided to verify whether the defect of autophagy induced by the lack of TG2 *in vivo* was characterized by the accumulation of ubiquitinated protein aggregates.

To this end, we analyzed the liver of TG2 knockout and wild-type mice upon starvation. Under fed condition

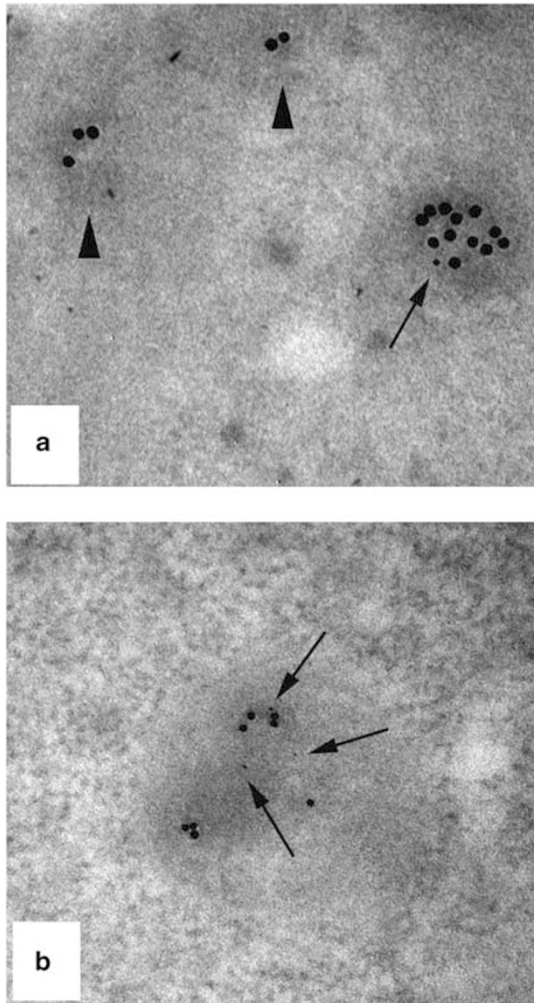


Figure 5 TG2 is present in cytosolic protein aggregates. (a and b) HEK293^{TG2} cells were cultured under starved condition in presence of MG132 for 2 h. Cells were double-labelled against TG2 (15-nm gold particles), and against p62 (5 nm gold particles). Immuno-gold analysis shows that small cytosolic membrane-free electron-dense structures (arrowheads) are positively stained for TG2 while larger aggregates display simultaneous positivity for TG2 and p62 (arrows). Original magnification: $\times 85\,000$

some ubiquitin-positive cells were found in TG2^{+/+} mice (Figures 7a and e). However, the amount of ubiquitinated protein aggregates was much more pronounced in TG2-deficient mouse (Figures 7b and e). Interestingly, following 48 h of starvation, the number of cells with ubiquitinated protein aggregates decreased in TG2^{+/+} mouse, as a result of their clearance by autophagy (Figures 7c and e). On the contrary, in the liver of TG2^{-/-} mouse, an increased number of cells with ubiquitinated protein aggregates was observed (Figures 7d and e), thus suggesting that, in the absence of TG2, elimination of protein aggregates is affected. In order to demonstrate that the accumulation of ubiquitinated proteins observed in knockout animals was indeed dependent on the lack of TG2, we analyzed the profile of ubiquitinated proteins in HEK293 cells lacking the enzyme and in the same cells overexpressing TG2 protein (HEK293^{TG2}). The data reported in Figure 7f clearly show that in the absence of the enzyme there was a marked accumulation of high-molecular-weight

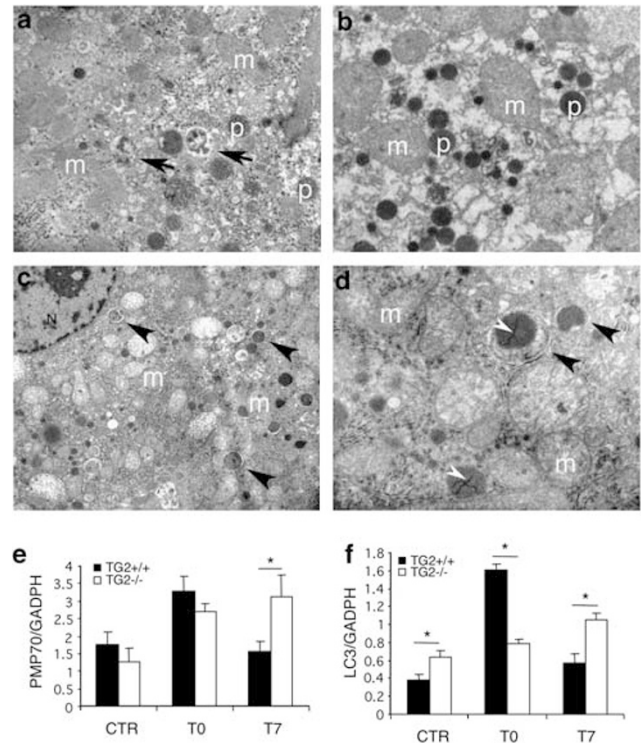


Figure 6 Impaired *in vivo* pexophagy after ciprofibrate-induced peroxisomal proliferation in the liver of TG2^{-/-} mice. Ultrastructural catalase cytochemistry of TG2^{+/+} (a) and TG2^{-/-} (b-d) mouse liver, after ciprofibrate treatment. Mice were given ciprofibrate-containing food for 10 days, then killed immediately (T0) or 7 days (T7) after suspension of treatment. Liver specimens were prepared as described in Materials and Methods and ultrathin sections were observed in a Zeiss EM 900 electron microscope. (a and b) Remarkable peroxisomal induction is observed in both TG2^{+/+} and TG2^{-/-} hepatocytes, at T0. However, while autophagosomes with partially degraded material are readily detected in the TG2^{+/+} samples (arrows), the knockout shows virtually no autophagic vacuoles. (c and d) Several autophagosomes are recognized in TG2^{-/-} samples at T7. These mostly contain indigested peroxisomes, with homogeneous catalase positivity (arrowheads). The higher magnification micrograph (d) shows the details of an autophagic vacuole (arrowhead), surrounding an intact peroxisome, in which the double membrane is clearly visible, catalase is cytochemically active and a typical peroxisomal core (white arrowhead) is present. N, nucleus; m, mitochondrion; p, peroxisome. Original magnification: (a and b) $\times 12\,000$; (c) $\times 4400$; (d) $\times 20\,000$. (e and f) Densitometric analysis of western blotting data, obtained on liver extracts from TG2^{+/+} and TG2^{-/-} mice before and after *in vivo* ciprofibrate administration, using the peroxisomal marker PMP70 (e) and the autophagic marker LC3 normalized to GADPH (f). LC3 levels are expressed as the ratio between LC3 II and LC3 I. Statistical analysis was performed by analysis of variance ($*P < 0.05$)

ubiquitinated proteins, particularly evident when the proteasome inhibition was carried out by MG132.

To characterize whether this effect is dependent on the TG2 crosslinking activity, we analyzed the importance of the enzyme's transamidating activity in the clearance of ubiquitinated protein aggregates. To this aim, we studied the direct interaction of ubiquitinated proteins with TG2 using the HEK293 cell line stably transfected with the wild-type enzyme and with its mutant lacking the transamidating activity (HEK293^{C277S}) (Supplementary Figure S1A). Interestingly, the active TG2 and its transamidating mutant both interact with high-molecular-weight ubiquitinated proteins

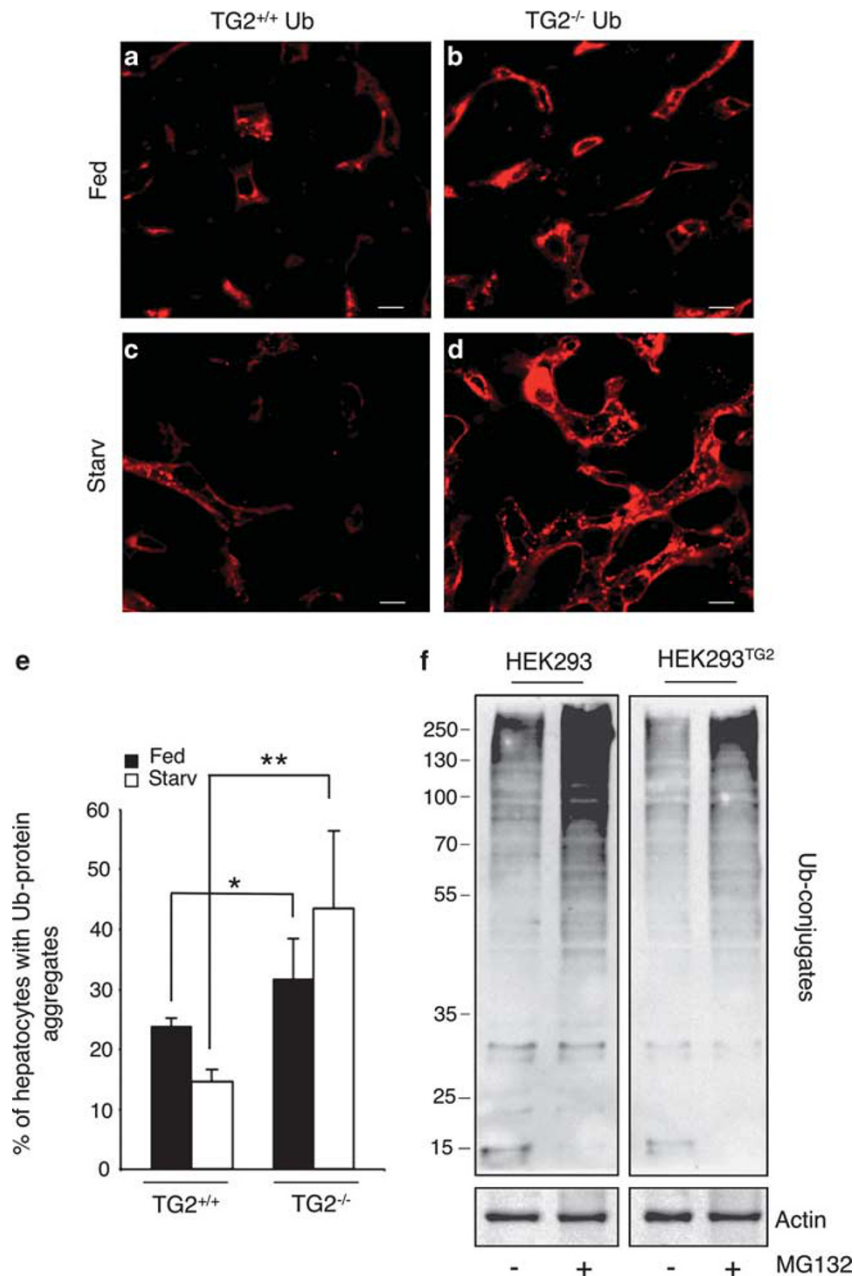


Figure 7 Effect of TG2 on ubiquitinated aggregates accumulation. (a–d) Immunofluorescence detection of ubiquitin in the liver of TG2^{+/+} and TG2^{-/-} mice before (a and b) and after starvation (c and d). Scale bar, 8 μ m. (e) Quantitative analysis of the formation of ubiquitin-positive aggregates in basal condition and after autophagy induction. The number of cells containing aggregates was counted in five independent fields of three independent mice. Results are expressed as the mean \pm S.D. Statistical analysis was performed by analysis of variance (* P < 0.05, ** P < 0.001). (f) Immunoblotting analysis of ubiquitinated proteins in HEK293 and HEK293^{TG2} cell lines. Cells were incubated with or without MG132 for 2 h, and ubiquitin expression levels were assayed by immunoblotting with anti-ubiquitin antibody. Actin was used as loading control

(Figure 8a), thus indicating that the transamidating activity is dispensable for the binding of ubiquitinated proteins. On the contrary, the transamidating activity is essential for their clearance, as shown by the accumulation of high-molecular-weight ubiquitinated proteins detected in cells expressing the C277S mutant (Figure 8b). Furthermore, the data reported in Figure 8a suggest that the interaction between TG2 and the ubiquitinated proteins is not dependent on p62, as protein complexes co-immunoprecipitating with

the TG2 mutant contain significant less amount of this cargo protein.

Discussion

The data reported in this study indicate that TG2 is an essential component for the proper maturation of autophagosomes under basal and particularly under stressful cellular conditions such as proteasome impairment or organelle

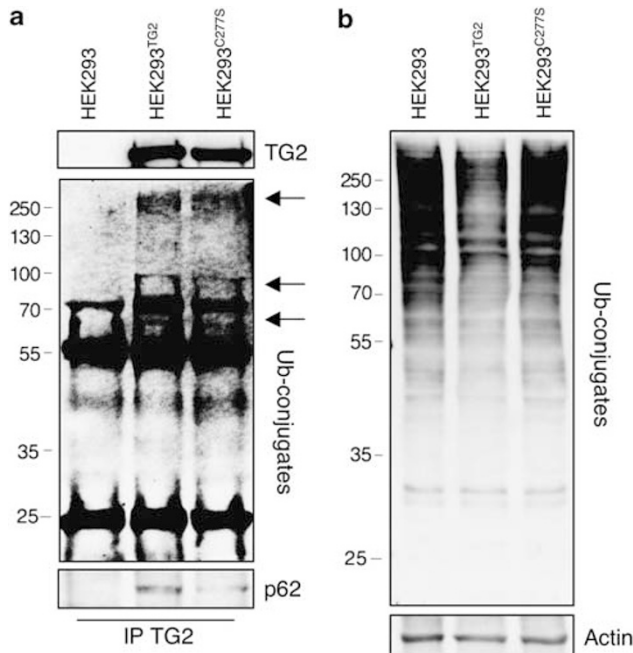


Figure 8 Effect of TG2 transamidating activity on the clearance of ubiquitinated protein aggregates. **(a)** Western blot analysis of p62 and ubiquitinated proteins in HEK293, HEK293^{TG2} and HEK293^{C277S} cell lines subjected to immunoprecipitation for TG2. Cells treated with MG132 for 2 h were lysed and proteins were immunoprecipitated using anti-TG2 antibody. Immuno- and co-immunoprecipitated proteins were separated by SDS-PAGE and immunoblotted using the indicated antibodies. Arrows indicate ubiquitinated proteins present in TG2 interacting protein complexes. **(b)** Immunoblotting analysis of ubiquitinated proteins in HEK293, HEK293^{TG2} and HEK293^{C277S} cell lines. Cells were incubated with MG132 for 2 h, and ubiquitin expression levels were assayed by immunoblotting with anti-ubiquitin antibody. Actin was used as loading control

hyper-proliferation. Indeed, we have previously shown that the ablation of TG2 results in an evident accumulation of LC3 II on pre-autophagic vesicles, pointing to a marked induction of autophagy.¹⁵ By contrast, the formation of the acidic vesicular organelles was very limited, as detected by the lack of acidification of the autophagolysosomes observed in TG2^{-/-} MEFs, suggesting an impairment in the autophagosome maturation process.¹⁵ In this paper, we demonstrate that the ablation of TG2 leads to the accumulation of ubiquitinated organelles and protein aggregates, which are not cleared by autophagy, thus indicating a role for the enzyme in the selection of the autophagy substrates. In fact, in the absence of TG2 and particularly under stressful conditions, we observed both *in vivo* and *in vitro* a marked accumulation of ubiquitinated proteins. We have also shown that the TG2-dependent posttranslational modification of its substrate proteins is increased by autophagy induction, and further potentiated upon proteasome inhibition. In connection with this, it is accepted that during the early stage of autophagy there is an accumulation of free calcium ions in the cytoplasm that may activate the TG2's transamidating activity.²⁷

Interestingly, TG2 is present in protein complexes containing two cargo proteins, p62 and NBR1, which are known to mediate the clearance of ubiquitinated proteins by autophagy. These cargo proteins contain UBA domains at their C-terminal regions, allowing them to interact with the aggregated protein

complexes and organelles that have to be degraded. Subsequently, by a LIR domain these cargo proteins interact with the ATG8-family members inside the nascent pre-autophagic vesicles.^{9,19} It is interesting to note that, although TG2 has two potentially canonical LIR domains, we were unable to detect by immunoprecipitation an interaction between TG2 and LC3 (unpublished observations). By contrast, our findings indicate that TG2 is localized in small protein aggregates where p62 is not present, while this cargo protein is later recruited on large aggregates where a high amount of TG2 is detected. In keeping with this finding, we detected an increased co-localization of the two proteins upon inhibition of the proteasome, a condition known to favor the formation of 'aggresomes'.²⁰ Furthermore, in cells lacking TG2, we detected the accumulation of ubiquitinated proteins suggesting that the enzyme is involved in the posttranslational modification of high-molecular-weight aggregates, which are then conveyed by cargo proteins to the autophagic machinery for degradation. Notably, only the reintroduction of the transamidating active TG2 in these cells favors the clearance of ubiquitinated proteins, highlighting that TG2's crosslinking activity has an important role in the formation/stabilization of substrates cleared by the autophagy pathway. These findings are in agreement with our previous results showing that the transamidating activity of the enzyme is required for the proper completion of the autophagic flux^{15,16} and the inhibition of the transamidating activity of TG2, by means of the specific inhibitor R283, results in a marked decrease of the number of acidic vesicular organelles.¹⁵ In this regard, it is important to mention that TG2 has been involved in the pathogenesis of several degenerative diseases characterized by the accumulation of mutated/misfolded proteins such as Lewy bodies in PD, neurofibrillary tangles in AD, Huntingtin aggregates in HD, as well as the Mallory bodies in the liver.^{13,14} Our previous studies, carried out in a mouse model for HD, suggested a possible involvement of TG2 in the neurodegenerative processes associated with autophagy impairment observed in this disease. In fact, the analysis of brains of the TG2^{-/-}/HD transgenic mice showed that the HD onset is associated with a large reduction in non-apoptotic cell death and with an increased number of nuclear protein inclusions, suggesting an impairment in their clearance by autophagy.²⁸

Taken together, these data indicate an important role for TG2-mediated posttranslational modifications in the maturation of autophagosomes. In support of this assumption is also the long-lasting use of a well-known competitive inhibitor of transglutaminase, the auto-fluorescent compound monodansyl-cadaverine (MDC), for *in vivo* labelling of autophagic vacuoles. MDC accumulates as a selective marker for autophagic vacuoles *in vivo*, and is not present in the early and late endosome.²⁹ In keeping with this, we have shown here that TG2 is present inside the autophagosomes, where the enzyme is selectively degraded similarly to its binding partner p62.

It is well known that autophagy has a crucial role in the turnover of cellular organelles; in particular it has been proposed that autophagy selectively degrades dysfunctional or supernumerary mitochondria and peroxisomes. Here, we show that pexophagy following ciprofibrate treatment is impaired in mice lacking TG2. Also, we have recently shown

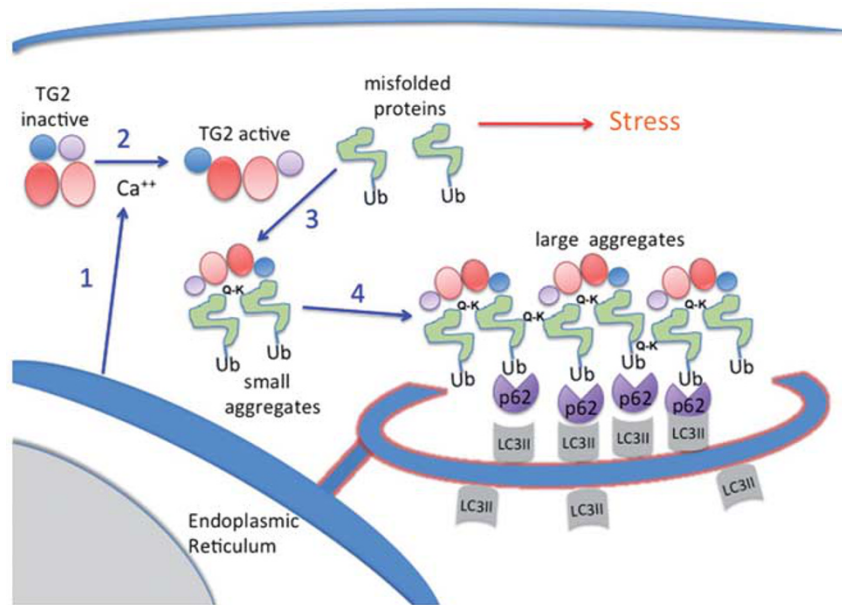


Figure 9 Tentative scheme of TG2 action during autophagy. The accumulation of misfolded ubiquitinated proteins, sensed by the cell as a stress, leads to the activation of autophagy at ER level determining the release of free calcium ions in the cytoplasm (1). This event leads to the activation of TG2 transamidating activity associated with its 3D structural change from the inactive 'closed conformation' to the active 'opened conformation' (2). The activated enzyme may catalyze the misfolded protein crosslinking, leading to the formation of small aggregates (3) and subsequently large aggregates (4). The formation of these ubiquitinated inclusions is recognized via the UBA domains by p62 or other cargo proteins. These complexes finally interact with LC3II through the LIR domains present on the cargo proteins, leading to their uploading inside the pre-autophagic vesicles

that the absence of TG2 is associated with the impairment of mitochondria that, in light of the present observations, could be due to the lack of clearance of the damaged ones.¹³

Finally, it is relevant to note that a large number of characterized TG2 candidate protein substrates interact with the ATG8 family members,³⁰ thus providing further evidence that the TG2-catalyzed posttranslational modifications may have a role in their clearance through the autophagosomes in collaboration with p62 and NBR1. The TG2 transamidating activity, acting at the level of glutamine and lysine residues of proteins, might be envisaged as a further regulatory step in the selection of protein substrates to be degraded into autophagosomes. In line with this assumption, it is important to mention that so far no clear consensus sequence has been described for the TG2's substrate proteins. Several authors have proposed that glutamine and lysine residues well exposed on the protein surface can act as possible targets for the enzyme, a condition likely to occur in misfolded proteins.³¹ On the basis of the data presented in this study we would like to propose that TG2 can be involved in the early steps of the recognition of the ubiquitinated proteins and organelles to be degraded. TG2 could favour by its transamidating activity the formation of intracellular structures, which are recognized by p62 and other cargo proteins leading to their recruitment in the pre-autophagic vesicles before degradation by autophagosomes (Figure 9).

Materials and Methods

Antibodies. Anti-tubulin, anti-actin and anti-PMP70 were from Sigma-Aldrich (Saint Louis, MO, USA), anti-LC3 was from Novus Biologicals (Littleton, CO, USA), anti-TG2 TG100 or CUB7402 were from Lab Vision NeoMarkers (Fremont, CA, USA), anti-mono and poly-ubiquitinated conjugates were from Enzo (Plymouth

Meeting, PA, USA), anti-p62/SQSTM1 was from MBL (Woburn, MA, USA), anti-VCP, anti-p27 (C-19), anti-p53 (FL-393) and anti-GADPH (FL-335) were from Santa Cruz (Santa Cruz, CA, USA), and anti-NBR1 was from Cell Signaling (Danvers, MA, USA). HRP-conjugated secondary antibodies were from Bio-Rad Laboratories (Hercules, CA, USA). Alexa Fluor 488- and Alexa Fluor 594-conjugated secondary antibodies were from Invitrogen (Carlsbad, CA, USA).

Generation of TG2^{-/-} GFP-LC3 mice. In order to obtain TG2^{-/-} mice expressing GFP-LC3 (TG2^{-/-} GFP-LC3), C57Bl/6 TG2^{-/-} mice were crossed with C57Bl/6 GFP-LC3 transgenic mice. TG2^{-/-} genotype was assessed by PCR using 5'-TCCTGACCTGAGTCCCTCGTC-3', 5'-TACTCCAGCTTCTCGTTCTG-3', and 5'-ACGAGACTAGTGAGACGTGC-3' primers, as previously described.³² To assess the presence of GFP-LC3 transgene, PCR was carried out with:

Primer 1 (5'-ATAACTTGCTGGCCTTCCACT-3')

Primer 2 (5'-CGGGCCATTTACCGTAAGTTAT-3')

Primer 3 (5'-GCAGCTCATTGCTGTTCCCTCAA-3')

(intron 3 of the LC3 genome as an internal control) following the conditions 94°C for 5 min, then 40 cycles at 94°C for 30 s + 55°C for 30 s + 72°C for 1 min, and then 72°C for 5 min.

Cell culture, transfection and drug treatments. HEK293 (human embryonic kidney) and 2fTGH were cultured in Dulbecco's modified Eagle's medium (Invitrogen Life Technologies Inc.) supplemented with 10% fetal bovine serum, 2 mM L-glutamine, 100 mg/ml streptomycin and 100 units/ml penicillin in a 5% CO₂ incubator. For generation of the TG2 stably expressing cells (HEK293^{TG2} and HEK293^{C277S}), HEK293 cells were transfected with pLPCX-TG2 or pLPCX-C277S¹⁶ using Lipofectamine 2000 (Invitrogen) according to the manufacturer's instructions and then selected for puromycin (Sigma-Aldrich) resistance using the antibiotic added to the culture medium (2 μg/ml). For the generation of 2fTGH-GFP-LC3 cells, 2fTGH cells were transiently transfected with pLPCX-GFP-LC3 vector using Lipofectamine 2000.

For amino-acid starvation (Starv), cells were washed two times in Earle's balanced salt solution (EBSS; Sigma-Aldrich) and incubated in EBSS for the indicated periods in the presence or not of 5 μM MG132 (Z-Leu-Leu-Leu-al; Sigma-Aldrich). For autophagy induction cells were incubated in full medium in the presence of 1 μM Rap (Sigma-Aldrich) or 10 mM 2-DG (Sigma-Aldrich).

Animals and treatment. Animals were fed with 0.025% ciprofibrate (Sigma Chemical Co., St. Louis, MO, USA). Mice were given 40 g ciprofibrate-containing food for 10 days, then killed immediately (T0) or 7 days (T7) after suspension of treatment.

For the autophagy induction mice were fed *ad libitum* or subjected to 24 or 48 h of starvation. For the autophagy inhibition the CQ was administered in the drinking water. Considering that the water uptake of mice is between 4 and 7 ml per day, we calculated a concentration of CQ salt of 0.375 mg/ml dissolved in normal tap water to deliver a daily oral dose of 1.5–2.6 mg.³³

Immunoblotting. Tissues were lysed in HEMG buffer (25 mM Hepes pH 8.0, 100 mM NaCl, 25 mM MgCl₂, 0.5% Triton X-100, 0.1 mM EDTA, and 10% glycerol) supplemented with protease and phosphatase inhibitor cocktail (1 mM sodium fluoride, 1 mM sodium orthovanadate and 1 mM sodium molybdate; Sigma-Aldrich).

Cells were rinsed in ice-cold phosphate-buffered saline (PBS) and collected in lysis buffer, containing 20 mM Tris-HCl pH 7.4, 150 mM NaCl and 1% Triton X-100 with protease inhibitor cocktail (Roche, Nutley, NJ, USA).

Protein concentrations were determined by the Bradford assay, using bovine serum albumin as a standard.

Aliquots of total protein extracts from cells and tissues after different treatments were resolved on SDS-polyacrylamide gel and transferred to a nitrocellulose membrane. Blots were blocked in 5% non-fat dry milk in T-PBS (PBS + 0.05% Tween 20) for 1 h at room temperature and then incubated overnight with the above-described antibodies. The membranes were incubated with HRP-conjugated secondary antibody for 1 h at room temperature and the signal was detected by Immuno-Star WesternC Kit (Bio-Rad Laboratories).

Statistical analysis. Densitometry measurements were used for statistical analysis using Graph Pad. Statistical significance was determined using the Student's *t*-test. A *P*-value ≤ 0.05 was considered to be significant.

Fluorescence microscopy. Tissues were washed by cardiac perfusion using PBS, dissected and fixed in 4% paraformaldehyde (PFA). Tissues were then cryoprotected with increasing concentrations of sucrose (15 and 30%, overnight) in phosphate buffer. Next, tissues were transferred to an embedding mold filled with Tissue-Teck OCT compound. The mold was rapidly submerged into isopentane cooled. The material was then frozen and stored at -80°C . The samples were sectioned at 10–20 μm thickness with cryostat (ref ex: CM3050 S, Leica, Deerfield, IL, USA) and stored at -80°C . For GFP observation, nuclei were stained with DAPI (20 min, 1 $\mu\text{g}/\text{ml}$) and then cryosections were examined under a Leica TCS SP5 confocal microscope equipped with an $\times 40$ (NA 1.25) or $\times 63$ (NA 1.4) oil-immersion objective (Deerfield, IL, USA). We used 'Leica confocal' software (Deerfield, IL, USA) for analysis. For immunohistochemical analysis, sections were permeabilized with 0.4% Triton X-100 in PBS for 1 h and then blocked in 3% NGS in HSPBS containing 0.2% Triton X-100 for 1 h. Sections were incubated with the above-indicated primary antibody.

Subconfluent cells (2fTGH and 2fTGH-GFP-LC3) grown on coverslips were washed with PBS and fixed in 4% PFA for 10 min at room temperature. Fixed cells were permeabilized with 0.1% Triton X-100 in PBS for 10 min, blocked with 3% BSA in PBS for 20 min, and incubated with primary antibodies for 1 h.

After washing, cells and tissue sections were incubated with Alexa Fluor 488- and Alexa Fluor 594-conjugated secondary antibodies. The coverslips were mounted on microscope slides, sealed with an antifade solution and examined with an image workstation DeltaVision (Applied Precision, Issaquah, WA, USA) Olympus 1X70 microscope.

Quantitative analysis of GFP-LC3 dots and ubiquitin-positive aggregates. The number of GFP-LC3 dots in the liver and heart was counted in five independent fields from three independent mice for each condition. Each point value represents the mean \pm S.D. Statistical analysis was performed by analysis of variance ($*P < 0.05$).

The number of ubiquitin-positive inclusions was counted in five independent fields from three independent mice for each condition. Each point value represents the mean \pm S.D. Statistical analysis was performed by analysis of variance ($*P < 0.05$).

Histological examination. Tissues were dissected, fixed in 4% PFA, paraffin embedded, and sectioned. Sections were stained by Meyer's hematoxylin and eosin.

Sudan Black (Sigma-Aldrich) staining was performed on cryostat liver sections, after dehydration in 70% ethanol for 30 min. Freshly prepared saturated Sudan Black solution was prepared in 70% ethanol. Sections were incubated with Sudan Black solution for 10 min, then treated with 70% ethanol for 1 min, and finally mounted using crystal mount (Biomedica, Burlingame, CA, USA).

Catalase ultrastructural cytochemistry. Liver specimens were fixed with 2.5% glutaraldehyde in 0.1 M cacodylate buffer, pH 7.4, for 45 min at 4°C . After extensive rinse in the same buffer, samples were incubated for 1 h at 37°C in the dark in 0.05 M 2-amino-2-methyl-1,3-propanediol, pH 9.4, containing 7.5% sucrose, 5 mM NaCN, 0.2% 3,3'-diaminobenzidine-tetra HCl (DAB) and 0.05% H₂O₂. For controls, the incubation medium was supplemented with 0.1 M 3-amino-1,2,4-triazole.

Specimens were then rinsed in 0.1 M cacodylate buffer, pH 7.4, postfixed in 1% OsO₄ in the same buffer for 1 h, at 4°C , dehydrated, and embedded in epoxy resin.

All the specimens were cut on a Leica UltraCut S ultramicrotome (Leica Microsystems, Wetzlar, Germany). Semithin sections were stained with toluidine blue and photographed, and ultrathin sections were briefly contrasted with aqueous 2% uranyl acetate for 20 min. Grids were observed and photographed in a Zeiss EM 900 electron microscope (Zeiss, Oberkochen, Germany).

Immunoprecipitation. Cell lysates were prepared in HEMG buffer (25 mM Hepes pH 8.0, 100 mM NaCl, 25 mM MgCl₂, 0.5% Triton X-100, 0.1 mM EDTA, and 10% glycerol) and protease inhibitor cocktail (Roche). The lysates were subjected to immunoprecipitation using specific antibodies in a combination with Protein G PLUS-Agarose (Santa Cruz). Immunoblot analysis was performed with indicated antibodies.

In situ TG assay. *In situ* TG activity was quantified by determining the incorporation of 5-(biotinamido)pentylamine into protein substrates. In brief, cells were pre-incubated for 20 min with 2 mM Ez-link pentylamine-Biotin (Thermo Scientific, Rockford, IL, USA) before each treatment. Cells were then harvested, lysed as above described, and proteins were resolved by SDS polyacrylamide gel. The blots were probed with streptavidin HRP-conjugated (Amersham Biosciences, Little Chalfont, UK) for 2 h at room temperature and then developed following the standard ECL protocol.

Immuno-electron microscopy. For immunolabelling, cells were fixed in 4% PFA, dehydrated in ethanol, and embedded in LR-White resin. Ultrathin sections were mounted on Formvar-coated copper grids, then washed three times with PBS and three times with PBS containing 1% bovine serum albumin and 0.15% glycine, followed by 30 min blocking with 5% normal goat serum. Samples were incubated overnight with the primary antibodies, mouse anti-TG2 1:25, and rabbit anti-p62 1.3:100. After washing in PBS, samples were incubated for 45 min with goat anti-mouse IgG conjugated to 15 nm gold particles and goat anti-rabbit IgG conjugated to 5 nm gold particles (BioCell, Cardiff, UK). Sections were stained with 2% uranyl acetate and observed under a Zeiss EM900 transmission electron microscope. Images were captured digitally with a Mega View II digital camera (Olympus SIS, Munster, Germany). The specificity of the immunoreaction was assessed in all cases by omitting the primary antibodies from the labelling protocol and incubating the sections only in the protein gold-conjugated secondary antibodies.

Conflict of Interest

The authors declare no conflict of interest.

Acknowledgements. The authors would like to thank Dr. P Mattioli from the Centre of Advanced Microscopy (CAM), Department of Biology, University of Rome Tor Vergata, for her skillful assistance in the use of the facility. This work was supported by grants from CHDI Foundation Inc. (USA), Compagnia di San Paolo, the Ministry of Health of Italy 'Ricerca Corrente' and 'Ricerca Finalizzata', and AIRC. The support of the EU grant 'Apo-Sys' and 'Transpath' Marie Curie project to MP is also acknowledged. FC is supported by grants from AIRC, Telethon and FISM.

1. Schubert U, Anton LC, Gibbs J, Norbury CC, Yewdell JW, Binnink JR. Rapid degradation of a large fraction of newly synthesized proteins by proteasomes. *Nature* 2000; **404**: 770–774.

2. Yao TP. The role of ubiquitin in autophagy-dependent protein aggregate processing. *Genes Cancer* 2010; **1**: 779–786.
3. Cyr DM, Hohfeld J, Patterson C. Protein quality control: U-box-containing E3 ubiquitin ligases join the fold. *Trends Biochem Sci* 2002; **27**: 368–375.
4. Willis MS, Townley-Tilson WH, Kang EY, Homeister JW, Patterson C. Sent to destroy: the ubiquitin proteasome system regulates cell signaling and protein quality control in cardiovascular development and disease. *Circ Res* 2010; **106**: 463–478.
5. Taylor JP, Tanaka F, Robitschek J, Sandoval CM, Taye A, Markovic-Plese S *et al*. Aggresomes protect cells by enhancing the degradation of toxic polyglutamine-containing protein. *Hum Mol Genet* 2003; **12**: 749–757.
6. Snyder H, Mensah K, Theisler C, Lee J, Matouschek A, Wolozin B. Aggregated and monomeric alpha-synuclein bind to the S6' proteasomal protein and inhibit proteasomal function. *J Biol Chem* 2003; **278**: 11753–11759.
7. Klionsky DJ, Emr SD. Autophagy as a regulated pathway of cellular degradation. *Science* 2000; **290**: 1717–1721.
8. Klionsky DJ. Autophagy: from phenomenology to molecular understanding in less than a decade. *Nat Rev Mol Cell Biol* 2007; **8**: 931–937.
9. Lamark T, Kirkin V, Dikic I, Johansen T. NBR1 and p62 as cargo receptors for selective autophagy of ubiquitinated targets. *Cell Cycle* 2009; **8**: 1986–1990.
10. Fesus L, Piacentini M. Transglutaminase 2: an enigmatic enzyme with diverse functions. *Trends Biochem Sci* 2002; **27**: 534–539.
11. Lai TS, Bielawska A, Peoples KA, Hannun YA, Greenberg CS. Sphingosylphosphocholine reduces the calcium ion requirement for activating tissue transglutaminase. *J Biol Chem* 1997; **272**: 16295–16300.
12. Fesus L, Thomazy V, Autuori F, Ceru MP, Tarcsa E, Piacentini M. Apoptotic hepatocytes become insoluble in detergents and chaotropic agents as a result of transglutaminase action. *FEBS Lett* 1989; **245**: 150–154.
13. Malomi W, Farrace MG, Rodolfo C, Piacentini M. Type 2 transglutaminase in neurodegenerative diseases: the mitochondrial connection. *Curr Pharm Des* 2008; **14**: 278–288.
14. Strnad P, Zatloukal K, Stumptner C, Kulaksiz H, Denk H. Mallory-Denk-bodies: lessons from keratin-containing hepatic inclusion bodies. *Biochim Biophys Acta* 2008; **1782**: 764–774.
15. D'Eletto M, Farrace MG, Falasca L, Reali V, Oliverio S, Melino G *et al*. Transglutaminase 2 is involved in autophagosome maturation. *Autophagy* 2009; **5**: 1145–1154.
16. Rossin F, D'Eletto M, Macdonald D, Farrace MG, Piacentini M. TG2 transamidating activity acts as a reostat controlling the interplay between apoptosis and autophagy. *Amino Acids* 2011. doi:10.1007/s00726-011-0899-x (in press).
17. Mizushima N, Yamamoto A, Matsui M, Yoshimori T, Ohsumi Y. *In vivo* analysis of autophagy in response to nutrient starvation using transgenic mice expressing a fluorescent autophagosome marker. *Mol Biol Cell* 2004; **15**: 1101–1111.
18. Luciani A, Villella VR, Esposito S, Brunetti-Pierri N, Medina DL, Settembre C *et al*. Cystic fibrosis: a disorder with defective autophagy. *Autophagy* 2011; **7**: 104–106.
19. Weidberg H, Shvets E, Elazar Z. Biogenesis and cargo selectivity of autophagosomes. *Annu Rev Biochem* 2011; **80**: 125–156.
20. Guthrie CR, Kraemer BC. Proteasome inhibition drives HDAC6-dependent recruitment of tau to aggresomes. *J Mol Neurosci* 2011; **45**: 32–41.
21. Kim PK, Hailey DW, Mullen RT, Lippincott-Schwartz J. Ubiquitin signals autophagic degradation of cytosolic proteins and peroxisomes. *Proc Natl Acad Sci USA* 2008; **105**: 20567–20574.
22. Fahimi HD, Reinicke A, Sujatta M, Yokota S, Ozel M, Hartig F *et al*. The short- and long-term effects of bezafibrate in the rat. *Ann NY Acad Sci* 1982; **386**: 111–135.
23. Islinger M, Luers GH, Li KW, Loos M, Volkl A. Rat liver peroxisomes after fibrate treatment: a survey using quantitative mass spectrometry. *J Biol Chem* 2007; **282**: 23055–23069.
24. Dzhokova-Stojkova S, Bogdanska J, Stojkova Z. Peroxisome proliferators: their biological and toxicological effects. *Clin Chem Lab Med* 2001; **39**: 468–474.
25. Ezaki J, Komatsu M, Yokota S, Ueno T, Kominami E. Method for monitoring pexophagy in mammalian cells. *Methods Enzymol* 2009; **452**: 215–226.
26. Singh R, Kaushik S, Wang Y, Xiang Y, Novak I, Komatsu M *et al*. Autophagy regulates lipid metabolism. *Nature* 2009; **458**: 1131–1135.
27. Hoyer-Hansen M, Bastholm L, Szyniarowski P, Campanella M, Szabadkai G, Farkas T *et al*. Control of macroautophagy by calcium, calmodulin-dependent kinase kinase-beta, and Bcl-2. *Mol Cell* 2007; **25**: 193–205.
28. Mastroberardino PG, Iannicola C, Nardacci R, Bernassola F, De Laurenzi V, Melino G *et al*. 'Tissue' transglutaminase ablation reduces neuronal death and prolongs survival in a mouse model of Huntington's disease. *Cell Death Differ* 2002; **9**: 873–880.
29. Biederbeck A, Kern HF, Elsässer HP. Monodansylcadaverine (MDC) is a specific *in vivo* marker for autophagic vacuoles. *Eur J Cell Biol* 1995; **66**: 3–14.
30. Behrends C, Sowa ME, Gygi SP, Harper JW. Network organization of the human autophagy system. *Nature* 2010; **466**: 68–76.
31. Hitomi K, Kitamura M, Sugimura Y. Preferred substrate sequences for transglutaminase 2: screening using a phage-displayed peptide library. *Amino Acids* 2009; **36**: 619–624.
32. De Laurenzi V, Melino G. Gene disruption of tissue transglutaminase. *Mol Cell Biol* 2001; **21**: 148–155.
33. Lewis MD, Pfeil J, Mueller AK. Continuous oral chloroquine as a novel route for Plasmodium prophylaxis and cure in experimental murine models. *BMC Res Notes* 2011; **4**: 262–266.

Supplementary Information accompanies the paper on Cell Death and Differentiation website (<http://www.nature.com/cdd>)

Mitochondrial BCL-2 inhibits AMBRA1-induced autophagy

Flavie Strappazon¹, Matteo Vietri-Rudan^{1,2},
Silvia Campello³, Francesca Nazio^{1,2},
Fulvio Florenzano⁴, Gian Maria Fimia⁵,
Mauro Piacentini^{5,6}, Beth Levine⁷ and
Francesco Cecconi^{1,2,*}

¹Laboratory of Molecular Neuroembryology, IRCCS Fondazione Santa Lucia, Rome, Italy, ²Department of Biology, Dulbecco Telethon Institute, University of Rome 'Tor Vergata', Rome, Italy, ³Department of Cell Physiology and Metabolism, University of Geneva Medical School, Geneva, Switzerland, ⁴Confocal Microscopy Unit, CNR-S.Lucia Foundation, Rome, Italy, ⁵National Institute for Infectious Diseases IRCCS 'L.Spallanzani', Rome, Italy, ⁶Department of Biology, University of Rome 'Tor Vergata', Rome, Italy and ⁷Howard Hughes Medical Institute and UT Southwestern Medical Center at Dallas, Dallas, TX, USA

BECLIN 1 is a central player in macroautophagy. AMBRA1, a BECLIN 1-interacting protein, positively regulates the BECLIN 1-dependent programme of autophagy. In this study, we show that AMBRA1 binds preferentially the mitochondrial pool of the antiapoptotic factor BCL-2, and that this interaction is disrupted following autophagy induction. Further, AMBRA1 can compete with both mitochondrial and endoplasmic reticulum-resident BCL-2 (mito-BCL-2 and ER-BCL-2, respectively) to bind BECLIN 1. Moreover, after autophagy induction, AMBRA1 is recruited to BECLIN 1. Altogether, these results indicate that, in normal conditions, a pool of AMBRA1 binds preferentially mito-BCL-2; after autophagy induction, AMBRA1 is released from BCL-2, consistent with its ability to promote BECLIN 1 activity. In addition, we found that the binding between AMBRA1 and mito-BCL-2 is reduced during apoptosis. Thus, a dynamic interaction exists between AMBRA1 and BCL-2 at the mitochondria that could regulate both BECLIN 1-dependent autophagy and apoptosis.

The EMBO Journal (2011) 30, 1195–1208. doi:10.1038/emboj.2011.49; Published online 25 February 2011

Subject Categories: membranes & transport; differentiation & death

Keywords: apoptosis; autophagy; endoplasmic reticulum; mitochondria

Introduction

Autophagy has a crucial role in many health and disease processes. This catabolic process in eukaryotic cells is involved in the degradation of cellular components through

*Corresponding author. Department of Biology, Dulbecco Telethon Institute, University of Rome 'Tor Vergata', Via della Ricerca Scientifica, Rome 00133, Italy. Tel.: +39 067 259 4230; Fax: +39 067 259 4222; E-mail: francesco.cecconi@uniroma2.it

Received: 23 August 2010; accepted: 4 February 2011; published online: 25 February 2011

the lysosome machinery. During this process, portions of cytoplasm are sequestered by double-membraned vesicles, the autophagosomes, and degraded after fusion with lysosomes for subsequent recycling. BECLIN 1, the mammalian ortholog of yeast Atg6, has an evolutionarily conserved role in macroautophagy. Several BECLIN 1-interacting proteins have been reported as regulating this function, both positively (e.g., hAtg14, Bif-1, UVRAG; Takahashi *et al*, 2007, 2009; Itakura *et al*, 2008; Liang *et al*, 2008; Sun *et al*, 2009) and negatively (e.g., Rubicon, Bcl-2 family members; Pattingre *et al*, 2005; Levine *et al*, 2008; Matsunaga *et al*, 2009). AMBRA1 is a positive regulator of the BECLIN 1-dependent programme of autophagy (Fimia *et al*, 2007). Its functional deficiency in mouse embryos leads to neuroepithelial hyperplasia associated with autophagy impairment and excessive apoptotic cell death (Cecconi *et al*, 2007). Further, we demonstrated that autophagosome formation is primed by AMBRA1 release from the cytoskeleton: When autophagy is induced, AMBRA1 is released from dynein in an ULK1-dependent manner, and re-localizes to the endoplasmic reticulum (ER), thus enabling autophagosome nucleation. Therefore, AMBRA1 can be considered as a crucial factor in regulating autophagy initiation (Di Bartolomeo *et al*, 2010).

A complex relationship between autophagy and cell death exists (Levine *et al*, 2008; Djavaheri-Mergny *et al*, 2010). Currently, the well-known antiapoptotic factor BCL-2 is a key player in this context. The pool of BCL-2 resident at the ER (ER-BCL-2) is able, indeed, with the contribution of NAF-1 (nutrient-deprivation autophagy factor-1), to negatively regulate the BECLIN 1-dependent autophagic programme (Chang *et al*, 2010). In contrast, the mitochondrial pool of BCL-2 (mito-BCL-2) is shown to exert only an antiapoptotic function (Pattingre *et al*, 2005; Levine *et al*, 2008) even though mitochondria have been recently demonstrated to be selected sites for autophagosome formation (Hailey *et al*, 2010). BCL-2-regulated apoptotic cell death has been extensively studied. Overexpression of BCL-2 promotes a protective effect against a wide range of inducers of apoptosis. This antiapoptotic action derives from the fact that BCL-2 neutralizes proapoptotic BCL-2 family members, preventing mitochondrial membrane permeabilization and consequent cell death (Adams and Cory, 2007).

As previous studies have demonstrated that Beclin 1/Vps34-mediated autophagy is negatively regulated through a direct interaction between BECLIN 1 and ER-BCL-2, we investigated whether the antiapoptotic BCL-2 protein and AMBRA1 could bind each other. In this context, we found that AMBRA1 is a new partner of BCL-2 in mammalian cells and that their binding is independent of BECLIN 1. More importantly, by targeting BCL-2 either to mitochondria (mito-BCL-2) or ER (ER-BCL-2), we demonstrated that mito-BCL-2 is able to bind AMBRA1 and that this binding is disrupted after both autophagy and apoptosis induction. Our findings indicate that AMBRA1 and BCL-2 bind BECLIN 1 on the same site. AMBRA1 can thus compete with mito- and ER-BCL-2 to

bind BECLIN 1. In addition, we demonstrated that, after autophagy induction, AMBRA1/BECLIN 1 interaction increases both in mitochondrial and microsomal fractions, whereas the AMBRA1-mito-BCL-2 interaction is disrupted. Altogether, these results lead us to propose a model in which, under normal conditions, a pool of AMBRA1 is docked by BCL-2 at the mitochondria, inhibiting its autophagic function; after autophagy induction, this mitochondrial pool of AMBRA1 separates from mito-BCL-2 and increases its binding to BECLIN 1 in order to favour the autophagic programme.

Results

AMBRA1 is a new partner of the antiapoptotic and antiautophagic factor BCL-2

AMBRA1 interacts with BECLIN 1 and its associated kinase Vps34, and favours BECLIN 1/Vps34 functional interaction (Fimia *et al*, 2007). This interaction, which requires the F2 fragment of AMBRA1 (Figure 1A), is crucial in the autophagic process; taken together, AMBRA1, BECLIN 1 and Vps34 have been defined as the autophagy core-complex (He and Levine, 2010). In contrast, BECLIN 1 is negatively regulated by a direct interaction with the antiapoptotic factor BCL-2. Therefore, we investigated the existence of a putative interaction between the antiapoptotic protein BCL-2 and AMBRA1 in a co-immunoprecipitation experiment. BCL-2 and AMBRA1 were found to be associated in HEK293 cells coexpressing both AMBRA1 and BCL-2 (Figure 1B, lane 2). Next, we wanted to find the AMBRA1 domain responsible for this binding. To this end, we transfected cells with cDNAs encoding various AMBRA1 portions (Figure 1A): FL (full length), F1 (amino acids 1–532), F2 (amino acids 533–750) and F3 (amino acids 767–1269). As shown in Figure 1B (lanes 3 and 5), F1 and F3 fragments (the N-terminal and C-terminal part of the protein, respectively) are sufficient to bind BCL-2, whereas the central region (F2), which is known to bind BECLIN 1 (Fimia *et al*, 2007), shows no interaction. Similar results were obtained following reciprocal co-immunoprecipitation experiments (Supplementary Figure S1). BCL-2 co-immunoprecipitates with AMBRA1 (lane 2) and its F1 and F3 fragments (lanes 3 and 5). To confirm these biochemical results, we performed a confocal microscopy analysis in HeLa cells expressing detectable endogenous levels of both AMBRA1 and BCL-2. As illustrated in Figure 1C, endogenous AMBRA1 and BCL-2 showed a partial colocalization. In order to give two quantitative outputs for this colocalization, we used Pearson (r_p) and Spearman (r_s) statistics. Both tests produce values in the range $(-1, 1)$, 0 indicating that there is no discernable correlation and -1 and $+1$ meaning strong negative and positive correlations, respectively. We obtained an $r_p = 0.38$ and an $r_s = 0.39$ confirming that AMBRA1 and BCL-2 colocalize in mammalian cells. This analysis indicates also that the interaction between the two proteins is partial. To confirm the result, we analysed the interaction between endogenous AMBRA1 and BCL-2 in HeLa cells. As illustrated in Figure 1D, we found that endogenous AMBRA1 binds specifically endogenous BCL-2. To strengthen our results on this interaction, we performed a Förster resonance energy transfer experiment to measure AMBRA1-BCL-2 proteins proximity within the cells. GFP and mCherry are two fluorescent proteins which use as an FRET pair that has been recently validated for reproducible quantitative determina-

tion of the energy transfer efficiency, both *in vivo* and *in vitro* (Albertazzi *et al* 2009). In order to study the interaction of BCL-2 and AMBRA1 proteins, they were fused with the GFP and mCherry fluorescent proteins and co-transfected in HEK293 cells. On a morphological ground, visual inspection of the fluorescence expression patterns in the histological material showed that BCL-2-GFP and AMBRA1-mCherry appeared to be coexpressed in structures mainly resembling mitochondria and ER. The colocalization of the two proteins was almost complete. The average FRET efficiency values measured was $11.14\% \pm 2.1$ (see Figure 1E). In a previous paper, the FRET behaviour of two tandem mCherry-EGFP fusion proteins (which differed for the distance, short linker and long linker) has been investigated (Albertazzi *et al* 2009). A FRET efficiency value of 0.41 for the short linker and of 0.29 for the long linker was achieved for the mCherry-EGFP tandem proteins. Comparison of our AMBRA1-BCL-2 FRET value with that of the mCherry-EGFP tandem construct suggests that AMBRA1 and BCL-2 are in proximity in the interacting complex.

BECLIN 1 is not required for AMBRA1-BCL-2 interaction

The F2 fragment of AMBRA1 is required for the interaction between AMBRA1 and BECLIN 1 (Fimia *et al*, 2007), but not for its binding to BCL-2. This suggests that BECLIN 1 is not necessary for this latter association. To confirm this hypothesis, we performed co-immunoprecipitation experiments using a mutant of BCL-2 unable to bind BECLIN 1. This mutant (EEE-BCL-2) possesses simultaneous glutamine substitutions at three phosphorylation sites (T69, S70 and S87), and mimics multi-phosphorylations that occur following autophagy induction (Wei *et al*, 2008). This impedes the interaction of BCL-2 with BECLIN 1 (Figure 2A and B). Vectors coding for AMBRA1 and for human-BCL-2 (h-BCL-2) or for the EEE-BCL-2 mutant were overexpressed in HEK293 cells; then, co-immunoprecipitations of AMBRA1 and BCL-2 were performed in normal conditions. As shown in Figure 2C, AMBRA1 is able to bind h-BCL-2 as well as the BCL-2 mutant (EEE-BCL-2) that cannot bind BECLIN 1.

Mitochondrial BCL-2 preferentially binds AMBRA1 and this interaction is disrupted after autophagy induction

BCL-2 is predominantly found on the outer mitochondrial and ER membranes (Germain and Shore, 2003), these subcellular localizations being related to BCL-2 function (Lithgow *et al*, 1994). To gain an insight into the functional significance of the interaction between AMBRA1 and BCL-2, we evaluated whether AMBRA1 differentially binds the ER resident or the mitochondrial pool of BCL-2. To this end, two BCL-2 mutants with restricted subcellular localization were used in co-immunoprecipitation experiments with AMBRA1. In the first mutant, the C-terminal hydrophobic sequence of BCL-2 is exchanged for an equivalent sequence from modified ActA, which binds specifically to the cytoplasmic face of mitochondrial outer membranes (Pistor *et al*, 1994). The other mutant possesses a C-terminal sequence exchanged for a sequence from cytochrome *b5* (DNA encoding the analogous 35 amino-acid sequence of the ER-specific isoform of rat hepatic cytochrome *b5* (Mitoma and Ito, 1992), resulting in ER-specific localization (Zhu *et al*, 1996)). As shown in Figure 3A, myc-AMBRA1 significantly co-immunoprecipitates with mito-targeted BCL-2 (lane 3), whereas only a

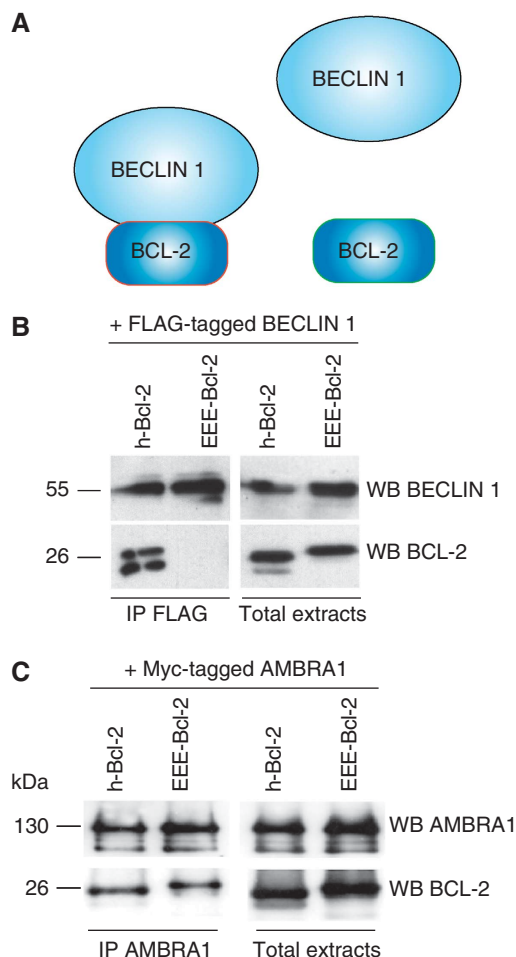


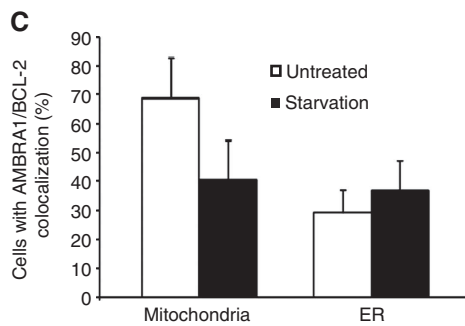
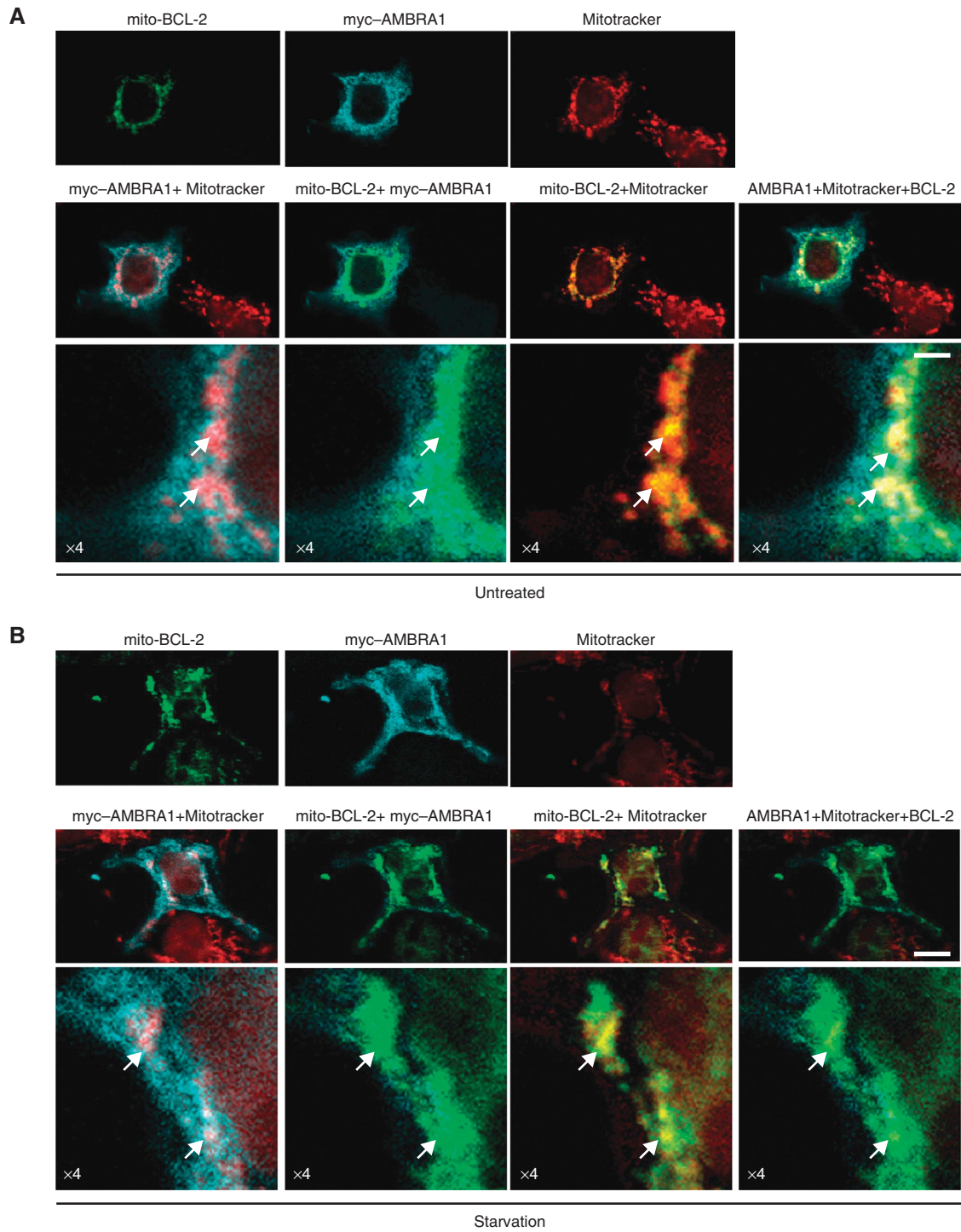
Figure 2 The interaction between AMBRA1 and BCL-2 does not require BECLIN 1. (A) Simultaneous glutamine substitutions at the three phosphorylation site on BCL-2 (EEE-BCL-2 mutant) induce a disruption of the BECLIN 1/BCL-2 complex (Pattingle *et al*, 2005). (B) BECLIN 1 co-immunoprecipitates with hBCL-2 but not with EEE-BCL-2 mutant in HEK293 cells. HEK293 cells were co-transfected with vectors encoding FLAG-BECLIN 1, and myc-h-BCL-2 or the EEE-BCL-2 mutant. Protein extracts were immunoprecipitated using an anti-FLAG antibody. Purified complexes and corresponding total extracts were analysed by WB using anti-BECLIN 1 and anti-BCL-2 antibodies. (C) AMBRA1 co-immunoprecipitates with both hBCL-2 and EEE-BCL-2 mutants in HEK293 cells. HEK293 cells were co-transfected with vectors encoding myc-AMBRA1, and myc-h-BCL-2 or the EEE-BCL-2 mutant. Protein extracts were immunoprecipitated using an anti-AMBRA1 antibody. Purified complexes and corresponding total extracts were analysed by WB using anti-AMBRA1 and anti-BCL-2 antibodies.

between AMBRA1 and mito-BCL-2 on autophagy induction. When cells were shifted for 4 h in an amino acid-free medium (EBSS medium), the interaction between AMBRA1 and mito-BCL-2 decreased, whereas no difference was observed in the binding between ER-BCL-2 and myc-AMBRA1. The reduction of p62/A170/SQSTM1, a ubiquitin-binding protein degraded by autophagy (Ichimura *et al*, 2008), was used as a marker to confirm autophagy induction (Figure 3A, lower panel). To control for the specificity of the co-immunoprecipitation between AMBRA1 and mito-BCL-2, negative controls using the myc antibody were performed in HEK293 cells, which do not overexpress myc-AMBRA1 or BCL-2 (Supplementary Figure S2B–D). The interaction between AMBRA1 and mito-BCL-2 can also be disrupted, at a lower extent, using rapa-

mycin as an autophagy inducer (Figure 3B). During autophagy, phosphorylation of BCL-2 by JNK1 kinase abrogates the binding between BECLIN 1 and BCL-2. Thus, we also tested whether inhibition of JNK1 would be responsible for the AMBRA1–BCL-2 binding regulation. However, as illustrated in Figure 3B, the JNK1 kinase inhibitor SP600125 does not impair the release of AMBRA1 from mito-BCL-2 after autophagy induction. Next, we observed binding between endogenous AMBRA1 and mito-BCL-2. To this end, we isolated mitochondrial fractions from cells grown in normal conditions or for 4 h in EBSS. We performed an immunoprecipitation of AMBRA1 in the mitochondrial fractions, and we were able to appreciate the binding with endogenous BCL-2 in normal conditions. In contrast, this binding was disrupted after autophagy induction (Figure 3C). Of note, when checking by densitometric analysis, we can observe a binding between endogenous AMBRA1 and BECLIN 1 in these mitochondrial fractions in normal conditions, with this binding being increased following autophagy induction (Supplementary Figure S2E). To consolidate these data, we decided to carry out a mitochondrial crosslink before performing a subcellular fractionation experiment in HEK293 cells grown in normal or starvation conditions. As illustrated in Figure 3D, when cells are not fixed, BCL-2 can be detected as a 26-kDa band (appropriate molecular weight) in normal condition, and this band decreases following autophagy induction. However, after cell fixation, this band is not detectable, whereas a band of ~170 kDa is detectable. The 170-kDa band may correspond most likely to a complex including at least endogenous AMBRA1 and BCL-2, thus confirming the interaction. Next, we set out to establish whether this dynamic interaction could be monitored by fluorescence microscopy. As illustrated in Figure 4A, mito-BCL-2 colocalizes perfectly with the mitotracker staining, as expected, and there is a significant colocalization between myc-AMBRA1 and mito-BCL-2 in normal conditions, whereas some cells showed only a slight colocalization between ER-BCL-2 and AMBRA1 (arrows in Supplementary Figure S3A, B). We performed the same type of staining at the endogenous level to confirm this colocalization (see Supplementary Figure S4). By performing statistical colocalization analysis, we found that AMBRA1 shows a very good colocalization with mito-BCL-2, as the r_p and r_s values are 0.7 and 0.8, respectively (Supplementary Figure S3C). When cells are shifted to EBSS a clear decrease in AMBRA1 and mito-BCL-2 colocalization is observed (Figure 4B, starvation lane). Furthermore, the percentage of cells where myc-AMBRA1 colocalizes either with mito-BCL-2 or ER-BCL-2 was determined. As illustrated in Figure 4C, 70% cells showing colocalization between AMBRA1 and mito-BCL-2 are found in normal conditions, whereas only 40% cells show the same colocalization after autophagy induction. Such a reduction of colocalization is not observed in the case of AMBRA1–ER-BCL-2 binding, where we found ~30% of colocalizing cells in both conditions. Of note, this colocalization seems to be due to a short ‘proximity’ between the stained compartments, rather than an overlap, as illustrated in Supplementary Figure S3B.

AMBRA1 partially localizes at mitochondria in normal conditions

AMBRA1 is a cytoplasmic protein showing a diffuse signal in normal conditions, mostly overlapping with dynein light



chains. After autophagy induction, a fraction of AMBRA1 translocates to the perinuclear region of the cell and more precisely to the ER (Di Bartolomeo *et al*, 2010). The binding of AMBRA1 with mito-BCL-2 led us to check whether there is a subcellular colocalization of AMBRA1 with mitochondria. As illustrated in Figure 5A, we found, indeed, that AMBRA1 presents a partial colocalization with mitochondria, as the r_p and r_s are 0.61 and 0.70, respectively. Of note, these quantitative results are similar to those obtained with the AMBRA1/mito-BCL-2 colocalization analysis.

In order to confirm our observation, we performed an immunogold assay using an anti-AMBRA1 antibody on HeLa cells grown in normal conditions and on their purified mitochondria (Figure 5B and Supplementary Figure S5). Altogether, these results indicate that a pool of AMBRA1 (corresponding to $49 \pm 10\%$ of the total protein) can localize at the mitochondria in normal conditions. Of note, after autophagy induction, this mitochondrial pool of AMBRA1 seems to be slightly reduced (see Supplementary Figure S6A). These results led us to hypothesize that mito-BCL-2 should anchor/inhibit AMBRA1 at the mitochondria in order to block its participation in the BECLIN 1-dependent autophagy

programme. Thus, we decided to evaluate the effect of mito-BCL-2 on autophagy induced by AMBRA1. We overexpressed AMBRA1 in the presence of a control plasmid (pCDNA3), or either with mito-BCL-2 or WT-BCL-2. LC3 protein conversion was used as a marker of autophagy induction (Mizushima *et al*, 2004, 2010). As shown in Figure 6, overexpression of mito-BCL-2 is sufficient to dramatically reduce AMBRA1-induced autophagy. However, the F2 fragment of AMBRA1, which is known to bind BECLIN 1 (Fimia *et al*, 2007), but not BCL-2 (see Figure 1A and B), is able to evade from mito-BCL-2 inhibition but not from ER-BCL-2 effect. Finally, in order to evaluate the autophagic flux (autophagosome *on-rate* versus *off-rate*), we treated cells with the lysosome inhibitor chloroquine (20 μ M) for 1 h. As shown in Figure 6B, chloroquine treatment leads to an increase of the intensity of the LC3-II bands in all the cases presented. Taken together, these results suggest that, in normal conditions, BCL-2 binds AMBRA1 at the mitochondria in order to inhibit its proautophagic function during autophagosome formation.

AMBRA1 competes with BCL-2 to bind BECLIN 1

BCL-2 is known to bind BECLIN 1 on its BH3 domain. Therefore, to better understand how AMBRA1 and BCL-2

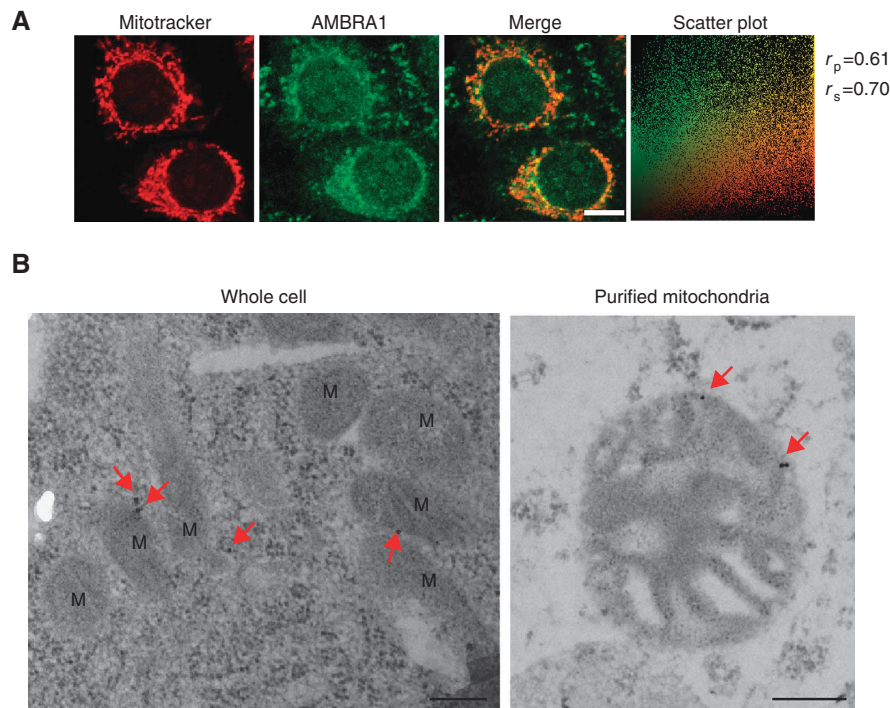


Figure 5 AMBRA1 partially colocalizes with the mitochondrial network. (A) HeLa cells grown in normal media were stained with Mitotracker (red) and an anti-AMBRA1 antibody (green). The merge of the two fluorescence signals is shown in the right panels. Scale bar, 6 μ m. The Pearson correlation coefficient r_p and Spearman correlation coefficient r_s are indicated on the scatter plot. (B) Immunogold analysis of whole cells and purified mitochondria from HeLa cells. Fifteen nm particles label the AMBRA1 protein (red arrows). Scale bar, 0.2 μ m. M, mitochondria.

Figure 4 AMBRA1 dynamic colocalization with mito-BCL-2 and the mitochondrial network. (A, B) HEK293 cells co-transfected with vectors encoding mito-BCL-2 and myc-AMBRA1, grown either in normal media (A) or in EBSS (B) for 4 h and stained with an anti-BCL-2 antibody (green), an anti-myc-AMBRA1 antibody (blu) and Mitotracker (red). The merge of the two or three fluorescence signals are shown in the bottom panels, as indicated. Scale bar, 6 μ m. White arrows point to strong triple colocalization areas. (C) AMBRA1-mito-BCL-2 colocalization decreases after autophagy induction. Quantification of cells showing colocalization between AMBRA1 and ER- or mito-BCL-2 in normal conditions and after autophagy induction is shown. Results are expressed as percentage of cells (\pm s.d.) showing colocalization between AMBRA1 and ER- or mito-BCL-2. Each point value represents the mean \pm s.d. of triplicate wells from three independent experiments. Statistical analysis was performed by analysis of variance (one-way ANOVA). * $P < 0.05$ versus mito-BCL-2 in normal conditions.

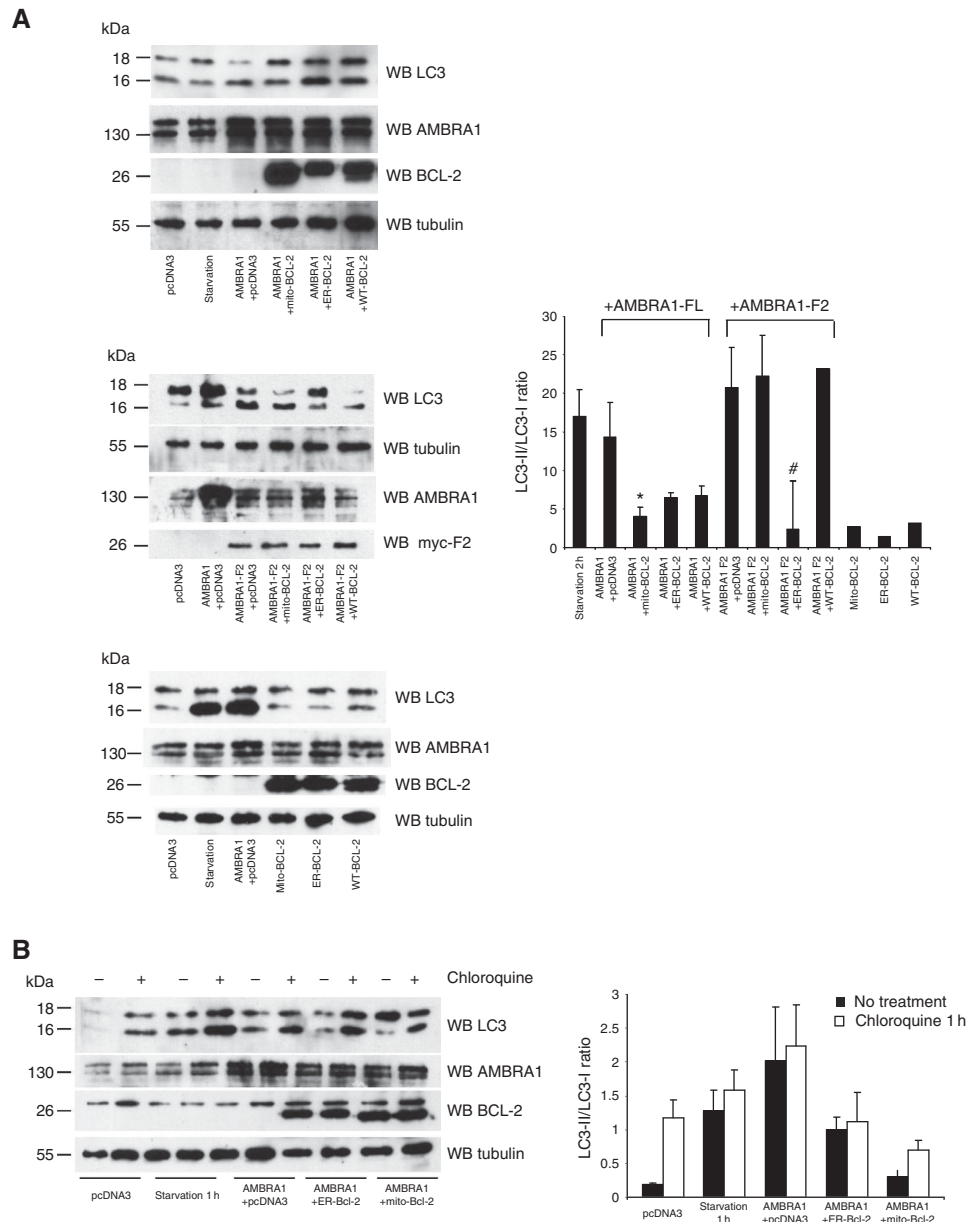


Figure 6 AMBRA1 proautophagic activity is inhibited by mito-BCL-2. **(A)** HEK293 cells were co-transfected either with the control vector pcDNA3, vectors encoding Mito-, ER- and WT-BCL-2 as controls and a vector encoding myc-AMBRA1 or AMBRA1-F2 with or without vectors encoding mito-, ER- or WT-BCL-2. As an additional positive autophagy control, 24 h untransfected cells were shifted in EBSS medium (starvation). Total extracts were then analysed by western blot (WB) using an anti-LC3 in order to analyse autophagy induction, anti-AMBRA1, anti-BCL-2 and anti-tubulin antibodies to control protein expressions. LC3-II/LC3-I ratio was quantified by densitometric analysis using the ImageQuant software. Results are expressed as LC3-II/LC3-I ratio as a percentage of control (pcDNA3 alone). Each point value represents the mean \pm s.d. from three independent experiments. Statistical analysis was performed by analysis of variance (one-way ANOVA). * $P < 0.05$ versus AMBRA1 + pcDNA3. # $P < 0.05$ versus AMBRA1 F2 + pcDNA3. **(B)** HEK293 cells were co-transfected either with the control vector pcDNA3 and a vector encoding myc-AMBRA1 with or without vectors encoding mito-, ER- or WT-BCL-2. Twenty-four hours after transfection, cells were treated with Chloroquine A or vehicle control for 2 h. Total extracts were then analysed by western blot (WB) using an anti-LC3 antibody in order to analyse autophagy induction, anti-AMBRA1, anti-BCL-2 and anti-tubulin antibodies to control protein expressions. LC3-II/LC3-I ratio was quantified by densitometric analysis using the ImageQuant software. Results are expressed as LC3-II/LC3-I ratio. Each point value represents the mean \pm s.d. from three independent experiments.

differentially regulate autophagy, we set out to determine the binding domain of AMBRA1 on BECLIN 1 by using different BECLIN 1 mutants in co-immunoprecipitation experiments with AMBRA1. In a first series of experiments, we found that three truncated BECLIN 1 mutants (aa 1–353, aa 141–353 and aa 141–450) are still able to interact with AMBRA1 (Figure 7A and B). We refined our search by using two BECLIN 1 deletion mutants: BECLIN 1 Δ Bcl-2 BD (binding domain)

(lacking aa 88–150) and BECLIN 1 Δ ECD (lacking aa 244–337). As shown in Figure 7C, AMBRA1 can still co-immunoprecipitate with BECLIN 1 Δ ECD, but not with the BECLIN 1 Δ Bcl-2 BD mutant. Consequently, it appears that a part of BECLIN 1 binding domain with BCL-2 is necessary for its binding to AMBRA1. By studying more in detail the amino acid sequence of BECLIN 1, it can be deduced that amino acids 141–150 are essential for the AMBRA1–BECLIN 1

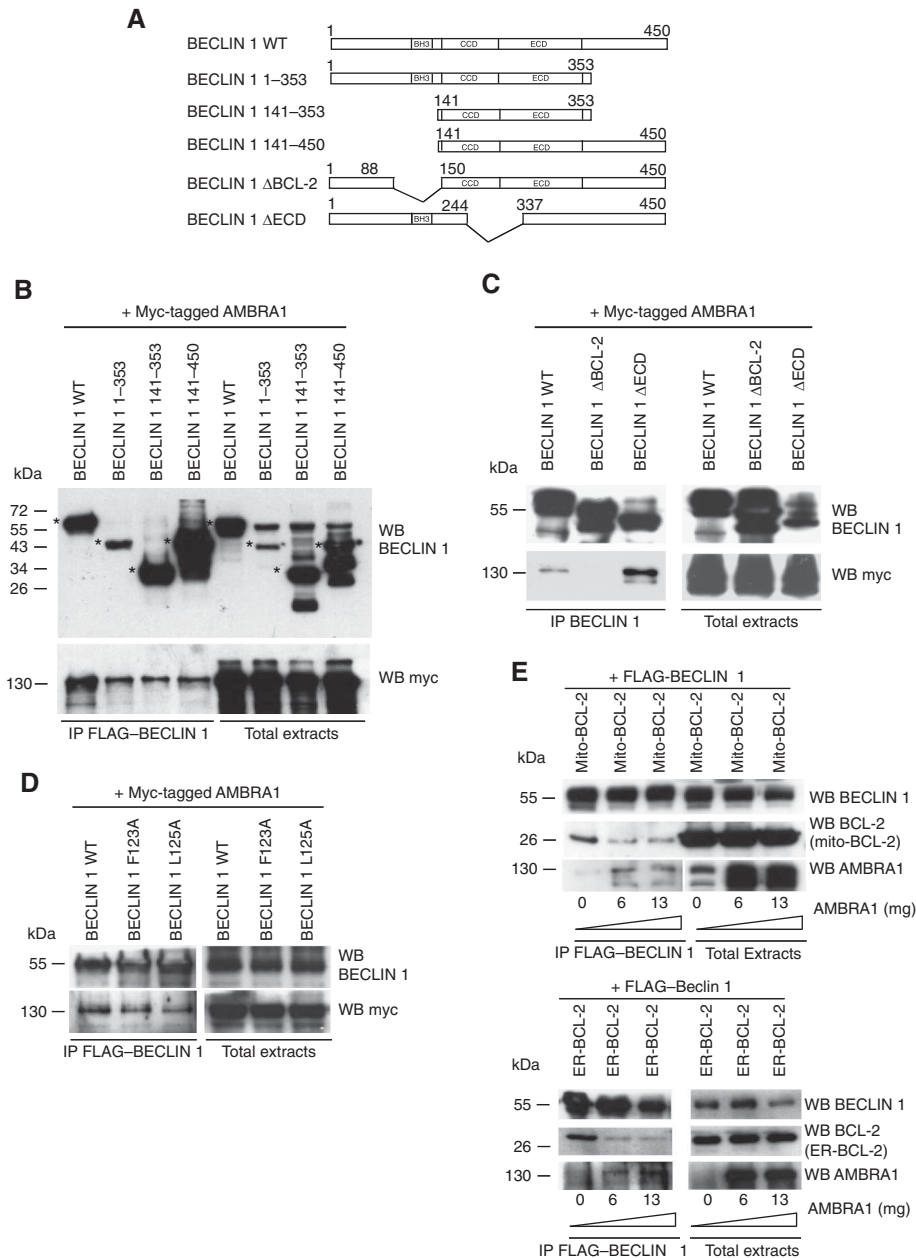


Figure 7 AMBRA1 competes with BCL-2 to bind BECLIN 1. **(A)** Illustration of the BECLIN 1 mutants. The coiled-coiled domain (CCD) and the evolutionary conserved domain (ECD) of BECLIN 1 are indicated. **(B)** AMBRA1 binds all truncated mutants of BECLIN 1. Co-immunoprecipitation of AMBRA1 and different mutants of BECLIN 1 in HEK293 cells is shown. HEK293 cells were co-transfected with vectors encoding myc-AMBRA1, FLAG-BECLIN 1 1-353, FLAG-BECLIN 1 141-353 or FLAG-BECLIN 1 141-459. Protein extracts were immunoprecipitated using an anti-FLAG antibody. Purified complexes and corresponding total extracts were analysed by WB, by using anti-AMBRA1 and anti-BECLIN 1 antibodies. Asterisks point to the molecular weight of proteins corresponding to the BECLIN 1 fragments. **(C)** AMBRA1 cannot be co-immunoprecipitated with the Beclin 1 ΔBcl-2 mutant. HEK293 cells were co-transfected with vectors encoding myc-AMBRA1 and BECLIN 1 ΔBcl-2 BD or BECLIN 1 ΔECD. Protein extracts were immunoprecipitated using an anti-BECLIN 1 antibody. Purified complexes and corresponding total extracts were analysed by WB, by using anti-AMBRA1 and anti-BECLIN 1 antibodies. **(D)** Intact BH3 binding site for BCL-2 is not required for the binding to AMBRA1. HEK293 cells were co-transfected with vectors encoding myc-AMBRA1 and BECLIN 1^{L125A} and BECLIN 1^{F123A}, which respectively interact or not with BCL-2 and BCL-X_L. Protein extracts were immunoprecipitated using a myc-AMBRA1 antibody. Purified complexes and corresponding total extracts were analysed by WB, by using anti-myc and anti-BECLIN 1 antibodies. **(E)** BECLIN 1 and mito- or ER-BCL-2 binding decreases when AMBRA1 is overexpressed. HEK293 cells were transfected both with FLAG-BECLIN 1, mito- and ER-BCL-2 and increasing concentrations of myc-AMBRA1 cDNAs. Protein extracts were immunoprecipitated using an anti-FLAG antibody. Purified complexes and corresponding total extracts were analysed by WB, by using anti-BECLIN 1, anti-BCL-2 and anti-AMBRA1 antibodies. In the upper panels, bands corresponding to AMBRA1 co-immunoprecipitated with BECLIN 1 are shown at a higher exposure than the others (mito-BCL-2 and FLAG-BECLIN 1) in order to better visualize it.

binding. We can conclude this because the Δ141-353 mutant binds AMBRA1, whereas the Δ88-150 mutant does not. We next analysed the binding between AMBRA1 and two BH3

mutants of BECLIN 1, BECLIN 1^{L125A} and BECLIN 1^{F123A}, which respectively interact or not with BCL-2 and BCL-X_L (Pattinre *et al*, 2005; Maiuri *et al*, 2007). In fact, BECLIN

1^{125A} mimicked the wild-type protein, while BECLIN 1^{F123A} possesses an unfunctional BH3 domain, a mutant known to induce a strong autophagy. Figure 7D shows that AMBRA1 can bind these two BECLIN 1 mutants, indicating that an intact BH3 binding site for BCL-2 and BCL-X_L is not required for the binding to AMBRA1. Even though AMBRA1 does not require a functional BH3 domain on BECLIN 1, it binds BECLIN 1 in a region similar to that used for binding BCL-2.

In order to substantiate the hypothesis that AMBRA1 and BCL-2 may compete for binding BECLIN 1, we conducted co-immunoprecipitation experiments with both mito/ER-BCL-2 and BECLIN 1, and increasing amounts of AMBRA1 (Figure 7E). Our results show that both mito- and ER-BCL-2/BECLIN 1 interaction decrease with increasing AMBRA1 levels. This suggests that, upon induction of autophagy, AMBRA1 can compete with mito/ER-BCL-2 to bind BECLIN 1. Of note, this competition is detectable also when we perform an inverse experiment, by using BCL-2 as a competitor for the binding between AMBRA1 and BECLIN 1 (see Supplementary Figure S7).

AMBRA1–BCL-2 interaction upon apoptosis induction

AMBRA1 functional deficiency in mouse embryos led to severe neural tube defects associated not only with autophagy impairment, but also with excessive apoptotic cell death (Fimia *et al*, 2007). Our observation that AMBRA1 binds the mitochondrial pool of BCL-2, which is known to exert an antiapoptotic effect, led us to examine the AMBRA1/BCL-2 interaction during apoptosis. First, we analysed AMBRA1–mito-BCL-2 interaction in HEK293 cells overexpressing both AMBRA1 and mito-BCL-2 and treated for 6 h with staurosporine (STS), an inducer of apoptosis. As illustrated in Figure 8A, we detected the same reduction of binding between AMBRA1 and mito-BCL-2 observed after induction of autophagy in the absence of cell death, as revealed by the absence of pycknotic nuclei (Figure 8B). In contrast, the interaction between AMBRA1 and ER-BCL-2 did not show any variations. In order to exclude a possible induction of autophagy by STS, cells were treated with STS in the presence of 10 mM 3-methyladenine (3-MA), an inhibitor of the kinase complex (Petiot *et al*, 2000). Also in this case, the disruption of AMBRA1–mito-BCL-2 complex occurs after apoptosis induction, clearly indicating that this event is independent of autophagy (Figure 8C). This decrease cannot be abrogated by addition of the general caspase inhibitor Q-VD-OPH (whose efficiency is demonstrated by PARP cleavage analysis), thus indicating that the disruption of the complex is upstream of caspase activation (Figure 8D). These results suggest that, after apoptosis induction, AMBRA1 early dissociates from mito-BCL-2.

Owing to the fact that AMBRA1 is a crucial protein for the development of the nervous system, where it is expressed from the first stages of neurulation onwards (Fimia *et al*, 2007), we investigated a putative involvement of AMBRA1 in neuronal survival. To this end, as a model of neuronal death, we used cerebellar granule neurons (CGNs) induced to die by suppression of trophic factors. Neurons were transfected with AMBRA1 and, 24 h later, cellular viability was assessed by analysis of nuclei morphology. As shown in Figure 8E, expression of AMBRA1 does not influence membrane-depolarization-induced CGN survival (K25 medium), thus excluding a proapoptotic role of AMBRA1. However, neurons overex-

pressing AMBRA1 (arrows) and shifted in K5 medium (cell death condition) for 15 h seems to better survive in this condition. These results may suggest that overexpression of wild-type AMBRA1 is probably sufficient to enhance CGN survival, early after K⁺ depletion.

Discussion

AMBRA1 binds the mitochondrial pool of BCL-2

Our work demonstrates the existence of an interaction between AMBRA1 and BCL-2. BCL-2 has been detected in different compartments of the cell: in particular, BCL-2 is not only detected in the mitochondrial fraction (17%) but also in cytoplasmic membranes including the ER (49%) and the nuclear envelope (34%; Lithgow *et al*, 1994; Hoetelmans *et al*, 2000; Portier and Tagliatalata, 2006). By looking at the different BCL-2 pools, we found that AMBRA1 binds preferentially and dynamically the mitochondrial pool of BCL-2, with the interaction being regulated by both autophagy and apoptosis induction.

Although ER-localized BCL-2, but not mitochondrial-localized BCL-2, has been shown to be important for the inhibition of autophagy (Pattingre *et al*, 2005), our results might imply that mitochondrial-localized BCL-2 can modulate the function of AMBRA1, so as to inhibit, in turn, the autophagic pathway. However, other studies are necessary to determine whether mito-BCL-2 is able to inhibit AMBRA1's role in the BECLIN 1/Vps34 complex formation. To this end, it will also be necessary to determine whether AMBRA1 can bind BCL-2 directly or through a cofactor. Different mechanisms have been proposed for regulating the binding of BCL-2/BCL-X_L to BECLIN 1 at the ER, including JNK1-mediated BCL-2 phosphorylation, competitive disruption of BCL-2–BECLIN 1 binding by other BH3 domain proteins (Sinha and Levine, 2008) and phosphorylation of the BH3 domain of BECLIN 1 by DAP kinase (Zalckvar *et al*, 2009). In this study, we found that AMBRA1 can compete with BCL-2 to bind BECLIN 1 and thus may act positively in the autophagic process.

The binding between AMBRA1 and mito-BCL-2 is disrupted following autophagy induction

BCL-2 has been mainly studied in the context of cell death; yet, it is also known to carry out other functions in different cellular processes, such as cell cycle progression, glucose homeostasis, transcriptional repression by p53 and autophagy (Reed, 1998; Danial and Korsmeyer, 2004; Pattingre *et al*, 2005; Maiuri *et al*, 2007). A subtle regulation of BCL-2 at the expression level exists, due to its long half-life (Reed, 1996). However, it is known that post-translational modifications of BCL-2, and in particular phosphorylation, have crucial roles in regulating its activity (Blagosklonny, 2001; Wei *et al*, 2008; Pattingre *et al*, 2009). Recently, it has been shown that BCL-2 phosphorylation on site T69, S70 and S87 by JNK1 inhibits its antiapoptotic function (Pattingre *et al*, 2009). How does the disruption of AMBRA1–mito-BCL-2 complex occur, following autophagy induction? We have evidence indicating that phosphorylation of BCL-2 by JNK1 does not regulate BCL-2 interaction with AMBRA1. Indeed, we found that AMBRA1 is able to co-immunoprecipitate with EEE-BCL-2, a mutant that phosphomimics the phosphorylation of BCL-2 at sites T69, S70 and S87 during autophagy

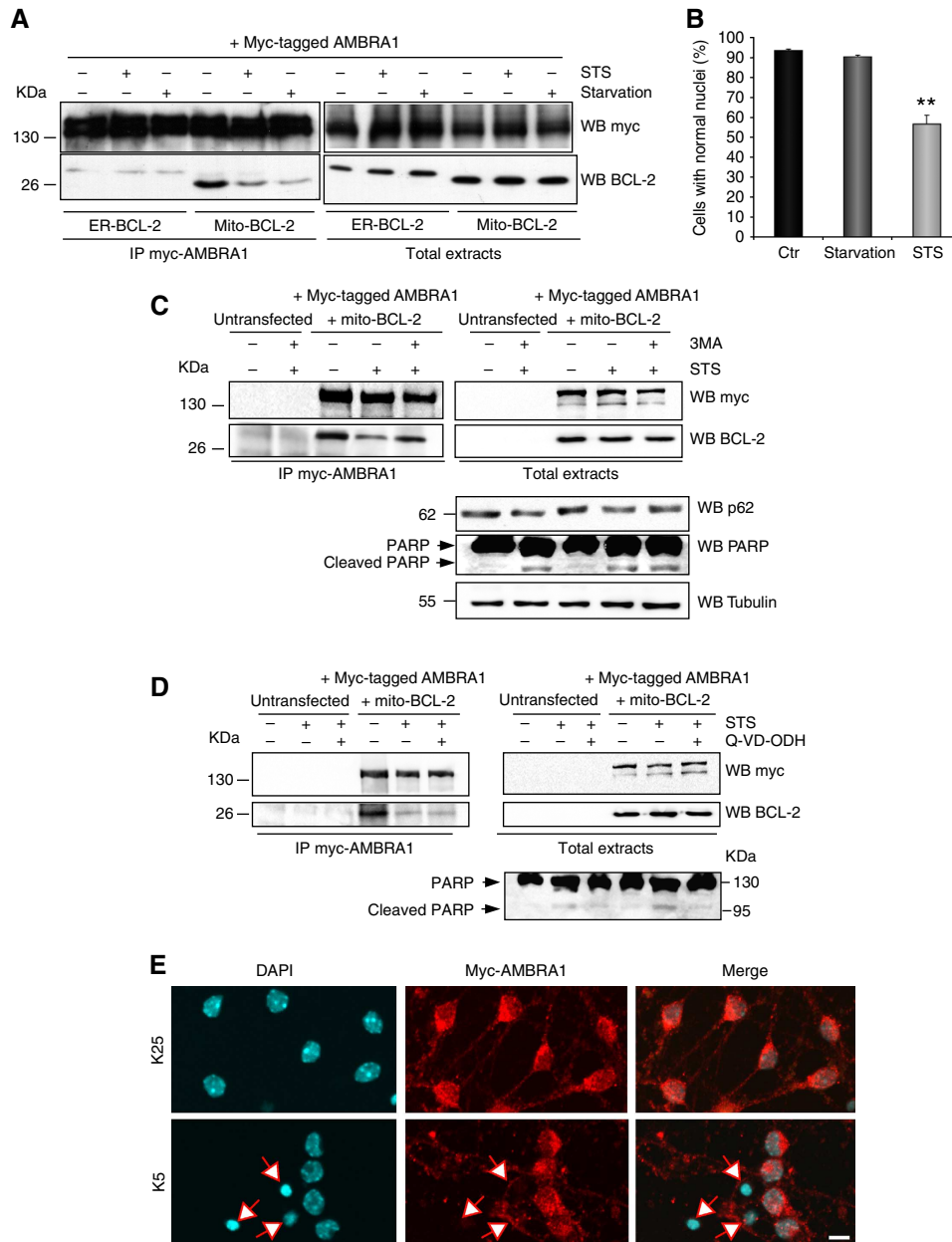


Figure 8 AMBRA1 does not possess a proapoptotic activity but, in contrast, it may participate to cell viability. **(A)** AMBRA1-BCL-2 interaction is disrupted after staurosporine (STS) treatment. HEK293 cells were co-transfected with vectors encoding mito-BCL-2 and myc-AMBRA1 FL and grown either in normal conditions, in starvation condition (EBSS 4 h) or in normal media plus STS (1 μ M, 6 h). Protein extracts were immunoprecipitated using a myc antibody (IP: myc-AMBRA1). Purified complexes and corresponding total extracts were analysed by WB, by using an anti-BCL-2 antibody. **(B)** STS but not EBSS treatment induces cell death of HEK293. HEK293 cells were co-transfected with vectors encoding mito-BCL-2 and myc-AMBRA1 and grown either in normal conditions, in starvation conditions (EBSS 4 h) or in normal media plus STS (1 μ M, 6 h). Cultures were then labelled with DAPI. Cells showing condensed or fragmented nuclei were scored as dying, and the percentage of viable cells was determined 6 h after EBSS or STS treatment. For each condition, cells were counted into 10 random fields in three different wells from three independent experiments. Statistical analysis was performed by analysis of variance (one-way ANOVA). * $P < 0.05$ versus control cells. **(C)** Apoptosis induced by STS treatment disrupts the complex AMBRA1/BCL-2. HEK293 cells were co-transfected or left untreated (as a negative control) with vectors encoding myc-AMBRA1 and mito-BCL-2. Cells were then treated with STS (1 μ M 4 h) in presence or not with 10 mM 3-MA. Protein extracts were immunoprecipitated using a myc antibody. Purified complexes and corresponding total extracts were analysed by WB using anti-BCL-2 and myc antibodies. p62 protein levels and PARP cleavage were also analysed in total extracts to control, respectively, autophagy and apoptosis induction. **(D)** Caspase inhibition does not block AMBRA1/BCL-2 complex disruption following STS treatment. HEK293 cells were co-transfected or left untreated (as a negative control) with vectors encoding mito-BCL-2 and myc-AMBRA1 and grown either in normal conditions, in normal conditions plus STS (1 μ M, 6 h) or plus caspase inhibitor Q-VD-ODH (10 μ M, 6 h). Protein extracts were immunoprecipitated using a myc antibody (IP: myc-AMBRA1). Purified complexes and corresponding total extracts were analysed by WB, by using an anti-BCL-2 antibody. Induction of cell death by STS or the inhibitory effect of Q-VD-ODH on caspases were evaluated using an anti-PARP antibody on corresponding total extracts. **(E)** AMBRA1 may protect neurons from death. Overexpression of myc-AMBRA1 in CGN grown in survival medium or after induction of apoptosis is shown. After 4 DIV, CGN were transfected with an expression vector encoding myc-AMBRA1. One day later, cultures were kept in K25 medium and grown for additional 24 h or shifted in K5 medium during 15 h. Cultures were then labelled with a myc antibody and DAPI. The transfected neurons showing condensed nuclei are visible on the overlay images. Arrows point to dead neurons. Scale bar, 6 μ m.

induction (Wei *et al*, 2008). In agreement with this observation, the interaction between AMBRA1 and mito-BCL-2 remains unchanged after induction of autophagy and treatment with a JNK1 kinase inhibitor.

Another hypothesis is that the disruption of the interaction between AMBRA1 and mito-BCL-2 is regulated by post-transcriptional modifications on AMBRA1. AMBRA1 can be directly phosphorylated by the serine/threonine kinase ULK1 and, indeed, when subjected to 2D-gel electrophoresis, it shows multiple spots, corresponding to a number of modifications (Di Bartolomeo *et al*, 2010). In line with this evidence, mito-AMBRA1 may be subjected to similar modifications during apoptosis and autophagy.

Another hypothesis concerning the function of AMBRA1 at the mitochondria comes from new data proposed by Hailey *et al* (2010), in which it is demonstrated that mitochondria can serve as a source of autophagosomal membranes during starvation in mammalian cells. Although isolation of mitochondria is likely to be contaminated with ER, in line with these results, we can speculate that AMBRA1 is present at the mitochondria to participate in the production of *mitochondrial autophagosomes*.

Indeed, our results highlight the important role played by the subcellular localization of AMBRA1 for its function. Noteworthy, we found an increase of binding between AMBRA1 and BECLIN 1 in the mitochondrial fraction, after autophagy induction. Given that we have recently demonstrated that a pool of AMBRA1 and BECLIN 1 form a complex and translocate together from the dynein motor complex to the ER upon autophagy (Di Bartolomeo *et al*, 2010), these results, combined with the recent findings from Hailey *et al* lead us to propose a model in which, in normal conditions, a pool of AMBRA1 (hereafter mito-AMBRA1) is docked by BCL-2 at the mitochondria: after autophagy induction, mito-AMBRA1 dissociates from mito-BCL-2, and increases its binding with a fraction of mito-resident BECLIN 1; Mito-AMBRA1 would have therefore the potential to enhance BECLIN 1-dependent autophagy (see Supplementary Figure S8, mitochondrial model). As we observed a reduction of AMBRA1 colocalization with mitochondria in response to autophagy (see Supplementary Figure S6A), accompanied with an increase of binding between AMBRA1 and BECLIN 1 in the microsomal fraction with a reciprocal decrease of binding between BCL-2 and BECLIN 1 (see Supplementary Figure S6B), we cannot exclude that a fraction of this mitochondrial pool of AMBRA1 translocates to the ER in order to bind ER-resident BECLIN 1 and further enhances the autophagic programme (see Supplementary Figure S8, omega-some model). Although AMBRA1 has not been shown to be in a stable complex with BECLIN 1 (Zhong *et al*, 2009; Funderburk *et al*, 2010), our present results indicate that AMBRA1 and BECLIN 1 can form 'transient' distinct complexes that can regulate the autophagic programme.

AMBRA1 and mito-BCL-2 interaction is disrupted after both autophagy and apoptosis induction

The fact that both STS treatment and autophagy induction are able to induce the dissociation of AMBRA1 from mito-BCL-2 led us to hypothesize that these two treatments induce a common pathway. Indeed, it is known that some apoptosis inducers can trigger, at first, an autophagic response (Colell *et al*, 2007); this being the case, autophagy could be

considered as a defensive response following stress-induced cell death. Our results, however, indicate that AMBRA1 and mito-BCL-2 interaction can be modulated by induction of both autophagy and apoptosis, thus underlying a double function of AMBRA1 both in autophagy and cell death control. Several authors have recently investigated the relationship between the proautophagic and proapoptosis activity of BECLIN 1 (Boya and Kroemer, 2009; Chang *et al*, 2010; Djavaheri-Mergny *et al*, 2010; Luo and Rubinsztein, 2010; Maiuri *et al* 2010). In particular, Djavaheri-Mergny *et al* (2010) reported that caspases can cleave BECLIN 1, thereby destroying its proautophagic activity. Thus, it will be very interesting to further investigate the relationship between AMBRA1 and caspase activities.

In conclusion, this work describes a novel interplay between the regulation of AMBRA1 function, BCL-2 and autophagy. For this reason, it opens up new areas of research in the complex relationship between apoptosis and autophagy.

Materials and methods

Antibodies

Polyclonal anti-FLAG (Sigma-Aldrich, F7425), monoclonal anti-myc 9E10 (Santa Cruz), polyclonal anti-myc A-14 (Santa Cruz), polyclonal anti-Beclin 1 (Santa Cruz), monoclonal anti-BECLIN 1 (Becton-Dickinson), mouse monoclonal anti-TUBULIN (Sigma-Aldrich), polyclonal anti-ACTIN (Sigma-Aldrich), monoclonal anti-BCL-2 (Santa Cruz, sc-7382), polyclonal anti-BCL-2 (Abcam, Ab7973), polyclonal anti-PARP antibody (Cell Signaling), polyclonal anti-MnSOD (Assay Designs), polyclonal anti-PDI (Stressgen), polyclonal anti-AMBRA1 (from SDI and Covalab), monoclonal anti-p62 (BD Transduction Laboratories) and polyclonal anti-LC3 (Cell Signaling).

Reagents and plasmid constructs

Constructs coding for AMBRA1 and its fragments were cloned in pLPCX vector (Clontech; Fimia *et al*, 2007). Plasmids containing either wild-type h-BCL-2-myc, EEE-BCL-2 mutant, ER-BCL-2, Mito-BCL-2, wild-type BECLIN 1 and all BECLIN 1 mutant cDNAs were present in Beth Levine's Laboratory (Howard Hughes Medical Institute, Dallas, Texas). Rapamycin and STS were purchased from Sigma-Aldrich. The Q-VD-ODH caspase inhibitor was from Kamyia Biomedical Company.

Immunoprecipitation

Cells were lysed either in HEMG buffer (25 mM HEPES (pH 8.0), 100 mM NaCl, 0.5% Nonidet P-40, 0.1 mM EDTA, 10% glycerol) plus protease and phosphatase inhibitors or in CHAPS buffer (40 mM HEPES (pH 7.4), 150 mM NaCl, 2 mM EDTA, 0.3% of CHAPS) in order to detect endogenous AMBRA1-BCL-2 interaction. After centrifugation at 4°C for 10 min at 13 000 g, equal amounts of protein were incubated with either anti-myc, anti-FLAG, anti-Beclin 1, anti-BCL-2 or anti-AMBRA1 antibodies (2 µg) overnight at 4°C, followed by 60 min incubation with 20 µl of protein A/G sepharose beads (Amersham Bioscience). The beads were collected by centrifugation and washed four times with the HEMG buffer. Proteins bound to the beads were eluted with 30 µl of SDS-polyacrylamide gel electrophoresis sample buffer and heated to 95°C for 10 min.

Immunocytochemistry

Cells were washed in PBS and fixed with 4% paraformaldehyde in PBS for 15 min. In order to stain mitochondria, mitotracker was applied to cells, prior to fixation, 15 min at 100 nM. After permeabilization with 0.2% Triton X-100 in PBS for 5 min, cells were blocked in 2% horse serum in PBS and incubated for 1 h at RT with primary antibodies. We used the antibodies directed against AMBRA1, BCL-2 and the myc Tag. Cells were then washed in blocking buffer and incubated for 1 h with labelled anti-mouse (Alexa Fluor-488 or Alexa Fluor555, Molecular Probes, Eugene, OR) or anti-rabbit (FITC or Cy3, Jackson ImmunoResearch, West Grove,

PA) secondary antibodies. Nuclei were stained with 1 µg/ml DAPI and examined under a Leica TCS SP5 confocal microscope equipped with a ×63 (NA 1.4) oil-immersion objective (Deerfield, IL). We used 'Leica confocal' software for analysis. In the case of AMBRA1 and mito-BCL-2 or ER-BCL-2 analysis, we used the Olympus IX70 microscope combined with SoftWorx software. Deconvolution was applied in standard condition (8 cycles). Image analysis was undertaken using the ImageJ analysis programme using the PSC colocalization plug-in (French *et al*, 2008) to calculate colocalization. At least 20 cells were analysed for each condition. Results are presented in terms of Pearson correlation coefficients, which represent the linear relationship of the signal intensity from the green and red channels of the analysed image.

Förster resonance energy transfer

For standard acceptor photobleaching FRET microscopy, HEK293 cells were seeded on coated glass coverslips and co-transfected with a vector encoding AMBRA1-mCherry and a vector encoding BCL-2-GFP. Twenty-four hours after transfection, cells were fixed with 4% paraformaldehyde for 10 min and, following three washes, nuclei were stained with 1 µg/ml DAPI 20 min and then placed on slides and embedded in mounting medium, as described above. FRET studies were performed on a confocal microscope (TCS SP5, Leica) using the implemented FRET acceptor photobleaching wizard. Acquisition settings were as follows: objective Plan-Apochromat ×63/1.4 NA oil immersion, pinhole 2 Airy units, image size 512 × 512. Prebleach and postbleach images were serially recorded by excitation of BCL-2-GFP at 488 nm (donor channel) with an argon laser, and mCherry-AMBRA1 at 543 nm (acceptor channel) with a helium-neon laser. Low laser intensities were used to avoid bleaching effects during acquisition, selection of the cells were made by visualizing only the donor channel to prevent premature partial bleaching of the acceptor. The acceptor was bleached with high intensity (100%) power at the 543 nm laser line for 10 iterations. This iteration time was found to be effective for bleaching mCherry-AMBRA1 in pilot experiments. The change in the fluorescence intensity between pre- and postbleach donor values (efficiency, *E*) was calculated using the formula $E = (\text{donor after} - \text{donor before}) \times 100 / \text{donor after}$, and was shown as a percentage; pseudo-coloured images showing FRET efficiency values were also generated. We analysed 10 cells from each of three independent experiments, where cells were maintained in basal conditions without starvation.

Isolation of microsomal fraction

HEK293 cells were plated in ten 10-cm Petri dishes and co-transfected with vectors encoding both FLAG-Beclin 1 and myc-AMBRA1. Five dishes were then shifted in EBSS media during 4 h and the other five dishes grown in normal media. Cells were washed twice with 5 ml of a solution of 0.137 M NaCl/2.7 mM KCl/8 mM Na₂HPO₄/1.5 mM KH₂PO₄ (PBS), harvested in a solution of 5 mM EDTA in PBS and washed with 5 ml of PBS. The cells were swollen at 0°C for 10 min in 2 ml of hypotonic solution of 10 mM Tris-HCl, pH 7.5/0.5 mM MgCl₂, and then protease inhibitor cocktail was added at 1 mM. Cells were homogenized with 30 strokes in a glass Dounce homogenizer and the homogenate was diluted in an equal volume of a solution of 0.5 M sucrose/6 mM 2-mercaptoethanol/40 µM CaCl₂/300 mM KCl/10 mM Tris-HCl, pH 7.5. The suspension was centrifugated at 10 000 g for 20 min to pellet nuclei and mitochondria. The supernatant was made at 0.6 M KCl. The suspension was centrifugated at 100 000 g for 60 min to sediment the microsomal fraction. The pellet was suspended in a solution containing 0.25 M sucrose, 0.15 M KCl, 3 mM 2-mercap-

toethanol, 20 µM CaCl₂, 10 mM Tris-HCl (pH 7.5), and centrifugated again at 100 000 g for 60 min. The pellet of protein was suspended in the same solution (Maruyama and MacLennan, 1988).

Transmission electron microscopy and immunogold staining

Mitochondria were isolated from HeLa cells by standard differential centrifugation, and suspended in isolation buffer (0.2 M sucrose, 10 mM Tris-MOPS (pH 7.4), 0.1 mM EGTA-Tris, 0.1% delipidated bovine serum albumin, BSA). They were then fixed in 2% freshly depolymerized paraformaldehyde and 0.2% glutaraldehyde in 0.1 M cacodylate buffer, pH 7.4, for 2 h at 4°C. Samples were rinsed in buffer partially dehydrated and embedded in Epon resin (Fluka), sectioned and collected on uncoated nickel grids. Ultrathin sections were processed for immunogold technique. Grids were preincubated with 10% normal goat serum in 10 mM PBS containing 1% BSA and 0.13% NaN₃ (medium A), for 15 min at RT; sections were then incubated with primary antibody, rabbit polyclonal anti-AMBRA1 (ProSci Inc.) diluted 1:50 in medium A, overnight at 4°C. After rinsing in medium containing 0.01% Tween-20 (Merck), a second incubation with primary antibody mouse anti-BCL-2 (Santa Cruz) diluted 1:50 in medium A was performed, for 2 h at RT. After incubation in medium A for 15 min at RT, sections were incubated for 1 h at RT in a solution of goat anti-rabbit IgG conjugated to 15 nm colloidal gold (British BioCell Int.) and goat anti-mouse IgG conjugated to 5 nm colloidal gold (British BioCell Int.) both diluted 1:30 in medium A containing fish gelatine 0.01%. Finally, grids were thoroughly rinsed in distilled water, contrasted with aqueous 2% uranyl acetate for 20 min, and Reynolds solution (3.5% tri-sodium citrate, 2.6% lead nitrate, Fluka) for 10 min, and then photographed in a Technai 20 (FEI Company, Eindhoven, the Netherlands) electron microscope.

Mitochondrial crosslinking

HEK293 cells were grown in normal medium or in EBSS medium during 4 h and fixed with PFA 0.5% during 10 min. After three washes with PBS, mitochondrial fractions were purified as described before. We also performed an immunoprecipitation of endogenous AMBRA1 with an antibody anti-AMBRA1 or with preimmune IgG as a negative control.

Supplementary data

Supplementary data are available at *The EMBO Journal* Online (<http://www.embojournal.org>).

Acknowledgements

This study was partly supported by the Associazione Italiana per la Ricerca sul Cancro (AIRC), the Telethon Foundation, the Italian Ministry of Health and the Italian Ministry of University and Research. Beth Levine lab is partly supported by the National Institute of Health (NIH ROI CA109618). Flavie Strappazzon is the recipient of a post-doctoral Marie Curie grant 'TRACKS' ITN. Silvia Campello is supported by a Fp-pEOPLE-IEF-2008 grant (grant agreement 235595). We thank Dr Palma Mattioli for confocal microscopy analysis, and Martin W Bennett and Magdalena Acuna Villa for excellent secretarial and editorial work.

Conflict of interest

The authors declare that they have no conflict of interest.

References

- Adams JM, Cory S (2007) Bcl-2-regulated apoptosis: mechanism and therapeutic potential. *Curr Opin Immunol* **19**: 488–496
- Albertazzi L, Arosio D, Marchetti L, Ricci F, Beltram F (2009) Quantitative FRET analysis with the EGFP-mCherry fluorescent protein pair. *Photochem Photobiol* **85**: 287–297
- Blagosklonny MV (2001) Unwinding the loop of Bcl-2 phosphorylation. *Leukemia* **15**: 869–874
- Boya P, Kroemer G (2009) Beclin 1: a BH3-only protein that fails to induce apoptosis. *Oncogene* **28**: 2125–2127
- Cecconi F, Di Bartolomeo S, Nardacci R, Fuoco C, Corazzari M, Giunta L, Romagnoli A, Stoykova A, Chowdhury K, Fimia GM, Piacentini M (2007) A novel role for autophagy in neuro development. *Autophagy* **3**: 506–508
- Chang NC, Nguyen M, Germain M, Shore GC (2010) Antagonism of Beclin 1-dependent autophagy by BCL-2 at the endoplasmic reticulum requires NAF-1. *EMBO J* **29**: 606–618
- Colell A, Ricci JE, Tait S, Milasta S, Maurer U, Bouchier-Hayes L, Fitzgerald P, Guio-Carrion A, Waterhouse NJ, Li CW,

- Mari B, Barbry P, Newmeyer DD, Beere HM, Green DR (2007) GAPDH and autophagy preserve survival after apoptotic cytochrome c release in the absence of caspase activation. *Cell* **5**: 983–997
- Daniel NN, Korsmeyer SJ (2004) Cell death: critical control points. *Cell* **116**: 205–219
- Di Bartolomeo S, Corazzari M, Nazio F, Oliverio S, Lisi G, Antoniolio M, Pagliarini V, Matteoni S, Fuoco C, Giunta L, D'Amelio M, Nardacci R, Romagnoli A, Piacentini M, Ceconi F, Fimia GM (2010) The dynamic interaction of Ambra1 with the dynein motor complex regulates mammalian autophagy. *J Cell Biol* **191**: 155–168
- Djavaheri-Mergny M, Maiuri MC, Kroemer G (2010) Cross talk between apoptosis and autophagy by caspase-mediated cleavage of Beclin 1. *Oncogene* **12**: 1717–1719
- Fimia GM, Stoykova A, Romagnoli A, Giunta L, Di Bartolomeo S, Nardacci R, Corazzari M, Fuoco C, Ucar A, Schwartz P, Gruss P, Piacentini M, Chowdhury K, Ceconi F (2007) Ambra1 regulates autophagy and development of the nervous system. *Nature* **447**: 1121–1125
- French AP, Mills S, Swarup R, Bennett MJ, Pridmore TP (2008) Colocalization of fluorescent markers in confocal microscope images of plant cells. *Nat Protoc* **3**: 619–628
- Funderburk SF, Wang QJ, Yue Z (2010) The Beclin 1-VPS34 complex-at the crossroads of autophagy and beyond. *Trends Cell Biol* **6**: 355–362
- Germain M, Shore GC (2003) Cellular distribution of Bcl-2 family proteins. *Sci STKE* **173**: pe10
- Hailey DW, Rambold AS, Satpute-Krishnan P, Mitra K, Sougrat R, Kim PK, Lippincott-Schwartz J (2010) Mitochondria supply membranes for autophagosome biogenesis during starvation. *Cell* **4**: 656–667
- He C, Levine B (2010) The Beclin 1 interactome. *Curr Opin Cell Biol* **2**: 140–149
- Hoetelmans R, van Slooten HJ, Keijzer R, Erkeland S, van de Velde CJ, Dierendonck JH (2000) Bcl-2 and Bax are present in interphase nuclei of mammalian cells. *Cell Death Differ* **4**: 384–392
- Ichimura Y, Kumanomidou T, Sou YS, Mizushima T, Ezaki J, Ueno T, Kominami E, Yamane T, Tanaka K, Komatsu M (2008) Structural basis for sorting mechanism of p62 in selective autophagy. *J Biol Chem* **283**: 22847–22857
- Itakura E, Kishi C, Inoue K, Mizushima N (2008) Beclin 1 forms two distinct phosphatidylinositol 3-kinase complexes with mammalian Atg14 and UVRAG. *Mol Biol Cell* **19**: 5360–5372
- Levine B, Sinha S, Kroemer G (2008) Bcl-2 family members: dual regulators of apoptosis and autophagy. *Autophagy* **4**: 600–606
- Liang C, Lee JS, Inn KS, Gack MU, Li Q, Roberts EA, Vergne I, Deretic V, Feng P, Akazawa C, Jung JU (2008) Beclin1-binding UVRAG targets the class C Vps complex to coordinate autophagosome maturation and endocytic trafficking. *Nat Cell Biol* **10**: 776–787
- Lithgow T, van Driel R, Bertram JF, Strasser A (1994) The protein product of the oncogene bcl-2 is a component of the nuclear envelope, the endoplasmic reticulum, and the outer mitochondrial membrane. *Cell Growth Differ* **5**: 411–417
- Luo S, Rubinsztein DC (2010) Apoptosis blocks Beclin 1-dependent autophagosome synthesis: an effect rescued by Bcl-xL. *Cell Death Differ* **17**: 268–277
- Maiuri MC, Ciriollo A, Kroemer G (2010) Crosstalk between apoptosis and autophagy within the Beclin 1 interactome. *EMBO J* **29**: 515–516
- Maiuri MC, Le Toumelin G, Ciriollo A, Rain JC, Gautier F, Juin P, Tasdemir E, Pierron G, Troulinaki K, Tavernarakis N, Hickman JA, Geneste O, Kroemer G (2007) Functional and physical interaction between Bcl-X(L) and a BH3-like domain in Beclin-1. *EMBO J* **26**: 2527–2539
- Maruyama K, MacLennan DH (1988) Mutation of aspartic acid-351, lysine-352, and lysine-515 alters the Ca²⁺ transport activity of the Ca²⁺-ATPase expressed in COS-1 cells. *Proc Natl Acad Sci* **85**: 3314–3318
- Matsunaga K, Saitoh T, Tabata K, Omori H, Satoh T, Kurotori N, Maejima I, Shirahama-Noda K, Ichimura T, Isobe T, Akira S, Noda T, Yoshimori T (2009) Two Beclin 1-binding proteins, Atg14L and Rubicon, reciprocally regulate autophagy at different stages. *Nat Cell Biol* **11**: 385–396
- Mitoma J, Ito A (1992) The carboxy-terminal 10 amino acid residues of cytochrome b5 are necessary for its targeting to the endoplasmic reticulum. *EMBO J* **11**: 4197–4203
- Mizushima N (2010) The role of the Atg1/ULK1 complex in autophagy regulation. *Curr Opin Cell Biol* **2**: 132–139
- Mizushima N, Yamamoto A, Matsui M, Yoshimori T, Ohsumi Y (2004) *In vivo* analysis of autophagy in response to nutrient starvation using transgenic mice expressing a fluorescent autophagosome marker. *Mol Biol Cell* **15**: 1101–1111
- Mizushima N, Yoshimori T, Levine B (2010) Methods in mammalian autophagy research. *Cell* **140**: 313–326
- Pattingre S, Bauvy C, Carpentier S, Levade T, Levine B, Codogno P (2009) Role of JNK1-dependent Bcl-2 phosphorylation in ceramide-induced macroautophagy. *J Biol Chem* **284**: 2719–2728
- Pattingre S, Tassa A, Qu X, Garuti R, Liang XH, Mizushima N, Packer M, Schneider MD, Levine B (2005) Bcl-2 antiapoptotic proteins inhibit Beclin 1-dependent autophagy. *Cell* **122**: 927–939
- Petiot A, Ogier-Denis E, Blommaert EF, Meijer AJ, Codogno P (2000) Distinct classes of phosphatidylinositol 3'-kinases are involved in signaling pathways that control macroautophagy in HT-29 cells. *J Biol Chem* **2**: 992–998
- Pistor S, Chakraborty T, Niebuhr K, Domann E, Wehland J (1994) The ActA protein of *Listeria monocytogenes* acts as a nucleator inducing reorganization of the actin cytoskeleton. *EMBO J* **13**: 758–763
- Portier BP, Tagliatalata G (2006) Bcl-2 localized at the nuclear compartment induces apoptosis after transient overexpression. *J Biol Chem* **281**: 40493–40502
- Reed JC (1996) Mechanisms of Bcl-2 family protein function and dysfunction in health and disease. *Behring Inst Mitt* **97**: 72–100
- Reed JC (1998) Bcl-2 family proteins. *Oncogene* **17**: 3225–3236
- Sinha S, Levine B (2008) The autophagy effector Beclin 1: a novel BH3-only protein. *Oncogene* **27**: 137–148
- Sun Q, Fan W, Zhong Q (2009) Regulation of Beclin 1 in autophagy. *Autophagy* **5**: 713–716
- Takahashi Y, Coppola D, Matsushita N, Cualing HD, Sun M, Sato Y, Liang C, Jung JU, Cheng JQ, Mule JJ, Pledger WJ, Wang HG (2007) Bif-1 interacts with Beclin 1 through UVRAG and regulates autophagy and tumorigenesis. *Nat Cell Biol* **9**: 1142–1151
- Takahashi Y, Meyerkord CL, Wang HG (2009) Bif-1/endophilin B1: a candidate for crescent driving force in autophagy. *Cell Death Differ* **16**: 947–955
- Wei Y, Pattingre S, Sinha S, Bassik M, Levine B (2008) JNK1-mediated phosphorylation of Bcl-2 regulates starvation-induced autophagy. *Mol Cell* **30**: 678–688
- Zalckvar E, Berissi H, Mizrachy L, Idelchuk Y, Koren I, Eisenstein M, Sabanay H, Pinkas-Kramarski R, Kimchi A (2009) DAP-kinase-mediated phosphorylation on the BH3 domain of beclin 1 promotes dissociation of beclin 1 from Bcl-XL and induction of autophagy. *EMBO Rep* **10**: 285–292
- Zhong Y, Wang QJ, Li X, Yan Y, Backer JM, Chait B, Heintz N, Yue Z (2009) Distinct regulation of autophagic activity by Atg14L and Rubicon associated with Beclin 1-phosphatidylinositol 3-kinase complex. *Nat Cell Biol* **4**: 468–476
- Zhu W, Cowie A, Wasfy GW, Penn LZ, Leber B, Andrews DW (1996) Bcl-2 mutants with restricted subcellular location reveal spatially distinct pathways for apoptosis in different cell types. *EMBO J* **15**: 4130–4141

AMBRA1 is able to induce mitophagy via LC3 binding, regardless of PARKIN and p62/SQSTM1

This article has been corrected since Advance Online Publication and a corrigendum is also printed in this issue.

F Strappazon^{1,2}, F Nazio¹, M Corrado^{1,3}, V Cianfanelli^{2,4}, A Romagnoli⁵, GM Fimia^{5,6}, S Campello¹, R Nardacci⁵, M Piacentini^{2,5}, M Campanella^{7,8} and F Cecconi^{*,1,2,4}

Damaged mitochondria are eliminated by mitophagy, a selective form of autophagy whose dysfunction associates with neurodegenerative diseases. PINK1, PARKIN and p62/SQSTM1 have been shown to regulate mitophagy, leaving hitherto ill-defined the contribution by key players in ‘general’ autophagy. In basal conditions, a pool of AMBRA1 – an upstream autophagy regulator and a PARKIN interactor – is present at the mitochondria, where its pro-autophagic activity is inhibited by Bcl-2. Here we show that, upon mitophagy induction, AMBRA1 binds the autophagosome adapter LC3 through a LIR (LC3 interacting region) motif, this interaction being crucial for regulating both canonical PARKIN-dependent and -independent mitochondrial clearance. Moreover, forcing AMBRA1 localization to the outer mitochondrial membrane unleashes a massive PARKIN- and p62-independent but LC3-dependent mitophagy. These results highlight a novel role for AMBRA1 as a powerful mitophagy regulator, through both canonical or noncanonical pathways.

Cell Death and Differentiation (2015) 22, 419–432; doi:10.1038/cdd.2014.139; published online 12 September 2014

Autophagy is an important eukaryotic process involved in the lysosomal degradation of cytosolic components in both physiological and pathological conditions. During autophagy, the autophagosomes – specific double-membraned vesicles – engulf a number of different cargoes and then fuse with the lysosomes for subsequent recycling of their content. Several key proteins are involved in autophagosome formation, such as BECLIN 1 and its positive regulator AMBRA1;^{1,2} a pool of AMBRA1 is localized at the mitochondria, where its pro-autophagic activity is inhibited by mitochondrial resident Bcl-2.³ Interestingly, mitochondria have been described as a source for autophagosome biogenesis;⁴ they play a key role in the cross-talk between autophagy and apoptosis regulation and they are involved in the cell death *versus* survival decision (reviewed in Strappazon *et al.*³).

Another mechanistic link exists between autophagy and mitochondria in mammals. Indeed, mitochondria damaged by the uncoupler CCCP (carbonyl cyanide *m*-chlorophenyl hydrazone) – because of a loss of their mitochondrial membrane potential ($\Delta\Psi_m$) – are subjected to a form of selective autophagy, termed mitophagy.^{5–7} During this process, depolarized mitochondria are ubiquitinated; they then recruit p62 (a protein involved in linking polyubiquitinated protein aggregates to the autophagic machinery) and next they are transported

along microtubules to the perinuclear region, where they form rough aggregate structures termed ‘mito-aggregates’,^{8–10} a step preceding their lysosomal degradation.

Although mitophagy has been described in a number of tissues and in various physiological or pathological conditions (reviewed in Andreux *et al.*¹¹), very few are the known molecular mechanisms that regulate mitophagy; this is despite the fact that its manipulation may represent a forefront strategy in several human diseases. Thus, rather scarce is yet the availability of chemicals and drug candidates to modulate the process. The autophagy receptor NIX and the kinase Ulk1 mediate developmental removal of mitochondria during reticulocyte differentiation.^{6,12,13} Smurf1 has been defined as a new recognized mediator of both viral autophagy and mitophagy.¹⁴ In contrast, the E3 ubiquitin ligase PARKIN and the Ser/Thr kinase PINK1, both found to be mutated in autosomal recessive forms of Parkinson’s disease (PD), regulate mitophagy after mitochondrial damage.⁵ In more detail, PINK1 recruits PARKIN to depolarized mitochondria in order to remove damaged mitochondria. This mitochondrial quality control, driven by PINK1/PARKIN proteins, has recently been better characterized by RNAi screens.¹⁵ In fact, new proteins such as HSPA1L, BAG4 and SIAH3

¹IRCCS Fondazione Santa Lucia, Rome, Italy; ²Department of Biology, University of Rome Tor Vergata, Rome, Italy; ³Dulbecco-Telethon Institute, Venetian Institute of Molecular Medicine, Padova, Italy; ⁴Unit of Cell Stress and Survival, Danish Cancer Society Research Center, Copenhagen, Denmark; ⁵IRCCS Istituto Nazionale Malattie Infettive Lazzaro Spallanzani, Rome, Italy; ⁶Department of Biological and Environmental Sciences and Technologies (DiSTeBA), University of Salento, Lecce, Italy; ⁷Department of Comparative Biomedical Sciences, The Royal Veterinary College, University of London and UCL Consortium for Mitochondrial Research (CfMR), London, UK and ⁸European Brain Research Institute (EBRI), Rita Levi-Montalcini Foundation, Rome, Italy

*Corresponding author: F Cecconi, IRCCS F. Santa Lucia and Department of Biology, University of Rome Tor Vergata, Via della Ricerca Scientifica, Rome 00133, Italy; Unit of Cell Stress and Survival, Danish Cancer Society Research Center, Strandboulevarden 49, 2100 Copenhagen, Denmark. Tel: +39 6 72594230; Fax: +39 6 72594222; E-mail: francesco.cecconi@uniroma2.it or cecconi@cancer.dk

Abbreviations: CCCP, carbonyl cyanide *m*-chlorophenyl hydrazone; $\Delta\Psi_m$, mitochondrial membrane potential; LIR, LC3 interacting region; FCCP, trifluorocarbonylcyanide phenylhydrazone; ETNA, embryonic telencephalic naive cell; ActA, Actin assembly-inducing protein; EM, electron microscope; 3-MA, 3-methyladenine; TMRM, Tetramethylrhodamine, methyl ester; DMEM, Dulbecco’s modified Eagle’s medium; FBS, fetal bovine serum; PD, Parkinson’s disease; MEF, mouse embryonic fibroblast

Received 12.6.14; revised 30.7.14; accepted 31.7.14; Edited by G Kroemer; published online 12.9.14

have been found to modulate translocation of PARKIN to damaged mitochondria, whereas TOMM7 stabilizes PINK1 on the mitochondria. Interestingly, it has been demonstrated that after mitochondrial depolarization, the cytosolic pool of AMBRA1 interacts with PARKIN to enhance mitochondrial clearance.¹⁶

In this study, we investigate the molecular mechanism(s) responsible for the AMBRA1-dependent enhancement of PARKIN-mediated mitophagy. We describe for the first time AMBRA1 as a new LIR (LC3 interacting region)-containing protein, and we demonstrate that this motif is essential for the binding between AMBRA1 and LC3, following mitophagy induction. Furthermore, we show that this interaction is crucial in a number of cell systems in order to both amplify PARKIN-mediated mitochondrial clearance and regulate PARKIN-independent mitophagy. In addition, to better understand the role of AMBRA1 at the mitochondria and as AMBRA1 does not possess a clear mitochondrial targeting sequence, we generated and expressed an organelle-targeted mutant of AMBRA1 in two different cell systems. Our data indicate that mitochondrial AMBRA1 induces (1) relocalization of the mitochondrial network around the nucleus, (2) depolarization and ubiquitylation of mitochondria and (3) recruitment of the molecular platform necessary to induce functional mitophagy through a PARKIN/p62-independent pathway.

This work thus places AMBRA1 as a central player of mitophagy: we suggest that this molecule facilitates mitochondrial clearance by bringing damaged mitochondria onto autophagosomes via its LIR-mediated LC3 interaction. In addition, we show that high levels of mitochondrial AMBRA1 trigger mitophagy, a finding that could herald new therapies to fight important human disorders, ranging from muscle dystrophy to neurodegeneration.

Results

FCCP induces AMBRA1 binding to LC3 through a previously undisclosed LIR motif, this enhancing PARKIN-mediated mitophagy. As AMBRA1 can localize at the mitochondria,³ and as this organelle has been described as a

source for autophagosome biogenesis,⁴ we checked whether AMBRA1 could bind LC3, an autophagosome cargo adapter, on the mitochondria, so as to enhance autophagosome production following mitochondrial damage.

The known *consensus* sequence for the core LIR motif is W/F/Y-x-x-L/I/V.¹⁷ Therefore, first of all, we examined *in silico* the AMBRA1 sequence and found that AMBRA1 possesses, indeed, a putative LIR motif in its C-terminal region (1012SGVEYYWxxL1023). Primed by the hypothesis that the two factors could interact only locally at a subcellular level, we enriched our samples for mitochondrial proteins, by performing a mitochondrial fractioning assay in HEK293 cells transiently overexpressing myc-AMBRA1^{WT} and after treatment with FCCP (trifluorocarbonylcyanide phenylhydrazide, 1 h, 10 μ M), a routinely adopted inducer of mitochondrial depolarization in *in vitro* assays. We then precipitated myc-AMBRA1^{WT}, and we checked for the presence of LC3-I and -II (hallmarks of autophagy). Interestingly, myc-AMBRA1^{WT} can be found associated with LC3-I and -II forms following FCCP treatment in both endogenous and overexpression conditions (Figure 1a and Supplementary Figure 1). It is noteworthy that no binding between AMBRA1 and LC3 could be found in total extracts of HEK293 cells following autophagy induction (EBSS treatment, Supplementary Figure 1b).

It is noteworthy that point mutations of both an aromatic residue and the conserved hydrophobic residue of the putative LIR motif (AMBRA1^{LIR-AA} (W1019A-L1022A) SGVEYYAxxA) almost abolished the interaction between myc-AMBRA1^{WT} and endogenous LC3 after mitophagy induction (Figure 1b). Next, as AMBRA1 overexpression has been shown to enhance PARKIN-mediated mitochondrial clearance,¹⁶ we set out to verify whether AMBRA1–LC3 interaction was required in this context. To this aim, we transiently coexpressed a vector encoding PARKIN and AMBRA1^{WT} or AMBRA1^{LIR-AA} in HEK293 cells. We then treated cells with FCCP in order to induce mitophagy, and then measured the expression of MnSOD, a mitochondrial marker. As shown in Figure 1c, overexpression of AMBRA1^{WT} potentiates PARKIN-mediated mitophagy, confirming previous results.¹⁶ In contrast, coexpression

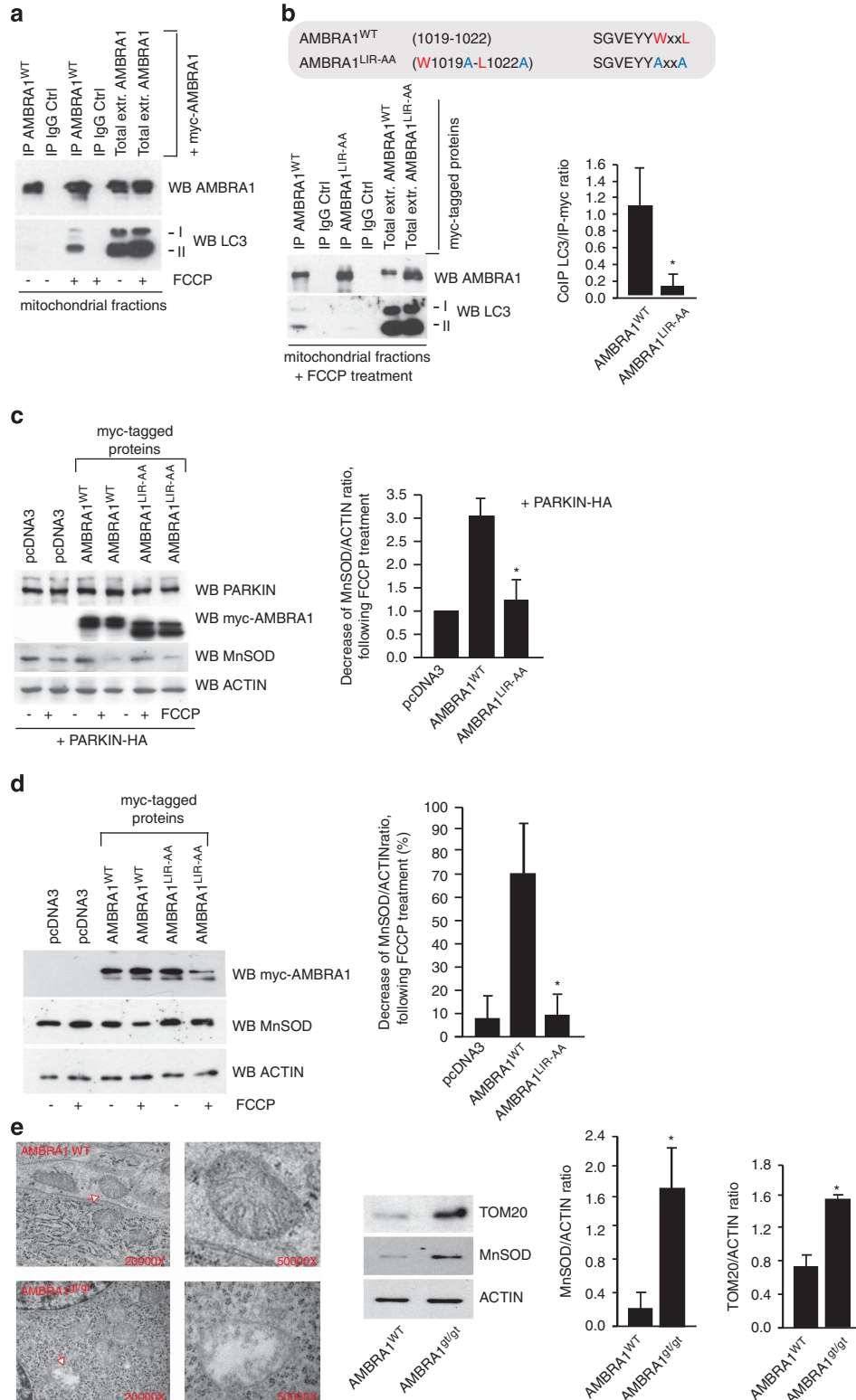
Figure 1 FCCP induces AMBRA1 binding to LC3 through a previously undisclosed LIR motif, enhancing PARKIN-mediated mitophagy. (a) HEK293 cells transfected with a vector encoding myc-AMBRA1^{WT}. At 24 h after transfection, cells were treated with DMSO (ctrl) or with FCCP for 1 h (10 μ M). Mitochondrial extracts were immunoprecipitated using an anti-myc antibody or with IgG control. Purified complexes and corresponding total extracts were analysed by western blot (WB) using anti-AMBRA1 and anti-LC3 antibodies. (b) Identification of a LIR motif within the AMBRA1 sequence. Point mutations of both an aromatic residue and the conserved hydrophobic residue are shown (AMBRA1-LIR^{AA} (W1019A-L1022A SGVEYYAxxA)). HEK293 cells were transfected with a vector encoding myc-AMBRA1^{WT} or myc-AMBRA1-LIR^{AA}. At 24 h after transfection, cells were treated with DMSO (ctrl) or FCCP for 1 h (10 μ M). Mitochondrial extracts were immunoprecipitated using an anti-myc antibody or with IgG control. Purified complexes and corresponding total extracts were analysed by WB using anti-AMBRA1 and anti-LC3 antibodies. The band density *ratio* of immunoprecipitated AMBRA1 relative to immunoprecipitated LC3 is analysed in three independent experiments; each point value represents the mean \pm S.D. from three independent experiments. Statistical analysis was performed using Student's test ($*P < 0.05$) versus AMBRA1. (c) HEK293 cells were transfected with a vector encoding myc-AMBRA1^{WT} or myc-AMBRA1-LIR^{AA}. At 24 h after transfection, cells were treated with DMSO (ctrl) or FCCP for 9 h (1 μ M). Protein extracts were analysed using anti-MnSOD and anti-ACTIN (loading control) antibodies. The graph illustrates the MnSOD/ACTIN *ratio* (\pm S.D.). Each point value represents the mean \pm S.D. from three independent experiments. Statistical analysis was performed using Student's test ($*P < 0.05$) versus AMBRA1 + PARKIN. (d) ETNA cells were transfected with a vector encoding myc-AMBRA1^{WT} or myc-AMBRA1^{LIR-AA}. At 24 h after transfection, cells were treated with DMSO (ctrl) or FCCP for 5 h (30 μ M). Protein extracts were analysed using anti-MnSOD (mitochondria) and anti-ACTIN (loading control) antibodies. The graph illustrates the MnSOD/ACTIN *ratio* decrease following FCCP treatment (%). Each point value represents the mean \pm S.D. from three independent experiments. Statistical analysis was performed using Student's test ($*P < 0.05$) versus AMBRA1^{WT}. (e) Ultrastructural analysis of brain from wild-type and *Ambra1*^{gt/gt} embryos. The arrow (in the *Ambra1*^{gt/gt} panel) indicates alterations of the cristae and the overall structure of the organelle in damaged mitochondria. Protein extracts from embryo heads (E13.5) were analysed by WB using anti-MnSOD, anti-TOM20 and anti-ACTIN (loading control) antibodies. Magnification is indicated (\times). Graphs represent MnSOD/ACTIN or TOM20/ACTIN *ratio* (\pm S.D.). Each point value represents the mean \pm S.D. from three independent experiments. Statistical analysis was performed by Student's test ($*P < 0.05$)

of PARKIN with AMBRA1^{LIR-AA} did not increase mitochondrial clearance to the same extent as AMBRA1^{WT}.

Next, we confirmed our results in a murine proneural cell line. We transiently coexpressed vectors encoding pcDNA3, AMBRA1^{WT} or AMBRA1^{LIR-AA} in embryonic telencephalic

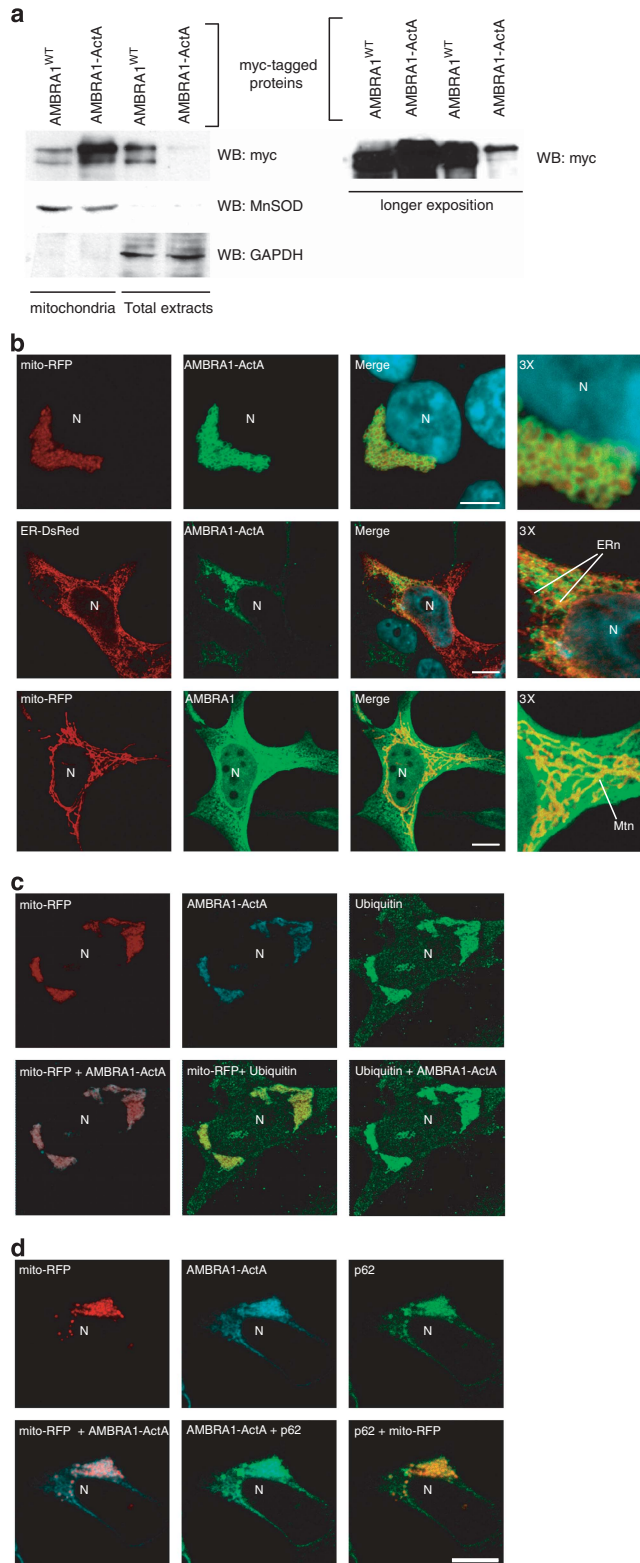
naive cells (ETNA).¹⁸ We then treated cells with FCCP, as in Figure 1c, and obtained even more striking results (Figure 1d).

Taken overall, these results indicate that, in different cell types, the LIR motif of AMBRA1 required for LC3 binding is



responsible for the described enhancement of PARKIN-mediated mitochondrial clearance.¹⁶

To investigate the mitophagic role of AMBRA1 *in vivo* in physiological conditions, we looked at the mitochondrial



content of embryonic forebrains (prosencephalon) from wild-type or AMBRA1-deficient embryos (*Ambra1^{gt/gt}*). As revealed by ultrastructural analysis using electron microscope (EM), brains from *Ambra1^{gt/gt}* embryos accumulated damaged mitochondria when compared with wild-type tissues. In addition, we observed a stronger expression of the two mitochondrial markers MnSOD and TOM20 in *Ambra1^{gt/gt}* embryonic brains (Figure 1e). These results support a crucial role, *in vivo*, for AMBRA1 in mitochondrial homeostasis.

High levels of mitochondria-targeted AMBRA1 specifically induce a perinuclear distribution of mitochondria.

To manipulate the dosage of the AMBRA1 mitochondrial pool, we generated a construct encoding myc-AMBRA1 fused to an 'insertion sequence' that can target the molecule to the outer mitochondrial membrane. To this end, we used a DNA sequence from the *Listeria monocytogenes* Actin assembly-inducing protein (ActA).¹⁹

First, we checked for the localization of the AMBRA1-ActA protein. As expected, AMBRA1-ActA is enriched in the mitochondrial fraction of HEK293 cells (Figure 2a).

To confirm these results we performed a confocal microscopy analysis in HEK293 cells co-transfected with a vector encoding fluorescent mito-RFP, in order to stain the mitochondrial network, and a tagged vector encoding AMBRA1-ActA. Indeed, AMBRA1-ActA surrounds swollen and aggregated mitochondria (Figure 2b). In contrast, only a slight colocalization of AMBRA1-ActA was found with the ER network (Figure 2b, upper and mid panels). AMBRA1^{WT} only partially colocalizes with mitochondria (Figure 2b, lower panels).

Most importantly, we observed that AMBRA1-ActA overexpression induces *per se* a strong relocalization of the mitochondrial network around the perinuclear envelope, leading to the formation of structures similar to those previously described as 'mito-aggregates'^{8,10} (Figure 2b, upper panels). These structures cannot be found after overexpression of Bcl-2-ActA (Supplementary Figure 2),

Figure 2 AMBRA1-ActA colocalizes with mitochondria and induces the formation of ubiquitin- and p62-positive mito-aggregates in HEK293 cells. (a) HEK293 cells were transfected with a vector encoding myc-AMBRA1-ActA. At 24 h after transfection, cells were lysed and mitochondrial extracts were analysed by western blot using an anti-myc antibody. The fraction purity was verified by means of antibodies against MnSOD (mitochondria) or GAPDH (cytosol). The longer exposure in the right panel shows the low levels of Ambra1-ActA outside mitochondria. (b) HEK293 cells were co-transfected with vectors encoding myc-AMBRA1-ActA (green) and mito-RFP (red) or ER-DsRed (red). As a control, HEK293 cells were co-transfected with vectors encoding myc-AMBRA1^{WT} and mito-RFP. At 24 h after transfection, cells were fixed and stained with an anti-myc antibody (green). Merge of the fluorescence signals is shown in the right panel, together with a higher magnification image ($\times 3$). N, nucleus; ERn, ER network; Mtn, mitochondrial network. Scale bar, 6 μ m. (c) HEK293 cells were co-transfected with vectors encoding myc-AMBRA1-ActA and mito-RFP (red). Twenty-four hours after transfection, cells were fixed and stained with anti-myc (blue) and anti-Ubiquitin (green) antibodies. Merged images of the two fluorescence signals are shown in the right panels. (d) HEK293 cells were co-transfected with vectors encoding myc-AMBRA1-ActA and mito-RFP (red). Twenty-four hours after transfection, cells were fixed and stained with anti-myc (blue) and anti-p62 (green) antibodies. Merged images of the two fluorescence signals are shown in the right panels. N, nucleus. Scale bar, 6 μ m.

confirming that they represent a specific effect of AMBRA1 mitochondrial overexpression.

To summarize, AMBRA1 localization at the outer mitochondrial membrane potently induces the formation of structures similar to mito-aggresomes.

Mitochondria-targeted AMBRA1 induces massive mitophagy in PARKIN-competent cells. We next studied the dynamics of the mitochondria shape changes induced by AMBRA1. As shown in Supplementary Figure 3, at 8 h after transfection, AMBRA1–ActA staining significantly overlaps with the mitochondrial network that seems to be normally well organized. However, at 10 h after transfection, AMBRA1–ActA staining in the majority of transfected cells ($\cong 75\%$) surrounds all mitochondria, forming a sort of ring. Finally, at 18 h after transfection, the mitochondrial network is completely redistributed around the perinuclear area and forms mito-aggresome-like structures.

Next, we characterized these structures and found that at 24 h following AMBRA1–ActA overexpression, mitochondria are stained for ubiquitin and p62 (Figure 2). This observation suggests that AMBRA1–ActA induces canonical mito-aggresomes, decorated by ubiquitin and p62.^{9,20} The appearance of mito-aggresomes led us to hypothesize that AMBRA1–ActA overexpression was able to induce mitophagy. Thus, we decided to check the occurrence of this event by the presence of LC3, a well-known marker of autophagosome formation.²¹ As shown in Figure 5a, a perfect colocalization between AMBRA1–ActA, mitochondria and LC3 can be observed. Cells overexpressing AMBRA1–ActA showed a colocalization of $\cong 82\%$ with ubiquitin, $\cong 69\%$ with p62 and $\cong 89\%$ with LC3 (see Supplementary Figure 4).

Furthermore, in order to better characterize the mito-aggresomes as regions with high density of mitochondria-containing autophagosomes, we performed an ultrastructural analysis by EM on cells overexpressing AMBRA1–ActA. The EM image at 24 h indicates the presence of mitochondria redistributed on one side of the nucleus. At 48 h after transfection, fewer mitochondria can be observed in whole cells and engulfment events of mitochondria by autophagosomes can be found (Figure 3b, 48 h + magnification panels). In contrast, after transfection of a vector encoding AMBRA1^{WT}, no changes in the mitochondrial distribution are observed (Supplementary Figure 5). To ascertain that mitophagy was induced by AMBRA1–ActA, we evaluated, by electronic microscopy, the mitochondria number 48 h after transfection of AMBRA1^{WT} or AMBRA1–ActA. As shown in the graph (Figure 3b), a third of mitochondria disappeared upon transfection of AMBRA1–ActA *versus* AMBRA1^{WT}. To confirm these data, we checked for mitochondrial proteins at different time points after AMBRA1–ActA overexpression. As shown in the graph in Figure 3c, at 48 h after AMBRA1–ActA overexpression, a third of mitochondria have disappeared, whereas almost all mitochondria have been degraded at 72 h after transfection. We can thus conclude that massive mitophagy is induced by AMBRA1–ActA.

To determine the role of PI3K on mitophagy induced by AMBRA1–ActA overexpression, HEK293 cells co-transfected with AMBRA1–ActA and mito-RFP were treated with 10 mM 3-MA (3-methyladenine) or 75 nM Wortmannin (two inhibitors

of PI3K^{22,23}). Aggregation of the mitochondrial network was reduced by treating the cells with 3-MA or Wortmannin (Figure 3d and Supplementary Figure 6a). Thus, AMBRA1–ActA-induced mitophagic sequestration seems to depend, at least in part, on the classical upstream PI3K pathway. We also examined the on/off rate of autophagy upon AMBRA1–ActA overexpression in the presence of a lysosomal-inhibiting agent, chloroquine. This treatment resulted in a significantly higher level of mito-aggresomes accumulation in AMBRA1–ActA-positive cells, hence indicating that autophagosomes induced by AMBRA1–ActA overexpression are normally degraded in the lysosome (Figure 3d). In addition, LAMP1/LC3 colocalization is present in AMBRA1–ActA-overexpressing cells, indicating a canonical lysosomal destination for the observed mito-aggresomes (Supplementary Figure 6b). We next confirmed the involvement of the PI3K pathway in AMBRA1–ActA-induced mitophagy by a more biochemical approach, that is, by analysing the expression of MnSOD and TOM20 following AMBRA1–ActA transfection in cells treated or not with 3-MA and Chloroquine. As shown in Figure 3e, both 3-MA and chloroquine treatments block MnSOD and TOM20 decrease following AMBRA1–ActA overexpression. Moreover, downregulation of *BECLIN 1*, an activator of the PI3K complex, is able to delay AMBRA1–ActA-induced mitophagy (Supplementary Figures 6c and d). It is noteworthy that AMBRA1–ActA overexpression is also sufficient to induce a massive mitochondrial clearance in the ETNA proneural cell line (Supplementary Figure 7).

Taken together, these observations demonstrate that AMBRA1–ActA transfection *per se* triggers a fully functional and massive mitophagy in different cell types.

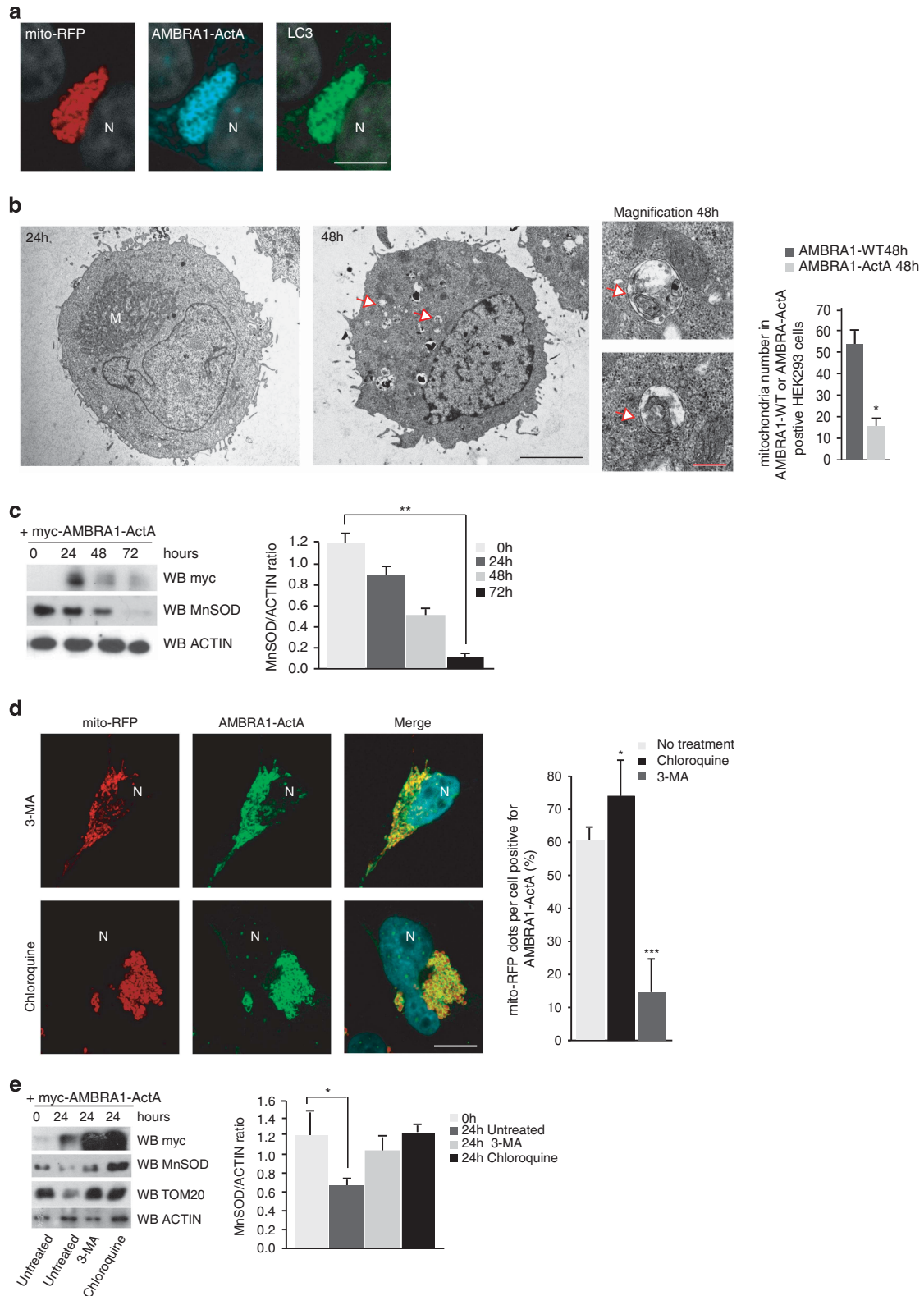
AMBRA1–ActA induces mitophagy independently of PARKIN and p62 recruitment. To identify the specific mitophagy pathway induced by AMBRA1–ActA, we decided to test whether our construct was able to induce mitophagy in a PARKIN-free system. We used HeLa cells as a cell line containing no PARKIN (Figure 4a), where AMBRA1–ActA induces mito-aggresomes (Figure 4b). Then we measured mitochondria degradation following AMBRA1–ActA overexpression. As shown in Figure 4c, at 48 h after transfection, 50% of mito-aggresomes disappear, when compared with the 24 h time point. At 72 h after transfection, it is also difficult to find cells with mito-aggresomes, and mitochondrial degradation is almost completed. This finding was also confirmed by western blot analysis, as revealed by the decrease of MnSOD and Tom20, two mitochondrial markers, following AMBRA1–ActA overexpression. Quantification of the MnSOD/ACTIN *ratio* indicates that 72 h after AMBRA1–ActA overexpression, almost all mitochondria are lost (Figure 4d). These results strongly suggest that AMBRA1–ActA is also able to induce mitophagy in a PARKIN-deficient cell line.

To confirm these results, we analysed HEK293 cells in which PARKIN-mediated autophagy normally takes place and where PARKIN recruitment to mitochondria also occurs upon AMBRA1–ActA transfection (Supplementary Figure 8). We downregulated PARKIN (ShPARKIN, see Figure 4e) and, in the same cells, we again coexpressed AMBRA1–ActA and mito-RFP. As shown in Figure 4e, AMBRA1–ActA staining

surrounds mitochondria in cells overexpressing either ShPARKIN or control ShRNA. Our measurement of mitochondria degradation at 24, 48 and 72 h post transfection was also consistent (see graph in Figure 4e). These data were also

confirmed by western blot analysis, by analysing the expression of MnSOD and TOM20 (Figure 4f).

Next, we decided to look at the formation of mito-aggregates following AMBRA1-ActA overexpression in



HeLa cells. Surprisingly, as shown in Figure 4e, we found that even though mitochondria are positive for ubiquitin (Supplementary Figure 9), p62 staining is almost negligible (at variance with what was observed in HEK293 cells, see Figure 4b). In more detail, cells overexpressing AMBRA1-ActA showed a colocalization of $\cong 80\%$ with ubiquitin; $\cong 15\%$ with p62 and $\cong 87\%$ with LC3 (Supplementary Figure 9).

Altogether, these data strongly suggest that high levels of AMBRA1 at the mitochondria can also drive this process in a PARKIN- or p62-independent manner.

AMBRA1-ActA surrounds depolarized mitochondria. A large body of evidence indicate that mitochondria depolarization is a 'call-out' signal to start mitophagy.²⁴ Therefore, we set out to establish whether or not AMBRA1-ActA overexpression was localized around depolarized mitochondria. We used Tetramethylrhodamine, methyl ester (TMRM).²⁵ As shown in Supplementary Figure 10A, AMBRA1-ActA is, indeed, localized around *depolarized* mitochondria, with AMBRA1-ActA-overexpressing cells showing an $\cong 60\%$ reduction in their mitochondrial potential (see graph), similar to the effect obtained by FCCP treatment ($\cong 80\%$). Overexpression of a vector coding for GFP-mito alone does not affect mitochondrial potential (Supplementary Figure 10B).

These data suggest that AMBRA1-ActA-mediated clearance of mitochondria is summoned into action by depolarized organelles.

The LIR motif of AMBRA1 is required for AMBRA1-ActA-induced mitophagy. Given our initial results regarding the importance of AMBRA1 LIR domain in mitophagy (see Figures 1c and d), we decided to check the occurrence of AMBRA1-ActA/LC3 interaction through this domain. We thus performed an immunoprecipitation between AMBRA1-ActA and LC3 on mitochondrial fractions. We found that, in the absence of any known mitophagy inducers, AMBRA1-ActA interacts with LC3, whereas no interaction can be found between AMBRA1^{WT} and LC3 (Figure 5a).

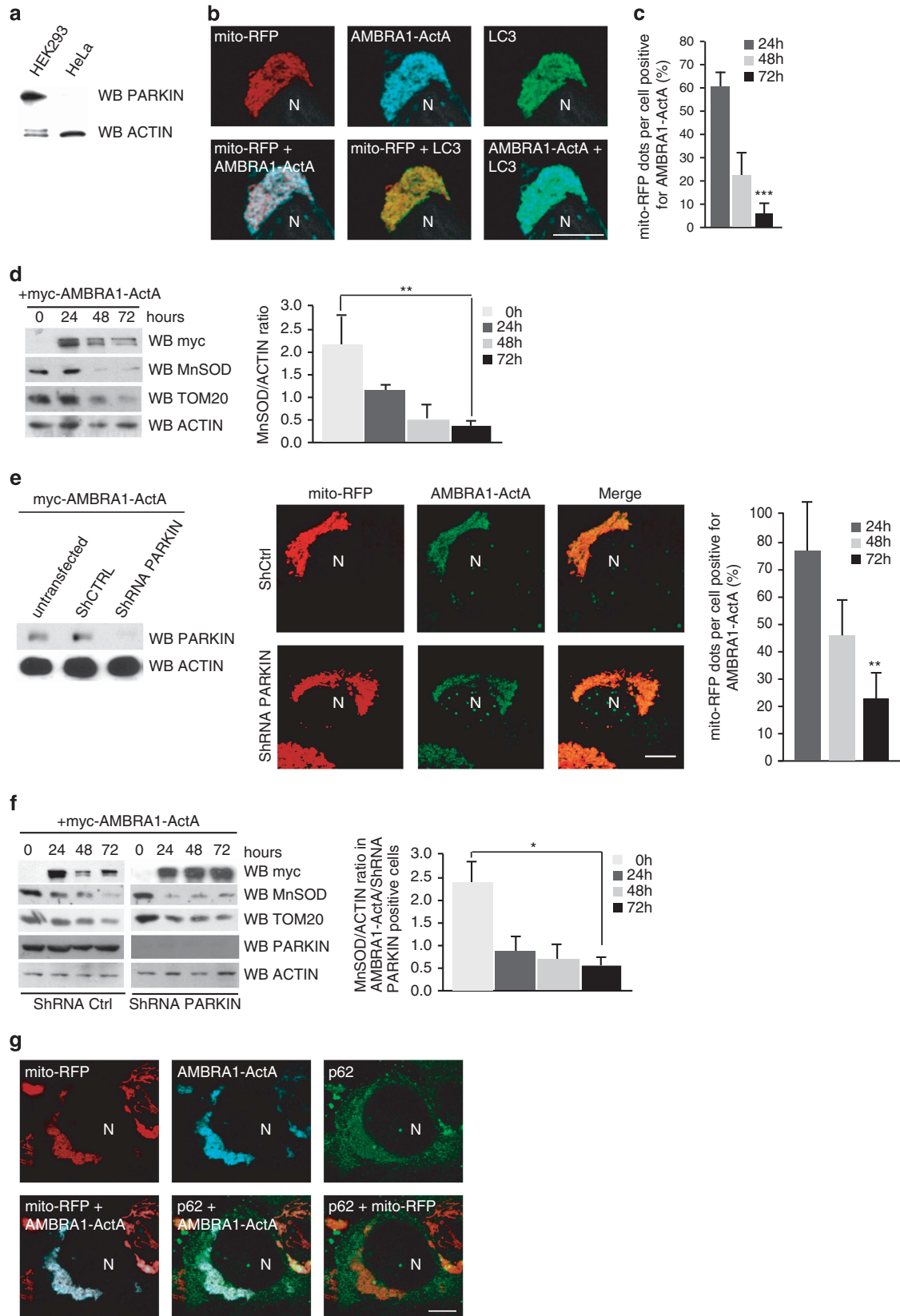
Point mutations of both the aromatic residue and the conserved hydrophobic residue of the LIR motif (AMBRA1^{LIR-AA}-ActA (W1019A-L1022A SGVEYYAxxA)) suppress the interaction between AMBRA1-ActA and endogenous LC3 (Figure 5b). In addition, we observed that AMBRA1^{LIR-AA}-ActA was able to colocalize with the mitochondrial network, but not, in contrast to AMBRA1-ActA, with mito-aggregates (Figure 5c).

Next, by measuring mitochondria degradation by western blot analysis, we found that the mitochondrial markers MnSOD and TOM20 were more stable after transfection of AMBRA1^{LIR-AA}-ActA when compared with cells overexpressing AMBRA1-ActA (Figure 5d).

Our data indicate that the LIR^{AA} mutation on AMBRA1-ActA delays mitochondrial clearance. We can thus conclude that AMBRA1-ActA-driven PARKIN-independent mitophagy also absolutely requires LC3 binding via the AMBRA1 LIR domain.

AMBRA1 mediates PINK1-PARKIN-independent mitophagy in different cell systems. Finally, to extend our analysis to the PINK1-PARKIN regulatory axis and to get an *in vivo* corroboration of our results, we decided to investigate whether AMBRA1^{WT} was able to induce mitochondrial clearance in several systems in which the PINK1-PARKIN pathway was deficient or absent. To this aim, we reconstituted *Parkin-Ambra1* double-deficient MEFs (*Ambra1^{gt/gt}*) with AMBRA1^{WT} or AMBRA1^{LIR-AA} and treated these cells with 30 μ M FCCP for 9 h, in order to induce mitophagy. As shown in Figure 6a, AMBRA1^{WT} is able to induce mitochondrial clearance, at variance with AMBRA1^{LIR-AA}, that is not able to promote mitophagy. We next decided to use mouse embryonic fibroblasts (MEFs) from *PINK1*^{-/-} mice in order to ascertain that the PINK1-PARKIN pathway was abolished. We overexpressed AMBRA1^{WT} or AMBRA1^{LIR-AA} and we treated cells with FCCP for 9 h (30 μ M). Again, as shown in Figure 6b, overexpression of AMBRA1^{WT} induces mitochondrial clearance, whereas overexpression of AMBRA1^{LIR-AA} did not increase mitochondrial clearance to

Figure 3 AMBRA1-ActA induces mitophagy in HEK293 cells. (a) HEK293 cells were co-transfected with vectors encoding myc-AMBRA1-ActA and mito-RFP (red). At 24 h after transfection, cells were fixed and stained with anti-myc (blue) and anti-LC3 (green) antibodies. Merge of the two fluorescence signals is shown in the right panel. Scale bar, 5 μ m. (b) An ultrastructural analysis by EM on whole cells. HEK293 cells were co-transfected with vectors encoding myc-AMBRA1-ActA and GFP mitochondria. At 24 or 48 h after transfection, GFP-positive cells were sorted by using FACS and fixed in glutaraldehyde. Morphological analysis was performed. In the left panel, mitochondria are already redistributed around the nucleus (24 h following transfection). M, mitochondria. The center panel (48 h following transfection) shows a whole cell containing less mitochondria than at 24 h. Arrows indicate fragmented mitochondria into autophagosomes. Scale bar, 5 μ m. The upper and lower panels on the right are two magnifications of the autophagosomes observed in the whole cell (see arrows in the middle panel, 48 h). Scale bar, 500 nm. The graph shows quantification of mitochondria number per cells positive for AMBRA1^{WT} and AMBRA1-ActA at 48 h post transfection. Each point value represents the mean \pm S.D. from three independent experiments. Statistical analysis was performed using Student's test ($*P < 0.05$) (c) HEK293 cells were transfected with a vector encoding myc-AMBRA1-ActA. At 24, 48 and 72 h after transfection, proteins extracts were analysed by western blot using the following antibodies: anti-MnSOD, anti-myc (to control AMBRA1-ActA expression) and anti-ACTIN (loading control). The graph represents the MnSOD/ACTIN ratio (\pm S.D.). Each point value represents the mean \pm S.D. from three independent experiments. Statistical analysis was performed using Student's test ($*P < 0.01$; 24 h versus 72 h). (d) 3-MA treatment partially inhibits AMBRA1-ActA/mito-DsRed vacuole formation. HEK293 cells were co-transfected with vectors encoding AMBRA1-ActA and mito-RFP and treated directly with 10 mM 3-MA. After 24 h, cells were fixed and stained with an anti-myc antibody (green). Nuclei were stained with 1 μ g/ μ l DAPI for 20 min. Merge of the three fluorescence signals is shown in the right panel. Scale bar, 6 μ m. Chloroquine treatment increases the percentage of AMBRA1-ActA/mito-RFP colocalizations on mito-aggregates per cell. HEK293 cells were co-transfected with a vector encoding AMBRA1-ActA and a vector encoding mito-RFP. After 24 h, cells were treated with chloroquine for 1 h, and cells were fixed and stained with an anti-myc antibody (green). Nuclei were stained with 1 μ g/ μ l DAPI for 20 min. Merge of the three fluorescence signals is shown in the right panel. Scale bar, 6 μ m. The graph shows the quantification of AMBRA1-ActA/mito-RFP colocalization on mito-aggregates per cell (\pm S.D.). Each point value represents the mean \pm S.D. from three independent experiments. Statistical analysis was performed using Student's test ($*P < 0.05$, no treatment versus Chloroquine; and $*P < 0.001$, no treatment versus 3-MA). N, nucleus. (e) HEK293 cells were co-transfected with vectors encoding AMBRA1-ActA and mito-RFP and treated directly with 10 mM 3-MA. After 24 h, proteins extracts treated with Chloroquine (1 h) or left untreated were analysed by western blot using the following antibodies: anti-MnSOD, anti-TOM20, anti-myc (to control AMBRA1-ActA expression) and anti-ACTIN (loading control). The graph represents the MnSOD/ACTIN ratio (\pm S.D.). Each point value represents the mean \pm S.D. from three independent experiments. Statistical analysis was performed using Student's test ($*P < 0.05$)



the same extent. To complete our analysis, we next used primary human cells from a PD patient with PINK1 loss of function (fibroblasts from Biobank of Genova, Italy). We introduced lentivirus expressing AMBRA1^{WT} or AMBRA1^{LIR-AA} in those cells and then treated them with FCCP for 5 h (40 μ M). As shown in Figure 6c, overexpression of AMBRA1^{WT} induces mitochondrial clearance. At variance, overexpression of AMBRA1^{LIR-AA} did not increase mitochondrial clearance to the same extent as AMBRA1^{WT}.

These results indicate that AMBRA1 expression can partially rescue mitochondrial clearance in different *ex vivo* models, including cells from a PD patient. In sum, AMBRA1 can induce mitophagy through its LIR domain, synergically with FCCP and in the absence of the PINK1–PARKIN pathway activity.

Discussion

AMBRA1 binds LC3 following mitophagy induction. We show that AMBRA1 uses a LIR motif to interact with LC3 following mitophagy induction. This interaction takes place both upon enhanced levels of AMBRA1 at the mitochondria and after FCCP treatment joint to PARKIN endogenous expression or overexpression. Our results thus suggest that LC3–AMBRA1 interaction is functional to an efficient mitochondrial clearance, rather than to the capture of AMBRA1 within the autophagosome in a sort of negative feedback control of autophagy. However, we cannot exclude that AMBRA1 is degraded by the autophagosomes in other conditions. Indeed, several ATG proteins are located on the outer surface of the phagophores, and some are also located within the autophagosomes.^{26–28} The interaction with LC3 may imply that a binding of AMBRA1 with other ATG proteins on LC3-positive structures could be required for correct autophagosome maturation.

AMBRA1–ActA induces depolarization and ubiquitylation of mitochondria. By another set of experiments, we demonstrate that all mitochondria found to be positive for AMBRA1–ActA are depolarized. An open question is how high levels of mitochondrial AMBRA1 would induce mitochondrial depolarization. We previously demonstrated that

AMBRA1 could bind mito-Bcl-2.³ Considering all our findings, we can now postulate that high levels of AMBRA1 at the mitochondria, by mimicking BH3-only proteins, could sequester the majority of mito-Bcl-2, thus inducing Bax/Bak activation and mitochondrial membrane depolarization. As for the fate of depolarized mitochondria, it is important to bear in mind that ubiquitin is a signal for selective autophagy in mammalian cells. In fact, in the PARKIN-induced mitophagy pathway, PARKIN, an E3-ubiquitin ligase, translocates from the cytosol to mitochondria in cells treated with CCCP.^{5,7} After translocation to the depolarized mitochondria, PARKIN catalyzes polyubiquitylation of several substrates, calling into play the autophagy receptor p62/SQSTM1 that simultaneously binds ubiquitin and autophagy-specific ubiquitin-like modifiers (LC3/GABARAP proteins).^{9,20} Here we found that all mitochondria are ubiquitylated after AMBRA1–ActA overexpression. As we also found mitochondrial ubiquitin in PARKIN-deficient cells, AMBRA1–ActA could serve, most likely, as an adaptor for other E3 ligases. Noteworthy, we have recently demonstrated that AMBRA1 can bind the E3 ubiquitin ligase TRAF6.²⁹ It will be interesting to investigate whether the binding between AMBRA1 and TRAF6 is an important event for mitochondria ubiquitylation. However, other candidates can help AMBRA1 to ubiquitylate mitochondria. In fact, AMBRA1 has also been found to be associated in a complex with the CUL4–DDB1 complex.^{30,31}

AMBRA1 mediates PINK1–PARKIN-independent mitophagy.

Another issue is the mechanism by which *endogenous* AMBRA1 participates in mitochondrial clearance. We confirm that AMBRA1 potentiates PARKIN-mediated mitophagy, in line with previous work.¹⁶ We show that AMBRA1–ActA promotes PARKIN translocation to depolarized mitochondria in HEK293 cells, where PARKIN is present. However, in PARKIN-deficient cells, AMBRA1–ActA alone can induce mitochondrial clearance, indicating that a parallel pathway for mitophagy may exist when PARKIN is not present. Of the highest importance, wild-type AMBRA1, in combination with FCCP treatment, can also induce mitochondrial clearance in a PARKIN-independent manner, as in *Pink1*- or *Parkin*-deficient mouse fibroblasts or in human fibroblasts in which a mutant inactive form of PARKIN is present.

Figure 4 AMBRA1–ActA induces mitophagy in PARKIN-deficient cell lines. (a) HeLa and HEK293 cells were grown in normal media. After extraction of proteins, we performed a western blot analysis by using antibodies against PARKIN and against ACTIN (as a loading control). (b) Colocalization between AMBRA1–ActA, mito-RFP and LC3 protein. HeLa cells were co-transfected with vectors encoding AMBRA1–ActA and mito-RFP, and grown in normal media. Cells were then stained using antibodies anti-myc (AMBRA1, blue) and anti-LC3 (green). Nuclei were stained with 1 μ g/ μ l DAPI for 20 min. Merge of the different fluorescence signals is illustrated. Scale bar, 8 μ m. (c) Quantification in HeLa cells of AMBRA1–ActA/mito-RFP mito-colocalizations at 24, 48 and 72 h after transfection per cell (\pm S.D.). Each time point value is the mean \pm S.D. from three independent experiments. Statistical analysis was performed using Student's test (** $P < 0.001$; 24 h versus 72 h). (d) HeLa cells were transfected with a vector encoding myc-AMBRA1–ActA. At 24, 48 and 72 h after transfection, proteins extracts were analysed by western blot using the following antibodies: anti-MnSOD, anti-TOM20, anti-myc (to control AMBRA1–ActA expression) and anti-ACTIN (loading control). The graph represents the MnSOD/ACTIN ratio (\pm S.D.). Each point value represents the mean \pm S.D. from three independent experiments. Statistical analysis was performed using Student's test (** $P < 0.01$; 24 h versus 72 h). (e) HEK293 cells were co-transfected with vectors encoding ShPARKIN or control ShRNA and myc-AMBRA1–ActA. At 24 h after transfection, expression of PARKIN was controlled by western blot analysis by means of anti-PARKIN and anti-ACTIN (loading control) antibodies. Cells were fixed and stained with an anti-myc antibody (green). The merge of the fluorescence signals is shown in the right panels. Scale bar, 4 μ m. The graph illustrates the quantification of AMBRA1–ActA/mito-RFP colocalizations on mito-aggregates per cell (\pm S.D.). Each point value represents the mean \pm S.D. from two independent experiments. Statistical analysis was performed using Student's test (* $P < 0.01$; 24 h versus 72 h). (f) HEK293 cells were co-transfected with vectors encoding ShPARKIN or control ShRNA, and myc-AMBRA1–ActA. At 24 h after transfection, expression of PARKIN was checked by western blot analysis by means of anti-PARKIN and anti-ACTIN (loading control) antibodies. At 24, 48 and 72 h after transfection, protein extracts were analysed by western blot using the following antibodies: anti-MnSOD, anti-TOM20, anti-myc (to control AMBRA1–ActA expression) and anti-ACTIN (loading control). The graph represents the MnSOD/ACTIN ratio (\pm S.D.). Each point value represents the mean \pm S.D. from three independent experiments. Statistical analysis was performed using Student's test (* $P < 0.05$; 24 h versus 72 h). (g) HeLa cells were co-transfected with vectors encoding myc-AMBRA1–ActA and mito-RFP (red). At 24 h after transfection, cells were fixed and stained with anti-myc (AMBRA1, blue) and anti-p62 antibodies (green). Merge of the fluorescence signals are shown. N, nucleus. Scale bar, 4 μ m

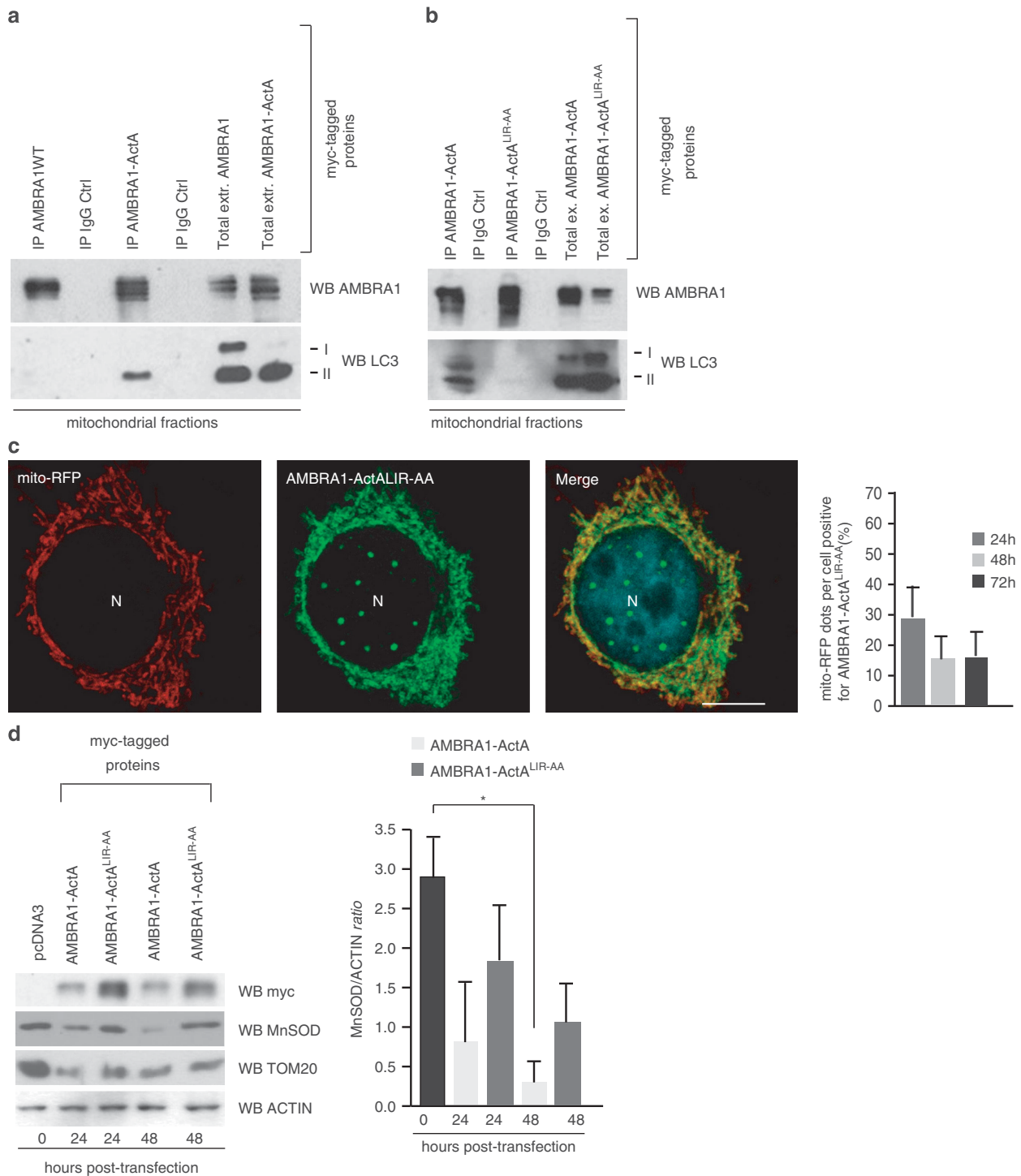


Figure 5 AMBRA1-ActA interacts with LC3, with this interaction being crucial for AMBRA1-ActA-induced mitophagy. **(a)** HEK293 cells were transfected with a vector encoding myc-AMBRA1-ActA. At 24 h after transfection, mitochondrial extracts were immunoprecipitated using an anti-myc antibody. Purified complexes and corresponding total extracts were analysed by western blot (WB), using anti-AMBRA1 and anti-LC3 antibodies. **(b)** HEK293 cells were transfected with a vector encoding myc-AMBRA1-ActA or myc-AMBRA1-ActA-LIR^{AA}. At 24 h after transfection, mitochondrial extracts were immunoprecipitated using an anti-myc antibody. Purified complexes and corresponding total extracts were analysed by WB using anti-AMBRA1 and anti-LC3 antibodies. **(c)** HEK293 cells were transfected with a vector encoding myc-AMBRA1-ActA-LIR^{AA} and mito-RFP. At 24 h after transfection, cells were fixed and stained with an anti-myc antibody (green). Merge of the fluorescence signals is shown in the right panels. Scale bar, 8 μ m. The graph reports the quantification of mitochondrial clearance in HEK293 cells overexpressing AMBRA1-ActA^{LIR-AA}/mito-RFP at 24, 48 and 72 h after transfection per cell (\pm S.D.). Each time point value is the mean \pm S.D. from three independent experiments. **(d)** HEK293 cells were transfected with a vector encoding myc-AMBRA1-ActA-LIR^{AA}. At 0, 24 and 48 h after transfection, protein extracts were analysed using anti-MnSOD, anti-myc (AMBRA1) and anti-ACTIN (loading control) antibodies. The graph represents the MnSOD/ACTIN ratio (\pm S.D.). Each point value represents the mean \pm S.D. from three independent experiments. Statistical analysis was performed by Student's test ($*P < 0.05$; 0 h versus 48 h)

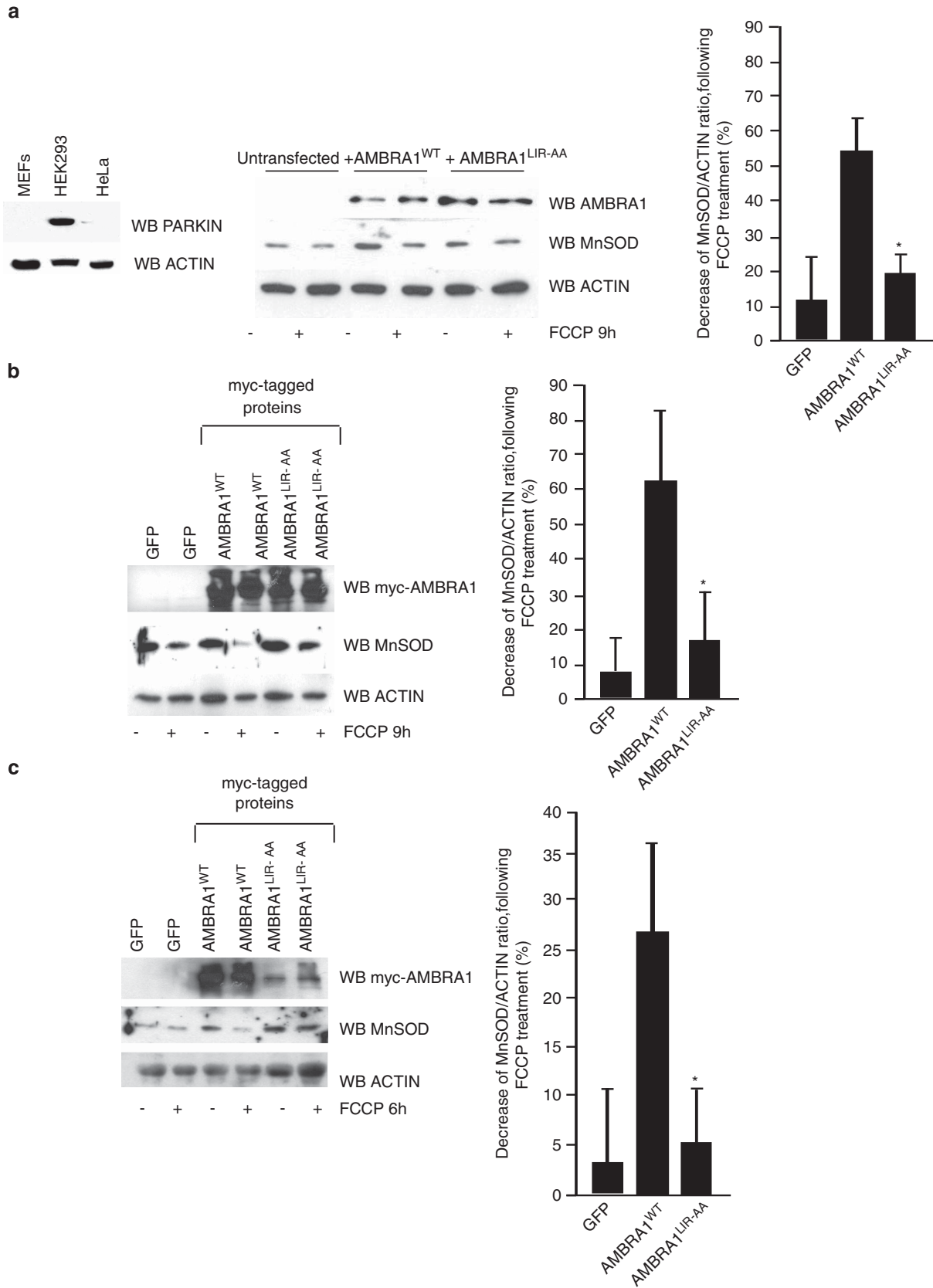


Figure 6 For caption see next page

In sum, it is certainly possible that different mitophagy pathways coexist, depending on the inducing conditions or the cell type. Moreover, we found a new mechanism accounting for the effect of AMBRA1 on PARKIN-mediated mitophagy. In fact, AMBRA1 binding to LC3 increases mitochondrial clearance. In the absence of PARKIN, we also found a binding between AMBRA1 and LC3 after AMBRA1-ActA overexpression. Therefore, in the absence of PARKIN, AMBRA1 could be proposed as a selective mitophagy receptor, similar to the factor Atg32 in yeast.^{32,33}

Interestingly, it has recently been demonstrated that BECLIN 1 interacts with PARKIN and regulates PARKIN translocation to mitochondria.³⁴ As we show that down-regulation of BECLIN 1 reduces AMBRA1-ActA-induced mitophagy, it would be interesting to investigate the role of BECLIN 1 in AMBRA1-ActA-induced mitophagy. We can hypothesize that BECLIN 1 is functional to bring a putative E3 Ubiquitin ligase (alternative to PARKIN) in order to ubiquitylate mitochondria in AMBRA1-ActA-induced mitophagy.

AMBRA1-ActA is a powerful inducer of mitophagy.

Hitherto, in mammalian cells, overexpression of PARKIN in combination with CCCP treatment is the only known method to induce mitophagy. We have now been able to prove that targeting AMBRA1 to mitochondria is sufficient to induce massive mitochondrial clearance. The next step will be to check whether AMBRA1-ActA induces mitophagy *in vivo*, this being of the highest importance in biomedicine. Furthermore, given the fact that AMBRA1 has a LIR motif used for its binding to LC3 during mitophagy, it would be interesting to investigate whether AMBRA1 could be mutated in this domain in neurodegenerative conditions, such as in PD. Similar mutations may also be associated with the risk of developing PD. At the same time, it could also be important to check AMBRA1 levels in other human disorders in which mitophagy is deregulated, such as muscular dystrophies.³⁵

Materials and Methods

Antibodies. The antibodies used were as follows: polyclonal anti-PARKIN (Santa Cruz Biotechnology, Santa Cruz, CA, USA, H-300- sc-30130, Abcam, Cambridge, UK, 15954), mouse monoclonal anti-ACTIN (Sigma-Aldrich, St. Louis, MO, USA), monoclonal anti-BCL-2 (Santa Cruz Biotechnology, sc-7382), polyclonal anti-MnSOD (Assay Designs, Danvers, MA, USA), polyclonal anti-AMBRA1 (Novus Biologicals, Littleton, CO, USA, 26190002), polyclonal anti-LC3 (Cell Signaling, Danvers, MA, USA), monoclonal anti-GAPDH and rabbit polyclonal anti-LAMP1 (Abcam 24170).

Cells. The human embryonic kidney HEK293 cells and HeLa cells were cultured in Dulbecco's modified Eagle's medium (DMEM, Sigma-Aldrich) supplemented with 10% FCS, 2 mM L-glutamine, and 1% penicillin/streptomycin solution at 37 °C under 5% CO₂. MEFs cells were cultured in DMEM supplemented with 10% fetal bovine serum (FBS, Sigma-Aldrich), 2 mM L-glutamine and 1% penicillin/streptomycin solution at 37 °C. Cells were incubated in the presence of 30 μM

FCCP (Sigma-Aldrich) for 9 h. Human fibroblasts (code: FFF0592011, Biobank Genova, Laboratorio di diagnosi Prenatale, Ist. Gaslini, Genova, Italy, kind gift of Dr. Filocamo) were obtained from a man bearing a mutation in the *PINK1* gene, who developed PD when he was 40 years old (early-onset form of the disease). Human fibroblasts were then cultured in RPMI-140 medium supplemented with 10% FBS (Sigma-Aldrich), 2 mM L-glutamine and 1% penicillin/streptomycin solution at 37 °C. *Pink1*^{-/-} mice were jointly provided by Professor Jie Shen (Harvard Medical School, Boston MA, USA) and Professor Antonio Pisani (IRCCS, Fondazione Santa Lucia, Roma, Italy). MEFs derived from *Pink1*^{-/-} embryos at day 13.5 p.c. were grown in DMEM supplemented with 10% FBS (Sigma-Aldrich), 2 mM L-glutamine and 1% penicillin/streptomycin solution at 37 °C.

Cloning and plasmids. To create AMBRA1-ActA fusion gene, we first amplified by PCR, with *PfuTurbo* DNA polymerase, the oligonucleotides corresponding to aa 613–639 of *Listeria ActA*, using a vector encoding Bcl-2-ActA (a kind gift of Dr. Beth Levine, Dallas, TX, USA). The AMBRA1 coding region has also been generated by PCR with *PfuTurbo* DNA Polymerase, using wild-type myc-AMBRA1. Next, we digested these two PCR products with two restriction enzymes *Apal* and *HindIII*, respectively, and then they were cloned into pCDNA3 vector (Invitrogen, Carlsbad, CA, USA). Construct coding for AMBRA1^{WT} was cloned in pLPCX vector (Clontech Laboratories, Mountain View, CA, USA).

Point mutations were generated using the QuickChange site-directed mutagenesis kit (Stratagene, La Jolla, CA, USA) and all plasmid constructs made in this study were verified by DNA sequencing (Eurofins, Rome, Italy). The oligonucleotides used for mutagenesis, PCR and DNA sequencing were purchased from Invitrogen.

ShRNA PARKIN. ShRNA PARKIN (PGIP2 449497) or shRNA Control (PGIP2) were transfected in HEK293 cells using Turbofect Transfection reagent (Fermentas, Thermo Fisher Scientific, Waltham, MA, USA, R0531), according to the manufacturer's instructions. At 24 or 48 h after transfection, PARKIN expression was controlled by western blot analysis.

Lentiviral production and infection. AMBRA1 cDNAs, wild-type and mutant, were subcloned from pLPCX, by cutting with *NheI* and *NotI* (blunted) restriction enzymes and transferred into the pRRL lentiviral plasmid digested with *XbaI* and *SaI* (blunted). For AMBRA1 ectopic expression in MEFs, lentiviral particles were produced by transfecting HEK293T cells with the lentiviral vector pRRLsinPPT.CMV.WPRE (Follenzi *et al.*³⁶) encoding AMBRA1^{WT} or AMBRA1-mutant (AMBRA1^{LIR-AA}), together with the pMDLg/pRRE, pMD2.G and pRSV-Rev plasmids. Supernatants were collected 48 h post transfection. The lentiviral suspension was supplemented with polybrene (4 μg/ml, Sigma-Aldrich), filtered (PES 0.45 μm filters, Corning, Santa Clara, CA, USA) to remove cell debris and incubated with target cells for 8–12 h. To increase the transduction efficiency, the infection was repeated twice. Infected cells were then analysed starting from 48 h after infection.

Reagents. 3-Methyladenine, Chloroquine and wortmannin were purchased from Sigma Chemical Co. (St. Louis, MO, USA). TMRM (cat. no. T668) was obtained from Invitrogen/Molecular Probes (Carlsbad, CA, USA). FCCP was from Sigma.

Western blot analysis. Cell extracts were centrifuged at 13000 g for 10 min at 4 °C. Protein concentrations were determined with the Bio-Rad Protein Assay (Bio-rad Laboratories, Hercules, CA, USA). Cell extracts or immunoprecipitates were separated by SDS-PAGE and transferred onto nylon membranes (Immobilon P, Millipore, Bedford, MA, USA). Membranes were incubated with primary antibodies followed by horseradish peroxidase-conjugate secondary antibody (Jackson Laboratories, Ann Arbor, MI, USA) and visualized with ECL plus (Amersham Bioscience, Little Chalfont, UK).

Figure 6 Wild-type AMBRA1, in combination with FCCP, induces mitophagy independently of the PINK1-PARKIN pathway. (a) Mouse embryonic fibroblasts (MEFs) homozygous (*Ambra1*^{gt/gt}) for the gene-trap mutation in the *Ambra1* locus were transduced with the AMBRA1^{WT} or AMBRA1^{LIR-AA} lentiviral vectors. MEFs were next treated with FCCP (30 μM) for 9 h in order to induce mitophagy. Protein extracts were analysed by western blotting using anti-AMBRA1, anti MnSOD and anti-ACTIN antibodies. The graph shows the MnSOD/ACTIN ratio decrease (± S.D.). Each point value represents the mean ± S.D. from three independent experiments. Statistical analysis was performed using Student's test (**P* < 0.05, versus AMBRA1). (b) *Pink1*^{-/-} MEFs were transduced with the GFP, AMBRA1^{WT} or AMBRA1^{LIR-AA} lentiviral vectors. MEFs were next treated with FCCP (30 μM) for 9 h in order to induce mitophagy. Protein extracts were analysed by western blotting as in (a). (c) Primary skin fibroblasts from a patient affected by an early-onset form of PD (mutation in *Pink1* gene) were transduced with the GFP, AMBRA1^{WT} or AMBRA1^{LIR-AA} lentiviral vectors. MEFs were next treated with FCCP (40 μM) for 6 h in order to induce mitophagy. Protein extracts were analysed by western blotting as in (a)

Immunocytochemistry. Cells were washed in PBS and fixed with 4% paraformaldehyde in PBS for 15 min. After permeabilization with 0.4% Triton X-100 in PBS for 5 min, cells were blocked in 3% normal goat serum in PBS and incubated overnight at 4 °C with primary antibodies. We used the antibodies directed against AMBRA1, PARKIN and LC3. Cells were then washed in blocking buffer and incubated for 1 h with labelled anti-mouse (Alexa Fluor 488 or Alexa Fluor 555, Molecular Probes, Eugene, OR, USA) or anti-rabbit (FITC or Cy3, Jackson ImmunoResearch, West Grove, PA, USA) secondary antibodies. Nuclei were stained with 1 µg/ml DAPI and examined under a Zeiss LSM 700 100 × oil-immersion objective (Zeiss, Oberkochen, Germany). We used 'ZEN 2009 Light edition' software for image analysis. All measurements in this work were performed by a blind approach. All colocalization analyses were performed in nonsaturated single z-confocal planes.

Mitochondria purification. Mitochondria were isolated from HEK293 cells by standard differential centrifugation, and suspended in isolation buffer (IB; 0.2 M sucrose, 10 mM Tris-MOPS (pH 7.4), 0.1 mM EGTA-Tris and 0.1% delipidated BSA).

Immunoprecipitation. Cells were lysed in RIPA buffer (plus protease inhibitors). Equal amounts of protein (500 µg) were incubated with 2 µl of monoclonal anti-Myc antibody conjugated with protein A agarose beads (Clontech and Sigma, respectively) for 4 h followed by 60 min incubation with 30 µl of protein A Sepharose beads (Roche, Boulogne-Billancourt, France). The beads were collected by centrifugation and washed four times with the RIPA buffer. Proteins bound to the beads were eluted with 30 µl of SDS-polyacrylamide gel electrophoresis sample buffer and heated to 95 °C for 10 min.

Electron microscopy. For conventional EM, HeLa cells previously transfected with AMBRA1–ActA and mito-GFP were sorted 24 or 48 h after transfection and fixed with 2.5% glutaraldehyde buffered with 0.1 M sodium phosphate, pH 7.4. Samples were postfixed with osmium tetroxide, then stained with uranyl acetate, dehydrated in ethanol and embedded in Epon resin (Fluka, Sigma-Aldrich). After sectioning, samples were collected on uncoated nickel grids and observed and photographed in a Technai 20 (FEI Company, Eindhoven, The Netherlands) EM.

Embryos lysis heads. Heads of embryos from stage E13.5 were subjected to mechanical lysis in 50 mM Tris HCl pH 7.5, 320 mM Sucrose, 50 mM NaCl, 1% Triton X-100 and protease inhibitors. Protein extracts were analysed by western blot analysis.

Ultrastructural analysis of brain from wild-type and *Ambra1^{g0/gt}* embryos. The embryos (E13.5) were extracted from the deciduas and fixed by immersion in 2.5% glutaraldehyde in 0.1 M cacodylate buffer, pH 7.4, for 45 min at 4 °C, rinsed in buffer, postfixed in 1% OsO₄ in 0.1 M cacodylate buffer, pH 7.4, dehydrated and embedded in Epon resin. Grids were thoroughly rinsed in distilled water, stained with aqueous 2% uranyl acetate for 20 min and photographed in a Zeiss EM 900 EM.

Conflict of Interest

The authors declare no conflict of interest.

Acknowledgements. We thank Mrs M Acuña Villa and Dr M Bennett for secretarial and proofreading work and A Di Rita for research assistance. We are indebted to Professor B Levine (Dallas, TX, USA) for kindly providing us with the Bcl-2-ActA construct. We acknowledge Professor J Shen (Boston, MA, USA) who provided Pink1/mice and Dr. P Bonsi from Professor A. Pisani's lab (Rome, Italy) for her help in breeding these mice. The cell line from patients affected by Parkinson's disease were obtained from the 'Cell Line and DNA Biobank from Patients affected by Genetic Diseases' (Istituto G. Gaslini) and the 'Parkinson Institute Biobank' (Milan, <http://www.parkinsonbiobank.com/>), members of the Telethon Network of Genetic Biobanks (<http://www.biobanknetwork.org>, project no. GTB12001), funded by Telethon Italy. This work was supported in part by grants from the Telethon Foundation (GGP10225), AIRC (IG2010 to FC and MyFAG 2009 to SC), FISM (2009), the Italian Ministry of University and Research (PRIN 2009 and FIRB Accordi di Programma 2011), the Italian Ministry of Health (Ricerca Finalizzata and

Ricerca Corrente to FC, Ricerca Finalizzata–Progetto Giovani Ricercatori to SC) and Ricerca Finalizzata RF-OGR-2008-120-3614 to MP.

- Cecconi F, Levine B. The role of autophagy in mammalian development: cell makeover rather than cell death. *Dev Cell* 2008; **3**: 344–357.
- Fimia GM, Stoykova A, Romagnoli A, Giunta L, Nardacci R, Corazzari M *et al*. Ambra1 regulates autophagy and development of the nervous system. *Nature* 2007; **447**: 1121–1125.
- Strappazzon F, Vietri-Rudan M, Campello S, Nazio F, Florenzano F, Fimia GM *et al*. Mitochondrial BCL-2 inhibits AMBRA1-induced autophagy. *EMBO J* 2011; **30**: 1195–1208.
- Lippincott-Schwartz J. Mitochondria supply membranes for autophagosomes biogenesis during starvation. *Cell* 2010; **4**: 656–667.
- Narendra N, Tanaka A, Suen DF, Youle RJ. Parkin is recruited selectively to impaired mitochondria and promotes their autophagy. *J Cell Biol* 2008; **183**: 795–803.
- Sandoval H, Thiagarajan P, Dasgupta SK, Schumacher A, Prchal JT, Chen M *et al*. Essential role for Nix in autophagic maturation of erythroid cells. *Nature* 2008; **454**: 232–235.
- Narendra DP, Jin SM, Tanaka A, Suen DF, Gautier CA, Shen S *et al*. PINK1 is selectively stabilized on impaired mitochondria to activate Parkin. *PLoS Biol* 2010; **8**: 1000298.
- Vives-Bauza C, Zhou C, Huang Y, Cui M, de Vries RL, Kim J *et al*. PINK1-dependent recruitment of Parkin to mitochondria in mitophagy. *Proc Natl Acad Sci USA* 2010; **107**: 378–383.
- Lee JY, Nagano Y, Taylor JP, Lim KL, Yao TP. Disease-causing mutations in parkin impair mitochondrial ubiquitination, aggregation, and HDAC6-dependent mitophagy. *J Cell Biol* 2010; **189**: 671–679.
- Okatsu K, Saisho K, Shimanuki M, Nakada K, Shitara H, Sou YS *et al*. p62/SQSTM1 cooperates with Parkin for perinuclear clustering of depolarized mitochondria. *Genes Cells* 2010; **15**: 887–900.
- Andreux PA, Houtkooper RH, Auwerx J. Pharmacological approaches to restore mitochondrial function. *Nat Rev Drug Discov* 2013; **6**: 465–483.
- Kundu M, Lindsten T, Yang CY, Wu J, Zhao F, Zhang J *et al*. Ulk1 plays a critical role in the autophagic clearance of mitochondria and ribosomes during reticulocyte maturation. *Blood* 2008; **112**: 1493–1502.
- Schweers RL, Zhang J, Randall MS, Loyd MR, Li W, Dorsey FC *et al*. NIX is required for programmed mitochondrial clearance during reticulocyte maturation. *Proc Natl Acad Sci USA* 2007; **104**: 19500–19505.
- Orvedahi A, Sumpster R, Xiao G, Ng A, Zou Z, Tang Y *et al*. Image-based genome-wide siRNA screen identifies selective autophagy factors. *Nature* 2011; **480**: 113–117.
- Hasson S, Kane LA, Yamano K, Huang CH, Sliter DA, Buehler E *et al*. High-content genome-wide RNAi screens identify regulators of parkin upstresam of mitophagy. *Nat Lett* 2013; **504**: 291–295.
- Van Humberbeck C, Cornelissen T, Hofkens H, Mandemakers W, Gevaert K, De Strooper B *et al*. Parkin interacts with Ambra1 to induce mitophagy. *J Neurosci* 2011; **28**: 10249–10261.
- Johansen T, Lamark T. Selective autophagy mediated by autophagic adapter proteins. *Autophagy* 2011; **7**: 279–296.
- Cozzolino M, Ferraro E, Ferri A, Rigamonti D, Quondamatteo F, Ding H *et al*. Apoptosome inactivation rescues proneural and neural cells from neurodegeneration. *Cell Death Differ* 2004; **11**: 1179–1191.
- Pistor S, Chakraborty T, Niebuhr K, Domann E, Wehland J. The ActA protein of *Listeria monocytogenes* acts as a nucleator inducing reorganization of the actin cytoskeleton. *EMBO J* 1994; **13**: 758–763.
- Geisler S, Holmstrom KM, Skujat D, Diesel FC, Rothfuss OC, Kahle PJ *et al*. PINK1/Parkin-mediated mitophagy is dependent on VDAC1 and p62/SQSTM1. *Nat Cell Biol* 2010; **12**: 119–131.
- Kabeya Y, Mizushima N, Ueno T, Yamamoto A, Kirisako T, Noda T *et al*. LC3, a mammalian homologue of yeast Apg8p, is localized in autophagosomal membranes after processing. *EMBO J* 2000; **19**: 5720–5728.
- Blommaert EF, Krause U, Schellens JP, Vreeling-Sindelarova H, Meijer AJ. The phosphatidylinositol 3-kinase inhibitors wortmannin and LY294002 inhibit autophagy in isolated rat hepatocytes. *Eur J Biochem* 1997; **243**: 240–246.
- Seglen PO, Gordon PB. 3-Methyladenine: specific inhibitor of autophagic/lysosomal protein degradation in isolated rat hepatocytes. *Proc Natl Acad Sci USA* 1982; **79**: 1889–1892.
- Twig G, Hyde B, Shirihai OS. Mitochondrial fusion, fission and autophagy as a quality control axis: the bioenergetic view. *Biochim Biophys Acta* 2008; **9**: 1092–1097.
- Campanella M, Parker N, Tan CH, Hall AM, Duchon MR. IF(1): setting the pace of the F(1)F(o)-ATP synthase. *Trends Biochem Sci* 2009; **7**: 343–350.
- Pankiv S, Clausen TH, Lamark T, Brech A, Bruun JA, Outzen H *et al*. p62/SQSTM1 binds directly to Atg9/LC3 to facilitate degradation of ubiquitinated protein aggregates by autophagy. *J Biol Chem* 2007; **282**: 24131–24145.

27. Itoh T, Kanno E, Uemura T, Waguri S, Fukuda M. OATL1, a novel autophagosome-resident Rab33B-GAP, regulates autophagosomal maturation. *J Cell Biol* 2011; **192**: 839–853.
28. Popovic D, Akutsu M, Novak I, Harper JW, Behrends C, Dikic I. Rab GTPase activating proteins in autophagy: regulation of endocytic and autophagy pathways by direct binding to human ATG8 modifiers. *Mol Cell Biol* 2012; **32**: 1733–1744.
29. Nazio F, Strappazzon F, Antonioli M, Bielli P, Cianfanelli V, Bordi M *et al*. mTOR inhibits autophagy by controlling ULK1 ubiquitination, self-association and function via AMBRA1 and TRAF6. *Nat Cell Biol* 2013; **4**: 406–416.
30. Jin J, Arias EE, Chen J, Harper JW, Walter JC. A family of diverse Cul4-Ddb1 interacting proteins includes Cdt2, which is required for S phase destruction of the replication factor Cdt1. *Mol Cell* 2006; **5**: 709–721.
31. Behrends C, Sowa ME, Gygi SP, Wade Harper J. Network organization of the human autophagy system. *Nature* 2010; **466**: 68–76.
32. Okamoto K, Kondo-Okamoto N, Ohsumi Y. Mitochondria-anchored receptor Atg32 mediates degradation of mitochondria via selective autophagy. *Dev Cell* 2009; **17**: 87–97.
33. Kanki T, Wang K, Cao Y, Baba M, Klionsky DJ. Atg32 is a mitochondrial protein that confers selectivity during mitophagy. *Dev Cell* 2009; **17**: 98–109.
34. Choubey V, Cagalinec M, Liiv J, Safiulina D, Hockey M, Kuum M *et al*. BECN1 is involved in the initiation of mitophagy. It facilitates PARK2 translocation to mitochondria. *Autophagy* 2014; **10**: 1092–1106.
35. Grumati P, Coletto L, Sabatelli P, Cescon M, Angelin A, Berteggia E *et al*. Autophagy is defective in collagen VI muscular dystrophies, and its reactivation rescues myofiber degeneration. *Nat Med* 2010; **11**: 1313–1320.
36. Follenzi A, Alles LE, Bakovic S, Geuna M, Naldini L. Gene transfer by lentiviral vectors is limited by nuclear translocation and rescued by HIV-1 pol sequences. *Nat Genet* 2000; **25**: 217–222.



This work is licensed under a Creative Commons Attribution-NonCommercial-NoDerivs 3.0 Unported License. The images or other third party material in this article are included in the article's Creative Commons license, unless indicated otherwise in the credit line; if the material is not included under the Creative Commons license, users will need to obtain permission from the license holder to reproduce the material. To view a copy of this license, visit <http://creativecommons.org/licenses/by-nc-nd/3.0/>

Supplementary Information accompanies this paper on Cell Death and Differentiation website (<http://www.nature.com/cdd>)

mTOR inhibits autophagy by controlling ULK1 ubiquitylation, self-association and function through AMBRA1 and TRAF6

Francesca Nazio^{1,2}, Flavie Strappazon^{1,2}, Manuela Antonioli³, Pamela Bielli², Valentina Cianfanelli^{1,2}, Matteo Bordi^{1,2}, Christine Gretzmeier^{4,5}, Joern Dengjel^{4,5}, Mauro Piacentini^{3,6}, Gian Maria Fimia³ and Francesco Cecconi^{1,2,7}

Autophagy is important in the basal or stress-induced clearance of bulk cytosol, damaged organelles, pathogens and selected proteins by specific vesicles, the autophagosomes. Following mTOR (mammalian target of rapamycin) inhibition, autophagosome formation is primed by the ULK1 and the beclin-1–Vps34–AMBRA1 complexes, which are linked together by a scaffold platform, the exocyst. Although several regulative steps have been described along this pathway, few targets of mTOR are known, and the cross-talk between ULK1 and beclin 1 complexes is still not fully understood. We show that under non-autophagic conditions, mTOR inhibits AMBRA1 by phosphorylation, whereas on autophagy induction, AMBRA1 is dephosphorylated. In this condition, AMBRA1, interacting with the E3-ligase TRAF6, supports ULK1 ubiquitylation by LYS-63-linked chains, and its subsequent stabilization, self-association and function. As ULK1 has been shown to activate AMBRA1 by phosphorylation, the proposed pathway may act as a positive regulation loop, which may be targeted in human disorders linked to impaired autophagy.

Autophagy is a highly conserved catabolic process, by which cytoplasmic material (for example, proteins, lipids and organelles) is transported to the lysosome for degradation by means of double-membraned vesicles, the autophagosomes. The process of *de novo* autophagosome formation has been shown to be regulated by at least four molecular complexes including the ULK1 complex, the beclin-1–VPS34–AMBRA1 complex, two transmembrane proteins, ATG9 and WIPI complexes, and two ubiquitin-like protein conjugation systems (ATG12 and LC3; ref. 1). The mammalian orthologue of yeast Atg1, the serine/threonine kinase ULK1, plays a key role in autophagy induction². ULK1 forms a stable complex with ATG13 (refs 3,4) and with FIP200 (ref. 5), the mammalian counterpart of ATG17. Under normal conditions, the ULK1 complex is de-activated by mTORC1 kinase-dependent phosphorylation of ULK1 and ATG13. Inhibition of mTORC1 enhances ULK1 kinase activity, which, in turn, triggers ATG13 and FIP200 phosphorylation^{4,6,7}. ULK1 also interacts with ATG101, another key player in autophagosome formation, in an ATG13-dependent manner^{6,8}. On autophagy, the ULK1 complex is localized in the isolation membranes⁵, where it promotes the formation of PI(3)P-enriched membrane compartments⁹ through

the beclin-1–VPS34–AMBRA1 complex, which recruits downstream effectors to the site where nucleation occurs. AMBRA1, on its ULK1-dependent release from a cytoskeletal docking site, induces autophagosome nucleation by promoting beclin 1 interaction with its target lipid kinase VPS34 (refs 10,11). In this work, we found that AMBRA1 is a ULK1-binding partner, required for ULK1 stability and kinase activity. Interestingly, during autophagy, ULK1 undergoes Lys 63-ubiquitylation and this modification is mediated by AMBRA1 and a specific RING finger E3 ubiquitin ligase, TRAF6 (tumour necrosis receptor-associated factor 6). Moreover, we determined that this Lys-63-linked ubiquitylation facilitates ULK1 self-association during autophagy.

Taken together, our results lead us to propose a role for AMBRA1 as a substrate receptor for the TRAF6 ligase in mediating ULK1 Lys-63-linked ubiquitylation that proves to be relevant for ULK1 protein stability and activation. Finally, we identified a specific inhibitory phosphorylation by mTOR on AMBRA1, which is removed during autophagy induction. We propose in this paper that mTOR, besides its negative regulation of ULK1 through its direct phosphorylation, may also indirectly inhibit ULK1 stability and activity by modifying AMBRA1 and impairing its E3-ligase-related functions.

¹Dulbecco Telethon Institute at the Department of Biology, University of Rome 'Tor Vergata', 00133 Rome, Italy. ²Laboratory of Molecular Neuroembryology, IRCCS Fondazione Santa Lucia, 00143 Rome, Italy. ³National Institute for Infectious Diseases IRCCS 'L. Spallanzani', 00149 Rome, Italy. ⁴Freiburg Institute for Advanced Studies (FRIAS), School of Life Sciences-LifeNet, University of Freiburg, Albertstr. 19, 79104 Freiburg, Germany. ⁵BIOS Centre for Biological Signalling Studies, University of Freiburg, Albertstr. 19, 79104 Freiburg, Germany. ⁶Department of Biology, University of Rome 'Tor Vergata', 00133 Rome, Italy. ⁷Correspondence should be addressed to F.C. (e-mail: francesco.cecconi@uniroma2.it)

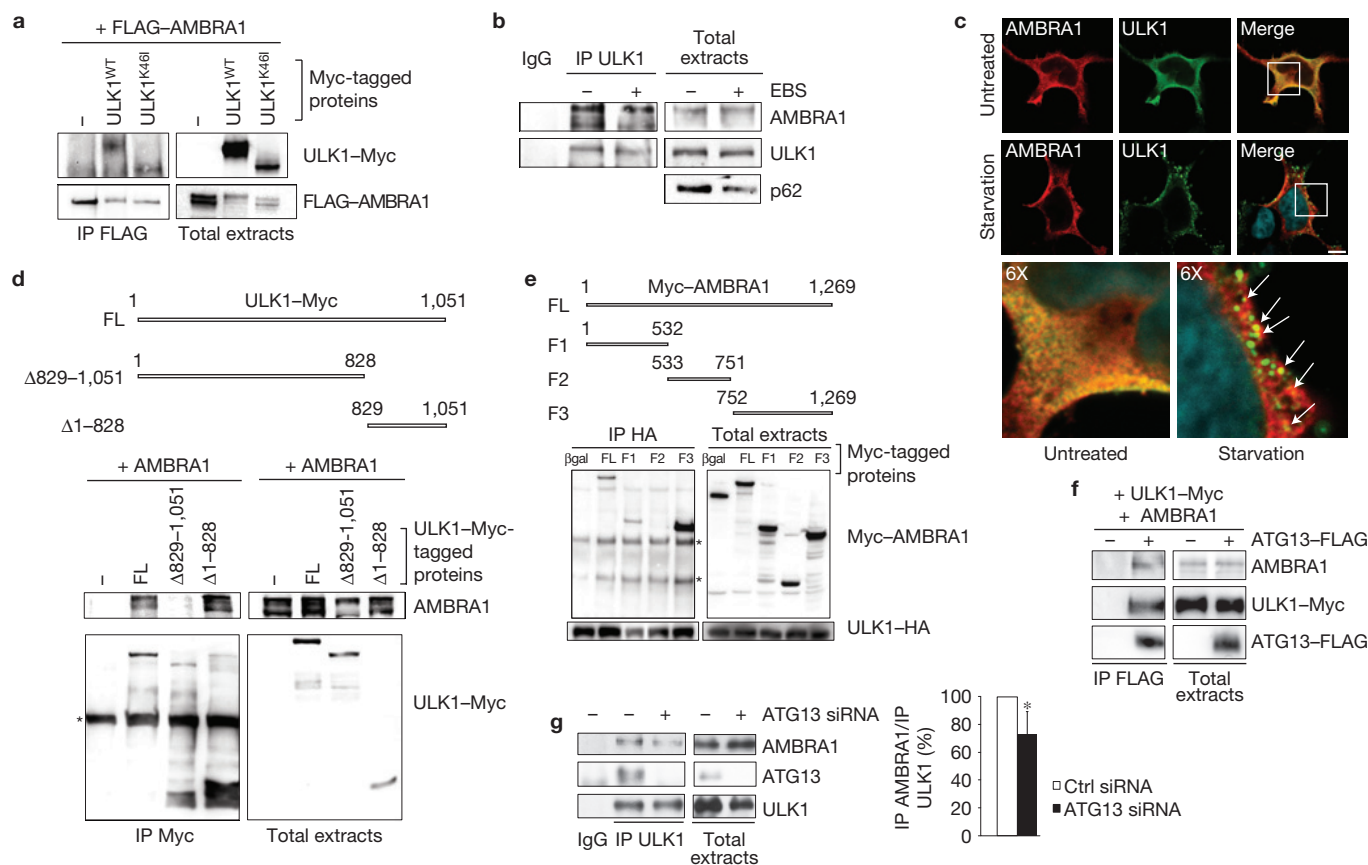


Figure 1 AMBRA1 interacts with the kinase ULK1 in mammalian cells. **(a)** FLAG-AMBRA1 was transfected into HEK293 cells together with ULK1^{WT} or ULK1^{K46I} Myc-tagged proteins. Protein extracts were immunoprecipitated (IP) using anti-FLAG antibody. **(b)** HEK293 cells were grown either in normal or in EBS medium for 1 h; protein extracts were immunoprecipitated using anti-ULK1 antibody or rabbit immunoglobulin as a negative control (IgG). Autophagy induction is shown by p62 degradation. **(c)** HEK293 cells were treated as in **b**, in the presence of leupeptin and stained by anti-AMBRA1 (red) and anti-ULK1 (green) antibodies. The merge of the two signals and DAPI (blue) for nuclear staining is shown in the right panels. Scale bar, 6 μm. The outlined areas are shown at a higher magnification in the lower panels. White arrows point to the co-localization puncta. Measurements by Metamorph indicate a co-localization ratio of 46% between ULK1 and AMBRA1 on autophagy induction. **(d,e)** ULK1 and AMBRA1 constructs are illustrated. Asterisks mark nonspecific bands corresponding to immunoglobulins. **(d)** HEK293 cells were co-transfected with vectors encoding AMBRA1 together with ULK1-Myc FL (full length) or its deletion mutants encoding the kinase and the proline-rich domains

(Δ829-1,051), and the ULK1 carboxy-terminal domain (Δ1-828). Protein extracts were immunoprecipitated using anti-Myc antibody. **(e)** HEK293 cells were co-transfected with vectors encoding ULK1-HA together with β-galactosidase-Myc (βgal), AMBRA1 full-length (FL), and F1, F2 or F3 Myc-tagged proteins. Protein extracts were immunoprecipitated using anti-HA antibody. The relative amounts of co-immunoprecipitated ULK1 and F1 or F3, respectively, are the same (see upper and lower left panel). **(f)** HEK293 cells were co-transfected with vectors encoding AMBRA1, ULK1-Myc and ATG13-FLAG. Protein extracts were immunoprecipitated using anti-FLAG antibody. **(g)** HEK293 cells were transfected with scramble siRNA or ATG13 siRNA. Protein extracts were immunoprecipitated using ULK1 antibody or IgG. The band density ratio of immunoprecipitated AMBRA1 relative to immunoprecipitated ULK1 is analysed, with the control ratio arbitrarily defined as 1.00. $n = 3$ extracts prepared from independent experiments; data are presented as means ± s.d. and significance is $P = 0.04$. Uncropped images of blots/gels are shown in Supplementary Fig. S6. Source data of statistical analysis are shown in Supplementary Table S1.

RESULTS

AMBRA1 interacts with the serine/threonine kinase ULK1 in mammalian cells

On autophagy induction, ULK1 phosphorylates AMBRA1, a modification essential for AMBRA1 translocation to the endoplasmic reticulum, where it can prime autophagosome formation¹¹. To examine the correlation between AMBRA1 and ULK1, we investigated whether AMBRA1 interacted with ULK1. Indeed, AMBRA1 interacts with both wild-type (WT) and K46I (dominant negative) ULK1 (ref. 3), showing that their interaction may not depend on ULK1 kinase activity (Fig. 1a). Furthermore, AMBRA1 and ULK1 form a stable protein complex in normal conditions and on autophagy induction by starvation (Fig. 1b,c), as revealed by co-immunoprecipitation and co-localization experiments.

Next, we attempted to identify the ULK1 domain responsible for this binding to AMBRA1. To this end, we used the full-length form of ULK1 (FL) and two different ULK1 deletion mutants (ULK1 Δ829-1,051 and Δ1-828; ref. 4). As shown in Fig. 1d, the carboxy-terminal domain (CTD) of ULK1, which binds ATG13 (ref. 3), is sufficient to bind AMBRA1. Vice versa, when mapping the AMBRA1 region responsible for ULK1 binding, we found that the AMBRA1 amino-terminal (F1) and C-terminal (F3) regions are sufficient to interact with ULK1, whereas the central region (F2), which binds beclin 1 (ref. 10), shows no interaction (Fig. 1e).

On the basis of these data, we examined the capacity of AMBRA1 to associate with ATG13, a ULK1-binding protein. As shown in Fig. 1f, AMBRA1 is able to interact with ATG13, suggesting

that ULK1, ATG13 and AMBRA1 coexist in a complex. However, AMBRA1–ULK1 interaction does not significantly depend on ULK1–ATG13 binding (Fig. 1g).

In conclusion, AMBRA1 forms a stable ternary complex with ULK1 and ATG13, which does not depend on ULK1 kinase activity or on ULK1 binding to ATG13.

AMBRA1 is important for ULK1 stability and kinase activity

By analysing ULK1 expression, we noticed that the ULK1 protein was expressed at higher levels on AMBRA1 transfection (Fig. 2a). Thus, we reasoned that AMBRA1 binding could stabilize ULK1 and analysed the expression of Ulk1/2 in *Ambra1*-deficient (*Ambra1*^{gt/gt}) mouse tissues. As illustrated in Fig. 2b and Supplementary Fig. S1a, the expression levels of Ulk1/2 in *Ambra1*^{gt/gt} embryos were much lower than in the wild type (*Ambra1*^{+/+}). Similar results were obtained in *Ambra1*^{+/gt} mouse embryonic fibroblasts (MEFs) (Supplementary Fig. S1b), suggesting an AMBRA1-dose-dependent effect in this stabilization. As shown in Supplementary Fig. S1c, there are no differences in the expression of beclin 1 and ATG12, two other autophagy-related proteins, in *Ambra1*^{+/+} versus *Ambra1*^{gt/gt} MEFs, indicating a ULK1-specific effect for AMBRA1. Furthermore, Ulk1 was detected as a smeared band with faster mobility in *Ambra1*^{gt/gt} tissues. As the faster gel migration of ULK1 indicates a reduced phosphorylation level of the protein^{2,5}, AMBRA1 could also be important for ULK1 basal phosphorylation. Indeed, the same results were observed by downregulation of AMBRA1 in HeLa cells, an effect that can be compensated by AMBRA1 reconstitution assays (Fig. 2c,d).

By analysing *Ulk1* messenger RNA expression, we found that there was no difference between *Ambra1*^{+/+} and *Ambra1*^{gt/gt} MEFs, and that *Ulk1* mRNA, as expected⁵, was enhanced after starvation in both the MEF genotypes analysed (Supplementary Fig. S1d). In contrast, an analysis of ULK1 decay in the presence of the translational inhibitor cycloheximide showed that, in the presence of AMBRA1, ULK1 expression remained essentially unchanged during the treatment (Fig. 2e). Also, ULK1 loss on AMBRA1 deficiency is proteasome dependent (Supplementary Fig. S1e). These results confirm that AMBRA1 is involved in ULK1 protein stability.

Next, to verify whether the ULK1 gel mobility shift, observed on AMBRA1 downregulation, was due to an impairment of ULK1 kinase activity, we investigated ATG13 phosphorylation (pATG13), a ULK1-mediated event. In AMBRA1-shRNA-treated cells, the pATG13 level decreases with respect to the control (Fig. 2d). In contrast, on AMBRA1 overexpression, the ATG13 phosphorylation level increases and an *in vitro* kinase assay shows that ULK1 kinase activity is, indeed, higher (Fig. 2f,g). However, by analysing the interaction between ULK1 and two known ULK1-binding partners, ATG13 and mTOR, we observed that the ULK1 complex is normally formed in AMBRA1-deficient cells (Supplementary Fig. S1f). Further, as previously reported, ULK1 forms, on autophagy induction, specific puncta within the cytosol¹²; although fewer ULK1 puncta could be seen in AMBRA1-deficient cells, highlighting a general decrease in ULK1 levels, no consequences could be detected on its mobilization and co-localization with LC3 puncta during autophagy (Supplementary Fig. S1g).

AMBRA1 is important for ULK1 Lys-63-linked ubiquitylation

Prompted by these findings, we analysed the molecular steps involved in this regulation. Post-translational modifications such as Lys-63-linked

ubiquitylation often regulate kinase activity and stability^{13–15}. In particular, ULK1 is a Lys-63-linked ubiquitylated protein during axon growth and endocytosis in the sensory growth cones of the nervous system¹⁶. How exactly polyubiquitylation affects the autophagy regulatory functions of ULK1 and whether this modification is sensitive to autophagy induction remain unknown.

Therefore, we investigated whether ULK1 underwent Lys-63-linked ubiquitylation in our cellular system and found that this was the case (Fig. 3a and Supplementary Fig. S2a). Furthermore, overexpression of a K63R ubiquitin mutant (unable to form Lys-63-linked chains) blocked the polyubiquitylation of ULK1, whereas a K48R mutant (unable to form K48-linked chains), as well as wild-type ubiquitin, did not (Fig. 3b), thus confirming that the polyubiquitylation we observed on ULK1 depends on Lys-63-linked ubiquitin. Furthermore, AMBRA1-siRNA-treated cells exhibit a decrease of Lys-63-linked ubiquitin in the ULK1 immunoprecipitates (Fig. 3c), while the amount of ULK1-linked ubiquitin is larger in cells transfected with AMBRA1 than in untransfected cells (Fig. 3d), indicating that AMBRA1 is required for ULK1 Lys-63-linked ubiquitylation.

Next, we analysed whether this modification on ULK1 was sensitive to autophagy induction. We found a rapid and transient increase in the Lys-63-linked ubiquitylation level of ULK1 using two different stimuli (rapamycin treatment and nutrient deprivation; Fig. 3e,f). Indeed, after autophagy induction by starvation, we observed a precise co-localization between ULK1 and Lys-63-linked ubiquitins (Supplementary Fig. S2b). Finally, we found that in the presence of a construct encoding ubiquitin Lys-63-linked chains, there was an appreciable increase in ULK1 levels and in the ATG13 phosphorylation level (Supplementary Fig. S2c). This supports our idea that this modification enhances ULK1 stability and activity. Of note, it is reasonable to believe that the population of Lys-63-ubiquitylated ULK1 is that which is released from the mTOR complex during autophagy².

AMBRA1 regulates ULK1 ubiquitylation by forming a complex with the TRAF6-ubiquitin ligase

We next attempted to identify the E3 ligase that could mediate this modification on ULK1. The E3 ligase TRAF6 can, indeed, ubiquitylate ULK1 *in vitro*¹⁶, and human TRAF6 is linked to the induction of autophagy in macrophages (through a physical interaction with beclin 1), resulting in its Lys-63-linked ubiquitylation¹⁷. In light of this evidence, we measured the expression levels of p62 and LC3 in TRAF6-overexpressing cells, observing a strong induction of autophagy on-rate, both in basal and starvation conditions (Fig. 4a and Supplementary Fig. S3a). However, when TRAF6 overexpression is coupled to simultaneous depletion of AMBRA1, the capability of TRAF6 to induce autophagy is reduced in all conditions analysed (Fig. 4b,c and Supplementary Fig. S3b), demonstrating that the TRAF6 pro-autophagic effect may depend, at least in part, on the presence of AMBRA1. Such a finding led us to examine whether TRAF6 was able to bind ULK1 and AMBRA1. As shown in Fig. 4d, FLAG–TRAF6 can bind AMBRA1 and ULK1 both in basal and starvation conditions and the three factors show vast subcellular co-localization (Supplementary Fig. S3c). Interestingly, when AMBRA1 is downregulated, the capability of TRAF6 to interact with ULK1 is strongly affected (Fig. 4e), proving that AMBRA1 is essential for the TRAF6–ULK1 interaction.

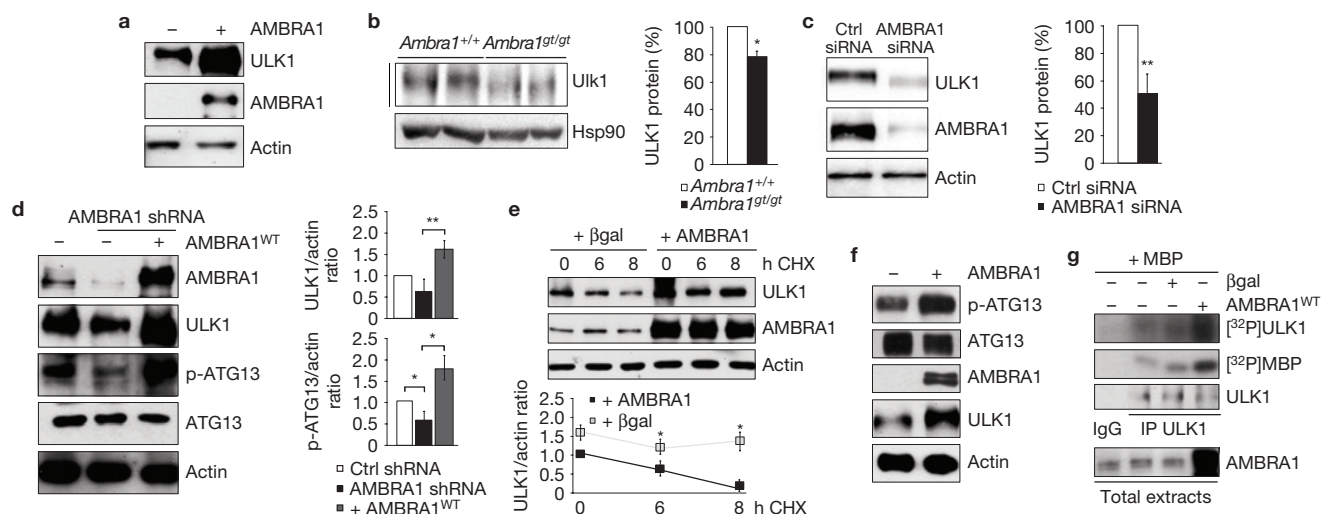


Figure 2 AMBRA1 is important for ULK1 stability and kinase activity. (a) HEK293 cells were transfected with AMBRA1 or the empty vector, as a control. ULK1, AMBRA1 and actin were analysed by western blotting. (b) Protein extracts from wild-type (*Ambra1*^{+/+}) and homozygous (*Ambra1*^{gt/gt}) embryos for the *Ambra1* gene-trap mutation at developmental day 14.5 were analysed by western blotting using anti-Ulk1 or anti-Hsp90 (loading control) antibodies. Quantification is shown on the right. $n = 6$ extracts prepared from independent experiments. Data are presented as means \pm s.d. and significance is $P = 0.037$. (c) AMBRA1, ULK1 and actin (as a protein loading control) were analysed by western blotting in HeLa cells transiently transfected with scramble siRNA or AMBRA1 siRNA. Quantification is shown on the right. $n = 5$ extracts prepared from independent experiments. Data are presented as means \pm s.d. and significance is $P = 0.007$. (d) HeLa cells stably interfered for AMBRA1 were transiently transfected with empty vector or AMBRA1 vector; AMBRA1, ULK1, ATG13, p-ATG13 and actin levels were analysed by western blotting. Quantification of ULK1 and pATG13 bands is shown on the right. $n = 3$ extracts prepared from independent experiments.

Next, we investigated whether TRAF6-mediated modification of ULK1 was as important as AMBRA1 deficiency for ULK1 protein stability. The depletion of TRAF6 promotes a massive proteasome-dependent reduction of ULK1, while TRAF6 overexpression enhances ULK1 levels (Fig. 4f and Supplementary Fig. S3a,d,f). These results demonstrate that both TRAF6 and AMBRA1 are required for ULK1 stability. In contrast, TRAF6 modulation has no such effect on the levels of other autophagy-related proteins, such as ATG13 or AMBRA1 (Fig. 4f).

Furthermore, the amount of ULK1-linked ubiquitin is larger in cells transfected with FLAG-TRAF6 than in control cells (Fig. 4g), the implication being that TRAF6 can ubiquitylate ULK1 *in vivo*. Interestingly, AMBRA1 downregulation led to a significant decrease in the capability of TRAF6 to ubiquitylate ULK1 (Fig. 4h), proving that AMBRA1 is necessary to mediate ULK1 ubiquitylation by TRAF6.

Last, we analysed ULK1 activation after TRAF6 overexpression by a kinase assay *in vitro* and found that, after TRAF6 overexpression, ULK1 proved more active (Fig. 4i). However, the capability of TRAF6 to induce ULK1 activation is impaired after AMBRA1 downregulation (Fig. 4i), as also confirmed by monitoring ULK1 gel mobility and ATG13 phosphorylation levels (Supplementary Fig. S3e–g).

Taken together, these findings demonstrate that, by promoting its ubiquitylation, both TRAF6 and AMBRA1 are required to enhance ULK1 phosphorylation.

Data are presented as means \pm s.d. and significance is $P = 0.006$ for ULK1 and $P = 0.044$ and $P = 0.011$ for pATG13. (e) HeLa cells were transfected or not with vector encoding AMBRA1 and treated with 35 μ M cycloheximide (CHX) for 6 and 8 h before extraction. ULK1, actin and AMBRA1 were analysed by western blotting. Quantification is shown below. $n = 3$ extracts prepared from independent experiments. Data are presented as means \pm s.d. and significance is $P = 0.049$ and $P = 0.02$. (f) HEK293 cells were transfected as in a; ATG13, pATG13, ULK1, AMBRA1 and actin were analysed by western blotting. (g) Endogenous ULK1 is immunoprecipitated from HeLa cells transfected with β -galactosidase or AMBRA1 plasmid respectively using an anti-ULK1 antibody. As a control, rabbit IgG was used. The resulting precipitates were subjected to ULK1 kinase assay using MBP as the substrate. Purified complexes were analysed by autoradiography and by western blotting using an anti-ULK1 antibody. Total extracts were analysed using an anti-AMBRA1 antibody. Uncropped images of blots/gels are shown in Supplementary Fig. S6. Source data of statistical analysis are shown in Supplementary Table S1.

AMBRA1-TRAF6 interaction is necessary for ULK1 Lys-63-linked ubiquitylation

By analysing the amino-acid sequence of human AMBRA1 we found five putative TRAF6-binding sites (P-X-E-X-X-aromatic/acidic)¹⁸ located at residues 618–623, 640–645, 681–686, 916–921 and 1,132–1,137, respectively. We mutated the glutamate residue to alanine in each potential binding site, and observed that the two sites identical to the canonical TRAF6-binding site (residues 618–623 and 681–686) are essential for AMBRA1-TRAF6 interaction (Fig. 5a,b and Supplementary Fig. S4a,b). By generating a double-mutant construct (AMBRA1^{AA}), we further confirmed the importance of these two sites in the AMBRA1-TRAF6 interaction, even though their mutation still allows AMBRA1 to bind ULK1 (Fig. 5c and Supplementary Fig. S4c).

We then examined the functional significance of AMBRA1-TRAF6 interaction in ULK1 ubiquitylation and activation. In the presence of the AMBRA1^{AA} construct, we found that ULK1 ubiquitylation and activation are almost abolished (Fig. 5d,e and Supplementary Fig. S4d,e), supporting the hypothesis that AMBRA1-TRAF6 binding is essential for ULK1-linked ubiquitylation and for regulating ULK1 stability and activity. TRAF6 overexpression only slightly rescued this phenotype (Supplementary Fig. S4d).

Finally, we investigated the importance of AMBRA1-TRAF6 interaction in autophagy induction. We confirmed that, in the presence of AMBRA1^{WT}, the autophagy on-rate is strongly induced, and the addition of AMBRA1^{AA} had a much lower effect ($\approx 50\%$; Fig. 5f,g and

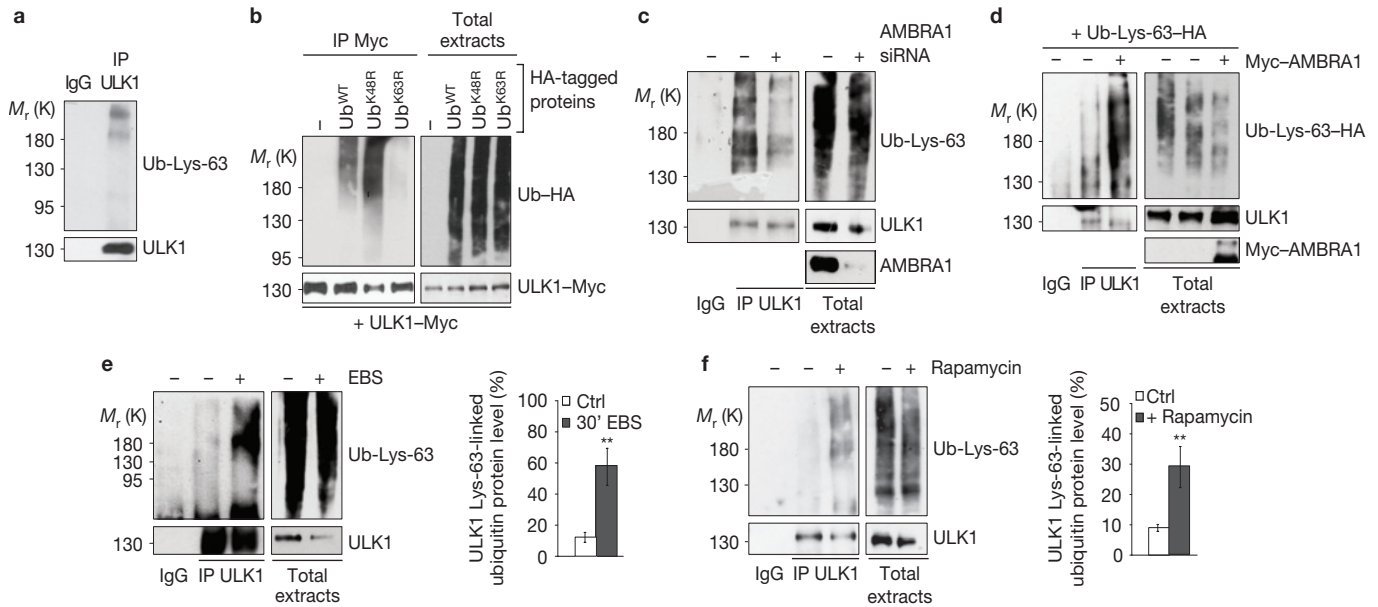


Figure 3 AMBRA1 is also important for ULK1 Lys-63-linked ubiquitylation. **(a)** Protein extracts from HeLa cells were immunoprecipitated using anti-ULK1 antibody or with IgG as a negative control and analysed by western blotting using anti-Lys63 specific ubiquitin and anti-ULK1 antibodies. **(b)** HeLa cells were co-transfected with ULK1-Myc alone or in combination with wild-type ubiquitin or its mutant (K48R or K63R) HA-tagged constructs. Protein extracts were immunoprecipitated using an anti-Myc antibody. Purified complexes and total extracts were analysed by western blotting using anti-Myc and anti-HA antibodies. **(c)** In HeLa cells, AMBRA1 was downregulated by RNAi. Protein extracts were immunoprecipitated using anti-ULK1 antibody or with IgG as a negative control. Purified complexes and total extracts were analysed by western blotting using anti-ULK1, anti-Lys-63 ubiquitin and anti-AMBRA1 antibodies. Of note, ULK1 levels in the co-immunoprecipitation experiment do not change in this case in the

Supplementary Fig. S4f), indicating that this interaction contributes to autophagy induction. **(d)** HeLa cells were co-transfected with vectors encoding for ubiquitin Lys-63-HA alone or in combination with AMBRA1. Protein extracts were immunoprecipitated using an anti-ULK1 antibody or with IgG as a negative control and Ub-Lys-63-HA, ULK1 and AMBRA1 were analysed by western blotting. **(e, f)** HeLa cells were cultured in complete or starvation medium for 30 min or in the presence of 100 nM of rapamycin for 3 h and then protein extracts were immunoprecipitated using anti-ULK1 antibody or with IgG as a negative control. Purified complexes and total extracts were analysed by western blotting as in **a**. Quantifications are shown on the right. In both panels, $n = 3$ extracts prepared from independent experiments. Data are presented as means \pm s.d. and significance is $P = 0.003$ and $P = 0.0015$, respectively. Uncropped images of blots/gels are shown in Supplementary Fig. S6. Source data of statistical analysis are shown in Supplementary Table S1.

Supplementary Fig. S4f), indicating that this interaction contributes to autophagy induction.

ULK1 Lys-63-linked ubiquitylation is required for ULK1 self-association

As Lys-63-linked ubiquitylation is often linked to protein self-association^{19,20} and a recent report shows that Atg1, the yeast ULK1 orthologue, is able to self-associate under autophagy induction²¹, we checked for this process in our system. We found that ULK1 is able to self-associate in mammalian cells and that autophagy induction by starvation enhances this capability (Fig. 6a). In contrast, downregulation of TRAF6 (Fig. 6b) or AMBRA1 (Fig. 6c) reduces the amount of ULK1-Myc interacting with ULK1-HA: this strongly suggests that both proteins are necessary for ULK1 self-association. Consistently, in the presence of the AMBRA1^{AA} mutant construct, ULK1 self-association is strongly reduced (Fig. 6d), implying that ULK1 ubiquitylation promotes ULK1 self-association.

mTOR phosphorylates AMBRA1 at Ser 52, inhibiting its role in ULK1 modification

Taken together, all of the results above indicate that AMBRA1 plays an upstream role in ULK1 regulation. On the basis of the observation that mTORC1 is a negative regulator of the ULK1 complex, and one of the more upstream factors in autophagy signalling, we reasoned that mTOR

could also modulate AMBRA1 activity. To identify potential AMBRA1 inhibitory modifications on autophagy induction, we performed a differential high-throughput mass spectrometry study (Supplementary Fig. S5a), by using cell extracts from starved and untreated cells. AMBRA1 was found to be phosphorylated in normal conditions at its Ser 52 residue, and the same site proved to be dephosphorylated on autophagy induction. Considering that the region surrounding this site is similar to the consensus phospho-acceptor motif for mTORC1 (ref. 22), we therefore postulated that mTOR could be responsible for this AMBRA1 phosphorylation in basal conditions, an event that would have an inhibitory role on autophagy (Supplementary Fig. S5b). Indeed, mutation of this site (AMBRA1^{S52A}) decreased the level of phosphorylation of AMBRA1 by mTOR *in vitro* (Fig. 7a), whereas AMBRA1 is able to physically interact with the mTORC1 complex (Fig. 7b), suggesting that AMBRA1 could be an mTOR substrate and that Ser 52 could be an mTOR target site. Moreover, we generated an antibody against phospho-Ser-52 AMBRA1 (Supplementary Fig. S5c) and, by means of this antibody, we confirmed a decrease in the phosphorylation status of AMBRA1 at Ser 52 in cells cultured in the presence of Torin1 (Fig. 7c), an mTOR inhibitor^{23,24}, or in nutrient-depleted media.

The functional role of this site in the capability of AMBRA1 to induce autophagy was then analysed by using LC3 and p62 antibodies, in the presence or the absence of chloroquine, an inhibitor of the autophagy flux (Fig. 7d). After AMBRA1^{WT} reintroduction in AMBRA1-deficient

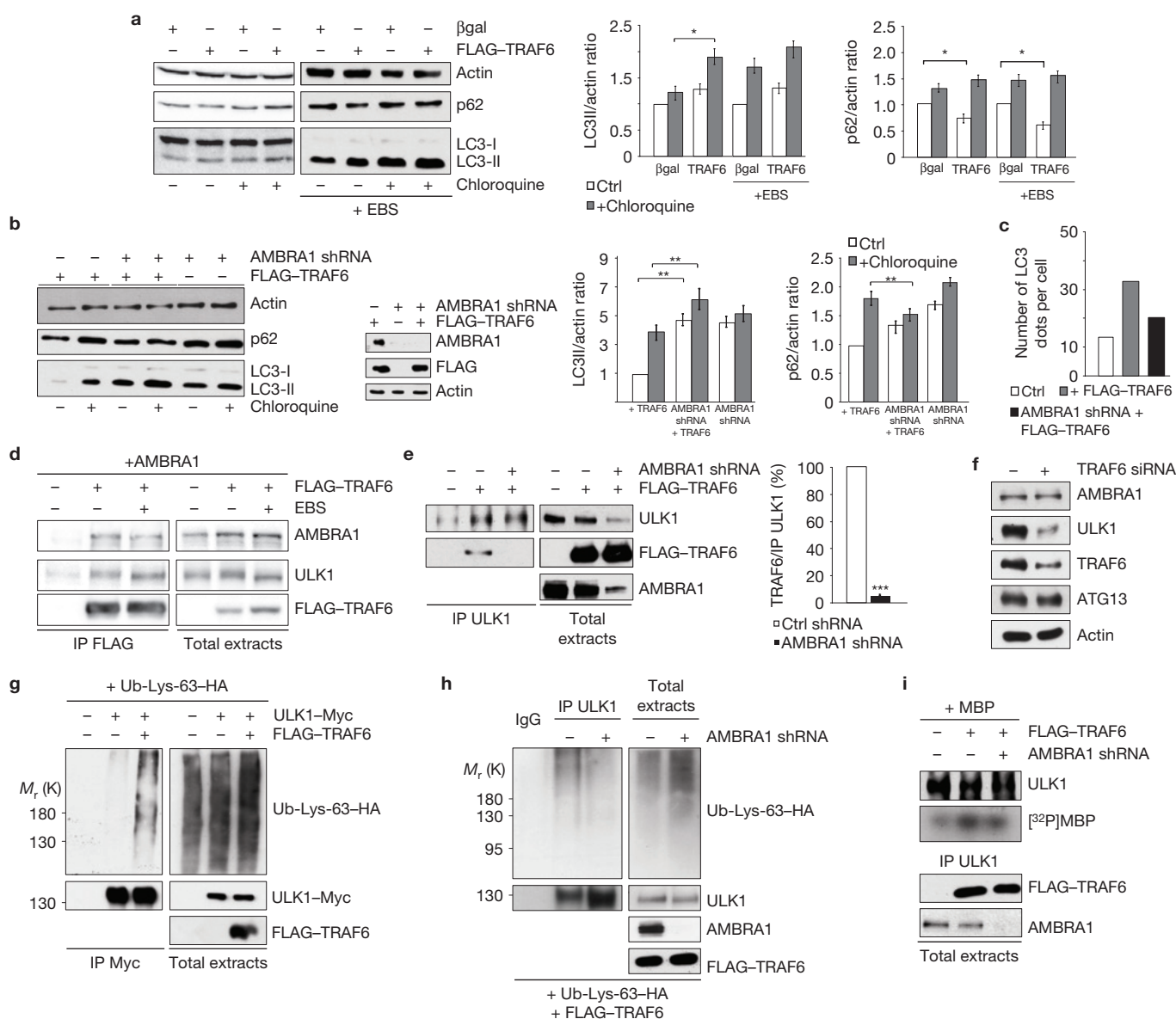


Figure 4 AMBRA1 regulates ULK1 ubiquitylation by forming a complex with the TRAF6 ubiquitin ligase. **(a)** HeLa cells were transfected with FLAG-TRAF6 or grown in starvation medium for 1 h. Some of them were treated with chloroquine. LC3, p62 and actin were analysed by western blotting. Quantification of LC3II and p62 bands is shown on the right. $n = 3$ extracts prepared from independent experiments. Data are presented as means \pm s.d. and significance is $P = 0.017$ for LC3 and $P = 0.01$ and $P = 0.04$ for p62. **(b)** HeLa cells were transduced with AMBRA1 lentiviral shRNA and transfected or not with FLAG-TRAF6. Quantification of LC3II and p62 bands is shown on the right. $n = 3$ extracts prepared from independent experiments. Data are presented as means \pm s.d. and significance is $P = 0.001$ and $P = 0.0018$ for LC3 and $P = 0.004$ for p62. **(c)** Count of LC3 puncta in HeLa cells transduced as in **b**. Five different confocal microscopy images for each experiment were randomly chosen and GFP-positive dots were examined on the images with identical brightness and contrast settings. The results are represented as the average number of LC3 dots with 100 cells analysed per sample. Confocal images are shown in Supplementary Fig. S3b. **(d)** HEK293 cells were transfected with AMBRA1

and FLAG-TRAF6 as indicated. Protein extracts were immunoprecipitated using an anti-FLAG antibody. **(e)** HeLa cells were transfected as in **b** and FLAG-TRAF6 was purified as in **d**. Quantification of immunoprecipitated TRAF6 is shown on the right. $n = 3$ extracts prepared from independent experiments. Data are presented as means \pm s.d. and significance is $P = 0.0003$. **(f)** In HeLa cells, TRAF6 was downregulated by RNAi. AMBRA1, ULK1, TRAF6, ATG13 and actin were analysed by western blotting. **(g)** HeLa cells were co-transfected with vectors encoding ULK1-Myc, FLAG-TRAF6 and Ub-Lys-63-HA, as indicated. Protein extracts were immunoprecipitated using an anti-Myc antibody. **(h)** HeLa cells stably interfered for AMBRA1 were transfected with FLAG-TRAF6 and Ub-Lys-63-HA as indicated. Protein extracts were immunoprecipitated using anti-ULK1 antibody. **(i)** Endogenous ULK1 is immunoprecipitated from HeLa cells transfected as in **b**. The resulting precipitates were subjected to a ULK1 kinase assay using MBP as the substrate. Purified complexes were analysed by autoradiography and by western blotting using an anti-ULK1 antibody. Uncropped images of blots/gels are shown in Supplementary Fig. S6. Source data of statistical analysis are shown in Supplementary Table S1.

HeLa cells, a strong induction of autophagy can be observed, as indicated by LC3 lipidation and p62 decrease. However, the addition of AMBRA1^{S52A} in the same system has a stronger effect, suggesting

that the dephosphorylation of this site contributes to the induction of autophagy. We also transfected HeLa cells with an AMBRA1^{S52E} phospho-mimicking mutant construct, again in an AMBRA1-deficient

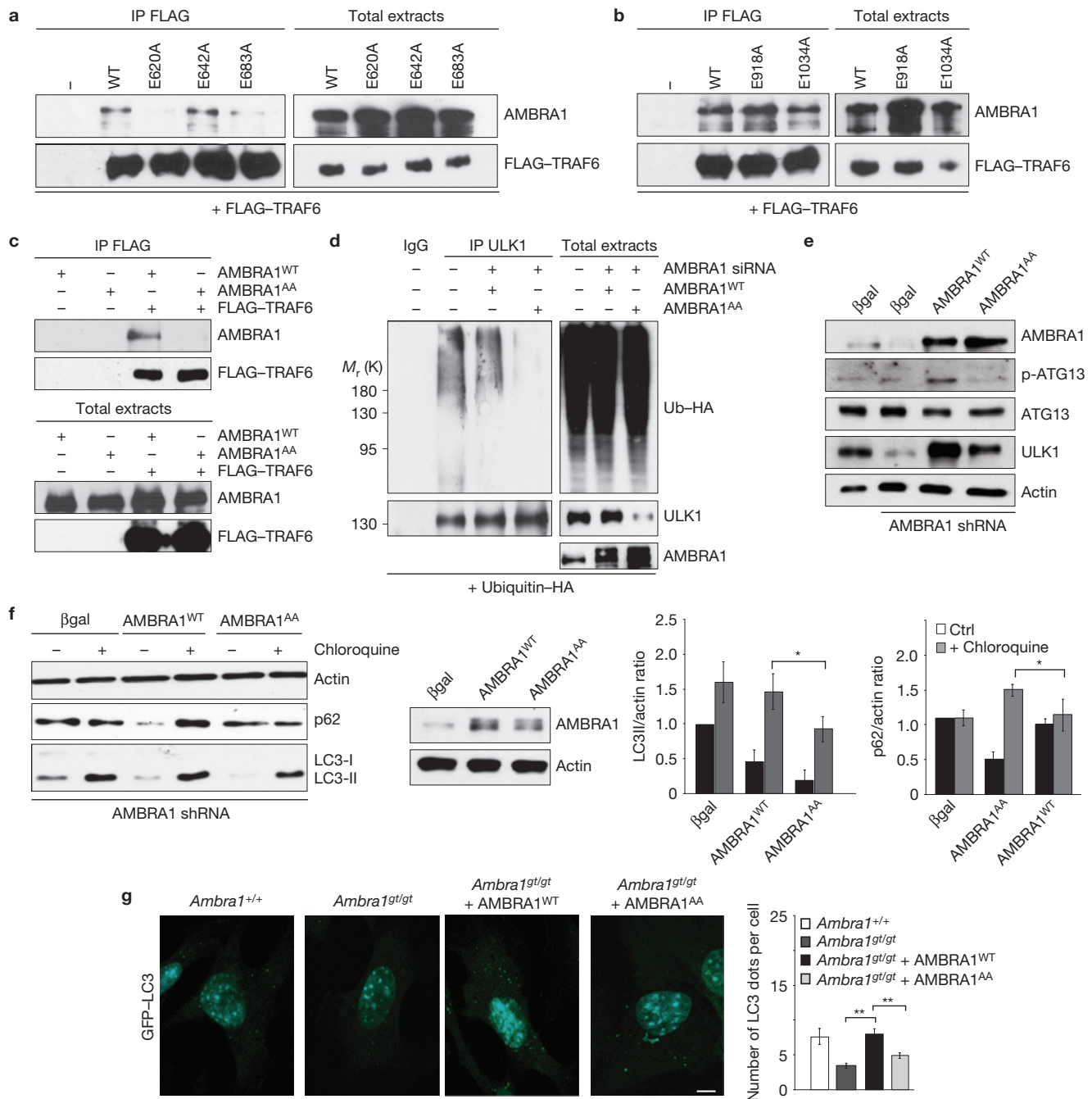


Figure 5 AMBRA1–TRAF6 interaction is necessary for ULK1 Lys-63-linked ubiquitylation. (**a–c**) Two canonical TRAF6-binding sites in AMBRA1 are essential for its interaction with TRAF6. HEK293 cells were co-transfected with vectors encoding FLAG–TRAF6 together with AMBRA1^{WT} and mutant constructs. Protein extracts were immunoprecipitated using an anti-FLAG antibody. AMBRA1 and FLAG–TRAF6 were analysed by western blotting. (**d**) HeLa cells were transfected with AMBRA1 RNAi oligonucleotide (siRNA AMBRA1). Then, cells were co-transfected with vectors encoding ubiquitin–HA and AMBRA1^{WT} or AMBRA1^{AA}, respectively. Protein extracts were immunoprecipitated using anti-ULK1 antibody; ubiquitin–HA, ULK1 and AMBRA1 were analysed by western blotting. (**e**) HeLa cells stably interfered for AMBRA1 were transduced with lentiviral vectors encoding β-galactosidase (negative control) AMBRA1^{WT} or AMBRA1^{AA} respectively; protein extracts were analysed by western blotting using anti-ULK1,

anti-AMBRA1 anti-ATG13, anti-pATG13 and anti-actin antibodies. (**f**) HeLa cells were transfected as in **e** and some of them were treated with chloroquine for 1 h. LC3, p62, AMBRA1 and actin were analysed by western blotting. Quantification of LC3II and p62 are shown on the right. $n = 3$ extracts prepared from independent experiments. Data are presented as means \pm s.d. and significance is $P = 0.03$ for LC3 and $P = 0.045$ for p62. (**g**) GFP–LC3 MEF cells from wild-type (*Ambra1*^{+/+}) and homozygous (*Ambra1*^{gt/gt}) embryos were transduced with the indicated lentiviral vectors and quantification of LC3 puncta per cells is shown on the right. Bars represent mean \pm s.e.m. of triplicate samples with 50 cells analysed per sample; $n = 3$ independent experiments. Significance is $P = 0.001$ and $P = 0.003$ ($n = 3$). Scale bar, 10 μ m. Uncropped images of blots/gels are shown in Supplementary Fig. S6. Source data of statistical analysis are shown in Supplementary Table S1.

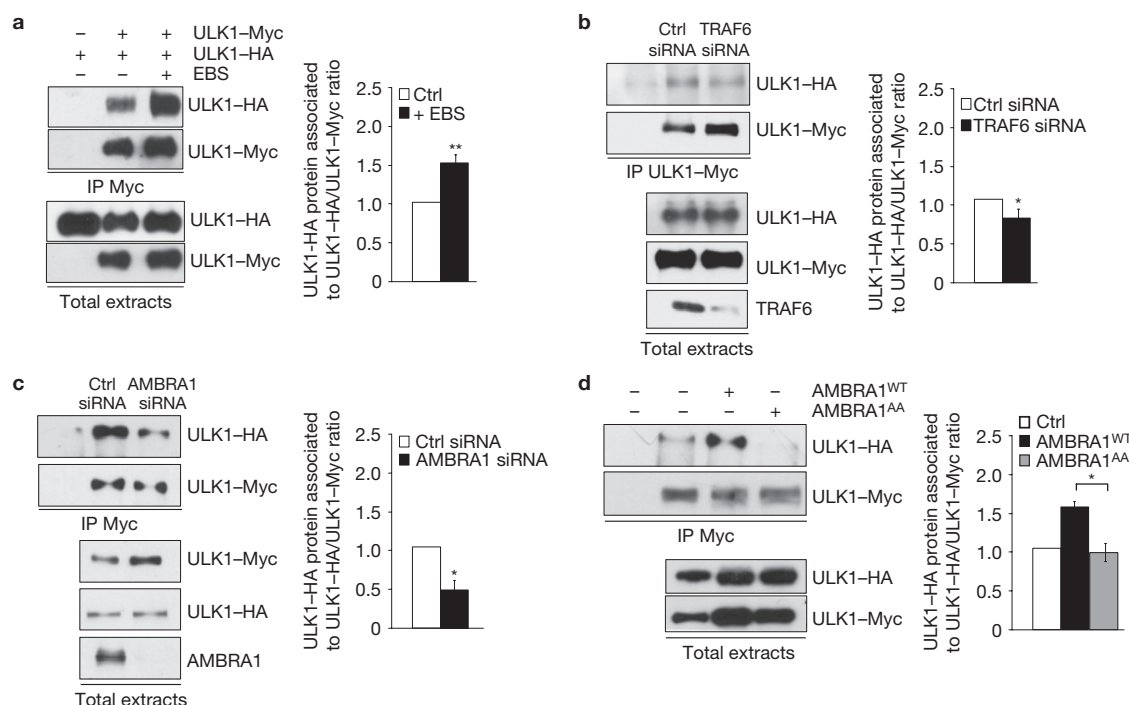


Figure 6 ULK1 Lys-63-linked ubiquitylation is necessary for ULK1 self-association. **(a)** HEK293 cells were co-transfected with vectors encoding ULK1-HA and ULK1-Myc and then grown either in normal (Ctrl) or in starvation (EBS) medium for 1 h. Protein extracts were immunoprecipitated using an anti-Myc antibody, and analysed by western blotting using anti-HA, and anti-Myc antibodies. Quantification is shown on the right. $n = 3$ extracts prepared from independent experiments. Data are presented as means \pm s.d. and significance is $P = 0.001$. **(b)** HEK293 cells were transfected with TRAF6 RNAi oligonucleotide (TRAF6 siRNA) or unrelated oligonucleotides as a control (Ctrl siRNA). Then, cells were co-transfected with vectors encoding ULK1-HA and ULK1-Myc and protein complexes were immunoprecipitated using anti-Myc antibody. Protein extracts were analysed by western blotting using anti-HA, anti-Myc and anti-TRAF6 antibodies. Quantification of ULK1-HA relative to ULK1-Myc is reported

on the right. $n = 3$ extracts prepared from independent experiments. Data are presented as means \pm s.d. and significance is $P = 0.037$. **(c)** HEK293 cells were transfected with AMBRA1 RNAi oligonucleotide (AMBRA1 siRNA) or unrelated oligonucleotides as a control (Ctrl siRNA). Then, cells were co-transfected and analysed as in **a**. Quantification is shown on the right. $n = 3$ extracts prepared from independent experiments. Data are presented as means \pm s.d. and significance is $P = 0.044$. **(d)** HEK293 cells were co-transfected with vectors encoding for ULK1-HA, ULK1-Myc and AMBRA1^{WT} or AMBRA1^{AA} respectively. Protein complexes were immunoprecipitated and analysed as in **a**. Quantification is shown on the right. $n = 3$ extracts prepared from independent experiments. Data are presented as means \pm s.d. and significance is $P = 0.014$. Uncropped images of blots/gels are shown in Supplementary Fig. S6. Source data of statistical analysis are shown in Supplementary Table S1.

context. In this case, the capability of AMBRA1 to induce autophagy was significantly reduced (Supplementary Fig. S5d).

To highlight the effect of this construct in *ex vivo* primary cells, we reconstituted *Ambra1*-deficient MEFs with AMBRA1^{S52A} and measured the occurrence of GFP-LC3-positive puncta, in comparison with AMBRA1^{WT}, obtaining an even stronger autophagy induction (Fig. 7e).

Then, the functional effect of Ser 52 phosphorylation in ULK1 modifications was analysed in the same reconstitution systems. As shown in Fig. 7f, in the presence of AMBRA1^{S52A}, ULK1 ubiquitylation is more abundant, compared with the expression of AMBRA1^{WT}. Furthermore, on transfection of the same construct, the level of ATG13 phosphorylation is increased, together with ULK1 protein levels and the capability of ULK1 to self-associate (see total extracts in Fig. 7f-h and Supplementary Fig. S5e).

Our conclusion, therefore, is that AMBRA1 phosphorylation by mTOR at Ser 52 impairs ULK1 ubiquitylation, stability, activity and self-association, besides inhibiting autophagy.

DISCUSSION

We have shown here that AMBRA1, a component of the beclin 1 complex, regulates the activation and stability of the kinase ULK1,

by promoting its Lys-63-linked ubiquitylation. Our data indicate that, on autophagy induction, ULK1 is rapidly Lys-63-ubiquitylated by an AMBRA1-TRAF6 complex, a key step in ULK1 self-association and in the enhancement of its kinase activity. In the absence of autophagy signalling, mTOR downregulates these series of events through a specific inhibitory phosphorylation on AMBRA1 (see Fig. 8).

Overall, these results imply that a much closer cross-talk between ULK1 and beclin 1 complexes exists long before their hierarchical localization at the omegasome on autophagy induction²⁵. Indeed, the exocyst, a protein scaffold complex involved in tethering intracellular vesicles to the plasma membrane, has been previously shown to provide an assembly and activation platform for members of the autophagy machinery. In this higher complex, all subcomplexes, including ULK1, beclin 1 and mTOR coexist, their interaction and functional reciprocal control being regulated by *ad hoc* protein modifications²⁶. mTOR, a master regulator of a cell life²⁷, is one of the more upstream negative regulators of autophagy: this protein, in response to the nutrient levels available to the cell, can inhibit ULK1 and ATG13 by phosphorylation²⁴. We here demonstrate that mTOR exerts a further brake on autophagy, by directly phosphorylating AMBRA1, thereby inhibiting its action on ULK1. AMBRA1 is thus one of the few known functional targets

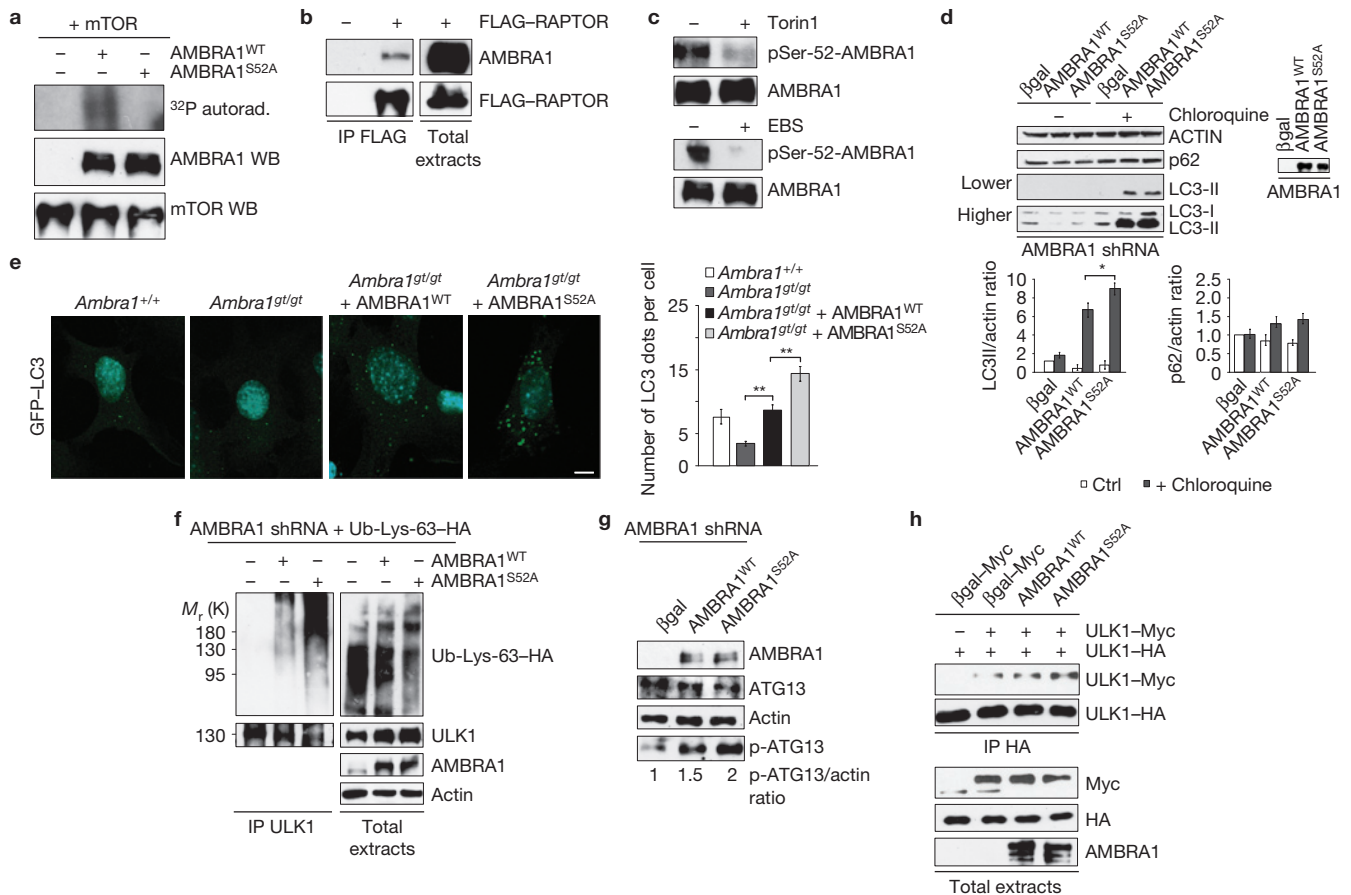


Figure 7 mTOR phosphorylates AMBRA1 at Ser 52, inhibiting its role in ULK1 modification. **(a)** Highly purified mTOR was incubated with radiolabelled ATP without substrate, with purified FLAG-AMBRA1 and purified FLAG-AMBRA1^{S52A} and analysed by autoradiography. The lower panels show a FLAG and mTOR western blot (WB). **(b)** HEK293 cells expressing FLAG-RAPTOR were subjected to FLAG immunoprecipitation. Protein complexes were analysed by western blotting using anti-FLAG and anti-AMBRA1 antibodies. **(c)** HEK293 cells were treated with Torin1 for 3 h or cultured in starvation medium for 2 h and protein extracts were analysed by western blotting using anti-pSer-52 and anti-AMBRA1 antibodies. **(d)** HeLa cells stably interfered for AMBRA1 were transduced with the indicated lentiviral vectors encoding for β-galactosidase, AMBRA1^{WT} or AMBRA1^{S52A} respectively and some of them were treated with chloroquine for 1 h. Protein extracts were analysed by western blotting using anti-LC3, anti-p62 and anti-actin antibodies. Quantification of LC3II and p62 bands is shown below. $n=3$ extracts prepared from independent experiments. Data are presented as means \pm s.d. and significance is $P=0.038$. **(e)** GFP-LC3 MEF cells from wild-type (*Ambra1*^{+/+}) and homozygous (*Ambra1*^{gt/gt})

embryos were transduced with indicated lentiviral vectors and quantification of LC3 puncta per cell is shown on the right. Bars represent mean \pm s.e.m. of triplicate samples and 50 cells analysed per sample. $n=3$ independent experiments. Significance is $P=0.001$ and $P=0.003$. Scale bar, 10 μ m. **(f)** HeLa cells stably interfered for AMBRA1 were co-transfected with vectors encoding Ub-Lys-63-HA and AMBRA1^{WT} or AMBRA1^{S52A}, respectively. Protein extracts were immunoprecipitated using an anti-ULK1 antibody and ubiquitin Lys-63-HA, ULK1, AMBRA1 and actin were analysed by western blotting. **(g)** HeLa cells stably interfered for AMBRA1 were transduced as in **d**; protein extracts were analysed by western blotting using anti-AMBRA1, anti-ATG13, anti-pATG13 and anti-actin antibodies. Quantification of the p-ATG13 band is shown below. **(h)** HeLa cells transfected with ULK1-HA, ULK1-Myc and different AMBRA1 constructs, respectively. Protein complexes were immunoprecipitated using anti-HA antibody and analysed by western blotting using anti-HA, anti-Myc and anti-AMBRA1 antibodies. Uncropped images of blots/gels are shown in Supplementary Fig. S6. Source data of statistical analysis are shown in Supplementary Table S1.

of mTOR and one of the more upstream autophagy signalers. Interestingly, and according to its secondary and tertiary putative sequence, AMBRA1 can be considered as an intrinsically disordered protein²⁸ (data not shown). These proteins are excellent candidates for the role of scaffold factors, linking different molecules and driving different cell processes, a capability that may explain the multi-task role of AMBRA1 at different steps during autophagy induction.

As for the role of Lys-63-linked ubiquitylation in autophagy, we show here that this modification is an early and crucial step of autophagy induction and is mediated by TRAF6. TRAF6-dependent Lys-63-linked ubiquitylation of beclin 1 was shown to be essential for beclin 1 pro-autophagic function¹⁷. TRAF6 is also known to be involved in

innate immune response by regulating the Toll-like pathway. In particular, in this signalling pathway, TRAF6 ubiquitylates some protein kinases such as TAK1 and IKK γ , leading to their subsequent activation²⁹. In our case, we found that TRAF6 overexpression enhances ULK1 activity and that the capability of TRAF6 to modify ULK1 is affected when AMBRA1 is downregulated. Interestingly, AMBRA1 has been identified as DDB1- and cullin4-associated factor 3 (DCAF3), and proposed to bridge this ligase complex to its target substrates^{30,31}, supporting the idea that AMBRA1 could act as a TRAF6 adaptor during autophagy. In fact, TRAF6 needs adaptor proteins to ubiquitylate its substrates, such as in the regulation of TAK1 kinase through the TAB1-TAB2 adaptor complex in the IL-1 signal

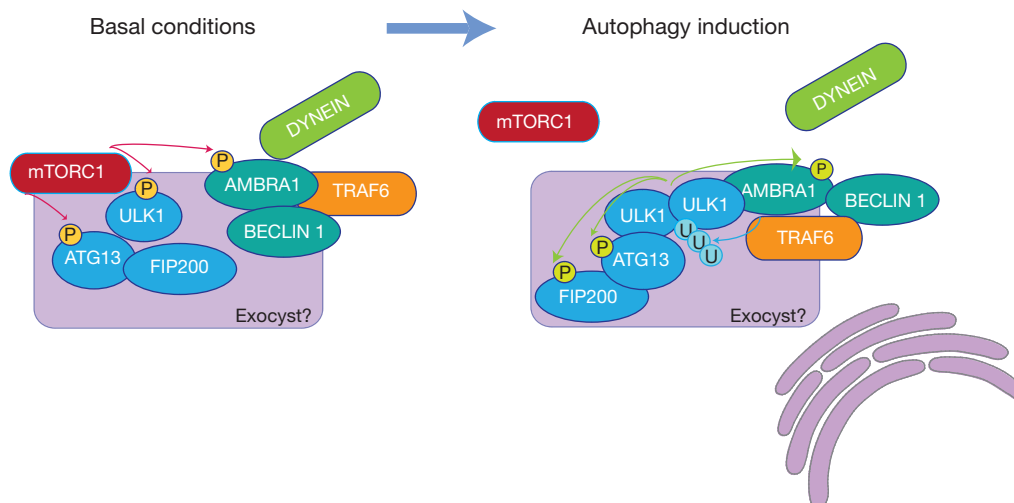


Figure 8 Proposed model of AMBRA1 regulation in ULK1 ubiquitylation. In basal conditions, AMBRA1 is maintained in an inactive state by mTOR phosphorylation and by its anchoring to the dynein motor complex. After autophagy induction, AMBRA1 and ULK1 are active; AMBRA1 enhances ULK1 kinase activity and stability by promoting its Lys-63-linked

ubiquitylation and self-association through TRAF6. ULK1 primes AMBRA1 detachment from the dynein complex through a positive phosphorylation. Coupling these regulatory events may represent a positive feedback to sustain autophagy in a continuous loop. The exocyst may act as a scaffold platform to keep the complexes involved grouped together.

transduction pathway³². Furthermore, it remains unknown how the failure in Lys-63-linked ubiquitylation of ULK1 affects its protein stability. It has been demonstrated that an enzyme called A20, a deubiquitylase for TRAF6, could deubiquitylate Lys-63-linked chains of TRAF6-target proteins to trigger K48-linked ubiquitylation, leading to these proteins degradation. A20 will therefore be a good candidate to exert this function on ULK1 (ref. 33). Of note, it has been recently published that, in yeast, the ULK1 orthologue Atg1 forms an Atg1–Atg1 complex, stimulating the autophosphorylation of Atg1 and autophagy induction²¹. According to our data, a self-association that enhances ULK1 activity occurs also in higher eukaryotes, and depends on the AMBRA1–TRAF6 complex.

Of note, we have previously shown that AMBRA1 itself is one of the targets of the ULK1 kinase activity¹¹. Indeed, this ULK1-mediated AMBRA1 phosphorylation has the potential to prime AMBRA1 detachment from cytoskeletal docking sites. Given the additional and more upstream role of AMBRA1 that we describe here, the ULK1-dependent regulation of AMBRA1 localization may represent a positive feedback loop regulating autophagy enhancement. As for the role of these two proteins *in vivo*, it should be noted that both AMBRA1 and ULK1 play crucial roles in the developing and adult brain compartments^{10,16,34}. Although these roles have not yet been clearly related to the ULK1 pro-autophagic functions, our findings reveal that AMBRA1 may participate in a common pathway in neurogenesis, linked to autophagy regulation. □

METHODS

Methods and any associated references are available in the [online version of the paper](#).

Note: Supplementary Information is available in the online version of the paper

ACKNOWLEDGEMENTS

We thank the Animal Facility (STA) of the University of Rome ‘Tor Vergata’ for the mouse work, M. Acuña Villa and M. W. Bennett for editorial and secretarial work, and G. Basile and M. Corrado for research assistance. We are indebted to S. A. Tooze (Cancer Research Institute London, UK), D. H. Kim (University of Minnesota

Cancer Center, USA), and D. M. Sabatini and R. Zoncu (Whitehead Institute for Biomedical Research, USA) for kindly providing us with ULK1 and ATG13 constructs and HEK293 cells stably expressing RAPTOR–FLAG, respectively. This work was supported in part by grants from the Telethon Foundation (GGP10225), AIRC (IG2010 and IG2012 to FC and MP), FISM (2009), the Italian Ministry of University and Research (PRIN 2009 and FIRB Accordi di Programma 2011) and the Italian Ministry of Health (Ricerca Finalizzata and Ricerca Corrente to F.C., M.P. and G.M.F.).

AUTHOR CONTRIBUTIONS

F.N. performed most experiments with crucial help from F.S. (immunofluorescence and confocal analyses), M.A. (mutagenesis and cloning), V.C. (immunoprecipitation analysis), M.B. (real-time PCR) and P.B. (kinase assay *in vitro*). C.G. and J.D. performed the mass spectrometry analysis; G.M.F. provided critical reagents. F.N. and F.C. wrote the manuscript with the help and suggestions of G.M.F. and M.P.; F.C. conceived and designed the research. All authors discussed the results and commented on the manuscript.

COMPETING FINANCIAL INTERESTS

The authors declare no competing financial interests.

Published online at www.nature.com/doi/10.1038/ncb2708

Reprints and permissions information is available online at www.nature.com/reprints

- Mizushima, N. & Komatsu, M. Autophagy: renovation of cells and tissues. *Cell* **147**, 728–741 (2012).
- Hosokawa, N. *et al.* Nutrient-dependent mTORC1 association with the ULK1–Atg13–FIP200 complex required for autophagy. *Mol. Biol. Cell.* **20**, 1981–1991 (2009).
- Chan, E. Y., Longatti, A., McKnight, N. C. & Tooze, S. A. Kinase-inactivated ULK proteins inhibit autophagy via their conserved C-terminal domains using an Atg13-independent mechanism. *Mol. Biol. Cell.* **29**, 157–171 (2009).
- Jung, C. H. *et al.* ULK–Atg13–FIP200 complexes mediate mTOR signaling to the autophagy machinery. *Mol. Biol. Cell.* **20**, 1992–2003 (2009).
- Hara, T. *et al.* FIP200, an ULK-interacting protein, is required for autophagosome formation in mammalian cells. *J. Cell Biol.* **181**, 497–510 (2008).
- Hokosawa, N. *et al.* Atg101, a novel mammalian autophagy protein interacting with Atg13. *Autophagy* **5**, 973–979 (2009).
- Ganley, I. G. *et al.* ULK1–ATG13–FIP200 complex mediates mTOR signaling and is essential for autophagy. *J. Biol. Chem.* **284**, 12297–12305 (2009).
- Mercer, C. A., Kaliappan, A. & Dennis, P. B. A novel, human Atg13 binding protein, Atg101, interacts with Ulk1 and is essential for macroautophagy. *Autophagy* **5**, 649–662 (2009).
- Hayashi-Nishino, M. *et al.* A subdomain of the endoplasmic reticulum forms a cradle for autophagosome formation. *Nat. Cell Biol.* **11**, 1433–1437 (2009).
- Fimia, G. M. *et al.* Ambra1 regulates autophagy and development of the nervous system. *Nature* **447**, 1121–1125 (2007).

11. Di Bartolomeo, S. *et al.* The dynamic interaction of AMBRA1 with the dynein motor complex regulates mammalian autophagy. *J. Cell Biol.* **191**, 155–168 (2010).
12. Chan, E. Y., Kir, S. & Tooze, S. A. siRNA screening of the kinome identifies ULK1 as a multidomain modulator of autophagy. *J. Biol. Chem.* **282**, 25464–25474 (2007).
13. Chen, Z. J. & Sun, L. J. Non proteolytic functions of ubiquitin in cell signaling. *Mol. Cell* **33**, 275–286 (2009).
14. Hoeller, D. & Dikic, I. Targeting the ubiquitin system in cancer therapy. *Nature* **458**, 438–444 (2009).
15. Raiborg, C. & Stenmark, H. The ESCRT machinery in endosomal sorting of ubiquitylated membrane proteins. *Nature* **458**, 445–445 (2009).
16. Zhou, X. *et al.* Unc-51-like kinase 1/2-mediated endocytic processes regulate filopodia extension and branching of sensory axons. *Proc. Natl Acad. Sci. USA* **104**, 5842–5847 (2007).
17. Shi, C. S. & Kehrl, J. H. Traf6 and A20 differentially regulate TLR4-induced autophagy by affecting the ubiquitination of Beclin 1. *Sci. Signal* **3**, 123 (2010).
18. Ye, H. *et al.* Distinct molecular mechanism for initiating TRAF6 signalling. *Nature* **418**, 443–447 (2002).
19. Liu, Z., Zhang, W. P., Xing, Q., Ren, X., Liu, M. & Tang, C. Noncovalent dimerization of ubiquitin. *Angew. Chem. Int. Ed. Engl.* **51**, 469–472 (2012).
20. Humphrey, R. K., Yu, S. M., Bellary, A., Gonuguntla, S., Yebra, M. & Jhala, U. S. Lysine 63-linked ubiquitination modulates mixed lineage kinase-3 interaction with JIP1 scaffold protein in cytokine-induced pancreatic β cell death. *J. Biol. Chem.* **288**, 2428–2440 (2012).
21. Yeh, Y. Y., Shah, K. H. & Herman, P. K. An Atg13 protein-mediated self-association of the Atg1 protein kinase is important for the induction of autophagy. *J. Biol. Chem.* **286**, 28931–28939 (2011).
22. Hsu, P. P. *et al.* The mTOR-regulated phosphoproteome reveals a mechanism of mTORC1-mediated inhibition of growth factor signaling. *Science* **332**, 1317–1322 (2011).
23. Feldman, M. E. *et al.* Active-site inhibitors of mTOR target rapamycin-resistant outputs of mTORC1 and mTORC2. *PLoS Biol.* **7**, e38 (2009).
24. Thoreen, C. C. *et al.* An ATP-competitive mammalian target of rapamycin inhibitor reveals rapamycin-resistant functions of mTORC1. *Biol. Chem.* **284**, 8023–8032 (2009).
25. Itakura, E. & Mizushima, N. Characterization of autophagosome formation site by a hierarchical analysis of mammalian Atg proteins. *Autophagy* **6**, 764–776 (2010).
26. Bodemann, B. O. *et al.* RalB and the exocyst mediate the cellular starvation response by direct activation of autophagosome assembly. *Cell* **144**, 253–267 (2011).
27. Hosking, R. mTOR: the master regulator. *Cell* **149**, 955–957 (2012).
28. Dyson, H. J. & Wright, P. E. Intrinsically unstructured proteins and their functions. *Nat. Rev. Mol. Cell Biol.* **6**, 253–267 (2005).
29. Sorrentino, A. *et al.* The type I TGF- β receptor engages TRAF6 to activate TAK1 in a receptor kinase-independent manner. *Nat. Cell Biol.* **10**, 1199–1207 (2008).
30. Jin, J., Arias, E. E., Chen, J., Harper, J. W. & Walter, J. C. A family of diverse Cul4-Ddb1-interacting proteins includes Cdt2, which is required for S phase destruction of the replication factor Cdt1. *Mol. Cell* **23**, 709–721 (2006).
31. Behrends, C., Sowa, M. E., Gygi, S. P. & Harper, J. W. Network organization of the human autophagy system. *Nature* **466**, 68–76 (2010).
32. Takaesu, G. *et al.* TAB2, a novel adaptor protein, mediates activation of TAK1 MAPKKK by linking TAK1 to TRAF6 in the IL-1 signal transduction pathway. *Mol. Cell* **5**, 649–658 (2000).
33. Wertz, I. E. *et al.* De-ubiquitination and ubiquitin ligase domains of A20 downregulate NF- κ B signalling. *Nature* **430**, 694–699 (2004).
34. Tomoda, T., Bhatt, R. S., Kuroyanagi, H., Shirasawa, T. & Hatten, M. E. A mouse serine/threonine kinase homologous to *C. elegans* UNC51 functions in parallel fiber formation of cerebellar granule neurons. *Neuron* **24**, 833–846 (1999).

METHODS

Antibodies. All antibodies were used at a dilution of 1:1,000 unless specified otherwise. Mouse monoclonal antibodies were from: Sigma (FLAG-F3165; HA-clone HA-7-H3663; TRAF6-D10 sc-8409), Santa Cruz (Myc-9E10 sc-40), Becton–Dickinson (beclin 1-612113). Rabbit polyclonal antibodies were from: Sigma (ATG13-SAB4200100; ULK1-A7481; actin-A2066 1:10,000; ULK2-U8008), Santa Cruz (ULK1 sc-33182), Novus (AMBRA1-26190002 1:3,000), Cell Signalling (LC3B #3868S 1:3,000; mTOR #2972; ATG12 #2011), Rockland (pATG13-600-401-C49), ProteinTech (FIP200-10043-2-AP 1:500). Rabbit monoclonal antibodies were from: Millipore (ubiquitin-Lys-63 specific-#05-1308), Epitomic (TRAF6 #1660-1). The antibody against phospho-AMBRA1S52 was raised by immunizing rabbits with a peptide (MERK) and was affinity-purified using the immunizing peptide (ABC80).

Immunoprecipitation and western blotting. Cells and embryonic tissues were lysed in CHAPS buffer as previously described². Lysates (1–3 mg) were then incubated at 4 °C for 30 min. Equal amounts of protein were incubated with 20 µl of monoclonal anti-Myc or anti-FLAG antibody conjugated with protein A agarose beads (Clontech and Sigma, respectively) for 4 h, or 2 µg of anti-ULK1 antibody overnight at 4 °C followed by 60 min incubation with 30 µl of protein A/G Sepharose beads (Roche). To detect ubiquitin and ULK1 modification by Lys-63-linked chains, after the lysis and before the immunoprecipitation 1% SDS was added and the lysates were incubated for 5 min at 90° to dissociate protein–protein interactions. The samples were diluted 10-fold with the same buffer and the immunoprecipitation assay was performed as previously described. Note that endogenous AMBRA1 usually migrates as a doublet band, whereas the overexpressed AMBRA1 shows additional lower-molecular-weight bands.

In vitro kinase assay. For ULK1 kinase assay, cells were lysed in ice-cold buffer (10 mM Tris–HCl (pH 7.4), 2 mM MgCl₂, 150 mM NaCl, 0.5% Triton X-100, 10% glycerol containing the Complete EDTA-free protease inhibitor cocktail (Sigma) and phosphatase inhibitors (NaV, NaF and β-glycerophosphate)). Lysates were incubated with anti-ULK1 antibody for 3 h and then washed three times with the buffer. Following the three washes, immunoprecipitates were further washed once with kinase reaction buffer (KRB; 20 mM HEPES, at pH 7.5, 20 mM MgCl₂, 25 mM β-glycerophosphate, 2 mM dithiothreitol and 100 µM sodium orthovanadate) and then incubated at a final volume of 20 µl in KRB containing 20 µM ATP, 5 µg myelin basic protein (MBP) and 5 µCi [³²P]ATP at 30 °C for 15 min. The reaction was stopped by the addition of sample buffer, boiled and analysed by SDS–PAGE followed by autoradiography. For the mTOR kinase assay, FLAG–AMBRA1^{WT} and FLAG–AMBRA1^{S52A} were purified from transiently transfected HEK293 cells using anti-FLAG affinity beads (Sigma). Cells were lysed using CHAPS buffer and immunocomplexes were washed four times in CHAPS buffer containing NaCl 150 mM and eluted for 1 h at 4 °C using a competing FLAG peptide (Sigma). Endogenous mTOR was purified using an anti-mTOR antibody. The kinase assay was performed for 30 min at 37 °C in a final volume of 25 µl consisting of kinase buffer (25 mM HEPES at pH 7.4, 50 mM KCl, 10 mM MgCl₂ and 4 mM MnCl₂), 50 µM ATP and 1 µCi [³²P]ATP. The reaction was stopped as described above.

Complementary DNA cloning. Constructs coding for AMBRA1 and its fragment were cloned in the pLPCX vector¹⁰ (Clontech) and these were used here for both transient expression and retroviral expression. Plasmids encoding for wild-type ULK1–Myc, wild-type ULK1–HA, K461 Ulk1–Myc and ATG13–FLAG were provided by S. A. Tooze. ULK1 deletion constructs were provided by D. H. Kim. AMBRA1 mutants for TRAF6-binding sites and for Ser 52 were generated by using the site-directed mutagenesis kit (Agilent Technologies). The sequences used were as follows: E620A 5'-GGCAGCCAGTTGCCACCTCTCGCGCGGACTGAGGGCCAAACG-3'; E682A 5'-CCTTACATCAGGATATGCCTGAGGCCGAGCTCTGAGGAGGATTC-3'; S52A 5'-GAGAGTAGAACTGCCGAGATGCTCCACGCTCTACCTTC-3'; S52E 5'-GAGAGTAGAACTGCCGAGATGACCCACGCTCTACCTTC-3'. TRAF6 and ubiquitin constructs were from Addgene. Ambra1 cDNA wild-type and mutants were subcloned from pLPCX, by cutting with NdeI and NotI (blunted) restriction enzymes, and transfer into the pRRL lentiviral plasmid digested with NdeI and SalI (blunted).

Cell culture and reagents. HEK293, MEF and HeLa cells were cultured in Dulbecco's modified Eagle's medium (DMEM, Sigma) supplemented with 10% fetal bovine serum (FBS, Sigma), 2 mM L-glutamine and 1% penicillin/streptomycin

solution at 37 °C. All co-immunoprecipitation and co-localization experiments were performed in HEK293 cells; instead, the gene modulation and functional assays were carried out in HeLa cells. For autophagy induction, cells were washed with PBS and cultured for 1–2 h in Earle's balanced salt solution (EBSS; Invitrogen) or treated with rapamycin (100 nM), 35 µM cycloheximide (Sigma), 20 µM MG132 (Sigma) or with 250 nM Torin1 (Tocris). HeLa and HEK293 cells were transiently transfected using Lipofectamine 2000 (Invitrogen) as indicated by the supplier.

Retrovirus and lentiviral generation and infection. The retroviral vectors (15 µg) were co-transfected with 5 µg of an expression plasmid for the vesicular stomatitis virus G protein into the HEK293 gp/bsr cell line. At 48 h later, the supernatant containing the retroviral particles was recovered and supplemented with Polybrene (4 µg ml⁻¹). HeLa cells were infected by incubation with retrovirus-containing supernatant for 6–8 h. For AMBRA1 ectopic expression, lentiviral particles were produced by transfecting HEK293 cells with pRRL–Ambra1 pMDLg, pRRE and pRSV–Rev plasmids. For stable Ambra1 RNA interference, a pLKO.1 plasmid carrying a short hairpin sequence targeting Ambra1 mRNA, obtained from Sigma–Aldrich (clone TRCN0000168652), was co-transfected with pMDLg and psPAX2 plasmids in HEK293 and supernatants were collected 48 h post-transfection. A pLKO.1 plasmid carrying a short hairpin sequence that does not target known mammalian genes was used as a control in lentiviral infection.

RNA interference. AMBRA1 siRNA oligonucleotides were described previously¹⁰. Stealth RNAi oligonucleotides were used for human ATG13 and the sequences used were as follows: sense, 5'-CCAUGUGUGGAGAUUUUACUUAA-3'; antisense, 5'-UUAAGUAAUCUCCACACACAUGG-3'. TRAF6 siRNA oligonucleotides were as follows: sense, 5'-CCACGAAGAGAUAAUGGAUGCCAAA-3'; antisense, 5'-UUUGCAUCCAUUAUCUCUUGGUGG-3'. For stable downregulation of AMBRA1 we used lentiviral vectors as indicated.

Immunocytochemistry. Cells were washed in PBS and fixed with 4% paraformaldehyde in PBS for 15 min. After permeabilization with 0.4% Triton X-100 in PBS for 5 min, cells were blocked in 3% horse serum in PBS and incubated overnight at 4 °C with primary antibodies. Cells were then washed and incubated for 1 h with labelled anti-mouse (Alexa Fluor-488, Molecular Probes) or anti-rabbit (FITC, Jackson ImmunoResearch; Alexa Fluor-647 donkey anti-Rabbit) secondary antibodies. Images were examined under a Zeiss LSM 700 confocal microscope equipped with a ×100 (NA 1.4) oil-immersion objective (Deerfield).

Real-time PCR. RNA was isolated by using the RNeasy Micro Kit (Qiagen), according to the manufacturer's instructions. Real-time PCR was performed using the SensiMix Plus SYBR Kit (Quantace). The primer sets used were as follows: mouse Ulk1 forward, 5'-TTACCAGCGCATCGAGCA-3'; reverse, 5'-TGGGGAGAAGGTGTGTGTA-GGG-3'. Real-time quantification was performed by using a Fast-Real Time PCR System (Applied Biosystems). Data were normalized to β-actin. Fold-change was determined by using the 2^{-ΔΔCT} method and all reactions were performed in triplicate.

Mass spectrometry. Samples were taken up in SDS–PAGE loading buffer, reduced with 1 mM dithiothreitol (Sigma) for 5 min at 95 °C and alkylated using 5.5 mM iodoacetamide (Sigma) for 30 min at 25 °C. Protein mixtures were separated by SDS–PAGE, and the gel lanes were cut into 10 equal slices, which were in-gel digested with trypsin (Promega). Peptides were incubated with 10 µl of a 30% TiO₂ slurry (MZ-Analysentechnik) in 30 mg ml⁻¹ DHB (Sigma–Aldrich) for 30 min at room temperature. Beads were washed with 100 µl of 10% ACN and 1% TFA followed by 100 µl 80% ACN and 1% TFA and finally 100 µl water. Phosphopeptides were eluted using 25% ammonium hydroxide in 20% and 40% ACN, respectively. Mass spectrometric measurements were performed on an LTQ Orbitrap XL mass spectrometer (Thermo Fisher Scientific) coupled to an Agilent 1200 nanoflow-HPLC (Agilent Technologies GmbH). Samples were applied directly onto the column without a pre-column. A gradient of A (0.5% acetic acid in water) and B (0.5% acetic acid in 80% ACN) with increasing organic proportion was used for peptide separation. The flow rate was 250 nl min⁻¹ and for sample application 500 nl min⁻¹. The mass spectrometer was operated in the data-dependent mode and switched automatically between MS (maximum of 1 × 10⁶ ions) and MS/MS. Each MS scan was followed by a maximum of five MS/MS scans in the linear ion trap using 35% collision energy and a target value of 5,000. Parent ions with a charge state of

$z = 1$ and unassigned charge states were excluded for fragmentation. For MS/MS, wideband activation and multi-stage activation were enabled with the neutral loss mass list of singly, doubly and triply phosphorylated peptides. The mass range for MS was $m/z = 350\text{--}2,000$ and the signal threshold was 1,000. The resolution was set to 60,000. Mass spectrometric parameters were as follows: spray voltage 2.3 kV; no sheath and auxiliary gas flow; ion-transfer tube temperature 200 °C.

Statistical analysis. For all experiments shown, n is indicated in the figure legends. Densitometric analysis was performed using the ImageJ software: the average of the values from different experiments (as indicated) related to the control ratio was arbitrarily defined as 1.00. Each point value represents the mean \pm s.d. from three independent experiments unless specified otherwise. Comparison between control

and sample in the western blot intensity measurement was made from the same western blot. Statistical significance was measured by an unpaired t -test. For the count of GFP-LC3-positive autophagosomes, five different confocal microscopy images were randomly chosen and GFP-positive dots were examined on the images with identical brightness and contrast settings. The total number of cells on images was determined by nuclei staining with DAPI (4',6-diamidino-2-phenylindole). Quantification was carried out by counting 50 or 100 cells for each experiment as indicated in the figure legends and calculating the percentage of cells with each phenotype after each experiment. The graphs relative to the count of puncta show the average percentage \pm s.e.m. A statistic checklist file, including single values corresponding to the graphs, is included as a separate spreadsheet (Supplementary Table S1).

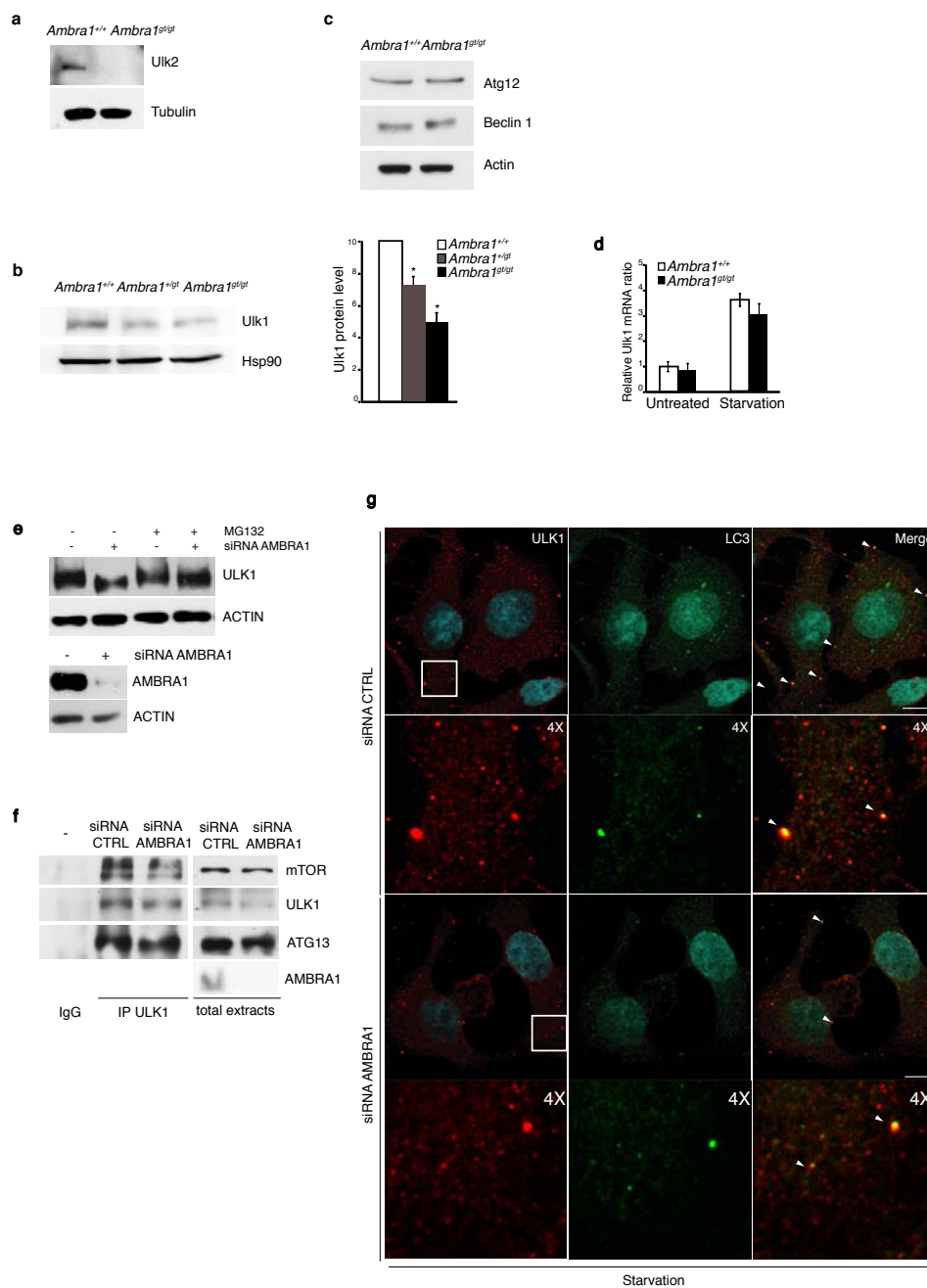


Figure S1 Expression analysis of autophagy-related molecules upon AMBRA1 regulation. **(a)** Protein extracts from wild-type (*Ambra1*^{+/+}) and homozygous (*Ambra1*^{glt/glt}) embryos for the *Ambra1* gene-trap mutation at developmental day 14.5 were analysed by WB using anti-Ulk2 or anti-Tubulin (loading control) antibodies. **(b)** Protein extracts from *AMBRA1*^{+/+}, *AMBRA1*^{+/glt} and *AMBRA1*^{glt/glt} MEFs were analysed by WB using an anti-Ulk1 or anti-Hsp90 (loading control) antibodies. Quantification is shown **(b, right)**. n=3 extracts prepared from independent experiments. Data are presented as means±s.d and significance is P=0.04 and P=0.02. **(c)** Protein extracts from *AMBRA1*^{+/+} and *AMBRA1*^{glt/glt} MEFs were analysed by WB using an anti-Beclin 1, anti-Atg12 and anti-Actin antibodies. **(d)** *Ambra1*^{+/+} and *Ambra1*^{glt/glt} MEF cells were cultured in the complete or starvation medium for 2 hours. *Ulk1* mRNA expression was analysed by real-time PCR and normalized to β -Actin mRNA levels. The relative expression is presented as a fraction of the mRNA

level detected in wild-type MEFs cultured in complete medium. Data are presented as means±s.d; n=5 independent experiments. **(e)** HeLa cells were transfected with scramble siRNA or AMBRA1 siRNA and treated for 6 hours with MG132. ULK1, AMBRA1 and ACTIN were analysed by WB. **(f)** HeLa cells were transfected with AMBRA1 RNAi oligonucleotide (siRNA AMBRA1) or unrelated oligonucleotide as a control (siRNA CTRL) and protein extracts were immunoprecipitated using anti-ULK1 antibody or with IgG as a control. Purified complexes and total extracts were analysed by WB using anti-ULK1, anti-ATG13, anti-mTOR and anti-AMBRA1 antibodies. **(g)** HeLa cells were transfected as in **(f)** and grown in starvation medium for 1 hour. The cells were subjected to an immunofluorescence analysis using anti-ULK1 and anti-LC3 antibodies. Scale bar, 10 μ m. White arrows point to the co-localisation puncta. The inserts are shown at higher magnification in lower panels. Source data of statistical analysis are shown in the Supplementary Table 1.

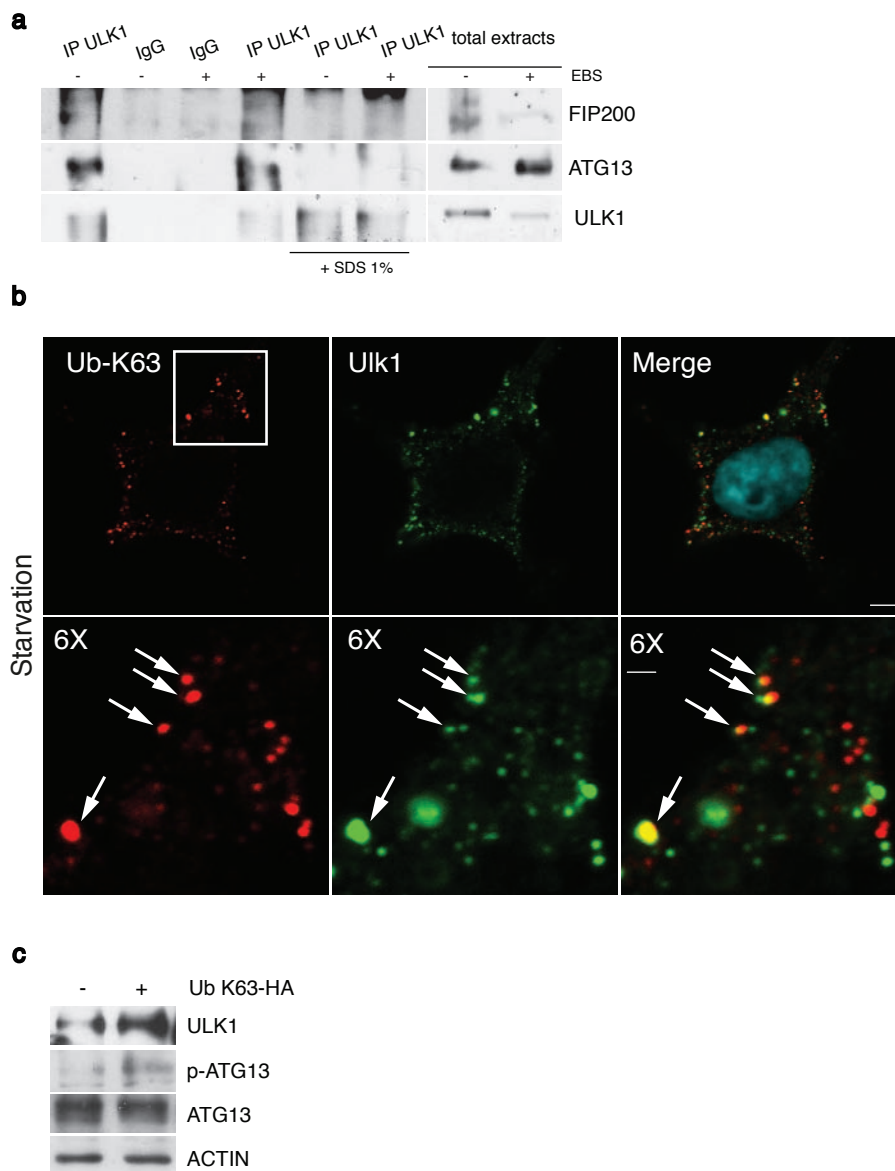


Figure S2 Analysis of ULK1 K63-linked ubiquitination. **(a)** HeLa cells were grown in normal medium or in starvation medium for 1 hour. Protein extracts were treated or not with SDS 1% as indicated and immunoprecipitated using anti-ULK1 antibody or with IgG as a control. Purified complexes and total extracts were analysed by WB using anti-ULK1, anti-ATG13, anti-FIP200 antibodies. **(b)** HEK293 cells grown in starvation medium for 30 minutes in presence of 15 μ M of leupeptin

and were stained by anti-ULK1 (Red) and anti-K63 ubiquitin (Green) antibodies. The merge of the two fluorescence signals is shown in the right panels. Scale bar, 6 μ m. The inserts are shown at higher magnification in lower panels. White arrows point to the co-localisation *puncta*. **(c)** HEK293 were transfected with vector encoding K63-ubiquitin chains and protein extracts were analysed using anti-ULK1, anti-ATG13, anti-pATG13 and anti-ACTIN antibodies.

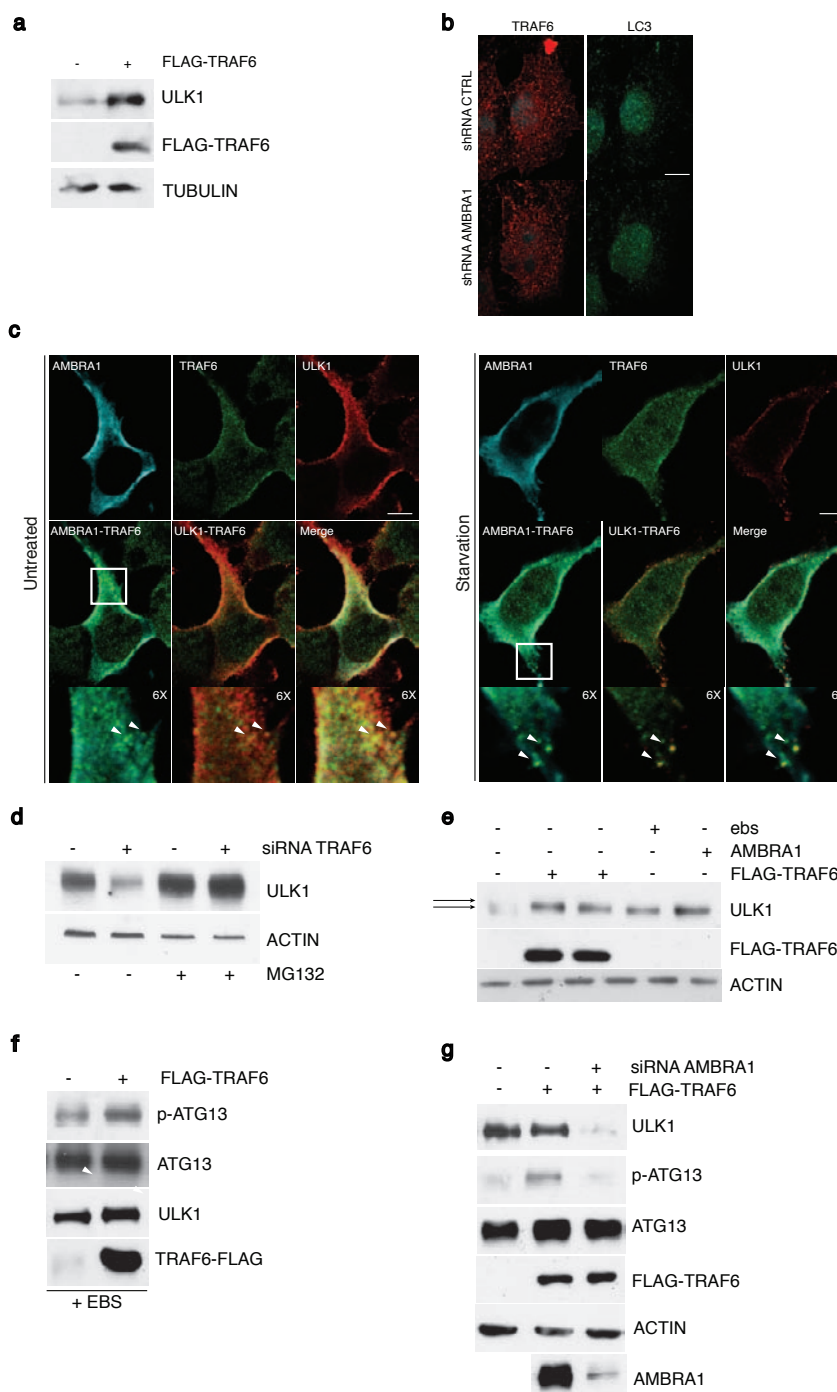


Figure S3 Study of TRAF6 activity on autophagy network regulation. **(a)** Total extracts relative to the experiment in Figure 4a are shown. ULK1, FLAG-TRAF6 and TUBULIN were analysed by WB. **(b)** The images are relative to the count of LC3 dots shown in Figure 4c. HeLa cells were transfected with indicated lentiviral vectors and transfected with TRAF6-FLAG. Cells were stained using TRAF6 (Red) and LC3 (Green) antibodies. **(c)** HEK293 cells, cultured in the complete or starvation medium for 1 hour, were stained by anti-ULK1 (Red), anti-TRAF6 (Green) and anti-AMBRA1 (blue) antibodies. The merge of AMBRA1-TRAF6 and ULK1-TRAF6 fluorescence signals is shown and also the merge of the three fluorescence signals. Scale bar, 6 μ m. The inserts are shown at higher magnification in lower panels. White

arrows point to the co-localisation *puncta*. **(d)** In HeLa cells, TRAF6 was downregulated by RNAi and then cells were treated for 6 hours with MG132. ULK1 and ACTIN were analysed by WB. **(e)** HeLa cells were transfected with FLAG-TRAF6 or AMBRA1 plasmids respectively; then, transfected cells were treated with starvation medium for 1 hour. ULK1, TRAF6-FLAG and ACTIN were analysed by WB. **(f)** HeLa cells were transfected or not with FLAG-TRAF6. ATG13, pATG13, ULK1 and FLAG-TRAF6 were analysed by WB. **(g)** In HeLa cells AMBRA1 was downregulated by RNAi. Then, the cells were newly transfected with FLAG-TRAF6. Protein extracts were analysed by WB using anti-pATG13, anti-ATG13, anti-ULK1, anti-FLAG, anti-AMBRA1 and anti-ACTIN antibodies.

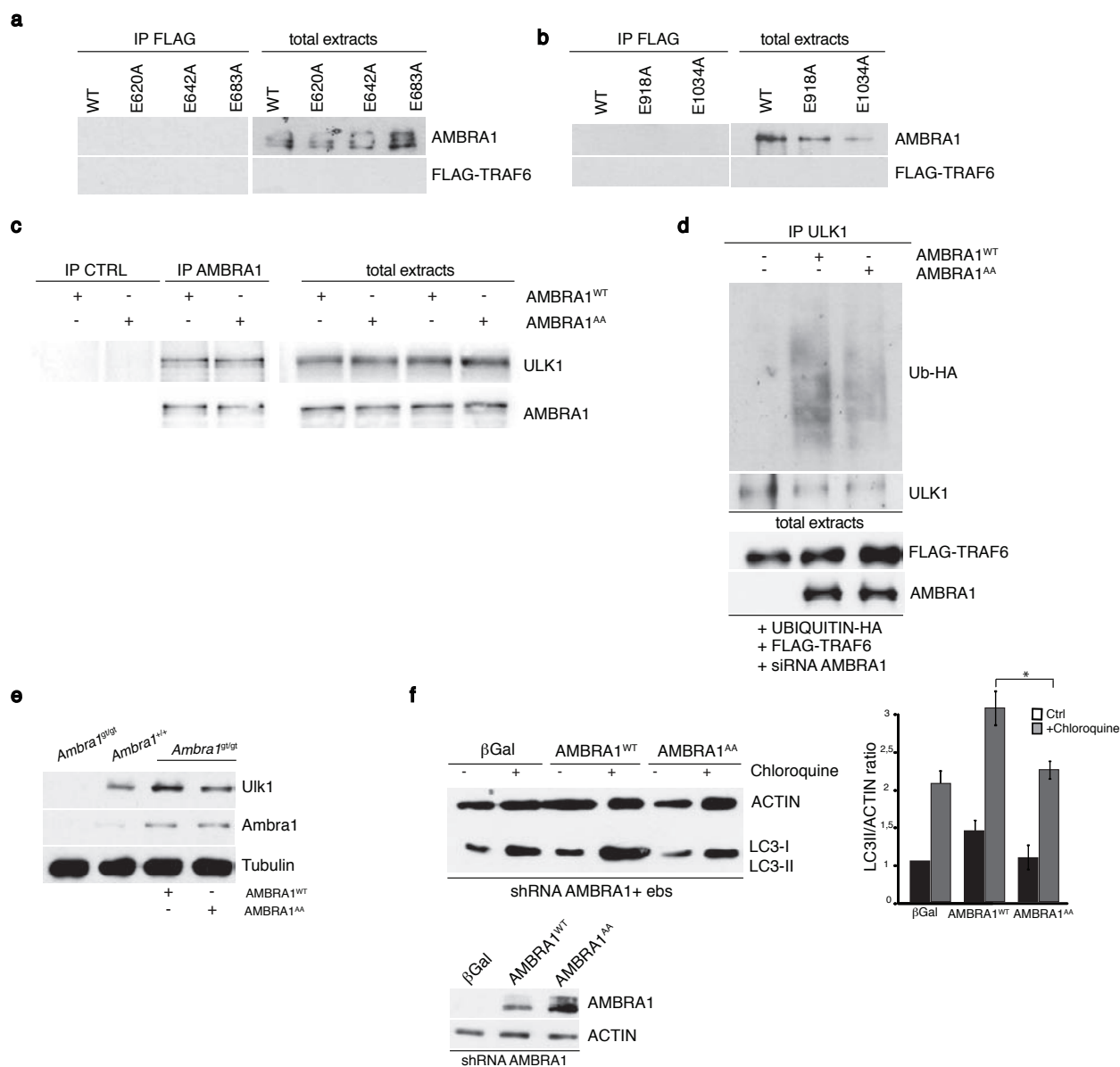


Figure S4 Structural and functional analysis of AMBRA1-TRAF6 interaction. **(a,b)** As control of the immunoprecipitations showed in Figure 5a-d, an anti-FLAG antibody was used for immunoprecipitation in the presence of the different AMBRA1 mutant constructs. Anti-FLAG and anti-AMBRA1 antibodies were used for WB. **(c)** HeLa cells were transfected with AMBRA1^{WT} and AMBRA1^{AA} constructs and immunoprecipitation was performed using anti-AMBRA1 antibody. Purified complexes and total extracts were analysed using anti-ULK1 and anti-AMBRA1 antibodies. **(d)** HeLa cells were transfected as in Figure 5d. After 24 hours, the cells were newly transfected with plasmids encoding FLAG-TRAF6 and Ubiquitin-HA. Protein extracts were

immunoprecipitated and analyzed as in **(5d)**. **(e)** Mefs cells from wild-type (*Ambra1*^{+/+}) and homozygous (*Ambra1*^{gt/gt}) embryos were transduced with lentiviral vectors coding for AMBRA1^{WT} or AMBRA1^{AA} respectively. Ulk1, Ambra1 and Tubulin were analysed by WB. **(f)** HeLa cells stably interfered for AMBRA1 were transduced with lentivirus coding for βGal (as negative control) AMBRA1^{WT} or AMBRA1^{AA} and starved for 1 hour; some of them were treated with chloroquine. LC3, AMBRA1 and ACTIN were analysed by WB. Quantification of LC3II is shown **(f, right)**. n=3 extracts prepared from independent experiments. Data are presented as means±s.d. and significance is P=0.04. Source data of statistical analysis are shown in the Supplementary Table 1.

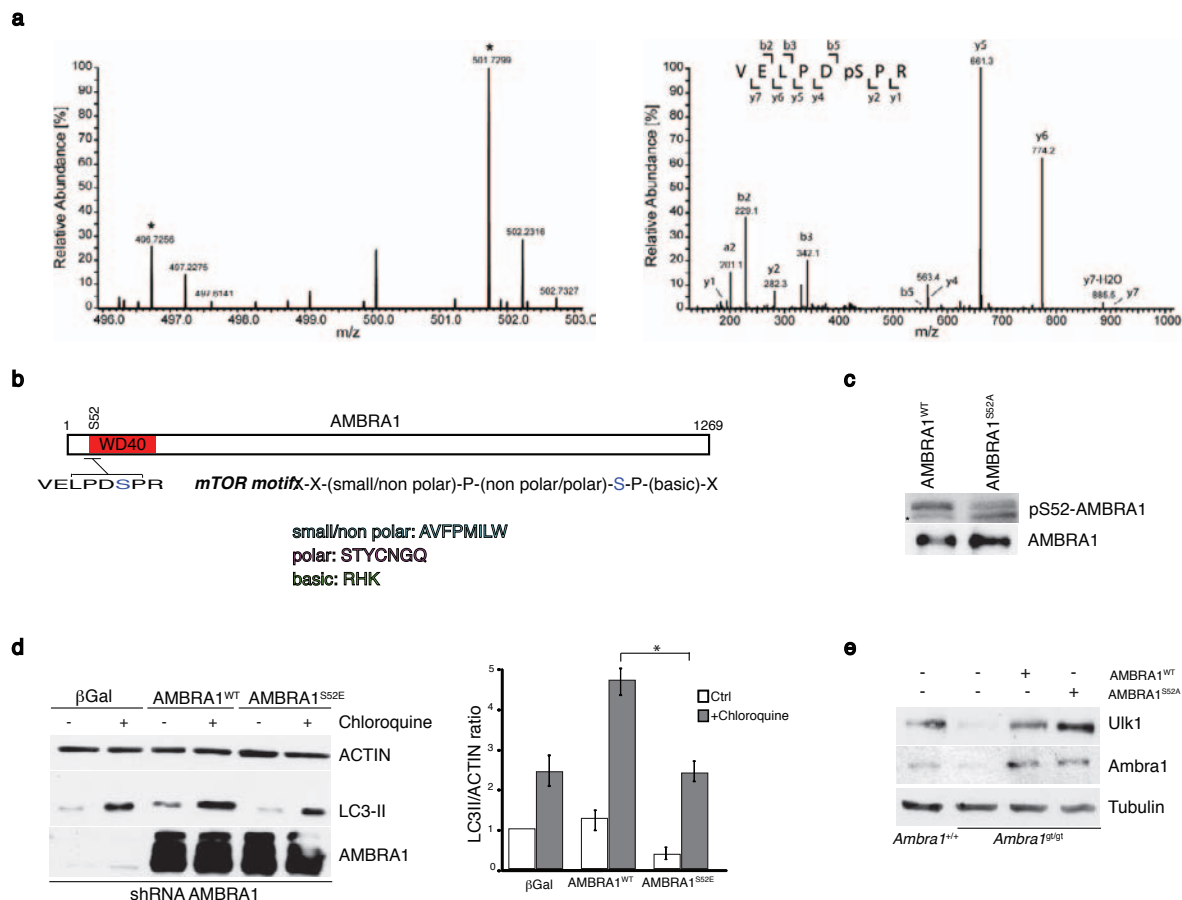


Figure S5 Study of AMBRA1 modification by mTOR. **(a)** Mass spectrometry analysis of AMBRA1 phosphorylation during autophagy. Cells were SILAC-labeled and starved for 0 h (Arg10) and 4 h (Arg0). Subsequently cells were combined, lysed, and AMBRA1-Flag-HA complexes purified by immunoprecipitation. Protein extracts were separated by SDS-PAGE and digested by trypsin. The resulting peptide mixtures were enriched for phosphorylated peptides by TiO_2 and analyzed by LC-MS/MS. The left panel shows the MS spectrum of the SILAC pair. Monoisotopic peaks are marked by asterisks. The right panel shows the fragment spectrum of the heavy labeled (Arg10) version of the peptide AMBRA1_{47-54} being phosphorylated on Ser_{52} . **(b)** Schematic representation of AMBRA1 protein structure with the mTOR target site Serine52 and its similarity to mTOR phosphoacceptor

motif. **(c)** Detection of p-S52-AMBRA1 using a p-S52 AMBRA1 antibody. Immunoblotting of protein extracts isolated from HEK293 cells transfected with FLAG-AMBRA1^{WT} or with FLAG-AMBRA1^{S52A} are probed with p-S52 AMBRA1 or FLAG antibodies. **(d)** HeLa cells stably interfered for AMBRA1 were transfected with vectors encoding βGal (as negative control) AMBRA1^{WT} or AMBRA1^{S52E} and some of them were treated with chloroquine. LC3, AMBRA1 and ACTIN were analysed by WB. Quantification of LC3II and is shown (f, right). n=3 extracts prepared from independent experiments. Data are presented as means±s.d. and significance is P=0.04. **(e)** Mef cells from wild-type (*Ambra1*^{+/+}) and homozygous (*Ambra1*^{g/gt}) embryos were transfected with indicated lentiviral vectors and Ulk1, Ambra1 and Tubulin were analysed by WB. Source data of statistical analysis are shown in the Supplementary Table 1.

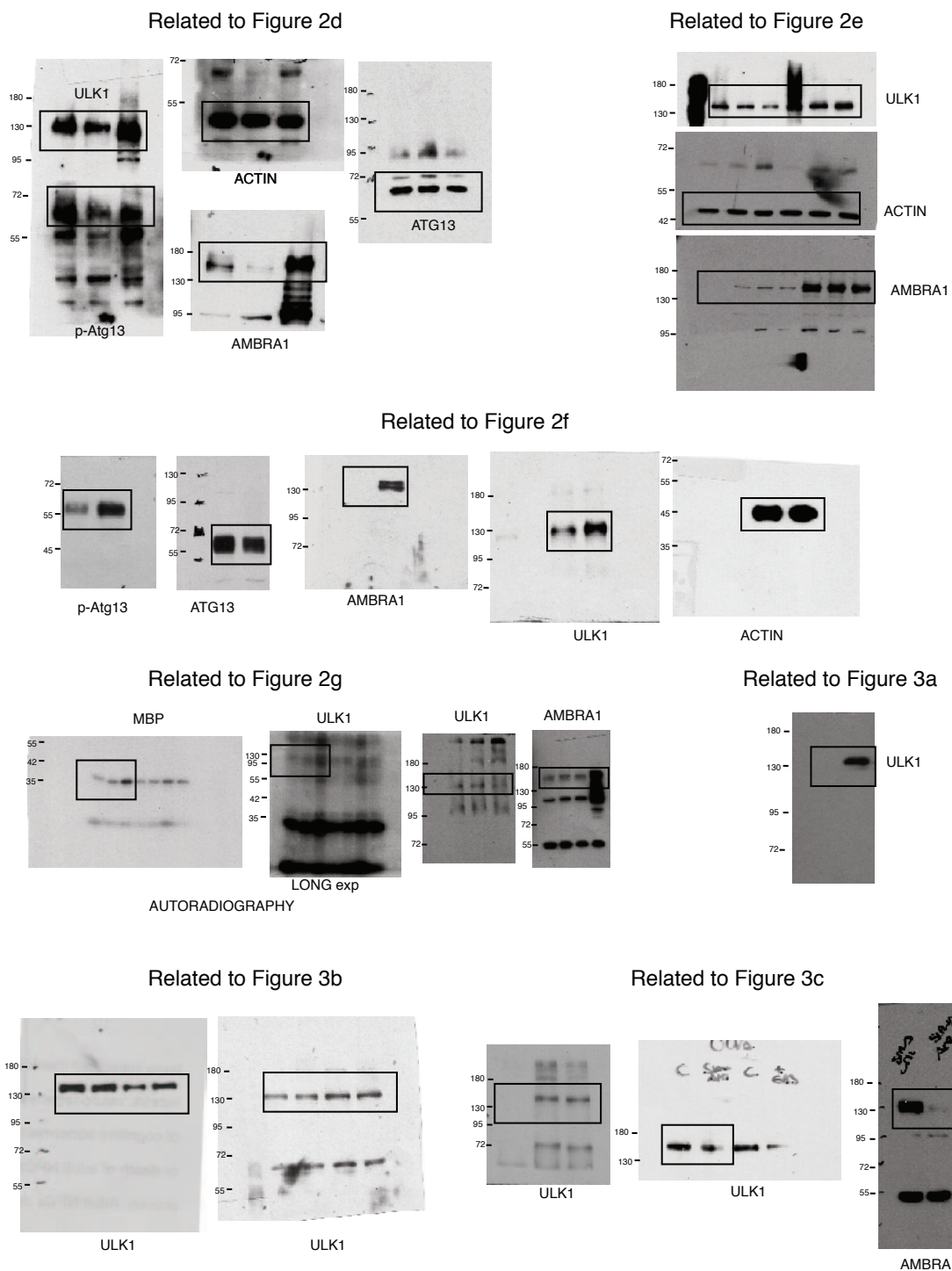


Figure S6 continued

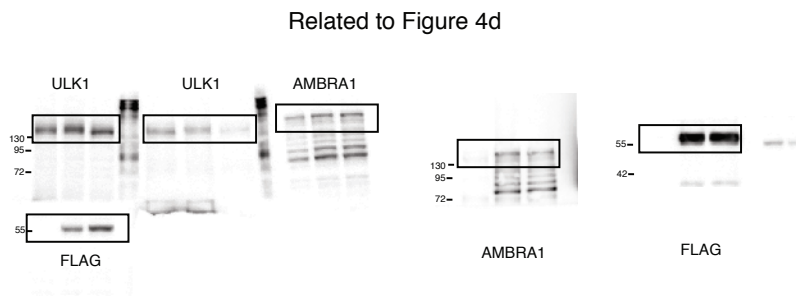
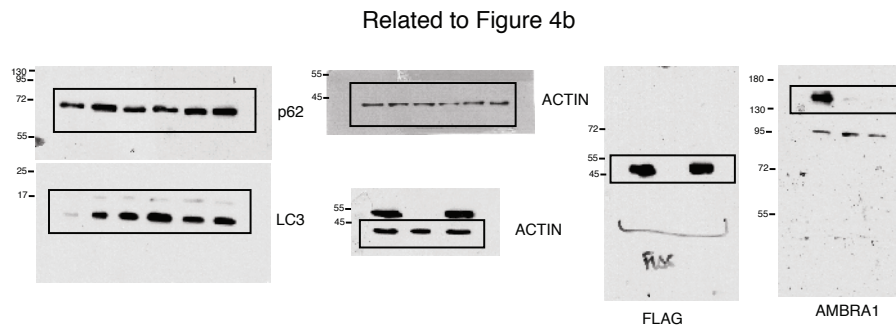
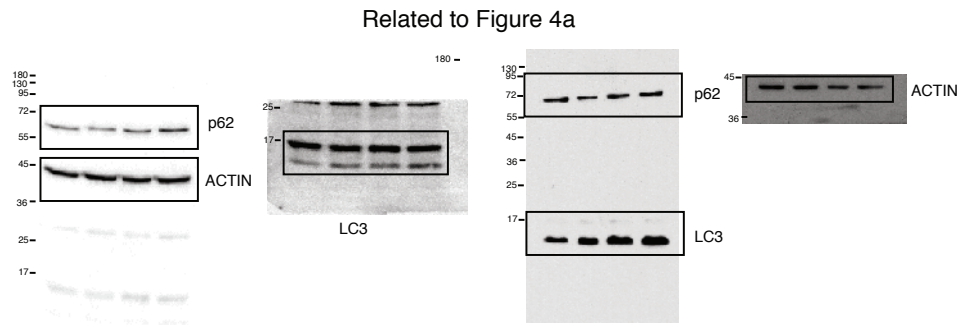
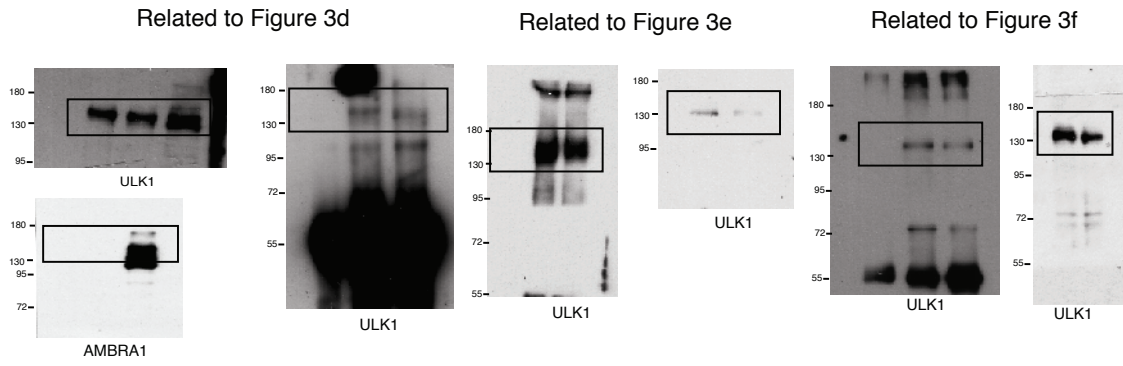


Figure S6 continued

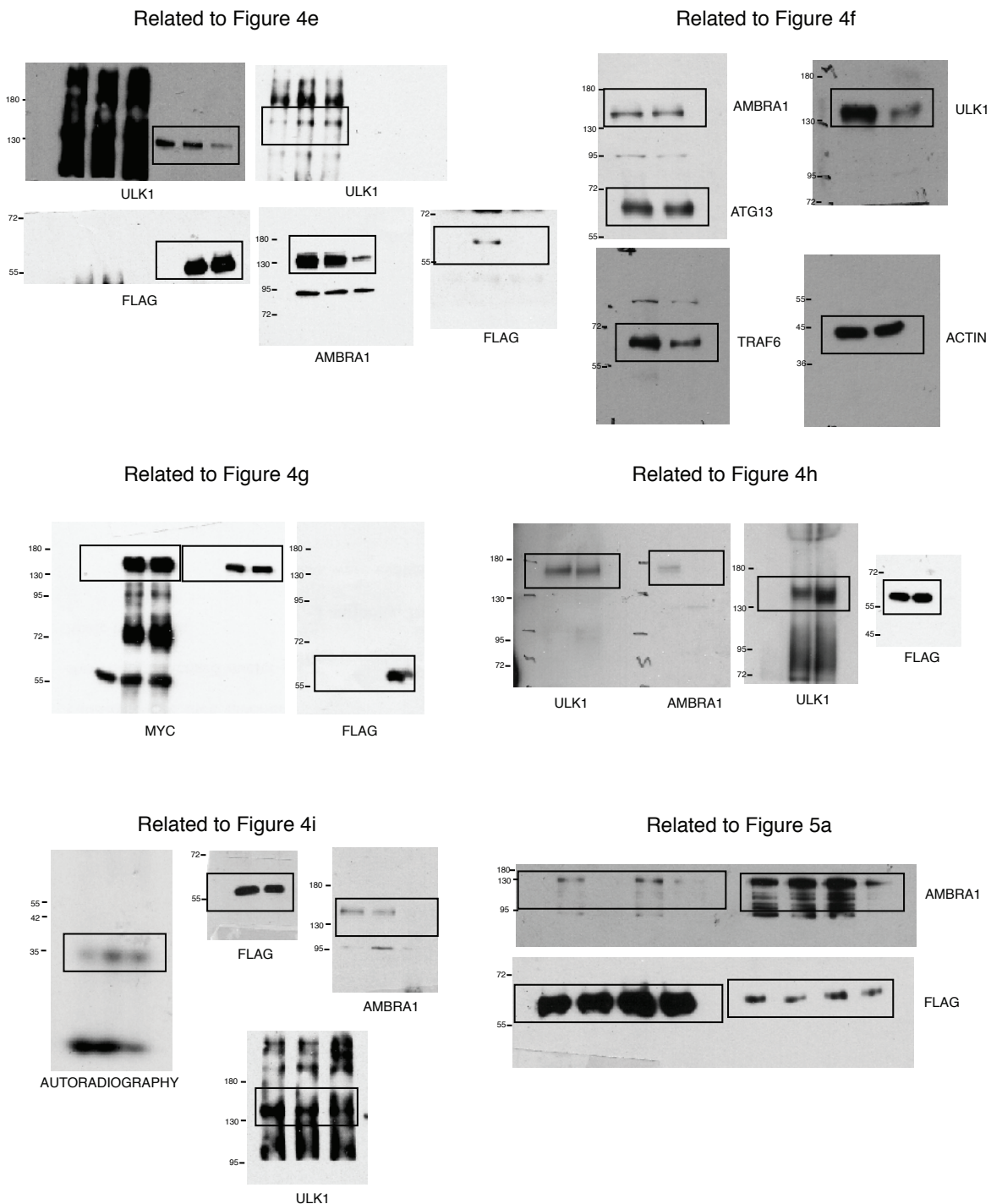


Figure S6 continued

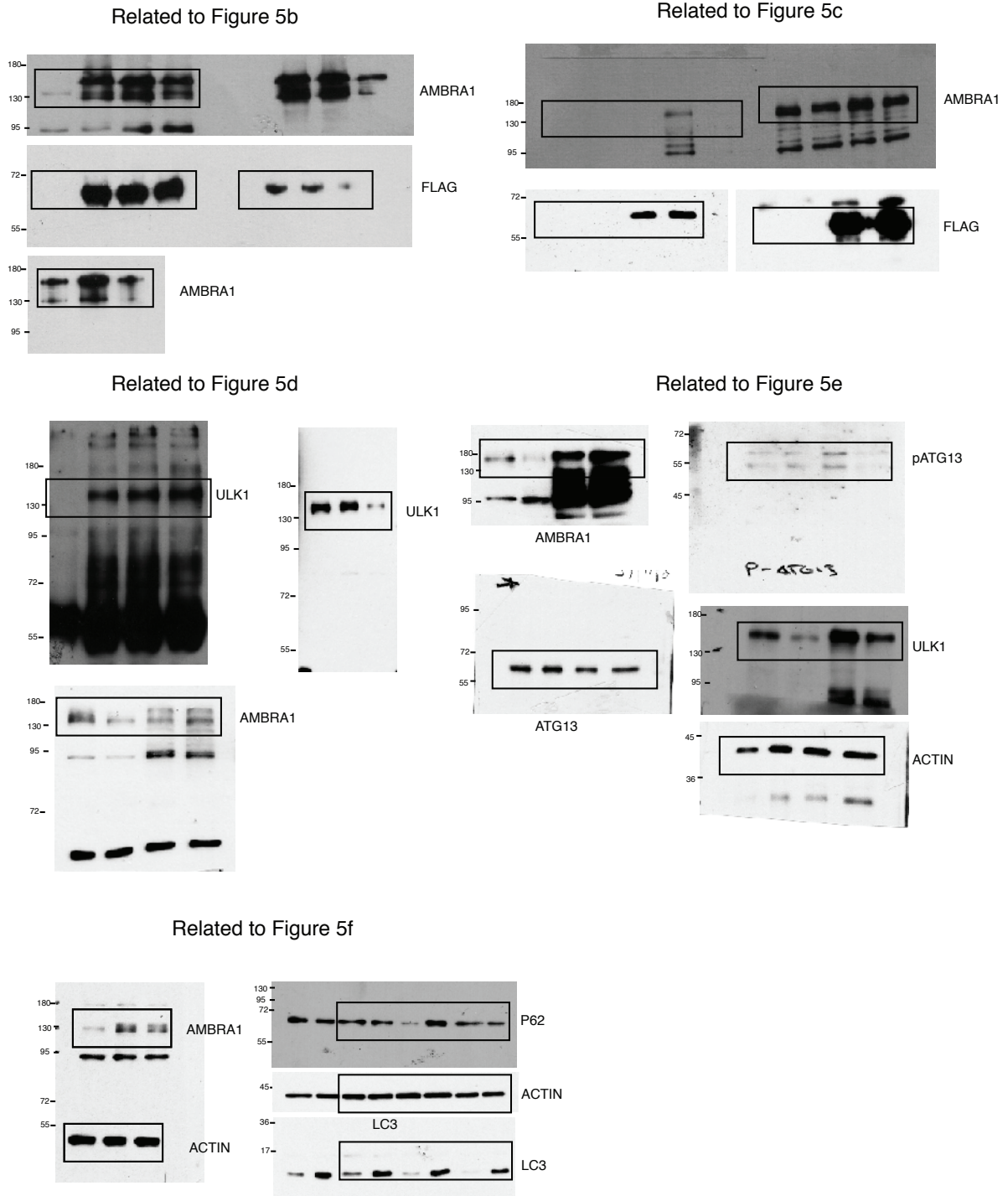
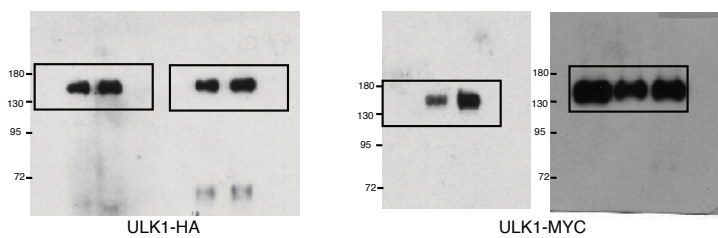
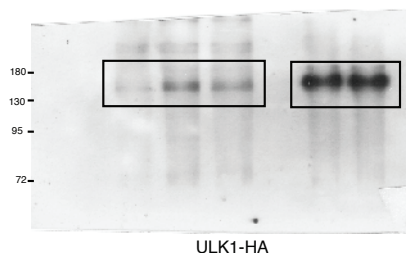


Figure S6 continued

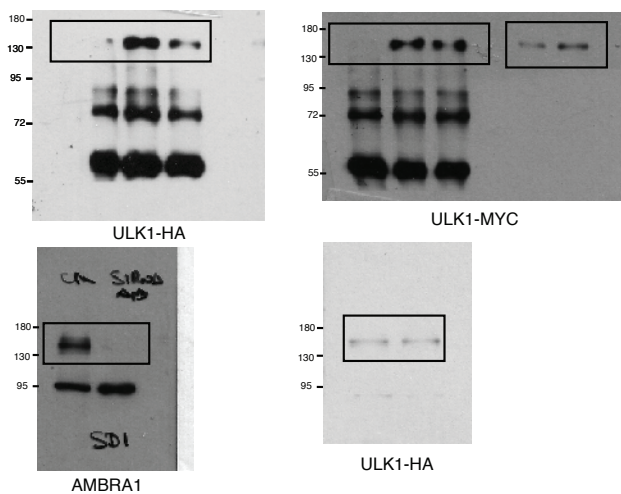
Related to Figure 6a



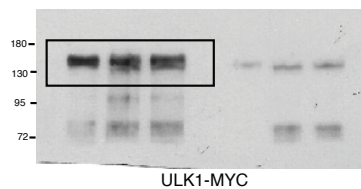
Related to Figure 6b



Related to Figure 6c



Related to Figure 6d



Related to Figure 7a

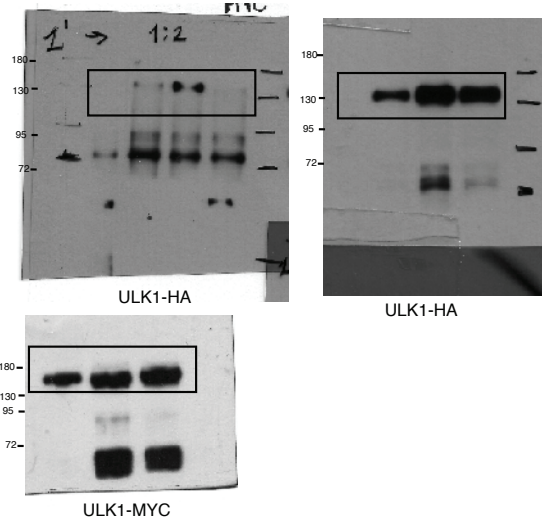
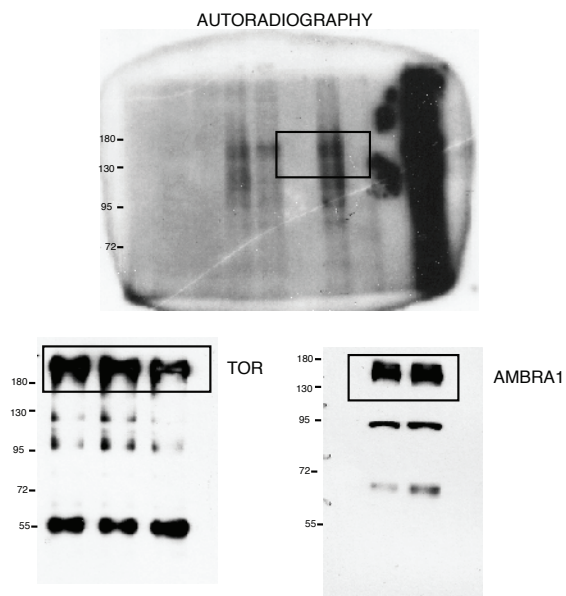


Figure S6 continued

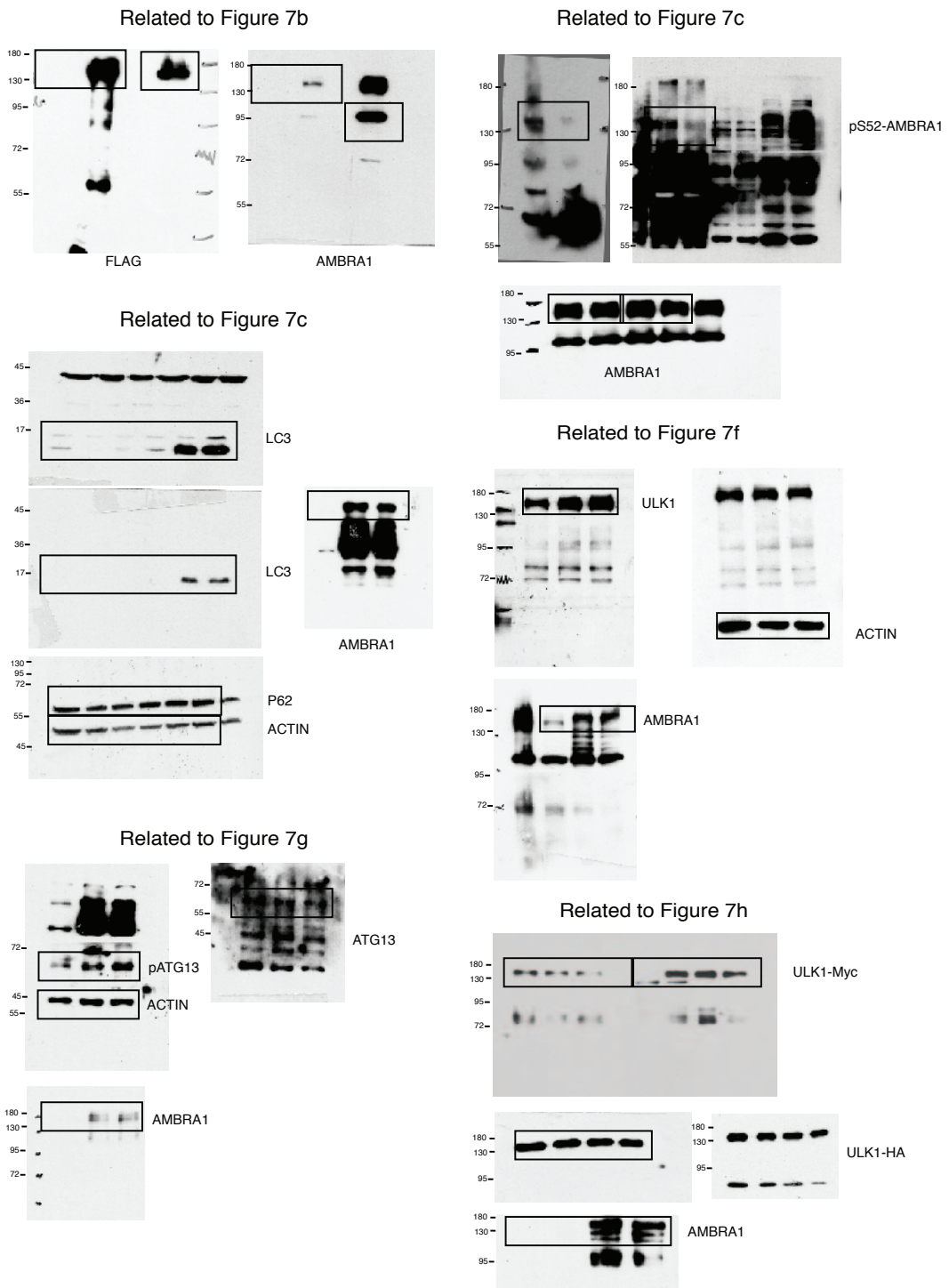


Figure S6 continued




MIR7-3HG, a MYC-dependent modulator of cell proliferation, inhibits autophagy by a regulatory loop involving AMBRA1

Mariacristina Capizzi, Flavie Strappazon, Valentina Cianfanelli, Elena Papaleo & Francesco Cecconi


To cite this article: Mariacristina Capizzi, Flavie Strappazon, Valentina Cianfanelli, Elena Papaleo & Francesco Cecconi (2017) *MIR7-3HG*, a MYC-dependent modulator of cell proliferation, inhibits autophagy by a regulatory loop involving AMBRA1, *Autophagy*, 13:3, 554-566, DOI: [10.1080/15548627.2016.1269989](https://doi.org/10.1080/15548627.2016.1269989)

To link to this article: <https://doi.org/10.1080/15548627.2016.1269989>


 View supplementary material [↗](#)

 Accepted author version posted online: 06 Jan 2017.
Published online: 06 Feb 2017.

 Submit your article to this journal [↗](#)

 Article views: 606

 View Crossmark data [↗](#)

 Citing articles: 5 View citing articles [↗](#)

BASIC RESEARCH PAPER

MIR7–3HG, a MYC-dependent modulator of cell proliferation, inhibits autophagy by a regulatory loop involving AMBRA1

Mariacristina Capizzi^{a,b}, Flavie Strappazon^b, Valentina Cianfanelli^c, Elena Papaleo^d, and Francesco Cecconi^{a,c,e}

^aDepartment of Biology, University of Tor Vergata, Rome, Italy; ^bIRCCS Fondazione, Santa Lucia, Rome, Italy; ^cUnit of Cell Stress and Survival, Danish Cancer Society Research Center, Copenhagen, Denmark; ^dComputational Biology Laboratory, Danish Cancer Society Research Center, Copenhagen, Denmark; ^eDepartment of Pediatric Hematology and Oncology, IRCCS Bambino Gesù Children's Hospital, Rome, Italy

ABSTRACT

Macroautophagy/autophagy is a tightly regulated intracellular catabolic pathway involving the lysosomal degradation of cytoplasmic organelles and proteins to be recycled into metabolic precursors. AMBRA1 (autophagy and Beclin 1 regulator 1) has a central role in the autophagy signaling network; it acts upstream of MTORC1-dependent autophagy by stabilizing the kinase ULK1 (unc-51 like autophagy activating kinase 1) and by favoring autophagosome core complex formation. AMBRA1 also regulates the cell cycle by modulating the activity of the phosphatase PPP2/PP2A (protein phosphatase 2) and degradation of MYC. Of note, post-transcriptional regulation mediated by noncoding microRNAs (MIRNAs) contributes significantly to control autophagy. Here we describe a new role for the microRNA *MIR7–3HG/MIR-7* as a potent autophagy inhibitor. Indeed, *MIR7–3HG* targets the 3' untranslated region (UTR) of *AMBRA1* mRNA, inducing a decrease of both *AMBRA1* mRNA and protein levels, and thus causing a block in autophagy. Furthermore, *MIR7–3HG*, through *AMBRA1* downregulation, prevents MYC dephosphorylation, establishing a positive feedback for its own transcription. These data suggest a new and interesting role of *MIR7–3HG* as an anti-autophagic MIRNA that may affect oncogenesis through the regulation of the tumor suppressor *AMBRA1*.

ARTICLE HISTORY

Received 26 February 2016
Revised 23 November 2016
Accepted 1 December 2016

KEYWORDS

BECN1; lung cancer; microRNA; MTOR; PPP2/PP2A

Introduction

Macroautophagy (hereafter referred to as autophagy) is a highly conserved catabolic pathway that is involved in cellular degradation of long-lived proteins or dysfunctional cellular components, through the action of lysosomes.¹ Central to this process is the formation of the autophagosome, a double-membraned vesicle, which is responsible for the delivery of cytosolic cargoes to the lysosome.² In addition to its housekeeping and homeostatic function, autophagy constitutes a key prosurvival response that allows adaptation to unfavorable conditions.^{3,4,5} Autophagy is essential for normal development,^{6,7} and defects in this process are linked to numerous human diseases, including neurodegeneration and cancer; this fact underlines why tight control of autophagy is essential.^{8,9} In a tumor microenvironment, autophagy promotes cancer cell survival in response to metabolic stress.^{10,11} However, hyperactivation of autophagy can lead to cell death, and human cancers often display inactivating mutations in autophagy-promoting genes.^{12,13} Thus, in relation to tumorigenesis, the role of autophagy is complex and likely depends on the genetic background of the cell as well as on the environmental cues the cell is exposed to.¹⁴


MicroRNAs (MIRNAs), a class of small noncoding RNAs, can bind the 3' untranslated region (UTR) of target messenger RNAs (mRNAs), causing translational inhibition or mRNA

destabilization.¹⁵ In recent years, MIRNAs have been closely linked to the post-translational regulation of almost all fundamental biological pathways, including autophagy.^{16,17,18,19} Conversely, autophagy is also important to maintain MIRNA homeostasis.²⁰ Recent data provide evidence that under stress conditions, a number of MIRNAs including MIR30A, MIR101, MIR130A, and MIR196 are capable of modulating autophagy activity by changing intracellular levels of key autophagy proteins.^{21,22}

This bidirectional crosstalk has been defined as the autophagoMIR pathway,²³ and its deregulation is obviously central to cancer oncogenesis and progression. Here we describe a new member of this pathway. In fact, *MIR7–3HG* turns out to be an anti-autophagic MIRNA that acts through the downregulation of *AMBRA1*, a key protein in autophagy. *AMBRA1* has been identified as a pivotal factor in regulating autophagy in vertebrates,^{24,25} which promotes the interaction of BECN1/Beclin 1 with its target lipid kinase, PI3K3C3/Vps34, thereby mediating the early phase of autophagy in autophagosome nucleation.²⁶ Several *AMBRA1* interaction partners have been identified so far,²⁷ highlighting the pivotal role of this protein as an efficient scaffold-molecule that is able to coordinate many intracellular processes with autophagy.^{28,29} Also, a number of *AMBRA1*

CONTACT Francesco Cecconi ✉ cecconi@cancer.dk; francesco.cecconi@uniroma2.it ✉ Department of Biology, University of Rome Tor Vergata, Via della Ricerca Scientifica, 00133 Rome, Italy; Danish Cancer Society Research Center, Strandboulevarden 49, 2100 Copenhagen, Denmark.

Color versions of one or more of the figures in the article can be found online at www.tandfonline.com/kaup.

 Supplemental data for this article can be accessed on the publisher's website.

post-translational modifications were characterized, while very little is known about its transcriptional regulation. In this study we have characterized MIR7-3HG and AMBRA1 regulatory interaction in a number of cell lines, and subsequently focused on a model of lung cancer (the A549 cell line) exhibiting low levels of AMBRA1 and high levels of the MIR7-3HG transcriptional regulator MYC.^{28,30} Of note, even though MIR7-3HG is generally described to have a tumor-suppressive role,³¹ in some instances the opposite effect has also been reported. In particular, in lung carcinomas, a poor prognosis is associated with MIR7-3HG overexpression.³⁰ Furthermore, inhibition of MIR7-3HG causes reduced proliferation and increased apoptosis in HeLa and lung carcinoma cell lines, respectively,³² suggesting that high MIR7-3HG expression is not necessarily beneficial in terms of inhibiting carcinogenesis. In the present study, we also highlight MIR7-3HG as an oncogenic MIRNA promoting its own MYC-mediated transcription through the downregulation of the tumor suppressor AMBRA1.

Results

In silico analysis of most significant MIRNA candidates to target the AMBRA1 3' UTR

In order to identify and study which MIRNAs could potentially regulate autophagy through targeting the AMBRA1 3' UTR, we performed a global analysis using 4 independent target prediction algorithms, DIANA-microT v3.032, TargetScan 5.2,^{33,34} microrna.org³⁵ and PicTar.³⁶ We thus obtained a list of the MIRNA families broadly conserved among vertebrates (Fig. S1A). The majority of predicted MIRNAs were unknown regulators of autophagy, with the exception of MIR23B. In fact, MIR23B regulates autophagy, associated with radio-resistance in pancreatic cancer cells, through the targeting of ATG12 and HMGB2.³⁷ By contrast, the other predicted MIRNAs (MIR7-3HG, MIR9 and MIR200B) we identified could be potentially novel regulators of autophagy. To determine whether these MIRNAs' binding sites were functional on the full-length AMBRA1 3'-UTR, HeLa cells were cotransfected with MIRNA overexpressing plasmids and a reporter plasmid, containing Renilla luciferase fused to the AMBRA1 full-length 3'-UTR sequence. Indeed, MIR7-3HG overexpression suppressed significantly (47%) the activity of Renilla luciferase compared to the control, whereas MIR200B and MIR23B over-dosage had no effects on the reporter activity (Fig S1B). MIR9 caused, as well, a mild decrease (27%) in Renilla expression. As a consequence, we decided to focus our attention on MIR7-3HG whose overexpression led to a remarkable downregulation of Renilla activity (Fig. S1B).

AMBRA1 mRNA is a direct target of MIR7-3HG

A stable interaction based on partial base pairing between mature MIRNA and the 3'-UTR region of an mRNA (the "MIRNA responsive element", MRE) is crucial for MIRNA-dependent regulation of target mRNA and protein levels. A seed sequence is essential for the MIRNA::mRNA interaction and it is located in the MIRNA 5'-end, at position 2 to 7. In the seed region occurs the perfect match between a MIRNA and its

mRNA target, while additional residues of the mature MIRNAs stabilize the contact.³⁸ To validate the effect of MIR7-3HG on AMBRA1, its wild-type 3'-UTR region was cloned downstream of the cDNA encoding Renilla luciferase in the psiCHECK-2 vector (Fig. 1A, upper panel). In parallel, we also created a mutant version of this construct by introducing 2 nonconsecutive base changes in the seed region of the AMBRA1-specific MRE for MIR7-3HG (Fig. 1A, lower panel). Co-transfection of

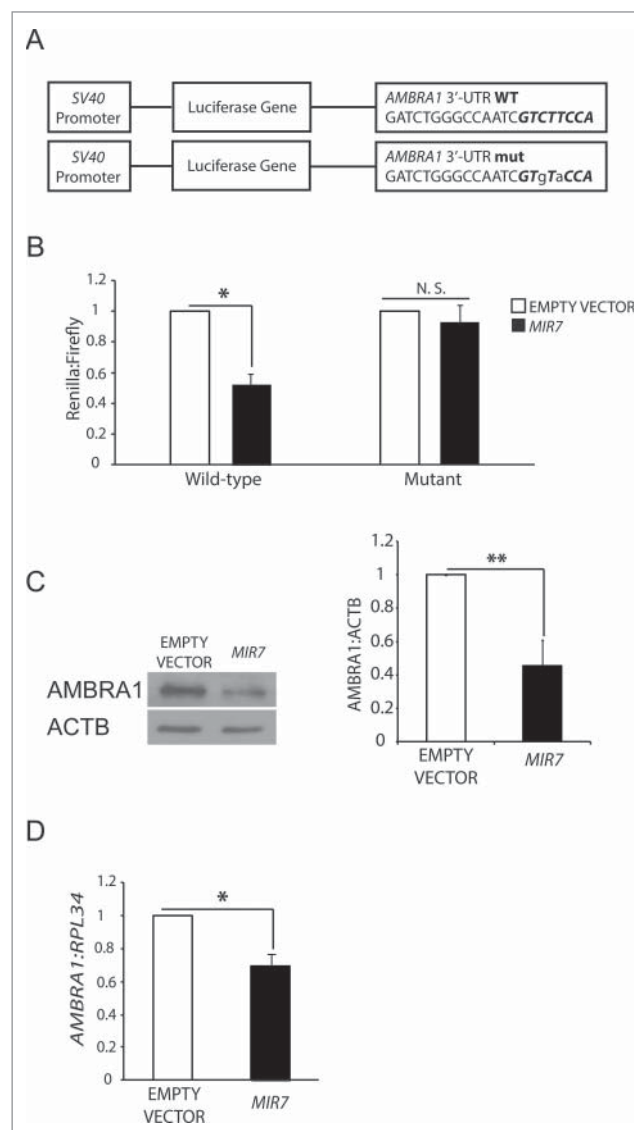


Figure 1. MIR7-3HG (MIR-7) targets AMBRA1. (A) Schematics representing sequences of AMBRA1 MRE (top sequence) or its artificially mutated form (bottom sequence) cloned within the 3'-UTR of the reporter Renilla luciferase in the vector psiCHECK-2. Mutations are marked in lower case letters. MIR7-3HG seed sequence is in bold. (B) Normalized luciferase activity in lysates from HEK293 cells, co-transfected with the wild-type or mutant AMBRA1 luciferase constructs and negative control (Empty Vector) or MIR7-3HG plasmids (indicated as MIR7; mean \pm SD of 3 independent experiments, * $p < 0.05$). N.S., not significant. (C) Western blot analysis of cytoplasmic AMBRA1 levels 24 h after transfection with MIR7-3HG-encoding plasmids (indicated as MIR7) or negative control (Empty Vector). ACTB was used as an endogenous control. One representative western blot of 3 independent experiments is shown. The right panel shows ImageJ densitometry analysis of 3 independent experiments (mean \pm SD of independent experiments, ** $p < 0.01$). (D) AMBRA1 mRNA expression was analyzed by quantitative RT-qPCR 24 h after transfection with MIR7-3HG-encoding plasmids (indicated as MIR7) or negative control (Empty Vector). Relative quantification was measured by means of the comparative cycle threshold ($\Delta\Delta Ct$) method (mean \pm SD of 3 independent experiments, * $p < 0.05$).

MIR7-3HG, together with the wild-type luciferase vector in HEK293 cells, resulted in a significant decrease in the luciferase activity, compared with control levels (Fig. 1B, wild-type). By contrast, MIR7-3HG had no significant effects on the luciferase levels expressed by the mutant construct (Fig. 1B, mutant). These results indicate that MIR7-3HG can downregulate AMBRA1 levels by directly targeting the above described MRE present in its 3'-UTR region.

Effect of MIR7-3HG overexpression on cellular AMBRA1 levels

To assess whether MIR7-3HG affected the translation of the endogenous AMBRA1, we analyzed its protein levels upon transfection with MIR7-3HG-overexpressing plasmid in HeLa cells (Fig. S1C). Western blot analysis indicates that MIR7-3HG reduces the endogenous levels of AMBRA1, coherently with the luciferase assay results (Fig. 1C). In addition, we also checked AMBRA1 mRNA levels, and demonstrated that they were, indeed, affected by MIR7-3HG overexpression (Fig. 1D). We could thus conclude that MIR7-3HG mediates the direct regulation of AMBRA1 expression.

Overexpression of MIR7-3HG results in an autophagy decrease in HeLa cells

Given the effect that MIR7-3HG has on AMBRA1, and considering the role of AMBRA1 in autophagy, we analyzed the role of this MIRNA in autophagy signaling and progression. To date, MAP1LC3/LC3 is the most reliable marker of autophagosomes, whose formation upon autophagy induction can be monitored by LC3-I to LC3-II conversion and by detecting LC3-positive cytosolic puncta. We found that, in basal conditions (DMEM with 10% serum), the overexpression of MIR7-3HG in HeLa cells reduced LC3 conversion compared to the control (Fig. 2A). Also, since autophagosome accumulation can result either from increased de novo autophagosome biosynthesis or inhibition of the autophagy flux, we also measured the on-rate/off-rate of autophagy by using the lysosomal inhibitor chloroquine. When we overexpressed MIR7-3HG, we observed a decrease in the accumulation of LC3-II, with respect to the control (Fig. 2A). To further confirm our data, we monitored the autophagy flux and autophagosome formation by measuring LC3-positive puncta in immunofluorescence analyses. In cells transfected with the control vector, we detected a significant number of LC3-II puncta and we observed accumulation of dots after chloroquine treatment (Fig. 2B, left panels). Conversely, MIR7-3HG did not increase LC3 puncta formation after chloroquine treatment (Fig. 2B, right panels and graph), supporting our finding that MIR7-3HG induces a block in the autophagic flux (autophagy on-rate). These observations were also strengthened by the analysis of LC3 conversion and dot accumulation upon autophagy induction by starvation (Fig. 2C, D). In line with what was observed in basal conditions, after MIR7-3HG overexpression LC3 puncta did not further increase upon starvation. To further assess the effect of MIR7-3HG on autophagy, we quantified the levels of the autophagy receptor SQSTM1/p62, a protein incorporated into phagophores (autophagosome precursors) and degraded in

autolysosomes³⁹ in basal and starvation conditions. Upon MIR7-3HG overexpression, there is a clear reduction in SQSTM1 degradation in both conditions and in comparison with the control vector (Fig. 2E).

Further, in order to verify whether or not the observed autophagy modulation was achieved by MIR7-3HG by downregulating other autophagy-related key molecules besides AMBRA1, we also analyzed the effect of MIR7-3HG on other autophagy proteins that play a central role in the regulation of autophagy; among them ULK1 and BECN1, both involved in autophagy induction⁴⁰ and a few crucial ATG genes (ATG3, ATG5, ATG7 and ATG12) in the elongation and closure of phagophores. Interestingly, we did not observe any changes in the protein levels of the analyzed autophagy markers after MIR7-3HG overexpression (Fig. S2A, B).

Last, we checked whether the observed regulation was specific for tumor cell lines, such as HeLa cells, or common to other nontumor cells, such as HEK293 (immortalized human kidney epithelium). We obtained, after MIR7-3HG overexpression, a decrease in AMBRA1 but also in autophagy flux and autophagosome formation level as seen with HeLa cells (Fig. S3). Moreover, we investigated the effect of MIR7-3HG also in 2 other nontumor cell lines, NIH3T3 (immortalized murine fibroblasts) or RPE1 (immortalized human retinal epithelium). In all cases MIR7-3HG downregulated AMBRA1 and inhibited autophagy flux (Fig. S4).

In summary, MIR7-3HG overexpression downregulates autophagy in both normal and starvation conditions.

MIR7-3HG affects autophagy by downregulating AMBRA1

To demonstrate that MIR7-3HG was acting on autophagy via AMBRA1, we investigated whether MIR7-insensitive AMBRA1 mRNA could rescue MIR7-3HG-dependent autophagy regulation. To this aim, we generated 2 new constructs carrying the AMBRA1 coding sequence with a wild-type or mutated AMBRA1 3'-UTR tail (AMBRA1[3'-UTR-WT] and AMBRA1[3'-UTR-MUT], respectively). The mutation is hypothesized to disrupt the specific MIR7-3HG binding to AMBRA1 mRNA (Fig. 3A). We then overexpressed these constructs simultaneously with MIR7-3HG in HEK293 cells and verified that, at variance with the wild-type form, the mutant construct was indeed unresponsive to MIR7-3HG (Fig. 3B). Of the greatest importance, the AMBRA1[3'-UTR-MUT] construct was able to completely rescue autophagy in the given conditions to control levels, as monitored by LC3 and SQSTM1/p62 in an autophagy flux assay (Fig. 3C).

Altogether, these results suggest the existence of a clear epistatic relationship between MIR7 and AMBRA1 in autophagy downregulation, irrespective of the cell type analyzed.

AntagoMIR against MIR7-3HG induces an increase of AMBRA1 protein levels and positively regulates autophagy

In the previous set of experiments, we observed that overexpression of MIR7-3HG caused a dramatic decrease in AMBRA1 protein levels, leading to an efficient block in the autophagy process. Based on these results, we next moved to

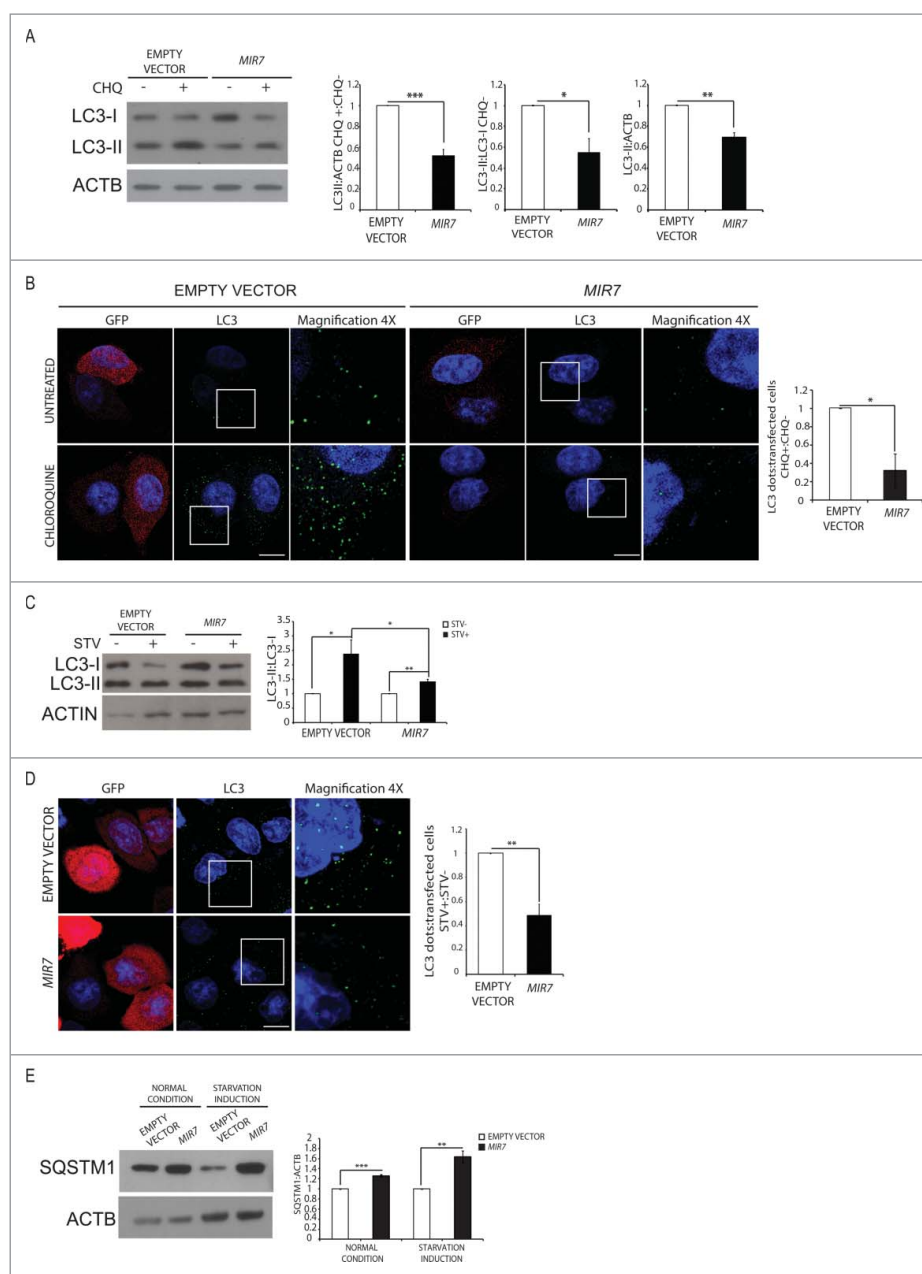


Figure 2. *MIR7-3HG* (*MIR7*) overexpression downregulates basal autophagy. (A) Analysis of cytoplasmic LC3-I and LC3-II levels, by using anti-LC3A/B antibody, on extracts from cells untreated or treated with chloroquine (CHQ; 20 μ M, 30 min). All samples were analyzed 24 h after transfection with *MIR7-3HG*-encoding plasmids (indicated as *MIR7*) or negative control (Empty Vector). ACTB was used as a loading control. One representative western blot of 3 independent experiments is shown. The right graphs show the quantification of autophagy flux as the ratio between LC3-II in chloroquine-treated and LC3-II in untreated cells, the rate of LC3-I in LC3-II conversion and the quantification of LC3-II in the untreated samples. ImageJ densitometry analysis of 3 independent experiments (mean \pm SD of independent experiments, * p < 0.05, *** p < 0.001). (B) *MIR7-3HG* blocked LC3 dot accumulation in samples treated with chloroquine. Cells were transfected with *MIR7-3HG* (indicated as *MIR7*) or Empty Vector and untreated (upper panels) or treated with chloroquine (20 μ M, 30 min, lower panels). Scale bar: 5 μ m. GFP fluorescence is shown in the red channel. The right graph shows the quantification of LC3 dots per transfected cell as the ratio between chloroquine-treated and -untreated cells (mean \pm SD of 3 independent experiments, * p < 0.05). Statistical analysis was performed using the Student t test. (C) Overexpression of *MIR7-3HG* downregulates starvation-induced autophagy. Starvation-induced and autophagy related LC3-I to LC3-II conversion, by using anti-LC3A/B antibody, after *MIR7-3HG* overexpression (indicated as *MIR7*) is shown by immunoblots of control or *MIR7-3HG*-transfected cells that were nonstarved (STV-) or starved for 2 h (STV+). ACTB was used as loading control. The right graph shows ImageJ densitometry analysis of 3 independent experiments (mean \pm SD of independent experiments, * p < 0.05, ** p < 0.01). (D) Analysis of LC3 dot formation in HeLa cells, transfected with *MIR7-3HG* (indicated as *MIR7*) or empty vector. Autophagy was assessed under starvation conditions (2 h, lower panels). Scale bar: 5 μ m. GFP fluorescence is shown in the red channel. The right graph shows the quantification of LC3 dots per transfected cell as the ratio between starved and nonstarved cells (mean \pm SD of 3 independent experiments, ** p < 0.01). Statistical analysis was performed using the Student t test. (E) Analysis of the starvation-induced and autophagy-related SQSTM1 degradation in *MIR7-3HG* transfected HeLa cells (indicated as *MIR7*). The right graph shows ImageJ densitometry analysis of 3 independent experiments (mean \pm SD of independent experiments, *** p < 0.001, ** p < 0.01).

another cellular system of tumor origin (A549 cells), exhibiting a very low level of *AMBRA1*.²⁸ siMIRNA are chemically engineered oligonucleotides conceived to block specific endogenous MIRNAs. To test whether silencing endogenous *MIR7-3HG*

could have an impact on target mRNA and protein levels, we obtained *MIR7-3HG*-specific siMIRNA (siMIR7-3HG, Fig. S5). We next transfected A549 cells with siMIR7-3HG or nonspecific control siMIRNA (Ctrl siRNA), and then

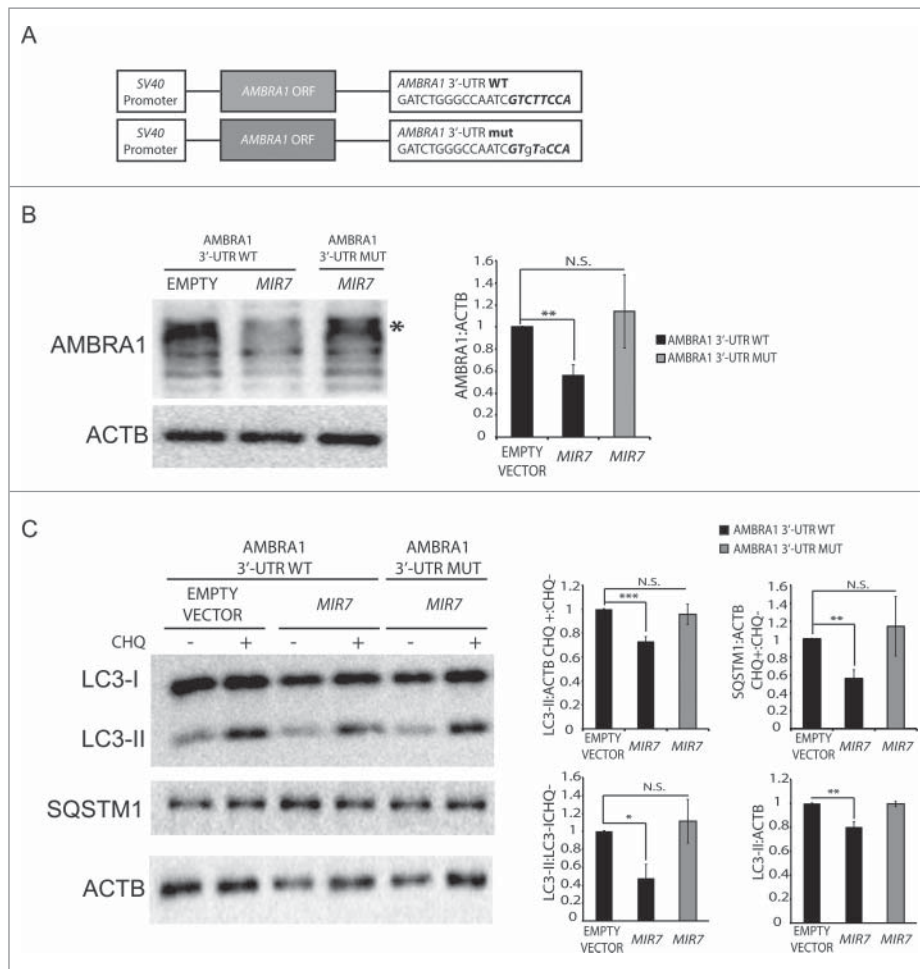


Figure 3. Overexpression of *MIR7-3HG*-insensible *AMBRA1* rescues the autophagy phenotype. (A) Scheme representing sequences of *AMBRA1* mRNA with wild-type 3'-UTR (top sequence) or its artificially mutated form in the *MIR7-3HG* responsive element (bottom sequence). Mutations are marked in lower case letters. *MIR7-3HG* seed sequence is in bold. (B) Western blot analysis of *AMBRA1* wild-type or mutated 24 h after cotransfection with *MIR7-3HG*-encoding plasmids (indicated as *MIR7*) or negative control (Empty Vector). Different bands are detected upon *AMBRA1* overexpression, with the band indicated by the arrow corresponding to the expected size-range for full-length *AMBRA1*. The other bands, with lower molecular weights, correspond to *AMBRA1* full-length cleavage products.²⁸ ACTB was used as endogenous control. One representative western blot of 3 independent experiments is shown. The right panel shows ImageJ densitometry analysis of the band of 3 independent experiments (mean \pm SD of independent experiments, ** $p < 0.01$). (C) Analysis of autophagy flux following overexpression of *AMBRA1* wild type or mutated, 24 h after cotransfection with *MIR7-3HG*-encoding plasmids (indicated as *MIR7*) or negative control (Empty Vector). Western blot analysis of LC3-II and SQSTM1 accumulation, using LC3B and SQSTM1 antibody, in extracts from cells untreated or treated with chloroquine (CHQ; 20 μ M, 30 min). ACTB was used as loading control. One representative western blot of 3 independent experiments is shown. The right graphs show the quantification of autophagy flux measures as the ratio between LC3-II and SQSTM1 in chloroquine-treated and untreated cells (upper graphs), the rate of LC3-I to LC3-II conversion and the quantification of LC3-II (lower graphs) in the untreated samples. The data show ImageJ densitometry analysis of 3 independent experiment (mean \pm SD of independent experiments, * $p < 0.05$, ** $p < 0.01$, *** $p < 0.001$).

monitored *AMBRA1* protein and mRNA levels. We observed that transfection with siMIR7-3HG led to an increase in *AMBRA1* protein (Fig. 4A) and a milder but significant increase in *AMBRA1* mRNA levels (Fig. 4B) compared to the control antagoMIRs, confirming the *MIR7-3HG*-dependent *AMBRA1* regulation.

Next, we analyzed autophagy upon biologically relevant inhibition of *MIR7-3HG* activity. In line with the previous experiments, interference of *MIR7-3HG* in the lung carcinoma cell line A549 by siMIR7-3HG caused an increase in the rate of LC3-I to LC3-II conversion and SQSTM1 degradation, when compared with control cells grown in basal conditions (Fig. 4A and Fig. 4C). The second step was to analyze the autophagic flux after *MIR7-3HG* silencing using the siMIR7-3HG antagoMIR. As shown in Figure 4C, after chloroquine treatment, we could appreciate a higher autophagosome accumulation in samples interfered for *MIR7-3HG*, respective to the control.

AntagoMIR against *MIR7-3HG* induces an increase of MYC phosphorylation at serine 62

Recently, we have demonstrated that *AMBRA1*, through a direct binding with the catalytic subunit of the serine/threonine-protein phosphatase 2A (PPP2/PP2A), is able to mediate the dephosphorylation of phospho-MYC on serine 62 (p-MYC [S62]) and, consequently, its proteasomal degradation.^{28,6}

Primed by this evidence, we analyzed the level of p-MYC (S62) upon transfection of A549 cells with siMIR7-3HG. Of note, this cell line exhibits a clear inverse correlation between *AMBRA1* (low) and p-MYC (S62) (high) protein levels.²⁸ When we transfected the A549 cell line with siMIR7-3HG, besides an *AMBRA1* increase, we observed a decrease of p-MYC (S62) (Fig. 5A). As previously shown,^{28,6} also in this system, the downregulation of p-MYC (S62) induced MYC degradation (Fig. 5B).

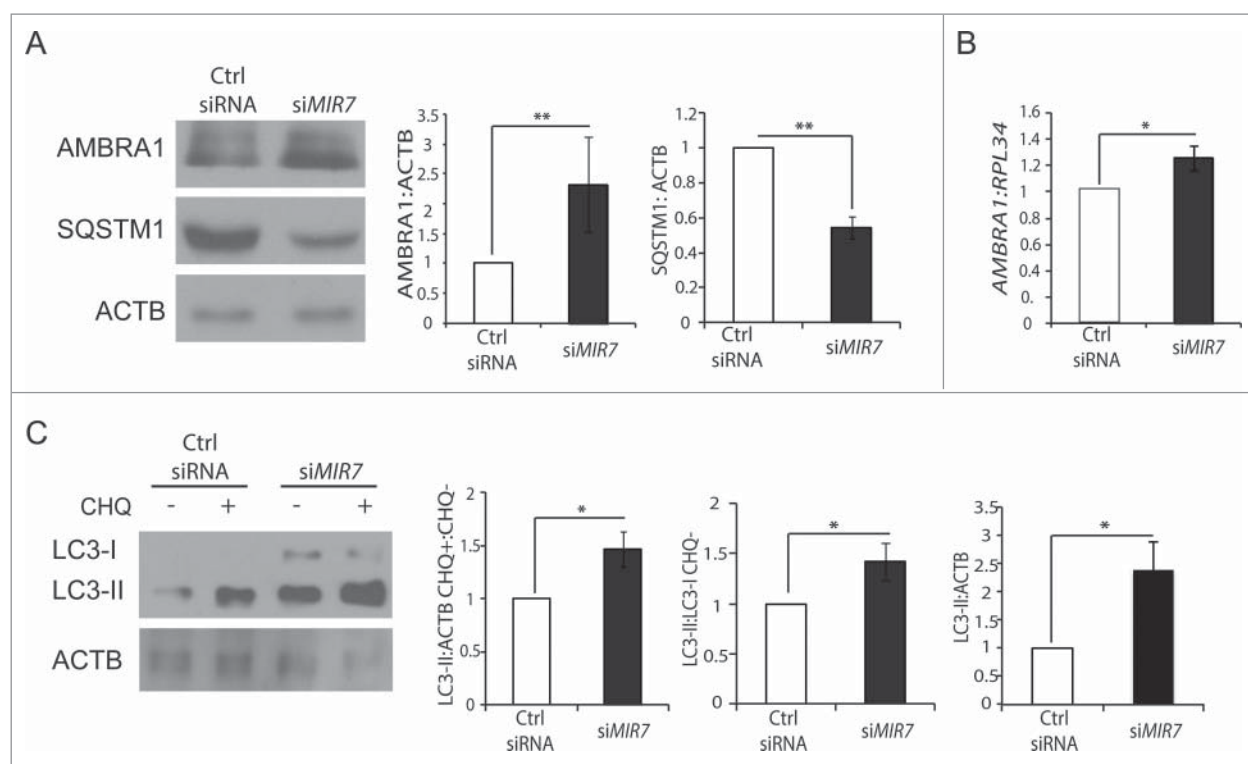


Figure 4. Inhibition of endogenous *MIR7-3HG* (*MIR7*) leads to *AMBRA1* upregulation and increased autophagy. (A) Western blot analysis in the A549 cell line of cytoplasmic *AMBRA1* and *SQSTM1* levels, 72 h after transfection with *siMIR7* (*siRNA* anti-*MIR7-3HG*) or negative control (Ctrl *siRNA*, control *siRNA*). *ACTB* was used as an endogenous control. One representative western blot of 3 independent experiments is shown. The right panels show ImageJ densitometry analysis of 3 independent experiments (mean \pm SD of independent experiments, ** $p < 0.01$). (B) *AMBRA1* mRNA expression was analyzed by quantitative RT-PCR, 72 h after overexpression of *siMIR7-3HG* (indicated as *siMIR7*). Relative quantification was measured by means of the comparative cycle threshold ($\Delta\Delta C_t$) method (mean \pm SD of 3 independent experiments, * $p < 0.05$). (C) Analysis of cytoplasmic LC3-I and LC3-II levels, by using anti-LC3A/B antibody, on extracts from cells untreated or treated with chloroquine (20 μ M, 30 min). All samples were analyzed 72 h after transfection with *siMIR7* (*siRNA* anti-*MIR7-3HG*) or negative control (Ctrl *siRNA*, control *siRNA*). *ACTB* was used as a loading control. One representative western blot of 3 independent experiments is shown. The right graphs show the quantification of autophagy flux as the ratio between LC3-II in chloroquine-treated and untreated cells, the rate of LC3-I to LC3-II conversion and the quantification of LC3-II in the untreated samples. ImageJ densitometry analysis of 3 independent experiments (mean \pm SD of independent experiments, * $p < 0.05$).

Given the reported activity of p-MYC (S62) on the *MIR7-3HG* promoter and *MIR7-3HG* transcription,³⁰ we sought to investigate whether an *AMBRA1* unable to bind the p-MYC (S62) phosphatase PPP2/PP2A (*AMBRA1*^{PXP})²⁸ decreased the impact of MYC on *MIR7-3HG* transcription. Interestingly, overexpression of wild-type *AMBRA1*, but not of its mutant form could regulate *MIR7-3HG* expression in lung cancer cells (Fig. 5C, right graph).

These data strongly suggest that *AMBRA1*-mediated regulation of p-MYC affects *MIR7-3HG* expression, thus establishing a feedback loop.

MIR7-3HG modulation in A549 cells has an impact on cell proliferation

Given the role of *AMBRA1* in cell cycle regulation²⁸ and in order to assess if *AMBRA1* modulation mediated by *MIR7-3HG* could have an effect on cell proliferation, we analyzed the proliferation rate of A549 cells after *MIR7-3HG* inhibition by a cell viability assay. Indeed, *MIR7-3HG* inhibition led to a decrease of proliferation when compared with control cells that was rescued upon *AMBRA1* overexpression (Fig. 6A). In line with this finding, overexpression of *MIR7-3HG* in HeLa cells, that express moderate levels of *MIR7*, led to a cell number increase (Fig. 6B). Also in this case, *AMBRA1* overexpression

compensated for the effect of *MIR7-3HG* overexpression, priming the cells to proliferate similar to the control.

MIR7-3HG and AMBRA1 expression inversely correlate in human lung tumor samples compared to normal tissues

Primed by our findings in the lung tumor cell line A549, we set out to investigate the reciprocal *AMBRA1*-*MIR7-3HG* regulation in silico in human lung tumor samples. To this aim, RNA-Seq data for 58 and 51 paired samples have been analyzed for LUAD (LUng ADenocarcinoma) and LUSC (LUng Small Cells cancer) data sets deposited in TCGA (The Cancer Genome Atlas database), respectively. We decided to focus only on the paired samples since the expression levels of *AMBRA1* vary remarkable from sample to sample. It is thus important to be able to compare the tumor samples to normal samples from the same patient as a reference to identify cases in which the gene is up- or downregulated.

We found that more than 40% and 60% of the LUAD and LUSC samples, respectively, have a negative log₂FC for the *AMBRA1* gene, indicating that in these tumor samples *AMBRA1* is downregulated with respect to the normal samples. The other cluster of patient data in which the log₂FC is positive have not been further investigated in this study, since other mechanisms such as the absence of other regulators of its

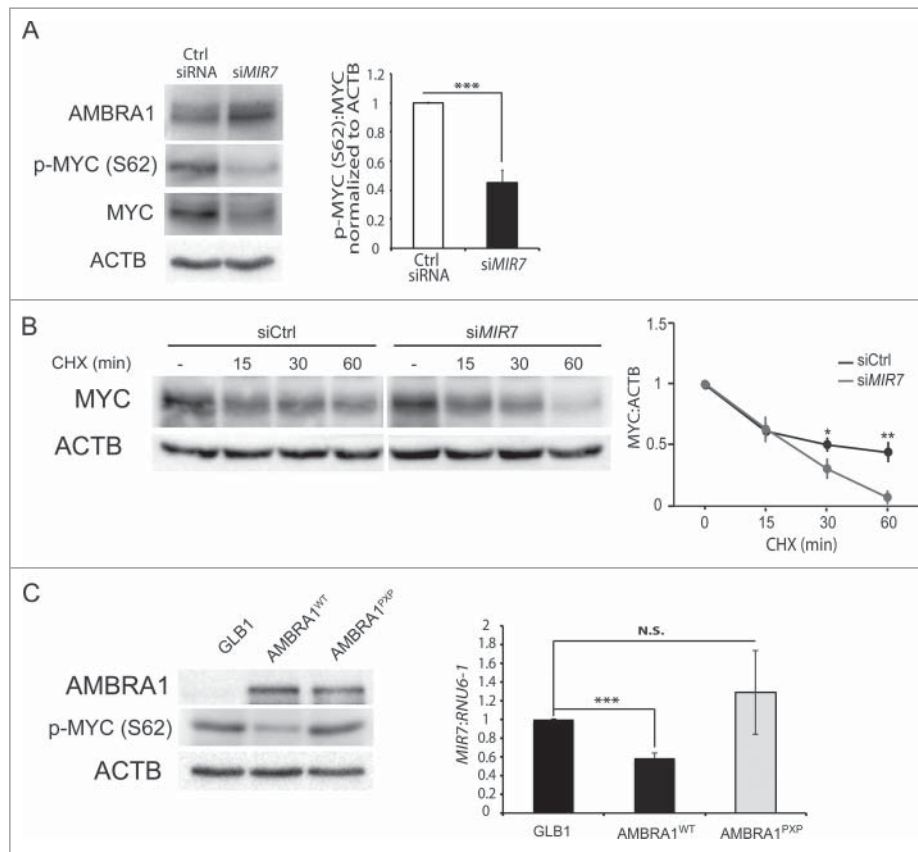


Figure 5. Inhibition of endogenous *MIR7-3HG* (*MIR7*) leads to an increase of *MYC* dephosphorylation and to a decrease in cell proliferation. (A) Western blot analysis of *AMBRA1*, p-*MYC* (S62) and *MYC* levels, 72 h after A549 cells transfection with *siMIR7* (siRNA anti-*MIR7-3HG*) or negative siRNA control (Ctrl siRNA, control siRNA). *ACTB* was used as a loading control. One representative western blot of 3 independent experiments is shown. The right graph shows the ratio between p-*MYC* (S62) and *MYC* proteins (ImageJ densitometry analysis of 3 independent experiments [mean \pm SD of independent experiments, *** p < 0.001]). (B) Cells transfected with *siMIR7-3HG* or negative siRNA control (Ctrl siRNA, control siRNA) were treated with 50 μ g ml⁻¹ cycloheximide (CHX) and collected at the indicated time points. Protein extracts of cells were analyzed by western blot, using antibodies against *MYC*. *ACTB* was used as a loading control. The right panel shows ImageJ densitometry analysis of the band of 3 independent experiments (mean \pm SD of independent experiments, ** p < 0.01, * p < 0.05). (C) Western blot analysis in the A549 cell line of cytoplasmic p-*MYC* (S62) 72 h after transfection with a plasmid encoding *AMBRA1*^{WT}, *AMBRA1*^{PXP} or with *GLB1*/ β -galactosidase, as a negative control. The right graph shows the relative quantification of endogenous *MIR7-3HG* in A549 cells after transfection. The level of endogenous *MIR7-3HG* was analyzed by quantitative RT-PCR. Relative quantification was measured using the comparative cycle threshold ($\Delta\Delta$ Ct) method (mean \pm SD of 3 independent experiments, * p < 0.05).

expression levels could account for expression changes, considering the high heterogeneous spectrum of cancer-related mechanisms. We thus focused on the samples characterized by log2FC, and we analyzed the levels of *MIR7-3HG* in tumor and normal samples. We observed that *MIR7-3HG* was always overexpressed in the given tumor cases for LUAD and in 90% of the LUSC samples where *AMBRA1* was downregulated (Figure 6C, D), supporting the existence of a tight correlation between *MIR7-3HG* and *AMBRA1* expression levels in cancer patient data.

Discussion

Autophagy plays essential roles in different cellular processes, and many studies have recently demonstrated the involvement of MIRNA-mediated regulation of proteins in the autophagy pathway. Very recently a correlation was described between *MIR23A* and *AMBRA1* in autophagy regulation during UV-stress-induced premature senescence.⁴¹ However, only few of these studies have investigated in depth the effect of MIRNAs on autophagic flux or attempted to identify the physiological context in which the MIRNA may be linked to autophagy. In

this study, we introduce *MIR7-3HG* as a new autophagy-regulating MIRNA that acts as an oncogene in lung cancer cells, by blocking autophagy in favor of cell proliferation.

Data obtained from the in silico analysis of *AMBRA1*, a key protein in autophagy regulation, identified *MIR7-3HG* as a strong candidate for *AMBRA1* regulation. Indeed, we observed that *MIR7-3HG* overexpression causes a significant decrease in *AMBRA1* levels; we also demonstrated that this regulation occurs through the binding of *MIR7-3HG* to a canonical *MIR7-3HG* responsive element present in the 3'-UTR region of *AMBRA1* mRNA, a domain that is broadly conserved among vertebrates. In fact, taking advantage of a luciferase assay, we validated *AMBRA1* mRNA as a direct target of *MIR7-3HG*.

To investigate the *AMBRA1*-*MIR7-3HG* axis in autophagy regulation we next decided to study LC3-II levels upon *AMBRA1* downregulation in both basal and starvation conditions or in a number of tumor and nontumor cell lines. We demonstrated by several approaches that *MIR7-3HG* overexpression decreases the conversion rate of LC3-I into LC3-II, positively modulates SQSTM1/p62 and plays an important role in blocking the autophagy flux. Also, we have proven the *AMBRA1* binding by *MIR7-3HG* to be functional to this

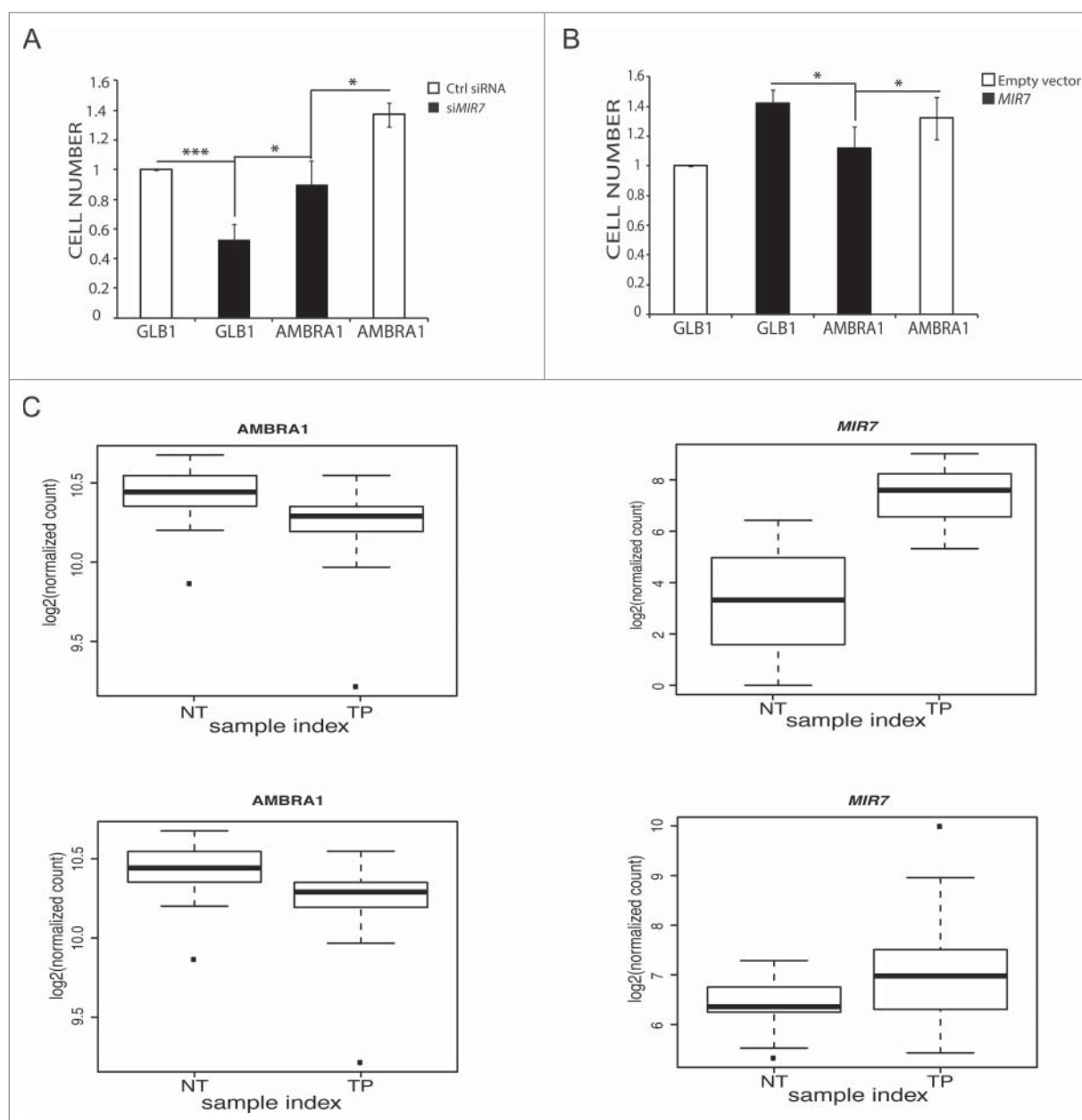


Figure 6. *MIR7-3HG (MIR7)* affects proliferation in an *AMBRA1*-dependent manner. (A) The graph shows the *MIR7-3HG* overexpression effect on cell proliferation in HeLa cells. (B) The left graph shows the *siMIR7-3HG* effect on cell proliferation in A549 cells. In (A) and (B) the proliferation rate was measured by the AlamarBlue® Cell Viability assay. All samples were analyzed 48 h after transfection with *siMIR7-3HG* or the negative control *siRCtrl* (mean \pm SD of independent experiments, * $p < 0.05$; *** $p < 0.001$). (C) Inverse correlation between *MIR7-3HG* levels and *AMBRA1* expression in lung cancer. Expression levels of *AMBRA1* (left graphs) and *MIR7-3HG* (right graphs) in LUAD (upper graphs) and LUSC (lower graphs) datasets from TCGA comparing normal (NT) to tumor primary (TP) samples. Center lines in the boxplot show the medians; box limits indicate the 25th and 75th percentiles as determined by R software; whiskers extend 1.5 times the interquartile range from the 25th and 75th percentiles, outliers are represented by dots.

regulation. Altogether, these results demonstrate that *MIR7-3HG* has a role in autophagy regulation via *AMBRA1*. It should be mentioned that an opposite and specific role for *MIR7-3HG* overexpression in human lung cancer cells has been previously reported,⁴² although based on a different protocol of transduction of *MIR7-3HG*, on a fluorescent-reporter detection method to monitor autophagy and, most important, at a very much later time point. Indeed, we cannot exclude, based on our data, that in a later phase of cell growth, autophagy gets primed as a secondary feedback response, resulting in decreased cell survival.

Recent data strongly support a physiological and pathological relevance for the crosstalk between autophagy and other

pathways.^{43,44} As an example, autophagy-related proteins also affect cell proliferation.^{26,28,45,46} Indeed, to adapt to nutrient deprivation or other cell stresses, a simultaneous regulation of autophagy and cell growth occurs in eukaryotic organisms. First, a plethora of signaling molecules and pathways have opposite effects on cell growth and autophagy, supporting the idea that these processes might represent mutually exclusive cell fates.⁴⁷ Such a reciprocal inhibition between autophagy and cell growth can occur either through direct regulatory mechanisms, most of which remain to be determined to date, or through the same signaling pathways that act independently and simultaneously on autophagy and cell growth.

AMBRA1, a well-characterized positive regulator of the autophagy pathway, affects cell proliferation both in vitro and in vivo.^{24,26,28} In more detail, embryos homozygous for the gene-trap mutation in the *Ambra1* locus (*Ambra1*^{gt/gt} embryos) are affected by a dramatic hyperproliferative phenotype of the neuroepithelium, appearing at the onset of neurulation.²⁶ Moreover, AMBRA1 downregulation or its overexpression in human cell lines result in a significant increase or decrease of the cell proliferation rate, respectively.^{26,28} By taking these lines of evidence into account, the relevance of AMBRA1 in controlling cell proliferation and guaranteeing cell survival upon autophagic stress is evident.

Primed by these findings, we thus investigated whether overexpression of MIR7-3HG, in our cellular model, could affect at the same time autophagy and cell proliferation. Overexpression of MIR7-3HG in HeLa and A549 cell lines resulted in a decrease of the autophagy flux, as previously described, and, at the same time, in a parallel increase in cell proliferation. By contrast, we obtained an opposite effect when we used an antagoMIR construct that decreases MIR7-3HG expression, leading to a decrease in cell proliferation and an increase in autophagy.

In recent years, AMBRA1 has emerged as a scaffold molecule that serves as a platform for autophagy-related complexes and as an early autophagy regulator, linking this process to a number of other cellular activities.²⁷ In this work, we have demonstrated that MIR7-3HG, via AMBRA1 downregulation, could be the circuit breaker between autophagy and cell proliferation. Indeed, through MIR7-3HG inhibition or activation, cells could be able to control both autophagy and proliferation.

Of note, we have previously demonstrated that AMBRA1, through its interaction with the phosphatase PPP2/PP2A, dephosphorylates the oncogene MYC, thereby enhancing its proteasomal degradation.²⁸ In this way, AMBRA1 is able to control MYC cellular levels, thus acting as a tumor suppressor. In various lung cancer cell lines, we observed a low expression level of AMBRA1 and high expression levels of phosphorylated MYC.²⁸ In lung cancer, MIR7-3HG expression is regulated by MYC, which promotes MIR7-3HG transcription.⁴⁸ Here, based on the interference of MIR7-3HG in A549 lung cancer cells, we suggest that MIR7-3HG maintains the balance of this inverse correlation between AMBRA1 and phospho-MYC. In fact, by blocking MIR7-3HG expression in A549 cells, we obtained an increase in AMBRA1; this finding correlates with a parallel enhancement in autophagy levels and a decrease in phosphorylated MYC levels. Through our experiments, we thus found that MIR7-3HG, through AMBRA1 downregulation, can regulate not only autophagy, but also the levels of MYC, a transcription factor regulating MIR7-3HG's own activity. This would establish a positive feedback for MIR7-3HG transcription.

In sum, we identified a regulatory loop, in which there is a mutual regulation between MIR7-3HG and AMBRA1. On the one hand, there is a direct post-transcriptional downregulation of MIR7-3HG on AMBRA1 expression; on the other hand, AMBRA1 is able to downregulate MIR7-3HG transcription by promoting proteasomal degradation of its transcriptional regulator MYC (Fig. 7). Such evidence, together with the observation that MIR7-3HG is deregulated in lung cancer cells, in which autophagy and AMBRA1 play a central role, leads us to

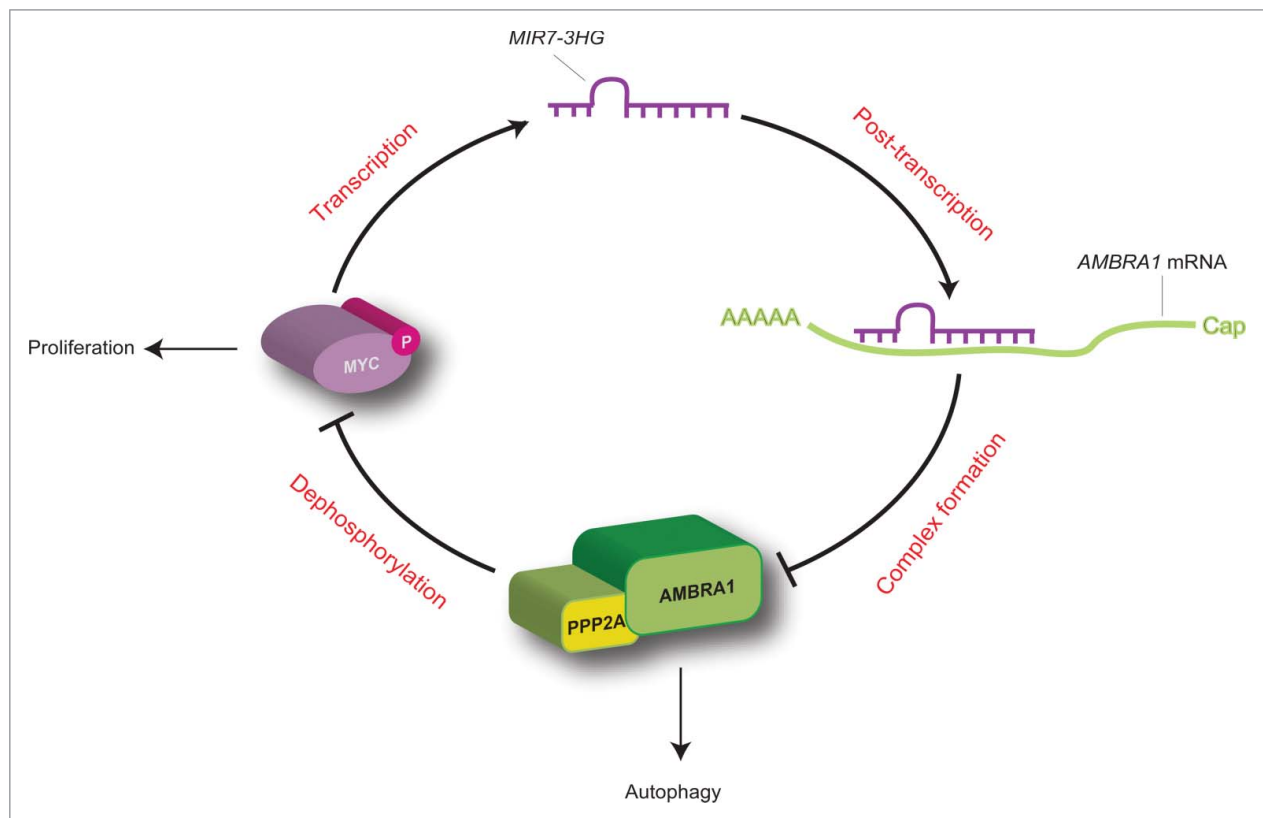


Figure 7. Proposed working model for the MYC-MIR7-3HG-AMBRA1 axis. In this regulatory loop, MIR7-3HG downregulates AMBRA1 expression, and promotes its own transcription mediated by MYC. This model favors cell proliferation to the detriment of autophagy (for details see the text).

hypothesize that MIR7-3HG and AMBRA1 interaction could be critical for the onset and progression of lung carcinoma. Of the highest importance, both LUAD and LUSC lung cancer in humans (with the A549 cell lined being derived from a LUAD tumor), show a striking inverse correlation between AMBRA1 mRNA and MIR7-3HG levels, which is lost in normal tumor from the same patients.

The importance of both autophagy and MIRNAs in cancer is emerging in recent years. It is widely demonstrated that altered autophagy is associated with tumor formation and progression, and with an altered response to several types of cancer treatment. The results reported here suggest that MIRNAs have the potential of modulating autophagy through regulation of expression of key autophagy genes, such as AMBRA1, providing evidence for a new role of MIRNAs highly correlated with cancer biology.

The finding that MIR7-3HG modulates the expression of the tumor suppressor AMBRA1, thereby promoting its expression, supports indeed the idea that MIR7-3HG is a promising prognostic biomarker and a therapeutic target for lung cancer. Our findings imply that by modulating MIR7-3HG in lung cancer cells, it could be possible to switch a cell phenotype towards a more autophagic profile and a less proliferative state.

In the future, it could be interesting to investigate, in non-malignant cells, whether there is a correlation between the presence of polymorphisms or genetic rearrangements of the AMBRA1 3'-UTR or if that could have a protective role in cancer insurgence and progression.

Material and methods

Cell culture and reagents

HEK293, NIH3T3, RPE1 and HeLa cells were cultured in Dulbecco's modified Eagle's medium (LONZA, BE12-604F) supplemented with 10% fetal bovine serum (GIBCO, 10270-106), in a CO₂-humidified incubator at 37°C. A549 cell lines were similarly cultured in RPMI 1640 (LONZA, BE12-702F) supplemented with 10% fetal bovine serum. For autophagy induction cells were washed with phosphate-buffered saline (UCS Diagnostic, PBS1199) and cultured for 2 h in Earle's balanced salt solution (Sigma-Aldrich, E2888). All the cell lines were transiently transfected with expression vectors using Lipofectamine 2000 (Invitrogen, 11668-019) as indicated by the supplier. Viral infection of A549 cells with the retroviral AMBRA1-coding constructs was performed as previously described.^{25,28} When indicated, cells were incubated in the presence of 50 µg ml⁻¹ cycloheximide (Sigma Aldrich, 200-636-0) and 20 µM chloroquine (Sigma Aldrich, 50-63-5).

Plasmid constructs

A construct coding for MIR7-3HG overexpression was produced by cloning the pri-MIRNA sequence, with 100 nucleotides upstream and downstream of the pre-MIRNA, in the pSP65 plasmid into the U1snRNA expression cassette (according to Denti⁴⁹). The full-length human 3'-UTR sequence of AMBRA1 was amplified by PCR and then directionally cloned in NotI and XhoI unique restriction site of the pscheck2 plasmid (Promega, C8021),

downstream of the Renilla luciferase gene. This kind of vector also contains the firefly luciferase to normalize transfection efficiency. AMBRA1-3'-UTR mutated in the MIR7-3HG recognition element was created by site-directed mutagenesis (Agilent Technologies, 200518), using AMBRA1 3' UTR as a template. The linker primers used during the study were; AMBRA1 5'- CATCTCGA-GAGACAAACGTTGCACTGGTG-3'; 5'- CATGC GGCCGCGAGGGGCATGTCATCATTTT-3'; AMBRA1 mutant primers 5'- AGCCTCCAGAGAGTGAACAGTGTACCAGATCT GGGCCAATCATCCT-3' and the exact reverse complement.

Target prediction

MIRNA targets were predicted using publicly available bioinformatics tools. Target scan (<http://www.targetscan.org/>); Pictar (http://pictar.mdc-berlin.de/cgi-bin/new_PicTar_vertibrate.cgi?species = vertebrate), MIRanda (<http://www.microrna.org/microrna/getGeneForm.do>), diana TOOLS (http://diana.imis.athena-innovation.gr/DianaTools/index.php?r = microT_CDS/index)

Immunoblotting and antibodies

Cells were lysed at the indicated time points in RIPA buffer (50 mM TRIS-HCl, pH 7.4, 150 mM NaCl, 1% NP40 [ThermoFisher Scientific, FNN0021], 0.25% Na-deoxycholate [ThermoFisher Scientific, 89904]) supplemented with complete protease inhibitor cocktail (Roche, 04-693-131-001) and 1 mM phenylmethylsulfonyl fluoride (Sigma-Aldrich, P7626). Protein extracts (20 mg per well) were analyzed using 7% or 12% SDS-polyacrylamide gels and then transferred onto nitrocellulose membranes (Millipore, IPVH00010). Membranes were blocked in 5% nonfat milk in TBST (50 mM Tris-Cl, pH 7.5, 150 mM NaCl, 0.1% Tween 20 [Sigma-Aldrich, P 9416], pH 7.4) for 1 h and then incubated with a 5% milk-containing TBST solution containing the following primary antibodies: Anti-ACTB (Sigma Aldrich, A2066; 1:2,000), anti-p-MYC (S62) (Abcam, ab78318), anti-SQSTM1 (Santa Cruz Biotechnology, sc-28359), anti-BECN1 (Santa Cruz Biotechnology, sc-11427), anti-AMBRA1 (Santa Cruz Biotechnology, sc-398204), and anti-LC3 (Cell Signaling Technology 27755 and 12741). Following incubation with horseradish peroxidase-coupled secondary anti-mouse (Bio-Rad, 170-6516) and anti-rabbit antibody (Bio-Rad, 170-6515), bands were revealed by chemiluminescence. Band intensities were quantified using ImageJ software.

Immunocytochemistry

Cells were washed in PBS and fixed with 4% paraformaldehyde in PBS for 30 min. After permeabilization with 0.4% Triton X-100 (Sigma-Aldrich, X100) in PBS for 5 min, cells were blocked in 3% normal goat serum (Sigma-Aldrich, G9023) in PBS and incubated overnight at 4°C with primary antibodies; we used the antibodies directed against LC3. Cells were then washed in blocking buffer and incubated for 1 h with labeled anti-mouse (Molecular Probes, Alexa Fluor 488, A11017 or Alexa Fluor 555, A20187) or anti-rabbit (Jackson Immuno Research, FITC, 111-095-003 or Cy3, 115-165-166) secondary antibodies.

Nuclei were stained with 1 mg/ml DAPI and examined under a Zeiss LSM 700 100_x oil-immersion objective (Zeiss, Oberkochen, Germany). We used 'ZEN 2009 Light edition' software for image analysis. All measurements in this work were performed by a blind approach. All analyses were performed in nonsaturated single z-confocal planes.

RNA isolation and real-time RT-PCR for *AMBRA1* mRNA quantification

RNA was extracted from HeLa and A549 cells using QIAGEN MIRNeasy kit (217004) following the manufacturer's instructions. Extracted RNA (800 ng) was used for reverse transcription and 500 ng of random primers for each μg of RNA was added to each tube. Samples were heated to 70°C for 5 min followed by immediate incubation on ice. M-MLV reaction buffer (1X), dNTPs, RNase inhibitor (1 U/ μl), and M-MLV reverse transcriptase (8U/reaction) (Promega, 9PIM170) were added to the mix and were incubated for 1 h at 37°C. Real-time PCR was performed using LightCycler 480 SYBR Green I Master and the LightCycler 480 System (Roche) following the manufacturer's instructions. mRNA change was quantified with the $2^{-\Delta\Delta\text{CT}}$ method using RPL34 as mRNA control. The following primers were used for quantitative real-time PCR: *Ambra1* (F: AACCTCCACTGCGAGTTGA, R: TCTACCTGTTCCGTGGTTCTCC), RPL34 (F: GTCCCGAACCCCTGGTAATAGA, R: GGCCCTGCTGACATGTTTCTT).

Real-time RT-PCR for endogenous *MIRNA* quantification

RNA was extracted from A549 cells. Extracted RNA (800 ng) was used for reverse transcription following the manufacturer's instructions using miScript Reverse Transcriptase Mix, miScript RT Buffer, RNase-Free Water (Quiagen, 218061). qPCR reactions were performed following manufacturer's instructions for QuantiTect SYBR Green PCR Master Mix, miScript Univerthe sal Primer (Quiagen, 218073). *MIRNA* change was quantified with the $2^{-\Delta\Delta\text{CT}}$ method using RNU6-1 (RNA, U6 small nuclear 1) as control.

Luciferase assay

Firefly and Renilla luciferase activities were measured 48 h post-transfection using the dual-luciferase reporter assay system (Promega, E1910) according to the manufacturer's instructions. Results were expressed as Renilla luciferase activity normalized to firefly luciferase activity.

siRNA *MIRNA*

The A549 cells were transfected with miRCURY LNATM, against *MIR7-3HG* (MIMAT0000252) and as control we utilized microRNA inhibitor negative control A purchase from Exigon.

Statistical analyses

Statistical analyses were performed using the Student 2-tailed *t* test. Data are shown as means \pm SD of *n* independent experiments. Values of *p* < 0.05 were considered significant.

Analyses of lung cancer data sets from The Cancer Genome Atlas database

RNA-Seq data for LUAD and LUSC paired samples have been downloaded from The Cancer Genome Atlas (TCGA) and pre-processed with the TCGAbiolinks R package.⁵⁰ In particular, we downloaded the data for 58 and 51 patient samples for lung adenocarcinoma (LUAD) and lung squamous cell carcinoma (LUSC), respectively. At first, we searched for possible outliers using the TCGAnalyze Preprocessing function of TCGAbiolinks, which performs an Array Array Intensity correlation analyses, i.e. a square symmetric matrix of Pearson correlation among all samples. According to this analysis we did not find samples with correlation lower than 0.6 in LUAD so all the samples have been retained for further analyses, whereas one of the samples was discarded for LUSC. Afterwards, using the TCGAnalyze_Normalization function of TCGAbiolinks, we normalized the mRNA transcripts using the EDASeq R package. In this step, we used normalization procedures to adjust for GC-content and gene-length effects on read counts and full quintile normalization.⁵¹ Fold change (FC) of tumor samples with respect to normal has been calculated and log₂ (log₂FC) transformed and used to classify the patient samples according to changes in *AMBRA1* expression levels of tumor versus normal samples. The *MIR7-3HG* microRNA expression levels corresponding to the same samples for which RNA-Seq data were available have been also analyzed as log₂ transformed normalized RSEM counts (for a total of 53 and 48 samples, for LUAD and LUSC, respectively). The data were produced using the Illumina HiSeq 2000 mRNA/MIRNA sequencing platform.

Abbreviations

A549	human lung carcinoma
<i>AMBRA1</i>	autophagy and Beclin 1 regulator 1
<i>AMBRA1</i> ^{PXP}	<i>AMBRA1</i> mutated in the PPP2/PP2A binding site
<i>AMBRA1</i> ^{3'-UTR-WT}	<i>AMBRA1</i> 3' untranslated region - wild type
<i>AMBRA1</i> ^{3'-UTR-MUT}	<i>AMBRA1</i> 3' untranslated region mutated in <i>MIR7-3HG</i> binding region
CHQ	chloroquine
HEK293	human embryonic kidney 293
MAP1LC3/LC3	microtubule associated protein 1 light chain 3
MIR	microRNAs
MRE	miRNA responsive element
MYC	v-myc avian myelocytomatosis viral oncogene homolog
PPP2/PP2A	protein phosphatase 2
UTR	untranslated region

Disclosure of Potential Conflicts of Interest

No potential conflicts of interest were disclosed.

Acknowledgements

We thank Mrs. M. Acuña Villa for secretarial work and Dr. Vanda Turcanova for the excellent technical support. We are indebted with Dr. Ubaldo Gioia,

(Rome, Italy) for kindly providing us with the *MIR7-3HG*, *MIR-9* and Dr. Francesca De Vito (Rome, Italy) for kindly providing us with the *MIR-200b*. We are grateful to Dr. Juliane Becher, Antonio Colaprico (Bruxelles, Belgium), and Richa Batra (Copenhagen, Denmark) for the useful advice and critical discussion of this work, and to Dr. Sandrine Humbert (Grenoble, France) to grant the execution of a number of the revision experiments in her laboratory.

Funding

This research was supported in part by grants from the Telethon Foundation (GGP14202), AIRC (IG2016-18906), FISM (2013), the Italian Ministry of Health (*Progetto Giovani Ricercatori* GR2011–2012 to FS) and the Danish National Supercomputer for Life Science Computerome. VC is supported by the Lundbeck Foundation (R209–2015–3505) and the KBVU (R146-A9471). This work has been also supported by a KBVU grant from the Danish Cancer Society (R146-A9364) to FC. We are also grateful to the Bjarne Saxhof Foundation, the Lundbeck Foundation (R167–2013–16100), the NovoNordisk Foundation (7559) and the European Union (Horizon 2020 MEL-PLEX, grant agreement 642295). Further, FC and EP labs in Copenhagen are part of the *Center of Excellence in Autophagy, Recycling and Disease* (CARD), funded by the Danish National Research Foundation.

References

- Mizushima N. Autophagy: process and function. *Genes Dev* 2007; 21:2861-73; PMID:18006683; <http://dx.doi.org/10.1101/gad.1599207>
- He C, Klionsky DJ. Regulation mechanisms and signaling pathways of autophagy. *Annu Rev Genet* 2009; 43:67-93; PMID:19653858; <http://dx.doi.org/10.1146/annurev-genet-102808-114910>
- Mathew R, Karantza-Wadsworth V, White E. Role of autophagy in cancer. *Nat Rev Cancer* 2007; 7:961-7; PMID:17972889; <http://dx.doi.org/10.1038/nrc2254>
- Mizushima N, Levine B, Cuervo AM, Klionsky DJ. Autophagy fights disease through cellular self-digestion. *Nature* 2008; 451(7182):1069-75.
- Abada A, Elazar Z. Getting ready for building: Signaling and autophagosome biogenesis. *EMBO Rep* 2014; 15:839-52; PMID:25027988; <http://dx.doi.org/10.15252/embr.201439076>
- Yeh E, Cunningham M, Arnold H, Chasse D, Monteith T, Ivaldi G, Hahn WC, Stukenberg PT, Shenolikar S, Uchida T, et al. A signalling pathway controlling MYC degradation that impacts oncogenic transformation of human cells. *Nat Cell Biol* 2004; 6:308-18; PMID:15048125; <http://dx.doi.org/10.1038/ncb1110>
- Kuma A, Hatano M, Matsui M, Yamamoto A, Nakaya H, Yoshimori T, Ohsumi Y, Tokuhisa T, Mizushima N. The role of autophagy during the early neonatal starvation period. *Nature* 2004; 432(7020):1032-6. Epub 2004 Nov 3; PMID:15525940; <http://dx.doi.org/10.1038/nature03029>
- Levine B, Kroemer G. Autophagy in the pathogenesis of disease. *Cell* 2008; 132:27-42; PMID:18191218; <http://dx.doi.org/10.1016/j.cell.2007.12.018>
- Chen N, Debnath J. Autophagy and tumorigenesis. *FEBS Lett* 2010; 584:1427-35; PMID:20035753; <http://dx.doi.org/10.1016/j.febslet.2009.12.034>
- Degenhardt K, Mathew R, Beaudoin B, Bray K, Anderson D, Chen G, Mukherjee C, Shi Y, Gélinas C, Fan Y, et al. Autophagy promotes tumor cell survival and restricts necrosis, inflammation, and tumorigenesis. *Cancer Cell* 2006; 10:51-64; PMID:16843265; <http://dx.doi.org/10.1016/j.ccr.2006.06.001>
- Karantza-Wadsworth V, White E. Role of autophagy in breast cancer. *Autophagy* 2007; 3:610-3; PMID:17786023; <http://dx.doi.org/10.4161/auto.4867>
- Corcelle EA, Puustinen P, Jäättelä M. Apoptosis and autophagy: Targeting autophagy signalling in cancer cells - 'trick or treats?'. *FEBS J* 2009; 276:6084-96; PMID:19788415; <http://dx.doi.org/10.1111/j.1742-4658.2009.07332.x>
- Chen N, Karantza V. Autophagy as a therapeutic target in cancer. *Cancer Biol Ther* 2011; 11:157-68; PMID:21228626; <http://dx.doi.org/10.4161/cbt.11.2.14622>
- Eisenberg-Lerner A, Kimchi A. The paradox of autophagy and its implication in cancer etiology and therapy. *Apoptosis* 2009; 14(4):376-91. Review; PMID:19172397; <http://dx.doi.org/10.1007/s10495-008-0307-5>
- Bartel DP. MicroRNAs: target recognition and regulatory functions. *Cell* 2009; 136:215-33; PMID:19167326; <http://dx.doi.org/10.1016/j.cell.2009.01.002>
- Gupta SK, Thum T. Non-coding RNAs as orchestrators of autophagic processes. *J Mol Cell Cardiol* 2015; 95:26-30; pii: S0022-2828(15)30116-4. [Epub ahead of print] Review.
- Jing Z, Han W, Sui X, Xie J, Pan H. Interaction of autophagy with microRNAs and their potential therapeutic implications in human cancers. *Cancer Lett* 2015; 356(2 Pt B):332-8. Epub 2014 Oct 7. Review; PMID:25304373; <http://dx.doi.org/10.1016/j.canlet.2014.09.039>
- Zhai H, Fesler A, Ju J. MicroRNA: A third dimension in autophagy. *Cell Cycle* 2013; 12(2):246-50. Epub 2012 Jan 15. Review; PMID:23255136; <http://dx.doi.org/10.4161/cc.23273>
- Frankel LB, Lund AH. MicroRNA regulation of autophagy. *Carcinogenesis* 2012; 33:2018-25; PMID:22902544; <http://dx.doi.org/10.1093/carcin/bgs266>
- Gibbins D, Mostowy S, Voinnet O. Autophagy selectively regulates MIRNA homeostasis. *Autophagy* 2013; 9(5):781-3. Epub 2013 Feb 19; PMID:23422216; <http://dx.doi.org/10.4161/auto.23694>
- Zhu H, Wu H, Liu X, Li B, Chen Y, Ren X, Liu CG, Yang JM. Regulation of autophagy by a beclin 1-targeted microRNA, *MIR-30a*, in cancer cells. *Autophagy* 2009; 5:816-23; PMID:19535919; <http://dx.doi.org/10.4161/auto.9064>
- Brest P, Lapaquette P, Souidi M, Lebrigand K, Cesaro A, Vouret-Craviari V, Mari B, Barbry P, Mosnier JF, Hébuterne X, et al. A synonymous variant in *IRGM* alters a binding site for *MIR-196* and causes deregulation of *IRGM*-dependent xenophagy in Crohn's disease. *Nat Genet* 2011; 43:242-5; PMID:21278745; <http://dx.doi.org/10.1038/ng.762>
- Gundara JS, Robinson BG, Sidhu SB. Evolution of the "autophagosome-MIR". *Autophagy* 2011; 7(12):1553-4; PMID:22024754; <http://dx.doi.org/10.4161/auto.7.12.17762>
- Di Bartolomeo S, Corazzari M, Nazio F, Oliverio S, Lisi G, Antonioli M, Pagliarini V, Matteoni S, Fuoco C, Giunta L, et al. The dynamic interaction of *AMBRA1* with the dynein motor complex regulates mammalian autophagy. *J Cell Biol* 2010; 191:155-68; PMID:20921139; <http://dx.doi.org/10.1083/jcb.201002100>
- Nazio F, Strappazon F, Antonioli M, Bielli P, Cianfanelli V, Bordini M, Gretzmeier C, Dengjel J, Piacentini M, Fimia GM, et al. mTOR inhibits autophagy by controlling ULK1 ubiquitylation, self-association and function through *AMBRA1* and *TRAF6*. *Nat Cell Biol* 2013; 15(4):406-16. Epub 2013 Mar 24; PMID:23524951; <http://dx.doi.org/10.1038/ncb2708>
- Fimia GM, Stoykova A, Romagnoli A, Giunta L, Di Bartolomeo S, Nardacci R, Corazzari M, Fuoco C, Ucar A, Schwartz P, et al. *Ambra1* regulates autophagy and development of the nervous system. *Nature* 2007; 447:1121-5; PMID:17589504
- Cianfanelli V, Nazio F, Cecconi F. Connecting autophagy: *AMBRA1* and its network of regulation. *Mol Cell Oncol* 2015; 2(1):e970059; PMID:27308402; <http://dx.doi.org/10.4161/23723548.2014.970059>
- Cianfanelli V, Fuoco C, Lorente M, Salazar M, Quondamatteo F, Gherardini PF, De Zio D, Nazio F, Antonioli M, D'Orazio M, et al. *AMBRA1* links autophagy to cell proliferation and tumorigenesis by promoting *c-Myc* dephosphorylation and degradation. *Nat Cell Biol* 2015; 17(5):706; PMID:25925585; <http://dx.doi.org/10.1038/ncb3171>
- Mei Y, Su M, Soni G, Salem S, Colbert CL, Sinha SC. Intrinsically disordered regions in autophagy proteins. *Proteins* 2014; 82:565-78; PMID:24115198; <http://dx.doi.org/10.1002/prot.24424>
- Chou YT, Lin HH, Lien YC, Wang YH, Hong CF, Kao YR, Lin SC, Chang YC, Lin SY, Chen SJ, et al. *EGFR* promotes lung tumorigenesis by activating *MIR-7* through a *Ras/ERK/Myc* pathway that targets

- the Ets2 transcriptional repressor ERF. *Cancer Res* 2010; 70:8822-31; PMID:20978205; <http://dx.doi.org/10.1158/0008-5472.CAN-10-0638>
- [31] Kalinowski FC, Brown RA, Ganda C, Giles KM, Epis MR, Horsham J, Leedman PJ. microRNA-7: a tumor suppressor miRNA with therapeutic potential. *Int J Biochem Cell Biol* 2014; 54:312-7. Epub 2014 Jun 5. Review; PMID:24907395; <http://dx.doi.org/10.1016/j.biocel.2014.05.040>
- [32] Cheng AM, Byrom MW, Shelton J, Ford LP. Antisense inhibition of human MIRNAs and indications for an involvement of MIRNA in cell growth and apoptosis. *Nucleic Acids Res* 2005; 33:1290-7; PMID:15741182; <http://dx.doi.org/10.1093/nar/gki200>
- [33] Maragkakis M, Reczko M, Simossis VA, Alexiou P, Papadopoulos GL, Dalamagas T, Giannopoulos G, Goumas G, Koukis E, et al. DIANA-microT web server: elucidating microRNA functions through target prediction. *Nucleic Acids Res* 2009; 37:W273-6; PMID:19406924; <http://dx.doi.org/10.1093/nar/gkp292>
- [34] Grimson A, Farh KK, Johnston WK, Garrett-Engele P, Lim LP, Bartel DP. MicroRNA targeting specificity in mammals: determinants beyond seed pairing. *Mol Cell* 2007; 27:91-105; PMID:17612493; <http://dx.doi.org/10.1016/j.molcel.2007.06.017>
- [35] Friedman RC, Farh KK, Burge CB, Bartel DP. Most mammalian mRNAs are conserved targets of microRNAs. *Genome Res* 2009; 19:92-105; PMID:18955434; <http://dx.doi.org/10.1101/gr.082701.108>
- [36] Betel D, Wilson M, Gabow A, Marks DS, Sander C. The microRNA.org resource: Targets and expression. *Nucleic Acids Res* 2008; 36:D149-53; PMID:18158296; <http://dx.doi.org/10.1093/nar/gkm995>
- [37] Wang P, Zhang J, Zhang L, Zhu Z, Fan J, Chen L, Zhuang L, Luo J, Chen H, Liu L, et al. MicroRNA 23b regulates autophagy associated with radioresistance of pancreatic cancer cells. *Gastroenterology* 2013; 145(5):1133-1143.e12. Epub 2013 Aug 2; PMID:23916944; <http://dx.doi.org/10.1053/j.gastro.2013.07.048>
- [38] Le Sage C, Agami R. Immense promises for tiny molecules: uncovering MIRNA functions. *Cell Cycle* 2006; 5:1415-21; PMID:16775415; <http://dx.doi.org/10.4161/cc.5.13.2890>
- [39] Pankiv S, Clausen TH, Lamark T, Brech A, Bruun JA, Outzen HF, Øvervatn A, Bjørkøy G, Johansen T. SQSTM1/p62 binds directly to Atg8/LC3 to facilitate degradation of ubiquitinated protein aggregates by autophagy. *J Biol Chem* 2007; 282:24131-45; PMID:17580304; <http://dx.doi.org/10.1074/jbc.M702824200>
- [40] Liang XH, Jackson S, Seaman M, Brown K, Kempkes B, Hibshoosh H, Levine B. Induction of autophagy and inhibition of tumorigenesis by beclin 1. *Nature* 1999; 402:672-6; PMID:10604474; <http://dx.doi.org/10.1038/45257>
- [41] Zhang JA, Zhou BR, Xu Y, Chen X, Liu J, Gozali M, Wu D, Yin ZQ, Luo D. MiR-23a-depressed autophagy is a participant in PUVA- and UVB-induced premature senescence. *Oncotarget* 2016; 7(25):37420-37435
- [42] Tazawa H, Yano S, Yoshida R, Yamasaki Y, Sasaki T, Hashimoto Y, Kuroda S, Ouchi M, Onishi T, Uno F, et al. Genetically engineered oncolytic adenovirus induces autophagic cell death through an E2F1-microRNA-7-epidermal growth factor receptor axis. *Int J Cancer* 2012; 131(12):2939-50; PMID:22492316; <http://dx.doi.org/10.1002/ijc.27589>
- [43] Boya P, Reggiori F, Codogno P. Emerging regulation and functions of autophagy. *Nat Cell Biol* 2013; 15(7):713-20. Review. Erratum in: *Nat Cell Biol*. 2013 Aug;15(8):1017; PMID:23817233; <http://dx.doi.org/10.1038/ncb2788>
- [44] Kroemer G, Mariño G, Levine B. Autophagy and the integrated stress response. *Mol Cell* 2010; 40(2):280-93. Review; PMID:20965422; <http://dx.doi.org/10.1016/j.molcel.2010.09.023>
- [45] Wei Y, Zou Z, Becker N, Anderson M, Sumpter R, Xiao G, Kinch L, Koduru P, Christudass CS, Veltri RW, et al. EGFR-mediated Beclin 1 phosphorylation in autophagy suppression, tumor progression, and tumor chemoresistance. *Cell* 2013; 154(6):1269-84; PMID:24034250; <http://dx.doi.org/10.1016/j.cell.2013.08.015>
- [46] Puustinen P, Rytter A, Mortensen M, Kohonen P, Moreira JM, Jäättelä M. CIP2A oncoprotein controls cell growth and autophagy through mTORC1 activation. *J Cell Biol* 2014; 204(5):713-27; PMID:24590173; <http://dx.doi.org/10.1083/jcb.201304012>
- [47] Neufeld TP. Autophagy and cell growth—the yin and yang of nutrient responses. *J Cell Sci* 2012; 125(Pt 10):2359-68. Epub 2012 May 30; PMID:22649254; <http://dx.doi.org/10.1242/jcs.103333>
- [48] Chou YT, Lin HH, Lien YC, Wang YH, Hong CF, Kao YR, Lin SC, Chang YC, Lin SY, Chen SJ, et al. EGFR promotes lung tumorigenesis by activating MIR-7 through a Ras/ERK/Myc pathway that targets the Ets2 transcriptional repressor ERF. *Cancer Res* 2010; 70:8822-31; PMID:20978205; <http://dx.doi.org/10.1158/0008-5472.CAN-10-0638>
- [49] Denti MA, Rosa A, Sthandier O, De Angelis FG, Bozzoni I. A new vector, based on the PolII promoter of the U1 snRNA gene, for the expression of siRNAs in mammalian cells. *Mol Ther* 2004; 10(1):191-9; PMID:15272480; <http://dx.doi.org/10.1016/j.ythe.2004.04.008>
- [50] Colaprico A, Silva TC, Olsen C, Garofano L, Cava C, Garolini D, Sabedot TS, Malta TM, Pagnotta SM, Castiglioni I, et al. TCGAAbio-links: An R/Bioconductor package for integrative analysis of TCGA data. *Nucleic Acids Res* 2016; 44(8):e71; PMID:26704973; <http://dx.doi.org/10.1093/nar/gkv1507>
- [51] Risso D, Schwartz K, Sherlock G, Dudoit S. GC-content normalization for RNA-Seq data. *BMC Bioinformatics* 2011; 12:480; PMID:22177264; <http://dx.doi.org/10.1186/1471-2105-12-480>



The multifaceted mitochondrion: An attractive candidate for therapeutic strategies



Flavie Strappazzon^{a,b,*}, Francesco Cecconi^{a,b,c}

^a IRCCS Fondazione Santa Lucia, 00143 Rome, Italy

^b Department of Biology, University of Rome Tor Vergata, 00133 Rome, Italy

^c Unit of Cell Stress and Survival, Danish Cancer Society Research Center, 2100 Copenhagen, Denmark

ARTICLE INFO

Article history:

Received 18 November 2014

Received in revised form 7 March 2015

Accepted 13 March 2015

Available online 24 March 2015

Keywords:

Mitochondrial biogenesis

Mitochondrial quality control

Mitochondrial plasticity

ABSTRACT

Mitochondria are considered the powerhouse of the cell and disturbances in mitochondrial functions are involved in several disorders such as neurodegeneration and mitochondrial diseases. This review summarizes pharmacological strategies that aim at modifying the number of mitochondria, their dynamics or the mitochondrial quality-control mechanisms, in several pathological instances in which any of these mechanisms are impaired or abnormal. The interplay between different cellular pathways that involve mitochondria in order to respond to stress is highlighted. Such a high mitochondrial plasticity could be exploited for new treatments.

© 2015 Published by Elsevier Ltd.

1. Introduction

In mitochondria, energy obtained by nutrients is converted, thanks to the oxidative phosphorylation system (OXPHOS) – located in the inner-membrane of the mitochondria, into ATP. Mitochondria plays many other roles, such as regulating signals through mitochondrial reactive oxygen species (ROS) [1] that they produce, in regulating the membrane potential [2] and cell death processes [3], and in modulating calcium signalling [4] and steroid production [5]. According to the endosymbiotic hypothesis, mitochondria were previously considered to be prokaryotic cells (derived from alphaproteobacteria) and able to carry out oxidative functions that were not possible for eukaryotic cells. Mitochondria next went on to be considered as endosymbionts inside the eukaryotes. This specificity renders the mitochondria a unique organelle with its own mitochondrial DNA (mtDNA). However, mtDNA encodes only a few crucial proteins (13 proteins). Consequently, a controlled importation of nuclear DNA (nuDNA)-encoded proteins is required to allow a proper mitochondria functionality [6].

Mitochondrial shape is also crucial for their function, this being regulated through an association with the cytoskeleton [7]. Moreover, mitochondria are highly dynamic organelles, undergoing

continuous fusion and fission in order to react to extra cellular stressors [8].

When the organelle is excessively damaged, it becomes dangerous for the cell, initiating the apoptotic pathway [9]. Fortunately, cells have developed a mitochondrial quality control system that can selectively degrade damaged mitochondria, through a selective autophagic process, called mitophagy [10]. Healthy and damaged mitochondria are illustrated in a simplified way in Fig. 1.

Considering that mitochondria, the principal source of energy for the cell, coordinate metabolism, and coordinate a subtle balance between mtDNA and nuDNA transcription and translation, it is not surprising that defects in these functions are involved in several diseases requiring therapy [11,12].

In particular, ageing-related diseases, such as neurodegenerative diseases and cancer are linked to mitochondrial disturbances. For instance, mitochondrial dysfunction and increased oxidative damage (high production of ROS that can in turn damage mtDNA) are often associated with Alzheimer disease (AD), and Parkinson disease (PD), suggesting that oxidative stress may play an important role in the pathophysiology of these diseases [13]. Moreover, mtDNA mutations could contribute to cancer progression by increasing mitochondrial oxidative damage and changing the energy capacities of the cell (reviewed in [14]). Finally, metabolic disorders such as obesity and type 2 diabetes, are also directly linked to mitochondrial dysfunction. A number of mitochondrial therapeutic interventions aimed at improving these metabolic disorders have been favourably reviewed [15].

* Corresponding author at: IRCCS Fondazione Santa Lucia, 00143 Rome, Italy.
Tel.: +39 6501703093.

E-mail address: f.strappazzon@hsantalucia.it (F. Strappazzon).

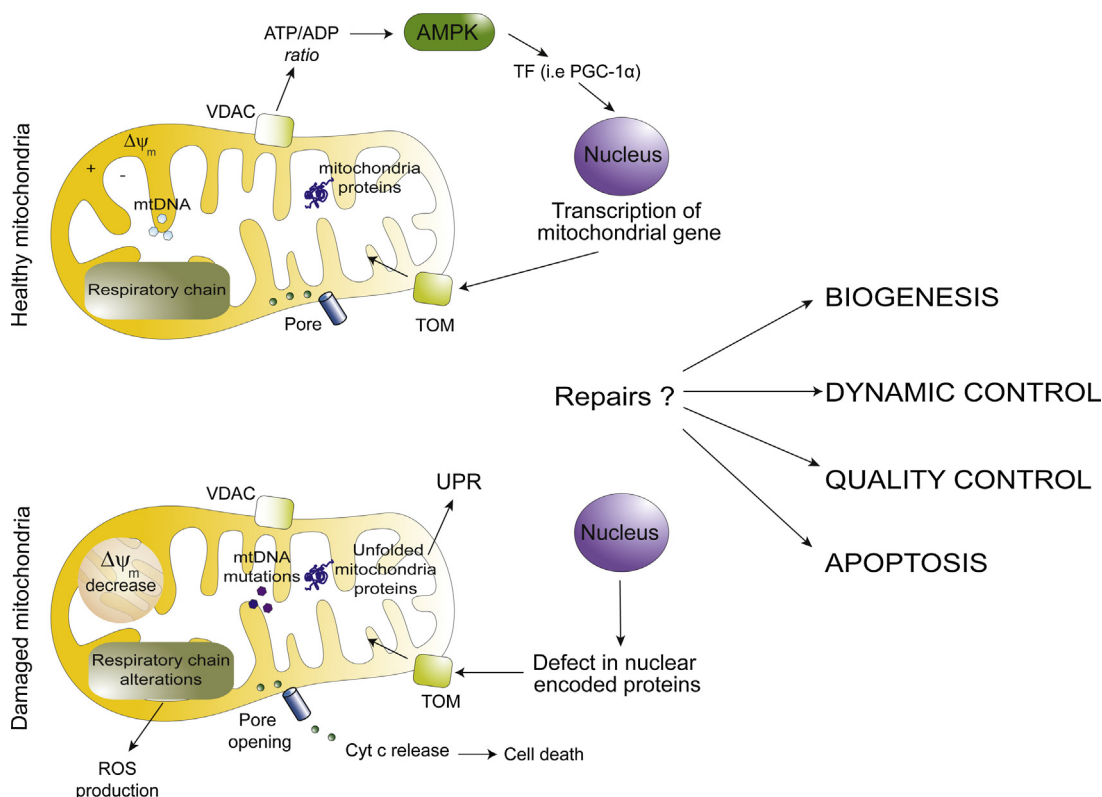


Fig. 1. Mitochondrial physiology and its major dysfunctions: principal pathways that can be manipulated to restore the organelle functions. Mitochondria produce ATP through the oxidative phosphorylation system (OXPHOS). When the cytosolic ATP/ADP ratio becomes too low, the AMP-dependent kinase (AMPK) is activated and acts principally on the transcriptional co-activator PGC-1 α . Mitochondrial DNA (mtDNA) encodes 13 key proteins responsible for respiratory chain synthesis and ATP synthase. The other mitochondrial proteins are imported from the cytosol after transcription of nuclear DNA (nuDNA). Mutations of the mitochondrial or nuclear DNA lead to alterations in the respiratory chain that, in turn, induce an increase in ROS production. Following apoptotic stimuli, the mitochondrial outer membrane becomes permeable (pore-opening) and cytochrome c (Cyt c) is released into the cytosol, where it can activate the apoptotic pathway.

Here are discussed the strategies aimed at repairing mitochondria functions in diseases in which they are damaged, such as PD, AD, Charcot–Marie–Tooth type 2A, the dominant optic atrophy and mitochondrial diseases such as the mitochondrial encephalopathy lactic acidosis. Thanks to the growing understanding of mitochondrial functions, we are now able to act, by using therapeutic compounds, on several functional aspects of the organelle. In this review, we present pharmacological strategies that affect mitochondria biogenesis, mitochondrial dynamics and mitochondria quality control, and we try to highlight the high plasticity that offers mitochondria a mechanism for coping with stress.

2. Strategies that affect mitochondrial biogenesis

Mitochondrial diseases are characterized by mutations on genes mtDNA- or nuDNA-encoded. For example, mitochondrial encephalopathy lactic acidosis is a disease due to a mutation in the mitochondrial tRNA gene that leads to defective assembly of oxidative phosphorylation complexes and defects in energy metabolism in the neuromuscular system [16]. Mutations on nuclear-encoded mitochondrial genes can also lead to defects in mitochondrial metabolic functions [17,18]. Cellular energy deficit is also a feature of several diseases, such as neurodegeneration, cancer, and metabolic diseases as obesity and type 2 diabetes [19]. Consequently, boosting mitochondria biogenesis, and thus the number of mitochondria, has considerable therapeutic potential since it may enhance ATP synthesis.

Physiologically, mitochondria number is stimulated following a workload or a reduction in nutrients. Indeed, caloric restriction is the well-known physiological intervention that can increase

lifespan [20]. A well-known way to stimulate mitochondrial biogenesis is to exert pressure on PGC-1 α (peroxisome proliferator-activated receptor gamma coactivator 1 alpha), a key player in mitochondrial biogenesis. PGC-1 α stimulates the activity of transcription factors such as nuclear respiratory factor (NRF-1), which, in turn, modulates the expression of other factors important for mtDNA replication and transcription [21]. More recently, synthetic chemicals that mimic the effects of a low-calorie intake have been identified and very well reviewed in Andreux et al. [22]. Here we summarize these principal components.

The Sirtuin family of histone deacetylase [23] is a good target to promote mitochondria biogenesis. In fact, these proteins depend on the metabolic co-factor NAD⁺ [24]; moreover, Sirtuin 1 (SIRT-1) is able to activate transcription factors such as PGC1 α [25]. The first compound discovered to act on Sirtuins was resveratrol, which by acting on AMPK (AMP-activated protein kinase), is responsible for an increase in NAD⁺ production that leads indirectly to Sirtuin activation [26,27]. Following this discovery, other SIRT-1-activating compounds have been identified, i.e., SRT1720 and SRT2014. The latest study describes a role for SRT1720 in extending the lifespan of mice by about 9% [28]. Again in order to activate sirtuins, researchers have developed a dietary supplemented with the NAD⁺ precursors nicotinamide mononucleotide (NMN) or nicotinamide riboside. In fact, NMN ameliorates glucose intolerance by restoring NAD⁺ levels in a type 2 diabetic mouse model [29].

The activation of AMPK is another way to increase mitochondrial biogenesis. AMPK is responsible of the enhancement of energy production which follows an increase of the AMP/ATP ratio [30]. AICAR (the AMPK agonist 5-aminoimidazole-4-carboxamide riboside) is responsible for AMPK activation and can then rescue

mitochondrial dysfunction [31]. The mTOR inhibitor Rapamycin can also act on AMPK activation, this action leading to a lifespan increase in mice and other organisms [32,33].

Other small molecules can trigger mitochondrial biogenesis by acting on downstream effectors, such as the nuclear receptors NRF-1 (nuclear respiratory factor 1) and TFAM (mitochondrial transcription factor A). Among them, we can mention compounds acting on the three peroxisome proliferator-activated receptors PPARs (agonists), such as L-16501L, GW501516, bezafibrate and rosiglitazone. Also compounds acting on oestrogen-related receptor- α can stimulate mitochondrial biogenesis, similarly to compounds acting more downstream on co-factors [22].

3. Strategies that affect mitochondrial dynamics

Mitochondria undergo a continuous fission and fusion. This dynamic process is very important for a normal morphology of the organelle, and to allow correct mitochondrial functions [34,35]. Key proteins regulate fusion events: MFN1 and MFN2 (Mitofusin 1 and 2), two GTPases anchored to the outer mitochondrial membrane [36] and another GTPase, OPA1 (optic atrophy 1), localized in the intermembrane space and the inner membrane of mitochondria [37,38]. A disturbance in the activity of these three proteins leads to excessive mitochondria fragmentation that in turn, impacts mitochondrial functions (depolarization of mitochondrial membrane, loss of mtDNA, respiratory chain alterations) [39]. Of note, these fusion factors are crucial for early development, as demonstrated by the fact that all mice lacking MFN1, MFN2 or OPA1 die at an early embryonic stage [39,40]. Mitochondrial fission is regulated by another GTPase, the dynamin-related protein 1 (DRP1) [41]. Drp1 is recruited to mitochondria through mitochondrial fission factor or MiD49/51 [41–43]. Cells lacking Drp1 present deficiency in mitochondrial fission with elongated mitochondria [44]. Most importantly, point mutations in *Mfn2* or *OPA1* lead to neurodegenerative diseases, such as Charcot–Marie–Tooth type 2A and the dominant optic atrophy [45,46].

As a result, in recent years, Drp1 has become an obvious target for these neurodegenerative diseases. One of the primary phenotypes associated with loss of fusion in mammalian cells is a severe defect in mitochondrial respiratory functions, caused in part by loss of mtDNA within a subset of mitochondria, this being due to excessive mitochondria division (an important factor contributing to the aetiology of these neurodegenerative diseases) [47,48]. Indeed, one of the fundamental roles of mitochondrial fusion is to provide an exchange mechanism that allows mtDNA maintenance [49].

Several chemical compounds have been reported to induce mitochondrial elongation through the inhibition of mitochondrial fission mediated by Drp1. In 2008, Cassidy-Stone et al. [50] identified mdivi-1 (mitochondrial division inhibitor 1) as the first selective inhibitor of mitochondrial division dynamins. The mechanism of mdivi-1 inhibition is distinct from the more general DRP inhibitor, dynasore, which was discovered in a chemical screen for inhibitors of dynamin-1 GTPase activity [51]. Dynasore inhibits the GTP hydrolysis of dynamin-1, dynamin-2 and Drp1 in a non-competitive manner, by binding to the GTPase domain in both assembled and unassembled states. Mdivi-1 selectively inhibits the activity of mitochondrial division DRPs by binding to an allosteric site, which does not exclusively act through the GTPase domain. Upon binding, mdivi-1 creates or stabilizes a conformational form of unassembled, and probably dimeric Dnm1 that can bind GTP, but at a significantly lower affinity. In addition, Mdivi-1 only partially blocks apoptosis by acting early in the pathway to inhibit mitochondrial outer membrane permeabilization (MOMP). Drp1 activity is regulated by covalent phosphorylation, ubiquitylation and sumoylation [52,53]. By attenuating mitochondrial division and increasing

mitochondrial connectivity, mdivi-1 is a selective inhibitor of mitochondrial division and apoptosis; this is highly beneficial in some of the many heteroplasmic mtDNA-linked diseases in humans.

Wang et al. [54] identified in 2012, from a phenotype image-based screen, the “M1 Hydrazone”, a small molecule that also promotes the fusion of fragmented mitochondria and protects cells from mitochondrial fragmentation associated cell death (M1 pre-treated cells showed decrease in Cytochrome c (Cyt c) release and higher survival rate). M1 regulates protein levels of the subunits of mitochondrial adenosine triphosphate (ATP5A and 5B). It is now considered as another approach to the treatment of diseases associated with mitochondrial dysfunction.

More recently, Yue et al. discovered a small natural compound, 15-oxospiramylactone (S3) derived from spiramine A of *Spiraea japonica* (rose family plant) which potently induces mitochondrial fusion. S3-induced inhibition of USP30, a mitochondrial-localized deubiquitinase, increased the ubiquitylation of MFN1 and MFN2 without affecting their protein levels. This non-degradative ubiquitylation of MFNs is involved in regulation of mitochondrial fusion [55]. S3 can restore the normal distribution of mtDNA and recover membrane depolarization; furthermore, it increases ATP levels and OXPHOS capacity. S3 has promising therapeutic implications in the treatment of diseases such as Charcot–Marie–Tooth type 2A and autosomal dominant optic atrophy. Hitherto, S3 is the first identified naturally derived small molecule from plants to activate mitochondrial fusion and facilitate restoration of the mitochondrial network.

The function of pharmacological compounds created to act on mitochondrial dynamics are illustrated in Fig. 2.

4. Strategies that could affect mitochondrial quality control

4.1. Mitophagy

Given the important mitochondria roles described above, damaged mitochondria could be detrimental to the cell. In fact, accumulation of dysfunctional mitochondria is a characteristic of many types of diseases, including Alzheimer's disease (AD), Parkinson's disease (PD), ageing and cancer [56,57]. AD is the most common age-associated neurodegenerative disorder, characterized by cognitive dysfunction and loss of memory, caused by neuronal death in cerebral cortex. Neurofibrillary tangles and extracellular amyloid plaques composed of beta-amyloid derived from amyloid precursor protein (APP) are observed in AD human brains. Mitochondrial damage has been implicated in the development of the disease: abnormalities in mitochondrial structure and accumulation of beta-amyloid fragment in mitochondria have been observed in AD patients [58,59]. PD is caused by loss of dopaminergic neurons in the *substantia nigra*, a region important for motor control and coordination. An increase of mutations and/or deletions of the mtDNA is observed in patients with PD [60,61]. Consistently, mitochondrial damage accumulation is observed in dopaminergic neurons of PD patients. Mitochondrial dysfunction has also been correlated with ageing. Indeed, mitochondria are the primary source of ROS [62]. Ageing particularly affects mitochondrial homeostasis with mtDNA mutations accumulating due to ROS generation in mitochondria, an event that has been correlated with age-related decreased autophagic activity [63,64].

Fortunately, cells have developed a mechanism to remove damaged mitochondria through a selective autophagy process called mitophagy. Stimulation of mitophagy may have a pivotal role in combating AD and PD development through the elimination of defective mitochondria. Autophagy (from ancient Greek, meaning *self-eating*) is a catabolic process occurring in all eukaryotic cells, by which cytoplasmic material (e.g., proteins, lipids and organelles)

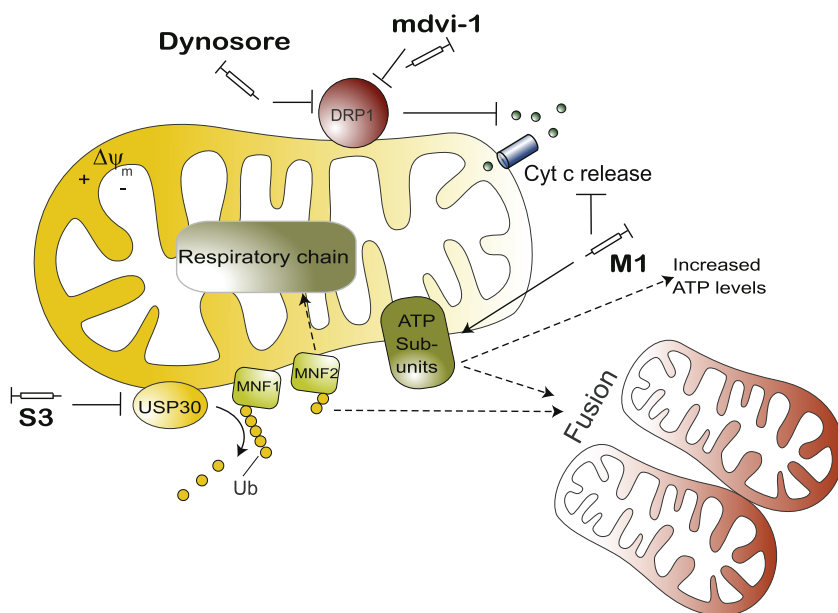


Fig. 2. Overview of the compounds acting on mitochondrial dynamics. Dynosore acts in a non-specific manner on DRP1 (inhibitor of dynamin-1, 2 and DRP1). By contrast, mdvi-1 inhibits DRP1 selectively and thus decreases division events that lead to a reduction of apoptosis by blocking Cyt c release. M1 Hydrazone is a small molecule that, by regulating levels of the subunits of mitochondrial adenosine phosphatase, promotes fusion of fragmented mitochondria and protects also cells from mitochondria-fragmentation-associated cell death. S3 induces mitochondrial fusion through inhibition of the deubiquitinase USP30. Consequently, USP30 cannot remove regulative ubiquitins on MFN1 and MFN2 which in turn increase their activity, promoting fusion events.

is degraded through the lysosome machinery. This process involves de novo formation of double-membraned vesicles, termed autophagosomes, which sequester the cytoplasm-derived materials and transport them to the lysosomes for degradation. There are three types of autophagy: microautophagy, chaperone-mediated autophagy (CMA), and macroautophagy. Macroautophagy is well conserved from yeast to mammals, and is the predominant pathway of autophagy. Non-selective autophagy (bulk autophagy) is induced by starvation, whilst selective autophagy is induced when organelles (such as mitochondria, and in this case the process is called mitophagy) are damaged or unwanted in the cell.

Fragmentation of the mitochondria is a critical step prior to engulfment of mitochondria into autophagosomes. Mitochondria damaged by the uncoupler CCCP (carbonyl cyanide *m*-chloro phenyl hydrazone) – due to a loss of their mitochondrial membrane potential ($\Delta\psi_m$), are subjected to mitophagy [65,66]. During this process, the protein kinase PINK1 is stabilized to the outer membrane of the mitochondria, where it can recruit the E3 ubiquitin ligase PARKIN. These two proteins are found to be mutated in autosomal recessive forms of PD [65]. The mitochondrial quality control, driven by PINK1/PARKIN proteins, has been more effectively characterized by RNAi screens [67]. New proteins such as HSPA1L (Heat shock 70 kDa protein 1-like), BAG4 (BAG family molecular chaperone regulator 4), and SIAH3 (siah E3 ubiquitin protein ligase family member 3) have been found to modulate translocation of PARKIN to damaged mitochondria, whereas TOMM7 (translocase of outer mitochondrial membrane 7 homolog) stabilizes PINK1 on the mitochondria. Interestingly, it has been demonstrated that after mitochondrial depolarization, the cytosolic pool of AMBRA1 interacts with PARKIN to enhance mitochondrial clearance [68]. We recently investigated the molecular mechanism responsible for the AMBRA1-dependent enhancement of PARKIN-mediated mitophagy. AMBRA1 was found to be a LIR-containing protein; as we have demonstrated, this motif is essential for the binding between AMBRA1 and LC3, following mitophagy induction. Furthermore, we have shown that this interaction is crucial in order to amplify PARKIN-mediated mitochondrial clearance [69].

In this system, it has recently been demonstrated that the other pro-autophagic factor BECLIN 1 also interacts with PARKIN and regulates PARKIN translocation to mitochondria [70].

In mammalian cells, mitophagy receptors are localized at the outer membrane of mitochondria and possess a consensus sequence (W/F/YxxL/I) that allows their binding with LC3 for selective autophagy. Until today, 2 types of mitophagy receptors have been identified: The group including NIX/BNIP3L and BNIP3 (BCL-2/adenovirus E1B 19 kDa protein-interacting protein 3-like) [71–73] and FUNDC1 (FUN14 domain-containing protein 1) [75].

NIX/BNIP3L and BNIP3 contain LIR motifs that can recruit LC3 to the mitochondria during red blood cell maturation [74]. Phosphorylation of BNIP3 on serine 17 and 24 are required to promote the binding with LC3 and thus needed for a correct mitophagy [76].

FUNDC1 is a mitochondrial outer membrane factor possessing three TM domains. The N-terminal region of FUNDC1 contains a LIR motif; it is exposed into the cytosol, where it can binds LC3 under hypoxia or after mitochondrial membrane depolarization. The activity of FUNDC1-mediated mitophagy is also regulated at a post-translational level. After membrane depolarization, FUNDC1 is phosphorylated on Serine 17 by the ULK1 kinase [75], whereas Liu et al. demonstrated that FUNDC1 required a dephosphorylation on tyrosine 18 and serine 13 to be active in the mitophagic pathway [76].

In addition to NIX and FUNDC1, AMBRA1 has been recently described as a novel regulator of mitophagy [69]. AMBRA1 has long been known to be a key mediator of autophagy, regulating positively the PI3K complex [77]. In 2011, a pool of AMBRA1 was demonstrated to be associated to BCL-2, in the outer mitochondrial membrane [78]. In addition, AMBRA1 possesses a LIR domain in its C-terminal part that allows its binding with LC3 upon mitophagy induction (after mitochondrial membrane depolarization). Furthermore, high levels of AMBRA1 at the mitochondria (obtained by overexpressing a mitochondria-targeted AMBRA1, also known as AMBRA1-ActA) are able to trigger massive mitophagy in both PARKIN-dependent or independent systems in mammalian cells. AMBRA1-ActA can thus be considered a novel inducer of mitophagy

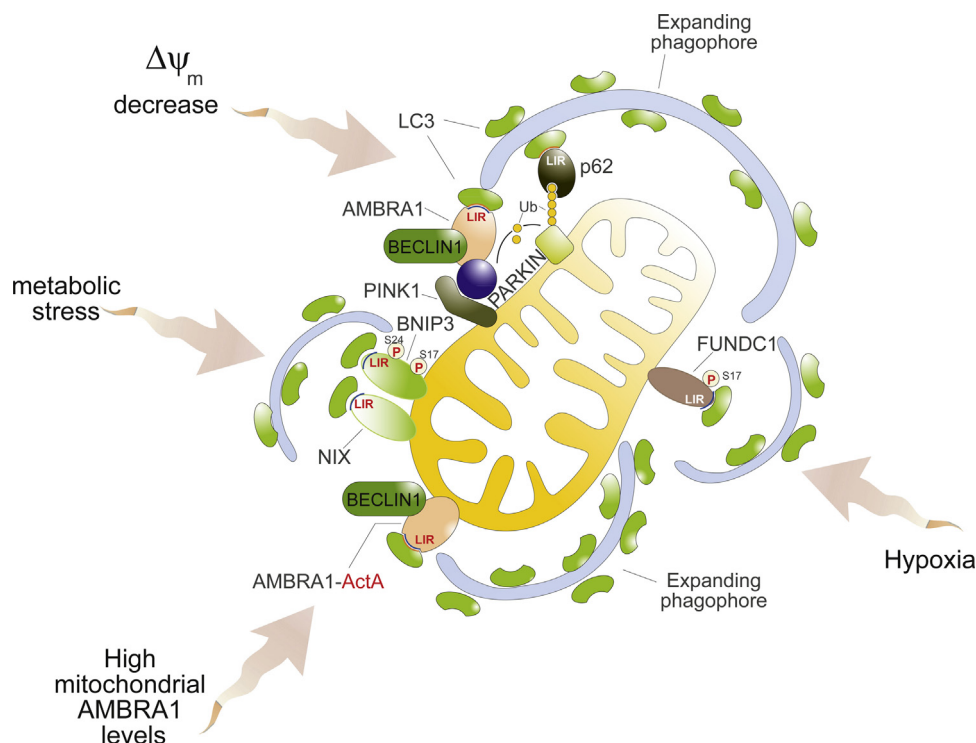


Fig. 3. Key players of mitophagy in mammalian cells. The PINK1/PARKIN pathway is induced after mitochondrial membrane depolarization. PINK1 is stabilized to mitochondria and allows mitochondrial recruitment of PARKIN. PARKIN ubiquitylates mitochondria that can subsequently be recognized by the scaffold protein p62. In this context, AMBRA1 is crucial to bring damaged mitochondria to degradation, by interacting with LC3 through its LIR motif. High levels of AMBRA1 at the mitochondria can induce massive mitophagy in a PARKIN-dependent or -independent context. AMBRA1 can thus be considered as a mitophagy receptor that binds LC3 through its LIR motif. FUNDC1, NIX/BNIP3L and BNIP also interact with LC3 through LIRs. Basically, FUNDC1 is phosphorylated on Tyr18 and Ser13. Hypoxia or mitochondrial depolarization induce dephosphorylation of the protein, leading to a stronger binding with LC3. By contrast, phosphorylation of BNIP3 on ser17 is necessary to favour its binding with LC3.

in the absence of any treatments with CCCP (a mitochondrial uncoupler known as the master mitophagy inducer), a finding which could herald new therapies to fight important human disorders, including age-associated pathologies such as PD, in which the PINK1/PARKIN pathway is mutated. Related to this, a pharmacological tool, named PMI (P62-mediated mitophagy) has been recently discovered to induce mitophagy in mammalian cells. This compound increases the expression and signalling of the autophagic adaptor molecule p62/SQSTM1 and induces mitochondrial removal. Even more interesting, this compound retains activity in cells devoid of a fully functional PINK1/PARKIN pathway [79]. This finding is of great interest in order to facilitate dissection of the molecular mechanisms underlying mitophagy. The mitophagy pathways described above are illustrated in Fig. 3.

4.1.1. Interplay between mitophagy and calcium

Gomez-Sanchez et al. [80] demonstrated that calcium overload is important in PINK1/PARKIN-mediated mitophagy. In fact, they found that increase of full-length PINK1 levels observed upon CCCP treatment is not due only to the stabilization of the protein but also to de novo PINK1 synthesis in a calcium dependent pathway. Since calcium chelators are able to inhibit mitochondrial removal following CCCP treatment, it will be interesting to test whether these kind of agents can directly decrease PINK1 transcription and thus act on mitophagy. Connected to this, Parkin mitochondrial localization increases the ER-mitochondrial crosstalk, favouring calcium transfer [81]. Since ER transfers calcium towards the mitochondria is fundamental for cell metabolism, it is not a surprise that disruption of proteins involved in ER/mitochondria connection induce calcium defects. Also, intracellular calcium has been shown to influence mitochondrial mobility [82]. In conclusion, all compounds that improve ER/mitochondria junction could be

opportune for the development of new therapies. Interestingly, the mitochondria-initiated calcium-mediated inter-organelle stress response is involved in cell death resistance in cancer cells [83]. In this review, we do not discuss apoptosis, which is another crucial feature of mitochondrial function, but this aspect has been extensively reviewed in [84].

4.2. Mitochondrial UPR

In addition to mitophagy, mammalian cells possess another quality control mechanism that involves the mitochondria-specific chaperones and proteases against misfolded proteins. Cancer cells, for example, survive in a highly oxidative environment. High levels of ROS induce oxidative damage to DNA, lipids and proteins, leading to their misfolding and aggregation in the mitochondria. Following an increase of misfolded and aggregated proteins into mitochondria, the cells triggers the mitochondrial unfolded protein response (UPR^{mt}), in order to decrease the proteotoxic stress and reach a good homeostasis. The UPR^{mt} is analogous to the UPR of the endoplasmic reticulum [85] but it was discovered more recently [86,87]. This signalling is controlled by 3 key proteins: (1) the transcription factor CHOP, which activates transcription of the mitochondrial chaperones and proteases [88]; there are two major mitochondrial chaperone systems that allow protein folding in the mitochondrial matrix: mtHSP70 and the HSP60-HSP10 machinery [89]; (2) the oestrogen receptor alpha (ER α), which exerts a cytoprotective action on the cell by acting on the proteasome and the protease Omi [90], and (3) SirT3, a novel major coordinator of the UPR^{mt} that orchestrates both the antioxidant machinery and mitophagy [91].

The UPR^{mt} is crucial for overcoming mitochondrial stress. Interestingly, Jin and Youle [92], demonstrated that a connection

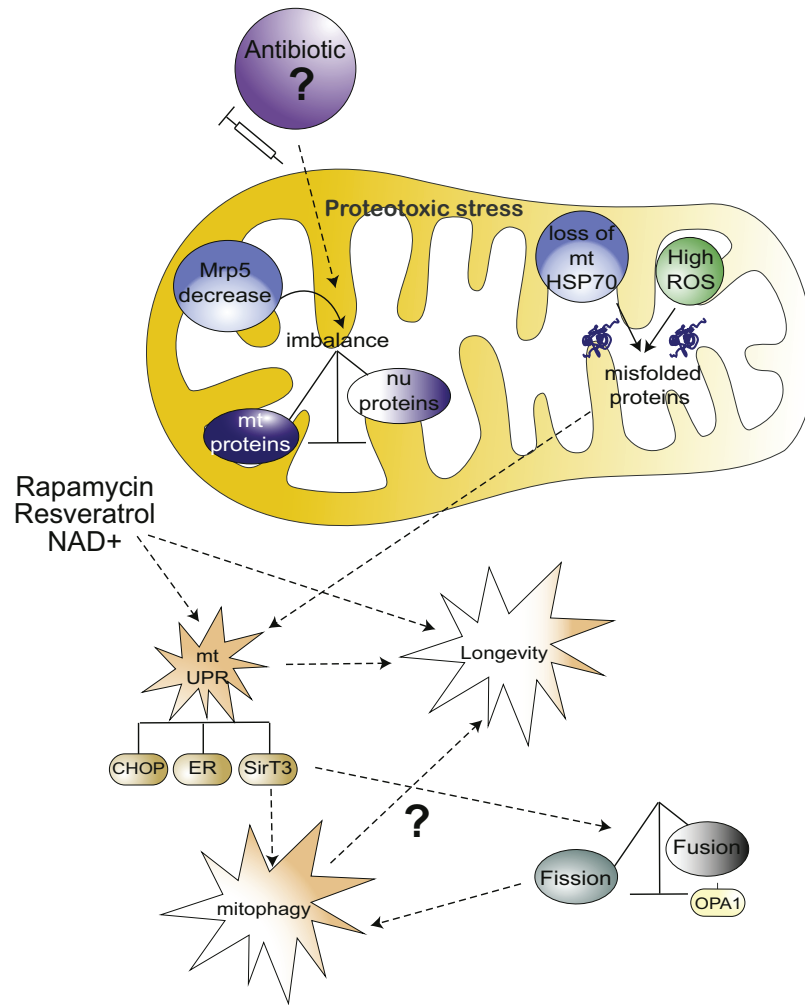


Fig. 4. UPR^{mt} signalling, as a target to develop therapeutic strategies in mammals. High levels of ROS induce oxidative damage to DNA, lipids and proteins, leading to their misfolding and aggregation. Following an increase of misfolded and aggregated proteins (mitochondrial proteotoxic stress) into mitochondria, the cells trigger the mitochondrial unfolded protein response (UPR^{mt}). UPR^{mt} can be activated after a loss of mtHSP70 that occurs in cells of PD patients, after a decrease of Mrps5 that triggers an imbalance between mitochondrial proteins and nuclear-encoded mitochondrial proteins. Three key proteins are involved in the UPR^{mt} signalling: CHOP, a transcription factor that activates transcription of chaperones and proteases; the oestrogen receptor alpha (ER α), that regulates proteasome activity, and the SirT3 protein that orchestrates both the antioxidant machinery and mitophagy. UPR^{mt} could thus be a novel target for therapeutic approaches. In fact, antibiotics seem to mimic, at least in *C. elegans*, Mrps5 decrease and then lead to longevity. Interconnection between UPR^{mt}, mitochondrial biogenesis, mitophagy, longevity and dynamics-related events are illustrated.

between the two quality control levels do, indeed, exist: expression of unfolded proteins in the matrix induces PINK1/PARKIN-mediated mitophagy and thus a reduction of unfolded protein load. Moreover, Papa et al. [91] recently demonstrated that if proteotoxic stress cannot be resolved, a mitophagic pathway, dependent of the protein SirT3, is triggered. SirT3 favours the activity of magnesium superoxide dismutase (MnSOD), a protein involved in the transformation of toxic superoxide into hydrogen peroxide and diatomic oxygen [93–95]. Consequently, a reduction of SirT3 is linked to an increase in ROS production [96]. Although the mechanism by which SirT3 coordinates the selection of damaged mitochondria has not been fully elucidated, it nevertheless shows mitochondria's remarkable plasticity in responding to stress.

Another study by Burbulla et al. illustrates the connection between UPR^{mt} and mitophagy: they showed that impaired intramitochondrial quality control, in PD, mediated by loss of mtHSP70 (also called Mortalin), can be compensated by PINK1/PARKIN-mediated mitophagy [97].

Of note, a gradual decrease of mitochondrial function occurs during ageing, as demonstrated by numerous studies, performed by using simple organisms as well as mammalian models [98]. Jovaisaite et al. [99] recently showed that activation of UPR^{mt} correlates

with longevity both in *Caenorhabditis elegans* and in mice [100]. The expression of mitochondrial ribosomal protein S5 (Mrps5) correlated with longevity. Knockdown of *mrps-5* expression decreases the translation of mtDNA-encoded components that leads to an imbalance between mtDNA and nuDNA-encoded OXPHOS complex components. This imbalance acts similarly to a proteotoxic stress for the host cell that – in turn, activates UPR^{mt} and prolongs lifespan. To pharmacologically mimic the reduction of *mrps-5*, Houtkooper et al. used antibiotics (doxycycline and chloramphenicol) that specifically targeted bacterial translation and thus also inhibited mitochondrial translation. They have obtained satisfactory results both in *C. elegans* and mouse hepatocyte cell cultures: Indeed, antibiotics are able to induce mito-nuclear imbalance leading to an UPR^{mt} and an increased of lifespan in *C. elegans*. Notably, exposition of worms or cells to mitochondrial biogenesis inducers, such as rapamycin and resveratrol (the well-known longevity agent described before) or NAD⁺ boosters (stimulator of the sirtuin 1 pathway), induce UPR^{mt} [100,101]. The next step is to better understand the physiological role of UPR^{mt} in mammals, although it seems that innovative therapeutic strategies can be developed, based on this process. In fact, given the studies performed in *C. elegans*, it is expected that pharmacological approaches that can mimic

UPR^{mt} could improve lifespan and health in age-related diseases such as AD or PD.

5. Discussion/conclusion

Mitochondria exhibit an ample range of stress responses in order to preserve the host cell. This feature underlines the fact that mitochondria are organelles with a high malleability. Therapeutic agents developed to restore mitochondrial function act principally on mitochondrial biogenesis and fusion/fission mechanisms. By gathering all information concerning possible ways to repair mitochondrial functions, it emerges that all pathways intended to save mitochondrial functions are interconnected. Biogenesis figures seem to be closely linked to the UPR^{mt} pathway, which is also linked to longevity. In addition, mitophagy, which is linked to mitochondrial dynamics (preceded by an increase in fission events), can be triggered if the UPR^{mt} pathway is not sufficient to help the cell. Finally, a recent study demonstrated that UPR^{mt} is directly linked to mitochondrial dynamics: SIRT3 binds and activates OPA1 to regulate mitochondrial dynamics during stress [102]. The interconnection between all mitochondrial pathways is illustrated in Fig. 4.

In conclusion, all therapies aimed at stimulating biogenesis can indirectly increase longevity, most likely by exerting pressure on the UPR^{mt} pathway. Further work should help to better understand whether mitophagy is important in increasing lifespan following caloric restriction. Finally, since novel molecules have been recently defined as novel mitophagy regulators (e.g., AMBRA1), efforts are now required to find new therapeutic approaches to exploit or target directly these novel mitophagic players. The same kind of studies are also required to find new compounds that can directly mimic UPR^{mt}, such as the antibiotics used in nematodes (that can create an imbalance between mtDNA and nuDNA).

Ideally, following from all the findings outlined here, the next step would be to identify a compound that acts on one of the pathways described before. This in turn would enhance the three other ways for restoring complete mitochondrial function under stresses.

Acknowledgements

We thank Mrs. M. Acuna Villa, Dr. M. Bennett and J. and D. Hodder for secretarial and proofreading work. The work performed by the author has been supported in part by from the Telethon Foundation (GGP14202), AIRC (IG2013 to FC), the Italian Ministry of University and Research (FIRB Accordi di Programma 2011), the Italian Ministry of Health (Ricerca Finalizzata and Ricerca Corrente to FC; GR2011-2012 to FS).

References

- [1] X. Li, P. Fang, J. Mai, E.T. Choi, H. Wang, X.F. Yang, Targeting mitochondrial reactive oxygen species as novel therapy for inflammatory diseases and cancers, *J. Hematol. Oncol.* 25 (2013) 6–19.
- [2] D. Voet, G. Judith, C. Voet, W. Pratt, *Fundamentals of Biochemistry*, 2nd ed., John Wiley and Sons, 2006, pp. 547.
- [3] D.R. Green, Apoptotic pathways: the roads to ruin, *Cell* 6 (1998) 695–698.
- [4] G. Hajnóczky, G. Csordás, S. Das, C. Garcia-Perez, M. Saotome, S. Sinha Roy, M. Yi, Mitochondrial calcium signalling and cell death: approaches for assessing the role of mitochondrial Ca²⁺ uptake in apoptosis, *Cell Calcium* 40 (5–6) (2006) 553–560.
- [5] M.F. Rossier, T channels and steroid biosynthesis: in search of a link with mitochondria, *Cell Calcium* 40 (2) (2006) 155–164.
- [6] M.T. Ryan, N.J. Hoogenraad, Mitochondrial nuclear communications, *Annu. Rev. Biochem.* 76 (2007) 701–722.
- [7] L. Rappaport, P. Oliviero, J.L. Samuel, Cytoskeleton and mitochondrial morphology and function, *Mol. Cell. Biochem.* 84 (1998) 101–105.
- [8] B. Westermann, Mitochondrial fusion and fission in cell life and death, *Nat. Rev. Mol. Cell Biol.* 11 (2010) 872–884.
- [9] J. Nunnari, A. Suomalainen, Mitochondria in sickness and in health, *Cell* 6 (2012) 1145–1159.
- [10] R. Youle, P. Narendra, Mechanism of mitophagy, *Nat. Rev. Mol. Cell Biol.* 12 (2011) 9–14.
- [11] D.C. Wallace, W. Fan, V. Procaccio, Mitochondrial energetics and therapeutics, *Annu. Rev. Pathol.* 5 (2010) 297–348.
- [12] M.R. Duchen, G. Szabadkai, Roles of mitochondria in human disease, *Essays Biochem.* 47 (2010) 115–137.
- [13] M.T. Lin, M.F. Beal, Mitochondrial dysfunction and oxidative stress in neurodegenerative diseases, *Nature* 7113 (2006) 787–795.
- [14] C. Hang, K. Yahui, Z. Hong, Oxidative stress mitochondrial dysfunction, and aging, *J. Signal Transduct.* (2012) 646354.
- [15] J. Szendroedi, E. Phielix, M. Roden, The role of mitochondria in insulin resistance and type 2 diabetes mellitus, *Nat. Rev. Endocrinol.* 8 (2012) 92–103.
- [16] K. Goto, M. Nagasawa, O. Yanagisawa, T. Kizuka, N. Ishii, K. Takamatsu, Muscular adaptations to combinations of high- and low-intensity resistance exercises, *J. Strength Cond. Res.* 4 (2004) 730–737.
- [17] J.A. Smeitink, O. Elpeleg, H. Antonicka, H. Diepstra, A. Saada, P. Smits, F. Sasarman, G. Vriend, J. Jacob-Hirsch, A. Shaag, G. Rechavi, B. Welling, J. Horst, R.J. Rodenburg, B. van den Heuvel, E.A. Shoubbridge, Distinct clinical phenotypes associated with a mutation in the mitochondrial translation elongation factor EFTs, *Am. J. Hum. Genet.* 5 (2006) 869–877.
- [18] C. Angelini, L. Bello, M. Spinazzi, C. Ferrati, Mitochondrial disorders of the nuclear genome, *Acta Myol.* 1 (2009) 16–23.
- [19] T.M. Wallace, D.R. Matthews, Poor glycemic control in type 2 diabetes: a conspiracy of disease suboptimal therapy and attitude, *QJM* 6(2000)369–374.
- [20] L. Fontana, L. Partridge, V.D. Longo, Extending healthy life span – from yeast to humans, *Science* 5976 (2010) 321–326.
- [21] R. Ventura-Clapier, Potentiating exercise training with resveratrol, *J. Physiol.* 590 (2012) 3215–3216.
- [22] P. Andreux, R.H. Houtkooper, J. Auwerx, Pharmacological approaches to restore mitochondrial function, *Nat. Rev. Drug Discov.* 12 (2013) 465–483.
- [23] R.H. Houtkooper, E. Pirinen, J. Auwerx, Sirtuins as regulators of metabolism and healthspan, *Nat. Rev. Mol. Cell Biol.* 4 (2012) 225–238.
- [24] S. Imai, C.M. Armstrong, M. Kaeberlein, L. Guarente, Transcriptional silencing and longevity protein Sir2 is an NAD-dependent histone deacetylase, *Nature* 6771 (2000) 795–800.
- [25] J.T. Rodgers, C. Lerin, W. Haas, S.P. Gygi, B.M. Spiegelman, P. Puigserver, Nutrient control of glucose homeostasis through a complex of PGC-1 α and SIRT1, *Nature* 7029 (2005) 113–118.
- [26] D. Beher, J. Wu, S. Cumine, K.W. Kim, S.C. Lu, L. Atangan, M. Wang, Resveratrol is not a direct activator of SIRT1 enzyme activity, *Chem. Biol. Drug Des.* 6 (2009) 619–624.
- [27] C. Cantó, L.Q. Jiang, A.S. Deshmukh, C. Matak, A. Coste, M. Lagouge, J.R. Zierath, J. Auwerx, Interdependence of AMPK and SIRT1 for metabolic adaptation to fasting and exercise in skeletal muscle, *Cell Metab.* 3 (2010) 213–219.
- [28] S.J. Mitchell, A. Martin-Montalvo, E.M. Mercken, H.H. Palacios, T.M. Ward, G. Abulwerdi, R.K. Minor, G.P. Vlasuk, J.L. Ellis, D.A. Sinclair, J. Dawson, D.B. Allison, Y. Zhang, K.G. Becker, M. Bernier, R. de Cabo, The SIRT1 activator SRT1720 extends lifespan and improves health of mice fed a standard diet, *Cell Rep.* 5 (2014) 836–843.
- [29] J. Yoshino, K.F. Mills, M.J. Yoon, S. Imai, Nicotinamide mononucleotide, a key NAD(+) intermediate, treats the pathophysiology of diet- and age-induced diabetes in mice, *Cell Metab.* 4 (2011) 528–536.
- [30] C. Cantó, J. Auwerx, NAD⁺ as a signaling molecule modulating metabolism, *Cold Spring Harb. Symp. Quant. Biol.* 76 (2011) 291–298.
- [31] C. Visconti, E. Bottani, G. Civiletto, R. Cerutti, M. Moggio, G. Fagioliari, E.A. Schon, C. Lamperti, M. Zeviani, In vivo correction of COX deficiency by activation of the AMPK/PGC-1 α axis, *Cell Metab.* 1 (2011) 80–90.
- [32] D.E. Harrison, R. Strong, Z.D. Sharp, J.F. Nelson, C.M. Astle, K. Flurkey, N.L. Nadon, J.E. Wilkinson, K. Frenkel, C.S. Carter, M. Pahor, M.A. Javors, E. Fernandez, R.A. Miller, Rapamycin fed late in life extends lifespan in genetically heterogeneous mice, *Nature* 7253 (2009) 392–395.
- [33] S. Robida-Stubbs, K. Glover-Cutter, D.W. Lamming, M. Mizunuma, S.D. Narasimhan, E. Neumann-Haefelin, D.M. Sabatini, T.K. Blackwell, TOR signaling and rapamycin influence longevity by regulating SKN-1/Nrf and DAF-16/FoxO, *Cell Metab.* 5 (2012) 713–724.
- [34] D.C. Chan, Mitochondria: dynamic organelles in diseases, aging, and development, *Cell* 7 (2006) 1241–1252.
- [35] S. Hoppins, L. Lackner, J. Nunnari, The machines that divide and fuse mitochondria, *Annu. Rev. Biochem.* 76 (2007) 751–780.
- [36] T. Koshiba, S.A. Detmer, J.T. Kaiser, H. Chen, J.M. McCaffery, D.C. Chan, Structural basis of mitochondrial tethering by mitofusin complexes, *Science* 305 (2004) 858–862.
- [37] S. Hiromi, M. Sheryl, M.P. Yaffe, R.E. Jensen, Mgm1p, a dynamin-related GTPase, is essential for fusion of the mitochondrial outer membrane, *Mol. Biol. Cell* 14 (2003) 2342–2356.
- [38] S. Cipolat, O. Martins de Brito, B. Dal Zilio, L. Scorrano, OPA1 requires mitofusin 1 to promote mitochondrial fusion, *Proc. Natl. Acad. Sci. U. S. A.* 101 (2004) 15927–15932.
- [39] H. Chen, S.A. Detmer, A.J. Ewald, E.E. Griffin, S.E. Fraser, D.C. Chan, Mitofusins Mfn1 and Mfn2 coordinately regulate mitochondrial fusion and are essential for embryonic, *J. Cell Biol.* 106 (2003) 189–200.
- [40] S. Cipolat, T. Rudka, D. Hartmann, V. Costa, L. Serneels, K. Craessaerts, K. Metzger, C. Frezza, W. Annaert, L. D'Adamio, C. Derks, T. Dejaegere, L. Pellegrini, R. D'Hooge, L. Scorrano, B. De Strooper, Mitochondrial rhomboid PARL regulates cytochrome c release during apoptosis via OPA1-dependent cristae remodeling, *Cell* 14 (2006) 163–175.

- [41] E. Smirnova, L. Griparic, D.L. Shurland, A.M. Van der Bliek, Dynamin-related protein Drp1 is required for mitochondrial division in mammalian cells, *Mol. Biol. Cell* 12 (2001) 2245–2256.
- [42] E. Ingerman, E.M. Perkins, M. Marino, J.A. Mears, J.M. McCaffery, J.E. Hinshaw, J. Nunnari, Dnm1 forms spirals that are structurally tailored to fit mitochondria, *J. Cell Biol.* 7 (2005) 1021–1027.
- [43] C.S. Palmer, L.D. Osellame, D. Laine, O.S. Koutsopoulos, A.E. Frazier, M.T. Ryan, Mid49 and Mid51, new components of the mitochondrial fission machinery, *EMBO Rep.* 6 (2011) 565.
- [44] N. Ishihara, M. Nomura, A. Jofuku, H. Kato, S.O. Suzuki, K. Masuda, H. Otera, Y. Nakanishi, I. Nonaka, Y. Goto, N. Taguchi, H. Morinaga, M. Maeda, R. Takayanagi, S. Yokota, K. Mihara, Mitochondrial fission factor Drp1 is essential for embryonic development and synapse formation in mice, *Nat. Cell Biol.* 8 (2009) 958–966.
- [45] S. Züchner, I.V. Mersianova, M. Muglia, N. Bissar-Tadmouri, J. Rochelle, E.L. Dadaei, M. Zappia, E. Nelis, A. Paticucci, J. Senderek, Y. Parman, O. Evgrafov, P.D. Jonghe, Y. Takahashi, S. Tsuji, M.A. Pericak-Vance, A. Quattrone, E. Battaloglu, A.V. Polyakov, V. Timmerman, J.M. Schröder, J.M. Vance, Mutations in the mitochondrial GTPase mitofusin 2 cause Charcot-Marie-Tooth neuropathy type 2A, *Nat. Genet.* 5 (2004) 449–451.
- [46] C. Alexander, M. Votruba, U.E. Pesch, D.L. Thiselton, S. Mayer, A. Moore, M. Rodriguez, U. Kellner, B. Leo-Kottler, G. Auburger, S.S. Bhattacharya, B. Wissinger, OPA1, encoding a dynamin-related GTPase, is mutated in autosomal dominant optic atrophy linked to chromosome 3q28, *Nat. Genet.* 2 (2000) 211–215.
- [47] A. Olichon, T. Landes, L. Arnauné-Pelloquin, L.J. Emorine, V. Mils, A. Guichet, C. Delettre, C. Hamel, P. Amati-Bonneau, D. Bonneau, P. Reynier, G. Lenaers, P. Belenguer, Effects of OPA1 mutations on mitochondrial morphology and apoptosis: relevance to ADOA pathogenesis, *J. Cell. Physiol.* 2 (2007) 423–430.
- [48] P.A. Parone, D.I. James, S. Da Cruz, Y. Mattenberger, O. Donzé, F. Barja, J.C. Martinou, Inhibiting the mitochondrial fission machinery does not prevent Bax/Bak-dependent apoptosis, *Mol. Cell. Biol.* 20 (2006) 7397–7408.
- [49] S. Hoppins, The regulation of mitochondrial dynamics, *Curr. Opin. Cell Biol.* 29C (August) (2014) 46–52.
- [50] A. Cassidy-Stone, J.E. Chipuk, E. Ingerman, C. Song, C. Yoo, T. Kuwana, M.J. Kurth, J.T. Shaw, J.E. Hinshaw, D.R. Green, J. Nunnari, Chemical inhibition of the mitochondrial division dynamin reveals its role in Bax/Bak-dependent mitochondrial outer membrane permeabilization, *Dev. Cell* 2 (2008) 193–204.
- [51] E. Macia, M. Ehrlich, R. Massol, E. Boucrot, C. Brunner, T. Kirchhausen, Dynasore, a cell-permeable inhibitor of dynamin, *Dev. Cell* 6 (2006) 839–850.
- [52] N. Nakamura, Y. Kimura, M. Tokuda, S. Honda, S. Hirose, MARCH-V is a novel mitofusin 2- and Drp1-binding protein able to change mitochondrial morphology, *EMBO Rep.* 10 (2006) 1019–1022.
- [53] N. Taguchi, N. Ishihara, A. Jofuku, T. Oka, K. Mihara, Mitotic phosphorylation of dynamin-related GTPase Drp1 participates in mitochondrial fission, *J. Biol. Chem.* 15 (2007) 11521–11529.
- [54] D. Wang, J. Wang, G.M. Bonamy, S. Meeusen, R.G. Bruschi, C. Turk, P. Yang, P.G. Schults, A small molecule promotes mitochondrial fusion in mammalian cells, *Angew. Chem. Int. Ed. Engl.* 37 (2012) 9302–9305.
- [55] W. Yue, Z. Chen, H. Liu, C. Yan, M. Chen, D. Feng, C. Yan, H. Wu, L. Du, Y. Wang, J. Liu, X. Huang, L. Xia, L. Liu, X. Wang, H. Jin, J. Wang, Z. Song, X. Hao, Q. Chen, A small natural molecule promotes mitochondrial fusion through inhibition of the deubiquitinase USP30, *Cell Res.* 4 (2014) 482–496.
- [56] K. Palikaras, N. Tavernarakis, Mitophagy in neurodegeneration and aging, *Front Genet.* 3 (2012) 297.
- [57] S.J. Goldman, R. Taylor, Y. Zhang, S. Jin, Autophagy and the degradation of mitochondria, *Mitochondrion* 4 (2010) 309–315.
- [58] J.W. Lustbader, M. Cirilli, C. Lin, H.W. Xu, K. Takuma, N. Wang, C. Caspersen, X. Chen, S. Pollak, M. Chaney, F. Trinchese, S. Liu, F. Gunn-Moore, L.F. Lue, D.G. Walker, P. Kuppasamy, Z.L. Zewier, O. Arancio, D. Stern, S.S. Yan, H. Wu, AβAD directly links Aβeta to mitochondrial toxicity in Alzheimer's disease, *Science* 306 (2004) 448–452.
- [59] C.S. Casley, J.M. Land, M.A. Sharpe, J.B. Clark, M.R. Duchon, L. Canevari, Beta-amyloid fragment 25–35 causes mitochondrial dysfunction in primary cortical neurons, *Neurobiol. Dis.* 10 (2012) 258–267.
- [60] K. Bender, J. Krishnan, C.M. Morris, G.A. Taylor, A.K. Reeve, R.H. Perry, E. Jaros, J.S. Hersheson, J. Betts, T. Klopstock, R.W. Taylor, D.M. Turnbull, High levels of mitochondrial DNA deletions in substantia nigra neurons in aging and Parkinson disease, *Nat. Genet.* 38 (5) (2006) 515–517.
- [61] S.J. Baloyannis, V. Costa, I.S. Baloyannis, Morphological alterations of the synapses in the locus coeruleus in Parkinson's disease, *J. Neurol. Sci.* (1–2) (2006) 35–41.
- [62] L.A. Sena, N.S. Chandel, Physiological roles of mitochondrial reactive oxygen species, *Mol. Cell* 2 (2012) 158–167.
- [63] A.M. Cuervo, Autophagy and aging: keeping that old broom working, *Trends Genet.* 24 (2008) 604–612.
- [64] V.M. Hubbard, R. Valdor, F. Macian, A.M. Cuervo, Selective autophagy in the maintenance of cellular homeostasis in aging organisms, *Biogerontology* 13 (2012) 21–35.
- [65] N. Narendra, A. Tanaka, D.F. Suen, R.J. Youle, Parkin is recruited selectively to impaired mitochondria and promotes their autophagy, *J. Cell Biol.* 183 (2008) 795–803.
- [66] S.M. Jin, A. Tanaka, D.F. Suen, C.A. Gautier, S. Shen, et al., PINK1 is selectively stabilized on impaired mitochondria to activate Parkin, *PLoS Biol.* 8 (2010) 1000298.
- [67] S. Hasson, L.A. Kane, K. Yamano, C.H. Huang, D.A. Sliter, E. Buehler, et al., High-content genome-wide RNAi screens identify regulators of parkin upstream of mitophagy, *Nat. Lett.* 504 (2013) 291–295.
- [68] C. Van Humbeek, T. Cornelissen, H. Hofkens, W. Mandemakers, K. Gevaert, De Strooper, et al., Parkin interacts with Ambra1 to induce mitophagy, *J. Neurosci.* 28 (2011) 10249–10261.
- [69] F. Strappazzon, F. Nazio, M. Corrado, V. Cianfanelli, A. Romagnoli, G.M. Fimia, S. Campello, R. Nardacci, M. Piacentini, M. Campanella, F. Ceconi, AMBRA1 is able to induce mitophagy via LC3 binding, regardless of PARKIN and p62/SQSTM1, *Cell Death Differ.* (2014), <http://dx.doi.org/10.1038/cdd.2014.139>.
- [70] V. Choubey, M. Cagalinec, J. Liiv, D. Safulina, M. Hockey, M. Kuum, et al., BECN1 is involved in the initiation of mitophagy. It facilitates PARK2 translocation to mitochondria, *Autophagy* 10 (2014) 1092–1106.
- [71] H. Sandoval, P. Thiagarajan, S.K. Dasgupta, A. Schumacher, J.T. Prchal, M. Chen, et al., Essential role for Nix in autophagic maturation of erythroid cells, *Nature* 454 (2008) 232–235.
- [72] I. Novak, V. Kirkin, D.G. McEwan, J. Zhang, P. Wild, A. Rozenknop, V. Rogov, F. Löhr, D. Popovic, A. Öchpinti, A.S. Reichert, J. Terzic, C.X. Deng, P.A. Ney, I. Dikic, Nix is a selective autophagy receptor for mitochondrial clearance, *EMBO Rep.* 1 (2010) 45–51.
- [73] I. Novak, I. Dikic, Autophagy receptors in developmental clearance of mitochondria, *Autophagy* 3 (2011) 301–303.
- [74] Y. Zhu, S. Massen, M. Terenzio, V. Lang, S. Chen-Lindner, R. Eils, I. Novak, I. Dikic, A. Hamacher-Brady, N.R. Brady, Modulation of serines 17 and 24 in the LC3-interacting region of Bnip3 determines pro-survival mitophagy versus apoptosis, *J. Biol. Chem.* 2 (2013) 1099–1113.
- [75] W. Wu, W. Tian, Z. Hu, G. Chen, L. Huang, W. Li, X. Zhang, P. Xue, C. Zhou, L. Liu, Y. Zhu, X. Zhang, L. Li, L. Zhang, S. Sui, B. Zhao, D. Feng, ULK1 translocates to mitochondria and phosphorylates FUNDC1 to regulate mitophagy, *EMBO Rep.* 5 (2014) 566–575.
- [76] L. Liu, D. Feng, G. Chen, M. Chen, Q. Zheng, P. Song, Q. Ma, C. Zhu, R. Wang, W. Qi, L. Huang, P. Xue, B. Li, X. Wang, H. Jin, J. Wang, F. Yang, P. Liu, Y. Zhu, S. Sui, Q. Chen, Mitochondrial outer-membrane protein FUNDC1 mediates hypoxia-induced mitophagy in mammalian cells, *Nat. Cell Biol.* 2 (2012) 177–185.
- [77] G.M. Fimia, A. Stoykova, A. Romagnoli, L. Giunta, R. Nardacci, M. Corazzari, et al., Ambra1 regulates autophagy and development of the nervous system, *Nature* 447 (2007) 1121–1125.
- [78] F. Strappazzon, M. Vietri-Rudan, S. Campello, F. Nazio, F. Florenzano, G.M. Fimia, et al., Mitochondrial BCL-2 inhibits AMBRA1-induced autophagy, *EMBO J.* 30 (2011) 1195–1208.
- [79] D.A. East, F. Fagiani, J. Crosby, N.D. Georgakopoulos, H. Bertrand, M. Schaap, A. Fowkes, G. Wells, Campanella PMI: a $\Delta\Psi_m$ independent pharmacological regulator of mitophagy, *Mol. Cell. Biol.* 11 (2014) 1585–1596.
- [80] R. Gómez-Sánchez, M.E. Gegg, J.M. Bravo-San Pedro, M. Niso-Santano, L. Alvarez-Erviti, E. Pizarro-Estrella, Y. Gutiérrez-Martín, A. Alvarez-Barrientos, J.M. Fuentes, R.A. González-Polo, A.H. Schapira, Mitochondrial impairment increases FL-PINK1 levels by calcium-dependent gene expression, *Neurobiol. Dis.* 62 (2014) 426–440.
- [81] T. Cali, D. Ottolini, A. Negro, M. Brini, Enhanced parkin levels favor ER-mitochondria crosstalk and guarantee Ca²⁺ transfer to sustain cell bioenergetics, *Biochim. Biophys. Acta* 4 (2013) 495–508.
- [82] Z.H. Sheng, Mitochondrial trafficking and anchoring in neurons: new insight and implications, *J. Cell Biol.* 7 (2014) 1087–1098.
- [83] H.K. Park, J.E. Lee, J. Lim, B.H. Kang, Mitochondrial Hsp90s suppress calcium-mediated stress signals propagating from mitochondria to the ER in cancer cells, *Mol. Cancer* 13 (2014) 148.
- [84] D.R. Green, L. Galluzzi, G. Kroemer, Mitochondria and the autophagy-inflammation-cell death axis in organismal aging, *Science* 6046 (2011) 1109–1112.
- [85] D.T. Rutkowski, R.J. Kaufman, A trip to the ER: coping with stress, *Trends Cell Biol.* 1 (2004) 20–28.
- [86] Q. Zhao, J. Wang, I.V. Levichkin, S. Stasinopoulos, M.T. Ryan, N.J. Hoogenraad, A mitochondrial specific stress response in mammalian cells, *EMBO J.* 17 (2002) 4411–4419.
- [87] J.E. Aldrige, T. Horibe, N.J. Hoogenraad, Discovery of genes activated by the mitochondrial unfolded protein response and cognate promoter elements, *PLoS ONE* 9 (2007) e874.
- [88] M.J. Backer, T. Tatsuda, T. Langer, Quality control of mitochondrial proteostasis, *Cold Spring Harb. Perspect. Biol.* 3 (7) (2011).
- [89] A. Chacinska, C.M. Koehler, D. Milenkovic, T. Lithgow, N. Pfanner, Importing mitochondrial proteins: machineries and mechanisms, *Cell* 4 (2009) 628–644.
- [90] S. Radke, H. Chander, P. Schäfer, G. Meiss, R. Krüger, J.B. Schulz, D. Germain, Mitochondrial protein quality control by the proteasome involves ubiquitination and the protease Omi, *J. Biol. Chem.* 19 (2008) 12681–12685.
- [91] L. Papa, D. Germain, SirT3 regulates the mitochondrial unfolded protein response, *Mol. Cell. Biol.* 4 (2014) 699–710.
- [92] S.M. Jin, R.J. Youle, PINK1- and Parkin-mediated mitophagy at a glance, *J. Cell Sci.* 125 (Pt 4) (2012) 795–799.
- [93] H.S. Kim, K. Patel, K. Muldoon-Jacobs, K.S. Bisht, N. Aykin-Burns, J.D. Pennington, R. van der Meer, P. Nguyen, J. Savage, K.M. Owens, A. Vassilopoulos, O. Ozden, S.H. Park, K.K. Singh, S.A. Abdulkadir, D.R. Spitz, C.X. Deng, D. Gius, SIRT3 is a mitochondria-localized tumor suppressor required for maintenance of mitochondrial integrity and metabolism during stress, *Cancer Cell* 1 (2010) 41–52.

- [94] N.R. Sundaresan, S.A. Samant, V.B. Pillai, S.B. Rajamohan, M.P. Gupta, SIRT3 is a stress-responsive deacetylase in cardiomyocytes that protects cells from stress-mediated cell death by deacetylation of Ku70, *Mol. Cell. Biol.* 20 (2008) 6384–6401.
- [95] R. Tao, M.C. Coleman, J.D. Pennington, O. Ozden, S.H. Park, H. Jiang, H.S. Kim, C.R. Flynn, S. Hill, W. Hayes McDonald, A.K. Olivier, D.R. Spitz, D. Gius, Sirt3-mediated deacetylation of evolutionarily conserved lysine 122 regulates MnSOD activity in response to stress, *Mol. Cell* 6 (2010) 893–904.
- [96] L.W. Finley, A. Carracedo, J. Lee, A. Souza, A. Egia, J. Zhang, J. Teruya-Feldstein, P.I. Moreira, S.M. Cardoso, C.B. Clish, P.P. Pandolfi, M.C. Haigis, SIRT3 opposes reprogramming of cancer cell metabolism through HIF1 α destabilization, *Cancer Cell* 3 (2011) 416–428.
- [97] L.F. Burbulla, J.C. Fitzgerald, K. Stegen, J. Westermeier, A.K. Thost, H. Kato, D. Mokranjac, J. Sauerwald, L.M. Martins, D. Voitalla, D. Rapaport, O. Riess, T. Proikas-Cezanne, T.M. Rasse, R. Krüger, Mitochondrial proteolytic stress induced by loss of mortalin function is rescued by Parkin and PINK1, *Cell Death Dis.* 5 (2014) e1180.
- [98] D.A. Pulliam, A. Bhattacharya, H. Van Remmen, Mitochondrial dysfunction in aging and longevity: a causal or protective role? *Antioxid. Redox Signal.* 12 (2013) 1373–1387.
- [99] V. Jovaisaite, L. Mouchiroud, J. Auwerx, The mitochondrial unfolded protein response, a conserved stress response pathway with implications in health and disease, *J. Exp. Biol.* 217 (Pt 1) (2014) 137–143.
- [100] R.H. Houtkooper, L. Mouchiroud, D. Ryu, N. Moullan, E. Katsyuba, G. Knott, R.W. Williams, J. Auwerx, Mitonuclear protein imbalance as a conserved longevity mechanism, *Nature* 497 (2013) 451–457.
- [101] L. Mouchiroud, R.H. Houtkooper, N. Moullan, E. Katsyuba, D. Ryu, C. Cantó, A. Mottis, Y.S. Jo, M. Viswanathan, K. Schoonjans, L. Guarente, J. Auwerx, The NAD(+)/Sirtuin pathway modulates longevity through activation of mitochondrial UPR and FOXO signaling, *Cell* 2 (2013) 430–441.
- [102] S.A. Samant, H.J. Zhang, Z. Hong, V.B. Pillai, N.R. Sundaresan, D. Wolfgeher, S.L. Archer, D.C. Chan, M.P. Gupta, SIRT3 deacetylates and activates OPA1 to regulate mitochondrial dynamics during stress, *Mol. Cell. Biol.* 5 (2014) 807–819.

Project performed as a Principal Investigator (PI) in the laboratory directed by my post-doctoral mentor Prof Cecconi. Santa Lucia Foundation, Rome, Italy (2014-2017).

My previous work demonstrated that, following AMBRA1-ActA expression, mitochondria are ubiquitylated prior their engulfment into the autophagosomes. Yet, since I discovered that AMBRA1 was able to induce mitophagy independently of the E3-ubiquitin ligase PARKIN, I sought to identify whether a novel E3 ubiquitin ligase could be involved in the mitophagy pathway mediated by AMBRA1. To do this project, I was awarded my first grant as a PI from the Italian Ministry of Health (Duration 3 years). These funds allowed me to acquire independence in the laboratory of Prof Cecconi. The grant covered my salary and the reagents necessary for the project and allowed me to co-supervise a PhD student.

By performing mass spectrometry analysis, we identified the E3 ubiquitin ligase HUWE1 as a novel key inducing factor in AMBRA1-mediated mitophagy, a process that takes place independently of the main *mitophagy receptors* (see Di Rita et al., 2018. *Nat Comm*). **Our results sheds new lights on the regulation of mitochondrial quality control and homoeostasis in mammalian cells.**

The same year we demonstrated that **AMBRA1-mediated mitophagy suppresses apoptosis in two *in vitro* models of Parkinson Disease** (see Di Rita et al., 2018. *Front in Cellular Neurosc.*). In parallel, I reported that AMBRA1 can act as a positive mediator of mitochondrial mediated apoptosis. Indeed, we observed that in a proapoptotic positive feedback loop, the C-terminal part of AMBRA1, generated by caspase cleavage upon apoptosis induction, inhibits the antiapoptotic factor Bcl-2 by a direct binding through its BH3-like domain (see Strappazon et al., 2016. *Autophagy*). Moreover a critical unresolved issue was how AMBRA1-mediated mitophagy was controlled in response to cellular stress. Therefore, I investigated the role of Bcl-2-family proteins on AMBRA1-dependent mitophagy and showed that the anti-apoptotic factor MCL1 delays AMBRA1-dependent mitophagy. Indeed, MCL1 overexpression is sufficient to inhibit recruitment to mitochondria of the E3 Ubiquitin ligase HUWE1, upon AMBRA1-mediated mitophagy induction. Our results demonstrated that MCL1 stability is regulated by the kinase GSK-3 β and the E3 ubiquitin ligase HUWE1, defining the anti-apoptotic factor MCL1 as an upstream stress-sensitive protein, functional in AMBRA1-mediated mitophagy (see Strappazon et al., 2019. *Cell Death and Diff.*). **Collectively, our results established**

that **AMBRA1** is at the crossroad between autophagy and cell death. A sum of these main researches on AMBRA1 has been published in “AMBRA1 at a Glance” and is illustrated in **Figure 1**.

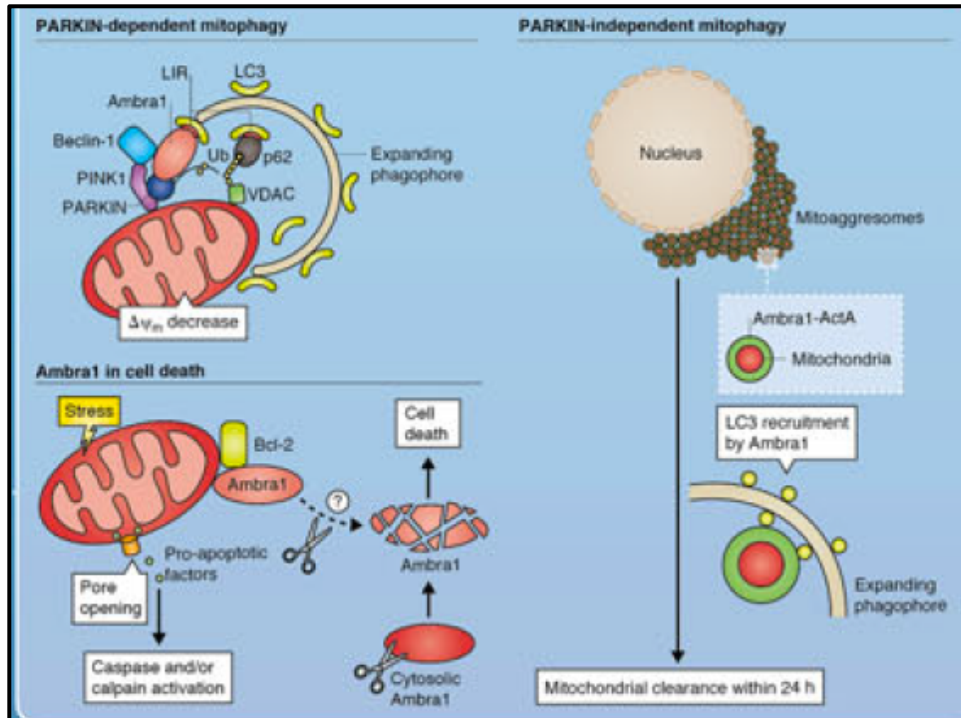


Figure 1: AMBRA1 is at the crossroad between mitophagy and cell death (from *AMBRA1 at a Glance*, 2015 *Journal of Cell Science*).

In addition, I participated to a study in which we used the iLID optogenetic bimodular system (a tool that I plan to use in one of the proposed projects, see **Figure 2**), based on the recruitment of AMBRA1 to mitochondrial outer membrane (MOM) after blue light irradiation, which can stimulate or switch off mitophagy when desired, *in vitro* and *in vivo*. We demonstrated effective mitophagy induction (I) *in vitro*, in HeLa cells, which don't express PARKIN (II) *ex vivo*, in human T lymphocytes, and (III) *in vivo*, in illuminated living *Danio rerio* embryos. Moreover, as a proof of concept of the potential beneficial contribution of our bimodular system to biomedicine, we tested whether AMBRA1-RFP-sspB-mediated mitophagy could block apoptosis in a cellular model of oxidative stress-induced neurotoxicity. We showed a light-dependent block of apoptosis in an *in vitro* model of oxidative stress-mediated proneural-like cell death.

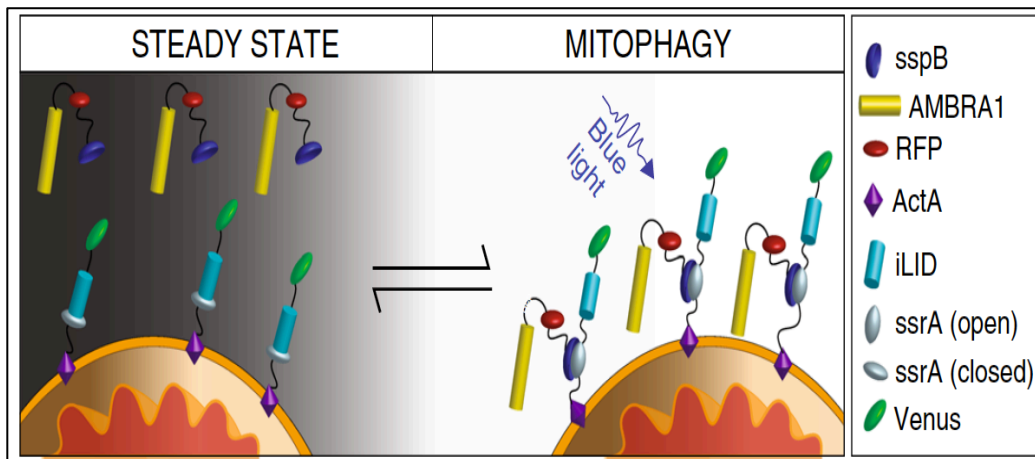


Figure 2: AMBRA1-RFP-sspB is relocalized to MOM upon blue light exposure. In resting conditions, Venus-iLID-ActA is tethered to the MOM, while AMBRA1-RFP-sspB is found in the cytosol. Upon blue light administration, iLID undergoes into a conformational change, which unmasks the ssrA peptide and permits the high-affinity binding between ssrA and sspB. Thus, the pro-autophagy protein AMBRA1 accumulates to the edge of the MOM where it promotes mitophagy.

This work is a great example of the potential application of optogenetic dimers to mediate, in this case, mitophagy that is not easily tuneable. While there are still many unanswered questions in the field of mitophagy, this optogenetic tool provides a necessary leap forward in understanding the basic cell biology behind this process. This work represents an important application that has been developed based on my discovery of AMBRA1-ActA-mediated mitophagy. I performed most of the confocal microscopy analysis presented in this work, and this illustrates the fact that I have the expertise required for the proposed project in order to study the temporal and spatial regulation of mitophagy in neurons.

In total, during this period I published two articles as **co-last and co-corresponding** author in *Nature Communication* and *Frontiers in Cellular Neurosciences*; two articles as **first and co-corresponding author** in *Autophagy* and *Cell Death and Differentiation* journals and one as second author in *Nature communication*.

ARTICLE

DOI: 10.1038/s41467-018-05722-3

OPEN

HUWE1 E3 ligase promotes PINK1/PARKIN-independent mitophagy by regulating AMBRA1 activation via IKK α

Anthea Di Rita^{1,2,14}, Angelo Peschiaroli³, Pasquale D'Acunzo², Daniela Strobbe^{1,4}, Zehan Hu⁵, Jens Gruber⁶, Mads Nygaard⁷, Matteo Lambrughini⁷, Gerry Melino⁸, Elena Papaleo⁷, Jörn Dengjel⁵, Said El Alaoui⁹, Michelangelo Campanella^{4,10,11}, Volker Dötsch⁶, Vladimir V. Rogov⁶, Flavie Strappazzon^{1,12} & Francesco Cecconi^{1,2,13}

The selective removal of undesired or damaged mitochondria by autophagy, known as mitophagy, is crucial for cellular homeostasis, and prevents tumour diffusion, neurodegeneration and ageing. The pro-autophagic molecule AMBRA1 (autophagy/beclin-1 regulator-1) has been defined as a novel regulator of mitophagy in both PINK1/PARKIN-dependent and -independent systems. Here, we identified the E3 ubiquitin ligase HUWE1 as a key inducing factor in AMBRA1-mediated mitophagy, a process that takes place independently of the main mitophagy receptors. Furthermore, we show that mitophagy function of AMBRA1 is post-translationally controlled, upon HUWE1 activity, by a positive phosphorylation on its serine 1014. This modification is mediated by the IKK α kinase and induces structural changes in AMBRA1, thus promoting its interaction with LC3/GABARAP (mATG8) proteins and its mitophagic activity. Altogether, these results demonstrate that AMBRA1 regulates mitophagy through a novel pathway, in which HUWE1 and IKK α are key factors, shedding new lights on the regulation of mitochondrial quality control and homeostasis in mammalian cells.

¹Department of Biology, University of Rome Tor Vergata, 00133 Rome, Italy. ²Department of Paediatric Haematology, Oncology and Cell and Gene Therapy, IRCCS Bambino Gesù Children's Hospital, Rome, Italy. ³National Research Council of Italy (CNR), Institute of Translational Pharmacology IFT, Via Fosso del Cavaliere 100, 00133 Rome, Italy. ⁴IRCCS- Regina Elena, National Cancer Institute, 00133 Rome, Italy. ⁵Department of Biology, University of Fribourg, Fribourg, Switzerland. ⁶Institute of Biophysical and Center for Biomolecular Magnetic Resonance, Goethe University, Frankfurt, Germany. ⁷Computational Biology Laboratory, Danish Cancer Society Research Center, 2100 Copenhagen, Denmark. ⁸Department of Experimental Medicine and Surgery, University of Rome Tor Vergata, 00133 Rome, Italy. ⁹Covalab, Villeurbanne, France. ¹⁰Department of Comparative Biomedical Sciences, Royal Veterinary College, London NW1 0TU, UK. ¹¹University College London Consortium for Mitochondrial Research, University College London, London WC1 6BT, UK. ¹²IRCCS FONDAZIONE SANTA LUCIA, 00143 Rome, Italy. ¹³Unit of Cell Stress and Survival, Danish Cancer Society Research Center, 2100 Copenhagen, Denmark. ¹⁴Present address: IRCCS FONDAZIONE SANTA LUCIA, 00143 Rome, Italy. Correspondence and requests for materials should be addressed to F.S. (email: f.strappazzon@hsantalucia.it) or to F.C. (email: cecconi@cancer.dk)

Mitophagy is an evolutionary-conserved mechanism that allows damaged or undesired mitochondria removal by an autophagosome-lysosome pathway¹. This high-quality clearance system is fundamental for preserving cellular homeostasis and for critical processes, such as inflammation and cell death or diseases, including cancer and neurodegeneration². The main mitophagy pathway is driven by the stabilization of the mitochondrial kinase PINK1, resulting in the recruitment of the E3 ubiquitin ligase PARKIN to damaged mitochondria, and in a ubiquitylation cascade targeting several outer mitochondrial membrane (OMM) proteins. Indeed, ubiquitylation events are fundamental during mitophagy, contributing to the normal turnover of mitochondrial proteins in basal conditions³, and promoting the recognition of UBD (ubiquitin binding domain)-containing proteins, which allow mitochondria selective autophagy⁴. Optineurin (OPTN) and NDP52 are the main mitophagy receptors, acting as bridges between ubiquitin-tagged mitochondria and the autophagosome-associated protein, MAP1LC3/LC3 (microtubule-associated proteins 1A/1B light chain 3), thus leading to mitochondria engulfment into autophagosomes, upon mitochondrial membrane depolarization^{5,6}. More recently, PHB2 (Prohibitin-2), an inner mitochondrial membrane protein, has also been demonstrated to be involved in selective mitochondria removal, cooperating with PARKIN in mammals⁷.

Besides the PINK1/PARKIN system, the OMM proteins NIX/BNIP3L, Bcl2-L-13 and FUNDC1 are also fundamental to trigger mitophagy in mammals, by interacting directly with LC3 and regulating mitochondrial clearance. In particular, (i) NIX/BNIP3L promotes mitochondria removal during reticulocytes differentiation^{8,9}; (ii) Bcl2-L-13 is the mammalian homologue of Atg32, and it stimulates mitochondria fragmentation and therefore mitophagy¹⁰; and lastly, (iii) FUNDC1 allows mitochondrial clearance upon hypoxia¹¹. Of note, these mitophagy receptors are post-translationally modified in order to regulate their interaction with LC3 during mitophagy¹².

We previously demonstrated that the LC3-interacting protein AMBRA1 plays a role in the selective degradation of ubiquitylated mitochondria, transducing both canonical PINK1/PARKIN-dependent and -independent mitophagy¹³. Here, we describe HUWE1 as the novel E3 ubiquitin ligase that collaborates with AMBRA1 to induce mitochondrial clearance, by inducing mitofusin 2 (MFN2) degradation. Moreover, since AMBRA1 exhibits (i) mitochondria localization¹⁴, (ii) a LIR (LC3-interacting region) motif and (iii) the capacity to induce mitophagy¹³, we decided to investigate whether AMBRA1 could be defined as a receptor, and to better characterize this pathway. We thus found that the activity of the mitophagy receptor AMBRA1 is regulated by a phosphorylation upstream of its LIR motif, mediated by the IKK α kinase.

Altogether, these findings highlight AMBRA1, HUWE1 and IKK α as three novel and crucial proteins for mammalian mitophagy regulation, following mitochondrial membrane depolarization in a PINK1/PARKIN-free context.

Results

HUWE1 is required for AMBRA1-mediated mitophagy. Since we have previously shown that AMBRA1 regulates the dismissal of ubiquitylated mitochondria in PINK1/PARKIN-independent mitophagy¹³, we searched for a novel putative E3 ubiquitin ligase, which could control mitochondrial protein ubiquitylation in cooperation with AMBRA1 during the mitophagy process.

To this aim, we performed a SILAC (stable isotope labelling by amino acids in cell culture)-based mass spectrometry (MS) analysis in order to detect AMBRA1-interacting proteins, upon

mitophagy stimulation, in a PARKIN-free cellular system. Thus, we immunoprecipitated Myc-AMBRA1^{ActA} (an AMBRA1 fusion protein targeted to the external membrane of mitochondria), which stimulates mitophagy¹³ in HeLa cells grown in two different isotope labelling media (light and heavy). The immunoprecipitated samples of the negative control (light medium lysate) and the experimental sample (heavy medium lysate) were mixed and then analysed by MS analysis¹⁵. Interestingly, this screening led us to identify a single E3 HECT-Ubiquitin ligase, HUWE1 (ARF-BP1, MULE, UREB1), whose role in macroautophagy/mitophagy was yet undisclosed (Fig. 1a).

In order to confirm these MS results, we performed a co-immunoprecipitation experiment in HeLa cells expressing a vector encoding for Myc-AMBRA1^{ActA}. Total lysates were immunoprecipitated with an anti-Myc antibody or an IgG control and the immune-complexes were analysed by western blotting. We found that AMBRA1^{ActA} was able to co-immunoprecipitate with HUWE1 (Fig. 1b). Since the expression of AMBRA1^{ActA} induces mitophagy per se¹³, we decided to compare the binding between AMBRA1^{WT} and HUWE1 in basal versus mitophagy conditions. To this end, we over-expressed HUWE1- and Myc-AMBRA1^{WT}-encoding constructs in HeLa cells, treated or not with oligomycin and antimycin (O/A) in order to induce mitophagy. Total lysates were immunoprecipitated using an anti-HUWE1 antibody or IgG control and the immune-complexes were analysed by western blot. As shown in Fig. 1c, AMBRA1^{WT} preferentially binds HUWE1 following mitophagy induction.

Given the evidence that HUWE1 is an AMBRA1-interacting protein preferentially upon mitophagy stimulation, we then focussed on a putative role of HUWE1 in mitophagy.

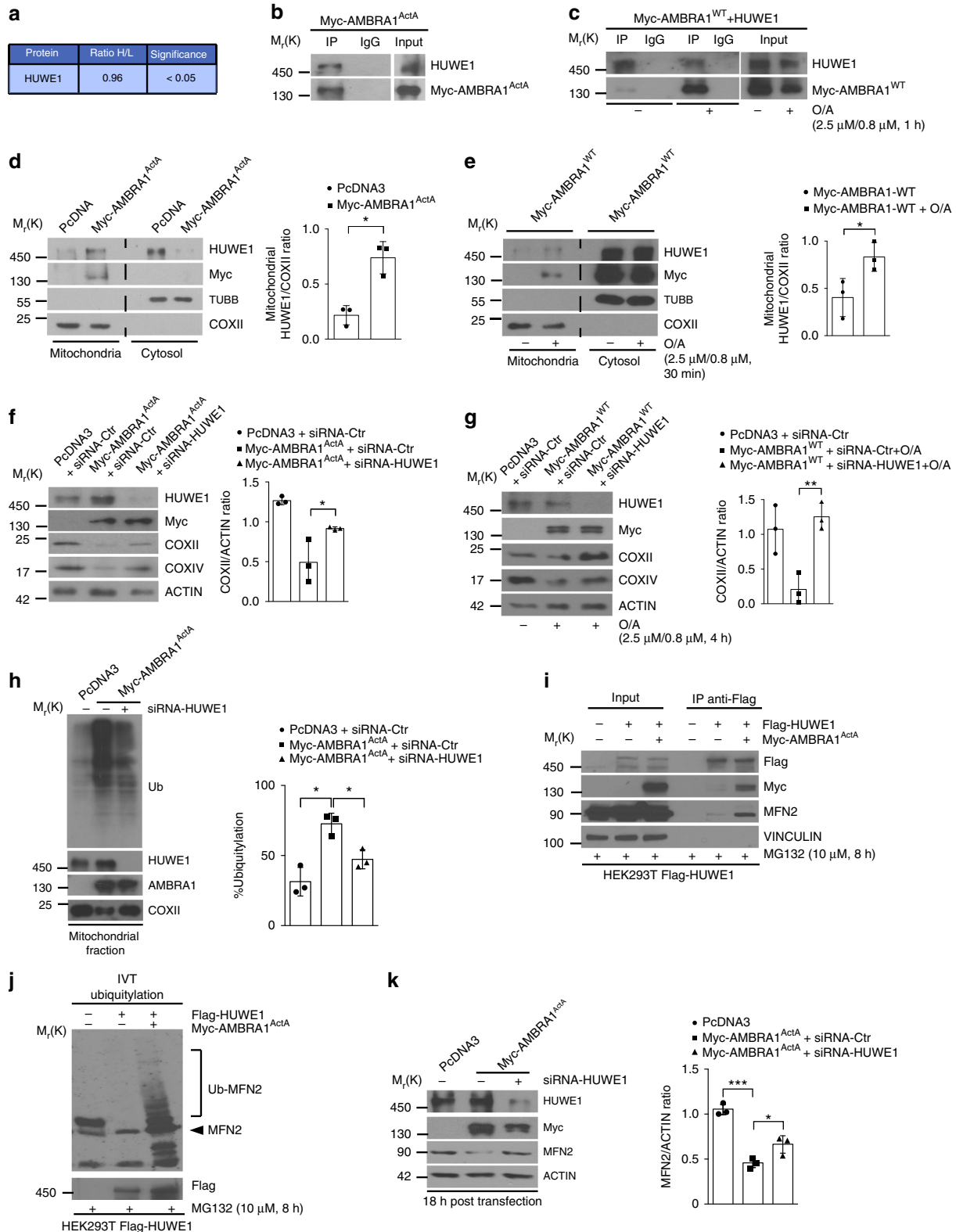
First, since HUWE1 is an E3 ubiquitin ligase mainly found in the cytoplasm¹⁶, we checked whether it was present at the mitochondria following mitophagy induction. By performing a mitochondria-cytosol fractionation in HeLa cells expressing Myc-AMBRA1^{ActA} or an empty vector (PcDNA3), we found that AMBRA1^{ActA} expression enables HUWE1 localization at the mitochondria (Fig. 1d). It is noteworthy that HUWE1 translocates to the mitochondria in also AMBRA1^{WT}-expressing cells upon mitophagy stimulation (Fig. 1e).

Next, in order to assess the effect of HUWE1 genetic silencing on AMBRA1^{ActA}-induced mitophagy, we checked mitophagy progression upon downregulation of HUWE1 via small interfering RNA (siRNA). As shown in Fig. 1f and in Supplementary Figure 1a, the decrease of mitochondrial markers associated with AMBRA1^{ActA} expression¹³, such as COXII and COXIV, is rescued in HUWE1-interfered cells. To confirm these data, we performed a confocal microscopy analysis in cells co-expressing both GFP-ShHUWE1 or GFP-ShCtr together with AMBRA1^{ActA}, and we measured the mitochondria amount in transfected green fluorescent protein (GFP)-positive cells. As expected, following AMBRA1^{ActA} expression with GFP-ShCtr, we observed the formation of mitochondria aggregates (mito-aggregates) around the nuclei, and a decrease in mitochondria staining; by contrast, GFP-ShHUWE1 transfected cells presented a delay in both mito-aggregates formation and mitochondrial clearance (Supplementary Fig. 1b). In addition, since we had previously demonstrated that AMBRA1 is able to induce mitophagy in a PINK1-independent manner¹³, we analysed AMBRA1-HUWE1 effect in mitophagy regulation also in mt-mKeima-expressing PINK1 knockout (mt-mKeima-PINK1-KO) HeLa cells⁵. As shown in Supplementary Fig. 1c, besides a strong localization of mitochondria into an acidic environment, following Myc-AMBRA1^{ActA} transfection, we also observed a reduction of acidic mt-mKeima upon HUWE1 downregulation. These data confirm that HUWE1

depletion impairs AMBRA1-mediated mitophagy. Finally, we also confirmed these data with the wild-type AMBRA1, following mitophagy induction. In fact, we transfected HeLa cells with Myc-AMBRA1^{WT} in combination or not with siRNA-HUWE1. Then, we treated cells with O/A (2.5 μM and 0.8 μM, respectively, 4 h). By western blot analysis, we observed a decrease of mitochondrial markers, COXII and COXIV, in the mitophagy context (Fig. 1g and Supplementary Fig. 1c).

In sum, these findings define a central role for the E3 ubiquitin ligase HUWE1 in controlling AMBRA1-dependent mitophagy.

Upon mitophagy, AMBRA1 acts as a cofactor for HUWE1 activity. Since HUWE1 depletion results in a block of AMBRA1-mediated mitophagy, we hypothesized that, in the meantime, mitochondria could be less ubiquitylated in that context.



To verify this hypothesis, we transfected HeLa cells with Ctr-siRNA or HUWE1-siRNA in combination with a vector encoding Myc-AMBRA1^{ActA}. We then performed a subcellular fractionation and analysed ubiquitylation in the mitochondria lysates, measuring the amount of total ubiquitin in these extracts, following AMBRA1^{ActA} transfection. As expected, we observed a reduction of the total mitochondrial ubiquitylation in HUWE1-interfered cells during AMBRA1^{ActA}-induced mitophagy when compared to control cells (Fig. 1h).

We next focalized our attention on MFN2, an OMM protein, whose ubiquitylation is known to be mediated by several E3 ubiquitin ligases, including HUWE1¹⁷, and whose degradation is known to be crucial for mitophagy induction¹⁸. We thus tested whether HUWE1–MFN2 interaction could be regulated by AMBRA1, upon mitophagy induction. To this aim, we transfected HEK293T cells stably expressing Flag-HUWE1 with a vector encoding Myc-AMBRA1^{ActA}. After treatment with the proteasome inhibitor MG132, we immunoprecipitated cell lysates with an anti-Flag antibody and observed that the expression of Myc-AMBRA1^{ActA} strongly favours the interaction between HUWE1 and MFN2 (Fig. 1i). Accordingly, by an *in vitro* ubiquitylation assay, we observed that Myc-AMBRA1^{ActA} expression in HEK293T-Flag-HUWE1 cell clones strongly increases MFN2 ubiquitylation compared to control conditions (Fig. 1j).

Last, we checked for MFN2 degradation in AMBRA1-mediated mitophagy (18 h following Myc-AMBRA1^{ActA} expression). By analysing MFN2 protein levels in Myc-AMBRA1^{ActA} transfected cells, we observed a decrease in this OMM protein. Interestingly, MFN2 decrease is rescued by downregulating HUWE1 or by treating cells with MG132 (Fig. 1k and Supplementary Fig. 1d). These data suggest that MFN2 ubiquitylation is an early event, following Myc-AMBRA1^{ActA} expression, controlled by HUWE1 and most likely required for AMBRA1-mediated mitophagy.

Altogether, these results indicate that AMBRA1 favours MFN2–HUWE1 interaction, thus leading to MFN2 ubiquitylation and subsequent degradation, with a final effect on mitophagy induction. AMBRA1 can be thus considered as a novel cofactor for HUWE1 ubiquitin ligase activity, underlining a new paradigm for the regulation of HUWE1.

AMBRA1 is a relevant mitophagy receptor. Next, since AMBRA1 (i) operates as a cofactor for HUWE1 activity in order to trigger mitophagy, (ii) displays mitochondrial localization¹⁴, (iii) exhibits a LIR motif on its sequence for LC3B binding, (iv) is able to regulate PINK1/PARKIN-independent mitophagy and (v) controls the PINK1/PARKIN-mediated mitophagy¹³, we investigated whether AMBRA1 can act as a mitophagy receptor.

To this aim, we checked for AMBRA1-mediated mitophagy efficiency using the well-known model of stable Penta-KO cells, unable to perform mitophagy⁵. Indeed, these cells are deficient for five mitophagy receptors, i.e., OPTN, NDP52, NBR1, P62 and TAX1BP1. In these cells, only the expression of NDP52 or OPTN (or TAX1BP1, in a few cases) is able to rescue the mitophagy pathway. In fact, the treatment of these cells with mitochondrial uncouplers does not induce mitophagy (Supplementary Fig. 2a). Thus, we transfected Penta-KO cells with a vector encoding Myc-AMBRA1^{ActA}. Western blot analysis, performed on extracts obtained 24 h after transfection, showed a decrease of mitochondrial markers, i.e., COXII, COXIV, and also HSP60 (Supplementary Fig. 2b), underlining that AMBRA1 expression at the mitochondria is sufficient per se to induce mitophagy in Penta-KO cells (Fig. 2a). Furthermore, by performing a confocal microscopy analysis, we observed that AMBRA1^{ActA} expression in Penta-KO cells led to mitochondria perinuclear re-localization, typical of mitophagy induction, followed by a decrease in the mitochondrial mass (Fig. 2b).

Given the powerful ability of AMBRA1^{ActA} to induce mitophagy in these cells, we also checked whether wild-type AMBRA1 could promote mitochondria selective removal. To this end, we transiently transfected Penta-KO cells with a vector encoding for Myc-AMBRA1^{WT} and treated cells with O/A for 24 h in order to induce mitophagy. By western blot analysis, we observed a decrease in the levels of the mitochondrial markers COXII and COXIV, thus confirming the central role of AMBRA1 in promoting mitophagy in this cell line (Fig. 2c). Of note, following overexpression of AMBRA1^{WT}, in the absence of any mitophagy treatments, all mitochondrial markers showed a marked decrease.

Also in this case, we confirmed the data by performing a confocal microscopy analysis in which we observed the formation of mito-aggregates and then a decrease of mitochondria content in cells overexpressing AMBRA1^{WT} (Fig. 2d). Finally, in order to ascertain that the AMBRA1-dependent mitochondrial decrease was well associated to lysosomal degradation, we treated cells with the lysosomal inhibitor NH₄Cl (Supplementary Fig. 2c). Indeed, an almost complete rescue of COXIV and COXII levels by NH₄Cl confirmed that a block in lysosomal degradation restored the total amount of mitochondria within the cells.

Taken together, our findings reveal that AMBRA1 acts as a relevant mitophagy receptor, capable to induce mitophagy in NDP52-, OPTN-, TAX1BP1-, NBR1- and P62-deficient cells.

AMBRA1 phosphorylation regulates AMBRA1-dependent mitophagy. A key process in the induction of selective autophagy is the interaction between mitophagy receptors and Atg8 (autophagy-related protein 8) protein family members¹⁹, which

Fig. 1 HUWE1 cooperates in AMBRA1-mediated mitophagy. **a** Table showing the E3 ubiquitin ligase interacting with AMBRA1 upon mitophagy stimuli in HeLa PARKIN-free cells. The ratio of heavy labelled peptides to the remaining non-labelled ones (ratio H/L) reflects is indicated. **b** Representative image of AMBRA1^{ActA}-HUWE1 co-immunoprecipitation (Co-IP); *n* = 3. **c** Representative image of AMBRA1^{WT}-HUWE1 co-immunoprecipitation (Co-IP) upon mitophagy stimulation (O/A); *n* = 3. **d** PcDNA3 or Myc-AMBRA1^{ActA} transfected HeLa cells were subjected to mitochondria-cytosol purification. Samples were blotted for the indicated antibodies; *n* = 3. **e** PcDNA3 or Myc-AMBRA1^{WT} transfected HeLa cells were treated with O/A for 30 min and subjected to mitochondria-cytosol purification; *n* = 3. **f** HeLa cells transfected with PcDNA3 or Myc-AMBRA1^{ActA} vectors were transfected with siRNA-Ctr or siRNA-HUWE1 constructs and then immunoblotted for the indicated proteins; *n* = 3. **g** Following O/A treatment, PcDNA3- or Myc-AMBRA1^{WT}-expressing HeLa cells transfected with siRNA-Ctr or siRNA-HUWE1 were immunoblotted for the indicated antibodies; *n* = 3. **h** PcDNA3, Myc-AMBRA1^{ActA} and Myc-AMBRA1^{ActA} transfected cells interfered for HUWE1 were blotted for the indicated antibodies. The graph shows the total ubiquitin amount in mitochondria fractionation sample (%); *n* = 3. **i** HEK293T stably expressing Flag-HUWE1, transfected with a vector coding for Myc-AMBRA1^{ActA} and treated with MG132 (10 μM, 8 h) were co-immunoprecipitated and immunoblotted for the indicated proteins; *n* = 3. **j** *In vitro* ubiquitylation assay of cells in **i**. Protein samples were resolved by SDS-PAGE and immunoblotted for Myc, MFN2 and HUWE1; *n* = 2. **k** HeLa cells transfected with Myc-AMBRA1^{ActA} (18 h) and interfered for HUWE1 (siRNA-HUWE1) were analysed by western blot; *n* = 3. The quantification results are the mean of three independent experiments (±S.D.). **P* < 0.05; ***P* < 0.01. Statistical analysis was performed using one-way ANOVA (**f**, **g**, **k**) and Student's *t*-test (**d**, **e**, **h**). M_r(K) = relative molecular mass expressed in kilodalton

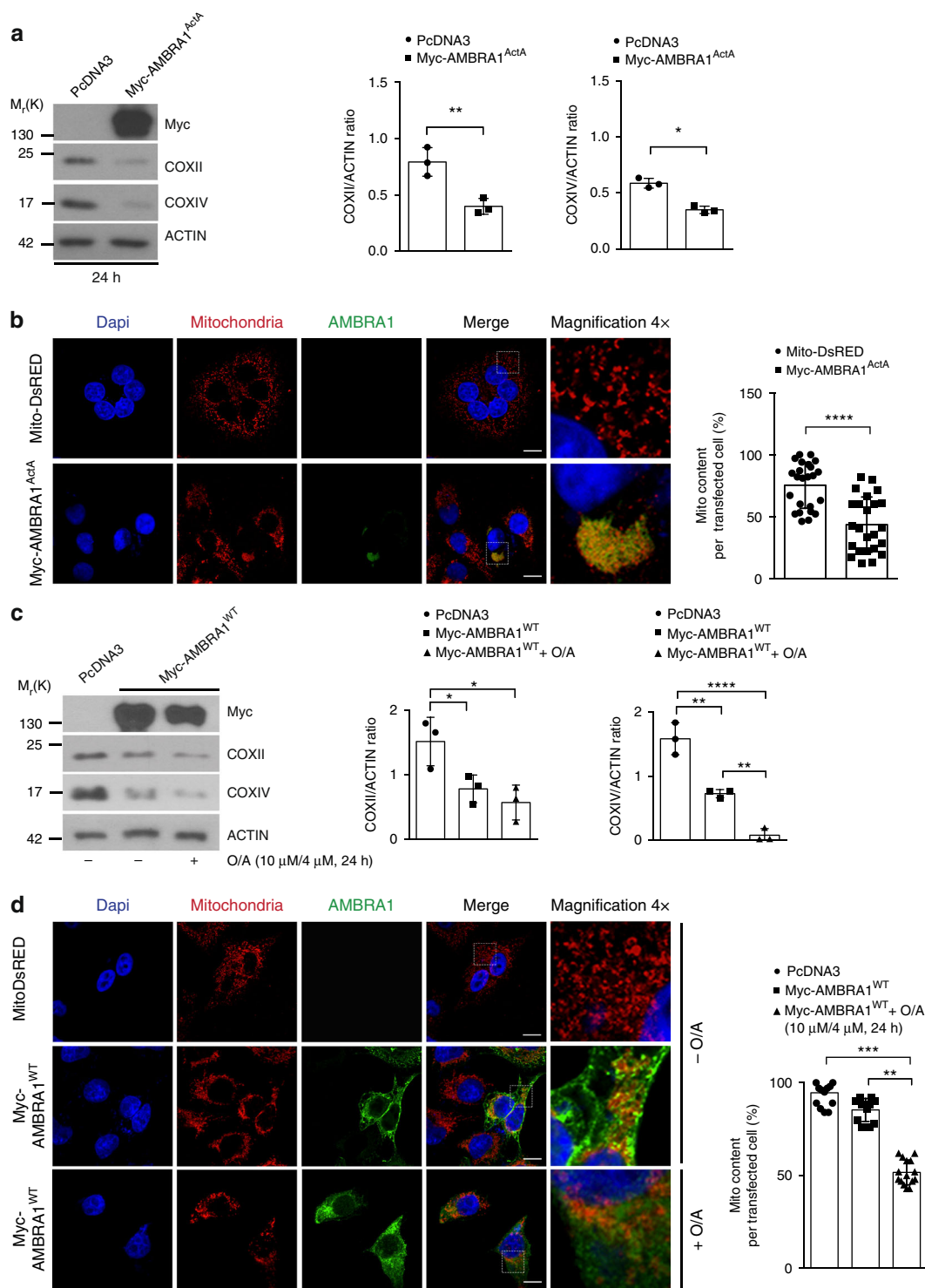
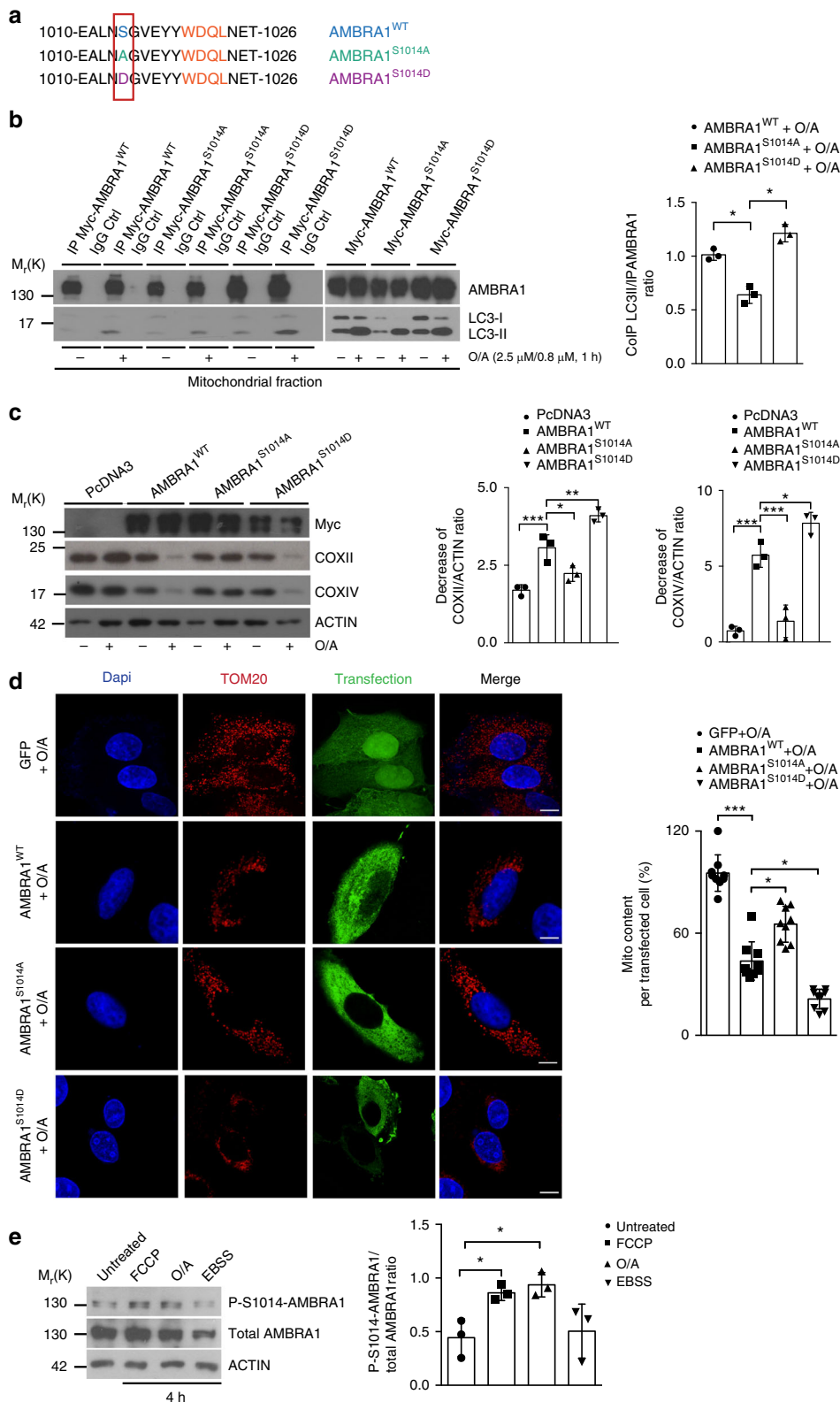


Fig. 2 AMBRA1 expression rescues mitophagy induction in Penta-KO cells. **a** Penta-KO cells transfected with a vector encoding for Myc-AMBRA1^{ActA} or an empty vector (PcDNA3) for 24 h were immunoblotted for the indicated antibodies; *n* = 3. **b** Myc-AMBRA1^{ActA} (red) or Mito-DsRED (red) transfected Penta-KO cells were fixed after 24 h. Scale bar, 10 μm. The graph shows the mito content (%) in single transfected cells (±S.D.); *n* = 4. Mito-DsRED = 12 individual fields; Myc-AMBRA1^{ActA} = 12 individual fields. **c** Penta-KO cells were transfected with vectors encoding Myc-AMBRA1^{WT} or PcDNA3 and treated with O/A (10 μM and 4 μM, respectively) for 24 h. Mitochondrial markers levels, COXII and COXIV, were evaluated by western blot; *n* = 3. **d** Cells transfected with Mito-DsRED or with Myc-AMBRA1^{WT} were immunostained with an anti-Myc (green) and anti-TOM20 (red) antibodies. Scale bar, 10 μm; *n* = 3. Mito-DsRED = 9 individual fields; Myc-AMBRA1^{WT} = 9 individual fields; Myc-AMBRA1^{WT}+O/A = 9 individual fields. **P* < 0.05; ***P* < 0.01; ****P* < 0.001; *****P* < 0.0001. The quantification results are the mean of three independent experiments (±S.D.) if not otherwise stated. Statistical analysis was performed using Student’s *t*-test (**a, b**) or one-way ANOVA (**c, d**). M_r(K) = relative molecular mass expressed in kilodalton

are LC3 and GABARAP proteins in mammals (mATG8). Since the phosphorylation status of a serine residue (Ser) flanking the LIR motifs of known mitophagy receptors, such as FUNDC1¹¹, BNIP3²⁰, NIX/BNIP3L^{9,21}, Bcl2-L-13¹⁰ and OPTN²², controls their binding with LC3, we investigated whether AMBRA1 could be post-translationally modified in a serine site in proximity of its LIR motif¹³.

First, through an in silico analysis of the AMBRA1 sequence, we identified serine 1014 (S1014) as a putative phosphorylation site close to the AMBRA1-LIR motif (Fig. 3a). Second, in order to demonstrate whether the phosphorylation on S1014 was able to influence AMBRA1-LC3B interaction in cells, we generated two AMBRA1 mutants, a phospho-dead mutant (AMBRA1^{S1014A}) and a phospho-mimetic mutant (AMBRA1^{S1014D}). By



performing co-immunoprecipitation experiments, we analysed AMBRA1–LC3B interaction in basal conditions and upon mitophagy stimulation (O/A treatment), obtained by overexpressing Myc-AMBRA1^{WT} and AMBRA1^{S1014A} or AMBRA1^{S1014D} in HeLa cells. First, we confirmed that AMBRA1 interacts mostly with LC3B following mitophagy stimuli¹³. Moreover, we observed that alanine substitution at residue 1014 reduced the binding between AMBRA1 and LC3B, following O/A treatment (Fig. 3b). By contrast, the AMBRA1^{S1014D} enhanced the ability of AMBRA1 to interact with LC3B during mitophagy.

These results highlight that the phosphorylation status of AMBRA1 on S1014 influences the interaction between AMBRA1 and LC3B during mitophagy.

Next, in order to ascertain whether S1014 is relevant in AMBRA1-induced mitophagy, we performed functional experiments to evaluate the mitophagy activity of AMBRA1^{WT} compared with its mutants on S1014. To this aim, we transfected HeLa cells with the empty vector PcDNA3 as a control, and vectors encoding Myc-AMBRA1^{WT} or Myc-AMBRA1^{S1014A} or Myc-AMBRA1^{S1014D} and checked, by western blot analysis, the levels of mitochondrial proteins COXII and COXIV.

Interestingly, upon mitophagy stimulation (by O/A treatment), HeLa cells transfected with AMBRA1^{WT} showed a decrease in COXII and COXIV levels, while cells expressing the AMBRA1^{S1014A} mutant showed a lower decrease in mitochondrial marker levels compared with AMBRA1^{WT} or AMBRA1^{S1014D} (Fig. 3c). Of note, the AMBRA1^{S1014D} mutant significantly increased the mitophagy ability of AMBRA1 when compared with the AMBRA1^{WT} form (Fig. 3c). Also, we analysed mitochondrial clearance by confocal immunofluorescence, looking at TOM20 levels, in HeLa cells expressing GFP, Myc-AMBRA1^{WT}, Myc-AMBRA1^{S1014A} or Myc-AMBRA1^{S1014D}. Indeed, we observed that the phospho-mimicking mutation (Myc-AMBRA1^{S1014D}) induced mito-aggregate formation and a clear decrease of mitochondria amount to a larger extent than AMBRA1^{WT} (Fig. 3d). Moreover, we also validated these data using HeLa cells expressing the mito-mKeima vector⁵. In analogy with our biochemistry and immunofluorescence analysis, mitochondria of Myc-AMBRA1^{S1014D}-expressing cells were predominantly found in an acidic environment, suggesting ongoing mitophagy. By contrast, Myc-AMBRA1^{S1014A} transfected cells, in which we previously observed a delay in mitophagy, were mostly present in a neutral environment (Supplementary Fig. 3a).

Since we demonstrated that phosphorylation of AMBRA1 on S1014 was a crucial event in order to regulate AMBRA1-mediated mitophagy, we next decided to check whether endogenous AMBRA1 was also subjected to such modification. We thus generated, through rabbit immunization, an anti-AMBRA1 serum that specifically recognized the phosphorylation at S1014 (anti-Phospho(P)-S1014-AMBRA1 serum). We tested its efficiency by comparing the level of phospho-S1014 in basal versus mitophagy (carbonyl cyanide-4-(trifluoromethoxy)

phenylhydrazone (FCCP), O/A) or autophagy conditions (Earle's balanced salt solution (EBSS)). As shown in the graph (Fig. 3e), we observed a significant increase in the phosphorylation signal following FCCP and O/A treatments, indicating that phosphorylation of AMBRA1 on S1014 was occurring specifically upon mitochondrial membrane depolarization during mitophagy induction. In addition, we proved that the anti-P-S1014-AMBRA1 antibody was able to specifically recognize AMBRA1 by analysing endogenous AMBRA1 levels in siRNA-Ctr- or AMBRA1-interfered cells by siRNA-AMBRA1 (Supplementary Fig. 3b). We also confirmed that this antibody was able to better recognize over-expressed AMBRA1^{WT} if compared to the phospho-dead AMBRA1^{S1014A} form (Supplementary Fig. 3c).

Taken together, these data indicate that the phosphorylation of S1014 on AMBRA1 regulates the AMBRA1–LC3B interaction and its mitophagy activity. We have also generated an anti-P-S1014-AMBRA1 antibody that recognized this AMBRA1 dynamic post-translational modification.

S1014-AMBRA1 phosphorylation increases the binding with mATG8s.

In order to characterize the binding affinity between AMBRA1-LIR and LC3/GABARAP proteins, and to confirm that the phosphorylation of S1014 in AMBRA1 increases this affinity, we performed isothermal titration calorimetry (ITC) experiments in which synthetic peptides spanning the AMBRA1-LIR at various phosphorylation states (P0: steady state and P1: phosphorylation state) were titrated into all six mATG8 proteins, including LC3A, LC3B, LC3C, GABARAP, GABARAP-L1 and GABARAP-L2 (Supplementary Fig. 4a–c, and Supplementary Note 1). The ITC experiments showed that the unmodified AMBRA1-LIR (P0) binds to LC3B with very low affinity (Fig. 4a left panel). K_D values for this interaction were in the range of >100 μ M, a value ~100 higher than the canonical p62-LIR, and comparable to the unphosphorylated NIX- and OPTN-LIR affinities^{13,22,23}. However, LC3B affinity to AMBRA1-LIR unambiguously increased upon S1014 phosphorylation, resulting in K_D of 53 μ M (Fig. 4a, right panel). Moreover, the nuclear magnetic resonance (NMR) titration experiments indicated a very similar effect of AMBRA1-LIR phosphorylation on its affinity to LC3B (Fig. 4b, c). Interestingly, although ITC experiments showed that the unmodified AMBRA1-LIR (P0) bound all 6 mATG8 proteins with low affinity (Supplementary Fig. 4a, upper plots), it exhibited some preference to GABARAP-subfamily proteins. In fact, strongest interaction appeared to the GABARAP protein, with K_D of ~40 μ M, while for the LC3 proteins and for GABARAP-L2 K_D values could be only estimated. Of note, the binding enthalpy for all mATG8 proteins is small, defining the entropy as the main driving force of the interactions. However, both phosphorylation of S1014 (P1, Supplementary Fig. 4b) and introduction of phospho-mimicking aspartate to this position (PM, Supplementary Fig. 4c) increased affinity of AMBRA1-LIR interaction with mATG8 analogues (K_D values decreased ~2–5 times). In particular, phosphorylation of

Fig. 3 S1014-AMBRA1 phosphorylation is crucial for AMBRA1-LC3 interaction. **a** Sequence alignment of AMBRA1-S1014 site, flanking its LIR motif, in comparison with the S1014A (phospho-dead) and S1014D (phospho-mimetic) generated mutants. **b** HeLa transfected with Myc-AMBRA1^{WT}, Myc-AMBRA1^{S1014A} or Myc-AMBRA1^{S1014D} were treated or not with O/A (2.5 μ M, 0.8 μ M, 1 h) and subjected to co-immunoprecipitation (Co-IP). The graph shows the ratio between Co-IP LC3II/IP-AMBRA1 upon mitophagy induction; $n = 3$. Statistical analysis was performed using Student's *t*-test versus the wild-type form of AMBRA1. **c** PcDNA3, Myc-AMBRA1^{WT}, Myc-AMBRA1^{S1014A} or Myc-AMBRA1^{S1014D} transfected HeLa cells were treated with O/A (2.5 μ M, 0.8 μ M, 4 h) and blotted for COXII, COXIV, Myc and ACTIN; $n = 3$. **d** Cells transfected with a vector encoding for GFP, Myc-AMBRA1^{WT}, or Myc-AMBRA1^{S1014A} or Myc-AMBRA1^{S1014D} were treated with O/A as indicated above and stained with anti-Myc and anti-TOM20 (red staining) antibodies. Scale bar, 10 μ m; $n = 3$. Myc-AMBRA1^{WT} = 9 individual fields; Myc-AMBRA1^{S1014A} = 9 individual fields; Myc-AMBRA1^{S1014D} = 9 individual fields. **e** Untransfected HeLa cells were treated with mitophagy inducers, such as FCCP (10 μ M) and O/A (2.5 μ M and 0.8 μ M) or with the starvation medium EBSS in order to induce autophagy for 4 h; $n = 3$. Data represent the mean of three different samples (\pm S.D.) and are representative of experimental triplicate. * $P < 0.05$; ** $P < 0.01$; *** $P < 0.001$. Statistical analysis was performed using Student's *t*-test (**b**) or one-way ANOVA (**c**, **d**, **e**). $M_r(K)$ = relative molecular mass expressed in kilodalton

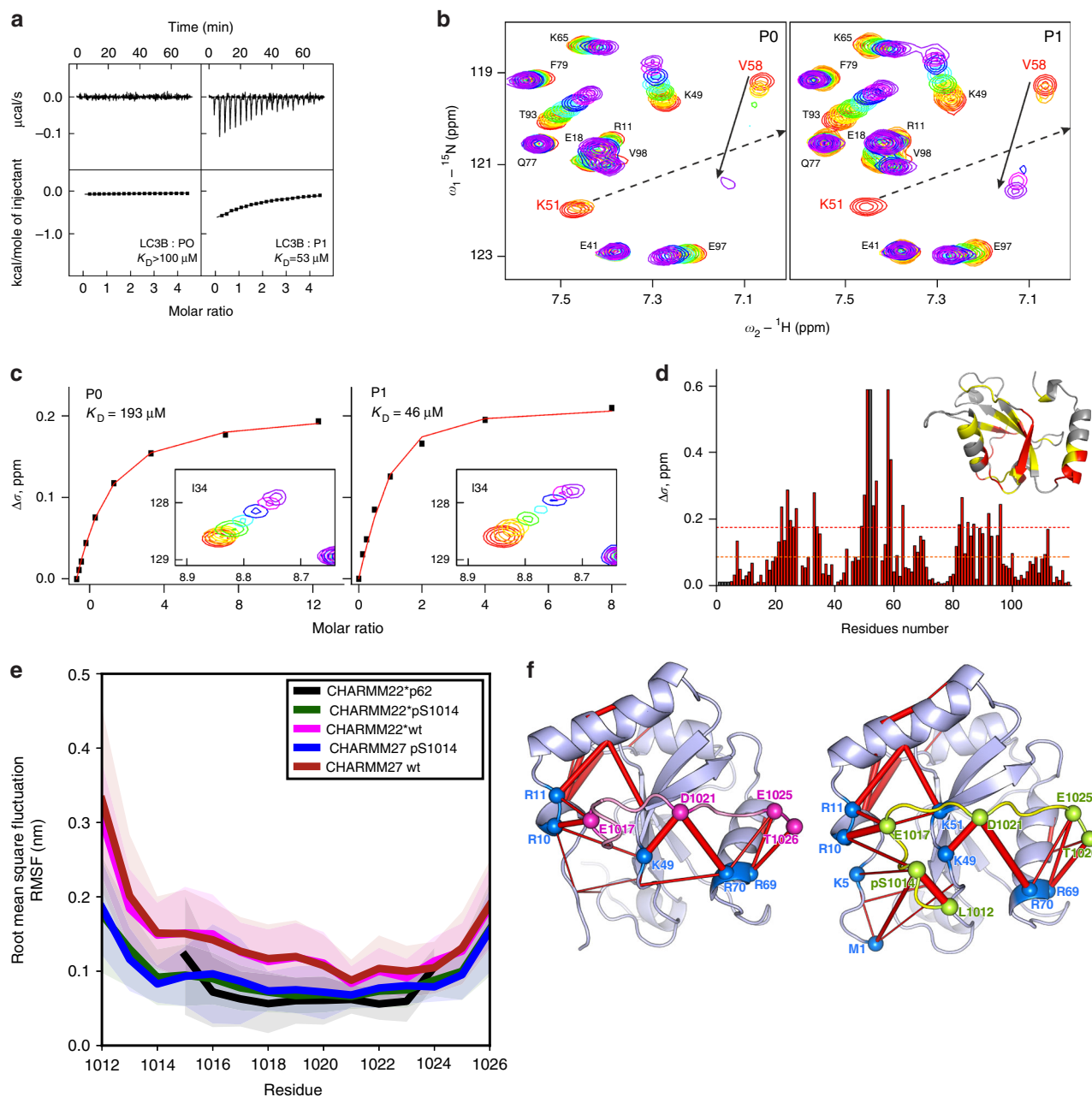


Fig. 4 S1014-AMBRA1 phosphorylation allows AMBRA1-LC3B binding. **a** ITC titrations of unmodified AMBRA1-LIR peptide (P0) compared with those of S1014-phosphorylated AMBRA1-LIR peptide (P1) into LC3B protein. The measurements were performed at 35 °C. Measured/estimated K_D values are indicated for each interaction. **b** Representative sections of HSQC spectra for ¹⁵N-labelled LC3B upon titration with P0 and P1. Both plots show fingerprint regions of the LC3B spectra (around HN resonance of K51). Molar ratios of protein/peptide are rainbow coloured (1:0, 1:0.125, 1:0.25, 1:0.5, 1:1, 1:2, 1:4 and 1:8; from red to violet) for each titration step. Arrows indicate the CSP for K51 and V58 HN backbone resonances. **c** K_D values calculated for the LC3B residue I34 upon titration with P0 and P1. Original CSP values are shown as black squares and the resulting fit is given as a red line in each plot. The original HSQC areas around I34 HN resonance are shown as a box under fitted curves. **d** CSP values ($\Delta\delta$) at the last titration stages for LC3B protein are plotted against residues numbers. The orange dashed line indicates the standard deviations (σ) over all residues within each dataset, and the red dashed line indicates double σ values. The CSP values mapped on the LC3B protein structure (ribbon diagrams, PDB ID 1UGM) are shown in the upper right corner. Residues with small ($\Delta\delta < \sigma$), intermediate ($\sigma < \Delta\delta < 2\sigma$) or strong ($2\sigma < \Delta\delta$) CSPs are marked in grey, yellow and red, respectively. **e** The root mean square fluctuation (RMSF) per residue of AMBRA1 decreases after S1014 phosphorylation (blue, green lines) compared to wt (magenta, red lines) and control P62 (black line) and is persistent with CHARMM22* (black, green and magenta lines) and CHARMM27 (blue and red lines) force fields. Shaded area corresponds to 1σ . **f** Superimposition of highly populated (>20%) electrostatic interactions (red bars, thickness indicates occurrence) over the LC3B/AMBRA1-LIR structure. Interactions identified between residues of S1014-phosphorylated AMBRA1-LIR (right panel) and LC3B are identified by spheres and reproduced on the wt (left panel). Similar patterns were seen for simulations using CHARMM22* (shown here) and CHARMM27 force fields

S1014 (P1, Supplementary Fig. 4b, low panel) enhanced the binding with the GABARAP protein and therefore the K_D shifted down to 21 μM , as determined by ITC. Based on chemical shift perturbations (CSP), we precisely calculated K_D values for LC3B interaction with unphosphorylated (P0) and phosphorylated (P1) AMBRA1-LIR peptides. We also mapped the CSP on the LC3B sequence and three-dimensional structure (Fig. 4d). Comparison of the mapped AMBRA1-LIR CSP pattern to previously published mappings indicated that the AMBRA1-LIR interacts with LC3B in a typical LIR mode and phosphorylation on S1014 close to the LIR motif enhances these interactions.

In order to understand the structural impact of S1014-AMBRA1 phosphorylation on the LC3B binding, we performed multi-replicate molecular dynamics (MD) simulations, evaluating conformations of the steady-state structure of AMBRA1 when compared to the phosphorylated structure. In this case, we used the P62-LIR/LC3B experimental structure as a template for modelling. As shown in the plot of Fig. 4e, in analogy to the canonical complex P62-LC3B, the root mean square fluctuation (RMSF), an index of structural flexibility of AMBRA1-LC3B interaction, showed a decrease in flexibility, upon phosphorylation of S1014 (blue and green lines; Fig. 4e). Interestingly, the phospho-variant was characterized by a flexibility profile comparable to the canonical p62-LIR (black line; Fig. 4e), suggesting that this post-translational modification is needed to compensate for the lower binding affinity of the unphosphorylated AMBRA1-LIR, with respect to other known LIR domains. Moreover, we observed that the stabilization induced by the phospho-S1014 was likely due to an increase in electrostatic interactions promoted by this residue (locally and long-range) (Fig. 4f).

Taken together, these results give a proof of concept that phosphorylation of S1014 is fundamental to stabilize the conformation of AMBRA1-LIR in the binding pocket of LC3B, thus promoting its interaction with LC3B (and most likely with all MATG8 proteins) and its mitophagy activity.

IKK α kinase phosphorylates AMBRA1 at S1014 during mitophagy. In order to define which kinase could regulate AMBRA1 phosphorylation at S1014 during mitophagy, we performed a bioinformatic analysis by using the Group-based Prediction System (GPS) software²⁴. One of the candidates with the highest score was the IKK α kinase (also termed CHUK), a serine–threonine kinase belonging to the IKK family that includes IKK α , IKK β , IKK γ , IKK ϵ and TBK1 proteins²⁵. The predicted IKK α consensus motif²⁶ was localized upstream of the LIR motif of AMBRA1 (Fig. 5a), suggesting a potential role of IKK α in AMBRA1-mediated mitophagy. To prove this biochemically, we first checked for a putative binding between AMBRA1 and the IKK α kinase. To this end, we over-expressed, in HeLa cells, the kinase-dead mutant of IKK α (HA-IKK α ^{K44M})²⁷ in order to avoid a kiss and run action between the wild-type kinase and AMBRA1, and then we immunoprecipitated the IKK α mutant with an anti-HA antibody and, finally, we checked for AMBRA1–IKK α complex by western blot analysis. As shown in Fig. 5b, we found a binding between the two proteins, suggesting that AMBRA1 could be a substrate for IKK α . To test this hypothesis, we decided to investigate the effect of the well-known IKK α -specific and irreversible inhibitor BAY-117082 on AMBRA1 phosphorylation at S1014 during mitophagy. As shown in Fig. 5c, we observed a clear reduction of AMBRA1 phosphorylation on S1014, when cells were treated with BAY-117082 compared to cells treated with the vehicle (dimethyl sulfoxide). These results suggested that the IKK α kinase was responsible for the phosphorylation on S1014 of AMBRA1 following mitophagy induction. To strengthen

these data, we decided to test the effect of the kinase-dead form of IKK α (IKK α ^{K44M}), which acts as a dominant negative mutant²⁷, on AMBRA1 phosphorylation at S1014. To this end, we over-expressed vectors encoding Flag-IKK α ^{WT} or HA-IKK α ^{K44M} in HeLa cells, and we induced mitophagy by using O/A. As shown in Fig. 5d, the expression of the kinase-dead version of IKK α was sufficient to abolish AMBRA1 phosphorylation at S1014 following O/A treatment, similarly to BAY-117082 (see Fig. 5c). Consistent with these results, we validated the IKK α -mediated phosphorylation on AMBRA1 at S1014 by an *in vitro* kinase assay, comparing the activity of IKK α ^{WT} to its kinase-dead mutant. To this end, we transfected HeLa cells with a vector encoding Myc-AMBRA1^{WT}, Flag-IKK α ^{WT} or HA-IKK α ^{K44M} and immunoprecipitated individually these three proteins from the mitochondrial fraction. Then, we combined the immunoprecipitated kinases (IP-IKK α ^{WT} or IP-IKK α ^{K44M}) with the immunoprecipitated substrate (IP-AMBRA1). The western blot analysis showed that the phosphorylation signal at AMBRA1–S1014 was present only in the IP-IKK α fraction (Fig. 5e). Subsequently, we also performed an *in vitro* kinase assay with human recombinant AMBRA1 as a substrate in order to formally prove a direct effect of the IKK α kinase on its novel substrate. As shown in Fig. 5f, the phosphorylated form of AMBRA1 at S1014 was detected when mixed with the IP-IKK α , but was not appreciated in the kinase-dead IP-IKK α ^{K44M} sample. Despite TBK1 and IKK α kinases shared a similar structure, we did not observe any effects of the TBK1 kinase on S1014 phosphorylation of AMBRA1 (Supplementary Fig. 5a).

These results prove that IKK α is the kinase responsible for AMBRA1 phosphorylation at S1014 upon mitophagy induction, and thus it represents a novel upstream factor accountable for mitophagy activation.

IKK α inhibition impairs AMBRA1-mediated mitophagy. In order to verify whether the abolishment of IKK α kinase activity could inhibit AMBRA1-mediated mitophagy, we tested the effect of IKK α inhibition on AMBRA1-mediated mitophagy. To this end, we checked for mitophagy induction in HeLa cells over-expressing AMBRA1^{ActA}, and treated or not with the IKK α inhibitor (BAY-117082) by detecting COXII and COXIV levels by western blot analysis. We observed that BAY-117082 treatment was able to rescue mitochondrial clearance following AMBRA1^{ActA} overexpression (Fig. 5g and Supplementary Fig. 5b).

Of the highest importance, the IKK α inhibitor also impacted AMBRA1-mediated mitophagy in Myc-AMBRA1^{WT} transiently transfected HeLa cells, in which we induced mitophagy by O/A. As shown in Fig. 5h and Supplementary Figure 5c, by analysing the mitochondrial clearance by western blotting, we also observed in this case a rescue of the mitochondrial markers COXII and COXIV upon BAY-117082 treatment.

To validate these data, we co-transfected HeLa cells with a vector encoding Myc-AMBRA1^{ActA} in combination with HA-IKK α ^{K44M} kinase-dead mutant. Again, by blocking IKK α activity, by using the dominant negative form of the kinase, we induced AMBRA1^{ActA}-mediated mitophagy inhibition (Fig. 5i and Supplementary Fig. 5d). As expected, AMBRA1^{WT}-induced mitophagy was also reduced in HA-IKK α ^{K44M} transfected cells, confirming that inhibition of IKK α also impaired AMBRA1^{WT}-mediated mitophagy (Fig. 5j and Supplementary Fig. 5e). Moreover, as a control, we checked whether the nuclear factor (NF)- κ B pathway was involved in this regulation by looking at p65 nuclear translocation upon mitophagy stimulation. As shown in Supplementary Figure 5f, no evident p65 translocation to the nucleus was observed upon O/A treatment compared to tumour necrosis

factors treatment, indicating that this inflammation pathway was not activated during mitophagy.

Altogether, these results point to IKK α as an essential factor in AMBRA1-mediated mitophagy, regulating AMBRA1 phosphorylation at S1014, and highlight a novel and alternative role (rather than in inflammation) of IKK α in mitophagy.

HUWE1 controls the S1014 phosphorylation of AMBRA1. In analogy with other mitophagy receptors, the phosphorylation of AMBRA1 at the S1014 site, flanking its LIR motif, is a crucial event for the engulfment of ubiquitin-tagged mitochondria into autophagosomes. Since we demonstrated that HUWE1 down-regulation results in a block of AMBRA1-mediated mitophagy,

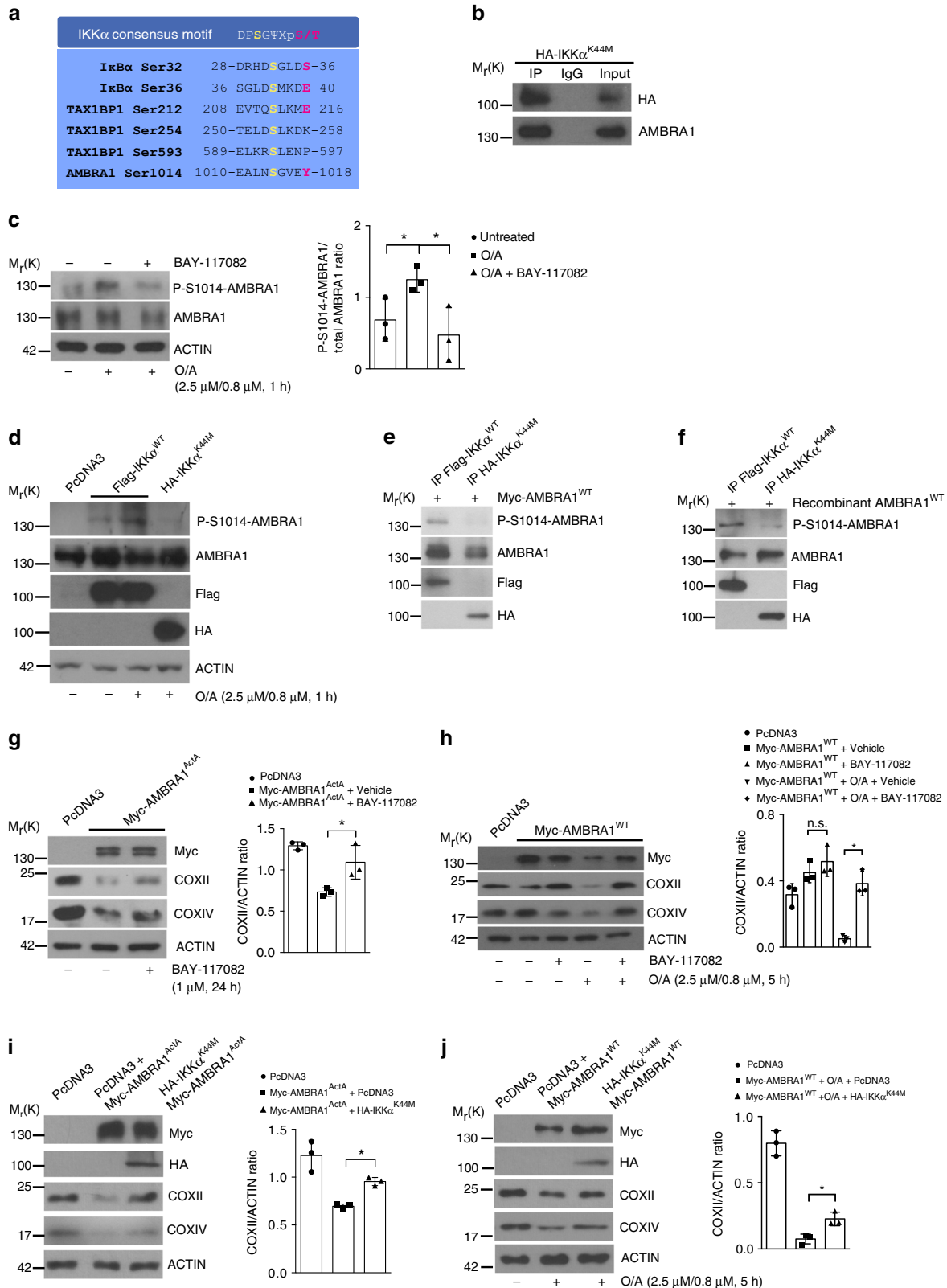


Fig. 5 IKK α controls AMBRA1 phosphorylation at S1014 during mitophagy. **a** Sequence alignment of the consensus sequence of IKK α -phosphorylation on I κ B α , TAX1BP1 and AMBRA1. **b** HA-IKK α^{K44M} transfected HeLa cells were subjected to Co-IP and blotted for the indicated antibodies; $n = 3$. **c** Untransfected HeLa cells were treated with O/A (2.5 μ M, 0.8 μ M, 1 h) and with the IKK α irreversible inhibitor BAY-117082 (2 μ M, 1 h); $n = 3$. **d** Representative image of HeLa cells transfected with PcDNA3, Flag-IKK α^{WT} or the kinase-dead HA-IKK α^{K44M} , treated with O/A and blotted for the indicated antibodies; $n = 3$. **e** In vitro kinase assay of immunoprecipitated-Flag-IKK α^{WT} - or HA-IKK α^{K44M} -expressing HeLa cells in which the substrate (Myc-AMBRA1^{WT}) was transcribed/translated in vitro. Samples were immunoblotted for the indicated proteins; $n = 2$. **f** In vitro kinase assay in which the immunoprecipitated fraction of IKK α^{WT} or IKK α^{K44M} were mixed to recombinant produced AMBRA1; $n = 2$. **g** HeLa cells transfected with Myc-AMBRA1^{ActA} or PcDNA3 (24 h) and treated with BAY-117082 inhibitor were blotted for the indicated antibodies; $n = 3$. **h** HeLa cells transfected with Myc-AMBRA1^{WT} or PcDNA3 and treated with O/A (2.5 μ M, 0.8 μ M, 5 h) and BAY-117082 inhibitor (2 μ M, 5 h) were immunoblotted for the indicated proteins; $n = 3$. **i** HeLa cells transfected with PcDNA3 or HA-IKK α^{K44M} constructs in combination with Myc-AMBRA1^{ActA} were analysed by western blot for the indicated antibodies; $n = 3$. **j** PcDNA3+Myc-AMBRA1^{WT} or Myc-AMBRA1^{WT}+HA-IKK α^{K44M} co-transfected HeLa cells treated with O/A were subjected to immunoblotting for COXII, COXIV, HA, Myc and ACTIN antibodies; $n = 3$. Data represent the mean of three different samples (\pm S.D.) and are representative of experimental triplicate. * $P < 0.05$. Statistical analysis was performed using one-way ANOVA (**c**, **g**, **h**, **i**, **j**). M_r(K) = relative molecular mass expressed in kilodalton

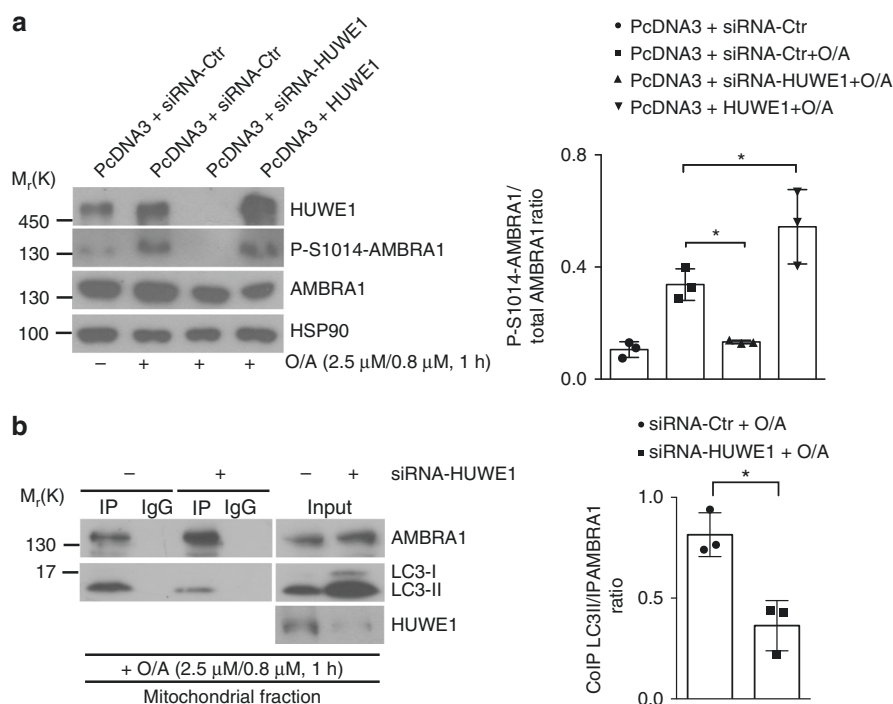


Fig. 6 HUWE1 is crucial for AMBRA1-S1014 phosphorylation. **a** HeLa cells were transfected with an empty vector (PcDNA3) in combination with a siRNA-Ctr or a siRNA-HUWE1 or a plasmid encoding for HUWE1. Cells were treated with O/A (2.5 μ M, 0.8 μ M, 1 h) and total lysates were blotted for the indicated antibodies; $n = 3$. **b** HeLa cells were transfected with siRNA-Ctr or siRNA-HUWE1 and treated with O/A (2.5 μ M, 0.8 μ M, 1 h). Mitochondrial fractions were immunoprecipitated using anti-AMBRA1 antibody; $n = 3$. Data represent the mean of three different samples (\pm S.D.) and are representative of experimental triplicate. * $P < 0.05$. Statistical analysis was performed using one-way ANOVA (**a**) or Student's *t*-test (**b**). M_r(K) = relative molecular mass expressed in kilodalton

we hypothesized that HUWE1 activity could influence AMBRA1 phosphorylation at S1014 upon mitophagy induction. Thus, we transfected HeLa cells with a siRNA-Ctr or siRNA-HUWE1 or with a vector encoding HUWE1, and then treated cells with O/A (2.5 μ M, 0.8 μ M, 1 h).

Interestingly, we observed that the downregulation of HUWE1 induced a significant reduction in AMBRA1-S1014 phosphorylation upon mitophagy induction. By contrast, HUWE1 overexpression resulted in increased phosphorylation of AMBRA1 at the same site (Fig. 6a). In analogy with this result, we observed that HUWE1 depletion produces a reduction in AMBRA1-LC3B binding upon mitophagy stimulation (Fig. 6b).

Taken together, these findings clearly define an epistatic role of HUWE1 in IKK α - and AMBRA1-mediated mitophagy.

AMBRA1 regulates mitochondrial clearance during ischaemia.

Following the evidence on AMBRA1-mediated mitophagy in relay with HUWE1 and IKK α , we checked the physiopathological relevance of this functional interplay in models of ischaemia. Indeed, there is general consensus that mitophagy can be triggered in similar conditions as it happens via receptors. For instance, NIX/BNIP3L mediates mitochondrial removal during cerebral²⁸ and cardiac²⁹ ischaemia/reperfusion (I/R) injury; also, FUNDC1 is a well-known regulator of mitophagy under hypoxia¹¹, and its implications in ischaemia have been recently elucidated^{30,31}. Of note, the intramitochondrial protein ATPIF1, during ischaemia-preconditioning context, has been reported to regulate selective degradation of potentially toxic mitochondria (i.e., those generating high doses of free radicals) by collapsing their membrane potential ($\Delta\Psi_m$)^{32,33}.

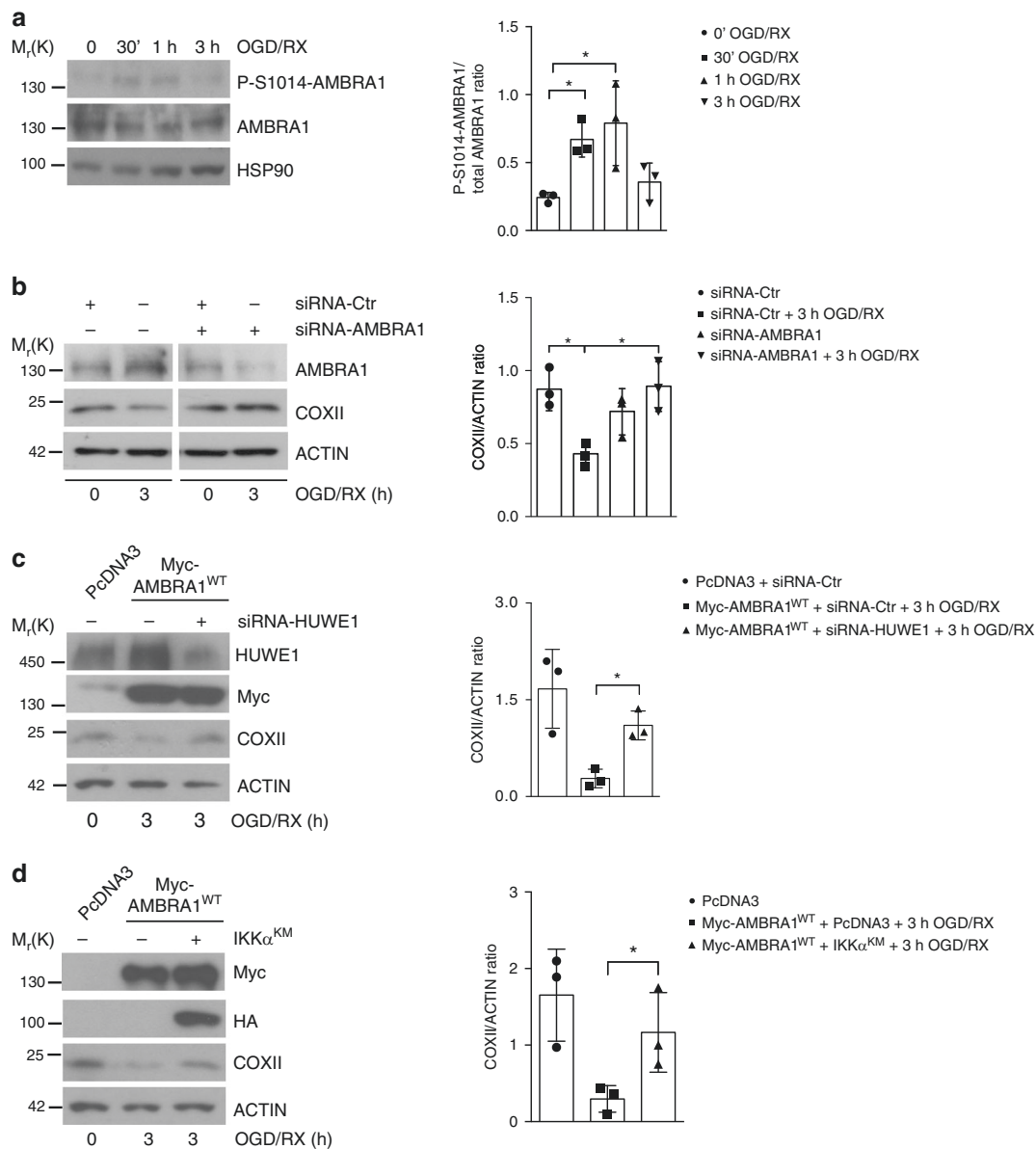


Fig. 7 AMBRA1 induce mitophagy in an in vitro model of ischaemia. **a** Lysates of SH-SY5Y cells exposed to different time points of OGD/RX (0 min, 30 min, 1 h and 3 h) were blotted with the indicated antibodies; $n = 3$. **b** Endogenous AMBRA1 levels were downregulated using siRNA-AMBRA1 in SH-SY5Y cells. Following exposure to 3 h OGD/RX, total lysates were subjected to western blot analysis in order to analyse mitochondria clearance, looking at COXII protein levels; $n = 3$. **c** PcDNA3 or Myc-AMBRA1^{WT}-expressing SH-SY5Y cells were transfected with siRNA-Ctr or siRNA-HUWE1 constructs and then immunoblotted for the indicated proteins; $n = 3$. **d** SH-SY5Y cells transfected with PcDNA3 or HA-IKKα^{K44M} constructs in combination with Myc-AMBRA1^{WT} were subjected to western blot analysis for the indicated antibodies; $n = 3$. Data represent the mean of three different experiments (\pm S.D.). * $P < 0.05$. Statistical analysis was performed using one-way ANOVA. M_r (K) = relative molecular mass expressed in kilodalton

Ischaemia and its prodromal phases are characterized by detrimental oxidative stress, which we showed to be counteracted by AMBRA1-induced mitophagy³⁴; this evidence prompted us to investigate whether AMBRA1 itself could drive mitophagy during I/R injury.

We thus tested the degree of AMBRA1 phosphorylation in SH-SY5Y cells exposed to an in vitro model of ischaemia mimicked by alternative time periods of oxygen-glucose deprivation/reoxygenation (OGD/RX)³³. Total lysates were then subjected to western blot analysis of P-S1014-AMBRA1, recording that AMBRA1 is neatly phosphorylated between 30 min and 1 h of OGD/RX treatment (Fig. 7a). Nevertheless, the role of endogenous AMBRA1 in this physiopathological activation of mitophagy was further corroborated by downregulating AMBRA1 in SH-

SY5Y cells exposed to the same OGD/RX protocols. In Fig. 7b, the decrease of COXII is utterly rescued when AMBRA1 is removed. Subsequently, we checked whether HUWE1 and IKKα also actively took part to AMBRA1-mediated mitophagy upon OGD/RX. In Myc-AMBRA1^{WT}-expressing SH-SY5Y cells, HUWE1 expression was repressed via siRNA; this primed a significant rescue of COXII during OGD/RX (Fig. 7c). In another experiment, we also abrogated IKKα activity by overexpressing the dominant negative kinase IKKα^{K44M} in SH-SY5Y cells transfected with Myc-AMBRA1^{WT}. Indeed, 3 h of exposure to OGD/RX impaired the clearance of mitochondria (Fig. 7d). In sum, these data lead us to conclude that AMBRA1, together with HUWE1 and IKKα, may well represent a novel regulator of ischaemia-induced mitophagy, thus highlighting the

physiopathological relevance of this pathway in mitochondria quality control.

Discussion

In the present study, we demonstrated that the mitophagy receptor AMBRA1 acts at two critical steps during mitochondrial membrane depolarization-induced mitophagy. First, we identified the E3 ubiquitin ligase HUWE1 as an important co-operator of AMBRA1 in order to induce mitophagy, following mitochondrial membrane depolarization. In particular, we demonstrated that AMBRA1^{ActA} strongly favours the interaction between HUWE1 and MFN2, thus acting as a cofactor for HUWE1 E3 ubiquitin ligase activity, and leading subsequently to MFN2 ubiquitylation and then to its degradation. The data highlight a novel important paradigm for HUWE1 E3 ubiquitin ligase activity regulation and open a wide range of studies to understand whether AMBRA1 may control HUWE1 activity in other contexts. Of note, HUWE1 depletion abolishes both MFN2 degradation and AMBRA1-mediated mitophagy in HeLa cells. Also, it has been established that MFN2 degradation is an important event for mitophagy induction³⁵. In line with this evidence, we showed that MFN2 is degraded in the early steps of AMBRA1-mediated mitophagy (18 h post transfection of Myc-AMBRA1^{ActA}). Moreover, HUWE1 depletion induces a clear reduction of total mitochondria ubiquitylation following AMBRA1^{ActA} expression. Since we found that MFN2 degradation correlates with AMBRA1-mediated mitophagy induction, it will be necessary to better understand in the future whether or not this event is a critical step for AMBRA1-mediated mitophagy. Also, although MFN2 is a favourite substrate of HUWE1, it will be important to investigate whether HUWE1 could ubiquitylate other mitochondrial substrates in order to control mitophagy induction.

We recently demonstrated that AMBRA1 is a BH3 (BCL2-homology domain 3)-like protein, containing a BH3 domain necessary for its interaction with BCL2 family proteins^{36,37}. Interestingly, HUWE1 has been defined as a unique BH3-containing E3 ubiquitin ligase³⁸; it would be interesting to characterize the binding between AMBRA1 and HUWE1 by checking, in particular, whether a BH3 mechanism is involved in this context. Of note, both HUWE1 and AMBRA1 can interact with the anti-apoptotic factor MCL1 (induced myeloid leukaemia cell differentiation protein Mcl-1)^{36,38}. In this scenario, it could also be interesting to define the relationship among AMBRA1–HUWE1-dependent mitophagy, mitochondrial dynamics and apoptosis.

The HUWE1–AMBRA1 axis in mitophagy defines a new pathway for damaged mitochondrial removal related to a novel E3 ligase, yet unwound in this field, but since AMBRA1 and HUWE1 are two large multi-domain proteins, they may cooperate in several processes, such as cancer, apoptosis and cell proliferation. In fact, HUWE1 has been described as a tumour suppressor gene controlling the proto-oncogene *c-Myc* regulation. HUWE1 participates to *c-Myc* degradation, leading to a reduction in tumour diffusion³⁹. It is opportune to underline that AMBRA1 also controls *c-Myc* expression, cooperating in the PP2A-mediated dephosphorylation of *c-Myc*⁴⁰. It could thus be interesting to analyse the correlation between AMBRA1–HUWE1 and *c-Myc* regulation upon mitophagy stimulation. As previously demonstrated, mitochondria are fundamental in cellular homeostasis and the HUWE1–AMBRA1 axis can represent a focal point of interconnection between healthy and tumour cells.

In addition, it is noteworthy that MFN2 degradation is also mediated by PARKIN activity⁴¹. Since we demonstrated that AMBRA1-dependent mitophagy is not controlled by the PINK1/PARKIN pathway, we propose here an alternative system that

regulates mitophagy. The removal and proteolysis of OMM proteins appears to be necessary for mitophagy⁴². Since the PINK1/PARKIN pathway is mutated in one of the most diffuse neurodegenerative disturb, Parkinson's Disease^{43,44}, AMBRA1–HUWE1-dependent mitophagy could offer a novel target therapy to counteract this disease as it may preserve cellular vitality. The mitophagy programme is a highly intricate system comprising different characters. In fact, PINK1-related mitophagy receptors present UBDs in their sequences that allow the interaction with Ser65-phosphoUb-containing mitochondria^{5,45}. By contrast, mitochondrial proteins, such as NIX, FUNDC1 and Bcl2-L-13, lacking an UBD, can anyway promote mitophagy of ubiquitylated mitochondria. In our current work, we added a piece to this heterogeneous puzzle, describing AMBRA1 as a new UBD-free mitophagy receptor, which acts following mitochondrial membrane depolarization. Indeed, we revealed that the expression of AMBRA1 is sufficient to restore mitochondrial clearance in cells depleted for PINK1/PARKIN-related mitophagy receptors, such as NDP52, OPTN, TAX1BP1, P62 and NBR1. In analogy with mitophagy receptors Bcl2-L-13, FUNDC1 and NIX/BNIP3L, we demonstrated that AMBRA1 is also able to stimulate mitochondrial clearance in the absence of any PINK1 phospho-ubiquitin signals. Indeed, we previously proved that AMBRA1 was able to induce mitophagy in *PINK1*^{-/-} MEFs cells¹³.

Moreover, we have proved that AMBRA1-mediated mitophagy activity is tightly dependent on its phosphorylation state. In particular, following mitophagy induction, the phosphorylation on S1014 increases the AMBRA1–LC3B binding thus promoting an enhancement in AMBRA1-mediated mitophagy. Moreover, we have revealed that the HUWE1 ubiquitylation signal is fundamental not only in tagging mitochondria for mitophagy, but also in activating AMBRA1 for mitophagy. In fact, we observed that downregulation of HUWE1 results in a reduction of AMBRA1-activated phosphorylation state, necessary for its interaction with the autophagosome marker LC3B. We can speculate that a fine dual relationship occurs between AMBRA1 and HUWE1: the former is necessary for HUWE1 recruitment to the mitochondria; the latter, once at the mitochondria, ubiquitylates OMM protein(s), thus inducing mitophagy and producing a signal for AMBRA1–S1014 phosphorylation, flanking its LIR motif. This event causes in turn a structural rearrangement necessary to make the AMBRA1–LIR motif more accessible to LC3B. In particular, we detected that the negative charge on S1014 of AMBRA1 produces an increase in electrostatic interactions in the proximity of the tryptophan site (W1020) on the AMBRA1–LIR motif. As shown in Supplementary Fig. 4, the importance of electrostatic interactions involving side chains of mATG8 proteins is confirmed by the NMR titration data. By performing ITC and NMR experiments, we observed that the phosphorylation on S1014 is important to increase the affinity between AMBRA1–LIR and mATG8 proteins (Supplementary Fig. 4) and this result led us to identify GABARAP proteins as more specific interacting proteins of AMBRA1. Of note, the S1014 site is not directly located prior to the core LIR aromatic residue W1020 of AMBRA1. Therefore, the increase of AMBRA1–mATG8 binding by S1014 phosphorylation is a quite unexpected event. For example, the OPTN phosphorylation on S170, flanking its LIR motif, shows a small increase in affinity to LC3B²⁴. Based on this, we cannot exclude that other factors (such as additional residues or structural elements in AMBRA1, or AMBRA1 additional post-translational modifications) could also affect the interactions between full-length AMBRA1 and mATG8 proteins. Moreover, since GABARAPs seem to be more involved in the PINK1/PARKIN-dependent mitophagy pathway than LC3s⁴⁶, it will be very interesting to investigate, in the future, whether AMBRA1 requires a preferentially binding to

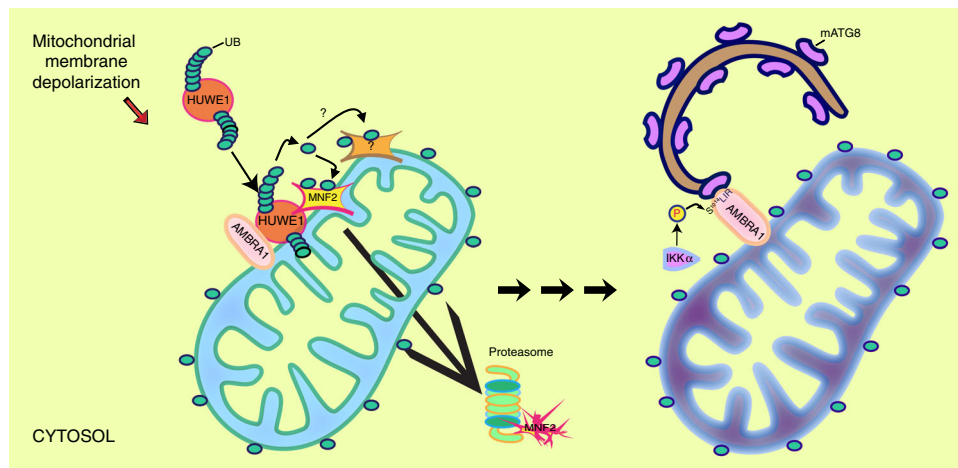


Fig. 8 AMBRA1 regulates mitophagy at two critical steps. Upon mitophagy stimulation, AMBRA1 mediates the HUWE1 E3 ubiquitin ligase translocation from cytosol to mitochondria (light blue). AMBRA1 acts as a cofactor for HUWE1 E3 ubiquitin ligase activity, favouring its binding to its substrate MFN2 (and maybe other OMM substrates) and targeting it to the proteasome. This event is crucial and required for AMBRA1-induced mitophagy. In a second step, in analogy with other mitophagy receptors, AMBRA1 is phosphorylated at S1014, flanking its LIR motif, in order to be able to interact with mATG8s. The final outcome is the engulfment of damaged mitochondria (dark blue) into autophagosomes. This post-translational modification is controlled by IKK α kinase upon mitophagy stimulation. Reproduced from ref.⁷¹ with permission from Elsevier

GABARAPs or to LC3s in mitophagy, depending on a particular context (PINK1/PARKIN dependent or independent) or on other processes (i.e., macroautophagy or different selective forms of autophagy).

Our results clearly define the importance of post-translational modifications on the phosphorylated site, in proximity of the identified LIR motif of AMBRA1. Several reports demonstrated the central role of kinase-mediated phosphorylation in cargo receptor-mediated autophagy^{11,47}. We here demonstrated a novel role of IKK α , independently of its role in NF- κ B pathway in mitophagy. Interestingly, Criollo et al.⁴⁸ proved that the IKK complex was able to promote macroautophagy activation in an NF- κ B-independent manner.

Although the IKK family is composed of several members, including IKK α , IKK β , IKK γ , TBK1 and IKK ϵ , the structure of these factors is very similar²⁵. Interestingly, one of these proteins, TBK1, plays a pivotal role in controlling selective autophagy, such as xenophagy and mitophagy^{6,23,47,49}. Here, we demonstrated that, in analogy with TBK1, which is mainly described to be involved in the phosphorylation of the mitophagy receptor OPTN upstream of its LIR motif in xenophagy²³ and in mitophagy⁵, IKK α is able to phosphorylate the mitophagy receptor AMBRA1 flanking its LC3-interacting region during mitochondrial clearance. It seems that such mechanisms are evolutionary conserved and we hypothesize that similar to OPTN, AMBRA1 could also be involved in other selective autophagy processes (i.e., xenophagy).

It is noteworthy that IKK α is also fundamental in mitochondrial dynamics regulation by favouring OPA1 activation and therefore mitochondrial fusion⁵⁰. Moreover, Bakkar et al.⁵¹ demonstrated that IKK α regulates mitochondrial biogenesis in muscle tissue. These data underline the complexity of IKK α function, which seems to be highly related to inflammation, mitochondria dynamics and mitophagy.

In sum, we prove that previously unravelled mitophagy-involved proteins, HUWE1 E3 ubiquitin ligase and IKK α kinase, play pivotal roles in AMBRA1-mediated mitophagy. HUWE1 is crucial to trigger AMBRA1-mediated mitophagy by favouring MFN2 degradation. This event is necessary for AMBRA1 phosphorylation on its S1014-mediated by IKK α . This kinase, in turn,

regulates the engulfment of damaged mitochondria into autophagosomes by phosphorylating AMBRA1-S1014, thus enabling AMBRA1-mATG8 interactions. Since either HUWE1 or IKK α depletion inhibit mitophagy mediated by AMBRA1, we propose that these two proteins strongly contribute to two different steps in the AMBRA1-mediated mitophagy control (Fig. 8).

Finally, we demonstrated that AMBRA1, in a model of ischaemia/re-oxygenation, regulates mitophagy together with HUWE1 and IKK α , thus implying that AMBRA1-mediated mitophagy plays a protective role in response to hypoxia. In the same line, it would also be interesting to test whether *Ambra1* heterozygous mice fail to show protection against ischaemic stress.

In sum, this work highlights this novel and alternative mitophagy pathway as a new target in developing therapy to counteract diseases characterized by malfunctioning mitochondria such as neurodegeneration, hypoxic-ischaemic encephalopathy and cancer.

Methods

Antibodies. Antibodies used for western blot or immunofluorescence analysis are listed in the Supplementary Table 1 with the appropriated dilutions.

Cell cultures and transfection. Cells were cultured in Dulbecco's modified Eagle's medium (DMEM; GIBCO 41966-029) supplemented with 10% foetal bovine serum (FBS; Thermo Fisher Scientific, 10270-106) and 1% penicillin-streptomycin solution (Lonza, 17-602 E) at 37 °C under 5% CO₂. HeLa and SH-SY5Y cells were purchased from Sigma-Aldrich (93021013 and 9403304, respectively). Penta-knockout HeLa cells (Penta-KO) and mt-mKeima expressing wild-type or PINK1 knockout HeLa cells (mt-mKeima HeLa; mt-mKeima PINK1-KO) were a gift of R. Youle⁵. HEK293T-HUWE1 cells were donated by T. Mak.

Transient transfections of expression plasmids into HeLa, Penta-KO, HEK293T-HUWE1 and SH-SY5Y cells were performed using TurboFect or Lipofectamine 2000 according to the supplier's instructions (Thermo Fisher Scientific, R0532; Invitrogen, 11668019).

Plasmids and cloning. All the transfected constructs presented in this article are described in Supplementary Table 2.

Mutations listed in the Supplementary Table 3 were generated using the QuickChange site-directed mutagenesis kit (Stratagene, 200519) and all plasmids generated in this study were verified by DNA sequencing (Eurofins).

siRNA-mediated knockdown. RNA-interference was performed using Lipofectamine 2000. A list of siRNA constructs is described in Supplementary Table 4.

Cell treatment. After 6 h of transfection or 24 h after cell seeding, cells were treated as described below. Penta-KO were treated with the combined treatment O/A (10 μ M oligomycin (Calbiochem)/4 μ M antimycin A (Sigma)), supplemented with 20 μ M QVD (Sigma-Aldrich, SML0063) in fresh growth medium for 24 h, as in ref. ⁵. HeLa cells were treated either with the combined treatment O/A (2.5 and 0.8 μ M) or FCCP 10 μ M (Sigma-Aldrich, C2920) or EBSS (Thermo Fisher Scientific, 24010043) for the indicated time. In order to block IKK α activity, cells were treated with the irreversible inhibitor BAY-117082 at 1 or 2 μ M, for the indicated time. Autophagosome-lysosome fusion was blocked with NH₄Cl 40 mM (Sigma-Aldrich, O9718).

Western blot analysis. Cells were rinsed in phosphate-buffered saline (PBS) on ice and lysed in RIPA buffer supplemented with a protease inhibitor cocktail (Sigma-Aldrich, P8340), Na₂VO₃ 0.1 mM (Sigma-Aldrich, S6508), NaF 1 mM (Sigma-Aldrich, S7920) and β -Glycerophosphate 5 mM (Sigma-Aldrich, G6376).

Cell extracts were centrifuged at 15,000 \times g for 10 min at 4 °C. Protein concentrations were determined with the Bio-Rad Protein Assay Kit (Bio-Rad, 5000001). Cell extracts or immunoprecipitates were separated by sodium dodecyl sulphate-polyacrylamide gel electrophoresis (SDS-PAGE). Polyvinylidene difluoride (PVDF; Merck-Millipore, IPVH00010) or Nitrocellulose (GE Healthcare, 10600002) membranes were incubated with primary antibodies followed by horseradish peroxidase-conjugate secondary antibodies (Bio-Rad, 1706515 and 1721011) and visualized with ECL (Merck-Millipore WBKLS0500). Uncropped scans of the most important blots are reported in the Supplementary Information, as Supplementary Figure 6.

Co-immunoprecipitation (Co-IP). After cell lysis, equal amounts of protein were incubated with primary antibodies with end-over-end rotation for 24 h. Then, 30 μ l of protein A agarose beads (Roche, 11719408001) were added for 60 min. The beads were collected by centrifugation and washed 3 times with the RIPA buffer. Immunocomplexes were eluted with 30 μ l of SDS sample buffer and heated at 95 °C for 10 min.

Immunofluorescence analysis. Cells were washed in PBS and fixed with 4% paraformaldehyde in PBS for 10 min. After permeabilization with 0.4% Triton X-100 (Sigma-Aldrich, X-100) in PBS for 5 min, cells were incubated overnight at 4 °C with primary antibodies and 2% normal goat serum (Sigma-Aldrich, G9023). Cells were then washed with PBS (GIBCO, BE17-512F) and incubated for 1 h with labelled anti-mouse (Thermo Fisher Scientific, A11017-A21425) or anti-rabbit (Thermo Fisher Scientific, A11070-A21430-A31573) secondary antibodies. Nuclei were stained with 1 μ g/ml DAPI (4',6-diamidino-2-phenylindole) and examined under a Zeiss LSM 700 100 \times oil-immersion objective (CLSM700; Jena, Germany). We used ImageJ software for image analysis. We calculated the mito content as percentage of cytosolic area occupied by mitochondria with Mitophagy macro⁵². For Supplementary Figure 1b, the quantification as mito-aggregate-positive transfected cells (%) was performed by a blind approach (the information on plasmid transfection was masked), counting the mitochondria with round and clumped shape. All acquisitions were performed in non-saturated single z-confocal planes.

Nuclei-mitochondria-cytosol purification. Cells, rinsed in ice-cold PBS and centrifuged at 800 \times g for 10 min, were resuspended in homogenization buffer (HB: 0.25 M sucrose (Sigma-Aldrich, S0389), 10 mM HEPES pH 7 (Sigma-Aldrich, H4034), EDTA (Sigma-Aldrich, ED-100)) with protease and phosphatase inhibitors cocktail. Nuclei, mitochondria and cytosol purifications proceed by standard differential centrifugations. After homogenization of the solution with 30–70 pulses (one pulse corresponds to approximately 1 s), cells were collected at 600 \times g for 10 min. The pellet containing the nuclear fraction was suspended in RIPA buffer, instead the supernatant was subjected to a further centrifugation at 11,000 \times g for 15 min at 4 °C. The mitochondrial pellet fraction was suspended in RIPA buffer. The supernatant fraction corresponded to soluble cytosolic proteins.

In vitro IP-kinase assay. HeLa cells were transiently transfected with a vector encoding for Myc-AMBRA1^{WT} or Flag-IKK α ^{WT} or HA-IKK α ^{K44M}. After 24 h, equal amounts of proteins (500 μ g) were immunoprecipitated using anti-Myc, anti-Flag and anti-HA antibodies, respectively, overnight. Protein A Agarose beads (30 μ l of 50% slurry) (Roche, 11719408001) were added to the samples at 4 °C with end-over-end rotation for 1 h. The immunoprecipitates were collected by centrifugation and washed 3 times with RIPA buffer. Pellets were washed for 3 min with 500 μ l 1 \times Kinase Buffer (KB: 20 mM Hepes pH 7.4, 10 mM MgCl₂, 25 mM Glycerophosphate, 0.1 Na₂VO₃, 4 mM NaF, 1 mM DTT (Sigma-Aldrich, GE17-1318-01)). The IP-Flag-IKK α ^{WT} or IP-HA-IKK α ^{K44M} final pellets were resuspended in 50 μ l of 1 \times Kinase Buffer, while IP-Myc-AMBRA1 was suspended in 50 μ l of RIPA buffer. In order to test kinase activity with a non-radioactive method, 1 μ l of 10 mM adenosine triphosphate (ATP) and 20 μ l of IP-Myc-AMBRA1 substrate were added to the IP kinases for 30 min at 30 °C. The reaction was stopped by adding 30 μ l of 4 \times SDS Sample Buffer and denaturing at 95 °C for 5 min. For

the kinase assay with recombinant AMBRA1, the wild-type AMBRA1 protein was transcribed and translated in vitro with standard procedures (Promega, L1170 TrnT[®] Quick Coupled Transcription/ Translation Systems). At the end of IKK α ^{WT} or IKK α ^{K44M} immunoprecipitation (as described above), 1 μ l of 10 mM ATP and 2 μ l of kinase substrate was added to the IP-kinases for 30 min at 30 °C. The reaction was stopped by adding 30 μ l of SDS Sample Buffer and denaturing at 95 °C for 5 min. For both of these kinase assays, samples were analysed by western blot.

Isothermal titration microcalorimetry. The ITC experiments were performed at 25 °C and 35 °C using a MicroCal VP-ITC microcalorimeter (Malvern Instruments Ltd, UK). The peptides at concentrations of 0.35 mM were titrated into 0.015 mM LC3 and GABARAP proteins in 21 steps. The ITC data were analysed with the ITC-Origin 7.0 software with a one-site binding model. The protein and peptide concentrations were calculated from the UV absorption at 280 nm through a Nanodrop spectrophotometer (Thermo Fisher Scientific, DE, USA).

NMR spectroscopy. All NMR experiments were performed at 298 K on Bruker Avance spectrometer operating at a proton frequencies of 600 MHz. Titration experiments were performed with 0.17 mM ¹⁵N-labelled LC3B and GABARAP protein samples to which the non-labelled AMBRA1-LIR peptides were added stepwise until 8 times excess to LC3B protein, or 4 times excess to the GABARAP protein. Chemical shift perturbations (CSP) analysis was done according to the most recent review⁵³. CSP values were calculated for each individual backbone proton using the formula: $\Delta\delta = [\Delta\delta_H^2 + (\Delta\delta_N/5)^2]^{1/2}$. The dissociation constants, K_D , were calculated by a least squares fit to the titration data under the assumptions of a fast exchange regime and a one binding site mode of the protein interaction. The obtained CSP values were mapped on LC3B (PDB ID 1UGM⁵⁴) and GABARAP (PDB ID 1GNU⁵⁵) structures.

ITC and NMR sample preparation. For ITC and NMR experiments, the unlabelled or ¹⁵N-labelled LC3 and GABARAP proteins were obtained based on the protocols described elsewhere^{56,57}. AMBRA1-LIR-containing peptides with different states of S1014 phosphorylation (unphosphorylated, P0: EALNSGVEYYWDQLNET; D-phosphomimicked, PM: EALNDGVEYYWDQLNET; and S1014 phosphorylated, P1: EALN{pS}GVEYYWDQLNET) were purchased from GenScript Inc. (NJ, USA). Before experiments, all proteins and peptides were equilibrated with a buffer containing 50 mM Na₂HPO₄, 100 mM NaCl, pH 7.0; and supplemented with 5 mM protease inhibitor cocktail.

AMBRA1-LC3B modelling. We used Modeller version 9.15⁵⁸ to generate structural models of the AMBRA1-LIR motif (L₁₀₁₃NSGVEYYWDQLNET₁₀₂₆) in complex with LC3B to use as starting structures for the all-atom MD simulations. For the modelling, we used the X-ray structure of p62-LIR motif in complex with LC3B (PDB entry 2ZJD)⁵⁹ as a template. We generated 1000 binding poses with Modeller and we then carried out structural clustering with the linkage algorithm based on the root mean square deviation (RMSD) of all the atoms of Ambra1-LIR peptide. We selected the average structures from each of the four more populated clusters (i.e., the conformer with the lowest RMSD to the other ones in the same cluster) and we used each of them as a starting structure for all-atom explicit solvent molecular simulations using multiple replicates. For the phosphorylated variant of Ambra1-LIR, we generated a second set of models by in silico phosphorylation (S2P; phosphoserine with a –2 charge) on position S1014 in each of the four models previously selected using the web interface of Vienna-PTM⁶⁰. We treated in our simulation the phosphoserine S1014 using the –2 state. Indeed, the pKa values of single protonated/un-protonated transition of phosphoserine suggest that both states are present at neutral pH, but the –2 state is predominant⁶¹.

We carried out 250-ns all-atom MD simulations in explicit solvent for each of the selected four models in both unphosphorylated and phosphorylated states, as well as a simulation of the known LC3B-p62 complex as a reference. The MD simulations were performed with Gromacs version 5.1⁶² with the protein force fields Charmm22/CMAP⁶³ and Charmm22⁶⁴ in conjunction with the TIP3P water model. Parameters for S2P were merged from ref. ⁶⁵. All systems were solvated in dodecahedral boxes with a minimum distance between protein and box edge of 1.8 nm and charged ions were added to set a concentration of 0.15 M NaCl. The productive MD simulations were carried out at 298 K with simulation parameters and equilibration protocol⁶⁶. The first 50 ns of each MD simulation required for equilibration of the system was discarded from downstream analyses.

For each trajectory we calculated, as a measure of protein flexibility, the average RMSF for each Ca atom in the Ambra1-LIR or the p62-LIR peptides averaging the RMSF over 10-ns time windows and estimating the associated standard deviations.

The four independent replicates of each system were merged into a concatenated trajectory for the analyses of electrostatic interactions.

We estimated intra- and inter-molecular electrostatic interactions, as implemented in the PyInterph suite of tools⁶⁷. The interactions are defined as distances between the charged groups in the residue side chains of arginine, lysine, aspartate, glutamate and the phosphoserine. We employed a 5 Å cutoff in the analyses. To filter out interactions with low occurrence in the simulations, we included in the final networks only those interactions which are present in at least

20% of the simulation frames, as previously tested in other cases of study⁶⁷. All the electrostatic interactions identified for each of the MD ensembles were visualized using the PyMOL plugin xPyder⁶⁸.

Mass spectrometry analysis of AMBRA1-interacting proteins. SILAC-based strategy is used for comparative and quantitative AMBRA1-interacting proteins analysis in HeLa cells in mitophagy condition. Cells were grown in SILAC DMEM (Silantes, 280001200), supplemented with FBS 10%, 1% penicillin–streptomycin solution, L-glutamine, L-arginine and L-lysine, according to the supplier's instructions. Accordingly, we obtained two different isotope amino-acid labelling media: Light Medium K0/R0 and SILAC Heavy medium (K6/R10). Cells were grown in these media for 2 weeks.

In order to analyse AMBRA1 interactors during mitophagy, Light and Heavy cells were transfected with a vector encoding for Myc-AMBRA1^{ActA} for 24 h. Equal amounts of harvested Light and Heavy lysates were immunoprecipitated with an anti-Myc antibody, as previously described in the immunoprecipitation protocol. Immunoprecipitated heavy proteins were then mixed 1:1 with light proteins and subjected to SDS-PAGE followed by band excision and trypsin-peptide digestion in order to allow LC-ESI-MS/MS (liquid chromatography-electrospray ionization-tandem mass spectrometry) analysis¹⁵.

In vitro ubiquitylation assay. HEK293T cells stably expressing Flag-HUWE1 were lysed with Triton Buffer (50 mM Tris-HCl pH 7.5, 250 mM NaCl, 50 mM NaF, 1 mM EDTA 1 pH 8, 0.1% Triton), supplemented with proteases and phosphatases inhibitors. Then, 3–5 mg of whole cell lysates were precleared with protein A/G-Sepharose beads (GE Healthcare) for 3 h and then incubated overnight at 4 °C with 5 mg of anti-Flag antibody (Sigma-Aldrich, F3165) per sample. Finally, the immunocomplexes have been absorbed on protein A/G-Sepharose beads, washed six times in Triton lysis buffer and used for in vitro ubiquitylation assay or eluted by boiling in SDS loading buffer.

In vitro ubiquitylation assay was carried out using HUWE1 complex immunopurified from HEK293T cells stably expressing Flag-HUWE1 using the method described above. The beads containing the HUWE1 immunocomplexes were washed twice with equilibration buffer (25 mM Tris-HCl pH 7.5, 50 mM NaCl, 1 mM EDTA, 0.01% Triton and 10% glycerol) and then added to the following reaction: 40 ng of E1, 0.5 µg of UbcH3, 0.5 µg of UbcH5, 0.3 µg of UbcH7, 1 µg of ubiquitin in the ubiquitylation buffer (2.5 mM Tris-HCl, 0.7 mM dithiothreitol (DTT), 4 mM ATP, 10 mM MgCl₂, 0.1 mM ubiquitin aldehyde) in a final volume of 30 µl. The assays have been carried out for 90 min at 30 °C, then the immunocomplexes were eluted by boiling in SDS loading buffer, loaded on SDS-PAGE, blotted onto PVDF membranes (Millipore) and then blocked with PBS-T (phosphate-buffered saline and 0.1% Tween-20) containing 5% non-fat dry milk for 1 h at room temperature (RT). The incubation with primary antibodies was performed for 2 h at RT, followed by appropriate horseradish peroxidase-conjugated secondary antibodies for 1 h at RT. After extensive washing, detection was performed with the ECL Western Blot Chemiluminescence Reagent (Perkin Elmer).

In vitro protocols of ischaemia. Preconditioning and ischaemia condition were recreated by exposing cells to 30 min and 3 h, respectively, of OGD⁶⁹. In addition, cells were exposed to 1 h of OGD. Initially, OGD was performed in a medium previously saturated with 95% N₂ and 5% CO₂ for 20 min and containing NaCl 116 mM, KCl 5.4 mM, MgSO₄ 0.8 mM, NaHCO₃ 26.2 mM, NaH₂PO₄ 1 mM, CaCl₂ 1.8 mM, glycine 0.001 mM and 0.001 w/v phenol red^{33,70}. Then, hypoxic conditions were maintained using a hypoxia chamber at 37 °C, 5% CO₂ and 95% N₂. At the end of OGD, the cells were incubated for 24 h in normoxic conditions using DMEM containing normal levels of O₂ in a CO₂ incubator at 37 °C RX) followed by lysis for western blot analysis. Whole cell lysate were prepared in RIPA buffer (50 mM Tris-HCl, 150 mM NaCl, 1% (v/v) Triton X-100, pH 8.0) containing protease and the phosphatase inhibitors.

mt-mKeima mitophagy assay. Wild-type and PINK1-KO HeLa cells stably expressing mitochondrial-targeted mKeima (mt-mKeima,⁷¹) were co-transfected with PcDNA3+GFP, Myc-AMBRA1^{WT}+GFP, Myc-AMBRA1^{S1014A}+GFP, Myc-AMBRA1^{S1014D}+GFP, PcDNA3+GFP-ShCtr, Myc-Ambra1^{ActA}+GFP-ShCtr or myc-Ambra1^{ActA}+GFP-ShHUWE1, and treated as indicated in the text. GFP was used as a reporter for co-transfected cells. Live cells were photographed at 37 °C/5% CO₂ through the live cell imaging microscope UltraView Vox (Perkin Elmer). mt-mKeima was excited both at 405 nm (neutral, pseudo-coloured in green) and 561 nm (acidic, red) and detected through the same emission filter (615 nm, W70), while GFP was captured with standard procedures (488 nm excitation, 525 nm W50 emission filter, pseudo-coloured in cyan). A total of 100 randomized fields per condition were detected in each experiment with a 100× objective. Randomization was performed through an automated function of the microscope. mt-mKeima fluorescence intensity was quantified in single GFP-positive cells with the integrated function of the microscope software Velocity (Perkin Elmer). Fields with no GFP-positive cells were excluded from the analysis.

Statistical analysis. All statistical calculations were performed and graphed using GraphPad Prism 6. Comparisons between two groups were analysed using Student's *t*-test assuming a two-tailed distribution. Three or more group comparisons were performed with one-way analysis of variance (ANOVA) and Tukey's post-test with a confidence interval of 95%. Significance is defined as **P* < 0.05; ***P* < 0.01; ****P* < 0.001; *****P* < 0.0001. No statistical methods were used to predetermine sample size.

Data availability

The data that support the findings of this study are available from the corresponding author upon reasonable request.

Received: 6 October 2017 Accepted: 27 June 2018

Published online: 14 September 2018

References

- Lemasters, J. J. Selective mitochondrial autophagy, or mitophagy, as a targeted defense against oxidative stress, mitochondrial dysfunction, and aging. *Rejuvenation Res.* **8**, 3–5 (2005).
- Tatsuta, T. & Langer, T. Quality control of mitochondria: protection against neurodegeneration and ageing. *EMBO J.* **27**, 306–314 (2008).
- Karbowsky, M. & Youle, R. J. Regulating mitochondrial outer membrane proteins by ubiquitination and proteasomal degradation. *Curr. Opin. Cell Biol.* **23**, 476–482 (2011).
- Yamano, K., Matsuda, N. & Tanaka, K. The ubiquitin signal and autophagy: an orchestrated dance leading to mitochondrial degradation. *EMBO Rep.* **17**, 300–316 (2016).
- Lazarou, M. et al. The ubiquitin kinase PINK1 recruits autophagy receptors to induce mitophagy. *Nature* **524**, 309–314 (2015).
- Heo, J. M., Ordureau, A., Paulo, J. A., Rinehart, J. & Harper, J. W. The PINK1-PARKIN mitochondrial ubiquitylation pathway drives a program of OPTN/NDP52 recruitment and TBK1 activation to promote mitophagy. *Mol. Cell* **60**, 7–20 (2015).
- Wei, Y., Chiang, W. C., Sumpter, R. Jr., Mishra, P. & Levine, B. Prohibitin 2 is an inner mitochondrial membrane mitophagy receptor. *Cell* **168**, 224–238 (2017).
- Sandoval, H. et al. Essential role for Nix in autophagic maturation of erythroid cells. *Nature* **454**, 232–235 (2008).
- Novak, I. et al. Nix is a selective autophagy receptor for mitochondrial clearance. *EMBO Rep.* **11**, 45–51 (2010).
- Murakawa, T. et al. Bcl-2-like protein 13 is a mammalian Atg32 homologue that mediates mitophagy and mitochondrial fragmentation. *Nat. Commun.* **6**, 7527 (2015).
- Liu, L. et al. Mitochondrial outer-membrane protein FUNDC1 mediates hypoxia-induced mitophagy in mammalian cells. *Nat. Cell Biol.* **14**, 177–185 (2014).
- Hamacher-Brady, A. & Brady, N. R. Mitophagy programs: mechanisms and physiological implications of mitochondrial targeting by autophagy. *Cell. Mol. Life Sci.* **73**, 775–795 (2016).
- Strappazzon, F. et al. AMBRA1 is able to induce mitophagy via LC3 binding, regardless of PARKIN and p62/SQSTM1. *Cell Death Differ.* **22**, 419–432 (2015).
- Strappazzon, F. et al. Mitochondrial BCL-2 inhibits AMBRA1-induced autophagy. *EMBO J.* **30**, 1195–1208 (2011).
- Sprenger, A. et al. Consistency of the proteome in primary human keratinocytes with respect to gender, age, and skin localization. *Mol. Cell. Proteom.* **12**, 2509–2521 (2013).
- Parsons, J. L. et al. Ubiquitin ligase ARF-BP1/Mule modulates base excision repair. *EMBO J.* **28**, 3207–3215 (2009).
- Leboucher, G. P. et al. Stress-induced phosphorylation and proteasomal degradation of mitofusin 2 facilitates mitochondrial fragmentation and apoptosis. *Mol. Cell* **47**, 547–557 (2012).
- Tanaka, A. et al. Proteasome and p97 mediate mitophagy and degradation of mitofusins induced by Parkin. *J. Cell Biol.* **191**, 1367–1380 (2010).
- Stolz, A. et al. Fluorescence-based ATG8 sensors monitor localization and function of LC3/GABARAP proteins. *EMBO J.* **36**, 549–564 (2017).
- Zhu, Y. et al. Modulation of serines 17 and 24 in the LC3-interacting region of Bnip3 determines pro-survival mitophagy versus apoptosis. *J. Biol. Chem.* **288**, 1099–1113 (2013).
- Rogov, V. V. et al. Phosphorylation of the mitochondrial autophagy receptor Nix enhances its interaction with LC3 proteins. *Sci. Rep.* **7**, 1131 (2017).
- Wild, P. et al. Phosphorylation of the autophagy receptor optineurin restricts Salmonella growth. *Science* **333**, 228–233 (2011).

23. Rogov, V. V. et al. Structural basis for phosphorylation-triggered autophagic clearance of Salmonella. *Biochem. J.* **454**, 459–466 (2013).
24. Xue, Y. et al. GPS: a comprehensive www server for phosphorylation sites prediction. *Nucleic Acids Res.* **33**, 184–187 (2005).
25. Xu, G. et al. Crystal structure of inhibitor of κ B kinase β . *Nature* **472**, 325–330 (2011).
26. Shembade, N., Pujari, R., Harhaj, N. S., Abbott, D. W. & Harhaj, E. W. The kinase IKK α inhibits activation of the transcription factor NF- κ B by phosphorylating the regulatory molecule TAX1BP1. *Nat. Immunol.* **12**, 834–843 (2011).
27. Tomita, H. et al. Troglitazone and 15-deoxy-delta(12,14)-prostaglandin J2 inhibit shear-induced coupling factor 6 release in endothelial cells. *Cardiovasc. Res.* **67**, 134–141 (2005).
28. Yuan, Y. et al. BNIP3L/NIX-mediated mitophagy protects against ischemic brain injury independent of PARK2. *Autophagy* **13**, 1754–1766 (2017).
29. Hamacher-Brady, A. et al. Response to myocardial ischemia/reperfusion injury involves Bnip3 and autophagy. *Cell Death Differ.* **14**, 146–157 (2007).
30. Zhang, W. et al. Hypoxic mitophagy regulates mitochondrial quality and platelet activation and determines severity of I/R heart injury. *eLife* **5**, e21407 (2016).
31. Zhou, H. et al. Pathogenesis of cardiac ischemia reperfusion injury is associated with CK2 α -disturbed mitochondrial homeostasis via suppression of FUNDC1-related mitophagy. *Cell Death Differ.* **25**, 1080–1093 (2018).
32. Campanella, M. et al. IF1, the endogenous regulator of the F(1)F(o)-ATP synthase, defines mitochondrial volume fraction in HeLa cells by regulating autophagy. *Biochim. Biophys. Acta* **1787**, 393–401 (2009).
33. Matic, I. et al. Neuroprotective coordination of cell mitophagy by the ATPase inhibitory factor 1. *Pharmacol. Res.* **103**, 56–68 (2016).
34. Di Rita, A. et al. AMBRA1-mediated mitophagy counteracts oxidative stress and apoptosis induced by neurotoxicity in human neuroblastoma SH-SY5Y cells. *Front. Cell. Neurosci.* **12**, 92 (2018).
35. Ashrafi, G. & Schwarz, T. L. The pathways of mitophagy for quality control and clearance of mitochondria. *Cell Death Differ.* **20**, 31–42 (2013).
36. Strappazzon, F. et al. Prosurvival AMBRA1 turns into a proapoptotic BH3-like protein during mitochondrial apoptosis. *Autophagy* **12**, 963–975 (2016).
37. Di Rita, A. & Strappazzon, F. AMBRA1, a novel BH3-like protein: new insights into the AMBRA1-BCL2-family proteins relationship. *Int. Rev. Cell Mol. Biol.* **330**, 85–113 (2017).
38. Zhong, Q., Gao, W., Du, F. & Wang, X. Mule/ARF-BP1, a BH3-only E3 ubiquitin ligase, catalyzes the polyubiquitination of Mcl-1 and regulates apoptosis. *Cell* **121**, 1085–1095 (2005).
39. Inoue, S. et al. Mule/Huwei1/Arf-BP1 suppresses Ras-driven tumorigenesis by preventing c-Myc/Miz1-mediated down-regulation of p21 and p15. *Gene Dev.* **27**, 1101–1114 (2013).
40. Cianfanelli, V. et al. AMBRA1 links autophagy to cell proliferation and tumorigenesis by promoting c-Myc dephosphorylation and degradation. *Nat. Cell Biol.* **17**, 20–30 (2015).
41. Chen, Y. & Dorn, G. W. 2nd PINK1-phosphorylated mitofusin 2 is a Parkin receptor for culling damaged mitochondria. *Science* **340**, 471–475 (2013).
42. Chan, N. C. et al. Broad activation of the ubiquitin-proteasome system by Parkin is critical for mitophagy. *Hum. Mol. Genet.* **20**, 1726–1737 (2011).
43. Valente, E. M. et al. PARK6-linked parkinsonism occurs in several European families. *Ann. Neurol.* **51**, 14–18 (2002).
44. Kitada, T. et al. Mutations in the parkin gene cause autosomal recessive juvenile parkinsonism. *Nature* **392**, 605–608 (1998).
45. Kane, L. A. et al. PINK1 phosphorylates ubiquitin to activate Parkin E3 ubiquitin ligase activity. *J. Cell Biol.* **205**, 143–153 (2014).
46. Nguyen, T. N. et al. Atg8 family LC3/GABARAP proteins are crucial for autophagosome-lysosome fusion but not autophagosome formation during PINK1/Parkin mitophagy and starvation. *J. Cell Biol.* **215**, 857–874 (2016).
47. Richter, B. et al. Phosphorylation of OPTN by TBK1 enhances its binding to Ub chains and promotes selective autophagy of damaged mitochondria. *Proc. Natl. Acad. Sci. USA* **113**, 4039–4044 (2016).
48. Criollo, A. et al. The IKK complex contributes to the induction of autophagy. *EMBO J.* **29**, 619–631 (2010).
49. Pilli, M. et al. TBK-1 promotes autophagy-mediated antimicrobial defense by controlling autophagosomal maturation. *Immunity* **37**, 223–234 (2012).
50. Laforge, M. et al. NF- κ B pathway controls mitochondrial dynamics. *Cell Death Differ.* **23**, 89–98 (2015).
51. Bakkar, N. et al. IKK α and alternative NF- κ B regulate PGC-1 β to promote oxidative muscle metabolism. *J. Cell Biol.* **196**, 497–511 (2012).
52. Dagda, R. K., Zhu, J., Kulich, S. M. & Chu, C. T. Mitochondrially localized ERK2 regulates mitophagy and autophagic cell stress. *Autophagy* **4**, 770–782 (2008).
53. Williamson, M. P. Using chemical shift perturbation to characterise ligand binding. *Prog. Nucl. Magn. Reson Spectrosc.* **73**, 1–16 (2013).
54. Sugawara, K. et al. The crystal structure of microtubule-associated protein light chain 3, a mammalian homologue of Saccharomyces cerevisiae Atg8. *Genes Cells* **9**, 611–618 (2004).
55. Knight, D. et al. The X-ray crystal structure and putative ligand-derived peptide binding properties of gamma-aminobutyric acid receptor type A receptor-associated protein. *J. Biol. Chem.* **277**, 5556–5561 (2002).
56. Rogov, V. V. et al. A universal expression tag for structural and functional studies of proteins. *Chembiochem* **13**, 959–963 (2012).
57. Rozenknop, A. et al. Characterization of the interaction of GABARAPL-1 with the LIR motif of NBR1. *J. Mol. Biol.* **410**, 477–487 (2011).
58. Sali, A. & Blundell, T. L. Comparative protein modelling by satisfaction of spatial restraints. *J. Mol. Biol.* **234**, 779–815 (1993).
59. Ichimura, Y. et al. Structural basis for sorting mechanism of p62 in selective autophagy. *J. Biol. Chem.* **283**, 22847–22857 (2008).
60. Margreiter, C., Petrov, D. & Zagrovic, B. Vienna-PTM web server: a toolkit for MD simulations of protein post-translational modifications. *Nucleic Acids Res.* **41**, 422–426 (2013).
61. Kitchen, J., Saunders, R. E. & Warwicker, J. Charge environments around phosphorylation sites in proteins. *BMC Struct. Biol.* **8**, 19 (2008).
62. Abraham, M. J. et al. Gromacs: high performance molecular simulations through multi-level parallelism from laptops to supercomputers. *SoftwareX* **1**, 19–25 (2015).
63. Bjelkmar, P., Larsson, P., Cuendet, M. A., Hess, B. & Lindahl, E. Implementation of the CHARMM force field in GROMACS: analysis of protein stability effects from correction maps, virtual interaction sites, and water models. *J. Chem. Theory Comput.* **6**, 459–466 (2010).
64. Piana, S., Lindorff-Larsen, K. & Shaw, D. E. How robust are protein folding simulations with respect to force field parameterization? *Biophys. J.* **100**, 47–49 (2011).
65. Khoury, G. A., Thompson, J. P., Smadbeck, J., Kieslich, C. A. & Floudas, C. A. Forcefield_PTMM: ab initio charge and AMBER forcefield parameters for frequently occurring post-translational modifications. *J. Chem. Theory Comput.* **9**, 5653–5674 (2013).
66. Tiberti, M., Papaleo, E., Bengtson, T., Boomsma, W. & Lindorff-Larsen, K. ENCORE: software for quantitative ensemble comparison. *PLoS Comput. Biol.* **11**, e1004415 (2015).
67. Tiberti, M. et al. PyInterph: a framework for the analysis of interaction networks in structural ensembles of proteins. *J. Chem. Inf. Model.* **54**, 1537–1551 (2014).
68. Pasi, M., Tiberti, M., Arrigoni, A. & Papaleo, E. xPyder: a PyMOL plugin to analyze coupled residues and their networks in protein structures. *J. Chem. Inf. Model.* **52**, 1865–1874 (2012).
69. Abramov, A. Y., Scorziello, A. & Duchon, M. R. Three distinct mechanisms generate oxygen free radicals in neurons and contribute to cell death during anoxia and reoxygenation. *J. Neurosci.* **27**, 1129–1138 (2007).
70. Choi, D. W. & Rothman, S. M. The role of glutamate neurotoxicity in hypoxic-ischemic neuronal death. *Annu. Rev. Neurosci.* **13**, 171–182 (1990).
71. Strappazzon, F. & Cecconi, F. The multifaceted mitochondrion: an attractive candidate for therapeutic strategies. *Pharmacol. Res.* **99**, 425–433 (2015).

Acknowledgements

We wish to thank: R. Youle (Bethesda, MD) for kindly providing us Penta-KO and mtmKeima expressing wild-type or PINK1 knockout HeLa cells; T. Mak (Toronto, CDN) for HUWE1 overexpressing cells; E. Meylan (Lausanne, CH), M. Karin (La Jolla, CA) and I. Dikic (Frankfurt, D) for supplying us the constructs Flag-IKK α ^{WT}, HA-IKK α ^{K44M} and Myc-TBK1, respectively. We thank Elsevier for giving us the opportunity to re-use on Fig. 8 our previous mitochondria draw image, published in Strappazzon and Cecconi. We are grateful to the Danish Supercomputing Center Computerome. This work was supported by grants: Italian Ministry of Health GR2011-02351433 and "Roche per la Ricerca 2017" to F.S.; AIRC (IG2016-18906), KBVU from the Danish Cancer Society (R72-A4408, R146-A9364), the Novo Nordisk Foundation (7559, 22544), the European Union (Horizon 2020 MEL-PLEX, grant agreement 642295), the Lundbeckfonden (R233-2016-3360), the LEO Foundation (LF17024), the Bjarne Saxhof Foundation to F.C.; PRACE-DECI14th GRANT for HPC resources on Archer (UK) to E.P. Further, F.C. and E.P. labs in Copenhagen are part of the Center of Excellence in Autophagy, Recycling and Disease (CARD), funded by the Danish National Research Foundation; and AIRC (MFAG#15523) to A.P. The work of J.G., V.D. and V.V.R. was supported by the German Research Foundation (CRC/SFB 1177 on selective autophagy). Research conducted by D. S. and M.C. was supported by the Umberto Veronesi Foundation, LAM-Bighi Grant Initiative, FIRB-Research Consolidator Grant [RBF13P392] and Italian Ministry of Health [IFO14/01/R/52]. We thank M. Acuña Villa for secretarial work and S. Verna and N. Rogova for technical assistance.

Author contributions

A.D.R. performed most experiments and designed the work plan together with F.S. and F.C. Experimental work: F.S. (cloning of serine mutants); A.P. (IVT ubiquitylation); M.

N., M.L., E.P. (molecular modelling of AMBRA1–LC3); J.G., V.D., V.V.R. (ITC and NMR); Z.H. and J.D. (mass spectrometry analysis); S.E.A. (P-S1014-AMBRA1 antibody generation); P.D.A. (mito-mKeima experiments); D.S. and M.C. (in vitro ischaemic experiments); and G.M. (contribution of reagents). A.D.R., F.S. and F.C. wrote the manuscript.

Additional information

Supplementary Information accompanies this paper at <https://doi.org/10.1038/s41467-018-05722-3>.

Competing interests: The authors declare no competing interests.

Reprints and permission information is available online at <http://npg.nature.com/reprintsandpermissions/>

Publisher's note: Springer Nature remains neutral with regard to jurisdictional claims in published maps and institutional affiliations.



Open Access This article is licensed under a Creative Commons Attribution 4.0 International License, which permits use, sharing, adaptation, distribution and reproduction in any medium or format, as long as you give appropriate credit to the original author(s) and the source, provide a link to the Creative Commons license, and indicate if changes were made. The images or other third party material in this article are included in the article's Creative Commons license, unless indicated otherwise in a credit line to the material. If material is not included in the article's Creative Commons license and your intended use is not permitted by statutory regulation or exceeds the permitted use, you will need to obtain permission directly from the copyright holder. To view a copy of this license, visit <http://creativecommons.org/licenses/by/4.0/>.

© The Author(s) 2018



AMBRA1-Mediated Mitophagy Counteracts Oxidative Stress and Apoptosis Induced by Neurotoxicity in Human Neuroblastoma SH-SY5Y Cells

Anthea Di Rita^{1,2,3}, Pasquale D'Acunzo³, Luca Simula³, Silvia Campello^{1,2}, Flavie Strappazzon^{1*} and Francesco Cecconi^{2,3,4*}

¹IRCCS Fondazione Santa Lucia, Rome, Italy, ²Department of Biology, University of Rome Tor Vergata, Rome, Italy,

³Department of Paediatric Haematology and Oncology, IRCCS Bambino Gesù Children's Hospital, Rome, Italy, ⁴Unit of Cell Stress and Survival, Danish Cancer Society Research Center, Copenhagen, Denmark

OPEN ACCESS

Edited by:

Galila Agam,
Ben-Gurion University of the Negev,
Israel

Reviewed by:

Kah-Leong Lim,
National University of Singapore,
Singapore
Gunnar P. H. Dietz,
Gesellschaft für Wissenschaftliche
Datenverarbeitung (MPG), Germany
Edgar Richard Kramer,
Plymouth University, United Kingdom

*Correspondence:

Francesco Cecconi
cecconi@cancer.dk
Flavie Strappazzon
f.strappazzon@hsantalucia.it

Received: 08 November 2017

Accepted: 20 March 2018

Published: 18 April 2018

Citation:

Di Rita A, D'Acunzo P, Simula L,
Campello S, Strappazzon F
and Cecconi F
(2018) AMBRA1-Mediated
Mitophagy Counteracts Oxidative
Stress and Apoptosis Induced by
Neurotoxicity in Human
Neuroblastoma SH-SY5Y Cells.
Front. Cell. Neurosci. 12:92.
doi: 10.3389/fncel.2018.00092

Therapeutic strategies are needed to protect dopaminergic neurons in Parkinson's disease (PD) patients. Oxidative stress caused by dopamine may play an important role in PD pathogenesis. Selective autophagy of mitochondria (mitophagy), mainly regulated by PINK1 and PARKIN, plays an important role in the maintenance of cell homeostasis. Mutations in those genes cause accumulation of damaged mitochondria, leading to nigral degeneration and early-onset PD. AMBRA1^{ActA} is a fusion protein specifically expressed at the mitochondria, and whose expression has been shown to induce a powerful mitophagy in mammalian cells. Most importantly, the pro-autophagy factor AMBRA1 is sufficient to restore mitophagy in fibroblasts of PD patients carrying PINK1 and PARKIN mutations. In this study, we investigated the potential neuroprotective effect of AMBRA1-induced mitophagy against 6-hydroxydopamine (6-OHDA)- and rotenone-induced cell death in human neuroblastoma SH-SY5Y cells. We demonstrated that AMBRA1^{ActA} overexpression was sufficient to induce mitochondrial clearance in SH-SY5Y cells. We found that apoptosis induced by 6-OHDA and rotenone was reversed by AMBRA1-induced mitophagy. Finally, transfection of SH-SY5Y cells with a vector encoding AMBRA1^{ActA} significantly reduced 6-OHDA and rotenone-induced generation of reactive oxygen species (ROS). Altogether, our results indicate that AMBRA1^{ActA} is able to induce mitophagy in SH-SY5Y cells in order to suppress oxidative stress and apoptosis induced by both 6-OHDA and rotenone. These results strongly suggest that AMBRA1 may have promising neuroprotective properties with an important role in limiting ROS-induced dopaminergic cell death, and the utmost potential to prevent PD or other neurodegenerative diseases associated with mitochondrial oxidative stress.

Keywords: cell death, oxidative stress, *in vitro* models, Parkinson's disease, mitophagy

INTRODUCTION

Parkinson's disease (PD) is a chronic and severe neurodegenerative disorder characterized by a progressive and selective death of dopaminergic neurons in the substantia nigra. The cellular loss (among 50%–70%) in the ventral area of the substantia nigra pars compacta is the main pathological hallmark of PD. Although Parkinsonism is usually a sporadic disease, there is also a familial component related to a growing number of single gene mutations. Among these, mutations in mitochondrial genes encoding PINK1, PARKIN and DJ-1 proteins promote autosomal recessive PD. Although the exact causes defining PD are largely unknown, mitochondrial oxidative stress and accumulated dysfunctional mitochondria are critical factors in the disease onset. The clearance of dysfunctional mitochondria can be regulated by a selective form of autophagy, known as mitophagy (Lemasters, 2005). Mitophagy is a self-degradative process that allows the elimination of ubiquitin-targeted mitochondria through lysosomal digestion. Both PINK1 and PARKIN are key factors in mitophagy induction: PINK1 is a Ser-Thr kinase that mediates the phospho-ubiquitin signal, thus recruiting the E3 ubiquitin ligase PARKIN at the mitochondria. Once at the mitochondria, PARKIN amplifies the ubiquitin signal on the mitochondrial surface, this leading to their recruitment into the autophagosome (Lazarou et al., 2015). We have previously demonstrated that a mitochondria-targeted fusion protein, AMBRA1^{ActA}, is a novel powerful inducer of mitophagy in mammalian cells (Strappazzon et al., 2015). Most importantly, we demonstrated that AMBRA1 restores mitophagy in mouse embryonic fibroblasts from *PINK1*^{-/-} mice, but also in fibroblasts from PD patients, in which PINK1 and PARKIN were mutated; altogether, these findings highlighted AMBRA1 as an alternative mediator of mitophagy to maintain mitochondrial homeostasis in PINK1-PARKIN-related PD (Strappazzon et al., 2015). In the PD context, oxidative stress is widely considered to be a key factor in both familial and sporadic forms of the disease (Sanders et al., 2014). It results from an imbalance of pro-oxidants/anti-oxidants homeostasis that leads to an abnormal production of reactive oxygen species (ROS), whose overproduction generates damage of both neurons and astrocytes (Lin and Beal, 2006).

In this study, we investigated the effect of AMBRA1^{ActA} protein in two oxidative stress models, evoked by disruption of the mitochondrial activity induced by: (1) blockade of mitochondrial complexes I and IV by using the pro-oxidant derivate of dopamine, 6-hydroxydopamine (6-OHDA; Glinka et al., 1997); or (2) blockade of mitochondrial complex I by using rotenone, a pesticide that has been associated with increased risk for PD (Li et al., 2003; Chin-Chan et al., 2015) in dopaminergic neural SH-SY5Y cells (Van Humbeeck et al., 2011). We further show that AMBRA1^{ActA} expression is sufficient to induce mitophagy also in SH-SY5Y cells. Moreover, the induction of mitophagy preserved cells from apoptosis induced by 6-OHDA and rotenone. Indeed, we observed an increase of cell viability in cells positive for AMBRA1^{ActA}, associated with a reduction of PARP-1 cleavage (caspase-3 substrate) and a number of pyknotic

nuclei. Finally, transfection of SH-SY5Y cells with a vector encoding AMBRA1^{ActA} significantly reduced 6-OHDA- and rotenone-induced generation of ROS. Our results thus indicate that AMBRA1^{ActA} is able to induce mitophagy in SH-SY5Y cells to suppress oxidative stress and apoptosis induced by 6-OHDA and rotenone. This evidence proves that AMBRA1^{ActA} may represent a novel molecular tool that could be used to induce mitophagy, in order to prevent accumulation of damaged mitochondria and neurodegeneration in PD.

MATERIALS AND METHODS

Cell Culture

Human neuroblastoma SH-SY5Y cells were cultured in Dulbecco's modified Eagle's medium (DMEM, GIBCO) supplemented with 10% FBS (GIBCO), at 37°C in a humidified atmosphere of 5% CO₂.

Reagents

3-(4,5-dimethylthiazol-2-yl)-5-(3-carboxymethoxyphenyl)-2-(4-sulfophenyl)-2H-tetrazolium (MTS) was purchased from Promega. 6-hydroxydopamine (6-OHDA), rotenone, the lysosome inhibitor NH₄Cl and the Carbonyl cyanide 4-(trifluoromethoxy)phenylhydrazone (FCCP) were purchased from Sigma Aldrich.

Transient Transfection and Plasmids

Human neuroblastoma SH-SY5Y cells were transfected using TransIT-X2[®] Dynamic Delivery System (MIR 6003, Mirus) according to the standard protocol. The Myc-AMBRA1^{ActA} plasmid was cloned as described in Strappazzon et al. (2015). The Mito-DsRED construct encodes for human Cox8A mitochondria signal peptide which is fused with wild-type-DsRED in PcDNA3 vector (Invitrogen). The Mito-DsRED-AMBRA1^{ActA} is a bidirectional vector encoding for both Mito-DsRED and AMBRA1^{ActA}. For small interfering RNA (siRNA)-mediated knockdown of AMBRA1, siRNA against AMBRA1 or siRNA-Ctr (Invitrogen), were transiently transfected using Lipofectamine 2000, according to the manufacturer's protocol. ShRNA PARKIN or shRNA Control were transfected in SH-SY5Y cells using Turbofect Transfection reagent (Thermo Fisher Scientific, R0531), according to the standard instructions.

Antibodies

We use the following antibodies: anti-Myc (Santa Cruz Biotechnology, 9E10), anti-ACTIN (Sigma-Aldrich, A2228), anti-PARP (Cell Signaling, 9542), anti-MnSOD (Enzo Life Sciences, 110F), anti-TOM20 (Santa Cruz Biotechnology, sc-FL145) and anti-HSP60 (Santa Cruz Biotechnology, sc-13966).

Immunoblotting Analysis

SH-SY5Y cells were lysed in RIPA buffer (50 mM Tris HCl pH 7.4, 1% Triton X-100, 0.5% NP40, 150 mM NaCl, 10% Glycerol, 2.5% Sodium Deoxycholate) plus protease inhibitor cocktail (Sigma Aldrich, S7920) and analyzed by SDS/PAGE and Western blot according to standard protocols.

Immunofluorescence Analysis

SH-SY5Y cells were fixed in 4% of paraformaldehyde and permeabilized with 0.4% Triton X-100. Fixed cells were blocked in 2% normal goat serum (Sigma-Aldrich, G9023) in PBS and incubated with primary antibody over night. Cells were then washed with PBS 3×5 min and incubated with secondary antibody for 1 h. After 3×5 min of PBS washing, coverslips were mounted on glass slides and finally analyzed by confocal microscopy analysis under Zeiss LSM 700 100 \times oil-immersion objective (CLSM700; Jena, Germany), Zoe Fluorescence cell imager (Biorad, 1450031) or Ultraview Vox (Perkin Elmer).

Confocal Image Analysis

The TOM20 and HSP60 intensities and the area occupied by the signal per cell, in conditions indicated in the text, were calculated through the NIH ImageJ software in 10 different fields of three independent experiments. Colocalization measurements were made through the JACOP plugin (Bolte and Cordelières, 2006) of the NIH ImageJ software. M1 manders colocalization coefficients (MCC) of mitochondria overlapping LC3, p62 and Ubiquitin were calculated on single cells in 10 different fields of three independent experiments upon overexpression of either Mito-DsRED or Mito-DsRED-AMBRA1^{ActA} to highlight wild type mitochondria and mitaaggresomes, respectively. Thresholds were not set by the operator, but automatically calculated by the software to avoid biased data. All microscope quantifications shown in the article were performed by a blind approach.

Determination of Cell Viability

Cell vitality was estimated by the MTS assay or by counting the number of condensed or fragmented nuclei (DAPI staining). For the MTS assay, the cytotoxicity of 6-OHDA or rotenone on SH-SY5Y cells was determined using the CellTiter96 Aqueous One Solution Assay (Promega, Madison, WI, USA). Indeed, SH-SY5Y cells were transfected using TransIT-X2[®] Dynamic Delivery System (MIR 6003, Mirus). Six hours after transfection, cells were split into 96-well dishes and treated with 6-OHDA (100 μ M) or rotenone (10 μ M). After 18 h, the CellTiter 96 Aqueous One Solution Reagent was added to each well. The plate was then read at 490 nm in a Victor³ plate reader at 37°C (PerkinElmer Life and Analytical Sciences, Shelton, CT, USA). For pyknotic nuclei counting, Mito-DsRED or Mito-DsRED-AMBRA1^{ActA} transfected cells were fixed in 4% paraformaldehyde (Merck Millipore, 104005) in PBS (GIBCO, BE17-512F) for 10 min at 37°C and stained with DAPI (Sigma Aldrich, D9542) in PBS for 15 min at room temperature. Cells were washed three times with PBS, then mounted and observed under Zoe microscope. For each condition, random images were captured and cell viability was then scored on the basis of nuclear morphology: cells containing condensed or fragmented nuclei were counted as dying or dead cells. All microscope quantifications shown in the article were performed by a blind approach.

Protein Oxidation Assay

SH-SY5Y cells were transfected and treated with 6-OHDA or rotenone, as described above. The DPN-derivatized proteins

containing carbonyl groups were evaluated by using the OxyBlot Protein Oxidation Detection Kit (Millipore S7150), according to the standard protocol.

Measure of $\Delta\psi_m$ and Superoxide Production

Cells were transfected with the bicistronic vector Tween-GFP-AMBRA1^{ActA} or Twen-GFP alone and subsequently treated or not with 100 μ M 6-OHDA and 10 μ M rotenone 6 h post transfection. After 18 h of treatment, cells were incubated with 5 nM Tetramethylrhodamine methyl ester (TMRM, Molecular Probes) in 10% FBS+DMEM for 30 min at 37°C or with 5 μ M MitoSOX Red reagent (Molecular Probes) in 10% FBS+DMEM for 10 min at 37°C in a 5% CO₂ incubator. Finally, cells were analyzed through the flow cytometer BD Accuri C6. TMRM and MitoSOX Red fluorescence intensities were measured in GFP positive cells and read in the FL3 channel upon stimulation at 488 nm.

Statistical Analysis

All statistical analysis were performed and graphed using GraphPad Prism 6. Comparisons between two groups were analyzed using Student's *T*-test. Three or more groups comparisons were performed with one-way ANOVA. Significance is defined as **P* < 0.05.

RESULTS

High Levels of Mitochondria-Targeted AMBRA1 (AMBRA1^{ActA}) in Human Neuroblastoma SH-SY5Y Cells Induce Perinuclear Distribution of Mitochondria, Accompanied by Mitochondria Clearance

To manipulate the dosage of the AMBRA1 mitochondrial pool in order to induce massive mitophagy, we previously generated a fusion construct encoding Myc-AMBRA1 and a sequence from the *Listeria monocytogenes* Actin assembly-inducing protein (ActA), that can target the molecule to the outer mitochondrial membrane (Strappazzon et al., 2015). In this case, we wanted to check for the localization of the AMBRA1^{ActA} protein and for a putative mitochondrial clearance in SH-SY5Y cells. To this end, we performed a confocal microscopy analysis in SH-SY5Y cells transfected with a vector encoding PcDNA3 as a control or Myc-AMBRA1^{ActA}. We then fixed cells and stained their mitochondria network by using an antibody directed against TOM20. We found that AMBRA1^{ActA} surrounds aggregated mitochondria. Most importantly, we observed that AMBRA1^{ActA} overexpression induces *per se* a strong relocalization of the mitochondrial network around the perinuclear envelope, thus leading to the formation of structures similar to those previously described as “mito-aggresomes” (Lee et al., 2010; **Figure 1A**). The reduction of both the area of mitochondria and the TOM20 signal intensity in AMBRA1^{ActA}-transfected cells confirmed that AMBRA1^{ActA} stimulates massive mitophagy also in SH-SY5Y cells. Moreover, in order to ascertain that mito-aggresome structures were

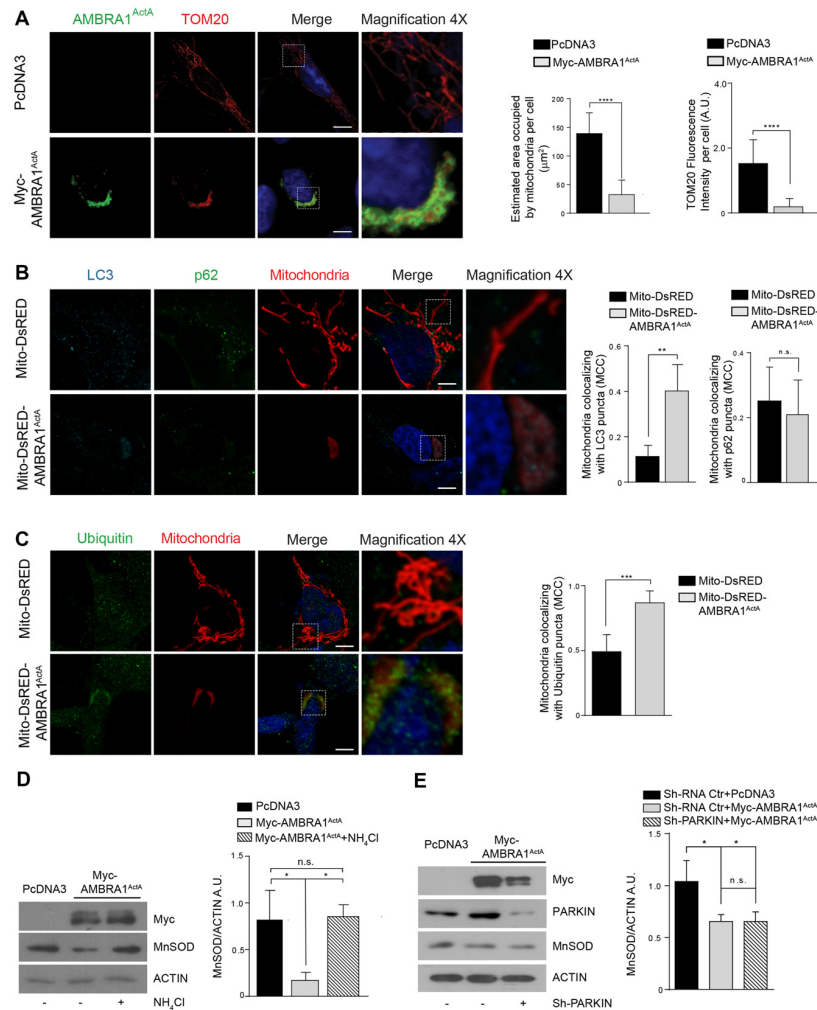


FIGURE 1 | **AMBRA1^{ActA}** induces mitophagy in SH-SY5Y cell line. **(A)** SH-SY5Y cells transfected with PcDNA3 or Myc-AMBRA1^{ActA} were immunostained with anti-Myc (green) and anti-TOM20 (red) antibodies. Scale bar, 10 μm. The upper and lower panels on the right are two magnifications (4×) of the mitochondria in transfected cells. The graphs show the estimated area occupied by mitochondria per cell and the TOM20 fluorescence intensity per cell (± S.D.). *n* = 3 independent experiments. Statistical analysis was performed using Student's *T*-test. *****P* < 0.0001. **(B)** SH-SY5Y cells were transfected with vectors encoding Mito-DsRED or Mito-DsRED-AMBRA1^{ActA} in order to mark wild type mitochondria and mitoaggregates, respectively. Subsequently, cells were fixed and immunostained for the autophagosome marker LC3 (blue), the mitophagy receptor p62 (green) and counterstained with DAPI (blue). The graphs summarize the quantification in single cells of the manders colocalization coefficient (MCC) of mitochondria on the LC3 signal (left) or p62 signal (right). The upper and lower panels on the right are two magnifications (4×) of the mitochondria in transfected cells. Ten random fields of three independent experiments were considered. Data are presented as Mean ± S.D. Statistical test: student *T*-test. Scale bar: 5 μm. ***P* < 0.01; n.s. not statistically significant. **(C)** SH-SY5Y cells transfected as described in **(B)**, were immunostained for Ubiquitin (green) and counterstained with DAPI (blue). The graph shows the quantification in single cells of the MCC of mitochondria on the Ub signal. The upper and lower panels on the right are two magnifications (4×) of the mitochondria in transfected cells. Ten random fields of three independent experiments were considered. Data are presented as Mean ± S.D. Statistical test: student *T*-test. Scale bar: 5 μm. ****P* < 0.001. **(D)** PcDNA3 or Myc-AMBRA1^{ActA} transfected cells, treated with the lysosome inhibitor NH₄Cl, were analyzed by western blotting analysis for the indicated antibody. The graph shows the MnSOD/ACTIN ratio. Statistical analysis was performed using One-way ANOVA. **P* < 0.05; n.s. not statistically significant. *n* = 3 independent experiments. **(E)** SH-SY5Y cells were transfected with Sh-PARKIN or Sh-RNA Ctr in combination with a vector coding for Myc-AMBRA1^{ActA}. Total lysates were subjected to western blotting analysis using anti-MnSOD (to analyze mitochondrial clearance), anti-Myc or anti-PARKIN to assess Myc-AMBRA1^{ActA} or Sh-PARKIN transfections, respectively. The quantification represents the MnSOD/ACTIN ratio. Statistical analysis was performed using One-way ANOVA. **P* < 0.05; n.s. not statistically significant. *n* = 3 independent experiments.

specific for AMBRA1 mitochondrial localization coupled with a reduction of mitochondrial marker levels, we performed a confocal microscope analysis, in which SH-SY5Y cells were transfected with PcDNA3, Myc-AMBRA1^{ActA}, Venus^{ActA}, a plasmid encoding the ActA sequence fused with the fluorescent

reporter protein Venus (Nagai et al., 2002), and with the wild-type form of AMBRA1 lacking the ActA sequence. Further, the AMBRA1^{ActA}-LIRAA plasmid, encoding an AMBRA1^{ActA} isoform mutated in its LIR motif and less active in mitophagy (due to a reduction of LC3B binding), was used to complete this

analysis (Strappazon et al., 2015; **Supplementary Figure S1**). We next analyzed whether AMBRA1^{ActA} expression was able to induce mitophagy, as we already described in HEK293, HeLa and MEF cells (Strappazon et al., 2015). To this end, SH-SY5Y cells were transfected with a bicistronic vector coding for Mito-DsRED alone (red staining of mitochondria) or encoding both Mito-DsRED and AMBRA1^{ActA} (Mito-DsRED-AMBRA1^{ActA}) for 24 h; first, we analyzed mitophagy induction by looking to well-known markers of autophagosome formation, such as LC3 and p62 (Kabeya et al., 2000; Pankiv et al., 2007). Indeed, we observed an increase in the accumulation of LC3 dots, but not p62, in Mito-DsRED-AMBRA1^{ActA}-positive mitochondria, suggesting that AMBRA1^{ActA} promotes an LC3-dependent, but p62-independent mitophagy in SHSY5Y cells (**Figure 1B**). In addition, we checked for ubiquitin staining and found that mito-aggregates are positive for Ubiquitin (**Figure 1C**). These data proved that AMBRA1^{ActA} induces mito-aggregates positive for LC3 and Ubiquitin, but negative for p62 also in SHSY5Y cells. We next confirmed that AMBRA1^{ActA} was able to induce mitophagy in these cells, by using a biochemical approach. Indeed, we checked the level of MnSOD, a mitochondrial protein, following AMBRA1^{ActA} transfection in SH-SY5Y cells in the presence or absence of a lysosomal inhibitor, ammonium chloride (NH₄Cl), known to prevent the autophagy flux by inhibiting the fusion of autophagosomes with lysosomes (Hart and Young, 1991). As expected, AMBRA1^{ActA} was able to induce a strong reduction of MnSOD protein levels. In addition, the NH₄Cl treatment resulted in a significantly higher level of mitochondrial protein accumulation in AMBRA1^{ActA}-positive cells, hence indicating that autophagosome formation induced by AMBRA1^{ActA} overexpression is responsible for MnSOD degradation by the lysosome (**Figure 1D**). The ability of AMBRA1^{ActA} to mediate mitophagy in these cells was confirmed also by looking at another mitochondrial marker, COXIV (data not shown). Finally, we checked in SH-SY5Y cells downregulated for PARKIN expression whether AMBRA1^{ActA} was able to induce mitophagy. As shown in **Figure 1E**, AMBRA1^{ActA} induces mitophagy also in PARKIN-deficient SH-SY5Y cells.

Altogether, these observations demonstrate that AMBRA1^{ActA} transfection triggers *per se* a fully functional and massive mitophagy in SH-SY5Y cells, which is independent of both PINK1/PARKIN and p62, but dependent of LC3 and Ubiquitin.

AMBRA1^{ActA}-Induced Mitophagy Protects SH-SY5Y Cells From Neurotoxicity Induced by 6-OHDA

We have previously demonstrated that AMBRA1-induced mitophagy is able to trigger mitophagy in fibroblasts from PD patients bearing PINK1 or PARKIN mutations, this highlighting the fact that AMBRA1 can serve as an alternative mediator of mitophagy to maintain mitochondrial turnover in PINK1/PARKIN-related PD. Thus, since mitophagy plays an important role in the quality control of mitochondria and in the maintenance of cell homeostasis, we hypothesized

that AMBRA1^{ActA}-induced mitophagy could be protective in well-known *in vitro* models of PD. We thus decided to test the potential effect of AMBRA1^{ActA} in SH-SY5Y cells treated with 6-OHDA (100 μM, 18 h). In this context, neurotoxicity is induced by blocking activities of mitochondria complexes I and IV (Glinka et al., 1997). In an MTS assay (3-(4,5-dimethylthiazol-2-yl)-5-(3-carboxymethoxyphenyl)-2-(4-sulfophenyl)-2H-tetrazolium) we observed, as expected, a reduction in the metabolic activity of PcDNA3-positive cells following 6-OHDA, when compared to PcDNA3-positive control cells, treated only with the vehicle. By contrast, MTS metabolism was improved in AMBRA1^{ActA}-positive cells (**Figure 2A**). These findings suggest that AMBRA1^{ActA}-positive cells are more resistant to neurotoxicity induced by 6-OHDA. To confirm this result, SH-SY5Y cells were transfected with Venus^{ActA} or Myc-AMBRA1^{ActA} or Myc-AMBRA1^{ActA}LIRAA for 24 h; cell viability was then measured by means of DAPI nuclear staining, following 6-OHDA treatment. After 6-OHDA treatment, about 80% of Venus^{ActA} or 64% of Myc-AMBRA1^{ActA}LIRAA positive cells exhibited condensed or fragmented nuclei, while only 40% of Myc-AMBRA1^{ActA}-positive cells showed these apoptotic features (**Figure 2B**). Therefore, high levels of AMBRA1 at the mitochondria improve the survival of SH-SY5Y cells following 6-OHDA treatment.

To strengthen our finding we next checked, by western-blot analysis, the occurrence of poly (ADP-ribose) polymerase-1 (PARP-1) cleavage, a well-known substrate of caspase-3, in cells over-expressing PcDNA3 or Myc-AMBRA1^{ActA} upon 6-OHDA treatment. As shown in **Figure 2C**, the cleavage of PARP-1 is reduced in cells overexpressing Myc-AMBRA1^{ActA} compared to cells expressing the control vector (**Figure 2C**). These results strongly support the existence of a protective effect of AMBRA1^{ActA} against neurotoxicity induced by 6-OHDA treatment in a human neuroblastoma cell line. Since Van Humbeeck et al. (2011) demonstrated that downregulation of AMBRA1 inhibits mitophagy in SH-SY5Y cells, we decided to check whether down-regulation of AMBRA1 expression by RNA interference (siRNA) could lead to a stronger apoptosis in 6-OHDA-treated cells. As shown in **Figure 2D**, downregulation of AMBRA1 increases apoptosis, as indicated by increased PARP cleavage, when compared to siRNA-Ctr positive cells. Moreover, the level of the mitochondrial marker MnSOD does not decrease in a toxic context affecting mitochondria in the absence of AMBRA1 (**Supplementary Figure S2A**). These results suggest that AMBRA1 plays pro-survival functions in SH-SY5Y cells following 6-OHDA treatment.

These results indicate that AMBRA1^{ActA} confers protection from cell death-induced by 6-OHDA thanks to its mitophagic activity.

AMBRA1^{ActA}-Induced Mitophagy Protects SH-SY5Y Cells From Neurotoxicity Induced by Rotenone

To ascertain that AMBRA1^{ActA} expression was also protective in another ROS-induced dopaminergic cell death model system,

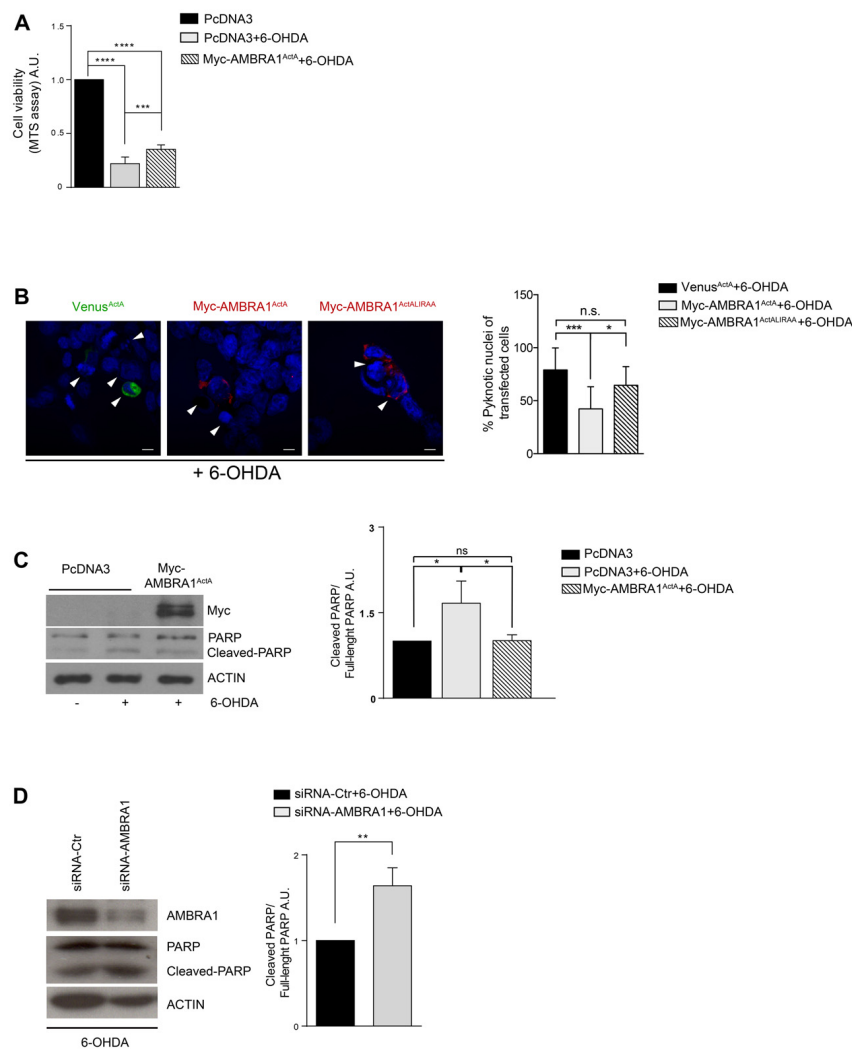


FIGURE 2 | AMBRA1^{ActA} improves vitality of SH-SY5Y cells treated with 6-hydroxydopamine (6-OHDA). **(A)** SH-SY5Y cells were transfected with vectors coding for PcDNA3 or for Myc-AMBRA1^{ActA} and 6 h after transfection, cells were treated with 6-OHDA (100 μ M). Viable cells were estimated using the MTS assay. Results are expressed as A.U. Each point represents the mean (\pm SD) of triplicate wells from three independent experiments. Statistical analysis was performed using One-way ANOVA. **** P < 0.0001; *** P < 0.001. **(B)** SH-SY5Y cells were transfected with vectors encoding Venus^{ActA} or Myc-AMBRA1^{ActA} or Myc-AMBRA1^{ActALIRAA} plasmids for 24 h. Six hours after transfection, cells were treated with 6-OHDA (100 μ M). Cells were then fixed and stained with DAPI. Cells with condensed or fragmented nuclei were scored as pyknotic (arrows indicate pyknotic nuclei). The graph shows the percentage of pyknotic nuclei in transfected cells. For each condition, transfected cells were counted in random fields from three independent experiments. Statistical analysis was performed using One-way ANOVA. *** P < 0.001; * P < 0.05; n.s. not statistically significant. **(C)** SH-SY5Y cells were transfected with vectors encoding PcDNA3 or Myc-AMBRA1^{ActA} for 24 h. Six hours after transfection, cells were treated with 6-OHDA (100 μ M). After proteins extraction, we performed a western blot analysis using antibodies directed against AMBRA1 (Myc), PARP and ACTIN. The graph shows the cleaved PARP/Full-length PARP ratio resulting as the mean of three independent experiments (\pm S.D). n = 3. Statistical analysis was performed using One-way ANOVA, * P < 0.05. **(D)** SHSY5Y cells transfected with a siRNA-Ctr or siRNA-AMBRA1 were treated with 6-OHDA for 18 h. Total lysates were immunoblotted for AMBRA1, PARP and ACTIN antibodies. Statistical analysis was performed using One-way ANOVA. ** P < 0.01. n = 3 independent experiments.

we decided to test the effect of AMBRA1^{ActA} in SH-SY5Y cells treated with another “well-known” dopaminergic neurotoxin, rotenone. In this context, neurotoxicity is induced by blocking activity of mitochondria complex I (Glinka et al., 1997). In analogy with 6-OHDA treatment, by using the MTS assay, we observed a reduction in metabolic activity of PcDNA3-positive cells following rotenone, when compared with PcDNA3-positive controls cells treated only with the vehicle. By contrast, MTS

metabolism was slightly improved in AMBRA1^{ActA}-positive cells (Figure 3A). These findings confirm that AMBRA1^{ActA}-positive cells are in general more resistant to neurotoxicity induced by different agents, in this case rotenone. In order to corroborate our results, we transfected SH-SY5Y cells with Venus^{ActA} or Myc-AMBRA1^{ActA} or Myc-AMBRA1^{ActALIRAA} plasmids for 24 h; cell viability was then evaluated by using DAPI nuclear staining upon rotenone treatment. As shown in

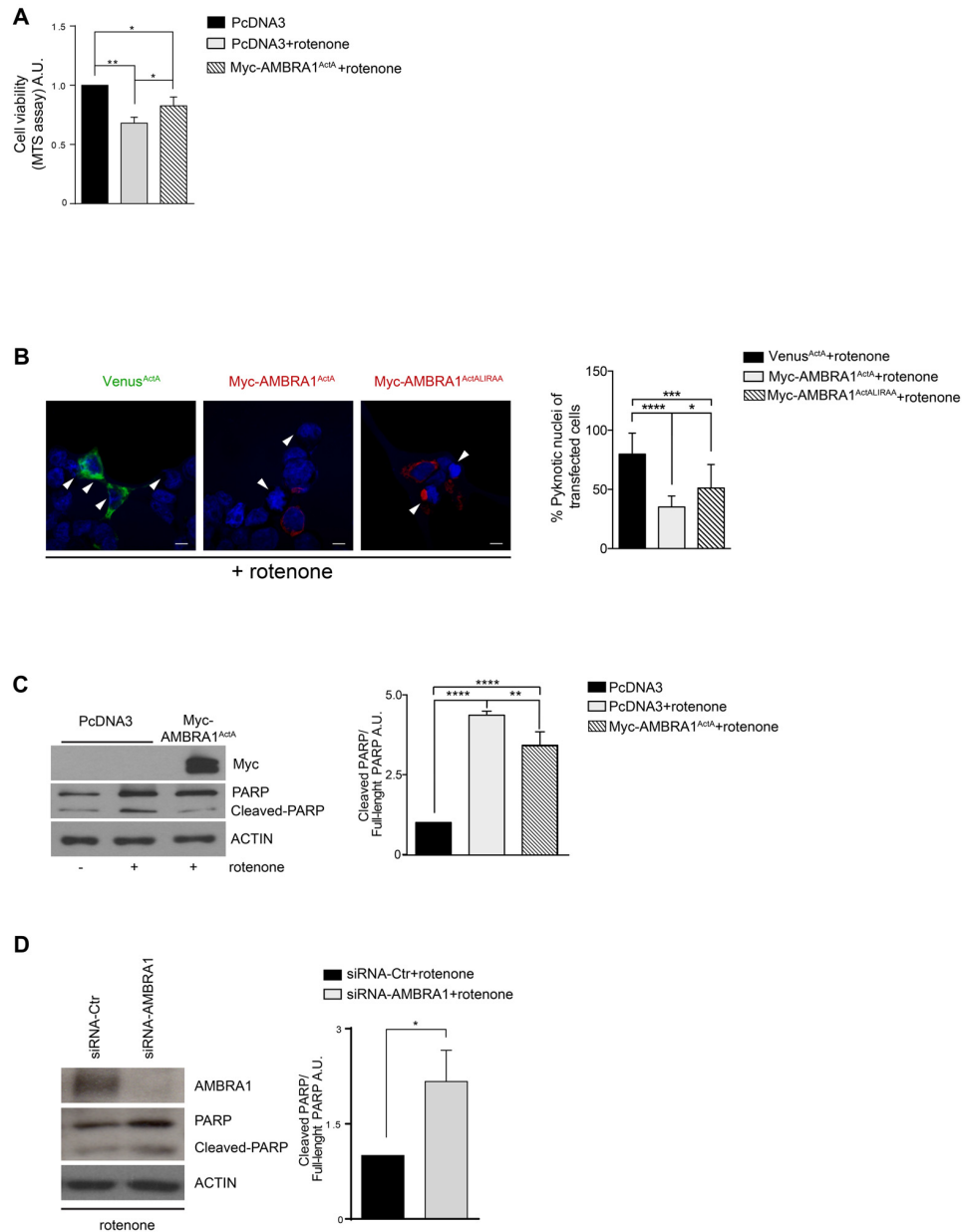


FIGURE 3 | AMBRA1^{ActA} improves vitality of SH-SY5Y cells treated with rotenone. **(A)** SH-SY5Y cells were transfected with vectors coding for PcDNA3 or for Myc-AMBRA1^{ActA} and then treated with rotenone (10 μ M). Viable cells were estimated using the MTS assay. Results are expressed as arbitrary unit (A.U.). Each point represents the mean (\pm SD) of triplicate wells from three independent experiments. Statistical analysis was performed using One-way ANOVA. $**P < 0.01$. $*P < 0.05$. **(B)** SH-SY5Y cells were transfected with vectors encoding Venus-ActA or Myc-AMBRA1^{ActA} or Myc-AMBRA1^{ActA}LIRAA for 24 h. Six hours after transfection, cells were treated with rotenone (10 μ M). After DAPI staining, cells with condensed or fragmented nuclei were scored as pyknotic (arrows indicate pyknotic nuclei). The graph shows the percentage of pyknotic nuclei in transfected cells (\pm S.D.). For each condition, transfected cells were counted in random fields from three independent experiments. Statistical analysis was performed using One-way ANOVA. $****P < 0.0001$; $***P < 0.001$; $*P < 0.05$. **(C)** SH-SY5Y cells were transfected with vectors encoding PcDNA3 or Myc-AMBRA1^{ActA} for 24 h. Six hours after transfection, cells were treated with rotenone (10 μ M). After extraction of proteins, we performed a western blot analysis using antibodies directed against AMBRA1 (Myc), PARP/Cleaved-PARP and ACTIN. The graph shows the cleaved PARP/full-length PARP ratio, resulting as the mean of three independent experiments (\pm S.D.). $n = 3$. One-way ANOVA, $*P < 0.05$. **(D)** SH-SY5Y cells transfected with a siRNA-Ctr or siRNA-AMBRA1 were treated with 6-OHDA for 18 h. Total lysates were subjected to immunoblotting for AMBRA1, PARP and ACTIN antibodies. The graph represents the cleaved PARP/Full-length PARP ratio (\pm S.D.). Statistical analysis was performed using One-way ANOVA. $*P < 0.05$. $n = 3$ independent experiments.

Figure 3B, AMBRA1^{ActA} expression is sufficient to robustly reduce the number of pyknotic nuclei in transfected individual

cells. Therefore, high levels of AMBRA1 at the mitochondria with a marked mitophagy activity (AMBRA1^{ActA}) greatly improve

survival of SH-SY5Y cells, following both 6-OHDA and rotenone treatments.

Again, by western-blot analysis upon rotenone treatment, we observed an inhibition of PARP-1 cleavage in cells over-expressing Myc-AMBRA1^{ActA} compared to PcDNA3-positive cells (Figure 3C). Altogether, these results strongly support a protective role for AMBRA1^{ActA} in the classical toxic *in vitro* model of PD induced by rotenone. We also checked in this context whether down-regulation of AMBRA1 expression using siRNA was able to trigger a stronger apoptosis following rotenone treatment. As shown in Figure 3D, downregulation of AMBRA1 increases apoptosis, as indicated by increased PARP cleavage. These results suggest that, also upon rotenone treatment of SH-SY5Y cells, endogenous AMBRA1 is involved in a pro-survival pathway. Moreover, SH-SY5Y cells in which AMBRA1 was downregulated through siRNA, were treated with rotenone in order to analyze the level of the mitochondrial marker MnSOD. In line with the 6-OHDA treatment, we observed no decrease in a toxic context affecting mitochondria in the absence of AMBRA1 (Supplementary Figure S2B).

These results indicate that AMBRA1^{ActA} confers protection from cell death-induced by rotenone thanks to its mitophagic activity.

AMBRA1^{ActA}-Induced Mitophagy Protects SH-SY5Y Cells From Oxidative Stress Generated by Both 6-OHDA and Rotenone

Although the exact molecular etiology of PD is largely unclear, mitochondrial oxidative stress and accumulated dysfunctional mitochondria are critical factors in the onset of the disease. Thus, we hypothesized that AMBRA1^{ActA}-induced mitophagy was able to also protect neuroblastoma cells from neurotoxicity, this being probably due to an anti-oxidative effect. In fact, accumulation of ROS by mitochondria can be reduced by activation of mitochondrial clearance. To test this hypothesis, we transfected SH-SY5Y cells with a vector encoding PcDNA3 or Myc-AMBRA1^{ActA}, and treated them with 6-OHDA (100 μ M) or rotenone (10 μ M) for 18 h. Oxidative modification of proteins by oxygen-free radicals and other reactive species occurs in physiological and pathological processes. As a consequence of the modification, carbonyl groups are introduced into protein side chains by a site-specific mechanism. We thus decided to immunodetect these carbonyl groups, which are hallmarks of protein oxidation status upon 6-OHDA or rotenone treatment in cells overexpressing Myc-AMBRA1^{ActA} or PcDNA3 as a control. As shown in Figures 4A,B, Myc-AMBRA1^{ActA} expression is sufficient to reduce protein carbonylation, upon 6-OHDA or rotenone treatments. To strengthen these results, we analyzed the ROS status through the fluorogenic dye MitoSOX Red coupled to flow cytometry analysis. SH-SY5Y cells were transfected with a bicistronic construct (Tween-GFP-AMBRA1^{ActA}) encoding AMBRA1^{ActA} and a cytosolic GFP, or the GFP alone, in order to select cells positive to transfection. Cells were then treated with 6-OHDA and rotenone, as indicated above. As shown in Figures 4C,D, 6-OHDA and rotenone strongly stimulate

ROS production, an effect attenuated upon AMBRA1^{ActA} overexpression.

These results indicate that AMBRA1^{ActA} expression reduces oxidative stress induction in SH-SY5Y cells, following induction of neurotoxicity. Next, since the formation of mitochondrial ROS (mtROS) is dependent on $\Delta\Psi_m$ (Korshunov et al., 1997), we checked for mitochondrial membrane status using Tetramethylrhodamine, methyl ester (TMRM) in AMBRA1^{ActA} positive cells, following 6-OHDA or rotenone treatments. As shown in Figure 4E, 6-OHDA or rotenone reduce the TMRM signal in control cells, thus confirming an alteration in the mitochondrial membrane potential. By contrast, as previously observed, we found that AMBRA1^{ActA} surrounds depolarized mitochondria and the 6-OHDA or rotenone treatment does not affect mitochondrial membrane potential in AMBRA1^{ActA}-transfected cells. Altogether, these data suggest that AMBRA1^{ActA} expression is sufficient to improve mitochondrial membrane status upon neurotoxin treatments.

DISCUSSION

Our previous study performed on mouse embryonic fibroblasts from *PINK1*^{-/-} mice or by using fibroblasts derived from PARKIN and PINK1-mutated PD patients provided evidence that AMBRA1 can mediate mitophagy in the absence of PARKIN or PINK1 activities (Strappazon et al., 2015). Here, primed by these findings, we decided to investigate the putative therapeutic potential of AMBRA1 to rescue mitochondrial dysfunction in two *in vitro* models of ROS-induced dopaminergic cell death.

Oxidative stress, which can be due to several genetic and environmental factors, is believed to be one of the major mediators of PD pathogenesis. The role of oxidative stress produced by dopamine for neuronal cell survival has been demonstrated in several works (Offen et al., 1996; Gilgun-Sherki et al., 2001). Interestingly, dysfunctional mitochondria are thought to be the predominant source of ROS (Jiang et al., 2016).

In this study, we first decided to mimic PD *in vitro*, by using 6-OHDA, the pro-oxidant derivate of dopamine widely used in ROS-induced dopaminergic cell death model systems. Indeed, 6-OHDA has been shown to increase protein oxidation (accumulation of carbonylated protein), and to increase both caspases-3/7 activity and nuclear fragmentation (Elkon et al., 2002; Hanrott et al., 2006). Interestingly, neurotoxicity of 6-OHDA is significantly attenuated by pre-incubation with catalase, this suggesting that hydrogen peroxide, at least in part, is responsible for cell death in this model. Here we report that AMBRA1^{ActA} expression is sufficient to induce functional mitophagy in neural dopaminergic SH-SY5Y cells. In addition, we found that cell metabolism was improved in the presence of AMBRA1^{ActA} and was associated to apoptosis reduction (reduction of PARP cleavage and occurrence of pyknotic nuclei), following 6-OHDA treatment.

We also investigated the putative beneficial role of AMBRA1^{ActA}-mediated mitophagy in a second model of

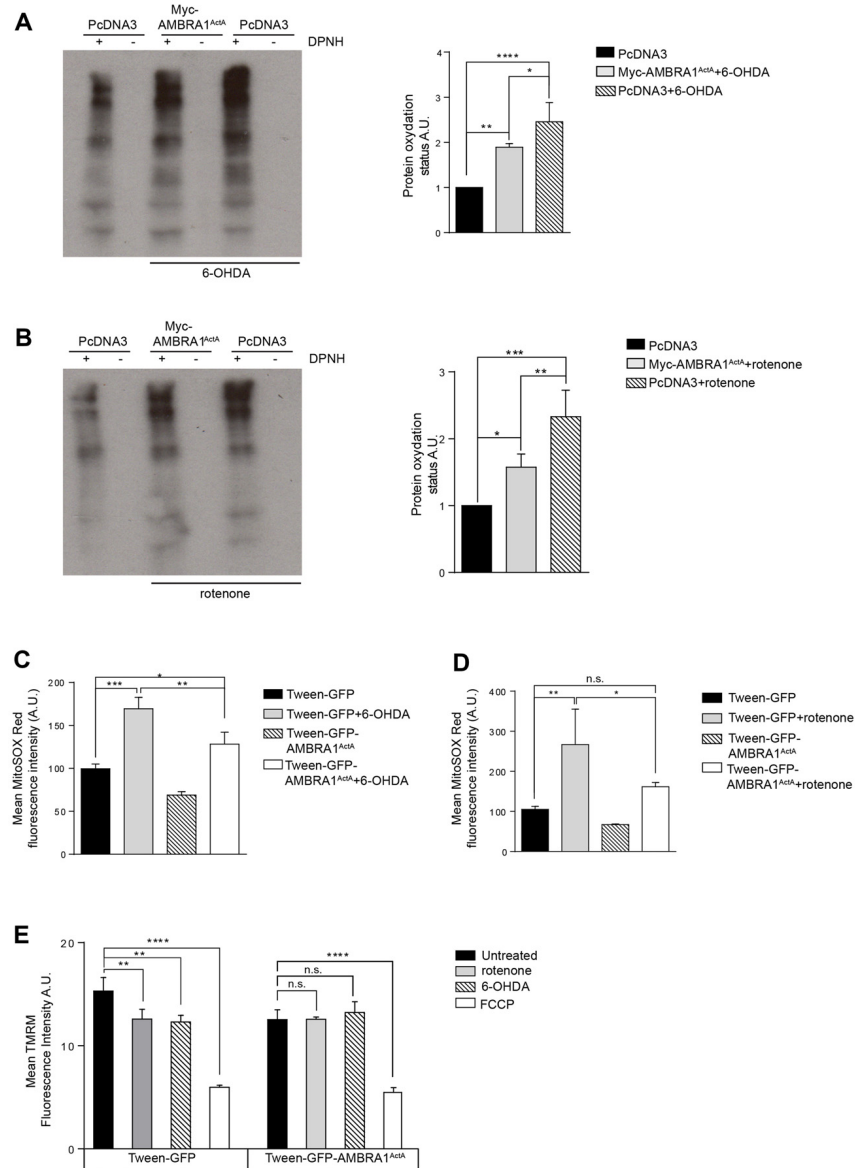


FIGURE 4 | AMBRA1^{ActA} reduces oxidative stress induced by 6-OHDA and rotenone treatments in SH-SY5Y cells. **(A)** Protein carbonylation analysis of SH-SY5Y cells transfected with vectors encoding PcDNA3 or Myc-AMBRA1^{ActA} for 24 h and treated or not with 6-OHDA. The graph showing protein oxidation status (A.U.) results as the mean of three independent experiments (\pm S.D.). Statistical analysis was performed using One-way ANOVA. **** $P < 0.0001$; ** $P < 0.01$; * $P < 0.05$. $n = 3$ independent experiments. **(B)** SH-SY5Y cells were transfected as indicated in **(A)** and treated or not with rotenone. The graph shows protein oxidation status (A.U.) and results as the mean of three independent experiments (\pm S.D.). Statistical analysis was performed using One-way ANOVA. *** $P < 0.001$; ** $P < 0.01$; * $P < 0.05$. $n = 3$ independent experiments. **(C)** SH-SY5Y cells were transfected with constructs encoding Tween-GFP or Tween-GFP-AMBRA1^{ActA} for 24 h and treated or not with 6-OHDA. Cells were subsequently stained with MitoSOX Red and analyzed by flow cytometry to measure the fluorescence intensity of the dye in GFP positive cells. Data are presented as Mean \pm S.D. of four independent experiments. Statistical test: One-way ANOVA. * $P < 0.05$; ** $P < 0.01$; *** $P < 0.001$. **(D)** SH-SY5Y cells were transfected with constructs encoding Tween-GFP or Tween-GFP-AMBRA1^{ActA} for 24 h and treated or not with rotenone. Cells were subsequently stained with MitoSOX Red and analyzed by flow cytometry to measure the fluorescence intensity of the dye in GFP positive cells. Data are presented as Mean \pm S.D. of four independent experiments. Statistical test: One-way ANOVA. * $P < 0.05$; ** $P < 0.01$; *** $P < 0.001$; n.s.: not statistically significant. **(E)** SH-SY5Y cells were transfected with a plasmid encoding Tween-GFP or Tween-GFP-AMBRA1^{ActA} and then treated or not with rotenone or 6-OHDA or FCCP. Cells were subsequently stained with 5 nM TMRM and analyzed by flow cytometry to measure the fluorescence intensity of the dye in GFP positive cells. Data are presented as Mean \pm S.D. of three independent experiments. Statistical test: One-way ANOVA. ** $P < 0.01$; **** $P < 0.0001$; n.s.: not statistically significant.

PD by using rotenone. Rotenone is, indeed, a commonly used pesticide, which has been associated with increased risk for PD (Chin-Chan et al., 2015). It is an inhibitor of mitochondrial

complex I (Degli Esposti et al., 1993) and it is believed to be a strong ROS producer (McLennan and Degli Esposti, 2000). Systemic chronic exposure of rats to rotenone causes a selective

degeneration of dopaminergic neurons in the substantia nigra (Betarbet et al., 2000; Sherer et al., 2003). *In vitro*, rotenone induces cytotoxicity via ROS-induced oxidative stress and mitochondria-mediated apoptosis involving p53, Bax/Bcl-2, and caspase-3 (Siddiqui et al., 2013). Again, by transfecting AMBRA1^{ActA} in SH-SY5Y cells treated with rotenone, we were able to delay apoptosis of human neuroblastoma cells.

These data are of the highest interest, since we were able to show that AMBRA1-mediated mitophagy is cell protective in two independent models of ROS-induced dopaminergic cell death (by 6-OHDA or rotenone). We thus here propose a model by which AMBRA1 expression at the mitochondria is sufficient to reduce ROS accumulation generated by neurotoxin (6-OHDA or rotenone) exposure. This protective effect is due to AMBRA1-mediated mitophagy that favors elimination of dysfunctional mitochondria, thus preventing cells from undergoing death. Indeed, our results strongly suggest that AMBRA1 is a promising target for limiting ROS production and toxin-induced cell death. Of note, it has been recently demonstrated that the mitochondria autophagy receptor Nip3-like protein X, named NIX [also known as BCL2/adenovirus E1B 19 kDa interacting protein 3-like (BNIP3L)] can restore mitophagy and mitochondrial function in fibroblasts from PINK1-PARKIN-mutated PD Patients (Koentjoro et al., 2017). Since NIX, similar to AMBRA1, induces alternative mitophagy (PINK1- and PARKIN-free), it would be of the highest interest to test in this context whether NIX-mediated mitophagy can rescue cell death following 6-OHDA or rotenone treatments in human neuroblastoma cell lines. Interestingly, AMBRA1 presents several common features with NIX such as: (1) a mitochondrial localization (Strappazzon et al., 2011); an LC3-Interacting Region (Strappazzon et al., 2015); a BH3-Like domain (Strappazzon et al., 2016). We could thus hypothesize that AMBRA1 and NIX work in synergy or by separate pathways that may compensate each other. Under physiological conditions, it has been demonstrated that NIX mediates mitophagy in erythrocytes. In particular, *Nix* knockout mice exhibit a reduced number of mature erythrocytes and show defects in mitochondrial clearance (Sandoval et al., 2008). To better understand the function of AMBRA1-alternative mitophagy *in vivo*, it will also be of great interest, and in line with the role of NIX, to examine *Ambra1* deficient mice in the hematopoietic system.

Further studies are needed to better understand the mechanisms by which AMBRA1-mediated mitophagy is initiated and to determine whether AMBRA1-mediated mitophagy could be pharmacologically induced *in vivo* in order to ameliorate the mitochondrial defects observed in human dopaminergic neurons in models of PD.

Finally, we reported here that AMBRA1 is able to favor the survival of SH-SY5Y cells following neurotoxic stimuli by attenuating oxidative stress. Interestingly, the endogenous antioxidant-reduced glutathione has been shown to improve cell viability following 6-OHDA treatment, this indicating that potent brain-penetrating antioxidants might act to slow down PD progression. We are now proposing AMBRA1 as a novel

target to reduce oxidative stress; indeed, this molecule could be modulated in the future as a pharmacological target in brains of PD patients or other patients with pathologies associated to oxidative stress.

In sum, our data strongly suggest that alternative mitophagy mediated by AMBRA1 can exert protective effects against PD-related neuronal injury, through inhibiting oxidative stress and mitochondrial dysfunction.

AUTHOR CONTRIBUTIONS

AD performed the majority of the experiments planned together with FS and FC. PD performed cloning, PD, LS and SC performed FACS analysis. AD, FS and FC wrote the manuscript.

FUNDING

This work was supported by grants GR2011-02351433 to FS; AIRC (IG2016-18906), Fondazione Roma, KBVU from the Danish Cancer Society (R146-A9364), the Novo Nordisk Foundation (7559, 22544) and the European Union (Horizon 2020 MEL-PLEX, grant agreement 195 642295) to FC. Further, FC lab in Copenhagen is part of the Center of Excellence in Autophagy, Recycling and Disease (CARD), funded by the Danish National Research Foundation.

ACKNOWLEDGMENTS

We wish to thank Prof. M. Campanella (Royal Veterinary College, University of London, UK) and Dr. P. P. Leoncini ("Bambino Gesù" Children's Hospital, Rome, Italy) for the gift of Short Hairpin PARKIN and Twee-GFP plasmids, respectively. We acknowledge Prof. D. Barilà (University of Rome, Tor Vergata, Italy) who kindly provided SH-SY5Y cells.

SUPPLEMENTARY MATERIAL

The Supplementary Material for this article can be found online at: <https://www.frontiersin.org/articles/10.3389/fncel.2018.00092/full#supplementary-material>

FIGURE S1 | The recombinant protein AMBRA1^{ActA} induces mitophagy in SH-SY5Y. SH-SY5Y cells transfected with PcDNA3 (empty vector) and with plasmids encoding the recombinant proteins Venus^{ActA}, Myc-AMBRA1^{ActA}, or Myc-AMBRA1^{ActA}^{LIRAA} and the wild-type protein Myc-AMBRA1 were fixed and stained for anti-HSP60 (red) and DAPI (blue). Scale bar, 6 μ m. The graph shows the HSP60 fluorescence intensity per cell (\pm S.D). $n = 3$ independent experiments. Statistical analysis was performed by using One-way ANOVA. **** $P < 0.0001$; * $P < 0.05$.

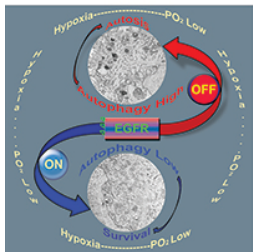
FIGURE S2 | *Endogenous* AMBRA1 downregulation produces a delay in mitochondrial clearance in 6-OHDA- or rotenone-treated cells. **(A)** SH-SY5Y cells were transfected with siRNA-Ctr or a siRNA against AMBRA1 and treated with 6-OHDA for 18 h. Total lysates were subjected to western blotting analysis for the indicated antibodies. **(B)** Total lysate of SH-SY5Y cells downregulated for AMBRA1, through siRNA-AMBRA1 transfection were treated with rotenone for 18 h and then analyzed by western blotting analysis looking to mitochondrial marker MnSOD level.

REFERENCES

- Betarbet, R., Sherer, T. B., MacKenzie, G., Garcia-Osuna, M., Panov, A. V., and Greenamyre, J. T. (2000). Chronic systemic pesticide exposure reproduces features of Parkinson's disease. *Nat. Neurosci.* 3, 1301–1306. doi: 10.1038/81834
- Bolte, S., and Cordelières, F. P. (2006). A guided tour into subcellular colocalization analysis in light microscopy. *J. Microsc.* 224, 213–232. doi: 10.1111/j.1365-2818.2006.01706.x
- Chin-Chan, M., Navarro-Yepes, J., and Quintanilla-Vega, B. (2015). Environmental pollutants as risk factors for neurodegenerative disorders: Alzheimer and Parkinson diseases. *Front. Cell. Neurosci.* 9:124. doi: 10.3389/fncel.2015.00124
- Degli Esposti, M., Ghelli, A., Crimi, M., Estornell, E., Fato, R., and Lenaz, G. (1993). Complex I and complex III of mitochondria have common inhibitors acting as ubiquinone antagonists. *Biochem. Biophys. Res. Commun.* 190, 1090–1096. doi: 10.1006/bbrc.1993.1161
- Elkon, H., Don, J., Melamed, E., Ziv, I., Shirvan, A., and Offen, D. (2002). Mutant and wild-type α -synuclein interact with mitochondrial cytochrome C oxidase. *J. Mol. Neurosci.* 18, 229–238. doi: 10.1385/jmn:18:3:229
- Gilgun-Sherki, Y., Melamed, E., and Offen, D. (2001). Oxidative stress induced-neurodegenerative diseases: the need for antioxidants that penetrate the blood brain barrier. *Neuropharmacology* 40, 959–975. doi: 10.1016/s0028-3908(01)00019-3
- Glinka, Y., Gassen, M., and Youdim, M. B. (1997). Mechanism of 6-hydroxydopamine neurotoxicity. *J. Neural Transm. Suppl.* 50, 55–66. doi: 10.1007/978-3-7091-6842-4_7
- Hanrott, K., Gudmunson, L., O'Neill, M. J., and Wonnacott, S. (2006). 6-hydroxydopamine-induced apoptosis is mediated via extracellular auto-oxidation and caspase 3-dependent activation of protein kinase Cdelta. *J. Biol. Chem.* 281, 5373–5382. doi: 10.1074/jbc.M511560200
- Hart, P. D., and Young, M. R. (1991). Ammonium chloride, an inhibitor of phagosome-lysosome fusion in macrophages, concurrently induces phagosome-endosome fusion, and opens a novel pathway: studies of a pathogenic mycobacterium and a nonpathogenic yeast. *J. Exp. Med.* 174, 881–889. doi: 10.1084/jem.174.4.881
- Jiang, L., Shestov, A. A., Swain, P., Yang, C., Parker, S. J., Wang, Q. A., et al. (2016). Reductive carboxylation supports redox homeostasis during anchorage-independent growth. *Nature* 532, 255–258. doi: 10.1038/nature17393
- Kabeya, Y., Mizushima, N., Ueno, T., Yamamoto, A., Kirisako, T., Noda, T., et al. (2000). LC3, a mammalian homologue of yeast Apg8p, is localized in autophagosome membranes after processing. *EMBO J.* 19, 5720–5728. doi: 10.1093/emboj/19.21.5720
- Koentjoro, B., Park, J. S., and Sue, C. M. (2017). Nix restores mitophagy and mitochondrial function to protect against PINK1/Parkin-related Parkinson's disease. *Sci. Rep.* 7:44373. doi: 10.1038/srep44373
- Korshunov, S. S., Skulachev, V. P., and Starkov, A. A. (1997). High protonic potential actuates a mechanism of production of reactive oxygen species in mitochondria. *FEBS Lett.* 416, 15–18. doi: 10.1016/s0014-5793(97)01159-9
- Lazarou, M., Sliter, D. A., Kane, L. A., Sarraf, S. A., Wang, C., Burman, J. L., et al. (2015). The ubiquitin kinase PINK1 recruits autophagy receptors to induce mitophagy. *Nature* 524, 309–314. doi: 10.1038/nature14893
- Lee, J. Y., Nagano, Y., Taylor, J. P., Lim, K. L., and Yao, T. P. (2010). Disease-causing mutations in parkin impair mitochondrial ubiquitination, aggregation, and HDAC6-dependent mitophagy. *J. Cell Biol.* 189, 671–679. doi: 10.1083/jcb.201001039
- Lemasters, J. J. (2005). Selective mitochondrial autophagy, or mitophagy, as a targeted defense against oxidative stress, mitochondrial dysfunction, and aging. *Rejuvenation Res.* 8, 3–5. doi: 10.1089/rej.2005.8.3
- Li, N., Ragheb, K., Lawler, G., Sturgis, J., Rajwa, B., Melendez, J. A., et al. (2003). Mitochondrial complex I inhibitor rotenone induces apoptosis through enhancing mitochondrial reactive oxygen species production. *J. Biol. Chem.* 278, 8516–8525. doi: 10.1074/jbc.m210432200
- Lin, M. T., and Beal, M. F. (2006). Mitochondrial dysfunction and oxidative stress in neurodegenerative diseases. *Nature* 443, 787–795. doi: 10.1038/nature05292
- McLennan, H. R., and Degli Esposti, M. (2000). The contribution of mitochondrial respiratory complexes to the production of reactive oxygen species. *J. Bioenerg. Biomembr.* 32, 153–162. doi: 10.1023/A:1005507913372
- Nagai, T., Ibata, K., Park, E. S., Kubota, M., Mikoshiba, K., and Miyawaki, A. (2002). A variant of yellow fluorescent protein with fast and efficient maturation for cell-biological applications. *Nat. Biotechnol.* 20, 87–90. doi: 10.1038/nbt0102-87
- Offen, D., Ziv, I., Sternin, H., Melamed, E., and Hochman, A. (1996). Prevention of dopamine-induced cell death by thiol antioxidants: possible implications for treatment of Parkinson's disease. *Exp. Neurol.* 141, 32–39. doi: 10.1006/exnr.1996.0136
- Pankiv, S., Clausen, T. H., Lamark, T., Brech, A., Bruun, J. A., Outzen, H., et al. (2007). p62/SQSTM1 binds directly to Atg8/LC3 to facilitate degradation of ubiquitinated protein aggregates by autophagy. *J. Biol. Chem.* 282, 24131–24145. doi: 10.1074/jbc.m702824200
- Sanders, L. H., McCoy, J., Hu, X., Mastroberardino, P. G., Dickinson, B. C., Chang, C. J., et al. (2014). Mitochondrial DNA damage: molecular marker of vulnerable nigral neurons in Parkinson's disease. *Neurobiol. Dis.* 70, 214–223. doi: 10.1016/j.nbd.2014.06.014
- Sandoval, H., Thiagarajan, P., Dasgupta, S. K., Schumacher, A., Prchal, J. T., Chen, M., et al. (2008). Essential role for Nix in autophagic maturation of erythroid cells. *Nature* 454, 232–235. doi: 10.1038/nature07006
- Sherer, T. B., Betarbet, R., Kim, J. H., and Greenamyre, J. T. (2003). Selective microglial activation in the rat rotenone model of Parkinson's disease. *Neurosci. Lett.* 341, 87–90. doi: 10.1016/s0304-3940(03)00172-1
- Siddiqui, M. A., Ahmad, J., Farshori, N. N., Saquib, Q., Jahan, S., Kashyap, M. P., et al. (2013). Rotenone-induced oxidative stress and apoptosis in human liver HepG2 cells. *Mol. Cell. Biochem.* 384, 59–69. doi: 10.1007/s11010-013-1781-9
- Strappazzon, F., Di Rita, A., Cianfanelli, V., D'Orazio, M., Nazio, F., Fimia, G. M., et al. (2016). Prosurvival AMBRA1 turns into a proapoptotic BH3-like protein during mitochondrial apoptosis. *Autophagy* 12, 963–975. doi: 10.1080/15548627.2016.1164359
- Strappazzon, F., Nazio, F., Corrado, M., Cianfanelli, V., Romagnoli, A., Fimia, G. M., et al. (2015). AMBRA1 is able to induce mitophagy via LC3 binding, regardless of PARKIN and p62/SQSTM1. *Cell Death Differ.* 22, 419–432. doi: 10.1038/cdd.2014.139
- Strappazzon, F., Vetri-Rudan, M., Campello, S., Nazio, F., Florenzano, F., Fimia, G. M., et al. (2011). Mitochondrial BCL-2 inhibits AMBRA1-induced autophagy. *EMBO J.* 30, 1195–1208. doi: 10.1038/emboj.2011.49
- Van Humbeek, C., Cornelissen, T., Hofkens, H., Mandemakers, W., Gevaert, K., De Strooper, B., et al. (2011). Parkin interacts with Ambra1 to induce mitophagy. *J. Neurosci.* 31, 10249–10261. doi: 10.1523/JNEUROSCI.1917-11.2011

Conflict of Interest Statement: The authors declare that the research was conducted in the absence of any commercial or financial relationships that could be construed as a potential conflict of interest.

Copyright © 2018 Di Rita, D'Acunzo, Simula, Campello, Strappazzon and Cecconi. This is an open-access article distributed under the terms of the Creative Commons Attribution License (CC BY). The use, distribution or reproduction in other forums is permitted, provided the original author(s) and the copyright owner are credited and that the original publication in this journal is cited, in accordance with accepted academic practice. No use, distribution or reproduction is permitted which does not comply with these terms.



Autophagy



ISSN: 1554-8627 (Print) 1554-8635 (Online) Journal homepage: <http://www.tandfonline.com/loi/kaup20>

Prosurvival AMBRA1 turns into a proapoptotic BH3-like protein during mitochondrial apoptosis

Flavie Strappazon, Anthea Di Rita, Valentina Cianfanelli, Melania D'Orazio, Francesca Nazio, Gian Maria Fimia & Francesco Cecconi

To cite this article: Flavie Strappazon, Anthea Di Rita, Valentina Cianfanelli, Melania D'Orazio, Francesca Nazio, Gian Maria Fimia & Francesco Cecconi (2016) Prosurvival AMBRA1 turns into a proapoptotic BH3-like protein during mitochondrial apoptosis, *Autophagy*, 12:6, 963-975, DOI: 10.1080/15548627.2016.1164359

To link to this article: <http://dx.doi.org/10.1080/15548627.2016.1164359>



© 2016 The Author(s). Published with license by Taylor & Francis Group, LLC
© 2016 Flavie Strappazon, Anthea Di Rita, Valentina Cianfanelli, Melania D'Orazio, Francesca Nazio, Gian Maria Fimia, and Francesco Cecconi.
Published online: 28 Apr 2016.



View supplementary material [↗](#)



Published online: 28 Apr 2016.



Submit your article to this journal [↗](#)



Article views: 942



View related articles [↗](#)



View Crossmark data [↗](#)



Citing articles: 1 View citing articles [↗](#)

BASIC RESEARCH PAPER

 OPEN ACCESS

Prosurvival AMBRA1 turns into a proapoptotic BH3-like protein during mitochondrial apoptosis

Flavie Strappazon^a, Anthea Di Rita^{a,b}, Valentina Cianfanelli^c, Melania D'Orazio^b, Francesca Nazio^{a,b}, Gian Maria Fimia^{d,e}, and Francesco Cecconi^{a,b,c}

^aIRCCS Fondazione Santa Lucia, Rome, Italy; ^bDepartment of Biology, University of Rome Tor Vergata, Rome, Italy; ^cUnit of Cell Stress and Survival, Danish Cancer Society Research Center, Copenhagen, Denmark; ^dDepartment of Biological and Environmental Sciences and Technologies (DiSTeBA), University of Salento, Lecce, Italy; ^eNational Institute for Infectious Diseases 'L. Spallanzani' IRCCS, Rome, Italy

ABSTRACT

Autophagy and apoptosis are 2 stress-response mechanisms that are closely interconnected. However, the molecular interplays between these 2 pathways remain to be clarified. Here we report that the crucial proautophagic factor AMBRA1 can act as a positive mediator of mitochondrial apoptosis. Indeed, we show that, in a proapoptotic positive feedback loop, the C-terminal part of AMBRA1, generated by CASP/CASPASE cleavage upon apoptosis induction, inhibits the antiapoptotic factor BCL2 by a direct binding through its BH3-like domain. The mitochondrial AMBRA1-BCL2 complex is thus at the crossroad between autophagy and cell death and may represent a novel target in development of therapeutic approaches in clinical diseases.

ARTICLE HISTORY

Received 24 September 2015
Revised 2 March 2016
Accepted 7 March 2016

KEYWORDS

AMBRA1; apoptosis; autophagy; BCL2; BH3 domain

Introduction

Autophagy is an important eukaryotic process involved in the lysosomal degradation of cytosolic components, both under physiological and pathological conditions. During autophagy, the autophagosomes—specific double-membrane vesicles—engulf a number of different cargoes and then fuse with lysosomes for subsequent recycling of their content. Several key proteins are involved in autophagosome formation, such as BECN1/Beclin 1 and its positive regulator AMBRA1; AMBRA1 and BECN1 are present in the class III phosphatidylinositol 3-kinase (PtdIns3K) complex,^{1,2} and are involved in autophagosome nucleation, an early step of autophagy induction. More recently, it has been demonstrated that AMBRA1 and BECN1 can also regulate autophagy at different steps of the process, by binding other key interactors.^{3–6} Interestingly, a pool of AMBRA1 is localized at the mitochondria, where its proautophagic activity is inhibited by mitochondrial resident BCL2.⁷ Moreover, AMBRA1 regulates mitophagy, a form of autophagy that ensures the specific removal of damaged mitochondria, both dependently or independently of the E3-ubiquitin Ligase PARK2/PARKIN.⁸


The fact that AMBRA1 interacts with the antiapoptotic factor BCL2 places it at the crossroad between autophagy and cell death. In fact, BCL2, a well-known antiapoptotic factor whose overexpression protects against a wide range of apoptotic inducers, can regulate BECN1-induced autophagy at the endoplasmic reticulum by a direct binding to the BECN1 BH3 domain and with the

contribution of Cisd2/NAF-1 (CDGSH iron sulfur domain 2).^{9,10} BCL2 can also regulate BECN1-induced autophagy by sequestering AMBRA1 (the activator of BECN1) at the mitochondria.⁶ Conversely, it has been demonstrated that a number of regulators of autophagy, such as BECN1 and PI3K3C3/Vps34,^{11,12,13,14,15} ATG4A/ATG4, ATG5,^{16,17,18,19} or AMBRA1,²⁰ are subjected to proteolytic cleavage during cell death so as to abrogate their proautophagic function. Another point of convergence between autophagy and apoptosis is the binding between ATG12 and BCL2 family members that takes place in order to induce mitochondrial apoptosis.²¹

Besides AMBRA1 binding to BCL2 in the mitochondrial fraction, we have previously demonstrated that this event is reduced following apoptosis induction,⁷ this indicating that AMBRA1 could be involved in cell death regulation.

In this work, we explore the relationship between AMBRA1 and the death machinery by investigating whether AMBRA1 could disrupt BCL2's ability to protect against apoptosis. In particular, because AMBRA1 is cleaved by CASP during apoptosis, we decided to study the effect of the C-terminal fragment of AMBRA1, which is released by this CASP cleavage, on BCL2. We found that this fragment, through a BH3-like domain, is able to inhibit the antiapoptotic function of BCL2 so as to enhance apoptosis. To summarize, we propose a model in which AMBRA1 is involved in both autophagy and apoptosis, depending upon the presence of its full-length or cleaved form.

CONTACT Flavie Strappazon  f.strappazon@hsantalucia.it; Francesco Cecconi  cecconi@cancer.dk, francesco.cecconi@uniroma2.it

 Supplemental data for this article can be accessed on the publisher's website.

© 2016 Flavie Strappazon, Anthea Di Rita, Valentina Cianfanelli, Melania D'Orazio, Francesca Nazio, Gian Maria Fimia, and Francesco Cecconi. Published with license by Taylor & Francis. This is an Open Access article distributed under the terms of the Creative Commons Attribution-Non-Commercial License (<http://creativecommons.org/licenses/by-nc/3.0/>), which permits unrestricted non-commercial use, distribution, and reproduction in any medium, provided the original work is properly cited. The moral rights of the named author(s) have been asserted.

Results

To test whether AMBRA1 could have an effect on BCL2 antiapoptotic functions, we first cotransfected HEK293 cells with a vector encoding AMBRA1 and a vector encoding mito-BCL2, a mutant of BCL2 which has a mitochondria-restricted subcellular localization and which is known to interact with AMBRA1.⁷ We next measured cell viability following treatment with staurosporin (STS), a pan-kinase inhibitor commonly used to induce rapid activation of mitochondrial apoptosis.

However, surprisingly, when AMBRA1 was cotransfected together with mito-BCL2, this protective effect was lost (Fig. 1A). This result was also observed by counting pyknotic nuclei in transfected cells (Fig. S1A). To elucidate the action of AMBRA1 on the protective effect of mito-BCL2, we performed a western blot analysis for the cleavage of PARP1 (fragment of 89 kDa), a CASP substrate. Again, cotransfection of AMBRA1 with mito-BCL2 abrogates this protective effect (Fig. 1B).

Next, we decided to investigate CYCS/cytochrome C release from mitochondria, another crucial step during apoptosis induction. To this end, we performed a confocal microscopy analysis on HEK293 cells cotransfected with a vector encoding mito-DsRED used in order to stain mitochondria (this vector contains a mitochondria targeting sequence fused with DsRED protein), and with AMBRA1 alone, mito-BCL2 alone or the 2 constructs together. As expected, mito-BCL2 overexpression was able to reduce CYCS release from mitochondria, as shown by an almost complete overlap between mitochondria (red staining) and CYCS (green staining) (Fig. 1C). However, the merging between mitochondria and CYCS was completely lost in cells overexpressing both AMBRA1 and mito-BCL2, so indicating a stronger release of CYCS in these cells. Quantification of CYCS release from mitochondria confirms that the BCL2 antiapoptotic effect is abolished when AMBRA1 is cotransfected with BCL2 (Fig. 1D). Overall, these results indicate that AMBRA1, in combination with mito-BCL2, may exert a proapoptotic activity.

Pagliarini et al. have previously demonstrated that AMBRA1 is subjected to proteolytic cleavage during apoptosis,²⁰ which leads to generation of 2 protein fragments. Of note, the C-terminal part of the protein proves to be more stable than the N-terminal fragment, which, instead, undergoes rapid degradation. Based on this finding, we thus hypothesized that one possible way by which AMBRA1 could regulate the BCL2 antiapoptotic effect, is via its C-terminal part (generated after CASP cleavage).

First, in order to test this hypothesis, we decided to investigate whether AMBRA1's C-terminal fragment (AMBRA1^{CT}), resulting from CASP cleavage, interacted with BCL2 during cell death. To answer this question, endogenous proteins extracted from HEK293 cells treated with DMSO (as control) or with STS were analyzed by size-exclusion fast protein liquid chromatography (sec-FPLC). The collected protein fractions were then studied by western blot analysis, using specific antibodies against AMBRA1 and BCL2. As shown in Fig. 2A, AMBRA1 (molecular mass of ~130 kDa) is copurified in the same fraction with BCL2 in DMSO conditions (fraction 24). In contrast, a fragment of AMBRA1 (molecular mass of ~100 kDa, only visible upon staurosporine treatment and likely corresponding

to endogenous AMBRA1^{CT}) and BCL2 are copurified in the same fractions (fractions 31 to 33, indicated with #), demonstrating the existence of a macromolecular complex comprising the 2 proteins, and with a molecular mass of ~120 kDa. This result indicates that the endogenous C-terminal part of AMBRA1 generated during cell death, as revealed by PARP cleavage in the given conditions (right panel in Fig. 2A), is in a macromolecular complex with endogenous BCL2.

Second, to assess BCL2 interaction with AMBRA1^{CT}, we transfected HEK293 cells with a construct encoding MYC-tagged AMBRA1 wild-type (AMBRA1^{WT}) or Flag-tagged AMBRA1^{CT} (Flag-AMBRA1^{CT}). We then treated these cells with STS in order to induce cell death; we next immunoprecipitated, using an anti-MYC antibody for the AMBRA1^{WT} construct or, with an anti-Flag antibody for the AMBRA1^{CT} construct, in normal and apoptotic conditions. As shown in Fig. 2B, BCL2 coimmunoprecipitates with AMBRA1^{WT} in normal conditions whereas this binding is disrupted following STS treatment. In contrast, AMBRA1^{CT} coimmunoprecipitates with BCL2 with higher affinity both in normal conditions and following cell death induction. To confirm this result, we performed a confocal microscopy analysis between AMBRA1^{WT} or AMBRA1^{CT} with endogenous BCL2, in normal conditions or following STS treatment. As shown in Fig. S1B, endogenous BCL2 strongly colocalizes with AMBRA1^{CT} following STS treatment when compared to AMBRA1^{WT}. Interestingly, we found that cleaved AMBRA1 competes with full-length AMBRA1 for binding to BCL2 (Fig. S2), suggesting that cleaved AMBRA1 is more prone to bind BCL2 than full-length AMBRA1. Since we previously have demonstrated that AMBRA1 is able to bind the mitochondrial pool of BCL2,⁶ in order to verify whether AMBRA1^{CT} was also able to bind the mitochondrial pool of BCL2, we performed a confocal microscopy analysis to check the subcellular distribution of AMBRA1^{WT} or AMBRA1^{CT}. In order to stain mitochondria, we overexpressed mito-DsRED with AMBRA1^{WT} or AMBRA1^{CT} alone (Fig. 2C, top panels) or with both AMBRA1^{WT} or AMBRA1^{CT} and mito-BCL2 (Fig. 2C, bottom panels). AMBRA1^{WT} and AMBRA1^{CT} (green staining) are widely distributed in the cytoplasm, and a partial colocalization with the mitochondrial network is detected (merged). Of note, the mitochondrial network (red staining) appears fragmented following AMBRA1^{CT} overexpression, indicating a putative proapoptotic effect of AMBRA1^{CT}. More interestingly, we observed that mito-BCL2 overexpressed together with AMBRA1^{CT} is sufficient to massively recruit AMBRA1^{CT} on mitochondria. Forty-eight h post-transfection, cells double-positive for AMBRA1^{CT} and mito-BCL2 undergo cell death (as shown by detection of apoptotic nuclei), exhibiting a mitochondrial network, which is completely aggregated around the nucleus (often defined as "mitoaggregates,"⁽²²⁾ Fig. 2D). These results led us to check whether AMBRA1^{CT}, in combination with mito-BCL2, was sufficient to induce apoptosis in the absence of any specific death stimuli, such as STS. To this end, we cotransfected HEK293 cells with AMBRA1^{CT} and mito-BCL2, and counted pyknotic nuclei in transfected cells, 24 h and 48 h after transfection. As shown in Fig. 2E, 24 h post-transfection more than 60% cells underwent death. Forty-eight h after transfection, we observed up to 100% of apoptosis in

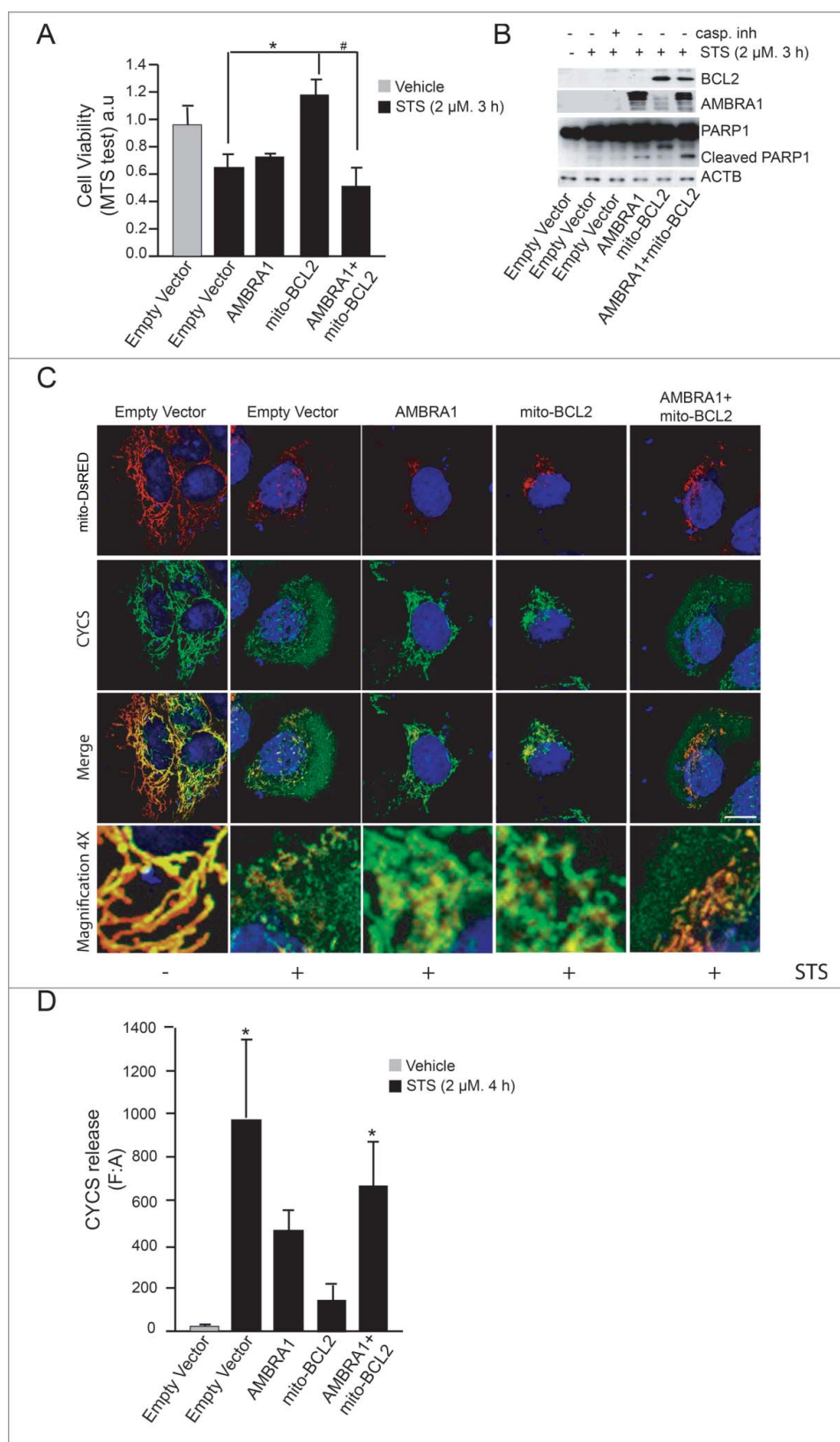


Figure 1. AMBRA1 becomes proapoptotic in combination with mito-BCL2. (A) HEK293 cells were transfected with an empty vector or vectors encoding AMBRA1, mito-BCL2 or cotransfected with both AMBRA1 and mito-BCL2. Twenty-four h after transfection, cells were treated or not with 2 μ M STS for 3 h and viable cells were estimated using the MTS assay. Results are expressed as arbitrary unit (a.u). Each point represents the mean (\pm SD) of triplicate wells from 3 independent experiments. Statistical analysis was performed using the Student *t* test ($^*P < 0.05$) versus pcDNA3 and ($^{\#}P < 0.05$) vs. mito-BCL2. (B) HEK293 cells were transfected with an empty vector or vectors encoding AMBRA1, mito-BCL2 or either cotransfected with both AMBRA1 and mito-BCL2. Twenty-four h after transfection, cells were treated with or without 2 μ M STS for 3 h. After extraction of proteins, we performed a western blot analysis by using antibodies against PARP1, AMBRA1, BCL2 and against ACTB (as a loading control). (C) HEK293 cells were cotransfected with an empty vector and mito-DsRED (in order to stain mitochondria) or with mito-DsRED and vectors encoding AMBRA1, mito-BCL2 or cotransfected with both AMBRA1 and mito-BCL2. Cells were then treated with STS 2 μ M during 4 h and stained using an anti-CYCS (green) antibody. Nuclei were stained with DAPI 1 μ g/ μ l 20 min. Merge of the different fluorescence signals are illustrated. Scale bar: 8 μ m. (D) Graphic of densitometry values of CYCS release, expressed as mean fluorescence of individual cells, normalized to total cellular surface (F:A, $n = 30$ cells/groups).

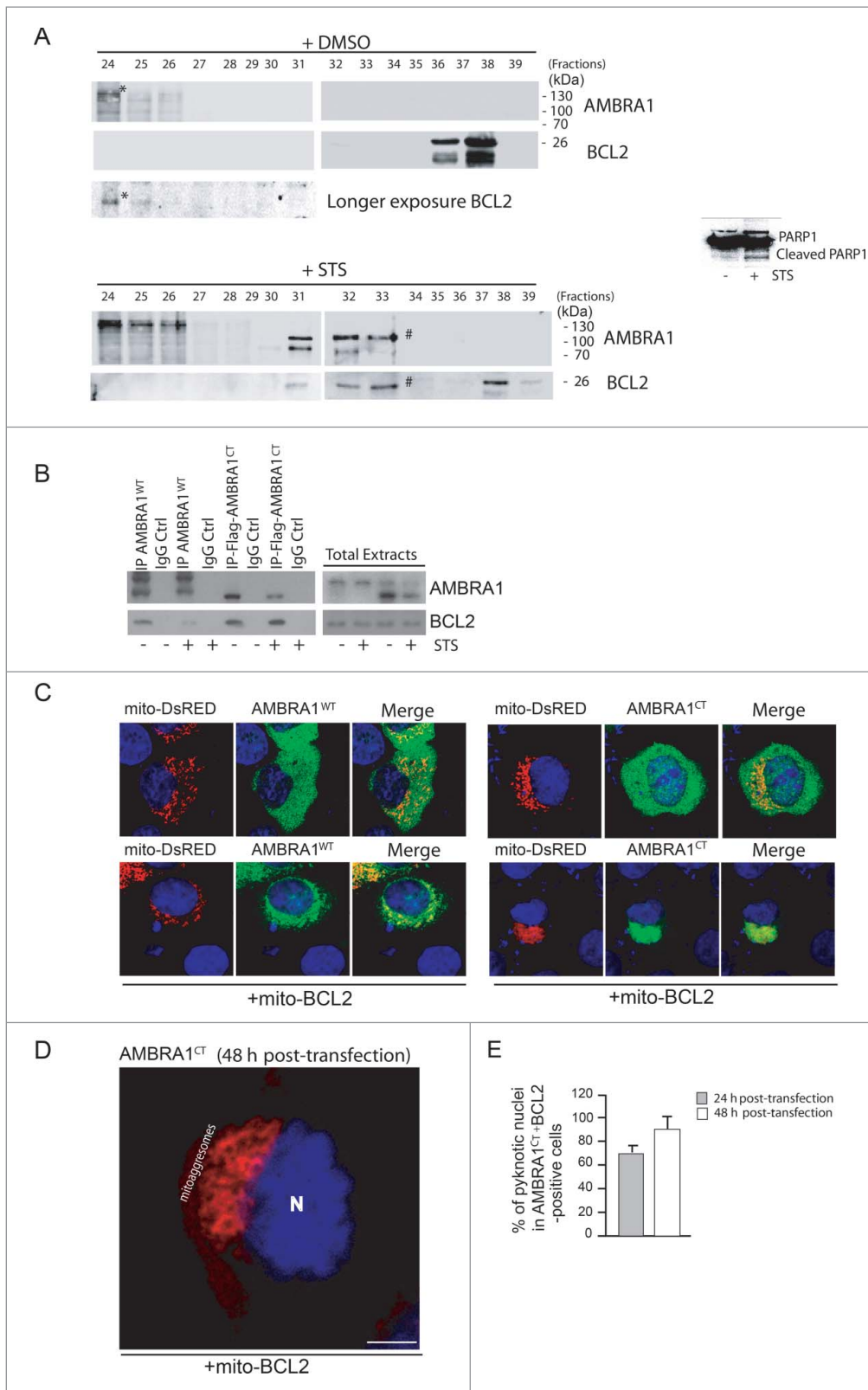


Figure 2. For figure legend, see next page.

cells overexpressing both AMBRA1^{CT} and mito-BCL2. These results demonstrate that AMBRA1^{CT}, in combination with mito-BCL2, induces apoptosis.

At this point, to demonstrate that the C-terminal fragment of AMBRA1 could become proapoptotic following cell death signals, we decided to use a mutant of AMBRA1 resistant to CASP cleavage (AMBRA1^{D482A}). In fact, the AMBRA1^{D482A} mutant, carrying a single-point mutation (D482 → A) was initially mutated in order to disrupt the predicted putative caspase cleavage site.²⁰ We overexpressed either a vector encoding AMBRA1^{D482A} or AMBRA1^{CT} in HEK293 cells, and treated them with STS to induce apoptosis. We next checked, by confocal microscope, CYCS release from mitochondria. As shown in Fig. 3A (top panels), AMBRA1^{D482A} did not induce CYCS release in normal condition. Also, following STS treatment, we observed that cells overexpressing AMBRA1^{D482A} were healthy, with a still significant overlap of CYCS staining with mitochondria, indicating an antiapoptotic activity of this mutant. By contrast, overexpression of AMBRA1^{CT} is sufficient to induce, in normal conditions, CYCS release from mitochondria (Fig. 3B, top panels), and this release is also visible in cells treated with STS (Fig. 3B, bottom panels). The graphic of Fig. 3C illustrates quantification of CYCS release. Last, by performing a western blot analysis, we observed that BAX activation, following STS treatment, is reduced in cells overexpressing AMBRA1^{D482A} compared with cells overexpressing AMBRA1^{WT} or AMBRA1^{CT} (Fig. 3D). Altogether, these results indicate that, during apoptosis, AMBRA1 cleavage by CASP is fundamental to support BAX activation.

This being the case, in contrast with cells overexpressing AMBRA1^{CT}, cells overexpressing AMBRA1^{D482A} are expected to be protected from cell death. We thus decided to monitor cell death by counting pyknotic nuclei in transfected cells. As shown in Fig. 3E, cells positive for AMBRA1^{D482A} undergo cell death to a lesser extent than to AMBRA1^{CT}-transfected cells. In fact, it has been demonstrated in another cell system that AMBRA1^{D482A} delays cell death by maintaining its proautophagic activity.²⁰ Our observation confirms that AMBRA1^{CT} favors apoptosis, whereas its mutant resistant to CASP cleavage can partially prolong cell survival.

Next, we decided to investigate the molecular mechanism of AMBRA1^{CT} activity on BCL2. BCL2 is a member of the BCL2 protein family; this family shares a consensus sequence called BH3 domain; often, proapoptotic members of this family regulate, through direct binding via their BH3 domain, other BH3-containing proteins. We thus hypothesized that AMBRA1^{CT}

could act on BCL2 as a BH3 protein. First, we used a well-known BH3-mimetic, ABT-737, to test whether the interaction between AMBRA1 and mito-BCL2 could occur through a BH3 domain. We thus treated HEK293 cells overexpressing MYC-AMBRA1^{WT} with 10 μM ABT-737 for 3 h. We next immunoprecipitated AMBRA1 with an anti-MYC antibody. As shown in Fig. 4A, mito-BCL2 is associated with AMBRA1 in normal conditions, this binding being reduced by ABT-737. We next examined in silico the AMBRA1 sequence and found that AMBRA1 possesses, indeed, a putative BH3 motif in its C-terminal region (1215LPEAGQLA1222, see Fig. 4B). Therefore, in principle, AMBRA1 could bind BCL2 through this motif. As expected, 2 point mutations of this putative BH3 domain (AMBRA1^{BH3-AE}, [L1215A and G1219E]) almost abolished the interaction between MYC-AMBRA1^{WT} and mito-BCL2 (Fig. 4A). These results indicate that AMBRA1 can interact with mito-BCL2 through a previously unrevealed BH3 domain. A quantification of the ratio between mito-BCL2 coimmunoprecipitated on the quantity of precipitated AMBRA1 is reported in the graph (Fig. 4B).

Finally, we investigated the effect of AMBRA1^{BH3-AE} on apoptosis induction. To this end, we performed a confocal microscopy analysis and checked for CYCS release from mitochondria, upon STS treatment, in cells overexpressing AMBRA1^{WT} or AMBRA1^{BH3-AE}. CYCS release was reduced in cells overexpressing AMBRA1^{BH3-AE} following STS treatment (Fig. 5B and C). Again, we quantified apoptosis upon STS treatment in cells overexpressing this novel mutant construct. As shown in Fig. 5D, AMBRA1^{BH3-AE} can delay apoptosis similarly to AMBRA1^{D482A}, confirming that the AMBRA1^{CT} acts on BCL2, through its BH3 domain, during apoptosis. Last, by performing a western blot analysis using an antibody against activated BAX, we observed that cells overexpressing AMBRA1^{BH3-AE} exhibited a lower basal activation of BAX when compared with AMBRA1^{CT} (Fig. 5E). Also, the capability of AMBRA1 fragments to bind BH3-domain-containing proteins is further proved by their dynamic interactions with other antiapoptotic members of the BH3 family, as shown in Fig. S4.

At this point, our data suggest that AMBRA1 can regulate the antiapoptotic effect of BCL2 during apoptosis induction by a direct binding of this protein through a BH3 motif. To strengthen these results, we decided to render AMBRA1 protein both autophagy deficient and BCL2-binding deficient. To this end, we performed 2 point mutations of the BH3 domain on the cleaved form of AMBRA1, which is deficient for autophagy activity (Pagliarini et al., and Fig. S5; AMBRA1^{CT-BH3-AE}).

Figure 2. (See previous page). The C-terminal part of AMBRA1, resulting from CASP cleavage, interacts with BCL2 and increases cell death following STS treatment. (A) 2 mg of HEK293 cell lysate, obtained from DMSO-treated cells (control cells) or staurosporine-treated cells, were injected onto a superose 6 HR 10/30 FPLC gel filtration column. Proteins were collected in 500 μl fractions. Equal amounts of each fraction have been analyzed by western blot using antibodies against AMBRA1 and BCL2. To control that the STS treatment was efficient, we analyzed PARP cleavage by using an antibody against PARP. (B) HEK293 cells were transfected with a vector encoding MYC-AMBRA1^{WT} or Flag-AMBRA1^{CT}. Twenty-four h after transfection, cells were treated or not with STS (2 μM, 2 h). Protein extracts were immunoprecipitated using an anti-MYC or anti-Flag antibodies. Purified complexes and corresponding total extracts were analyzed by western blot (WB) using anti-AMBRA1 and anti-BCL2 antibodies. (C) HEK293 cells were cotransfected with a vector encoding mito-DsRED (to stain mitochondria) and a vector encoding MYC-AMBRA1^{WT} or AMBRA1^{CT} (lane 1) or in addition with a vector encoding mito-BCL2 (lane 2). Twenty-four h after transfection, cells were then stained using antibody anti-AMBRA1 (AMBRA1^{WT} and AMBRA1^{CT}, green). Nuclei were stained with DAPI 1 μg/μl 20 min. The merging of the different fluorescence signals is illustrated. Scale bar: 8 μm. (D) HEK293 cells were cotransfected with a vector encoding AMBRA1^{CT} and a vector encoding mito-BCL2. Forty-eight h after transfection, cells were fixed and stained using anti-AMBRA1 antibody (AMBRA1^{CT}, red). Nuclei were stained with DAPI 1 μg/μl 20 min. The merging of the different fluorescence signals is illustrated. Scale bar: 8 μm. (E) HEK293 cells were cotransfected with a vector encoding Flag-AMBRA1^{CT} and a vector encoding mito-BCL2. Twenty-four or 48 h following transfection, cells were fixed and assessed by immunolabelling using anti-Flag antibody and cells with condensed or fragmented nuclei were scored as pyknotic. Results are expressed as the percentage of transfected cells displaying pyknotic nuclei. For each condition, transfected cells were counted in 10 random fields from 3 independent experiments. Values are given as a percentage (± SD) of cell death.

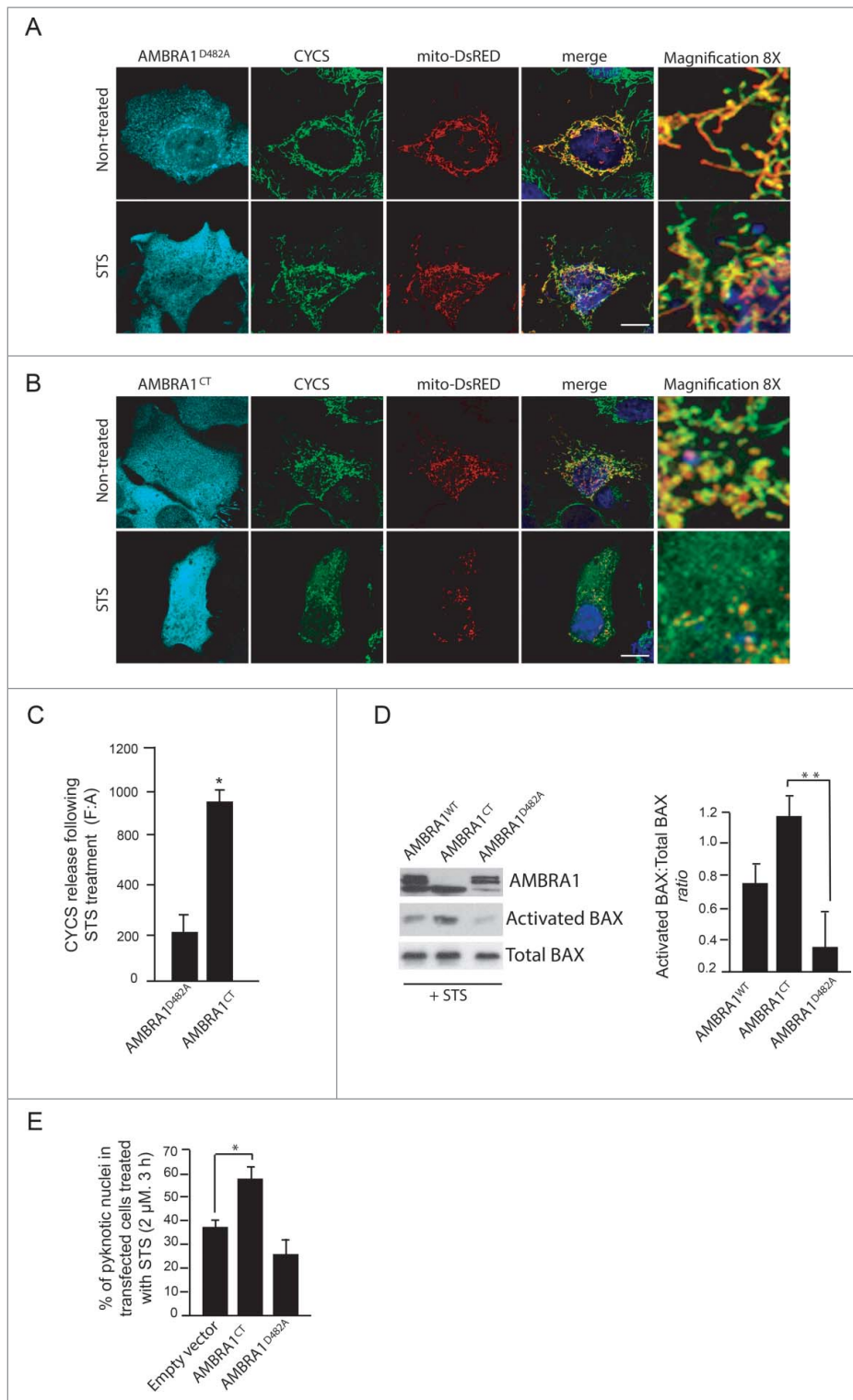


Figure 3. The C-terminal part of AMBRA1 functions upstream of MOMP. (A) HEK293 cells were cotransfected with a vector encoding AMBRA1^{D482A} and mito-DsRED (in order to stain mitochondria) or (B) with mito-DsRED and vectors encoding AMBRA1^{CT}. Twenty-four h after transfection, cells were treated with or without STS (2 μM) for 4 h. Cells were fixed and then stained using antibodies against CYCS (green) and against AMBRA1 (blue staining) that recognize only the overexpressed form of the protein. Nuclei were stained with DAPI 1 μg/μl 20 min. The merging of the different fluorescence signals is illustrated. Scale bar: 8 μm. (C) Graphic of densitometric values of CYCS release, expressed as mean fluorescence of individual cells, normalized to total cellular surface (F:A, n=30 cells/groups). (D) HEK293 cells were transfected with vectors encoding AMBRA1^{WT}, AMBRA1^{D482A} or AMBRA1^{CT}. Twenty-four h after transfection, cells were treated with 2 μM STS for 2 h. After extraction of proteins, we performed a western blot analysis using antibodies against AMBRA1, activated BAX, and total BAX (as a loading control). The band density ratio of activated BAX/total BAX was analyzed in 3 independent experiments; each point value represents the mean ± SD from 3 independent experiments. Statistical analysis was performed using the Student *t* test (*, *P* < 0.05). (E) HEK293 cells were transfected with an empty vector or with a vector encoding AMBRA1^{D482A} or AMBRA1^{CT}. Twenty-four h following transfection, cells were treated with 2 μM STS for 2 h. Cells were next fixed and examined by immunolabelling using anti-AMBRA1 antibody and cells with condensed or fragmented nuclei were scored as pyknotic. Results are expressed as the percentage of transfected cells displaying pyknotic nuclei. For each condition, transfected cells were counted in 10 random fields from 3 independent experiments. Values are given as a percentage (± SD) of cell death.

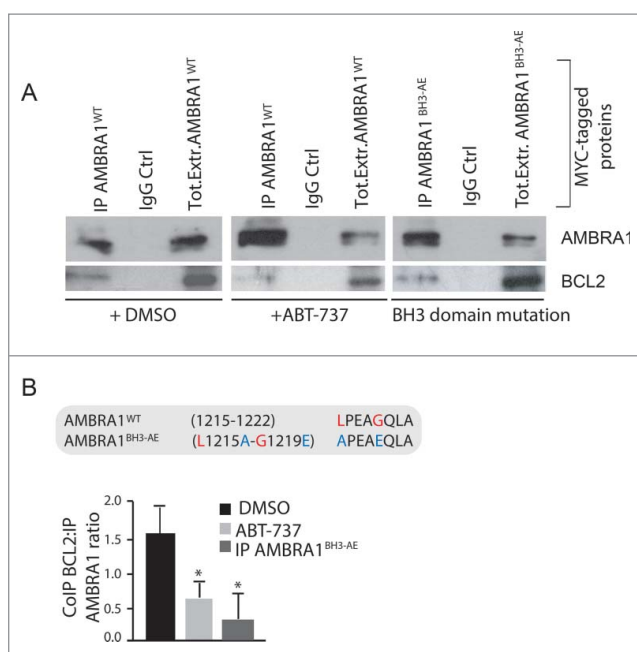


Figure 4. The C-terminal part of AMBRA1 interacts with mito-BCL2 via a BH3-like motif. (A) HEK293 cells were transfected with a vector encoding MYC-AMBRA1^{WT} or MYC-AMBRA1^{BH3-AE}. Twenty-four h after transfection, cells were treated with DMSO (ctrl) or with ABT-737 during 3 h (10 μ M). Total extracts were next immunoprecipitated using an anti-MYC antibody. Purified complexes were analyzed by western blot (WB) using anti-AMBRA1 and anti-BCL2 antibodies. (B) Identification of a BH3-like motif within the AMBRA1 sequence. Point mutations of both an aromatic residue and the conserved residue are shown (AMBRA1^{BH3-AE} [L1215A-G1219E; APEAEQLA]). The band density ratio of immunoprecipitated AMBRA1 relative to immunoprecipitated BCL2 was analyzed in 3 independent experiments; each point value represents the mean \pm SD from 3 independent experiments. Statistical analysis was performed using the Student *t* test (**P* < 0.05) versus the DMSO condition.

As expected, these mutations almost abolished the interaction between AMBRA1^{CT} and mito-BCL2 (Fig. 6A). A quantification of the ratio between coimmunoprecipitated mito-BCL2 and cleaved-AMBRA1 is reported in the graph (Fig. 6B). Further, by counting pyknotic nuclei in transfected cells, we observed that AMBRA1^{CT-BH3-AE} exhibits less apoptotic activity than AMBRA1^{CT} (Fig. 6C). Also, by looking at CYCS release (Fig. 6D), we found that AMBRA1^{CT-BH3-AE}-positive cells present less release of CYCS from mitochondria than cells overexpressing AMBRA1^{CT}. Altogether these results suggest that AMBRA1^{CT-BH3-AE} induces less mitochondrial permeabilization than AMBRA1^{CT}. Indeed, by monitoring BAX translocation from cytosol to mitochondria, we found that cells overexpressing AMBRA1^{CT-BH3-AE} present less translocated BAX on mitochondria than cells overexpressing AMBRA1^{CT} (Fig. 6F).

In conclusion, our data clearly indicate that AMBRA1 can regulate the antiapoptotic effect of BCL2 during apoptosis induction, by direct binding of this protein through a BH3 motif. A proposed working model for AMBRA1 in apoptosis is finally shown in Fig. 7.

Discussion

Our results indicate that AMBRA1, in addition to its roles in macroautophagy and mitophagy (reviewed in ref. 23), can act as a positive mediator of mitochondrial apoptosis. We propose

here that the C-terminal part of AMBRA1, AMBRA1^{CT}, generated by CASP cleavage, inactivates the BCL2 antiapoptotic factor, by a direct binding through its BH3-like domain. This work demonstrates the existence of a reciprocal regulation between AMBRA1 and BCL2 at the mitochondria.

The functional deficiency of *Ambra1* in mice induces a large number of supernumerary apoptotic cells in several areas of the nervous system.¹ Pagliarini et al.²⁰ have demonstrated that reduced levels of AMBRA1 in several cell lines lead to increased susceptibility to different apoptotic stimuli. Altogether, these results underline a prosurvival effect of AMBRA1; in line with these results, we demonstrated that cerebellar granule neurons overexpressing AMBRA1 are more resistant to trophic factor withdrawal than control neurons.⁷ Similarly to other proautophagic factors, such as ATG5 and ATG12,^{16,21} AMBRA1 is cleaved during apoptosis, in order to abolish its prosurvival effect. Since a mutant form of AMBRA1 resistant to CASP cleavage increases resistance to cell death by blocking both BAX activation and CYCS release from mitochondria, it can be postulated that AMBRA1 cleavage is involved in mitochondrial outer membrane permeabilization (MOMP). However, mutation of the AMBRA1 CASP cleavage site does not completely protect cells against cell death. This result can be explained by the fact that, in addition to CASP cleavage, AMBRA1 (or its cleaved fragments) may also be subjected to CAPN (calpain) cleavage, this leading to a complete destruction of the protein. In addition, other proautophagic proteins, and thus other prosurvival proteins, such as BECN1, are also cleaved during cell death, contributing to cell death induction. The fact that AMBRA1 requires to be cleaved in order to inhibit BCL2 opens the question about why the full-length form is not able to have such an effect. It is well possible that the N-terminal part of the protein, by binding other proteins, induces a particular conformation that blocks its inhibitory action on BCL2. This hypothesis is supported by the fact that AMBRA1 can dynamically binds the antiapoptotic proteins MCL1 and BCL2L1/BCLX. In particular, the cleaved form of AMBRA1 binds preferentially these antiapoptotic proteins when compared to full-length AMBRA1 during cell death. These data suggest that a conformational change of AMBRA1, that occurs during cell death, is necessary to allow its binding with antiapoptotic factors of the BCL2 family. Most likely, in addition to BCL2, in order to potentiate cell death, AMBRA1^{CT} could also act on MCL1 and BCL2L1. Interestingly, no binding can be found between AMBRA1 and the proapoptotic members of the BCL2 family proteins, such as BAX and BAK1/BAK.

BCL2 binds BECN1 on its BH3 domain. We show here that also AMBRA1 contains a BH3-like motif along its sequence. Of note, AMBRA1^{BH3-AE} partially loses its binding with mito-BCL2. In fact, we previously have proved that AMBRA1 binds dynamically to the mitochondrial pool of BCL2 with both the amino and the C-terminal domains of the protein. It is thus possible that the resistant binding observed with mutant AMBRA1^{BH3-AE} is mediated by the N-terminal part of the protein. It will be interesting to identify the precise region of binding between AMBRA1 and BCL2 in this N-terminal region.

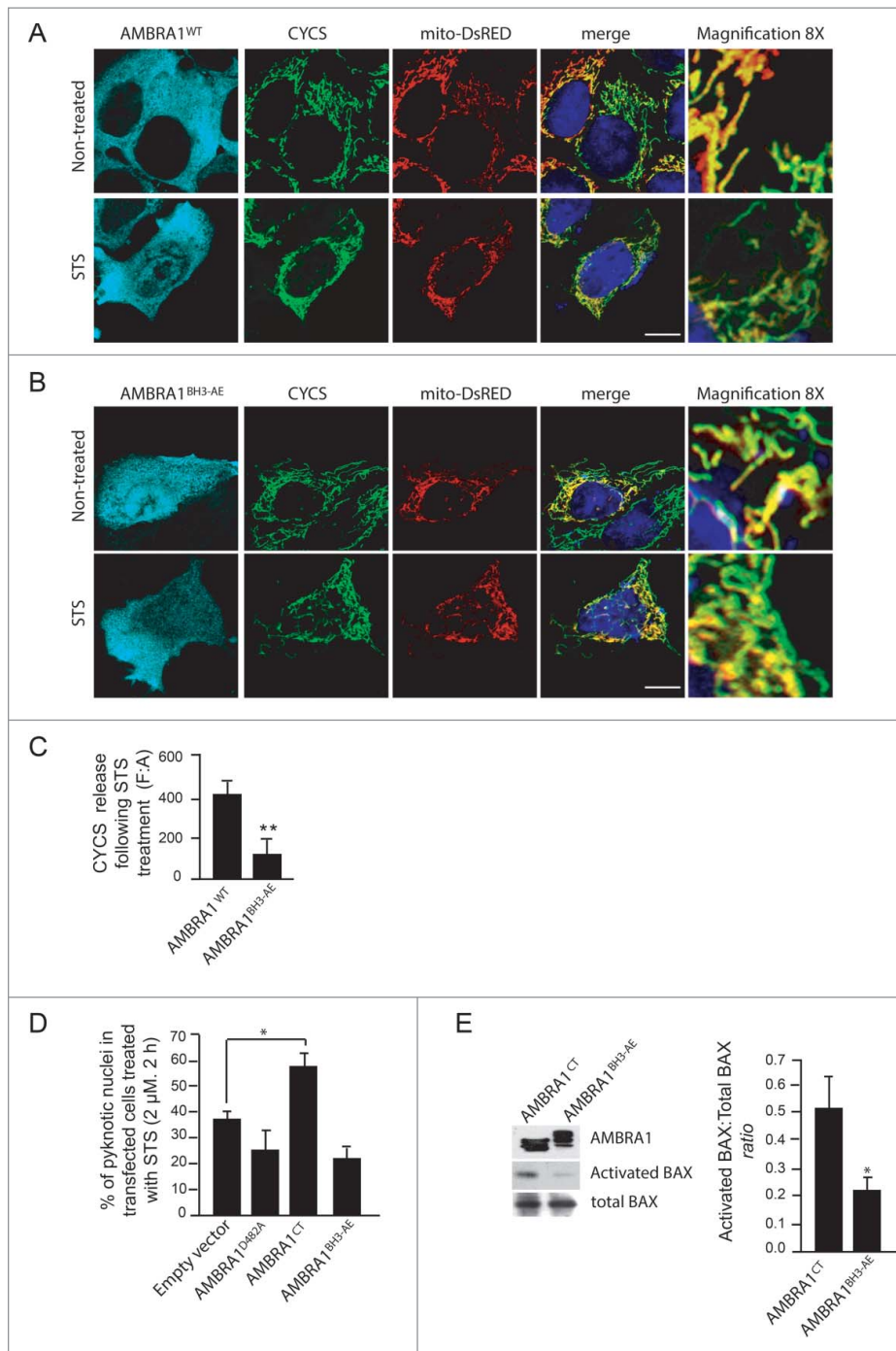


Figure 5. The mutant of AMBRA1 that cannot bind BCL2 loses its proapoptotic effect during cell death. (A) HEK293 cells were cotransfected with a vector encoding AMBRA1^{WT} or (B) AMBRA1^{BH3-AE} and mito-DsRED (in order to stain mitochondria). Twenty-four h after transfection, cells were treated with or without STS (2 μM) for 4 h. Cells were fixed and then stained using the anti-CYCS (green) antibody. Nuclei were stained with DAPI 1 μg/μl 20 min. The merging of the different fluorescence signals is illustrated. Scale bar: 8 μm. (C) HEK293 cells were transfected with an empty vector or with a vector encoding AMBRA1^{D482A}, AMBRA1^{CT} (see Fig. 3D) or with a vector encoding AMBRA1^{BH3-AE}. Twenty-four h following transfection, cells were treated with 2 μM STS during 3 h. Cells were next fixed and examined by immunolabelling using anti-AMBRA1 antibody that recognizes only the overexpressed form of the protein and cells with condensed or fragmented nuclei were scored as pyknotic. Results are expressed as the percentage of transfected cells displaying pyknotic nuclei. For each condition, transfected cells were counted in 10 random fields from 3 independent experiments. Values are given as a percentage (± SD) of cell death. (D) Graphic of densitometric values of CYCS release, expressed as mean fluorescence of individual cells, normalized to total cellular surface (F:A, n=30 cells/groups). (E) HEK293 cells transfected with a vector encoding AMBRA1^{CT} or AMBRA1^{BH3-AE} were analyzed by western blot using antibodies against activated BAX and total BAX. The band density ratio of activated BAX/total BAX was analyzed in 3 independent experiments; each point value represents the mean ± SD from 3 independent experiments. Statistical analysis was performed using the Student *t* test (**P* < 0.05).

Human cancer grows by evading cell death. In fact, some cancers, and in particular breast cancers, express high levels of BCL2. Proteins from the BCL2 family are involved in MOMP, a phenomenon mediating CYCS release from mitochondria (essential in cell death induction) and, for this

reason, MOMP is a good target in cancer therapy. Indeed, BH3 mimetics are already used in chemotherapy and have provided beneficial insights into the regulation of the BCL2-BECN1 complex as well as in identifying additional pathways involved in autophagic cell death. ABT-737 and

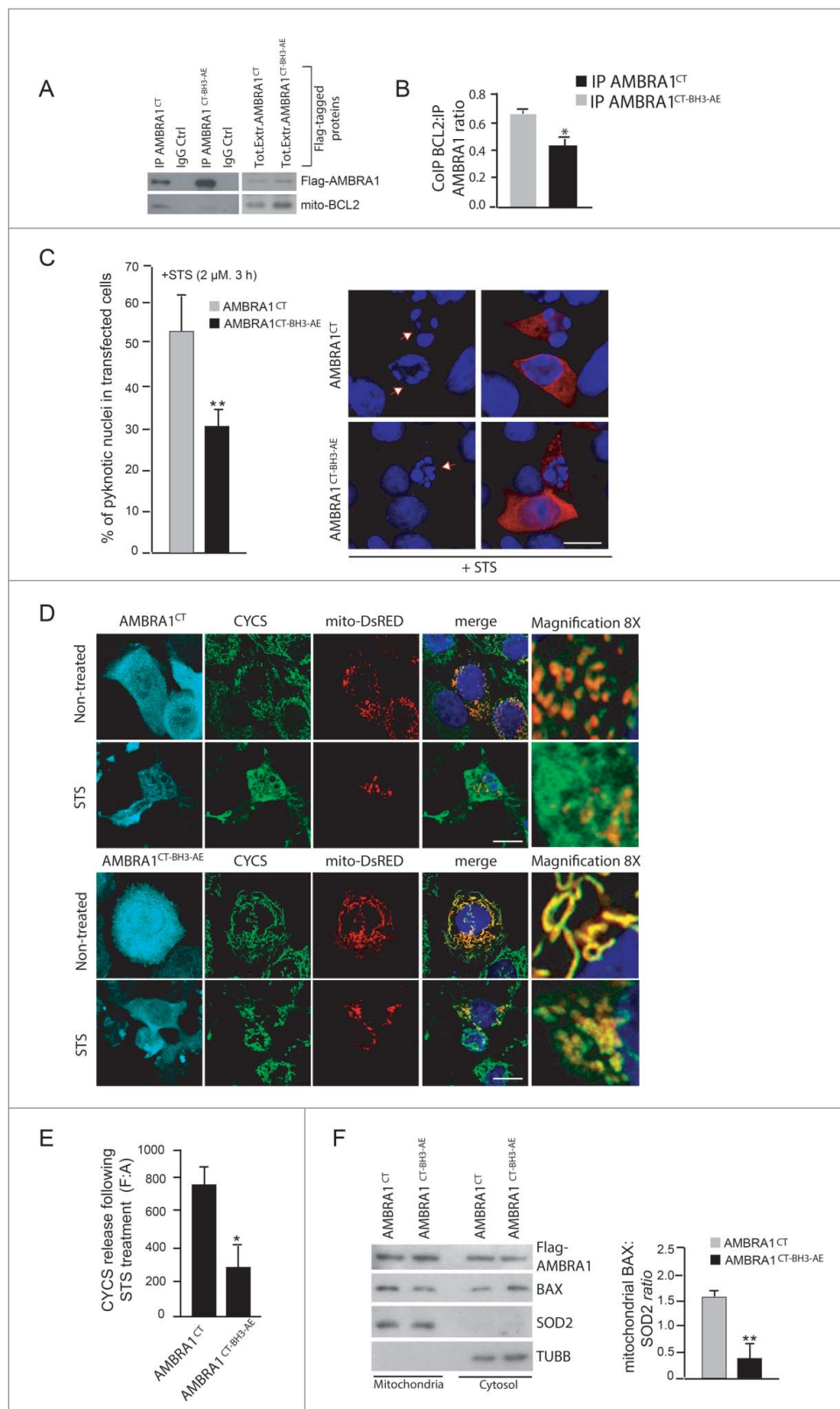


Figure 6. For figure legend, see next page.

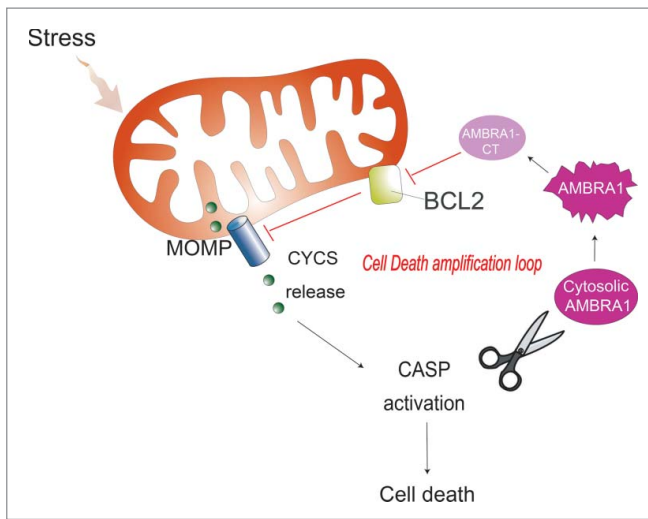


Figure 7. The proposed working model for AMBRA1 in mitochondrial apoptosis. Upon induction of apoptosis, AMBRA1 is subjected to CASP cleavage. In the initial phase of apoptosis, the C-terminal fragment of AMBRA1 is stable and interacts directly with BCL2 through its BH3-like domain, thus likely increasing cell death (cell death amplification loop).

HA14-1 also stimulate other proautophagic pathways and hence activate the nutrient sensors SIRT1 (sirtuin 1) and AMPK, inhibit MTOR, deplete cytoplasmic TP53/p53, and trigger the CHUCK/IKK α and IKBKB/IKK β kinases.²⁴ Here we propose a novel mechanism of action of ABT-737, which disrupts the interaction between AMBRA1 and mito-BCL2, thus contributing to autophagy induction. Consequently, exploiting the AMBRA1-BCL2 interaction could be used to develop novel anticancer therapies.

BCL2 is upregulated in human breast cancers and mediates the resistance of these cancers to chemotherapeutic strategies,^{25,26} while, by contrast, AMBRA1 is an haploinsufficient tumor suppressor gene;²⁷ given both these factors, modulating the reciprocal AMBRA1 and BCL2 levels in cancer cells by targeting their interaction could contribute to early diagnosis and to predicting prognosis for breast cancer.

Further studies are needed to discover binding partners that can alter the reciprocal affinity of BCL2 and AMBRA1 at the mitochondria. It should also be interesting to investigate whether post-translational modifications on AMBRA1 (such as its phosphorylation by kinases) regulate this

binding. Developing combination therapies between BH3 mimetics and kinase activators could provide a powerful “double effect” on the AMBRA1-BCL2 complex. In conclusion, identification of the mechanisms that maintain or disrupt this complex may allow us to develop additional drugs that can target it, thus ensuring an improved therapeutic outcome.

Materials and methods

Antibodies

Mouse monoclonal anti-ACTB/ β actin (Sigma-Aldrich, A2228), monoclonal anti-BCL2 (Santa Cruz Biotechnology, sc-7382), polyclonal anti-AMBRA1 (Novus, 26190002), monoclonal anti-AMBRA1 (Santa Cruz Biotechnology, sc-398204), mouse monoclonal anti-CYCS (Assay designs-Enzo Life Sciences, 6H2-B4), polyclonal anti-LC3 (Cell Signaling Technology, 2775), monoclonal anti-SQSTM1/p62 (Santa Cruz Biotechnology, sc-28369), polyclonal anti-activated BAX (6A7; Abcam 5714), polyclonal anti-BAX (Santa Cruz Biotechnology, sc-493, N-20), polyclonal anti-PARP1 (Cell Signaling Technology, 9542), goat anti-BAK1 (G-23; Santa Cruz Biotechnology, sc-832), mouse monoclonal anti-MYC (9E10; Santa Cruz Biotechnology, sc-4), mouse monoclonal anti-Flag (Sigma-Aldrich, F3165), rabbit polyclonal anti-SOD2/MnSOD (Enzo Life Sciences, 110F) and mouse monoclonal anti-TUBB/ β tubulin (Sigma-Aldrich, T9026).

Cloning and plasmids

Construct coding for AMBRA1^{WT}, AMBRA1^{D482A} and AMBRA1^{CT} (483-1300 amino acids) was cloned in pLPCX vector (Clontech, 631511).¹⁸

The construct coding for “mito-BCL2,” a mitochondrial-targeted BCL2 in which the C-terminal hydrophobic sequence of BCL2 is exchanged for an equivalent sequence from modified ActA (*Listeria monocytogenes* actin assembly-inducing protein) which binds specifically to the cytoplasmic face of mitochondrial outer membranes, was kindly provided by Beth Levine⁹ and was cloned in pRCMV vector.

The mito-DsRED construct encodes for human Cox8A mitochondria signal which is fused with wild-type-DsRED in pcDNA3 vector (Invitrogen).

We summarized in the table all constructs used in the present work:

Figure 6. (See previous page). The mutant form of cleaved AMBRA1 that cannot bind BCL2 loses its proapoptotic effect during cell death. (A) HEK293 cells were transfected with a vector encoding Flag-AMBRA1^{CT} or Flag-AMBRA1^{CT-BH3-AE}. Twenty-four h after transfection, total extracts were next immunoprecipitated using an anti-Flag antibody. Purified complexes were analyzed by western blot (WB) using anti-AMBRA1 and anti-BCL2 antibodies. (B) The band density ratio of immunoprecipitated AMBRA1 relative to immunoprecipitated BCL2 was analyzed in 3 independent experiments; each point value represents the mean \pm SD from 3 independent experiments. Statistical analysis was performed using the Student *t* test (*, $P < 0.05$) vs. CT. (C) HEK293 cells were transfected with a vector encoding Flag-AMBRA1^{CT} or Flag-AMBRA1^{CT-BH3-AE}. Twenty-four h following transfection, cells were treated with 2 μ M STS during 2 h. Cells were next fixed and examined by immunolabelling using anti-AMBRA1 antibody that recognizes only the overexpressed form of the protein and cells with condensed or fragmented nuclei were scored as pyknotic. Results are expressed as the percentage of transfected cells displaying pyknotic nuclei. For each condition, transfected cells were counted in 10 random fields from 3 independent experiments. Values are given as a percentage (\pm SD) of cell death. (D) HEK293 cells were cotransfected with a vector encoding Flag-AMBRA1^{CT} or Flag-AMBRA1^{CT-BH3-AE} and mito-DsRED (in order to stain mitochondria). Cells were then treated with STS 2 μ M during 4 h and stained using an anti-CYCS antibody (green). Nuclei were stained with DAPI 1 μ g/ μ l during 20 min. The merging of the different fluorescence signals is illustrated. Scale bar: 8 μ m. (E) Graphic of densitometric values of CYCS release, expressed as mean fluorescence of individual cells, normalized to total cellular surface (F:A, n=30 cells/groups). (F) HEK293 cells were transfected with a vector encoding Flag-AMBRA1^{CT} or Flag-AMBRA1^{CT-BH3-AE}. Twenty-four h after transfection, cytosolic and mitochondrial fractions were analyzed by western blot (WB) using anti-BAX and anti-SOD2 antibodies. The band density ratio of translocated BAX on mitochondria was analyzed in 3 independent experiments; each point value represents the mean \pm SD from 3 independent experiments. Statistical analysis was performed using the Student *t* test (**, $P < 0.01$) versus CT.

Constructs	Type of mutation	Feature
Flag-tagged-AMBRA1 ^{D482A}	Single-point mutation (D482 → A) on the predicted caspase cleavage site of AMBRA1	This mutant of AMBRA1 is uncleavable by caspases following apoptosis induction and maintains its proautophagic activity
MYC-tagged-AMBRA1 ^{WT}	No mutation	This construct encodes for the wild-type form of AMBRA1
MYC-tagged-AMBRA1 ^{BH3-AE}	Two-point mutations in the BH3 domain of AMBRA1 L1215 → A and G1219 → E	This mutant of AMBRA1 partially loses its binding with mito-BCL2 protein
Flag-tagged-AMBRA1 ^{CT}	Terminal fragment of AMBRA1 resulting from caspase cleavage (483-1300 amino acids)	This construct encodes for the C-terminal part of AMBRA1 resulting from caspase cleavage. This fragment binds mito-BCL2
Flag-tagged-AMBRA1 ^{CT-BH3-AE}	Two-point mutations in the BH3 domain of the C-terminal fragment of AMBRA1 L1215 → A and G1219 → E resulting from caspase cleavage (483-1300 amino acids)	This construct encodes a C-terminal fragment of AMBRA1 which partially loses its binding with mito-BCL2
Mito-BCL2	The mitochondrial-targeted BCL2 presents the C-terminal hydrophobic sequence of BCL2 exchanged for an equivalent sequence from modified ActA (<i>Listeria monocytogenes</i> Actin assembly-inducing protein), which binds specifically to the cytoplasmic face of mitochondrial outer membranes. In this case BCL2 is fused with ActA sequence.	This construct encodes a BCL2 protein that is specifically targeted to the mitochondria where it acts as an antiapoptotic factor.
Mito-DsRED	Human Cox8A mitochondria signal is fused with wild-type-DsRED protein in pCDNA3 vector.	This construct encodes for a red protein that is targeted to the mitochondria. It is used in microscopy analysis in order to stain the mitochondria network.

Point mutations were generated using the QuickChange site-directed mutagenesis kit (Stratagene, 200519) and all plasmid constructs made in this study were verified by DNA sequencing (Eurofins). The oligonucleotides used for mutagenesis, PCR, and DNA sequencing were purchased from Invitrogen.

Cell cultures

The human embryonic kidney HEK293 cells and HeLa cells were cultured in Dulbecco's modified Eagle's medium (Lonza, BE12-604F) supplemented with 10% FBS (Gibco; Thermo Fisher Scientific, 10270-106), and 1% penicillin-streptomycin solution (Lonza, 17-602 E) at 37°C under 5% CO₂.

Cell culture transfection

Transient transfections of expression plasmids into HEK293 cells were performed using TurboFect according to the supplier's instructions (Thermo Fisher Scientific, R0532).

Determination of cell viability

Cell survival was estimated by using the MTS assay or by counting the number of condensed or fragmented nuclei as observed using DAPI (Sigma Aldrich, D9542) staining. The tetrazolium salt MTS (3-[4,5-dimethyl-2-thiazolyl]-2-5diphenyl-2H tetrazolium bromide; Sigma Aldrich, M2128) was added to cell cultures (1 mg/ml) and incubated for 30 min at 37°C. Cells were then lysed in DMSO (Sigma Aldrich, 472301). Formazan production by living cells was assessed by measuring absorbance at 540 nm using a Biotek Elx-800 microplate reader (Mandel Scientific Inc.) For cell counting, cultures were fixed in 4% paraformaldehyde (Merck Millipore, 104005) in PBS (UCS Diagnostic, PBS1199) for 10 min at 4°C and stained with DAPI in PBS for 20 min at room temperature. Cells were washed 3 times with PBS, then mounted and observed under a ZEISS confocal laser microscope (CLSM700; Jena, Germany). For each condition, random images were captured and analyzed using Zen Light edition software. Cell viability was then scored on the basis of nuclear morphology: cells containing condensed or fragmented nuclei were counted as dying or dead cells.

Immunocytochemistry

Cells were washed in PBS and fixed with 4% paraformaldehyde in PBS for 15 min. After permeabilization with 0.4% Triton X-100 (Sigma Aldrich, X100) in PBS for 5 min, cells were blocked in 3% normal goat serum (Sigma-Aldrich, G9023) in PBS and incubated overnight at 4 degrees with primary antibodies. We used the antibodies directed against AMBRA1 and CYCS. Cells were then washed in blocking buffer and incubated for 1 h with labeled anti-mouse (Alexa Fluor 488; Thermo Fisher Scientific, A11017) or anti-rabbit (CyTM3; Jackson ImmunoResearch, 115-165-166) secondary antibodies. Nuclei were stained with 1 μg/ml DAPI and examined under a Zeiss LSM 700 100x oil-immersion objective (CLSM700; Jena, Germany). We used "ZEN 2009 Light edition" software for image analysis. All acquisitions were performed in non-saturated single z-confocal planes.

Western blot analysis

Cell extracts were centrifuged at 13,000 g for 10 min at 4°C. Protein concentrations were determined with the Bio-Rad Protein Assay Kit (Bio-Rad, 5000001). Cell extracts or immunoprecipitates were separated by SDS-PAGE and transferred onto nylon membranes (Immobilon P; Merck-Millipore, IPFL10100). Membranes were incubated with primary antibodies followed by horseradish peroxidase-conjugate secondary antibody (Bio-Rad, 1706515 and 1721011) and visualized with ECL (Merck-Millipore WBKLS0500).

Immunoprecipitation

Cells were lysed in RIPA buffer plus protease inhibitor cocktail (Sigma Aldrich, P8340). Equal amounts of protein (500 μg) were incubated with 2 μl of monoclonal anti-MYC antibody for 4 h followed by 60 min incubation with 30 μl of protein A

agarose beads (Roche, 11719408001). The beads were collected by centrifugation and washed 4 times with the RIPA buffer. Proteins bound to the beads were eluted with 30 μ l of SDS-polyacrylamide gel electrophoresis sample buffer and heated to 95°C for 10 min.

Mitochondria/cytosol purification

Mitochondria and cytosol purification occurs by standard differential centrifugations. HEK293 cells were suspended in homogenization buffer (0.25 M sucrose, 10 mM HEPES, pH 7, 1 mM EDTA [Sigma-Aldrich, S0389, H4034, and ED-100, respectively]) with protease and phosphatase inhibitors. Mitochondria suspensions were obtained homogenizing the solution with 40°–60 pulses (one pulse corresponds to approximately one sec), in vertical movements. After homogenization, the suspension was centrifuged at 11 000 g for 15 min at 4°C. The mitochondrial pellet fraction was suspended in isolation buffer (0.2 M sucrose, 10 mM Tris-MOPS [Sigma, M1254], pH 7.4, 0.1 mM EGTA-Tris [Sigma Aldrich, E4378]). The supernatant fraction corresponded to soluble cytosolic proteins.

Size-exclusion fast protein liquid chromatography (sec-FPLC)

Two milligrams of HEK293 cell lysate, obtained from DMSO-treated cells or staurosporine-treated cells, were injected onto a Superose 6 HR 10/30 fast protein liquid chromatography (FPLC) gel filtration column (Amersham Pharmacia Biosciences, 17-0537-01) connected to a Pharmacia LKB LCC 501 Plus FPLC System (Amersham Pharmacia LKB Biotechnologies, Piscataway, N.J.). Lysate preparation and column equilibration have been previously described.⁵ CAPN (calpain II inhibitor, 50 μ M; Sigma-Aldrich, A6060) and CASP (Q-VD-OPH, 100 μ M; Santa Cruz Biotechnology, sc-222230) inhibitors were added in the lysis buffer in order to prevent AMBRA1 cleavage during the fraction separation. Proteins were collected in 500 μ l fractions, precipitated with 10% trichloroacetic acid, and resolved in SDS-PAGE for western blot analyses. Gel filtration column was calibrated as previously described.²⁵ Equal amounts of each fraction were analyzed by western blot.

Quantification of CYCS release

Quantification of CYCS release from mitochondria was performed on transfected cells by densitometric analyses, as previously described.²⁸ After background subtraction, CYCS cell-associated signals were quantified by manually outlining individual cells and measuring cell-associated fluorescence intensity with the ImageJ software (<http://rsb.info.nih.gov/ij/>). The F:A ratio defines mean fluorescence of individual cells (F) normalized to total cellular surface (A).

Statistical analyses

Statistical analyses were performed using the Student 2-tailed *t*-test. Data were shown as means \pm SD of 3 independent experiments. Values of $p < 0,05$ were considered significant.

Abbreviations

AMBRA1	autophagy/Beclin 1 regulator 1
AMBRA1 ^{BH3-AE}	autophagy/Beclin 1 regulator 1, mutated in BH3 motif
AMBRA1 ^{CT}	C-terminal part of AMBRA1
AMBRA1 ^{CT-BH3-AE}	C-terminal part of AMBRA1, mutated in BH3 motif
BAX	BCL2-associated X protein
BCL2	B-cell CLL/lymphoma 2
BECN1	Beclin 1, autophagy related
BH3	BCL2 homology domain 3
CASP	caspace
CYCS	cytochrome c, somatic
FPLC	fast protein liquid chromatography
HEK293	human embryonic kidney
MOMP	mitochondrial outer membrane permeabilization
Mito-BCL2	mitochondrial targeted BCL2
PARK2	parkin RBR E3 ubiquitin protein ligase
STS	staurosporin

Disclosure of potential conflicts of interest

The authors declare no conflict of interest.

Acknowledgments

We thank M. Acuña Villa and M. Bennett for secretarial and proofreading work, and V. Nanni and B. Biferali for research assistance. We are indebted to B. Levine (Dallas, TX), for kindly providing us with the mito-BCL2 construct and M. Priault (Bordeaux, France) for kindly providing us with the MCL1 and BCL2L1 constructs.

Funding

This work was supported in part by grants from the Telethon Foundation (GGP14202), AIRC (IG2013 to FC, IG2012-13529 and IG 2015-17404 to GMF), FISM (2013), the Italian Ministry of University and Research (FIRB Accordi di Programma 2011), the Italian Ministry of Health (Ricerca Finalizzata and Ricerca Corrente to FC and GMF, Progetto Giovani Ricercatori GR2011-2012 to FS). VC is supported by the Lundbeck Foundation (R165-2013-15982). This work has been also supported by a KBVU grant from the Danish Cancer Society (R72-A4408). We are also grateful to the Bjarne Saxhof Foundation, the Lundbeck Foundation (R167-2013-16100), and the NovoNordisk Foundation (7559). Further, FC lab in Copenhagen is part of the Center of Excellence in Autophagy, Recycling and Disease (CARD), funded by the Danish National Research Foundation.

References

- [1] Fimia GM, Stoykova A, Romagnoli A, Giunta L, Nardacci R, Corazzari M, Fuoco C, Ucar A, Schwartz P, Gruss P, et al. Ambra1 regulates autophagy and development of the nervous system. *Nature* 2007; 447: 1121-1125; PMID:17589504
- [2] Di Bartolomeo S, Corazzari M, Nazio F, Oliverio S, Lisi G, Antonioli M, Paglierini V, Mattoni S, Fuoco C, Giunta L, et al. The dynamic interaction of AMBRA1 with the dynein motor complex regulates mammalian autophagy. *J Cell Biol.* 2010; 191:155-68; PMID:20921139; <http://dx.doi.org/10.1083/jcb.201002100>
- [3] He C, Levine B. The Beclin 1 interactome. *Curr Opin Cell Biol.* 2010; 2:140-9; <http://dx.doi.org/10.1016/j.ccb.2010.01.001>
- [4] Nazio F, Strappazzon F, Antonioli M, Bielli P, Cianfanelli V, Bordini M, Gretzmeier C, Dengjel J, Piacentini M, Fimia GM, et al. mTOR inhibits autophagy by controlling ULK1 ubiquitination, self-association and function via AMBRA1 and TRAF6. *Nat Cell Biol.* 2013; 4:406-16; <http://dx.doi.org/10.1038/ncb2708>

- [5] Cianfanelli V, Fuoco C, Lorente M, Salazar M, Quondamatteo F, Gherardini PF, De Zio D, Nazio F, Antonioli M, D'Orazio M, et al. AMBRA1 links autophagy to cell proliferation and tumorigenesis by promoting c-Myc dephosphorylation and degradation. *Nat Cell Biol.* 2015; 17:20-30; PMID:25438055; <http://dx.doi.org/10.1038/ncb3072>
- [6] Antonioli M, Albiero F, Nazio F, Vescovo T, Perdomo AB, Corazzari M, Marsella C, Piselli P, Greztmeier P, Denjiel J, et al. AMBRA1 interplay with cullin E3 ubiquitin ligases regulates autophagy dynamics. *Dev Cell.* 2014; 6:734-46; <http://dx.doi.org/10.1016/j.devcel.2014.11.013>
- [7] Strappazzon F, Vietri-Rudan M, Campello S, Nazio F, Florenzano F, Fimia GM, Piacentini M, Levine B, Cecconi F. Mitochondrial BCL-2 inhibits AMBRA1-induced autophagy. *Embo j.* 2011; 30:1195-208; PMID:21358617; <http://dx.doi.org/10.1038/emboj.2011.49>
- [8] Strappazzon F, Nazio F, Corrado M, Cianfanelli V, Romagnoli A, Fimia GM, Campello S, Nardacci R, Piacentini M, Campanella M, et al. AMBRA1 is able to induce mitophagy via LC3 binding, regardless of PARKIN and p62/SQSTM1. *Cell Death Differ.* 2015; 3:419-32; <http://dx.doi.org/10.1038/cdd.2014.139>
- [9] Pattingre S, Tassa A, Qu X, Garuti R, Liang XH, Mizushima N, Packer M, Schneider MD, Levine B. Bcl-2 antiapoptotic proteins inhibit Beclin 1-dependent autophagy. *Cell* 2005; 122:927-39; PMID:16179260; <http://dx.doi.org/10.1016/j.cell.2005.07.002>
- [10] Chang NC, Nguyen M, Germain M, Shore GC. Antagonism of Beclin 1-dependent autophagy by BCL-2 at the endoplasmic reticulum requires NAF-1. *Embo J* 2010; 29:606-18; PMID:20010695; <http://dx.doi.org/10.1038/emboj.2009.369>
- [11] Cho DH, Jo YK, Hwang JJ, Lee YM, Roh SA, Kim JC. Caspase-mediated cleavage of ATG6/Beclin-1 links apoptosis to autophagy in HeLa cells. *Cancer Lett.* 2009; 274:95-100; PMID:18842334; <http://dx.doi.org/10.1016/j.canlet.2008.09.004>
- [12] Luo S, Rubinsztein DC. Apoptosis blocks Beclin 1-dependent autophagosome synthesis: an effect rescued by Bcl-xL. *Cell Death Differ* 2010; 17:268-277; PMID:19713971; <http://dx.doi.org/10.1038/cdd.2009.121>
- [13] Zhu Y, Zhao L, Liu L, Gao P, Tian W, Wang X, Jin H, Xu H, Chen Q. Beclin 1 cleavage by caspase-3 inactivates autophagy and promotes apoptosis. *Protein Cell* 2010; 1:468-477; PMID:21203962; <http://dx.doi.org/10.1007/s13238-010-0048-4>
- [14] Djavaheri-Mergny M, Maiuri MC, Kroemer G. Cross talk between apoptosis and autophagy by caspase-mediated cleavage of Beclin 1. *Oncogene* 2010; 12:1717-9; <http://dx.doi.org/10.1038/onc.2009.519>
- [15] Maiuri MC, Ciriollo A, Kroemer G. Crosstalk between apoptosis and autophagy within the Beclin 1 interactome. *Embo J* 2010; 29:515-6; PMID:20125189; <http://dx.doi.org/10.1038/emboj.2009.377>
- [16] Pyo JO, Jang MH, Kwon YK, Lee HJ, Jun JI, Woo HN, Cho DH, Choi B, Lee H, Kim JH, et al. Essential roles of Atg5 and FADD in autophagic cell death: dissection of autophagic cell death into vacuole formation and cell death. *J. Biol. Chem.* 2005; 280:20722-9; PMID:15778222; <http://dx.doi.org/10.1074/jbc.M413934200>
- [17] Yousefi S, Perozzo R, Schmid I, Ziemiecki A, Schaffner T, Scapozza L, Brunner T, Simon HU. Calpain-mediated cleavage of Atg5 switches autophagy to apoptosis. *Nat. Cell Biol.* 2006; 8:1124-32; PMID:16998475; <http://dx.doi.org/10.1038/ncb1482>
- [18] Zalckvar E, Yosef N, Reef S, Ber Y, Rubinstein AD, Mor I, Sharan R, Ruppin E, Kimchi A. A systems level strategy for analyzing the cell death network: implication in exploring the apoptosis/autophagy connection. *Cell Death Differ.* 2010; 17:1244-53; PMID:20150916; <http://dx.doi.org/10.1038/cdd.2010.7>
- [19] Maskey D, Yousefi S, Schmid I, Zlobec I, Perren A, Friis R, Simon HU. ATG5 is induced by DNA-damaging agents and promotes mitotic catastrophe independent of autophagy. *Nat Commun.* 2013; 4:2130; PMID:23945651; <http://dx.doi.org/10.1038/ncomms3130>
- [20] Pagliarini V, Wirawan E, Romagnoli A, Ciccocanti F, Lisi G, Lippens S, Cecconi F, Fimia GM, Vandenabeele P, Corazzari M, et al. Proteolysis of Ambra1 during apoptosis has a role in the inhibition of the autophagic pro-survival response. *Cell Death Differ.* 2012; 9:1495-504; <http://dx.doi.org/10.1038/cdd.2012.27>
- [21] Rubinstein AD, Eisenstein M, Ber Y, Bialik S, Kimchi A. The autophagy protein Atg12 associates with antiapoptotic Bcl-2 family members to promote mitochondrial apoptosis. *Mol Cell.* 2011; 5:698-709; <http://dx.doi.org/10.1016/j.molcel.2011.10.014>
- [22] Lee JY, Nagano Y, Taylor JP, Lim KL, Yao TP. Disease-causing mutations in parkin impair mitochondrial ubiquitination, aggregation, and HDAC6-dependent mitophagy. *J Cell Biol.* 2010; 4:671-9; <http://dx.doi.org/10.1083/jcb.201001039>
- [23] Cianfanelli V, De Zio D, Di Bartolomeo S, Nazio F, Strappazzon F, Cecconi F. Ambra1 at a glance. *Cell Science at a glance* 2015; 11:2003-8; <http://dx.doi.org/10.1242/jcs.168153>
- [24] Malik SA, Shen S, Mariño G, BenYounès A, Maiuri MC, Kroemer G. BH3 mimetics reveal the network properties of autophagy-regulatory signaling cascades. *Autophagy.* 2011; 8:914-6; <http://dx.doi.org/10.4161/auto.7.8.15785>
- [25] Huang Z. Bcl-2 family proteins as targets for anticancer drug design. *Oncogene* 19:6627-31; PMID:11426648; <http://dx.doi.org/10.1038/sj.onc.1204087>
- [26] Karnak D, Xu L. Chemosensitization of prostate cancer by modulating Bcl-2 family proteins. *Curr Drug Targets* 2010; 11:699-707; PMID:20298153; <http://dx.doi.org/10.2174/138945010791170888>
- [27] Cianfanelli V, D'Orazio M, Cecconi F. AMBRA1 and BECLIN 1 interplay in the crosstalk between autophagy and cell proliferation. *Cell cycle* 2015; 14:959-63; PMID:25803737; <http://dx.doi.org/10.1080/15384101.2015.1021526>
- [28] Oddi S, Latini L, Viscomi MT, Bisicchia E, Molinari M, Maccarrone M. Distinct regulation of nNOS and iNOS by CB2 receptor in remote delayed neurodegeneration. *J Mol Med (Berl)* 2012; 90:371-87; PMID:22198001; <http://dx.doi.org/10.1007/s00109-011-0846-z>



HUWE1 controls MCL1 stability to unleash AMBRA1-induced mitophagy

Flavie Strappazon¹ · Anthea Di Rita^{1,2} · Angelo Peschiaroli³ · Pier Paolo Leoncini⁴ · Franco Locatelli^{4,5} · Gerry Melino^{6,7} · Francesco Ceconi^{2,8,9}

Received: 28 January 2019 / Revised: 24 July 2019 / Accepted: 26 July 2019
© The Author(s), under exclusive licence to ADMC Associazione Differenziamento e Morte Cellulare 2019

Abstract

Receptor-mediated mitophagy is a crucial process involved in mitochondria quality control. AMBRA1 is a mitophagy receptor for the selective removal of damaged mitochondria in mammalian cells. A critical unresolved issue is how AMBRA1-mediated mitophagy is controlled in response to cellular stress. Here, we investigated the role of BCL2-family proteins on AMBRA1-dependent mitophagy and showed that MCL1 delays AMBRA1-dependent mitophagy. Indeed, MCL1 overexpression is sufficient to inhibit recruitment to mitochondria of the E3 Ubiquitin ligase HUWE1, a crucial dynamic partner of AMBRA1, upon AMBRA1-mediated mitophagy induction. In addition, we found that during mitophagy induced by AMBRA1, MCL1 levels decreased but were sustained by inhibition of the GSK-3 β kinase, which delayed AMBRA1-mediated mitophagy. Also, we showed that MCL1 was phosphorylated by GSK-3 β at a conserved GSK-3 phosphorylation site (S159) during AMBRA1-mediated mitophagy and that this event was accompanied by HUWE1-dependent MCL1 degradation. Altogether, our results demonstrate that MCL1 stability is regulated by the kinase GSK-3 β and the E3 ubiquitin ligase HUWE1 in regulating AMBRA1-mediated mitophagy. Our work thus defines MCL1 as an upstream stress-sensitive protein, functional in AMBRA1-mediated mitophagy.

Introduction

Autophagy is an important eukaryotic process involved in the lysosomal degradation of cytosolic components in

both physiological and pathological conditions. During autophagy, the autophagosomes engulf a number of different cargoes and then fuse with lysosomes for subsequent recycling of their content [1]. Several key proteins are involved in the autophagosome formation, such as BECLIN 1 and its positive regulator AMBRA1 [1, 2]. Mitophagy is a selective form of autophagy essential for the elimination of impaired or depolarized mitochondria. It is important for a cell to remove damaged mitochondria, since wanton release of reactive oxygen

Edited by H.-U. Simon

Supplementary information The online version of this article (<https://doi.org/10.1038/s41418-019-0404-8>) contains supplementary material, which is available to authorized users.

✉ Flavie Strappazon
f.strappazon@hsantalucia.it

✉ Francesco Ceconi
ceconi@cancer.dk

¹ IRCCS Fondazione Santa Lucia, 00143 Rome, Italy

² Department of Biology, University of Rome Tor Vergata, 00133 Rome, Italy

³ National Research Council of Italy (CNR) Institute of Translational Pharmacology IFT Via Fosso del Cavaliere 100, 00133 Rome, Italy

⁴ Department of Paediatric Oncohematology and Cell and Gene

therapy, IRCCS Ospedale pediatrico Bambino Gesù, 00143 Rome, Italy

⁵ Department of Gynecology/Obstetrics and Pediatrics, Sapienza University, Rome, Italy

⁶ Department of Experimental Medicine, TOR, University of Rome Tor Vergata, 00133 Rome, Italy

⁷ MRC Toxicology Unit, University of Cambridge, Cambridge, UK

⁸ Unit of Cell Stress and Survival, Center for Autophagy, Recycling and Disease (CARD), Danish Cancer Society Research Center, 2100 Copenhagen, Denmark

⁹ Department of Pediatric Hematology and Oncology, IRCCS Bambino Gesù Children's Hospital, Rome, Italy

intermediates leads to inflammasome activation, genotoxic stress, promotion of tumorigenesis, and aging. Accordingly, alteration of the mitophagic pathway may contribute to neurodegenerative or inflammatory diseases, cancer, and decreased lifespan [3]. Damaged mitochondria activate the PINK1/PARKIN pathway, the major mitophagic molecular axis described so far. PINK1, which is constantly degraded, is instead stabilized to mitochondria, resulting in the recruitment of the PARKIN E3 ubiquitin ligase to damaged mitochondria and in the ubiquitination of several outer mitochondria membrane proteins. Mitophagy receptors that bind ubiquitin, such as NDP52 and OPTINEURIN, and the autophagosome-associated protein LC3, then favor the engulfment of damaged mitochondria into autophagosomes [4, 5].

Mitophagy occurs also in cells lacking detectable PARKIN, through alternative mitophagy receptors. For example, BNIP3 (BCL2/adenovirus E1B 19 kDa interacting protein 3) and its homolog NIX/BNIP3L (BCL2/adenovirus E1B 19 kDa interacting protein 3 like) are two mitophagy receptors able to regulate mitochondrial clearance during reticulocyte development. They possess a LC3-interacting region (LIR) that facilitate the binding to LC3B (Microtubule-associated protein 1A/1B light chain 3B) (for BNIP3) [6] or to the other mATG8-family member Gamma-AminoButyric Acid Receptor-Associated Protein (for NIX/BNIP3L) [7]. FUN14 domain-containing protein 1 is another mitophagy receptor located at the mitochondria, with a LIR domain that mediates its association with LC3B during hypoxia or following mitochondrial membrane depolarization [8]. Prohibitin 2, an inner mitochondria membrane protein, is another key mitophagy receptor for both PARKIN-mediated mitophagy in mammalian cells and for paternal mitochondrial clearance in *C. elegans* [9]. Recently, we showed that AMBRA1, also a LIR-containing protein, is a new mitophagic receptor crucial in order to both amplify PARKIN-mediated mitochondrial clearance and regulate PARKIN-independent mitophagy [10, 11]. Similar to BNIP3, NIX/BNIP3L, and FUNDC1, AMBRA1 can be positively regulated by a specific phosphorylation upstream its LIR domain [11].

Since BCL2-family proteins [12–17] can control mitophagy [18, 19] and since we previously demonstrated that AMBRA1 can bind BCL2-family proteins [20, 21], we decided to investigate a putative regulatory role for BCL2-family members on AMBRA1-dependent mitophagy. We thus found that MCL1 is a potent inhibitor of AMBRA1-mediated mitophagy, and discovered that MCL1 destabilization by the Glycogen Synthase kinase-3 β (GSK-3 β) and the E3 ubiquitin ligase HUWE1 is a key event for this specific mitophagy pathway. In sum, this work unveils a novel mechanism for mitophagy regulation, linking it to the BCL2 death factors.

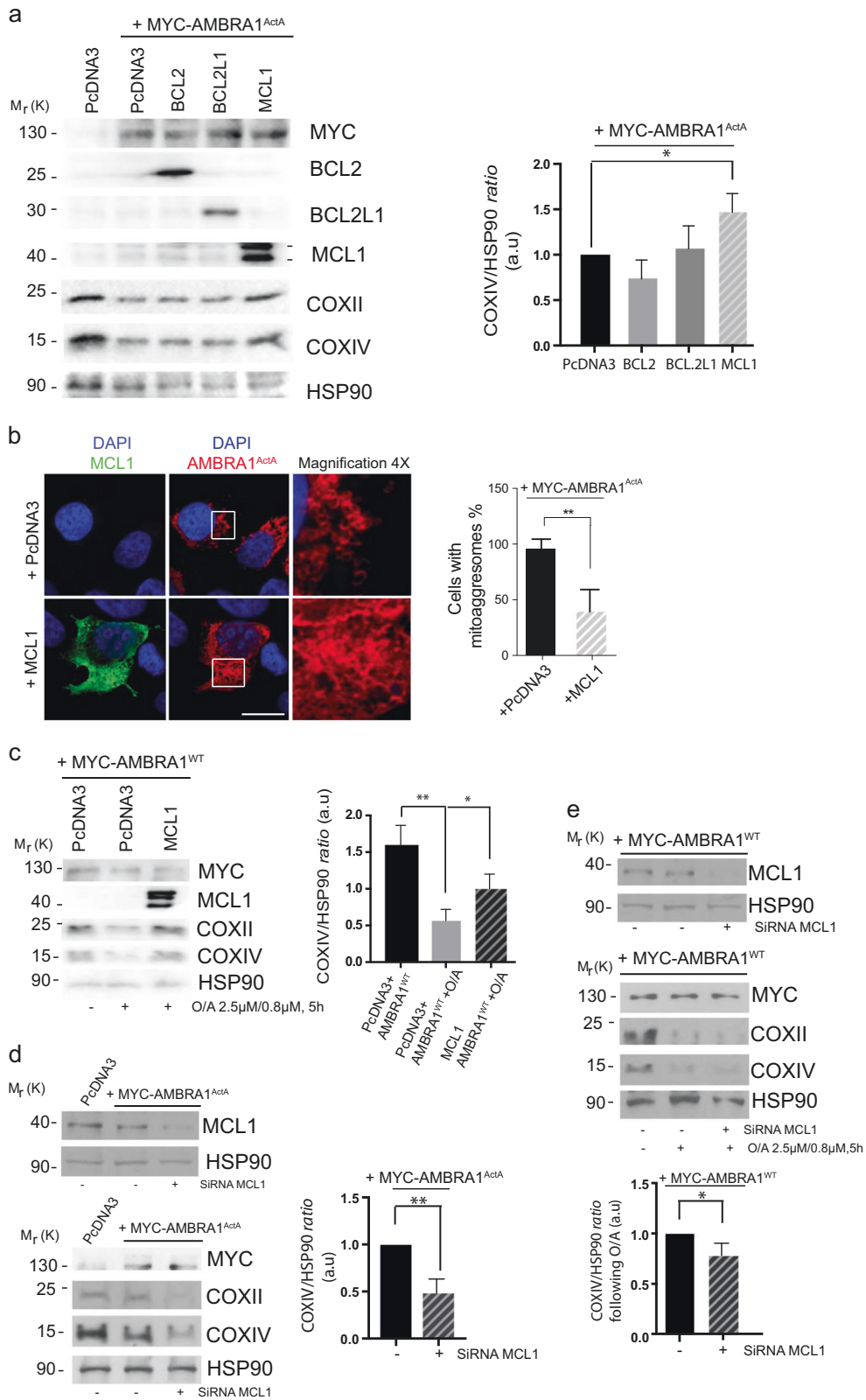
Results

AMBRA1-dependent mitophagy is inhibited by the anti-apoptotic factor MCL1

HeLa cells (a well-known PARKIN-free cellular system) rapidly undergo mitophagy when overexpress either AMBRA1^{ActA}, a protein fusion that specifically targets AMBRA1 to the mitochondria, or AMBRA1^{WT} in combination with mitophagy inducers [i.e. Olygomycin/Actinomycin (O/A), or protonophores such as CCCP or FCCP] [10, 11, 22]. To characterize the role of BCL2-family proteins on AMBRA1-mediated mitophagy, we first checked whether overexpression of these proteins was capable to regulate mitophagy in HeLa cells. Interestingly, we found that MCL1 expression was sufficient to reduce mitophagy induced by AMBRA1^{ActA}. First, by performing a western blot analysis upon the coexpression of AMBRA1^{ActA} and individual BCL2 proteins, we observed a strong decrease in the clearance of both COXII and COXIV, two mitochondrial markers (Fig. 1a and Supplementary Fig. 1a). Of note, no other members of the BCL2-family did significantly inhibit mitophagy in the same conditions. We next confirmed these results by performing a confocal microscopy analysis, by which we checked for AMBRA1^{ActA}-induced mitoagosome formation, a typical feature of AMBRA1^{ActA}-mediated mitophagy [10]. As illustrated in Fig. 1b, the mitochondrial network is less aggregated around the nucleus when cells are expressing MCL1 in combination with AMBRA1^{ActA}, at variance with cells expressing only AMBRA1^{ActA}. Then, we decided to check whether MCL1 was able to inhibit mitophagy induced by wild-type AMBRA1 (AMBRA1^{WT}) in combination with a mitophagy inducer. As shown in Fig. 1c and Supplementary Fig. 1b, both COXII and COXIV loss is decreased in cells overexpressing AMBRA1^{WT} and MCL1 and treated with O/A for 5 h. Primed by these results, we next decided to interfere MCL1 by using specific siRNAs against human MCL1 in HeLa cells overexpressing AMBRA1^{ActA} or AMBRA1^{WT} cells treated with O/A. Our results indicate that downregulation of MCL1 is sufficient to stimulate AMBRA1-mediated mitophagy, as demonstrated by a more evident reduction of the mitochondrial markers COXII and COXIV, when compared with cells transfected with control siRNA (Fig. 1d, e and Supplementary Fig. 1c, d).

In addition, we found that MCL1 overexpression was sufficient to reduce the number of autophagosomes following AMBRA1-mediated mitophagy, as illustrated by a reduction of LC3-II band appearance (Supplementary Fig. 1e, f).

Altogether, these data suggest that the prosurvival factor MCL1 is important for preventing mitophagy governed by the mitophagic receptor AMBRA1.



◀ **Fig. 1** MCL1 antagonizes AMBRA1-dependent mitophagy. **a** HeLa cells were cotransfected with Myc-AMBRA1^{ActA} and PcDNA3, BCL2, BCL2L1 or MCL1. After 24 h of transfection, protein extracts were analyzed using the indicated antibodies and anti-HSP90 was used as a loading control. The graph illustrates the COXIV/HSP90 ratio (\pm S.D.) as an arbitrary unit (a.u). Each point value represents the mean \pm S.D. from three independent biological replicas. Statistical analysis was performed using Student's test ($*P < 0.05$). **b** HeLa cells were cotransfected with a vector encoding MYC-AMBRA1^{ActA} and PcDNA3 or MCL1. Following 24 h of transfection, cells were fixed and assessed by immunolabeling using anti-MCL1 and MYC antibodies. Nuclei were stained with DAPI 1 μ g/ μ l 20 min. Scale bar: 8 μ m. Percentage of AMBRA1^{ActA}-transfected cells with mitoaggregosomes has been quantified following pcDNA3 or MCL1 overexpression. Each point value represents the mean \pm S.D. from three independent experiments. Statistical analysis was performed using Student's test ($**P < 0.01$). **c** HeLa cells were cotransfected with Myc-AMBRA1^{WT} and PcDNA3 or MCL1. After 24 h of transfection, cells were treated with O/A (2.5 μ M, 0.8 μ M, 5 h), total extracts were immunoblotted using the indicated antibodies and anti-HSP90 was used as a loading control. The graph illustrates the COXIV/HSP90 ratio (\pm S.D.) as an arbitrary unit (a.u). Each point value represents the mean \pm S.D. from three independent experiments. Statistical analysis was performed using Student's test ($*P < 0.05$, $**P < 0.01$). **d** HeLa cells were transfected with an empty vector (PcDNA3) or Myc-AMBRA1^{ActA} in combination with SiRNA-CTRL or SiRNA-MCL1. Cells were treated with O/A (2.5 μ M, 0.8 μ M, 5 h) and total lysates were blotted for the indicated antibodies. The graph illustrates the COXIV/HSP90 ratio (\pm S.D.) as an arbitrary unit (a.u). Each point value represents the mean \pm S.D. from three independent experiments. Statistical analysis was performed using Student's test ($**P < 0.01$). **e** HeLa cells were transfected with Myc-AMBRA1^{WT} in combination with SiRNA-CTRL or SiRNA-MCL1. Cells were treated with O/A (2.5 μ M, 0.8 μ M, 5 h) and total lysates were blotted for the indicated antibodies. The graph illustrates the COXIV/HSP90 ratio (\pm S.D.) as an arbitrary unit (a.u). Each point value represents the mean \pm S.D. from three independent experiments. Statistical analysis was performed using Student's test ($*P < 0.05$)

MCL1 antagonizes mitochondria ubiquitylation following AMBRA1^{ActA} expression by inhibiting mitochondrial translocation of HUWE1

Since we demonstrated that mitochondria ubiquitylation is an early event in AMBRA1-mediated mitophagy [10, 11], in order to better understand the mechanisms by which MCL1 was able to inhibit AMBRA1-mediated mitophagy, we checked for mitochondria ubiquitylation following AMBRA1^{ActA} expression and in the presence or absence of MCL1. By performing a mitochondrial-fractioning assay, we found that mitochondria ubiquitylation was strongly inhibited following MCL1 expression (Fig. 2a), with this suggesting that prosurvival MCL1 inhibits AMBRA1-dependent mitophagy at an early stage in the process, prior to mitochondria tagging by ubiquitin.

We recently discovered that AMBRA1-dependent ubiquitylation of mitochondria is carried out by the E3 Ubiquitin ligase HUWE1 [11]; we thus explored whether HUWE1 translocation to mitochondria was affected by

MCL1. Indeed, we found that HUWE1 mitochondrial translocation was clearly reduced in the presence of MCL1, at variance with control cells. Of note, the E3 Ubiquitin ligase PARKIN was undetectable in our mitochondrial fractions (Fig. 2a). Next, we strengthened these data by performing a quantification of HUWE1 translocation from cytosol to mitochondria, which confirms that HUWE1 expression clearly decreases in mitochondria when MCL1 is overexpressed (Supplementary Fig. 2).

Moreover, by performing a confocal microscopy analysis, we confirmed that the ubiquitin staining on mitochondria (whose aggregation into mitoaggregosomes is almost abolished by MCL1) was also reduced in cells overexpressing MCL1 (Fig. 2b).

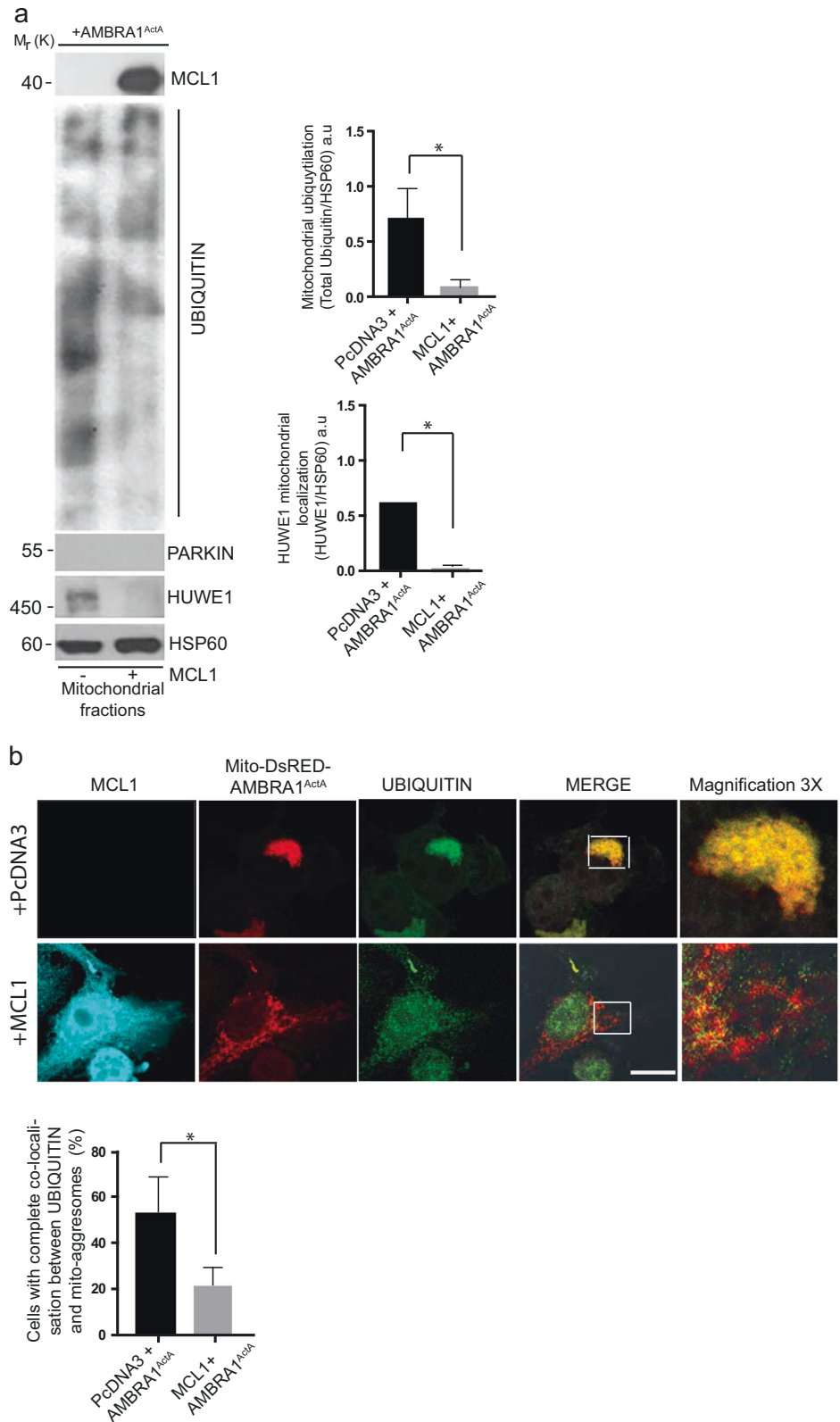
In conclusion, we found that prosurvival MCL1 may interfere with the recruitment of HUWE1 to mitochondria, thus inhibiting ubiquitylation of mitochondria, an early event necessary for AMBRA1-mediated mitophagy.

GSK-3 β modulates MCL1 protein levels during AMBRA1-mediated mitophagy

The finding that MCL1 is capable to significantly reduce AMBRA1-mediated mitophagy led us to hypothesize that this prosurvival factor needs to be tightly regulated during that process. We thus checked for its stability during AMBRA1-mediated mitophagy. Indeed, overexpression of AMBRA1^{ActA} is sufficient to induce a clear reduction in the levels of endogenous MCL1 (Fig. 3a). In a similar manner, cells overexpressing AMBRA1^{WT} and then treated with O/A for 5 h, present a decrease in MCL1 protein levels (Fig. 3b). Interestingly, such decrease of MCL1 levels can be blocked by treating both AMBRA1^{ActA} and AMBRA1^{WT}-positive HeLa cells with the proteasome inhibitor MG132 (Fig. 3a, b). These data indicate that MCL1 is degraded by the proteasome upon AMBRA1-mediated mitophagy induction. Since phosphorylation of serine 159 (S159) of MCL1 is correlated to MCL1 degradation [23], we hypothesized that MCL1 is phosphorylated on this site during mitophagy. To check for this modification event, we induced mitophagy in HeLa cells by overexpressing AMBRA1^{ActA} or AMBRA1^{WT} + O/A and then monitored phospho-S159 by means of a specific antibody. As shown in Fig. 3c, d, MCL1 is indeed phosphorylated on S159 in the early phase of the AMBRA1-mediated mitophagy (24 h following AMBRA1^{ActA} expression and 30 min following O/A treatment).

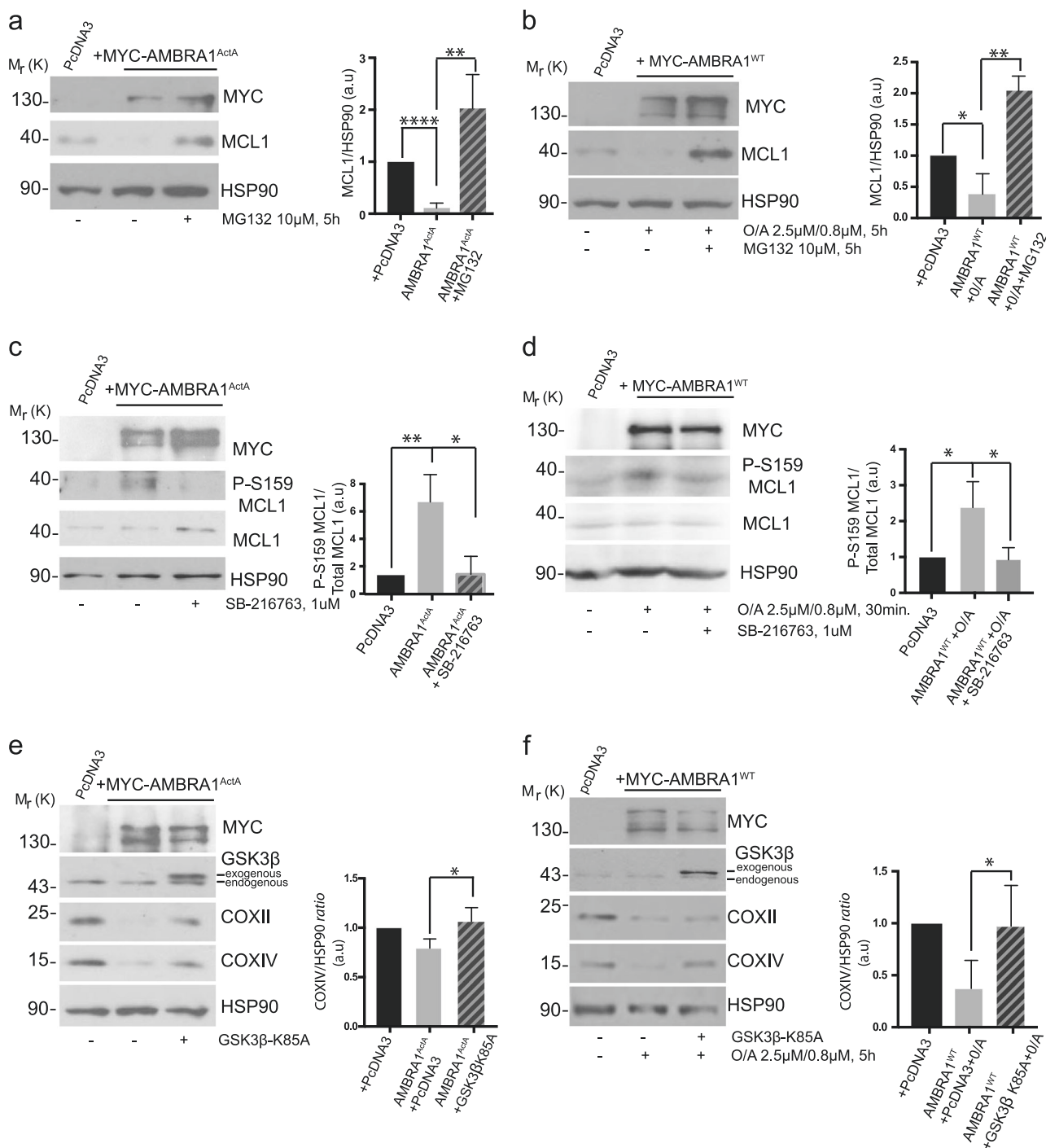
One protein kinase responsible for MCL1 phosphorylation at S159 is the GSK-3 β kinase [23]; we thus speculated that GSK-3 β was the kinase responsible for MCL1 phosphorylation and consequently for its degradation, in order to allow mitophagy. We thus checked the effect of GSK3 pharmacological inhibition on MCL1 phospho-

Fig. 2 Upon AMBRA1-mediated mitophagy, MCL1 inhibits HUWE1 translocation to mitochondria and their ubiquitylation. **a** HeLa cells were cotransfected with Myc-AMBRA1^{ActA} and PcDNA3 or MCL1. After 24 h of transfection, mitochondrial enrichment was performed through differential centrifugations, mitochondrial fractions were analyzed using the indicated antibodies and anti-HSP60 was used as a loading control. The graphs illustrate UBIQUITIN/HSP60 and HUWE1/HSP60 ratio (\pm S.D.) as an arbitrary unit (a.u). Each point value represents the mean \pm S.D. from three independent experiments. Statistical analysis was performed using Student's test ($*P < 0.05$). **b** HeLa cells were cotransfected with a vector encoding Mito-DsRED-AMBRA1^{ActA} and PcDNA3 or MCL1. Following 24 h of transfection, cells were fixed and assessed by immunolabelling using anti-MCL1 and UBIQUITIN antibodies. Nuclei were stained with DAPI 1 μ g/ μ l 20 min. The merging of the fluorescence signals is illustrated. Scale bar: 8 μ m. The graph illustrates the percentage of cells showing a complete colocalization between UBIQUITIN and the mitochondrial network (\pm S.D). Each point value represents the mean \pm S.D. from three independent experiments. Statistical analysis was performed using Student's test ($*P < 0.05$)



S159 during AMBRA1-mediated mitophagy. As expected, S159-phosphorylated MCL1 can be observed during AMBRA1-mediated mitophagy but is reduced when GSK-

β is inhibited by means of SB-216763, a small-molecule inhibitor of GSK-3 (Fig. 3c, d). These results strongly suggest that GSK-3 β may be the kinase responsible for



MCL1 phosphorylation following mitophagy induction. Primed by this result, we next investigated the contribution of GSK-3 β in mitophagy induction upon AMBRA1 expression in HeLa cells. To this end, we interfered genetically the kinase activity of the specific GSK-3 β isoform by means of a plasmid encoding GSK-3 β K85A, a kinase-dead mutant that inhibits endogenous GSK-3 β in a dominant negative manner [24]. As shown in Fig. 3e, f and Supplementary Fig. 3a, b, overexpression of the GSK-3 β

K85A is sufficient to inhibit both AMBRA1^{ActA} and AMBRA1^{WT} + O/A-mediated mitophagy.

Last, we found that inhibition of GSK-3 β was sufficient to reduce the number of autophagosomes following AMBRA1-mediated mitophagy, as shown by a reduction of LC3-II band appearance (Supplementary Fig. 3c, d).

These results strongly imply that GSK-3 β is functional to the regulation of AMBRA1-mediated mitophagy and that it acts, at least in part, through MCL1 destabilization.

◀ **Fig. 3** MCL1 is phosphorylated on serine 159 by GSK3 β during mitophagy and GSK3 β inhibition delays AMBRA1-dependent mitophagy. **a** HeLa cells were transfected with MYC-AMBRA1^{ActA} or PcDNA3 and treated with the proteasome inhibitor MG132 (10 μ M, 24 h) or not (DMSO). Total extracts were immunoblotted using the indicated antibodies and anti-HSP90 was used as a loading control. The graph illustrates the COXIV/HSP90 ratio (\pm S.D) as an arbitrary unit (a.u). Each point value represents the mean \pm S.D. from three independent experiments. Statistical analysis was performed using Student's test (**** P < 0.0001, ** P < 0.01). **b** HeLa cells were transfected with PcDNA3 or MYC-AMBRA1^{WT} and treated with O/A (2.5 μ M, 0.8 μ M, 5 h) and proteasome inhibitor (MG132, 10 μ M, 5 h) or not (DMSO). Total extracts were immunoblotted using the indicated antibodies and anti-HSP90 was used as a loading control. The graph illustrates the COXIV/HSP90 ratio (\pm S.D) as an arbitrary unit (a.u). Each point value represents the mean \pm S.D. from three independent experiments. Statistical analysis was performed using Student's test (* P < 0.05, ** P < 0.01). **c** HeLa cells were transfected with MYC-AMBRA1^{ActA} or PcDNA3 and treated with GSK3 inhibitor (SB-216763, 1 μ M, 24 h) or not (DMSO). Total extracts were immunoblotted using the indicated antibodies and anti-HSP90 was used as a loading control. The graph illustrates the P-S159MCL1/MCL1 ratio (\pm S.D) as an arbitrary unit (a.u). Each point value represents the mean \pm S.D. from three independent experiments. Statistical analysis was performed using Student's test (* P < 0.05). **d** HeLa cells were transfected with PcDNA3 or MYC-AMBRA1^{WT} and treated with O/A (2.5 μ M, 0.8 μ M, 5 h) and GSK3 inhibitor (SB-216763, 1 μ M, 5 h) or not (DMSO). Total extracts were immunoblotted using the indicated antibodies and anti-HSP90 was used as a loading control. The graph illustrates the COXIV/HSP90 ratio (\pm S.D) as an arbitrary unit (a.u). Each point value represents the mean \pm S.D. from three independent experiments. Statistical analysis was performed using Student's test (* P < 0.05, ** P < 0.01). **e** HeLa cells were cotransfected with MYC-AMBRA1^{ActA} and PcDNA3 or GSK3 β dead kinase (GSK3 β -K85A). After 24 h of transfection, total extracts were immunoblotted using the indicated antibodies and anti-HSP90 was used as a loading control. The graph illustrates the COXIV/HSP90 ratio (\pm S.D) as an arbitrary unit (a.u). Each point value represents the mean \pm S.D. from three independent experiments. Statistical analysis was performed using Student's test (* P < 0.05). **f** HeLa cells were cotransfected with MYC-AMBRA1^{WT} and PcDNA3 or GSK3 β dead kinase (GSK3 β -K85A) and treated with O/A (2.5 μ M, 0.8 μ M, 5 h). After 24 h of transfection, total extracts were immunoblotted using the indicated antibodies and anti-HSP90 was used as a loading control. The graph illustrates the COXIV/HSP90 ratio (\pm S.D) as an arbitrary unit (a.u). Each point value represents the mean \pm S.D. from three independent experiments. Statistical analysis was performed using Student's test (* P < 0.05)

HUWE1 is responsible for MCL1 ubiquitylation and degradation upon AMBRA1-mediated mitophagy

AMBRA1 cooperates with the E3 ubiquitin ligase HUWE1 in order to mediate mitophagy [11]. Interestingly, MCL1 is a well-known substrate of HUWE1 [25]. We could thus candidate HUWE1 as the E3 Ubiquitin ligase responsible for MCL1 degradation during AMBRA-dependent mitophagy. To investigate this possibility, we first downregulated HUWE1 in HeLa cells overexpressing AMBRA1^{ActA} or AMBRA1^{WT} and treated with O/A, and next checked for MCL1 protein levels during mitophagy. As shown in Fig. 4a, b,

downregulation of HUWE1 is sufficient to reduce MCL1 degradation upon mitophagy induction. Of note, AMBRA1-mediated mitophagy inhibition, by blocking MCL1 degradation through the use of HUWE1 siRNA, is accompanied by a reduction of the autophagosome number as shown by a reduction of the LC3-II band appearance (Supplementary Fig. 4a, b). HUWE1 should then be able to cooperate with GSK-3 β to induce MCL1 degradation following AMBRA1-induced mitophagy. To test this hypothesis, we checked whether HUWE1 was able or not to bind its substrate MCL1 upon AMBRA1^{ActA}-mediated mitophagy dependently or not from GSK-3 β inhibitor. Indeed, HUWE1 strongly binds endogenous MCL1 upon AMBRA1^{ActA}-mediated mitophagy and this binding is reduced when GSK-3 β is inhibited (Fig. 4c), with this indicating that GSK-3 β is a priming kinase important for MCL1 recognition by HUWE1.

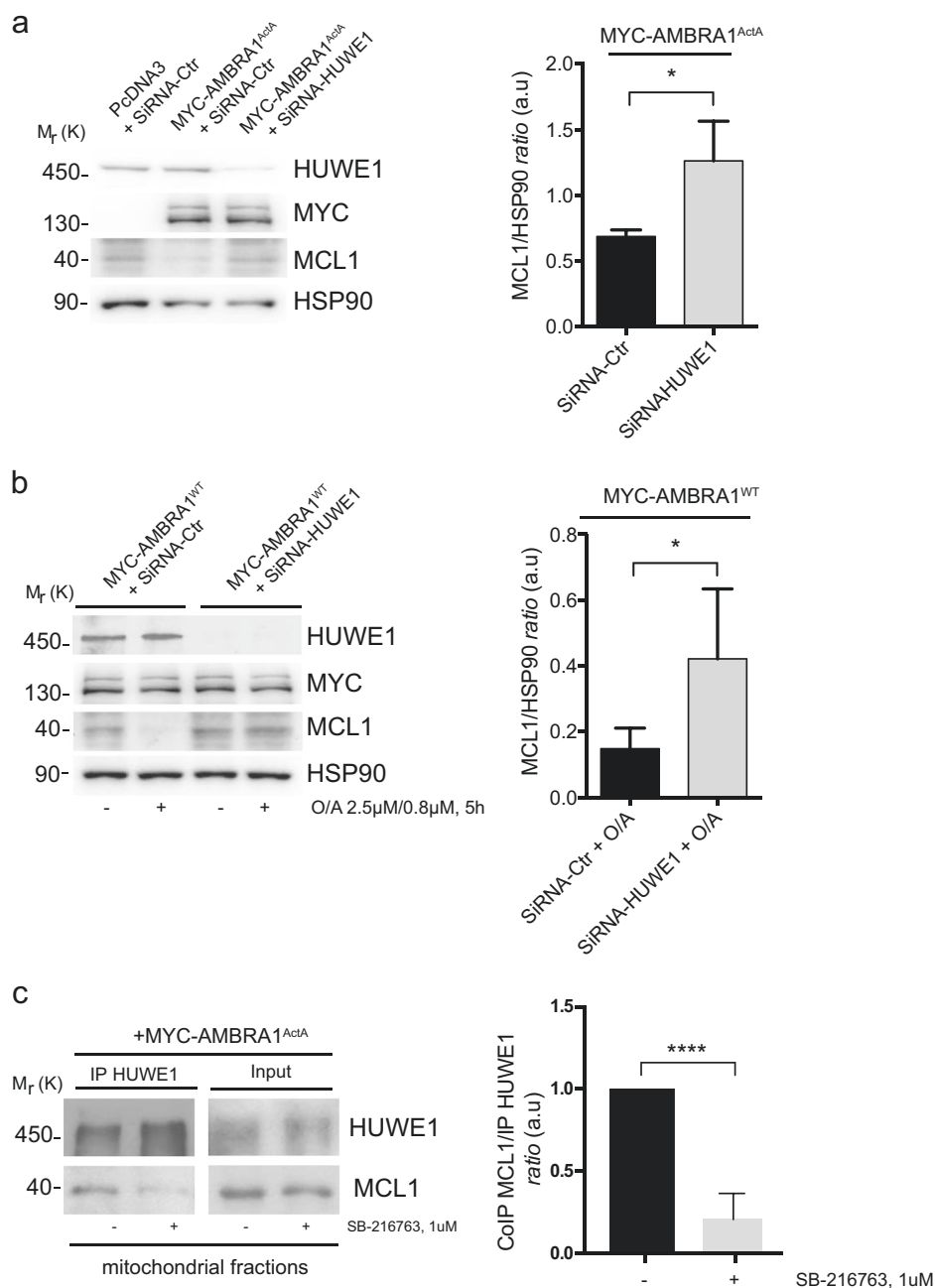
AMBRA1-mediated mitophagy operates through the HUWE1-GSK3 axis in MCF7 breast cancer cells, in order to degrade MCL1 for a correct mitophagy occurrence

Next, we decided to validate our main findings obtained in HeLa cells in an other cell line, in which high endogenous levels of MCL1 are detected. To this end, we have chosen the MCF7 cells, a breast cancer cell line known to be resistant to some drugs, with this being due, in part, to the high levels of MCL1 they display [26]. In particular, we confirmed that MCL1 was highly expressed in these cells compared with HeLa cells (Fig. 5a). In addition, we showed that MCL1 is able to delay mitoagosome formation (Fig. 5b), to reduce ubiquitin on mitochondria (Fig. 5c). Moreover, as already demonstrated in HeLa cells, we found that AMBRA1-mediated mitophagy induction is able to induce MCL1 degradation through the HUWE1-GSK3 axis (Fig. 5f–j). These data indicate that AMBRA1-mediated mitophagy induction is sufficient to reduce high levels of endogenous MCL1 in a breast cancer cell line, in order to properly induce mitophagy.

AMBRA1^{ActA} ectopic expression delays the potential of clonogenicity of primary CD34⁺ cells of a CN-AML patient

Interestingly, MCL1 is an essential survival factor for hematopoiesis, and in humans, hematopoietic stem cells express MCL1 at the highest level in response to FMS-like tyrosine kinase-3 (FLT3) signaling. Patients suffering from acute myeloid leukemias (AML) with FMS-like tyrosine kinase-3-internal tandem duplications (FLT3-ITD) have poor outcomes following induction of several therapies and this is mainly attributed to drug resistance due to the

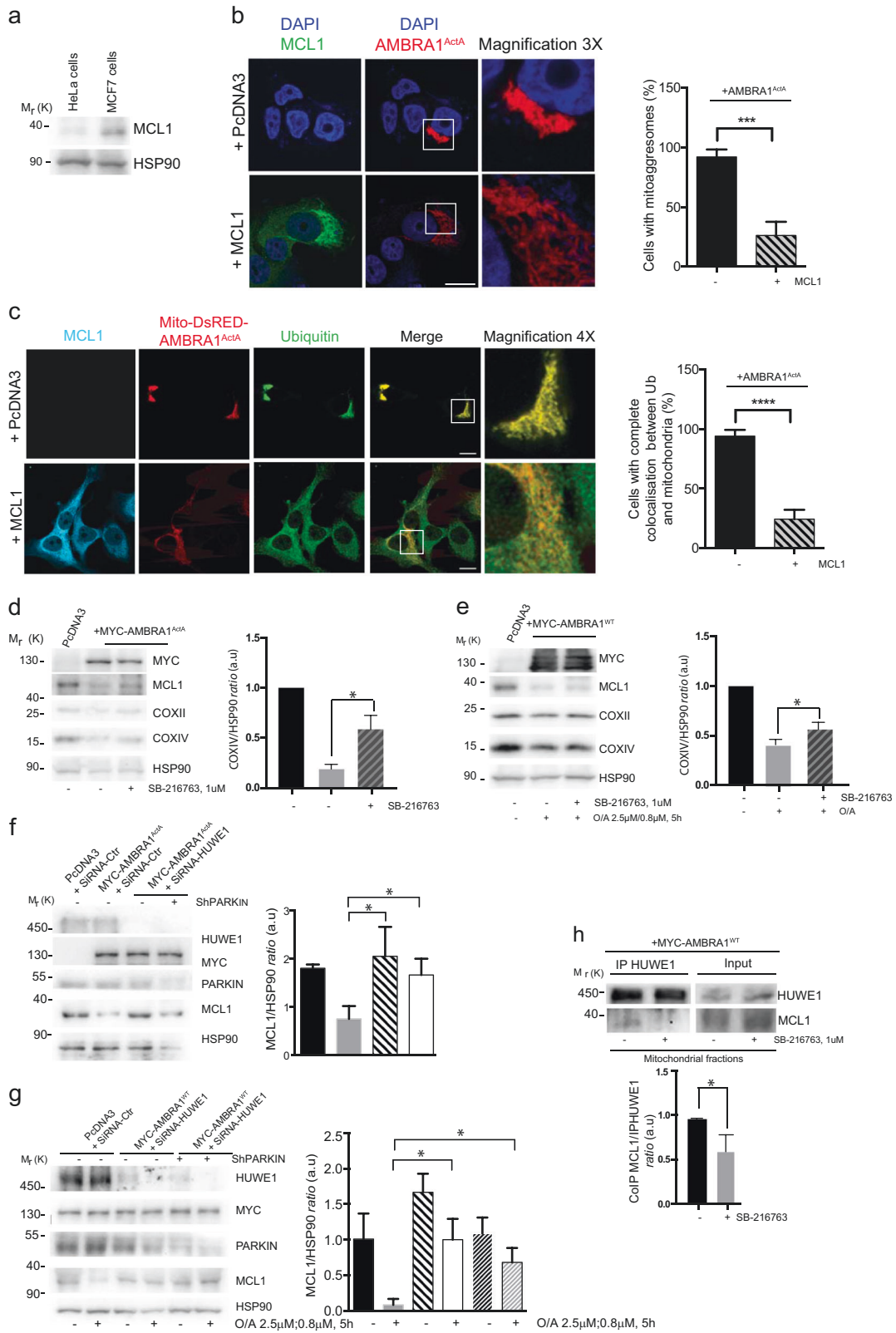
Fig. 4 HUWE1 is responsible for MCL1 degradation during AMBRA1-mediated mitophagy. **a** HeLa cells transfected with MYC-AMBRA1^{ActA} (18 h) and interfered for HUWE1 (SiRNA-HUWE1) were analyzed by western blot. The quantification results are the mean of three independent experiments (\pm S.D.). Statistical analysis was performed using Student *t*-test (** $P < 0.01$). **b** HeLa cells transfected with MYC-AMBRA1^{WT} and interfered for HUWE1 (SiRNA-HUWE1) were treated with O/A and analyzed by western blot. The quantification results are the mean of four independent experiments (\pm S.D.). * $P < 0.05$. Statistical analysis was performed using Student *t*-test. **c** Representative image of HUWE1-MCL1 co-immunoprecipitation (Co-IP), upon mitophagy stimulation (AMBRA1^{ActA} overexpression) in the mitochondrial fractions. The graph illustrates the levels of MCL1 coimmunoprecipitated with HUWE1 in normal condition or following GSK3 inhibition (\pm S.D.). Statistical analysis was performed using Student *t*-test (**** $P < 0.0001$)



upregulation of MCL1 in primary mononuclear cells (MNC) from AML patients compared with FLT3-wild-type controls [27]. Since therapeutic targeting of MCL1 is a promising strategy for FLT3-ITD-positive AML patients and since we demonstrated that AMBRA1-mediated mitophagy induces MCL1 downregulation, we hypothesized that AMBRA1^{ActA} expression, by mediating MCL1 downregulation, would affect the clonogenic potential of CD34+ AML cells. To this end, we retrovirally infected CD34+ of a paediatric CN-AML patient harboring FLT3-ITD mutation. As shown in Fig. 6, AMBRA1^{ActA} infection in CD34+

cells induced a significant reduction of the in vitro CFUs compare with control cells; this was accompanied by a reduction of MCL1 levels in these primary AMBRA1^{ActA}-positive CD34+ AML cells.

In sum, targeting MCL1 by overexpressing AMBRA1^{ActA} reduces the clonogenic activity (by >50%) in a primary AML case tested. These findings demonstrate that targeting MCL1 through AMBRA1-mediated mitophagy induction may have the potential to reduce proliferation of CD34+ cells and could be able to suppress human leukemic stem and progenitor cells.



◀ **Fig. 5** MCL1 antagonizes AMBRA1-dependent mitophagy and its HUWE1-dependent degradation, is necessary for a correct mitophagy in MCF7 cells. **a** Protein extracts of HeLa and MCF7 cells were analyzed using the MCL1 antibody and anti-HSP90 was used as a loading control. **b** MCF7 cells were cotransfected with a vector encoding MYC-AMBRA1^{ActA} and PcDNA3 or MCL1. Following 24 h of transfection, cells were fixed and assessed by immunolabelling using anti-MCL1 and MYC antibodies. Nuclei were stained with DAPI 1 µg/µl 20 min. Scale bar: 8 µm. Percentage of AMBRA1^{ActA} transfected cells with mitoaggregates has been quantified following pcDNA3 or MCL1 overexpression. Each point value represents the mean ± S.D. from three independent experiments. Statistical analysis was performed using Student's test (***P* < 0.001). **c** MCF7 cells were cotransfected with a vector encoding Mito-DsRED-AMBRA1^{ActA} and PcDNA3 or MCL1. Following 24 h of transfection, cells were fixed and assessed by immunolabelling using anti-MCL1 and UBIQUITIN antibodies. Nuclei were stained with DAPI 1 µg/µl 20 min. The merging of the fluorescence signals is illustrated. Scale bar: 8 µm. The graph illustrates the percentage of cells showing a complete colocalization between UBIQUITIN and the mitochondrial network (± S.D.). Each point value represents the mean ± S.D. from three independent experiments. Statistical analysis was performed using Student's test (*****P* < 0.0001). **d** MCF7 cells were transfected with MYC-AMBRA1^{ActA} or PcDNA3 and treated with GSK3 inhibitor (SB-216763, 1 µM, 24 h) or not (DMSO). Total extracts were immunoblotted using the indicated antibodies and anti-HSP90 was used as a loading control. The graph illustrates the COXIV/HSP90 ratio (± S.D.) as an arbitrary unit (a.u). Each point value represents the mean ± S.D. from three independent experiments. Statistical analysis was performed using Student's test (**P* < 0.05). **e** MCF7 cells were transfected with PcDNA3 or MYC-AMBRA1^{WT} and treated with O/A (2.5 µM, 0.8 µM, 5 h) and GSK3 inhibitor (SB-216763, 1 µM, 5 h) or not (DMSO). Total extracts were immunoblotted using the indicated antibodies and anti-HSP90 was used as a loading control. The graph illustrates the COXIV/HSP90 ratio (± S.D.) as an arbitrary unit (a.u). Each point value represents the mean ± S.D. from three independent experiments. Statistical analysis was performed using Student's test (**P* < 0.05). **f** MCF7 cells transfected with MYC-AMBRA1^{ActA} (18 h) and interfered for HUWE1 (SiRNA-HUWE1) and PARKIN (Sh-PARKIN), or not, were analyzed by western blot. The quantification results are the mean of three independent experiments (± S.D.). Statistical analysis was performed using Student *t*-test (**P* < 0.05). **g** MCF7 cells transfected with MYC-AMBRA1^{WT} and interfered for HUWE1 (SiRNA-HUWE1) and PARKIN (Sh-PARKIN), or not, were treated with O/A and analyzed by western blot. The quantification results are the mean of four independent experiments (± S.D.). Statistical analysis was performed using Student's *t*-test (**P* < 0.05). **h** Representative image of HUWE1-MCL1 co-immunoprecipitation (Co-IP), upon mitophagy stimulation (AMBRA1^{ActA} overexpression) in mitochondrial fractions of MCF7 cells. The graph illustrates the levels of MCL1 coimmunoprecipitated with HUWE1 in normal condition or following GSK3 inhibition (± S.D.). Statistical analysis was performed using Student's *t*-test (**P* < 0.05)

Discussion

Here, we have shown that MCL1, a member of the BCL2-family, inhibits HUWE1 recruitment to mitochondria, a critical event for AMBRA1-mediated mitophagy. We also found that MCL1 stability is regulated during mitophagy by the priming kinase GSK-3β, which phosphorylates MCL1 on S159, this leading to its proteasomal degradation by HUWE1. In sum, we propose that MCL1 is degraded by

this axis during mitophagy and that this event is important to remove the MCL1 inhibitory effect on mitophagy (Fig. 7).

Interestingly, MCL1 degradation has been found in serum withdrawal conditions and its deletion exacerbates autophagy, this highlighting a function for MCL1 in autophagy regulation [28]. Our data indicate that MCL1 is also capable to regulate selective autophagy, and in particular mitochondria removal governed by the mitophagy receptor AMBRA1. Hollville et al. demonstrated that MCL1, BCL2L1, and BCL2 are able to inhibit PARKIN-mediated mitophagy by blocking PARKIN translocation to mitochondria [18]. Moreover, Wu et al. demonstrated that BCL2L1 inhibits FUNDC1-mediated mitophagy [19]. Our results are thus in line with the concept that BCL2-family proteins are important regulators of the mitophagic process.

Since both PARKIN and HUWE1 are mainly cytoplasmic E3 ubiquitin ligases, our work together with those of Hollville et al. suggest that a general mechanism for the BCL2-family proteins could exist in order to decide to maintain healthy mitochondria, by inhibiting E3 ubiquitin ligase translocation. One open question is how HUWE1 is recruited to mitochondria. Since HUWE1 is a E3 ubiquitin ligase containing a BH3 domain [25], we can speculate that overexpressed MCL1 is able to compete with HUWE1 for an interaction with another BH3 protein that serves as a "mitochondrial anchor" for HUWE1.

Interestingly, at variance with PARKIN-mediated mitophagy, we found here that MCL1 possesses a unique function, distinct from that of BCL2L1 and BCL2 on AMBRA1-mediated mitophagy.

Further, we validated our main findings also in MCF7 cells, a cancer cell line expressing high levels of endogenous MCL1. Since targeting MCL1 is a current strategy to fight breast cancer, our results indicate that also AMBRA1-mediated mitophagy may be a target to fight such cancer, in which MCL1 is found upregulated.

Moreover, by demonstrating that AMBRA1^{ActA}-infected CD34+ AML cells showed a lower clonogenic potential compared with infected control cells, we highlighted the potential of a novel strategy, based on the stimulation of AMBRA1-mediated mitophagy, for the development of specific MCL1-targeting pathways in order to eliminate residual FLT3-ITD leukemic blasts and stem cells resistant to cytotoxic agents.

Further, deletion of the *AMBRA1* gene causes unbalanced cell proliferation accompanied by defects of neuronal development [2]; since MCL1 is strongly involved in neuron survival [29], we can hypothesize that MCL1, by mediating a tight regulation of the balance between mitophagy and apoptosis, may control AMBRA1-mediated mitophagy during brain development. Finally, Hollville et al. [18] found that BH3-only proteins, such as BAD,

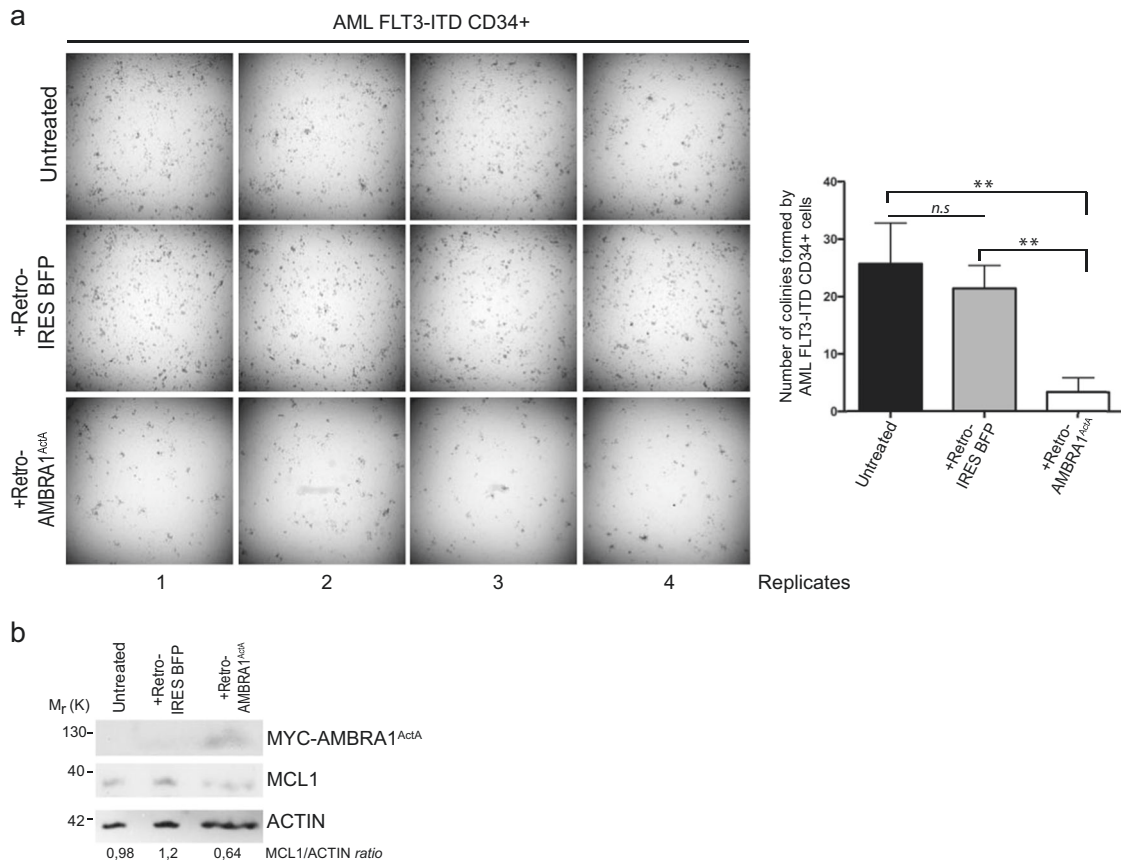


Fig. 6 Ectopic expression of AMBRA1^{ActA} fusion gene impairs colony formation and MCL1 expression in FLT3-ITD-mutated AML CD34+ cells. **a** Colony-formation assay (CFU-assay) shows reduced colony-formation capacity after 15 days in culture in AMBRA1^{ActA} (+Retro-AMBRA1^{ActA}) overexpressing CD34+ cells, compared with non-infected (Untreated; *t*-test $P=0.0068$) and empty vector infected (+Retro IRES BFP; *t*-test $P=0.0028$) CD34+ cells. (Four technical

replicates are shown). Histograms show the median number of colonies and SDs for the three conditions mentioned above. Difference between untreated and +Retro IRES BFP conditions is not statistically significant (*t*-test $P=0.41$). **b** Western blot shows expression of ectopic AMBRA1^{ActA} fusion gene in +Retro-AMBRA1^{ActA} infected CD34+ cells along with MCL1 reduction compared with controls cells after 15 days in culture

BIM, PUMA, and NOXA, as well as a BH3-only mimetics, were capable of accelerating PARKIN recruitment in order to impact mitochondria, most likely through neutralization of endogenous BCL2-family proteins. It will be interesting, in the future, to understand whether this happens or not in the context of AMBRA1-mediated mitophagy.

In conclusion, the ability of MCL1 to regulate the mitophagy process driven by AMBRA1 suggests that MCL1 acts as important sensor of mitochondria healthy status, thus impacting on both apoptosis and mitophagy control.

Methods

Antibodies

Rabbit anti-MCL1 (Santa Cruz Biotechnology, sc-819), monoclonal anti-BCL2 (Santa Cruz Biotechnology, sc-7382),

mouse monoclonal anti-COXII (Abcam, ab110258); mouse monoclonal anti-COXIV (Abcam, ab33985), mouse monoclonal anti-MYC (9E10; Santa Cruz Biotechnology, sc-40), mouse monoclonal anti-FLAG (Sigma-Aldrich, F3165), rabbit polyclonal anti-FLAG (Sigma-Aldrich, F7425), rabbit polyclonal anti-phospho S159 MCL1 (Cell signaling, #45795), mouse monoclonal anti-GSK3 β (E-11) (Santa Cruz Biotechnology, sc-377213), rabbit polyclonal anti-HSP90 (Santa Cruz Biotechnology, sc-7947), rabbit polyclonal anti-HUWE1 (Bethyl, A300-486A), mouse monoclonal anti-UBIQUITIN (Santa Cruz Biotechnology, sc-8017), anti-GAPDH (Santa Cruz Biotechnology sc-47724), and anti-HSP60 (Santa Cruz Biotechnology, sc-13966).

Cloning and plasmids

Construct coding for AMBRA1^{WT} was cloned in pLPCX vector (Clontech, 631511).¹⁸. The constructs coding for BCL2L1 and MCL1 were a gift of Muriel Priault (Bordeaux,

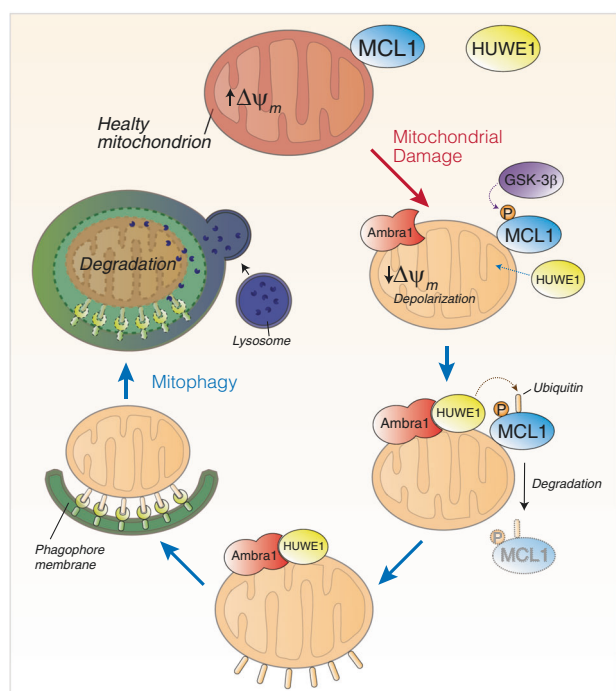


Fig. 7 MCL1 antagonizes AMBRA1-dependent mitochondrial quality control. In normal condition, HUWE1 is an E3 ubiquitin ligase mostly found in the cytoplasm. Upon AMBRA1-mediated mitophagy induction, AMBRA1 favors HUWE1 E3 ubiquitin ligase translocation from the cytosol to mitochondria [11]. Here we demonstrate that the pro-survival factor MCL1, when highly expressed, antagonizes the mitochondrial access of the E3 Ubiquitin ligase HUWE1 upon mitophagy induction. In normal condition, MCL1 is thus, most likely, a stress-sensitive protein which is able to preserve the mitochondrial membrane from the E3 ubiquitin ligase HUWE1 access. When mitophagy is induced, by expressing high quantities of AMBRA1 to the mitochondria, MCL1 is phosphorylated by GSK3 β on Serine 159 and degraded by the proteasome through HUWE1

France). The Myc-AMBRA1^{ActA} plasmid was cloned as described in Strappazzon et al. (2015). The Mito-DsRED construct encodes for human Cox8A mitochondria signal peptide which is fused with wild-type-DsRED in PcDNA3 vector (Invitrogen). The Mito-DsRED-AMBRA1^{ActA} is a bidirectional vector encoding for both Mito-DsRED and FLAG-AMBRA1^{ActA}. Plasmid encoding for HA GSK3- β K85A pcDNA3 was purchased from Addgene.

Interference using siRNAs

All the RNA-interference was performed using Lipofectamine 2000. We used MCL1 (h) siRNA from Santa Cruz (sc:43912); siRNA-HUWE1 from Integrated DNA Technologies (IDT) #150971213.

Cell cultures

HeLa cells were cultured in Dulbecco's Modified Eagle's Medium (Lonza, BE12-604F) supplemented with 10% fetal

bovine serum (FBS) (Gibco; Thermo Fisher Scientific, 10270-106), and 1% penicillin–streptomycin solution (Lonza, 17-602 E) at 37 °C under 5% CO₂.

Cell culture transfection

Transient transfections of expression plasmids into HeLa cells were performed using TurboFect according to the supplier's instructions (Thermo Fisher Scientific, R0532). MCF7 cells were transiently transfected using Lipofectamine 2000 according to the supplier's instructions (Thermo Fisher Scientific, #11668019).

Cells treatments

In order to induce mitophagy, HeLa cells were treated with the combined treatment O/A [2.5 μ M Oligomycin (Calbiochem)/0.8 μ M Antimycin A (Sigma)] in fresh growth medium for 5 h. In order to block GSK3 activity, cells were treated with SB-216763 (Sigma-Aldrich S3442) at 1 μ M. MG132 (Sigma-Aldrich, M7449) was used to inhibit the proteasome at 10 μ M.

Immunocytochemistry

Cells were washed in PBS and fixed with 4% paraformaldehyde in PBS for 15 min. After permeabilization with 0.4% Triton X-100 (Sigma-Aldrich, X100) in PBS for 5 min, cells were blocked in 3% normal goat serum (Sigma-Aldrich, G9023) in PBS and incubated overnight at 4 °C with primary antibodies. We used the antibodies directed against rabbit anti-MCL1, rabbit anti-FLAG-HUWE1 and mouse anti-UBIQUITIN (1:100 overnight). Cells were then washed in blocking buffer and incubated for 1 h with labeled anti-mouse (Alexa Fluor 488; Invitrogen, A11017), anti-rabbit (Alexa Fluor 555; Invitrogen, A21430) or anti-rabbit (Alexa Fluor 647; Invitrogen, A31573) secondary antibodies. Nuclei were stained with 1 μ g/ml DAPI and examined under a Zeiss LSM 700 100 \times oil-immersion objective (CLSM700; Jena, Germany). We used "ZEN 2009 Light edition" software for image analysis. All acquisitions were performed in single z-confocal planes.

Western blot analysis

Cell extracts were centrifuged at 13,000 \times g for 10 min at 4 °C. Protein concentrations were determined with the Bio-Rad Protein Assay Kit (Bio-Rad, 5000001). Cell extracts were separated by SDS-PAGE and transferred onto nylon membranes (Immobilon P; Merck-Millipore, IPFL10100). Membranes were incubated with primary antibodies (1:1000, overnight) followed by horseradish peroxidase-conjugated

secondary antibody (Bio-Rad, 1706515 and 1721011) and visualized with ECL (Merck-Millipore WBKLS0500).

Co-immunoprecipitation (Co-IP)

After cell lysis, equal amounts of protein were incubated with the primary antibody (Anti-HUWE1) with rotation for 24 h. Then 30 μ l of protein A agarose beads (Roche, 11719408001) were added for 60 min. The beads were collected by centrifugation and washed three times with the RIPA buffer. Immuno-complexes were eluted with 30 μ l of SDS sample buffer and heated at 95 °C for 10 min.

Cytosol/mitochondria fraction preparation

For cytosol/mitochondria fractionation, cells were lysed by mechanical breaking (~100 potter strokes) into a detergent-free buffer (0.25 M sucrose, 10 mM HEPES pH 7.5, 1 mM EDTA). A first centrifugation (600 \times g for 10 min at 4 °C) was employed to pellet nuclei; subsequently, supernatants were recentrifuged at 12,000 \times g for 15 min at 4 °C to separate a cytosolic upper phase from a mitochondrial pellet. The latter was lysed in RIPA buffer. All protein extracts were quantified through the Bradford Protein Assay (Bradford solution from Bio-Rad Laboratories) according to the manufacturer's protocols.

Retrovirus production and infection protocol

CD34+ AML cells were infected using a pMSCV-IRES-Blue FP Retroviral construct (pMSCV-IRES-Blue FP was a gift from Dario Vignali—Addgene plasmid # 52115) carrying a MYC-AMBRA-ActA fusion gene or the Empty vector. Noninfected CD34+ cells were also considered as control. Retroviral particles were generated using pCMV-VSV-G (Envelope; pCMV-VSV-G was a gift from Bob Weinberg—Addgene plasmid # 8454) and pUMVC (Packaging; pUMVC was a gift from Bob Weinberg—Addgene plasmid # 8449) in 293T cells. MYC-AMBRA-ActA fusion gene was cloned into the multiple cloning site using SnaBI and ApaI restriction enzymes (New England Biolabs). Retrovirus was concentrated using Retro-X™ Concentrator (Takara) and infection was performed after coating the culture plates with RetroNectin (Takara—RetroNectin® GMP grade) following manufacturer protocol. After 24 h in culture, in presence of retroviral particles, cells were washed three times with D-PBS and cultured for colony-forming assay.

Colony formation assay

In vitro colony-forming unit (CFU) assay was performed in order to test clonogenic potential of CD34+ after 15 days of expansion using MethoCult H4434 methylcellulose

medium (Stem Cell Technologies, Vancouver, CA). Colonies were counted with CellSens Standard 1.14 (Olympus, Tokyo, JP) with a minimum imposition of 200 nm diameter per colony unit. Unpaired *t*-test was performed to determine if the means of the datasets were significantly different from each other using Bioconductor and GraphPad Prism version 6.00 for MacOSX (GraphPad Software, La Jolla California USA). Frozen bone marrow sample from newly diagnosed AML pediatric patient was collected by Ospedale Pediatrico Bambino Gesù. The patient harbored FLT3-ITD mutation in a CN-AML. Informed consent was obtained from either parents or legal guardians according to the Declaration of Helsinki. Approvals for this study were obtained from the Institutional Review Boards of the institution. MNC were isolated by density gradient centrifugation, diluted in 90% FBS plus 10% dimethyl sulfoxide and stored in liquid nitrogen. CD34+ cells were magnetically separated using MACS CD34+ microbead kit (Miltenyi Biotech, Bergish Gladbach, DE).

Statistical analyses

Data were analyzed and graphs were plotted using GraphPad Prism 6 software. Statistical analyses were performed using the Student two-tailed *t*-test. Data were shown as means \pm SD of three independent experiments. Values of $p < 0.05$ were considered significant (* $p < 0.05$; ** $p < 0.01$; *** $p < 0.001$).

Acknowledgements We wish to thank Dr Muriel Priault for kindly providing us the constructs BCL2L1 and MCL1; Prof. M. Campanella for the gift of Short Hairpin PARKIN and Dr V. Stagni and Prof. Barilà for the gift of MCF7 cells. We are grateful to Dr Salvatore Rizza for his help with Fig. 7. We thank M. Acuña Villa for secretarial work and F. Maria Orecchio, S. Verna, T. Maiorino, K. Bruqi for technical assistance.

Funding This work was also supported by grants: GR2011-02351433 (Italian Ministry of Health), ROCHE (Roche per la ricerca 2017) and 5XMILLE Italian Ministry of Health (2017) to FS; AIRC (MFAG#15523) to AP; MRC, LazioInnova (85-2017-14986) and AIRC (IG#20473) to GM; grants from the Italian Ministry of Education, University and Research (Research Project of National Relevance 2017 ID 2017WC8499) and AIRC (Associazione Italiana Ricerca sul Cancro, 5 \times 1000 ID 9962, AIRC IG 2018 ID 21724) to FL. P.L. was supported by FUV Grant 2019. Francesco Ceconi's laboratory is supported by grants from the Bjarne Saxhof Foundation, the Danish Cancer Society (KBVU R72-A4408, R146-A9364), the Novo Nordisk Foundation (7559, 22544), the Lundbeckfonden (R233-2016-3360), the LEO Foundation (LF17024), "Associazione Italiana per la Ricerca sul Cancro" (AIRC IG-15180). FC lab in Copenhagen are part of the Center of Excellence for Autophagy, Recycling and Disease (CARD), funded by the Danmarks Grundforskningsfond (DNR125).

Compliance with ethical standards

Conflict of interest The authors declare that they have no conflict of interest.

Publisher's note: Springer Nature remains neutral with regard to jurisdictional claims in published maps and institutional affiliations.

References









- Cecconi F, Levine B. The role of autophagy in mammalian development: cell makeover rather than cell death. *Dev Cell*. 2008;3:344–57.
- Fimia GM, Stoykova A, Romagnoli A, Giunta L, Nardacci R, Corazzari M, et al. Ambra1 regulates autophagy and development of the nervous system. *Nature*. 2007;447:1121–5.
- Levine B, Elazar Z. Development. Inheriting maternal mtDNA. *Science*. 2011;25:1069–70.
- Pickrell AM. The roles of PINK1, parkin, and mitochondrial fidelity in Parkinson's disease. *2015*;21:257–73.
- Lazarou M, Sliter DA, Kane LA, Sarraf SA, Wang C, Burman JL, et al. The ubiquitin kinase PINK1 recruits autophagy receptors to induce mitophagy. *Nature*. 2015;524:309–14.
- Hanna RA, Quinsay MN, Orogo AM, Giang K, Rikka S, Gustafsson ÅB. Microtubule-associated protein 1 light chain 3 (LC3) interacts with Bnip3 protein to selectively remove endoplasmic reticulum and mitochondria via autophagy. *J Biol Chem*. 2012;287:19094–104. 1
- Schwarten M, Mohrlüder J, Ma P, Stoldt M, Thielmann Y, Stangler T, et al. Nix directly binds to GABARAP: a possible crosstalk between apoptosis and autophagy. *Autophagy*. 2009;5:690–8.
- Liu L, Feng D, Chen G, Chen M, Zheng Q, Song P, et al. Mitochondrial outer-membrane protein FUNDC1 mediates hypoxia-induced mitophagy in mammalian cells. *Nat Cell Biol*. 2014;14:177–85.
- Wei Y, Chiang WC, Sumpter R Jr, Mishra P, Levine B. Prohibitin 2 Is an Inner Mitochondrial Membrane Mitophagy Receptor. *Cell*. 2017;168:224–38.
- Strappazzon F, Nazio F, Corrado M, Cianfanelli V, Romagnoli A, Fimia GM, et al. AMBRA1 is able to induce mitophagy via LC3 binding, regardless of PARKIN and p62/SQSTM1. *Cell Death Differ*. 2015;22:419–32.
- Di Rita A, Peschiaroli A, D'Acunzo P, Strobbe D, Hu Z, Gruber J, et al. HUWE1 E3 ligase promotes PINK1/PARKIN-independent mitophagy by regulating AMBRA1 activation via IKK α . *Nat Commun*. 2018;9:3755. 14
- Adams JM, Cory S. The BCL-2 arbiters of apoptosis and their growing role as cancer targets. *Cell Death Differ*. 2018;25:27–36.
- Kale J, Osterlund EJ, Andrews DW. BCL-2 family proteins: changing partners in the dance towards death. *Cell Death Differ*. 2018;25:65–80.
- Kalkavan H, Green DR. MOMP, cell suicide as a BCL-2 family business. *Cell Death Differ*. 2018;25:46–55.
- Mukherjee A, Williams DW. More alive than dead: non-apoptotic roles for caspases in neuronal development, plasticity and disease. *Cell Death Differ*. 2017;24:1411–21.
- Opferman JT, Kothari A. Anti-apoptotic BCL-2 family members in development. *Cell Death Differ*. 2018;25:37–45.
- Strasser A, Vaux DL. Viewing BCL2 and cell death control from an evolutionary perspective. *Cell Death Differ*. 2018;25:13–20.
- Hollville E, Carroll RG, Cullen SP, Martin SJ. Bcl-2 family proteins participate in mitochondrial quality control by regulating Parkin/PINK1-dependent mitophagy. *Mol Cell*. 2014;55:451–66.
- Wu H, Xue D, Chen G, Han Z, Huang L, Zhu C, et al. The BCL2L1 and PGAM5 axis defines hypoxia-induced receptor-mediated mitophagy. *Autophagy*. 2014;10:1712–25.
- Strappazzon F, Vietri-Rudan M, Campello S, Nazio F, Florenzano F, Fimia GM, et al. Mitochondrial BCL-2 inhibits AMBRA1-induced autophagy. *EMBO J*. 2011;30:1195–208.
- Strappazzon F, Di Rita A, Cianfanelli V, D'Orazio M, Nazio F, Fimia GM, et al. Prosurvival AMBRA1 turns into a proapoptotic BH3-like protein during mitochondrial apoptosis. *Autophagy*. 2016;12:963–75.
- Di Rita A, D'Acunzo P, Simula L, Campello S, Strappazzon F, Cecconi F. AMBRA1-Mediated Mitophagy Counteracts Oxidative Stress and Apoptosis Induced by Neurotoxicity in Human Neuroblastoma SH-SY5Y Cells. *Front Cell Neurosci*. 2018;12:92.
- Maurer U, Charvet C, Wagman AS, DeJardin E, Green DR. Glycogen synthase kinase-3 regulates mitochondrial outer membrane permeabilization and apoptosis by destabilization of MCL-1. *Mol Cell*. 2006;21:749–60.
- Dominguez I, Itoh K, Sokol SY. Role of glycogen synthase kinase 3b as a negative regulator of dorsoventral axis formation in *Xenopus* embryos. *Proc Natl Acad Sci USA*. 1995;92:8498–502.
- Zhong Q, Gao W, Du F, Wang X. Mule/ARF-BP1, a BH3-only E3 ubiquitin ligase, catalyzes the polyubiquitination of Mcl-1 and regulates apoptosis. *Cell*. 2015;121:1085–95.
- Placzek WJ, Wei J, Kitada S, Zhai D, Reed JC, Pellecchia M. A survey of the anti-apoptotic bcl-2 subfamily expression in cancer types provides a platform to predict the efficacy of bcl-2 antagonists in cancer therapy. *Cell Death Dis*. 2010;1:e40.
- Kasper S, Breitenbuecher F, Heidel F, Hoffarth S, Markova B, Schuler M, et al. Targeting MCL-1 sensitizes FLT3-ITD-positive leukemias to cytotoxic therapies. *Blood*. 2012;2:e60.
- Germain M, Nguyen AP, Le Grand JN, Arbour N, Vanderluit JL, Park DS, et al. MCL-1 is a stress sensor that regulates autophagy in a developmentally regulated manner. *EMBO J*. 2011;30:395–407.
- Fogarty LC, Flemmer RT, Geizer BA, Licursi M, Karunanithy A, Opferman JT, et al. Mcl-1 and Bcl-xL are essential for survival of the developing nervous system. *Cell Death Differ*. 2018;26:1501–15.

ARTICLE

<https://doi.org/10.1038/s41467-019-09487-1>

OPEN

Reversible induction of mitophagy by an optogenetic bimodular system

Pasquale D'Acunzo ¹, Flavie Strappazon ^{2,3}, Ignazio Caruana ¹, Giacomo Meneghetti ⁴, Anthea Di Rita^{2,3}, Luca Simula^{1,3}, Gerrit Weber¹, Francesca Del Bufalo ¹, Luisa Dalla Valle ⁴, Silvia Campello ^{2,3}, Franco Locatelli^{1,5} & Francesco Cecconi ^{1,3,6}

Autophagy-mediated degradation of mitochondria (mitophagy) is a key process in cellular quality control. Although mitophagy impairment is involved in several patho-physiological conditions, valuable methods to induce mitophagy with low toxicity *in vivo* are still lacking. Herein, we describe a new optogenetic tool to stimulate mitophagy, based on light-dependent recruitment of pro-autophagy protein AMBRA1 to mitochondrial surface. Upon illumination, AMBRA1-RFP-sspB is efficiently relocated from the cytosol to mitochondria, where it reversibly mediates mito-aggresome formation and reduction of mitochondrial mass. Finally, as a proof of concept of the biomedical relevance of this method, we induced mitophagy in an *in vitro* model of neurotoxicity, fully preventing cell death, as well as in human T lymphocytes and in zebrafish *in vivo*. Given the unique features of this tool, we think it may turn out to be very useful for a wide range of both therapeutic and research applications.

¹ Department of Paediatric Haematology, Oncology and Cell and Gene Therapy, IRCCS Bambino Gesù Children's Hospital, Piazza Sant'Onofrio 4, 00165 Rome, Italy. ² IRCCS Fondazione Santa Lucia, Via del Fosso di Fiorano 64, 00143 Rome, Italy. ³ Department of Biology, University of Tor Vergata, Via della Ricerca Scientifica 1, 00133 Rome, Italy. ⁴ Department of Biology, University of Padova, Via Ugo Bassi 58/b, 35131 Padova, Italy. ⁵ Department of Gynecology/Obstetrics and Pediatrics, Sapienza University of Rome, Piazzale Aldo Moro 5, 00185 Rome, Italy. ⁶ Unit of Cell Stress and Survival, Danish Cancer Society Research Center, Strandboulevarden 49, DK-2100 Copenhagen, Denmark. Correspondence and requests for materials should be addressed to F.C. (email: cecconi@cancer.dk)

Autophagy-mediated degradation of mitochondria (hereafter mitophagy) is a pivotal quality control mechanism in cellular homeostasis¹. Briefly, in normal conditions, aged and damaged mitochondria are ubiquitinated and engulfed in double membrane vesicles called autophagosomes (APs), which, in turn, are transported and fused to lysosomes in order to release their cargo. Given the importance of mitochondria in adenosine triphosphate (ATP) production, calcium buffering, redox reactions, reactive oxygen species (ROS) generation, and death/survival choice², cells need to finely regulate the turnover of these organelles to maintain internal stability. Accordingly, mitophagy defects have been implicated in the initial steps of several diseases, such as neurodegenerative diseases, muscle atrophy, and carcinogenesis, in which this housekeeping process is strongly downregulated³.

Nonetheless, valuable methods to selectively and reversibly induce mitophagy with low-level side effects are still lacking, restraining the study of mitophagy to selected cases and conditions.

In conventional cell biology studies, the most-widely used strategy encompasses the dissipation of the H⁺ proton gradient across the inner mitochondrial membrane, through administration of uncoupling agents—carbonyl cyanide-4-(tri-fluoromethoxy)phenylhydrazone (FCCP), 2,4-dinitrophenol (2,4-DNP or simply DNP), etc.—or electron transport chain inhibitors (oligomycin/antimycin-A). Accordingly, uncouplers cause rapid depolarization of mitochondrial potential ($\Delta\Psi_m$) and mitochondrial damage. Consequently, E3 ubiquitin ligases, such as Parkin, are recruited to depolarized mitochondria, where they ubiquitinate their substrates and induce mitochondrial clearance².

Administration of these compounds carries several disadvantages. First of all, they show a broad spectrum of off-target activities, e.g., plasma membrane depolarization⁴, ATP production block⁵, mitochondrial permeability transition pore opening⁶, cytotoxicity⁷ and, ultimately, cell death^{8–10}. Second, uncoupler treatments are not suitable in vivo, since the fast H⁺ influx into the mitochondrial matrix is responsible for strong hyperthermia in mammals¹¹. Third, mitophagy activation by $\Delta\Psi_m$ depolarization seems to require PINK1/Parkin activity, at least in a number of model systems¹². This pathway, however, has been found to be mutated or impaired in some diseases, such as Parkinson's disease (PD)¹³.

One way, usually followed, to overcome some of these issues had been the genetic manipulation of specific genes along the mitophagy pathway. Downregulation of the mitochondrial deubiquitinase USP30, for instance, has been shown to provoke a strong mitophagy response with low toxicity, and was able to counteract oxidative stress-driven neurotoxicity in vivo in *Drosophila melanogaster*¹⁴. Likewise, the forced relocalization of the pro-autophagy protein AMBRA1 (autophagy and beclin-1 regulator 1) to the mitochondrial outer membrane (MOM) directly stimulates mitophagy¹⁵. In fact, endogenous AMBRA1 can be found at mitochondria¹⁶ and is able to directly recruit APs to damaged organelles through Microtubule-associated proteins 1A/1B light chain 3B (LC3) binding upon stress induction¹⁵. When fused C-terminally to a small signal peptide from the *Lysteria monocytogenes* ActA (actin assembly inducing) protein, it could be relocalized to the MOM¹⁵, where it induces mitophagy per se, in the absence of any other stimulus, in both Parkin-dependent or -independent ways¹⁵. Notably, AMBRA1-ActA-mediated mitophagy was sufficient to alleviate oxidative stress and significantly reduce cell death in commonly used in vitro models of PD, namely in rotenone and 6-hydroxydopamine(6-OHDA)-intoxicated neuroblastoma cells¹⁷.

Although genetic manipulation led to good results in terms of toxicity and specificity, in practice it is rarely used as mitophagic

tool, since the cellular response is hardly tuneable and cannot be switched off.

Herein, we present an optogenetic bimodular system, based on the recruitment of AMBRA1 to mitochondria after blue light irradiation, which stimulates mitophagy in a specific and reversible fashion. As a proof of concept, we demonstrate effective mitophagy induction (I) in vitro, in HeLa cells, which are worldwide considered a Parkin-free cell line¹⁸, (II) ex vivo, in human T lymphocytes collected from peripheral blood of healthy donors, and (III) in vivo, in illuminated living *Danio rerio* embryos. Moreover, we also show a light-dependent block of apoptosis in an in vitro model of oxidative stress-mediated neuronal-like cell death.

Besides its relevance as a putative therapeutic tool, this is a formidable example of the potential application of optogenetic dimers to mediate not easily tuneable cellular processes in an efficient and reversible way.

Results

AMBRA1 is recruited to the MOM upon blue light stimulation. To date, diverse blue light-induced dimerizers have been described; among others, we have chosen the iLID/sspB_{micro} system¹⁹. In fact, this system is characterized by fast kinetics, large changes in binding affinity upon irradiation, low (if any) binding in the dark state, no requirement of exogenous chromophores and very low-molecular weight of the modules, so making it one of the most attractive optogenetic pairs hitherto published²⁰.

Thus, we N-terminally fused the sequence encoding AMBRA1 to the already published TagRFPT-sspB_{micro} protein (hereafter, AMBRA1-RFP-sspB). Its counterpart (Venus-iLID-ActA) carried a more stable modified version of the green fluorescent protein (Venus), the blue-light sensor element iLID and the MOM signal peptide of the ActA protein (Fig. 1a). In our working model, AMBRA1-RFP-sspB is present in the cytosol in a basal state, while its partner is tethered to the mitochondrial membrane. Upon blue light stimulus, iLID undergoes a conformational change which unlocks the ssrA peptide and allows its binding to the sspB stretch¹⁹ (Fig. 1a). The expected final result would be a blue-light inducible shuttling of AMBRA1 from its main diffuse cytosolic localization to the MOM; this event should then trigger mitophagy without additional stimuli, de facto reproducing the phenotype we obtained by overexpressing AMBRA1-ActA in different cell types¹⁵. Note that the local irradiance necessary for sspB/iLID binding (500 μW per cm^2)²⁰ is lower, by several orders of magnitude, than that used for classical optogenetic opsins (~ 1 mW per mm^2 , corresponding to 10^5 μW per cm^2)²¹, strongly limiting unspecific effects and photodamage in prolonged experiments.

To confirm our hypothesis, Venus-iLID-ActA was transfected alone in HeLa cells, which were, in turn, kept in the dark or illuminated for 72 h at an irradiance of 500 μW per cm^2 with a blue pulsed light LED emitter (cycles of 1 s of light spaced by 1 min of dark resting state). Cells showed a healthy, fused and elongated mitochondrial network, even after prolonged pulsed illumination, this suggesting that neither overexpression of the MOM-tagged Venus-iLID-ActA nor blue light exposure were altering per se mitochondrial dynamics. Moreover, as expected, Venus-iLID-ActA was found to entirely co-localize with the MOM-marker Tom20 (Supplementary Figure 1).

Next, Venus-iLID-ActA and AMBRA1-RFP-sspB were co-expressed and complete recruitment of AMBRA1-RFP-sspB to mitochondria in irradiated cells was obtained (Fig. 1b–d). First, we analyzed the subcellular distribution of AMBRA1-RFP-sspB by Western blot (WB) assay, by separating the mitochondrial

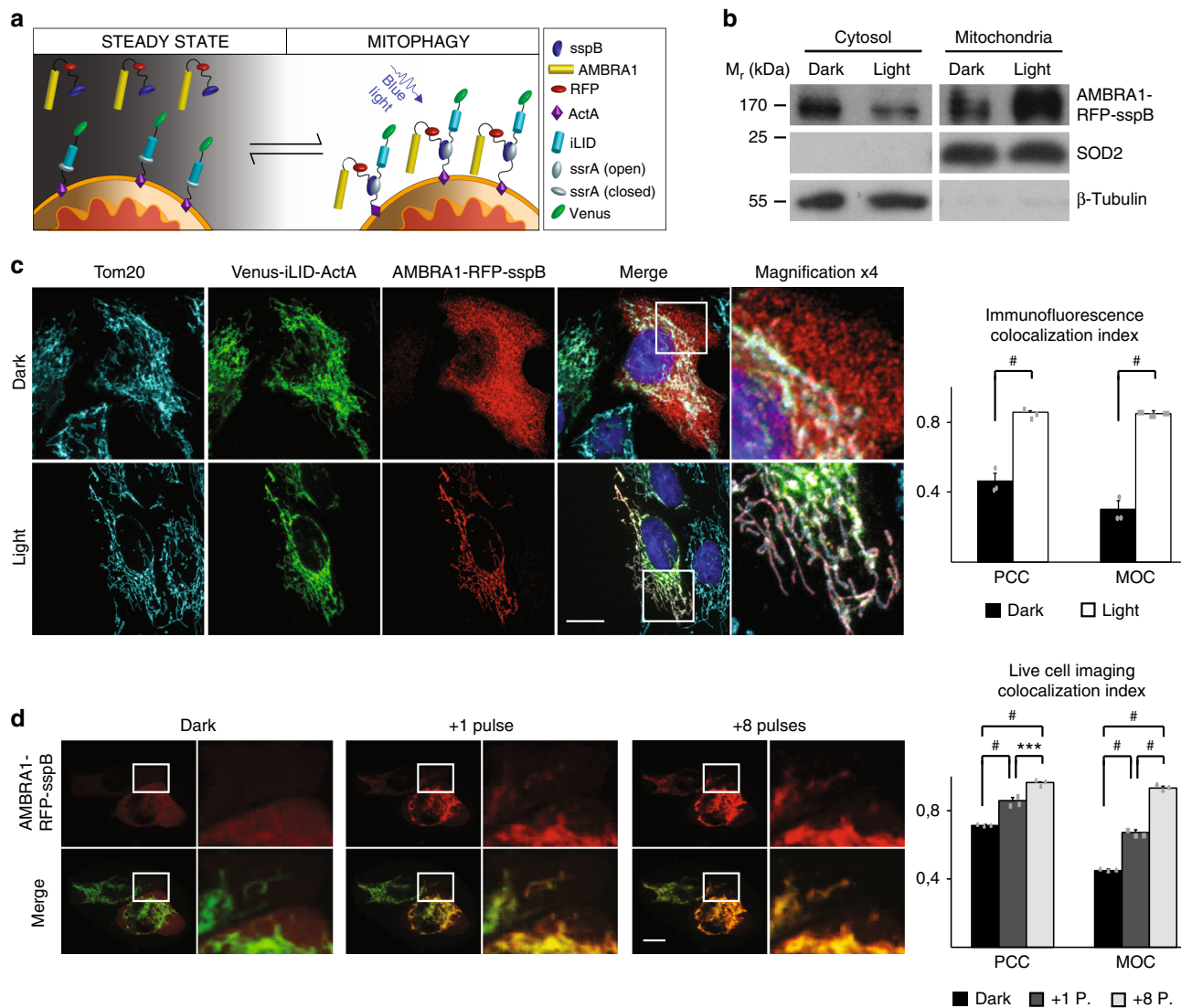


Fig. 1 AMBRA1-RFP-sspB is relocalized to MOM upon blue light exposure. **a** Scheme of the blue light-dependent, AMBRA1-RFP-sspB-mediated induction of mitophagy. In resting conditions, Venus-iLID-ActA is tethered to the MOM, while AMBRA1-RFP-sspB is found in the cytosol (STEADY STATE panel, left). Upon blue light administration, iLID undergoes into a conformational change, which unmasks the ssrA peptide and permits the high-affinity binding between ssrA and sspB (MITOPHAGY panel, Right). Thus, the pro-autophagy protein AMBRA1 (covalently bound to sspB) accumulates to the edge of the MOM where it promotes autophagy-mediated clearance of mitochondria (mitophagy). **b** HeLa cells, transfected with plasmids encoding Venus-iLID-ActA/AMBRA1-RFP-sspB, were exposed to continuous blue light for 30 s or kept in the dark. Crude mitochondrial and cytosolic extracts were analyzed by WB through an anti-AMBRA1 antibody to reveal AMBRA1-RFP-sspB. SOD2 and β-tubulin were used as loading control for mitochondrial and cytosolic lysates, respectively. M_r (kDa): relative molecular mass expressed in kilodalton. **c** HeLa cells were transfected and treated as described in (b). Subsequently, cells were fixed and immuno-stained with antibodies against AMBRA1 (red) and Tom20 (MOM marker, cyan). The green signal shown in the figure is the intrinsic fluorescence of the Venus-iLID-ActA protein. Pearson's correlation coefficient (PCC) and Manders' overlap coefficient (MOC) of the red over the green signal were quantified in ten random fields of three independent experiments. Nuclei (blue) were stained with DAPI. **d** HeLa cells overexpressing Venus-iLID-ActA/AMBRA1-RFP-sspB were filmed through the UltraVox (PerkinElmer) live cell imaging spinning disk microscope before (Dark in the panel) and during 8 irradiation cycles, consisting of 1 pulse (50 ms) of blue light followed by 35 s of dark resting state. The graph shows PCC and MOC quantifications of the red over the green signal for three conditions (Dark, one pulse, eight pulses) in ten random fields of three independent experiments. Images are the sum of a three frames Z-stack. Insets: 4× magnification. Scale bars: 10 μm. Data shown: mean ± S.E.M. Hypothesis tests: Student's *t* test in (c) and ANOVA test in (d). ****p* < 10⁻³. #*p* < 10⁻⁴. Source data are provided as a Source Data file

from the cytosolic protein pools in Venus-iLID-ActA/AMBRA1-RFP-sspB-overexpressing cells lysates. Upon blue light exposure, the AMBRA1-RFP-sspB signal clearly decreased into the cytosolic fractions whilst increased in the mitochondrial one (Fig. 1b). Second, AMBRA1-RFP-sspB relocalization after a single burst of blue light was confirmed in fixed cells incubated with antibodies against Tom20 and AMBRA1. In cells kept in the dark, AMBRA1-RFP-sspB was found in the cytosol, while it was

almost completely co-localized with Tom20 and Venus-iLID-ActA after stimulus—Pearson's correlation coefficient (PCC): 0.86 ± 0.04 (mean ± standard deviation); Manders' overlap coefficient (MOC): 0.85 ± 0.05 Fig. 1c. We also report 9.4 ± 1.4% of cells in which a faint signal was retained in the cytoplasm upon illumination, mostly in Venus-iLID-ActA low-expressing cells (Supplementary Figure 2). Last, to better understand the binding kinetics in our conditions, we recorded AMBRA1-RFP-sspB

shuttling from cytosol to mitochondria within the same cell, by live cell imaging (Supplementary Movie 1). A single 50 ms pulse was enough to efficiently drive the vast majority of AMBRA1-RFP-sspB to mitochondria (MOC: 0.67 ± 0.04 vs. 0.45 ± 0.02 , ANOVA test, $p < 10^{-4}$); nevertheless, a rising number of spikes permitted a slightly increase of the co-localization rate. After 8 spikes, the translocation of the protein reached the plateau (MOC: 0.93 ± 0.04 , ANOVA test, $p < 10^{-4}$ Fig. 1d).

Prolonged AMBRA1 repositioning to the MOM induces mitophagy. Next, we wondered whether the persistent presence of AMBRA1-RFP-sspB on the MOM was able to trigger mitophagy as already observed in the case of AMBRA1-ActA ectopic expression¹⁵. HeLa cells (a bona fide Parkin-free cell line) were transfected with the two plasmids encoding Venus-iLID-ActA and AMBRA1-RFP-sspB and irradiated with pulsed blue light for 30 min, 1 h, 2 h, or 4 h to monitor the status of their mitochondria. In the given conditions, sporadically after 30 min and more prominently after 4 h, mitochondria appeared fragmented, round-shaped and accumulated next to the nuclei, usually in 1 or 2 opposite poles (Fig. 2a), with these structures strongly resembling mito-aggregates, a hallmark of ongoing mitophagy²². The appearance of AMBRA1-RFP-sspB rings around mito-aggregates was also evident at higher magnification (Fig. 2a, inset), as already reported for AMBRA1-ActA¹⁵. Of note, as an internal control, nontransfected neighbor cells showed normal-looking mitochondria, suggesting that the effect described is not due to unspecific phenomena related to illumination. Upon light exposure the percentage of transfected cells with mito-aggregates increased over time, raising from $10.8 \pm 1.5\%$ to $31.9 \pm 4.5\%$, while the extent of normal cells decreased accordingly (Supplementary Figure 3). When pulsed irradiation was prolonged to 24 h, more evident phenotypes were detected, as $13.4 \pm 3.7\%$ of double-transfected cells had only mitochondrial remnants (Supplementary Figure 4). Remarkably, little (if any) pyknosis is seen by DAPI staining of irradiated Venus-iLID-ActA/AMBRA1-RFP-sspB cells (Fig. 2a, Supplementary Figure 3, Supplementary Figure 4), suggesting lack of apoptosis when mito-aggregates are formed. To better elucidate this point, we analyzed the percentage of Venus-iLID-ActA/AMBRA1-RFP-sspB double-positive viable cells by flow cytometry when either kept in the dark or illuminated for 24 h, finding no differences (Supplementary Figure 5); moreover, at a single-cell level, no release of cytochrome-c from mito-aggregates was documented (Supplementary Figure 6). These data suggest that AMBRA1-RFP-sspB-mediated mitophagy was not followed by cell death in our conditions.

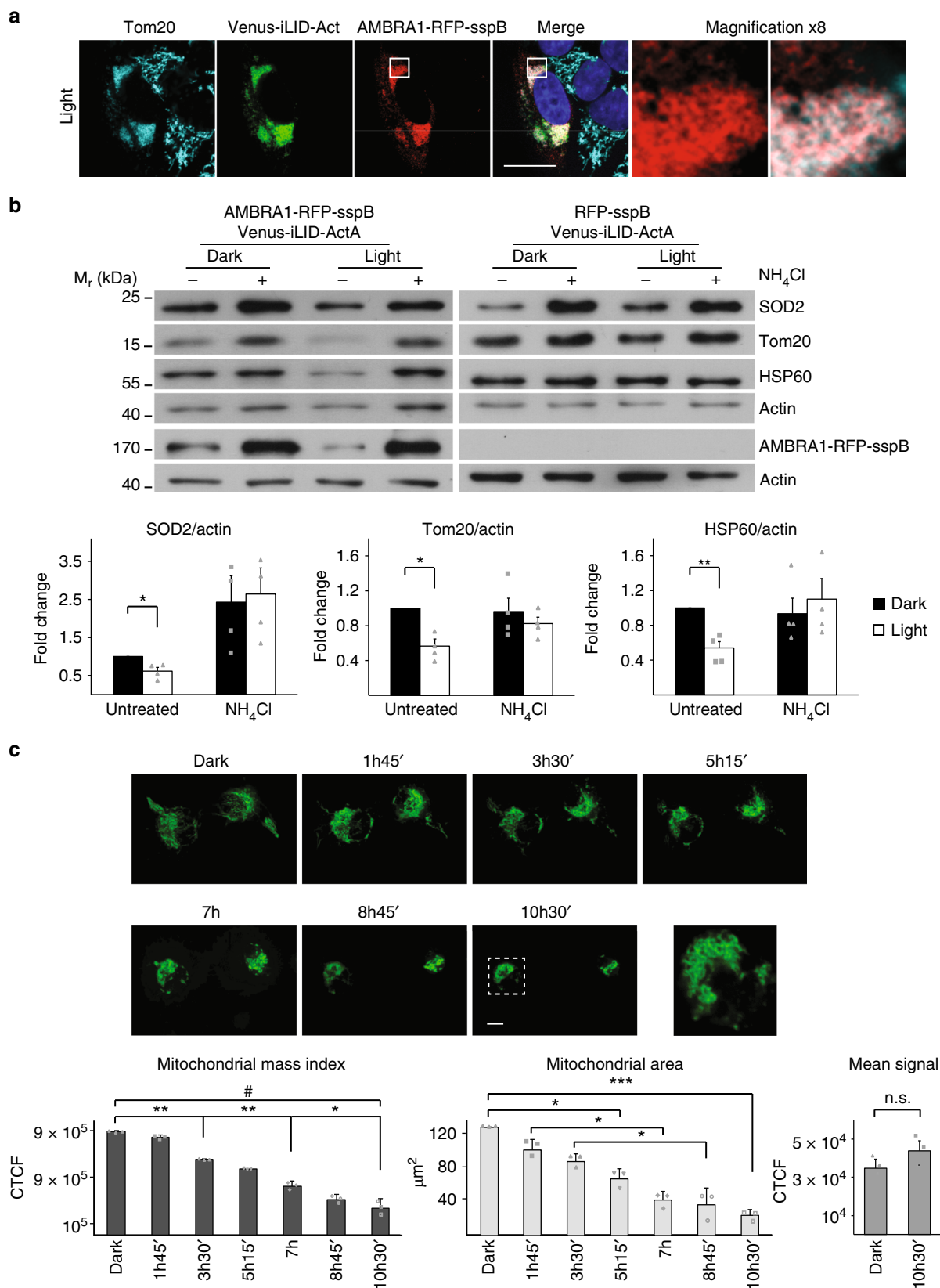
Subsequently, to better understand if upon illumination the autophagy machinery led to a reduction in mitochondrial mass, we assessed by WB the amount of three distinct mitochondrial markers in cells treated with the lysosome inhibitor ammonium chloride (NH_4Cl , 40 mM) and in the presence or absence of pulsed blue light for 24 h (Fig. 2b, left panel). More specifically, we analyzed the signal of Tom20 (MOM protein), and two mitochondrial matrix proteins, SOD2 and HSP60. As previously described²³, mitochondrial matrix proteins are the best markers to estimate mitochondrial mass since they are preferentially degraded by mitophagy. Indeed, all markers were reduced in irradiated cells compared to their dark counterparts, while no changes were documented in NH_4Cl -treated cells, strongly suggesting that reduction of the signal mediated by AMBRA1-RFP-sspB translocation to the MOM is mitophagy dependent. As a negative control, we repeated the same experiment in Venus-iLID-ActA/RFP-sspB co-expressing cells. RFP-sspB retains the ability to bind its partner upon blue light exposure, but it does not carry the pro-autophagy effector protein AMBRA1. As expected,

no alteration in mitochondrial morphology and no decrease in mitochondrial markers were detected after illumination (Fig. 2b, right panel, Supplementary Figure 7 and Supplementary Figure 8). Since wild-type HeLa cells are Parkin-deficient and almost insensitive to mitophagy-inducing insults without overexpression of Parkin or other mitophagic receptors²⁴, a direct comparison between our optogenetic tool and pre-existing methods has been prohibitive for this cell line. However, in Parkin-competent cells (HEK293T) the AMBRA1-RFP-sspB-mediated, light-induced reduction in mitochondrial mass was comparable to that triggered with classical methods, as the Oligomycin/Antimycin A treatment (Supplementary Figure 9). Next, in order to corroborate the relationship existing between the reduction of mitochondrial markers and autophagy induction, we performed a pulse-chase experiment in which a modified methionine analogue (L-azidohomoalanine, AHA) has been incorporated into nascent proteins before the illumination procedures. After 24 h of pulsed blue light illumination or 24 h of dark resting state, AHA levels have been quantified and a significant decrease was reported in Venus-iLID-ActA/AMBRA1-RFP-sspB double-transfected and irradiated cells when compared to control cells that were treated in the same way (Supplementary Figure 10). Given that a long chase time (24 h in our experiments) guaranteed the exclusive measurement of the long-lived proteins proteolytic rate, our data strongly suggest that blue light irradiation stimulated autophagy specifically in Venus-iLID-ActA/AMBRA1-RFP-sspB co-expressing cells.

Finally, mitochondrial rearrangement and reduction during AMBRA1-mediated mitophagy was recorded over time by live cell imaging (Supplementary Movie 2, Supplementary Figure 11 and Fig. 2c). Since Venus-iLID-ActA is constantly anchored to the MOM, live visualization over time of this protein in not-bleaching conditions makes it possible both to estimate mitochondrial mass within single cells (proportional to Venus-iLID-ActA fluorescence) and to monitor how mitochondria behave when AMBRA1 shuttles to their surface. A progressive remodeling of mitochondria was appreciable, this leading to a fragmented perinuclear signal. Mitochondrial aggregation was also confirmed by the reduction of the area occupied by mitochondria (from 123 ± 2 to $25 \pm 6 \mu\text{m}$, ANOVA test, $p < 10^{-3}$). While the mean signal did not decrease (ensuring no photobleaching), the decrease of green fluorescence per whole cell was also evident (from a coefficient of $8.9 \pm 0.1 \times 10^5$ down to $2.3 \pm 0.6 \times 10^5$, ANOVA test, $p < 10^{-3}$) again suggesting ongoing mitochondrial clearance in our given conditions.

AMBRA1-RFP-sspB-mediated mitophagy is reversible. Venus-iLID/RFP-sspB binding is reversible, as previously described¹⁹ and as confirmed by us (Supplementary Figure 12). Therefore, by live cell imaging, we set up to establish whether our fusion proteins maintained this important property and conferred the same feature to the phenotype. To this aim, we first stimulated AMBRA1-RFP-sspB repositioning to MOM in Venus-iLID-ActA/AMBRA1-RFP-sspB overexpressing cells; then, we examined AMBRA1-RFP-sspB shuttling when the dark state was restored. After 3 min, the AMBRA1-related mitochondrial signal was highly weakened, while the cytosolic one had an opposite tendency, revealing an ongoing detachment of AMBRA1-RFP-sspB from mitochondria (Fig. 3a, Supplementary Figure 13, Supplementary Movie 3). However, a new burst of blue light was able to fully bring back the protein to the former position, thus proving that AMBRA1-RFP-sspB displacement could be precisely regulated.

We next checked if a continuous dark state could be sufficient to thwart previous induction of mitophagy by pulsed light, in



Venus-iLID-ActA/AMBRA1-RFP-sspB co-expressing cells. Hence, cells were illuminated for 24 h followed by 24 h of dark (a condition that we termed Rescue). Then, we compared the levels of the mitochondrial marker SOD2 with those derived from cells treated in the opposite way (24 h resting, then 24 h light) in

order to estimate mitochondrial mass in the two given conditions. As controls, cells were also kept either 48 h in the dark or 48 h under blue light, respectively; additionally, the experiment was repeated in Venus-iLID-ActA/RFP-sspB co-expressing cells to highlight the specificity of SOD2 decrease, as explained before

Fig. 2 AMBRA1-RFP-sspB shuttling to the MOM induces mitophagy. **a** Venus-iLID-ActA/AMBRA1-RFP-sspB overexpressing HeLa cells were irradiated or not for 4 h with pulsed, blue light. Cells were subsequently fixed and stained for Nuclei (DAPI, blue), AMBRA1 (red) and Tom20 (cyan). Inset: 8× magnification. Scale bar: 10 μm. **b** HeLa cells, transfected with plasmids encoding Venus-iLID-ActA/AMBRA1-RFP-sspB (left panel), were stimulated with a blue LED irradiator or left in the dark for 24 h. In the meantime, they were treated or not with 40 mM NH₄Cl, a lysosome inhibitor. As a negative control, the same experiment was repeated in Venus-iLID-ActA/RFP-sspB co-expressing cells (right panel). In the subsequent WB analysis, Tom20, SOD2, and HSP60 were used as mitochondrial markers, while actin was the loading control. AMBRA1-RFP-sspB was detected to verify the rate of overexpression. Graphs recapitulate the normalized ratio between the densitometric signals of the three mitochondrial markers over actin in four independent experiments involving Venus-iLID-ActA/AMBRA1-RFP-sspB overexpressing cells. For the quantification of the same parameters in the negative control see Supplementary Figure 7. Data shown: mean ± S.E.M. Hypothesis test: Student's *t* test. **p* < 5 × 10⁻². ***p* < 10⁻². *M_r* (kDa): Relative molecular mass expressed in kilodalton. **c** Single-HeLa cells co-expressing Venus-iLID-ActA/AMBRA1-RFP-sspB were followed in time for 10 h 30 min during mitophagy progression through live cell imaging of the protein Venus-iLID-ActA (50 ms blue laser spikes alternated by 1 min dark). Each frame depicts mitochondria morphology every 1 h 45 min of stimulation. Images are the sum of a three frames Z-stack. Graphs show the area occupied by mitochondria over time, the overall reduction per whole cell of the Venus-iLID-ActA signal intensity corrected for the background and the mean fluorescence intensity in three independent experiments. Inset: 4× magnification of a single plane after 10 h 30 min of stimulation, highlighting mitoagosome formation. CTF corrected total cell fluorescence. Scale bar: 10 μm. Data shown: mean ± S.E.M. Hypothesis test: ANOVA test for Area and Mito Mass Index, Student's *t* test for the mean signal. n.s. not statistically significant. **p* < 5 × 10⁻². ***p* < 10⁻². ****p* < 10⁻³. #*p* < 10⁻⁴. Source data are provided as a Source Data file

(Fig. 3b). Strikingly, the Rescue condition permitted the re-establishment of normal SOD2 levels, which were significantly higher than what observed in the 24 h lane, this strongly suggesting a complete halt in mitophagy progression. As expected, no effect was observed for Venus-iLID-ActA/RFP-sspB co-expressing cells.

Last, in order to further elucidate the molecular mechanisms at the basis of AMBRA1-RFP-sspB-mediated mitophagy in a Parkin-independent context, we checked whether inhibition of the HUWE1 E3 Ubiquitin Ligase or the IKKα kinase (two key factors in AMBRA1-dependent mitophagy²⁴) were able to block mitophagy in HeLa cells. As expected, both the downregulation of HUWE1 and the pharmacological irreversible inhibition of IKKα were able to fully prevent reduction of mitochondrial mass upon blue light stimulus in Venus-iLID-ActA/AMBRA1-RFP-sspB co-expressing HeLa cells (Supplementary Figure 14). This suggests that the HUWE1/IKKα-axis is a crucial pathway to fully trigger AMBRA1-RFP-sspB-mediated mitophagy.

Optogenetic mitophagy induction in physiological contexts.

In order to assess if our bimodular system could be used in other applications besides in vitro studies, we checked whether mitophagy could be induced in ex vivo human T lymphocytes taken from healthy donors and in living animals in vivo. To this aim, we co-infected T cells with retroviral vectors encoding for Venus-iLID-ActA/AMBRA1-RFP-sspB or Venus-iLID-ActA/RFP-sspB as a control (Supplementary Figure 15) and illuminated or not these cells for 24 h by pulsed blue light as indicated above. AMBRA1-RFP-sspB shuttling to mitochondria as well as a reduction in mitochondrial mass was confirmed also in this experimental condition (Fig. 4). AMBRA1-RFP-sspB but not RFP-sspB-expressing cells showed a marked decrease in Tom20 staining when illuminated (from a coefficient of 31.7 ± 3.1 to 7.6 ± 1.6, *p* < 10⁻⁴, Student's *t* test, Fig. 4a) as well as decreased mitochondrial markers by WB (Fig. 4b), with this indicating blue light-driven mitochondrial clearance.

For in vivo stimulation of AMBRA1-RFP-sspB-mediated mitophagy, we chose zebrafish (*D. rerio*) as a model organism for several reasons. Technically, the optical transparency of zebrafish embryos permitted an easier penetration of blue light when compared to rodents. Functionally, it has already been demonstrated that AMBRA1 is highly conserved in this species²⁵, and that injection of human AMBRA1 mRNA is able to rescue the phenotype of zebrafish morphants in which endogenous genes were knocked-down²⁶, strongly suggesting overlapping functions across species. Intriguingly, zebrafish *ambra1a* knockdown larvae display accumulation of swollen and aberrant mitochondria in

skeletal muscle fibers²⁶, while the protein sequence is predicted in silico²⁷ to carry a LC3-interacting region domain in its C-terminal region (Supplementary Figure 16), similarly to human AMBRA1¹⁵; this clearly indicates a possible role for *ambra1a* in zebrafish mitophagic pathways.

In view of that, we microinjected Venus-iLID-ActA/AMBRA1-RFP-sspB expressing plasmids in zebrafish embryos and checked whether mitophagy could be induced by blue light. Preliminarily, we demonstrated a proper MOM distribution for Venus-iLID-ActA alone (Fig. 5a) and a correct mitochondrial shuttling of AMBRA1-RFP-sspB from and to mitochondria of zebrafish muscle fibers with similar kinetics observed in human cells in vitro (MOC of 0.877 ± 0.09 after light, down to 0.402 ± 0.11 when dark was restored, *p* < 10⁻², ANOVA test, Fig. 5b). Lastly, double-positive Venus-iLID-ActA/AMBRA1-RFP-sspB or Venus-iLID-ActA/RFP-sspB (negative control) were analyzed by live cell imaging before and after 8 h of pulsed blue light stimulation (Fig. 5c). Upon light stimulus, mitochondria appeared round-shaped (arrowheads), while Venus-iLID-ActA intensity per single fiber was significantly decreased, suggesting ongoing mitochondrial clearance. No changes could be detected in Venus-iLID-ActA/RFP-sspB-positive embryos.

Mitophagy prevents cell death in a model of neurotoxicity.

As a proof of concept of the potential beneficial contribution of our bimodular system to biomedicine in a functional study, we tested whether AMBRA1-RFP-sspB-mediated mitophagy could be able to block apoptosis in a cellular model of oxidative stress-induced neurotoxicity. The role of mitochondria dysfunction as a priming event for ROS accumulation has been widely discussed in the literature, and mitophagy impairment has been postulated to be a key feature during ROS-derived neurodegeneration²⁸. Indeed, a class of compounds called Parkinsonian toxins (among the others, Paraquat, rotenone, and 6-OHDA) directly impair mitochondrial activity through diverse mechanisms while being responsible of a PD-like phenotype both in vivo and in vitro²⁹. Above all, the FDA-approved herbicide Paraquat (PQ; N,N'-dimethyl-4,4'-bipyridinium dichloride) has been epidemiologically linked to sporadic PD cases in humans³⁰, and it seems to provoke similar effects in rats³¹, *Caenorhabditis elegans*³² and *D. melanogaster*¹⁴, as well as cell death in neuronal cell lines³³. We already demonstrated that AMBRA1-ActA-mediated mitophagy is able per se to counteract apoptosis in parkinsonian toxins SHSY-5Y intoxicated cells;¹⁷ moreover, the protective role of mitophagy upon PQ treatment has also been thoroughly proved in vivo, at least in *D. melanogaster*¹⁴.

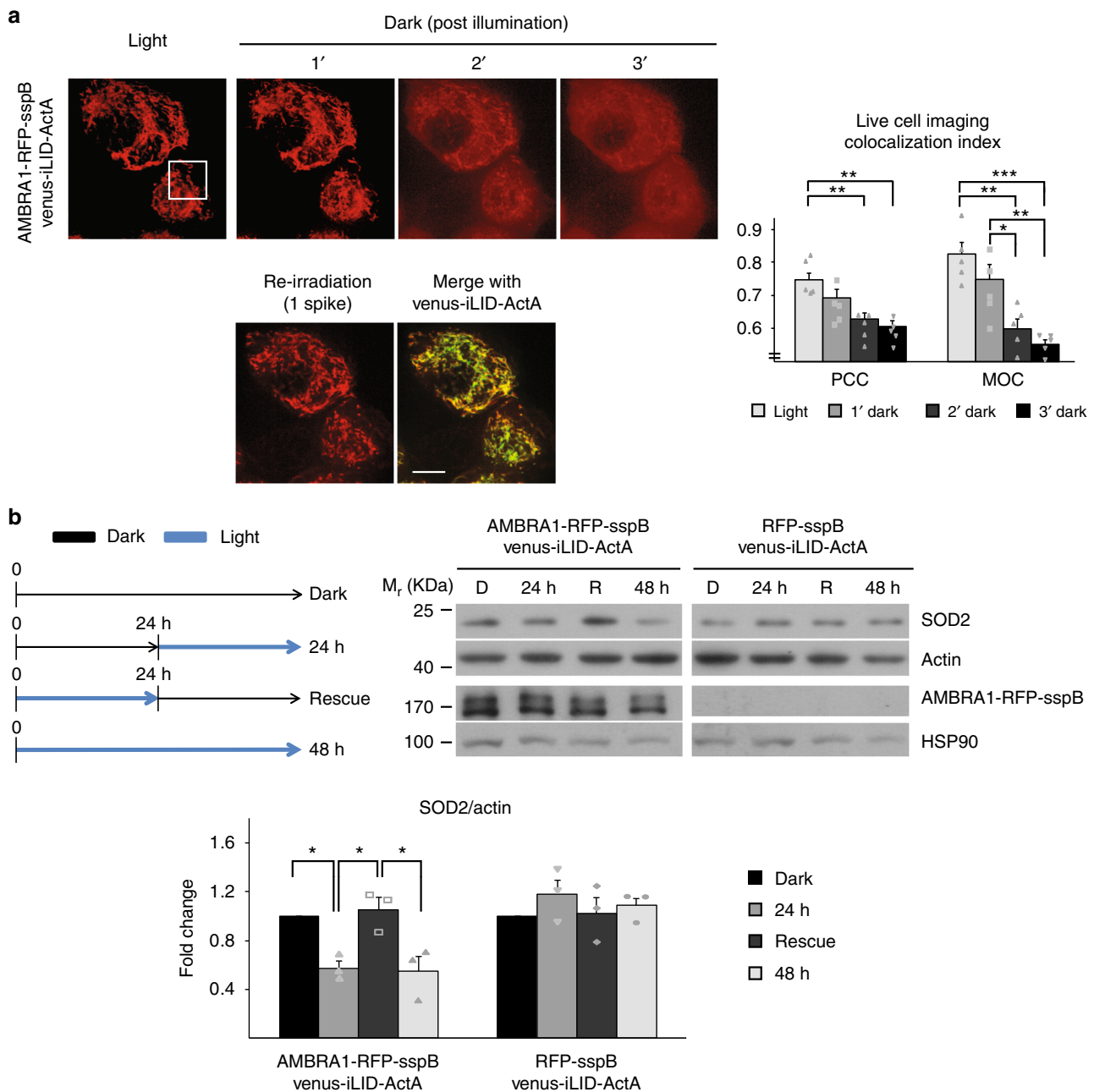


Fig. 3 AMBRA1-RFP-sspB-mediated mitophagy is reversible. **a** AMBRA1-RFP-sspB shuttling from mitochondria was assessed by live cell imaging in single Venus-iLID-ActA/AMBRA1-RFP-sspB overexpressing HeLa cells. Upon blue light irradiation AMBRA1-RFP-sspB was found at mitochondria. Subsequently, AMBRA1-RFP-sspB subcellular distribution was recorded every minute without blue light administration. After 3 min, one spike of blue light was reapplied. Images are the sum of a three frames Z-stack. PCC and MOC of the red over the green signal were quantified in ten random fields of five independent experiments. For a $\times 4$ magnification of the inset see Supplementary Figure 13. Scale bar: 10 μ m. Data shown mean \pm S.E.M. Hypothesis test: ANOVA test. * $p < 5 \times 10^{-2}$. ** $p < 10^{-2}$. *** $p < 10^{-3}$. **b** Transfected HeLa cells were treated as follows: 48 h of dark (lane Dark or D), 24 h of dark + 24 h pulsed blue light (1 s light + 1 min dark, lane 24 h), 24 h of pulsed blue light + 24 h of dark state (lane Rescue or R), and 48 h of pulsed blue light only. Cell lysates were loaded on a polyacrylamide gel and immuno-blotted. Levels of the mitochondrial marker SOD2 were investigated; AMBRA1-RFP-sspB was detected to verify the rate of overexpression. Actin and HSP90 were used as loading controls of the two gels, respectively. The graph shows the normalized densitometric SOD2 over actin ratio in three independent experiments. The experiments were repeated in Venus-iLID-ActA/RFP-sspB overexpressing HeLa cells as a control (right panel). Data shown: mean \pm S.E.M. Hypothesis test: ANOVA test. * $p < 5 \times 10^{-2}$. M_r (kDa): Relative molecular mass expressed in kilodalton. Source data are provided as a Source Data file

Primed by this evidence, we first verified mitophagy stimulation upon pulsed blue light exposure in Venus-iLID-ActA/AMBRA1-RFP-sspB co-expressing embryonic telencephalic nAive (ETNA) cells, a line derived from murine E14 striatum primordia neurons³⁴. Subsequently, we investigated its protective action upon PQ-mediated damage (Fig. 6).

In these cells, mito-aggresome formation was confirmed (Fig. 6a), as well as the decrease of mitochondrial mass as measured by the protein levels of the marker HSP60 (Fig. 6b, left panel). In our system, mitochondrial damage primed by PQ seemed not to trigger mitophagy in basal conditions, whilst it robustly potentiated mitochondrial loss when

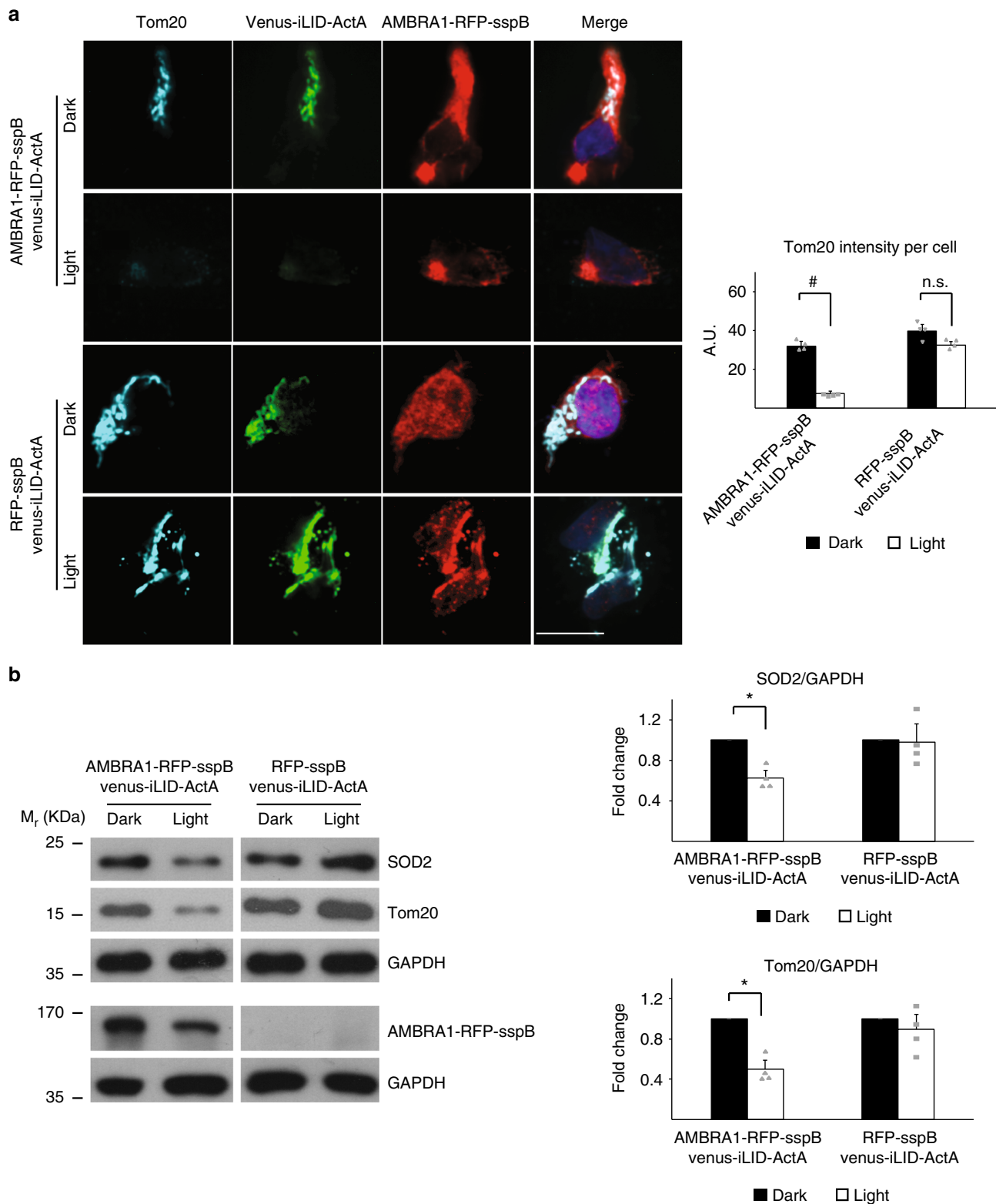


Fig. 4 AMBRA1-RFP-sspB-mediated mitophagy can be induced in T lymphocytes. **a** Human T lymphocytes from healthy donors were double infected with viral vectors encoding Venus-iLID-ActA/AMBRA1-RFP-sspB or Venus-iLID-ActA/RFP-sspB (negative control). Cells were subsequently illuminated 24 h with pulsed (1 s light, 1 min dark) blue light or kept in the dark, then fixed and immunostained for Tom20 (cyan). Nuclei were counterstained with DAPI (blue). The graph shows the intensity per cell of the Tom20 signal from four different donors. A minimum of 50 cells were analyzed per donor. Scale bar: 10 μ m. Data shown: mean \pm S.E.M. Hypothesis test: ANOVA test. $\#p < 10^{-4}$. n.s. not statistically significant. **b** Human T lymphocytes, manipulated as described in (a), were lysed and analyzed by WB. Tom20 and SOD2 were used as mitochondrial markers, while GAPDH was the loading control. AMBRA1-RFP-sspB was detected to verify the rate of overexpression. Graphs recapitulate the normalized ratio between the densitometric signals of the two mitochondrial markers over GAPDH in four different donors. Data shown: Mean \pm S.E.M. Hypothesis test: ANOVA test. $*p < 5 \times 10^{-2}$. M_r (kDa): Relative molecular mass expressed in kilodalton. Source data are provided as a Source Data file

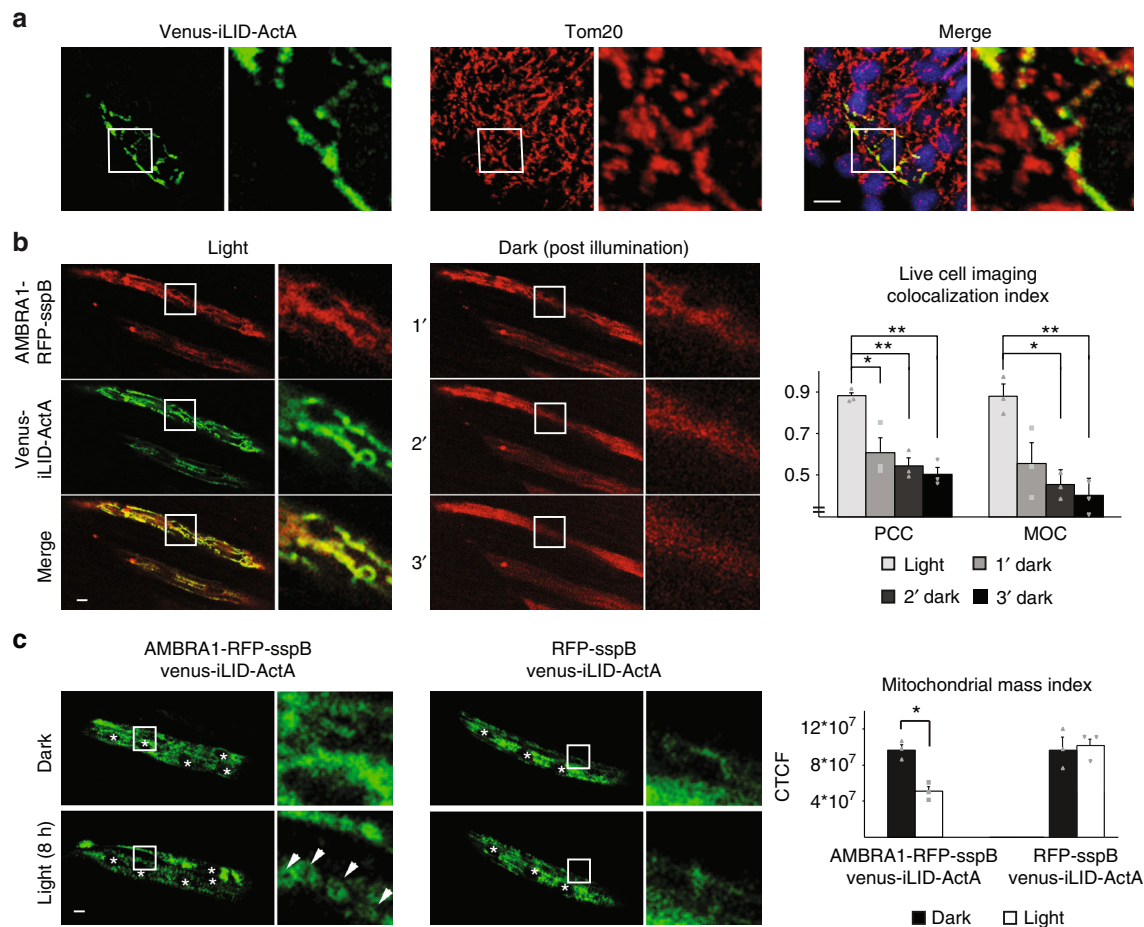


Fig. 5 In vivo induction of mitophagy through an optogenetic bimodular system. **a** Zebrafish embryos were microinjected with a Venus-iLID-ActA overexpressing plasmid, then fixed 48-hpf and whole mount immuno-stained for Tom20 (red). Nuclei were counterstained with DAPI (blue). Inset: $\times 4$ magnification. Scale bar: 10 μm . **b** Venus-iLID-ActA/AMBRA1-RFP-sspB microinjected zebrafish embryos were illuminated with blue light and then kept in the dark for 3 min, mimicking the experiment shown in Fig. 3a. Double-positive muscle fibers were photographed in order to analyze Venus-iLID-ActA/AMBRA1-RFP-sspB dynamic interactions. PCC and MOC of the red over the green signal were quantified in three independent experiments. Inset: $\times 6$ magnification. Scale bar: 10 μm . Data shown: mean \pm S.E.M. Hypothesis test: ANOVA test. $^*p < 5 \times 10^{-2}$. $^{**}p < 10^{-2}$. **c** Venus-iLID-ActA/AMBRA1-RFP-sspB or Venus-iLID-ActA/RFP-sspB (negative control) double positive zebrafish embryos were illuminated for 8 h with a pulsed (2 s light/2 min dark) blue light; muscle fibers were analyzed. Upon light stimulation, round-shaped mitochondria (arrowheads) were clearly visible in AMBRA1-RFP-sspB but not RFP-sspB positive fibers. Images are the sum of three frames Z-stack. Stars indicate nuclei. Graphs show the overall reduction per single fiber of the Venus-iLID-ActA signal intensity corrected for the background in three independent experiments. Inset: $\times 8$ magnification. Scale bar: 10 μm . Data shown: mean \pm S.E.M. Hypothesis test: ANOVA test. $^*p < 5 \times 10^{-2}$. Source data are provided as a Source Data file

AMBRA1-RFP-sspB relocated to MOM. Conversely, a slight increase of HSP60 signal in PQ-treated cells was detected in the control experiment (Fig. 6b, right panel), this being probably due to upregulation of the protein related to mitochondrial ROS accumulation³⁵.

Finally, we assessed cell death during PQ treatment by WB assay of the apoptotic marker cleaved PARP (cl-PARP, Fig. 6c). As expected, PQ caused apoptosis in the dark (lane 2, left panel), while the concomitant presence of blue light (lane 4, left panel) strongly attenuated cell death; no reduction of cl-PARP was seen in control conditions (Fig. 6c, lane 2/4, right panel). This trend was also confirmed when cleaved caspase3, a different protein of the same pathway, was analyzed (Supplementary Figure 17). Altogether, these data confirmed a cytoprotective function of AMBRA1-RFP-sspB-mediated mitophagy during PQ intoxication.

Discussion

Here, we describe an optogenetically driven tool to specifically and reversibly induce mitophagy in the absence of any

mitochondrial poisons. This is particularly relevant in physiological conditions, making its use an attractive (and mostly unexplored) strategy to ameliorate the phenotype of diseases in which dysfunctional mitochondria are involved. Loss of mitochondrial quality control has been postulated to be the keystone of many human diseases, such as tumorigenesis, muscle atrophy, diabetes, and Alzheimer's Disease, but the strongest correlations have been established with PD³⁶. The electron transport chain, most of all Complex I and III, has been shown to be severely impaired in PD sporadic cases, likely causing a huge increase in intracellular ROS levels. Accordingly, signs of oxidative stress (lipid and protein peroxidation, GSH depletion, mtDNA damage, and peroxynitrites accumulation) are validated hallmarks of PD³⁶. Although the reason why mainly Substantia nigra pars compacta dopaminergic neurons are targeted is not known, it is possible that there is a relation with their energy needs, given that they express a self-generated pacemaker activity in basal conditions and are metabolically hyperactive³⁶. Accordingly, understanding the role that mitophagy plays in vivo in its homeostatic control of mitochondrial-derived ROS is an urgent need. To date,

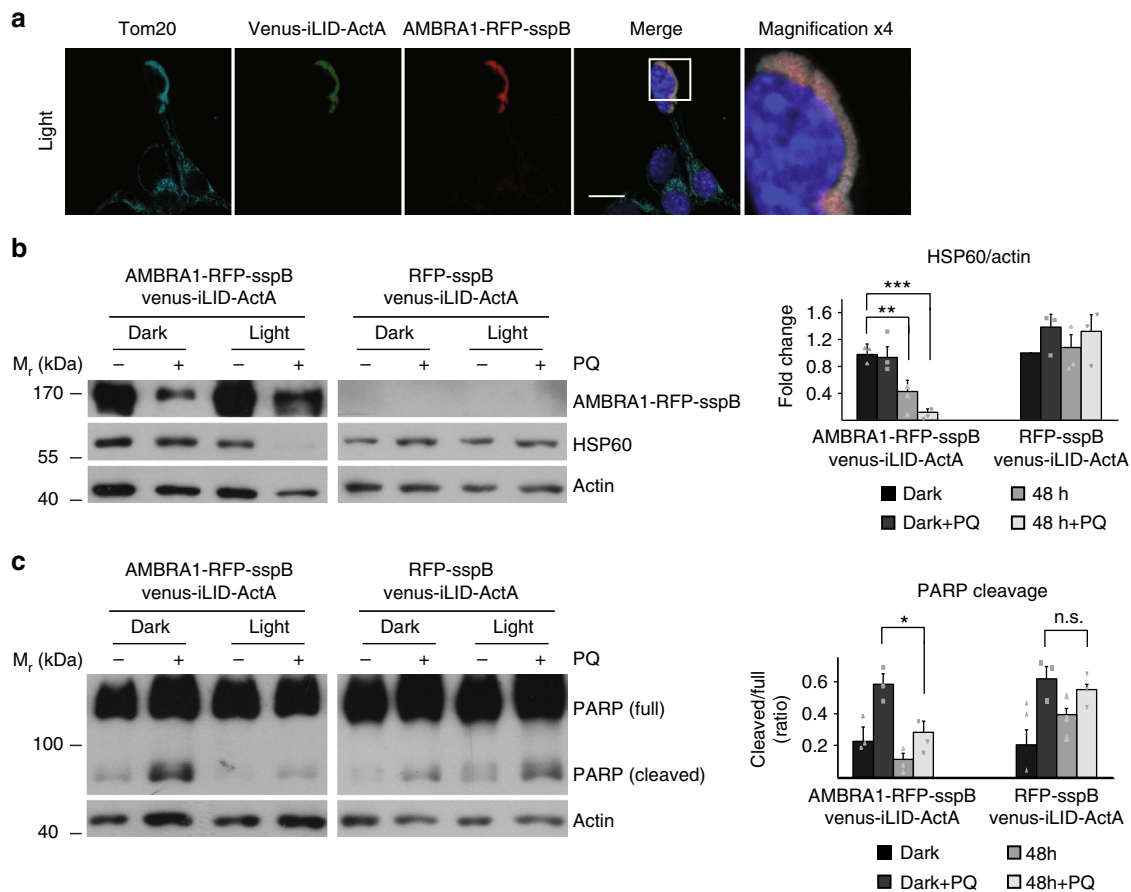


Fig. 6 Optogenetic-mediated mitophagy prevents apoptosis in a model of neurotoxicity. **a** ETNA (Embryonic Telencephalic NAïve) cells co-expressing Venus-iLID-ActA/AMBRA1-RFP-sspB were irradiated with pulsed (1 s light + 1 min dark) light for 4 h, then fixed and stained for nuclei (DAPI, blue) AMBRA1 (red) and Tom20 (cyan). Inset: $\times 4$ magnification. Scale bar: 10 μ m. **b** ETNA cells, transfected with Venus-iLID-ActA/AMBRA1-RFP-sspB or Venus-iLID-ActA/RFP-sspB (negative control), were irradiated with pulsed blue light (1 s light + 1 min dark) for 48 h or left in the dark upon treatment with 250 μ M PQ. Cell lysates were prepared and HSP60 levels (mitochondrial marker) explored in three independent experiments. Actin was used as a loading control. The graph reports the means of the normalized densitometric ratio between HSP60 and actin. Data shown: mean \pm S.E.M. Hypothesis test: ANOVA test. ** $p < 10^{-2}$. *** $p < 10^{-3}$. M_r (kDa): Relative molecular mass expressed in kilodalton. **c** Venus-iLID-ActA/AMBRA1-RFP-sspB or Venus-iLID-ActA/RFP-sspB (negative control) ETNA cells were handled as described in (**b**). WB was performed to reveal PARP protein in cell lysates. Upper band: full length PARP. Lower band: cleaved PARP. Actin: loading control. The graph summarizes the densitometric quantification of cleaved/full PARP in three independent experiments. Data shown: mean \pm S.E.M. Hypothesis test: ANOVA test. * $p < 5 \times 10^{-2}$. n.s. not statistically significant. M_r (kDa): Relative molecular mass expressed in kilodalton. Source data are provided as a Source Data file

the high toxicity and the broad off-target effects of uncouplers and of other mitochondria poisons make it impossible to investigate this aspect. Remarkably, depolarizing agents' efficacy depends on the PINK1/Parkin axis, but these proteins are often mutated, both in sporadic and genetic variants of PD³⁷. In line with that, as a proof of concept, we examined the cytoprotective role of AMBRA1-RFP-sspB-mediated mitophagy in a well-established experimental model of ROS-induced neurotoxicity. As expected, cell survival of PQ-treated proneural cells was strongly sustained (Fig. 6). In this sense, the possibility to stimulate this process in vivo (Fig. 5) opens new windows for research and therapeutic innovative strategies in neuroscience. In fact, AMBRA1-RFP-sspB/Venus-iLID-ActA bimodular system provides remarkable intrinsic advantages over any other mitophagy-based therapeutic candidates published so far.

First, AMBRA1-mediated mitophagy is Parkin dispensable¹⁵. This feature may hypothetically circumvent the problem that alterations of PINK1-Parkin pathway are often observed in neurodegenerative diseases³⁷.

Second, the quick temporal reversibility of the sspB/iLID binding permits to switch off the signal when undesired, and to

finely tune the extent of the induction by regulating the time of illumination and/or frequency of spikes. Accordingly, we showed (Fig. 3) that AMBRA1 detachment from mitochondria restored normal levels of the mitochondrial mass in 24 h.

Third, optogenetics guarantees a high-spatial resolution, unattainable with other methods. It has been observed that just focusing the laser beam it is possible to push sspB/iLID binding in a subcellular fashion¹⁹. Thus, even if not demonstrated here, ideally the stimulation of mitophagy can be restricted to a single cellular compartment within polarized cells, such as neurons. We already reported that mitochondria from dendrites, but not cell somata, may contribute to the first stages of neurodegeneration in a mouse model of Alzheimer's disease³⁸. Thus, it would be of great interest in the near future to stimulate mitophagy in subcellular zones and assess the resulting phenotype. It is also worth pointing out that in our conditions the iLID/sspB system can be used in living animals, and that we studied optogenetic dimers, as a whole, in functional assays in vivo.

To stress the versatility of the Venus-iLID-ActA/AMBRA1-RFP-sspB system we also demonstrated an effective mitophagy induction in human T cells collected from healthy donors. Since

mitophagy seems to be a key process in ROS control and cell survival of these cells³⁹, in the next future it would be highly intriguing to see, upon *ex vivo* reprogramming and reinfusion into patients, if an *in loco* boost of light-driven mitophagy could improve immune response in different hostile milieus, such as tumors or circumscribed sites of infection. It has also recently been demonstrated that T-cell mitochondrial dynamics have a huge impact on their metabolism and fate⁴⁰, this giving other perspectives to finely manipulate immunomodulation in specific sites and circumstances just by focusing a laser beam.

In sum, the AMBRA1-RFP-sspB/Venus-iLID-ActA bimodular system can represent a useful tool for several applications in various fields, either for basic research or as a therapeutic agent. Further understanding of the exact mechanisms by which AMBRA1 operates at mitochondria is still needed, in order to optimize the system and guide operators in future experiments.

Methods

Ethical aspects. The authors declare that all relevant ethical regulations for animal testing and research have been complied with peripheral blood mononuclear cells (PBMC) were isolated from buffy coats obtained from healthy donors from Bambino Gesù Children's Hospital (OPBG) in Rome, Italy, who signed a written informed consent, in accordance with rules set by the Institutional Review Board of OPBG (Approval of Ethical Committee N° 969/2015 prot. N° 669LB). All husbandry and experimental procedures involving *D. rerio* embryos complied with European Legislation for the Protection of Animals used for Scientific Purposes (Directive 2010/63/EU).

Plasmids and subcloning. pLL 7.0 Venus-iLID-ActA and pLL 7.0 tgRFPt-sspB_{micro} were purchased from Addgene (Cambridge, UK, #60413 and #60416, respectively). We took advantage of an AgeI unique restriction site upstream of tgRFPt-sspB_{micro} to insert human AMBRA1 DNA sequence. Thus, AMBRA1 was PCR amplified through high fidelity PfuTurbo Polymerase (Stratagene, La Jolla, USA) from our pLPCX-AMBRA1 vector adding AgeI sites in the two primers (AMBRA1_F: ATTAACCGGTCCGCCACCATGAAGTTGTCCAGAAAAG; AMBRA1_R: ATTAACCGGTCCGCCACCCCTGTTCCGTGGTTCCTC. The forward primer contained a strong Kozak sequence (GCCACC) upstream the first Methionine. Moreover, a small linker (Gly-Gly-Gly-Pro-Val-Ala-Thr) was inserted between the C-terminus of AMBRA1 and the N-terminus of tgRFPt to guarantee flexibility and prevention of sterical artefacts. Lastly, to ensure sustained expressions of transgenes, cDNAs were subcloned downstream a strong CMV promoter and upstream a WPRE post-transcriptional regulatory element. After subcloning, sequence and frame were confirmed by sequencing in the certificated laboratory Eurofins Genomics (Ebersberg, Germany).

Cell cultures and transfections. HeLa (catalog number 93021013, Sigma-Aldrich, St. Louis, USA), HEK293T (ECACC 12022001) and ETNA cells (in-house cell line derived from murine E14 striatum primordia neurons and immortalized with a retrovirus transducing the tsA58/U19 large T antigen) were cultured in Dulbecco's Modified Eagle's Medium (DMEM, Gibco, USA) supplemented with 10% fetal bovine serum (FBS, ThermoScientific, Pittsburgh, USA) under 5% CO₂ at 37 and 33 °C, respectively. Cotransfections were performed using a 1:3 ratio of total plasmids DNA over Lipofectamine2000 (ThermoScientific) in Opti-MEM (ThermoScientific) for 6 h. HUWE1 interference was achieved through transient transfection of the siRNA-HUWE1 5'-GCAGAUAAAUCUGAUCCUAAACCTG-3' 3'-UUCGUCUAUUUAGACUAGGAUUUGGAC-5' (Integrated DNA Technologies #150971213) by means of Lipofectamine 2000 according to the supplier's instructions. Prior all irradiation experiments, cell media were discarded and replaced by the phenol red-free FluoroBrite DMEM (ThermoScientific) added with 10% FBS, 2 mM L-glutamine (ThermoScientific) and 1% PenStrep (ThermoScientific). Cell treatments encompassed 40 mM NH₄Cl (Sigma-Aldrich) for 24 h, O/A [2.5 μM oligomycin (Calbiochem)/0.8 μM Antimycin A (Sigma-Aldrich)], supplemented with 20 μM QVD (Sigma-Aldrich) for 24 h or 250 μM Paraquat (Sigma-Aldrich) for 48 h. In order to block IKKα activity, cells were treated with the irreversible inhibitor BAY-117082 at 1 μM for 24 h, during illumination.

The 293T/17 packaging cell line (ATCC® CRL-11268) was cultured with IMDM (Gibco) supplemented with 10% FBS (Thermo Scientific) and 2 mM GlutaMax (Invitrogen, CA, USA). Cells were maintained in a humidified atmosphere containing 5% CO₂ at 37 °C. Cell lines were routinely tested for mycoplasma and authenticated by short tandem repeat analysis in the certificated laboratory Eurofins Genomics.

Illumination procedures. Cells were illuminated inside a standard cell incubator at an irradiance of 500 μW per cm² with a 7.2 W low-energy blue light LED irradiator plugged to a high accuracy (error rate: 0.1 s per cycle) intervalometer (Model 451,

GraLab, Centerville, OH, USA). Cells were routinely irradiated with cycles of 1 s of light spaced by 1 min of dark resting state.

Cell lysis and fractionation. HeLa, HEK293T and ETNA total extracts were obtained as follows. After ×3 washing steps in ice cold phosphate-buffered saline (PBS) (Lonza, Basel, Switzerland), cells were lysed in homemade RIPA lysis buffer (150 mM NaCl, 50 mM Tris-HCl pH 7.5, 1% NP40, 0.5% sodium deoxycholate, 0.1% sodium dodecyl sulfate (SDS), 2.5 mM Na₃VO₄, 5 mM NaF, 1 mM DTT, all reagents purchased from Sigma-Aldrich) complemented with protease inhibitor cocktail (Sigma-Aldrich). Samples were collected and centrifuged at 13,000g for 10 min at 4 °C; supernatants were saved.

For cytosol/mitochondria fractionation, cells were lysed by mechanical breaking (~100 potter strokes) into a detergent-free buffer (0.25 M sucrose, 10 mM HEPES pH 7.5, 1 mM EDTA). A first centrifugation (600g for 10 min at 4 °C) was employed to pellet nuclei; subsequently, supernatants were recentrifuged at 12,000g for 15 min at 4 °C to separate a cytosolic upper phase from a mitochondrial pellet. The latter was eventually lysed in RIPA buffer.

All protein extracts were quantified through the Bradford Protein Assay (Bradford solution from Bio-Rad Laboratories) according to the manufacturer's protocols.

Western blotting. A 5 μg per sample were loaded on polyacrylamide gels and SDS-polyacrylamide performed. Gels were transferred onto PVDF membranes (Immobilion P, Millipore, Burlington, US) at 300 mA for 2 h. Membranes were subsequently blocked in 5% non-fat dry milk in TBS-T (50 mM Tris-HCl pH 7.5, 150 mM NaCl, 0.1% Tween-20) for 1 h at room temperature. Specific primary antibodies were used, followed by 3× 10 min washing steps in TBS-T and incubation with appropriate HRP (Horseradish Peroxidase)-conjugated secondary antibodies for 2 h at room temperature (1:3000 in blocking solution, Bio-Rad). Finally, bands were impressed on X-ray films (Aurogene, Rome, Italy) upon exposure of the chemiluminescent substrate ECL (Millipore) for 3 min. Primary antibodies used were: Rabbit anti-Actin (1:100,000, #4967 Cell Signaling Technology, Danvers, US), Mouse anti-AMBRA1 (1:3000, sc-398204 Santa Cruz Biotechnology, Dallas, USA), Rabbit anti-Casp3 (1:1000, #9662 Cell Signaling), Mouse anti-GAPDH (1:1000000, Mab374 Chemicon International, Temecula, USA), Rabbit anti-HSP60 (1:2000, sc-13966 Santa Cruz Biotechnology), Rabbit anti-PARP (1:1000, #9542 Cell Signaling), Rabbit anti-SOD2 (1:5000, ADI-SOD-110 Enzo LifeScience, Farmingdale, USA), Rabbit and Mouse anti-Tom20 (1:10000, sc-11415 and sc-17764 Santa Cruz Biotechnology), Mouse anti-Tubulin (1:50000, T6199 Sigma-Aldrich), Rabbit anti-HUWE1 (1:1000, A300-486A Bethyl Laboratories, Montgomery, USA). Uncropped and unprocessed blots are provided in the attached Source Data file

Immunofluorescence. Transfected or transduced cells grown on glass coverslips were washed and fixed with 4% formaldehyde (Sigma-Aldrich) in PBS for 15 min at 37 °C. After a permeabilization step (0.4% Triton X-100, Sigma-Aldrich, in PBS for 10 min at room temperature) cells were simultaneously incubated overnight at 4 °C with mouse anti-AMBRA1 (1:200, sc-398204 Santa Cruz Biotechnology) and rabbit anti-Tom20 (1:500, sc-11415 Santa Cruz Biotechnology) primary antibodies, dissolved in 3% Normal Goat Serum in PBS. Next day, cells were washed three times and treated with goat anti-mouse Alexa Fluor 555 (1:300, A-21425 Life Technologies) and donkey anti-rabbit Alexa Fluor 647 (1:300, A-31573 Life Technologies) secondary antibodies for 2 h at room temperature. Nuclei were counterstained with DAPI 1 μg per ml for 5 min, and then coverslips were mounted on polylysinated slides with an aqueous mounting medium (Sigma-Aldrich).

Microscopy and image processing. Immunofluorescence images represent a single-focus plane taken by a Zeiss LSM 700 confocal microscope (Carl Zeiss, Oberkochen, Germany). Live cell imaging was performed through a UltraVox Cellular Imaging Microscope (PerkinElmer, Waltham, USA) in a 37 °C thermostat chamber at 5% of CO₂. Small adjustments in term of brightness and contrast were achieved through the software Adobe Photoshop CS6 (Adobe Systems, San Jose, US). The Area occupied by the signal was estimated through ImageJ. Corrected total cell fluorescence (CTCF) was calculated according to the following formula: CTCF = ID - AxB, where ID stays for integrated density of single cells, A for the area of the signal and B for Integrated density of the background. The mean signal was calculated through ImageJ as the mean of ten different points per cell.

Pulse-chase assay. After 16 h of transfection, cells have been incubated for 4 h with AHA 50 μM (Invitrogen) in DMEM medium without Methionine (Gibco). Then cells have been washed twice with Dulbecco's PBS (Gibco) and illuminated (Light) or not (Dark) for 24 h. Cells have been fixed and permeabilized using Click-iT Cell Reaction Buffer Kit (Invitrogen) and conjugated with Alexa-647 alkyne (Invitrogen) following manufacturer instructions. AHA-alkyne-Alexa647 fluorescence have been measured with BD FACS-Celesta (using DIVA software) gated on Venus-positive cells.

Retroviral constructs and production. The expression cassette encoding for Venus-iLID-ActA, Ambra1-TagRFPT-sspB_{micro} and the corresponding control TagRFPT-sspB_{micro} were cloned inside a SFG retrovirus backbone. To produce the retroviral supernatant, 293T/17 were cotransfected with the retroviral vectors codifying for MoMLV gag-pol and the RD114 envelope, using the Genejuice transfection reagent (Merck Millipore, Germany), according to the manufacturer's instruction. Supernatant containing the retrovirus was collected 48 and 72 h later.

Isolation and transduction of T lymphocytes. PBMC were isolated from buffy coats obtained from healthy donors from Bambino Gesù Children's Hospital (OPBG) in Rome, Italy, who signed a written informed consent, in accordance with rules set by the Institutional Review Board of OPBG (Approval of Ethical Committee N°969/2015 prot. N° 669LB), using lymphocytes separation medium (Eurobio, Les Ulis, France). T lymphocytes were activated with immobilized anti-OKT3 (1 µg per ml, 14-0037-82 e-Bioscience, San Diego, USA) and anti-CD28 (1 µg per ml, 555726 BD Biosciences, Eysins, Switzerland) monoclonal antibodies in the presence of recombinant human interleukin-7 (IL7, 10 ng per ml; R&D, USA) and 15 (IL15, 5 ng per ml; R&D). Activated T cells were transduced on day 3 in 24-well plates pre-coated with recombinant human RetroNectin (Takara-Bio, Japan) using a specific retroviral supernatant. On day 5 after transduction, T cells were expanded in medium containing 45% RPMI1640 and 45% Click's medium (Sigma-Aldrich) supplemented with 10% FBS and 2 mM Glutamax and replenished twice a week.

Cytofluorimetric analysis. Expression of the CD3 cell surface molecule, the green and red fluorescence proteins were determined by flow-cytometry using standard methodology. Samples were analyzed with a BD LSRFortessa X-20. Data were analyzed using the FACSDiva software (BD Biosciences). For each sample, we analyzed a minimum of 20,000 events. For assessing apoptosis, AnnexinV Apoptosis Detection Kit has been used (eBioscience) on a BD Accuri C6 Cytometer (BD Bioscience). Gating strategies are shown in Supplementary Figure 18.

Fish maintenance and embryos collection. Zebrafish (*D. rerio*) of wild type strain were maintained at 28.5 °C in a Tecniplast aquarium system. Embryos were obtained by natural breeding and raised in Petri dishes containing Fish Water solution at 28.5 °C with a photoperiod of 14 h light/10 h dark. Developmental stages of embryos were determined according to the time after fertilization and morphological criteria.

Microinjection of zebrafish embryos. One- to two-cells stage embryos were microinjected into the yolk mass with 10 nl of a solution containing 30 ng per µl of pCS2 + hAMBRA1-RFP-sspB (or pCS2 + RFP-sspB as a control) and 15 ng per µl of pCS2 + Venus-iLID-ActA in ×1 Danieau's buffer. Injections were performed under a dissecting microscope using a microinjector attached to a micro-manipulator (Leica Microsystems, Milan, Italy). Injected embryos were raised to the desired stages for in vivo imaging or collected for further analyses.

In vivo imaging of zebrafish embryos. Microinjected embryos were anesthetized with 0.04% tricaine (Sigma-Aldrich, E10521), embedded in 0.8% low-melting agarose prepared in fish water and lateral mounted on a depression slide. A Nikon C2 confocal system was used to record images that were analyzed with Fiji (ImageJ) software. Dynamic of interaction between AMBRA1 and mitochondrial outer membrane was studied by time-lapse confocal microscopy analysis of 32-hpf (hours post fertilization) zebrafish embryos treated with 488 nm wavelength laser (at 1/10 of the maximum intensity) for 2 s every 30 s over a period of 3 min. Acquisitions were made every 30 s in both green and red channels.

For functional experiments, microinjected embryos images were captured every 2 min over a period of 8 h from 34 hpf to 42 hpf with the same laser's settings.

Immunofluorescence on zebrafish. Totally, 48-hpf zebrafish embryos were fixed in 4% PFA overnight at 4 °C and then dechorionated. Embryos were stored in 100% MeOH at -20 °C, rehydrated in 1× PTW (1× PBS at pH 7.3, 0.1% Tween), incubated in 150 mM Tris-HCl at pH 9.0 for 5 min, followed by heating at 70 °C for 15 min. Subsequently, embryos were permeabilized with acetone for 20 min at -20 °C. After 3 h of incubation with blocking buffer (2% sheep serum, 1% bovine serum albumin, 1% DMSO in PBS), embryos were incubated for 3 days in primary antibody using 1:200 rabbit anti-Tom20 (sc-11415, Santa Cruz Biotechnology).

Alexa Fluor 555 goat anti-rabbit IgG (H + L) (A-27039, Invitrogen) was used 1:500 as secondary antibody for 2 h at room temperature. Nuclear counter staining was performed with the DNA binding dye Hoechst 33342. Images were taken using a Leica (Wetzlar, Germany) SP5 confocal microscope.

Statistics. All statistical calculations were performed and graphed using GraphPad Prism 6.01. Statistical analysis has been performed using two-tailed, paired (when the same cell was analyzed over time, as for the live cell imaging colocalization experiments) or unpaired (all other cases) Student's *t* test (two groups; 95% confidence interval) or with two-tailed one-way ANOVA with Tukey's post hoc test (multiple groups; 95% confidence interval). No other statistical tests were used.

Data are shown as mean ± SEM (single measurements indicated by dots and attached in the Source Data file). All experiments have been performed at least three times independently. No statistical methods were used to predetermine sample size. Pearson's and Manders' colocalization coefficients were automatically calculated using ImageJ software and the Jacop plug-in.

Data availability

The authors declare that all data supporting the findings of this study are available within the paper and its supplementary information files. No datasets were generated in this study. The source data underlying Figs. 1b–d, 2b, c, 3a, b, 4a, b, 5b, c, 6b, c and Supplementary Figures 1, 3, 5, 7, 8b, 9, 10, 14, and 17 are provided as a Source Data file

Received: 1 August 2018 Accepted: 12 March 2019

Published online: 04 April 2019

References

- Strappazzon, F. & Cecconi, F. The multifaceted mitochondrion: an attractive candidate for therapeutic strategies. *Pharmacol. Res.* **99**, 425–433 (2015).
- Hsu, C. C., Tseng, L. M. & Lee, H. C. Role of mitochondrial dysfunction in cancer progression. *Exp. Biol. Med.* **241**, 1281–1295 (2016).
- Strappazzon, F. & Cecconi, F. AMBRA1-induced mitophagy: a new mechanism to cope with cancer? *Mol. Cell Oncol.* **2**, e975647 (2015).
- Park, K. S. et al. FCCP depolarizes plasma membrane potential by activating proton and Na⁺ currents in bovine aortic endothelial cells. *Pflug. Arch.* **443**, 344–352 (2002).
- Tretter, L., Chinopoulos, C. & Adam-Vizi, V. Plasma membrane depolarization and disturbed Na⁺ homeostasis induced by the protonophore carbonyl cyanide-p-trifluoromethoxyphenyl-hydrazon in isolated nerve terminals. *Mol. Pharmacol.* **53**, 734–741 (1998).
- Scorrano, L., Petronilli, V. & Bernardi, P. On the voltage dependence of the mitochondrial permeability transition pore. A critical appraisal. *J. Biol. Chem.* **272**, 12295–12299 (1997).
- Maro, B., Marty, M. C. & Bornens, M. In vivo and in vitro effects of the mitochondrial uncoupler FCCP on microtubules. *EMBO J.* **1**, 1347–1352 (1982).
- Han, Y. H., Kim, S. H., Kim, S. Z. & Park, W. H. Carbonyl cyanide p-(trifluoromethoxy) phenylhydrazon (FCCP) as an O₂(^{•-}) generator induces apoptosis via the depletion of intracellular GSH contents in Calu-6 cells. *Lung Cancer* **63**, 201–209 (2009).
- Han, Y. H., Yang, Y. M. & Park, W. H. Carbonyl cyanide p-(trifluoromethoxy) phenylhydrazon induces caspase-independent apoptosis in As4.1 juxtaglomerular cells. *Anticancer Res.* **30**, 2863–2868 (2010).
- Mlejnek, P. & Dolezel, P. Loss of mitochondrial transmembrane potential and glutathione depletion are not sufficient to account for induction of apoptosis by carbonyl cyanide 4-(trifluoromethoxy)phenylhydrazon in human leukemia K562 cells. *Chem. Biol. Interact.* **239**, 100–110 (2015).
- Grundlingh, J., Dargan, P. I., El-Zanfaly, M. & Wood, D. M. 2,4-dinitrophenol (DNP): a weight loss agent with significant acute toxicity and risk of death. *J. Med. Toxicol.* **7**, 205–212 (2011).
- Narendra, D., Tanaka, A., Suen, D. F. & Youle, R. J. Parkin is recruited selectively to impaired mitochondria and promotes their autophagy. *J. Cell Biol.* **183**, 795–803 (2008).
- Kitada, T. et al. Mutations in the parkin gene cause autosomal recessive juvenile parkinsonism. *Nature* **392**, 605–608 (1998).
- Bingol, B. et al. The mitochondrial deubiquitinase USP30 opposes Parkin-mediated mitophagy. *Nature* **510**, 370–375 (2014).
- Strappazzon, F. et al. AMBRA1 is able to induce mitophagy via LC3 binding, regardless of PARKIN and p62/SQSTM1. *Cell Death Differ.* **22**, 419–432 (2015).
- Strappazzon, F. et al. Mitochondrial BCL-2 inhibits AMBRA1-induced autophagy. *EMBO J.* **30**, 1195–1208 (2011).
- Di Rita, A. et al. AMBRA1-mediated mitophagy counteracts oxidative stress and apoptosis induced by neurotoxicity in human neuroblastoma SH-SY5Y Cells. *Front. Cell Neurosci.* **12**, 92 (2018).
- Denison, S. R. et al. Alterations in the common fragile site gene Parkin in ovarian and other cancers. *Oncogene* **22**, 8370–8378 (2003).
- Guntas, G. et al. Engineering an improved light-induced dimer (iLID) for controlling the localization and activity of signaling proteins. *Proc. Natl Acad. Sci. USA* **112**, 112–117 (2015).
- Hallett, R. A., Zimmerman, S. P., Yumerefendi, H., Bear, J. E. & Kuhlman, B. Correlating in vitro and in vivo activities of light-inducible dimers: a cellular optogenetics guide. *ACS Synth. Biol.* **5**, 53–64 (2016).
- Yizhar, O., Fenko, L. E., Davidson, T. J., Mogri, M. & Deisseroth, K. Optogenetics in neural systems. *Neuron* **71**, 9–34 (2011).

22. Okatsu, K. et al. p62/SQSTM1 cooperates with Parkin for perinuclear clustering of depolarized mitochondria. *Genes Cells* **15**, 887–900 (2010).
23. Yoshii, S. R., Kishi, C., Ishihara, N. & Mizushima, N. Parkin mediates proteasome-dependent protein degradation and rupture of the outer mitochondrial membrane. *J. Biol. Chem.* **286**, 19630–19640 (2011).
24. Di Rita, A. et al. HUWE1 E3 ligase promotes PINK1/PARKIN-independent mitophagy by regulating AMBRA1 activation via IKK α . *Nat. Commun.* **9**, 3755 (2018).
25. Benato, F. et al. Ambra1 knockdown in zebrafish leads to incomplete development due to severe defects in organogenesis. *Autophagy* **9**, 476–495 (2013).
26. Skobo, T. et al. Zebrafish ambra1a and ambra1b knockdown impairs skeletal muscle development. *PLoS ONE* **9**, e99210 (2014).
27. Kalvari, I. et al. iLIR: A web resource for prediction of Atg8-family interacting proteins. *Autophagy* **10**, 913–925 (2014).
28. Von Stockum, S., Nardin, A., Schrepfer, E. & Ziviani, E. Mitochondrial dynamics and mitophagy in Parkinson's disease: a fly point of view. *Neurobiol. Dis.* **90**, 58–67 (2016).
29. Dagda, R. K., Das Banerjee, T. & Janda, E. How Parkinsonian toxins dysregulate the autophagy machinery. *Int J. Mol. Sci.* **14**, 22163–22189 (2013).
30. Nandipati, S. & Litvan, I. Environmental exposures and Parkinson's disease. *Int. J. Environ. Res. Public Health* **13**, 9 (2016).
31. Ossowska, K. et al. A slowly developing dysfunction of dopaminergic nigrostriatal neurons induced by long-term paraquat administration in rats: an animal model of preclinical stages of Parkinson's disease? *Eur. J. Neurosci.* **22**, 1294–1304 (2005).
32. Palikaras, K., Lionaki, E. & Tavernarakis, N. Coordination of mitophagy and mitochondrial biogenesis during ageing in *C. elegans*. *Nature* **521**, 525–528 (2015).
33. Yang, W. & Tiffany-Castiglioni, E. Paraquat-induced apoptosis in human neuroblastoma SH-SY5Y cells: involvement of p53 and mitochondria. *J. Toxicol. Environ. Health A* **71**, 289–299 (2008).
34. Cozzolino, M. et al. Apoptosome inactivation rescues proneural and neural cells from neurodegeneration. *Cell Death Differ.* **11**, 1179–1191 (2004).
35. Kaetsu, A., Fukushima, T., Inoue, S., Lim, H. & Moriyama, M. Role of heat shock protein 60 (HSP60) on paraquat intoxication. *J. Appl. Toxicol.* **21**, 425–430 (2001).
36. Keane, P. C., Kurzawa, M., Blain, P. G. & Morris, C. M. Mitochondrial dysfunction in Parkinson's disease. *Park. Dis.* **2011**, 716871 (2011).
37. Clark, L. N. et al. Case-control study of the parkin gene in early-onset Parkinson disease. *Arch. Neurol.* **63**, 548–552 (2006).
38. D'Amelio, M. et al. Caspase-3 triggers early synaptic dysfunction in a mouse model of Alzheimer's disease. *Nat. Neurosci.* **14**, 69–76 (2011).
39. Pua, H. H., Guo, J., Komatsu, M. & He, Y. W. Autophagy is essential for mitochondrial clearance in mature T lymphocytes. *J. Immunol.* **182**, 4046–4055 (2009).
40. Simula, L. et al. Drp1 controls effective T cell immune-surveillance by regulating T cell migration, proliferation, and cMyc-dependent metabolic reprogramming. *Cell Rep.* **25**, 3059–3073 (2016).

Acknowledgements

We thank Mrs. M. Acuña Villa and Dr. M. Bennett for secretarial and proofreading work respectively, Dr. C. Rodolfo, V. Turcanova, and M. Sorrenti for the technical support, Dr. L. Motta-Mena (Department of Biophysics, University of Texas) for kind suggestions. We also thank G. Milletti for the kind help in preparing Fig. 1a. Francesco Cecconi's laboratory is supported by grants from the Danish Cancer Society (KBVU R72-A4408,

R146-A9364), the Novo Nordisk Foundation (7559, 22544), the Lundbeckfonden (R233-2016-3360), the LEO Foundation (LF17024). F. Cecconi's lab in Copenhagen is part of the newly established Center of Excellence for Autophagy, Recycling and Disease (CARD), funded by the Danmarks Grundforskningsfond (DNRF125). The Bjarne Saxhof Foundation also provided financial support. This research was also supported in part by grants from, FISM (2013 to F. Cecconi), the Italian Ministry of Health (Progetto Giovani Ricercatori GR2011-2012 to F. Strappazzon and Ricerca Corrente to I. Caruana), the Italian Ministry of Education, University and Research (Research Project of National Relevance 2017 ID 2017WC8499 to F. Locatelli), Roche (Roche per la ricerca 2017 to F. Strappazzon) and AIRC (Associazione Italiana Ricerca sul Cancro, 5x1000 ID 9962, AIRC IG 2018 ID 21724 to F. Locatelli, Start-up grant to I. Caruana and AIRC IG-2017 19826 to S. Campello).

Author contributions

P.D'A. and F.C. had the ideas, designed the work plan, and wrote the paper. P.D'A. performed most of the experiments and all the cloning procedures. F.C. coordinated and supervised the work. P.D'A. and F.S. performed together most of the microscopy imaging. F.S. helped also in defining the strategies for the in vitro experiments. I.C., G.W., F. D.B., and F.L. provided human T lymphocytes, produced viral vectors, and infected the cells for the ex vivo experiments. G.M. and L.D.V. microinjected D. rerio embryos and performed the in vivo experiments. A.D.R. performed the experiments shown in Supplementary Figures 8, 9, 14, and in Supplementary Figure 10, the latter together with L.S. L.S. and S.C. performed the cytofluorimetric analysis in Supplementary Figures 5 and 10.

Additional information

Supplementary Information accompanies this paper at <https://doi.org/10.1038/s41467-019-09487-1>.

Competing interests: The authors declare no competing interests.

Reprints and permission information is available online at <http://npg.nature.com/reprintsandpermissions/>

Journal peer review information: *Nature Communications* thanks the anonymous reviewers for their contribution to the peer review of this work. Peer reviewer reports are available.

Publisher's note: Springer Nature remains neutral with regard to jurisdictional claims in published maps and institutional affiliations.



Open Access This article is licensed under a Creative Commons Attribution 4.0 International License, which permits use, sharing, adaptation, distribution and reproduction in any medium or format, as long as you give appropriate credit to the original author(s) and the source, provide a link to the Creative Commons license, and indicate if changes were made. The images or other third party material in this article are included in the article's Creative Commons license, unless indicated otherwise in a credit line to the material. If material is not included in the article's Creative Commons license and your intended use is not permitted by statutory regulation or exceeds the permitted use, you will need to obtain permission directly from the copyright holder. To view a copy of this license, visit <http://creativecommons.org/licenses/by/4.0/>.

© The Author(s) 2019

Head of the laboratory “Cellular and Molecular Neurosciences” (2018 –2021):**“Study of mitophagy in physiopathological contexts”**. Santa Lucia Foundation, Rome, Italy.

In 2018, I started my research group working on selective autophagy and, in particular, on mitophagy in the context of autoimmune and neurodegenerative diseases. My lab contributed to the molecular understanding of this process in order to define new therapeutical approaches for neurodegeneratives. In date, as a head of laboratory, I was awarded grants from ROCHE (private funds), AIRC (Associazione Italiana per la Ricerca sul Cancro) and Airalz (Associazione Italiana Ricerca Alzheimer Onlus).

It is possible to modulate autophagy thanks to several pharmacological approaches (ie: Chloroquine, Rapamycin, 3-MA etc.), however, very few tools are available to modulate selective autophagy of mitochondria. In particular mitophagy inhibition may be beneficial in some human diseases. For instance, it has been demonstrated that melatonin exerts neuroprotective effects against glutamate-induced excitotoxicity by reducing mitophagy-related oxidative stress and maintaining mitochondrial function [1]. In the context of cancer, mitophagy was initially thought to be an onco-suppressor that helps in maintaining cellular homeostasis [2], but now emerging evidence indicates that mitophagy inhibition may favor cancer cell survival by eliminating damaged mitochondria and reducing, in this way, mitochondrial reactive oxygen species [3]. The mitophagy manipulation is thus crucial for cancer therapy.

In 2020, my team focused his attention on microRNAs, as potential regulators of mitophagy. In particular, since PARKIN was suspected to be a target of mir-218 [4], we decided to investigate a potential role of miR-218 in mitophagy mediated by PINK1 and Parkin. We demonstrated that Parkin is a target of miR218 in human cells. Moreover, we discovered that following mitophagy induction, miR-218 expression is sufficient to reduce the level of Parkin protein, limiting its translocation to mitochondria and thus reducing its ability to potentiate the ubiquitylation signal requested for the PINK1/Parkin-dependent mitophagy. Finally, we demonstrated that miR-218 expression is sufficient to delay mitochondrial clearance following mitophagy induction (see Di Rita et al. 2020 *IJMS*). **These results define a novel role of miR-218 in mitophagy and highlight a novel negative mechanism for mitochondria selective removal regulation. miR-218 could thus be a novel molecular mechanism that could be hijacked to treat several diseases such as cancer and neurodegenerative pathologies.**

Since nanoparticles represent incredible opportunities for cell specific controlled delivery of miRNAs in the treatment of cancer or neurodegenerative disorders, our findings thus provide a potential therapeutic strategy for cancer, such as breast cancer. Moreover, inhibition of miR-218 (e.g., AntagomiR) is expected to be beneficial in several neurodegenerative diseases in which the mitophagy process is not sufficient.

Afterwards, I wrote a review that specifically focused on studies that highlight the miRNAs implicated in the regulation of mitophagic pathways. In particular, I underlined the importance of these discoveries in order to define new therapeutic approaches in the context of age-related diseases involving mitochondrial dysfunctions, such as cancers and neurodegenerative diseases (see Strappazzon 2020 *Prog Mol Biol Transl Sci*).

In parallel to this work, in 2018, my team started to study the role of mitophagy in the context of Multiple Sclerosis (MS), a demyelinating disease associated with dysfunctional mitochondria. Multiple sclerosis (MS) is a very debilitating chronic autoimmune disease. Depending on the region of the world, the incidence is of 50 to 300 per 100,000 individuals. MS generally affects young adults with a prevalence of 3 female patients for every male patient. Currently, the processes that trigger the disease are not known, but genetic predispositions, environmental agents (such as bacteria or virus infections) and social components (such as tobacco consumption) participate in the pathogenesis of MS. There are three types of MS. A cyclic or remitting form (relapsing-remitting MS, RR-MS), which affects 80–85% of patients without progression of the handicap between relapses. This MS can progress to secondarily progressive MS (or MS-SP). There is also a primary progressive form (or PP-MS) in which the phases of the disease are not interspersed with phases of remission, affecting approximately 15% of patients. In all cases, the disease is characterized by the onset of varying disabilities all due to the progressive infiltration of cells of the adaptive immune system, T and B lymphocytes, into the central nervous system. These activated cells are responsible for the destruction of the myelin sheath of neurons and the development of neuronal and axonal damage. One characteristic of MS is the presence of oxidative stress and mitochondrial dysfunctions associated with the pathology.

It has been demonstrated that ATG5, a protein involved in autophagy, and PARKIN increase in cerebrospinal fluid and serum of MS patients, highlighting these autophagy/mitophagy elements as new molecular markers of the disease' s active phases [5,6]. **However, at that time, the role played by mitophagy remained completely**

obscure in MS pathogenesis.

We thus decided to quantitatively and qualitatively analyzed three indispensable proteins for the PINK1-mediated mitophagy pathway, i.e., PINK1, Optineurin (OPTN), and NDP52 (also known as CALCOCO2), in peripheral blood mononuclear cells (PBMCs) of relapsing–remitting (RR)-MS patients. We discovered that a variant of one of the major mitophagy receptors, NDP52, confers protection against MS. Mechanistically, we identified residue 140 of NDP52 as a crucial modulator of NDP52/LC3C binding, promoting the formation of autophagosomes in order to drive efficient mitophagy. In addition, we found that NDP52 is mainly expressed in B cells (among PBMCs) and by ensuring efficient mitophagy, it is able to limit the production of the pro-inflammatory cytokine TNF- α following cell stimulation. **Our work highlights NDP52 as a novel target for the diagnosis and treatment of MS.** I published this work as **last author** (Di Rita et al., 2021 *Cell Death and Differentiation*) and we wrote a comment on this work in the *Autophagy J* (See Di Rita & Strappazzon, 2021 *Autophagy*).

References

1. Wang, D.D.; Jin, M.F.; Zhao, D.J.; Ni, H. Reduction of Mitophagy-Related Oxidative Stress and Preservation of Mitochondria Function Using Melatonin Therapy in an HT22 Hippocampal Neuronal Cell Model of Glutamate-Induced Excitotoxicity. *Front. Endocrinol.* (2019).
2. Strappazzon, F.; Cecconi, F. AMBRA1-induced mitophagy: A new mechanism to cope with cancer? *Mol. Cell. Oncol.*, 2, e975647 (2015).
3. Yan, C.; Li, T.S. Dual role of mitophagy in cancer drug resistance. *Anticancer Res.* 2018, 38, 617–621.
4. Amin, N.D.; Bai, G.; Klug, J.R.; Bonanomi, D.; Pankratz, M.T.; Giord, W.D.; Hinckley, C.A.; Sternfeld, M.J.; Driscoll, S.P.; Dominguez, B.; et al. Loss of motoneuron-specific microRNA-218 causes systemic neuromuscular failure. *Science*, 350, 1525–1529 (2015).
5. Patergnani S, Castellazzi M, Bonora M, Marchi S, Casetta I, Pugliatti M, et al. Autophagy and mitophagy elements are increased in body fluids of multiple sclerosis-affected individuals. *J Neurol Neurosurg Psychiatry.* 89:439–41 (2018).
6. Castellazzi M, Patergnani S, Donadio M, Giorgi C, Bonora M, Fainardi E, et al. Correlation between auto/mitophagic processes and magnetic resonance imaging activity in multiple sclerosis patients. *J Neuroinflammation.*16:131 (2019).



Article

miR-218 Inhibits Mitochondrial Clearance by Targeting PRKN E3 Ubiquitin Ligase

Anthea Di Rita ^{1,2} , Teresa Maiorino ¹, Krenare Bruqi ^{1,2}, Floriana Volpicelli ^{3,4} , Gian Carlo Bellenchi ^{1,3,5} and Flavie Strappazon ^{1,*}

¹ IRCCS Fondazione Santa Lucia, 00143 Rome, Italy; antheadirita@gmail.com (A.D.R.); maiorino.teresa@gmail.com (T.M.); krenare.bruqi@gmail.com (K.B.); bellenchi@igb.cnr.it (G.C.B.)

² University of Rome Tor Vergata, 00133 Rome, Italy

³ Institute of Genetics and Biophysics “Adriano Buzzati Traverso”, CNR, 80131 Naples, Italy; floriana.volpicelli@unina.it

⁴ Department of Pharmacy, University of Naples Federico II, 80131 Naples, Italy

⁵ Department of Systems Medicine, University of Rome Tor Vergata, 00133 Rome, Italy

* Correspondence: f.strappazon@hsantalucia.it; Tel.: +39-06501703093

Received: 2 December 2019; Accepted: 3 January 2020; Published: 5 January 2020



Abstract: The selective elimination of dysfunctional mitochondria through mitophagy is crucial for preserving mitochondrial quality and cellular homeostasis. The most described mitophagy pathway is regulated by a positive ubiquitylation feedback loop in which the PINK1 (PTEN induced kinase 1) kinase phosphorylates both ubiquitin and the E3 ubiquitin ligase PRKN (Parkin RBR E3 ubiquitin ligase), also known as PARKIN. This event recruits PRKN to the mitochondria, thus amplifying ubiquitylation signal. Here we report that miR-218 targets PRKN and negatively regulates PINK1/PRKN-mediated mitophagy. Overexpression of miR-218 reduces PRKN mRNA levels, thus also reducing protein content and deregulating the E3 ubiquitin ligase action. In fact, following miR-218 overexpression, mitochondria result less ubiquitylated and the autophagy machinery fails to proceed with correct mitochondrial clearance. Since mitophagy defects are associated with various human diseases, these results qualify miR-218 as a promising therapeutic target for human diseases.

Keywords: microRNA; mitochondria; miR-218; PARKIN/PRKN; mitophagy

1. Introduction

Autophagy is an important eukaryotic process involved in the lysosomal degradation of cytosolic components in both physiological and pathological conditions. During autophagy, some vesicles named autophagosomes engulf a number of different cargoes and then fuse with lysosomes for subsequent recycling of their content [1]. Selective elimination of undesired or dysfunctional mitochondria through autophagy is called mitophagy [2]. This evolutionary-conserved mechanism removes damaged mitochondria in order to reduce reactive oxygen intermediates that are known to participate in inflammation, genotoxic stress, promotion of tumorigenesis, and aging [3]. Accordingly, defects of the mitophagic pathway contribute to neurodegenerative or inflammatory diseases and cancers. However, mitophagy inhibition may also be beneficial in some human diseases. For instance, it has been demonstrated that melatonin exerts neuroprotective effects against glutamate-induced excitotoxicity by reducing mitophagy-related oxidative stress and maintaining mitochondrial function [4]. In the context of cancer, mitophagy was initially thought to be an onco-suppressor that helps in maintaining cellular homeostasis [5], but now emerging evidence indicates that mitophagy inhibition may favor cancer cell survival by eliminating damaged mitochondria and reducing, in this

way, mitochondrial reactive oxygen species [6]. The mitophagy manipulation is thus crucial for cancer therapy. During mitophagy, two post-translational modifications, such as ubiquitylation and phosphorylation, orchestrate an efficient mechanism for mitochondria specific elimination [7]. To date, the most characterized mitophagy pathway is regulated by the PINK1 (PTEN induced kinase 1) protein. PINK1 is a serine-threonine kinase that phosphorylates both ubiquitin and the E3 ubiquitin ligase PRKN (Parkin RBR E3 ubiquitin ligase), also known as PARKIN, at serine 65 (S65). PRKN phosphorylation is necessary for recruiting and activating the E3 ubiquitin ligase activity on dysfunctional mitochondria [8–10]. This event leads PRKN to conjugate ubiquitin chains on outer mitochondrial membrane proteins. Ubiquitins are thus phosphorylated on S65 to further stimulate in a positive feedback loop PRKN recruitment and activation [11–16]. This rapid amplification of pS65-Ub chains on the mitochondria is fundamental to autophagy machinery recognition. In fact, some proteins, known as mitophagy receptors, bind ubiquitin chains and act as a bridge between the autophagosome marker MAP1LC3A/LC3 (microtubule associated protein 1 light chain 3 alpha) and the dysfunctional mitochondria. In PINK1/PRKN system, OPTN (Optineurin) and CALCOCO2/NDF52 (calcium binding and coiled-coil domain 2) are the primary mitophagy receptors [17–20]. Besides the PINK1/PRKN-dependent mitophagy, mammalian mitochondria selective clearance is also controlled by other proteins, which function in an alternative pathway, including BNIP3L (BCL2 interacting protein 3 like) [21,22], FUNDC1 (FUN14 domain containing 1) [23], AMBRA1 (Autophagy and Beclin 1 regulator 1) [24], BCL2L13 (BCL2 like 13) [25] or that can cooperate with the PINK1/PRKN system, such as AMBRA1 [26] and PHB2 (Prohibitin 2) [27].

In the last few years, studies have demonstrated the involvement of microRNAs (abbreviated miRNAs), which are small non-coding RNA molecules (containing about 22 nucleotides), in a large spectrum of processes, including autophagy [28,29]. Moreover, it has been shown that miRNAs control also mitochondria selective autophagy. In fact, Barde and colleagues demonstrated that a persistent expression of miRNAs causes a hematopoietic-restricted deletion of Kap1 that inhibits mitophagy and retains mitochondria into erythroblasts [30]. In addition, a hypoxia-responsive miRNA, miR-137 targets both FUNDC1 and BNIP3L thus inhibiting hypoxia-induced mitophagy. Furthermore, miR-124 protects against spinal cord ischemia–reperfusion injury by probably stimulating mitophagy [31]. Concerning the PINK1-mediated mitophagy, two specific regulations by miRNA have been proposed: (1) in 2016, it was shown that miR-181 controls mitochondrial clearance by targeting the E3 ligase PRKN [32]; (2) in the same year, it was established that miR-27a and miR-27b target PINK1 and abrogate the mitophagy pathway [33].

As it has been reported that PRKN E3 ubiquitin ligase could be a putative target of miR-218 [34] and since regulations are emerging between microRNA action and mitochondria selective removal, we decided here to investigate a potential role of miR-218 in mitophagy mediated by PINK1 and PRKN.

We demonstrated that PRKN is a target of miR218 in human cells. Moreover, we discovered that following mitophagy induction, miR-218 expression is sufficient to reduce the level of PRKN protein, limiting its translocation to mitochondria and thus reducing its ability to potentiate the ubiquitylation signal requested for the PINK1/PRKN-dependent mitophagy. Finally, we demonstrated that miR-218 expression is sufficient to delay mitochondrial clearance following mitophagy induction.

These results define a novel role of miR-218 in mitophagy and highlight a novel negative mechanism for mitochondria selective removal regulation. miR-218 could thus be a novel molecular mechanism that could be hijacked to treat several diseases such as cancer and neurodegenerative pathologies.

2. Results

2.1. miR-218 Targets PRKN E3 Ubiquitin Ligase

As it has been reported that PRKN may be a target of miR-218 [34], we first investigated whether miR-218 was able to target PRKN. In order to solve this question, by using target Scan software, we searched for putative miR-218 binding sites to the 3' un-translated region (3'UTR) of PRKN. We did

not find conserved matches in the human transcripts; however, two specific sites were identified in the 3'UTR of the mouse sequence for PRKN. These sites were located respectively at 80 bp and at 250 bp after the PRKN stop codon (Figure 1a).

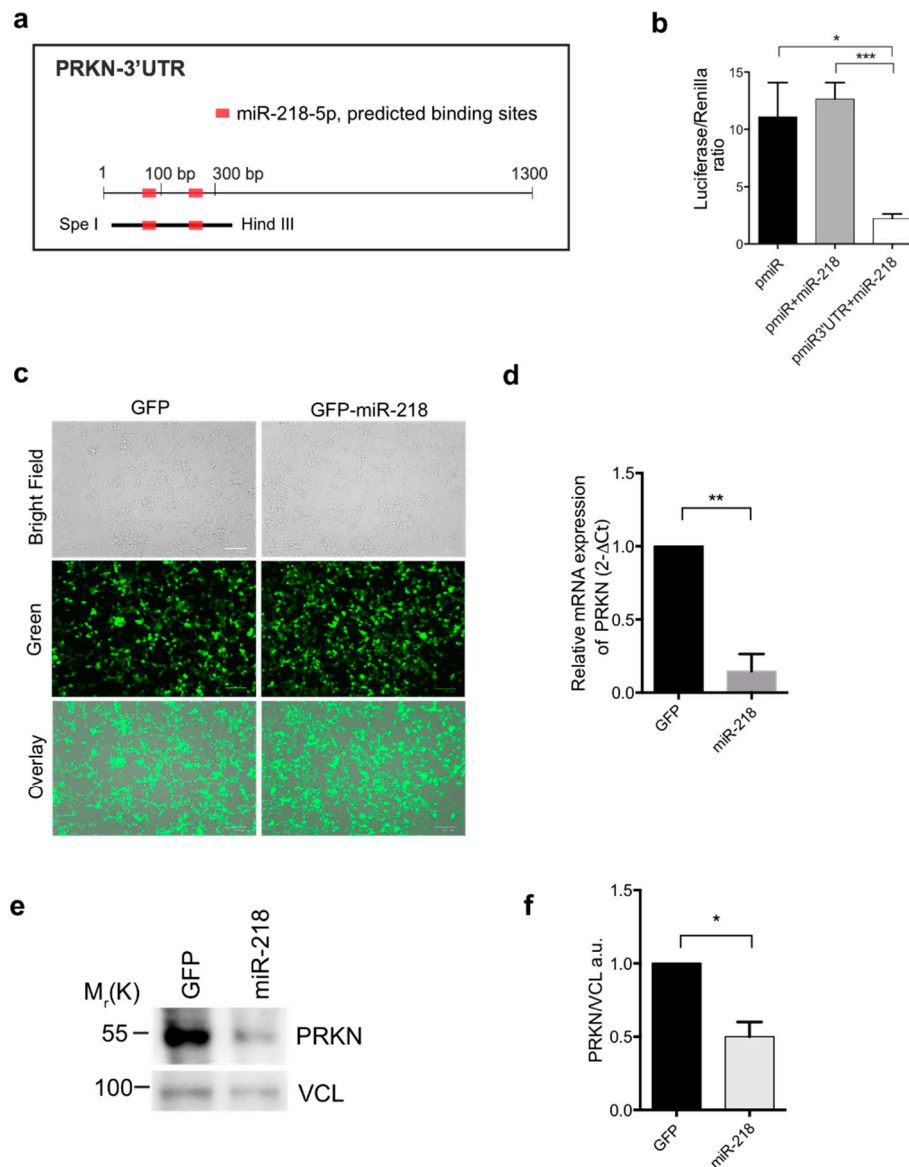


Figure 1. (a) Scheme of the 3'UTR (Untranslated region) of PRKN (Parkin RBR E3 ubiquitin ligase). The location of the two predicted binding sites for miR-218 are indicated in red. The region cloned in the pMiR Report miRNA expression vector is shown below the 3'UTR. The restriction enzymes used are indicated as well. (b) Luciferase assay. pMiR-Reports containing a portion of the PRKN 3'UTR (pMiR-3'UTR) or the empty pMiR vector (pMiR) were co-transfected in presence or absence of miR-218. All luciferase data have been normalized to the Renilla (RL-SV40) activity. The graph reports the Luciferase/renilla ratio. (c) Representative images of HEK293 cells transfected with GFP (Green Fluorescence Protein) or GFP-miR-218 vectors (left part) that were then analyzed by quantitative PCR (qPCR) in order to analyze the mRNA of PRKN (right part). Scale bar 100 μm. (d) The graph shows the relative expression of PRKN, normalized on B2M as loading control. (e) Protein lysates of GFP or GFP-miR-218 transfected HEK293 cells were subjected to western blot analysis against PRKN antibody. (f) The graph reports the PRKN/VCL ratio. VCL/Vinculin is used as loading control. All data are representative of experimental triplicate (± s.e.m.). Statistical analysis was performed using Student t-test with Welch's correction. * $p < 0.05$; ** $p < 0.01$; *** $p < 0.001$ $M_r(K)$ = relative molecular mass expressed in Kilo Dalton.

To confirm the ability of miR-218 to bind this region we cloned a 350 bp portion of the PRKN 3'UTR, containing the two predicted binding sites, downstream the pMiR-REPORTER vector encoding the Renilla luciferase hereafter called pMiR-3'UTR (Figure 1b). Co-transfection of miR-218, with the pMiR-3'-UTR vector in HeLa cells results in a significant decrease in the luciferase activity, compared with empty vector (Figure 1b).

This result indicates that miR-218 is potentially able to down-regulate PRKN by binding specific sites at the 3'-UTR region.

The physiological role of such binding between miR-218 and PRKN has not been explored yet. In order to investigate, from a functional point of view, such an interaction, we overexpressed a vector encoding miR-218 comparing with an empty vector expressing the green fluorescent protein GFP alone in HEK293 cells, which are PRKN competent cells (Figure 1c). Then, we analyzed the mRNA levels of PRKN in the presence or absence of miR-218. As expected, we found that overexpression of miR-218 substantially reduced PRKN transcript levels (Figure 1d). Moreover, we analyzed the PRKN protein levels by performing a western blot analysis. As illustrated in Figure 1e, HEK293 cells transfected with a vector encoding miR-218 show a decrease in PRKN protein level compare to GFP-positive control cells (Figure 1e,f).

These results indicate that miR-218 down-regulates PRKN levels in HEK293 cells.

2.2. miR-218 Inhibits Mitochondrial Clearance

Since we demonstrated that PRKN is a novel target of miR-218 in HEK293 cells (Figure 1) and since PRKN is important for a correct amplification of the PINK1-mediated mitophagy, we hypothesized here that miR-218 expression was able to interfere with mitochondrial clearance by reducing PRKN levels. To test this hypothesis, HEK293 cells transfected with GFP or GFP-miR-218 vectors were treated with oligomycin and antimycin A (O/A), two agents commonly used to induce mitochondrial damage in order to activate mitophagy [13,20]. We next checked for mitophagy occurrence; to do this, we analyzed levels of two mitochondrial proteins, a common method used to monitor mitophagy. As expected, we observed a strong decrease of both SOD2/MnSOD (superoxide dismutase 2) and TOMM20 (translocase of outer mitochondria membrane 20) following mitophagy induction, suggesting that mitochondrial clearance occurs (Figure 2a–c). However, when we overexpressed miR-218, we found no evident reduction of mitochondrial proteins upon O/A treatment, suggesting that mitochondrial clearance was blocked by miR-218 overexpression. Then, we decided to strengthen our biochemical data by performing a confocal microscopy analysis. We confirmed that miR-218 was able to inhibit mitochondrial clearance following mitophagy stimulation. In fact, in GFP-transfected cells treated with O/A, we observed a huge decrease of mitochondrial content; however, when we over-expressed miR-218, no evident decrease was observed in transfected cells (Figure 2d,e).

Overall, these results suggest that miR-218 over-expression delays mitochondria selective removal following mitophagy induction.

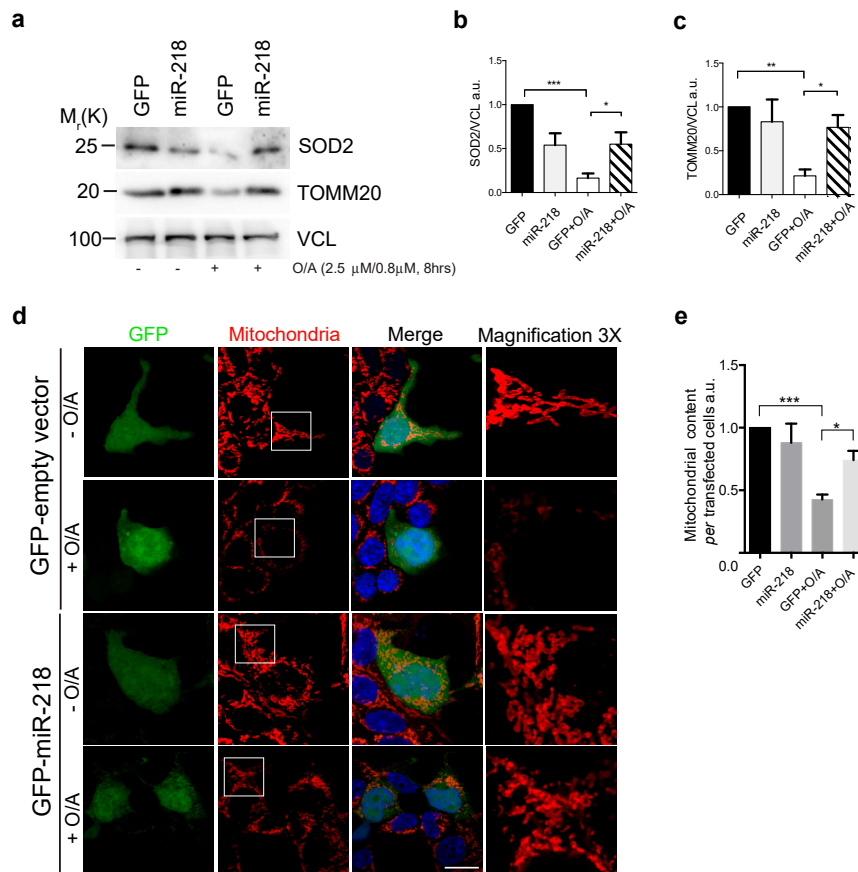


Figure 2. (a) HEK293 cells transfected with GFP or GFP-miR-218 vectors and then treated with O/A (Oligomycin and Antimycin A 2.5 μ M, 0.8 μ M, 8 h) were immunoblotted for the indicated antibodies. (b,c) The graphs show the SOD2 (superoxide dismutase 2) and TOMM20 (translocase of outer mitochondria membrane 20) protein level normalized on the VCL (Vinculin) loading control. (d,e) Representative immunofluorescence image and related graph in which GFP or GFP-miR-218 overexpressing HEK293 cells were immunostained with an anti-TOMM20 to detect mitochondria (red). Magnifications (3X) of the areas localized in the white frames are illustrated for each immunofluorescence. Scale bar, 10 μ m. All data represent the mean of experimental triplicate (\pm s.e.m.). Statistical analysis was performed using One-Way ANOVA with Sidak's correction. * $p < 0.05$; ** $p < 0.01$; *** $p < 0.001$. Mr(K) = relative molecular mass expressed in Kilo Dalton.

2.3. miR-218 Inhibits Mitophagy by Reducing Prkn Expression and Function

Since we found that one of the main players of mitophagy pathway, PRKN, is a target of miR-218, and since this miRNA negatively controls mitochondria selective removal, we expected that miR-218 would delay mitochondrial clearance by targeting PRKN protein levels and thus affecting its known function in mitophagy. In order to address this point, we first evaluated the PRKN translocation to the mitochondria, a necessary event for a correct mitophagy induction. In fact, upon mitophagy stimulation, the cytosolic E3 ubiquitin ligase PRKN is known to be recruited to the mitochondria in order to amplify the ubiquitylation events necessary for the recruitment of mitophagy receptors [8–10]. To test this, HEK293 cells over-expressing GFP or GFP-miR-218 plasmids were treated with O/A in order to stimulate mitophagy. Cells were then subjected to mitochondria fractionation and immunoblotting analysis. As shown in Figure 3a,b we observed a reduction of mitochondrial PRKN comparing with the control condition following mitophagy induction. Since a reduction in PRKN mitochondrial level is evident, we hypothesized that, in the meantime, mitochondria could be less-ubiquitylated in that context. To verify this hypothesis, we transfected HEK293 cells with GFP or GFP-miR-218 constructs and we treated cells with O/A in order to induce mitophagy. We then performed a mitochondrial

fractionation in which we analyzed ubiquitylation by measuring the amount of total ubiquitin in these extracts. The ubiquitylated mitochondrial proteins decreased upon miR-218 over-expression, suggesting that the PRKN-dependent ubiquitin amplification signal is reduced (Figure 3c,d).

Our findings reveal that miR-218 over-expression promotes a reduction of PRKN levels during mitophagy, leading to a decrease of PRKN translocation to mitochondria and most likely to a reduction of PRKN mitophagy activity.

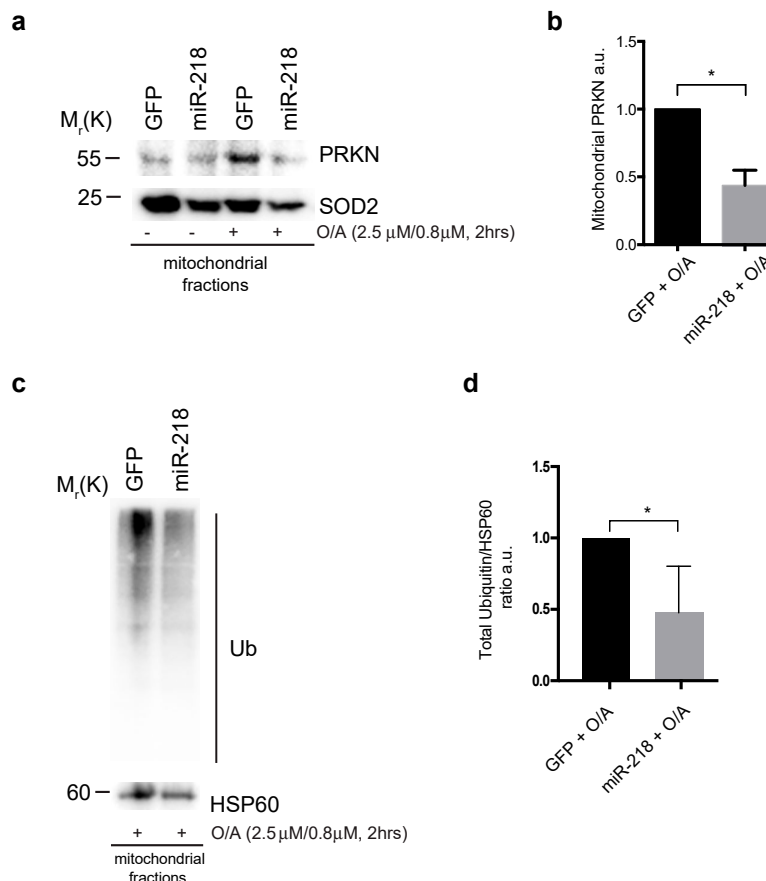


Figure 3. (a) HEK293 cells overexpressing GFP or GFP-miR-218 vectors were treated with O/A for 2 h and subjected to mitochondria purification. (b) The graph shows the mitochondrial PRKN normalized on the mitochondrial loading control. (c) Representative image of HEK293 cells transfected with GFP or GFP-miR-218 constructs and treated with O/A for 2 h in order to analyze total ubiquitin amount in mitochondria. (d) The graph shows total Ub (Ubiquitin) normalized on the mitochondrial protein HSP60 (Heat Shock Protein 60). All data represent the mean of three experiments (\pm s.e.m.). * $p < 0.05$. Statistical analysis was performed using Student t-test with Welch's correction. Mr(K) = relative molecular mass expressed in Kilo Dalton.

2.4. miR-218 Inhibits Mitochondria Co-Localization with Autophagosomes

In order to demonstrate that miR-218 was able to negatively control a mitochondria clearance related to the autophagy pathway, we transfected HEK293 cells with vectors encoding GFP or GFP-miR-218 plasmids in order to determine the co-localization between the autophagy machinery substrate (mitochondria) and the autophagosome marker protein MAP1LC3A, upon mitophagy stimulation. As expected, we observed a high co-localization rate between mitochondria (in cyano) and MAP1LC3A-labelled autophagosomes (in red) in GFP transfected cells treated with O/A, by performing confocal microscopy analysis. Instead, by overexpressing miR-218, we observed no such increase in mitochondria and autophagosome co-localization (Figure 4a,b). Moreover, since during mitophagy, dysfunctional mitochondria, engulfed into autophagosomes, are delivered to lysosomes for degradation,

we decided to verify whether miR-218 expression was efficient like the effect of Chloroquine (CQ), a well-known inhibitor of the fusion between autophagosomes and lysosomes [35]. To address this question, we transfected HEK293 cells with GFP or GFP-miR-218 and then we treated them or not with CQ, (Figure 4c). Upon mitophagy stimulation (O/A treatment), we detected a decrease of the mitochondrial marker SOD2 that was similarly rescued by overexpressing miR-218 or by blocking the fusion of autophagosomes and lysosomes with CQ.

Together these results demonstrate that miR-218 exerts an inhibitory effect on mitochondrial clearance through the autophagic pathway.

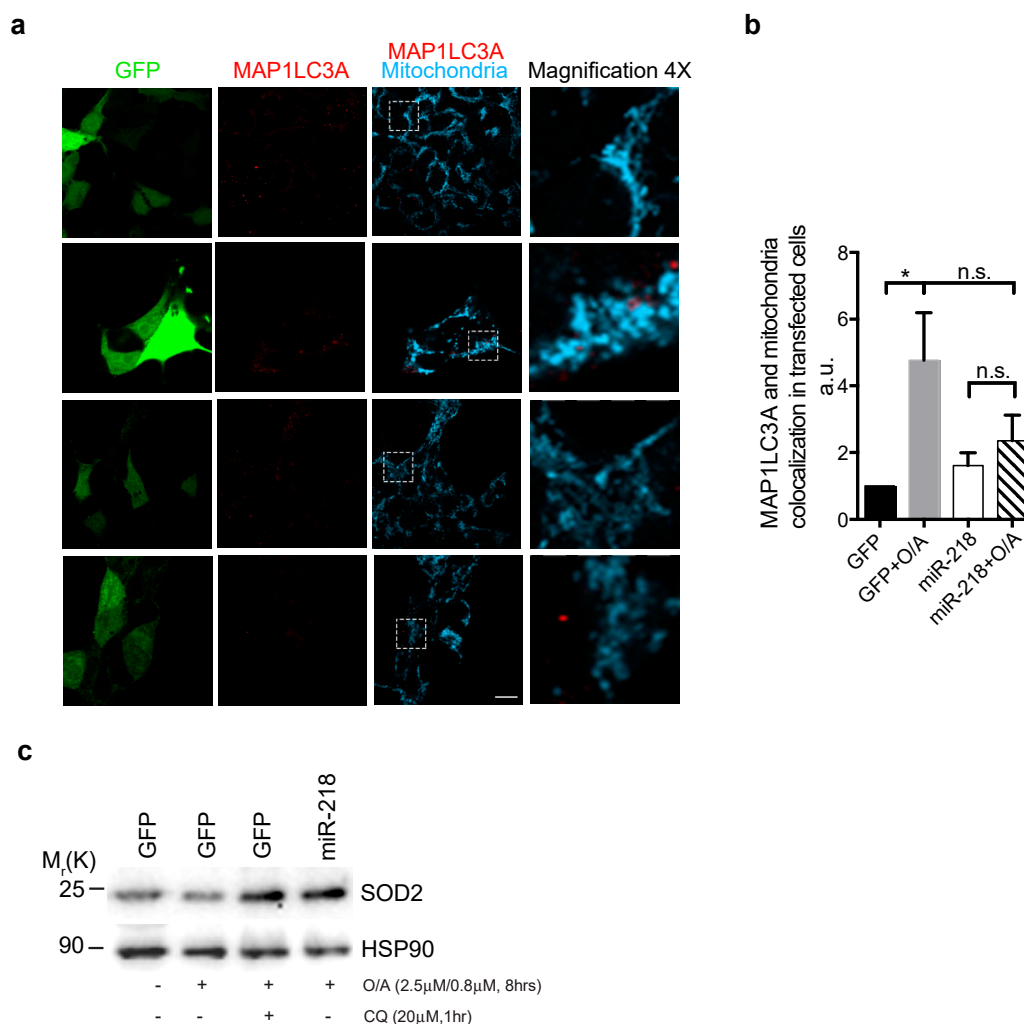


Figure 4. (a,b) Representative immunofluorescence image and related graph of HEK293 cells transfected with GFP or GFP-miR-218 vectors were treated with O/A for 5 h and immunostained with an anti-MAP1LC3A antibody (red) and an anti-TOMM20 (cyan) to detect mitochondria. Scale bar, 7 μm. The right panels report the magnifications (4X) of the images that are in the white dotted frames. Data represent the mean of three different samples (\pm s.e.m.) and are representative of experimental triplicate. * $p < 0.05$, n.s. (not significant). Statistical analysis was performed using One-Way ANOVA with Sidak's correction. (c) Representative image of HEK293 cells transfected as in (a) and treated with O/A for 8 h in combination or not with the autophagosome-lysosome fusion inhibitor chloroquine (CQ), were immunoblotted for the indicated antibodies.

3. Discussion

An involvement of microRNAs in regulating highly controlled systems such as mitochondrial selective removal through autophagy pathway, also called mitophagy, has recently emerged [30–33].

Here, we analyzed the role of miR-218 in mitophagy, discovering its new target PRKN. Interestingly, we found that miR-218 is able to down-regulate PRKN mRNA in HEK293 cells demonstrating a novel function of miR-218. PRKN is fundamental in various neurodegenerative diseases, including Parkinson's disease, Alzheimer's disease, Amyotrophic Lateral Sclerosis and Huntington's disease [36–39]. Furthermore, several studies have reported the ability of PRKN to protect neurons against neurotoxins and metallic ions [40]. Thus, maintaining an optimal PRKN expression and function appears to be crucial for neuron homeostasis.

In addition, PRKN is also involved in cancer regulation and the levels of its mRNA and protein are frequently down-regulated in ovarian and lung cancers [41–46].

Of note, the PRKN activity is strictly connected to mitochondria. In fact, in 2003, studies on *Drosophila* documented that, in absence of PRKN, mitochondria present abnormalities [47]. In addition, in 2008, Youle's group demonstrated that PRKN regulates mitophagy in mammalian cells collaborating with PINK1 [48,49]. In this study, we showed that miR-218 action on PRKN could, at least, affect its function during the mitophagy process; in fact, miR-218 over-expression in HEK293 cells suppresses mitochondrial inhibitors-induced mitophagy by reducing the degradation of mitochondrial proteins. Besides the mitophagic process, mitochondrial-derived vesicles (MDVs) are known to be involved in the maintenance of mitochondrial homeostasis. MDVs are generated by selective incorporation of mitochondrial cargo into small vesicles, which transit to the lysosome for subsequent degradation. Interestingly, the MDVs transit to the lysosome is PINK1/PRKN-dependent [50]. Therefore, considering that both MDVs and mitophagy share common regulation pathways, our work places miR-218 as a novel attractive target in regulating the mitochondrial quality processes. Further studies are required to investigate a putative link between miR-218 and MDVs transit to lysosomes.

Preserving a correct mitophagy process is necessary for limiting reactive oxygen species (ROS) production, mitochondrial DNA mutations, metabolic inflexibility, and inflammation [51]. Upon PINK1 phosphorylation, PRKN mediates the amplification of the ubiquitylation signal necessary for mitophagy receptors recruitment to mitochondria [8–10]. We identified miR-218 as a promising candidate to switch off PRKN gene, thus inhibiting mitophagy. Of note, autophagy inhibition has been widely accepted as a therapeutic strategy in cancer. In fact, autophagy regulators (e.g., chloroquine, hydrochloroquine) are already used in clinical studies on anticancer therapy. Now a general interest in mitophagy manipulation to improve cancer therapy is emerging. Indeed, inhibition of mitophagy (by targeting different stages of the autophagic/mitophagic process, genetically or pharmacologically) enhances drug sensitivity in several cases. For instance, the block of autophagosome formation and the inhibition of autophagosomes-lysosomes fusion were investigated [52–54]. The block of mitophagy by BNIP3L down-regulation enhanced doxorubicin sensitivity in colorectal cancer stem cells [55]. This said, few tools are available in order to specifically modulate the mitophagy pathway (and not only the general autophagy pathway). Here, we found that miR-218 is a novel powerful inhibitor of mitophagy through PRKN down-regulation. Interestingly, miR-218 was found significantly decreased in breast cancer tissues and negatively associated with Ki-67 [56]. The authors of this work demonstrated, *in vitro*, that over-expression of miR-218 induces apoptosis and decreases cell proliferation. In this regard, miR-218 mediated down-regulation of PRKN could be a potential mechanism that may contribute to apoptosis in breast cancer cells. Further studies are required to investigate this point.

Since nanoparticles offer incredible opportunities for cell specific controlled delivery of miRNAs in the treatment of cancer or neurodegenerative disorders [57], our findings thus provide a potential therapeutic strategy for cancer, such as breast cancer. Moreover, inhibition of miR-218 (e.g., AntagomiR) is expected to be beneficial in several neurodegenerative diseases in which the mitophagy process is not sufficiently efficient.

Interestingly, this E3 ubiquitin ligase is also the substrate of another miRNA, miR-181 [32]. It seems that both miR-218 and miR-181 have the same function in mammalian cells; as such, it would be interesting to understand if their functions are redundant or whether they could compensate each other. Since miR-218 is down-regulated in several cancers [58–61], we can suppose that expression of

miR-181 could compensate these defects. However, when a strong stimulus promotes mitochondrial depolarization and thus powerful mitochondria selective removal is required, this pro-survival process can exceed in deregulated clearance that leads to apoptosis [62]. In this context, over-expressing miR-218 or generating a miR-218 agonist could turn out to be a promising weapon in order to combat mitophagy system's dysregulation.

Finally, it has been recently demonstrated that despite its function in targeting PRKN during mitophagy, miR-181 control also genes implicated in mitochondrial biogenesis, functionality, and antioxidant response [63]. In analogy with this microRNA, it would be interesting to study whether miR-218 cover additional functions in controlling mitochondrial homeostasis beyond mitophagy.

In summary since PRKN and the mitophagy process play a pivotal role in neurodegeneration and tumor progression, our findings identify in miR-218 a potential therapeutic target for counteracting neurodegenerative and cancer diseases.

4. Materials and Methods

4.1. Cloning and Luciferase Assay

A portion of the 3'UTR sequence containing two predicted binding sites for miR-218 was cloned in the pMiR reporter vector by using the following oligonucleotides: forward: GCGCACTAGT-CGCACAACCTCAAGGGAAACTC (containing the cloning site for Spe I); reverse: GCGCAAGCTT-GCAGCGTTCCTCAGATCTCAAG (containing the cloning site for Hind III). The assay was performed by using the Luciferase Reporter Assay System (Promega, Milan, Italy), following the manufacturer's instructions. The 3'UTR-containing pmiR-Report was co-transfected with the Tet-O-FUW miRNA-overexpressing vector and the rtTA-expressing vector in HeLa cells. A pRL-SV40 Renilla luciferase reporter vector (Promega, Milan, Italy) was also used to quantify the transfection efficiency. Firefly luciferase luminescent signal was normalized on the Renilla luciferase signal (Promega, Milan, Italy). Control experiments using the empty pMiR-Report vector in presence or absence of the microRNA were performed.

4.2. Cell Cultures and Transfection

Cells were cultured in Dulbecco's modified Eagle's medium (DMEM; GIBCO 41966-029, Monza, Italy) supplemented with 10% fetal bovine serum (FBS; Thermo Fisher Scientific, 10270-106, Monza, Italy) at 37 °C under 5% CO₂. Transient transfections of expression plasmids into Hek293 cells were performed using TurboFect (Thermo Fisher Scientific, R0532, Monza, Italy).

4.3. Plasmids

The GFP-miR-218 construct was generated by cloning 400 bps encompassing the sequence for miR-218-1 into a Tet-O-FUW-Ires-GFP vector under the control of the tetracycline operator. Proper expression of mature miR-218 was tested by TaqMan (Thermo Fisher Scientific, Monza, Italy) assay as previously described [64]. Transfection was performed in combination with the rtTA transactivator supplied with doxycycline (2 mg/mL, Clontech, Mountain View, California, USA). An empty Tet-O-FW GFP vector was used as control.

4.4. Cell Treatment

HEK293 cells were treated with the combined treatment O/A (2.5 and 0.8 μM) for the indicated time. Autophagosome-lysosome fusion was blocked with CQ 20 μM for 1 h (Sigma-Aldrich, O9718, Milan, Italy).

4.5. Quantitative PCR (qPCR)

cDNA was isolated from Hek293 cells using the ReliaPrep RNA Cell Miniprep System (Promega, Milan, Italy) according to the manufacturer's instruction. The quantitative analysis

of PRKN was performed using quantitative real time polymerase chain reaction (PCR) for PRKN (Primer FW: GGGTCGTGAACAACTGCCGATCATT; Primer RV: AGGAGCCCCGTCCTGGTTTT). We used B2M as housekeeping gene (Primer FW: CTCCGTGGCCTTAGCTGTG; Primer RV: TCTCTGCTGGATGACGTGAG). Each 20 μ L reaction contained 5 μ L of template, 1 μ L of each primer (10 μ M), 10 μ L SensiFAST SYBR MIX 2 \times (Bioline, Milan, Italy) and 3 μ L of nuclease-free water. The experiment was run in triplicate on a LC480 LightCycler (Roche, Milan, Italy). PRKN content was calculated with the $\Delta\Delta$ Ct method after normalization on B2M.

4.6. Western Blot Analysis

Cells were rinsed in phosphate-buffered saline (PBS) on ice and lysed in RIPA (Radioimmunoprecipitation assay buffer) buffer supplemented with a protease inhibitor cocktail (Sigma-Aldrich, P8340, Milan, Italy), Na₄VO₃ 0.1 mM (Sigma-Aldrich, S6508, Milan, Italy), NaF 1 mM (Sigma-Aldrich, S7920, Milan, Italy) and β -Glycerophosphate 5 mM (Sigma-Aldrich, G6376, Milan, Italy). Cell extracts were centrifuged at 15,000 \times g for 10 min at 4 $^{\circ}$ C. Protein concentrations were determined with the Bio-Rad Protein Assay Kit (Bio-Rad, 5000001, Milan, Italy). Cell extracts were separated by sodium dodecyl sulphate–polyacrylamide gel electrophoresis (SDS–PAGE). Primary antibodies used were: anti-SOD2 (Enzo-Lifesciences, Milan, Italy), anti-TOMM20 (Santa Cruz Biotechnology, Milan, Italy), anti-PRKN (Cell signalling, Milan, Italy), anti-VCL (Santa Cruz Biotechnology, Milan, Italy), anti-Ub (Santa Cruz Biotechnology, Milan, Italy), anti-Ub (KK2, Enzo-Lifesciences, Milan, Italy), anti-HSP60 (Santa Cruz Biotechnology, Milan, Italy). All uncropped images are illustrated in Supplementary Figure S1).

4.7. Immunofluorescence Analysis

Cells were washed in PBS and fixed with 4% paraformaldehyde in PBS for 10 min. After permeabilization with 0.4% Triton X-100 (Sigma-Aldrich, X-100, Milan, Italy) in PBS for 5 min, cells were incubated overnight at 4 $^{\circ}$ C with primary antibodies and 2% normal goat serum (Sigma-Aldrich, G9023). Primary antibodies used were: anti-TOM20 (Santa Cruz Biotechnology, Milan, Italy), anti-LC3 (Cell Signaling, Milan, Italy). Cells were then washed with PBS (GIBCO, BE17-512F, Monza, Italy) and incubated for 1 h with labelled anti-mouse (Thermo Fisher Scientific, A11017-A21425, Monza, Italy) or anti-rabbit (Thermo Fisher Scientific, A11070-A21430-A31573, Monza, Italy) secondary antibodies. Nuclei were stained with 1 μ g/mL DAPI (4',6-diamidino-2-phenylindole) and examined under a Zeiss LSM 700 63 \times oil-immersion objective (CLSM700; Jena, Germany). We used ImageJ software for image analysis. We calculated the mito content as percentage of cytosolic area occupied by mitochondria with Mitophagy macro [65,66]. Co-localization measurements were made through the JACOP plugin of the NIH ImageJ software [67]. M1 manders co-localization coefficients (MCC) of mitochondria overlapping LC3. All acquisitions were performed by a blind approach in non-saturated single z-confocal. The images in Figure 1a were captured with Zoe Fluorescence Cell Imager (Biorad, Milan, Italy).

4.8. Statistical Analysis

All statistical analyses were performed and graphed using GraphPad Prism 6. Comparisons between two groups were analyzed using two-tailed Student's T-test with Welch's correction. Three or more groups comparisons were performed with one-way ANOVA with Sidak's correction. Significance is defined as * $p < 0.05$, ** $p < 0.01$ and *** $p < 0.001$. Standard error of the mean is indicated as s.e.m.

Supplementary Materials: The following are available online at <http://www.mdpi.com/1422-0067/21/1/355/s1>.

Author Contributions: A.D.R. performed most experiments and designed the work plan together with F.S.; Experimental work: T.M. (Figures 2d and 3c,d and contribution in Figure 4c); K.B. (contribution in Figures 1e, 2d and 4c); F.V. and G.C.B. (contribution in Figure 1a,b, cloning, luciferase assay and contribution of reagents). A.D.R. and F.S. wrote the manuscript. All authors have read and agreed to the published version of the manuscript.

Funding: This work was supported by grants: ROCHE (Roche per la ricerca 2017) and 5XMILLE Italian Ministry of Health (2017) to Flavie Strappazon and PRIN 2017 protocol n. 2017T9JNLT to Gian Carlo Bellenchi.

Acknowledgments: We wish to thank Martin Bennett for proofreading of this work and Daniele Guerrucci (SIAL company) for fees management.

Conflicts of Interest: The authors declare no conflict of interest. Funders had no role in the design of the study; in the collection, analyses, or interpretation of data; in the writing of the manuscript, or in the decision to publish the results.

Abbreviations

PINK1HP	TEN induced kinase 1
PRKN	Parkin RBR E3 ubiquitin ligase
SOD2	superoxide dismutase 2
TOMM20	translocase of outer mitochondrion membrane 20
VCL	vinculin
OPTN	optineurin
CALCOCO2	calcium binding and coiled-coil domain 2
BNIP3L	BCL2 interacting protein 3 like
AMBRA1	Autophagy and Beclin 1 regulator 1
FUNDC1	FUN14 domain containing 1
BCL2L13	BCL2 like 13
PHB2	Prohibitin 2
MAP1LC3A	microtubule associated protein 1 light chain 3 alpha
UTR	Un-translated Region
MDVs	Mitochondrial-Derived Vesicles
GFP	Green Fluorescent protein
Mr(K)	Relative molecular mass expressed in Kilo Dalton
O/A	Oligomycin/Antimycin A
CQ	Cloroquine
s.e.m.	Standard Error of the Mean

References

- Cecconi, F.; Levine, B. The role of autophagy in mammalian development: Cell makeover rather than cell death. *Dev. Cell* **2008**, *3*, 344–357. [[CrossRef](#)] [[PubMed](#)]
- Lemasters, J.J. Selective mitochondrial autophagy, or mitophagy, as a targeted defense against oxidative stress, mitochondrial dysfunction, and aging. *Rejuvenation Res.* **2005**, *8*, 3–5. [[CrossRef](#)] [[PubMed](#)]
- Tatsuta, T.; Langer, T. Quality control of mitochondria: Protection against neurodegeneration and ageing. *EMBO J.* **2008**, *27*, 306–314. [[CrossRef](#)] [[PubMed](#)]
- Wang, D.D.; Jin, M.F.; Zhao, D.J.; Ni, H. Reduction of Mitophagy-Related Oxidative Stress and Preservation of Mitochondria Function Using Melatonin Therapy in an HT22 Hippocampal Neuronal Cell Model of Glutamate-Induced Excitotoxicity. *Front. Endocrinol.* **2019**. [[CrossRef](#)] [[PubMed](#)]
- Strappazon, F.; Cecconi, F. AMBRA1-induced mitophagy: A new mechanism to cope with cancer? *Mol. Cell. Oncol.* **2015**, *2*, e975647. [[CrossRef](#)]
- Yan, C.; Li, T.S. Dual role of mitophagy in cancer drug resistance. *Anticancer Res.* **2018**, *38*, 617–621.
- Yamano, K.; Matsuda, N.; Tanaka, K. The ubiquitin signal and autophagy: An orchestrated dance leading to mitochondrial degradation. *EMBO Rep.* **2016**, *17*, 300–316. [[CrossRef](#)]
- Kane, L.A.; Lazarou, M.; Fogel, A.I.; Li, Y.; Yamano, K.; Sarraf, S.A.; Banerjee, S.; Youle, R.J. PINK1 phosphorylates ubiquitin to activate Parkin E3 ubiquitin ligase activity. *J. Cell Biol.* **2014**, *205*, 143–153. [[CrossRef](#)]
- Koyano, F.; Okatsu, K.; Kosako, H.; Tamura, Y.; Go, E.; Kimura, M.; Kimura, Y.; Tsuchiya, H.; Yoshihara, H.; Hirokawa, T.; et al. Ubiquitin is phosphorylated by PINK1 to activate parkin. *Nature* **2014**, *510*, 162–166. [[CrossRef](#)]

10. Kazlauskaite, A.; Kondapalli, C.; Gourlay, R.; Campbell, D.G.; Ritorto, M.S.; Hofmann, K.; Alessi, D.R.; Knebel, A.; Trost, M.; Muqit, M.M. Parkin is activated by PINK1-dependent phosphorylation of ubiquitin at Ser65. *Biochem. J.* **2014**, *460*, 127–139. [[CrossRef](#)]
11. Ordureau, A.; Sarraf, S.A.; Duda, D.M.; Heo, J.M.; Jedrychowski, M.P.; Sviderskiy, V.O.; Olszewski, J.L.; Koerber, J.T.; Xie, T.; Beausoleil, S.A. Quantitative proteomics reveal a feedforward mechanism for mitochondrial PARKIN translocation and ubiquitin chain synthesis. *Mol. Cell* **2014**, *56*, 360–375. [[CrossRef](#)] [[PubMed](#)]
12. Pickrell, A.M.; Youle, R.J. The roles of PINK1, parkin, and mitochondrial fidelity in Parkinson's disease. *Neuron* **2015**, *85*, 257–273. [[CrossRef](#)] [[PubMed](#)]
13. Wauer, T.; Simicek, M.; Schubert, A.; Komander, D. Mechanism of phospho-ubiquitin-induced PARKIN activation. *Nature* **2015**, *524*, 370–374. [[CrossRef](#)] [[PubMed](#)]
14. Okatsu, K.; Koyano, F.; Kimura, M.; Kosako, H.; Saeki, Y.; Tanaka, K.; Matsuda, N. Phosphorylated ubiquitin chain is the genuine Parkin receptor. *J. Cell Biol.* **2015**, *209*, 111–128. [[CrossRef](#)] [[PubMed](#)]
15. Kumar, A.; Chaugule, V.K.; Condos, T.E.C.; Barber, K.R.; Johnson, C.; Toth, R.; Sundaramoorthy, R.; Knebel, A.; Shaw, G.S.; Walden, H. Parkin-phosphoubiquitin complex reveals cryptic ubiquitinbinding site required for RBR ligase activity. *Nat. Struct. Mol. Biol.* **2017**, *24*, 475–483. [[CrossRef](#)] [[PubMed](#)]
16. Trempe, J.F.; Sauvé, V.; Grenier, K.; Seirafi, M.; Tang, M.Y.; Ménade, M.; Al-Abdul-Wahid, S.; Krett, J.; Wong, K.; Kozlov, G.; et al. Structure of parkin reveals mechanisms for ubiquitin ligase activation. *Science* **2013**, *340*, 1451–1455. [[CrossRef](#)] [[PubMed](#)]
17. Lazarou, M.; Sliter, D.A.; Kane, L.A.; Sarraf, S.A.; Wang, C.; Burman, J.L.; Sideris, D.P.; Fogel, A.I.; Youle, R.J. The ubiquitin kinase PINK1 recruits autophagy receptors to induce mitophagy. *Nature* **2015**, *524*, 309–314. [[CrossRef](#)]
18. Wong, Y.C.; Holzbaur, E.L. Optineurin is an autophagy receptor for damaged mitochondria in parkin-mediated mitophagy that is disrupted by an ALS-linked mutation. *Proc. Natl. Acad. Sci. USA* **2014**, *111*, E4439–E4448. [[CrossRef](#)]
19. Heo, J.M.; Ordureau, A.; Paulo, J.A.; Rinehart, J.; Harper, J.W. The PINK1- PARKIN mitochondrial ubiquitylation pathway drives a program of OPTN/NDP52 recruitment and TBK1 activation to promote mitophagy. *Mol. Cell* **2015**, *60*, 7–20. [[CrossRef](#)]
20. Richter, B.; Sliter, D.A.; Herhaus, L.; Stolz, A.; Wang, C.; Beli, P.; Zaffagnini, G.; Wild, P.; Martens, S.; Wagner, S.A.; et al. Phosphorylation of OPTN by TBK1 enhances its binding to Ub chains and promotes selective autophagy of damaged mitochondria. *Proc. Natl. Acad. Sci. USA* **2016**, *113*, 4039–4044. [[CrossRef](#)]
21. Sandoval, H.; Thiagarajan, P.; Dasgupta, S.K.; Schumacher, A.; Prchal, J.T.; Chen, M.; Wang, J. Essential role for Nix in autophagic maturation of erythroid cells. *Nature* **2008**, *454*, 232–235. [[CrossRef](#)] [[PubMed](#)]
22. Novak, I.; Kirkin, V.; McEwan, D.G.; Zhang, J.; Wild, P.; Rozenknop, A.; Rogov, V.; Löhr, F.; Popovic, D.; Occhipinti, A.; et al. Nix is a selective autophagy receptor for mitochondrial clearance. *EMBO Rep.* **2010**, *11*, 45–51. [[CrossRef](#)] [[PubMed](#)]
23. Liu, L.; Feng, D.; Chen, G.; Chen, M.; Zheng, Q.; Song, P.; Ma, Q.; Zhu, C.; Wang, R.; Qi, W.; et al. Mitochondrial outer-membrane protein FUNDC1 mediates hypoxia-induced mitophagy in mammalian cells. *Nat. Cell Biol.* **2014**, *14*, 177–185. [[CrossRef](#)] [[PubMed](#)]
24. Di Rita, A.; Peschiaroli, A.; D'Acunzo, P.; Strobbe, D.; Hu, Z.; Gruber, J.; Nygaard, M.; Lambrugh, M.; Melino, G.; Papaleo, E.; et al. HUWE1 E3 ligase promotes PINK1/PARKIN-independent mitophagy by regulating AMBRA1 activation via IKK α . *Nat. Commun.* **2018**, *9*, 3755. [[CrossRef](#)] [[PubMed](#)]
25. Murakawa, T.; Yamaguchi, O.; Hashimoto, A.; Hikoso, S.; Takeda, T.; Oka, T.; Yasui, H.; Ueda, H.; Akazawa, Y.; Nakayama, H.; et al. Bcl-2-like protein 13 is a mammalian Atg32 homologue that mediates mitophagy and mitochondrial fragmentation. *Nat. Commun.* **2015**, *6*, 7527. [[CrossRef](#)] [[PubMed](#)]
26. Strappazzon, F.; Nazio, F.; Corrado, M.; Cianfanelli, V.; Romagnoli, A.; Fimia, G.M.; Campello, S.; Nardacci, R.; Piacentini, M.; Campanella, M.; et al. AMBRA1 is able to induce mitophagy via LC3 binding, regardless of PARKIN and p62/SQSTM1. *Cell Death Differ.* **2015**, *22*, 419–432. [[CrossRef](#)]
27. Wei, Y.; Chiang, W.C.; Sumpter, R., Jr.; Mishra, P.; Levine, B. Prohibitin 2 Is an Inner Mitochondrial Membrane Mitophagy Receptor. *Cell* **2017**, *168*, 224–238. [[CrossRef](#)]
28. Frankel, L.B.; Lund, A.H. MicroRNA regulation of autophagy. *Carcinogenesis* **2012**, *33*, 2018–2025. [[CrossRef](#)]
29. Jing, Z.; Han, W.; Sui, X.; Xie, J.; Pan, H. Interaction of autophagy with microRNAs and their potential therapeutic implications in human cancers. *Cancer Lett.* **2015**, *356*, 332–338. [[CrossRef](#)]

30. Barde, I.; Rauwel, B.; Marin-Florez, R.M.; Corsinotti, A.; Laurenti, E.; Verp, S.; Offner, S.; Marquis, J.; Kapopoulou, A.; Vanicek, J.; et al. A KRAB/KAP1-miRNA cascade regulates erythropoiesis through stage-specific control of mitophagy. *Science* **2013**, *340*, 350–353. [[CrossRef](#)]
31. Liu, K.; Yan, L.; Jiang, X.; Yu, Y.; Liu, H.; Gu, T.; Shi, E. Acquired inhibition of microRNA-124 protects against spinal cord ischemia-reperfusion injury partially through a mitophagy-dependent pathway. *J. Thorac. Cardiovasc. Surg.* **2017**, *154*, 1498–1508. [[CrossRef](#)] [[PubMed](#)]
32. Cheng, M.; Liu, L.; Lao, Y.; Liao, W.; Liao, M.; Luo, X.; Wu, J.; Xie, W.; Zhang, Y.; Xu, N. MicroRNA-181a suppresses parkin-mediated mitophagy and sensitizes neuroblastoma cells to mitochondrial uncoupler-induced apoptosis. *Oncotarget* **2016**, *7*, 42274–42287. [[CrossRef](#)] [[PubMed](#)]
33. Kim, J.; Fiesel, F.C.; Belmonte, K.C.; Hudec, R.; Wang, W.X.; Kim, C.; Nelson, P.T.; Springer, W.; Kim, J. miR-27a and miR-27b regulate autophagic clearance of damaged mitochondria by targeting PTEN-induced putative kinase 1 (PINK1). *Mol. Neurodegener.* **2016**, *11*, 55. [[CrossRef](#)] [[PubMed](#)]
34. Amin, N.D.; Bai, G.; Klug, J.R.; Bonanomi, D.; Pankratz, M.T.; Gifford, W.D.; Hinckley, C.A.; Sternfeld, M.J.; Driscoll, S.P.; Dominguez, B.; et al. Loss of motoneuron-specific microRNA-218 causes systemic neuromuscular failure. *Science* **2015**, *350*, 1525–1529. [[CrossRef](#)]
35. Mauthe, M.; Orhon, I.; Rocchi, C.; Zhou, X.; Luhr, M.; Hijlkema, K.J.; Coppes, R.P.; Engedal, N.; Mari, M.; Reggiori, F. Chloroquine inhibits autophagic flux by decreasing autophagosome-lysosome fusion. *Autophagy* **2018**, *14*, 1435–1455. [[CrossRef](#)]
36. Dawson, T.M.; Dawson, V.L. Parkin plays a role in sporadic Parkinson's disease. *Neurodegener. Dis.* **2014**, *13*, 69–71. [[CrossRef](#)]
37. Tsai, Y.C.; Fishman, P.S.; Thakor, N.V.; Oyler, G.A. Parkin facilitates the elimination of expanded polyglutamine proteins and leads to preservation of proteasome function. *J. Biol. Chem.* **2003**, *278*, 22044–22055. [[CrossRef](#)]
38. Rosen, K.M.; Moussa, C.E.; Lee, H.K.; Kumar, P.; Kitada, T.; Qin, G.; Fu, Q.; Querfurth, H.W. Parkin reverses intracellular beta-amyloid accumulation and its negative effects on proteasome function. *J. Neurosci. Res.* **2010**, *88*, 167–178. [[CrossRef](#)]
39. Hebron, M.; Chen, W.; Miessau, M.J.; Lonskaya, I.; Moussa, C.E. Parkin reverses TDP-43-induced cell death and failure of aminoacid homeostasis. *J. Neurochem.* **2014**, *129*, 350–361. [[CrossRef](#)]
40. Kubo, S.; Hatano, T.; Takanashi, M.; Hattori, N. Can parkin be a target for future treatment of Parkinson's disease? *Expert Opin. Ther. Targets* **2013**, *17*, 1133–1144. [[CrossRef](#)]
41. Liu, J.; Zhang, C.; Hu, W.; Feng, Z. Parkinson's disease-associated protein Parkin: An unusual player in cancer. *Cancer Commun.* **2018**, *26*, 40. [[CrossRef](#)] [[PubMed](#)]
42. Cesari, R.; Martin, E.S.; Calin, G.A.; Pentimalli, F.; Bichi, R.; McAdams, H.; Trapasso, F.; Drusco, A.; Shimizu, M.; Masciullo, V.; et al. Parkin, a gene implicated in autosomal recessive juvenile parkinsonism, is a candidate tumor suppressor gene on chromosome 6q25–q27. *Proc. Natl. Acad. Sci. USA* **2003**, *100*, 5956–5961. [[CrossRef](#)]
43. Denison, S.R.; Wang, F.; Becker, N.A.; Schüle, B.; Kock, N.; Phillips, L.A.; Klein, C.; Smith, D.I. Alterations in the common fragile site gene Parkin in ovarian and other cancers. *Oncogene* **2003**, *22*, 8370–8378. [[CrossRef](#)]
44. Picchio, M.C.; Martin, E.S.; Cesari, R.; Calin, G.A.; Yendamuri, S.; Kuroki, T.; Pentimalli, F.; Sarti, M.; Yoder, K.; Kaiser, L.R.; et al. Alterations of the tumor suppressor gene Parkin in non-small cell lung cancer. *Clin. Cancer Res.* **2004**, *10*, 2720–2724. [[CrossRef](#)] [[PubMed](#)]
45. Tay, S.P.; Yeo, C.W.; Chai, C.; Chua, P.J.; Tan, H.M.; Ang, A.X.; Yip, D.L.; Sung, J.X.; Tan, P.H.; Bay, B.H.; et al. Parkin enhances the expression of cyclin-dependent kinase 6 and negatively regulates the proliferation of breast cancer cells. *J. Biol. Chem.* **2010**, *285*, 29231–29238. [[CrossRef](#)] [[PubMed](#)]
46. Liu, J.; Zhang, C.; Zhao, Y.; Yue, X.; Wu, H.; Huang, S.; Chen, J.; Tomsky, K.; Xie, H.; Khella, C.A.; et al. Parkin targets HIF-1alpha for ubiquitination and degradation to inhibit breast tumor progression. *Nat. Commun.* **2017**, *8*, 1823. [[CrossRef](#)]
47. Greene, J.C.; Whitworth, A.J.; Kuo, I.; Andrews, L.A.; Feany, M.B.; Pallanck, L.J. Mitochondrial pathology and apoptotic muscle degeneration in *Drosophila* parkin mutants. *Proc. Natl. Acad. Sci. USA* **2003**, *100*, 4078–4083. [[CrossRef](#)]
48. Narendra, D.; Tanaka, A.; Suen, D.F.; Youle, R.J. Parkin is recruited selectively to impaired mitochondria and promotes their autophagy. *J. Cell Biol.* **2008**, *183*, 795–803. [[CrossRef](#)]

49. Matsuda, N.; Sato, S.; Shiba, K.; Okatsu, K.; Saisho, K.; Gautier, C.A.; Sou, Y.S.; Saiki, S.; Kawajiri, S.; Sato, F.; et al. PINK1 stabilized by mitochondrial depolarization recruits Parkin to damaged mitochondria and activates latent Parkin for mitophagy. *J. Cell Biol.* **2010**, *189*, 211–221. [[CrossRef](#)]
50. Sugiura, A.; McLelland, G.L.; Fon, E.A.; McBride, H.M. A new pathway for mitochondrial quality control: Mitochondrial-derived vesicles. *EMBO J.* **2014**, *33*, 2142–2156. [[CrossRef](#)]
51. Gottlieb, R.A.; Thomas, A. Mitophagy and Mitochondrial Quality Control Mechanisms in the Heart. *Curr. Pathobiol. Rep.* **2017**, *5*, 161–169. [[CrossRef](#)] [[PubMed](#)]
52. Zhou, J.; Li, G.; Zheng, Y.; Shen, H.M.; Hu, X.; Ming, Q.L.; Huang, C.; Li, P.; Gao, N. A novel autophagy/mitophagy inhibitor liensinine sensitizes breast cancer cells to chemotherapy through DNMI1L-mediated mitochondrial fission. *Autophagy* **2015**, *11*, 1259–1279. [[CrossRef](#)] [[PubMed](#)]
53. Mauro-Lizcano, M.; Esteban-Martinez, L.; Seco, E.; Serrano-Puebla, A.; Garcia-Ledo, L.; Figueiredo-Pereira, C.; Vieira, H.L.; Boya, P. New method to assess mitophagy flux by flow cytometry. *Autophagy* **2015**, *11*, 833–843. [[CrossRef](#)] [[PubMed](#)]
54. Radogna, F.; Cerella, C.; Gaigneaux, A.; Christov, C.; Dicato, M.; Diederich, M. Cell type-dependent ROS and mitophagy response leads to apoptosis or necroptosis in neuroblastoma. *Oncogene* **2016**, *35*, 3839–3853. [[CrossRef](#)] [[PubMed](#)]
55. Yan, C.; Luo, L.; Guo, C.Y.; Goto, S.; Urata, Y.; Shao, J.H.; Li, T.S. Doxorubicin-induced mitophagy contributes to drug resistance in cancer stem cells from HCT8 human colorectal cancer cells. *Cancer Lett.* **2017**, *388*, 34–42. [[CrossRef](#)]
56. Liu, B.; Tian, Y.; Li, F.; Zhao, Z.; Jiang, X.; Zhai, C.; Han, X.; Zhang, L. Tumor-suppressing roles of miR-214 and miR-218 in breast cancer. *Oncol. Rep.* **2016**, *35*, 3178–3184. [[CrossRef](#)]
57. Lee, S.W.L.; Paoletti, C.; Campisi, M.; Osaki, t.; Adriani, G.; Kann, R.D.; Mattu, C.; Chiono, V. MicroRNA delivery through nanoparticles. *J. Controll. Release* **2019**, *313*, 80–95. [[CrossRef](#)]
58. Yu, J.; Wang, Y.; Dong, R.; Huang, X.; Ding, S.; Qiu, H. Circulating microRNA-218 was reduced in cervical cancer and correlated with tumor invasion. *J. Cancer Res. Clin. Oncol.* **2012**, *138*, 671–674. [[CrossRef](#)]
59. He, X.; Dong, Y.; Wu, C.W.; Zhao, Z.; Ng, S.S.; Chang, F.K.; Sung, J.J.; Yu, J. MicroRNA-218 inhibits cell cycle progression and promotes apoptosis in colon cancer by downregulating BMI1 polycomb ring finger oncogene. *Mol. Med.* **2012**, *18*, 1491–1498. [[CrossRef](#)]
60. Sher, Y.P.; Wang, L.J.; Chuang, L.L.; Tsai, M.H.; Kuo, T.T.; Huang, C.C.; Chuang, E.Y.; Lai, L.C. ADAM9 up-regulates N-cadherin via miR-218 suppression in lung adenocarcinoma cells. *PLoS ONE* **2014**, *9*, e94065. [[CrossRef](#)]
61. Uesugi, A.; Kozaki, K.; Tsuruta, T.; Furuta, M.; Morita, K.; Imoto, I.; Omura, K.; Inazawa, J. The tumor suppressive microRNA miR-218 targets the mTOR component Rictor and inhibits AKT phosphorylation in oral cancer. *Cancer Res.* **2011**, *71*, 5765–5778. [[CrossRef](#)] [[PubMed](#)]
62. Liu, D.H.; Lv, J.X. The progress research of mitophagy. *J. Cell Biol.* **2008**, *30*, 467–471.
63. Indrieri, A.; Carrella, S.; Romano, A.; Spaziano, A.; Marrocco, E.; Fernandez-Vizarra, E.; Barbato, S.; Pizzo, M.; Ezhova, Y.; Golia, F.M.; et al. miR-181a/b downregulation exerts a protective action on mitochondrial disease models. *EMBO Mol. Med.* **2019**, *11*, e8734. [[CrossRef](#)] [[PubMed](#)]
64. De Gregorio, R.; Pulcrano, S.; De Sanctis, C.; Volpicelli, F.; Guatteo, E.; von Oerthel, L.; Latagliata, E.C.; Esposito, R.; Piscitelli, R.M.; Perrone-Capano, C.; et al. miR-34b/c Regulates Wnt1 and Enhances Mesencephalic Dopaminergic Neuron Differentiation. *Stem Cell Rep.* **2018**, *10*, 1237–1250. [[CrossRef](#)] [[PubMed](#)]
65. Dagda, R.K.; Zhu, J.; Kulich, S.M.; Chu, C.T. Mitochondrially localized ERK2 regulates mitophagy and autophagic cell stress. *Autophagy* **2008**, *4*, 770–782. [[CrossRef](#)] [[PubMed](#)]
66. Zhu, J.; Dagda, R.K.; Chu, C.T. Monitoring mitophagy in neuronal cell cultures. *Methods Mol. Biol.* **2011**, *793*, 325–339.
67. Bolte, S.; Cordelières, F.P. A guided tour into subcellular colocalization analysis in light microscopy. *J. Microsc.* **2006**, *224*, 213–232. [[CrossRef](#)]





A global view of the miRNA-mitophagy connexion

Flavie Strappazon*

IRCCS Fondazione Santa Lucia, Rome, Italy

*Corresponding author: e-mail address: f.strappazon@hsantalucia.it

Contents

1. Introduction	38
2. Mammalian key proteins in mitophagy	39
3. MicroRNAs	41
4. Mammalian mitophagy regulation by microRNAs	42
4.1 MicroRNAs and physiological mitophagy control	42
4.2 MicroRNAs that regulate mitophagy by directly targeting some mitophagic players	42
4.3 MicroRNAs that modulate mitophagy in pathological condition	43
5. Interconnecting microRNAs and mitophagy to favor new therapeutic approaches for neurodegenerative diseases and cancers	48
5.1 Neurodegenerative diseases	48
5.2 Cancers	49
6. Conclusions	50
Acknowledgments	51
References	51

Abstract

Mitochondria are highly dynamics organelles that provide the necessary energy for cellular functions. However, when they are dysfunctional, they can, by contrast, be very harmful for the cell. Mitophagy ensures their recycling and preserves cell performance. This mechanism is particularly important in neurons because they use a lot of energy. Failed mitophagy can thus affect the development of neurons and lead to brain problems. In this regard, a tight regulation of this process is needed. In recent years microRNAs, as regulators of several biological processes, have attracted attention in the field of mitophagy. In this review, we focused on the studies that highlight the miRNAs implicated in the regulation of mitophagic pathways. In particular, we described the first study carried out 7 years ago, in the context of mitophagy during erythroid differentiation. Next, we have cited all the other works to date on microRNAs and mitophagy regulation. Finally, we have underlined the importance of these discoveries in order to define new therapeutic approaches in the context of age-related diseases involving mitochondrial dysfunctions, such as cancers and neurodegenerative diseases.

Abbreviations

AMBRA1	autophagy and beclin 1 regulator 1
Atg8	protein linked to autophagy 8
BNIP3L	BCL2 interacting protein 3 like
CALCOCO2	calcium binding and coiled-coil domain 2
FUNDC1	FUN14 domain containing 1
HEK293	human embryonic kidney 293
HMBG1	<i>high mobility group box 1</i>
I/R	ischemia/reperfusion
KRAB-ZFPs	KRAB-containing zinc finger proteins
LC3	proteins associated with microtubules 1A/1B light chain 3B
LIR	LC3 interaction region
OMM	outer mitochondrial membrane (OMM)
OPTN	optineurin
PD	Parkinson's disease
PINK1	PTEN-induced kinase 1
ROS	reactive oxygen species
TRAF3	TNF receptor-associated factor 3
UBD	ubiquitin binding domain
UTR	untranslated region
VDAC1	voltage-dependent anion channel 1



1. Introduction

Autophagy is one of the processes of cellular degradation that has been preserved in all eukaryotic organisms. It involves molecular machinery and specific degradation compartments, which in mammals are represented by lysosomes and by vacuoles in plants and yeast.

Three common forms of autophagic pathways are defined: microautophagy, chaperone-mediated autophagy (CMA) and macroautophagy. Microautophagy is mediated by direct engulfment of the cytoplasmic material that needs to be degraded. Cytoplasmic material is trapped in the lysosome/vacuole by a random process of membrane invagination. This pathway is crucial for survival of cells under conditions of starvation, nitrogen deprivation, or after treatment with rapamycin. CMA contributes to cellular quality control through the removal of damaged or malfunctioning proteins through the lysosome and this is performed specifically through a recognition motif in the amino acid sequences of proteins. Macroautophagy is instead considered the main form of autophagy and is characterized by a discernible

morphological feature. Indeed, it involves the formation of membranes, called phagophores, which close by sequestering cytoplasmic content and form vesicles, named autophagosomes. These autophagosomes will then merge with the lysosome, their content being degraded due to the different enzymes present in this compartment. Many diseases such as neurodegenerative diseases and cancers have been associated with defects in autophagy.^{1,2}

Autophagy has been long considered a mechanism used only for the random degradation of cytosolic components (proteins, organelles, ribosomes, etc.). However, numerous studies have now reported that autophagy degradation can be selective for specific substrates, such as ribosomes, peroxisome, nucleus, endoplasmic reticulum or mitochondria.³ Because maintaining damaged mitochondria is harmful for cells, eukaryotic species have developed a specific mitochondrial degradation process called mitophagy. It is a crucial process for the specific removal of damaged or excess mitochondria by micro or macroautophagy.⁴ Microautophagic pathways have been observed in yeast cells following nitrogen deprivation. In this context, one mitophagic receptor has been described as playing a key role and is called Uth1/taking part of the SUN family protein UTH1).⁵ Like for macroautophagy, the macromitophagy is widespread in a variety of model organisms such as yeast, nematodes, flies and mammals, making it the best path molecularly described to date. This process is important to remove superfluous mitochondria that have no apparent defects but also damaged mitochondria.⁶ The mitophagy process was introduced in 2005 by John Lemasters.⁷ He observed, in rat hepatocytes placed under deficiency conditions, that some of the mitochondria were sequestered in autophagosomes.⁸ To be degraded by mitophagy, certain proteins of the outer mitochondria membrane (OMM) must be labeled by ubiquitin. Mitochondria are then recognized by proteins that specifically bind ubiquitin or by specific mitophagy receptors present in the OMM. The interaction of these effectors with LC3 (microtubule-associated protein 1A/1B-light chain 3), a protein localized in the membranes of phagophores would allow the recruitment and sequestration of mitochondria into autophagosomes (Fig. 1).



2. Mammalian key proteins in mitophagy

At the physiological level, the macroautophagic removal of mitochondria was revealed to be crucial in two contexts: (i) during maturation of reticulocytes into erythrocytes. Indeed, mitochondrial clearance is required during this differentiation process in order to deplete erythrocytes from mitochondria. In such conditions, the NIX protein, also known as

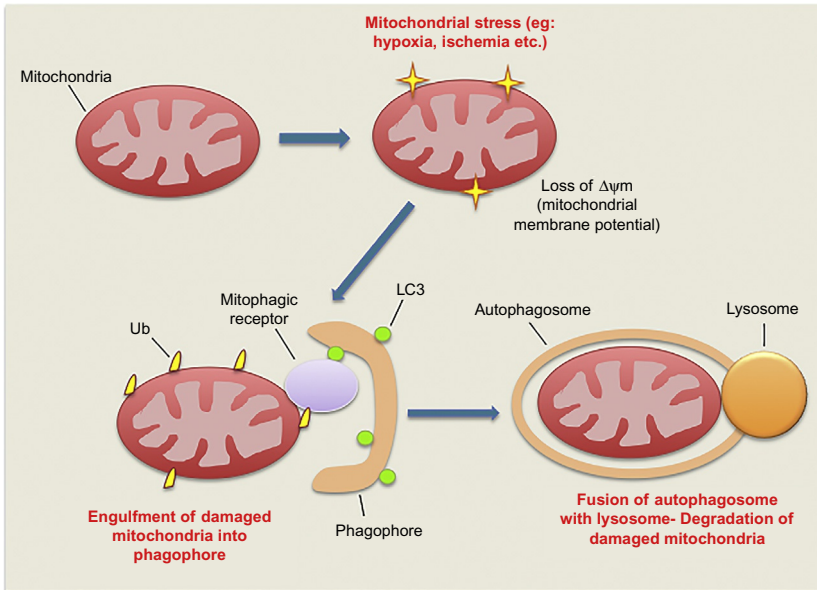


Fig. 1 The mitophagy mechanism in mammalian cells. The molecular pathway of mitophagy is illustrated. The principal major steps in the process are shown in red. Ub: Ubiquitin.

beclin-2 (BCL2)/adenovirus E1B 19 kDa protein interacting on proteins 3 (BNIP3L), increases and is responsible for the mitochondria elimination by directly binding LC3B thanks to its LC3 interaction region (LIR)⁹; (ii) during the first step of embryogenesis^{10,11} when paternal mitochondria need to be removed. In this context, paternal mitochondria which are fragmented and depolarised^{10,12} are removed thanks to some molecular players such as endonuclease G in yeast,¹³ prohibitin 2 (PHB2),¹⁴ PTEN-induced putative kinase 1 (PINK1), and Parkin (PARK2) in mammals that contribute to tag mitochondria to be removed.

In mammals, mitophagy has been extensively studied since 2007 and, depending to the mitochondrial stress stimuli, various proteins that will be mentioned below, were found to regulate this process.

The main mitochondria degradation path described today occurs following depolarization of mitochondria. It is governed after the activation of the PINK1 kinase and the E3 Ubiquitin ligase, Parkin. After the loss of mitochondrial membrane potential, PINK1 accumulates in the OMM,¹⁵ this in turn, allows PINK1-dependent recruitment of Parkin and its phosphorylation at Serine 65,¹⁶ which promotes its dimerization and activation of its

E3 ubiquitin ligase activity. Activation of Parkin is followed by the ubiquitination of different OMM substrates. Afterwards, this phospho-ubiquitin signaling induces the recruitment of mitophagy cargo receptors such as SQSTM1 (also known as p62), Optineurin (OPTN) and CALCOCO2/Nuclear dot protein 52 (NDP52). These receptors are capable of binding ubiquitylated mitochondria through their UBD (Ubiquitin Binding domain) and thanks to a LIR (LC3-Interacting Region) motif, they bind Atg8 (protein linked to autophagy 8) /LC3 (proteins associated with microtubules 1A/1B light chain 3B) proteins on the membranes of phagophore in order to deliver mitochondria in autophagosomes.¹⁷

Other “alternative” mitophagy pathways, PINK1/Parkin-independent, have been described. For instance, in conditions of hypoxia, it has been shown that FUNDC1 (FUN14 domain containing 1), a protein of the OMM, activates mitophagy. In this context, FUNDC1 is mitophagic receptor that directly binds LC3 via its LIR domain.¹⁸ Moreover NIX/Bcl-2-like 13 (BCL2L13), another mitophagic receptor of the OMM, is also known to favor mitophagy following hypoxia through a direct binding with LC3.⁹ In addition, AMBRA1 is a cytosolic protein that can be located on damaged mitochondria after mitochondrial depolarization or ischemia, and that directly binds LC3 via its LIR motif, stimulating mitophagy.^{19,20} This protein can be recruited to damaged mitochondria in contexts dependent²¹ or independent of Parkin.¹⁹ In this latest condition, AMBRA1 cooperates with the E3 Ubiquitin ligase HUWE1 in order to induce mitophagy.^{19,22} Some members of the Fanconi Anemia (FA) protein family, Transglutaminase 2 (TG2), SMAD-specific E3 ubiquitin protein ligase 1 (SMURF1), peroxisomal biogenesis factor 3 (PEX3) and PEX13 also play a role in the mitophagy regulation. Their exact role, however, needs to be clarified.^{23–26}



3. MicroRNAs

MicroRNAs (miRNAs or miRs), recently called “master regulators of gene expression,”⁶ are a class of small non-coding RNAs (approximately 22 nucleotides long). They regulate the expression of genes via base complementarity between the seed region of the microRNA and the 3′-untranslated region (UTR) of the target mRNA.^{27,28} miRNA binding induces degradation of the mRNA, translational repression, or both, depending on their level of complementarity.^{29–31}

The post-transcriptional regulation of gene expression by microRNAs is huge since it could reach 60% of all genes encoding human proteins.³² For this reason, miRNAs are involved in multiple cellular processes, such as proliferation, differentiation, apoptosis, carcinogenesis and energy metabolism.^{33–39}



4. Mammalian mitophagy regulation by microRNAs

4.1 MicroRNAs and physiological mitophagy control

As said before, the mitophagy process is carried out by crucial proteins of the OMM or by proteins that translocate from the cytosol to mitochondria following mitochondrial stress. Hitherto it appears that mitophagy can be actively regulated by miRNAs in several contexts.

The first study which linked microRNAs to mitophagy was carried out in the context of erythroid differentiation, and therefore in a physiological mitophagic context. Indeed, in 2013, Barde et al. demonstrated that, during hematopoiesis, the mitophagy process is controlled through the induction of specific members of the large family of KRAB-containing zinc finger proteins (KRAB-ZFPs), which represses the expression of microRNAs targeting the transcripts of mitophagy effector genes.⁴⁰ Indeed, miR-351 and several other miRNAs, with predicted targets in the mitophagy pathway, are up-regulated in *kap1*-deleted murine erythroblasts. In human erythroblasts, the same authors demonstrated that KAP1 represses the NIX-targeting miR-125a-5p. These results underline a tight transcriptional regulation of mitophagy by microRNAs during hematopoiesis.

4.2 MicroRNAs that regulate mitophagy by directly targeting some mitophagic players

Here we cite the microRNAs that have been revealed as directly targeting some of the main players in mitophagy.

4.2.1 MicroRNAs and PINK1/Parkin-mediated mitophagy

Initially, miR-27a and miR-27b have been shown to regulate PINK1 expression at the translational level, which subsequently decreases the mitophagy efficiency. In particular, the authors of the study demonstrated that miR-27a,b expressions reduce ubiquitin phosphorylation, Parkin translocation, and LC3-II accumulation in damaged mitochondria.⁴¹ The same year, miR-181a emerged as another inhibitor of mitophagy by targeting Parkin expression and consequently blocking the co-localization of

mitochondria and autophagosomes. On the other hand, the authors demonstrated that the knockdown of miR-181 was sufficient to accelerate mitophagy in neuroblastoma cells.⁴² More recently, miR-218 emerged as another Parkin targeting microRNA, able to delay mitochondrial clearance in HEK293 cells, by reducing Parkin expression to mitochondria, ubiquitinylation of OMM proteins and mitochondria co-localization with LC3-II.⁴³

4.2.2 *MicroRNAs and hypoxia-mediated mitophagy*

In 2014, a study revealed a link between miR-137 and hypoxia-mediated mitophagy. miR-137 was found to be a novel hypoxia-responsive microRNA, which inhibits mitochondrial degradation by autophagy. The authors demonstrated that miR-137 directly downregulates the expression of the two main mitophagy receptors involved in hypoxia-induced mitophagy: FUNDC1 and NIX. They showed that the defect on mitophagy, due to the expression of miR-137, could be rescued by re-introduction of FUNDC1 and NIX expression constructs that lack the miR-137 pairing sites.⁴⁴

4.2.3 *MicroRNAs and starvation-mediated mitophagy*

CREB1-driven expression of miR-320a was shown to promote mitophagy in HeLa cells following serum deprivation. In this context, miR-320a targets VDAC1 (voltage-dependent anion channel 1) expression and favors mitochondrial clearance.⁴⁵

In summary, almost all mitophagy pathways that have been hitherto described can be regulated by microRNAs. This microRNAs/mitophagy interconnexion in mammalian cells is illustrated in [Fig. 2](#).

4.3 MicroRNAs that modulate mitophagy in pathological condition

We report here some other microRNAs that can influence mitophagy without acting on a known “mitophagic target” or acting indirectly on mitophagy proteins.

4.3.1 *MicroRNA and mitophagy mediated by injuries*

Spinal cord injury. Liu and colleagues have postulated a protective role for mitophagy in spinal cord injury. In particular, they demonstrated, in rats with spinal cord ischemia-reperfusion (I/R), that the down-regulation of miR-124 (using antagonomiR-124) protects against spinal cord injury, by

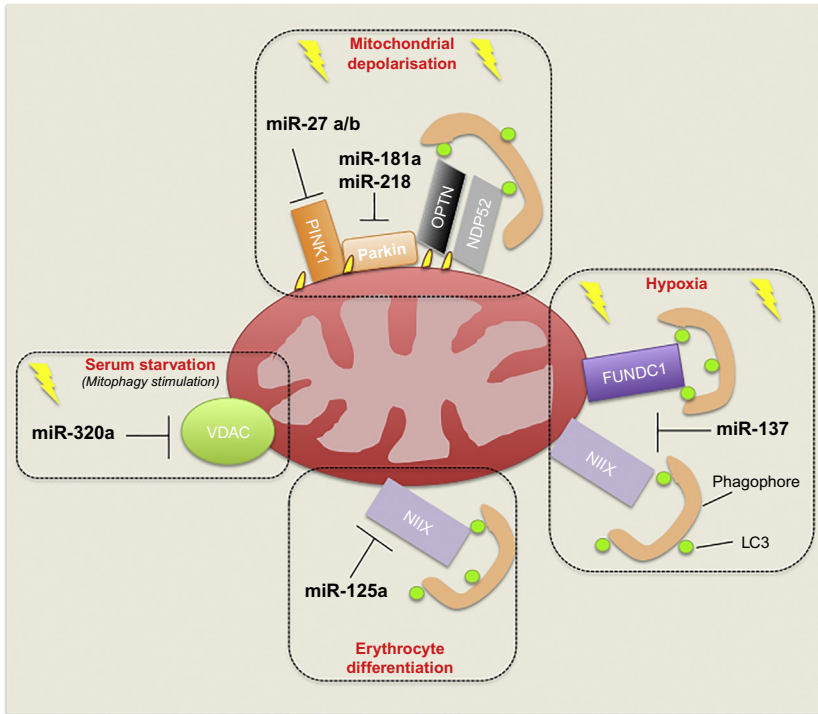


Fig. 2 Overview of the microRNAs controlling mammalian mitophagy pathways. Following mitochondrial depolarization, miR-27 a/b inhibit mitophagy through PINK1 down-regulation, whereas both miR-181a and miR-218 interfere with Parkin expression. During hypoxia, miR-137 inhibits both FUNDC1 and NIX expression, thus interfering with the main mitophagic receptor involved in hypoxia-mediated mitophagy. In the context of erythrocyte differentiation, miR-125 blocks NIX expression and thus mitophagy. Finally, following serum deprivation, miR-320 targets VDAC1 on the OMM, so favoring mitophagy. See text for more details.

increasing mitophagy.⁴⁶ Other studies are needed in order to understand the inhibitory mechanism of miR-124 on mitophagy since the authors did not analyze which target of miR-124 may be repressed following spinal cord injury.

Cardiac injury. Mitochondrial dysfunctions are critical in the cardiac system. Yang and coll. demonstrated that miR-410 inhibits mitophagy after cardiac I/R injury by modulating the heat shock protein B1 activity targeting HMGB1 (high-mobility group box 1 protein). This work opens thus new path for mitophagy modulation in heart injury related to I/R.⁴⁷

Liver injury. 2,20,4,40-Tetrabromodiphenyl ether (BDE-47) induces mitochondrial dysfunction accumulation through a block of PINK1

mediated mitophagy in mouse liver and thus plays a role in liver injury. In this context, miR-34a-5p-mediates mitophagy impairment by targeting NAMPT expression reducing NAD production and favoring oxidation injury in mouse livers. miR-34a-5p-mediated mitophagy defect thus emerges as a potential target for the therapeutic intervention of BDE-47 toxicity.⁴⁸

4.3.2 MicroRNA and mitophagy-related to inflammation

Adipose inflammation. In the context of obesity, miR-103 is a positive regulator of adipose inflammation by blocking mitophagy through TRAF3 (Tumor necrosis factor receptor-associated factor 3) down-regulation.⁴⁹ Further studies aiming to manipulate miR-103 and thus mitophagy could offer new opportunities for improving adipose inflammation in obesity.

Facial neuritis. Inflammatory response is involved in the development of facial neuritis. Liu and coll. explored the role of mitophagy in facial nerve damage induced by tumor necrosis factor α (TNF α). They indicated that TNF α treatment induces apoptosis in SH-SY5Y and suppressed mitophagy by reducing the expression of Bnip3. Functional studies have indicated that miR-145 inhibited Bnip3 transcription and expression, leading to mitophagy inhibition. In this context, miR-145/Bnip3/mitophagy axis may be considered as a potential target for the treatment of facial neuritis.⁵⁰

Antiviral signaling pathways. During innate immune response, which plays a crucial role in the host defense against pathogens, miR-33/33* targets adenosine monophosphate activated protein kinase (AMPK), impeding the formation of active aggregates done by the mitochondrial adaptor mitochondrial antiviral-signaling protein (MAVS). This in turns inhibits mitophagy and generates an imbalance mitochondrial homeostasis, which is required for efficient MAVS activation. miR-33/33* thus emerges as a negative regulator of the RNA virus-triggered innate immune response.⁵¹

4.3.3 MicroRNA, mitophagy and cancers

Several connections between miRNAs, mitophagy and cancers have been discovered in the recent years, highlighting some potential new strategies in cancer prevention or treatments.

Mitochondrial dynamics is a highly deregulated process in cancer. Purhoit et al. have shown that miR-195 exerts pro-apoptotic effects in breast cancer cells by targeting mitofusin2. This in turn, favors mitochondria fission and cell death of breast cancer. Of note mitochondrial mass was decreased in this context but without increase of PINK1. Even if the precise

mitophagy path induced in this system needs to be clarified, it appears that miR-195 expression could be used to fight breast cancer.⁵²

Stem cell-based therapies are attractive for treating various human diseases, including cancer. Among the cell types that can be used for this end, mesenchymal stem cells (MSCs) are considered as promising source of stem cells. It has been shown that miR-155 disturbs mitophagy in MSCs.⁵³ In particular, miR-155 targets Bcl-2 associated athanogene 5 (BAG5) and this destabilizes the PINK1 kinase and consequently disrupted mitophagy. This study suggests a novel mechanism connecting mitochondrial dysfunction in stem cells through a miRNA-mediated mechanism and could offer new strategy for cancer therapies.

Also, because cancer stem cells are often resistant to anti-cancer treatment, modulation of their viability is becoming highly attractive. Zang et al. demonstrated that overexpression of miR-1 induces mitochondrial damage of cancer stem cells by targeting GPD2 (glycerol-3-phosphate dehydrogenase 2), MINOS1 (mitochondrial inner membrane organizing system 1) genes and interacting with LRPPRC (leucine-rich pentatricopeptide-repeat containing) protein. The role of mitophagy induction in this context is not well defined, but it suggests that miRNA-1-mediated regulation of mitochondria morphology may be a strategy to modulate cancer stem cells' viability.⁵⁴

Another miRNA has been connected to mitophagy regulation and cancer, this in the context of lung tumors. In particular, in a mouse model of silicosis, it has been demonstrated that the expression of miR-1224-5p is increased both in lung tissues of silica-induced pulmonary fibrosis and fibroblasts exposed to TGF-1. Repression of miR-1224-5p expression attenuated silica-induced fibrotic progression in vivo and TGF-1-induced myofibroblast differentiation in vitro. miR-1224-5p facilitated silica-induced pulmonary fibrosis primarily by repressing one of target genes, Beclin1, thereby blocking Parkin translocation to mitochondria and inducing the accumulation of damaged mitochondria. These data indicate that miR-1224-5p exerts key functions in silica-induced pulmonary fibrosis and may represent a potential therapeutic target for lung tumors.⁵⁵

Finally, because ROS production emerged as a strategy to kill cancer cells, Guo et al. proposed a novel strategy for cancer prevention or treatment through the use of miR-346.⁵⁶ Indeed, they found that following ER stress induced by thapsigargin treatment, the expression of miR-346 was increased. They next demonstrated that miR-346 reduced HeLa cell apoptosis following ER stress, this through a mechanism

autophagy/mitophagy-dependent. In particular they found that miR-346 favors the expression of GSK β , which disrupts Beclin1 (a well-known pro-autophagy protein) from its inhibitor Bcl-2, favoring like this the autophagy/mitophagy path and decreasing ROS production. The exact induction of autophagy and/or mitophagy in this context needs to be clarified but the reduction of Bcl-2 by miR-346 could be a therapeutic strategy for cancer prevention or treatment.

In summary, mitophagy processes induced by several pathological conditions such as spinal cord cardiac or liver injuries, inflammations or cancers are widely controlled by microRNAs. We illustrated these regulations in Figs. 3 and 4.

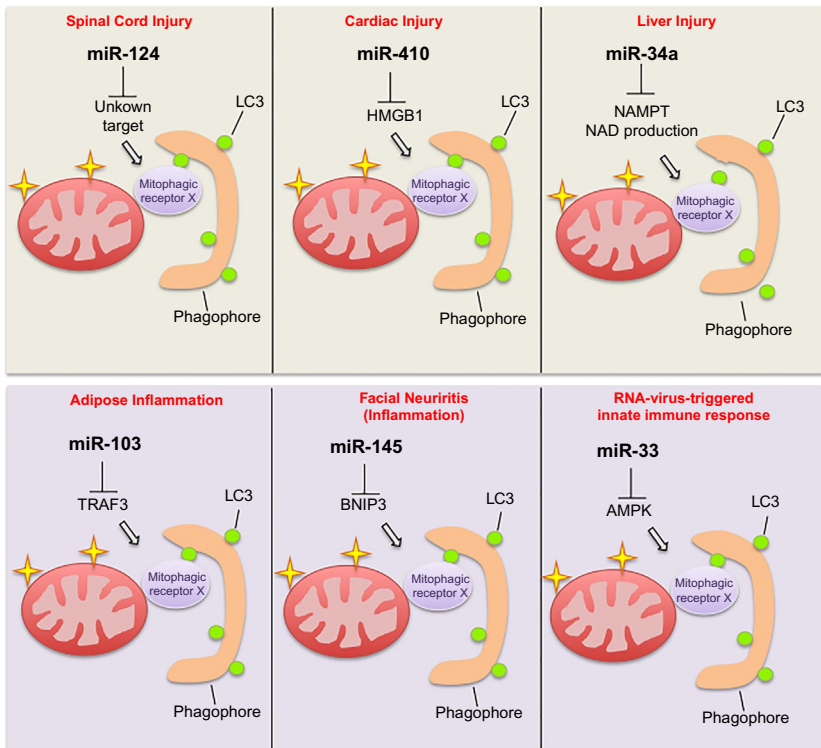


Fig. 3 Overview of microRNAs controlling mitophagy in pathological conditions. Following spinal cord, cardiac or liver injuries, protective mitophagy pathways are activated and can be repressed, respectively by miR-124, miR-410 and miR-34a. miR-410 targets HMGB1 which decreases its expression and inhibits mitophagy. In the context of obesity, miR-103 represses TRAF3, which in turn inhibits mitophagy and participates in adipose inflammation. Following BDE-47 treatment, miR-34a inhibits mitophagy and favors liver injury. See text for more details.

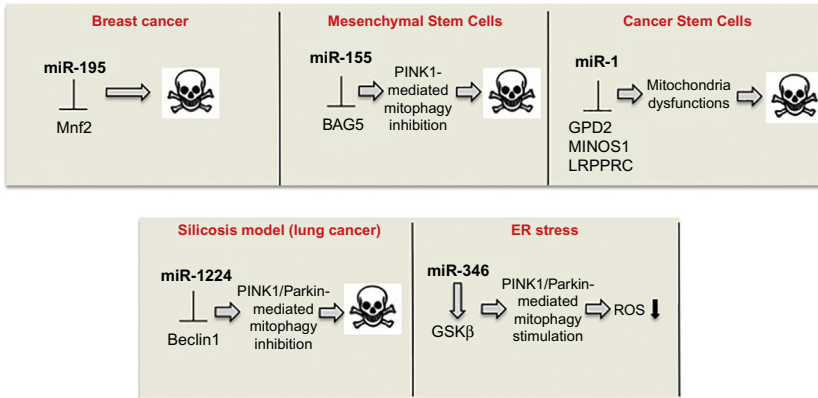


Fig. 4 Overview of microRNAs controlling mitochondria function/mitophagy in contexts related to cancers. Mir-195 expression induces cell death of breast cancer cells through mitofusin2 (Mfn2) down-regulation and thus mitochondrial dysfunction induction. miR-155 expression targets BAG5 which in turn inhibits PINK1-mediated mitophagy and favors cell death of mesenchymal stem cells. miR-1 targets GPD2, MINOS1 and LRPPRC, inducing mitochondrial dysfunctions and thus cell death of cancer stem cells. In the context of silicosis, miR-1224 targets Beclin1 and inhibits Parkin translocation to mitochondria, blocking mitophagy and favoring cell death. Following ER stress, miR-346 favors the expression of GSKB, which disrupts Beclin1 from its inhibitor Bcl2, favoring the autophagy/mitophagy path and decreasing ROS production. See text for more details.



5. Interconnecting microRNAs and mitophagy to favor new therapeutic approaches for neurodegenerative diseases and cancers

Mitochondrial clearance efficiency declines with age, leading to progressive accumulation of damaged and/or unwanted mitochondria, deterioration of cellular function, and cell death. For this reason, mitophagy modulation emerges as a potential therapeutic approach to tackle age-associated pathologies such as neurodegenerative diseases and cancers.⁵⁷ Because microRNAs are involved in several human diseases, such as cancer and disorders of the brain⁵⁸ their interconnection with the mitophagy process may offer novel attractive therapies.

5.1 Neurodegenerative diseases

PINK1 and Parkin are genetically associated with Parkinson's disease (PD) and play critical role in the mitophagy process. Endogenous miR-27a

and- miR-27b regulate PINK1 expression in human dopaminergic-like M17 cells,⁴¹ suggesting that miR27a/b may regulate PINK1 expression in dopaminergic neurons (main neurons involved in PD pathology). Endogenous miR-181 has been shown to be responsive to mitophagic agents in SH-SY5Y cells,⁴² which are neuronal-like cells commonly used as an in vitro model of PD, suggesting a potential role of miR-181a in this pathology. In order to investigate potential contributions of these microRNAs in PD pathology, an accurate analysis of their specific brain expression should be investigated in the course of PD progression. Of note miR-181a, by targeting ATG5 mRNA and thus its protein level, has been recently described as an important inhibitor of macroautophagy induced by starvation and rapamycin in MCF-7, Huh-7 and K562 cells.⁵⁹ Moreover a key role of this microRNA has been demonstrated in mitochondrial homeostasis. Indeed, by favoring mitochondrial biogenesis and mitophagy, miR-181 inactivation delays neuronal death in two animal models of mitochondrial diseases (Microphthalmia with linear skin lesions and Leber's hereditary optic neuropathy).⁶⁰ This study thus highlights miR-181 as a therapeutic target for mitochondrial diseases.

Moreover, it is important to bear in mind that miR-218 is found enriched in motoneurons and mutant mice lacking miR-218 die neonatally and exhibit hallmarks of motoneuron diseases such as amyotrophic lateral sclerosis and spinal muscular atrophy.⁶¹ In this regard, inhibition of mitophagy mediated by miR-218 may play an important role in controlling motoneurons homeostasis.

5.2 Cancers

Many studies have highlighted the role of autophagy in maintaining proper mitochondrial function. Concerning the role of mitophagy, some studies based on the analysis of the phenotypes in mice deleted for Parkin or PINK1 or for the BNIP3 and NIX mitophagy receptors have indicated a tumor suppressor function for mitophagy.^{62,63} Preserving a correct mitophagy process is necessary for limiting reactive oxygen species (ROS) production, inflammation etc. By contrast, a block of mitophagy can lead to excessive ROS production and favor apoptosis. From this point of view, a general interest in mitophagy manipulation in order to improve cancer therapy is emerging. Indeed, taking advantage of the technological advances, chemotherapeutic agents can be administered with miRNAs to provide synergistic effects on patient. Interestingly, inhibition

of autophagy/mitophagy enhanced drug sensitivity in several cases in which autophagosome formation or autophagosomes-lysosomes fusion events were inhibited.^{64,65} The block of mitochondrial clearance by BNIP3L down-regulation enhanced doxorubicin sensitivity in colorectal cancer stem cells.⁶⁶ Even if macroautophagy inhibition has been already accepted as a therapeutic strategy in cancer, few tools that specifically block selective autophagy of mitochondria are available. Therefore, microRNAs that target mitophagy through PINK1, Parkin or mitophagic receptors down-regulation, are attractive. Interestingly, miR-218 was found significantly decreased in breast cancer tissues.⁶⁷ The authors demonstrated, *in vitro*, that miR-218 overexpression induces apoptosis. miR-218 mediated down-regulation of Parkin could be thus a potential mechanism that may contribute to apoptosis in breast cancer cells. Further studies are required to investigate this point. This microRNA is also strongly down-regulated in human glioma and it has been shown to work as a tumor suppressor in glioma cells.⁶⁸⁻⁷⁰ Again, the role of mitophagy mediated by Parkin should be investigated in this context in order to understand whether mitophagy could regulate tumorigenesis in glioma cells. Interestingly, both miR-181a and Parkin siRNA sensitizes SH-SY5Y cells to apoptosis in response to mitochondrial stresses.⁴² miR-181a mediated down-regulation of Parkin, as well as other potential known targets (i.e., anti-apoptotic proteins) may thus contribute to apoptosis and underline miR-181a as a potential therapeutic strategy for neuroblastoma.

Finally microRNAs have emerged as key modulators of cellular senescence.^{71,72} Since autophagy seems to be a causative agent for senescence, it would be interesting to evaluate the role of microRNA that control mitophagy in this context. Since autophagy induction is known to favor the immunogenic cell death (ICD) and thus to help in the success of chemotherapy,⁷³ it would also be interesting to test the use of miRNA's modulators of mitophagy in order to elucidate the role of mitophagy in ICD.



6. Conclusions

Since miRNAs/AntagoMirs deliverances can be easily performed through the use of nanoparticles, their application in cancer or neurodegenerative disorders has started to become highly attractive.⁷⁴ However, because miRNA-based therapeutic is quite recent, there are some challenges and limitations in their application. One major point is the fact that the

modulation of miRNAs expression could have undesirable actions due to certain off-target effects (numerous mRNAs targets can be regulated by a single miRNA⁷⁵). Further investigation in this regard is thus required in order to ensure a safe application of this kind of biotechnologies. Taken together, by linking microRNAs and mitophagy modulation, the studies cited in this review provide novel and promising therapeutic strategies for the treatment of mitochondrial-related diseases.

Acknowledgments

This work was supported by grants: ROCHE (Roche per la ricerca 2017) and 5XMILLE Italian Ministry of Health (2017) to Flavie Strappazon. I thank M. Bennett for his proofreading.

References

1. Gallagher LE, Williamson LE, Chan EY. Advances in autophagy regulatory mechanisms. *Cells*. 2016;5:pii: E24.
2. Levine B, Packer M, Codogno P. Development of autophagy inducers in clinical medicine. *J Clin Invest*. 2015;125:14–24.
3. Stolz A, Andreas Ernst A, Dikic I. Cargo recognition and trafficking in selective autophagy. *Nat Cell Biol*. 2014;16:495–501.
4. Galluzzi L, Baehrecke EH, Ballabio A, et al. Molecular definitions of autophagy and related processes. *EMBO J*. 2017;13:1811–1836.
5. Kissova I, Salin B, Schaeffer J, Bhatia S, Manon S, Camougrand N. Selective and non-selective autophagic degradation of mitochondria in yeast. *Autophagy*. 2017;3:329–336.
6. Palikaras K, Tavernarakis N. Mitochondrial homeostasis: the interplay between mitophagy and mitochondrial biogenesis. *Exp Gerontol*. 2014;56:182–188.
7. Lemasters JJ. Selective mitochondrial autophagy, or mitophagy, as a targeted defense against oxidative stress, mitochondrial dysfunction, and aging. *Rejuvenation Res*. 2005;8:3–5.
8. Kim I, Rodriguez-Enriquez S, Lemasters JJ. Selective degradation of mitochondria by mitophagy. *Arch Biochem Biophys*. 2007;462:245–253.
9. Novak I, Kirkin V, McEwan DG, et al. Nix is a selective autophagy receptor for mitochondrial clearance. *EMBO Rep*. 2010;11:45–51.
10. Al Rawi S, Louvet-Vallee S, Djeddi A, et al. Postfertilization autophagy of sperm organelles prevents paternal mitochondrial DNA transmission. *Science*. 2010;334:1144–1147.
11. Sato M, Sato K. Degradation of paternal mitochondria by fertilization triggered autophagy in *Caenorhabditis elegans* embryos. *Science*. 2011;334:1141–1144.
12. Wang Y, Zhang Y, Chen L, et al. Kinetics and specificity of paternal mitochondrial elimination in *Caenorhabditis elegans*. *Nat Commun*. 2016;7:12569.
13. Zhou Q, Li H, Li H, et al. Mitochondrial endonuclease G mediates breakdown of paternal mitochondria upon fertilization. *Science*. 2016;353:394–399.
14. Wei Y, Chiang WC, Sumpter Jr R, Mishra P, Levine B. Prohibitin 2 is an inner-mitochondrial membrane mitophagy receptor. *Cell*. 2017;168:224–238.
15. Okatsu K, Oka T, Iguchi M, et al. PINK1 autophosphorylation upon membrane potential dissipation is essential for Parkin recruitment to damaged mitochondria. *Nat Commun*. 2012;3:1016.
16. Koyano F, Okatsu K, Kosako H, et al. Ubiquitin is phosphorylated by PINK1 to activate parkin. *Nature*. 2014;510(7503):162–166.

17. Lazarou M, Sliter DA, Kane LA, et al. The ubiquitin kinase PINK1 recruits autophagy receptors to induce mitophagy. *Nature*. 2015;524:309–314.
18. Chen M, Chen Z, Wang Y, et al. Mitophagy receptor FUNDC1 regulates mitochondrial dynamics and mitophagy. *Autophagy*. 2016;12:689–702.
19. Strappazzon F, Nazio F, Corrado M, et al. AMBRA1 is able to induce mitophagy via LC3 binding, regardless of PARKIN and p62/SQSTM1. *Cell Death Differ*. 2015;22:419–432.
20. Di Rita A, Peschiaroli A, D’Acunzo P, et al. HUWE1 E3 ligase promotes PINK1/PARKIN-independent mitophagy by regulating AMBRA1 activation via IKKalpha. *Nat Commun*. 2018;9:3755.
21. Van Humbeeck C, Cornelissen T, Hofkens H, et al. Parkin interacts with Ambra1 to induce mitophagy. *J Neurosci*. 2011;31:10249–10261.
22. Strappazzon F, Di Rita A, Peschiaroli A, et al. HUWE1 controls MCL1 stability to unleash AMBRA1-induced mitophagy. *Cell Death Differ*. 2019;21:1–14. <https://doi.org/10.1038/s41418-019-0404-8>.
23. Orvedahl A, MacPherson S, Sumpter Jr R, Talloczy Z, Zou Z, Levine B. Autophagy protects against Sindbis virus infection of the central nervous system. *Cell Host Microbe*. 2010;7:115–127.
24. Rossin F, D’Eletto M, Falasca L, et al. Transglutaminase 2 ablation leads to mitophagy impairment associated with a metabolic shift towards aerobic glycolysis. *Cell Death Differ*. 2015;22:408–418.
25. Lee MY, Sumpter Jr R, Zou Z, et al. Peroxisomal protein PEX13 functions in selective autophagy. *EMBO Rep*. 2017;18:48–60.
26. Sumpter Jr R, Sirasanagandla S, Fernandez AF, et al. Fanconi anemia proteins function in mitophagy and immunity. *Cell*. 2016;165:867–881.
27. Lee RC, Feinbaum RL, Ambros V. The *C. elegans* heterochronic gene *lin-4* encodes small RNAs with antisense complementarity to *lin-14*. *Cell*. 1993;75:843–854.
28. Wightman B, Ha I, Ruvkun G. Posttranscriptional regulation of the heterochronic gene *lin-14* by *lin-4* mediates temporal pattern formation in *C. elegans*. *Cell*. 1993;75:855–862.
29. Behm-Ansmant I, Rehwinkel J, Doerks T, Stark A, Bork P, Izaurralde E. mRNA degradation by miRNAs and GW182 requires both CCR4:NOT deadenylase and DCP1:DCP2 decapping complexes. *Genes Dev*. 2006;20:1885–1898.
30. Behm-Ansmant I, Rehwinkel J, Izaurralde E. MicroRNAs silence gene expression by repressing protein expression and/or by promoting mRNA decay. *Cold Spring Harb Symp Quant Biol*. 2006;71:523–530.
31. Vella MC, Choi E-Y, Lin S-Y, Reinert K, Slack FJ. The *C. elegans* microRNA *let-7* binds to imperfect *let-7* complementary sites from the *lin-41* 3’UTR. *Genes Dev*. 2004;18:132–137.
32. Friedman RC, Farh KK-H, Burge CB, Bartel DP. Most mammalian mRNAs are conserved targets of microRNAs. *Genome Res*. 2009;19:92–105.
33. Roccaro AM, Sacco A, Thompson B, et al. MicroRNAs 15a and 16 regulate tumor proliferation in multiple myeloma. *Blood*. 2009;113:6669–6680.
34. Chen J-F, Tao Y, Li J, et al. microRNA-1 and microRNA-206 regulate skeletal muscle satellite cell proliferation and differentiation by repressing Pax7. *J Cell Biol*. 2010;190:867–879.
35. Yamakuchi M, Ferlito M, Lowenstein CJ. miR-34a repression of SIRT1 regulates apoptosis. *Proc Natl Acad Sci U S A*. 2008;105:13421–13426.
36. Schickel R, Park S-M, Murmann AE, Peter ME. miR-200c regulates induction of apoptosis through CD95 by targeting FAP-1. *Mol Cell*. 2010;38:908–915.
37. Otsubo T, Akiyama Y, Hashimoto Y, Shimada S, Goto K, Yuasa Y. MicroRNA-126 inhibits SOX2 expression and contributes to gastric carcinogenesis. *PLoS One*. 2011;6:e16617.

38. Hu Q, Du K, Mao X, Ning S. miR-197 is downregulated in cervical carcinogenesis and suppresses cell proliferation and invasion through targeting forkhead box M1. *Oncol Lett.* 2018;15:10063–10069.
39. Lu H, Buchan RJ, Cook SA. MicroRNA-223 regulates Glut4 expression and cardiomyocyte glucose metabolism. *Cardiovasc Res.* 2010;86:410–420.
40. Barde I, Rauwel B, Marin-Florez RM, et al. A KRAB/KAP1-miRNA cascade regulates erythropoiesis through stage-specific control of mitophagy. *Science.* 2013;340:350–353.
41. Kim J, Fiesel FC, Belmonte KC, et al. miR-27a and miR-27b regulate autophagic clearance of damaged mitochondria by targeting PTEN-induced putative kinase 1. *Mol Neurodegener.* 2016;11:55.
42. Cheng M, Liu L, Lao Y, et al. MicroRNA-181a suppresses parkin-mediated mitophagy and sensitizes neuroblastoma cells to mitochondrial uncoupler-induced apoptosis. *Oncotarget.* 2016;7:42274–42287.
43. Di Rita A, Maiorino T, Bruqi K, Volpicelli F, Belenchi GC, Strappazzon F. miR-218 inhibits mitochondrial clearance by targeting PRKN E3 ubiquitin ligase. *Int J Mol Sci.* 2020;21(1):355.
44. Li W, Zhang X, Zhuang H, et al. MicroRNA-137 is a novel hypoxia-responsive microRNA that inhibits mitophagy via regulation of two mitophagy receptors FUNDC1 and NIX. *J Biol Chem.* 2014;289:10691–10701.
45. Li QQ, Zhang L, Wan HY, Liu M, Li X, Tang H. CREB1-driven expression of miR-320a promotes mitophagy by down-regulating VDAC1 expression during serum starvation in cervical cancer cells. *Oncotarget.* 2015;6:34924–34940.
46. Liu K, Yan L, Jiang X, et al. Inhibition of microRNA-124 protects against spinal cord ischemia-reperfusion injury partially through a mitophagy-dependent pathway. *J Thorac Cardiovasc Surg.* 2017;154:1498–1508.
47. Yang F, Li T, Dong Z, Mi R. MicroRNA-410 is involved in mitophagy after cardiac ischemia/reperfusion injury by targeting high-mobility group box 1 protein. *J Cell Biochem.* 2018;119:2427–2439.
48. Chen F, Feng L, Zheng YL, et al. 2', 4, 4'-tetrabromodiphenyl ether (BDE-47) induces mitochondrial dysfunction and related liver injury via eliciting miR-34a-5p-mediated mitophagy impairment. *Environ Pollut.* 2020;258:113693.
49. Zhang Z, Zhang T, Feng R, Huang H, Xia T, Sun C. circARF3 alleviates mitophagy-mediated inflammation by targeting miR-103/TRAF3 in mouse adipose tissue. *Mol Ther Nucleic Acids.* 2019;14:192–203.
50. Liu H, Huang H, Li R, et al. Mitophagy protects SH-SY5Y neuroblastoma cells against the TNF α -induced inflammatory injury: involvement of microRNA-145 and Bnip3. *Biomed Pharmacother.* 2019;109:957–968.
51. Liu D, Tan Q, Zhu J, et al. MicroRNA-33/33* inhibit the activation of MAVS through AMPK in antiviral innate immunity. *Cell Mol Immunol.* 2019;4:329–336.
52. Purohit PK, Edwards R, Tokatlidis K, Saini N. MiR-195 regulates mitochondrial function by targeting mitofusin-2 in breast cancer cells. *RNA Biol.* 2019;16:918–929.
53. Tsujimoto T, Mori T, Houri K, et al. miR-155 inhibits mitophagy through suppression of BAG5, a partner protein of PINK1. *Biochem Biophys Res Commun.* 2020;523:707–712.
54. Zhang S, Liu C, Zhang X. Mitochondrial damage mediated by miR-1 overexpression in cancer stem cells. *Mol Ther Nucleic Acids.* 2019;18:938–953.
55. Wu Q, Xu T, Liu Y, et al. miR-1224-5p mediates mitochondrial damage to affect silica-induced pulmonary fibrosis by targeting BECN1. *Int J Mol Sci.* 2017;18(11):2357.
56. Guo J, Yang Z, Yang X, Li T, Liu M, Tang H. miR-346 functions as a pro-survival factor under ER stress by activating mitophagy. *Cancer Lett.* 2018;413:69–81.
57. Markaki M, Palikaras K, Tavernarakis N. Novel insights into the anti-aging role of mitophagy. *Int Rev Cell Mol Biol.* 2018;340:169–208.
58. Enciu AM, Popescu BO, Gheorghisan-Galateanu A. MicroRNAs in brain development and degeneration. *Mol Biol Rep.* 2012;39:2243–2252.

59. Tekirdag KA, Korkmaz G, Ozturk DG, Agami R, Gozuacik D. MIR181A regulates starvation- and rapamycin-induced autophagy through targeting of ATG5. *Autophagy*. 2013;9:374–385.
60. Indrieri A, Carrella S, Romano A, et al. miR-181a/b downregulation exerts a protective action on mitochondrial disease models. *EMBO Mol Med*. 2019;11(5):e8734.
61. Amin ND, Bai G, Klug JR, et al. Loss of motoneuron-specific microRNA-218 causes systemic neuromuscular failure. *Science*. 2015;350:1525–1529.
62. Anderson CM, Macleod KF. Autophagy and cancer cell metabolism. *Int Rev Cell Mol Biol*. 2019;347:145–190.
63. Strappazzon F, Cecconi F. AMBRA1-induced mitophagy: a new mechanism to cope with cancer? *Mol Cell Oncol*. 2015;2(2):e975647.
64. Zhou J, Li G, Zheng Y, et al. A novel autophagy/mitophagy inhibitor liensinine sensitizes breast cancer cells to chemotherapy through DNMT1-mediated mitochondrial fission. *Autophagy*. 2015;11:1259–1279.
65. Mauro-Lizcano M, Esteban-Martínez L, Seco E, et al. New method to assess mitophagy flux by flow cytometry. *Autophagy*. 2015;11:833–843.
66. Yan C, Luo L, Guo CY, et al. Doxorubicin-induced mitophagy contributes to drug resistance in cancer stem cells from HCT8 human colorectal cancer cells. *Cancer Lett*. 2017;388:34–42.
67. Liu B, Tian Y, Li F, et al. Tumor-suppressing roles of miR-214 and miR-218 in breast cancer. *Oncol Rep*. 2016;35:3178–3184.
68. Song L, Huang Q, Chen K, et al. miR-218 inhibits the invasive ability of glioma cells by direct downregulation of IKK- β . *Biochem Biophys Res Commun*. 2010;402:135–140.
69. Setty M, Helmy K, Khan AA, et al. Inferring transcriptional and microRNA-mediated regulatory programs in glioblastoma. *Mol Syst Biol*. 2012;8:605.
70. Skalsky RL, Cullen BR. Reduced expression of brain-enriched microRNAs in glioblastomas permits targeted regulation of a cell death gene. *PLoS One*. 2011;6:e24248.
71. Neault M, Couteau F, Bonneau É, De Guire V, Mallette FA. Molecular regulation of cellular senescence by MicroRNAs: implications in cancer and age-related diseases. *Int Rev Cell Mol Biol*. 2017;334:27–98.
72. Munk R, Panda AC, Grammatikakis I, Gorospe M, Abdelmohsen K. Senescence-associated MicroRNAs. *Int Rev Cell Mol Biol*. 2017;334:177–205.
73. Castoldi F, Vacchelli E, Zitvogel L, Maiuri MC, Pietrocola F, Kroemer G. Systemic autophagy in the therapeutic response to anthracycline-based chemotherapy. *Oncotargets Ther*. 2018;8(1):e1498285.
74. Lee SWL, Paoletti C, Campisi M, et al. MicroRNA delivery through nanoparticles. *J Control Release*. 2019;313:80–95.
75. Chakraborty C, Wen Z-H, Agoramorthy G, Lin C-S. Therapeutic microRNA delivery strategies with special emphasis on cancer therapy and tumorigenesis: current trends and future challenges. *Curr Drug Metab*. 2016;17:469–477.



Characterization of a natural variant of human NDP52 and its functional consequences on mitophagy

Anthea Di Rita^{1,2} · Daniela F. Angelini³ · Teresa Maiorino⁴ · Valerio Caputo^{5,6} · Raffaella Cascella^{5,6} · Mukesh Kumar⁷ · Matteo Tiberti⁷ · Matteo Lambrughi⁷ · Nicole Wesch⁸ · Frank Löhr⁸ · Volker Dötsch^{8,9} · Marianna Carinci¹⁰ · Pasquale D'Acunzo^{11,12} · Valerio Chiurchiù^{3,13} · Elena Papaleo^{7,14} · Vladimir V. Rogov^{8,9,15} · Emiliano Giardina^{5,6} · Luca Battistini³ · Flavie Strappazon³

Received: 10 August 2020 / Revised: 17 February 2021 / Accepted: 25 February 2021 / Published online: 15 March 2021
© The Author(s), under exclusive licence to ADMC Associazione Differenziamento e Morte Cellulare 2021

Abstract

The role of mitophagy, a process that allows the removal of damaged mitochondria from cells, remains unknown in multiple sclerosis (MS), a disease that is found associated with dysfunctional mitochondria. Here we have qualitatively and quantitatively studied the main players in PINK1-mediated mitophagy in peripheral blood mononuclear cells (PBMCs) of patients with relapsing–remitting MS. We found the variant c.491G>A (rs550510, p.G140E) of NDP52, one of the major mitophagy receptor genes, associated with a MS cohort. Through the characterization of this variant, we discovered that the residue 140 of human NDP52 is a crucial modulator of NDP52/LC3C binding, promoting the formation of autophagosomes in order to drive efficient mitophagy. In addition, we found that in the PBMC population, NDP52 is mainly expressed in B cells and by ensuring efficient mitophagy, it is able to limit the production of the proinflammatory cytokine TNF- α following cell stimulation. In sum, our results contribute to a better understanding of the role of NDP52 in mitophagy and underline, for the first time, a possible role of NDP52 in MS.

Edited by H. Zhang

Supplementary information The online version contains supplementary material available at <https://doi.org/10.1038/s41418-021-00766-3>.

✉ Flavie Strappazon
f.strappazon@hsantalucia.it

- 1 Department of Life Sciences, University of Siena, Siena, Italy
- 2 Fondazione Toscana Life Sciences, Siena, Italy
- 3 IRCCS Fondazione Santa Lucia, Rome, Italy
- 4 Department of Molecular Medicine and Medical Biotechnology, University of Naples “Federico II”, Naples, Italy
- 5 Genomic Medicine Laboratory UILDM, IRCCS Santa Lucia Foundation, Rome, Italy
- 6 Department of Biomedicine and Prevention, Tor Vergata University, Rome, Italy
- 7 Computational Biology Laboratory, Danish Cancer Society Research Center, Copenhagen, Denmark
- 8 Institute of Biophysical Chemistry and Center for Biomolecular Magnetic Resonance, Goethe University Frankfurt, Frankfurt am Main, Germany

Introduction

Multiple sclerosis (MS) is an autoimmune disease with a chronic inflammatory response in the central nervous system that leads to demyelination and axonal damage

- 9 Structural Genomics Consortium, Buchmann Institute for Life Sciences, Goethe University Frankfurt, Frankfurt, Germany
- 10 Department of Medical Sciences, University of Ferrara, Ferrara, Italy
- 11 Center for Dementia Research, Nathan S. Kline Institute for Psychiatric Research, Orangeburg, NY, USA
- 12 Department of Psychiatry, New York University School of Medicine, New York, NY, USA
- 13 Institute of Translational Pharmacology, National Council Research, Rome, Italy
- 14 Translational Disease Systems Biology, Faculty of Health and Medical Sciences, Novo Nordisk Foundation Center for Protein Research University of Copenhagen, Copenhagen, Denmark
- 15 Institute of Pharmaceutical Chemistry, Goethe University Frankfurt, Frankfurt, Germany

resulting in motor, sensory, and cognitive loss. The causes of the inflammatory process are not yet known but a well-accepted theory indicates that several factors are involved, including genetic predisposition to develop the disease and environmental agents able to stimulate the immune system and trigger the autoimmune reaction. Among these hypotheses, there is the involvement of bacterial or viral infections [1, 2]. Immune responses are triggered and driven, upon microbial infection, by the recognition of pathogen-associated molecular patterns (PAMPs), by means of a broad spectrum of pattern-recognition receptors (PRRs) expressed on several innate and adaptive immune cells [3]. Toll-like receptors (TLRs) are generally perceived as the main PRRs and serve as immune sensors for the detection of specific PAMPs related to different pathogens [4].

Another characteristic of MS is the presence of mitochondrial dysfunctions associated with the pathology [5–7]. A mechanism called mitophagy selectively eliminates altered mitochondria, in order to regulate the functional quality of mitochondria and to reduce oxidative stress [8]. This removal mainly happens by a selective form of autophagy after activation of the kinase PINK1 and the E3 ubiquitin ligase PARKIN. Following the loss of mitochondrial membrane potential, PINK1 is stabilized on the outer mitochondrial membrane where it phosphorylates ubiquitin at Ser65 and recruits two crucial redundant mitophagy receptors OPTINEURIN (OPTN) and CALCOCO2/Nuclear dot protein 52 (NDP52) [9, 10]. These receptors bind ubiquitinated mitochondria through their ubiquitin-binding domain (UBD) and thanks to a LC3-interacting region (LIR) motif, they bind Atg8 (autophagy-related protein 8)/LC3 (*microtubule-associated proteins 1A/1B light chain 3B*) proteins onto autophagosome membranes in order to deliver mitochondria to the autophagosomes [11]. More recently, the LIR motif has been shown to serve as amplifiers of mitophagy by recruiting additional OPTN or NDP52 to growing phagophore membranes [12].

It has been demonstrated that ATG5, a protein involved in autophagy, and PARKIN increase in cerebrospinal fluid and serum of MS patients, highlighting these autophagy/mitophagy elements as new molecular markers of the disease's active phases [13, 14]. However, the role of PINK1-mediated mitophagy pathway in MS remains obscure.

In the present work, we, quantitatively and qualitatively analyzed three indispensable proteins for the PINK1-mediated mitophagy pathway, i.e., PINK1, OPTN, and NDP52, in peripheral blood mononuclear cells (PBMCs) of relapsing–remitting (RR)-MS patients. We identified a possible protective variant of *NDP52* associated with MS pathology, by promoting a more efficient clearance of damaged mitochondria with respect to the wild-type (WT) form. Finally, we discovered that, among PBMCs, NDP52 is

mainly expressed in the B cell subpopulation ensuring effective mitophagy following B cell stimulation and reducing the release of the proinflammatory cytokine TNF- α .

Results

PINK1-mediated mitophagy genes are upregulated in PBMCs of RR-MS patients and damaged mitochondria are accumulated

We evaluated mRNA expression of *PINK1*, *OPTN*, and *NDP52*, the three indispensable PINK1-mediated mitophagy genes in PBMCs isolated from RR-MS patients ($n = 35$) and healthy donors (HD, $n = 24$). Our data indicate that *PINK1* and *NDP52* genes are upregulated in RR-MS patients with respect to controls (Fig. 1a, b). Of note, no particular increase in mRNA *OPTN* was observed (Fig. 1c). We found that both PINK1 and NDP52 protein levels were also increased in RR-MS subjects compared to HD (Fig. 1d, e). Again, *OPTN* protein levels were unchanged between HD and MS subjects (Fig. 1f).

These findings provide evidence that the production of two main mitophagy elements of the PINK1-mediated mitophagy is induced in PBMCs of MS patients, suggesting that mitophagy is most likely stimulated in PBMCs of RR-MS patients.

Since mitophagy induction is typically characterized by a decreased mitochondrial mass, we thought to examine mitochondrial content in PBMCs by checking the levels of two inner mitochondrial membrane markers, the cytochrome c oxidase subunit II (COXII) and cytochrome c oxidase subunit IV (COXIV). We observed an increase in both COXII and COXIV protein levels in MS patients compared to HD (Fig. 1g), suggesting a putative block in mitochondrial clearance. Consistent with this increase, we observed an increase in the mitochondrial DNA (mtDNA)/nuclear DNA ratio (mtDNA:nucDNA ratio) in RR-MS patients compared to HD (Fig. 1h).

Our results show that mitochondria of RR-MS patients display a reduced membrane potential ($\Delta\Psi_m$) compared to HD (Fig. 1i), indicating that the accumulated mitochondria in RR-MS patients were corresponding to damaged mitochondria. We next thought to assess whether such mitochondrial dysfunction was associated with oxidative stress by evaluating the content of putative carbonyl groups introduced into proteins. As shown in Fig. 1j, protein extracts from PBMCs of RR-MS patients show an increase in protein carbonylation compared to HD.

Altogether, these data indicate that, even if PINK1 and NDP52 genes are induced in RR-MS patients, damaged mitochondria are found accumulated, participating most likely in oxidative stress production and in inflammation.

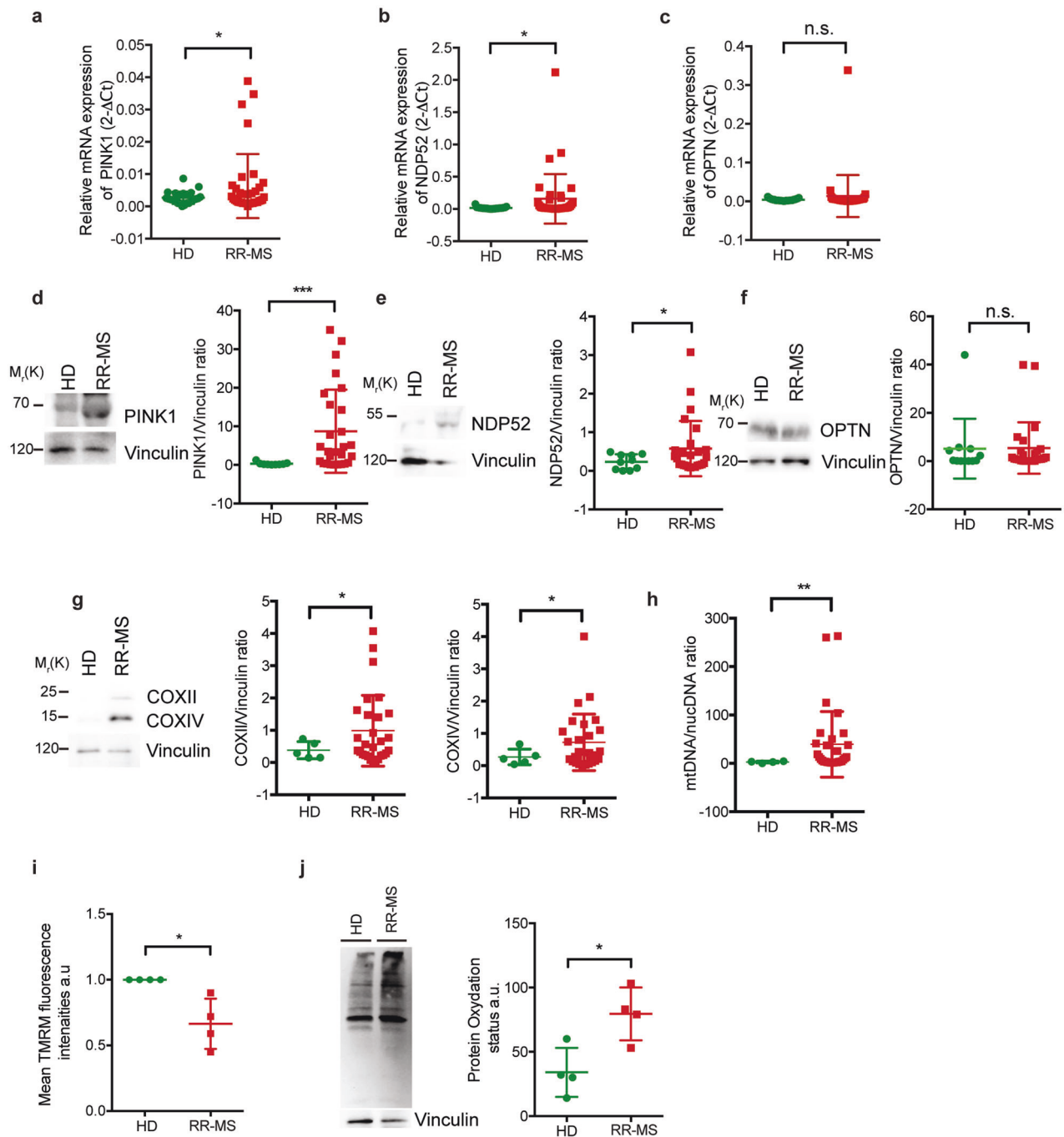


Fig. 1 PINK1-mediated mitophagy genes are increased in PBMCs of multiple sclerosis patients. **a–c** PINK1, NDP52, and OPTN mRNA levels, respectively, were analyzed in PBMCs of healthy donors (HD = 24) or multiple sclerosis patients (RR-MS = 35) by qPCR analysis. B2M was used as housekeeping gene. **d** PBMCs from HD or RR-MS people were lysated and immunoblotted for PINK1 and Vinculin antibodies (HD = 10; RR-MS = 28). The graph reports the PINK1/Vinculin ratio. **e** PBMCs from HD or RR-MS people were lysated and immunoblotted for NDP52 and Vinculin antibodies (HD = 10; RR-MS = 28). The graph reports the NDP52/Vinculin ratio. **f** Protein lysates from PBMCs were immunoblotted for OPTN (HD = 10; RR-MS = 26). Vinculin was used as loading control. The graphs show and OPTN/Vinculin ratio. **g** PBMCs from HD (*n* = 5) or RR-MS

(*n* = 28) subjects were lysated and immunoblotted for the indicated antibodies. **h** The graph analyzed the mtDNA/nucDNA ratio in PBMCs of HD (*n* = 4) or RR-MS patients (*n* = 28) by qPCR analysis. **i** Four HD or 4 RR-MS PBMCs were stained with 10 nM of TMRM and analyzed by flow cytometry to measure the fluorescence intensity of the dye. The median FL-2A of HD patients were reported to 1 and compared to RR-MS patients. **j** Representative image of protein carbonylation analysis from HD or RR-MS PBMCs. The graph showing protein oxidation status (a.u.). All the quantifications resulting as the mean of at least three independent experiments (±SD). Statistical analysis was performed using Student *t*-test with Welch’s correction (**P* < 0.05; ***P* < 0.01; ****P* < 0.001, n.s.: not significant).

Table 1 *NDP52* c.491G>A (rs550510, p.G140E) associates with a decreased susceptibility to MS.

Gene	SNP	Allele	Allele frequencies (cases)	Allele frequencies (controls)	<i>P</i>	OR (95% CI)
<i>NDP52</i>	rs550510 G/A	G	0.870	0.814	0.007	G: 1.53 (1.12–2.08)
		A	0.130	0.186		A: 0.65 (0.48–0.89)
		Genotype	Genotype frequencies (cases)	Genotype frequencies (controls)	<i>P</i>	OR (95% CI)
		GG	0.750	0.667	0.022	–
		GA	0.240	0.293		GA: 0.73 (0.52–1.04)
		AA	0.010	0.040		AA: 0.22 (0.05–0.92)

Results obtained by the biostatistical analysis performed on the genotyping results of 203 RR-MS patients and 1000 healthy control subjects. *SNP* single nucleotide polymorphism, *OR* odds ratio, *CI* confidence interval.

***NDP52* G140E variant was associated and genetically protective in MS**

We next qualitatively analyzed the main mitophagy receptors involved in PINK1-mediated mitophagy in RR-MS patients. To this end, we extracted cDNA from PBMCs of RR-MS patients and amplified the two main functional fragments of both *NDP52* and *OPTN*: the UBD and the LIR domains. We sequenced the extracted cDNA of 35 RR-MS patients in order to search for putative point mutations or specific polymorphisms in these functional fragments. We did not find any changes in the *OPTN* gene (data not shown). Instead, we observed the presence of c.491G>A (rs550510, p.G140E) variant in the LIR region of *NDP52*. We thus performed a genotyping analysis on a cohort of 203 RR-MS patients and 1000 control subjects. The frequency distribution of the alleles showed a higher frequency of the variant allele (A) in the control group with respect to cases. Similarly, the frequency distribution of the genotypes in our cohort showed a higher frequency of heterozygous (GA) and homozygous (AA) genotypes in the control group. The biostatistical analysis revealed a statistically significant association of c.491G>A variant with the disease ($P=0.007$), with the A allele being protective (odds ratio, OR, A = 0.65, 95% CI: 0.48–0.89) for MS (Table 1). The allele association has been further confirmed by the genotype association, as shown by the *P* and OR of GA and AA genotypes, respectively (Table 1). Taken together, these results suggest that the *NDP52* variant may confer protection to MS.

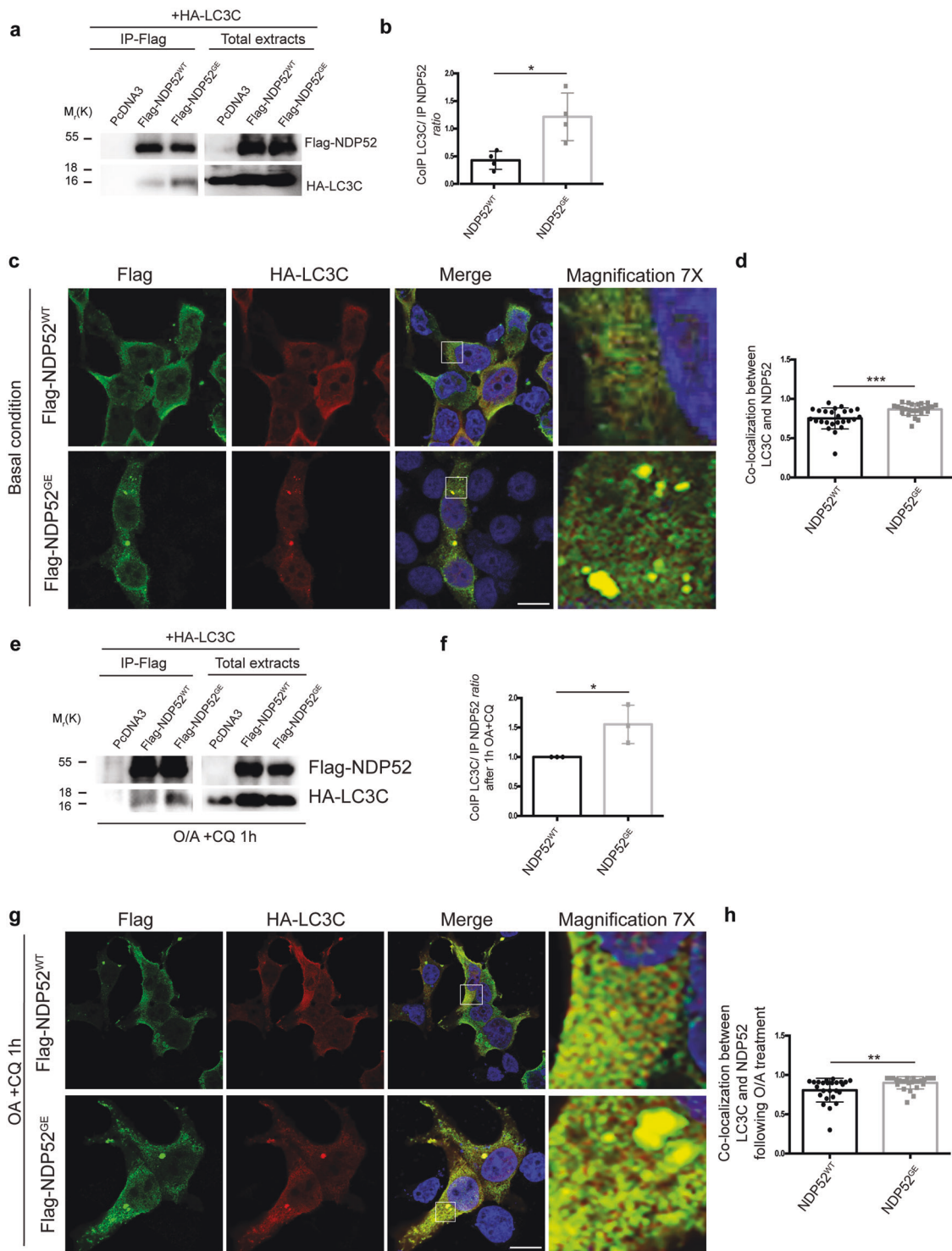
***NDP52* G140E substitution increases the binding with LC3C**

NDP52 is known to negatively regulate TLR-triggered NF- κ B activation and to be degraded in the course of TLR activation [15]. Because enhanced immune response may benefit MS patients by eliminating microbes, we first anticipated that *NDP52* G140E variant might be protective in MS by being more stable than the WT form of the protein after TLR3 stimulation and therefore by favoring activation

of NF- κ B. In order to verify this aspect in cells, we generated the *NDP52* G140E mutant (hereafter called *NDP52*^{GE}). We evaluated the stability of *NDP52*^{GE} under Polyinosinic: polycytidylic acid treatment (Poly (I:C))-triggered TLR-activating conditions and whether *NDP52*^{GE} was capable of dampening proinflammatory signaling. To this end, we transfected HeLa cells (that are known to express TLR3) with vectors encoding *NDP52*^{WT} or *NDP52*^{GE} and we treated cells with Poly (I:C) in order to mimic viral infection. TLR activation resulted in similar degradation of both *NDP52*^{WT} and *NDP52*^{GE} variants (Supplementary Fig. 1a). Moreover, by quantifying the ratio of nuclear/cytoplasmic presence of p65/NF- κ B in *NDP52*-expressing cells, we did not observe differences of NF- κ B activation between *NDP52*^{WT} and *NDP52*^{GE} expressing cells (Supplementary Fig. 1b). These data indicate that the substitution G140E of *NDP52* did not affect its function in regulating TLR signaling.

At this point we hypothesized that *NDP52*^{GE} may mitigate MS disease by clearing more efficiently damaged mitochondria compared to the WT form of the protein. Since the *NDP52*^{GE} variant is subjected to an amino acid modification near its cLIR motif, we postulated that *NDP52*^{GE} may favor the binding between LC3C, its preferential LC3 binding partner [16]. By performing co-immunoprecipitation experiments, we analyzed *NDP52*–LC3C interaction in basal conditions. We co-transfected HEK293 cells with a vector encoding HA-LC3C and a vector encoding FLAG-*NDP52*^{WT} or FLAG-*NDP52*^{GE}. We observed that G substitution in E at residue 140 enhanced the ability of *NDP52* to interact with LC3C (Fig. 2a, b). We reinforced these data by performing a confocal microscopy analysis in which we analyzed the colocalization between *NDP52* variants and LC3C. As shown on Fig. 2c, d, the colocalization between *NDP52*^{GE} and LC3C is higher with respect to the one between *NDP52*^{WT} and LC3C.

To verify whether the highest ability of *NDP52*^{GE} to bind LC3C occurs also following mitophagy induction, we checked for this binding following Oligomycin/Antimycin-A treatment (O/A), two agents commonly used to induce



mitochondrial damage. We did not observe an increase of binding between NDP52 and LC3C following O/A (Supplementary Fig. 2a). We thus hypothesized that the stimulus of mitophagy induction plus the variant NDP52^{GE} was too strong, accelerating the autophagy/mitophagy flux. We thus blocked the autophagy flux by adding Chloroquine (CQ) to O/A treatment and we found a stronger binding between

NDP52^{GE} and LC3C under mitochondrial stress compared with the NDP52^{WT} condition (Fig. 2e, f). We confirmed these data by performing confocal microscopy analysis (Fig. 2g, h and Supplementary Fig. 2b).

Altogether, these results indicate that the amino acid on position 140 of NDP52 influences its interaction with LC3C both in basal condition and following mitophagy induction.

◀ Fig. 2 The NDP52 G140E variant increases NDP52-LC3C binding. **a** Representative image of co-immunoprecipitation experiment in which HEK293 cells were co-transfected with Flag-NDP52^{WT} or Flag-NDP52^{GE} vectors in combination with HA-LC3C. **b** The graph represents the ratio between LC3C and NDP52 ($n = 4$). **c** HEK293 cells co-transfected as indicated in (a) were subjected to confocal immunofluorescence in order to evaluate LC3C-NDP52 colocalization. Scale bar 8 μm . **d** The graph indicates the colocalization value between LC3C and wild-type or mutant NDP52. **e** HEK293 cells co-transfected with pcDNA3 (empty vector) or Flag-NDP52^{WT} or Flag-NDP52^{GE} vectors in combination with HA-LC3C were treated with O/A (10 μM /4 μM) and CQ (20 μM) for the indicated times and subjected to co-immunoprecipitation analysis. **f** The graph represents the ratio between LC3C and NDP52 in O/A + CQ condition ($n = 3$). **g** HEK293 cells co-transfected as indicated in (a) were treated with O/A in order to induce mitophagy. Confocal immunofluorescence analysis evaluates LC3C-NDP52 colocalization. Scale bar 8 μm . **h** The graph indicates the colocalization (Pearson coefficient) between LC3C and wild-type or mutant NDP52, upon mitophagy induction. All the quantifications resulting as the mean of at least three independent experiments ($\pm\text{SD}$). Statistical analysis was performed using Student t -test (* $P < 0.05$; ** $P < 0.01$).

NDP52 G140E substitution induces a conformational changes around LIR motif, enhancing the binding between NDP52 and LC3C

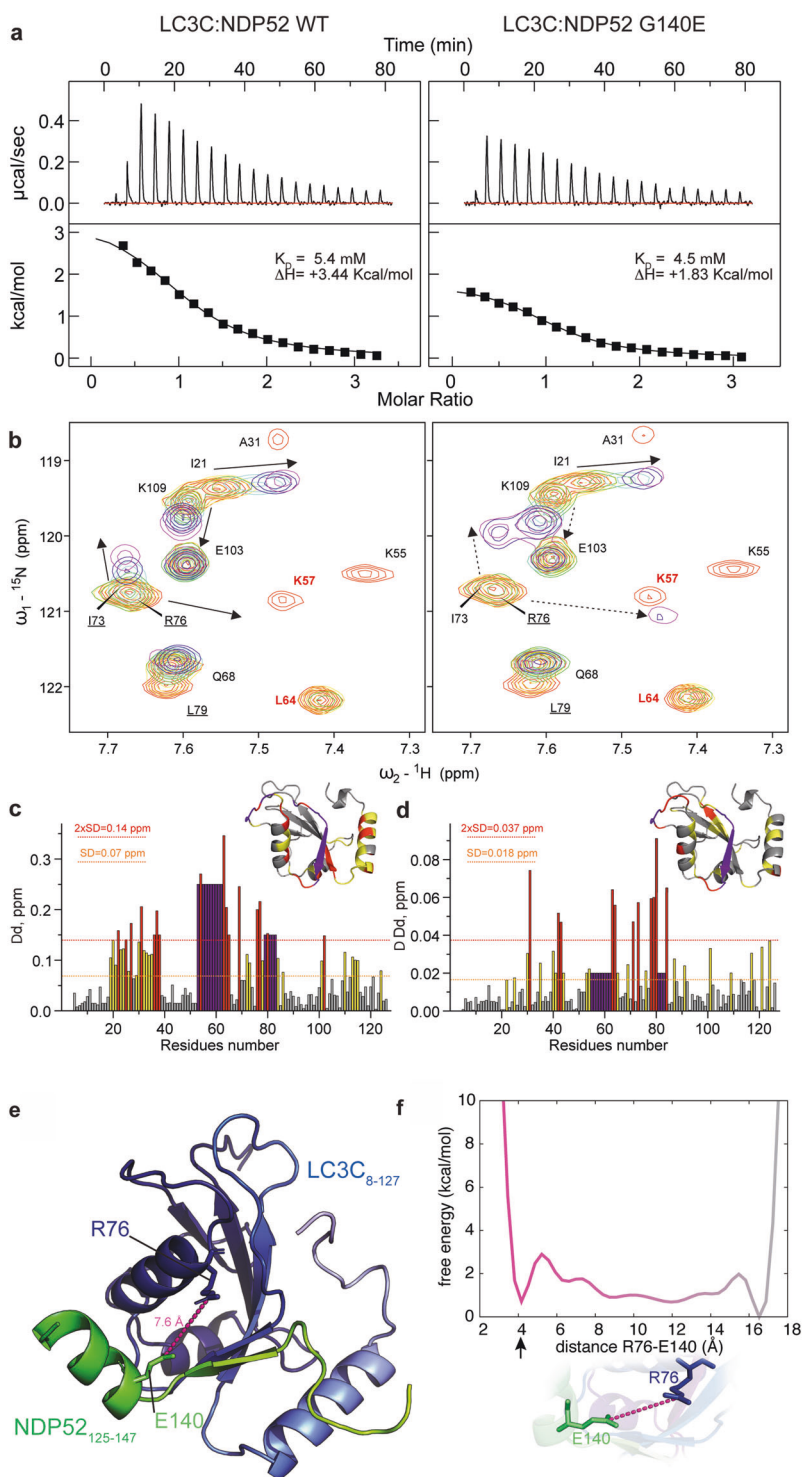
In order to characterize the interaction between NDP52 and LC3C protein, we performed isothermal titration calorimetry (ITC) experiments in which synthetic peptides spanning the short NDP52 cLIR motif were titrated into LC3C protein. We observed a very small increase in affinity for the mutated NDP52 peptide (K_D values are 5.4 μM for NDP52_{128–155}, and 4.5 μM for NDP52^{GE}_{128–155}) and decrease of unfavorable (positive) binding enthalpy (Fig. 3a). The same tendency was observed in LC3B-based ITC experiments (Supplementary Fig. 3a–d and Supplementary Table 2). The decrease in unfavorable enthalpy indicates that the “enthalpically” favorable interactions could play a role in the G140E-mediated NDP52 affinity increase to LC3C and LC3B proteins. ITC results are in agreement with the affinities reported previously and indicated preference of LC3C for interaction with NDP52 cLIR [16].

In order to validate the ITC data and understand the mechanism of the affinity increase, we performed nuclear magnetic resonance (NMR) titration experiments, in which we titrated non-labeled NDP52_{128–224} and NDP52^{GE}_{128–224} into the ¹⁵N-labeled LC3C sample (Fig. 3b–d). Both titration experiments showed that the chemical shift perturbations (CSPs) undergo intermediate to slow exchange modes, confirming low μM K_D values for both NDP52 constructs. The resonances in the most relevant LC3C regions (β -strand 2 and in close proximity to it, HP1 and HP2) disappeared upon interaction with NDP52 and did not appear again, indicating specific dynamics of the NDP52 constructs with equilibria between unfolded and α -helical conformations of

the fragments observed by 1D NMR spectra (Supplementary Fig. 3e). It was possible to map CSPs on LC3C sequence and 3D structure (Fig. 3c). We observed few differences between the CSPs. The first difference is the CSP altitude—addition of NDP52^{GE}_{128–224} induced either larger CSP (like R76 HN resonance, Fig. 3b) or different direction CSP (like V89 HN resonance, Supplementary Fig. 3f) for a set of LC3C residues. These differences are overviewed in Fig. 3d where the different CSP values ($\Delta\Delta\delta$) were mapped on the LC3C sequence and surface. The second difference is the dynamic behavior of the CSPs—a number of LC3C resonances showed more slow exchange mode upon titration with NDP52^{GE}_{128–224} construct when with NDP52_{128–224} (I73 HN resonance in Fig. 3b). The larger CSP values and “slower” exchange mode indicate clear preference of LC3C protein to the NDP52^{GE} variant, while different direction CSPs indicate changes in the resonance’s microenvironment upon addition of mutated NDP52 fragment.

Since the data suggest that the NDP52 G140E mutation affects intermolecular electrostatic interactions and conformational equilibria of close proximity to G/E140, we used molecular modeling and simulations to address this hypothesis. It is known that the C-terminal LIR extensions can modulate its binding affinity to human ATG8 proteins [17–21]. For example, FYCO1 LIR C-terminal extension was reported to form an α -helix and a key network of intermolecular electrostatic interactions was mediated by E1246, forming intermolecular hydrogen bonds with LC3B residue R70 [22]. G140 in NDP52 corresponds to E1246 in FYCO1 with respect to the position in sequence of the LIR motifs in these two proteins. We thus speculate that increased affinity of the NDP52^{GE} variant to LC3C could be due to a similar scenario, including the formation of a salt bridge between E140 in NDP52^{GE} and LC3C R76. G140 is located at the N-terminus of the predicted α -helical area (coiled-coil (cc) region) and the G140E substitution could also stabilize the helical structure.

We thus built a model for the LC3C_{8–127}-NDP52^{GE}_{125–147} complex and carried out unbiased molecular dynamics (MD) simulations (see GitHub repository) (Fig. 3e). We used MD simulations to see if conformational changes that favor the formation of a salt bridge or other electrostatic interactions in proximity of R76 are likely to occur. During unbiased hundreds ns MD simulations, we observed a low tendency for intermolecular salt bridge or hydrogen bond formation for E140 with LC3C residues. For example, we only found a salt bridge interaction between the charged groups of R76 and E140, in less than 1% of the MD structures (see GitHub repository). This is likely due to inherent limitations in the sampling of the conformational space that classical MD can provide [23], as our starting structures did not feature the salt bridge in question. We thus applied another approach based on the metadynamics



algorithm in the well-tempered ensemble flavor to boost the sampling of the conformational space [24, 25]. We observed two main free energy minima separated by other less populated states. The first one is in the range of 3–5 Å, which is compatible with the salt bridge formation between E140 and R76 and the second one is in the range of

16–18 Å, which is similar to the distance between the two groups at the beginning of the simulation. The latter is likely to be overestimated due to the starting conformation of our model (Fig. 3f).

Taken together, these results give a proof of concept that the point mutation in G140 in “E” induces a specific

Fig. 3 The NDP52 variant G140E shows propensity for an intermolecular salt bridge with R76 of LC3C. NDP52 G140E mutation enhances interaction between NDP52 and LC3C. **a** ITC analysis of the interaction between LC3C and peptides contained NDP52 LIR motif. Titrations of the NDP52_{128–155} peptide (NDP52 WT, left panel) and NDP52^{GE}_{128–155} peptide (NDP52 G140E, right panel) to LC3C protein showed slight preference of LC3C to the NDP52^{GE}_{128–155} (K_D values and enthalpies for each interaction are indicated at the plots). The upper graph shows the raw measurement; the lower diagram represents the intergraded heat per injection (squares) and best fit function (solid line). All thermodynamic parameters are summarized in Supplementary Table 2. **b** NMR titration of ¹⁵N-labeled LC3C with NDP52_{128–224} and NDP52^{GE}_{128–224} peptides. The representative area (the “fingerprint” area, containing LC3C K55 and L64 HN resonances) of the LC3C ¹⁵N-¹H-TROSY-HSQC spectra upon titration with NDP52_{128–224} (left panel) and NDP52^{GE}_{128–224} (right panel). Increasing concentrations of peptide are indicated with the rainbow color code from red (free LC3C) to violet (four times peptides excess). Identified CSP are highlighted by solid line arrows, the CSP exhibited difference between NDP52_{128–224} and NDP52^{GE}_{128–224} peptides are showed by dashed arrows at the right plot. **c** CSP values ($\Delta\delta$) for LC3C HN resonances at the last titration stages with NDP52_{128–224} are plotted against residues numbers. The bars for $\Delta\delta$ below standard deviation value (σ , calculated for all identified CSPs) are colored gray; for $\sigma < \Delta\delta < 2\sigma$ —yellow; and for $\Delta\delta$ above 2σ —red. Violet bars represent the residues that resonances disappear upon addition of NDP52_{128–224} and do not appear again (strong interaction with intermediate to slow exchange mode). Their $\Delta\delta$ values are set to the $\Delta\delta$ values of neighbor residues. The CSP values mapped on the LC3C protein structure (ribbon diagrams, PDB ID 1GNU) are shown in the upper right corner with the same color code. **d** Differences of CSP values ($\Delta\Delta\delta$) induced upon titration of NDP52_{128–224} and NDP52^{GE}_{128–224} into ¹⁵N-labeled LC3C are mapped on the LC3C sequence and structure. The color code is the same as at **c**. **e** The cartoon representation shows one of the selected models of LC3C_{13–126}-NDP52_{125–147} G140E as a reference with a gradient of colors from N- to C-terminal (light blue to dark blue for LC3C_{13–126} and yellow to green for NDP52_{125–147}). The stick representation highlights the residue E140 of NDP52 and R76 of LC3C forming possible electrostatic interaction. The dotted line (hot pink) indicates the distance between the atoms C δ of E140 and C ζ of R76. **f** The plot shows the one-dimensional free energy surface of the distance between E140 of NDP52 and R76 of LC3C as calculated by WTE-metaD simulation. The profile indicates two main minima, separated by less populated states. We highlighted the first minima (hot pink) in the range of distance (3–5 Å) compatible with the formation of a salt bridge for sake of clarity. The bottom panel highlights the side chain of E140 (green) and R76 (blue) and the distance between their C δ and C ζ atoms (hot pink dotted line) that we used as a collective variable in the well-tempered metadynamics simulation.

conformation of the region near the NDP52-LIR domain, which favor its interaction with LC3C (and most likely with all mATG8 proteins).

NDP52^{GE} promotes a more efficient initiation of mitophagy compared to the wild-type form of NDP52

Several studies have demonstrated the importance of the LIR motif for selective autophagy [26, 27]. More recently, the LIR motif has been shown to mediate the translocation of autophagy receptors to mitochondria independently of

the ubiquitin binding [12]. Since NDP52 plays a key role during autophagosome initiation by promoting the recruitment of the ULK1 complex to mitochondria, thanks to its LC3 binding [28], we hypothesized that NDP52^{GE}, by binding more efficiently LC3C, could be localized at the mitochondrial surface at higher levels when compared to its WT isoform. We thus checked, by performing confocal microscopy analysis, NDP52 localization on mitochondria in HEK293. Cells were transfected with vectors encoding NDP52^{WT} or NDP52^{GE} and mitochondria were stained with TOM20 antibody. We found a higher localization of NDP52^{GE} to mitochondria respect to its WT form in basal condition (Fig. 4a–c). Moreover, we noticed that the mitochondrial network was reduced in NDP52^{GE} positive cells compared to the NDP52^{WT} positive cells, suggesting a basal mitophagy induction in NDP52^{GE} positive cells.

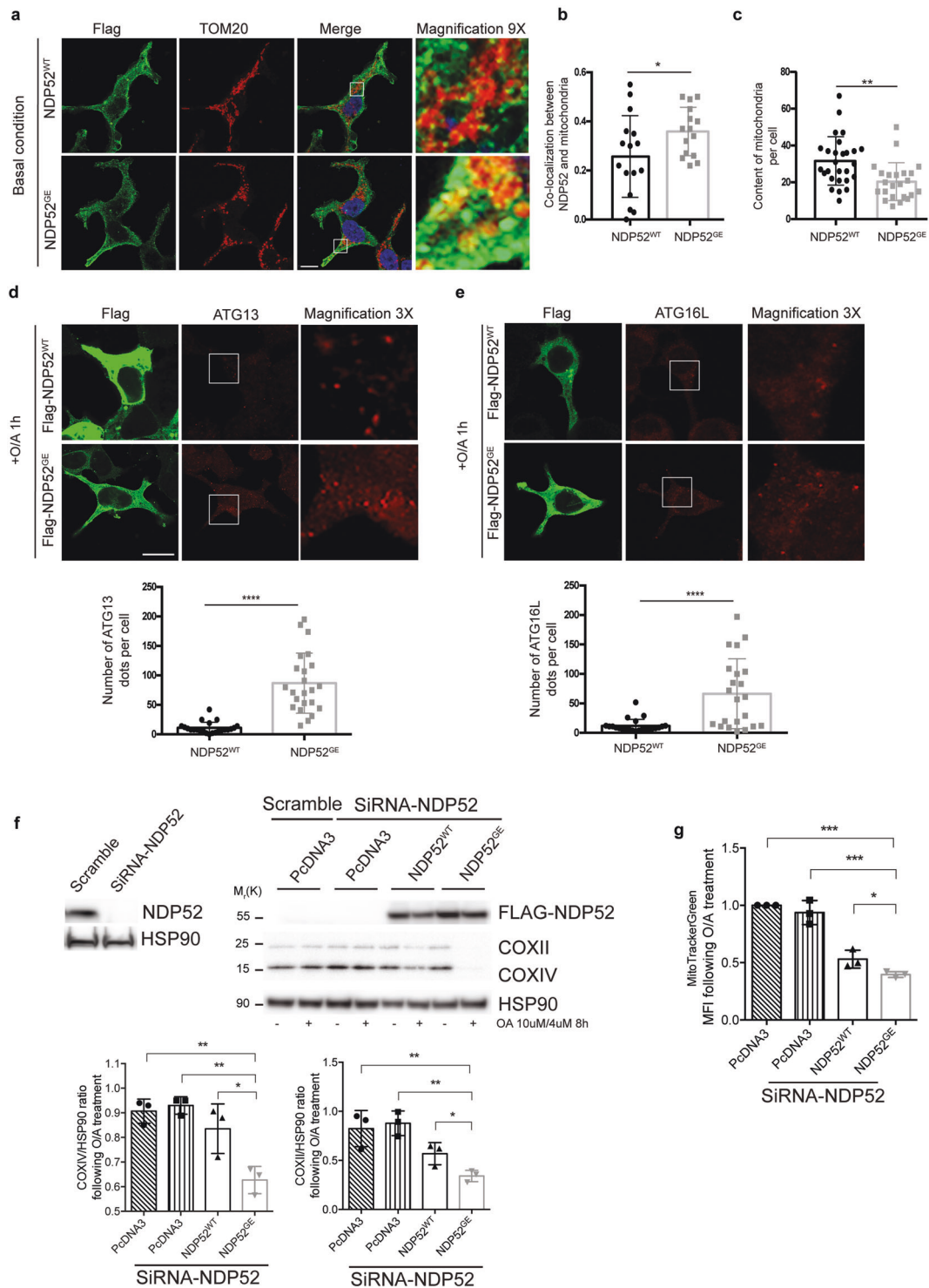
These data indicate that NDP52^{GE}, which binds LC3C with a higher affinity, is more translocated to mitochondria compared to the WT form.

We next postulated that NDP52^{GE} may favor the recruitment of the machinery necessary for autophagosome formation. We thus quantified the formation of autophagosome initiation dots containing the ULK1 complex subunit ATG13 [28, 29] in cells expressing NDP52^{WT} or NDP52^{GE} after O/A treatment. Our data indicate that the overall number of ATG13 dots in cells expressing NDP52^{GE} was significantly higher than those expressing NDP52^{WT} (Fig. 4d). Consistent with this, the recruitment of ATG16L1, a downstream autophagy effector, was also enhanced in cells expressing NDP52^{GE} (Fig. 4e). We next assessed the mitophagy activity of LIR-mutant NDP52^{GE} and NDP52^{WT} in endogenous NDP52-downregulated HEK293 cells. We found that NDP52^{GE} significantly degraded COXII and COXIV compared to NDP52^{WT} (Fig. 4f). In agreement, we found that NDP52^{GE} is degraded to a higher level than the WT form of the protein following O/A treatment (Supplementary Fig. 4). We confirmed these data by evaluating the mitochondrial mass using the MitoTracker-Green dye (Fig. 4g).

These results demonstrate that NDP52^{GE} recruits, with more efficiency, the platform necessary for autophagosome formation during mitophagy and promotes a rapid clearance of damaged mitochondria compared to the WT form of NDP52.

NDP52, predominantly expressed in B cells, ensures effective mitophagy and reduces secretion of the proinflammatory cytokine TNF- α following B cell stimulation

To better understand the role of NDP52 in blood cells, we checked in which subpopulation of PBMCs NDP52 was expressed. We discovered that NDP52 was highly expressed



in B cells compared to T cells or monocytes (Fig. 5a, b). In order to exclude that the increase of NDP52 expression found in MS patients (Fig. 1e) was due to an increase in B cells population, we compared the number of B cells in healthy patients versus MS patients. As illustrated in Supplementary Fig. 5, no difference between the two populations was observed, confirming that NDP52 is upregulated in

B cells of MS patients compared to healthy controls. Since B cells play a key role in MS disease [30], we checked the levels of NDP52 after stimulation of B cells and found that the expression of NDP52 was increased after stimulation with PMA and Ionomycin (PMA/Iono) (Fig. 5c, d).

We thus hypothesized that NDP52 may be a key element for correct mitophagy occurrence in B cells, reducing the

◀ Fig. 4 The NDP52 G140E variant favors phagophore formation and efficient mitophagy. **a** HEK293 cells transfected Flag-NDP52^{WT} or Flag-NDP52^{GE} vectors were fixed and immunostained with antibodies against TOM20 in order to label mitochondria and Flag to detect NDP52 transfected cells. Scale bar 5 μ m. **b** The graph represents the colocalization (Pearson coefficient) between mitochondrial marker TOMM20 and NDP52 evaluated on in single transfected cells from three independent experiments. **c** The graph represents mitochondrial content in Flag-NDP52^{WT} or Flag-NDP52^{GE} transfected cells (27 cells in total from three independent experiments) following mitophagy induction. **d, e** Representative confocal microscopy images in which HEK293 cells transfected and treated as indicated in (a). Scale bar 8 μ m. The graphs report the number of ATG13 (d) or ATG16L (e) foci per cell ($n = 23$ cells), respectively. **f** HEK293 cells downregulated for NDP52 using specific siRNA were next transfected with pcDNA3, Flag-NDP52^{WT} or Flag-NDP52^{GE} vectors and treated with O/A (10 μ M/4 μ M) for 8 h. Mitochondrial markers COXII and COXIV were detected by western blot. HSP90 was used as loading control. The graphs represent the COXII/HSP90 or COXIV/HSP90 ratio in mitophagy condition, resulting as the mean of three independent experiments (\pm SD). **g** Cell treated as in (f) were stained with the MitoTracker Green probe and analyzed by FACS analysis. All statistical analysis were performed using Student *t*-test (* $P < 0.05$; ** $P < 0.01$; *** $P < 0.001$; **** $P < 0.0001$).

release of proinflammatory cytokines that trigger inflammation in MS patients. To test this, in order to manipulate NDP52 expression, we moved to a lymphoblastoid cell line (LCL) derived from a healthy patient. First, we checked whether NDP52 could be also modulated following stimulation of these cells. As illustrated in Fig. 5c, the PMA/Iono treatment was sufficient to induce an upregulation of NDP52. In addition, we found that NDP52 increase was accompanied by a decrease of COXII protein, indicating induction of mitophagy. By contrast, downregulation of NDP52 favors COXII accumulation thus inhibiting mitochondrial clearance (Fig. 5e–g). Also, by performing enzyme-linked immunosorbent assay (ELISA), we found that human proinflammatory cytokine TNF- α was increased in LCL cells downregulated for NDP52 compared to control cells stimulated with PMA/Iono (Fig. 5h).

In summary, our data underline NDP52 as a novel regulator of the immune response in B cells. In particular, we found that NDP52, by ensuring correct mitochondrial clearance following B cell stimulation, limits proinflammatory cytokine production.

Altogether our data suggest that NDP52^{GE} variant may be protective in MS thanks to its higher ability to induce mitophagy respect to the WT form and we can assume that, by acting on B cells, this pro-mitophagic activity may reduce inflammation in MS patients (Fig. 6).

Discussion

Our study reveals that PINK1 and NDP52 expressions are induced in PBMCs of RR-MS patients. Since RR-MS

patients displayed an accumulation of NDP52 and a block in mitochondrial clearance, we suggest that mitophagy induction is not sufficient to remove damaged mitochondria. In fact, we found an accumulation of mitochondria accompanied by oxidative stress in PBMCs of RR-MS patients. Interestingly, an increase of PINK1 protein has been found in MS brain lesions [31]. These data suggest that most likely, PINK1-mediated mitophagy may also be stimulated in the brain of MS patients. Of note, we did not find positive correlation between high expression of PINK1 and NDP52 in PBMCs of single MS patients (Supplementary Fig. 6). Moreover, we cannot exclude that an increase in the OPTN mRNA levels is necessary for correct mitophagy induction in PBMCs of RR-MS patients. Therefore, further investigation of this aspect may explain why mitophagy is not sufficient to remove damaged mitochondria in PBMCs of RR-MS subjects.

Our results reveal a significant association of *NDP52* c.491G>A (rs550510, p.G140E) with a decreased susceptibility to MS. Interestingly, a risk polymorphism in the *NDP52* gene has been found to be associated with Crohn's disease [32]. Functionally, the authors found that the *NDP52* risk variant is more stable compared to the WT form following TLR signaling stimulation, favoring inflammation. We did not find differences between our variants in regulating TLR signaling but our data showed that the NDP52^{GE} variant is more efficient in mitochondria removal. We have identified an amino acid in NDP52 sequence that is crucial in order to extend the cLIR motif and favor its binding with LC3C, inducing a positive feedback loop on phagophore formation and thus on mitophagy. Our data support the ubiquitin-independent mechanism of autophagy receptor recruitment discovered by Padman et al. [12]. The exact mechanism of the affinity enhancement still needs a careful investigation. It is necessary to understand the role of the G140E mutation in the stabilization of the predicted NDP52 cc-region C-terminally to the cLIR motif. Interestingly, another non-canonical LIR-like motif is located in the cc-regions (residues 203-DYWE-206, [33]). This LIR-like motif showed preference for LC3B protein and seems could prompt autophagosome maturation. Indeed, NDP52 constructs possessing both cLIR and LIR-like motifs showed more complex ITC profile (Supplementary Fig. 3c). We cannot exclude that other signals could affect the length and stability of the cc-region in order to induce a stronger pro-mitophagy activity of NDP52^{GE}. A more comprehensive computational study should be carried to quantitatively estimate the propensity for hydrogen bonds or/and salt bridge formation.

Of note, available data on rs550510 variant (reported on 1000Genomes and GnomAD databases of genetic variants annotation) indicate that the protective allele is more common in some populations (i.e., East Asian) than others (i.e., Europe). Since genetic features, environmental factors and habits influence variant distribution, it is not a surprise that,

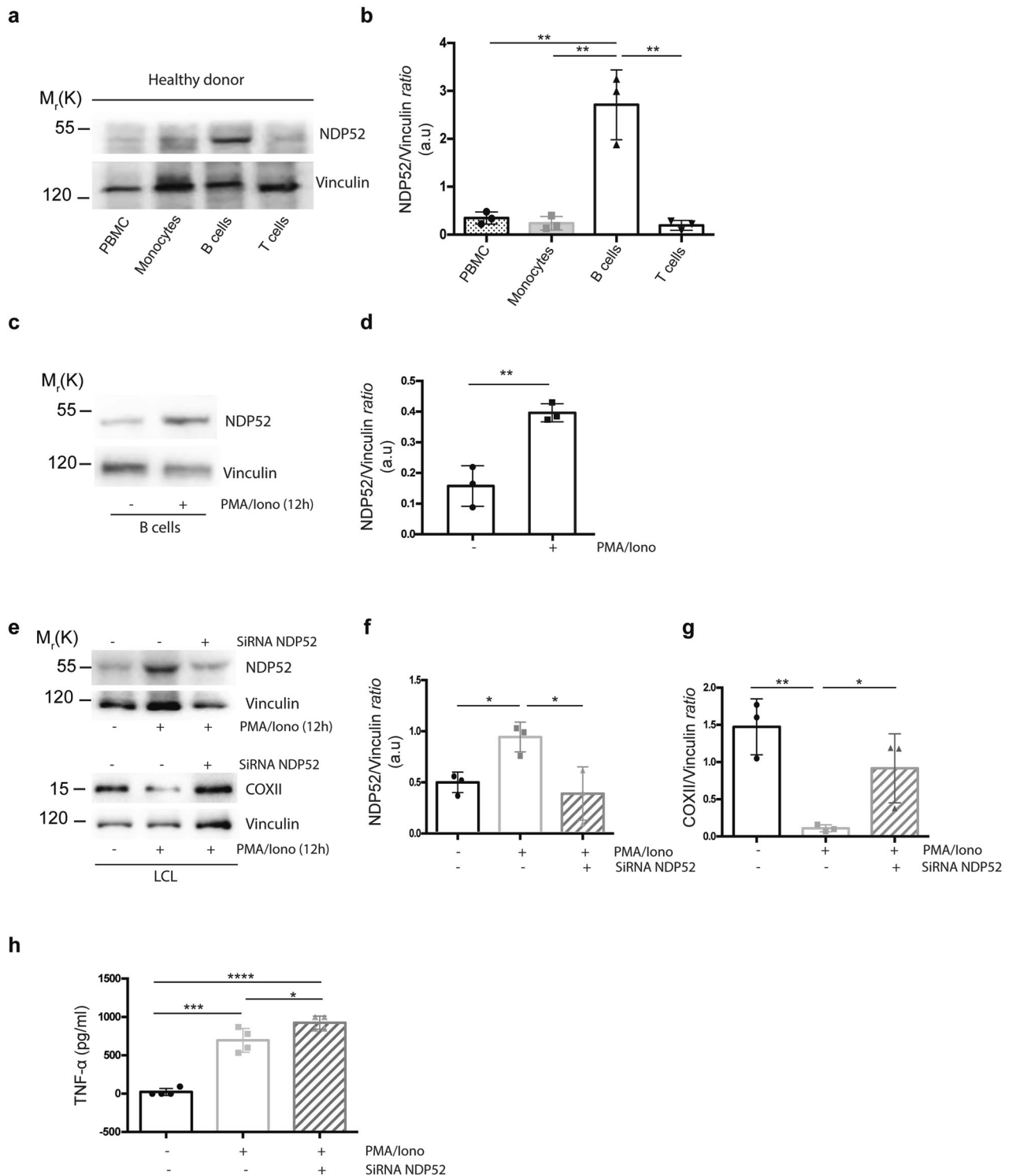


Fig. 5 The NDP52 G140E substitution decreases the production of proinflammatory cytokine in B cells. **a** Total PBMCs, monocytes, B or T cells from healthy donors (HD) were lysated and immunoblotted for NDP52 and Vinculin antibodies (HD = 3). **b** The graph reports the NDP52/Vinculin ratio of three independent experiments. **c** Immunoblotting image of B cells from HD were stimulated with PMA (20 ng/ml) and Ionomycin (200 ng/ml) treatment for 12 h. **d** The graph reports the NDP52/Vinculin ratio in basal or PMA/Iono condition of three independent experiments. **e** LCL cells were downregulated or not for NDP52 using specific siRNA and then stimulated with PMA (20 ng/ml)

and Ionomycin (200 ng/ml) treatment for 12 h. The levels of NDP52, COXII and Vinculin (as a loading control) have been detected by western blot. **f** The graph reports the NDP52/Vinculin ratio of three independent experiments. **g** The graph reports the COXII/Vinculin ratio of three independent experiments. **h** The graphs report the results of ELISA test performed to detect TNF-α in the supernatant of LCL cells (n = 4). All quantifications resulting as the mean of at least three independent experiments (±SD). Statistical analysis was performed using Student *t*-test (**P* < 0.05; ***P* < 0.01).

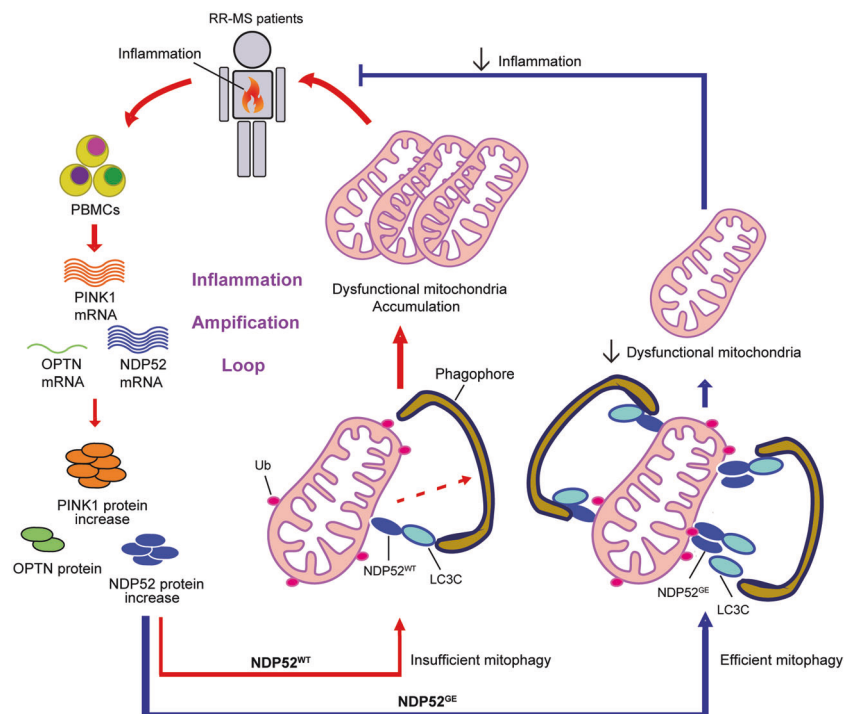


Fig. 6 The “protective” variant NDP52^{GE} potentiates PINK1-mediated mitophagy and may reduce inflammation in RR-MS patients. The PBMC inflammatory state in RR-MS patients induces a robust production of PINK1-mediated mitophagy elements (PINK1 and NDP52). Despite this fact, we noticed a block in mitochondrial clearance and thus an accumulation of dysfunctional mitochondria. The defect in mitochondrial clearance may thus favor a feedback

inflammation loop in PBMCs of RR-MS patients. The substitution G140E of NDP52 (NDP52^{GE}, protective variant in MS) improves the efficiency of mitophagy compared to the WT (NDP52^{WT}) form of the protein (by binding more LC3C and thus favoring phagophore formation) and this allows most likely B cells to decrease their proinflammatory cytokine production thus reducing inflammation.

like other genetic polymorphism, the NDP52^{GE} variant shows a variable frequency distributions among the worldwide populations. It should be interesting to investigate, in the future, why such an efficient variant has not been selected too much in the European population.

Our results highlight that NDP52 protein is mainly expressed in B cell subset. We found that the absence of NDP52 is associated with a block in mitochondrial clearance and an increased production of the proinflammatory cytokine TNF- α following B cell stimulation, underlying a critical role of NDP52 in regulating mitophagy in B cells. Interestingly, defects in mitochondrial clearance predispose human monocytes to interleukin-1 β hyper-secretion [34]. In the future, it would be interesting to check whether B cells isolated from MS patients bearing the NDP52^{GE} variant exhibit a particular cytokines profile. Since we found that NDP52^{GE} is more “mitophagic” than the WT form of the protein, we believe that this variant may prevent the release of proinflammatory cytokines (and maybe mitochondrial factors) that trigger inflammation in MS patients and most likely in other autoimmune diseases. However, we cannot exclude that, as a mitophagy and xenophagy receptor, NDP52 has other protective effects. Hence, additional studies will be needed to clarify this point.

Our work indicates that small molecule development to treat complex diseases, such as MS, may focus on compounds enhancing/stabilizing LIR-dependent interactions between NDP52 and human ATG8-family proteins, thereby opening an important path for the generation of therapeutic agents in addition to compounds that can enhance autophagy/mitophagy process.

Materials and methods

Human samples

Blood samples were collected from 238 untreated patients (females and males, age mean: 35 years) admitted to the neurological clinic of Santa Lucia Foundation of Rome or already stored in its biobank, and diagnosed as suffering from RR-MS, according to internationally established criteria [34]. The diagnosis of MS was established at the end of the diagnostic protocol by clinical, laboratory, and magnetic resonance imaging parameters, and matched published criteria. The Expanded Disability Status Scale scores were always <3 for RR-MS. All RR-MS patients

were treatment-naïve, and blood collection was performed at least 1 month after the last corticosteroid therapy [35]. All peripheral blood samples were collected after obtaining the written informed consent of the study participants, in accordance with the Helsinki Declaration. Most of the samples were stored in the Biobank and a small part of them comes from the project CE/AG4-PROG.246–121. The study protocol was approved by the local ethic committee of the recruitment center.

PBMCs were separated by density gradient over Ficoll-Hypaque, according to standard procedures. Briefly, heparinized blood was diluted with one volume of PBS and gently layered over the Ficoll. Following centrifugation at 660 g for 30 min, cells at the interface of the gradient were collected and washed three times.

Sorting of cells

To separate the different immune populations present in the peripheral blood, we used magnetic beads for cell isolation of Miltenyi Biotec. Specifically, we used anti human antibodies CD19 PE, CD3 PE, and CD14 PE followed by anti-PE Microbeads to separate B lymphocytes, T lymphocytes, and monocytes, respectively. After separation the samples were analyzed by CytoFLEX cytometer (Beckman Coulter) and only samples with a purity greater than 90% were considered for the study.

Count of B cells

Antibodies against CD45, CD3, CD19 and CD20 were added to 1 ml of whole blood from 31 HD and 24 patients with MS at the predetermined concentrations. After lysis of the red blood cells they were resuspended in 1 ml of PBS and analyzed by CytoFLEX (Beckman Coulter) flow cytometer that allows to have the event count per microliter.

Quantitative real-time PCR (qRT-PCR)

RNA from thawed PBMCs samples of MS and HD subjects was isolated and then retro-transcribed using the ReliaPrep RNA Cell Miniprep System (Promega) according to the manufacturer's instruction.

The quantitative analysis of cDNA in PBMCs was performed using quantitative real-time polymerase chain reaction (PCR) for PINK1 (Primer FW: GGGAGTATGGA GCAGTCAC; Primer RW: AGCACATCAGGGTAGTCG), NDP52 (Primer FW: CCTTTCCAATTCCGTCCAG; Primer RW: TGAGTTCTGCTTCTGGAGG), OPTN (Primer FW: GGAGCACAGAGAAAGAGAATG; Primer RW: CGCTGAGTTTTGTATGAGCC), and the housekeeping gene B2M (Primer FW: CTCCGTGGCCTTAGCTGTG; Primer RW: TCTCTGCTGGATGACGTGAG). All genes

content were calculated with the $\Delta\Delta\text{Ct}$ method after normalization on B2M.

mtDNA levels assessment

We checked for the mtDNA/nuclear DNA ratio (mtDNA:nucDNA ratio) levels in PBMCs by performing RT-PCR for mitochondrial COXII (Primer FW: GTCCTGTATGC CCTTTTCCTAACACTC; Primer RV: GACCTCGTCT GTTATGTAAAGGATGCG). We used B2M as housekeeping gene (Primer FW: CTCCGTGGCCTTAGCTGTG; Primer RV: TCTCTGCTGGATGACGTGAG). DNA were isolated from PBMCs using the ReliaPrep RNA Cell Miniprep System (Promega) according to the manufacturer's instruction. COXII content was calculated with the $\Delta\Delta\text{Ct}$ method after normalization on B2M.

Measurement of the mitochondrial membrane potential and mitochondrial mass

Mitochondrial membrane potential ($\Delta\Psi_m$) was estimated by probing the fluorescent intensity. PBMCs were washed and incubated at 37 °C with 10 nM of TMRM⁺ for 30 min in DPBS. After the incubation, cells were washed with PBS and trypsinized off and resuspended in 0.5 ml of DPBS. TMRM⁺ were excited at 488 nm, and fluorescence emitted at 588 nm were measured with (FL2) channel by FACS using the CytoFLEX flow cytometer (Beckman Coulter). For each sample, approximately 300,000 lymphocytes were selected based on physical size (FSC) and grain size (SSC) parameters, and analysis was conducted using the FlowJo v10.5 software (TreeStar, Ashland, OR). The data were expressed in mean fluorescence intensity. Mitochondrial mass was analyzed by FACS analysis by using the MitoTracker Green FM dye (Thermo Fisher). HEK293 cells were exposed to 150 nM MitoTracker Green FM for 30 min at 37 °C, washed in PBS and analyzed by flow cytometry. FACS analysis were conducted using the FlowJo v10.5 software (TreeStar, Ashland, OR).

Protein oxidation assay

PBMCs from healthy or MS subjects were lysed in RIPA buffer as described above. The DPN-derivatized proteins containing carbonyl groups were evaluated by using the OxyBlot Protein Oxidation Detection Kit (Millipore S7150), according to the manufacture's protocol.

Cell lines and primary cells cultures

HeLa and HEK293 cells were cultured in Dulbecco modified Eagle medium (GIBCO 41966-029) supplemented with 10% fetal bovine serum (FBS) (Thermo Fisher

Scientific, 10270-106) at 37 °C under 5% CO₂. These cells were coming from an in-house stock. All cell lines were routinely tested for mycoplasma contamination. B cells (isolated by FACS from healthy patients) and LCL cell line (kind gift from Dr Battistini Lab, IRCCS Fondazione Santa Lucia) were cultured in RPMI 1640 medium (Thermo Fisher 21875) supplemented with 10% FBS.

Cells transfection, cell interference, and treatment

Transient transfections of WT or mutant plasmids or siRNA oligo were performed using Lipofectamine 2000 according to the supplier's instructions (Invitrogen, 11668019). Cells were treated with the combined treatment O/A [10 μM Oligomycin (Calbiochem)/4 μM Antimycin A (Sigma)] in order to induce mitophagy. Cells were treated with PMA/Iono (Sigma, 20 and 200 ng/ml, respectively) in order to stimulate B cells or with Poly (I:C) (Sigma, 50 μg/ml) in order to mimic viral infection in HeLa cells.

Plasmid, cloning, and siRNA

3x-Flag-NDP52 plasmid into p3xFLAG CMV10 vector, kindly donated by Prof. Honglin Luo (Vancouver, Canada) was subjected to mutagenesis in order to generate the 3x-FLAG-NDP52^{GE} mutant according to the manufacturer's protocol of QuickChange site-directed mutagenesis kit (Stratagene).

(Primer FW: CAATCTCTCCACCTCTTCCTGAGTGGTAACAACC; Primer RV: GGTTGTTACCACTCAGGAAGAGGTGGAAGAGATTG). The sequence was verified using the primer: GCATGTCTGAGTTCTGCTTCGGAG by DNA sequencing (BioFab Research, Rome, Italy). The oligonucleotides used for mutagenesis, PCR, and DNA sequencing were purchased from Sigma. HA-LC3C vector was a gift from Dr Christian Berhendts (Boston, USA). PcDNA3 empty vector was used as control plasmid. The oligo siRNA-NDP52 was purchased from Santa Cruz Biotechnology (sc-93738).

Western blot analysis

PBMCs of RR-MS or healthy subjects were lysed with 100 μl of RIPA buffer (50 mM Tris HCl pH 7.4, 1% Triton X-100, 0.5% NP40, 150 mM NaCl, 10% Glycerol) plus protease and phosphatase inhibitor cocktail (Sigma-Aldrich). After 15 min on ice, cells were centrifuged at 11,000 g for 10 min at 4 °C. HeLa and HEK293 cells lysed in RIPA buffer plus protease inhibitor cocktail (Sigma-Aldrich, P8340), Na₄VO₃ 0.1 mM (Sigma-Aldrich, S6508), NaF 1 mM (Sigma-Aldrich, S7920), β-Glycerophosphate 5 mM (Sigma-Aldrich, G6376) were centrifuged at 13,000 rpm for 10 min at 4 °C. PBMCs or cell lines protein concentrations

were determined with the Bio-Rad Protein Assay Kit (Bio-Rad, 5000001). Proteins were separated by SDS-PAGE and transferred into PVDF membranes (Millipore). We next incubated membranes with the following antibodies: anti-PINK1 (Novus #BC100-49455), anti-NDP52 (Cell Signaling, #60732), anti-OPTN (Abcam, Ab236666), anti-FLAG (Sigma-Aldrich, F7425), anti-HA (Sigma-Aldrich, H3663), anti-TOMM20 (Santa Cruz Biotechnology, sc-FL145), anti-HSP90 (Santa Cruz Biotechnology, sc-7947), anti-COXII (Abcam, ab110258) anti-COXIV (Abcam, Ab33985), anti-Vinculin (Santa Cruz Biotechnology, sc-73614).

Densitometry analyses of the western blot were performed using the ImageJ software.

Co-Immunoprecipitation (Co-IP)

After HEK293 cell lysis, proteins were incubated with primary antibody (anti-Flag rabbit) for 24 h. Then 20 μl of protein A agarose beads (Roche, 11719408001) was added for 1 h. The beads were collected by centrifugation and washed three times with the RIPA buffer. Finally, immunocomplexes were eluted with 20 μl of SDS sample buffer and heated to 95 °C for 10 min.

Immunofluorescence analysis

HEK293 cells were washed in PBS and fixed with 4% paraformaldehyde in PBS for 10 min. After permeabilization with 0.4% Triton X-100 (Sigma-Aldrich, X-100) in PBS for 5 min, cells were incubated at 4 °C with primary antibodies (24 h) with 2% normal goat serum (Sigma-Aldrich, G9023). Cells were then washed with PBS (GIBCO, BE17-512F) and incubated for 1 h with labeled anti-mouse (Thermo Fisher Scientific, A11017-A21425) or anti-rabbit (Thermo Fisher Scientific, A11070-A21430-A31573) secondary antibodies. Then cells were stained with 1 μg/ml DAPI in order to detect the nuclei and analyzed with Zeiss LSM 700 63x oil-immersion objective (CLSM700; Jena, Germany). Colocalization measurement were performed for each transfected individual cells using ImageJ colocalization 2 plugin (Pearson value). In order to measure cellular mitochondrial area, RGB images captured were processed using ImageJ software that calculates total area occupied by mitochondria particles in the cell of interest using the outline algorithm of the "Analyse particles." The count of ATG13 and ATG16L foci was performed using the same "analysis particles" with ImageJ software. All acquisitions were performed in non-saturated single z-confocal planes.

Genotyping and association analysis

Samples from 203 RR-MS patients and 1000 healthy controls have been subjected to automated DNA extraction, in accordance with the Declaration of Helsinki. All

subjects were asked to provide written and signed informed consent. The extracted DNA was employed for the genotyping analysis through a predesigned TaqMan assay on QuantStudio[®] 5 Real-Time PCR System (Applied Biosystems). Each real-time PCR run was performed using a negative control and three positive samples that were previously tested by direct sequencing (BigDye Terminator v3.1) and run on ABI3130xl (Applied Biosystems) [36]. The genotyping results have been subsequently tested for biostatistical analysis, in order to evaluate the association and the effect of the identified variants. The Hardy–Weinberg equilibrium was confirmed in both cases' and controls' cohorts. In particular, the obtained data were evaluated by calculating the *P* value through a 2 × 2 (allele association) and 2 × 3 (genotype association) contingency tables. The statistical associations were considered significant for *P* < 0.05 with a 95% confidence interval. The strength of association was established by calculating the OR [37].

ITC and NMR samples preparation

For ITC and NMR experiments, the non-labeled or ¹⁵N-labeled LC3C and LC3B proteins were obtained based on the protocols described elsewhere [38]. The shortest NDP52 LIR-contained peptides (with Trp residue added to the N-terminus of each peptide in order to calculate peptides concentration):

NDP52_{128–152}WENEEDILVVTQTQGEVEEIEQHNKEL
 NDP52_{128–155}WENEEDILVVTQTQGEVEEIEQHNKE
 LCKE
 NDP52^{GE}_{128–152}WENEEDILVVTQTQEEVEEIEQHN
 KEL
 NDP52^{GE}_{128–155}WENEEDILVVTQTQEEVEEIEQHN
 KELCKE

were purchased from GenScript Inc (NJ, USA). The longer NDP52 fragments (WT or with mutation) were subcloned into pNIC28_Ub19_Bsa4 vector by ligation-independent cloning technology. The expression, isolation, and purification of the NDP52 fragments were performed based on the protocols described elsewhere [37]. The NDP52 constructs used in this study are overviewed in Supplementary Table 1 and presented schematically at Supplementary Fig. 3a. Before experiments, all proteins and peptides were equilibrated with a buffer containing 25 mM HEPES, 100 mM NaCl, pH 7.0; and supplied with 5 mM protease inhibitors cocktail.

Isothermal titration microcalorimetry (ITC)

The ITC experiments were performed at 25 °C using a MicroCal VP-ITC microcalorimeter (Malvern Instruments Ltd., UK). The peptides at concentrations of 0.3 mM were

titrated into 0.015 mM LC3 proteins in 21 steps. The ITC data were analyzed with the ITC-Origin 7.0 software with a “one-site” binding model. The proteins and peptides concentrations were calculated from the UV-absorption at 280 nm by Nanodrop spectrophotometer (Thermo Fisher Scientific, DE, USA).

Nuclear magnetic resonance spectroscopy

All NMR experiments were performed at a sample temperature of 298 K on Bruker Avance III spectrometer operating at a proton frequencies of 950 MHz. Titration experiments were performed with a 0.190 mM ¹⁵N-labeled LC3C protein samples to which the non-labeled NDP52_{128–224} and NDP52^{GE}_{128–224} constructs were added stepwise until four times excess to LC3C protein. CSP analysis was done according to the most recent review [39]. CSP values were calculated for each individual backbone HN resonance using the formula: $\Delta\delta = [\Delta\delta_H^2 + (\Delta\delta_N/5)^2]^{1/2}$. The obtained CSP values were mapped on LC3C (PDB ID 3WAM [40]) structure.

Molecular modeling

We modeled the three-dimensional structure of the complex between LC3C_{8–127} and the cLIR of NDP52 (NDP52_{125–147}) using a multi-step procedure based on MODELLER version 9.15 [41]. In the first step, we collected a model of the complex with WT NDP52 using the X-ray structure of LC3C_{13–126}-NDP52_{125–141} as partial template (PDB entry 3VWV, [16]) to reconstruct the missing coordinates for the N- and C-terminal residues of LC3C. We generated a set of structures and selected one, as detailed in the GitHub repository associated with the publication. We performed another round of modeling using the model collected at the first step for LC3C_{8–127}-NDP52_{125–141} and the X-ray structure of the complex between FYCO1_{1235–1253} and LC3B_{4–120} (PDB entry 5WRD, [21]) as templates. The alignment between LC3B and LC3C to guide the modeling was provided by Clustal Omega [42]. The crystal asymmetric unit of 5WRD contains two conformations of the FYCO1-LC3C complex; therefore, we carried out this procedure as two independent MODELLER runs using each of them as templates and generating 1000 models for each. We then selected the model having the shortest distance between the C α atom of G140 in NDP52 and the C ζ atom of R76 in LC3C from each run. We introduced the mutation of interest (G140E) in both structures using PyMOL, selecting the rotamer of E140 characterized by the lowest number of interatomic clashes with the surrounding atoms.

Notably, as the C-terminal region of FYCO1 corresponding to our region of interest in NDP52 with respect to the core LIR motif (residues 1235–1239) is in a helical

conformation which is stabilized by intermolecular electrostatic interactions [21], we constrained the helical conformation for NDP52 C-terminal region (residues 138–147) during the modeling procedure.

Molecular dynamics and metadynamics simulations

Using the two models selected above for the complex of LC3C_{13–126}-NDP52_{125–141}, we carried out all-atom 250-ns MD simulations in explicit solvent using GROMACS version 5.1.5 [43]. We employed the CHARMM22* force field [44] together with the TIPS3P water model [45]. To avoid artificial interactions formed by charged N- and C-terminal groups, we used a N- and C-terminal capping for both LC3C and NDP52 (see GitHub repository for details). We performed the MD simulations employing a dodecahedral box of water to solvate the protein, with a minimum distance between protein atoms and the box edges of 18 Å using periodic boundary conditions. We applied different steps of energy minimization, solvent equilibration, thermalization, and pressurization to prepare the systems for simulation (see GitHub repository). We performed the productive MD simulations using an integration step of 2 fs in the canonical ensemble with the Bussi thermostat [46] at a temperature of 298 K. We used a 9-Å cutoff for both Van Der Waals and short-range Coulomb electrostatic interactions. We also applied the particle mesh Ewald scheme for electrostatics [47]. Additional details are reported in the input files in the GitHub repository.

We used the well-tempered metadynamics (WTE-metaD) [23] to enhance the sampling of the free energy surface of salt bridge formation by adding the history-dependent bias potential on the distance between E140 C δ of NDP52 and R76 C ζ of LC3C. Gaussians with width of 0.1 nm and height of 2.5 KJ/mol were added every 500 simulation steps (1 ps). The bias factor ($\gamma = 10$) and temperature (298 K) were kept constant throughout the simulations. A restraining potential was used to limit the sampling of the CV below 1.7 nm, with a force constant of 10,000 kJ/(mol nm²). We collected two WTE-metaD simulations starting from the two selected models of the complex LC3C_{8–127}-NDP52_{125–147}, to ensure convergence—in fact, two independent simulations starting from different starting structures should converge to the same free energy surface. Simulations were performed using GROMACS 2019.4 and PLUMED 2.5.3 [48].

Simulations analyses

We estimated the occurrence, in the unbiased MD ensembles, of intermolecular salt bridge and hydrogen bonds using PyInterph [49]. We applied a distance cutoff of 4.5

and 3 Å, respectively. We also tested higher cutoffs for salt bridges (i.e., 5–6 Å) to rule out that the charged groups of E140 and positively charged residues of LC3C could be overlooked.

The free energy landscape was reconstructed from the deposited bias during the metadynamics simulation using the *sum_hills* tool available in PLUMED using a stride of 1000. We have used three different strategies to assess the convergence of our metadynamics simulations. The details are reported in the GitHub repository.

Detection of human TNF- α by ELISA

Human TNF- α Quantikine ELISA kits (Invitrogen) was used according to the manufacturer's protocol. Absorbance was measured by Thermo Multiskan EX Microplate Photometer (Thermo Fisher Scientific) at 450 nm with wavelength correction set at 540 nm.

Statistical analysis

All statistical calculations were performed and graphed using GraphPad Prism 6. Comparisons between two groups were analyzed using unpaired Student *t*-test. Significance were defined as * $P < 0.05$; ** $P < 0.01$; *** $P < 0.001$; **** $P < 0.0001$.

Data availability

All the software used is freely available. The scripts, input, and outputs files generated during the study will be freely available in a GitHub repository associated with our publication (https://github.com/ELELAB/LC3C_NDP52_GE_mutant). The MD trajectories will be available in Open Science Framework (OSF): <https://osf.io/48wzq/>.

Acknowledgements We wish to thank Dr Christian Behrends for kindly providing us the construct encoding HA-LC3C; Prof. Honglin Luo for the gift of 3x-Flag-NDP52 plasmid; Dr Anna Kabanova for granting the execution of some revision experiments in her laboratory; Krenare Bruqi for her technical assistance and D.Hodder for his proofreading. We are grateful to Meike Crecelius, Natalia Rogova, and Viktoria Morasch for their help with cloning of NDP52 fragments for ITC and NMR experiments, protein/peptide sample preparation, and ITC data collection.

Author contributions FS designed the project. ADR and FS wrote the paper. ADR performed analysis in MS patients (Fig. 1), on B cells (Fig. 5a–d) and performed the cloning of NDP52^{GE}. TM investigated the role of NDP52 variants in the TLR signaling (Supplementary Fig. 1) and helped FS in performing Immunofluorescences of Figs. 2, 3, and 5e–g. FS characterized the binding between LC3C and NDP52 variants, performed the mitophagy analysis and Fig. 5e–g. MC helped FS in the characterization of LC3C-NDP52 interaction. PDA participated in the amplification of NDP52-LIR motif from MS patients and HD donors. DFA and LB provided PBMCs of MS patients and the LCL cell line. VC provided

PBMCs of HD and MS patients and helped in preparing some cDNAs (Fig. 1). DFA performed FACS analysis (TMRM) and sorted monocytes, B and T cells from healthy patients (Fig. 5a). GC, RC, and VC performed the genetical study. MK, MT, ML, FL, VD, and EP performed Fig. 3e, f. The ITC and NMR experiments were designed by VD and VVR, and performed by NW and FL (Fig. 3 and Supplementary Fig. 2). ADR, EP, VVR, EG, and FS analyzed data. All authors commented on the final draft of the paper.

Funding This work was supported by grants: ROCHE (Roche per la ricerca 2017) and 5XMILLE Italian Ministry of Health (2017) to FS. The study was partially supported by the Italian Ministry of Health (Progetto di ricerca Finalizzata RF-2018-12366111) and by the Italian Foundation for Multiple Sclerosis (Fism Progetto Speciale 2018/S/5) to LB. The work of NW, VD, and VVR was supported by the DFG-funded Collaborative Research Centre on Selective Autophagy (SFB 1177 “Molecular and Functional Characterization of Selective Autophagy”), Germany. VD and VVR also received funding from Structural Genomic Consortium (SGC). The SGC is a registered charity (no: 1097737) that receives funds from AbbVie, Bayer AG, Boehringer Ingelheim, Canada Foundation for Innovation, Eshelman Institute for Innovation, Genentech, Genome Canada through Ontario Genomics Institute [OGI-196], EU/EFPIA/OICR/McGill/KTH/Diamond, Innovative Medicines Initiative 2 Joint Undertaking [EUbOPEN grant 875510], Janssen, Merck KGaA (aka EMD in Canada and USA), Merck & Co (aka MSD outside Canada and USA), Pfizer, São Paulo Research Foundation-FAPESP, Takeda and Wellcome [106169/ZZ14/Z]. The work of VC was supported by Italian Foundation of Multiple Sclerosis (FISM grant 2017/R/08) and by Ministry of Health, Progetto Giovani Ricercatori (GR-2016-02362380). The work of MK, MT, ML, FL, VD, and EP is supported by Danmarks Grundforskningsfond (DNRF125) and a Carlsberg Foundation Distinguished Fellowship (CF18-0314) to EP’s group. Moreover, the project has been supported by a Netaji Subhash ICAR international fellowship, Government of India to MK to work in EP group. The calculations described in this paper were performed using the DeIC National Life Science Supercomputer Computerome at DTU (Denmark), and a DeIC-Pilot Grant on Abacus (Denmark).

Compliance with ethical standards

Conflict of interest The authors declare no competing interests.

Ethical approval Refer to Human samples paragraph in the Materials and methods section.

Publisher’s note Springer Nature remains neutral with regard to jurisdictional claims in published maps and institutional affiliations.

References

- Compston A, Coles A. Multiple sclerosis. *Lancet*. 2002;359:1221–31.
- Noseworthy JH, Lucchinetti C, Rodriguez M, Weinshenker BG. Multiple sclerosis. *N Engl J Med*. 2000;343:938–52.
- Dendrou CA, Fugger L, Friese MA. Immunopathology of multiple sclerosis. *Nat Rev Immunol*. 2015;15:545–58.
- Brown J, Wang H, Hajishengallis GN, Martin M. TLR-signaling networks: an integration of adaptor molecules, kinases, and cross-talk. *J Dent Res*. 2011;90:417–27.
- Su K, Bourdette D, Forte M. Mitochondrial dysfunction and neurodegeneration in multiple sclerosis. *Front Physiol*. 2013;4:169.
- Chiurchiu V. Novel targets in multiple sclerosis: to oxidative stress and beyond. *Curr Top Med Chem*. 2014;14:2590–9.
- Gonzalo H, Noguera L, Gil-Sánchez A, Hervás JV, Valcheva P, González-Mingot C, et al. Impairment of mitochondrial redox status in peripheral lymphocytes of multiple sclerosis patients. *Front Neurosci*. 2019;13:938.
- Lou G, Palikaras K, Lautrup S, Scheibye-Knudsen M, Tavernarakis N, Fang EF. Mitophagy and neuroprotection. *Trends Mol Med*. 2020;26:8–20.
- Koyano F, Okatsu K, Kosako H, Tamura Y, Go E, Kimura M, et al. Ubiquitin is phosphorylated by PINK1 to activate parkin. *Nature*. 2014;510:162–6.
- Kazlauskaitė A, Kondapalli C, Gourlay R, Campbell DG, Ritorto MS, Hofmann K, et al. Parkin is activated by PINK1-dependent phosphorylation of ubiquitin at Ser65. *Biochem J*. 2014;460:127–39.
- Lazarou M, Sliter DA, Kane LA, Sarraf SA, Wang C, Burman JL, et al. The ubiquitin kinase PINK1 recruits autophagy receptors to induce mitophagy. *Nature*. 2015;524:309–14.
- Padman BS, Nguyen TN, Uoselis L, Skulsupaisarn M, Nguyen LK, Lazarou M. LC3/GABARAPs drive ubiquitin-independent recruitment of Optineurin and NDP52 to amplify mitophagy. *Nat Commun*. 2019;10:408.
- Patergnani S, Castellazzi M, Bonora M, Marchi S, Casetta I, Pugliatti M, et al. Autophagy and mitophagy elements are increased in body fluids of multiple sclerosis-affected individuals. *J Neurol Neurosurg Psychiatry*. 2018;89:439–41.
- Castellazzi M, Patergnani S, Donadio M, Giorgi C, Bonora M, Fainardi E, et al. Correlation between auto/mitophagic processes and magnetic resonance imaging activity in multiple sclerosis patients. *J Neuroinflammation*. 2019;16:131.
- Inomata M, Niida S, Shibata KI, Into T. Regulation of toll-like receptor signaling by NDP52-mediated selective autophagy is normally inactivated by A20. *Cell Mol Life Sci*. 2012;69:963–79.
- von Muhlinen N, Akutsu M, Ravenhill BJ, Foeglein Á, Bloor S, Rutherford TJ, et al. LC3C, bound selectively by a noncanonical LIR Motif in NDP52, is required for antibacterial autophagy. *Mol Cell*. 2012;48:329–42.
- Skytte Rasmussen M, Mouilleron S, Kumar Shrestha B, Wirth M, Lee R, et al. ATG4B contains a C-terminal LIR motif important for binding and efficient cleavage of mammalian orthologs of yeast Atg8. *Autophagy*. 2017;13:834–53.
- Wirth M, Zhang W, Razi M, Nyoni L, Joshi D, O’Reilly N, et al. Molecular determinants regulating selective binding of autophagy adaptors and receptors to ATG8 proteins. *Nat Commun*. 2019;10:2055.
- Cheng X, Wang Y, Gong Y, Li F, Guo Y, Hu S, Liu J, Pan L. Structural basis of FYCO1 and MAP1LC3A interaction reveals a novel binding mode for Atg8-family proteins. *Autophagy*. 2016;12:1330–9.
- Kirkin V, Rogov VV. A diversity of selective autophagy receptors determines the specificity of the autophagy pathway. *Mol Cell*. 2019;76:268–85.
- Johansen T, Lamark T. Selective autophagy: ATG8 family proteins, LIR motifs and cargo receptors. *J Mol Biol*. 2020;432:80–103.
- Sakurai S, Tomita T, Shimizu T, Ohto U. The crystal structure of mouse LC3B in complex with the FYCO1 LIR reveals the importance of the flanking region of the LIR motif. *Acta Crystallogr F Struct Biol Commun*. 2017;73:130–7.
- Laio A, Parrinello M. Escaping free-energy minima. *Proc Natl Acad Sci USA*. 2002;99:12562–6.
- Bonomi M, Barducci A, Parrinello M. Reconstructing the equilibrium boltzmann distribution from well-tempered metadynamics. *J Comput Chem*. 2009;30:1615–21.

25. Bussi G, Laio A. Using metadynamics to explore complex free-energy landscapes. *Nat Rev Phys.* 2020;2:200–12.
26. Richter B, Sliter DA, Herhaus L, Stolz A, Wang C, Beli P, et al. Phosphorylation of OPTN by TBK1 enhances its binding to Ub chains and promotes selective autophagy of damaged mitochondria. *Proc Natl Acad Sci USA.* 2016;113:4039–44.
27. Moore AS, Holzbaur ELF. Dynamic recruitment and activation of ALS-associated TBK1 with its target optineurin are required for efficient mitophagy. *Proc Natl Acad Sci USA.* 2016;113:3349–58.
28. Turco E, Fracchiolla D, Martens S. Recruitment and activation of the ULK1/Atg1 kinase complex in selective autophagy. *J Mol Biol.* 2020;432:123–34.
29. Karanasios E, Stapleton E, Manifava M, Kaizuka T, Mizushima N, Walker SA, et al. Dynamic association of the ULK1 complex with omegasomes during autophagy induction. *J Cell Sci.* 2013;126:5224–38.
30. Sabatino JJ, Pröbstel AK, Zamvil SS. B cells in autoimmune and neurodegenerative central nervous system diseases. *Nat Rev Neurosci.* 2019;20:728–45.
31. Wilhelmus MM, van der Pol SM, Jansen Q, Witte ME, van der Valk P, Rozemuller A, et al. Association of Parkinson disease-related protein PINK1 with Alzheimer disease and multiple sclerosis brain lesions. *Free Radic Biol Med.* 2011;50:469–76.
32. Ellinghaus D, Zhang H, Zeissig S, Lipinski S, Till A, Jiang T, et al. Association between variants of PRDM1 and NDP52 and crohn's disease, based on exome sequencing and functional studies. *Gastroenterology.* 2013;145:339–47.
33. Verlhac P, Grégoire IP, Azocar O, Petkova DS, Baguet J, Viret C, Faure M. Autophagy receptor NDP52 regulates pathogen-containing autophagosome maturation. *Cell Host Microbe.* 2015;17:515–25.
34. van der Burgh R, Nijhuis L, Pervolaraki K, Compeer EB, Jongeneel LH, van Gijn M, et al. Defects in mitochondrial clearance predispose human monocytes to interleukin-1 β hypersecretion. *J Biol Chem.* 2014;289:5000–12.
35. McNicholas N, Hutchinson M, McGuigan C, Chataway J. 2017 McDonald diagnostic criteria: a review of the evidence. *Mult Scler Relat Disord.* 2018;24:48–54.
36. Cascella R, Strafella C, Ragazzo M, Manzo L, Costanza G, Bowes J, et al. KIF3A and IL-4 are disease-specific biomarkers for psoriatic arthritis susceptibility. *Oncotarget.* 2017;8:95401–11.
37. Cascella R, Strafella C, Longo G, Ragazzo M, Manzo L, De Felici C, et al. Uncovering genetic and non-genetic biomarkers specific for exudative age-related macular degeneration: significant association of twelve variants. *Oncotarget.* 2018;9:7812–21.
38. Rogov VV, Rozenknop A, Rogova NY, Löhr F, Tikole S, Jaravine V, et al. A universal expression tag for structural and functional studies of proteins. *ChemBioChem.* 2012;13:959–63.
39. Williamson MP. Using chemical shift perturbation to characterise ligand binding. *Prog Nucl Magn Reson Spectrosc.* 2013;73:1–16.
40. Suzuki H, Tabata K, Morita E, Kawasaki M, Kato R, Dobson RC, et al. Structural basis of the autophagy-related LC3/Atg13 LIR complex: recognition and interaction mechanism. *Structure.* 2014;22:47–58.
41. Webb B, Sali A. Comparative protein structure modeling using MODELLER. *Curr Protoc Bioinformatics.* 2016;54:5.6.1–5.6.37.
42. Sievers F, Wilm A, Dineen D, Gibson TJ, Karplus K, Li W, et al. Fast, scalable generation of high-quality protein multiple sequence alignments using Clustal Omega. *Mol Syst Biol.* 2011;7:539.
43. Abraham MJ, Murtola T, Schultz R, Pall S, Smith JC, Hess B, et al. Gromacs: high performance molecular simulations through multi-level parallelism from laptops to supercomputers. *SoftwareX.* 2015;1:19–25.
44. Piana S, Lindorff-Larsen K, Shaw DE. How robust are protein folding simulations with respect to force field parameterization? *Biophys J.* 2011;100:47–9.
45. Jorgensen WL, Chandrasekhar J, Madura JD, Impey RW, Klein ML. Comparison of simple potential functions for simulating liquid water. *J Chem Phys.* 1983;79:926.
46. Bussi G, Donadio D, Parrinello M. Canonical sampling through velocity rescaling. *J Chem Phys.* 2007;126:014101.
47. Harvey MJ, De Fabritiis G. An implementation of the smooth particle mesh Ewald method on GPU hardware. *J Chem Theory Comput.* 2009;5:2371–7.
48. Tribello GA, Bonomi M, Branduardi D, Camilloni C, Bussi G. PLUMED 2: new feathers for an old bird. *Comput Phys Commun.* 2014;185:604–13.
49. Tiberti M, et al. PyInteraph: a framework for the analysis of interaction networks in structural ensembles of proteins. *J Chem Inf Model.* 2014;54:1537–51.



A protective variant of the autophagy receptor CALCOCO2/NDP52 in Multiple Sclerosis (MS)

Anthea Di Rita & Flavie Strappazon

To cite this article: Anthea Di Rita & Flavie Strappazon (2021) A protective variant of the autophagy receptor CALCOCO2/NDP52 in Multiple Sclerosis (MS), *Autophagy*, 17:6, 1565-1567, DOI: [10.1080/15548627.2021.1924969](https://doi.org/10.1080/15548627.2021.1924969)

To link to this article: <https://doi.org/10.1080/15548627.2021.1924969>



Published online: 10 May 2021.



Submit your article to this journal [↗](#)



Article views: 349



View related articles [↗](#)



View Crossmark data [↗](#)

A protective variant of the autophagy receptor CALCOCO2/NDP52 in Multiple Sclerosis (MS)

Anthea Di Rita^a and Flavie Strappazzon^b

^aReiThera Srl, Rome, Italy; ^bIRCCS Fondazione Santa Lucia, Rome, Italy

ABSTRACT

Multiple sclerosis (MS) is an autoimmune disease of the central nervous system, which has been found associated with dysfunctional mitochondria. In order to advance our understanding of the complex molecular mechanisms underlying this disease, we analyzed mitophagy, a process fundamental for the elimination of damaged mitochondria through the autophagic process, in peripheral blood mononuclear cells (PBMCs) of MS patients. Through a genetic analysis carried out on 203 MS patients and 1000 healthy controls, we identified a natural variant of CALCOCO2/NDP52, a well-known autophagic receptor, associated with and protective in MS. Structural modeling of the CALCOCO2 variant and functional studies highlighted an amino acid substitution (G140E) located near the LC3-interacting region (LIR) motif of CALCOCO2, crucial in controlling mitophagy. In addition, we found that among PBMCs, CALCOCO2 is mainly expressed in B cells and, by mediating mitophagy, it reduces pro-inflammatory cytokine production following stimulation of these cells. Here we summarize these recent findings, discuss the putative protective roles of CALCOCO2 in B cells and its novel association with an autoimmune disease such as MS.

Abbreviations: LIR: LC3-interacting region; MS: multiple sclerosis; PBMC: peripheral blood mononuclear cells; RR-MS: relapsing-remitting MS; TLR: toll like receptor.

ARTICLE HISTORY

Received 21 April 2021

Revised 26 April 2021

Accepted 28 April 2021

KEYWORDS

B cells; CALCOCO2; inflammation; mitochondria; mitophagy; multiple sclerosis

Multiple sclerosis (MS) is a very debilitating chronic autoimmune disease. Depending on the region of the world, the incidence is of 50 to 300 per 100,000 individuals. MS generally affects young adults with a prevalence of 3 female patients for every male patient. Currently, the processes that trigger the disease are not known, but genetic predispositions, environmental agents (such as bacteria or virus infections) and social components (such as tobacco consumption) participate in the pathogenesis of MS.

There are three types of MS. A cyclic or remitting form (relapsing-remitting MS, RR-MS), which affects 80–85% of patients without progression of the handicap between relapses. This MS can progress to secondarily progressive MS (or MS-SP). There is also a primary progressive form (or PP-MS) in which the phases of the disease are not interspersed with phases of remission, affecting approximately 15% of patients.

In all cases, the disease is characterized by the onset of varying disabilities all due to the progressive infiltration of cells of the adaptive immune system, T and B lymphocytes, into the central nervous system. These activated cells are responsible for the destruction of the myelin sheath of neurons and the development of neuronal and axonal damage.

One characteristic of MS is the presence of oxidative stress and mitochondrial dysfunctions associated with the pathology. However, the role played by mitophagy – a process that selectively eliminates altered mitochondria through the

autophagic process to regulate the functional quality of mitochondria and to reduce oxidative stress – remains completely obscure in MS pathogenesis.

In our recent article [1], we identified and characterized a variant of the autophagic receptor CALCOCO2/NDP52 that links mitophagy and MS pathogenesis. Indeed, by sequencing the DNA coming from peripheral blood mononuclear cells (PBMCs) of 203 RR-MS patients with specific probes for the genes encoding two main mitophagic receptors, CALCOCO2 and OPTN, we revealed a significant association of CALCOCO2 c.491 G > A mutation (rs550510, p. G140E) with a decreased susceptibility to MS, suggesting that the CALCOCO2 variant CALCOCO2^{G140E} may confer protection to MS. Functional analyses were performed for the two CALCOCO2 forms, wild-type (WT) CALCOCO2 and protective CALCOCO2^{G140E}, using overexpression of tagged protein variants in a human cell line under different conditions.

First, because enhanced immune response may benefit MS patients by eliminating microbes and because CALCOCO2 negatively regulates TLR (toll like receptor)-triggered NFκB activation, we thought to test whether the CALCOCO2^{G140E} variant was protective in MS by favoring activation of NFκB, following TLR stimulation. However, our data indicate that the substitution of G140E of CALCOCO2 does not affect its function in regulating TLR signaling.

Second, because mitochondrial dysfunctions are related to MS pathogenesis and CALCOCO2 serves as a bridge between

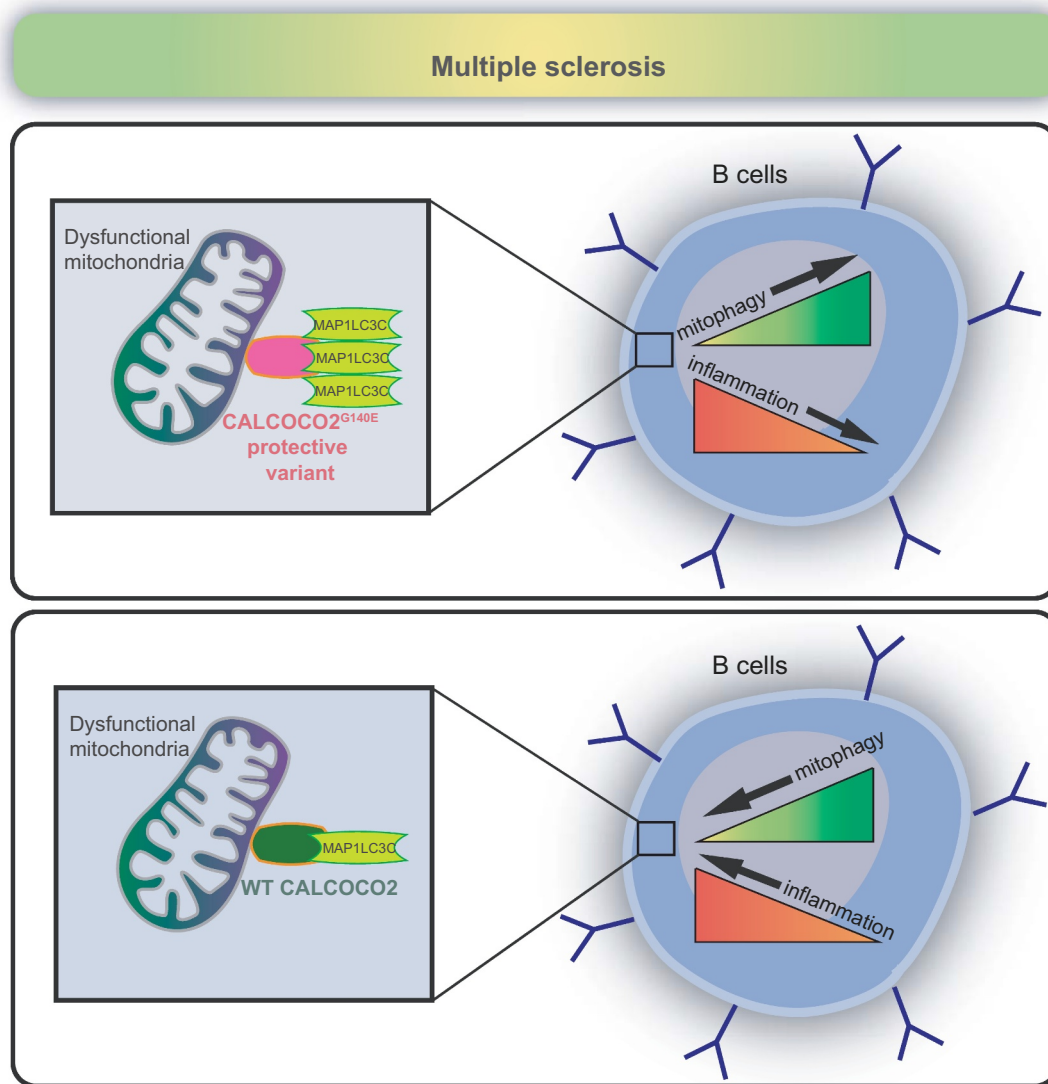


Figure 1. Hypothetical model of the protective role of CALCOCO2^{G140E} variant in B cells of RR-MS patients. In multiple sclerosis, the protective variant of CALCOCO2 (CALCOCO2^{G140E}) can inhibit pro-inflammatory cytokine production (TNF) in B cells by increasing its binding with MAP1LC3C and thus favoring the selective degradation of damaged mitochondria (mitophagy) (upper panel). WT CALCOCO2, instead, has a restricted interaction with MAP1LC3C, and this can reduce the elimination of dysfunctional mitochondria and enhance inflammation in MS patients (lower panel).

mitochondria and phagophores during degradation of damaged mitochondria by autophagy, we then decided to focus our attention on the role played by CALCOCO2^{G140E} in mitophagy.

Our study showed that the CALCOCO2^{G140E} variant is more efficient in removing damaged mitochondria compared with WT CALCOCO2. The single amino acid substitution in the CALCOCO2 sequence is crucial for extending its non-canonical LIR motif (cLIR) and promoting its binding with LC3C, thus favoring mitophagy.

Our structural and biochemical analysis indicated that the CALCOCO2^{G140E} variant exhibits a better affinity with the LC3C protein. Further studies will be necessary to quantitatively estimate the propensity to form hydrogen bonds and/or to the formation of salt bridges induced by this point mutation.

We demonstrated that, despite the efficiency of the protective CALCOCO2^{G140E} variant, the available data on the rs550510 variant (reported on 1000Genomes and GnomAD databases of genetic variants annotation) indicate that the protective allele is more common in some populations (i.e., East Asian) than others (i.e., European). This correlates with the global distribution of MS; however, from a genetic point of view, the cause of the lower distribution of CALCOCO2^{G140E} in the European population will be an interesting point to examine in future studies.

We discovered that among PBMCs, CALCOCO2 is mainly expressed in B cells. In MS pathology, B lymphocytes are involved in the secretion of pro-inflammatory cytokines, in the presentation of autoantigens to T lymphocytes and in the secretion of autoantibodies. Depleting B-cells, using specific antibodies in RR-MS patients, leads to the suppression of an inflammatory response, thus reducing the formation of new lesions.

Interestingly, our findings pointed out that, following B cell stimulation, CALCOCO2 ensures effective mitophagy thus reducing the release of a pro-inflammatory cytokine, TNF/TNF- α .

We do not exclude the possibility that, despite our findings that highlight a pro-mitophagy function of CALCOCO2^{G140E} in MS, this variant may also emerge as a novel link among 1) xenophagy, a form of selective autophagy of pathogens (such as bacteria and virus), 2) B cells and 3) viral infections known to be associated with MS (i.e., Epstein-Barr virus, one of the main environmental risk factors for MS). Hence, future studies will be required to better characterize and understand the molecular mechanisms underlying the novel function of CALCOCO2 in B cells in the context of MS.

In conclusion, our results allow us to propose a model in which the variant G140E of CALCOCO2 may prevent the release of pro-inflammatory cytokines from B cells (and maybe mitochondrial factors such as mitochondrial DNA) that trigger inflammation in MS patients and most likely in other autoimmune diseases (See [Figure 1](#)).

Altogether, this work highlights a potentially druggable mechanism that links CALCOCO2-mediated mitophagy to fine tuning pro-inflammatory signaling cascades in B lymphocytes. Small molecule development may focus on compounds enhancing/stabilizing LIR-dependent interactions between CALCOCO2 and human LC3 in B cells, thereby opening an important path for the generation of new therapeutic tools.

Disclosure statement

No potential conflict of interest was reported by the author(s).

Reference

- [1] Di Rita A, Angelini DF, Maiorino T, et al. Characterization of a natural variant of human NDP52 and its functional consequences on mitophagy. *Cell Death Differ.* 2021 Mar 15. DOI:10.1038/s41418-021-00766-3.

ONGOING PROJECTS

My current research is aimed at studying the cellular and molecular mechanisms underlying selective autophagy in two physiopathological contexts. In particular, in 2020 (the same year I applied to the CRCN-CNRS context), as a PI (under 40 years old), I was granted by the Italian Association to fight Alzheimer disease (Airalzh-Grants-for-Young-Researchers) and the Italian Association to fight Cancers (My first AIRC) in order to:

- 1) Investigate the putative beneficial role of the autophagy receptor NDP52 in the context of Alzheimer Disease (AD);**

- 2) Investigate the putative beneficial role of mitophagy inhibition in the context of resistance to Breast Cancer (BC) therapy.**

These grants provided me the necessary financial, instrumental and human resources to perform these two on-going projects described below. The two projects are carried out at the IRCCS Santa Lucia Foundation (Rome, Italy) with the help of two post-doc fellows. I thus periodically organize meetings with the team in order to evaluate the state of advancement of the projects and to plan the programmed activities.

ONGOING PROJECT N°1: A natural variant of the autophagic receptor NDP52 as a possible target for novel treatments in Alzheimer's disease (2021-2022).

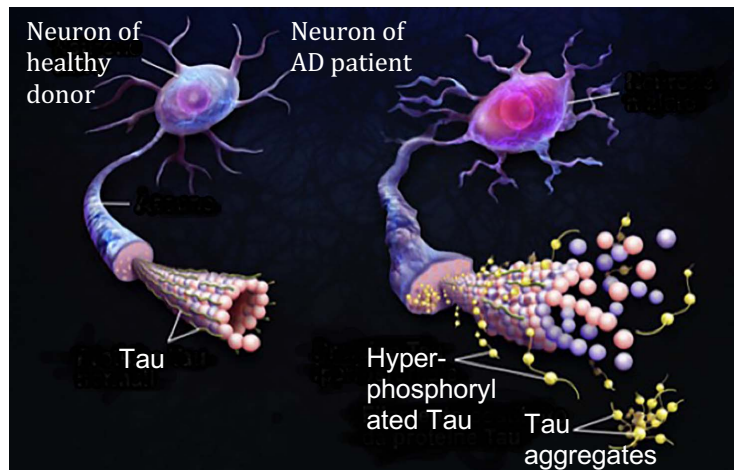


Background

In Alzheimer's disease (AD), the Tau protein (Microtubule Associated Protein Tau) becomes aberrantly phosphorylated and oligomerized, which contributes to neuronal dysfunction [1]. It is thus important to develop therapeutic approaches that may favour its selective elimination.

Figure 1: Accumulation of phosphorylated Tau is a key pathological feature of Alzheimer's disease.

Phosphorylated tau accumulation causes synaptic impairment, neuronal dysfunction and formation of neurofibrillary tangles (aggregates of Tau) that are toxic for neurons.



Pathological Tau can be degraded through the autophagic pathway [2]. During this process, an autophagy receptor directly links the cargo and brings it into a double membrane vesicle called autophagosome that fuse then with lysosome to degrade the engulfed material [3]. To do so, the autophagy receptor binds, on one side its cargo (ie: proteins, organelles) and on the other side, through a LIR (LC3-Interacting Region) motif, it binds Atg8 (autophagy-related protein 8)/LC3 (*Microtubule-associated proteins 1A/1B light chain 3B*) proteins onto autophagosome membranes in order to deliver its cargo to the autophagosomes [4]. Interestingly, NDP52 (Nuclear dot protein 5), one of the major autophagy receptors in mammals, has been found to play a potential protective role in AD pathogenesis by directly binding pathological Tau and facilitating its autophagic clearance [5] (**Figure 2**).

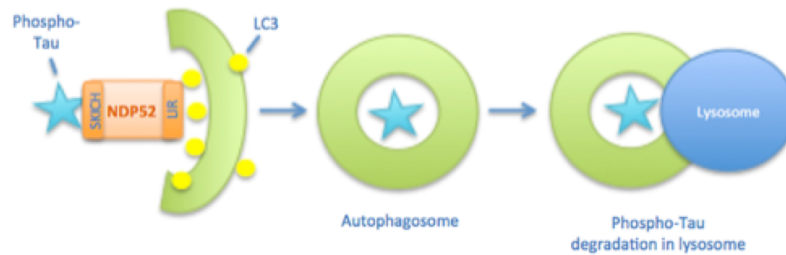


Figure 2: A schematic illustration of pathological Tau clearance mediated by the autophagic receptor NDP52.

By binding phospho-Tau through its SKICH domain, NDP52 brings pathological Tau into autophagosomes, which then fuse with lysosomes to degrade their contents.

General objectives of the project

The LIR motif of the autophagy receptors is crucial for their function in autophagy. It has been demonstrated that post-translational modifications of residues flanking the LIR motifs of known autophagic receptors are key processes regulating autophagy, by inducing specific conformational changes, that favour their binding with LC3 and thus their autophagic activity [6].

Since we found in 2021 (in the context of MS) in a natural variant of NDP52 (rs550510), an amino acid modification near its canonical LIR motif (G140E) that favours its binding with LC3 [7], we hypothesised that this amino acid change (compared to the WT form of NDP52) may modulate its binding with LC3C also in the context of neuronal cells. In addition, because NDP52 plays an important role in the clearance of phosphorylated Tau [5], we anticipated that the NDP52^{GE} variant may be able to mitigate AD disease by clearing more efficiently Tau protein compared to the WT form of NDP52, and this through its higher capacity to bind LC3C.

The project was designed to investigate this hypothesis by addressing the following issues:

- 1-Demonstrate in neuronal-like cells, that NDP52^{GE} binds more efficiently LC3C compared to the WT form of the protein;**
- 2- Demonstrate that NDP52^{GE} induces a robust clearance of phospho-tau compared to the WT form of the protein.**

We are currently concluding this project (Manuscript Mattioni et al. *in preparation*). Here bellow, a sum of the results already obtained.

Results

The cLIR motif of NDP52 is required for hTau degradation.

NDP52 is known to be a crucial autophagy receptor that facilitates the recognition of infected pathogens and damaged mitochondria [8]. Since the cLIR motif of NDP52 is required for its function in selective autophagy of these cargos, we wondered whether the effect of NDP52 on Tau clearance was cLIR-dependent. To this end, we generated a construct encoding for NDP52^{WT} lacking the LC3-binding (NDP52 V136S) [9], and we assessed its effect on Tau degradation. As expected, the point mutation V136S was sufficient to strongly reduce the binding of NDP52 with LC3C (**Figure 3A**) and interestingly, this mutation inhibits hTau degradation by NDP52. In fact, NDP52^{WT} overexpression in combination with hTau is sufficient to induce a degradation of Tau but, NDP52V136S mutant is almost unable to degrade hTau (**Figure 3B**), indicating that the LIR motif and thus the binding between NDP52 and LC3C, is required for hTau degradation.

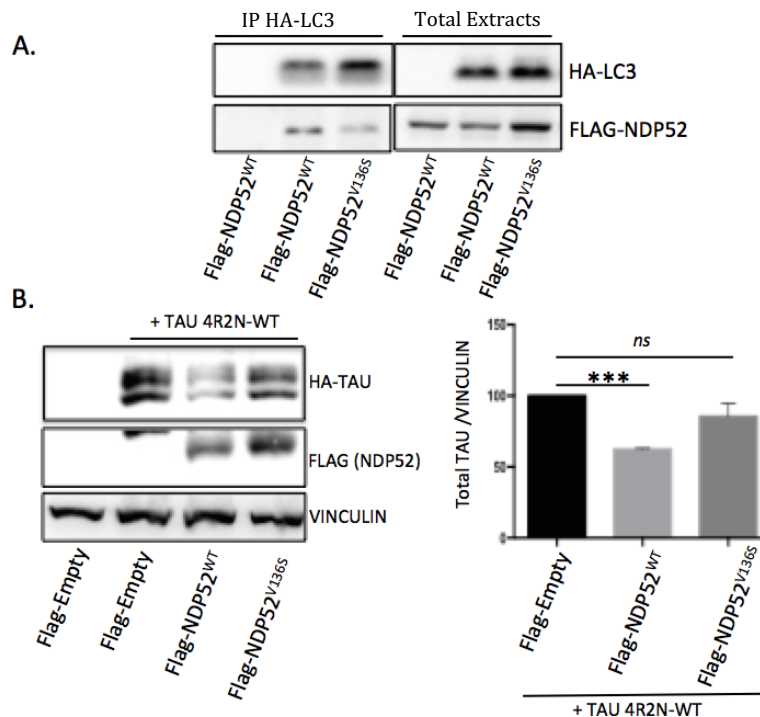


Figure 3: NDP52 requires its binding to LC3C in order to induce degradation of hTAU. A. Representative image of co-immunoprecipitation experiment in which SH-S5Y cells were co-transfected with Flag-NDP52^{WT} or Flag-NDP52^{GE} vectors in combination with HA-LC3C. We used an antibody anti-HA to immunoprecipitate LC3C. B. SH-S5Y cells were co-transfected with a Flag-empty vector, Flag-NDP52^{WT} or Flag-NDP52^{V136S} vectors in combination with the longest human brain tau protein

splice variant (HA- 4R2N-Tau). hTau levels were detected by western blot using antibody anti-HA. VINVULIN was used as loading control. The graphs represent the hTAU/VINCULIN, resulting as the mean of three independent experiments (\pm SD). Statistical analysis was performed using Student *t*-test ($***P < 0.001$; *ns*: non statistical).

NDP52GE binds more efficiently LC3C compared to the WT form of the protein also in neuronal-like cells.

Milestone 1 of Aim1 was dedicated to investigate the binding between the 2 allelic variants of NDP52 and LC3C in neuronal like cells. As predicted, we achieved this task 1. Briefly, human neuroblastoma SH-SY5Y cells were cultured in Dulbecco's modified Eagle's medium supplemented with 10% FBS at 37°C in a humidified atmosphere of 5% CO₂. We co-transfected these cells with vectors encoding Flag-NDP52^{WT} or ^{GE} with a vector encoding HA-LC3C and by performing co-immunoprecipitation (Co-IP) experiments, we analysed NDP52–LC3C interaction. As shown in **figure 4A**, we found that NDP52^{GE} binds LC3C in a higher manner compared to the WT form of the protein, confirming our previous data obtained in HEK293 cells [7]. We next reinforced these data by performing a confocal microscopy analysis in SH-S5SY cells in which we analysed the co-localization between NDP52 variants and LC3C. As shown in **figure 4B**, the co-localisation between NDP52^{GE} and LC3C is higher than with NDP52^{WT}.

Altogether, these data demonstrate that G substitution in E, at residue 140 enhances the ability of NDP52 to interact with LC3C in neuronal-like cells.

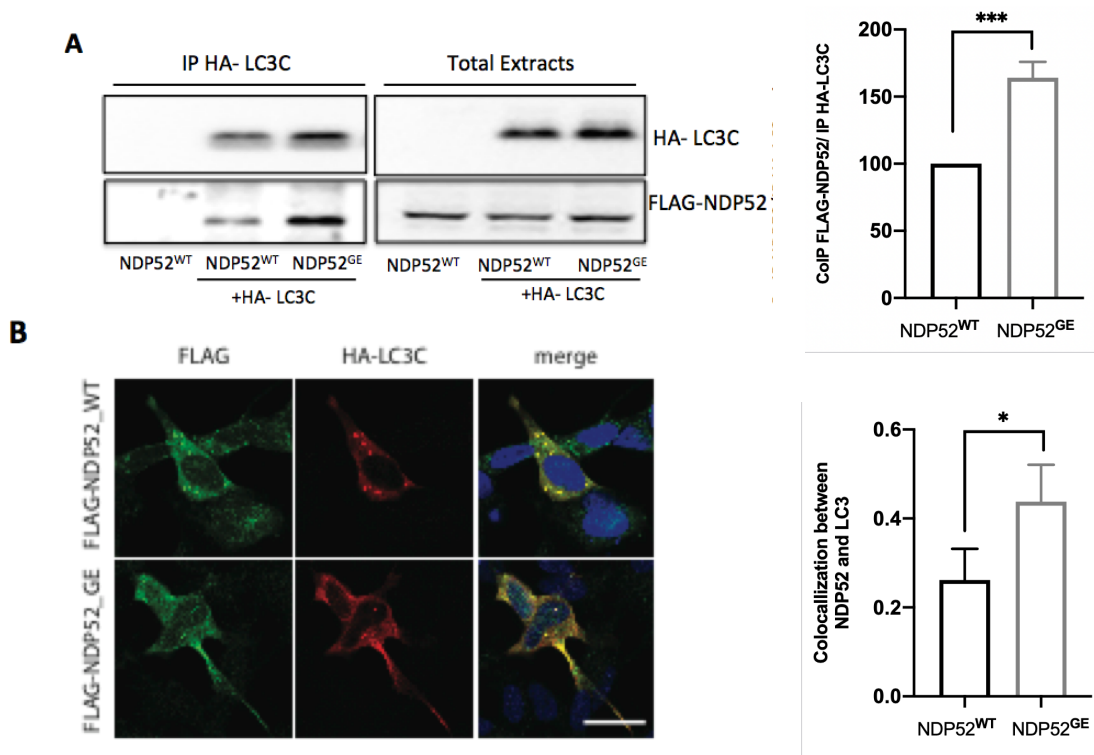


Figure 4. The NDP52 G140E variant increases NDP52-LC3C binding in neuronal-like cells.

A. Representative image of co-immunoprecipitation experiment in which SHS5SY cells were co-transfected with Flag-NDP52^{WT} or Flag-NDP52^{GE} vectors in combination with HA-LC3C. The graph represents the ratio between LC3C and NDP52 (n = 3). B. SHS5SY cells co-transfected as indicated in (A) were subjected to confocal immunofluorescence in order to evaluate LC3C-NDP52 co-localization. The graph indicates the co-localization value between LC3C and wild-type or mutant NDP52. All the quantifications resulting as the mean of at least three independent experiments (±SD). Statistical analysis was performed using Student t test (**P < 0.01). Scal bar 10 μM

NDP52^{GE} is a powerful “cleaner” of pathological tau

The fact that the cLIR motif of NDP52 is required for hTau degradation, lead us to anticipate that NDP52^{GE} may be able to enhance clearance of pathological Tau thanks to its higher binding with LC3C. In order to evaluate the effect of NDP52 variants on Tau clearance, we generated an *in vitro* model in order to mimic the accumulation of phospho-Tau in SH-S5SY cells by using Okadaic acid (Oka) treatment, an inhibitor of phosphatase-2A, the most effective phosphatase in dephosphorylating hyperphosphorylated Tau from AD brains [10,11]. We showed that treatment of SH-S5SY cells with Oka for 1h or 2h is sufficient to induce a hypermobility shifts of endogenous hTau at 50 kDa and 70 kDa which correspond to the molecular weights of the main group of isoforms of Tau (**Figure 5A**). These hypermobility shifts suggest that Tau isoforms could be hyperphosphorylated under Oka treatment. To ascertain this, we treated our cells with Oka in combination with lambda phosphatase (PP), a Mn²⁺-dependent protein phosphatase with activity towards phosphorylated serine, threonine and tyrosine residues. As shown in **figure 5B**, treatment with lambda PP is sufficient to reduce the hypermobility shifts of Tau, confirming that these shifts were due to hyperphosphorylations of Tau. We also checked the efficiency of lambda PP on a specific phosphorylation site of Tau on Serine 396, a phosphorylation known to correlate with cognitive decline in AD patients [12] and that we found up-regulated after Oka treatment (**figure 5A, C**).

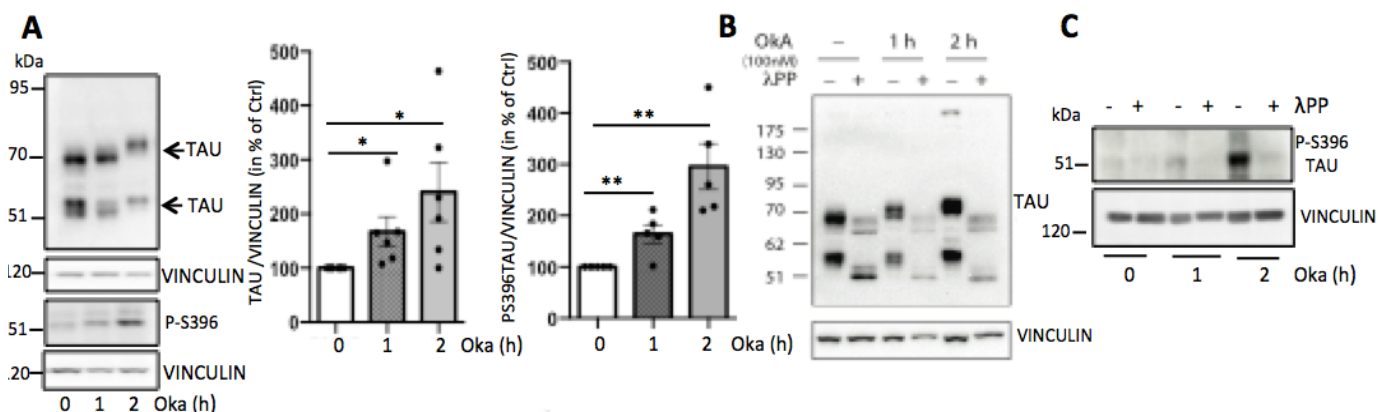


Figure 5: Okadaic Acid treatment induces hyperphosphorylation of Tau in SH-SY5Y cells.

A) Treatment of SH-SY5Y cells with Oka (100nM) induces a higher mobility shift of Tau proteins (indicating a putative hyperphosphorylation of endogenous forms of tau) as well as phosphorylation of Tau at S396, a site known to be higher phosphorylated in AD brain respect to developing brain. B) The lambda phosphatase treatment of SH-SY5Y cells in combination with Oka treatment at 1h and 2h abrogates hyperphosphorylation of Tau proteins, as well as C) the S396 phosphorylation site of Tau.

Having validated the *in vitro* model, we tested the effect of NDP52^{GE} and NDP52^{WT} overexpressions on a putative degradation of hyperphosphorylated forms of Tau in that system. As shown in **figure 6A**, SH-SY5Y cells overexpressing NDP52^{WT} and treated with Oka, show lower levels of total Tau than in control cells. Most interestingly, overexpression of NDP52^{GE} further decreases hyperphosphorylated Tau as indicated by a decrease in the mobility shift of total Tau. The graphic illustrates the quantification of total Tau on vinculin in cells expressing the empty vector or NDP52 variants. These data indicate that the variant NDP52^{GE} is a powerful “cleaner” of pathological Tau and thus could be a protective factor for AD.

We are currently showing that this effect of NDP52^{GE} is autophagy-dependent through the generation of a construct encoding for NDP52^{GE} lacking LC3-binding and assessing its effect on Tau degradation. In addition, by performing confocal microscopy analysis we observed that the NDP52^{GE} variant has a powerful effect on P-S396 Tau since almost no accumulation of P-S396 Tau was found in NDP52^{GE}-positive cells under Oka treatment (**Figure 6B**).

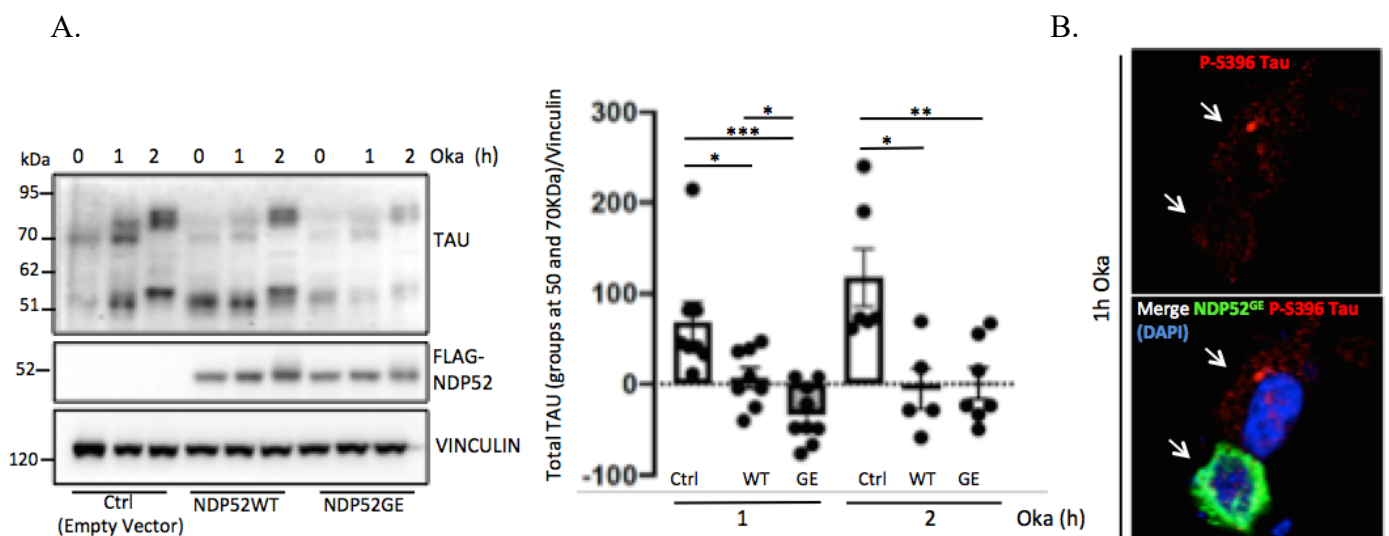


FIGURE 6. NDP52^{GE} favours degradation of pathological Tau in a higher manner than NDP52^{WT}. A) SH-SY5Y cells overexpressing FLAG-NDP52^{WT} or -^{GE} were treated with Oka and we checked for Tau accumulation in these cells. As illustrated on the western-blot and the corresponding

graphic, NDP52^{GE} clears more efficiently hyperphosphorylated tau compared to NDP52^{WT} following Oka treatment. B) Illustration of the powerful effect of NDP52^{GE} on P-396-Tau clearance under Oka treatment (arrows indicate untransfected- versus NDP52-transfected cell (green)). All the quantifications are the mean of three independent experiments (\pm S.D.). Statistical analysis was performed using Student t-test (* P <0.05; **<0.01; ***<0.001).

In sum, our data indicate that G substitution in E, at residue 140 enhances the ability of NDP52 to interact with LC3C also in neuronal-like cells. Moreover, we demonstrated that NDP52^{WT} favours degradation of phospho-Tau and that NDP52^{GE} robustly degrade Tau protein compared to NDP52^{WT}. The higher ability of NDP52^{GE} to drive pathological tau degradation seems to indicate that the point mutation near the LIR motif of NDP52 is essential for optimal tau clearance. These results indicate that the variant NDP52^{GE} is a powerful and promising candidate able to mitigate the early events of AD disease and thus could be a novel target to improve the quality of life of AD patients.

These data prompted us to directly move to an *in vivo* model of AD in order to obtain the proof-of-concept that 1) NDP52^{WT} may be able to reduce neuronal Tau toxicity *in vivo* and 2) the NDP52^{GE} variant may enhance this beneficial effect of NDP52 on AD.

Since *Drosophila* has been extensively used to study Tau biology, we generated transgenic drosophila co-expressing NDP52^{WT} or ^{-GE} and human Tau (in collaboration with GL. Cestra, CNR- Rome and Best Gene Inc Compagny, USA). For this we cloned NDP52^{WT} and ^{-GE} into the pUASTattB vector and generated UAS-hNDP52^{WT} or ^{-GE} *Drosophila* fly lines. Next, we crossed these lines with UAS-hTAU (2N4R) flies and used the eye-specific Eyeless-Gal4 promoter to expressed hTAU and NDP52 genes in the eyes.

The expression of human Tau in the eyes of *drosophila* (which represent a simple nervous system) is known to generate an abnormal eye phenotype, named “rough eye” and this is due to neuronal Tau toxicity (**Figure 7**).

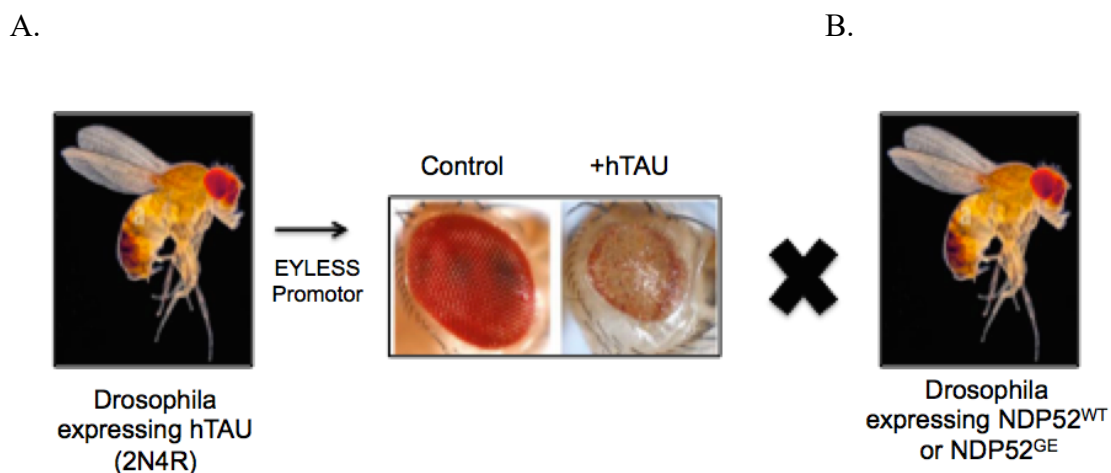


Figure 7. hTau in the eyes of *Drosophila* induces rough eyes.

A. Accumulation of phospho-Tau in the eyes induces neuronal death and “rough eyes” of the transgenic

drosophila. B. We crossed Drosophila fly lines transgenic for NDP52 variants with UAS-hTau (2N4R) Drosophila fly line, a well-known AD model.

We first checked in our new transgenic drosophila for NDP52 expression. Both variants of NDP52 are well expressed in Drosophila using the eye-specific Eyeless-Gal4 promoter. Moreover, we did not detect any sign of eye alteration following NDP52 expression in the eyes (data not shown). We next monitored adult eye morphology in drosophila expressing hTau alone or in combination with NDP52^{WT} or ^{-GE}. As expected, we found that the co-expression of NDP52 increased the area of the eyes compared to hTau controls, and that NDP52^{GE} ameliorates this phenotype better than NDP52^{WT} (**Figure 8A, B**).

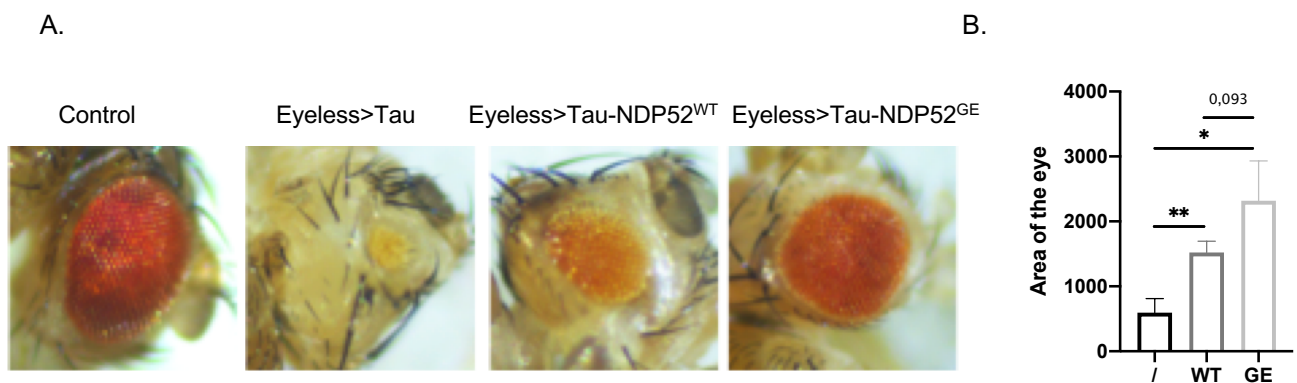


Figure 8: NDP52 expression improves the Tau Rough Eye Phenotype

A. Images of adult eye morphology in drosophila expressing hTau alone or in combination with NDP52^{WT} or ^{-GE}. **The overexpression of hTAU in Drosophila eyes using the eye-specific EYEless-GAL4 promoter decreased eye size.** The Eye specific overexpression of NDP52 WT or GE together with hTau increased eye size relative to hTau controls. B. The graph represents the area of the eye quantification. Statistical analysis was performed using Student t-test (*P<0.05; **<0.01; ***<0.001; ****<0.0001).

Conclusion

Altogether, this work is very innovative because it highlights the contribution of a specific polymorphism of NDP52 in the pathology of AD, thus tackling a new subject both in the field of autophagy and AD. In particular, the project has demonstrated that G substitution in E, at residue 140 enhance the ability of NDP52 to interact with LC3C in neuronal cells. Moreover, we found that NDP52^{GE} robustly degrades Tau protein compared to NDP52^{WT}. The higher ability of NDP52^{GE} to drive pathological Tau degradation indicates that the point mutation near the LIR motif of NDP52 is essential for optimal Tau clearance. Finally, we discovered for the first time that NDP52 is beneficial in

an *in vivo* model of AD and that the variant NDP52^{GE} is able to almost completely recover eye phenotype of AD's *Drosophila*. **This project turns the spotlight on NDP52^{GE}, as a powerful “cleaner” of pathological Tau and thus as a potential protective factor for AD.**

References

1. Ballatore, C., Lee, V. M. & Trojanowski, J. Q. Tau-mediated neurodegeneration in Alzheimer's disease and related disorders. *Nat. Rev. Neurosci.* 8, 663–672 (2007).
2. Yipeng Wang, Marta Martinez-Vicente, Ulrike Krüger, Susmita Kaushik, Esther Wong, Eva-Maria Mandelkow, Ana Maria Cuervo, Eckhard Mandelkow. Tau fragmentation, aggregation and clearance: the dual role of lysosomal processing *Hum Mol Genet.* Nov 1; 18(21): 4153–4170 (2009).
3. Dikic I, Elazar Z. Mechanism and medical implications of mammalian autophagy. *Nat Rev Mol Cell Biol.* Jun;19(6):349-364 (2018).
4. Johansen, T. & Lamark, T. Selective autophagy mediated by autophagic adapter proteins. *Autophagy* 7, 279–296 (2011).
5. Chulman Jo, Soner Gundemir, Susanne Pritchard, Youngnam N. Jin, Irfan Rahman, Gail V.W. Johnson. Nrf2 reduces levels of phosphorylated tau protein by inducing autophagy adaptor protein NDP52. *Nat Commun.* Sep 25. 5: 3496. (2014)
6. Brigisdottir Asa Birna, Johansen Terje. Lamark Trond, The LIR motif-crucial for selective autophagy. *J Cell Sci.* Aug 1;126:3237-47 (2013).
7. Di Rita A, Angelini DF, Maiorino T, Caputo V, Cascella R, Kumar M, Tiberti M, Lambrughini M, Wesch N, Löhr F, Dötsch V, Carinci M, D'Acunzo P, Chiurchiù V, Papaleo E, Rogov VV, Giardina E, Battistini L, Strappazzon F. Characterization of a natural variant of human NDP52 and its functional consequences on mitophagy. *Cell Death Differ.* Aug;28(8):2499-2516 (2021).
8. Kim BW, Kwon DH, Song HK. Structure biology of selective autophagy receptors. *BMB Rep.* Feb;49(2):73-80 (2016).
9. Padman BS, Nguyen TN, Uoselis L, Skulsuppaisarn M, Nguyen LK, Lazarou M. LC3/GABARAPs drive ubiquitin-independent recruitment of Optineurin and NDP52 to amplify mitophagy. *Nat. Commun.*;10:408 (2019).
10. Zhang Z, Simpkins JW. Okadaic acid induces tau phosphorylation in SH-SY5Y cells in an estrogen-preventable manner. *Brain Res.* Jul 23;1345:176-81 (2010).
11. Voronkov M, Braithwaite SP, Stock JB. Phosphoprotein phosphatase 2A: a novel druggable target for Alzheimer's disease. *Future Med Chem.* May;3(7):821-33 (2011).
12. Petersen RC. Mild cognitive impairment as a diagnostic entity. *J Intern Med.* Sep;256(3):183-94 (2004).

ONGOING PROJECT N°2: Dissecting the role of mitophagy in breast cancer therapy resistance



The duration of this project is 5 years (2020-2025).

State-of-the-art

Breast cancer (BC) is the most frequently diagnosed cancer in women and its treatment remains challenging due to drug resistance [1]. It is thus crucial to discover new players in this context in order to provide new therapies for durable disease remission and long-term survival of cancer patients. Several reports suggested that mitophagy, a selective form of autophagy aimed to degradate damaged mitochondria, contributes to drug resistance in several cancers such as Melanoma, Glioma or colorectal cancer [2,3,4]. In the context of BC, Liensinie, an isoquinoline alkaloid, sensitizes BC cells to chemotherapy by accumulating autophagosome/mitophagosomes, suggesting a putative block of autophagy/mitophagy by this agent [5]. **However, the role of mitophagy in BC treatment remains largely unclear and this is due in part to the fact that specific inhibitors of this selective autophagy, are lacking.** The main mitophagy path described today is governed after the activation of the PINK1 kinase and the E3 Ubiquitin ligase Parkin. After mitochondrial damage, PINK1 accumulates in the outer mitochondrial membrane (OMM) and this in turn, allows PINK1-dependent recruitment of Parkin and activation of its E3 ubiquitin ligase activity, which is followed by the ubiquitination of different OMM substrates. Afterwards, ubiquitin signalling induces the recruitment of mitophagy cargo receptors capable of delivering mitochondria into double membrane vesicles called autophagosomes, which fuse then with lysosome to degrade their contents [6]. In 2021, we discovered that miR-218, a small non-coding RNAs, is a powerful inhibitor of mitophagy in mammalian cells. We reported that miR-218 expression reduces Parkin mRNA and protein levels and deregulates its E3 ubiquitin ligase action. Consequently, following mitochondrial stress, miR-218 expression is sufficient to reduce ubiquitylation of mitochondria and the autophagy machinery fails to proceed with a correct mitochondrial clearance [7]. Interestingly, miR-218 expression has been found reduced in BC cells and its expression favours cell death of BC cells [8]. However, its role as a putative tumor

suppressor in vivo and in cancer treatment resistance has not been yet investigated.

Preliminary data

Since we demonstrated that miR-218 impairs mitophagy in HEK293 by inhibiting Parkin expression [7], we hypothesized that miR-218 expression could inhibit mitophagy also in BC cells and this could be a way to deprive cells from energy (blocking the removal of mitochondria), to favour accumulation of reactive oxygen species (ROS) and thus their death. To test this hypothesis, we checked, by performing qPCR (**Figure 1A**) and western-blot analysis (**Figure 1B,C**), whether miR218 was able to target Parkin expression also in breast cancer MCF7 cells. As shown in Figure 1, miR-218 is able to inhibit Parkin expression in MCF7 cells as well.

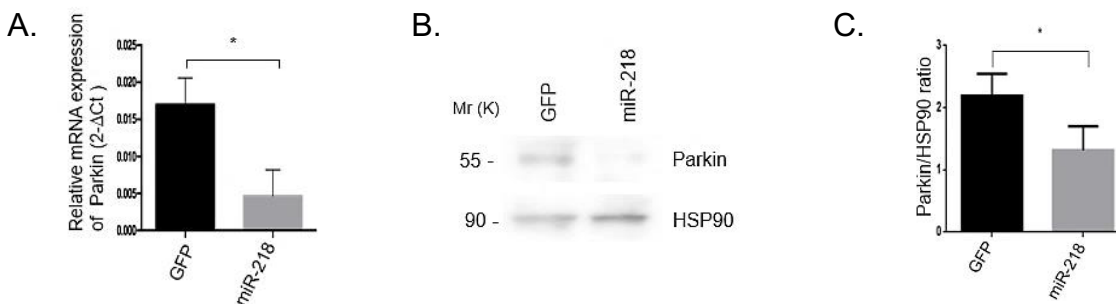


Figure 1: miR-218 targets Parkin in BC MCF7 cells

A) qPCR analysis representative graph of mRNA level of Parkin in control *versus* miR-218 transfected cells. Normalization of Parkin was done on B2M (loading control). (B, C) Western blot analysis of the protein level of Parkin in control *versus* miR-218 overexpressing cells and the representative graph of Parkin/HSP90 ratio (HSP90 was used as loading control). All data represent the mean of experimental triplicate (\pm s.e.m.). Statistical analysis was performed using t-test * $p < 0.05$.

We next investigated whether miR-218 was able to block mitophagy in BC cells. As shown in **Figure 2 A,B** cells overexpressing miR-218, upon mitophagy induction (Oligomycin/Antimycin (O/A) treatment), show a higher level of the two mitophagy markers (MnSOD and TOMM20), compared to control GFP positive cells, indicating an inhibition in the mitochondrial clearance pathway.

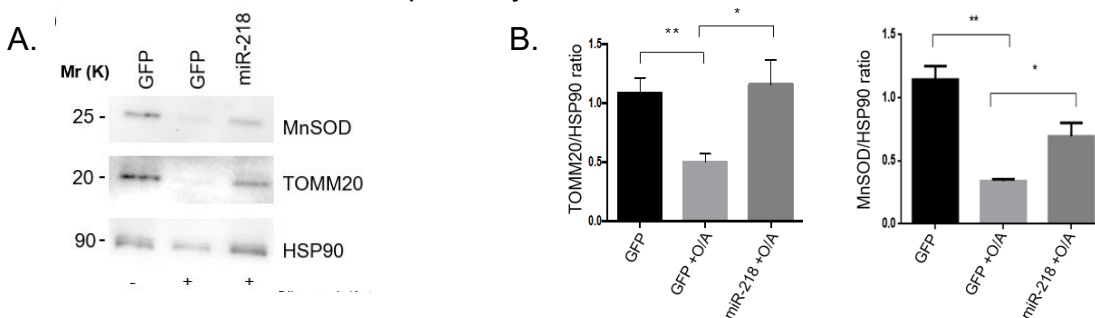


Figure 2: miR-218 inhibits mitochondrial clearance induced by O/A treatment in MCF7 cells. Western blot analysis image of MnSOD and TOMM20 protein level of MCF7 transfected cells treated with O/A (10 μ M; 4 μ M), overnight and the corresponding graphs for MnSOD and TOMM20 protein level normalized on HSP90 (loading control), representing the mean of experimental triplicate (\pm s.e.m.). Statistical analysis was performed using Bonferroni corrected t-test. * $p < 0.05$; ** $p < 0.01$.

We strengthen our results by performing a confocal microscopy analysis. For this, transfected GFP or GFP-miR-218 cells have been subjected to O/A treatment. Untreated cells show a normal mitochondria network (TOM20, red staining) typical of cells grown in normal condition. Meanwhile, upon stimulation of mitophagy (+O/A), mitochondria content is decreasing in GFP positive cells but expression of miR-218 is sufficient to block the mitochondrial clearance (**Figure 3 A, B**).

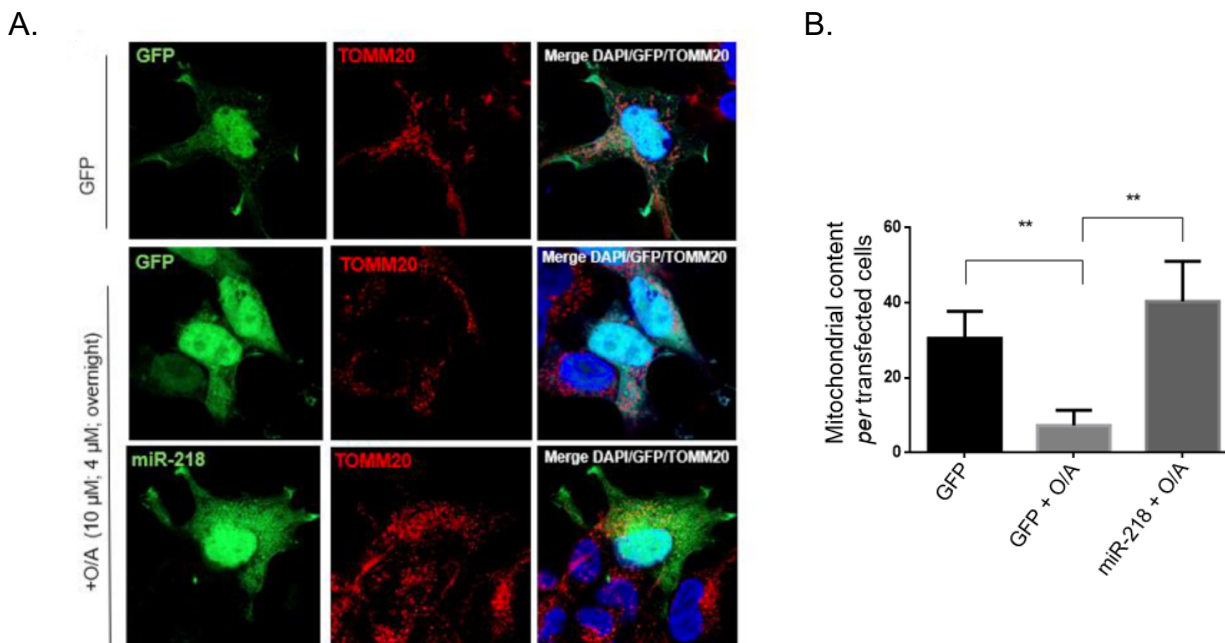


Figure 3. miR-218 inhibits mitophagy induced by O/A in MCF7 cells. A) Confocal microscopy analysis of MCF7 cells transfected with GFP or GFP-miR-218, treated or not with O/A (10 μ M; 4 μ M; overnight) and stained for mitochondria (TOMM20). B) The content of mitochondria/ cells was evaluated in 3 independent experiments in transfected cells. Statistical analysis was performed using Bonferroni corrected t-test. * $p < 0.05$; ** $p < 0.01$.

We next hypothesized that Doxorubicin (DXR), a common chemotherapeutic agent in cancer treatment, which has been shown to induce mitophagy in Cancer Stem Cells (CSC) of colorectal cancer [3], may stimulate mitophagy in BC cells and that miR-218 could block this putative mitophagy. As illustrated in **figure 4 (A-D)**, DXR treatment of MCF7 cells favours mitochondria clearance and underline miR-218 as a novel inhibitor of mitophagy induced by DXR.

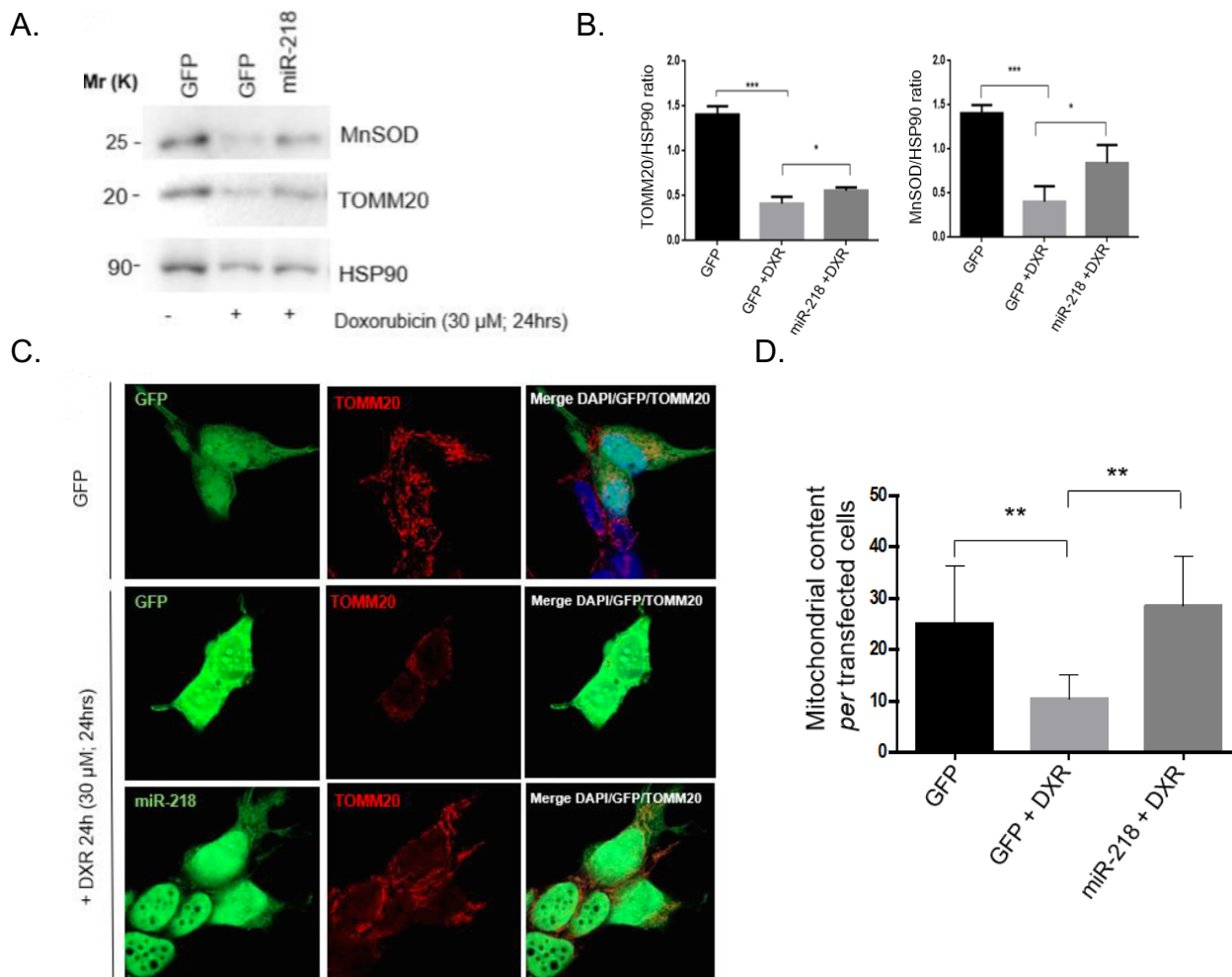


Figure 4. miR-218 inhibits Doxorubicin-induced mitophagy in MCF7 cells. A. Western blot images of mitophagy related proteins, MnSOD and TOMM20 in GFP versus miR-218 transfected cells in basal condition and following DXR treatment (30 μ M; 24hrs) B. Representative graphs of the protein level of MnSOD and TOMM20 normalized on HSP90 representing the mean of experimental triplicate (\pm s.e.m.). C-D. Immunofluorescence analysis and corresponding graph of mitochondria content in GFP and miR-218 transfected cells. Statistical analysis was performed using Bonferroni corrected t-test. . * $p < 0.05$; ** $p < 0.01$.

We next anticipated that miR-218, by blocking mitophagy may favor cell death induced by DXR treatment. Indeed, our preliminary data suggest that, by inhibiting mitophagy, miR-218 improves DXR-mediated cell death (figure 5A, B). Such data point the possible and promising role of mitophagy inhibition in improving treatment efficiency in BC.

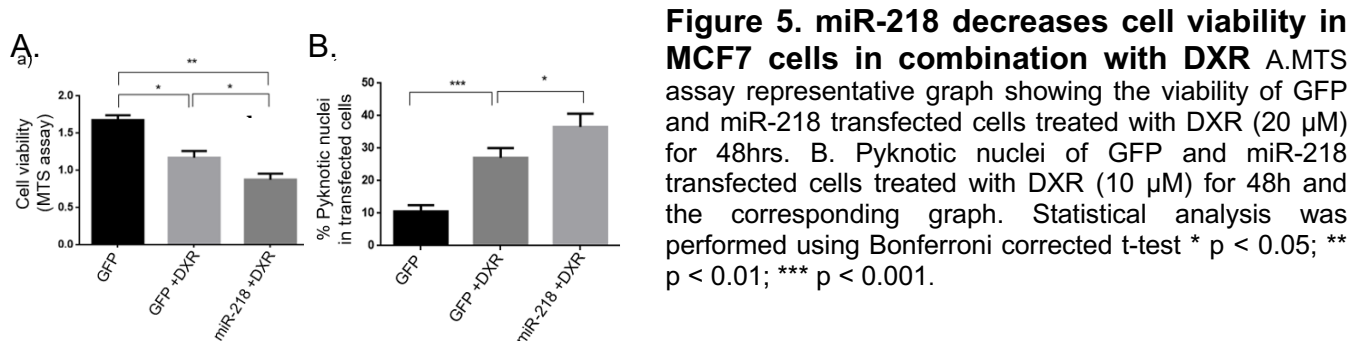


Figure 5. miR-218 decreases cell viability in MCF7 cells in combination with DXR A. MTS assay representative graph showing the viability of GFP and miR-218 transfected cells treated with DXR (20 μ M) for 48hrs. B. Pyknotic nuclei of GFP and miR-218 transfected cells treated with DXR (10 μ M) for 48h and the corresponding graph. Statistical analysis was performed using Bonferroni corrected t-test * $p < 0.05$; ** $p < 0.01$; *** $p < 0.001$.

At this point we hypothesised that *PARKIN* expression may be correlated to DXR-resistance in patients affected with BC. To place *PARKIN* in a wider context of molecular connections, we preliminary combined the mitophagic genes from three lists of relevant human genes in public databases (Gene Ontology, KEGG, Reactome): by this analysis we found that *PARKIN* is part of a complex biological network of 101 highly connected proteins (prot-prot interaction enrichment $p\text{-value} < 1.0 \times 10^{-16}$, StringDB database).

Overall, our preliminary data indicated that miR-218 targets Parkin and impair mitophagy in MCF7 cells. Most importantly, we discovered that DXR treatment of MCF7 BC cells induces mitophagy, suggesting that mitophagy induction could be a pro-survival path induced by DXR, hence favoring drug resistance. **We here anticipate that BC cells may avoid the effect of drug treatment by enhancing their mitophagy activity. Our goal is to identify a novel relationship between mitophagy gene expressions and drug resistance in BC cells and to mechanistically confirm our hypothesis by interfering with mitophagy proteins in BC (i.e Parkin) and to investigate cell response to drug treatment.**

The project was designed to investigate this hypothesis by addressing the following issues:

1. Demonstration that it exists a relationship between mitophagic genes and DXR resistance.
2. Demonstration that DXR induces mitophagy PINK1-Parkin dependent in two luminal subtypes of cell lines, MCF7 and SKBR3 and a basal subtype cell line, MDA-MB-231 cells and in stem like cells growth as mammospheres.
3. Demonstration that mitophagy inhibition through miR-218 expression can improve the sensitivity to the chemotherapeutic agent DXR in BC cell lines. In this context we will elucidate which molecular mechanism is responsible for cell death increase. The same study will be performed in stem like cells growth as mammospheres derived from BC cells
4. Demonstration, *in vivo*, using conditional miR-218 knock-out mice that miR-218 expression could be crucial to fight mammary tumors
5. Considering that nanoparticles (NPs) offer excellent opportunities for cancer cell specific controlled delivery of miRNAs but also for chemotherapeutic agents, we plan to synthesize miR-218/DXR NPs and to intratumorally inject them to target, *in vivo*, the mitophagy PINK1/Parkin-dependent and to improve therapy efficiency in a BC mouse model.

Impact: By performing a global mitophagy genes analysis, the project has a high potential to demonstrate that it may exist a strong relationship between expression of mitophagic genes and DXR resistance. Mitophagy genes could thus become novel specific targets for BC treatment. In 2020 my team discovered a powerful inhibitor of mitophagy (miR-218) that will be used in the present project in order to interfere with the mitophagic E3 ubiquitin ligase Parkin. To the best of our knowledge, this project could be the first report able to demonstrate the effectiveness of specific mitophagy inhibition in BC therapy. Indeed, blocking this ligase might make cancer cells more sensitive to DXR treatment in BC cells *in vitro* and *in vivo* both in stem and non-stem BC cells. Our approach will combine two ways of tumor cell killing (mitophagy inhibition and chemotherapy) and could represent a new strategy for clinical practice when injecting nanoparticles intratumorally. Moreover, by using conditional miR-218 KO mice, we could provide the innovative proof-of-concept that miR-218 is involved, *in vivo*, in BC tumorigenesis. Also, by using miR-218/DXR nanoparticles, we hope to target both tumors and their resident stem cells and this could have the potential to improve survival of patients. If successful, this proposal will thus not only enhance our knowledge on the mitophagic process related to BC cells but will also provide novel target for therapeutic intervention.

Experimental Design and results

TASK1. Is there a relationship between mitophagic genes and DXR resistance in breast cancer?

Description/methods

Resistance to DXR is the most common clinical problem in breast cancer therapy, and the underlying molecular mechanisms remain to be investigated. With this task we aim to demonstrate that mitophagy-induced by DXR may be a novel way of resistance to chemotherapy. This part of the project could provide crucial information of how parental BC cells but also stems like cells could resist to therapy.

Milestone a. Does mitophagic genes are found up-regulated in BC patients treated with DXR?

In order to investigate whether mitophagic genes may be modulated in BC patients treated

with DXR, we performed a bioinformatical analysis in collaboration with Dr Ivan Arisi, a Bioinformatics scientist (EBRI, Rome, Italy). To this end, the list of mitophagic genes has been extracted from several lists of RNA profiles coming from BC patients from the KEGG, Reactome and AmiGO databases using the mitophagy-related keywords. We analyzed the expression of main mitophagic genes (ie: *PINK1*, *PARKIN*, *NDP52*, *OPTN*, *p62*, *AMBRA1*, *LC3* etc.) in transcriptomic datasets extracted from the Gene Expression Omnibus and ArrayExpress public databases and from the scientific literature. Filtered normalized expression data downloaded from these databases have been analyzed by R-Bioconductor. Differentially expressed genes have been selected using the R packages Limma for microarray data and edgeR or DESeq2 for RNA-Seq data. As illustrated in **figure 6** the main genes involved in PINK1-mediated mitophagy such as the kinase PINK1, the autophagic receptor Optineurin (OPTN), LC3B (MAP1LC3B), GABARAPL2 or TBK1 are found up-regulated following DXR treatment in MCF7 cells suggesting that this pathway may be stimulated.

Interestingly, our analysis indicates that a part of these genes are up-regulated in the polysomal fraction, suggesting that mitophagic gene levels may be finely regulated during DXR response in BC cells and thus that the mitophagy response may be finely regulated at the transcriptional and translational levels.

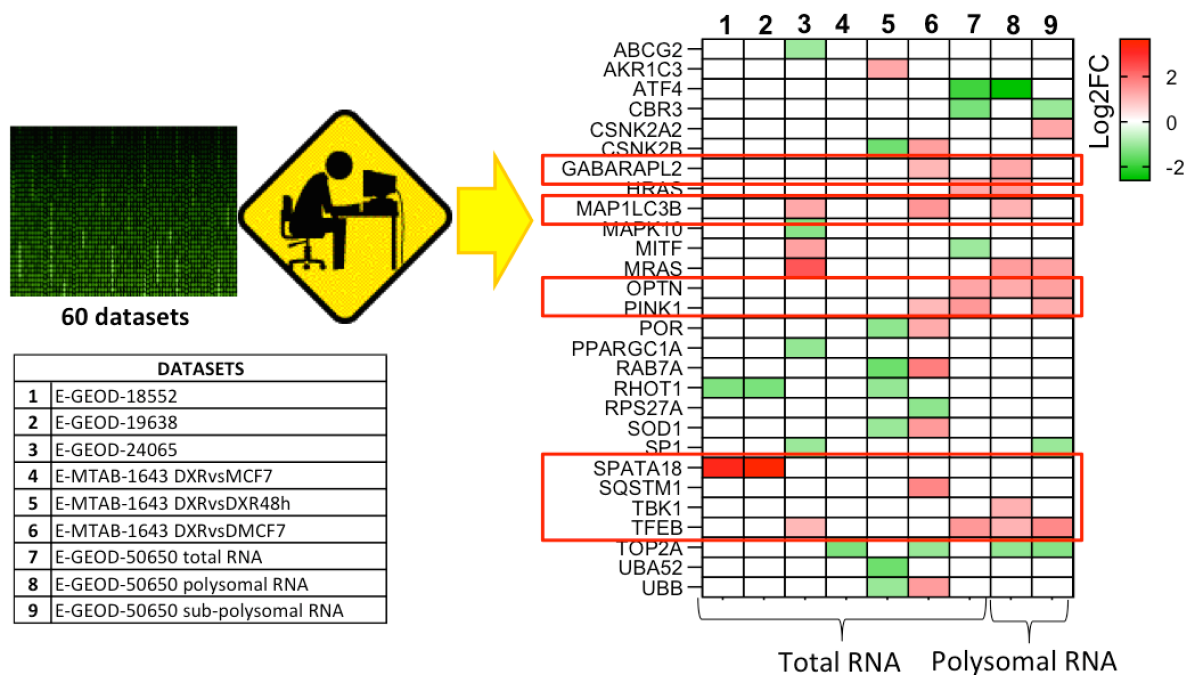


Figure 6. DXR treatment modulates mitophagy-related genes expression in MCF7 BC cells. Heatmap showing the fold change expression of representative mitochondrial quality control/autophagy-related genes in MCF7 cells treated with different timings and concentrations of DXR vs untreated culture. Up-regulated genes are shown in red, down-regulated genes are in green. The table

shows the datasets used for the analysis.

Milestone b. Does mitophagic gene expression increase in BC cells following DXR treatment?

We next analysed the effect of DXR treatment on mitophagy gene expression, on MCF7 cells. For this, we treated human MCF7 cells with DXR and by performing a microarray analysis, we evaluated a potential increase of genes encoding key proteins regulating the mitophagy pathway in the cells treated with DXR compared to control cells treated with vehicle. Briefly, RNA has been extracted from these cells, three biological replicas have been produced and the analysis has been performed in collaboration with Dr M. D’Onofrio (EBRI, Roma, Italy). Of note, the same procedure will be repeated on MCF7 resistant to DXR (generation of these cells in progress) and on MCF7 cells grown as mammospheres (in progress).

Our data indicate that around 5000 genes are up- or down-regulated following DXR treatment. Among genes up regulated, we confirmed, in our hands, that the kinase PINK1 is up-regulated together with LC3B and p62 (**Figure 7**). Interestingly MFN1 and 2, two genes, involved in the elongation of mitochondria, appeared down-regulated, supporting the idea of the presence of a fragmented mitochondrial network (which is required for mitophagy).

Symbol	Log2fc	FDR
ATG12	■	1.3E-14
ATG5	■	8.0E-09
CSNK2A1	■	6.4E-13
CSNK2A2	■	4.5E-16
CSNK2B	■	4.4E-17
FUNDC1	■	1.7E-04
MAP1LC3B	■	5.3E-13
MFN1	■	5.2E-14
MFN2	■	5.3E-11
MTERF3	■	3.0E-10
PGAM5	■	3.2E-12
PINK1	■	1.7E-05
RPS27A	■	2.2E-17
SQSTM1	■	1.1E-07
SRC	■	1.5E-15
TOMM20	■	8.9E-12
TOMM22	■	1.5E-16
TOMM40	■	7.3E-10
TOMM5	■	2.7E-16
TOMM6	■	3.0E-16
TOMM7	■	4.0E-19
TOMM70	■	8.2E-17
UBA52	■	1.9E-20
UBB	■	5.9E-05
UBC	■	1.6E-20
ULK1	■	2.4E-13
VDAC1	■	3.6E-17

Figure 7. PINK1-mediated mitophagy genes expression are up-regulated in MCF7 treated with DXR. The table shows the mitophagy-related gene list from the database Reactome. Fold change of each gene has been represented with bar green (down-regulated) and red (up-regulated). FDR values are shown.

We are currently validating up-regulation of mitophagic genes by carrying out by qRT-PCR on BC cells treated or not with DXR. We next plan to downregulate the candidate genes with siRNAs and to evaluate the putative cell death improvement by performing MTT assays and quantifying, by microscopy, the pycknotic nucleci in transfected cells.

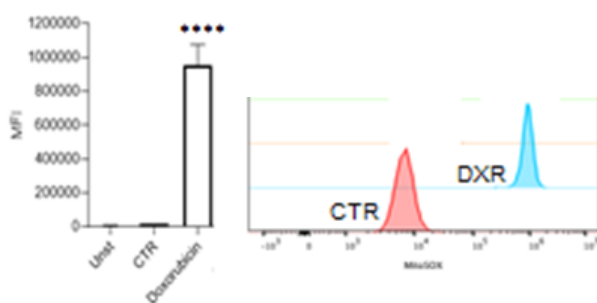
TASK2. Does DXR induce mitophagy PINK1-Parkin dependent in BC cells and in stem like cells derived from parental BC cells?

Description/methods

Interestingly, we discovered that DXR treatment of MCF7 BC cells induces the clearance of two mitochondrial markers (**Figure 4**). Since mitophagy is often acting as a prosurvival pathway, this suggests that induction of mitophagy could be a DXR-induced pro-survival pathway, thereby promoting drug resistance.

Here we confirmed that DXR induces mitophagy dependent of PINK1/Parkin, in the luminal subtype of cell line MCF7 (we are also checking this aspect in the basal subtype, triple negative cell line MDA-MB-231). By performing FACS analysis and confocal microscopy, we found that DXR treatment induces mitochondrial superoxide generation and mitochondrial degradation in MCF7 cells (**Figure 8**).

A.



B.

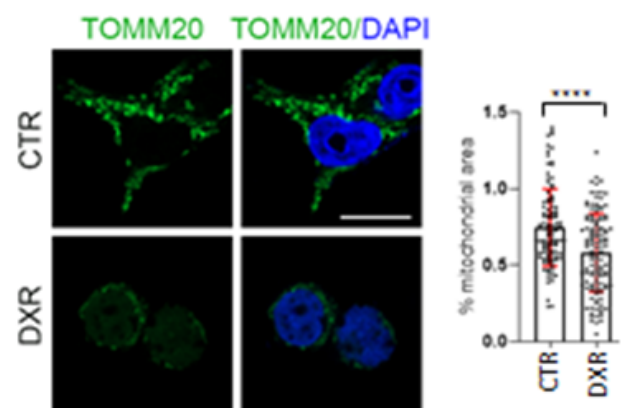


Figure 8. DXR treatment induces ROS generation and mitochondria degradation. A. FACS analysis of mitochondrial superoxide (MitoSOX). The histogram shows the intensity of the signal in the indicated condition. B. Illustration of the mitochondrial network in untreated (CTR) and treated (DXR) cultures. The graph shows the area of mitochondrial network quantified in the indicated condition. Standard deviations (S.D.) are shown in red. Statistical analysis was performed using one way ANOVA (A) and Mann-Whitney test (B); **** $p < 0.0001$.

We next check for autophagosome formation following DXR treatment through confocal microscopy analysis using anti-LC3 antibody. As shown in **Figure 9**, DXR induces LC3 dots formation that is further increased with Ammonium chloride (NH_4Cl), a well-known autophagy inhibitor, confirming that an autophagy flux is induced following DXR treatment in BC cells.

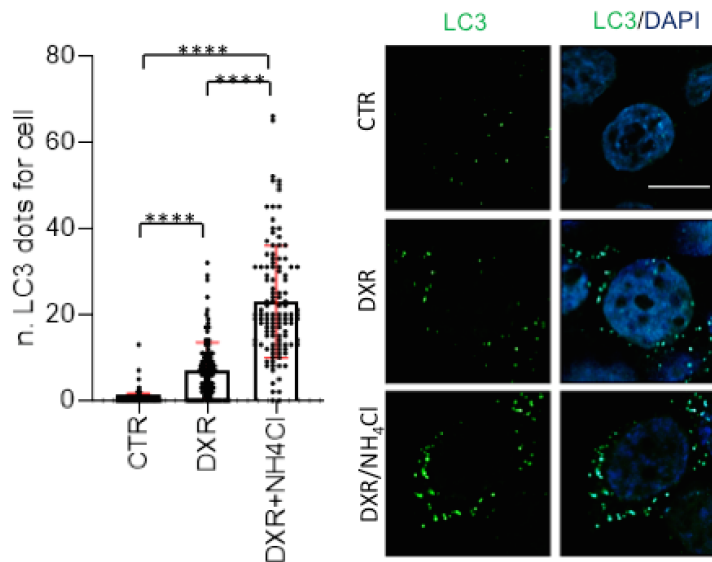


Figure 9. DXR induces LC3 dots formation. Each dot in the graphic represents the number of autophagosomes for cell. Standard deviations (S.D.) are shown in red. Images illustrate LC3 dots accumulation following DXR treatment and NH_4Cl . Statistical analysis was performed using t-test **** $p < 0.0001$.

To ascertain that mitochondria degradation is occurring through the autophagy/lysosomal degradation, we treated our cells with NH_4Cl . As shown in **Figure 10**, NH_4Cl treatment is sufficient to inhibit degradation of both COXII and COXIV, confirming that mitochondria are degraded through the autophagy pathway following DXR treatment.

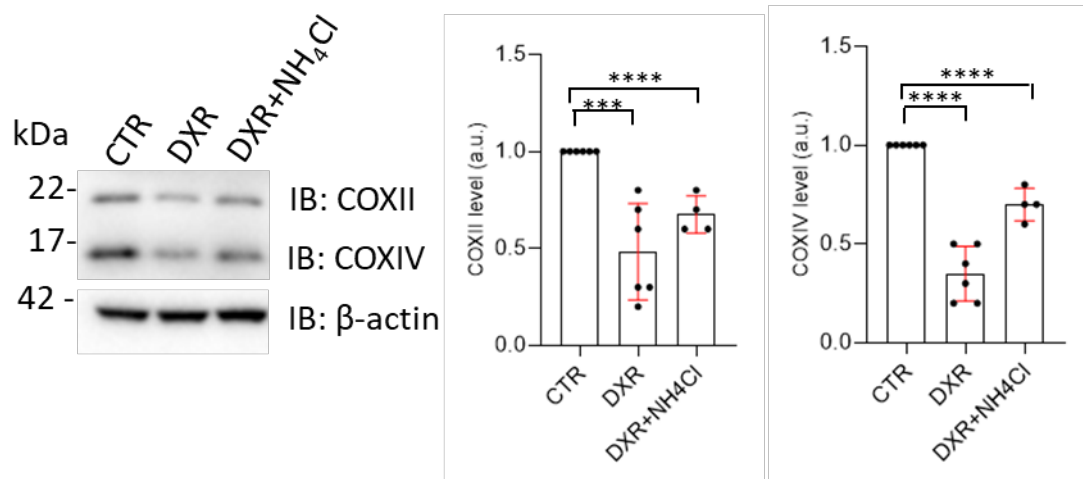
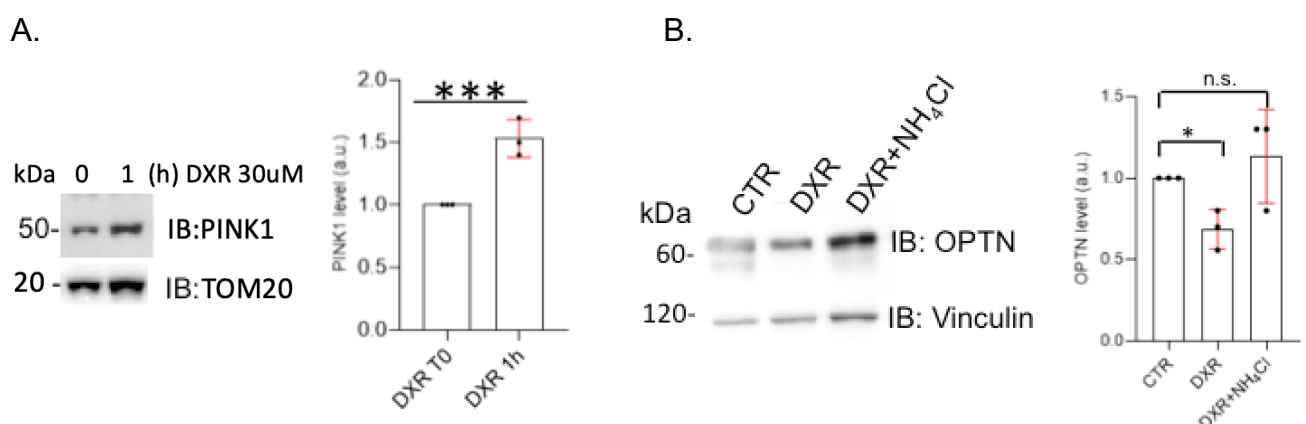


Figure 10. DXR-mediated mitochondria degradation requires autophagy. Western blot analysis of mitochondrial markers in cells treated with DXR and DXR+NH₄Cl. Histograms represent the mean of at least 4 experimental replicates of COXII and COXIV level normalised with Actin, in treated (DXR or DXR+NH₄Cl) vs untreated sample (CTR). Standard deviations (S.D.) are shown in red. Statistical analysis was performed using t-test ***p<0.001; **** p<0.0001.

Afterwards we checked for PINK1 accumulation on mitochondria following DXR, which is a hallmark of mitophagy induction together with the modulation of the two main mitophagic receptors involved in PINK1-mediated mitophagy, which are NDP52 and Optineurin (OPTN). As expected, PINK1 levels increase following DXR treatment and both NDP52 and OPTN levels are accumulating following DXR treatment in combination with NH₄Cl, indicating that these two autophagic receptors are involved in the mitophagic pathway stimulated by DXR.

To reinforce these data, we are currently analysing PINK1 activity (phospho-PINK1) and the translocation of the E3 Ubiquitin ligase Parkin to mitochondria after DXR treatment. We are also testing the potential induction of mitophagy in stem like cells growth as mammospheres [8].



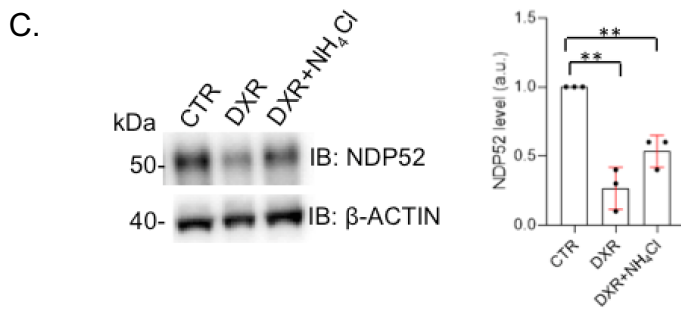


Figure 11: DXR induces PINK1 accumulation and autophagy receptor expression modulations in MCF7 cells. The Western-blot shows stabilisation of PINK1 after DXR treatment (30 μ M, 1h) A. Main mitophagic receptors Optineurin and NDP52 decrease in presence of DXR (30 μ M, 24h) and accumulate with NH₄Cl (20 μ M, 24h) B-C. Histograms represent the mean of at least 3 experimental replicate of the indicated protein level, normalized with actin (A,B) or vinculin (C), in treated (DXR or DXR+NH₄Cl) vs untreated sample (CTR). Standard deviations (S.D.) are shown in red. Statistical analysis was performed using t-test. n.s. not significant; * $p < 0.05$; ** $p < 0.01$; *** $p < 0.001$.

Finally, to understand whether mitophagy should be a real mechanism of resistance to treatment, we generated MCF7 cells resistant to DXR. To this end, we treated the cell culture with low doses of DXR, increasing the concentration until cells have shown an adaptation (restart to grow). When cells survive to specific high concentration of DXR for several weeks, we call them “resistant”. We performed a confocal microscopy on DXR-sensitive MCF7 or DXR-resistant MCF7 cells with antibodies against TOM20 and LC3 in order to stain mitochondria and autophagosomes, respectively. In basal condition, few dots of LC3 are found colocalized with mitochondria in sensitive-MCF7 cells (**Figure 12A**). However, this colocalisation is strongly up-regulated in resistant-cells (**Figure 12B**). We are currently quantifying TOMM20-LC3 colocalization in these two conditions. This preliminary data indicate that mitophagy is a process that could be strongly stimulated in cells resistant to DXR. We are also reinforcing these results by performing qPCR of mitophagic genes and mir-218 in resistant cells. We expect that mir218 will be inversely correlated with PINK1-mediated mitophagy genes.

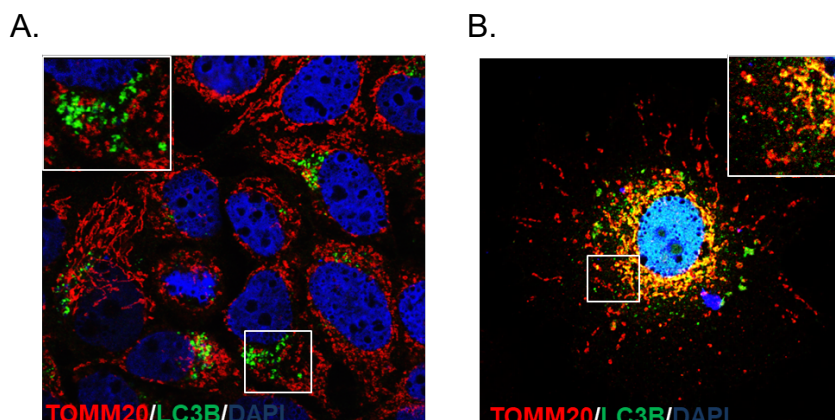


Figure 12. DXR resistant MCF7 cells display an increase colocalization between mitochondria and autophagosomes. Confocal images of sensitive-MCF7 cells (A) stained with anti-LC3 (green) and TOMM20 (red) or resistant cells to 160 nM DXR (B).

TASK3. Does mitophagy inhibition through miR-218 expression improve the sensitivity to the chemotherapeutic agent DXR in BC cell lines?

Description/methods

We found that miR-218 overexpressing cells, by inhibiting DXR-induced mitophagy, improves BC cell death (**Figure 5**), thus, supporting our hypothesis, that inhibition of mitophagy could further improve the efficacy of the chemotherapeutic agent. Of note, autophagy inhibitors such as chloroquine, hydrochloroquine already find a wide application in cancer therapy [9], meanwhile the role of mitophagy inhibition in this context, remains complex, partly due to the fact that inhibitors of mitophagy are lacking. Our preliminary data put thus under the spotlight miR-218 as a novel inhibitor of mitophagy that could be useful in fighting resistance to chemotherapy treatment in BC. This task is aimed to test this hypothesis. Considering that CSC play a pivotal role in cancer development and regeneration, we plan to study the role of miR-218 in combination with DXR also in stem like cells grown as mammosphere.

TASK4 and TASK 5 described bellow were planned for the third to fifth year of the project (2023-2025).

Task 4 is dedicated to demonstrate, in vivo, that miR-218 expression is crucial to fight against breast tumorigenesis.

Milestone a. Does loss of miR-218 predispose the mammary gland to spontaneously induce mammary tumour formation

Description/methods

It has been demonstrated that miR-218 expression is reduced in BC cells and its expression favors their death [10]. To gain insight into the function of miR-218 in mammary gland, we will generate a mammary-specific miR-218 knockout mouse model. To this end, we will take advantage of conditional miR-218 knock-out mice, already generated by our

collaborator Dr GC Bellenchi (Institute of Genetics and Biophysics "Adriano Buzzati Traverso", CNR, Naples, Italy) and which are available in the host institution. Of note, two identical isoforms for miR-218 are present in the mammalian genome, named miR-218-1 and miR-218-2. While miR-218-1 KO is vital, fertile and does not show any phenotype [11, Bellenchi, unpublished observation] miR-218-2 is perinatal lethal. Thus to study the biological role of miR-218, our collaborator generated a mouse line with the following miR-218s genotype: miR-218-1^{-/-}; miR-218-2^{flox/flox}, where the first isoform is constitutively deleted and the second isoform can be deleted by using a tissue-specific Cre deleter. From hereafter, we will refer to this mouse line as conditional miR-218 (miR-218^{fl/fl}).

Since we don't know which isoform of miR-218 is mainly expressed in the mammary gland (mostly because they produce identical mature miR-218), it will be first necessary to discriminate which miR-218 is highly expressed in the mammary gland. To this end, our collaborator, Dr Bellenchi, will perform real-time PCR (RT-PCR) using the Taqman array system and focalizing on the promoter regions of each isoform. If the results obtained will indicate that miR-218-1 is the main miR218 expressed in the mammary gland, since we already possess the constitutive knock out mice for Mir218-1, we plan to directly analyse mammary tumors development in these mice (Milestone b). By contrast, if we find that miR-218-2 (together with mir 218-1 or not), is expressed in the mammary gland, we will have to interfere specifically with this isoform in the mammary gland. To this end, we plan to use a conditional knockout mouse where the Cre transgene will be under the control of the β -lactoglobulin (BLG) promoter [12]. In order to induce activation of the BLG promoter and subsequent complete miR-218 knockout, a pituitary isograft will be surgically inserted into the renal capsule of 6-week-old BLG-Cre; miR-218 fl/fl (Cre+) and miR-218 fl/ fl (Cre-) control mice [13]. The pituitary transplant containing prolactin and ovarian hormones will trigger epithelial proliferation and lobuloalveolar differentiation in the mammary gland. The presence of milk in the mammary glands will indicate the correct activation of the BLG promoter approximately 50 days after pituitary implantation [14]. 6 BLG-Cre; miR-218^{fl/fl} and miR-218^{fl/fl} mice that had undergone at least 2 pregnancies will be monitored for spontaneous mammary tumour formation. We will check in Cre-positive mice for miR-218 downregulation from isolated mammary epithelial cells by performing WB of isolated mammary epithelial cells at multiple stages of mammary development and immunohistochemical staining in the mammary epithelium. We will estimate the number of potential spontaneous developed mammary tumors in Cre+ and Cre- mice. All mice will be monitored weekly by palpation for evidence of mammary tumour formation. Mice will be

sacrificed when the largest of the tumors will have a final volume of 1cm³ (tumors volumes will be calculated according to the formula $V = (4/3) \pi R_1^2 R_2$ (radius $R_1 < R_2$)). All mammary tumors and normal mammary glands will be dissected. For histological studies, needed to analyse which subtypes of BC tumour will be developed (i.e. adenocarcinoma, carcinosarcoma), half of the tumors will be fixed in 10% formalin buffer, embedded in paraffin wax, and then stained with hematoxylin and eosin (H&E) and the other half of the tumors will be frozen in liquid nitrogen and stored in -70 °C for Western-blot analysis.

Milestone b. Does loss of miR-218 predispose the mammary gland to chemically induced mammary tumour formation.

Description/methods

We plan here to check whether loss of miR-218 predisposes the mammary gland to chemically induced mammary tumour formation. We anticipate that miR-218-mammary gland deficient mice will have a greater susceptibility to breast tumorigenesis or aggressive breast cancer progression.

For mammary tumors induction, mice (8 BLG-Cre; miR-218^{fl/fl} mice and 8 miR-218^{fl/fl} control mice), will be treated once a week with the carcinogen 7,12-dimethylbenz(α)anthracene (DMBA) or corn oil for 5 weeks (1mg per 25g) by gavage. We will check in Cre-positive mice for miR-218 downregulation from isolated mammary epithelial cells by performing WB of isolated mammary epithelial cells at multiple stages of mammary development and immunohistochemical staining in the mammary epithelium. We will also estimate the number of developed primary mammary tumors, as well as developed multiple tumors in DMBA-treated Cre⁺ mice compared to Cre⁻ mice. Lungs will be also evaluated for evidence of metastases. All mice will be monitored weekly by palpation for evidence of mammary tumor formation. Mice will be sacrificed when the largest of the tumors will have a final volume of 1cm³. All experimental procedures will be approved by the Committee on the Ethics of Animal Experiments and the number of animals planned for this task has been justified in the 3R section using the power analysis.

TASK 5 is dedicated to demonstrate that miR-218/DXR lipid-based nanoparticles intratumorally injected in vivo, may improve therapy efficiency in BC mouse model

Description/methods

We preliminarily discovered that DXR treatment of MCF7 BC cells induces mitophagy (**Fig.4**). In addition, miR-218 overexpressing cells by inhibiting DXR-induced mitophagy,

improves BC cell death (**Fig.5**), thus, supporting the fact that inhibition of mitophagy could further improve the efficacy of the chemotherapeutic agent. In view of the drug-resistant BC cells, there is a need for therapeutic alternatives. Keeping this in mind, the task 5 will be aimed at testing the synergism between miR-218 (a powerful inhibitor of mitophagy) and DXR against BC tumorigenesis. Since nanotechnology-mediated drug deliveries of a combinatorial drug have shown to be promising in multiple cancers [15], we aim to develop nanoparticles for co-encapsulation and co-delivery of miR-218/DXR (milestone a). We will then check the correct co-delivery of miR-218 and DXR into DXR-resistant MCF7 cells and wild-type MCF7 cells and we will evaluate the effect of NPs on cell proliferation and apoptosis *in vitro* (Milestone b). We will then check whether the co-delivery of miR-218 and DXR by NPs can synergistically have anti-proliferative effects, tumor inhibition, in MCF7/resistant-bearing nude mice. Finally, we will test whether NPs can prolong the average survival time of tumor-bearing mice (Milestone c).

Milestone a. Synthesis of miR-218/DXR nanoparticles

Nanoparticles improve the bioavailability of the drug as well as the selectivity of the anticancer drug [16]. They have sizes between 1 and 1000 nm and among the many nanoformulations used in oncology, in order to achieve the goal of the project, three suitable drug delivery systems will be considered based on three different type of nanoparticles: i) polymeric (such as alginate and chitosan) [17] ii) lipid (such as Cetyl Palmitate and proper emulsifiers) [18,19], iii) inorganic (such as graphene quantum dots, GQD) nanoparticles [20,21].

All the selected nanoparticles have shown successful application as drug delivery system in many cancer types. Polymeric and lipid systems are remarkable for the biocompatible matrix, protection from degradation, sustained release of the encapsulated drug, reduced cytotoxicity as well as cell uptake. On the other hand, GQD nanoparticles have shown low cytotoxicity (up to 100 $\mu\text{g mL}^{-1}$) and ability to penetrate effortlessly tumor cells, especially MCF7 BC [21]. Moreover, the GQD fluorescence properties make it a good candidate for imaging/detection issue, too.

We plan to synthesize in collaboration with Prof S Bellucci (INFN-Laboratori Nazionali Di Frascati, Rome, Italy), miR-218/DXR nanoparticles. For this aim, nano-complexes will be prepared using the proper method (i.e. i) gelation process for polymer, ii) cold water of oil-in-water microemulsions for lipid iii) liquid exfoliation for GQD), which simultaneously encapsulate positive charged DXR and negative charged miR-218. In order to achieve the double encapsulation, proper functionalization of the nanomaterials

will be designed to modify surface charge and hydrophobicity. The NPs will be prepared and optimized, and the physicochemical properties of nanoparticles will be characterized from morphological and spectroscopic point of view. The DXR/miR-218 encapsulation efficiency, particle stability in various solutions and *in vitro* release will be analyzed. The most promising drug delivery system will be chosen (milestone a) and tested *in vitro/in vivo* studies.

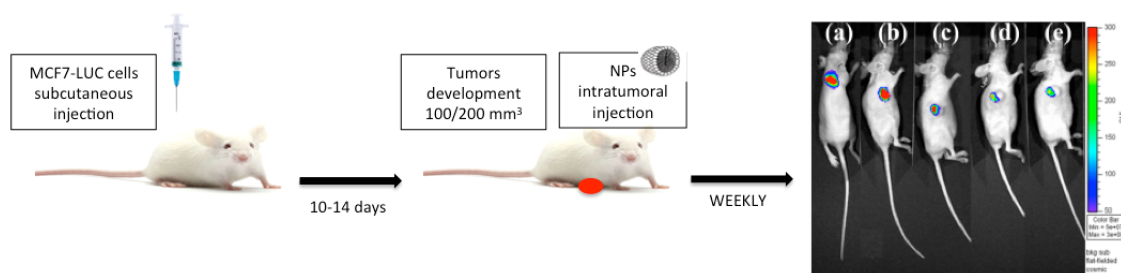
Milestone b. Does miR-218/DXR nanoparticles increase, in vitro, cell death of BC cell compared to DXR treated BC cells?

In order to verify the intracellular co-delivery efficiency of nanoparticles in MCF7 BC cells, miR-218 will be labeled with GFP in order to visualize the cell uptake of miR-218 compared with red fluorescence of DXR. We will follow the cellular uptake of the miR-218/DXR complex by fluorescent microscopy for 48 h. qPCR of miR-218 expression will be performed to confirm that NPs can be used as efficient miRNA delivery systems, using miR-218 oligonucleotides, in comparison with that of a classical transfection using RNAiMAX Lipofectamine. We will check by western-blot analysis and confocal microscopy for miR218 efficiency on Parkin expression and thus on mitophagy inhibition in nanoparticle-positive cells. Toxicity and apoptosis assays: human BC cells MCF7 but also MCF7/DXR-resistant will be incubated with miR-218 and DXR for 24 h or 48 h, respectively. 100 nM of miRNA will be constantly used, while DXR will be loaded with 3 different drug concentrations 0.1, 0.5 and 2.5 mM, which correspond to low, moderate and high doses of DXR. Control cells will be cultured in the same conditions without nanoparticles treatment. Cell viability will be determined at indicated time points using MTT assay. We plan also to use the AnnexinV/propidium iodide (PI) apoptosis detection kit for apoptosis assessment. At 48 h post treatment, cells will be harvested and processed by using AnnexinV/propidium iodide (PI) apoptosis detection kit and will be subjected to flow cytometric analysis. Each experiment will be performed in triplicate.

Milestone c. Does miR-218/DXR nanoparticles reduce, in vivo, breast tumorigenesis more than the DXR treatment alone?

To further study the *in vivo* anti-tumor effects of miR-218/DXR NPs in DXR-resistant tumors, we plan to establish a xenograft model by orthopic injection of MCF7 resistant cells into the abdominal mammary gland of eight-week-old nude female mice (1 x 10⁶ cells, mixed with 50uL of Matrigel) will be subcutaneously injected into nude female

mice (BALB/c). When the tumor will reach approximately 50 mm³, the mice will be randomly divided into groups, with 7 per group (saline, blank NPs, DXR, miR-218/DXR NPs). The mice will be treated four times by intratumoral injection of miR-218/DXR NPs every 3 days and the tumor growth (size and weight) will be analysed after 21 days of treatment.



Group	Cell line used for xenograft	Number of cells	Treatment	Quantity	Description	Number of animals
1	MCF7-Luc	50x10 ⁵	NPs	Vol?	NP	12(6+6)
2	MCF7-Luc	50x10 ⁵	DXR in NPs	5mg/kg	NP and DXR	12(6+6)
3	MCF7-Luc	50x10 ⁵	DXR and miR218 in NPs	5mg/kg 2mg	NP with DXR and miR218	12(6+6)

The tumors volume and body weight will be measured every other day. The tumor volume will be monitored using calipers and calculated using the approximate formula $V \sim 1/2 * (\text{length} * \text{width}^2)$ [mm³] derived from the ellipsoid volume [22]. The tumors of the four groups will be dissected and weighed at 3 days after the last administration. A TUNEL assay will be performed in order to quantify apoptotic tumor cells. Elimination of actively dividing tumor cells will be analysed by performing immunofluorescence of Ki67 staining. The survival time of tumor-bearing mice will be evaluated. By using miR-218/DXR NPs, we hope to target both tumors and their resident CSCs. To check this later aspect, downregulation of BC CSC markers such as Aldehyde Dehydrogenase 1-A1 (ALDH1), CD44+/CD24- will be analysed by performing FACS analysis. All experiments will be performed in accordance with the procedures and protocols of the Animal Ethics Committee and the number of animals planned for this task has been justified in the 3R section using the power analysis.

Statistical analysis: Statistical tests will be performed using GraphPad Prism. To analyse the percentage of tumor free mice over time, Kaplan-Meier curves will be used and the

logrank test will be performed to compare two different conditions. In vitro mitophagy, cell death, palpable tumour, average number of tumour/ mouse and average growth rate will be evaluated using the two tailed Mann-Whitney test to compare two independent groups. Kruskal-Wallis with Tukey's post hoc tests will be used to compare more than two independent groups. In case of multiple testing, Bonferroni correction will be applied to p-values. For any statistical design, p-value < 0.05 will be considered significant.

Risk assessment and contingency plans:

Modulation of miRNAs expression could have undesirable actions due to certain off-target effects. However, in the context of BC, miR-218 has already been shown to target Survivin, a protein involved in drug resistance of BC cells. We can thus hope to obtain a positive dual effect of miR-218 in targeting both a pro survival protein and mitophagy. We may also consider that mitophagy inhibition will not improve cell death of stem like cells grown as mammospheres as we preliminary obtained in MCF7 cells. In this case we could think to change the nanoparticles strategy in order to avoid side effects, for example, by engineering nanoparticles that can target only parental cells and not stem like cells.

References

- 1.Chun KH, Park JH, Fan S. Predicting and Overcoming Chemotherapeutic Resistance in Breast Cancer. *Adv Exp Med Biol.* 2017;1026:59-104.
- 2.Kim EH, Sohn S, Kwon HJ, Kim SU, Kim MJ, Lee SJ, Choi KS. Sodium selenite induces superoxide-mediated mitochondrial damage and subsequent autophagic cell death in malignant glioma cells. *Cancer Res* 2007;67(13):6314-24.
- 3.Yan C, Luo L, Guo CY, Goto S, Urata Y, Shao JH, Li TS. Doxorubicin-induced mitophagy contributes to drug resistance in cancer stem cells from HCT8 human colorectal cancer cells. *Cancer Lett.* 2017; 388:34-42.
4. Yao N, Wang C, Hu N, Li Y, Liu M, Lei Y, Chen M, Chen L, Chen C, Lan P, Chen W, Chen Z, Fu D, Ye W, Zhang D. Inhibition of PINK1/Parkin-dependent mitophagy sensitizes multidrug-resistant cancer cells to B5G1, a new betulonic acid analog. *Cell Death Dis.* 2019;10(3):232.
5. Zhou J, Li G, Zheng Y, Shen HM, Hu X, Ming QL, Huang C, Li P, Gao N. A novel autophagy/mitophagy inhibitor liensinine sensitizes breast cancer cells to chemotherapy through DNMT1-mediated mitochondrial fission. *Autophagy.* 2015;11(8):1259-79.
6. Lazarou M, Sliter DA, Kane LA, Sarraf SA, Wang C, Burman JL, Sideris DP, Fogel AI, Youle RJ. The ubiquitin kinase PINK1 recruits autophagy receptors to induce mitophagy. *Nature.* 2015;524(7565):309-314.
7. Di Rita A, Maiorino T, Bruqi K, Volpicelli F, Bellenchi GC, Strappazon F. miR-218 Inhibits Mitochondrial Clearance by Targeting PRKN E3 Ubiquitin Ligase. *Int J Mol Sci.* 2020 Jan 5;21(1):355.

8. Dontu G, Abdallah WM, Foley JM, Jackson KW, Clarke MF, Kawamura MJ, Wicha MS. In vitro propagation and transcriptional profiling of human mammary stem/progenitor cells. *Genes Dev.* 2003;17(10):1253-70.
9. Chen C, Lu L, Yan S, Yi H, Yao H, Wu D, He G, Tao X, Deng X. Autophagy and doxorubicin resistance in cancer. *Anticancer Drugs.* 2018;29(1):1-9.
10. Liu B, Tian Y, Li F, Zhao Z, Jiang X, Zhai C, Han X, Zhang L. Tumor-suppressing roles of miR-214 and miR-218 in breast cancer. *Oncol Rep.* 2016;35(6):3178-84.
11. Amin ND, Bai G, Klug JR, Bonanomi D, Pankratz MT, Gifford WD, Hinckley CA, Sternfeld MJ, Driscoll SP, Dominguez B, Lee KF, Jin X, Pfaff SL. Loss of motoneuron-specific microRNA-218 causes systemic neuromuscular failure. *Science.* 2015; 350(6267):1525-9.
12. Stewart MK, Bechberger JF, Welch I, Naus CC, Laird DW. Cx26 knockout predisposes the mammary gland to primary mammary tumors in a DMBA-induced mouse model of breast cancer. *Oncotarget.* 2015;6(35):37185-99.
13. Lydon JP, Ge G, Kittrell FS, Medina D, O'Malley BW. Murine mammary gland carcinogenesis is critically dependent on progesterone receptor function. *Cancer Res.* 1999;59(17):4276-84.
14. Wang RA, Zhang H, Balasenthil S, Medina D, Kumar R. PAK1 hyperactivation is sufficient for mammary gland tumor formation. *Oncogene.* 2006;25(20):2931-6.
15. Li Z, Tan S, Li S, Shen Q, Wang K. Cancer drug delivery in the nano era: An overview and perspectives. *Oncol Rep.* 2017;38(2):611-624.
16. Miele E, Spinelli GP, Miele E, Di Fabrizio E, Ferretti E, Tomao S, Gulino A. Nanoparticle-based delivery of small interfering RNA: challenges for cancer therapy. *Int J Nanomedicine.* 2012;7:3637-57.
17. Zhao N, Woodle MC, Mixson AJ. Advances in delivery systems for doxorubicin. *J Nanomed Nanotechnol.* 2018;9(5):519.
18. Montenegro L, Trapani A, Latrofa A, Puglisi G. In vitro evaluation on a model of blood brain barrier of idebenone-loaded solid lipid nanoparticles. *J Nanosci Nanotechnol.* 2012;12(1):330-7.
19. Cormode D.P., Naha P.C., Fayad Z.A. Nanoparticle contrast agents for computed tomography: A focus on micelles. *Contrast Media Mol. Imaging.* 2014;9:37-52.
20. Dong Y, Chen C, Zhen X, Gao L, Cui Z, Yang H, Guo C, Chi Y and Li CM. One-step and high yield simultaneous preparation of single- and multi-layer graphene quantum dots from CX-72 carbon black. *Journal of Materials Chemistry.* 2012; 10.1039/C2JM30658A
21. Zhang, Mo, et al. Facile synthesis of water-soluble, highly fluorescent graphene quantum dots as a robust biological label for stem cells. *Journal of materials chemistry* 22.15 2012; 7461-746. 10.1039/C2JM16835A
22. Faustino-Rocha A, Oliveira PA, Pinho-Oliveira J, Teixeira-Guedes C, Soares-Maia R, da Costa RG, Colaço B, Pires MJ, Colaço J, Ferreira R, Ginja M. Estimation of rat mammary tumor volume using caliper and ultrasonography measurements. *Lab Anim (NY).* 2013;42(6):217-24.
23. Strappazon F, Di Rita A, Peschiaroli A, Leoncini PP, Locatelli F, Melino G, Cecconi F. HUWE1 controls MCL1 stability to unleash AMBRA1-induced mitophagy. *Cell Death Differ.* 2020;27(4):1155-1168.
24. Antonelli M, Strappazon F, Arisi I, Brandi R, D'Onofrio M, Sambucci M, Manic G, Vitale I, Barilà D, Stagni V. ATM kinase sustains breast cancer stem-like cells by promoting ATG4C expression and autophagy. *Oncotarget.* 2017;8(13):21692-21709.

PROPOSED PROJECTS

Along my “small career” I acquired a strong expertise in autophagy and neurosciences. I became independent in 2018 working in my own laboratory in Rome. As a PI, I obtained 5 grants among which the Neuroscience prize from ROCHE and AGYR grant (Alzheimer Italian Association). In 2022, as a newly recruited CR-CNRS, I joined the team of J. Courchet at INMG (Lyon), a centre dedicated to study the pathophysiology of the nervous system and muscles.

I plan to develop my sub-group to pursue the project on Alzheimer disease (project N°1) and to develop new projects that will be in perfect harmony with the laboratory directed by J Courchet and my Host Institution (See project N°2 and N°3).

The research project N°1 detailed below constitutes the core of my current team’s activity that has been under support from AGYR. I hope to obtain soon from “France Alzheimer”, the necessary necessary financial and human resources to perform the proposed project n°1 (The time-frame planned is 2022-2024).

The project N°2 corresponds to my CRCN-CNRS proposed project. I plan to obtained robust preliminary data in these months in order to next apply to funding’s including national grants such as ANR, FRM and AFM. This project has been initiated directly following my relocation from Rome (Italy) since I performed myself a part of the experiments described in this proposal. In addition, I plan to recruit a Master and PhD student to assist me on this project.

Furthermore, our team belongs to the MyoNeurAlp alliance, a research consortium gathering teams from the Rhone Alpes Auvergne region and focusing on the study of neuromuscular diseases under the impulsion of the AFM-Telethon. It is a multi-PI grant and is given in a global envelope for the team (450k€ including 150k€ of funds for me (PhD grant + consumable). I am thus PI of the research proposed project N°3 detailed below and that will be conducted under the MyoNeurAlp consortium.

PROPOSED PROJECT 1:

NDP52, a protein that protects against Alzheimer's (Acronym "VITAL"- Time frame: Jan 2023- Jan 2025)

With project N°1, we plan to provide evidence that the variant NDP52^{GE}, that we are currently demonstrating to be beneficial *in vitro* and *in vivo* in two AD-related models (Neuroblastoma cells + *Drosophila*), could be also beneficial in an *in vivo* mouse model of Tau-related AD. Due to the close evolutionary relationship of mice with humans, **this part of the project could bring the innovative proof-of-concept that NDP52 is a novel therapeutic target in mammals.**

Moreover, through a genetic analysis, we plan to show that **NDP52 G140E variant may be protective for AD patients.** This project could undoubtedly highlight NDP52^{GE} as a new target for AD patients.

To do so, I plan to combine my unique knowledge on NDP52^{GE} with the expertise of my host team (stereotaxic injections; cognitive tests) and with Dr D Blum, an expert in Tau-related AD. Also, the host institution has state-of-the-art Biochemistry, Cellular and Molecular Biology facilities, an animal house facility and is equipped with a confocal microscope and a 2-photon microscope with a stereotaxic frame adapted to live imaging in the mouse brain. Overall, I am in a highly favourable environment to successfully reach the proposed objectives.

AIMS

Because NDP52 plays an important role in the clearance of phosphorylated Tau [5,6], we here anticipate that the NDP52^{GE} variant may be able to mitigate AD by clearing more efficiently Tau proteins as compared to the WT form of NDP52 through a higher capacity to bind LC3C. Our data indicate that NDP52^{GE} is able to bind more LC3C in neuronal-like cells and that it induces, *in vitro*, a robust clearance of phospho-Tau compared to its WT form (See Ongoing Project 1). In addition, we preliminary suggest that the variant NDP52^{GE} could be genetically associated to AD as a protective factor.

In that context, the present project is designed to investigate this hypothesis as follows:

1. **Demonstrating that NDP52GE may be beneficial *in vivo*, in a hTau mouse model of AD (Aim1);**
2. **Demonstrating that NDP52 G140E variant is genetically protective in AD patients (Aim2).**

Aim1: We will investigate the beneficial impact of the NDP52GE variant in an *in vivo* model of AD-like Tau pathology, the THY-Tau22 (Tau22) strain, developed by our partner laboratory, which progressively develops hippocampal Tau pathology and memory deficits [10]. We aim at demonstrating that NDP52GE neuronal expression mitigates the development of hippocampal Tau pathology, related synaptic loss and subsequently improves cognitive features of these mice (spatial and non-spatial memory).

Aim2: Because NDP52GE variant is naturally presents in human, we plan to demonstrate that it could be a novel protective factor for AD patients. To this end, through genotyping of the rs550510 (G/A) variant, c. 419 G> A, p.Gly140Glu of the NDP52 gene , we plan to compare the presence of the variant in healthy donors versus AD patients. Our preliminary results allow us to anticipate that, by increasing the number of AD patients in our cohort, the variant NDP52GE could result as a genetic protective factor for AD patients.

Methodology and experimental plan

AIM1. Demonstration that NDP52GE may be beneficial *in vivo*, in a hTau mouse model of AD

We plan to test the beneficial effect of NDP52GE variant in a hTau mouse model of AD (THY-Tau22) kindly provided by our partner Dr Blum (UMR-S1172 LiNCog - Alzheimer & Taupathies, Lille, France). THY-Tau22 mice ((B6.Cg-Tg(Thy1- MAPT)22Schd) express mutant human 4R Tau (G272V and P301S) driven by a neuron-specific promoter (Thy1.2). These mice are maintained in the C57BL/6J background [10]. They are a classical model for Tau aggregation, a pathological hallmark of AD as well as numerous tauopathies. With age these mice develop a variety of Tau-related neuropathological changes, including Tau hyperphosphorylation, neurofibrillary-like Tau inclusions and tangles. Tau pathology is generally mild at three to four months of age, moderate at six to seven months, and

extensive at nine months and beyond. Behaviourally, these mice display progressive learning and memory impairments, including deficits in spatial, social, and contextual learning. Non-spatial memory is affected as early as six months, whereas spatial is impaired later, from 8.5 months [16].

We plan to use Adeno-associated virus (AAV) as a shuttle vector in order to deliver NDP52 safely and effectively in mice [17]. We will generate AAV2/5 encoding GFP as a control, NDP52WTp2AGFP or NDP52Gep2AGFP under synapsin neuronal promoter (Addgene AAV production). To test the effect of NDP52 variants, we will inject, through stereotaxy (n=15 /group), AAV encoding “GFP control”, NDP52WTp2AGFP or NDP52Gep2AGFP in the hippocampus of adult mice (Both females and males, 3 months of age).

We next plan to analyse mice phenotype with the help of our partner, Dr Blum, expert in Tauopathy:

-Non-spatial memory (known to be affected already at 6 months) and spatial memory (known to be affected after 9 months) [10] will be evaluated through cognitive tests mastered in the host laboratory. In particular, we plan to perform several behavioural tests such as the Y-Maze and Barnes Maze.

-Once behavioral analysis is completed, we will sacrifice animals and the hippocampal Tau pathology will be investigated as described [18-20]: i) Tau immunohistochemistry against hyperphosphorylated (AT8) and conformational epitopes (MC1, AT100); ii) 2D and Western blot using against hyperphosphorylated (T181,S199,S262,S396,S404) or abnormally phosphorylated epitopes (AT100); iii) Sarkosyl fractionation of insoluble Tau.

-Further, since it has been shown that diminished levels of total spines is a characteristic of the CA1 regions of THY-Tau22 mice [21,22], we plan to check whether NDP52 expression prevents Tau-induced synaptic loss. To this end, we will quantify on brain slices the number of dendritic spines in GFP-positive neurons by performing stainings against VGluT1 and PSD-95, respectively pre- and post-synaptic markers of excitatory synapses, predominantly affected in Thy-Tau22 mice. The number of synapses will be quantified through the colocalisation of the two markers following images acquisitions of dendritic segments of GFP-labeled CA1 pyramidal neurons using a confocal microscope (Nikon C2) equipped with 63 objective and Imaris software.

-Finally, we plan thus to check, at that time, for a putative neuronal loss in the hippocampus by using NeuN immunohistochemistry and Nissl/cresyl-violet [10].

All animal studies will be conducted following the protocols approved by the Institutional Animal Care and Utilization Committee.

AIM2. Demonstration that *NDP52* G140E variant is genetically protective in AD patients

Preliminary observations

We recently performed a genotyping of the rs550510 (G/A) variant, c. 419 G> A, p.Gly140Glu of the *NDP52* gene in 189 AD and 1000 matched-control subjects. The allelic association is (weakly) significant ($p = 0.03$ approximately) and the A allele is "protective" with OR A = 0.69, which is in line with our molecular hypothesis.

Alzheimer Disease (189) versus Healthy Controls (1000)						
Gene	SNP	Allele	Allele Frequencies (Cases)	Allele Frequencies (Controls)	P	OR (95% CI)
<i>NDP52</i>	rs550510 G/A	G	0,862	0,814	0,028	G:1,44 (1,05-1,96)
		A	0,138	0,186		A:0,69 (0,51-0,96)
		Genotype	Genotype Frequencies (Cases)	Genotype Frequencies (Controls)	P	
		GG	0,741	0,667	0,07	-
		GA	0,243	0,293		-
		AA	0,016	0,040		-

These preliminary data indicate an allelic association between *NDP52*GE variant and AD patients, however we do not obtained an association at the genotype level and this is most likely due to the limited number of patients analysed until now.

In order to obtain more robust results, we plan to improve our preliminary genetic analysis by increasing our cohort of AD patients. For this, 220 additional blood samples have been already collected from sporadic AD patients (In collaboration with Dr Gabelli, Padou, Italy). The selection of AD patients was made on the basis of the clinical criteria of the National Institute on Aging and the Alzheimer's Association [23]. Samples have been subjected to DNA extraction. These DNA will be employed for the genotyping analysis

through a predesigned TaqMan assay (in collaboration with Dr Giardina, Rome, Italy). The genotyping results will be tested for biostatistical analysis to evaluate the association and the effect of the identified variants. We will calculate the P value through a 2×2 (allele association) and 2×3 (genotype association) contingency tables. The statistical associations will be considered significant for $P < 0.05$ with a 95% confidence interval. The strength of association will be established by calculating the OR.

Expected results

The “VITAL” program could demonstrate the effectiveness of NDP52GE to drive pathological Tau degradation in *in vitro* and *in vivo* models of AD and define this factor as protective in AD patients. The project is innovative for two reasons. First, so far, no data have been reported on the role of the specific polymorphism of NDP52 “GE” in Tau clearance. Second, this variant is present naturally in human, hence supporting a great potential for therapeutic interventions for AD in patients. The project will thus tackle a new subject both in the field of autophagy and AD. Also, since there is currently no *in vivo* evidence for the role of NDP52 in defence against pathological Tau, this project may bring to the scientific community the innovative proof-of-concept that NDP52 is beneficial in AD. Our proposal, initiated in cell culture will take advantage of a robust transgenic mice model, which recapitulates the main features of Tau pathology [10]. Moreover, through a genetic analysis on AD patients, the VITAL project could further support that NDP52GE is a protective factor in AD patients, opening exciting avenues for novel therapeutic strategies. Overall, this work may serve as a template for future explorations in the field of translational medicine for improving AD patients ‘life (i.e.: drug development that could activate NDP52 such as small molecule that may enhance interactions between NDP52 and LC3 proteins). Having already demonstrated, *in vitro*, that NDP52GE is a powerful cleaner of pathological Tau, the present project is highly relevant and has a strong potential for providing important results that can be translated to therapy in human in the future. Since we plan to use the mouse as the next model of Alzheimer's, if successful, this project will be a key step to next make possible to test the approach with AAV-NDP52 in humans suffering from the AD.

Organizational issues

As PI, (Physiopathologie Génétique du Neurone et du Muscle, INMG Lyon, France), I will take responsibility of the training and professional growth of a Master II student involved in

the project. I have indeed this ability since I already trained/supervised 9 master students, 1 PhD and 1 Junior fellow and 2 post-doctoral fellows. One young technician will be hired. I will supervise the work of the young technician involved in this project. Expert in autophagy and neurodegeneration, I will also actively participate to some experiments (see below). Finally, I will coordinate Aim2 that will be performed in collaboration with Dr Emiliano Giardina (Rome, Italy).

AIM1: Is NDP52^{GE} beneficial in an *in vivo* mouse model of AD? (0-24 months)

Milestone 1. After production of AVVs, the PhD Student **Salma Ellouze** (Team Courchet, Lyon France), expert in stereotaxic injections in mice, will perform AVVs injections in the hippocampus of THY-22 mice. **One young technician** and **FS** will technically help S Ellouze (0-6 months).

Milestone 2. **Geraldine Meyer-Dilhet**, engineer expert in Neurosciences (strong experience in mice breeding, behavioural tests) (team Courchet, INMG Lyon, France) will perform the cognitive tests that she perfectly knows on mice at 9 months of age. **Dr David Blum, expert in Tau-related AD** will provide the Thy-22 mice and will contribute to this task by sharing his strong knowledge on Thy22 mice, on behavioural tests and biochemical approaches (i.e: 2D western-blot, Sarkosyl fractioning).

One young technician (experience less than 3 years, to be determined) with cellular and molecular skills and experience with mice, will be hired. She/he will be full-time involved on this project for 18 months and will assist G. Meyer-Dilhet and Salma Ellouze in performing breeding mice, stereotaxic injections of AVV and behavioural tests.

At 9 months of age, **FS** with the expertise of **DB** and the technical help of the **young technician** will analyse the number of dendritic spines and cell death in CA1 hippocampus.

AIM2: Is NDP52^{GE} a protective factor against AD? (from 6 to 10 months)

FS will coordinate the genetic analysis. She will provide Dr Emiliano Giardina (Expert in genetic, IRCCS Santa Lucia, Rome, Italy) with 220 additional DNAs coming from AD patients (from Dr Gabelli, Padova, Italy). In collaboration, these DNAs will be employed for the genotyping analysis.

Risk assessment:

Since NDP52 is involved in selective autophagy of mitochondria, its expression could have “undesirable” actions on this selective autophagy. However, in the context of AD, it is known that Tau accumulation may damage mitochondria. Because we previously demonstrated that NDP52 is also more “pro-mitophagic” compared to its WT form [8], we can thus hope to obtain a positive dual effect of NDP52GE in targeting both damaged mitochondria and pathological Tau in AD context.

References

1. Tiwari S, Atluri V, Kaushik A, Yndart A, Nair M. Alzheimer's disease: pathogenesis, diagnostics, and therapeutics. *Int J Nanomedicine*. 2019 Jul 19;14:5541-5554.
2. Long JM, Holtzman DM. Alzheimer Disease: An Update on Pathobiology and Treatment Strategies. *Cell*. 2019 Oct 3;179(2):312-339.
3. Ballatore, C., Lee, V. M. & Trojanowski, J. Q. Tau-mediated neurodegeneration in Alzheimer's disease and related disorders. *Nat. Rev. Neurosci.* 8, 663–672 (2007).
4. Dikic I, Elazar Z. Mechanism and medical implications of mammalian autophagy. *Nat Rev Mol Cell Biol*. 2018 Jun;19(6):349-364.
5. Jo C, Gundemir S, Pritchard S, Jin YN, Rahman I, Johnson GV. Nrf2 reduces levels of phosphorylated tau protein by inducing autophagy adaptor protein NDP52. *Nat Commun*. 2014 Mar 25;5:3496.
6. Kim S, Lee D, Song JC, Cho SJ, Yun SM, Koh YH, Song J, Johnson GV, Jo C. NDP52 associates with phosphorylated tau in brains of an Alzheimer disease mouse model. *Biochem Biophys Res Commun*. 2014 Nov 7;454(1):196-201.
7. Birgisdottir ÁB, Lamark T, Johansen T. The LIR motif - crucial for selective autophagy. *J Cell Sci*. 2013 Aug 1;126(Pt 15):3237-47.
8. Di Rita A, Angelini DF, Maiorino T, Caputo V, Cascella R, Kumar M, Tiberti M, Lambrughini M, Wesch N, Löhner F, Dötsch V, Carinci M, D'Acunzo P, Chiurchiù V, Papaleo E, Rogov VV, Giardina E, Battistini L, Strappazzon F. Characterization of a natural variant of human NDP52 and its functional consequences on mitophagy. *Cell Death Differ*. 2021 Aug;28(8):2499-2516.
9. Di Rita A, Strappazzon F. A protective variant of the autophagy receptor CALCOCO2/NDP52 in Multiple Sclerosis (MS). *Autophagy*. 2021 Jun;17(6):1565-1567.
10. Schindowski K, Bretteville A, Leroy K, Bégard S, Brion JP, Hamdane M, Buée L. Alzheimer's disease-like tau neuropathology leads to memory deficits and loss of functional synapses in a novel mutated tau transgenic mouse without any motor deficits. *Am J Pathol*. 2006 Aug;169(2):599-616.
11. Kim BW, Kwon DH, Song HK. Structure biology of selective autophagy receptors. *BMB Rep*. 2016 Feb;49(2):73-80.
12. Padman BS, Nguyen TN, Uoselis L, Skulsuppaisarn M, Nguyen LK, Lazarou M. LC3/GABARAPs drive ubiquitin-independent recruitment of Optineurin and NDP52 to amplify mitophagy. *Nat Commun*. 2019 Jan 24;10(1):408.
13. Zhang Z, Simpkins JW. Okadaic acid induces tau phosphorylation in SH-SY5Y cells in an estrogen-

preventable manner. *Brain Res.* 2010 Jul 23;1345:176-81.

14. Voronkov M, Braithwaite SP, Stock JB. Phosphoprotein phosphatase 2A: a novel druggable target for Alzheimer's disease. *Future Med Chem.* 2011 May;3(7):821-33.

15. Petersen RC. Mild cognitive impairment as a diagnostic entity. *J Intern Med.* 2004 Sep;256(3):183-94.

16. Van der Jeugd A, Vermaercke B, Derisbourg M, Lo AC, Hamdane M, Blum D, Buée L, D'Hooge R. Progressive age-related cognitive decline in tau mice. *J Alzheimers Dis.* 2013;37(4):777-88.

17. Stoica L, Ahmed SS, Gao G, Sena-Esteves M. Gene transfer to the CNS using recombinant adeno-associated virus. *Curr Protoc Microbiol.* 2013;Chapter 14:Unit14D.5.

18. Leboucher A, Laurent C, Fernandez-Gomez FJ, Burnouf S, Troquier L, Eddarkaoui S, Demeyer D, Caillierez R, Zommer N, Vallez E, Bantubungi K, Breton C, Pigny P, Buée-Scherrer V, Staels B, Hamdane M, Tailleux A, Buée L, Blum D. Detrimental effects of diet-induced obesity on τ pathology are independent of insulin resistance in τ transgenic mice. *Diabetes.* 2013 May;62(5):1681-8.

19. Laurent C, Burnouf S, Ferry B, Batalha VL, Coelho JE, Baqi Y, Malik E, Mariciniak E, Parrot S, Van der Jeugd A, Faivre E, Flaten V, Ledent C, D'Hooge R, Sergeant N, Hamdane M, Humez S, Müller CE, Lopes LV, Buée L, Blum D. A2A adenosine receptor deletion is protective in a mouse model of Tauopathy. *Mol Psychiatry.* 2016 Jan;21(1):97-107. doi: 10.1038/mp.2014.151. Epub 2014 Dec 2. Erratum in: *Mol Psychiatry.* 2016 Jan;21(1):149.

20. Carvalho K, Faivre E, Pietrowski MJ, Marques X, Gomez-Murcia V, Deleau A, Huin V, Hansen JN, Kozlov S, Danis C, Temido-Ferreira M, Coelho JE, Mériaux C, Eddarkaoui S, Gras SL, Dumoulin M, Cellai L; NeuroCEB Brain Bank, Landrieu I, Chern Y, Hamdane M, Buée L, Boutillier AL, Levi S, Halle A, Lopes LV, Blum D. Exacerbation of C1q dysregulation, synaptic loss and memory deficits in tau pathology linked to neuronal adenosine A2A receptor. *Brain.* 2019 Nov 1;142(11):3636-3654

21. Burlot MA, Braudeau J, Michaelsen-Preusse K, Potier B, Ayciriex S, Varin J, Gautier B, Djelti F, Audrain M, Dauphinot L, Fernandez-Gomez FJ, Caillierez R, Laprévotte O, Bièche I, Auzeil N, Potier MC, Dutar P, Korte M, Buée L, Blum D, Cartier N. Cholesterol 24-hydroxylase defect is implicated in memory impairments associated with Alzheimer-like Tau pathology. *Hum Mol Genet.* 2015 Nov 1;24(21):5965-76.

22. Chatterjee S, Mudher A. Alzheimer's Disease and Type 2 Diabetes: A Critical Assessment of the Shared Pathological Traits. *Front Neurosci.* 2018 Jun 8;12:383.

23. McKhann GM, Knopman DS, Chertkow H, Hyman BT, Jack CR Jr, Kawas CH, Klunk WE, Koroshetz WJ, Manly JJ, Mayeux R, Mohs RC, Morris JC, Rossor MN, Scheltens P, Carrillo MC, Thies B, Weintraub S, Phelps CH. The diagnosis of dementia due to Alzheimer's disease: recommendations from the National Institute on Aging-Alzheimer's Association workgroups on diagnostic guidelines for Alzheimer's disease. *Alzheimers Dement.* 2011 May;7(3):263-9.

PROPOSED PROJECT N°2: “Local modulation of mitophagy and refinement of cortical connectivity during axonal development”
(Time Frame 2022-2027)

My current research is mainly aimed at studying the cellular and molecular mechanisms underlying mitophagy regulation in physiopathological contexts. The team “Energy Metabolism and Neuronal Development” (PI: Julien Courchet, hereafter J. Courchet’s team) recently highlighted the crucial role that mitochondrial metabolism plays in circuit formation in the developing brain. Having a strong expertise to study mitophagy and a particular interest in neurobiology since my PhD, I would like to combine my expertise with the one of J Courchet in order to explore the involvement of mitophagy in axonal branching during neurodevelopment of the brain.

Scientific context of the project

The cerebral cortex is the siege of higher cognitive functions such as attention, perception, language, memory and consciousness. It is established by coordinated developmental processes leading to the formation of a functional network of several billions of neurons connected by thousands of synapses. The wiring of the cortex relies on energy consuming cellular mechanisms, which are exacerbated during the phase of remodelling of neural circuits in young children [1]. If these mechanisms go wrong, neuronal circuit formation can be impaired, potentially leading to NeuroDevelopmental Disorders (NDD) such as Autism Spectrum Disorders (ASD), schizophrenia, epilepsy or intellectual disability [2].

If axon growth and branch addition are critical steps to make new connections supporting circuit formation, it is equally crucial to eliminate supernumerary connections. Indeed during the normal course of development, there is a significant physiological removal of axonal branches, a process known as pruning, and allowing the refinement of neural circuits. Many examples in the literature demonstrate that axon pruning can occur on a large scale to eliminate long-range connections (*e.g.* the pruning of the infrapyramidal tract from neurons of the Dentate Gyrus, or the pruning of spinal projections of Layer V cortical neurons from the visual cortex) or to refine local connections [3]. Despite these marked differences in scale, pruning events rely on largely conserved cellular

mechanisms, which often engage metabolic molecules revolving around the mitochondria such as NAD⁺ or caspases [4].

Objectives and hypothesis

It is now well established that mitochondria play an essential role in neuronal development and cortical circuits formation. Mechanistically, mitochondria are actively transported to and captured at presynapses [5,6] and this allows maintaining a correct presynaptic metabolism for short-term synaptic plasticity and prolonged synaptic efficacy [7,8].

In order to maintain their crucial functions, mitochondria must constantly be qualitatively and quantitatively well-controlled. For a rapid removal of dysfunctional or excessive mitochondria, cells employ the so-called *mitophagy* process, a selective form of autophagy allowing removal of organelles in a lysosome-dependent manner [9]. In the axon, mitophagosomes are retrogradely transported to be degraded in the soma, where the mature lysosomes are predominantly located [10]. However, it has been reported that PINK1 and PARKIN can mediate mitophagy in response to local damage in hippocampal axons suggesting that mitophagy could also occur in the axon, and suggesting that mitophagy could be regulated locally [11].

Data from the Courchet team underline a crucial role for mitochondria in axonal development. They identified that the signaling pathway formed by the kinases LKB1 (STK11) and NUAK1 (ARK5) controls cortical axon branching through an original cellular mechanism involving the regulation of mitochondria capture at immature presynaptic sites [12]. NUAK1 belongs to the so-called AMPK-related kinases (AMPKRK) family [13], which is formed by 14 kinases related to the metabolic regulator AMPK (PRKAA). NUAK1 is an autism-associated kinase [14] and strongly expressed in the mouse-developing cortex [18]. Recent evidence from the team demonstrate that NUAK1 controls not only the proper localization of mitochondria, but also mitochondrial metabolic activity, and that both are required to support axon branching [8]. Because a healthy mitochondrial population preserve intact energy metabolism it is therefore expected that a basal mitophagy, by allowing a correct mitochondrial turnover, may be required for early axonal branching. Interestingly, data from Courchet's team also indicate that the removal of mitochondria from axonal branches is a prerequisite for their elimination (see **Figure 1**). This data raises the hypothesis that a stronger local induction of mitophagy is rather necessary to remove

excessive mitochondria from axonal branches before their elimination during early development.

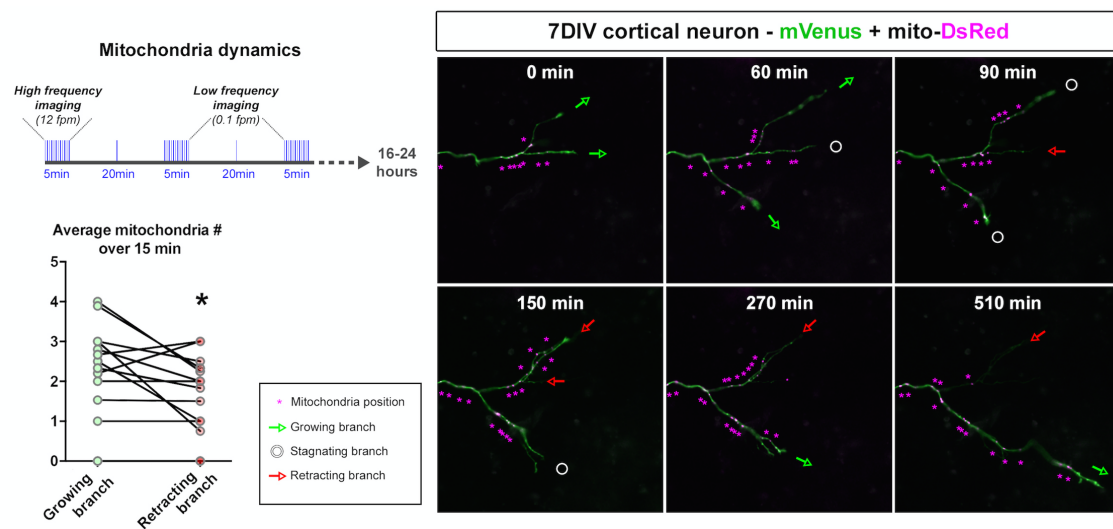


Figure 1: Timing of mitochondria recruitment and removal in relation with branch growth or retraction. (Left) Mitochondria trafficking was observed in cultured cortical neurons by time-lapse imaging over 24 hours. Short periods of high frequency imaging were alterned with 20 minutes pauses with low frequency imaging, to avoid phototoxicity and preserve a normal axon growth. (Right) Position of mitochondria in the branches on one representative axon. (bottom left) quantification of the average number of mitochondria *per* axonal branch, during growth or retraction phase.

In the first part of the present project I propose to investigate the importance of mitochondria turnover to refine axonal arborizations. I anticipate that mitophagy could be a physiologically regulated process for axonal growth and pruning (Aims 1+2). To do this I will take advantage of the NUAK1 conditional knockout mouse model (already present in the host laboratory) in which axonal branching and cortical circuits formation are affected [5,12]. Although the results of the host laboratory underline a central role of NUAK1 in the regulation of mitochondrial homeostasis, a possible "mitophagic" activity of NUAK1 and if a deregulation of this mitophagic activity could contribute to the axonal defects in NUAK1 knockout animals has never been analysed. I discovered that NUAK1 is predicted to contain a LIR motif, which suggests it can play a role in selective autophagy. This also led me to observe some interesting homologies between the kinase NUAK1 and ULK1, a well known kinase involved in mitophagy and in axonal growth of embryonic sensory neurons by promoting endocytosis of neurotrophins [15]. ***Aim 3 of the project will be devoted to characterize the involvement of NUAK1 as a novel kinase-***

containing LIR domain in axonal morphogenesis through its putative new fonction in mitophagy and/or in the control of neurotrophines endocytosis.

Aim 1. Demonstration that mitophagy may be involved in physiological conditions during axonal morphogenesis

Milestone 1. Is global or local mitophagy modulated during developing cortical neurons?

Our preliminary data suggest that mitochondria leave branches before the removing of these branches (**Figure 1**). What triggers mitochondrial elimination and specifically whether basal mitophagy plays a role during early development of the axon remains to be explored. I hypothesize here that basal mitophagy could take place locally in the axon to ensure mitochondria removal and the elimination of supernumerary axonal branches. I will thus check when mitophagy could be relevant in developing cortical neurons, whether it correlates with specific stages of axonal development and whether the process could be locally regulated.

Methods: I will check for global mitophagy by analysing, through western-blot, mitochondrial markers and LC3 conversion in extracts of WT cortical neurons corresponding to distinct stages of neuronal development (Days In Vitro (DIV) 3-21; eg. DIV3 : neuronal polarization, DIV7 : axon branching etc.). The same kind of analysis will be done, by confocal microcopy, on fixed cortical neurons at DIV3-21 both in the soma and axon, in order to determine whether mitochondria in distal axons could locally recruit autophagosomes. To examine endogenous lysosome distribution, dissociated cortical neurons will be immunostained for LAMP1, a late endosome/lysosome marker. To determine whether lysosomes would be recruited to autophagosomes containing mitochondria, we will analyse co-localisation between mitochondria, LAMP1 and LC3. Finally, to elucidate whether mitophagy could occurs locally, I will perform live imaging on neurons expressing the mito-mKeima construct, a mitochondria-targeted pH-sensitive fluorescent protein construct which has been developed as a sensitive readout of mitophagy [16] (see **Figure2**).

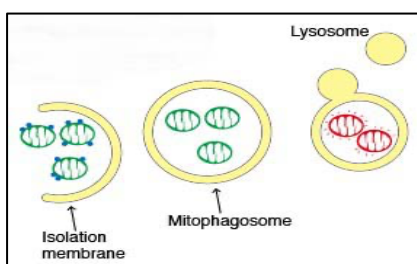


Figure 2: Detection of mitophagy with mito-Keima construct.

A fluorescent protein derived from coral, Keima, changes color upon conversion of an autophagosome to an autolysosome. The pH sensitivity of the fluorophore allows for discrimination between healthy mitochondria at neutral pH (green) and mitochondria undergoing degradation in low-pH autolysosomes (red) (Keima is resistant to lysosomal degradation allowing for accumulation of the signal, which is interpreted as an integration of the extent of mitophagic flux over time).

This will allow us to understand whether mitochondria degradation occurs locally or back to the soma during early development of cortical neurons.

Milestone 2. Is mitophagy locally regulated following mitochondrial stress?

Since several lines of work including by the Courchet team demonstrated that metabolic stress affects directly axon development [8,17], I will analyse a putative mitophagy induction in the axon under a metabolic stress, by performing Chromophore-Assisted Light Inactivation (CALI) of mitochondria using Killer-Red (mt-KR), a genetically encoded photosensitizer targeted to mitochondria, which is already mastered by the host laboratory [8]. Light-induced activation of mt-KR causes local ROS-mediated damage to mitochondria in a spatiotemporally controlled manner, while preserving the overall integrity of the mitochondrial network. I will thus check for putative subcellular mitophagy modulation in axon of neurons following mitochondrial stress.

Methods: To evaluate the formation of mitochondrion-containing autophagosomes, I will quantify GFP-LC3 accumulation on mitochondria after activation of mt-KR in cortical neurons. I will check the presence mitophagolysosome by performing LAMP1 staining together with mitochondria, LC3 staining and a far-red stained axonal marker. Also, because mt-KR is sufficient to promote branch eliminations [8], I will check whether mitophagy could be modulated locally by mtKR during this process in single branches of neurons. To this end, I will perform live imaging with long time-lapse on neurons expressing GFP-LC3, mt-BFP, and a far-red stained axonal marker to see the branches that will be eliminated.

Milestone 3. Could a powerful stimulation of axonal mitophagy promote the elimination of axonal branches?

Milestone 2 could demonstrate how mitochondrial stress (induced with mtKR) triggers the mitophagy process locally. Here, I will test whether the induction of the mitophagy process in a spatially restricted fashion, is sufficient to cause branch elimination, even without any metabolic stress. My prediction is that the local induction of a powerful mitophagy in one collateral branch of the axon will trigger the elimination of mitochondria, which precedes branch elimination. To test this hypothesis, I will use, in collaboration with Prof Cecconi, the optogenetic tool that we developed previously [18] by recruiting the mitophagic receptor AMBRA1 to the outer mitochondrial membrane (OMM) of cortical neurons (AMBRA1-RFP-sspB-mediated induction of mitophagy). This tool will

guarantee a high-spatial resolution, unattainable with other methods. Basically, in resting conditions, Venus-iLID-ActA will be tethered to the MOM, while AMBRA1-RFP-sspB will be found in the cytosol. Upon blue light, iLID will undergo into a conformational change, which will unmask the ssrA peptide and permits the high-affinity binding between ssrA and sspB.

Methods: First and because AMBRA1-RFP-sspB constructs have never been used in cortical neurons, I will determine the optimal parameters for an efficient elimination of mitochondria in these neurons electroporated with vectors encoding Venus-iLID-ActA/AMBRA1-RFP-sspB or Venus-iLID-ActA/RFP-sspB. Mitophagy progression will be followed in time through live cell imaging by estimating the area occupied by mitochondria and the overall reduction per whole cell of the Venus signal intensity. Following this initial step of calibration, I will use the optimal parameters to stimulate mitophagy and test its effect on axon morphogenesis. To this end, I will illuminate in Region of Interest (ROI), 5DIV single-neurons expressing Venus-iLID-ActA/AMBRA1-RFP-sspB and a cyan *fluorescent protein* (mTurquoise) with 488 nm laser for several times ranging from 2h to 10h. By performing live imaging, I will follow the morphology of neurons and after acquisitions at several times, we plan to quantify axonal branch elimination.

In sum, with Aim1, I will demonstrate that local mitophagy may be physiologically regulated during brain development. If I do not find any signs of mitophagy in basal condition due to a low mitophagy flux (milestone 1), I plan to analyse local mitophagy induction under metabolic stress condition which is known to affect axon formation (milestone 2). Finally, with milestone 3, I plan to demonstrate that a potent axonal mitophagy could be a rapid and local mechanism responsible for removing superfluous mitochondria from the axonal branch and needed before their own removal.

Aim 2: Demonstration that mitophagy impairment could be linked to pathological conditions such as abnormalities in cortical development

Preliminary data: I analysed cortical extracts from mice with a conditional deletion of NUA1 (hereafter NUA1^{ckO}) in cortical glutamatergic neurons (NexCRE ; NUA1F/F) [12]. I observed that the levels of LC3-II and MnSOD are increased in these extracts as compared to WT, indicating a putative accumulation of autophagosomes and mitophagy substrate. Moreover, I found an up-regulation of PINK1 and PARKIN, which suggests an accumulation of damaged mitochondria (**Figure 3**). These data support the fact that mitophagy might be altered in absence of NUA1 and this could contribute to defect in

mitochondrial homeostasis at presynaptic sites. Aim 2 will be dedicated to test this hypothesis.

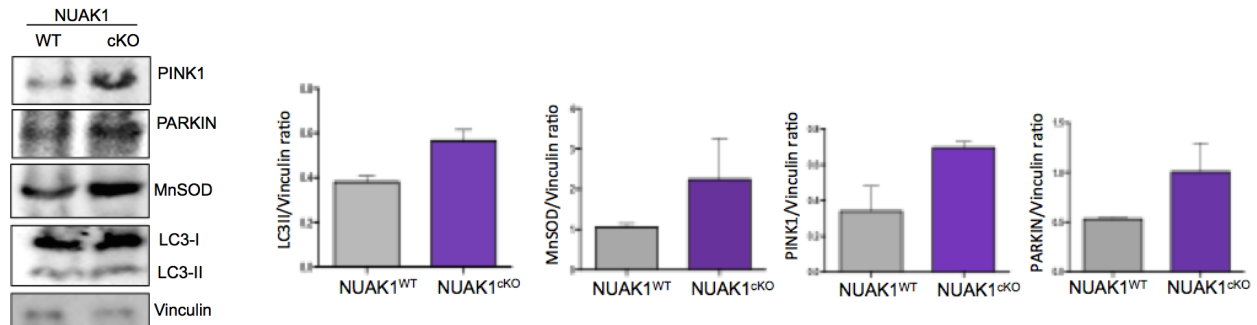


Figure 3. PINK1, PARKIN, MnSOD and LC3 protein levels in cortical extracts NUAK1^{cKO}. The graphs show the normalized densitometric LC3-II, MnSOD, PINK1 and PARKIN over Vinculin *ratio* in two independent experiments.

Milestone 1: Characterisation of mitophagy impairment in NUAK1^{-/-} neurons

I will check which mitophagy pathway are deregulated in *Nuak1*-deficient developing cortical neurons by biochemical and confocal microscopy analyses.

Methods: I will perform western blots on extracts of NUAK1^{cKO} cortical neurons to analyse mTOR and ULK1 activation, which are two kinases known to be linked to mitophagy control [19, 20], but also specific signalling related to the main mitophagic receptors such as FUNDC1, AMBRA1 or NIX [22, 24, 37]. I will perform mitochondrial/cytosol fractioning in WT or NUAK1^{cKO} neurons in order to check for PINK1 and PARKIN accumulation on mitochondria. In parallel, I will perform confocal microscopy analyses to quantify the number of mitophagosomes (defined as co-localized LC3 dots with mitochondria) in axonal collateral branches, and in immature presynaptic sites of WT *versus* NUAK1^{cKO} cortical neurons. Finally, by performing confocal microscopy analysis, I will test the mitophagic response in NUAK1^{cKO} neurons by treating neurons with Antimycin A, which leads to a rapid loss of mitochondrial membrane potential. To examine the late stages of mitophagy, I will analyse the autophagic delivery of mitochondria to lysosomes by quantifying mitochondria (marked by mito-DsRed expression) co-localisation with LAMP1 following mitophagy induction. My results will provide the complete description of the alterations of mitophagy in the axon of NUAK1 deficient neurons.

Milestone 2. Does local mitophagy stimulation improve neuronal circuit defects observed in NUAK1^{cKO} mice?

Milestone 1 will expectedly identify specific mitophagy pathways altered in NUAK1^{ckO} neurons. I predict that restoring mitophagy would in turn improve mitochondrial homeostasis, leading to a partial normalization of axonal phenotypes. To test this hypothesis, I will use the optogenetic tool described in Aim1 in order to stimulate mitophagy through AMBRA1 recruitment on OMM.

Methods: I will activate “moderate” mitophagy and test its effect on axonal branching in NUAK1^{ckO} neurons. To do so I will use a laser and time setting that we will have defined and retained "moderate" during the realization of the milestone 2 of Aim1. I will illuminate in ROI, single-NUAK1^{ckO} neurons expressing Venus-iLID-ActA/AMBRA1-RFP-sspB and a cyan *fluorescent protein* (mTurquoise) for several times ranging from 2h to 10h. The morphology of these neurons (number of axonal branching and axon length) will be analysed over 24 hours, which is sufficient to see branch dynamics ([8], see also **Figure 1**). In case I need to look at even longer axon development periods, I will resolve to alternative strategies, with more spaced imaging points, that are currently developed in the host team and allow to visualize axon development over 4 days. The same experiment will be performed on single neurons expressing Venus-iLID-ActA/AMBRA1-RFP-sspB and the synaptic vesicle marker mTurquoise-vGlut1, which will be useful to quantify the formation of immature presynaptic boutons. If my local, optogenetic based strategy does not provide significant improvement, I plan to turn to general treatments that disrupt the mitochondrial membrane potential ($\Delta\Psi_m$) and induce mitochondrial degradation (e.g. CCCP or O/A), which are routinely used to induce “global” mitophagy.

Finally, I aim to get some insight into the **physiologically-relevant but more challenging environment of organotypic brain slices**. Venus-iLID-ActA/AMBRA1-RFP-sspB plasmids will be expressed by *in utero* cortical electroporation at E15.5 to target callosal-projecting layer 2/3 cortical pyramidal neurons. At E18.5, I will perform organotypic slice cultures as described [21, 22], a method that the host lab masters. Following a short incubation time (2-4 days), I will follow axon elongation and axonal branching by confocal microscopy. This part will be challenging but have the potential to bring the innovative proof-of-concept that *ex-in vivo* stimulation of mitophagy may directly modulate axonal branching.

In sum, the second Aim will seek to identify how a deregulation of axonal mitophagy can contribute to mis-wiring of the brain in pathological states. The model of study will be the kinase NUAK1, for which the host team has expertise and tools readily available. On the

long-term, this work could provide conceptual insight on a deregulation of mitophagy in the context of an altered development where neuronal metabolism is affected.

Aim 3: Characterisation of NUAK1 as a novel LIR-containing protein in axonal morphogenesis

Preliminary data: I performed an *in silico* analysis of the sequence of NUAK1 and identified a xLIR motif in position 581 to 586, a motif that correspond to the shortest sequence required for the interaction with Atg8-family proteins (e.g. LC3) [23] (**Figure 4**). This observation strongly suggests that NUAK1 may be a novel player involved in mitochondrial clearance. Interestingly, in a recent work from 2020, it has been suggested a novel role of NUAK1 in clearance of protein aggregates in the context of *Drosophila* larval muscles [24].

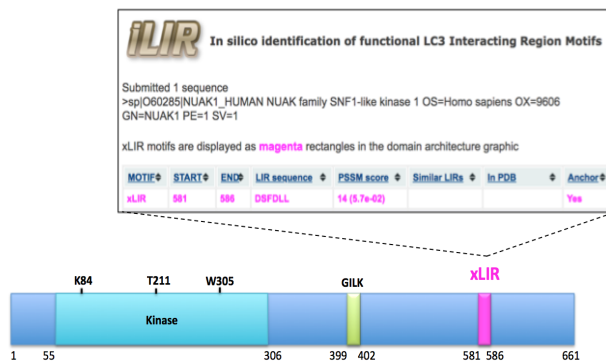


Figure 4: An undisclosed xLIR motif in NUAK1. The catalytic domain of NUAK1 protein is located in the N-terminal at residues 55 to 306. K84 is an ATP binding site. T211 is phosphorylated by LKB1, which activates NUAK1 (Lizzano et al 2004). W305 is required for binding of USP9X. The GILK motif is a binding site for protein phosphatase PPP1CB (Zagorska et al., 2010). We identified a xLIR domain (DSFDLL) in the C-terminal part of NUAK at residues 581 to 586 .

I will thus test whether the xLIR domain in NUAK1 is functional. I preliminary performed co-immunoprecipitation experiments in HEK293 cells, in order to test for a putative binding between WT or a truncated mutant of NUAK1 in its C-terminal part (hereafter named NUAK1^{STOP}) and LC3 protein. I found that NUAK1 and LC3 could indeed interact each other and this through the C-terminal part of the protein in which I identified the LIR domain.

Milestone 1.1. Is the LIR domain of NUAK1 crucial for mitochondrial clearance and axonal branching regulation?

Based on my preliminary results, I will confirm the interaction between NUAK1 and LC3 by co-immunoprecipitation assays. Experiments will be performed in cell lines (U87MG glioma cells which are NUAK1-free but also in SH-S5SY neuroblastoma cells) upon overexpression of tagged NUAK1 and LC3 proteins. I will test whether this

interaction may be modulated upon mitochondrial stress. These results will be confirmed in a second time at the endogenous level in cortical neurons. I will next check, by performing confocal microscopy analysis, whether NUA1 may be recruited to autophagosome-like structures (LC3-II positive vesicles), which could be functionally important for autophagosome formation and/or maturation. Afterward, I will use site-directed mutagenesis to introduce two crucial point mutations in the LIR domain of NUA1 (NUAK1-581DSFDLL586)). I will take advantage of tools readily available in my host team to assess the subcellular location, stability and catalytic activity of this new mutant NUA1^{LIRmut}. In parallel, I will determine how this mutation affects binding to LC3, and the formation and turnover of autophagosomes in response to mitochondrial stress or starvation (deprivation of nutrients) through western-blot analysis of mitochondrial markers and by performing confocal microscopy analysis, using the Mito-Keima probe. I will evaluate the mitophagy process in cortical neurons NUA1^{WT} *versus* neurons NUA1^{LIRmut}. Finally, I will express either WT or mutant NUA1^{LIRmut} proteins in NUA1-null neurons *in vitro* to determine axon morphology. The same strategy will be adapted *in vivo* in NUA1^{CKO} mice through *in utero* electroporation of vector encoding for NUA1^{LIRmut} to observe the consequences of disrupting the NUA1-LC3 interaction on terminal axon branching.

Milestone 1.2 Are there any post-translational modifications of NUA1 (specific signaling?) upstream its LIR domain, that could favour mitochondrial clearance and axonal branching?

LIR-containing proteins are often phosphorylated on a serine localized upstream their LIR motif that induce a local conformational change and favour binding with Atg8-family proteins [25]. Using prediction softwares, I identified two phosphorylation sites (S560, S565) upstream the LIR motif (**Figure 5**). Primed by this evidence, I will check *in vitro* whether one of these sites can be phosphorylated in order to modulate NUA1 mitophagic activity and thus axonal branching. After identification of the serine, which could modulate NUA1 activity in mitophagy, I will identify the kinase responsible for its phosphorylation.



Figure 6: Serine candidates that may be subjected to phosphorylation upstream the LIR motif of NUA1.

I will generate phosphomimetic or phosphodead NUA1 mutants on S560 or S565 and check whether these mutants will modify the NUA1 capability to bind LC3 and to regulate mitophagy in U87MG cells or SH-S5Y cells. Moreover, I will check, by overexpressing these mutants in cortical neurons, whether they could regulate mitochondria homeostasis at presynaptic site and thus axonal branching. Because phosphorylation upstream of the LIR motif usually activates the mitophagic process [25], I anticipate that a phospho-dead mutant of NUA1 on S560 and/or S565 will have a reduced mitophagy activity and thus could generate defect of axonal branching. Next, I will seek to identify the kinase responsible for the putative phosphorylation at S560 or S565, at first through a candidate-based strategy. I expect here that a specific cellular signalling (ie: presynaptic mitochondrial stress or putative neurotrophin-mediated signalling etc.) may activate locally NUA1 activity in selective autophagy. *In silico* analyses suggest that AKT could be the kinase upstream of S560 and S565 phosphorylation (**Figure 6**). Given the major roles of AKT in axon growth and branching [26,27], I will test this candidate, by performing *in vitro* kinase assays. However, if AKT is not the kinase involved in this context, I plan to perform, in collaboration with Dr Jörn Dengjel (University of Fribourg, Switzerland), with who I have already established successful collaborations, a mass spectrometry analysis on NUA1 immunoprecipitation in normal condition *versus* stress conditions (mitophagy/metabolic stress) in cortical neurons.

Milestone 2. Does NUA1 play a role in neurotrophin endocytosis and thus in axonal growth

With milestone 1, I will characterize NUA1 as a novel LIR-containing kinase that may regulate selective autophagy. The Courchet team recently observed that the LKB1/NUA1 pathway integrates signaling by the neurotrophin BDNF and its receptor TrkB to induce collateral branch formation in cortical neurons (*Garcia et al., in preparation*). Interestingly an other LIR-containing kinase well-known to regulate selective autophagy and named ULK1, has been found to regulate axonal length by allowing an efficient endocytosis of the Nerve Growth Factor (NGF) in embryonic sensory neurons [15]. We preliminary found that down-regulation of ULK1/2 induce defects in axon formation of cortical neurons that are very similar to defects upon knockdown of NUA1/2 (**Figure 7,a**). Both ULK1/2 and NUA1/2 possess a kinase domain followed by an xLIR motif which is present in a disordered region predicted to have the potential to transit from a disordered to an ordered state, suggesting that these kinases may work in similar manners in a similar

context. Since I observed these homologies (**Figure 7b**), I hypothesize here that NUAK1/2 and ULK1/2, could be important for the endocytosis of BDNF in cortical neurons and this could explain their important function in the control of axonal growth. In addition, since how ULK1 exerts its function on endocytosis in sensory neurons is not clear and given that the xLIR motif of NUAK1 is very similar to the one identified in ULK1, **I hypothesize that the LIR motif of these two kinases could play an essential and completely unknown role in the control of endocytosis of growth factor in order to control a correct axon morphogenesis.** This part of the project will be devoted to study this hypothesis

Methods: I will electroporate cortical neurons with shRNAs against NUAK1 or ULK1 (co-electroporated with a GFP-coding plasmid), then apply Cy3-BDNF. On these cultures I will analyse BDNF internalization into the growth cones and at branchpoints of GFP-expressing neurons, and I will check whether BDNF may stimulate recruitment of NUAK1 or ULK1 to the TrkB receptor complex. In order to understand whether the LIR domain of ULK1 and NUAK1 may be involved in the control of endocytosis, the same experiments, as described above will be conducted using GFP-NUAK1^{LIRmut} and GFP-ULK1^{LIRmut}. Since NGF signalling has been found to favour ULK1 K63-ubiquitination, we will check whether BDNF could control polyubiquitination of NUAK1 (specific k63-polyubiquitination? Which E3 Ubiquitin ligase involved in?) and could favor its interaction with the BDNF signaling complex. Since it has been demonstrated that the pharmacological drug “MRT68921” exerts a dual inhibition of NUAK1 and ULK1 [28], I plan to test this drug on cortical neurons, in order to test whether their kinase activities are involved in axon growth regulation. Finally, because downregulation of these kinases show the same phenotype on axon growth of cortical neurons, I will test whether they have a redundant function in the BDNF signaling by complementing neurons downregulated for NUAK1/2 with ULK1/2 and *viceversa*.

In sum, the results of aim 3 could highlight NUAK1 and ULK1 kinases as regulators of cortical axon outgrowth through regulating TrkB receptor signaling.

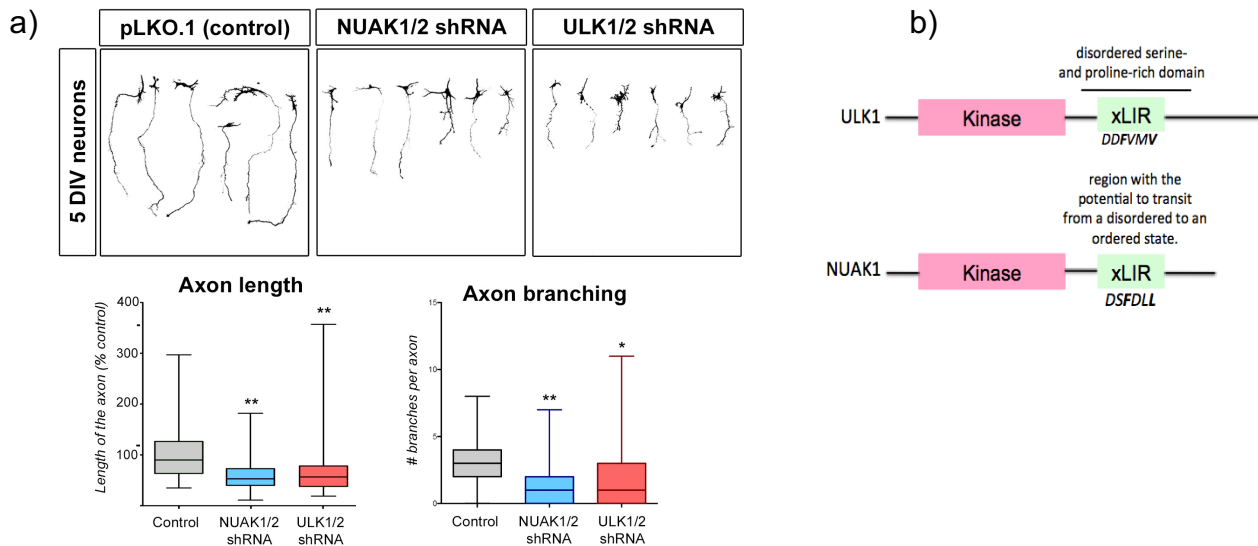


Figure 7. Homologies between NUAK1 and the kinase ULK1.

a) Both downregulation of NUAK1/2 or ULK1/2 induce reduction of axon formation and length in cortical neurons

b) Both ULK1 and NUAK1 possess a similar xLIR motif (consensus sequence— referred to as the xLIR motif— is (ADEFGLPRSK)(DEGMSTV) (**WFY**)(DEILQTV)(ADEFHIKLPSTV)(**ILV**), where the residues marked in bold (positions 3 and 6) correspond to the most crucial residues for the interaction with Atg8-family proteins). Also, interestingly, the LIR motif of ULK1 is located in its disordered serine- and proline-rich domain and the one that we discovered in NUAK1 is also predicted to overlaps a region with the potential to transit from a disordered to an ordered state. These two proteins, in addition to their xLIR motif, possess a kinase domain; this feature highlights NUAK1, in addition to ULK1, as the second kinase with a LIR motif that could play a role in autophagy/selective autophagy

Significance/Innovation

The project will address a novel aspect both in the field of mitophagy and neurodevelopment. It has a high potential to provide the scientific community with the innovative proof-of-concept that a fine regulation of axonal mitophagy may be a crucial denominator for a correct axonal branching formation and elimination. The study of mitochondrial quality control in neurons has been hampered by the lack of methods to induce a specific mitophagy in a specific compartment of the neurons. To the best of my knowledge, this project could be the first report able to demonstrate the effectiveness of local and tunable mitophagy stimulation in neurons in order to improve axonal branching refinement and thus could improve, in the future, trouble linked to neurodevelopmental disorders such as ASD and ID. Also, by identifying NUAK1 kinase as a novel protein containing an LIR domain, I plan to uncover new molecular mechanisms underlying

mitophagy and/or neurotrophin endocytosis control that may be involved in axonal morphogenesis and thus in neurodevelopmental-related. This project could thus underline the NUAK1 LIR motif as a new therapeutic target in neurodevelopmental disorders such as autism and ID. We believe that all of these goals are of the utmost importance in the biology of neurodevelopmental disorders.

Feasibility

The project proposed above will be developed in the host team, with the support of the local environment. Specifically, I will benefit from the mutualization of support personnel from the team. This line of research is naturally complementary to the research carried out by Julien Courchet. With my expertise in the field of mitophagy, I will be able to develop a sub-group within the team to pursue this project, pending successful application to funding and recruitment of a student. I will take advantage of the NUAK1^{ckO} mice as an experimental model of neurodevelopmental disorders and of mt-KR, which are in possess by the host laboratory. Moreover, I will exploit a unique optogenetic tool in order to stimulate mitophagy in neurons, a tool that I developed during my post-doctoral training and that will be made available to us through collaboration with Pr. Cecconi [18]. In addition, well-trained collaborators will help me in other various aspects: the host laboratory routinely perform *in utero* plasmid electroporations, live imaging and has a strong background in axonal morphogenesis. They possess a microscope dedicated for live imaging and photomanipulation of neurons, which is compatible with the proposed experiments. Having already identified exciting preliminary results, the present project is coherent therefore has good potential to provide important results. Finally, the host institution (INMG) has state-of-the-art Biochemistry/Cellular and Molecular Biology but also microscopy and animal house facilities. Overall, I am in a highly favourable environment to successfully reach the proposed objectives.

References

1. Goyal MS et al. Aerobic glycolysis in the human brain is associated with development and neotenus gene expression. *Cell Metab.* 2014 Jan 7;19(1):49-57.
- 2 Del Pino I et al. . Neural circuit dysfunction in mouse models of neurodevelopmental disorders. *Curr Opin Neurobiol.* 2018 Feb;48:174-182.
- 3 Hassan BA, Hiesinger PR. Beyond Molecular Codes: Simple Rules to Wire Complex Brains. *Cell.* 2015 Oct 8;163(2):285-91.

4. Simon DJ, Pitts J, Hertz NT, Yang J, Yamagishi Y, Olsen O, Tešić Mark M, Molina H, Tessier-Lavigne M. Axon Degeneration Gated by Retrograde Activation of Somatic Pro-apoptotic Signaling. *Cell*. 2016 Feb 25;164(5):1031-45.
5. Courchet J et al. Terminal axon branching is regulated by the LKB1-NUAK1 kinase pathway via presynaptic mitochondrial capture. *Cell*. 2013 Jun 20;153(7):1510-25
6. Devine MJ, Kittler JT. Mitochondria at the neuronal presynapse in health and disease. *Nat Rev Neurosci*. 2018 Jan 19;19(2):63-80
7. Li S et al. The cross-talk of energy sensing and mitochondrial anchoring sustains synaptic efficacy by maintaining presynaptic metabolism. *Nat Metab*. 2020 Oct;2(10):1077-1095.
8. Lanfranchi M et al. The AMPK-related kinase NUAK1 controls cortical axons branching through a local modulation of mitochondrial metabolic functions. *BioRxiv* <https://doi.org/10.1101/2020.05.18.102582>.
9. Lemasters JJ. Selective mitochondrial autophagy, or mitophagy, as a targeted defense against oxidative stress, mitochondrial dysfunction, and aging. *Rejuvenation Res*. 2005 Spring;8(1):3-5.
10. Cai Q et al. Spatial parkin translocation and degradation of damaged mitochondria via mitophagy in live cortical neurons. *Curr Biol*. 2012 Mar 20;22(6):545-52.
11. Ashrafi G et al. Mitophagy of damaged mitochondria occurs locally in distal neuronal axons and requires PINK1 and Parkin. *J Cell Biol*. 2014 Sep 1;206(5):655-70.
12. Courchet V et al. Haploinsufficiency of autism spectrum disorder candidate gene NUAK1 impairs cortical development and behavior in mice. *Nat Commun*. 2018 Oct 16;9(1):4289.
13. Lizcano et al., 2004
14. Iossifov I et al. De novo gene disruptions in children on the autistic spectrum. *Neuron*. 2012 Apr 26;74(2):285-99.
15. Zhou X et al. Unc-51-like kinase 1/2-mediated endocytic processes regulate filopodia extension and branching of sensory axons. *Proc Natl Acad Sci U S A*. 2007 Apr 3;104(14):5842-7.
16. Katayama H et al. A sensitive and quantitative technique for detecting autophagic events based on lysosomal delivery. *Chem Biol*. 2011 Aug 26;18(8):1042-52.
17. Amato S, Man HY. AMPK links cellular bioenergy status to the decision making of axon initiation in neurons. *Cell Logist*. 2011 May;1(3):103-105.
18. D'Acunzo P et al. Reversible induction of mitophagy by an optogenetic bimodular system. *Nat Commun*. 2019 Apr 4;10(1):1533
19. Dunlop EA, Tee AR. mTOR and autophagy: a dynamic relationship governed by nutrients and energy. *Semin Cell Dev Biol*. 2014 Dec;36:121-9.
20. Tian W et al. Phosphorylation of ULK1 by AMPK regulates translocation of ULK1 to mitochondria and mitophagy. *FEBS Lett*. 2015 Jul 8;589(15):1847-54.
21. Polleux F, Ghosh A. The slice overlay assay: a versatile tool to study the influence of extracellular signals on neuronal development. *Sci STKE*. 2002 Jun 11;2002(136):pl9.
22. Turchetto S, Broix L and Nguyen L. *Ex Vivo* Recording of Axonal Transport Dynamics on Postnatal Organotypic Cortical Slices *Stratoprotocols*, Oct 2020.
23. Popelka H, Klionsky DJ. Analysis of the native conformation of the LIR/AIM motif in the Atg8/LC3/GABARAP-binding proteins. *Autophagy*. 2015;11(12):2153-9.

- 24 Brooks D et al. Drosophila NUAK functions with Starvin/BAG3 in autophagic protein turnover. PLoS Genet. 2020 Apr 22;16(4):e1008700.
25. Birgisdottir ÁB, Lamark T, Johansen T. The LIR motif - crucial for selective autophagy. J Cell Sci. 2013 Aug 1;126(Pt 15):3237-47
26. Bilimoria PM, Bonni A. Molecular control of axon branching. Neuroscientist. 2013 Feb;19(1):16-24.
27. Grider MH et al.. Lipid raft-targeted Akt promotes axonal branching and growth cone expansion via mTOR and Rac1, respectively. J Neurosci Res. 2009 Nov 1;87(14):3033-42.
28. Chen Y et al. Dual targeting of NUA1 and ULK1 using the multitargeted inhibitor MRT68921 exerts potent antitumor activities. Cell Death Dis. 2020 Sep 1;11(8):712.

PROPOSED PROJECT N°3: Selective autophagy and skeletal striated muscle: identification of novel molecular mechanisms involved in myotonic dystrophy type 1 (DM1) (Time frame: 2021-2026).



Background

In the context of the MyoNeurAlp alliance, I plan to study skeletal striated muscle autophagy and to investigate biological function of the kinase DMPK in order to identify novel molecular mechanisms involved in myotonic dystrophy type 1 (DM1). The ability of skeletal muscle to maintain its homeostasis is severely compromised in patients with neuromuscular diseases. Myotonic dystrophy type 1 (DM1) is an autosomal dominant disease affecting skeletal striated muscle as well as cardiac muscle, resulting in myofiber atrophy and skeletal muscle weakness. DM1 is caused by a CTG expansion in the 3'UTR of the DMPK gene transcript. Toxic mRNAs, carrying CUG repeats, accumulate in the nucleus of myofibers, disrupting mRNA splicing and thus altering the expression of genes involved in muscle differentiation [1].

In fibroblasts from patients with DM1, impaired mitochondria function results in a decrease in ATP production and in an increase of the production of reactive oxygen species. Patients with DM1 show an accumulation of mitochondria in their muscle cells. These data suggest that mitophagy is impaired in DM1 patients.

Despite huge efforts, the pathophysiological mechanisms underlying DM1 still remain elusive. This project will englobe tow aims that will be mainly performed by a PhD that I will co-supervise with Dr Rémi Mounier (DR-CNRS at PGNM-INMG institut), an expert in skeletal striated muscle and AMPK.

Aim1. What are the benefits of activation of AMPK kinase and/or NUA1 kinase on mitochondrial dysfunction and skeletal muscle atrophy?

AMPK kinase is a major regulator of mitophagy in muscle and AMPK signalling has been shown to be repressed in DM1 skeletal muscle. In addition, the Mounier/Courchet teams have observed that the absence of the kinase NUA1 in skeletal muscle, disrupts muscle fiber homeostasis. By using a combination of *in vivo* (mouse) and

in vitro (primary culture of muscle cells) models associated with biochemical, molecular, cellular and physiological approaches mastered by the host teams, the objective of this part of the project will be to understand what are the benefits of activation of AMPK kinase and/or NUAK1 kinase on mitochondrial dysfunction and skeletal muscle atrophy while providing insights on novel therapies for DM1.

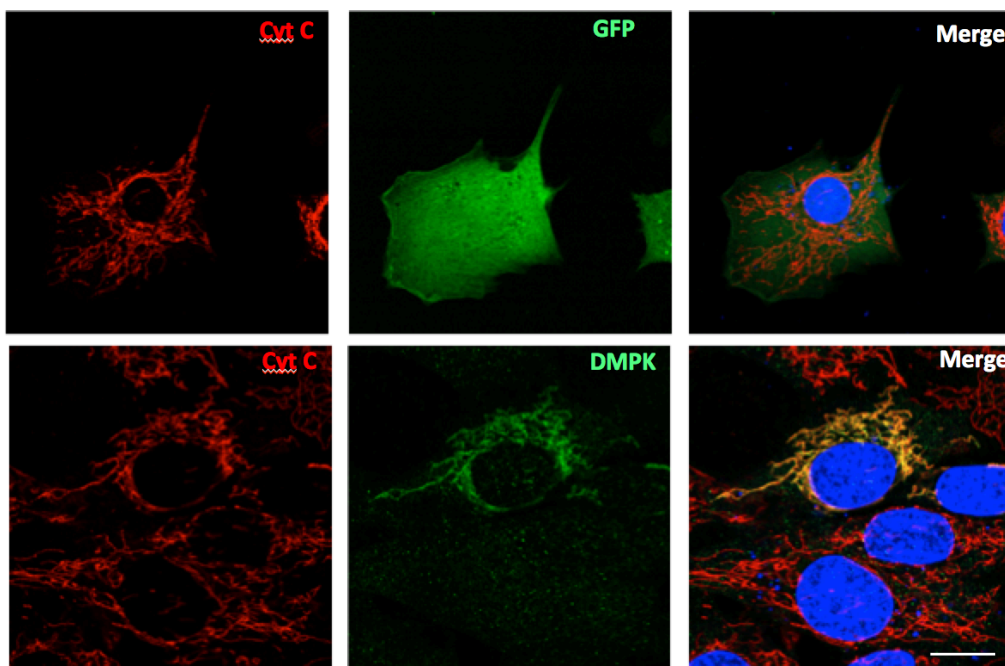
Aim2. Does DMPK kinase directly involve in DM1 pathogenesis?

Studies on the DMPK gene and gene products have far mainly concentrated on the fate of length mutation in the (CTG)_n repeat at the DNA level and consequences of repeat expansion at the RNA level in DM1 patients and disease models. Little is known about the function of DMPK protein products and a direct role for DMPK in the pathogenesis of DM1 has never been linked to the disease. It cannot be excluded that protein haploinsufficiency due to transcript retention in the nucleus may contribute to certain DM1 symptoms. Few studies have addressed individual protein products from the *DMPK* gene, including their normal structure function relationship [2,3]. Six major DMPK splice isoforms exist and are conserved between mouse and man. Individual isoforms are characterized by presence of either one of two types of long C-termini (tail versions 1 or 2; DMPK isoforms A to D) or a rather short C-terminus (tail 3; isoforms E and F), combined with absence or presence of an internal VSGGG-motif (A vs B, C vs D, E vs F) [4]. DMPK isoforms A–D are typical tail-anchored proteins with a membrane segment in their C-terminus. These isoforms are mainly expressed in heart, skeletal muscle and brain. Isoforms E and F are cytosolic proteins, predominantly found in smooth muscle cells [4,5]. Tail anchors in DMPK A/B and DMPK C/D drive binding to specific organelle membranes [6]. In mouse, this results in binding of mDMPK A and B to the endoplasmic reticulum (ER) and in binding of mDMPK C (and D) to the mitochondrial outer membrane (MOM). In humans, hDMPK A/B and C/D have also distinct tails, but these isoforms all anchor to the MOM. Isoform hDMPK A is unique in that its transient expression causes mitochondrial morphology. In particular, the protein's C-terminal tail is sufficient for induction of perinuclear clustering of mitochondria that results in autophagy induction, loss of cell-functional integrity and in the initiation of apoptosis [7,8].

Since I preliminary found *in silico* that DMPK kinase could be a kinase capable to phosphorylate NUAK1, I checked for putative phosphorylation and interaction between NUAK1 and DMPK kinases. I started my researches using the DMPK isoform B since its transient expression was not known to affect mitochondrial morphology.

By performing this preliminary analysis, I obtained surprising data that were not expected. In fact, I did not find any colocalization between NUAK1 and DMPK-B but our preliminary data suggest that **DMPK-B may be involved in DM1 pathogenesis through a specific myoblast cell cycle control**. Indeed, after overexpression of DMPK-B in C2C12 cells (a subclone of myoblasts), in addition to find, as expected, DMPK-B often localized on the outer mitochondrial membrane (Figure 1A), I noticed that a large number of DMPK-B transfected cells were in mitosis compared to GFP transfected cells (Figure 1B), suggesting that DMPK-B may favour mitosis in C2C12 cells.

A.



B.

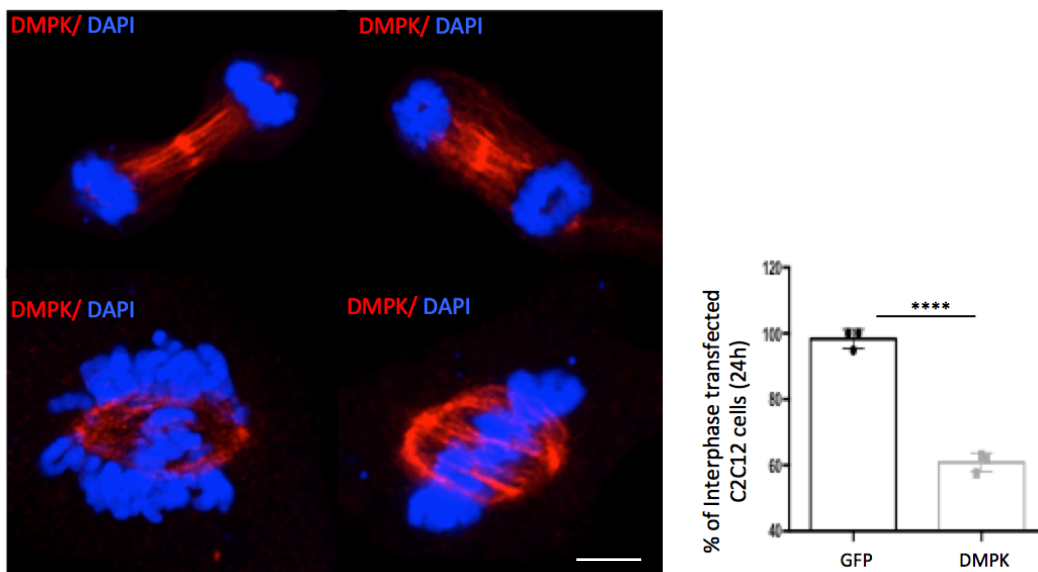


Figure 1. hDMPK-B is mainly localized on mitochondria in interphase but favors mitosis in C2C12 cells. A. C2C12 cells were transfected with a vector encoding hDMPK-B or GFP for 24h. Cells were next fixed and stained with an antibody against Cytochrome c to stain mitochondria (Cyt c, red signal), DMPK (green signal) and DAPI (blu signal). Scale bar 8 μ m. B. C2C12 cells were transfected with a vector encoding hDMPK-B or GFP for 24h. Cells were next fixed and stained with an antibody against DMPK (red signal) and DAPI (blu signal). Scale bar: 2 μ m. The number of transfected cells in interphase were quantified and compared to GFP transfected cells as a control and is illustrated on the graphic as the mean of three independent experiments (\pm SD). Statistical analysis was performed using Student *t*-test ($***P < 0.001$).

Of note, we performed a point mutation in the kinase domain of DMPK (K100A) and found that the kinase activity of hDMPK-B is required to induce mitosis in C2C12 cells (data not shown). Also, we noticed that DMPK-B loses its localization to mitochondria during mitosis (Figure 2).

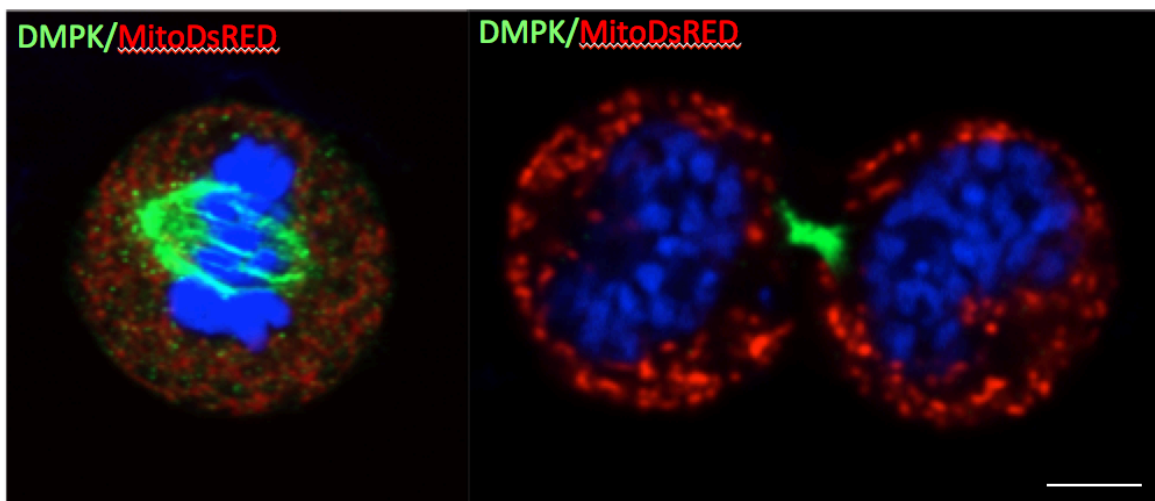


Figure 2. hDMPK-B is mainly localised on mitochondria in interphase but detaches from mitochondria during mitosis and re-localises on mitotic structures. C2C12 cells were transfected with a vector encoding hDMPK-B and mito-DsRED for 24h. Cells were next fixed and stained with an antibody against DMPK (green signal), mitochondria are red and with DAPI (blu signal). Scale bar: 1 μ m No colocalization was found between mitochondria (red) and DMPK (green) during mitosis.

In order to estimate the mitotic progression of the cells transfected with GFP alone or with DMPK, we next synchronised cells (by performing a deprivation of serum) and we quantified each phases of mitosis. We discovered that DMPK-B favours mostly telophases which correspond to the late phase of mitosis (Figure 3).

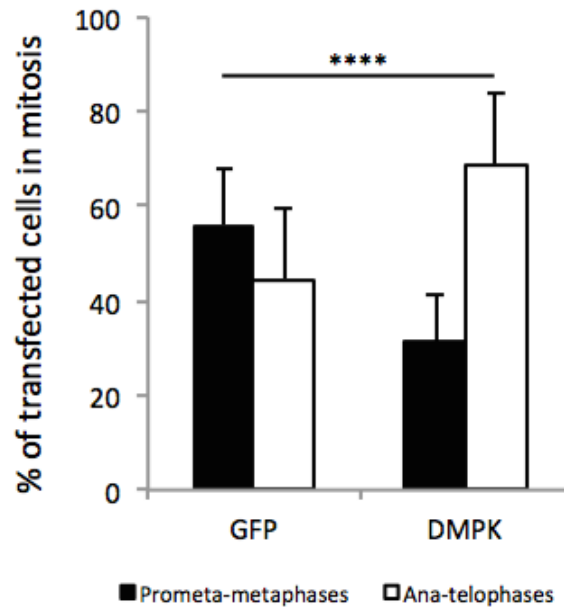


Figure 3. hDMPK-B favours ana-telophases in C2C12 cells. Cells were transfected with vectors encoding GFP and hDMPK-B and synchronized in medium deprived of serum for 12h. They were next fixed and stained for DMPK and DAPI. The number of prometa-metaphases was counted together with ana-telophases in GFP and DMPK transfected cells. The graphic represents the mean of three independent experiments (\pm SD). Statistical analysis was performed using Student *t*-test (**** $P < 0.0001$).

In addition, we found that DMPK-B re-localises considerably during the cell cycle. It concentrates mainly on cytoplasm or mitochondria in interphase, but moves partially to spindle poles in metaphase, and finally localizes to the spindle midzone and the midbody in telophase and during cytokinesis. On the midbody, DMPK-B localizes in a characteristic ring-like arrangement that is embraced by PRC1 (protein regulator of cytokinesis 1) and microtubules, indicating that DMPK is associated with the midbody ring (Figure 4). Since PRC1 is known to regulate cytokinesis, this data suggests that DMPK may regulate cytokinesis. We will thus check for a putative role of DMPK in cytokinesis regulation. Also, we identified DMPK-B as a constant companion of the midbody ring. We plan thus to check whether DMPK-B is required for its normal assembly. Altogether, these preliminary data provide evidences for the involvement of DMPK-B in regulation of mitosis. One of the aims of our PhD candidate work will be to unravel the mechanisms by which this regulation is achieved. Given the highly dynamic localization pattern of DMPK-B during cell division, we will search for binding partners and ask whether DMPK-B might target mitotic proteins. We plan also to verify whether DMPK-A that is very similar to DMPK-B (only 5 amino acids different) is able to control the cell cycle. One other main goal of the project will be to

understand how DMPK detaches from mitochondria to control cell cycle (ie: identification of a specific signalling) and whether it exist a link between its mitochondria localization and its capability to favour mitosis. Moreover, we plan to demonstrate the importance of this novel function of DMPK in the context of DM1, by using myoblasts coming directly from DM1 patients (in collaboration with Rémi Mounier from INMG, who already possesses these cells).

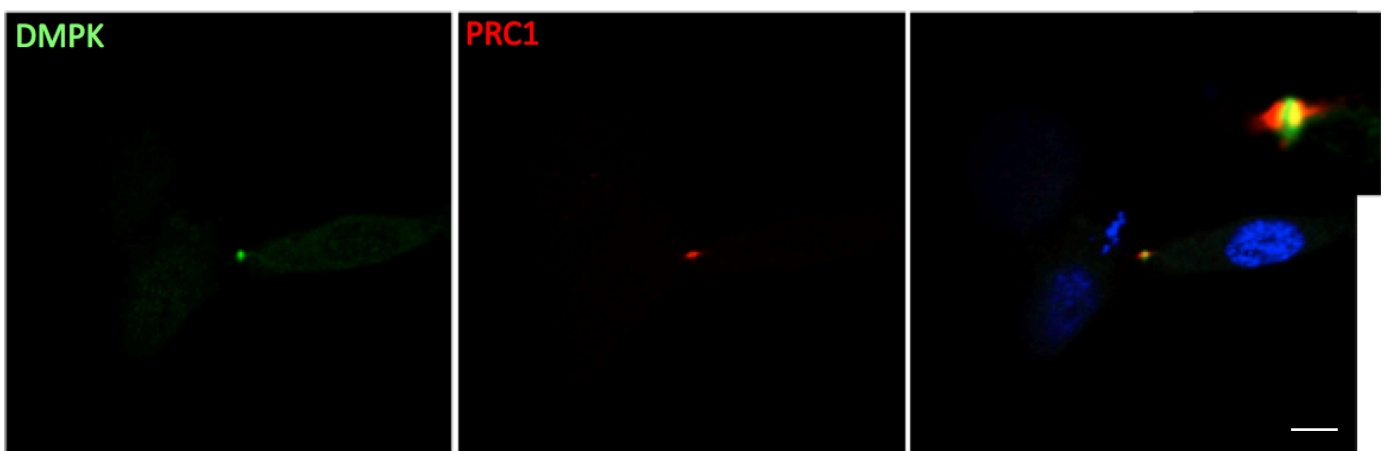
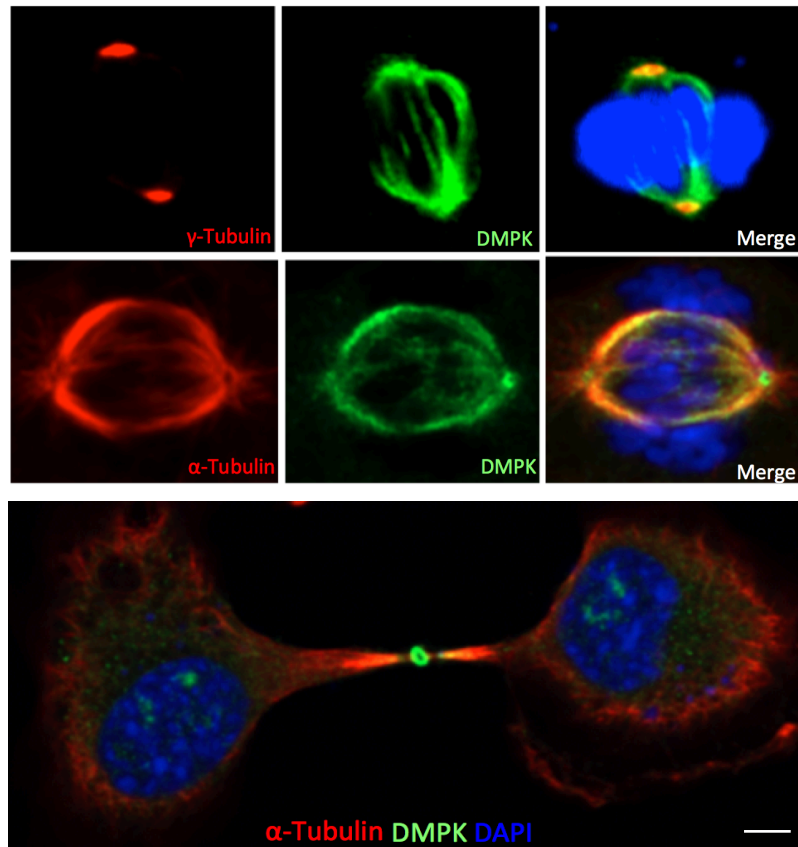


Figure 4. DMPK-B re-localises during the cell cycle. C2C12 cells were transfected with a vector encoding for hDMPK-B for 24h. Cells were next fixed and stained with antibody against DMPK (green staining), against γ -Tubulin (centrosome marker), α -Tubulin (microtubule marker) and PRC1 (Midbody marker). Scale bar: 1 μ m upper panels and 5 μ m on the lower panel.

By performing the two aims of this project (proposed project N°3), we hope to provide novel important pathophysiological mechanisms underlying DM1 in order to define new therapeutical approaches for this disease.

References

1. Mahadevan MS, Amemiya C, Jansen G, Sabourin L, Baird S, et al. Structure and genomic sequence of the myotonic dystrophy (DM kinase) gene. *Hum Mol Genet* 2: 299–304 (1993)
2. Wansink DG, van Herpen RE, Wieringa B. Normal and pathophysiological significance of myotonic dystrophy protein kinase. In: Wells RD, Ashizawa T, editors. *Genetic Instabilities and Neurological Diseases*. 2nd ed. San Diego, CA: Elsevier-Academic Press, Inc. pp. 79–97 (2006).
3. Kaliman P, Llagostera E. Myotonic dystrophy protein kinase (DMPK) and its role in the pathogenesis of myotonic dystrophy 1. *Cell Signal*. (2008)
4. Groenen PJ, Wansink DG, Coerwinkel M, van den Broek W, Jansen G, et al. Constitutive and regulated modes of splicing produce six major myotonic dystrophy protein kinase (DMPK) isoforms with distinct properties. *Hum Mol Genet* 9: 605–616 (2000)
5. Oude Ophuis RJ, Mulders SA, van Herpen RE, van de Vorstenbosch R, Wieringa B, et al. DMPK protein isoforms are differentially expressed in myogenic and neural cell lineages. *Muscle Nerve* 40: 545–555 (2009).
6. Snapp EL, Hegde RS, Francolini M, Lombardo F, Colombo S, et al. Formation of stacked ER cisternae by low affinity protein interactions. *J Cell Biol* 163: 257–269 (2003).
7. van Herpen RE, Oude Ophuis RJ, Wijers M, Bennink MB, van de Loo FA, et al. Divergent mitochondrial and endoplasmic reticulum association of DMPK splice isoforms depends on unique sequence arrangements in tail anchors. *Mol Cell Biol* 25: 1402–1414 (2005).
8. Oude Ophuis RJ, Wijers M, Bennink MB, van de Loo FA, Fransen JA, Wieringa B, Wansink DG. A tail-anchored myotonic dystrophy protein kinase isoform induces perinuclear clustering of mitochondria, autophagy, and apoptosis. *PLoS One*. Nov 25;4(11):e8024 (2009).

ANNEX

This section gathers additional work published in collaboration during my post-doctoral training (directly with Cecconi's group) or with other groups:

-The first work describes a collaboration with Bonaldo's laboratory (Padova, Italy) in which we demonstrated that **Ambra1 deficiency impairs mitophagy in skeletal muscle**. In 2015 I was granted by a trampoline AFM-Telethon grant as a junior PI. I proposed to demonstrate the role of Ambra1 as a positive regulator of mitophagy, by exploiting in vivo overexpression of a mitochondria-targeted form of Ambra1 in skeletal muscle. This part of my grant is illustrated in the first figure of this work by Gambarotto et al. 2022.

-The second and third works highlight a collaboration that I develop during these last years with Natascia Ventura (Group leader at the University of Dusseldorf) who is focusing her attention on the role of mitochondria in developmental- as well as age-associated neurodegenerative diseases, with the ultimate goal of promoting health-span. We published a work in 2015 (Schiavi et al., 2015) in which we show that **Iron-Starvation-Induced Mitophagy Mediates Lifespan Extension upon Mitochondrial Stress in C. elegans**. In 2020 we wrote review in which I am co-first author and that describes the link between **Mitophagy and Iron: two actors sharing the stage in age-associated neuronal pathologies** (Schiavi, Strappazzon et al., 2020). From this collaboration, we have currently another work in revision in the journal *Frontiers in Cell and Developmental Biology*.

-The fourth and fifth articles are collaborations with the group of Francesco Cecconi that I performed during my post-doctoral training. In Nazio et al., 2020, we found that a **Fine-tuning of ULK1 mRNA and protein levels is required for autophagy oscillation**. These results placed NEDD4L and ULK1 in a key position to control oscillatory activation of autophagy during prolonged stress to keep the levels of this process under a safe and physiological threshold. In Becher et al., 2018, we demonstrated that **AMBRA1 controls regulatory T-cell differentiation and homeostasis upstream of the FOXO3-FOXP3 axis**.

-The sixth article underlines a collaboration that I developed with Venturina Stagni (Researcher CNR, Rome, Italy) in which we discovered that **ATM kinase sustains breast**

cancer stem-like cells by promoting ATG4C expression and autophagy.

-Finally, the other articles represent some reviews that I wrote in principal position (First or last author) that highlighted the importance of the role played by mitochondria in diseases such as cancers and neurodegenerative diseases.

Ambra1 deficiency impairs mitophagy in skeletal muscle

Lisa Gambarotto^{1,2†}, Samuele Metti^{1†}, Martina Chrisam¹, Cristina Cerqua³, Patrizia Sabatelli^{4,5}, Andrea Armani^{6,7}, Carlo Zanon³, Marianna Spizzotin², Silvia Castagnaro¹, Flavie Strappazon^{8,9}, Paolo Grumati¹⁰, Matilde Cescon¹, Paola Braghetta¹, Eva Trevisson^{3,11}, Francesco Cecconi¹² & Paolo Bonaldo^{1*} 

¹Department of Molecular Medicine, University of Padova, Padova, Italy; ²Department of Biology, University of Padova, Padova, Italy; ³Institute of Pediatric Research IRP, Fondazione Città della Speranza, Padova, Italy; ⁴IRCCS Istituto Ortopedico Rizzoli, Bologna, Italy; ⁵CNR - Institute of Molecular Genetics "Luigi Luca Cavalli-Sforza", Unit of Bologna, Bologna, Italy; ⁶Department of Biomedical Sciences, University of Padova, Padova, Italy; ⁷Fondazione per la Ricerca Biomedica Avanzata, VIMM, Padova, Italy; ⁸IRCCS Fondazione Santa Lucia, Rome, Italy; ⁹Institut NeuroMyogène, CNRS UMR5261 - INSERM U1315, Université Claude Bernard Lyon 1, Lyon, France; ¹⁰Telethon Institute of Genetics and Medicine, Pozzuoli, Italy; ¹¹Clinical Genetics Unit, Department of Women's and Children's Health, University of Padova, Padova, Italy; ¹²Danish Cancer Society Research Center, Copenhagen, Denmark

Abstract

Background Maintaining healthy mitochondria is mandatory for muscle viability and function. An essential surveillance mechanism targeting defective and harmful mitochondria to degradation is the selective form of autophagy called mitophagy. Ambra1 is a multifaceted protein with well-known autophagic and mitophagic functions. However, the study of its role in adult tissues has been extremely limited due to the embryonic lethality caused by full-body Ambra1 deficiency.

Methods To establish the role of Ambra1 as a positive regulator of mitophagy, we exploited *in vivo* overexpression of a mitochondria-targeted form of Ambra1 in skeletal muscle. To dissect the consequence of Ambra1 inactivation in skeletal muscle, we generated muscle-specific *Ambra1* knockout (*Ambra1*^{fl/fl}:*Mlc1f*-Cre) mice. Mitochondria-enriched fractions were obtained from muscles of fed and starved animals to investigate the dynamics of the mitophagic flux.

Results Our data show that Ambra1 has a critical role in the mitophagic flux of adult murine skeletal muscle and that its genetic inactivation leads to mitochondria alterations and myofibre remodelling. Ambra1 overexpression in wild-type muscles is sufficient to enhance mitochondria clearance through the autophagy-lysosome system. Consistently with this, Ambra1-deficient muscles display an abnormal accumulation of the mitochondrial marker TOMM20 by +76% ($n = 6-7$; $P < 0.05$), a higher presence of myofibres with swollen mitochondria by +173% ($n = 4$; $P < 0.05$), and an alteration in the maintenance of the mitochondrial membrane potential and a 34% reduction in the mitochondrial respiratory complex I activity ($n = 4$; $P < 0.05$). Lack of Ambra1 in skeletal muscle leads to impaired mitophagic flux, without affecting the bulk autophagic process. This is due to a significantly decreased recruitment of DRP1 ($n = 6-7$ mice; $P < 0.01$) and Parkin ($n = 6-7$ mice; $P < 0.05$) to the mitochondrial compartment, when compared with controls. Ambra1-deficient muscles also show a marked dysregulation of the endolysosome compartment, as the incidence of myofibres with lysosomal accumulation is 20 times higher than wild-type muscles ($n = 4$; $P < 0.05$). Histologically, Ambra1-deficient muscles of both 3- and 6-month-old animals display a significant decrease of myofibre cross-sectional area and a 52% reduction in oxidative fibres ($n = 6-7$; $P < 0.05$), thus highlighting a role for Ambra1 in the proper structure and activity of skeletal muscle.

Conclusions Our study indicates that Ambra1 is critical for skeletal muscle mitophagy and for the proper maintenance of functional mitochondria.

Keywords Ambra1; Skeletal muscle; Mitophagy; Mitochondria

Received: 5 January 2022; Revised: 21 March 2022; Accepted: 14 April 2022

*Correspondence to: Paolo Bonaldo, Department of Molecular Medicine, University of Padova, Via Ugo Bassi 58/B, 35131 Padova, Italy. Phone: (+39) 049 827 6084, Fax: (+39) 049 827 6079, Email: bonaldo@bio.unipd.it

Lisa Gambarotto and Samuele Metti contributed equally to this work.

Introduction

Mitochondria are dynamic organelles providing energy and metabolites to eukaryotic cells, thus ensuring their metabolic needs.¹ Mitochondria also act as signalling organelles that orchestrate several cellular processes, such as programmed cell death, autophagy, cell cycle regulation, and redox balance.² The presence of healthy and functional mitochondria is imperative for cellular homeostasis. Therefore, cells need surveillance mechanisms able to recognize and remove dysfunctional mitochondria.³

Macroautophagy (hereafter referred as autophagy) is a tightly regulated self-eating process, highly conserved among species, which plays essential roles in ensuring quality control of cell components and in the maintenance of cell homeostasis. The autophagic machinery removes damaged or unnecessary organelles, protein aggregates, and pathogens through double-membrane vesicles called autophagosomes, which are delivered to the endo-lysosomal pathway.⁴ Besides bulk autophagy, several forms of autophagy involved in the turnover of distinct cell components were recognized. Among them, mitophagy ensures the clearance of defective mitochondria during different physiological and pathological conditions, thus preventing their toxic accumulation. The mitophagic process is critical in post-mitotic and energy-demanding cells, such as neurons and muscle fibres, because their low regenerative capacity and the production of reactive oxygen species require high turnover rates of proteins and organelles to cope with cellular damages that may accumulate over time.⁵

Skeletal muscle is a plastic tissue, able to adapt to different physiological and pathological stimuli, such as variations in nutrients, mechanical stress, physical activity, and hormones. Given its abundance within body mass, skeletal muscle plays fundamental roles in the maintenance of whole-body metabolic homeostasis. Therefore, the fine regulation of mitochondria activity and turnover is critical for muscle function.⁶ Indeed, mitophagy dysregulation was found to be involved in the aetiopathology of a broad range of disorders affecting muscles, including cancer cachexia,⁷ age-related sarcopenia,⁸ insulin resistance,⁹ and muscular dystrophies.^{10,11} However, the molecular players participating in the regulation of mitophagy in muscle are still largely unknown.

Activating molecule in Beclin 1-regulated autophagy (Ambra1) is an intrinsically disordered protein acting as a scaffold and involved in multiple cellular processes, including cell cycle, proliferation, and autophagy.^{12,13,51} During autophagy, Ambra1 interacts with Beclin 1, thus stabilizing and potentiating the activity of class-III-phosphoinositide-3-kinase (PI3K) initiation complex upon pro-autophagic stimuli.¹⁴ Ambra1 also plays a pivotal role in regulating mitophagy, being recruited to depolarized mitochondria where it mediates

their selective clearance by interacting with the E3 ubiquitin ligase Parkin.^{15,52} In addition, Ambra1 facilitates the transport of mitophagic cargoes into nascent autophagosomes, thus acting as a mitophagy receptor through the interaction of microtubule-associated protein 1 light chain 1 β (MAP1LC3B, hereafter LC3) with the LC3-interacting region (LIR) of Ambra1.^{16,17,53}

Initial studies, exploiting a randomly mutated *Ambra1* locus (*Ambra1^{gt/gt}*) in mice, showed that Ambra1 deficiency is embryonic lethal and causes exencephaly and spina bifida, associated with autophagy impairment, unbalanced cell proliferation, and excessive apoptosis.¹⁸ Notably, besides altered neurogenesis, Ambra1 deficiency also leads to impaired muscle development in both zebrafish and mouse embryos.^{18–20}

Because the embryonic lethality of *Ambra1^{gt/gt}* mice prevents to investigate Ambra1 function in adults, we generated a new *Ambra1^{fl/fl}:Mlc1f-Cre* mouse model, in which Ambra1 depletion occurs in skeletal muscle. Here we show that Ambra1-deficient muscles display myofibre defects, with progressive accumulation of dysfunctional mitochondria. Notably, while bulk autophagy appears unaffected, the mitophagic flux is compromised in Ambra1-deficient muscles due to impaired recruitment of Parkin and DRP1 to depolarized mitochondria.

Methods

Generation of *Ambra1* knockout mice

Whole-body and muscle-specific *Ambra1* knockout mice were produced from *Ambra1*<tm1a(EUCOMM)Wtsi> embryonic stem cells (EUCOMM Consortium), which contain a targeted conditional mutation (tm1a; reference⁵⁴) within exon 4 of *Ambra1* gene in the C57BL/6N background (see Supporting Information, *Figure S1a* for details). Cells were aggregated with E2.5 morulas of CD1 mice, following standard procedures.⁵⁵ The nucleotide sequence of *Ambra1*<tm1a(EUCOMM)Wtsi> mutant allele is deposited in GenBank (#JN964599.1). Mice bearing the *Ambra1^{tm1a}* allele were crossed with FLP transgenic mice,⁵⁶ to remove *lacZ* and *neo* cassettes (tm1c allele; *Figure S1a*). The obtained *Ambra1^{fl/+}* mice were backcrossed with C57BL/6N mice for one generation to get rid of the FLP transgene and then crossed with CAG-Cre mice,⁵⁷ to generate whole-body *Ambra1* knockout (*Ambra1^{-/-}*) mice. Skeletal muscle-specific *Ambra1* (*Ambra1^{fl/fl}:Mlc1f-Cre*) knockout mice were generated by crossing *Ambra1^{fl/+}* mice with *Mlc1f-Cre* mice.⁵⁸ *Ambra1^{fl/fl}:Mlc1f-Cre* and *Ambra1^{fl/fl}* littermate controls were obtained by subsequent crossings (*Figure S1a*). All studies were carried out in mice with C57BL/6N genetic background. Genotyping

was determined by PCR with specific primers, listed in *Table S1*.

Animals

The newly generated mice and GFP-LC3 mice⁵⁹ were housed in controlled temperature (23°C) and light (12 h light/12 h dark cycle) conditions, with free access to water and food. Animal procedures were approved by the Animal Ethics Committee of the University of Padova and by the Italian Ministry of Health (n. 581/2017-PR). For starvation experiments, at 8 AM, mice were transferred for 24 h to clean cages without chow but with free water access. For colchicine treatment, mice were i.p. injected with 0.4 mg/kg/day of colchicine (Sigma-Aldrich), 24 and 12 h before sacrifice. For chloroquine treatment, mice were i.p. injected with 50 mg/kg/day of chloroquine (Sigma-Aldrich) for three consecutive days and sacrificed 3 h after last injection.⁵¹⁰ For all experiments, mice were sacrificed within 7:30 and 10:00 AM.

In vivo muscle transfection

Tibialis anterior (TA) muscles were transfected by *in vivo* electroporation as described.⁵¹¹ Briefly, animals were anaesthetized, TA was exposed, and 30–40 µg of naked plasmid DNA was injected in the central region of muscle. Spatula electrodes were placed and five 200-ms-long electric pulses were delivered at 100 V/cm with Nepagene NEPA21 electroporator. Muscles were collected 10–12 days after wound closure. For transfection of flexor digitorum brevis (FDB) muscle, DNA was injected in the foot without any skin incision after hyaluronidase pre-treatment and delivered to cells by 20 electric pulses with needle electrodes.

Histology and immunofluorescence

Embryos were fixed overnight at 4°C with 4% paraformaldehyde in phosphate-buffered saline (PBS), dehydrated in increasing alcohol solutions, cleared with xylene, and paraffine-embedded. Seven-micrometre-thick sections were deparaffinized in xylene and rehydrated in decreasing alcohol solutions before staining. TA and quadriceps muscles were frozen in pre-cooled isopentane and stored at –80°C until analysis. Ten-micrometre-thick cryosections were stained with haematoxylin and eosin, dehydrated, and mounted with Eukitt Quick-hardening mounting medium (Sigma-Aldrich). Bright-field micrographs were captured by a Leica DM-R microscope equipped with digital camera. Cross-sectional area (CSA) measurements were carried out manually using haematoxylin–eosin-stained images. Immunostainings were performed as described⁵¹² and hybridized overnight with primary antibodies (listed in *Table S2*) and with the appropri-

ate secondary antibodies (Jackson ImmunoResearch). Nuclei were counter-stained with Hoechst 33258 (Sigma-Aldrich). Slides were mounted with 80% glycerol in PBS and observed with Zeiss LSM700 and Leica SP5 confocal microscopes. Confocal images were processed by FIJI Software⁵¹³ and quantitative analysis was performed with Squassh software,⁵¹⁴ always maintaining the same parameters. Fibre type analysis and the relative CSA measurements were carried out by exploiting Myosoft automated macro for FIJI software.⁵¹⁵

Transmission electron microscopy

Tibialis anterior muscles from 6-month-old mice were fixed overnight at 4°C with 2.5% glutaraldehyde in 0.1 M cacodylate buffer, washed with 0.1 M cacodylate buffer, post-fixed for 2 h with 1% osmium tetroxide, and embedded in Epon812 (Electron Microscopy Sciences). Ultrathin sections were stained with uranyl acetate and lead citrate and observed with a Philips EM400 electron microscope operating at 100 kV.

Western blotting

Frozen murine samples (whole embryos, skeletal muscles, and heart) were ground in liquid nitrogen and lysed as described.⁵¹² For subcellular fractionation of mitochondria and nuclei, freshly collected quadriceps were processed as described⁵¹⁶ and lysates stored at –80°C until use. Equal amounts of proteins, quantified by BCA Protein Assay Kit (Thermo-Fisher), were loaded in polyacrylamide Novex NuPAGE Bis-Tris gels (Invitrogen) and electrotransferred onto PVDF membranes (Millipore). Membranes were stained with Ponceau (Sigma-Aldrich), saturated, and incubated overnight with primary antibodies (listed in *Table S2*). Horseradish peroxidase-conjugated secondary antibodies (1:2000; Bethyl Laboratories) were used, and the signal detected with SuperSignal West Pico (Thermo-Fisher). Densitometric quantification was carried out by FIJI software.⁵¹³

Real-time quantitative polymerase chain reaction

Whole frozen embryos or muscles were ground in liquid nitrogen. Total RNA was isolated by TRIzol (Invitrogen), quantified, and retrotranscribed with SuperScript III First-Strand Synthesis System (Invitrogen) using random hexamers. Real-time PCR reactions were performed with RotorGeneQ (Qiagen), using SYBR green mastermix (Qiagen). Data were analysed with the instrument's software, using *Actb* as a reference gene. Primers sequences are listed in *Table S1*.

Mitochondrial DNA copy number

Total DNA was isolated from entire quadriceps muscles by phenol:chloroform extraction and quantified. For each sample, same DNA amounts were amplified by real-time PCR, using primers for nuclear (*Tert*) and mitochondrial (*Nd4*) DNA (Table S1). Mitochondrial DNA copy number was calculated using *Tert* as a reference for nuclear DNA content.

Mitochondrial membrane potential

Mitochondrial membrane potential was measured in *ex vivo* FDB myofibres. Briefly, freshly dissected FDB muscles were incubated for 1 h in ice and 50 min at 37°C in the presence of 0.4% collagenase I (Sigma-Aldrich). Fibres were mechanically dissociated and seeded in microscope slides pre-coated with laminin (Sigma-Aldrich). The following day, slides were incubated for 30 min at 37°C in a saline buffer (20 mM HEPES, 35 mM NaCl, 5 mM KCl, 1 mM CaCl₂, 1 mM MgCl₂, 1 mM MgSO₄, 0.4 mM KH₂PO₄, 5 mM glucose) supplemented with 20 nM tetramethylrhodamine methyl ester (TMRM), and myofibres were analysed with SP5 inverted confocal microscope (Leica). Sequential images of TMRM fluorescence were acquired every 5 s. When indicated, 10 μM oligomycin or 10 μM carbonyl cyanide *m*-chlorophenyl hydrazone (CCCP) were added. Quantification of TMRM fluorescence was performed using FIJI software.^{S13}

Treadmill exercise

Six-month-old mice were first adapted for two consecutive days to treadmill, set in horizontal position, for 15 min at a speed of 8 cm/s. Acute exercise was performed, by setting treadmill in uphill position (+5° slope) at increasing speeds (10 min at 0 cm/s, 5 min at 11 cm/s, 10 min at 18 cm/s, 15 min at 25 cm/s, and 50 min at 33 cm/s).

Respiratory chain activity

Activities of NADH:coenzyme Q1 oxidoreductase (Complex I), succinate dehydrogenase (Complex II), ubiquinol:cytochrome c oxidoreductase (Complex III), NADH:cytochrome c reductase (Complex I–III), succinate:cytochrome c reductase (Complex II–III), cytochrome c oxidase (Complex IV), and citrate synthase (CS) in skeletal muscles were determined by spectrophotometric assays as described.^{S17}

RNA extraction and library preparation

Total RNA was extracted from TA muscles with TRIzol (Invitrogen), and its concentration measured with

QuantiFluor RNA System (Promega). RNA integrity was assessed by Agilent 2100 Bioanalyzer. From each sample, 800 ng total RNA was used to prepare two pools, one from *Ambra1^{fl/fl}* TA and one from *Ambra1^{fl/fl}:Mlc1f-Cre* TA, which provided inputs for sample preparations. Libraries for RNA-seq were constructed with the TruSeq Stranded mRNA Kit (Illumina), according to manufacturer's instructions.

RNA-seq analysis

Fastq files were processed with the 'Salmon' software v.1.3.0^{S18} to quantify transcript expression, using mm10.refMn mouse transcripts as reference. Log2ratios for each transcript were calculated from transcript per million bases (TPM) values. Differentially expressed transcripts were shortlisted by setting the minimum TPM value of 3 and the minimum absolute log2ratio of 0.7. Pathway enrichment analysis was performed for selected transcripts using the PANTHER Overrepresentation Test (<http://pantherdb.org/tools/compareToRefList.jsp>), and the results were graphically reported using the function barplot of R v.4.1.1 software (<https://www.R-project.org/>).

Statistics

Observed and expected outcomes of mouse matings (Figure S1d) were compared by χ^2 test. All comparisons were made by using two-tailed unpaired Student's *t*-test, except when indicated in figure captions, and *P* < 0.05 was considered as statistically significant. Data are provided as mean ± SEM. The number of biological replicates (always greater than three) is indicated in figures' captions.

Results

In vivo Ambra1-ActA overexpression in skeletal muscle induces mitochondria clearance through the autophagy-lysosome system

To study the contribution of Ambra1 in regulating mitophagy in adult skeletal muscle, we first exploited *in vivo* overexpression of a mitochondria-targeted form of Ambra1 (Ambra1-ActA) in TA and FDB muscles of GFP-LC3 reporter mice, which allow to easily monitor autophagy by fluorescence microscopy.¹⁶ We transfected muscles with a bicistronic vector that simultaneously drives the expression of FLAG-tagged Ambra1-ActA and mitoDsRed, thus allowing for mitochondria labelling in transfected myofibres. Fluorescence microscopy of TA cross-sections showed more GFP-LC3B-positive puncta in Ambra1-ActA-transfected myofibres, and many of these puncta colocalized with mitochondrial signal (Figure 1A).

Moreover, when acidification of lysosomes was inhibited by chloroquine administration, with a resulting block of the autophagic flux, myofibres transfected with Ambra1-ActA showed increased mitochondrial signal co-localizing with GFP-LC3-positive dots, when compared with fibres transfected with control plasmid (Figure 1A). These data suggested that Ambra1-ActA overexpression enhances mitochondrial clearance by triggering autophagosome formation. In agreement with this, western blotting highlighted a significant chloroquine-dependent accumulation of the mitochondrial protein cytochrome c oxidase subunit 4 (COX4) only when Ambra1-ActA was overexpressed (Figure 1B). Interestingly, even transfected Ambra1-ActA protein itself accumulated after autophagy inhibition, suggesting that it was subjected to the same clearance process as other autophagosome proteins (Figure 1C). In addition, Ambra1-ActA overexpression in muscle led to increased accumulation of the lipidated form of LC3, a well-known autophagosome marker, when chloroquine was provided (Figure 1D). Taken together, these results indicate that overexpression of a mitochondria-targeted form of Ambra1 is sufficient to enhance mitochondrial degradation through the autophagy-lysosome degradative system in adult muscle.

Whole-body Ambra1 knockout is embryonic lethal

To assess the consequences of *in vivo* Ambra1 ablation, we generated Ambra1 conditional knockout mice (Materials and Methods and Figure S1a). Global, whole-body Ambra1 null (*Ambra1*^{-/-}) mice were obtained by crossing *Ambra1*^{fl/fl} mice with transgenic mice expressing Cre recombinase under the control of a promoter active at the zygote stage. Western blotting and RT-qPCR confirmed correct ablation of Ambra1 mRNA and protein in *Ambra1*^{-/-} embryos (Figure S1b,c). We found that no homozygous *Ambra1*^{-/-} pups were present in litters, whereas heterozygous *Ambra1*^{fl/-} were born at the expected Mendelian ratios (Figure S1d), confirming that Ambra1 null allele in homozygosity causes embryonic lethality at mid-gestation. Macroscopic and histological analyses at E13.5 showed major abnormalities in *Ambra1*^{-/-} embryos, with severe disruption of brain and neural tube development (Figure S1e), thus resembling the exencephaly and spina bifida defects of *Ambra1*^{gt/gt} embryos.¹⁸ Western blotting for autophagic markers revealed a significant increase of p62/SQSTM1 levels and a concurrent decrease of LC3-II levels in *Ambra1*^{-/-} embryos (Figure S1f), pointing at autophagic impairment with decreased autophagosome formation and accumulation of SQSTM1-tagged autophagic cargoes. These results support the essential role of Ambra1 for proper neural development and confirm that its global inactivation leads to embryonic lethality at mid-gestation.

Conditional inactivation of Ambra1 in skeletal muscle leads to myofibre remodelling in postnatal life

Muscle-specific ablation of Ambra1 was obtained by crossing *Ambra1*^{fl/fl} mice with *Mlc1f*-Cre mice, which express Cre recombinase in differentiated myofibres.⁵⁸ *Ambra1*^{fl/fl}:*Mlc1f*-Cre mice did not display any major difference in body weight, life expectancy, or fertility when compared with *Ambra1*^{fl/fl} littermate controls (data not shown). Western blotting confirmed depletion of Ambra1 in skeletal muscles (Figure S2a), but not in heart or other tissues (Figure 2A and data not shown). Haematoxylin–eosin staining of Ambra1-deficient muscles did not show any overt alteration of the three-dimensional architecture of skeletal muscles (Figure 2B). Nevertheless, morphometric analyses revealed that Ambra1 deletion led to decreased myofibre sizes in both juvenile (3-month-old) and adult (6-month-old) *Ambra1*^{fl/fl}:*Mlc1f*-Cre mice, with a significant decrease of the mean myofibre CSA and of the percentage of myofibres with larger CSA, when compared with *Ambra1*^{fl/fl} control mice (Figure 2C). In addition, *Ambra1*^{fl/fl}:*Mlc1f*-Cre muscles displayed a significant decrease in the percentage of type IIA myofibres, pointing at a switch from oxidative to glycolytic myofibres (Figure 2D). Analysis of the CSA distributions within different fibre types at 6 months of age showed decreased CSA in both type IIB/IIX and type IIA myofibres of *Ambra1*^{fl/fl}:*Mlc1f*-Cre muscles (Figure S2b). RNA-seq experiments on TA, aimed at the identification of differentially expressed genes between *Ambra1*^{fl/fl}:*Mlc1f*-Cre and *Ambra1*^{fl/fl} muscles, highlighted changes in several gene ontology (GO) transcripts classes. Among the most enriched GO classes for ‘biological process’ (Figure 2E) and ‘cellular components’ (Figure 2F), there was significant enrichment in transcripts coding for proteins involved in sarcomere structure and function. Furthermore, these experiments revealed altered expression of genes coding for mitochondria-related proteins in Ambra1-depleted muscles (Figure 2F), prompting us to investigate further the mitochondrial compartment. Altogether, these data indicate that Ambra1 ablation in skeletal muscle leads to extensive remodelling both in terms of myofibre size and gene expression.

Ambra1-deficient muscles accumulate mitochondria and endo-lysosomal vesicles

Considering that Ambra1 is a positive regulator for autophagy, we investigated bulk autophagy in Ambra1-depleted muscles. Unexpectedly, analysis of the autophagic flux upon colchicine administration did not reveal any significant difference in LC3 lipidation and LC3-II accumulation between *Ambra1*^{fl/fl}:*Mlc1f*-Cre and *Ambra1*^{fl/fl} muscles, thus suggesting that bulk autophagy is not overtly affected by lack of

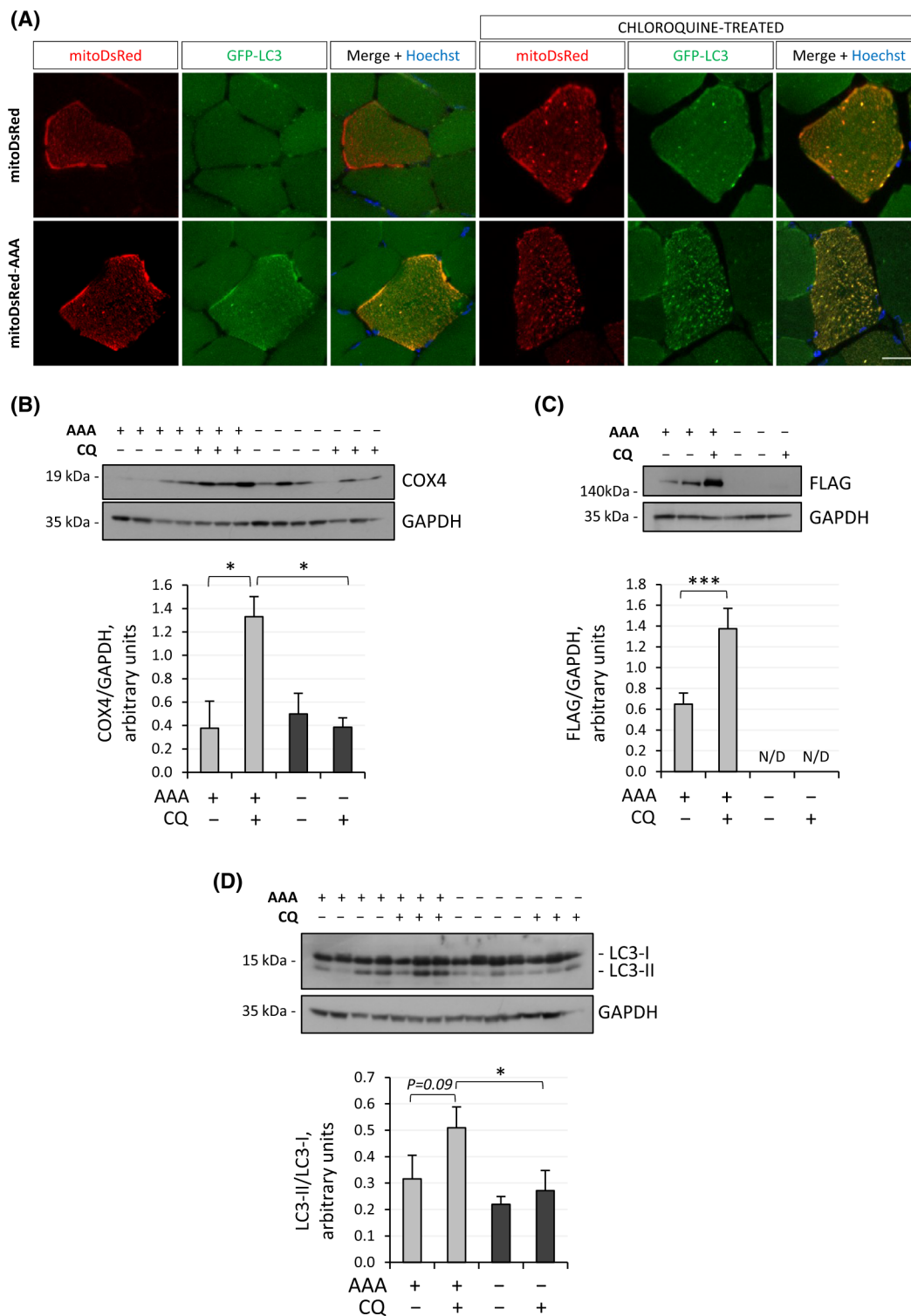
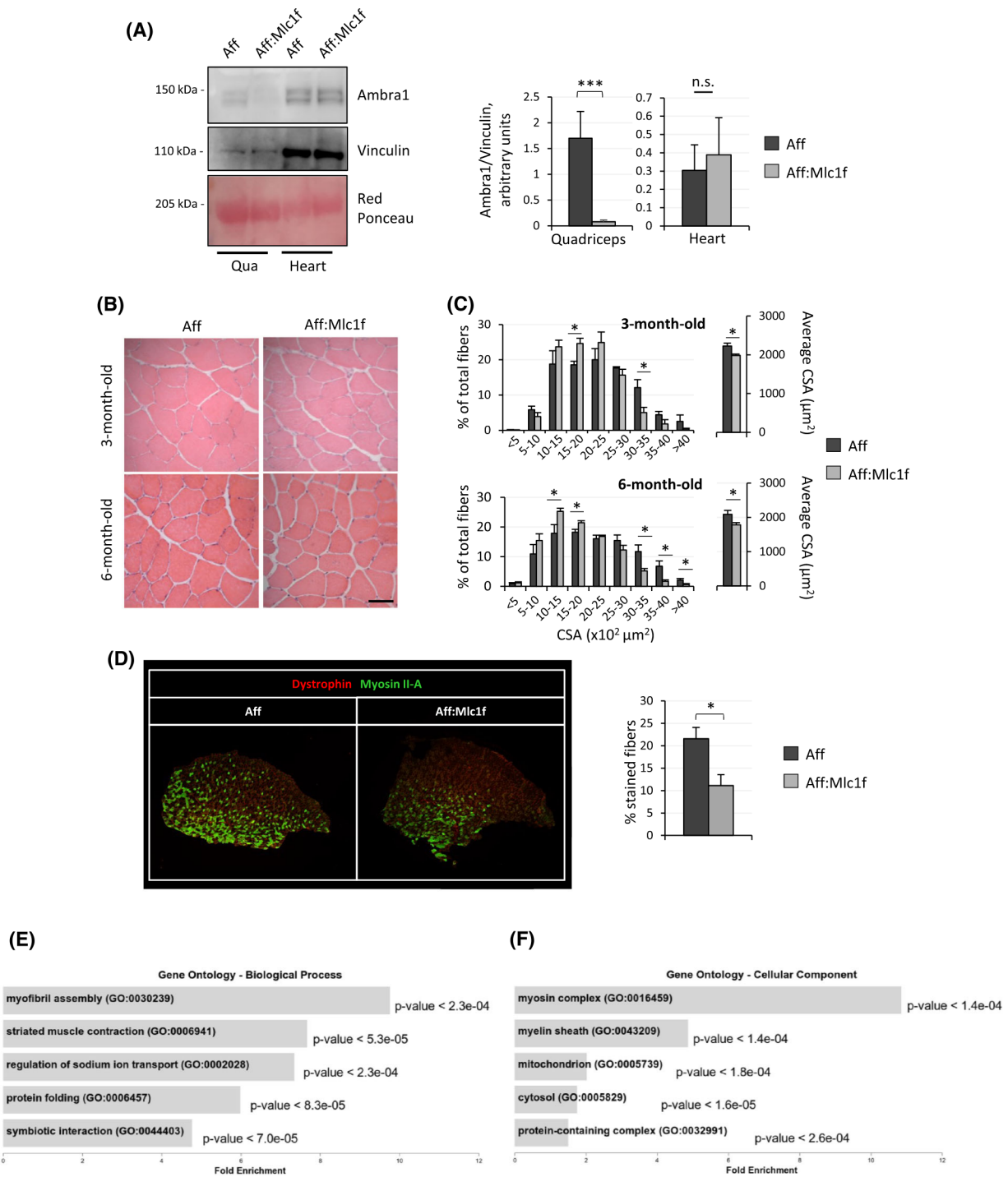


Figure 1 *In vivo* Ambra1-ActA overexpression in skeletal muscle induces mitophagy. (A) Representative confocal immunofluorescence images for mitoDsRed (red) and GFP-LC3 (green) in cross sections of TA muscles electroporated with control plasmid (mitoDsRed) or Ambra1-ActA-FLAG plasmid (mitoDsRed-AAA), in GFP-LC3 reporter mice treated or not with chloroquine. Nuclei were counterstained with Hoechst (blue). Scale bar, 20 μ m. (B–D) Western blot analysis for COX4 (B), FLAG (C), and LC3 (D) in protein lysates of FDB muscle electroporated with Ambra1-ActA-FLAG plasmid (AAA, +) or control plasmid (–), in wild-type mice treated (+) or not (–) with chloroquine (CQ). GAPDH was used as loading control. The densitometric quantifications of FLAG vs. GAPDH, COX4 vs. GAPDH, and LC3-II vs. LC3-I are shown below the respective western blot panels. Data are provided as mean \pm SEM ($n = 3–4$, each condition; *, $P < 0.05$; ***, $P < 0.001$). N/D, not detectable.



Ambra1 in muscles (Figure S2c). Because we found that Ambra1-ActA overexpression led to mitochondria degradation via the autophagy-lysosome system (see Figure 1), we investigated the mitochondrial and endo-lysosomal compartments in Ambra1-deficient TA and quadriceps muscles. Western blotting (Figure 3A; Figure S2d) and quantitative immuno-

fluorescence (Figure 3B,C) revealed that lysosome-associated membrane protein 1 (LAMP1) and translocase of outer mitochondrial membrane 20 (TOMM20), which respectively mark endo-lysosomes and mitochondria, were significantly increased in *Ambra1^{fl/fl};Mlc1f-Cre* muscles, pointing at an accumulation of mitochondria and endo-lysosomes. This

Figure 2 Muscle-specific ablation of *Ambra1* leads to myofibre remodelling. (A) Western blotting for *Ambra1* in protein extracts of quadriceps muscle (Qua) and heart from 6-month-old *Ambra1^{fl/fl}* (Aff) and *Ambra1^{fl/fl}:Mlc1f-Cre* (Aff:Mlc1f) mice. Vinculin was used as loading control. Densitometric quantifications of *Ambra1* vs. vinculin, as determined by at least three independent experiments, are shown on the right. Data are provided as mean \pm SEM ($n = 4$, each condition; ***, $P < 0.001$; n.s., not significant). (B) Haematoxylin–eosin staining of TA cross sections from 3- and 6-month-old *Ambra1^{fl/fl}* (Aff) and *Ambra1^{fl/fl}:Mlc1f-Cre* (Aff:Mlc1f) mice. Scale bar, 50 μ m. (C) Morphometric analysis for cross-sectional area (CSA) distribution among myofibres (left) and average cross-sectional area (right), as determined by microscopy images of TA muscle cross sections as in (B). Data are shown as mean \pm SEM ($n = 4$ –9 mice, each genotype; *, $P < 0.05$; **, $P < 0.01$). (D) Merged immunofluorescence confocal images for Dystrophin (red) and Myosin IIA (green) in cross cryosections of TA muscle from 6-month-old *Ambra1^{fl/fl}* (Aff) and *Ambra1^{fl/fl}:Mlc1f-Cre* (Aff:Mlc1f) mice. Quantification of the percentage of green-positive fibres is shown on the right. Data are shown as mean \pm SEM ($n = 6$ –7 mice, each genotype; *, $P < 0.05$). (E,F) Bar plots representing the five most enriched gene ontology (GO) classes for biological process (E) and cellular component (F) categories, as determined from RNA-seq data for differentially expressed genes in tibialis anterior muscles of 6-month-old *Ambra1^{fl/fl}* and *Ambra1^{fl/fl}:Mlc1f-Cre* mice. Fold enrichment is shown in x axes; P -value for each class is shown on the right of each bar.

prompted us to explore whether the increased mitochondria content of *Ambra1*-depleted muscles was attributable to defective degradation or to enhanced biogenesis. Quantification of gene expression and protein levels for peroxisome proliferator-activated receptor gamma coactivator 1-alpha (PGC-1 α) and mitochondrial transcription factor A (TFAM), two key regulators of mitochondrial biogenesis, showed that their levels were unaltered in *Ambra1^{fl/fl}:Mlc1f-Cre* muscles (Figure S3a–c), thus ruling out a major impact of increased mitochondrial biogenesis in the observed differences. In agreement with this, mitochondrial DNA content was not significantly different between *Ambra1^{fl/fl}:Mlc1f-Cre* and *Ambra1^{fl/fl}* muscles (Figure S3d). Accumulation of structurally abnormal mitochondria in *Ambra1*-deficient muscles was confirmed by transmission electron microscopy, which showed an increased percentage of myofibres with swollen mitochondria and abnormal cristae in *Ambra1^{fl/fl}:Mlc1f-Cre* TA sections (Figure 3D,E). Electron microscopy also confirmed increased lysosomal content of *Ambra1*-deficient muscles, with markedly increased percentages of myofibres with lysosomal accumulation in *Ambra1^{fl/fl}:Mlc1f-Cre* TA sections (Figure 3D,E). Altogether, these data indicate that *Ambra1* deficiency in skeletal muscle strongly impinges on the mitochondrial compartment and the endo-lysosomal system, with no overt defects in the bulk autophagic pathway.

Ambra1 null muscles display dysfunctional mitochondria

To understand whether defective mitochondria accumulated along postnatal life in *Ambra1*-deficient muscles and how the observed ultrastructural defects impacted on mitochondrial function, we carried out further studies in mice at different ages. Transmission electron microscopy showed that mitochondria were moderately affected in 3-month-old *Ambra1^{fl/fl}:Mlc1f-Cre* muscles, whereas they became markedly swollen in 6-month-old *Ambra1^{fl/fl}:Mlc1f-Cre* samples (Figure 4A). Confocal TMRM analysis for mitochondrial membrane potential in myofibres isolated from FDB muscles of 6-month-old *Ambra1^{fl/fl}:Mlc1f-Cre* and *Ambra1^{fl/fl}* mice revealed that *Ambra1*-depleted myofibres did not hyperpolar-

ize upon oligomycin addition, at difference from control myofibres, pointing at mitochondrial dysfunction (Figure 4B). Finally, we investigated the activity of respiratory chain complexes in mitochondria isolated from muscles of *Ambra1^{fl/fl}:Mlc1f-Cre* and *Ambra1^{fl/fl}* mice. As the activity of the different respiratory chain complexes was not significantly affected in mice kept in standard resting conditions (Figure S3e), we subjected mice to acute treadmill exercise, to assess the impact of locomotor activity in the observed mitochondrial defects. This experiment highlighted a significant decrease of complex I activity in *Ambra1*-deficient mitochondria, together with a trend towards decreased activities of complex III and complex I + III (Figure 4C). Altogether, these data indicated that lack of *Ambra1* affects the structure and function of the mitochondrial compartment of skeletal muscles.

Ambra1 ablation in muscles affects mitophagy and leads to defective mitophagic flux

Mitochondrial dynamics and mitophagy are highly interconnected mechanisms, and the recruitment of pro-fission factors at the mitochondrial compartment is an essential prerequisite for mitochondria turnover.²¹ Therefore, we investigated key mitophagic proteins in mitochondrial fractions isolated from quadriceps muscles of 3- and 6-month-old mice. Western blot quantifications revealed that both dynamin-related protein 1 (DRP1), a key regulator of mitochondria fission, and Parkin (PARK2), an E3 ubiquitin ligase with a central role in mitophagy, were significantly less recruited to mitochondria in muscles of both 3- and 6-month-old *Ambra1^{fl/fl}:Mlc1f-Cre* animals when compared with *Ambra1^{fl/fl}* controls (Figure 5A,B). These findings pointed at a defective regulation of the mitophagic process in *Ambra1*-deficient muscles. To investigate this aspect in further detail, we studied the mitophagic flux by quantifying the amount of lipidated LC3 recruited to muscle mitochondria upon starvation, as an inducing stimulus, and following *in vivo* administration of colchicine, to block the flux and fusion with lysosomes.²² These experiments revealed that LC3-II did not accumulate after colchicine treatment in mitochondria of *Ambra1*-deficient muscles, at difference from

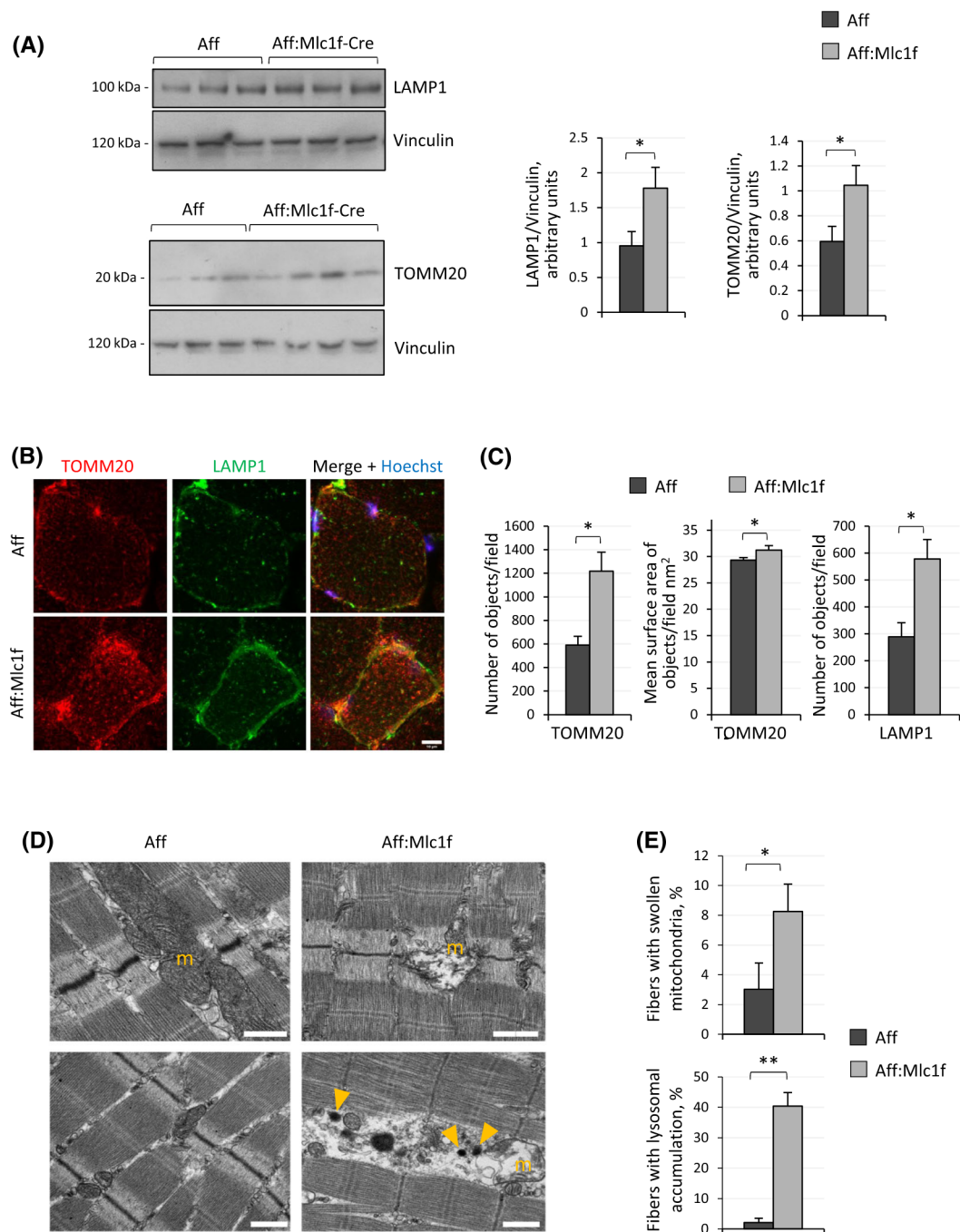


Figure 3 Mitochondria and endo-lysosomal accumulation in *Ambra1* null muscles. (A) Western blotting for LAMP1 and TOMM20 in protein extract of quadriceps muscle from 6-month-old *Ambra1^{fl/fl}* (Aff) and *Ambra1^{fl/fl}:Mlc1f-Cre* (Aff:Mlc1f-Cre) mice. Vinculin was used as loading control. Densitometric quantifications of LAMP1 vs. Vinculin and of TOMM20 vs. Vinculin, as determined by at least three independent experiments, are shown on the right panels. Data are provided as mean ± SEM ($n = 6-7$ mice, each genotype; *, $P < 0.05$). (B) Representative confocal immunofluorescence images for TOMM20 (red) and LAMP1 (green) in cross cryosections of quadriceps muscle from 6-month-old *Ambra1^{fl/fl}* (Aff) and *Ambra1^{fl/fl}:Mlc1f-Cre* (Aff:Mlc1f) mice. Nuclei were counterstained with Hoechst (blue). Scale bar, 10 μm. (C) Automated quantifications of the number of objects per cell and of the mean surface of objects per cell for TOMM20 (left and middle panels) and LAMP1 (right panel) signals, as determined by confocal immunofluorescence images as in (B). Data are shown as mean ± SEM ($n = 4$ mice, each genotype; *, $P < 0.05$). (D) Representative transmission electron microscopy images of longitudinal sections of TA muscle from 6-month-old *Ambra1^{fl/fl}* (Aff) and *Ambra1^{fl/fl}:Mlc1f-Cre* (Aff:Mlc1f) mice. Yellow arrowheads point at lysosomes. Scale bar, 1 μm. m, mitochondria. (E) Quantification of the percentage of myofibers with swollen mitochondria (upper panel) and with lysosomal accumulation (lower panel), based on electron microscopy images as in (D). Data are shown as mean ± SEM ($n = 4$ mice, each genotype; Mann-Whitney test; *, $P < 0.05$; **, $P < 0.01$).

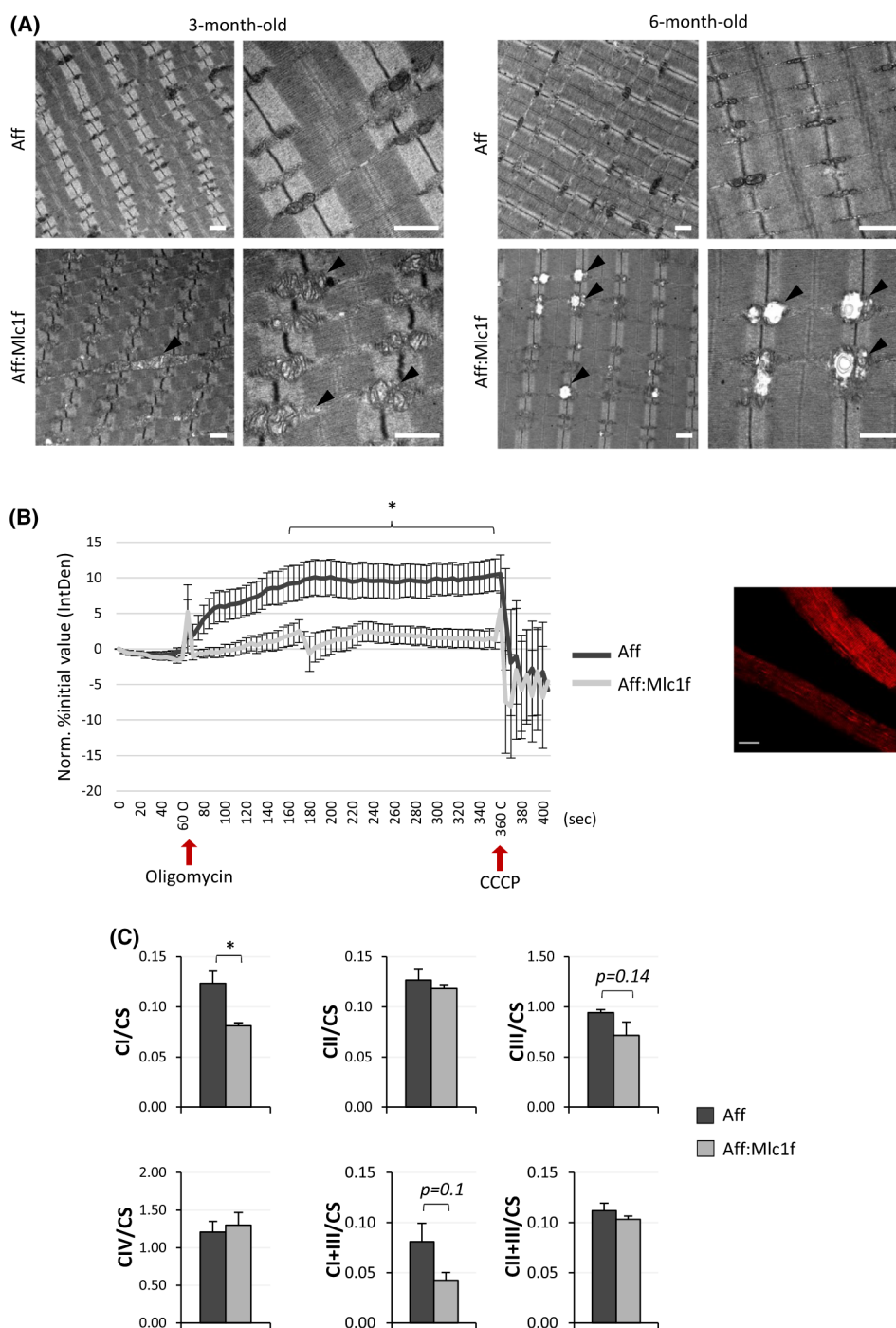


Figure 4 *Ambra1* null muscles display dysfunctional mitochondria. (A) Representative transmission electron microscopy images of longitudinal sections of TA muscle from 3- and 6-month-old *Ambra1*^{fl/fl} (*Aff*) and *Ambra1*^{fl/fl}:*Mlc1f*-Cre (*Aff:Mlc1f*) mice. Black arrowheads point at some structurally abnormal mitochondria displayed by *Ambra1*-deficient muscles. Scale bar, 1 μ m. (B) Quantification of TMRM fluorescence in isolated FDB myofibres from 6-month-old *Ambra1*^{fl/fl} (*Aff*) and *Ambra1*^{fl/fl}:*Mlc1f*-Cre (*Aff:Mlc1f*) mice. Red arrows indicate the time points of oligomycin and CCCP addition, respectively. The graph shows the integrated density value (IntDen) normalized as the percentage of the initial value. Data are shown as mean \pm SEM ($n = 23$ – 24 myofibres from four different mice, each genotype; *, $P < 0.05$). A representative confocal microscopy image of TMRM-labelled myofibres from control *Ambra1*^{fl/fl} mice is shown on the right. Scale bar, 20 μ m. (C) Quantification of the activity of respiratory chain complex I (CI), complex II (CII), complex III (CIII), complex IV (CIV), complex I + III (SCI + III), and complex II + III (SCII + III) in mitochondria isolated from quadriceps muscles of 6-month-old *Ambra1*^{fl/fl} (*Aff*) and *Ambra1*^{fl/fl}:*Mlc1f*-Cre (*Aff:Mlc1f*) mice subjected to acute treadmill exercise as described in Methods section. The activity of the different complexes was normalized on citrate synthase (CS) activity. Data are shown as mean \pm SEM ($n = 4$ mice, each genotype; *, $P < 0.05$).

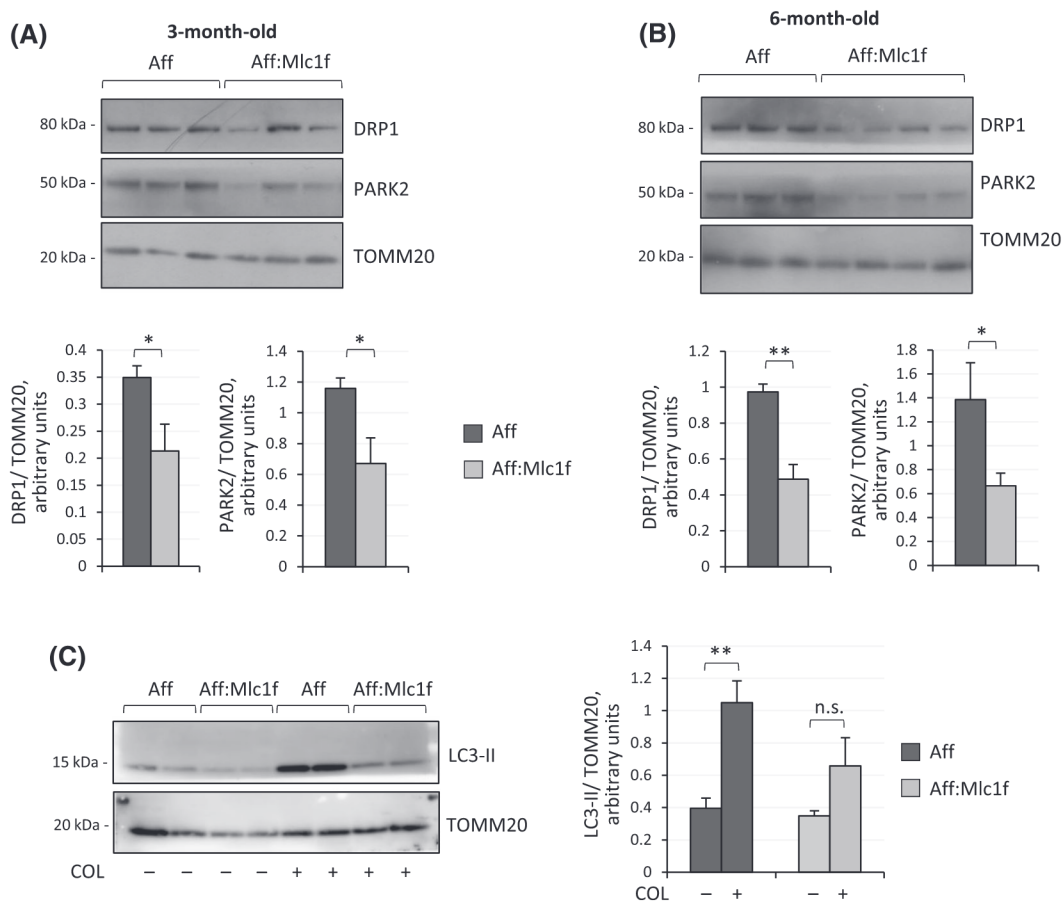


Figure 5 Ambra1 ablation in muscles leads to defective mitophagy. (A,B) Western blotting for DRP1 and PARK2 in mitochondria-enriched protein extracts of quadriceps muscle from 3-month-old (A) and 6-month-old (B) *Ambra1^{fl/fl}* (Aff) and *Ambra1^{fl/fl}:Mlc1f-Cre* (Aff:Mlc1f) mice. TOMM20 was used as loading control. Densitometric quantifications of DRP1 vs. TOMM20 and of PARK2 vs. TOMM20, as determined by at least three independent experiments, are shown on the bottom panels. Data are shown as mean \pm SEM ($n = 6-7$ mice, each genotype; *, $P < 0.05$; **, $P < 0.01$). (C) Western blotting for LC3 in mitochondria-enriched protein extract of quadriceps muscle from 6-month-old *Ambra1^{fl/fl}* (Aff) and *Ambra1^{fl/fl}:Mlc1f-Cre* (Aff:Mlc1f) mice, starved for 24 h to induce mitophagy and treated (+) or not (–) with colchicine (COL). TOMM20 was used as loading control. The right panel shows the densitometric quantifications of LC3-II vs. TOMM20, as determined by at least three independent experiments. Data are shown as mean \pm SEM ($n = 5-6$ mice, each condition; **, $P < 0.01$; n.s., not significant).

control samples (Figure 5C). Taken together, these data indicate that Ambra1 ablation in skeletal muscles leads to defective recruitment of LC3 to mitochondria, thus reducing the rate of mitophagic flux and prompting to an abnormal accumulation of dysfunctional mitochondria.

Discussion

Both bulk and selective autophagy play fundamental roles in skeletal muscles, because myofibres are continuously subjected to mechanical and metabolic stress during their activity. In particular, mitophagy is critical for the maintenance of myofibre homeostasis, by selectively removing dysfunctional mitochondria, which otherwise would undergo a grad-

ual accretion within cells and dramatically compromise the functionality of the entire muscle.^{23–25}

In skeletal muscle, the autophagy-lysosome system was extensively studied mainly by focusing on transcription factors and cofactors that govern its transcriptional regulation, such as FOXOs^{26,511} and PGC-1 α .²⁷ Further, it is well known how these proteins regulate autophagy upon muscle denervation, starvation, and exercise, as well as in pathological conditions, such as muscular dystrophies, myopathies, and age-related sarcopenia.²¹ Despite this, there is a knowledge gap in the field. Indeed, there is still a limited number of studies in which proteins directly involved in mediating either bulk or selective autophagy were targeted for *in vivo* manipulation in mammalian skeletal muscles. Among such mediators of the autophagic process, Ambra1 emerged as a major inducer of mitophagy via direct binding to LC3.^{15,16} In addition, recent findings

highlighted an important involvement of Ambra1 in cell cycle regulation, in particular controlling the abundance of D-type cyclins.^{28,51,519} These findings, together with the identification of a c-Myc/Ambra1/STAT3 oncogenic pathway,²⁹ pointed at cancer as one major field of study for Ambra1.

Although Ambra1 was described as a positive regulator of autophagy, little is known about its physiological role in a post-mitotic tissue such as adult skeletal muscle. Previous studies showed that Ambra1 deficiency during development causes abnormal muscle structure in both zebrafish and mouse embryos, together with several neurological defects.^{18,19} Moreover, *in vitro* studies showed that Ambra1 controls the interaction between TRIM32 E3-ubiquitin ligases and ULK1 serine/threonine kinase for induction of the atrophy process in a muscle cell line.³⁰

Here, we investigated the role of Ambra1 in mediating autophagy and mitophagy in skeletal muscle, by exploiting different *in vivo* approaches in mice. First, we found that mitochondria undergo massive autophagy-dependent degradation upon forced *in vivo* expression of a mitochondria-targeted form of Ambra1 in muscle. Based on this finding, we moved forward and generated both full body and muscle-specific knockout mouse models for Ambra1. Interestingly, our data indicate that Ambra1-deficient muscles accumulate dysfunctional mitochondria, with disorganized cristae and impaired regulation of mitochondrial membrane potential, with no significant impact on the rate of mitochondria biogenesis. In spite of these defects, the bulk autophagic flux is not appreciably affected by Ambra1 ablation in muscle. Instead, Ambra1-deficient muscles display a marked enhancement of LAMP1-positive endo-lysosomal vesicles, thus providing evidence that the degradative pathways are actually compromised, leading to the accumulation of dysfunctional mitochondria. To further investigate this aspect, we isolated mitochondria-enriched fractions from fresh muscles and assessed the selective clearance of mitochondria by mitophagy. The data reveal that upon starvation and colchicine treatment, the lipidated form of LC3 does not accumulate in Ambra1-deficient mitochondria, thus indicating that the mitophagy flux is compromised in muscles lacking Ambra1.

Mitochondrial dynamics and the occurrence of mitochondrial fission and fusion events play prominent roles in the clearance of dysfunctional mitochondria within cells by mitophagy. Indeed, mitochondrial fission is a mandatory step that precedes mitochondrial clearance via mitophagy.²¹ In agreement with this concept, our data indicate that in the absence of Ambra1, the pro-fission protein DRP1 and the E3 ubiquitin ligase Parkin are not properly recruited to mitochondria, even when the mitophagic flux is induced, thus accounting for the impaired mitophagy of Ambra1-deficient muscles. Previous studies demonstrated that Ambra1 is a major interactor of Parkin and plays a critical role in recruiting Parkin to dysfunctional mitochondria.^{15,31} Indeed, if Parkin is not properly translocated to the membrane of damaged

mitochondria, it cannot be activated by the PTEN-induced kinase 1 (PINK1). Thus, ubiquitination of mitochondrial outer membrane proteins, which in turn leads to the recruitment of autophagic cargo receptors, does not occur in such conditions.^{32,33} Our data support a role for the Ambra1/Parkin axis in the maintenance of muscle homeostasis, by promoting the selective removal of dysfunctional mitochondria in myofibres. In agreement with this concept, a recent work showed that Parkin ablation in mice negatively impacts muscle homeostasis. Indeed, *Park2* knockout mice display mild impairment in muscle contractility accompanied by defective mitochondrial function, with decreased activity of respiratory chain complexes, and deregulation of DRP1 turnover.³⁴ This latter evidence is of particular interest, as literature studies identified DRP1 as a substrate for Parkin-mediated ubiquitination,³⁵ thus highlighting a further level of regulation between mitophagy and mitochondrial dynamics. Consistently, muscle-specific *Drp1* knockout leads to postnatal lethality in mice, with several major negative effects on muscle homeostasis.³⁶ In addition, inducible *Drp1* ablation in skeletal muscles of adult mice still results in mitochondrial alterations,³⁶ further pointing at mitophagy and mitochondrial dynamics as fundamental for muscle function.

So far, few other autophagy-related proteins were specifically inactivated in skeletal muscle *in vivo*. These include muscle-specific *Atg5*,^{37,38} *Atg7*,³⁹ and *Vps15*⁴⁰ knockout mouse models. As expected, these models display markedly compromised bulk autophagy, with a detrimental accumulation of dysfunctional organelles, leading to severe muscle atrophy with myopathy. The severe phenotypes and the overtly compromised bulk autophagy of these mouse models make it difficult to elucidate the roles of these proteins in the regulation of the selective removal of mitochondria via mitophagy. Conversely, the relatively mild phenotype of muscle-specific *Ambra1* knockout mice and the data we obtained in the present work point at Ambra1 as an autophagy protein with a main role for the mitophagic pathway in muscles, being involved in the recruitment of DRP1 and Parkin on dysfunctional mitochondria.

Interestingly, similar to our Ambra1-depleted model, muscles lacking ATG5 show increased lysosomal size and density.³⁷ The endo-lysosomal compartment represents the final district of the autophagic pathway, and thus, it is not surprising that lysosomes are altered when autophagy is impaired. On the other hand, accumulation of endo-lysosomal vesicles, clearly displayed by Ambra1 knockout muscles, was not described before in other *in vitro* and *in vivo* Ambra1-deficient models. Therefore, in the near future, it would be interesting to further investigate new lysosomal-related functions of Ambra1, under both physiological and pathological conditions.

Finally, our data suggest that Ambra1 may be a valuable molecular target to selectively enhance mitophagy and improve mitochondria health in myofibres, with possible implications for the prospective treatment of muscular

dystrophies and metabolic diseases in which the mitophagy pathway is affected, as well as in age-related sarcopenia. Furthermore, they point at the search for *AMBRA1* gene mutations in patients affected by myopathies with abnormal mitochondrial buildup and hinting at defective mitophagy regulation.

Acknowledgements

We are thankful to Dr. Gaia Gherardi for advice and technical support with TMRM analysis, to Dr. Pasquale D'Aquino for the cloning of the bicistronic vector, and to Dr. Dario Bizzotto for the maintenance of mouse colonies. We gratefully thank Prof. Noboru Mizushima for providing us with GFP-LC3 reporter mice. We also thank Prof. Leonardo Salviati and Prof. Marco Sandri for their helpful discussions. We acknowledge the light and electron microscopy facility of the Biology Department of the University of Padova and the Next Gener-

ation Sequencing facility of the Istituto di Ricerca Pediatrica (IRP, Padova). We also thank all the members of Bonaldo laboratory for daily discussions and suggestions. This work was supported by the Italian Ministry of University and Research (Grants 2015FBNB5Y and 201742SBXA), the Telethon Foundation (Grants GGP14202 and GGP19229), the Cariparo Foundation, and the University of Padova. FS was supported by an AFM-Telethon trampoline grant (AFM-18376).

Conflict of interest

The authors declare that they have no conflict of interest.

Online supplementary material

Additional supporting information may be found online in the Supporting Information section at the end of the article.

References

- Spinelli JB, Haigis MC. The multifaceted contributions of mitochondria to cellular metabolism. *Nat Cell Biol* 2018;**20**:745–754.
- Giacomello M, Pyakurel A, Glytsou C, Scorrano L. The cell biology of mitochondrial membrane dynamics. *Nat Rev Mol Cell Biol* 2020;**21**:204–224.
- Nunnari J, Suomalainen A. Mitochondria: in sickness and in health. *Cell* 2012;**148**:1145.
- Mizushima N. Autophagy: process and function. *Genes Dev* 2007;**21**:2861–2873.
- Drake J, Yan Z. Mitophagy in maintaining skeletal muscle mitochondrial proteostasis and metabolic health with ageing. *J Physiol* 2017;**595**:6391–6399.
- Romanello V, Sandri M. Mitochondrial quality control and muscle mass maintenance. *Front Physiol* 2015;**6**:422.
- van der Ende M, Grefte S, Plas R, Meijerink J, Witkamp RF, Keijer J, et al. Mitochondrial dynamics in cancer-induced cachexia. *Biochimica et Biophysica Acta (BBA) - Rev Cancer* 2018;**1870**:137–150.
- Sebastián D, Soriano E, Segalés J, Irazoki A, Ruiz-Bonilla V, Sala D, et al. Mfn2 deficiency links age-related sarcopenia and impaired autophagy to activation of an adaptive mitophagy pathway. *EMBO J* 2016;**35**:1677.
- Su Z, Nie Y, Huang X, Zhu Y, Feng B, Tang L, et al. Mitophagy in hepatic insulin resistance: therapeutic potential and concerns. *Front Pharmacol* 2019;**10**:1193.
- Bernardi P, Bonaldo P. Mitochondrial dysfunction and defective autophagy in the pathogenesis of collagen VI muscular dystrophies. *Cold Spring Harb Perspect Biol* 2013;**5**:a011387.
- de Palma C, Morisi F, Cheli S, Pambianco S, Cappello V, Vezzoli M, et al. Autophagy as a new therapeutic target in Duchenne muscular dystrophy. *Cell Death Dis* 2012;**3**:e418.
- Cianfanelli V, de Zio D, di Bartolomeo S, Nazio F, Strappazon F, Cecconi F. Ambra1 at a glance. *J Cell Sci* 2015;**128**:2003–2008.
- Maiani E, Milletti G, Nazio F, Holdgaard SG, Bartkova J, Rizza S, et al. AMBRA1 regulates cyclin D to guard S-phase entry and genomic integrity. *Nature* 2021;**592**:799–803.
- di Bartolomeo S, Corazzari M, Nazio F, Oliverio S, Lisi G, Antonioli M, et al. The dynamic interaction of AMBRA1 with the dynein motor complex regulates mammalian autophagy. *J Cell Biol* 2010;**191**:155–168.
- van Humbeek C, Cornelissen T, Hofkens H, Mandemakers W, Gevaert K, Strooper B, et al. Parkin interacts with Ambra1 to induce mitophagy. *J Neurosci* 2011;**31**:10249–10261.
- Strappazon F, Nazio F, Corrado M, Cianfanelli V, Romagnoli A, Fimia GM, et al. AMBRA1 is able to induce mitophagy via LC3 binding, regardless of PARKIN and p62/SQSTM1. *Cell Death Differ* 2015;**22**:419–432.
- Strappazon F, di Rita A, Peschiaroli A, Leoncini PP, Locatelli F, Melino G, et al. HUWE1 controls MCL1 stability to unleash AMBRA1-induced mitophagy. *Cell Death Differ* 2019;**27**:1155–1168.
- Fimia GM, Stoykova A, Romagnoli A, Giunta L, di Bartolomeo S, Nardacci R, et al. Ambra1 regulates autophagy and development of the nervous system. *Nature* 2007;**447**:1121–1125.
- Skobo T, Benato F, Grumati P, Meneghetti G, Cianfanelli V, Castagnaro S, et al. Zebrafish *ambra1a* and *ambra1b* knock-down impairs skeletal muscle development. *PLoS ONE* 2014;**9**:e99210.
- Meneghetti G, Skobo T, Chrisam M, Fontana CM, Facchinello N, Nazio F, et al. Zebrafish *ambra1a* and *ambra1b* silencing affect heart development. *Zebrafish* 2020;**17**:163–176.
- Romanello V, Sandri M. The connection between the dynamic remodeling of the mitochondrial network and the regulation of muscle mass. *Cell Mol Life Sci* 2020;**78**:1305–1328.
- Oost LJ, Kustermann M, Armani A, Blaauw B, Romanello V. Fibroblast growth factor 21 controls mitophagy and muscle mass. *J Cachexia Sarcopenia Muscle* 2019;**10**:630–642.
- Grumati P, Coletto L, Sabatelli P, Cescon M, Angelin A, Bertaggia E, et al. Autophagy is defective in collagen VI muscular dystrophies, and its reactivation rescues myofiber degeneration. *Nat Med* 2010;**16**:1313–1320.
- Luan P, Amico D D, Andreux PA, Laurila P-P, Wohlwend M, Li H, et al. Urolithin A improves muscle function by inducing mitophagy in muscular dystrophy. *Sci Transl Med* 2021;**13**:319.

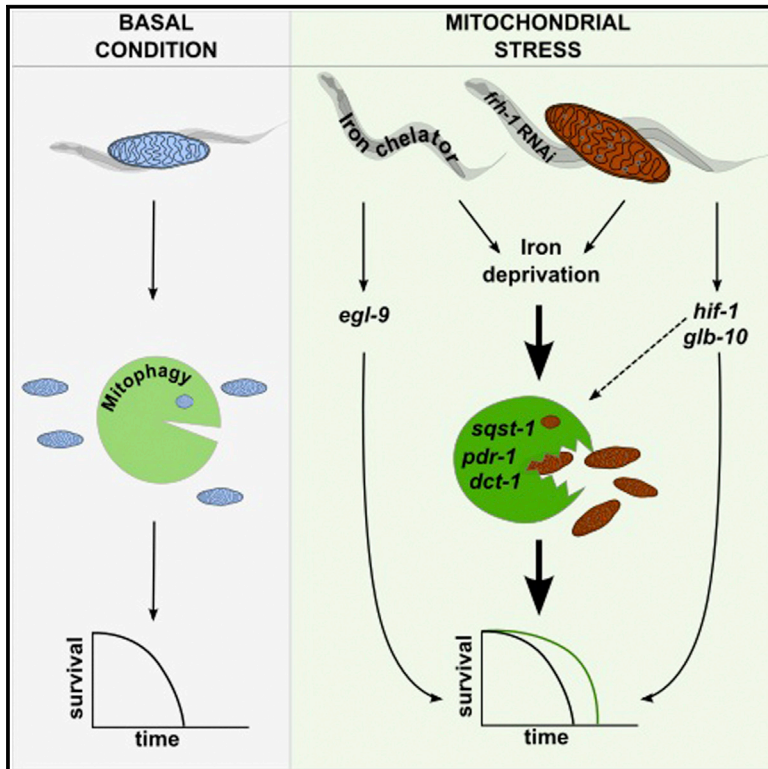
25. Xia Q, Huang X, Huang J, Zheng Y, March ME, Li J, et al. The role of autophagy in skeletal muscle diseases. *Front Physiol* 2021;**12**:291.
26. Mammucari C, Milan G, Romanello V, Masiero E, Rudolf R, del Piccolo P, et al. FoxO3 controls autophagy in skeletal muscle in vivo. *Cell Metab* 2007;**6**:458–471.
27. Vainshtein A, Desjardins EM, Armani A, Sandri M, Hood DA. PGC-1 α modulates denervation-induced mitophagy in skeletal muscle. *Skel Musc* 2015;**5**:1–17.
28. di Leo L, Bodemeyer V, Bosisio FM, Claps G, Carretta M, Rizza S, et al. Loss of Ambra1 promotes melanoma growth and invasion. *Nat Commun* 2021;**12**:1–17.
29. Nazio F, Po A, Abballe L, Ballabio C, Diomedes Camassei F, Bordi M, et al. Targeting cancer stem cells in medulloblastoma by inhibiting AMBRA1 dual function in autophagy and STAT3 signalling. *Acta Neuropathol* 2021;**142**:537–564.
30. di Rienzo M, Piacentini M, Fimia GM. A TRIM32-AMBRA1-ULK1 complex initiates the autophagy response in atrophic muscle cells. *Autophagy* 2019;**15**:1674–1676.
31. Cianfanelli V, Nazio F, Cecconi F. Connecting autophagy: AMBRA1 and its network of regulation. *Mol Cell Oncol* 2015;**2**:e970059.
32. Narendra D, Tanaka A, Suen D-F, Youle RJ. Parkin is recruited selectively to impaired mitochondria and promotes their autophagy. *J Cell Biol* 2008;**183**:795–803.
33. Jin SM, Youle RJ. PINK1- and Parkin-mediated mitophagy at a glance. *J Cell Sci* 2012;**125**:795–799.
34. Gospillou G, Godin R, Piquereau J, Picard M, Mofarrahi M, Mathew J, et al. Protective role of Parkin in skeletal muscle contractile and mitochondrial function. *J Physiol* 2018;**596**:2565–2579.
35. Wang H, Song P, Du L, Tian W, Yue W, Liu M, et al. Parkin ubiquitinates Drp1 for proteasome-dependent degradation: implication of dysregulated mitochondrial dynamics in parkinson disease. *J Biol Chem* 2011;**286**:11649–11658.
36. Favaro G, Romanello V, Varanita T, Andrea Desbats M, Morbidoni V, Tezze C, et al. DRP1-mediated mitochondrial shape controls calcium homeostasis and muscle mass. *Nat Commun* 2019;**10**:1–17.
37. Raben N, Hill V, Shea L, Takikita S, Baum R, Mizushima N, et al. Suppression of autophagy in skeletal muscle uncovers the accumulation of ubiquitinated proteins and their potential role in muscle damage in Pompe disease. *Hum Mol Genet* 2008;**17**:3897–3908.
38. Masiero E, Agatea L, Mammucari C, Blaauw B, Loro E, Komatsu M, et al. Autophagy is required to maintain muscle mass. *Cell Metab* 2009;**10**:507–515.
39. Raben N, Schreiner C, Baum R, Takikita S, Xu S, Xie T, et al. Suppression of autophagy permits successful enzyme replacement therapy in a lysosomal storage disorder—murine Pompe disease. *Autophagy* 2010;**6**:1078–1089.
40. Nemazany I, Blaauw B, Paolini C, Caillaud C, Protasi F, Mueller A, et al. Defects of Vps15 in skeletal muscles lead to autophagic vacuolar myopathy and lysosomal disease. *EMBO Mol Med* 2013;**5**:870–890.



Current Biology

Iron-Starvation-Induced Mitophagy Mediates Lifespan Extension upon Mitochondrial Stress in *C. elegans*

Graphical Abstract



Authors

Alfonso Schiavi, Silvia Maglioni,
Konstantinos Palikaras, ...,
Francesco Cecconi,
Nektarios Tavernarakis,
Nataschia Ventura

Correspondence

nataschia.ventura@uni-duesseldorf.de

In Brief

Mitophagy is a fundamental mitochondrial quality control mechanism. Schiavi et al. identify a conserved Parkin/Bnip3-regulated mitophagy pathway required for lifespan extension induced by mitochondrial stress in *C. elegans*. Mitophagy also mediates a pro-longevity iron starvation response activated to cope with frataxin suppression.

Highlights

- Mitochondrial stress induces Parkin/Bnip3-regulated mitophagy in *C. elegans*
- Frataxin silencing triggers a pro-longevity iron starvation response
- Mitochondrial stress and iron depletion extend *C. elegans* lifespan via mitophagy
- Frataxin and iron depletion extend lifespan via overlapping and unique mechanisms



Iron-Starvation-Induced Mitophagy Mediates Lifespan Extension upon Mitochondrial Stress in *C. elegans*

Alfonso Schiavi,^{2,3} Silvia Maglioni,^{1,2} Konstantinos Palikaras,⁴ Anjumara Shaik,^{1,2} Flavie Strappazon,^{6,7} Vanessa Brinkmann,² Alessandro Torgovnick,² Natascha Castelein,⁹ Sasha De Henau,⁹ Bart P. Braeckman,⁹ Francesco Ceconi,^{6,7,8} Nektarios Tavernarakis,^{4,5} and Nataschia Ventura^{1,2,3,*}

¹Institute for Clinical Chemistry and Laboratory Diagnostic, Medical Faculty of the Heinrich Heine University, 40225 Düsseldorf, Germany

²IUF-Leibniz Research Institute for Environmental Medicine, 40225 Düsseldorf, Germany

³Department of Biomedicine and Prevention, University of Rome Tor Vergata, 00133 Rome, Italy

⁴Institute of Molecular Biology and Biotechnology, Foundation for Research and Technology – Hellas, Heraklion 70013, Crete, Greece

⁵Department of Basic Sciences, Faculty of Medicine, University of Crete, Heraklion 71110, Crete, Greece

⁶IRCCS Fondazione Santa Lucia, 00143 Rome, Italy

⁷Department of Biology, University of Rome Tor Vergata, 00133 Rome, Italy

⁸Unit of Cell Stress and Survival, Danish Cancer Society Research Center, 2100 Copenhagen, Denmark

⁹Biology Department, Ghent University, 9000 Ghent, Belgium

*Correspondence: nataschia.ventura@uni-duesseldorf.de

<http://dx.doi.org/10.1016/j.cub.2015.05.059>

SUMMARY

Frataxin is a nuclear-encoded mitochondrial protein involved in the biogenesis of Fe-S-cluster-containing proteins and consequently in the functionality of the mitochondrial respiratory chain. Similar to other proteins that regulate mitochondrial respiration, severe frataxin deficiency leads to pathology in humans—Friedreich’s ataxia, a life-threatening neurodegenerative disorder—and to developmental arrest in the nematode *C. elegans*. Interestingly, partial frataxin depletion extends *C. elegans* lifespan, and a similar anti-aging effect is prompted by reduced expression of other mitochondrial regulatory proteins from yeast to mammals. The beneficial adaptive responses to mild mitochondrial stress are still largely unknown and, if characterized, may suggest novel potential targets for the treatment of human mitochondria-associated, age-related disorders. Here we identify mitochondrial autophagy as an evolutionarily conserved response to frataxin silencing, and show for the first time that, similar to mammals, mitophagy is activated in *C. elegans* in response to mitochondrial stress in a *pdr-1*/*Parkin*-, *pink-1*/*Pink*-, and *dct-1*/*Bnip3*-dependent manner. The induction of mitophagy is part of a hypoxia-like, iron starvation response triggered upon frataxin depletion and causally involved in animal lifespan extension. We also identify non-overlapping *hif-1* upstream (HIF-1-prolyl-hydroxylase) and downstream (globins) regulatory genes mediating lifespan extension upon frataxin and iron depletion. Our findings indicate that mitophagy induction is part of an adaptive iron starvation response induced as a protective mechanism against mitochondrial stress,

thus suggesting novel potential therapeutic strategies for the treatment of mitochondrial-associated, age-related disorders.

INTRODUCTION

Frataxin is a nuclear-encoded mitochondrial protein that regulates the biogenesis of iron-sulfur-cluster (ISC)-containing proteins and, as a consequence, the functionality of the mitochondrial respiratory chain (MRC). Complete absence of frataxin is lethal in different species, including the nematode *Caenorhabditis elegans* (*C. elegans*), and its severe deficiency leads in humans to Friedreich’s ataxia (FRDA), the most frequently inherited recessive ataxia [1]. Similar to other life-threatening mitochondrial-associated diseases, residual levels of the pathogenic protein (frataxin) is critical for survival and inversely correlates with disease onset, progression, and severity of symptoms. According to a threshold effect, moderate depletion of the *C. elegans* frataxin homolog FRH-1, similar to suppression of other mitochondrial-associated diseases proteins, extends animal lifespan [2]. The evolutionarily conserved nature of this pro-longevity effect [3] indicates that cellular adaptation to partial mitochondrial dysfunction induces beneficial responses, which, if identified, may suggest novel therapeutic strategies for human diseases associated with progressive mitochondrial deterioration [4].

Changes in animal metabolism and induction of cellular stress responses and detoxification systems (e.g., mtUPR, antioxidants, and autophagy) have been associated with, although not always causally involved in, lifespan extension in animals with genetic- or RNAi-mediated suppression of MRC regulatory proteins (the so-called mitochondrial [*Mit*] mutants [4, 5]). However, the key molecular players underlying mitochondrial-stress control of longevity are still largely uncharacterized. To date, only some autophagy (*unc-51* and *bec-1*) and mtUPR (*ubl-5*) regulatory genes [6, 7], as well as a handful of transcription factors [5] (the *C. elegans* p53 ortholog CEP-1, the homeobox protein CEH-23,

a component of the TFIID mRNA transcription complex TAF-4, the *C. elegans* TFEB ortholog HLH-30, and the hypoxia-inducible factor HIF-1), were shown to mediate *Mit* mutants longevity.

HIF-1 overexpression or stabilization through hypoxia or reduced expression of *egl-9* or *vhl-1* extends *C. elegans* lifespan [8, 9]. EGL-9 is the prolyl-hydroxylase that in normoxia conditions targets HIF-1 to the proteasome for degradation through VHL-1, the von Hippel Lindau protein that is part of an E3 ubiquitin-ligase complex. The activity of EGL-9 is inhibited by low oxygen levels but also by reduced levels of iron and of the tricarboxylic cycle acid intermediate (α KG) [10]. Induction of autophagy is an evolutionarily conserved protective response to hypoxia and to reduced frataxin expression, and it is required for mitochondrial-stress extension of lifespan in *C. elegans* [6, 11]. Mitochondrial autophagy (or mitophagy) is a selective form of autophagy dedicated to mitochondrial quality control by recycling unhealthy mitochondria [12]. It can be activated in a HIF-1- and Beclin-dependent manner to protect mammalian cells against hypoxia [13]. Whether mitophagy plays a role in mitochondrial-stress control of longevity remains speculative [14, 15] and was the main question addressed in this study.

Here we provide evidence that in *C. elegans* a hypoxia-like iron starvation response is causally involved in the lifespan-extending effect elicited by frataxin suppression, and we identify mitochondrial autophagy as part of this beneficial response. We find that mitophagy is induced in an evolutionarily conserved manner upon frataxin silencing, and we show for the first time that, similar to mammals, it is activated in *C. elegans* in response to mitochondrial stress in a Parkin/*pdr-1*-, Pink/*pdr-1*-, and Bnip3/*dct-1*-dependent manner. Furthermore, although different mitophagy regulatory homologs mediate *C. elegans* lifespan extension upon frataxin or iron depletion, we find that the two treatments can extend lifespan also through unique, non-overlapping mechanisms. We, therefore, provide further insight into molecular mechanisms of mitochondrial-stress control of longevity and point to mitophagy as a novel potential therapeutic target for FRDA and possibly other mitochondrial-associated diseases.

RESULTS

C. elegans Homologs of Mitophagy Regulatory Genes Mediate Lifespan Extension

Induction of autophagy is an evolutionarily conserved response to reduced frataxin expression, causally involved in the longevity of different *C. elegans* *Mit* mutants including frataxin (*frh-1*)-depleted animals [6]. Mitochondrial autophagy is a selective form of autophagy dedicated to mitochondrial quality control, which is activated to recycle unhealthy mitochondria. We thus asked whether mitophagy could play a specific role in mitochondrial-stress control of longevity. In mammals, Pink1 kinase cooperates with Parkin, a cytosolic E3 ubiquitin ligase, to signal damaged mitochondria for degradation through autophagy [16]. Homologs of the genes that encode for these proteins have been identified in *C. elegans*, respectively named *pink-1* and *pdr-1*, and their deletion increases animal's sensitivity to oxidative stress [17, 18]. Silencing of *pink-1* was also recently shown to prevent proper elimination of damaged mtDNA after UVC irradiation [19]. To address the role of *pink-1* and *pdr-1* in longevity specification in response to mitochondrial stress, we assessed

the lifespan of corresponding mutant strains upon frataxin silencing. We found that the lifespan-extending effect of *frh-1* RNAi was almost completely prevented in the *pdr-1*(*gk448*) mutant strain (Figures 1A and 1B; Table S1). Two additional *pdr-1* alleles (*tm598* and *tm395*), as well as *pdr-1* RNAi, also suppressed the lifespan-extending ability of frataxin silencing (Figures S1A–S1C; Table S1), thus establishing a clear role for *pdr-1* in frataxin-regulated longevity. To our surprise, but consistent with recent finding from Bess et al. [19] showing seemingly contrasting results between *pink-1* mutant and silencing, two different *pink-1* mutant alleles (*tm1779* and *ok3538*) did not affect *frh-1* RNAi longevity, while *pink-1* RNAi completely abolished it (Figures S1D–S1F; Table S1).

We then tested the effect of other possible mitophagy regulatory genes, such as Bnip3 (*dct-1* in *C. elegans* [20]), the Bcl-2/adenovirus E1B 19-kDa-interacting protein 3, and the adaptor protein p62/SQST1 (*sqst-1* in *C. elegans* [21]). We found that deletion or silencing of *C. elegans* *dct-1* suppressed *frh-1* RNAi extension of lifespan compared to its effect on the wild-type strain (Figures 1C and S1G; Table S1). Moreover, *C. elegans* *sqst-1* mutants completely abolished the lifespan-extending effect of *frh-1* RNAi (Figure 1D). In mammals, Bnip3 is induced to eliminate dysfunctional mitochondria in response to hypoxia in an HIF-1-dependent manner [13], while p62 facilitates cargo degradation, including mitochondria, and it is selectively degraded in response to hypoxia through the autophagic machinery [22]. Likewise, we now found that in *C. elegans* hypoxia upregulates the expression of *dct-1* in an *hif-1*-dependent manner (Figures S1H and S1I). Moreover, hypoxia reduced the content of the SQST-1 protein in a wild-type background and upon loss of the ribosomal protein *rpl-43*, which has been shown to cause an accumulation of SQST-1 aggregates [23] (Figures S1J and S1K). Of note, similar to a hypoxia mechanism, frataxin silencing increased the expression of *dct-1* transcript in an *hif-1*-dependent manner and reduced that of SQST-1 protein (Figures 1E and 1F). We did not observe any change in p62 transcript expression upon *frh-1* RNAi (data not shown), indicating that its degradation occurs at the posttranscriptional level, possibly through an intact autophagic flux [6] induced by a hypoxia-like signaling. Taken together, these findings revealed an evolutionarily conserved protective role for mitophagy regulatory genes, which are required for frataxin-silencing extension of lifespan in *C. elegans*.

Induction of Mitophagy Is an Evolutionarily Conserved Response to Mitochondrial Stress

The inability of *frh-1* RNAi to extend lifespan in mutants of mitophagy regulatory homologs could be ascribed to mitophagy-independent functions of the corresponding *C. elegans* proteins. Indeed, whether *C. elegans* mitophagy is induced upon mitochondrial stress and regulated by the same genes is not known. We, therefore, assessed whether *frh-1* silencing affects mitophagy. Compared to control animals, *frh-1* RNAi-treated animals displayed a substantial co-localization between mitochondria and autophagosomal marker LGG-1 (Figures 2A and S2A), a prerequisite for mitochondrial elimination through the autophagic pathway. To further prove the induction of mitochondrial autophagy, we generated additional transgenic strains and found that frataxin silencing significantly increased the co-localization between DCT-1 and LGG-1 and between DCT-1 and PDR-1

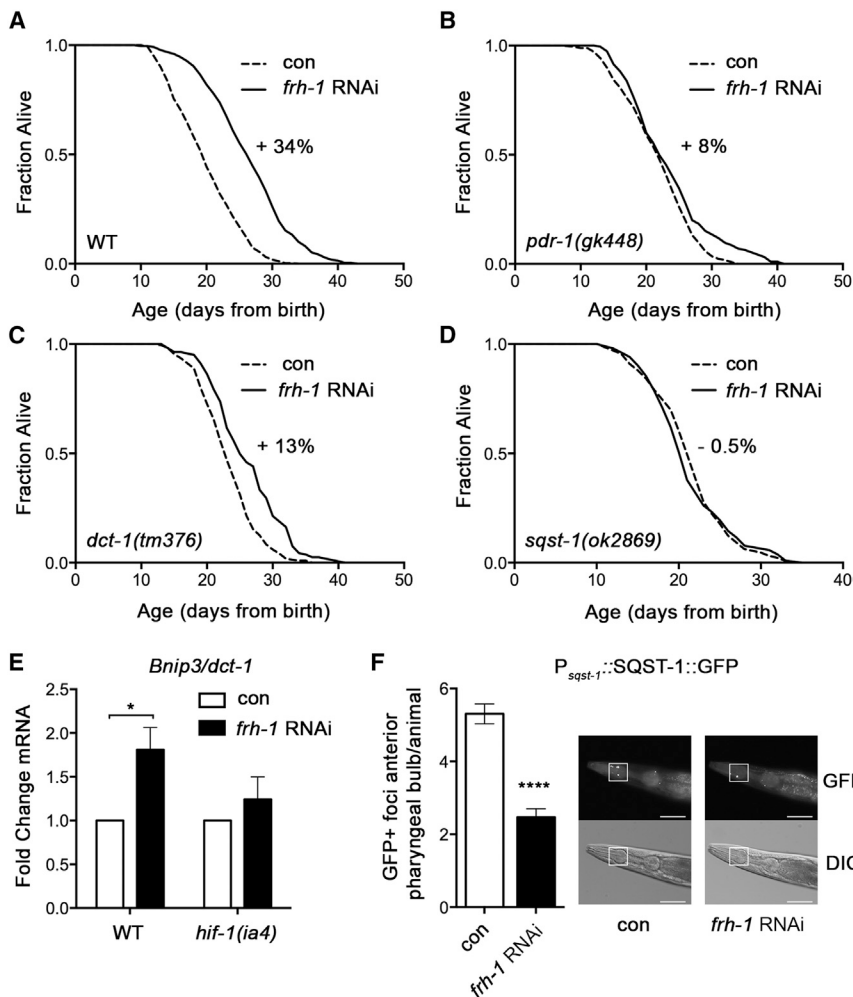


Figure 1. *C. elegans* Homologs of Mitophagy Regulatory Genes Mediate Lifespan Extension upon Frataxin Silencing

(A–D) Kaplan-Meier survival curves of wild-type (WT) (A), *pdr-1(gk448)* (B), *dct-1(tm376)* (C), and *sqst-1(ok2869)* (D) *C. elegans* strains fed bacteria transformed with either empty-vector (con) or vector-expressing dsRNA against *frh-1* (*frh-1* RNAi). Percentages indicate increase in mean lifespan of *frh-1* RNAi-treated over control animals. (E) Quantification of *dct-1* transcript expression in WT animals and *hif-1* mutants fed as in (A). Bar graph represents means \pm SEM (n = 3); *p < 0.05. (F) Quantification of GFP+ foci in the anterior pharyngeal bulb of *P_{sqst-1}::SQST-1::GFP* transgenic strain fed as in (A). (Right) Representative pictures have red squares indicating the region used to count the number of foci. (Top) Green fluorescence channel images (GFP) are shown. (Bottom) Differential (Nomarski) interference contrast images (DICs) are shown. Scale bars in white represent 50 μ m. Bar graph represents means \pm SEM (n = 5); ****p < 0.0001. See also Figures S1 and S3.

compared to wild-type animals (Figures S2B and S2C). Collectively, these data clearly demonstrate that *frh-1*-depleted animals display an increased number of mitoautophagosomes compared to wild-type animals.

To confirm the induction of mitochondrial autophagy in *C. elegans*, we expressed a dual fluorescent pH-sensitive biosensor with a mitochondrial tag that, in normal conditions, marks mitochondria in red and green fluorescence. Upon mitophagy induction, the delivery of mitochondria into the acidic lysosome compartment mainly quenches the green, but not the red, fluorescence, thus reducing the GFP to dsRed ratio (see the Supplemental Experimental Procedures). We observed that *frh-1* RNAi significantly reduced the ratio of GFP versus dsRed fluorescence (Figures 2B and 2C), a clear indication of mitochondria redistribution into the lysosomal compartment. Of note, silencing of mitophagy regulatory genes required for frataxin longevity significantly prevented the induction of mitochondrial autophagy upon *frh-1* RNAi without affecting it in basal conditions (Figure 2C), indicating that mitophagy is required for lifespan extension upon mitochondrial stress.

Remarkably, considering the potential role of mitophagy in the context of neurodegenerative diseases [15], we also found that mitochondrial autophagy is triggered by frataxin silencing in

mammalian cells. In agreement with our previous findings [6], compared to control cells, frataxin small hairpin RNA (shRNA)-treated cells expressed increased levels of LC3II (Figure 2D). Consistent with an increased mitochondrial autophagy, frataxin-depleted cells also contained fewer mitochondrial proteins, such as MnSOD and TOM20 (Figure 2D). Moreover, confocal microscopic analysis revealed Parkin translocation from the cytosol to the mitochondria (Figure S2D), a signal required for targeting mitochondria to the autophagic machinery [16]. Cellular fractionation analysis confirmed a significant increase in Parkin as well as Pink accumulation on mitochondria (Figures 2E, 2F, S2E, and S2F). Notably, similar to what we observed in the worms, the expression of p62/SQSTM1, which cooperates with Parkin to facilitate mitochondrial degradation through the lysosomes [24], was reduced in total extracts and mitochondrial-enriched fractions of frataxin shRNA mammalian cells (Figures 2D and S2F), indicating an intact autophagic flux. To maintain an appropriate mitochondrial network homeostasis, induction of mitophagy typically is preceded by mitochondrial fragmentation [25], which favors the elimination of dysfunctional mitochondria, and is accompanied by the biogenesis of new healthy mitochondria. We observed an altered mitochondrial distribution in both mammalian cells and *C. elegans* subjected to frataxin silencing, an indication of an effective integration of mitochondrial quality control pathways. Indeed, confocal analysis of frataxin shRNA-treated cells revealed a clear perinuclear clustering of highly fragmented mitochondria (Figure S2D), a typical distribution of mitochondria undergoing mitophagy [24]. Similarly, *frh-1* silencing in *C. elegans* increased the density of muscle mitochondria, which also presented with a fragmented pattern (Figure S2G).

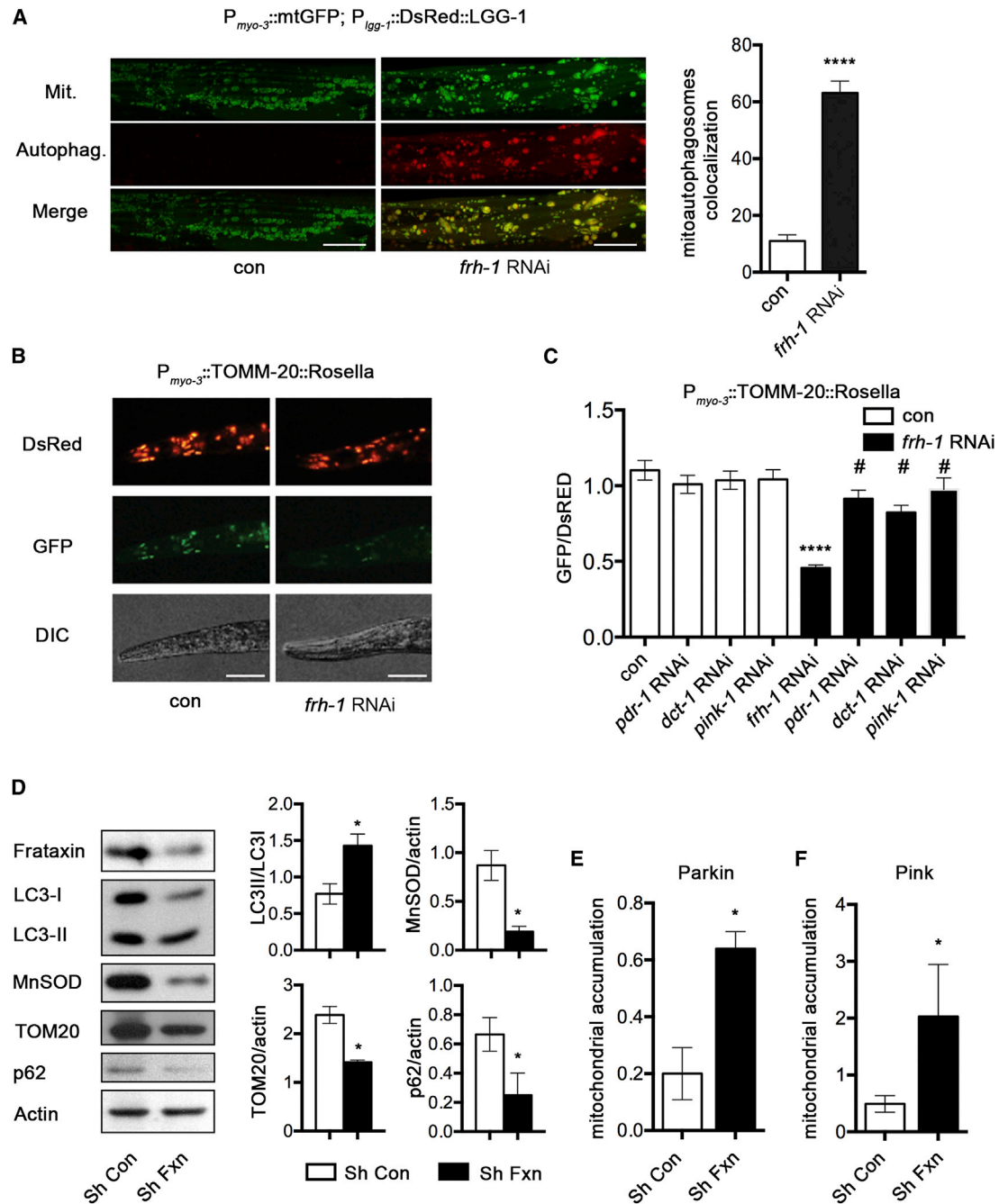


Figure 2. Induction of Mitophagy Is an Evolutionarily Conserved Response to Frataxin Silencing

(A) Quantification of the colocalization between mitochondria and autophagosomes in $P_{myo-3}::mtGFP; P_{lgg-1}::DsRed::LGG-1$ transgenic animals fed bacteria transformed with either empty-vector (con) or vector-expressing dsRNA against *frh-1* (*frh-1* RNAi). (Left) Representative confocal picture of *C. elegans* muscles was acquired using a 100 \times objective lens; green, muscle mitochondria (Mit); red, autophagosomes (Autophag.); and yellow, overlapping of the two (Merge). Size bars, 20 μ m. (B) Representative pictures show $P_{myo-3}::TOMM-20::Rosella$ transgenic strain fed as in (A). In red is shown the total amount of mitochondria as revealed by pH-insensitive Rosella red tag (dsRED), and in green is shown the amount of mitochondria that is transported to the lysosome as revealed by pH-sensitive Rosella green tag (GFP). (Bottom) DIC shows the part of the animals used for quantification.

(C) Mitochondrial autophagy was quantified using the ratio between green and red fluorescence (GFP/DsRED) in $P_{myo-3}::TOMM-20::Rosella$ transgenic animals fed bacteria transformed with either empty vector (con) or vector expressing the indicated dsRNA.

(D) Representative western blots and quantifications of the expression of the indicated proteins from human embryonic kidney HEK293 cells transiently transfected with vector-expressing shRNA control (Sh Con) or shRNA Frataxin (Sh Fxn) are shown.

(E and F) Quantification of Parkin (E) and Pink (F) accumulation on mitochondria from enriched mitochondrial extract of HEK293 cells treated as in (D).

Bar graphs represent means \pm SEM ($n = 3$); *p value versus con < 0.05, ****p value versus con < 0.0001, #p value versus *frh-1* RNAi < 0.0001. See also Figures S2 and S3.

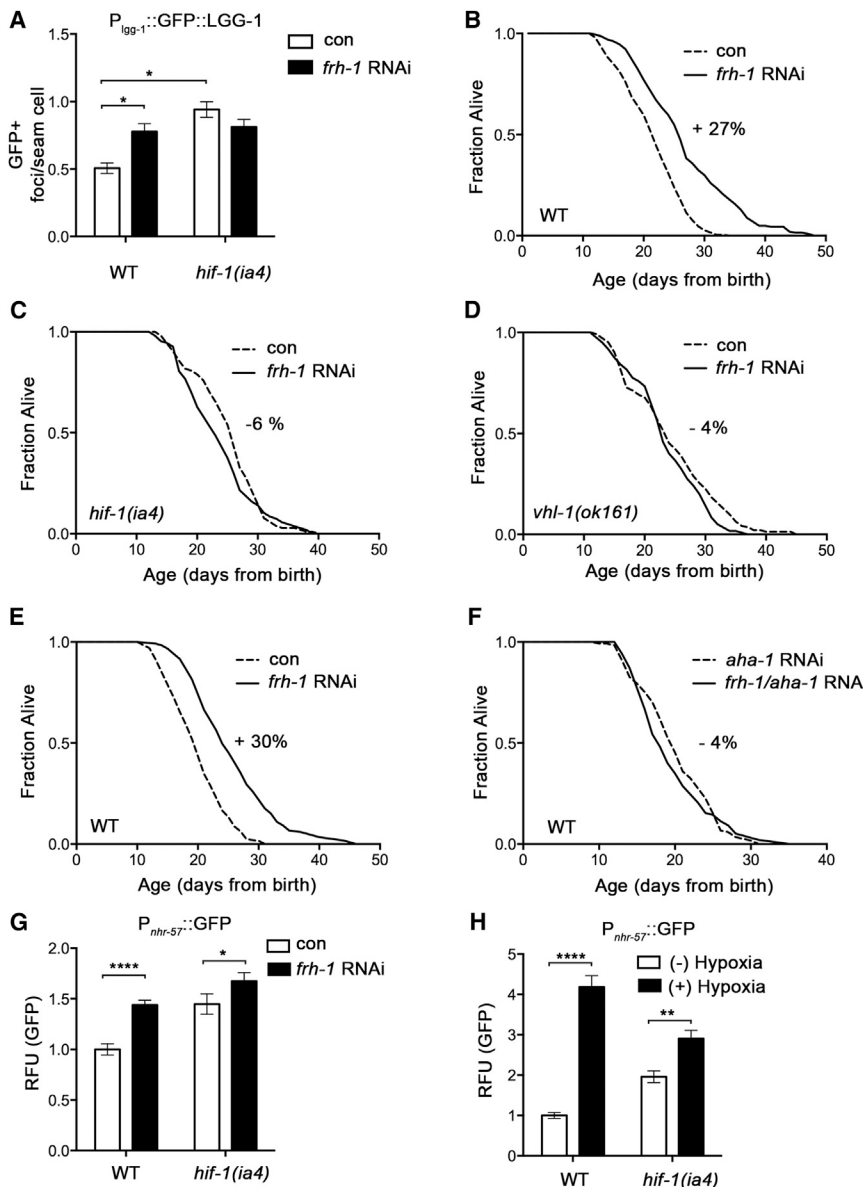


Figure 3. Frataxin Silencing Induces a Hypoxia-like Signaling

(A) Quantification of GFP+ foci in the seam cells of $P_{lgg-1}::GFP::LGG-1$ (WT) and $P_{lgg-1}::GFP::LGG-1$; $hif-1(ia4)$ transgenic strains fed bacteria transformed with either empty-vector (con) or vector-expressing dsRNA against $frh-1$ ($frh-1$ RNAi). Bar graph represents means \pm SEM (n = 5); *p < 0.05. (B–D) Kaplan-Meier survival curves of WT (B), $hif-1(ia4)$ (C), and $vhl-1(ok161)$ (D) *C. elegans* strains fed as in (A) are shown. (E and F) Kaplan-Meier survival curves of WT animals fed bacteria transformed either with empty-vector (con) or with vector-expressing dsRNA against $frh-1$ ($frh-1$ RNAi), $aha-1$ ($aha-1$ RNAi), or both ($frh-1/aha-1$ RNAi). Percentages indicate increase or decrease in mean lifespan of $frh-1$ RNAi-treated over control animals. (G) Quantification of GFP expression in WT and $hif-1(ia4)$ strains expressing the $P_{nhr-57}::GFP$ transgene fed as in (A) is shown. (H) Quantification of GFP expression in WT and $hif-1(ia4)$ strains expressing the $P_{nhr-57}::GFP$ transgene and fed empty vector transformed bacteria were left untreated or treated for 4 hr with hypoxia (<1% O_2 at 20°C). Bar graph represents means \pm SEM (n = 3); *p value vs con < 0.05, ****p value versus con < 0.0001. See also Figure S4.

Finally, in support of a general conserved role for mitophagy in response to mitochondrial stress, we found that silencing other MRC regulatory proteins, similar to $frh-1$ RNAi [6], reduced reactive oxygen species (ROS) levels (Figure S3A); increased the accumulation of autophagosomes (Figure S3B); promoted a $pdr-1$ -, $dct-1$ -, and $pink-1$ -dependent mitophagy (Figure S3C); and required mitophagy regulatory genes for optimal lifespan extension (Figures S3D–S3G). Collectively, the results described so far indicate that the induction of mitochondrial autophagy is an evolutionarily conserved response to reduced frataxin expression, and they identify a role for $pdr-1$ /Parkin- and $dct-1$ /Bnip3-regulated mitophagy in mitochondrial-stress control of longevity.

Frataxin Silencing Induces a Pro-longevity Iron Starvation Response

In search of a mechanism that could explain how frataxin depletion stimulates mitochondrial autophagy, we speculated a

possible hypoxia-like signal triggered by altered mitochondrial physiology. Indeed, frataxin suppression affects intracellular levels of ATP, ROS, and iron [6, 26], which can initiate a hypoxia-like signaling [27, 28]. Hypoxia, in turn, can trigger autophagy in *C. elegans* [11] as well as in mammals, and in the latter this can occur either in an HIF-1-dependent manner [29] or in an HIF-1-independent manner through AMP-regulated kinases (AMPKs) [30]. Although ATP content is reduced in $frh-1$ RNAi-depleted animals and in other RNAi-derived *Mit* mutants, levels of ATP do not correlate with, and AMPKs do not mediate, animal longevity [6, 31], thus arguing against a potential AMPK-regulated, HIF-1-independent activation of autophagy. Instead, $hif-1$ is required for lifespan extension in other *Mit* mutants [28, 32], and we found that it mediates autophagy and longevity in $frh-1$ RNAi animals (Figures 3A–3C). Specifically, LGG-1 is the nematode homolog of the microtubule-associated protein light chain 3 (LC3), and its pattern changes from diffuse to punctate during the autophagic process, reflecting the formation of the autophagosomes [33]. While $frh-1$ RNAi induces the accumulation of LGG-1-positive foci in wild-type animals [6], it could not further increase it in the $hif-1$ mutants, which already presented with a significantly higher number of autophagosomes compared to wild-type animals (Figure 3A). Either stabilization of HIF-1, through hypoxia or through reduced expression of VHL-1, or its loss of function can extend *C. elegans* lifespan [8, 9].

Consistent with an intact autophagy flux being required for *frh-1* RNAi longevity [6], we now found that either *hif-1* or *vhl-1* depletion completely blocked lifespan extension in response to frataxin silencing (Figures 3B–3D). The hypoxia-inducible factor acts in a heterodimeric transcription complex, consisting of HIF-1 and AHA-1 in *C. elegans*, encoded by homologs of the mammalian HIF-1-alpha and -beta subunits, respectively [34]. *aha-1* recently was identified as one of the *C. elegans* transcription factors required for lifespan extension in genetic-mediated *Mit* mutants [32]. In line with the *hif-1* findings, *frh-1* RNAi could not extend lifespan in animals depleted of *aha-1* (Figures 3E and 3F; Table S1). In further support of frataxin silencing activating a hypoxia-like response, it increased the expression of hypoxia-inducible genes such as *nhr-57* (Figure 3G) and *dct-1* (Figure 1E) in an *hif-1*-dependent manner, and reduced the expression of p62 (Figure 1F). In *C. elegans*, *nhr-57* belongs to the large family of nuclear hormone receptors and it is the most reliable marker for HIF-1 activation under hypoxic conditions ([35] and Figure 3H). Moreover, we found that *frh-1* RNAi tends to increase the transcriptional expression of different globins, *glb-1*, *glb-10*, *glb-13*, *glb-19*, and *glb-28*, especially in an RNAi-sensitized background; but, a *frh-1* double-stranded RNA (dsRNA) construct that reduced frataxin expression above the threshold for lifespan extension [6] did not significantly modulate the expression of any of them (Figures S4A and S4B). Globin genes encode for iron-containing proteins that can regulate the redox status of the cells in response to hypoxia [36]. Thirty-three globins were identified in *C. elegans*, all containing HIF-1 regulatory elements, and some of them can be induced by hypoxia in an *hif-1*-dependent manner ([37] and Figure S4C).

We then asked how frataxin silencing could mimic a hypoxia-like state. HIF-1 is a central player of oxygen and iron homeostasis in mammals as well as in *C. elegans* and can be activated by increased levels of ROS or reduced levels of cytosolic oxygen or iron [27, 38]. Although ROS-dependent activation of HIF-1 mediates longevity of the genetic-derived *Mit* mutants [28], ROS levels were actually reduced following silencing of different MRC regulatory subunits, including *frh-1* (Figure S3A) [6]. Iron deprivation can also activate a hypoxia-like signaling in mammals as well as in *C. elegans* [26, 27], and, accordingly, it increased the expression of *nhr-57* in an *hif-1*-dependent manner (Figure 4A), similar to the above-described effect with *frh-1* RNAi or hypoxia (Figures 3G and 3H). We thus speculated that *frh-1* RNAi activates the hypoxia-like response through cytosolic iron deprivation, a condition associated with reduced frataxin expression from yeast to mammals as a consequence of progressive mitochondrial iron accumulation [26, 39]. Consistent with this possibility, we found that the expression of the *C. elegans* cytosolic aconitase (*aco-1*), which is downregulated in response to iron overload like its mammalian homolog iron regulatory protein-1 (IRP1) [40], was significantly increased in *frh-1*-depleted animals compared to wild-type (Figure 4B). The mitochondrial Fe/S-cluster protein aconitase (*aco-2*) was also upregulated by *frh-1* RNAi (Figure 4B). These effects on the two aconitases possibly represent compensatory responses to the reduced cytosolic iron content and Fe/S-cluster biogenesis induced by frataxin deficiency [26]. The two aconitases also tended to be induced by hypoxia in an *hif-1*-dependent manner (Figures S4D and S4E).

A reduced iron content upon frataxin suppression is expected to decrease animal sensitivity to iron supplementation while increasing their sensitivity to iron deprivation. Accordingly, although iron supplementation through the entire life significantly shortened lifespan [41] of control (–18%) and of *frh-1*-depleted (–8%) animals, the latter were much less affected, as clearly underlined by the differences in their mean lifespan (Figure 4C; Table S1). Frataxin-deficient animals were also more sensitive to the detrimental effects induced by severe iron deprivation on development (Figure 4D), fertility, and fecundity (Figure 4E; Figure S4F). Furthermore, electron microscopic analysis revealed an elevated number of electron-dense granules, indicative of iron deposits [42], in mitochondria, but not in the cytosol, of *frh-1*-depleted animals, which was not observed in wild-type animals (Figure S4G). Of note, these electron-dense granules were detected in mitochondria of tissues, such as the intestine and the muscle, where we also observed the induction of autophagy (Figures S4H and 1F) and mitophagy (Figures 2A–2C).

Remarkably, similar to the opposite effects on lifespan induced by different levels of mitochondrial stress, while severe iron deficiency was lethal (Figure 4D), we found that milder iron deprivation significantly extended lifespan in wild-type animals (Figure 4F; Table S1). In support of frataxin silencing acting through an iron starvation response, iron chelation did not significantly extend lifespan of *frh-1*-depleted animals (Figure 4F; Table S1), while iron supplementation suppressed it (Figure 4C). Moreover, DMT1 is a divalent metal transporter whose expression is induced in mammals to increase intestinal iron transport in conditions of iron deficiency, and a *C. elegans* mutant for the DMT1 homolog, *smf-3*, displays low levels of iron compared to wild-type [38]. In agreement with previous results, we found that *smf-3* mutants have an extended lifespan that is not further prolonged by *frh-1* RNAi (Figures 4I and 4J; Table S1). To validate the iron starvation response induced in frataxin-depleted animals, we quantified the expression of the *C. elegans* ferritin homolog, *ftn-2*, an iron storage protein whose expression is induced in the presence of excessive iron and reduced in response to iron deprivation in an *hif-1*-dependent manner [38]. As expected, the expression of a *ftn-2::gfp* reporter was significantly reduced by iron depletion (Figure 4G). Of note we observed that *frh-1* RNAi also reduced *ftn-2* expression, and, consistent with the survival analysis, the combined treatment with iron depletion did not additively affect the expression of the two *hif-1* target genes, *ftn-2* and *nhr-57* (Figures 4G and 4H). Non-additive effects on *ftn-2* and *nhr-57* expression were similarly observed following iron chelation treatment in animals depleted of other MRC regulatory proteins (unpublished data), suggesting a more general iron starvation response upon mitochondrial stress. Taken together, the results shown so far reveal an iron starvation response as an evolutionarily conserved response to frataxin depletion, with pro-longevity effects in *C. elegans*.

Frataxin and Iron Depletion Extend Lifespan through Overlapping and Independent Mechanisms

Finally, we asked whether frataxin-silencing extension of lifespan via iron depletion could be ascribed to the induction of mitochondrial autophagy. Consistent with this possibility, we found that a lifespan-extending dose of iron chelation significantly induced

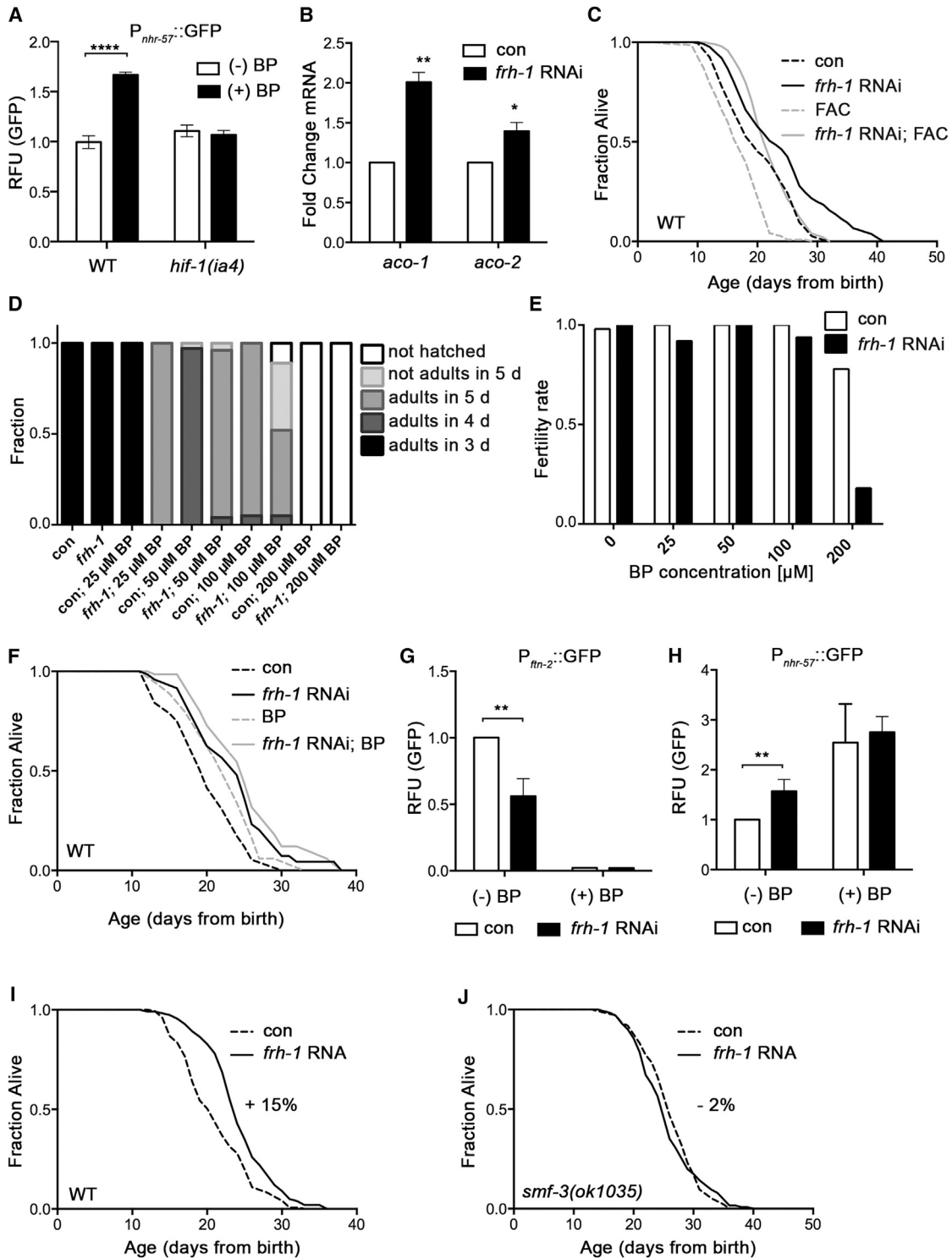


Figure 4. Frataxin Silencing Extends Lifespan through Iron Deprivation

(A) Quantification of GFP expression in WT and *hif-1(ia4)* strains expressing the $P_{nhr-57}::GFP$ transgene, left untreated or treated for 24 hr with 100 μ M of the iron chelator 2,2'-dipyridyl (BP), is shown.

(B) Quantification of *aconitases* transcript expression in WT animals fed bacteria transformed with either empty-vector (con) or vector-expressing dsRNA against *frh-1* (*frh-1* RNAi) is shown.

(C) Kaplan-Meier survival curves of WT animals fed as in (B) and left untreated or treated from eggs with life-shortening concentration (6.6 mg/ml) of an iron donor [ammonium iron (III) citrate, FAC] are shown.

(D) Developmental rate of WT animals fed as in (B), and left untreated or treated from eggs with the indicated concentrations of BP, is shown.

(legend continued on next page)

mitophagy (Figure 5A). Depletion of mitophagy regulatory genes significantly prevented this effect (Figure 5A) and also partially suppressed lifespan extension in response to iron depletion (Figures 5B–5E; Table S1). Notably, frataxin silencing did not further increase the effects of iron chelation on the accumulation of the autophagosomes and mitophagy (Figures 5F and 5G). This correlates with the lack of cumulative effect of the two treatments on lifespan (Figure 4F), and it suggests mitochondrial degradation by the lysosomal pathway as a specific mechanism induced by frataxin suppression to extend lifespan via cytosolic iron deprivation.

Whereas mitochondrial stress and iron deprivation converge on mitophagy to extend lifespan, the different phenotypic appearances of long-lived iron-depleted and frataxin-deficient animals (Figure 6A) also suggest the induction of incompletely overlapping signaling between the two treatments. While 4-day-old frataxin-depleted animals displayed their typical reduced size and fecundity compared to control animals, life-extending doses of iron chelation affected neither animal size nor fecundity (Figure 6A). The iron chelator reduced fecundity to the same level of *frh-1* RNAi only at doses of 100 μ M (Figure S4G), which also dramatically impaired animal development (Figure 4D). As a first indication that frataxin and iron depletion can also act through non-overlapping mechanisms, while *frh-1* RNAi did not extend lifespan of the *hif-1* mutants (Figure 3C), iron chelation could still do so (although the two treatments were not fully additive) (Figures 6B and 6C).

We then looked at *hif-1* upstream and downstream regulatory genes. The absence of EGL-9, the *C. elegans* homolog of the HIF-1 prolyl-hydroxylase, stabilizes *hif-1* in normoxia conditions and extends lifespan [9]. As expected by the fact that the prolyl-hydroxylase can be inhibited by low iron content [10], iron chelation did not extend lifespan of the long-lived *egl-9* mutants (Figures 6D and 6E). However, contrary to our expectation, *frh-1* RNAi not only further extended lifespan of the long-lived *egl-9* mutants but it also significantly suppressed animals internal bagging due to the egg-laying defect described in this strain (Figures 6D and 6E; Table S1). We then confirmed the induction of some globin genes (*glb-10*, *glb-19*, and *glb-28*) and the reduction of *glb-26* upon *frh-1* RNAi by quantifying the expression of the corresponding GFP reporter strains through an unbiased automated microscopy platform (Figure 6F). Iron chelation also upregulated *glb-10* expression and this was not further increased by *frh-1* RNAi (Figure 6G). However, surprisingly, loss of *glb-10* suppressed *frh-1* RNAi longevity, but did not prevent the pro-longevity effect of the iron chelator (Figures 6H, 6I, S5A, and S5B; Table S1). Taken together, our data reveal that overlapping (mitophagy) as well as unique (*egl-9* and *glb-10*) hypoxia-related pathways specify longevity of frataxin- and iron-depleted animals.

DISCUSSION

Collectively, our findings indicate that an iron starvation, hypoxia-like response is triggered by frataxin silencing and activates an evolutionarily conserved *pdr-1*/Parkin- and *dct-1*/Bnip3-regulated mitophagy, which ultimately mediates lifespan extension in *C. elegans*. To our knowledge, this is the first study that addressed and clearly identified a causal role for mitochondrial autophagy in longevity specification. ROS-dependent activation of HIF-1 is required for the lifespan extension of genetic-derived *Mit* mutants [28]. However, ROS are not deemed to be the main longevity determinants of RNAi-derived *Mit* mutants [7, 43], and induction of mitophagy can reduce ROS levels in response to hypoxia [13]. Consistent with these observations, we found that silencing of different MRC regulatory genes reduces ROS content. Although it is still possible that a transient elevation of ROS during animal development activates *hif-1*, our findings are in agreement with the notion that genetic- and RNAi-mediated *Mit* mutants can elicit distinct pro-longevity responses [44]. In fact, our study identifies reduced cytosolic iron, rather than increased ROS levels, as a trigger of the pro-longevity response induced by frataxin silencing. Accordingly, iron is active in the generation of ROS via the Fenton reaction, and, therefore, its reduced cytosolic content may concur to the observed reduced ROS levels in the different RNAi-mediated *Mit* mutants.

Iron is an essential element involved in the biogenesis and activity of different proteins and enzymes, and alteration in iron homeostasis is often observed in mitochondrial-associated disorders. Severe iron deficiency leads in humans to different diseases often associated with developmental defects, and in *C. elegans* it leads to a developmental arrest, which also is seen in response to severe hypoxia or mitochondrial stress. Interestingly, as with mild hypoxia or mitochondrial stress, we found that moderate iron depletion can also have beneficial, pro-longevity effects. This adaptive response, coupled with the resistance to hypoxia observed in the *Mit* mutants ([45] and data not shown), resembles the evolutionarily conserved beneficial effects elicited by hypoxia preconditioning [46]. In neurons and cardiomyocytes, this can be ascribed to activation of autophagy [47], thus suggesting that mitochondrial autophagy could also specifically contribute to its protective effect. Our findings are, therefore, extremely relevant in light of (1) the growing body of evidence implicating altered mitophagy in the pathogenesis of different genetic or age-related (neuro)degenerative disorders [15, 16], and (2) the beneficial effects that could be provided by the hypoxia mimetic effect of iron chelators in these pathological conditions.

In support of mitophagy being induced as part of the protective iron starvation response activated to cope with mitochondrial

(E) Number of eggs hatched per worm was quantified and normalized against the number of eggs laid (fertility rate) in WT animals fed bacteria transformed as in (B), after L4 larvae were left untreated or treated for 24 hr with the indicated concentrations of BP.

(F) Kaplan-Meier survival analysis of WT animals fed bacteria transformed with either empty-vector (con) or vector-expressing dsRNA against *frh-1* (*frh-1* RNAi), and left untreated or treated from eggs with 10 μ M BP, is shown.

(G) Automated fluorescent quantification of GFP expression in *P_{frh-2}::GFP* transgenic strain fed as in (F), and left untreated or treated for 18 hr as L4 with 100 μ M BP, is shown.

(H) Automated fluorescent quantification of GFP expression in *P_{frh-57}::GFP* transgenic strain treated as in (G) is shown.

(I and J) Kaplan-Meier survival analysis of WT animals and *smf-3(ok1035)* mutants fed as in (B).

Bar graph represents means \pm SEM (n = 3); *p value versus con < 0.05, **p value versus con < 0.01, ****p value versus con < 0.0001. See also Figure S4D.

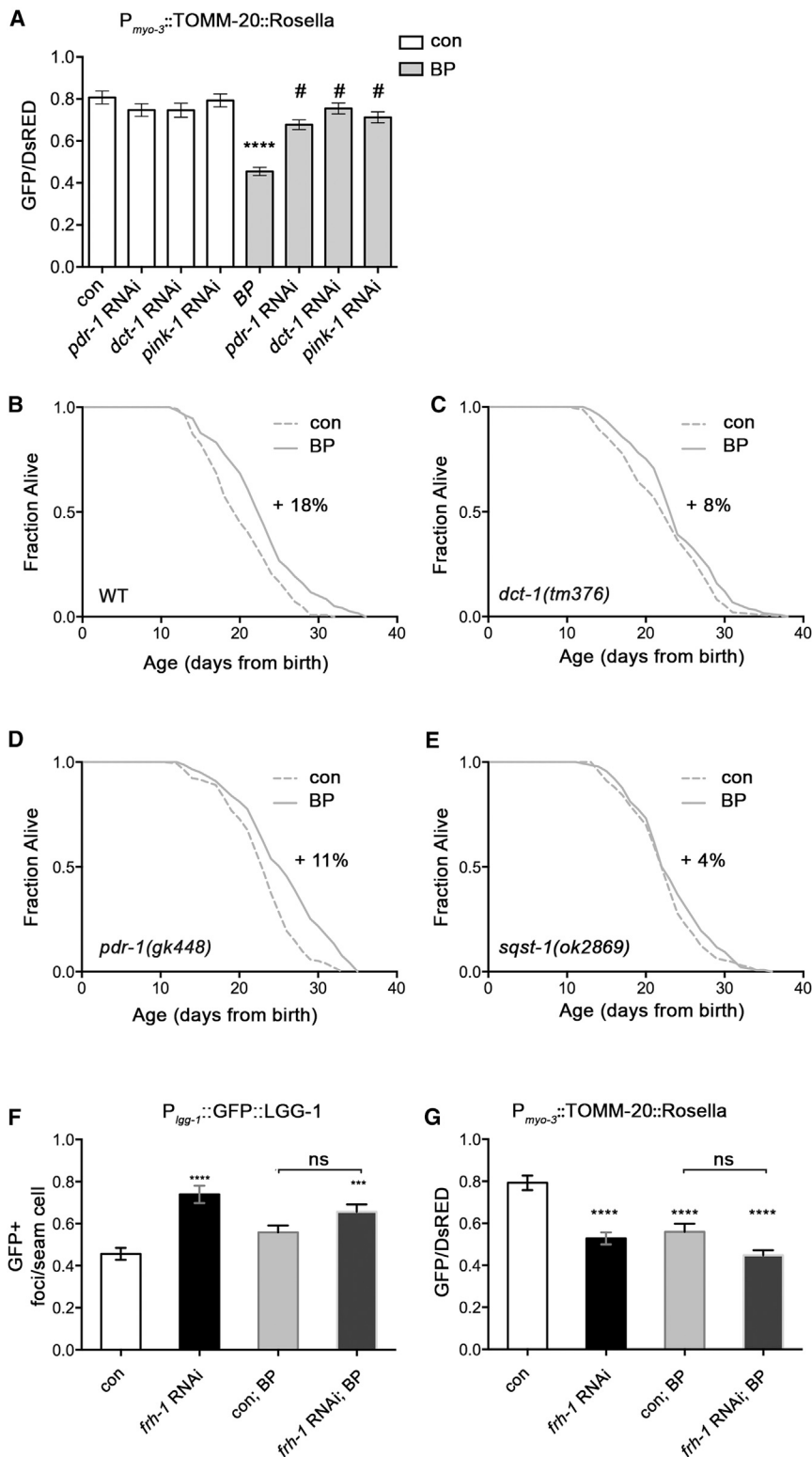


Figure 5. Iron Deprivation Extends Lifespan through the Induction of Mitophagy

(A) Quantification of the ratio between GFP/DsRED in $P_{myo-3}::TOMM-20::Rosella$ transgenic animals fed bacteria transformed with either empty vector (con) or vector expressing the indicated dsRNA, and left untreated or treated from eggs with 10 μ M of the iron chelator BP, is shown.

(B–E) Kaplan-Meier survival curves of WT animals, *dct-1(tm376)*, *pdr-1(gk448)*, and *sqst-1(ok2869)* strains, left untreated or treated from eggs with 10 μ M BP, are shown.

(F and G) Quantifications of GFP+ foci in the seam cells and of the ratio between GFP/DsRED, respectively, in $P_{igg-1}::GFP::LGG-1$ (F) and in $P_{myo-3}::TOMM-20::Rosella$ (G) transgenic strains fed bacteria transformed with empty-vector (con) or with vector-expressing dsRNA against *frh-1* (*frh-1* RNAi), and left untreated or treated from eggs with 10 μ M of BP, are shown.

Bar graphs represent means \pm SEM (n = 5); ***p value versus con < 0.001, ****p value versus con < 0.0001, #p value versus *frh-1* RNAi < 0.0001; NS, non-significant.

prisingly, while mutants or silencing of different mitophagy regulatory genes, namely *pdr-1*, *dct-1*, and *sqst-1*, as well as silencing of *pink-1*, in part or completely suppressed lifespan extension upon frataxin suppression, two different *pink-1* alleles did not. These findings are consistent with those of Bess et al. [19] showing that *pink-1* mutants do not exacerbate the developmental arrest elicited by UVC-induced mtDNA damage, while *pink-1* silencing prevents proper elimination of damaged mtDNA after UVC irradiation and suggests that *pink-1* mutants may retain some residual functions required for animal somatic maintenance (development or longevity) in response to mitochondrial stress. Taken together, we revealed a conserved function for mitophagy regulatory genes in mitochondrial elimination in *C. elegans*, and we identified a novel protective role for mitophagy in longevity specification in response to mitochondrial stress and iron deprivation.

Interestingly, while we were working on this paper, it was shown that iron chelators can induce mitophagy in mammalian cells [48] and in *C. elegans* [49], possibly as a way of recycling iron from the mitochondrial storage. These findings insinuate that, although frataxin silencing

stress, we show that different mitophagy regulatory genes mediate mitophagy induction and lifespan extension upon frataxin or iron depletion, and that the effect of the two combined treatments on mitophagy and on lifespan is not additive. Sur-

can induce mitophagy via cytosolic iron deprivation, the non-additive effects of the two combined treatments could also be a consequence of iron depletion-induced mitochondrial damage. It will be important to further elucidate underlying molecular

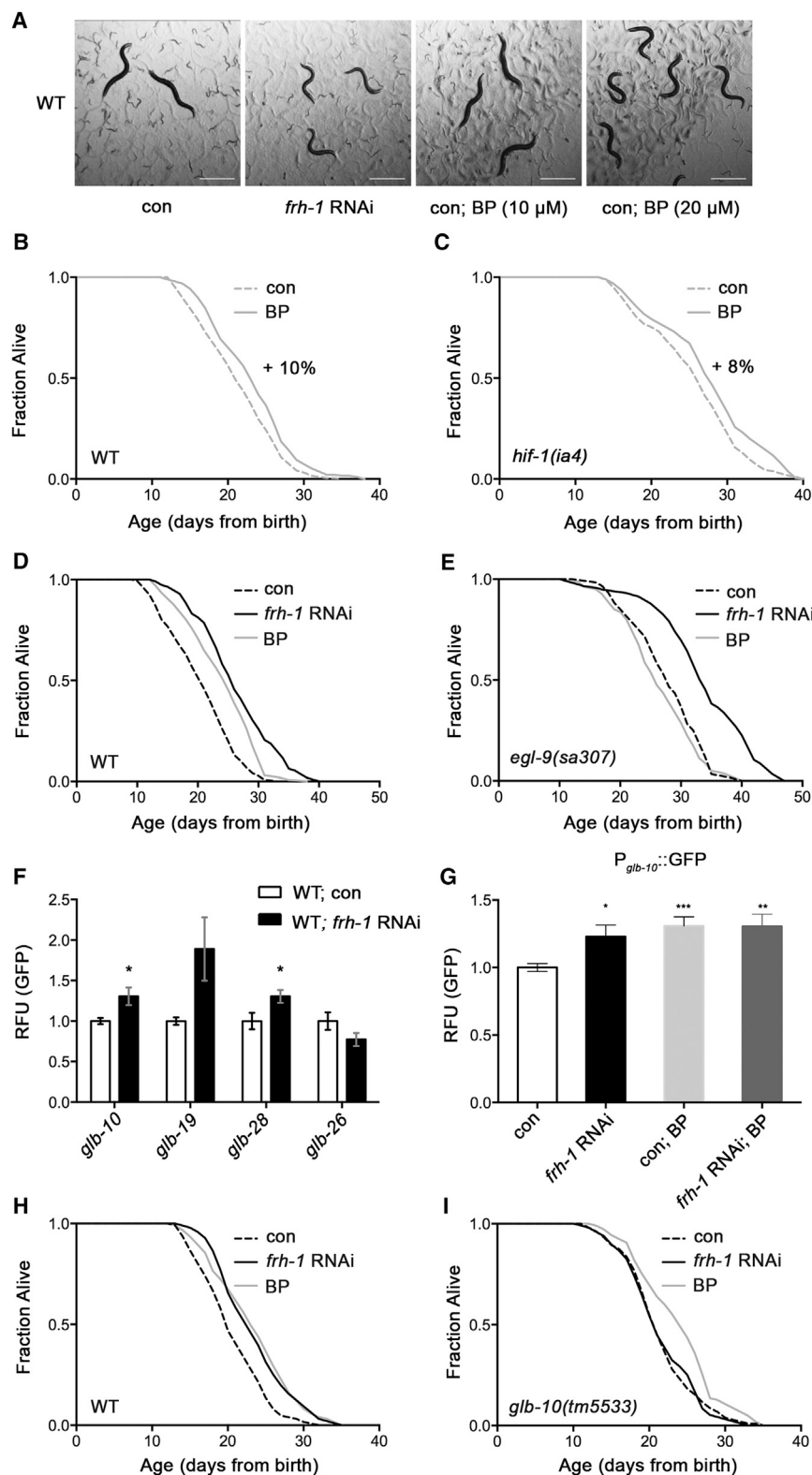


Figure 6. Frataxin and Iron Depletion Act through Independent Pathways

(A) Representative picture of 4-day-old WT worms fed bacteria transformed with empty-vector (con) or with vector-expressing dsRNA against *frh-1* (*frh-1* RNAi) or fed empty vector expressing bacteria and treated from eggs with the indicated concentrations of the iron chelator BP. Pictures were acquired using 40-fold magnification on a stereomicroscope (Leica MZ10F). White scale bars, 500 μ m.

(B and C) Kaplan-Meier survival curves of WT (B) and *hif-1(ia4)* (C) strains left untreated or treated from eggs with 10 μ M of BP are shown.

(D and E) Kaplan-Meier survival curves of WT (D) and *egl-9(sa307)* (E) strain fed bacteria transformed with empty-vector left untreated (con) or treated from eggs with 10 μ M BP or fed bacteria transformed with vector-expressing dsRNA against *frh-1* (*frh-1* RNAi) are shown.

(F) Automated fluorescent quantification of GFP expression in $P_{glb-10}::GFP$, $P_{glb-19}::GFP$, $P_{glb-28}::GFP$ and $P_{glb-26}::GFP$ transgenic strains fed bacteria transformed with empty-vector (con) or with vector-expressing dsRNA against *frh-1* (*frh-1* RNAi). Bars and errors represent means \pm SEM (n = 3); *p value versus con < 0.05.

(G) Automated fluorescent quantification of GFP expression in the $P_{glb-10}::GFP$ transgenic strain fed as in (F) and left untreated or treated from eggs with the iron 10 μ M BP is shown. Bars and errors represent means \pm SEM (n = 3); *p value versus con < 0.05, **p value versus con < 0.01, ***p value versus con < 0.001.

(H and I) Kaplan-Meier survival curves of WT and *glb-10(tm5533)* strains fed as in (D) and (E). See also Figure S5.

mechanisms of iron- and frataxin-depletion induction of mitophagy and to understand whether mitophagy plays a causal role in health span determination in other pathophysiological conditions.

span. Indeed, although *glb-10* was upregulated also by iron chelation, *glb-10* mutants did not affect their longevity, and *glb-10* overexpression by transgene injection did not positively impact on lifespan in otherwise wild-type animals (data not shown). On

the other hand, contrary to frataxin silencing, the lifespan-extending effect of iron deprivation was still present in the *hif-1* mutants, while it was completely abolished by lack of EGL-9, the prolyl-hydroxylase responsible for HIF-1 degradation in normoxia conditions, suggesting the parallel existence of *hif-1*-independent pathways to modulate iron-depletion extension of lifespan possibly mediated by other *egl-9* substrates. Interestingly, EGL-9 is inhibited by low oxygen levels but also by reduced levels of iron, and it can act in an *hif-1*-dependent or -independent manner [51], while globins can act as oxygen sensing, as NADH oxidase to sustain anaerobic respiration, and as ROS/NOS-scavenging proteins, and their expression can be induced in an *hif-1*-dependent manner [36, 37]. Additional studies to accurately assess tissue-specific expression of the different globins and to investigate possible links between the different *hif-1*-dependent or -independent signaling networks are required to elucidate their role in longevity specification in response to mitochondrial stress and/or iron depletion.

In *C. elegans*, *hif-1* can promote or limit longevity through distinct molecular mechanisms [52], and our data indicate that it can also act as a positive or negative regulator of autophagy. We found that *hif-1* was partially required for frataxin extension of lifespan and induction of autophagy. Given that additional transcription factors, such as p53/CEP-1 or HLH-30, can regulate *Mit* mutants' longevity through autophagy [6, 53], it is attractive to speculate a crosstalk between transcription factors in mediating mitochondrial stress and/or iron-depletion extension of lifespan through autophagy. In line with this possibility, iron chelation and hypoxia modulate the expression of common HIF-1 and p53 targets, including mitophagy in mammals [13, 48], and frataxin participates in the hypoxia-induced response together with the two transcription factors [54]. In conclusion, this is the first study that to our knowledge identifies a causal role for mitophagy as part of a pro-longevity iron starvation response induced to cope with mitochondrial stress, thus opening new interesting possibilities for healthy aging medicine. Since autophagy is implicated in the pathogenesis and treatment of several neurodegenerative disorders, it is time to speculate that the same could hold true also for more dedicated forms of autophagy, such as mitophagy, especially in those neurodegenerative disorders, such as FRDA, or age-related diseases associated with progressive mitochondrial deterioration.

EXPERIMENTAL PROCEDURES

Mammalian Cells

Transfection and Protein Expression Analysis

HEK293 cells were transiently transfected with expression plasmids Sh-scramble and Sh-Frataxin using TurboFect Transfection Reagent (Thermo Scientific), and the expression of the indicated proteins was analyzed by western blot in total cell extracts or mitochondrial fractions or by immunofluorescence analysis. See the [Supplemental Experimental Procedures](#) for details.

C. elegans

Nematode Strains and Culture Conditions

Standard conditions for *C. elegans* strains culture and RNAi experiments were used. All experiments were performed at 20°C on nematode growth media (NGMs) agar supplemented with *Escherichia coli* (OP50 or transformed HT115), unless otherwise indicated. A list of strains utilized in this work is provided in the [Supplemental Experimental Procedures](#).

Lifespan and Statistical Analysis

Survival analysis started from hatching using synchronous populations of 70–100 animals per strain. Survival curves and statistical analyses were carried out following standard procedures in the *C. elegans* aging field [55]. Briefly, we calculated mean, SD of the mean, and p value using the log-rank test (Mantel-Cox) from Kaplan-Meier survival analysis of pooled data resulting from at least two independent replicas. See the [Supplemental Experimental Procedures](#) for the detailed procedure and [Table S1](#) for the summary of lifespan data analysis.

Quantification of Gene Expression

GFP expression was quantified either by acquiring pictures with a Imager2 Zeiss fluorescence microscope, followed by ImageJ analysis, or through automated quantification, by transferring transgenic adult-stage worms to 96-well plates followed by image acquisition and analysis with the ArrayScan V^{TI} HCS Reader (Cellomics, Thermo Fisher Scientific) [56]. The qRT-PCR was carried out as we previously described. See the [Supplemental Experimental Procedures](#) for detailed quantification methods and analysis.

Electron Microscopy

Synchronized populations of about ~1,000 first-day adult animals were mixed with a thick pellet of *Escherichia coli* and immediately flash frozen. Thin sections of osmium tetroxide-fixed samples were stained with 2% uranyl acetate and Reynold's lead citrate and imaged at 80 kV on a Phillips CM10 electron microscope. Representative images were acquired from two experiments. None of the wild-type animals displayed dark electron-dense granules, while all sections from *frh-1* RNAi animals displayed dark deposits in at least one mitochondrion. See the [Supplemental Experimental Procedures](#) for more details.

Iron Chelation Sensitivity

The iron chelator 2,2'-dipyridyl (BP, Carl Roth) was supplemented to NGM at the indicated concentrations, and its effect was investigated on development, fecundity, and fertility of synchronized populations of worms. Transgene expression in response to iron chelation was measured on synchronized larvae grown for 24 hr on NGM plates and then transferred as L4 larvae to NGM plates supplemented with 100 μM BP for 18 hr before quantification.

Hypoxia Treatment

For generation of hypoxic status, worms were placed into a modular incubator chamber (Billups-Rothenberg). For almost complete replacement of the oxygen (<0.1%), a gas mixture (95% N₂, 5% CO₂) was flushed (15 l/min) into the chamber for 10 min. Young adult worms were then left in the hypoxic chamber for 4 hr at 20°C. Immediately after the hypoxia treatment, the worms were placed on a slide and acquired with the respective control left untreated.

Autophagy Measurements

Different transgenic strains were used to quantify autophagosomes using 100-fold magnification on a Zeiss Axio Imager 2 microscope. GFP-positive foci were counted in the seam cells of *gfp::lgg-1* L3 larvae and in the anterior pharyngeal bulb of young adult *sqst-1::gfp* animals. mCherry/*lgg-1*-positive foci were counted in the intestine of young adult worms. See the [Supplemental Experimental Procedures](#) for the detailed procedure.

Mitophagy Measurement

For monitoring of mitophagy, the following four newly generated *C. elegans* transgenic strains were employed: (1) N2;*s*[*p_{myo-3}::mtGFP*];*Ex*[*p_{lgg-1}::DsRed::LGG-1*], (2) N2;*Ex*[*p_{myo-3}::PDR-1::DsRed*; *p_{dct-1}::DCT-1::GFP*], (3) N2;*Ex*[*p_{myo-3}::DsRed::LGG-1*; *p_{dct-1}::DCT-1::GFP*], and (4) N2;*Ex*[*p_{myo-3}::TOMM-20::Rosella*]. See the [Supplemental Experimental Procedures](#) for details.

Mitochondrial Density

Mitochondrial density, expressed as the percentage of mitochondrial volume in the total analyzed volume, was quantified through 3D reconstruction of z stack images acquired using confocal laser scanning microscopy from *rps-0p::gas-1::DENDRA2* transgenic strain, as previously described. See the [Supplemental Experimental Procedures](#) for details.

Statistical Analysis

Data are represented as mean ± SEM from at least three independent biological replica carried out with blinded genotypes where possible. Statistical analyses were performed using two-tailed Student's t test or one-way ANOVA for multiple comparisons (GraphPad software) to calculate significance as follows: *p = 0.01 to 0.05, **p = 0.001 to 0.01, ***p = 0.0001 to 0.001, and ****p < 0.0001 versus respective control conditions.

SUPPLEMENTAL INFORMATION

Supplemental Information includes Supplemental Experimental Procedures, five figures, and one table and can be found with this article online at <http://dx.doi.org/10.1016/j.cub.2015.05.059>.

AUTHOR CONTRIBUTIONS

Conceptualization, N.V.; Methodology, A. Schiavi, S.M., K.P.; Investigation, A. Schiavi, S.M., A. Shaik, K.P., F.S., V.B., A.T., N.C., S.D.H., N.V.; Formal Analysis, A. Schiavi, N.V.; Writing – Original Draft, N.V., A. Schiavi; Writing – Review & Editing, N.V., A. Schiavi, A.T., B.P.B., N.T.; Resources, N.V., B.P.B., F.C., N.T.; Funding Acquisition and Supervision, N.V.

ACKNOWLEDGMENTS

Most nematode strains utilized in this work were provided by the *Caenorhabditis* Genetics Center, funded by the NIH Office of Research Infrastructure Programs (P40 OD010440). Other strains were kindly provided by Jo Anne Powell-Coffman (ZG120 and ZG175), Chris Link (VC1024 and RB2547), and Joshua Romney (XA6901). We thank Virginia Fonte for critical reading of the manuscript and technical help with electron microscopy, Anthea Di Rita and Beatrice Biferali for technical assistance with experiments in mammalian cells, and Roberto Testi for Sh-Frataxin and control plasmids. B.P.B. is indebted to the Fund for Scientific Research – Flanders (G008912N). This work was financially supported by funding to N.V. from the following: Italian Association for Cancer Research (MFA11509), Strategic Research Funding of the Heinrich Heine University (701301988), and Start-up Competitive Research Funding of the Medical Faculty of the Heinrich Heine University (Forschungskommision 43/2013).

Received: January 28, 2015

Revised: May 4, 2015

Accepted: May 27, 2015

Published: July 2, 2015

REFERENCES

- Campuzano, V., Montermini, L., Moltò, M.D., Pianese, L., Cossée, M., Cavalcanti, F., Monros, E., Rodius, F., Duclos, F., Monticelli, A., et al. (1996). Friedreich's ataxia: autosomal recessive disease caused by an intronic GAA triplet repeat expansion. *Science* *271*, 1423–1427.
- Ventura, N., and Rea, S.L. (2007). *Caenorhabditis elegans* mitochondrial mutants as an investigative tool to study human neurodegenerative diseases associated with mitochondrial dysfunction. *Biotechnol. J.* *2*, 584–595.
- Dell'agnello, C., Leo, S., Agostino, A., Szabadkai, G., Tiveron, C., Zulian, A., Prella, A., Roubertoux, P., Rizzuto, R., and Zeviani, M. (2007). Increased longevity and refractoriness to Ca(2+)-dependent neurodegeneration in Surf1 knockout mice. *Hum. Mol. Genet.* *16*, 431–444.
- Ventura, N., Rea, S.L., and Testi, R. (2006). Long-lived *C. elegans* mitochondrial mutants as a model for human mitochondrial-associated diseases. *Exp. Gerontol.* *41*, 974–991.
- Munkácsy, E., and Rea, S.L. (2014). The paradox of mitochondrial dysfunction and extended longevity. *Exp. Gerontol.* *56*, 221–233.
- Schiavi, A., Torgovnick, A., Kell, A., Megalou, E., Castelein, N., Guccini, I., Marzocchella, L., Gelino, S., Hansen, M., Malisan, F., et al. (2013). Autophagy induction extends lifespan and reduces lipid content in response to frataxin silencing in *C. elegans*. *Exp. Gerontol.* *48*, 191–201.
- Durieux, J., Wolff, S., and Dillin, A. (2011). The cell-non-autonomous nature of electron transport chain-mediated longevity. *Cell* *144*, 79–91.
- Mehta, R., Steinkraus, K.A., Sutphin, G.L., Ramos, F.J., Shamieh, L.S., Huh, A., Davis, C., Chandler-Brown, D., and Kaerberlein, M. (2009). Proteasomal regulation of the hypoxic response modulates aging in *C. elegans*. *Science* *324*, 1196–1198.
- Zhang, Y., Shao, Z., Zhai, Z., Shen, C., and Powell-Coffman, J.A. (2009). The HIF-1 hypoxia-inducible factor modulates lifespan in *C. elegans*. *PLoS ONE* *4*, e6348.
- Epstein, A.C., Gleadle, J.M., McNeill, L.A., Hewitson, K.S., O'Rourke, J., Mole, D.R., Mukherji, M., Metzen, E., Wilson, M.I., Dhanda, A., et al. (2001). *C. elegans* EGL-9 and mammalian homologs define a family of dioxygenases that regulate HIF by prolyl hydroxylation. *Cell* *107*, 43–54.
- Samokhvalov, V., Scott, B.A., and Crowder, C.M. (2008). Autophagy protects against hypoxic injury in *C. elegans*. *Autophagy* *4*, 1034–1041.
- Wang, K., and Klionsky, D.J. (2011). Mitochondria removal by autophagy. *Autophagy* *7*, 297–300.
- Zhang, H., Bosch-Marce, M., Shimoda, L.A., Tan, Y.S., Baek, J.H., Wesley, J.B., Gonzalez, F.J., and Semenza, G.L. (2008). Mitochondrial autophagy is an HIF-1-dependent adaptive metabolic response to hypoxia. *J. Biol. Chem.* *283*, 10892–10903.
- Schiavi, A., and Ventura, N. (2014). The interplay between mitochondria and autophagy and its role in the aging process. *Exp. Gerontol.* *56*, 147–153.
- Palikaras, K., and Tavernarakis, N. (2012). Mitophagy in neurodegeneration and aging. *Front. Genet.* *3*, 297.
- Narendra, D.P., and Youle, R.J. (2011). Targeting mitochondrial dysfunction: role for PINK1 and Parkin in mitochondrial quality control. *Antioxid. Redox Signal.* *14*, 1929–1938.
- Springer, W., Hoppe, T., Schmidt, E., and Baumeister, R. (2005). A *Caenorhabditis elegans* Parkin mutant with altered solubility couples alpha-synuclein aggregation to proteotoxic stress. *Hum. Mol. Genet.* *14*, 3407–3423.
- Sämann, J., Hegermann, J., von Gromoff, E., Eimer, S., Baumeister, R., and Schmidt, E. (2009). *Caenorhabditis elegans* LRK-1 and PINK-1 act antagonistically in stress response and neurite outgrowth. *J. Biol. Chem.* *284*, 16482–16491.
- Bess, A.S., Crocker, T.L., Ryde, I.T., and Meyer, J.N. (2012). Mitochondrial dynamics and autophagy aid in removal of persistent mitochondrial DNA damage in *Caenorhabditis elegans*. *Nucleic Acids Res.* *40*, 7916–7931.
- Yasuda, M., D'Sa-Eipper, C., Gong, X.L., and Chinnadurai, G. (1998). Regulation of apoptosis by a *Caenorhabditis elegans* BNIP3 homolog. *Oncogene* *17*, 2525–2530.
- Tian, Y., Li, Z., Hu, W., Ren, H., Tian, E., Zhao, Y., Lu, Q., Huang, X., Yang, P., Li, X., et al. (2010). *C. elegans* screen identifies autophagy genes specific to multicellular organisms. *Cell* *141*, 1042–1055.
- Pursiheimo, J.P., Rantanen, K., Heikkinen, P.T., Johansen, T., and Jaakkola, P.M. (2009). Hypoxia-activated autophagy accelerates degradation of SQSTM1/p62. *Oncogene* *28*, 334–344.
- Guo, B., Huang, X., Zhang, P., Qi, L., Liang, Q., Zhang, X., Huang, J., Fang, B., Hou, W., Han, J., and Zhang, H. (2014). Genome-wide screen identifies signaling pathways that regulate autophagy during *Caenorhabditis elegans* development. *EMBO Rep.* *15*, 705–713.
- Okatsu, K., Saisho, K., Shimanuki, M., Nakada, K., Shitara, H., Sou, Y.S., Kimura, M., Sato, S., Hattori, N., Komatsu, M., et al. (2010). p62/SQSTM1 cooperates with Parkin for perinuclear clustering of depolarized mitochondria. *Genes Cells* *15*, 887–900.
- Palikaras, K., and Tavernarakis, N. (2014). Mitochondrial homeostasis: the interplay between mitophagy and mitochondrial biogenesis. *Exp. Gerontol.* *56*, 182–188.
- Huang, M.L., Becker, E.M., Whitnall, M., Suryo Rahmanto, Y., Ponka, P., and Richardson, D.R. (2009). Elucidation of the mechanism of mitochondrial iron loading in Friedreich's ataxia by analysis of a mouse mutant. *Proc. Natl. Acad. Sci. USA* *106*, 16381–16386.
- Kirienko, N.V., Kirienko, D.R., Larkins-Ford, J., Wählby, C., Ruvkun, G., and Ausubel, F.M. (2013). *Pseudomonas aeruginosa* disrupts *Caenorhabditis elegans* iron homeostasis, causing a hypoxic response and death. *Cell Host Microbe* *13*, 406–416.

28. Lee, S.J., Hwang, A.B., and Kenyon, C. (2010). Inhibition of respiration extends *C. elegans* life span via reactive oxygen species that increase HIF-1 activity. *Curr. Biol.* *20*, 2131–2136.
29. Bellot, G., Garcia-Medina, R., Gounon, P., Chiche, J., Roux, D., Pouyssegur, J., and Mazure, N.M. (2009). Hypoxia-induced autophagy is mediated through hypoxia-inducible factor induction of BNIP3 and BNIP3L via their BH3 domains. *Mol. Cell. Biol.* *29*, 2570–2581.
30. Papandreou, I., Lim, A.L., Laderoute, K., and Denko, N.C. (2008). Hypoxia signals autophagy in tumor cells via AMPK activity, independent of HIF-1, BNIP3, and BNIP3L. *Cell Death Differ.* *15*, 1572–1581.
31. Dillin, A., Hsu, A.L., Arantes-Oliveira, N., Lehrer-Graiwer, J., Hsin, H., Fraser, A.G., Kamath, R.S., Ahringer, J., and Kenyon, C. (2002). Rates of behavior and aging specified by mitochondrial function during development. *Science* *298*, 2398–2401.
32. Khan, M.H., Ligon, M., Hussey, L.R., Hufnal, B., Farber, R., 2nd, Munkacsy, E., Rodriguez, A., Dillow, A., Kahlig, E., and Rea, S.L. (2013). TAF-4 is required for the life extension of *isp-1*, *clk-1* and *tpk-1* Mit mutants. *Aging (Albany NY)* *5*, 741–758.
33. Meléndez, A., Tallóczy, Z., Seaman, M., Eskelinen, E.L., Hall, D.H., and Levine, B. (2003). Autophagy genes are essential for dauer development and life-span extension in *C. elegans*. *Science* *301*, 1387–1391.
34. Jiang, H., Guo, R., and Powell-Coffman, J.A. (2001). The *Caenorhabditis elegans* *hif-1* gene encodes a bHLH-PAS protein that is required for adaptation to hypoxia. *Proc. Natl. Acad. Sci. USA* *98*, 7916–7921.
35. Shen, C., Nettleton, D., Jiang, M., Kim, S.K., and Powell-Coffman, J.A. (2005). Roles of the HIF-1 hypoxia-inducible factor during hypoxia response in *Caenorhabditis elegans*. *J. Biol. Chem.* *280*, 20580–20588.
36. Hoogewijs, D., Terwilliger, N.B., Webster, K.A., Powell-Coffman, J.A., Tokishita, S., Yamagata, H., Hankeln, T., Burmester, T., Rytönen, K.T., Nikinmaa, M., et al. (2007). From critters to cancers: bridging comparative and clinical research on oxygen sensing, HIF signaling, and adaptations towards hypoxia. *Integr. Comp. Biol.* *47*, 552–577.
37. Hoogewijs, D., Geuens, E., Dewilde, S., Vierstraete, A., Moens, L., Vinogradov, S., and Vanfleteren, J.R. (2007). Wide diversity in structure and expression profiles among members of the *Caenorhabditis elegans* globin protein family. *BMC Genomics* *8*, 356.
38. Romney, S.J., Newman, B.S., Thacker, C., and Leibold, E.A. (2011). HIF-1 regulates iron homeostasis in *Caenorhabditis elegans* by activation and inhibition of genes involved in iron uptake and storage. *PLoS Genet.* *7*, e1002394.
39. Gabrielli, N., Ayté, J., and Hidalgo, E. (2012). Cells lacking *pfh1*, a fission yeast homolog of mammalian frataxin protein, display constitutive activation of the iron starvation response. *J. Biol. Chem.* *287*, 43042–43051.
40. Kim, Y.I., Cho, J.H., Yoo, O.J., and Ahnn, J. (2004). Transcriptional regulation and life-span modulation of cytosolic aconitase and ferritin genes in *C. elegans*. *J. Mol. Biol.* *342*, 421–433.
41. Gourley, B.L., Parker, S.B., Jones, B.J., Zumbrennen, K.B., and Leibold, E.A. (2003). Cytosolic aconitase and ferritin are regulated by iron in *Caenorhabditis elegans*. *J. Biol. Chem.* *278*, 3227–3234.
42. Puccio, H., Simon, D., Cossée, M., Criqui-Filipe, P., Tiziano, F., Melki, J., Hindelang, C., Matyas, R., Rustin, P., and Koenig, M. (2001). Mouse models for Friedreich ataxia exhibit cardiomyopathy, sensory nerve defect and Fe-S enzyme deficiency followed by intramitochondrial iron deposits. *Nat. Genet.* *27*, 181–186.
43. Rea, S.L., Ventura, N., and Johnson, T.E. (2007). Relationship between mitochondrial electron transport chain dysfunction, development, and life extension in *Caenorhabditis elegans*. *PLoS Biol.* *5*, e259.
44. Yang, W., and Hekimi, S. (2010). Two modes of mitochondrial dysfunction lead independently to lifespan extension in *Caenorhabditis elegans*. *Aging Cell* *9*, 433–447.
45. Butler, J.A., Ventura, N., Johnson, T.E., and Rea, S.L. (2010). Long-lived mitochondrial (Mit) mutants of *Caenorhabditis elegans* utilize a novel metabolism. *FASEB J.* *24*, 4977–4988.
46. Dasgupta, N., Patel, A.M., Scott, B.A., and Crowder, C.M. (2007). Hypoxic preconditioning requires the apoptosis protein CED-4 in *C. elegans*. *Curr. Biol.* *17*, 1954–1959.
47. Park, H.K., Chu, K., Jung, K.H., Lee, S.T., Bahn, J.J., Kim, M., Lee, S.K., and Roh, J.K. (2009). Autophagy is involved in the ischemic preconditioning. *Neurosci. Lett.* *451*, 16–19.
48. Allen, G.F., Toth, R., James, J., and Ganley, I.G. (2013). Loss of iron triggers PINK1/Parkin-independent mitophagy. *EMBO Rep.* *14*, 1127–1135.
49. Kirienko, N.V., Ausubel, F.M., and Ruvkun, G. (2015). Mitophagy confers resistance to siderophore-mediated killing by *Pseudomonas aeruginosa*. *Proc. Natl. Acad. Sci. USA* *112*, 1821–1826.
50. Maglioni, S., Schiavi, A., Runci, A., Shaik, A., and Ventura, N. (2014). Mitochondrial stress extends lifespan in *C. elegans* through neuronal homeostasis. *Exp. Gerontol.* *56*, 89–98.
51. Luhachack, L.G., Visvikis, O., Wollenberg, A.C., Lacy-Hulbert, A., Stuart, L.M., and Irazoqui, J.E. (2012). EGL-9 controls *C. elegans* host defense specificity through prolyl hydroxylation-dependent and -independent HIF-1 pathways. *PLoS Pathog.* *8*, e1002798.
52. Leiser, S.F., and Kaerberlein, M. (2010). The hypoxia-inducible factor HIF-1 functions as both a positive and negative modulator of aging. *Biol. Chem.* *391*, 1131–1137.
53. Lapiere, L.R., De Magalhaes Filho, C.D., McQuary, P.R., Chu, C.C., Visvikis, O., Chang, J.T., Gelino, S., Ong, B., Davis, A.E., Irazoqui, J.E., et al. (2013). The TFEB orthologue HLH-30 regulates autophagy and modulates longevity in *Caenorhabditis elegans*. *Nat. Commun.* *4*, 2267.
54. Guccini, I., Serio, D., Condò, I., Rufini, A., Tomassini, B., Mangiola, A., Maira, G., Anile, C., Fina, D., Pallone, F., et al. (2011). Frataxin participates to the hypoxia-induced response in tumors. *Cell Death Dis.* *2*, e123.
55. Ventura, N., Rea, S.L., Schiavi, A., Torgovnick, A., Testi, R., and Johnson, T.E. (2009). p53/CEP-1 increases or decreases lifespan, depending on level of mitochondrial bioenergetic stress. *Aging Cell* *8*, 380–393.
56. Maglioni, S., Arsalan, N., Franchi, L., Hurd, A., Oipari, A.W., Glick, G.D., and Ventura, N. (2015). An automated phenotype-based microscopy screen to identify pro-longevity interventions acting through mitochondria in *C. elegans*. *Biochim Biophys Acta*. Published online May 12, 2015. <http://dx.doi.org/10.1016/j.bbabi.2015.05.004>.



Mitophagy and iron: two actors sharing the stage in age-associated neuronal pathologies



Alfonso Schiavi^{a,b,1}, Flavie Strappazon^{c,1}, Natascia Ventura^{a,b,*}

^a Institute of Clinical Chemistry and Laboratory Diagnostic, Medical Faculty, Heinrich Heine University, Düsseldorf, Germany

^b IUF- Leibniz Research Institute for Environmental Medicine, Düsseldorf, Germany

^c IRCCS Fondazione Santa Lucia, Rome, Italy

ARTICLE INFO

Keywords:

Mitochondria

Iron

Aging

Alzheimer disease

Parkinson disease

Amyotrophic Lateral Sclerosis

ABSTRACT

Aging is characterized by the deterioration of different cellular and organismal structures and functions. A typical hallmark of the aging process is the accumulation of dysfunctional mitochondria and excess iron, leading to a vicious cycle that promotes cell and tissue damage, which ultimately contribute to organismal aging. Accordingly, altered mitochondrial quality control pathways such as mitochondrial autophagy (mitophagy) as well as altered iron homeostasis, with consequent iron overload, can accelerate the aging process and the development and progression of different age-associated disorders. In this review we first briefly introduce the aging process and summarize molecular mechanisms regulating mitophagy and iron homeostasis. We then provide an overview on how dysfunction of these two processes impact on aging and age-associated neurodegenerative disorders with a focus on Alzheimer's disease, Parkinson's disease and Amyotrophic Lateral Sclerosis. Finally, we summarize some recent evidence showing mechanistic links between iron metabolism and mitophagy and speculate on how regulating the crosstalk between the two processes may provide protective effects against aging and age-associated neuronal pathologies.

1. AGING

Aging is a complex and still not completely understood process characterized by the progressive deterioration of cellular components with consequent decline in different physiological functions and increased frailty, and it represents the most important risk factor for the development of a wide range of diseases such as cancer, cardiovascular and neurodegenerative pathologies, the principal causes of death in the industrialized world. Aging is a multifactorial process concurrently shaped by genetic and environmental factors. Despite several theories of aging having been postulated in the past 150 years [1–8], it is only in the last 50 years that aging research, also thanks to the growing number of studies exploiting simple but powerful model organisms, has enormously increased our knowledge of molecular mechanisms underlying the aging process. Although it is impossible to identify a main culprit of aging or a unifying theory, attempts have been made in the latest years to establish evolutionarily conserved signs of the aging process [9–11]. Namely, nine main hallmarks of aging were identified based on evidence that these changes manifest during physiological aging, accelerate or delay the aging process when experimentally

exacerbated or ameliorated respectively. These hallmarks were sub-grouped in three functional categories: the potentially *primary* culprits of cellular damage (genome instability, telomere attrition, epigenetic alterations, loss of proteostasis), the *antagonistic* mechanisms, which try to compensate the initial damage but once overwhelmed actually contribute to the aging process (deregulated nutrient sensing, mitochondrial dysfunction, cellular senescence), and the *integrative hallmarks* resulting from the integration of previous changes and eventually leading to organism functional decline (stem cells exhaustion and altered intracellular communication). The number of features falling into the identified categories is expected to increase as aging research progresses; altered metabolic processes such as metal homeostasis with iron overload has been for instance increasingly recognized as a typical feature aging and associated disorders. Although this classification oversimplifies a much more complex scenario, the definition of the aging hallmarks should facilitate studies aiming at distinguishing actual players causally involved in promoting the aging process from pure bystanders or consequences, with the ultimate goal of developing targeted preventive and symptomatic therapeutics to fight aging and most importantly age-related pathologies.

* Corresponding author at: Institute of Clinical Chemistry and Laboratory Diagnostic, Medical Faculty, Heinrich Heine University, Düsseldorf, Germany.

E-mail address: natascia.ventura@uni-duesseldorf.de (N. Ventura).

¹ Equal contribution.

2. MITOPHAGY

One of the hallmarks of aging is mitochondrial dysfunction. Given the central importance of mitochondria in cellular homeostasis it is not surprising that cells developed a variety of protective mechanisms to cope with, prevent and repair their damage, and that, failure of these mechanisms or severe non-repairable mitochondrial damage, lead to a plethora of disorders and accelerate the aging process. One of these mechanisms, *mitophagy*, has the role of selectively degrading mitochondria by taking advantage of the autophagy process (or autophagocytosis), a genetically regulated mechanism of the cells that removes and recycles unnecessary or dysfunctional components through the lysosome [12,13]. The first observation of mitochondria selectively degraded by autophagy was made in *Saccharomyces cerevisiae*, in 2004, when these yeasts were cultivated in the presence of a strictly respiratory carbon source and subjected to nutrient deprivation [14]. The name “mitophagy” was subsequently introduced by Lemasters and described as a protective mechanism against mitochondrial damage [15]. Mitophagy was then revealed to be a fundamental process also in two physiological contexts, namely during maturation of reticulocytes into erythrocytes [16] and during the first step of embryogenesis for the removal of paternal mitochondria [17,18]. Mitochondria, by providing cells with adenosine triphosphate (ATP) through the oxidative phosphorylation system (OXPHOS), play a central role in bioenergetic pathways and can rapidly adjust their respiratory capacity to respond to the metabolic needs of the cell. Increased demand of energy is accomplished by mitochondrial biogenesis and fusion of individual mitochondria into dynamic networks; on the other hand, a decrease in energy demand results in the clearance of superfluous mitochondria through fission mechanisms and mitophagy. While mitochondrial autophagy occurs in physiological conditions to maintain optimal cellular homeostasis, it can also be induced in response to different types of mitochondrial damage, thus acting as a mechanism to control the functional quality of mitochondria and prevent the consequence of their dysfunction, such as oxidative stress.

At the molecular level, in mammalian cells, removal of damaged mitochondria mainly occurs after activation of the PTEN-induced kinase 1 (PINK1) and the E3 ubiquitin ligase Parkin. After the loss of mitochondrial membrane potential, PINK1 accumulates in the outer mitochondrial membrane (OMM) associating to the translocase of the outer membrane (TOM) complex [19] and leading to its homodimerization and autophosphorylation at S228, T257, and S402. This, in turn, allows PINK1-dependent recruitment and phosphorylation of Parkin at S65 in the OMM [20], which promotes its dimerization and activation of its E3 ligase activity, leading to ubiquitination of different OMM substrates [21,22]. Phospho-ubiquitin signalling of OMM proteins next induces the recruitment of mitophagy cargo receptors. Two main cargo receptors, Optineurin (OPTN) and CALCOCO2/Nuclear dot protein 52 (NDP52) are involved in PINK1-mediated mitophagy. These receptors are able to bind ubiquitylated mitochondria through their Ubiquitin Binding Domain (UBD) and thanks to a LC3-Interacting Region (LIR) motif, they bind Autophagy-related protein 8 (Atg8)/Microtubule-associated proteins 1A/1B light chain 3B (LC3) proteins onto autophagosomal membranes in order to deliver mitochondria into autophagosomes [23]. The LIR and UBD motifs of these autophagy receptors are thus crucial for their function in mitophagy. Parkin-mediated degradation of OMM proteins exposes Prohibitin (PHB2), a protein of the inner mitochondrial membrane (IMM), to LC3. PHB2 is thus an accessory protein that could get into the game when PINK1/Parkin-mediated mitophagy pathway is activated [24]. Another element of the IMM, namely the membrane lipid Cardiolipin, is involved in mitophagy regulation. Besides other functions, Cardiolipin, when externalized to the OMM can serve as a receptor for LC3 following mitochondrial membrane depolarization. However, in contrast to PHB2, the binding between Cardiolipin and LC3 occurs independently of Parkin [25]. Of note, the players involved in the mitophagy processes that occur during

physiological conditions have also been identified. In particular, during erythrocyte differentiation, the protein NIX, which is also known as beclin-2 (BCL2)/adenovirus E1B 19 kDa protein-interacting protein 3-like (BNIP3L), emerged as the key protein responsible for the elimination of mitochondria by direct binding of its LIR domain to LC3B [26]. Instead, paternal mitochondria degradation during embryogenesis is mediated by the two redundant E3 ubiquitin ligases, PARKIN and MUL1, which then require FIS1, P62, and PINK1 kinase for degradation [27].

PINK1/Parkin-mediated mitophagy is the best characterized mitophagy pathway, but “alternative” pathways have been also described. Indeed, other E3 ubiquitin protein ligases are involved in PINK-Parkin-independent mitophagy modulation, such as SMURF1, SIAH1, MUL1, Gp78, ARIH1 and HUWE1 [28–35]. Under hypoxia condition, it has been demonstrated that FUNDC1, another OMM protein, is able to activate mitophagy. In this context, it can recruit directly LC3 through its LIR domain [36]. Bcl-2-like 13 (BCL2L13), another OMM protein and homologue of Atg32, a well-known mitophagic receptor in yeast, can also bind LC3 directly through its LIR motif and favour mitophagy [37]. Finally, Ambra1, a cytosolic protein mainly described as a main positive regulator of autophagy [38–40] can be recruited to damaged mitochondria in Parkin-dependent [41] or Parkin-independent contexts. In particular, Ambra1, in analogy with the other mitophagic receptors can be localized on damaged mitochondria following mitochondrial depolarization or ischemia, and directly binds LC3 via its LIR motif, stimulating mitophagy [34,42].

Mitophagy is a crucial mechanism to maintain a healthy population of mitochondria therefore it needs to be tightly regulated. To this end, almost all mitophagy-regulatory proteins are post-translationally modified (primarily by phosphorylation), in order to induce a correct mitophagy process. Anti-apoptotic proteins belonging to the Bcl-2 family confer an additional level of regulation of the mitophagic pathway. Upon mitochondrial damage PINK1 is auto-phosphorylated at S228, T257 and S402, and, in turn, PINK1 phosphorylates Parkin on Ub-S65 in order to start the mitophagic process [22]. Moreover, this process is repressed by Bcl2 family proteins (i.e., BCL2, MCL1 and Bcl-XL), which inhibit the translocation of the E3 Ubiquitin ligase Parkin on damaged mitochondria [43]. To induce mitophagy, FUNDC1 needs to be phosphorylated at S17 by Ulk1 and dephosphorylated at S13 by PGAM5 under hypoxia condition. In this context, BCL2L1/Bcl-XL is able to block dephosphorylation of FUNDC1 by PGAM5 and thus inhibit mitophagy [44]. *In vitro* studies mimicking phosphorylation events on LIR domains, showed that phosphorylation of NIX LIR domain at S34/35 stabilizes the Nix:LC3B complex and enhances autophagosome recruitment in HeLa Cells [45]. IKK α kinase instead phosphorylates Ambra1 at S1014, favouring the binding between LC3B and Ambra1 and thus mitophagy [34]. This process is regulated by the anti-apoptotic factor MCL-1, which inhibits mitochondrial translocation of HUWE1, the E3 Ubiquitin ligase known to collaborate with Ambra1 for a correct mitophagy induction [46]. Finally, BCL2L13-mediated mitophagy is also stimulated after phosphorylation of S272, which favours its binding with LC3 [37,47]. It is expected that, similar to bulk or other specialized forms of autophagy, the number of modifications and mechanisms regulating the functions of mitophagy-regulatory proteins will increase exponentially as mitophagy studies will expand.

3. IRON

Iron is one of the most abundant components on our planet and it is essential for every living organism on Earth. Iron is indeed necessary for diverse biological functions, ranging from oxygen transport primarily as a component of hemoglobin [48], to DNA synthesis and repair for instance as co-factor in ribonucleotide reductase [49], to oxidative phosphorylation being an essential component of iron-sulfur complexes and cytochromes [50]. Consistent with its vital role, altered iron metabolism has been shown during aging and in a variety of diseases

[51–53] and either iron excess or its deficiency can lead to deleterious consequences. It is interesting to note that altered iron levels seem to mainly affect the organism through antagonist pleiotropy effects: iron deficiency is especially detrimental during early development and childhood while iron excess has primary undesirable effects during aging. On the one hand, in conditions of iron deficiency, the organism lacks the required amounts of iron to produce iron-containing proteins (see below) [54]. Iron deficiency can thus promote several conditions such as anemia, due to the inability to produce hemoglobin [55], and for instance impair the cognitive function and psychomotor development in children [56]. On the other hand, iron overload has been described as another typical sign of aging and its excess may directly or indirectly contribute to the aging process and to the pathogenesis of different disorders ranging from genetic diseases such as Friedreich ataxia [57] and hemochromatosis aceruloplasminemia [58], to age-associated diseases such as Alzheimer's [59–61] or Parkinson's disease [62–64]. It is therefore clear that iron homeostasis has to be finely tuned throughout life to avoid deleterious consequences associated with its either excessive or defective levels. Iron concentration and homeostasis are in fact tightly regulated both at the systemic level, through its absorption mainly by the intestinal enterocytes [65], and at the cellular level, through its sensing (Iron Regulatory Proteins), uptake (transferrins, mitoferrins, divalent metal transporters), usage, storage (ferritins), and excretion (ferroportin) [66–68].

3.1. Proteins regulating iron metabolism

The amount of iron in an adult is around 3 to 5 g with a slight difference between males and females. Approximately 70% of total iron is utilized to bind and transport oxygen as heme. The second most abundant fraction, around 20%, is stored in the hepatocytes [69]. Maintenance of appropriate systemic iron levels is primarily regulated by hepcidin, [70] in response to serum iron concentration, erythropoiesis, hypoxia and inflammation [70–73]. Iron is absorbed mainly from enterocytes covering the villi of the duodenum. Iron can switch between two oxidative states, ferrous (Fe^{2+}) and ferric (Fe^{3+}) iron [74] simply through a one-electron oxidation-reduction reaction [74], and the switch facilitates several biological reactions that require electron transfer and pH variation. Fe^{3+} is reduced by different reductases such as the cytochrome b reductase 1 (DCYTB) in the intestinal lumen [75]. The divalent transporter 1 (DMT1) [76] then transfers Fe^{2+} to the apical membrane of enterocytes. From the apical membrane, iron is transferred to the basolateral membrane of the enterocytes where ferroportin (FPN1) [77,78], a transmembrane iron exporter expressed on the cells membrane, permits the export of Fe^{2+} to the circulation supported by the oxidases ceruloplasmin and hephaestin [79]. Systemic iron excess increases hepcidin, which binds to FPN1 inducing its degradation through the lysosomes to minimize the amount of circulating iron; while iron deficiency decreases hepcidin levels to promote intestinal iron intake [80,81].

At the cellular level, iron homeostasis is instead maintained by several proteins, including iron transporters such as Transferrin (Tf) and Tf-Receptor 1 (TfR1), iron storage proteins such as Ferritins (FTs), Mitochondrial Ferritin (FTMT) and Frataxin (FXN) [82,83] and iron regulatory proteins IRP1 and IRP2 (IRPs). Tf, produced for the majority by the liver, is a glycoprotein that binds reversibly to Fe^{3+} for delivery into the cells. Iron binding to Tf promotes a conformational change which allows the recognition and binding to its receptor, TfR1, on the cell membranes [84,85]. The complex Tf-TfR1 is then internalized by endocytosis and once in the endosome the complex is disassembled and recycled on the cell surface [84,86], while Fe^{3+} is reduced to Fe^{2+} and released into the cytosol by DMT1 [87]. Then, to maintain intracellular iron homeostasis, different proteins exist to store iron. FT is an intracellular iron storage protein composed by 24 subunits of two types, the heavy and the light chain respectively named H- and L-chain disposed in a hollow spherical shape around an iron core that can contain

up to 4500 iron atoms [88,89]. Moreover, iron can be stored in the mitochondria by FTMT, which is therefore important for iron balance between cytoplasm and mitochondria. FTMT is expressed mainly in tissue with high oxygen consumption like the central nervous system [90,91], where it may play a role in protecting the mitochondria and the tissues from iron-induced ROS [92,93]. FXN is yet another protein which in mammals it is involved in different aspects of iron metabolism: iron-sulfur clusters (ISC) biogenesis [94], heme biogenesis [95], iron-binding/storage and ferroxidase activity [96–98] and iron chaperone [99]. Frataxin deficiency results in iron accumulation inside mitochondria, at the expense of cytosolic iron, in an evolutionarily conserved manner [100–102]. Iron is imported inside mitochondria by the mitoferrins (Mfrn1 and Mfrn2), and Mfrn2 is overexpressed in response to reduced frataxin expression, which in turn promote the accumulation of iron inside mitochondria [103].

Iron homeostasis inside the cells is primarily regulated by IRPs (IRP1 is expressed in most tissue while IRP2 is expressed mainly in the brain and small intestine), cytosolic RNA-binding proteins that regulate the expression of iron metabolic proteins by binding to the iron-responsive element sequences (IRE) on their mRNA [82]. In the presence of a high concentration of iron, IRPs binds ISC proteins (4Fe–4S) losing the capacity to bind the IRE of TfR1 and DMT1, which consequently are poorly translated and iron uptake is reduced, while FPN1 and FT are stabilized promoting iron storage and export [104–106]. On the contrary, when the iron is low, IRPs stabilizes TfR1 and DMT1 mRNA by binding their IRE sequence at 3'-UTR, and inhibits FT and FPN1 mRNA. Thus, IRPs promote iron absorption into cells and inhibits iron storage and export. Finally, it has been described that IRPs and hepcidin coordinately maintain appropriate levels of FPN1 expression in the brain: degradation of FPN1 by hepcidin increases cellular levels of iron, which in turn bind to IRPs and promote its detachment from FPN1 IRE mRNA, leading to increase FPN1 translation [107].

Besides IRPs, iron levels modulate the activity of different other proteins necessary to maintain its appropriate concentrations at systemic and cellular levels. Moreover, as a cofactor, iron is involved in the regulation of a wide range of other proteins critical for cellular homeostasis.

3.2. Proteins regulated by iron

Together with inorganic sulfur, iron is widely present in [2Fe–2S] or [4Fe–4S] iron-sulfur-cluster (ISC), and in this form is contained in several proteins involved in different functions such as electron transfer (e.g. ferredoxins [108]), non-redox catalysis (e.g. Fumarase A and B [109]), gene regulation (e.g. IRP1 [82]), DNA repair (e.g. XPD [110]), and iron sensors (Fra2-Grx3 [111]). The biogenesis of ISCs-containing proteins mainly requires mitochondria, but eukaryotic cells also possess a cytosolic ISC assembly machinery necessary for the maturation of cytosolic and nuclear proteins [112–114].

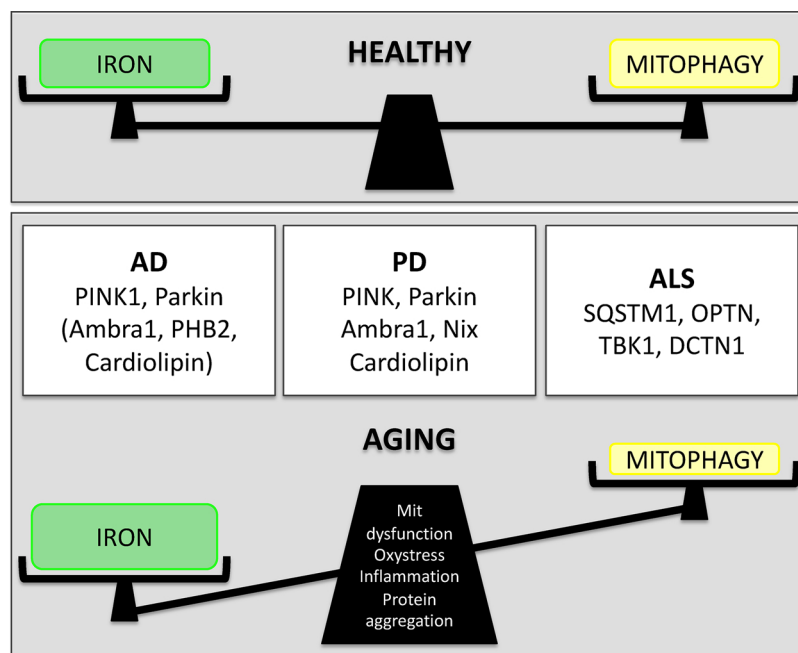
Iron is also largely found in the form of haem prosthetic groups in haemoproteins, a large class of metalloproteins required for several functions such as oxygen carrier and reduction, and electron transfer [115]. Examples of haemoproteins are haemoglobin, myoglobin, and cytochromes. Haemoglobin is the prevalent protein in erythrocytes and is mainly required for transporting oxygen and carbon dioxide between the lung and the tissues [48,116]. Haemoglobins are tetramers formed by two α -like globin subunits and two non- α globin subunits (β , γ , or δ). The haem group is associated with each globin subunit by noncovalent interaction and it is the site of oxygen binding [48]. Myoglobin instead is a monomeric globular protein containing only one haem group that binds oxygen more tightly than haemoglobin, and it functions as an oxygen reservoir to suit the oxygen needs of muscle and particularly of striated and cardiac muscle [117]. Another important category of proteins containing haem as cofactor are cytochromes, divided in four categories (a, b, c, and d) according to the characteristics of the haem group and the amino acid sequence similarity [118]. Cytochromes are

mainly involved in processes which require electron-transfer, such as respiration and photosynthesis, and this is achieved by reversible state variation of the iron atom contained in the haem unit [119]. For instance, cytochrome c is a small protein located in the mitochondrial intermembrane [120,121], it has a globular shape and it is involved in the electron transport chain (ETC) function carrying electrons between different complexes of the ETC. Another family of proteins containing iron in the form of haem are oxygenase enzymes that catalyse the reactions of O₂ with the substrates. They are divided into two groups: dioxygenases which can integrate both oxygen atoms into the product, and monooxygenases which can integrate one oxygen atom while the other one is discarded as a H₂O [122]. Many of the monooxygenases contain a specific haem group named cytochrome P-450. The cytochrome P-450 are involved in different steps of biosynthesis and biodegradation of endogenous compound (e.g. fatty acids) and in detoxification of exogenous compounds such as drugs or other environmental toxicants [123].

Another class of proteins is instead regulated by iron as a cofactor. For instance, prolyl hydroxylases (PHDs) regulate the stability, and therefore the expression, of the hypoxia-inducible factor (HIF1, composed by two subunits, HIF1 α and HIF1 β) by proline hydroxylation using iron and oxygen as cofactors. Under normal concentrations of oxygen and iron, HIF1 α is hydroxylated by PHD, which leads to the polyubiquitylation of HIF1 α by the von Hippel-Lindau tumour suppressor protein (VHL) and its consequent degradation through the proteasome [124]. Decreased levels of either oxygen or iron inactivate PHD resulting in HIF1 stabilization. Stabilized HIF1 can, in turn, regulated the transcription of different genes, including some involved in iron homeostasis (Tf, TfR, DMT-1, FPN1) [125]. Iron also regulates the activity of proteins involved in DNA maintenance. Ribonucleotide reductase (RNR) is an enzyme required for DNA synthesis to catalyse the reduction of ribonucleotides to deoxyribonucleotides. Different classes of RNR are involved in the DNA synthesis, which differ for the cofactor used (iron or manganese) or the amino acid sequences [49,126].

4. MITOPHAGY AND IRON IN AGING AND AGE-ASSOCIATED NEURODEGENERATIVE DISEASES

Mitochondrial integrity and functionality are crucial for appropriate



iron homeostasis, cell survival and organismal health (Fig. 1). Different mitochondrial quality control pathways, therefore, have evolved to maintain mitochondria quality and quantity, such as mitophagy, and these processes are especially important in cells like neurons or cardiomyocytes defined as long-lived post-mitotic cells, that are heavily dependent on mitochondrial energy metabolism (e.g. for ATP-dependent neurotransmission or contraction) and that cannot dilute cellular and mitochondrial damage through cell division [127,128]. Although it is still controversial whether mitochondrial dysfunction represents a cause or a consequence of aging there is no doubt that impaired mitochondrial quality control pathways and mitochondrial dysfunction, can accelerate the aging process [128,129] and concur to the development of age-associated neuronal (and not only) pathologies [130–134]. During aging indeed mitophagy decreases its efficiency [135], which can contribute to age-related disorders in mammals and lead to the accumulation of mitochondria in the nematode *Caenorhabditis elegans* (*C. elegans*) [136]. Accordingly, induction of mitophagy by Urolithin A, NAD + supplementation, iron-chelation and suppression of mitochondrial proteins, promote health and lifespan in *C. elegans* [101,137–139]. In line with the pro-longevity effect of iron chelation, iron accumulation has been described as another typical feature of molecular aging and iron excess can itself accelerate aging across species [101,140–142]. Notably, iron accumulation can concur to the pathogenesis of different age-associated neurodegenerative disorder and increased generation of reactive oxygen (ROS) species through the Fenton reaction, increased aggregation of toxic proteins, induction of cell death (e.g. ferroptosis) and inflammation, have been all causally linked to its detrimental effects in the nervous system [143–151]. In this review we specifically decided to focus on three main age-related diseases, Alzheimer's (AD), Parkinson's (PD) diseases and Amyotrophic Lateral Sclerosis (ALS) for which a role for altered mitophagy and iron overload have been described or proposed (Fig. 1). Interestingly, an *in silico* analysis using the integrative searchable database GeneCards, which combine information on human genes coming from omics, genetic, clinical and functional data, revealed 334 genes commonly associated with the keywords PD, AD, ALS, Mitophagy and Iron (Fig. 2).

Fig. 1. Mitophagy and iron in aging and associated neuronal pathologies. *Top panel.* Appropriate levels of mitophagy and iron are required to maintain cell homeostasis and organismal health. *Bottom panel.* Abnormal levels of iron (excess amount) and mitophagy (reduced amount) accelerate the aging process and concur to the pathogenesis of age-associated neurodegenerative disorders, also through the induction of typical hallmarks of aging such as mitochondrial dysfunction, oxidative stress, inflammation and protein aggregation. Specifically, Alzheimer's Disease (AD), Parkinson's Disease (PD) and Amyotrophic Lateral Sclerosis (ALS) (white boxes), have been linked to mutations and/or altered expression of different genes regulating mitophagy, and were shown to display increased iron accumulation in specific parts of the brain. Accordingly, interventions inducing mitophagy or reducing iron levels promote healthy aging in an evolutionarily conserved manner and iron-chelators inducing mitophagy may thus represent new interesting anti-aging strategies.

formation of amyloid oligomers and fibrils. [182–184]. Conversely, iron may accumulate in the brain as a direct activity of APP, which can support the iron export from neuron maintaining FPN1 on the neuronal surface [59,61,185]. Interestingly, many common polymorphisms associated with high levels of iron (e.g TF and FPN1) are also associated with AD [186,187]. Myelin production and sustainment are highly dependent on iron, which make the oligodendrocytes the cell types with the highest iron content in the Central Nervous System (CNS) [188,189]. Additionally, oligodendrocytes are also more sensitive to oxidative stress since they contain low levels of antioxidants and the stress can promptly increase with iron increase [190–192]. All together, these works, along with promising observation showing beneficial effects of iron chelators in early AD patients and animal models, implicate that iron overload in the progression of AD [193,194].

4.2. Parkinson Disease (PD)

After AD, PD is the second most common age-associated neurodegenerative disorder. PD is characterized by the loss of dopaminergic neurons in the substantia nigra with consequent motor neuron dysfunction [195]. Similar to AD, both environmental and genetic factors play an important role in PD pathogenesis and specifically in affecting several biological processes involved in the development of the disease, such as misfolded proteins, mitochondria dysfunction, ROS, and iron imbalance [63,64,179]. Genetic mutations in mitophagy regulatory proteins including PINK1 can lead to autosomal recessive forms of familial PD [196]. Of note, expression of an Ambra1-ActA fusion protein, targeting Ambra1 to the OMM, induces a powerful mitophagy in mammalian cells and can restore mitophagy in fibroblasts of PD patients carrying PINK1 and Parkin mutations [42]. Mitochondrial targeting toxins such as 6-hydroxydopamine (6-OHDA)- and rotenone can also mimic PD pathology and Ambra1-induced mitophagy also has a protective effect against 6-OHDA- and rotenone-induced cell death in human neuroblastoma SH-SY5Y cells by reducing compounds-induced oxidative stress [197]. Similar to Ambra1 overexpression, also genetic and pharmacological induction of Nix improves mitochondrial ATP production and restores mitophagy in PINK1- and Parkin-related PD patient cell lines [198], indicating that Nix is able to induce mitophagy independently of the PINK1/Parkin-mediated pathway. Nix could thus represent a promising target for neuroprotective treatment in PINK1/Parkin-related PD. Cardiolipin is also capable to drive mitophagy by directly binding LC3. This interaction is particularly important in the context of 6-OHDA- and rotenone-induced PD model, indicating that this interaction between Cardiolipin and LC3 may be a novel target to fine tune mitophagy in the context of PD [25].

Similar to AD, iron accumulation has been also documented in the substantia nigra pars compacta, which can lead to the degeneration of dopaminergic neurons through oxidative stress and/or increased aggregation of toxic proteins typically mutated in familial forms of PD, such as α -synuclein [199,200]. Different mechanisms have been proposed to explain the role of the iron imbalance in PD. Iron transporters (Tf and TfR) are important for iron import in the brain [201]: TfR2 is mainly expressed in the dopaminergic mitochondrial neurons in the substantia nigra and is dysregulated in PD, which may contribute to iron accumulation [149,202,203]. The iron not bound to Tf is transported by DMT1, which is also expressed in neurons, astrocytes and microglia of substantia nigra pars compacta [204]: DMT1 expression significantly increases in the brain of PD patients and animal models and may, therefore, contribute to the iron overload and neurodegeneration [205–207]. Another alternative pathway for iron uptake comprises the iron transporter lactoferrin (LF), produced and released only by activated microglia, and the lactoferrin receptor (LFR), present in blood vessels and dopaminergic neurons of substantia nigra: PD patients show an increased expression of LF and LFR, which may lead to neuronal iron accumulation [208,209]. Finally, Fe^{2+} exported to the bloodstream by FPN1, is promptly oxidized to Fe^{3+} by the ferroxidases

such as hephaestin or ceruloplasmin, whose activity is reduced in the cerebrospinal fluid in PD patients [210,211]. Interestingly, many of the genes implicated in familiar forms of PD are also implicated in iron accumulation. Indeed, it has been shown that PD patients with mutations of Parkin, DJ-1, α -synuclein, or PINK1 exhibited an increased iron level in the nigral region [63,212]. For instance, besides post-transcriptional regulation by IRE/IRP, DMT1 is degraded through the ubiquitin proteasome system (UPS) by the E3 ligase Parkin, and this may contribute to the increased DMT1, and consequent iron accumulation, observed in PD models [205,213]. Overall, data described so far indicate a cross talk between PD-related genes and iron metabolism, which may lead to iron accumulation possibly aggravated by altered mitophagy and consequent accumulation of dysfunctional mitochondria.

4.3. Amyotrophic lateral sclerosis (ALS)

ALS is a devastating disease, which is characterized by motor neuron degeneration mainly ascribed to accumulation of abnormal misfolded proteins or aggregates. Aggregation of the protein TDP-43 (transactive response DNA-binding protein 43 kDa) is one of the features of the pathology. As well as for the other neurodegenerative diseases, an accumulation of defective mitochondria with consequence OXPHOS defects, altered Ca^{2+} buffering and increased ROS production are hallmarks of this disease [214]. Moreover, the C- and N-terminal fragments of TDP-43 have been found associated with mitochondria, and animal models of TDP-43 pathology present dysfunctional mitochondria [215–217]. Most importantly some mutations of “autophagic/mitophagic” related-genes have been associated with ALS. Among them, DCTN1 (p150 subunit of dynactin) encodes a component of the microtubule-based motor complex that contribute to the transport of autophagosomes from the axon toward the soma [218]. Two mitophagy regulatory ubiquitin-binding proteins were also found mutated in ALS, namely the mitophagy receptors p62/SQSTM1 [219] and OPTN [220]. The ALS-associated E478 G ubiquitin binding-deficient mutant of OPTN cannot properly attach to the mitochondrial surface [220] thus impairing targeting of damaged mitochondria to the autophagosomes for degradation, while ALS-associated p62 mutant revealed that p62 serves as an important adaptor between mutant superoxide dismutase (SOD1) and the autophagy machinery [218]. Finally, TBK1 (TANK-binding kinase 1), a kinase known to phosphorylate both p62 and OPTN, was identified as an ALS-linked gene by exome sequencing and its ALS-associated mutant reduces OPTN and LC3B recruitment to damaged mitochondria [221–223].

ALS patients have been also reported to have increased levels of iron in the cerebrospinal fluid, in the motor cortex, and in the spinal neuron [224–227], while mouse models show that iron is increased also in the spinal cord [228]. Serum ferritin is significantly increased in advanced ALS patients [229] and is often associated with short survival rate [230]. Reduced levels of transferrin have been reported in ALS patients [231,232]. Taken together these findings suggest that altered iron metabolism may contribute to the development and progression of ALS. Accordingly, iron accumulation increases oxidative stress, which promotes neuronal degeneration in ALS patients [233,234]. On the other hand, oxidative stress can be induced by the mutations in the SOD1 gene, which is often mutated in ALS patients [235]. SOD1 it is required to remove superoxide radicals produced by the mitochondrial ETC and consequently to mitigate the ROS production. A link between iron and ALS is also indicated by the presence of genes variation in iron regulatory genes associated with ALS, for example, mutation in HFE increases oxidative stress and exacerbated ALS symptoms in mice [236,237]. HFE is known to regulate transferrin mediated iron uptake [238,239]. Moreover, a polymorphism variant (rs407135) in the DMT1 gene is associated with faster disease progression in ALS patients with lower limb onset [240]. Of note, promising treatment with iron chelators [241,242] support a role of iron overload in ALS pathogenesis, but

Table 1
Iron depletion induce mitophagy across species.

Iron Chelators	Mitophagy genes involved	Model	Reference
Deferiprone Deferoxamine	PINK/Parkin/ BNIP3/ -independent	primary human fibroblasts	[247]
Ferrozine 2,2'-dipyridyl	ATG32 PINK/ <i>pink-1</i> Parkin/ <i>pdn-1</i> BNIP3/ <i>dct-1</i>	<i>Candida glabrata</i> <i>Caenorhabditis elegans</i>	[248] [101]
Pyoverdine Phenanthroline	PINK1/ <i>pink-1</i>	<i>Caenorhabditis elegans</i> HEK293 T cells	[249,250]

further studies are required to define whether iron dysregulation is a cause or a consequence of the disease.

5. Crosstalk between mitophagy and iron

While mitochondrial damage may disrupt iron homeostasis [243,244], altered iron metabolism may, in turn, affect mitochondrial function [245,246], leading to a detrimental vicious cycle, which is concurrently a cause and a consequence of the aging process. Interestingly, a PubMed search for iron and mitophagy gives 56 items, a very limited number when compared to the literature on the single terms alone: 218289 items for iron, and 3930 items for mitophagy. Out of these 56 papers, only 5 established a direct functional crosstalk between the two processes by showing that iron depletion induces mitophagy across species [101,247–250] (Table 1).

Specifically, it has been demonstrated that iron chelators induce PINK1- and Parkin-independent mitophagy in human primary skin fibroblasts: mitophagy induction requires a metabolic switch from oxidative phosphorylation to glycolysis and is associated with HIF1 α and BNIP3L overexpression [247]. Hypoxia was shown to induce mitophagy via HIF1 α stabilization-induced BNIP3L expression [251]. However, whether similar to hypoxia, HIF1 α is also required for iron-chelation-induced mitophagy remains to be established. Interestingly, and of relevance for the aging process, mild mitochondrial-stress and iron-chelation, non-additively extend lifespan in *C. elegans* through iron-starvation-induced *pink-1*/PINK1, *park-1*/Parkin, and *dct-1*/BNIP3-dependent mitophagy [101]. Although the exact underlying molecular mechanisms through which iron depletion induces mitophagy remain to be identified, mitophagy could be induced to promote mitochondrial turnover in response to iron depletion-induced mitochondria damage [101,249,250]. Additionally, mitophagy could aid restoring proper iron levels by recycling the iron stored in the mitochondria, similar to the degradation of ferritin through iron chelation-induced autophagy (e.g. ferritinophagy) [252]. In line with these possibilities, in *C. elegans*, mitophagy is induced to mitigate the infection of *Pseudomonas aeruginosa*, which infects the host and secrete the iron-binding siderophore pyoverdine disrupting iron and mitochondrial homeostasis [249,250]. Moreover, it has been shown that the pathogenic yeast *Candida glabrata* during host infection experiences iron-depletion mainly due to the action of host's iron-chelating proteins such as transferrin [253]; to compensate for iron-depletion-induced mitochondrial stress *Candida glabrata* triggers mitophagy to maintain mitochondrial integrity [248]. It will be thus interesting to further gain insight into the underlying molecular mechanism of a direct functional crosstalk between mitophagy and iron metabolism to understand its implication at cellular and organismal levels for health, aging and diseases.

6. Conclusion and perspectives

Appropriate levels of mitophagy and iron are required to maintain cell homeostasis and organismal health (Fig. 1). In line with their

critical role, reduced mitophagy induction and excess iron accumulation, also through the induction of a variety of detrimental effects such as mitochondrial dysfunction, oxidative stress, inflammation and protein aggregation (four typical hallmarks of aging), concur to accelerate aging and the development and progression of age-associated neuronal pathologies (Fig. 1). Accordingly, interventions inducing mitophagy or reducing iron levels promote healthy aging in an evolutionarily conserved manner. Interestingly, although only 5 papers so far made a direct functional crosstalk between iron deprivation and activation of mitophagy (Table 1) a few more papers indicate indirect links. Thus, understanding the possible molecular mechanisms linking mitophagy and iron homeostasis may help developing novel therapeutic approaches to promote healthy aging and ameliorate specific age-associated neurodegenerative diseases where mitochondrial dysfunction and/or an iron overload are clearly identified.

Declaration of Competing Interest

The authors declare that the research was conducted in the absence of any commercial or financial relationships that could be construed as a potential conflict of interest.

Acknowledgments

We would like to apologize for all papers from valued scientists and colleagues, which we could not cite. We are in debt with David Weinkove for careful reading and editing of the manuscript. NV would like to thank the Deutsche Forschungsgemeinschaft (DFG VE663/1-6) and the Bundesministeriums für Bildung und Forschung (BMBF HDHL/JPI MiTyrAge project) for funding. This work was also supported by 5XMILLE Italian Ministry of Health (2017) to FS.

References

- Hamilton, W.D., 1966. The moulding of senescence by natural selection. *J Theor Biol* 12 (1), 12–45.
- Harman, D., 1956. Aging: a theory based on free radical and radiation chemistry. *J Gerontol* 11 (3), 298–300.
- Kirkwood, T.B., 1977. Evolution of ageing. *Nature* 270 (5635), 301–304.
- Villeponteau, B., 1997. The heterochromatin loss model of aging. *Exp Gerontol* 32 (4-5), 383–394.
- Williams, G.C., 1957. Pleiotropy, natural selection and the evolution of senescence. *Evolution* 11, 398–411.
- Kirkwood, T.B., Holliday, R., 1979. The evolution of ageing and longevity. *Proc R Soc Lond B Biol Sci* 205 (1161), 531–546.
- Hulbert, A.J., et al., 2007. Life and death: metabolic rate, membrane composition, and life span of animals. *Physiol Rev* 87 (4), 1175–1213.
- Blagosklonny, M.V., 2012. Answering the ultimate question "what is the proximal cause of aging? *Aging (Albany NY)* 4 (12), 861–877.
- Lopez-Otin, C., et al., 2013. The hallmarks of aging. *Cell* 153 (6), 1194–1217.
- Tigges, J., et al., 2014. The Hallmarks of Fibroblast Ageing. *Mech Ageing Dev.*
- Aunan, J.R., et al., 2016. Molecular and biological hallmarks of ageing. *Br J Surg* 103 (2), e29–46.
- Klionsky, D.J., 2008. Autophagy revisited: a conversation with Christian de Duve. *Autophagy* 4 (6), 740–743.
- Mizushima, N., Komatsu, M., 2011. Autophagy: renovation of cells and tissues. *Cell* 147 (4), 728–741.
- Kisova, I., et al., 2004. Uth1p is involved in the autophagic degradation of mitochondria. *J Biol Chem* 279 (37), 39068–39074.
- Kim, I., Rodriguez-Enriquez, S., Lemasters, J.J., 2007. Selective degradation of mitochondria by mitophagy. *Arch Biochem Biophys* 462 (2), 245–253.
- Novak, I., et al., 2010. Nix is a selective autophagy receptor for mitochondrial clearance. *EMBO Rep* 11 (1), 45–51.
- Al Rawi, S., et al., 2011. Postfertilization autophagy of sperm organelles prevents paternal mitochondrial DNA transmission. *Science* 334 (6059), 1144–1147.
- Sato, M., Sato, K., 2011. Degradation of paternal mitochondria by fertilization-triggered autophagy in *C. elegans* embryos. *Science* 334 (6059), 1141–1144.
- Lazarou, M., et al., 2012. Role of PINK1 binding to the TOM complex and alternate intracellular membranes in recruitment and activation of the E3 ligase Parkin. *Dev Cell* 22 (2), 320–333.
- Okatsu, K., et al., 2012. PINK1 autophosphorylation upon membrane potential dissipation is essential for Parkin recruitment to damaged mitochondria. *Nat Commun* 3, 1016.
- Koyano, F., et al., 2014. Ubiquitin is phosphorylated by PINK1 to activate parkin. *Nature* 510 (7503), 162–166.
- Kondapalli, C., et al., 2012. PINK1 is activated by mitochondrial membrane potential

- depolarization and stimulates Parkin E3 ligase activity by phosphorylating Serine 65. *Open Biol* 2 (5), 120080.
- Lazarou, M., et al., 2015. The ubiquitin kinase PINK1 recruits autophagy receptors to induce mitophagy. *Nature* 524 (7565), 309–314.
- Wei, Y., et al., 2017. Prohibitin 2 Is an Inner Mitochondrial Membrane Mitophagy Receptor. *Cell* 168 (1–2), 224–238 e10.
- Chu, C.T., Bayir, H., Kagan, V.E., 2014. LC3 binds externalized cardiolipin on injured mitochondria to signal mitophagy in neurons: implications for Parkinson disease. *Autophagy* 10 (2), 376–378.
- Sandoval, H., et al., 2008. Essential role for Nix in autophagic maturation of erythroid cells. *Nature* 454 (7201), 232–235.
- Rojansky, R., Cha, M.Y., Chan, D.C., 2016. Elimination of paternal mitochondria in mouse embryos occurs through autophagic degradation dependent on PARKIN and MUL1. *Elife* 5.
- Yuan, Y., et al., 2019. Mul1 promotes autophagy flux to suppress the development of clear cell renal cell carcinomas. *Cancer Sci*.
- Puri, R., et al., 2019. Mul1 restrains Parkin-mediated mitophagy in mature neurons by maintaining ER-mitochondrial contacts. *Nat Commun* 10 (1), 3645.
- Szargel, R., et al., 2016. The PINK1, synphilin-1 and SH3A1 complex constitutes a novel mitophagy pathway. *Hum Mol Genet* 25 (16), 3476–3490.
- Xu, Y., Shen, J., Ran, Z., 2019. Emerging views of mitophagy in immunity and autoimmune diseases. *Autophagy* 1–15.
- Orvedahl, A., et al., 2011. Image-based genome-wide siRNA screen identifies selective autophagy factors. *Nature* 480 (7375), 113–117.
- Villa, E., et al., 2017. Parkin-Independent Mitophagy Controls Chemotherapeutic Response in Cancer Cells. *Cell Rep* 20 (12), 2846–2859.
- Di Rita, A., et al., 2018. HUWE1 E3 ligase promotes PINK1/PARKIN-independent mitophagy by regulating AMBRA1 activation via IKKalpha. *Nat Commun* 9 (1), 3755.
- Fu, M., et al., 2013. Regulation of mitophagy by the Gp78 E3 ubiquitin ligase. *Mol Biol Cell* 24 (8), 1153–1162.
- Chen, M., et al., 2016. Mitophagy receptor FUNDC1 regulates mitochondrial dynamics and mitophagy. *Autophagy* 12 (4), 689–702.
- Murakawa, T., et al., 2015. Bcl-2-like protein 13 is a mammalian Atg32 homologue that mediates mitophagy and mitochondrial fragmentation. *Nat Commun* 6, 7527.
- Fimia, G.M., et al., 2007. Ambra1 regulates autophagy and development of the nervous system. *Nature* 447 (7148), 1121–1125.
- Nazio, F., et al., 2013. mTOR inhibits autophagy by controlling ULK1 ubiquitination, self-association and function through AMBRA1 and TRAF6. *Nat Cell Biol* 15 (4), 406–416.
- Strappazzon, F., et al., 2011. Mitochondrial BCL-2 inhibits AMBRA1-induced autophagy. *EMBO J* 30 (7), 1195–1208.
- Van Humbeeck, C., et al., 2011. Parkin interacts with Ambra1 to induce mitophagy. *J Neurosci* 31 (28), 10249–10261.
- Strappazzon, F., et al., 2015. AMBRA1 is able to induce mitophagy via LC3 binding, regardless of PARKIN and p62/SQSTM1. *Cell Death Differ* 22 (3), 419–432.
- Hollville, E., et al., 2014. Bcl-2 family proteins participate in mitochondrial quality control by regulating Parkin/PINK1-dependent mitophagy. *Mol Cell* 55 (3), 451–466.
- Wu, H., et al., 2014. The BCL2L1 and PGAM5 axis defines hypoxia-induced receptor-mediated mitophagy. *Autophagy* 10 (10), 1712–1725.
- Rogov, V.V., et al., 2017. Phosphorylation of the mitochondrial autophagy receptor Nix enhances its interaction with LC3 proteins. *Sci Rep* 7 (1), 1131.
- Strappazzon, F., et al., 2019. HUWE1 controls MCL1 stability to unleash AMBRA1-induced mitophagy. *Cell Death Differ*.
- Otsu, K., Murakawa, T., Yamaguchi, O., 2015. BCL2L13 is a mammalian homolog of the yeast mitophagy receptor Atg32. *Autophagy* 11 (10), 1932–1933.
- Gell, D.A., 2018. Structure and function of haemoglobins. *Blood Cells Mol Dis* 70, 13–42.
- Puig, S., et al., 2017. The elemental role of iron in DNA synthesis and repair. *Metallomics* 9 (11), 1483–1500.
- Papa, S., et al., 2012. The oxidative phosphorylation system in mammalian mitochondria. *Adv Exp Med Biol* 942, 3–37.
- Ploumi, C., Kyriakakis, E., Tavernarakis, N., 2019. Dynamics of Iron Homeostasis in Health and Disease: Molecular Mechanisms and Methods for Iron Determination. *Thermodynamics and Biophysics of Biomedical Nanosystems*. pp. 105–145.
- Conrad, M.E., Umbreit, J.N., Moore, E.G., 1999. Iron absorption and transport. *Am J Med Sci* 318 (4), 213–229.
- Harigae, H., 2018. Iron metabolism and related diseases: an overview. *Int J Hematol* 107 (1), 5–6.
- Zimmermann, M.B., Hurrell, R.F., 2007. Nutritional iron deficiency. *Lancet* 370 (9586), 511–520.
- DeLoughery, T.G., 2017. Iron Deficiency Anemia. *Med Clin North Am* 101 (2), 319–332.
- Pivina, L., et al., 2019. Iron Deficiency, Cognitive Functions, and Neurobehavioral Disorders in Children. *J Mol Neurosci* 68 (1), 1–10.
- Cook, A., Giunti, P., 2017. Friedreich's ataxia: clinical features, pathogenesis and management. *Br Med Bull* 124 (1), 19–30.
- Sebastiani, G., Pantopoulos, K., 2011. Disorders associated with systemic or local iron overload: from pathophysiology to clinical practice. *Metallomics* 3 (10), 971–986.
- Wan, L., et al., 2011. beta-Amyloid peptide increases levels of iron content and oxidative stress in human cell and *Caenorhabditis elegans* models of Alzheimer disease. *Free Radic Biol Med* 50 (1), 122–129.
- Everett, J., et al., 2014. Ferrous iron formation following the co-aggregation of ferric iron and the Alzheimer's disease peptide beta-amyloid (1–42). *J R Soc Interface* 11 (95), 2014 0165.
- Wong, B.X., et al., 2014. beta-Amyloid precursor protein does not possess ferroxidase activity but does stabilize the cell surface ferrous iron exporter ferroportin. *PLoS One* 9 (12), e114174.
- Patel, D., et al., 2018. Alpha-synuclein inhibits Snx3-retromer-mediated retrograde recycling of iron transporters in *S. cerevisiae* and *C. elegans* models of Parkinson's disease. *Hum Mol Genet* 27 (9), 1514–1532.
- Jiang, H., et al., 2017. Brain Iron Metabolism Dysfunction in Parkinson's Disease. *Mol Neurobiol* 54 (4), 3078–3101.
- Mostile, G., et al., 2017. Iron and Parkinson's disease: A systematic review and meta-analysis. *Mol Med Rep* 15 (5), 3383–3389.
- Papanikolaou, G., Pantopoulos, K., 2017. Systemic iron homeostasis and erythropoiesis. *IUBMB Life* 69 (6), 399–413.
- Lawen, A., Lane, D.J., 2013. Mammalian iron homeostasis in health and disease: uptake, storage, transport, and molecular mechanisms of action. *Antioxid Redox Signal* 18 (18), 2473–2507.
- Pantopoulos, K., et al., 2012. Mechanisms of mammalian iron homeostasis. *Biochemistry* 51 (29), 5705–5724.
- Hentze, M.W., Muckenthaler, M.U., Andrews, N.C., 2004. Balancing acts: molecular control of mammalian iron metabolism. *Cell* 117 (3), 285–297.
- Gkouvatsos, K., Papanikolaou, G., Pantopoulos, K., 2012. Regulation of iron transport and the role of transferrin. *Biochim Biophys Acta* 1820 (3), 188–202.
- Nemeth, E., et al., 2004. Hcpidin regulates cellular iron efflux by binding to ferroportin and inducing its internalization. *Science* 306 (5704), 2090–2093.
- Nicolas, G., et al., 2002. The gene encoding the iron regulatory peptide hepcidin is regulated by anemia, hypoxia, and inflammation. *The Journal of clinical investigation* 110 (7), 1037–1044.
- Merle, U., et al., 2007. The iron regulatory peptide hepcidin is expressed in the heart and regulated by hypoxia and inflammation. *Endocrinology* 148 (6), 2663–2668.
- Sangkhae, V., Nemeth, E., 2017. Regulation of the Iron Homeostatic Hormone Hepcidin. *Advances in nutrition* (Bethesda, Md) 8 (1), 126–136.
- Wessling-Resnick, M., 1999. Biochemistry of iron uptake. *Crit Rev Biochem Mol Biol* 34 (5), 285–314.
- McKie, A.T., 2008. The role of Dcytb in iron metabolism: an update. *Biochem Soc Trans* 36 (Pt 6), 1239–1241.
- Yanatori, I., Kishi, F., 2019. DMT1 and iron transport. *Free Radic Biol Med* 133, 55–63.
- Sharp, P., Srai, S.K., 2007. Molecular mechanisms involved in intestinal iron absorption. *World J Gastroenterol* 13 (35), 4716–4724.
- Ward, D.M., Kaplan, J., 2012. Ferroportin-mediated iron transport: expression and regulation. *Biochim Biophys Acta* 1823 (9), 1426–1433.
- Knutson, M.D., et al., 2005. Iron release from macrophages after erythrophagocytosis is up-regulated by ferroportin 1 overexpression and down-regulated by hepcidin. *Proc Natl Acad Sci U S A* 102 (5), 1324–1328.
- Preza, G.C., et al., 2013. Cellular catabolism of the iron-regulatory peptide hormone hepcidin. *PLoS One* 8 (3), e58934.
- Aschemeyer, S., et al., 2018. Structure-function analysis of ferroportin defines the binding site and an alternative mechanism of action of hepcidin. *Blood* 131 (8), 899–910.
- Rouault, T.A., 2006. The role of iron regulatory proteins in mammalian iron homeostasis and disease. *Nat Chem Biol* 2 (8), 406–414.
- Kuhn, L.C., 2015. Iron regulatory proteins and their role in controlling iron metabolism. *Metallomics* 7 (2), 232–243.
- Huebers, H.A., Finch, C.A., 1987. The physiology of transferrin and transferrin receptors. *Physiol Rev* 67 (2), 520–582.
- Dalhoj, J., Wiggers, P., 1988. Transferrin and transferrin receptors. *Physiology and clinical aspects*. *Ugeskr Laeger* 150 (32), 1914–1918.
- Aisen, P., 1992. Entry of iron into cells: a new role for the transferrin receptor in modulating iron release from transferrin. *Ann Neurol* (32 Suppl), S62–8.
- Kawabata, H., 2019. Transferrin and transferrin receptors update. *Free Radic Biol Med* 133, 46–54.
- Theil, E.C., 1987. Ferritin: structure, gene regulation, and cellular function in animals, plants, and microorganisms. *Annu Rev Biochem* 56, 289–315.
- Koorts, A.M., Viljoen, M., 2007. Ferritin and ferritin isoforms I: Structure-function relationships, synthesis, degradation and secretion. *Arch Physiol Biochem* 113 (1), 30–54.
- Shi, Y., et al., 2009. Human ISD11 is essential for both iron-sulfur cluster assembly and maintenance of normal cellular iron homeostasis. *Hum Mol Genet* 18 (16), 3014–3025.
- Ward, D.M., Cloonan, S.M., 2019. Mitochondrial Iron in Human Health and Disease. *Annu Rev Physiol* 81, 453–482.
- Wu, W.S., et al., 2013. Mitochondrial ferritin attenuates beta-amyloid-induced neurotoxicity: reduction in oxidative damage through the Erk/P38 mitogen-activated protein kinase pathways. *Antioxid Redox Signal* 18 (2), 158–169.
- Shi, Z.H., et al., 2010. Neuroprotective mechanism of mitochondrial ferritin on 6-hydroxydopamine-induced dopaminergic cell damage: implication for neuroprotection in Parkinson's disease. *Antioxid Redox Signal* 13 (6), 783–796.
- Stehling, O., et al., 2004. Iron-sulfur protein maturation in human cells: evidence for a function of frataxin. *Hum Mol Genet* 13 (23), 3007–3015.
- Yoon, T., Cowan, J.A., 2004. Frataxin-mediated iron delivery to ferroxidase in the final step of heme biosynthesis. *J Biol Chem* 279 (25), 25943–25946.
- Cavadini, P., et al., 2002. Assembly and iron-binding properties of human frataxin, the protein deficient in Friedreich ataxia. *Hum Mol Genet* 11 (3), 217–227.
- Soderberg, C.A., et al., 2013. The molecular basis of iron-induced oligomerization of frataxin and the role of the ferroxidation reaction in oligomerization. *J Biol Chem* 288 (12), 8156–8167.
- Park, S., et al., 2002. The ferroxidase activity of yeast frataxin. *J Biol Chem* 277 (41), 38589–38595.
- Bulteau, A.L., et al., 2004. Frataxin acts as an iron chaperone protein to modulate mitochondrial aconitase activity. *Science* 305 (5681), 242–245.
- Babcock, M., et al., 1997. Regulation of mitochondrial iron accumulation by Yfh1p, a putative homolog of frataxin. *Science* 276 (5319), 1709–1712.
- Schiavi, A., et al., 2015. Iron-Starvation-Induced Mitophagy Mediates Lifespan Extension upon Mitochondrial Stress in *C. elegans*. *Curr Biol* 25 (14), 1810–1822.

- Soriano, S., et al., 2013. Deferiprone and idebenone rescue frataxin depletion phenotypes in a *Drosophila* model of Friedreich's ataxia. *Gene* 521 (2), 274–281.
- Huang, M.L., et al., 2009. Elucidation of the mechanism of mitochondrial iron loading in Friedreich's ataxia by analysis of a mouse mutant. *Proc Natl Acad Sci U S A* 106 (38), 16381–16386.
- Wallander, M.L., Leibold, E.A., Eisenstein, R.S., 2006. Molecular control of vertebrate iron homeostasis by iron regulatory proteins. *Biochim Biophys Acta* 1763 (7), 668–689.
- Andolfo, I., et al., 2010. Regulation of divalent metal transporter 1 (DMT1) non-IRE isoform by the microRNA Let-7d in erythroid cells. *Haematologica* 95 (8), 1244–1252.
- Zhou, Z.D., Tan, E.K., 2017. Iron regulatory protein (IRP)-iron responsive element (IRE) signaling pathway in human neurodegenerative diseases. *Mol Neurodegener* 12 (1), 75.
- Wang, L., et al., 2019. Hepcidin and iron regulatory proteins coordinately regulate ferroportin 1 expression in the brain of mice. *J Cell Physiol* 234 (5), 7600–7607.
- Cassier-Chauvat, C., Chauvat, F., 2014. Function and Regulation of Ferredoxins in the Cyanobacterium, *Synechocystis* PCC6803: Recent Advances. *Life (Basel)* 4 (4), 666–680.
- Flint, D.H., Allen, R.M., 1996. Ironminus signSulfur Proteins with Nonredox Functions. *Chem Rev* 96 (7), 2315–2334.
- Rudolf, J., et al., 2006. The DNA repair helicases XPD and FancJ have essential iron-sulfur domains. *Mol Cell* 23 (6), 801–808.
- Li, H., et al., 2011. Histidine 103 in Fra2 is an iron-sulfur cluster ligand in the [2Fe-2S] Fra2-Grx3 complex and is required for in vivo iron signaling in yeast. *J Biol Chem* 286 (1), 867–876.
- Netz, D.J., et al., 2014. Maturation of cytosolic and nuclear iron-sulfur proteins. *Trends Cell Biol* 24 (5), 303–312.
- Lill, R., Freibert, S.A., 2020. Mechanisms of Mitochondrial Iron-Sulfur Protein Biogenesis. *Annu Rev Biochem*.
- Stehling, O., et al., 2018. Biochemical Analyses of Human Iron-Sulfur Protein Biogenesis and of Related Diseases. *Methods Enzymol* 599, 227–263.
- Li, T., Bonkovsky, H.L., Guo, J.T., 2011. Structural analysis of heme proteins: implications for design and prediction. *BMC Struct Biol* 11, 13.
- D'Alessandro, A., et al., 2017. Red blood cell proteomics update: is there more to discover? *Blood Transfus* 15 (2), 182–187.
- Vanek, T., Kohli, A., 2020. Biochemistry, Myoglobin. *StatPearls*. Treasure Island, FL. Nomenclature Committee of the International Union of Biochemistry (NC-IUB). Nomenclature of electron-transfer proteins. Recommendations 1989. *J Biol Chem* 267 (1), 665–677.
- Liu, J., et al., 2014. Metalloproteins containing cytochrome, iron-sulfur, or copper redox centers. *Chem Rev* 114 (8), 4366–4469.
- UniProt, C., 2019. UniProt: a worldwide hub of protein knowledge. *Nucleic Acids Res* 47 (D1), D506–D515.
- Wan, J., et al., 2019. Regulation of Respiration and Apoptosis by Cytochrome c Threonine 58 Phosphorylation. *Sci Rep* 9 (1), 15815.
- Messerschmidt, A., 2004. Handbook of metalloproteins. Wiley, Chichester.
- Hannemann, F., et al., 2007. Cytochrome P450 systems—biological variations of electron transport chains. *Biochim Biophys Acta* 1770 (3), 330–344.
- Semenza, G.L., 2001. HIF-1, O(2), and the 3 PHDs: how animal cells signal hypoxia to the nucleus. *Cell* 107 (1), 1–3.
- Goralska, M., Fleisher, L.N., McGahan, M.C., 2014. Hypoxia induced changes in expression of proteins involved in iron uptake and storage in cultured lens epithelial cells. *Exp Eye Res* 125, 135–141.
- Kolberg, M., et al., 2004. Structure, function, and mechanism of ribonucleotide reductases. *Biochim Biophys Acta* 1699 (1-2), 1–34.
- Dorn 2nd, G.W., Vega, R.B., Kelly, D.P., 2015. Mitochondrial biogenesis and dynamics in the developing and diseased heart. *Genes Dev* 29 (19), 1981–1991.
- Fivenson, E.M., et al., 2017. Mitophagy in neurodegeneration and aging. *Neurochem Int* 109, 202–209.
- Markaki, M., Palikaras, K., Tavernarakis, N., 2018. Novel Insights Into the Anti-aging Role of Mitophagy. *Int Rev Cell Mol Biol* 340, 169–208.
- Park, J.S., Davis, R.L., Sue, C.M., 2018. Mitochondrial Dysfunction in Parkinson's Disease: New Mechanistic Insights and Therapeutic Perspectives. *Curr Neurol Neurosci Rep* 18 (5), 21.
- Perez Ortiz, J.M., Swerdlow, R.H., 2019. Mitochondrial dysfunction in Alzheimer's disease: Role in pathogenesis and novel therapeutic opportunities. *Br J Pharmacol* 176 (18), 3489–3507.
- Nunnari, J., Suomalainen, A., 2012. Mitochondria: in sickness and in health. *Cell* 148 (6), 1145–1159.
- Evans, C.S., Holzbaur, E.L.F., 2019. Autophagy and mitophagy in ALS. *Neurobiol Dis* 122, 35–40.
- Rodolfo, C., Campello, S., Cecconi, F., 2018. Mitophagy in neurodegenerative diseases. *Neurochem Int* 117, 156–166.
- Sun, N., et al., 2015. Measuring In Vivo Mitophagy. *Mol Cell* 60 (4), 685–696.
- Palikaras, K., Lionaki, E., Tavernarakis, N., 2015. Coordination of mitophagy and mitochondrial biogenesis during ageing in *C. elegans*. *Nature* 521 (7553), 525–528.
- Ryu, D., et al., 2016. Urolithin A induces mitophagy and prolongs lifespan in *C. elegans* and increases muscle function in rodents. *Nat Med* 22 (8), 879–888.
- Fang, E.F., et al., 2019. NAD(+) augmentation restores mitophagy and limits accelerated aging in Werner syndrome. *Nat Commun* 10 (1), 5284.
- Fang, E.F., et al., 2019. Mitophagy inhibits amyloid-beta and tau pathology and reverses cognitive deficits in models of Alzheimer's disease. *Nat Neurosci* 22 (3), 401–412.
- Sfera, A., et al., 2018. Ferrosenescence: The iron age of neurodegeneration? *Mech Ageing Dev* 174, 63–75.
- Wawer, A.A., Jennings, A., Fairweather-Tait, S.J., 2018. Iron status in the elderly: A review of recent evidence. *Mech Ageing Dev* 175, 55–73.
- Ashraf, A., Clark, M., So, P.W., 2018. The Aging of Iron Man. *Front Aging Neurosci* 10, 65.
- Andersen, H.H., Johnsen, K.B., Moos, T., 2014. Iron deposits in the chronically inflamed central nervous system and contributes to neurodegeneration. *Cell Mol Life Sci* 71 (9), 1607–1622.
- Zucca, F.A., et al., 2017. Interactions of iron, dopamine and neuromelanin pathways in brain aging and Parkinson's disease. *Prog Neurobiol* 155, 96–119.
- Klang, I.M., et al., 2014. Iron promotes protein insolubility and aging in *C. elegans*. *Ageing (Albany NY)* 6 (11), 975–991.
- Masaldan, S., et al., 2018. Iron accumulation in senescent cells is coupled with impaired ferritinophagy and inhibition of ferroptosis. *Redox Biol* 14, 100–115.
- Nakamura, T., Naguro, I., Ichijo, H., 2019. Iron homeostasis and iron-regulated ROS in cell death, senescence and human diseases. *Biochim Biophys Acta Gen Subj* 1863 (9), 1398–1409.
- Latunde-Dada, G.O., 2017. Ferroptosis: Role of lipid peroxidation, iron and ferritinophagy. *Biochim Biophys Acta Gen Subj* 1861 (8), 1893–1900.
- Ward, R.J., et al., 2014. The role of iron in brain ageing and neurodegenerative disorders. *Lancet Neurol* 13 (10), 1045–1060.
- Connor, J.R., et al., 1992. Regional distribution of iron and iron-regulatory proteins in the brain in aging and Alzheimer's disease. *J Neurosci Res* 31 (2), 327–335.
- Agrawal, S., et al., 2017. Impact of high iron intake on cognition and neurodegeneration in humans and in animal models: a systematic review. *Nutr Rev* 75 (6), 456–470.
- Stelzer, G., et al., 2016. The GeneCards Suite: From Gene Data Mining to Disease Genome Sequence Analyses. *Curr Protoc Bioinformatics* 54, 1 30 1–1 30 33.
- Scheltens, P., et al., 2016. Alzheimer's disease. *Lancet* 388 (10043), 505–517.
- Sadigh-Eteghad, S., Talebi, M., Farhoudi, M., 2012. Association of apolipoprotein E epsilon 4 allele with sporadic late onset Alzheimer's disease. A meta-analysis. *Neurosciences (Riyadh)* 17 (4), 321–326.
- Genin, E., et al., 2011. APOE and Alzheimer disease: a major gene with semi-dominant inheritance. *Mol Psychiatry* 16 (9), 903–907.
- Machado, A., et al., 2014. Chronic stress as a risk factor for Alzheimer's disease. *Rev Neurosci* 25 (6), 785–804.
- de Bruijn, R.F., et al., 2015. The potential for prevention of dementia across two decades: the prospective, population-based Rotterdam Study. *BMC Med* 13, 132.
- Jessen, N.A., et al., 2015. The Glymphatic System: A Beginner's Guide. *Neurochem Res* 40 (12), 2583–2599.
- Chen, X.Q., Mobley, W.C., 2019. Alzheimer Disease Pathogenesis: Insights From Molecular and Cellular Biology Studies of Oligomeric Abeta and Tau Species. *Front Neurosci* 13, 659.
- Roher, A.E., et al., 2017. APP/Abeta structural diversity and Alzheimer's disease pathogenesis. *Neurochem Int* 110, 1–13.
- Reiss, A.B., et al., 2018. Amyloid toxicity in Alzheimer's disease. *Rev Neurosci* 29 (6), 613–627.
- Herrup, K., 2015. The case for rejecting the amyloid cascade hypothesis. *Nat Neurosci* 18 (6), 794–799.
- Gibson, G.E., Shi, Q., 2010. A mitocentric view of Alzheimer's disease suggests multi-faceted treatments. *J Alzheimers Dis* 20 (Suppl 2), S591–607.
- Cai, Q., Jeong, Y.Y., 2020. Mitophagy in Alzheimer's Disease and Other Age-Related Neurodegenerative Diseases. *Cells* 9 (1).
- Hirai, K., et al., 2001. Mitochondrial abnormalities in Alzheimer's disease. *J Neurosci* 21 (9), 3017–3023.
- Moreira, P.I., et al., 2007. Increased autophagic degradation of mitochondria in Alzheimer disease. *Autophagy* 3 (6), 614–615.
- Martin-Maestro, P., et al., 2016. PARK2 enhancement is able to compensate mitophagy alterations found in sporadic Alzheimer's disease. *Hum Mol Genet* 25 (4), 792–806.
- Sorrentino, V., et al., 2017. Enhancing mitochondrial proteostasis reduces amyloid-beta proteotoxicity. *Nature* 552 (7684), 187–193.
- Ye, X., et al., 2015. Parkin-mediated mitophagy in mutant hAPP neurons and Alzheimer's disease patient brains. *Hum Mol Genet* 24 (10), 2938–2951.
- Du, F., et al., 2017. PINK1 signalling rescues amyloid pathology and mitochondrial dysfunction in Alzheimer's disease. *Brain* 140 (12), 3233–3251.
- Khandelwal, P.J., et al., 2011. Parkin mediates beclin-dependent autophagic clearance of defective mitochondria and ubiquitinated Abeta in AD models. *Hum Mol Genet* 20 (11), 2091–2102.
- Cummins, N., et al., 2019. Disease-associated tau impairs mitophagy by inhibiting Parkin translocation to mitochondria. *EMBO J* 38 (3).
- Jacobsen, J.S., et al., 2006. Early-onset behavioral and synaptic deficits in a mouse model of Alzheimer's disease. *Proc Natl Acad Sci U S A* 103 (13), 5161–5166.
- Sepe, S., et al., 2014. Expression of Ambral in mouse brain during physiological and Alzheimer type aging. *Neurobiol Aging* 35 (1), 96–108.
- Merkwirth, C., et al., 2012. Loss of prohibitin membrane scaffolds impairs mitochondrial architecture and leads to tau hyperphosphorylation and neurodegeneration. *PLoS Genet* 8 (11), e1003021.
- Monteiro-Cardoso, V.F., et al., 2015. Cardiolipin profile changes are associated to the early synaptic mitochondrial dysfunction in Alzheimer's disease. *J Alzheimers Dis* 43 (4), 1375–1392.
- Ndayisaba, A., Kaindlstorfer, C., Wenning, G.K., 2019. Iron in Neurodegeneration - Cause or Consequence? *Front Neurosci* 13, 180.
- Khan, A., Dobson, J.P., Exley, C., 2006. Redox cycling of iron by Abeta42. *Free Radic Biol Med* 40 (4), 557–569.
- Joppe, K., et al., 2019. The Contribution of Iron to Protein Aggregation Disorders in the Central Nervous System. *Front Neurosci* 13, 15.
- Raven, E.P., et al., 2013. Increased iron levels and decreased tissue integrity in hippocampus of Alzheimer's disease detected in vivo with magnetic resonance imaging. *J Alzheimers Dis* 37 (1), 127–136.
- Ding, B., et al., 2009. Correlation of iron in the hippocampus with MMSE in patients with Alzheimer's disease. *J Magn Reson Imaging* 29 (4), 793–798.

- Meadowcroft, M.D., et al., 2009. MRI and histological analysis of beta-amyloid plaques in both human Alzheimer's disease and APP/PS1 transgenic mice. *J Magn Reson Imaging* 29 (5), 997–1007.
- Telling, N.D., et al., 2017. Iron Biochemistry is Correlated with Amyloid Plaque Morphology in an Established Mouse Model of Alzheimer's Disease. *Cell Chem Biol* 24 (10), 1205–1215 e3.
- Boopathi, S., Koldaival, P., 2016. Fe(2+) binding on amyloid beta-peptide promotes aggregation. *Proteins* 84 (9), 1257–1274.
- Guo, C., et al., 2013. Intranasal deferroxamine reverses iron-induced memory deficits and inhibits amyloidogenic APP processing in a transgenic mouse model of Alzheimer's disease. *Neurobiol Aging* 34 (2), 562–575.
- Pramanik, D., Dey, S.G., 2011. Active site environment of heme-bound amyloid beta peptide associated with Alzheimer's disease. *J Am Chem Soc* 133 (1), 81–87.
- Nandar, W., Connor, J.R., 2011. HFE gene variants affect iron in the brain. *J Nutr* 141 (4), 729S–739S.
- Bartzokis, G., 2004. Age-related myelin breakdown: a developmental model of cognitive decline and Alzheimer's disease. *Neurobiol Aging* 25 (1), 5–18 author reply 49–62.
- Bartzokis, G., 2011. Alzheimer's disease as homeostatic responses to age-related myelin breakdown. *Neurobiol Aging* 32 (8), 1341–1371.
- French, H.M., et al., 2009. Oxidative stress disrupts oligodendrocyte maturation. *J Neurosci Res* 87 (14), 3076–3087.
- Nasrabady, S.E., et al., 2018. White matter changes in Alzheimer's disease: a focus on myelin and oligodendrocytes. *Acta Neuropathol Commun* 6 (1), 22.
- Thorburne, S.K., Juurlink, B.H., 1996. Low glutathione and high iron govern the susceptibility of oligodendroglial precursors to oxidative stress. *J Neurochem* 67 (3), 1014–1022.
- Nunez, M.T., Chana-Cuevas, P., 2018. New Perspectives in Iron Chelation Therapy for the Treatment of Neurodegenerative Diseases. *Pharmaceuticals (Basel)* 11 (4).
- Singh, Y.P., et al., 2019. A review on iron chelators as potential therapeutic agents for the treatment of Alzheimer's and Parkinson's diseases. *Mol Divers* 23 (2), 509–526.
- Kalia, L.V., Lang, A.E., 2015. Parkinson's disease. *Lancet* 386 (9996), 896–912.
- Song, S., et al., 2013. Characterization of PINK1 (PTEN-induced putative kinase 1) mutations associated with Parkinson disease in mammalian cells and *Drosophila*. *J Biol Chem* 288 (8), 5660–5672.
- Di Rita, A., et al., 2018. AMBRA1-Mediated Mitophagy Counteracts Oxidative Stress and Apoptosis Induced by Neurotoxicity in Human Neuroblastoma SH-SY5Y Cells. *Front Cell Neurosci* 12, 92.
- Koentjoro, B., Park, J.S., Sue, C.M., 2017. Nix restores mitophagy and mitochondrial function to protect against PINK1/Parkin-related Parkinson's disease. *Sci Rep* 7, 44373.
- Bastian, T.W., et al., 2010. Perinatal iron and copper deficiencies alter neonatal rat circulating and brain thyroid hormone concentrations. *Endocrinology* 151 (8), 4055–4065.
- Dexter, D.T., et al., 1989. Increased nigral iron content and alterations in other metal ions occurring in brain in Parkinson's disease. *J Neurochem* 52 (6), 1830–1836.
- McCarthy, R.C., Kosman, D.J., 2015. Iron transport across the blood-brain barrier: development, neurovascular regulation and cerebral amyloid angiopathy. *Cell Mol Life Sci* 72 (4), 709–727.
- Mastroberardino, P.G., et al., 2009. A novel transferrin/TFR2-mediated mitochondrial iron transport system is disrupted in Parkinson's disease. *Neurobiol Dis* 34 (3), 417–431.
- Pellegrino, R.M., et al., 2016. Transferrin Receptor 2 Dependent Alterations of Brain Iron Metabolism Affect Anxiety Circuits in the Mouse. *Sci Rep* 6, 30725.
- Skjorringe, T., et al., 2015. Divalent metal transporter 1 (DMT1) in the brain: implications for a role in iron transport at the blood-brain barrier, and neuronal and glial pathology. *Front Mol Neurosci* 8, 19.
- Salazar, J., et al., 2008. Divalent metal transporter 1 (DMT1) contributes to neurodegeneration in animal models of Parkinson's disease. *Proc Natl Acad Sci U S A* 105 (47), 18578–18583.
- Jiang, H., et al., 2010. Up-regulation of divalent metal transporter 1 in 6-hydroxydopamine intoxication is IRE/IRP dependent. *Cell Res* 20 (3), 345–356.
- Song, N., et al., 2007. Divalent metal transporter 1 up-regulation is involved in the 6-hydroxydopamine-induced ferrous iron influx. *J Neurosci Res* 85 (14), 3118–3126.
- Wang, B., et al., 2019. Lactoferrin: Structure, function, denaturation and digestion. *Crit Rev Food Sci Nutr* 59 (4), 580–596.
- Jiang, H., et al., 2019. Iron Pathophysiology in Parkinson Diseases. *Adv Exp Med Biol* 1173, 45–66.
- Boll, M.C., et al., 1999. Reduced ferroxidase activity in the cerebrospinal fluid from patients with Parkinson's disease. *Neurosci Lett* 265 (3), 155–158.
- Olivieri, S., et al., 2011. Ceruloplasmin oxidation, a feature of Parkinson's disease CSF, inhibits ferroxidase activity and promotes cellular iron retention. *J Neurosci* 31 (50), 18568–18577.
- Lee, D.W., Andersen, J.K., 2010. Iron elevations in the aging Parkinsonian brain: a consequence of impaired iron homeostasis? *J Neurochem* 112 (2), 332–339.
- Lu, L.N., et al., 2017. Expression of Iron Transporters and Pathological Hallmarks of Parkinson's and Alzheimer's Diseases in the Brain of Young, Adult, and Aged Rats. *Mol Neurobiol* 54 (7), 5213–5224.
- Muyderman, H., Chen, T., 2014. Mitochondrial dysfunction in amyotrophic lateral sclerosis - a valid pharmacological target? *Br J Pharmacol* 171 (8), 2191–2205.
- Shan, X., et al., 2010. Altered distributions of Gemini of coiled bodies and mitochondria in motor neurons of TDP-43 transgenic mice. *Proc Natl Acad Sci U S A* 107 (37), 16325–16330.
- Xu, Y.F., et al., 2010. Wild-type human TDP-43 expression causes TDP-43 phosphorylation, mitochondrial aggregation, motor deficits, and early mortality in transgenic mice. *J Neurosci* 30 (32), 10851–10859.
- Davis, S.A., et al., 2018. TDP-43 interacts with mitochondrial proteins critical for mitophagy and mitochondrial dynamics. *Neurosci Lett* 678, 8–15.
- Chia, R., Chio, A., Traynor, B.J., 2018. Novel genes associated with amyotrophic lateral sclerosis: diagnostic and clinical implications. *Lancet Neurol* 17 (1), 94–102.
- Gal, J., et al., 2009. Sequestosome 1/p62 links familial ALS mutant SOD1 to LC3 via an ubiquitin-independent mechanism. *J Neurochem* 111 (4), 1062–1073.
- Wong, Y.C., Holzbaur, E.L., 2014. Optineurin is an autophagy receptor for damaged mitochondria in parkin-mediated mitophagy that is disrupted by an ALS-linked mutation. *Proc Natl Acad Sci U S A* 111 (42), E4439–48.
- Moore, A.S., Holzbaur, E.L., 2016. Dynamic recruitment and activation of ALS-associated TBK1 with its target optineurin are required for efficient mitophagy. *Proc Natl Acad Sci U S A* 113 (24), E3349–58.
- Freischmidt, A., et al., 2015. Haploinsufficiency of TBK1 causes familial ALS and fronto-temporal dementia. *Nat Neurosci* 18 (5), 631–636.
- Cirulli, E.T., et al., 2015. Exome sequencing in amyotrophic lateral sclerosis identifies risk genes and pathways. *Science* 347 (6229), 1436–1441.
- Kwan, J.Y., et al., 2012. Iron accumulation in deep cortical layers accounts for MRI signal abnormalities in ALS: correlating 7 tesla MRI and pathology. *PLoS One* 7 (4), e35241.
- Kasarskis, E.J., et al., 1995. Aluminum, calcium, and iron in the spinal cord of patients with sporadic amyotrophic lateral sclerosis using laser microprobe mass spectroscopy: a preliminary study. *J Neurol Sci* 130 (2), 203–208.
- Kokic, A.N., et al., 2005. Biotransformation of nitric oxide in the cerebrospinal fluid of amyotrophic lateral sclerosis patients. *Redox Rep* 10 (5), 265–270.
- Hozumi, I., et al., 2011. Patterns of levels of biological metals in CSF differ among neurodegenerative diseases. *J Neurol Sci* 303 (1–2), 95–99.
- Jeong, S.Y., et al., 2009. Dysregulation of iron homeostasis in the CNS contributes to disease progression in a mouse model of amyotrophic lateral sclerosis. *J Neurosci* 29 (3), 610–619.
- Yu, J., et al., 2018. Serum ferritin is a candidate biomarker of disease aggravation in amyotrophic lateral sclerosis. *Biomed Rep* 9 (4), 333–338.
- Nadjar, Y., et al., 2012. Elevated serum ferritin is associated with reduced survival in amyotrophic lateral sclerosis. *PLoS One* 7 (9), e45034.
- Mitchell, R.M., et al., 2010. Plasma biomarkers associated with ALS and their relationship to iron homeostasis. *Muscle Nerve* 42 (1), 95–103.
- Qureshi, M., et al., 2008. Serum ferritin and metal levels as risk factors for amyotrophic lateral sclerosis. *Open Neurol J* 2, 51–54.
- Bozzo, F., Mirra, A., Carri, M.T., 2017. Oxidative stress and mitochondrial damage in the pathogenesis of ALS: New perspectives. *Neurosci Lett* 636, 3–8.
- Bu, X.L., Xiang, Y., Guo, Y., 2019. The Role of Iron in Amyotrophic Lateral Sclerosis. *Adv Exp Med Biol* 1173, 145–152.
- Yoshida, M., et al., 2010. A mutation database for amyotrophic lateral sclerosis. *Hum Mutat* 31 (9), 1003–1010.
- Li, M., et al., 2014. Mutations in the HFE gene and sporadic amyotrophic lateral sclerosis risk: a meta-analysis of observational studies. *Braz J Med Biol Res* 47 (3), 215–222.
- Nandar, W., et al., 2014. H63D HFE genotype accelerates disease progression in animal models of amyotrophic lateral sclerosis. *Biochim Biophys Acta* 1842 (12 Pt A), 2413–2426.
- Barton, J.C., Edwards, C.Q., Acton, R.T., 2015. HFE gene: Structure, function, mutations, and associated iron abnormalities. *Gene* 574 (2), 179–192.
- Drakesmith, H., Townsend, A., 2000. The structure and function of HFE. *Bioessays* 22 (7), 595–598.
- Blasco, H., et al., 2011. Association between divalent metal transport 1 encoding gene (SLC11A2) and disease duration in amyotrophic lateral sclerosis. *J Neurol Sci* 303 (1–2), 124–127.
- Wang, Q., et al., 2011. Prevention of motor neuron degeneration by novel iron chelators in SOD1(G93A) transgenic mice of amyotrophic lateral sclerosis. *Neurodegener Dis* 8 (5), 310–321.
- Moreau, C., et al., 2018. Could Conservative Iron Chelation Lead to Neuroprotection in Amyotrophic Lateral Sclerosis? *Antioxid Redox Signal* 29 (8), 742–748.
- Kollberg, G., et al., 2009. Clinical manifestation and a new ISC mutation in iron-sulphur cluster deficiency myopathy. *Brain* 132 (Pt 8), 2170–2179.
- Puccio, H., et al., 2001. Mouse models for Friedreich ataxia exhibit cardiomyopathy, sensory nerve defect and Fe-S enzyme deficiency followed by intramitochondrial iron deposits. *Nat Genet* 27 (2), 181–186.
- Walter, P.B., et al., 2002. Iron deficiency and iron excess damage mitochondria and mitochondrial DNA in rats. *Proc Natl Acad Sci U S A* 99 (4), 2264–2269.
- Gao, X., et al., 2009. Mitochondrial DNA damage in iron overload. *J Biol Chem* 284 (8), 4767–4775.
- Allen, G.F., et al., 2013. Loss of iron triggers PINK1/Parkin-independent mitophagy. *EMBO Rep* 14 (12), 1127–1135.
- Nagi, M., et al., 2016. Iron-depletion promotes mitophagy to maintain mitochondrial integrity in pathogenic yeast *Candida glabrata*. *Autophagy* 12 (8), 1259–1271.
- Kirienko, N.V., Ausubel, F.M., Ruvkun, G., 2015. Mitophagy confers resistance to siderophore-mediated killing by *Pseudomonas aeruginosa*. *Proc Natl Acad Sci U S A* 112 (6), 1821–1826.
- Kang, D., et al., 2018. Pyoverdine, a siderophore from *Pseudomonas aeruginosa*, translocates into *C. elegans*, removes iron, and activates a distinct host response. *Virulence* 9 (1), 804–817.
- Zhang, H., et al., 2008. Mitochondrial autophagy is an HIF-1-dependent adaptive metabolic response to hypoxia. *J Biol Chem* 283 (16), 10892–10903.
- De Domenico, I., Ward, D.M., Kaplan, J., 2009. Specific iron chelators determine the route of ferritin degradation. *Blood* 114 (20), 4546–4551.
- Sasaki, K., et al., 2011. Improved quantification for non-transferrin-bound iron measurement using high-performance liquid chromatography by reducing iron contamination. *Mol Med Rep* 4 (5), 913–918.

Fine-tuning of ULK1 mRNA and protein levels is required for autophagy oscillation

Francesca Nazio,^{1,2} Marianna Carinci,² Cristina Valacca,² Pamela Bielli,³ Flavie Strappazzon,³ Manuela Antonioli,^{4,5} Fabiola Ciccocanti,⁵ Carlo Rodolfo,² Silvia Campello,^{2,3} Gian Maria Fimia,^{5,6} Claudio Sette,^{3,7} Paolo Bonaldo,⁸ and Francesco Cecconi^{1,2,9}

¹Department of Pediatric Hematology and Oncology, Istituto di Ricovero e Cura a Carattere Scientifico Bambino Gesù Children's Hospital, 00146 Rome, Italy

²Department of Biology, University of Rome Tor Vergata, 00133 Rome, Italy

³Istituto di Ricovero e Cura a Carattere Scientifico Fondazione Santa Lucia, 00143 Rome, Italy

⁴Freiburg Institute for Advanced Studies, University of Freiburg, 79104 Freiburg, Germany

⁵National Institute for Infectious Diseases, Istituto di Ricovero e Cura a Carattere Scientifico "L. Spallanzani," 00149 Rome, Italy

⁶Department of Biological and Environmental Sciences and Technologies, University of Salento, 73100 Lecce, Italy

⁷Department of Biomedicine and Prevention, University of Rome Tor Vergata, 00133 Rome, Italy

⁸Department of Molecular Medicine, University of Padova, 35131 Padova, Italy

⁹Danish Cancer Society Research Center, 2100 Copenhagen, Denmark

Autophagy is an intracellular degradation pathway whose levels are tightly controlled to secure cell homeostasis. Unc-51–like kinase 1 (ULK1) is a conserved serine–threonine kinase that plays a central role in the initiation of autophagy. Here, we report that upon autophagy progression, ULK1 protein levels are specifically down-regulated by the E3 ligase NEDD4L, which ubiquitylates ULK1 for degradation by the proteasome. However, whereas ULK1 protein is degraded, *ULK1* mRNA is actively transcribed. Upon reactivation of mTOR-dependent protein synthesis, basal levels of ULK1 are promptly restored, but the activity of newly synthesized ULK1 is inhibited by mTOR. This prepares the cell for a new possible round of autophagy stimulation. Our results thus place NEDD4L and ULK1 in a key position to control oscillatory activation of autophagy during prolonged stress to keep the levels of this process under a safe and physiological threshold.

Introduction

Autophagy is a catabolic process occurring in all eukaryotic cells so as to maintain cellular viability and homeostasis during basal conditions by controlling long-lived proteins and damaged organelles. Autophagy can also be stimulated to maintain cell survival in response to sublethal stresses, such as nutrient or growth factor deprivation, hypoxia, reactive oxygen species, or viral and pathogen invasion (Choi et al., 2013). This process requires both the ULK1 serine–threonine kinase and the BECLIN 1–VPS34 core complex for its upstream signaling to generate double-membraned vesicles, the autophagosomes, which transfer portions of cytosolic content to lysosomes (Wirth et al., 2013).

ULK1 is one of the most upstream autophagy-related factors; in fact, it forms a stable complex with ATG13, FIP200, and ATG101, playing a crucial role in the initiation steps of autophagy (Noda and Fujioka, 2015). Furthermore, ULK1 regulates its substrates and is itself regulated by phosphorylation

events. mTOR and 5' AMP-activated protein kinase are among its well-known upstream regulators (Kim et al., 2011). Other posttranslational modifications, including ubiquitylation and acetylation, have been reported to modulate the pace of ULK1 turnover and kinase activity in different cellular contexts (Lin et al., 2012; Kuang et al., 2013; Jiao et al., 2015). Indeed, Hsp90 and Cdc37 are chaperones that regulate ULK1 stability and activity by forming a complex with ULK1, which subsequently influences ATG13-mediated mitophagy (Joo et al., 2011). Further, soon after autophagy induction, the stability of ULK1 is regulated by K63-linked ubiquitin chains, which are mediated by the AMBRA1 complex with the E3 ligase TRAF6 (Nazio et al., 2013). Of note, it has been found that AMBRA1 protein levels are also significantly modulated by E3 ligases during the autophagy response (Antonioli et al., 2014; Xia et al., 2014). Several additional E3 ligases have been identified as ULK1 regulators (Nazio et al., 2013; Li et al., 2015; Liu et al., 2016), and it is now apparent that activation of protein kinases can initiate irreversible down-regulation by ubiquitin proteasome system

Correspondence to Francesco Cecconi: cecconi@cancer.dk

Abbreviations used: Act D, actinomycin D; ANOVA, analysis of variance; Baf A1, bafilomycin A1; CHX, cycloheximide; Clq, chloroquine; co-IP, Co-Immunoprecipitation; EBSS, Earle's balanced salt solution; HECT, Homologous to E6AP C terminus; IP, immunoprecipitation; MALDI-TOF/TOF, matrix-assisted laser desorption/ionization time of flight/time of flight; MS, mass spectrometry; Ni-NTA, nickel-nitrilotriacetic acid; oligo, oligonucleotide; qPCR, quantitative real-time PCR; ULK, Unc-51–like kinase; UPS, ubiquitin proteasome system; WB, Western blotting.

© 2016 Nazio et al. This article is distributed under the terms of an Attribution–Noncommercial–Share Alike–No Mirror Sites license for the first six months after the publication date (see <http://www.rupress.org/terms/>). After six months it is available under a Creative Commons License (Attribution–Noncommercial–Share Alike 4.0 International license, as described at <https://creativecommons.org/licenses/by-nc-sa/4.0/>).



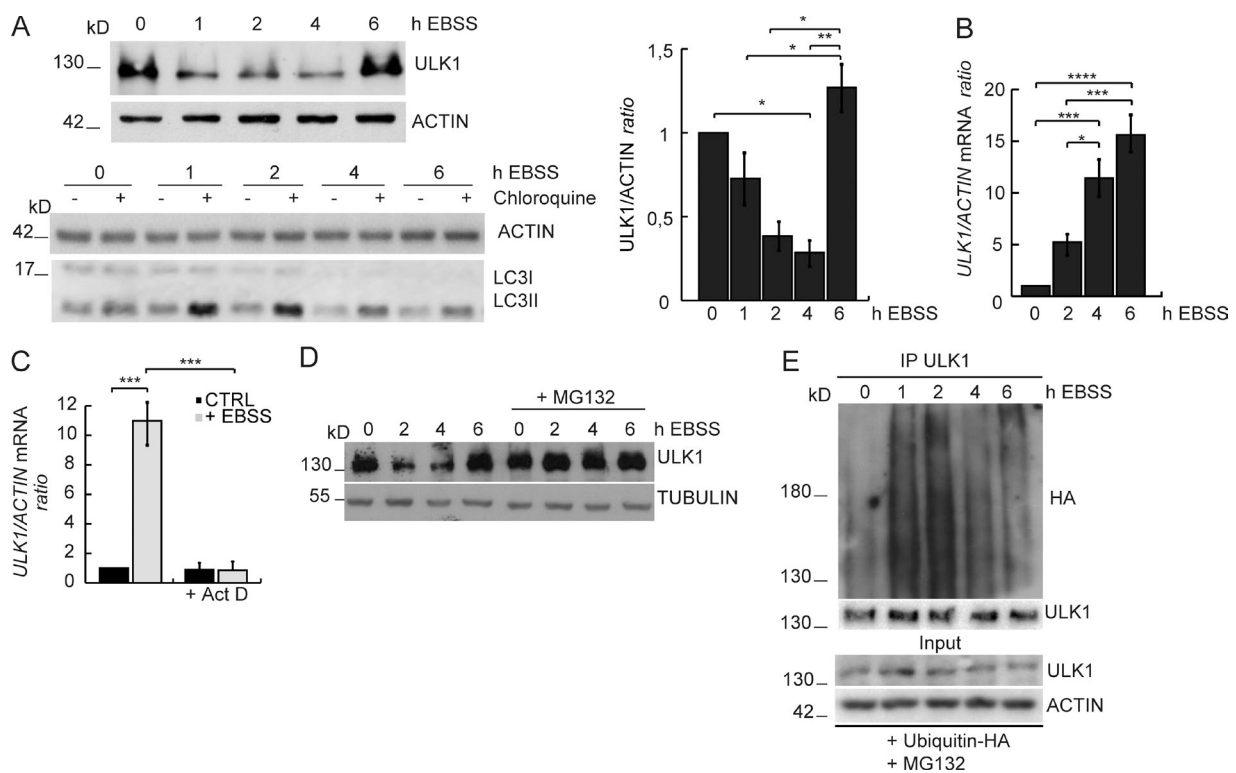


Figure 1. ULK1 mRNA and protein levels are regulated in a controlled time course during autophagy. (A) HeLa cells were treated with EBSS for the indicated time periods in the presence or not of Clq, and the levels of ULK1, ACTIN, and LC3 were detected by WB. Densitometric analysis of ULK1 over ACTIN is also shown (right graph). Data are expressed as the mean \pm SEM ($n = 4$). (B) qPCR analysis of *ULK1* mRNA levels in HeLa cells incubated in EBSS medium for the indicated time periods. Data are expressed as mean \pm SEM ($n = 3$). (C) qPCR analysis of *ULK1* mRNA levels in HeLa cells incubated in EBSS medium for 4 h in the presence or not of Act D. Data are expressed as mean \pm SEM ($n = 3$). (D) HeLa cells were treated with EBSS for the indicated time periods in the presence or not of MG132. Protein levels of ULK1 and TUBULIN were detected by WB. (E) HeLa cells were transfected with ubiquitin-HA and treated with EBSS for the indicated time periods in the presence of MG132. Protein extracts were immunoprecipitated in denaturing conditions using an anti-ULK1 antibody; ubiquitin, ULK1, and ACTIN were analyzed by WB. In A and B, data were analyzed by one-way analysis of variance (ANOVA) followed by Tukey post hoc test. *, $P < 0.05$; **, $P < 0.01$; ***, $P < 0.001$; ****, $P < 0.0001$. In C, data were analyzed by two-way ANOVA followed by Bonferroni's multiple comparison post test. ***, $P < 0.001$.

(UPS)-mediated protein degradation and that this can be an important mechanism of signal termination (Lu and Hunter, 2009).

Here, we report that ULK1 levels are finely regulated during an autophagy response at the transcriptional, translational, and degradation levels. We show that ULK1 protein is down-regulated during the first few hours of starvation through the activity of the E3 ligase NEDD4L (neural precursor cell-expressed developmentally down-regulated 4-like) and restored to basal levels during prolonged starvation. This ULK1 rescue requires a constant transcription of *ULK1* mRNA and mTOR-dependent de novo protein synthesis reactivation.

mTOR may then inhibit ULK1 activity and block autophagy progression in the absence of new stimuli. Autophagy, if re-induced, can proceed, through this novel pathway of regulation, by tightly controlled pulses, by which a cell can avoid excessive self-digestion culminating in cell death.

Results

ULK1 mRNA and protein levels are regulated in a controlled time course during autophagy

Because the protein levels of AMBRA1, a key regulator of ULK1 protein stability, are regulated by UPS during autophagy (Nazio et al., 2013; Antonioli et al., 2014), we first analyzed ULK1 protein levels in HeLa cells under starvation conditions (lacking

both amino acids and serum). We found that ULK1 protein levels are reduced during the first 4 h of starvation, being later restored to almost basal levels after starvation for 6 h (Fig. 1 A). Autophagy flux is analyzed in the presence or absence of the lysosomal inhibitor chloroquine (Clq) by LC3 lipidation. We also analyzed the levels of some ULK1-interacting proteins, such as FIP200 and ATG13. As shown in Fig. S1 A, ATG13 protein levels also decrease during starvation. Moreover, by analyzing the ULK1-dependent phosphorylation of ATG13 (S318), we found an increase in ULK1 kinase activity during the first 2 h of starvation, this being later decreased after starvation for 4–6 h (Fig. S1 A). Such a starvation-induced decrease in ULK1 levels, even though slightly delayed, was also found in HEK293 cells (Fig. S1 B), suggesting that different cell types share this regulation. Next, we decided to analyze *ULK1* mRNA by quantitative real-time PCR (qPCR) during amino acid and serum starvation, and we found that it is greatly increased (by ~ 15 -fold after 6-h starvation; Fig. 1 B). Furthermore, actinomycin D (Act D), a potent inhibitor of transcription, completely inhibited starvation-induced *ULK1* mRNA up-regulation (Fig. 1 C).

Then, we decided to verify whether the UPS regulates ULK1 protein stability. By treating cells with the proteasome inhibitor MG132 during starvation, we found that ULK1 protein levels increase (Fig. 1 D). Consistently, in the presence of MG132, ULK1 proves to be ubiquitylated during starvation (with this modification showing a rapid increase 1–2 h after

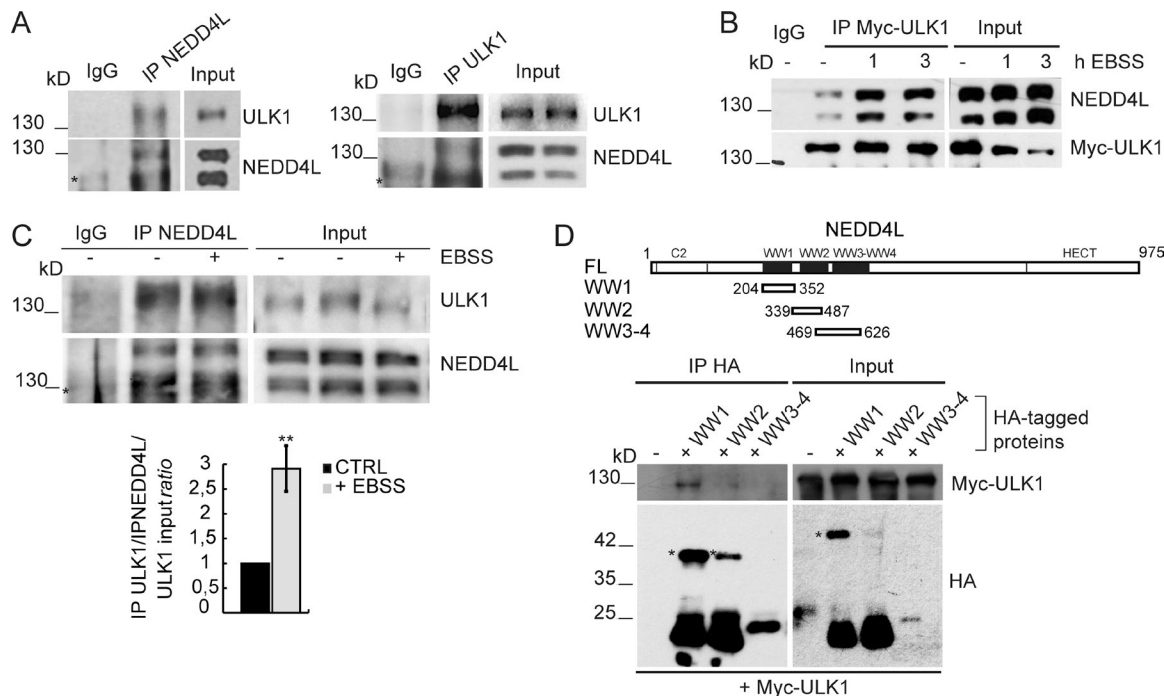


Figure 2. ULK1 interacts with the E3 ligase NEDD4L. (A) Protein extracts from HeLa cells were immunoprecipitated using anti-NEDD4L, anti-ULK1 antibodies and with IgG as a negative control. NEDD4L and ULK1 were analyzed by WB. The two NEDD4L bands correspond to two different spliced isoforms. (B) HeLa cells were transiently transfected with Myc-ULK1 and then grown in normal or EBSS medium for 1 and 3 h, respectively. Protein extracts were immunoprecipitated using an anti-Myc antibody or with IgG as a negative control; Myc-ULK1 and NEDD4L were analyzed by WB. (C) HeLa cells were grown either in normal or in EBSS medium for 90 min, respectively. Protein extracts were immunoprecipitated using an anti-NEDD4L antibody or with IgG as a negative control. ULK1 and NEDD4L analyzed by WB. The band density ratio of immunoprecipitated ULK1, relative to immunoprecipitated NEDD4L normalized on the input amount of ULK1, is analyzed ($n = 3$). Data are expressed as the mean \pm SD, and statistical analysis was performed using an unpaired Student's *t* test. **, $P < 0.01$. (D) Scheme of NEDD4L full length and fragments showing the N-terminal C2 domain, four WW domains (black boxes), and the HECT domain. HeLa cells were cotransfected with vectors encoding Myc-ULK1 together with NEDD4L-HA fragments encoding the WW1, WW2, and WW3-4 domains, respectively. Protein extracts were immunoprecipitated using an anti-HA antibody; Myc-ULK1 and NEDD4L-HA fragments are analyzed by WB. Asterisk represents unspecific bands.

nutrient starvation), thus suggesting that ULK1 stability is regulated by the proteasome during autophagy (Fig. 1 E).

ULK1 interacts with the E3 ubiquitin ligase NEDD4L

Prompted by this finding, we then moved to the identification of the E3 ubiquitin ligase responsible for the first steps of ULK1 proteasome-dependent degradation. Given the role of TRAF6 on ULK1 positive regulation and our preliminary data on ULK1 interactors based on mass spectrometry (MS) analysis, and because NEDD4L acts as an E3 ligase in the opposite way of TRAF6 in regulating the nerve growth factor receptor TrkA, another kinase and ULK1 interactor (Geetha et al., 2005; Zhou et al., 2007; Georgieva et al., 2011), we decided to investigate the existence of a putative NEDD4L–ULK1 interaction by a biochemical approach. To verify this, coimmunoprecipitation (co-IP) analyses were performed in HeLa cells using both NEDD4L and ULK1 antibodies. These analyses reveal the interaction between endogenous NEDD4L and ULK1 (Fig. 2 A). Moreover, by analyzing the interaction between ULK1 and NEDD4L after autophagy induction by starvation, we found an increase in their binding both in endogenous or overexpression conditions (Fig. 2, B and C). Next, because NEDD4L substrates interact specifically with the WW domains of Homologous to E6AP C terminus (HECT) E3 ligase to be ubiquitinated (Harvey et al., 1999), we tested which NEDD4L WW domains mediate the interaction with ULK1. As shown in Fig. 2 D, the WW1 domain of NEDD4L is capable of binding

ULK1, with WW2 showing only a very modest interaction. Unfortunately, no canonical WW-binding PPXY motifs are present in ULK1, suggesting that critical phosphorylated residues could mediate this binding or some adaptor proteins bearing PPXY-like sequences could be involved (Lu et al., 1999; Shearwin-Whyatt et al., 2006; León and Haguenaer-Tsapais, 2009).

NEDD4L ubiquitylates ULK1 and induces its degradation via the proteasome

As NEDD4L is a HECT domain-containing E3 ubiquitin ligase, we then tested whether NEDD4L could regulate the protein levels of ULK1. Indeed, wild-type NEDD4L (NEDD4L^{WT}) efficiently promotes ULK1 protein decrease, but at variance with its C821A mutant lacking ubiquitin ligase activity (NEDD4L^{CA}; Bruce et al., 2008; Yang and Kumar, 2010; Fig. 3, A and B). This effect is specific because overexpression of NEDD4L does not show any effects on other known ULK1-binding proteins, such as ATG13, AMBRA1, and BECLIN 1 (Fig. S2 A). The decrease in ATG13 levels that we find during starvation is therefore most likely regulated by another degradation mechanism.

Because of the high degree of homology between NEDD4 and NEDD4L, and the fact that NEDD4 is involved in the degradation of another key proautophagic protein BECLIN 1 (Platta et al., 2012), we tested whether NEDD4 could also regulate ULK1 protein degradation. However, at variance with NEDD4L, NEDD4 overexpression is not able to induce ULK1 protein decrease (Fig. S2 B).

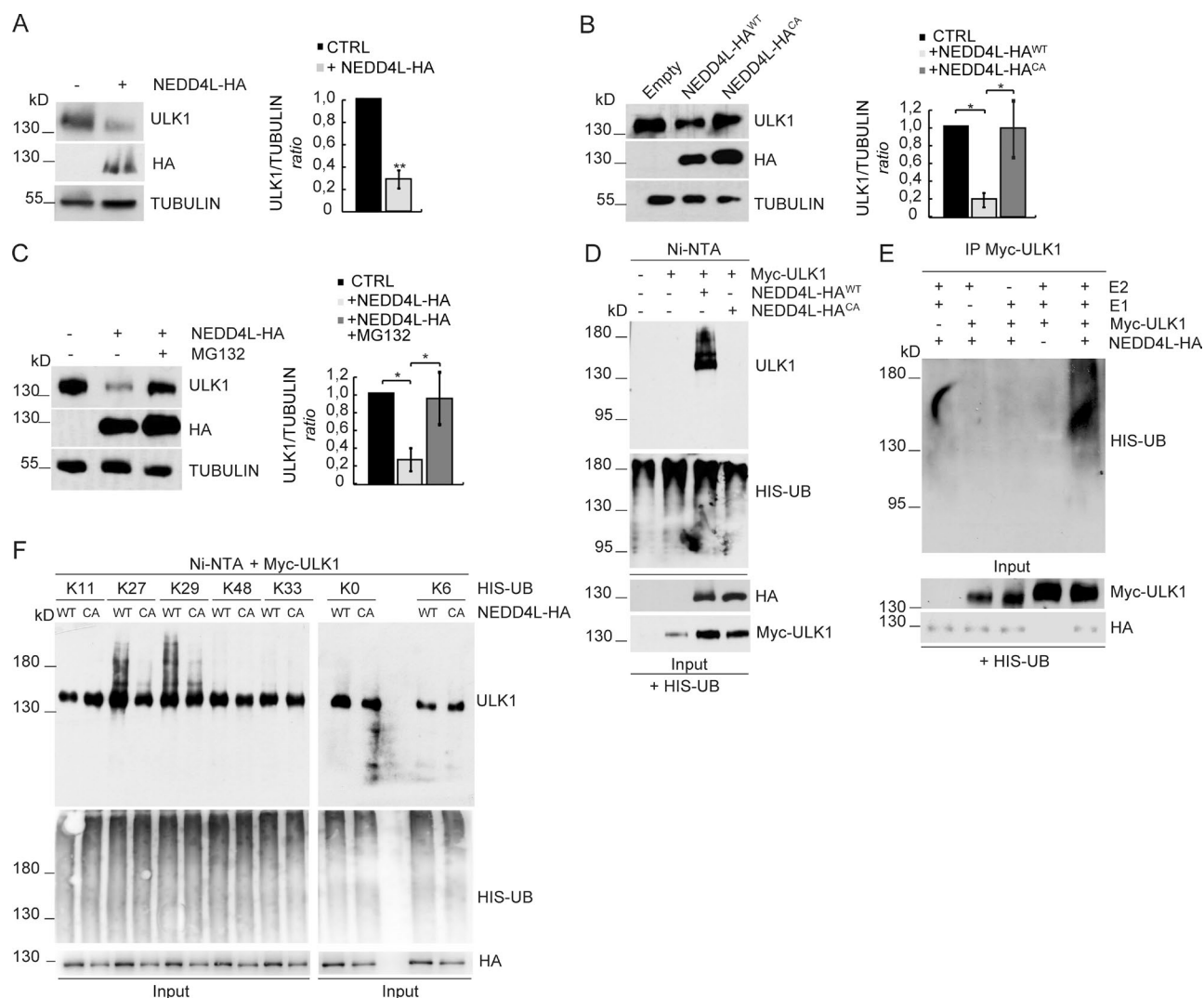


Figure 3. NEDD4L ubiquitylates ULK1 and induces its degradation via proteasome. (A) HeLa cells were transfected with empty or NEDD4L-HA vectors; levels of ULK1, NEDD4L, and TUBULIN were detected by WB. Densitometric analysis of ULK1 over TUBULIN is also shown (right graph). Data are expressed as the mean \pm SD ($n = 3$) and statistical analysis was performed using an unpaired Student's *t* test. **, $P < 0.01$. (B) HeLa cells were transfected with cDNAs coding for NEDD4L^{WT} and NEDD4L^{CA} HA-tagged proteins; ULK1, NEDD4L, and TUBULIN protein levels were detected by WB. Densitometric analysis of ULK1 over TUBULIN is also shown (right graph). Data are expressed as the mean \pm SEM ($n = 4$). (C) HeLa cells were transfected with NEDD4L-HA in the presence or not of MG132 for 4 h. Levels of ULK1, NEDD4L, and TUBULIN were detected by WB. Densitometric analysis of ULK1 over TUBULIN is also shown (right graph). Data are expressed as the mean \pm SEM ($n = 3$). (D) HeLa cells were cotransfected with a vector encoding a 6xHIS-tag ubiquitin and Myc-ULK1 in combination or not with NEDD4L^{WT} and NEDD4L^{CA} in the presence of MG132. Protein extracts were prepared in a denaturing urea buffer and subjected to Ni-NTA purification. The amount of ubiquitylated Myc-ULK1 copurified with 6xHIS-ubiquitin was evaluated by WB. (E) An *in vitro* ubiquitylation assay was performed by mixing immunopurified Myc-ULK1 and NEDD4L-HA, together with recombinant HIS-tag ubiquitin. ULK1 ubiquitylation is evaluated using an anti-Ubiquitin antibody to detect the incorporation of recombinant HIS-ubiquitin. The levels of ULK1 and NEDD4L were analyzed by WB. (F) HeLa cells were cotransfected independently with vectors encoding for 6xHIS-tag specific ubiquitin constructs and Myc-ULK1 in combination or not with HA-tagged NEDD4L^{WT} or NEDD4L^{CA} as a negative control. Protein extracts were prepared as in (D) and the amount of ubiquitylated ULK1 copurified with 6xHIS-Ubiquitin was evaluated by WB. The higher expression levels of NEDD4L^{CA} construct are caused by the lack of activity on itself (Bruce et al., 2008). In B and C, data were analyzed by one-way ANOVA followed by Tukey post hoc test. *, $P < 0.05$.

Next, we found that down-regulation of the ULK1 protein by NEDD4L is blocked by proteasome inhibitors (MG132 and lactacystin), but not by lysosomal inhibitors (leupeptin and Clq; Figs. 3 C and S2 C), indicating that NEDD4L triggers ULK1 degradation exclusively through the proteasome pathway.

Prompted by this finding, we investigated whether NEDD4L could induce ULK1 ubiquitylation. We found that NEDD4L^{WT}, but not NEDD4L^{CA} mutant, efficiently promotes ULK1 ubiquitylation *in vivo* (Fig. 3 D). To exclude the possibility that NEDD4L might act indirectly on ULK1, we investigated whether NEDD4L could directly ubiquitylate ULK1 in

vitro. Indeed, the ubiquitylation assay *in vitro* reveals a direct ubiquitylation of ULK1 by NEDD4L (Fig. 3 E).

K48-linked ubiquitylation is mainly believed to target substrates for proteasome degradation, whereas K63-linked ubiquitylation is involved in regulating protein activity. It has been reported that NEDD4L is able to promote K11-, K48-, K63-, K29-, K27-, and K6-linked ubiquitylation to mediate the degradation of its substrates (Fotia et al., 2006; Ding et al., 2013). This raised the intriguing question as to what type of degradative ubiquitylation NEDD4L induces on ULK1. To address this, we used a series of HIS-tagged ubiquitin constructs possessing a

single lysine in the presence of NEDD4L^{WT} or NEDD4L^{CA} as a negative control; as shown in Fig. 3 F, we found that NEDD4L^{WT} promotes noncanonical K27- and K29-linked polyubiquitylation of ULK1. Then, we verified whether ULK1 could be modified by K27- and K29-linked ubiquitin during autophagy; being in ULK1 overexpressing conditions, we analyzed ULK1 ubiquitylation after 4 and 6 h of starvation. As shown in Fig. S2 D, ULK1-linked K27 and K29 ubiquitylation increases after autophagy induction by starvation. Finally, because of the established role in vitro of NEDD4 family members in K63-mediated ubiquitylation (Kim and Huijbrechtse, 2009; Maspero et al., 2013), we also checked the capability of NEDD4L to promote this kind of modification on ULK1. Indeed, by overexpressing NEDD4L, an increase of K63 ubiquitylation is detectable on ULK1 (Fig. S2 E), implying a putative additional role for ubiquitin K63 chains in regulating ULK1 activity in this context of regulation. Of note, we previously showed that the alternative E3 ligase TRAF6 could favor a similar modification on ULK1 early during autophagy activation (Nazio et al., 2013).

NEDD4L degrades ULK1 protein during prolonged starvation

Given that NEDD4L induces ULK1 proteasomal degradation and that ULK1 is degraded by UPS during starvation, we decided to analyze ULK1 protein levels in cells knocked down for NEDD4L. As shown in Fig. 4 (A–C) and Fig. S3 A, NEDD4L down-regulation induces an increase in ULK1 protein levels in fed conditions and prevents its degradation after prolonged nutrient starvation. Interestingly, we found that ULK2, another Atg1 orthologue in mammals often shown to compensate for ULK1 functions (Alers et al., 2012), also undergoes a similar regulation (Fig. S3 B).

Because ULK1 kinase is active during autophagy induction, we set out to find whether NEDD4L is able to distinguish the active form of ULK1 from the inactive one for the purpose of triggering its proteasomal degradation. We thus cotransfected the cells with three different Myc-tagged ULK1 constructs, the wild-type (ULK1^{WT}), the kinase-dead (ULK1^{K46I}), and the ULK1^{S1047A} (Dorsey et al., 2009) mutated form in its autophosphorylation site (Fig. S3 C) in NEDD4L^{WT}-overexpressing cells, and we analyzed the ability of NEDD4L to degrade and ubiquitylate ULK1. As shown in Figs. 4 D and S3 D, we found that NEDD4L is able to induce the ubiquitylation and subsequently the degradation of only the active form of ULK1, supporting the hypothesis that this regulation occurs specifically upon autophagy.

Moreover, we analyzed the capability of NEDD4L to bind the kinase-dead form of ULK1, and we found that both the wild-type and mutant form of ULK1 are able to interact with NEDD4L (Fig. S3 E), suggesting that ULK1 needs activation to undergo conformational changes functional to its NEDD4L-mediated ubiquitylation, but not to interact with NEDD4L.

Last, because NEDD4L is regulated by self-ubiquitylation (Bruce et al., 2008) and phosphorylation (An et al., 2014), we decided to investigate whether these modifications are regulated during autophagy. First, we analyzed NEDD4L self-ubiquitylation in basal conditions and after autophagy induction by starvation. As shown in Fig. 4 E, NEDD4L displays higher self-ubiquitylation levels after autophagy induction than in control conditions. Next, we noticed that two sites (S342 and S448) flanking the NEDD4L WW domains can be phosphorylated by several AGC kinase family members, including SGK1,

Akt, and PKA (Lee et al., 2007; Gao et al., 2009). These phosphorylation events inhibit NEDD4L function as a regulator of ENACs and TGF- β signaling. For this reason, we analyzed the phosphorylation status of NEDD4L during autophagy induction by starvation at different time points. As shown in Fig. 4 F, NEDD4L phosphorylation is reduced during the first 4 h of starvation. Interestingly this modification pattern parallels that of ULK1 expression levels (Fig. 1 A). Moreover, using qPCR, we found a significant increase in *NEDD4L* mRNA during starvation (Fig. 4 G), supporting that NEDD4L is positively regulated during autophagy progression.

Collectively, both of these findings support the hypothesis that NEDD4L is more active during autophagy than in standard conditions, and this facilitates ULK1 proteasomal degradation.

NEDD4L is a negative regulator of autophagy

Based on the evidence that NEDD4L degrades ULK1 during autophagy, we decided to explore whether NEDD4L inactivation, and the resulting stabilization of ULK1 in prolonged starvation, can alter the duration of the autophagy response. To this aim, we down-regulated NEDD4L by RNAi and induced autophagy for different time periods; we then analyzed autophagy using three different methods: LC3 lipidation and p62 protein levels by Western blotting (WB; Fig. 5, A and B) and both LC3 and ATG16L puncta detection by immunofluorescence (Fig. 5, C and D). As shown, in control cells, autophagy rapidly increases at 1–2 h and then declines at 4–6 h of starvation. In NEDD4L-silenced cells, an increased and persistent autophagy flux is observed, suggesting a correlation between ULK1 protein degradation and the on-rate of autophagy.

NEDD4L ubiquitylates ULK1 at lysine 925 and lysine 933

To finely dissect ULK1 regulation by NEDD4L at a structural level, we next determined the NEDD4L-dependent ubiquitylation sites on ULK1. By MS analysis, we identified two lysine residues on the same ULK1 peptide (K925 and K933) that proved to be ubiquitylated (Table S1). By mutating the lysine residues to arginines, we generated three mutant constructs (ULK1^{K925R}, ULK1^{K933R}, and ULK1^{K925R+K933R}). First, we analyzed the half-life of the single-mutant constructs in the presence of cycloheximide (CHX), a protein translation inhibitor, or CHX+MG132, and found that the ULK1^{K925R} and ULK1^{K933R} constructs are as active and functional as ULK1^{WT} but more stable than ULK1^{WT} (Fig. 6 A and Fig. S4, A and B).

Then, we evaluated the capability of all the mutant constructs to be degraded by NEDD4L in standard conditions (Fig. 6, B and C) or during autophagy (Fig. 6, D and E), in the presence or not of MG132. We thus found that both mutations affect NEDD4L-dependent degradation of ULK1 during autophagy. Finally, we analyzed the capability of NEDD4L to ubiquitylate ULK1^{K925R}, ULK1^{K933R}, and ULK1^{K925R+K933R} (Fig. 6, F and G) and found a significant decrease in the ubiquitylation status of all the mutant constructs analyzed when compared with the wild type. However, a residual ubiquitylation is found in this context, arguing for the presence for other unknown ubiquitylation site(s).

Because the NEDD4L-dependent ubiquitylation sites are located in the region of ULK1 that is known to mediate the interaction with ATG13 (Jung et al., 2009), we analyzed whether the ULK1-ATG13 binding is affected during autophagy induction

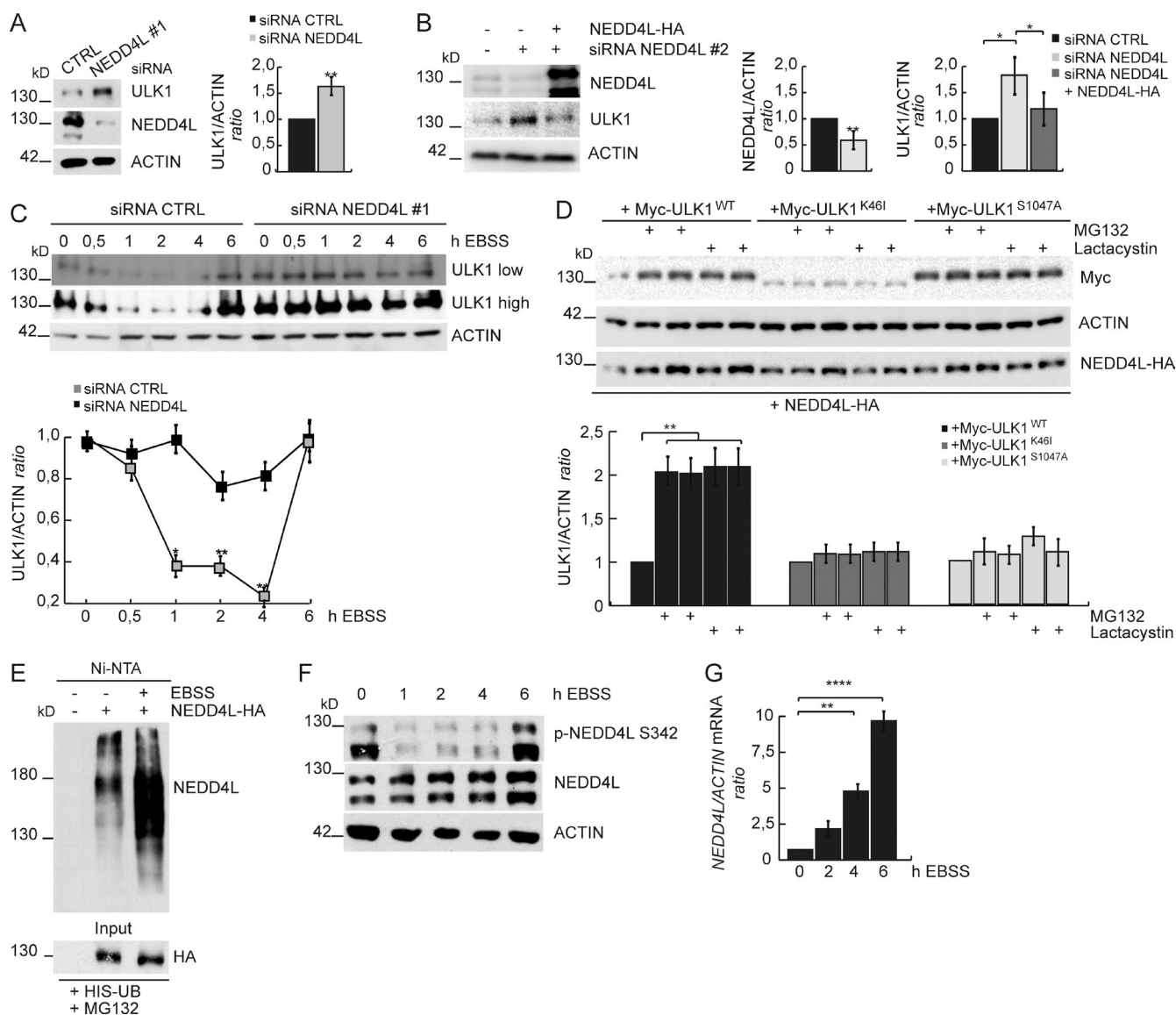


Figure 4. NEDD4L degrades ULK1 during prolonged starvation. (A) NEDD4L expression was down-regulated in HeLa cells using specific RNAi oligonucleotides (oligos; siRNA NEDD4L#1) or unrelated oligos as negative control (siRNA CTRL). Densitometric analysis of ULK1 over ACTIN is also shown (right graph). Data are expressed as the mean value \pm SD ($n = 3$), and statistical analysis was performed using an unpaired Student's *t* test. **, $P < 0.01$. (B) NEDD4L expression was down-regulated in HeLa cells using specific RNAi oligos targeting NEDD4L 3' UTR (siRNA NEDD4L#2) or unrelated oligos as negative control (siRNA CTRL). Some of them were then transfected with empty vector or NEDD4L-HA. Levels of ULK1, NEDD4L, and ACTIN were detected by WB. Densitometric analyses of both ULK1 and NEDD4L over ACTIN are also shown (right graphs). Data are expressed as the mean value \pm SEM ($n = 3$). (C) NEDD4L expression was down-regulated in HeLa cells as in (A) and autophagy was induced by starving cells for the indicated time periods. Levels of ULK1 and ACTIN were detected by WB. Densitometric analysis of ULK1 over ACTIN is also shown (below graph). Data are expressed as the mean \pm SEM ($n = 3$). Two different expositions (low and high) for ULK1 bands are shown. (D) HeLa cells were cotransfected with cDNAs coding for Myc-tagged ULK1^{WT} or ULK1^{S1047A} or ULK1^{K46I} together with NEDD4L^{WT}-HA in the presence or absence of MG132 or lactacystin for two different time periods (1 h and 2 h). Levels of ULK1, NEDD4L, and ACTIN were detected by WB. Densitometric analysis of ULK1 over ACTIN is also shown (below graph). Data are expressed as the mean \pm SEM ($n = 3$). (E) HeLa cells were cotransfected with a vector encoding 6xHis-tag Ubiquitin and in some of them with NEDD4L-HA and autophagy was induced for 3 h in the presence of MG132. Protein extracts were prepared in a denaturing urea buffer and subjected to Ni-NTA purification. The amount of ubiquitylated NEDD4L copurified with 6xHis-ubiquitin was evaluated by WB. (F) HeLa cells were treated with EBSS for the indicated time periods, and the levels of p-NEDD4L, NEDD4L, and ACTIN were detected by WB. (G) qPCR analysis of *NEDD4L* mRNA levels in HeLa cells incubated in EBSS medium for the indicated time periods. Data are expressed as mean \pm SEM ($n = 3$). In B–D and G, data were analyzed by one-way ANOVA followed by Tukey post hoc test. *, $P < 0.05$; **, $P < 0.01$; ****, $P < 0.0001$.

or after NEDD4L overexpression. As shown in Fig. S4 (C and D), no impairment is found, suggesting that ATG13–ULK1 binding is not necessary for ULK1 degradation.

Finally, we decided to analyze autophagy in the presence of ULK1 mutant constructs. Thus, we expressed, in independent experiments, ULK1^{WT} and ULK1^{K925R+K933R} mCherry-tagged plasmids in ULK1 knockdown cells, and we analyzed ATG16L

puncta formation after autophagy induction by starvation at two different time points. As shown in Figs. 6 H and S4 E, the ULK1 mutant construct increases autophagy with respect to the ULK1^{WT}, as we found after NEDD4L down-regulation. A similar autophagy alteration is also found by only increasing ULK1 levels by expression of ULK1^{WT} or ULK1^{K925R+K933R} in control cells (Fig. S4 F). Moreover, also using the single-mutant

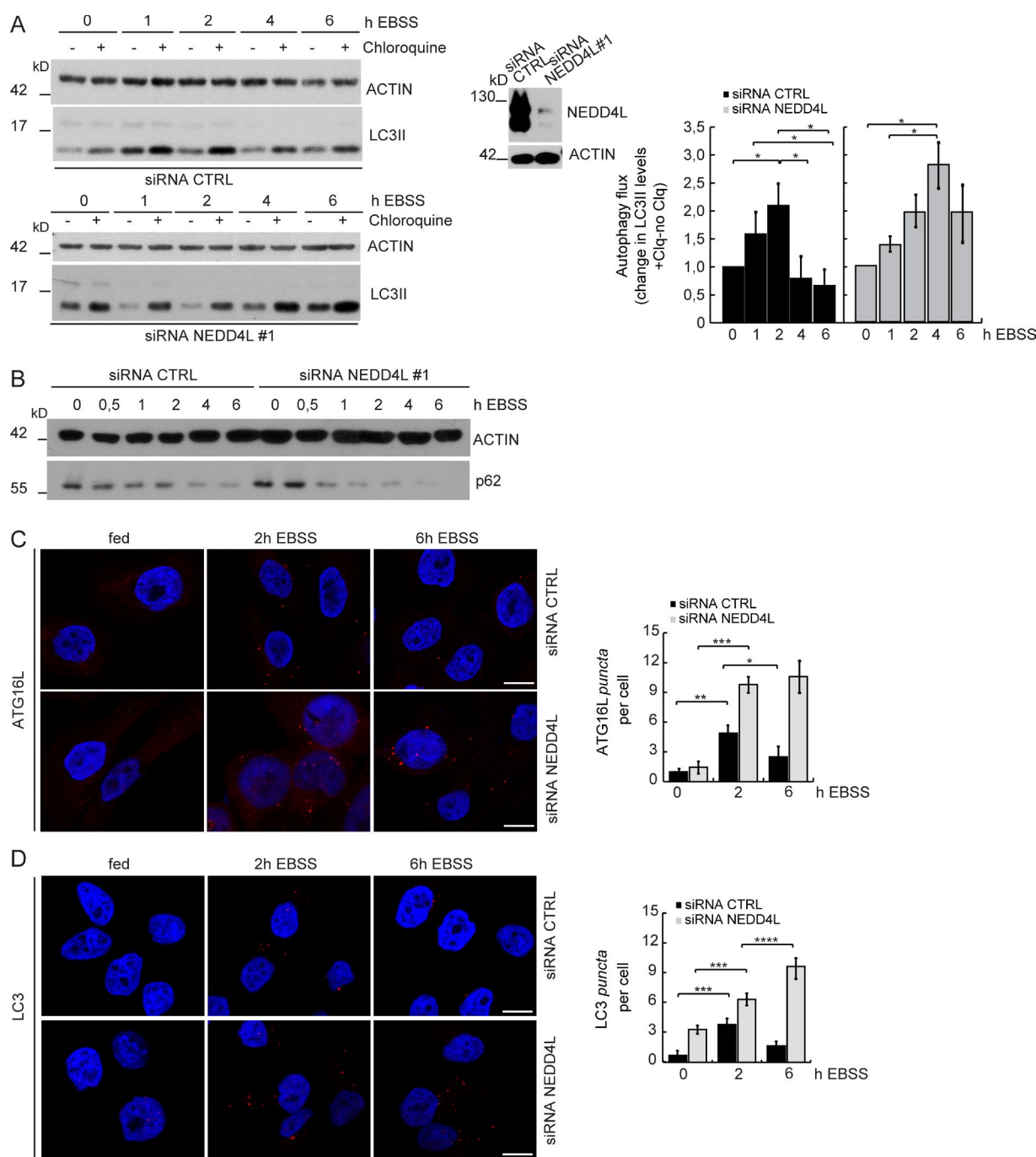


Figure 5. NEDD4L down-regulation increases autophagy. (A) NEDD4L expression was down-regulated in HeLa by RNAi. Cells were nutrient-starved for the indicated time periods in the presence or not of Clq. Protein extracts were analyzed by WB for the expression of LC3, ACTIN, and NEDD4L. Densitometric analysis of LC3II+Clq-LC3II control over ACTIN band is shown. Data are expressed as the mean \pm SEM of three independent experiments ($n = 3$). (B) HeLa cells were treated as in A. Protein extracts were analyzed by WB for the expression of p62 and ACTIN. (C and D) NEDD4L expression was down-regulated by RNAi as in A; cells were nutrient-starved for the indicated time periods and fixed and labeled with anti-ATG16L or anti-LC3 antibodies (red puncta) and visualized by confocal microscopy. Analysis of the number of both ATG16L and LC3 puncta occurrence per cell is shown in the graph. Data are expressed as the mean \pm SEM ($n = 3$); representative images are shown. Bar, 20 μ m (>50 cells analyzed per sample). In A, data were analyzed by one-way ANOVA followed by Tukey post hoc test. *, $P < 0.05$. In C and D, data were analyzed by two-way ANOVA followed by Bonferroni's multiple comparison post test. *, $P < 0.05$; **, $P < 0.01$; ***, $P < 0.001$; ****, $P < 0.0001$.

constructs (ULK1^{K925R} and ULK1^{K933R}), LC3 lipidation is increased and stable during the starvation period (Fig. S4 G). Further, this effect is not additive to NEDD4L down-regulation (Fig. S4 H). All these experiments support the idea that there is a correlation between ULK1 protein degradation and termination of the autophagy response.

ULK1 restoration requires de novo mTOR-dependent protein synthesis

Last, we investigated the mechanism underlying the restoration of ULK1 during prolonged starvation. Because it is known that mTOR is reactivated during prolonged starvation (Yu et al., 2010; Sahani et al., 2014) and its activity also reported as

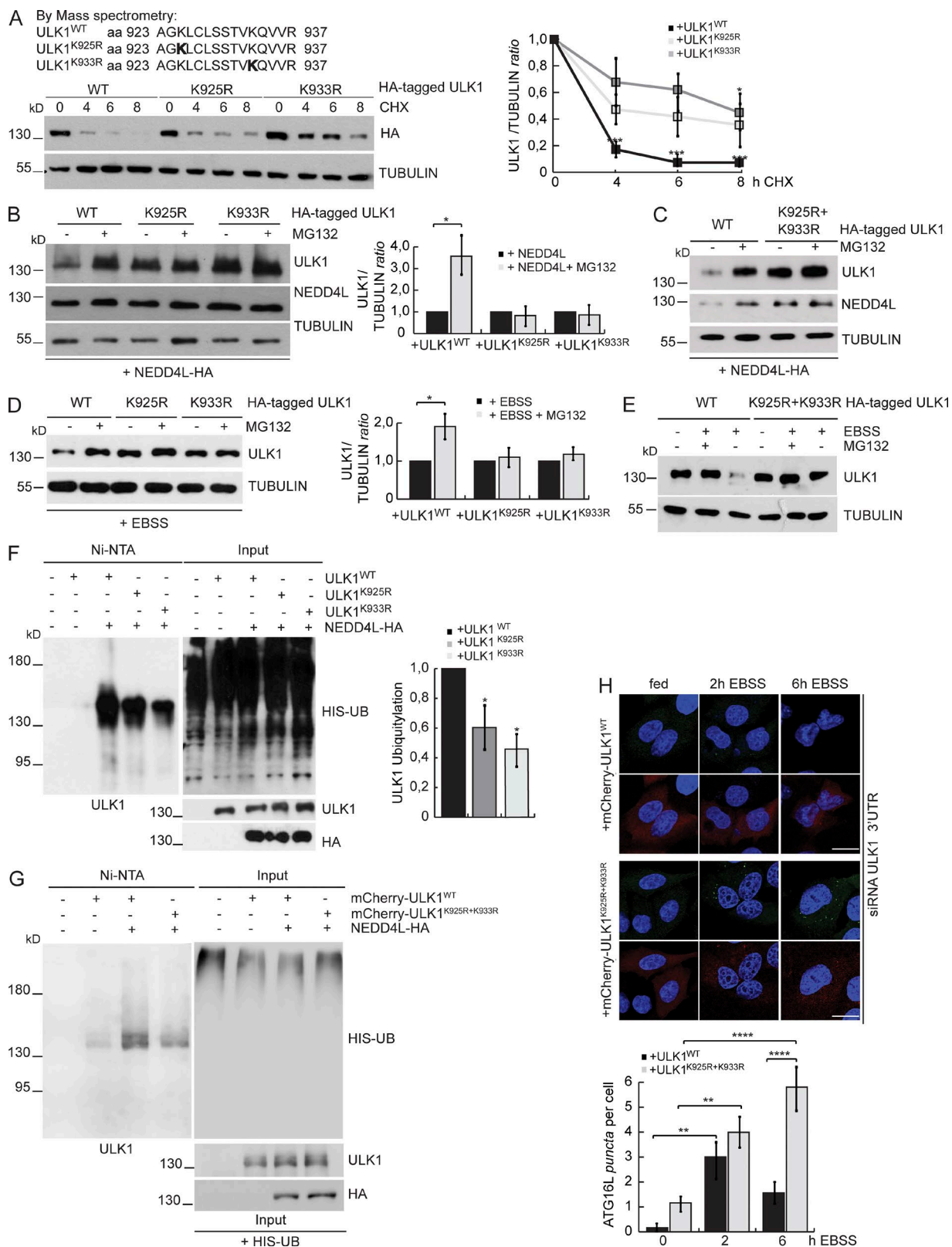


Figure 6. NEDD4L ubiquitylates ULK1 at lysine 925 and lysine 933. (A) HeLa cells were transfected with ULK1^{WT}, ULK1^{K925R}, and ULK1^{K933R} HA-tagged proteins and treated with CHX (50 μ M) for different time periods. Levels of ULK1 and TUBULIN were detected by WB. Densitometric analysis of ULK1 over TUBULIN is also shown (right graph). Data are expressed as the mean \pm SEM ($n = 3$). (B and C) HeLa cells were transfected ULK1^{WT}, ULK1^{K925R}, ULK1^{K933R}, and ULK1^{K925R+K933R} HA-tagged proteins together with NEDD4L-HA in the presence or not of MG132 (4 h) and all were treated with CHX for 3 h. Levels of ULK1, NEDD4L, and TUBULIN were detected by WB. (B) Densitometric analysis of ULK1+MG132/ULK1 control over TUBULIN bands is also shown. Data are expressed as the mean \pm SEM ($n = 3$). (D and E) HeLa cells were transfected with ULK1^{WT}, ULK1^{K925R}, ULK1^{K933R}, and ULK1^{K925R+K933R} HA-tagged proteins in the presence or not of MG132 and autophagy was induced with EBSS for 4 h. The levels of ULK1 and TUBULIN were detected by WB.

oscillatory in lymphocytic subpopulation in response to proliferative stimuli (Procaccini et al., 2010), we first analyzed the involvement of mTOR kinase.

As shown in Fig. 7 A and Fig. S5 A, mTOR is active after 6 h with both amino acid and serum starvation or with amino acid alone. We analyzed both the autophosphorylation of mTOR and the mTOR-mediated phosphorylation of ULK1 and found that the newly synthesized pool of ULK1 is directly inhibited by mTOR phosphorylation, contributing to maintain autophagy inhibition after prolonged starvation. Next, when cells were treated with two different mTOR inhibitors, rapamycin and Torin1 at 4 h of starvation, we found that mTOR inhibition effectively suppressed both ULK1 protein level restoration and ULK1 neophosphorylation by mTOR (Fig. 7, B and C), suggesting an involvement of mTOR reactivation in ULK1 restoration. Then, to evaluate whether the restoration of ULK1 required de novo protein synthesis, we used CHX after 4 h of starvation and found that this treatment also abolished ULK1 restoration, even though CHX is known to secondarily activate mTOR (Fig. 7 C).

Because we found an increase in *ULK1* mRNA level transcription during autophagy (Fig. 1 B), we analyzed whether transcriptional up-regulation was required for ULK1 protein restoration. As shown in Fig. 7 D, Act D is able to inhibit ULK1 restoration after 6 h of starvation, supporting the role of *ULK1* mRNA transcription as propaedeutical for de novo synthesis of ULK1 protein.

To determine whether increased translation of *ULK1* mRNA accounted for the increased protein levels at 6 h of starvation, we performed sucrose gradients to profile ULK1 mRNA distribution in translationally active polysomes or in translationally inactive RNPs (Bianchini et al., 2008). Autophagy was induced by starvation for 2 and 6 h, and polysome–mRNA complexes were fractionated by sucrose gradient centrifugation. Figs. 7 E and S5 B show a decrease in polysome-associated *ULK1* mRNA in cells grown under starvation conditions for 2 h, indicating translational repression of the mRNA. However, a strong recruitment of *ULK1* mRNA was observed after 6 h of starvation, strongly suggesting that increased translation of *ULK1* mRNA at 6 h of starvation (after mTOR reactivation) contributes to de novo synthesis of ULK1 protein.

Because prolonged autophagy is known to influence cell death (Füllgrabe et al., 2013; Antonioli et al., 2014), we analyzed cell viability in both control conditions and after NEDD4L down-regulation during prolonged starvation and in the presence or not of a low dose of bafilomycin A1 (Baf A1). As shown in Figs. 7 F and S5 C, when NEDD4L is down-regulated and autophagy remains high, we can detect an increase in starvation-induced cell death, which is

blocked by Baf A1, suggesting that persistent autophagy may trigger cell demise.

Autophagy restimulation requires mRNA preaccumulation and is amplified by NEDD4L down-regulation

To gain insight into the physiological relevance of ULK1 protein and mRNA modulation during prolonged starvation, we first decided to analyze ULK1 protein levels after reinduction of autophagy in the system by nutrient replenishment. As shown in Fig. 8 A, ULK1 protein levels can be down-regulated again as soon as autophagy is reinduced, indicating an oscillating regulation for this autophagy key factor. Then, to evaluate the importance of mRNA transcription in general (and of *ULK1* mRNA in particular; Fig. 1 D) in this oscillation, we used Act D for the first 4 h of starvation and analyzed both ULK1 protein levels and autophagy occurrence. As shown in Fig. 8 B, the temporary inhibition of mRNA transcription is sufficient to block autophagy reinduction by starvation after nutrient replenishment, as analyzed by counting ATG16L puncta. On the contrary, when NEDD4L is down-regulated and ULK1 protein levels cannot be decreased, we observed a stronger reinduction of autophagy (Fig. 8 C) when compared with the control. These results, collectively, confirm the importance of ULK1 fine-tuning in autophagy restimulation, which confers an oscillatory behavior to autophagy progression.

Discussion

Autophagy is the last resource to help cells survive during starvation, but self-degradation has a limit, beyond which the cell will die. For instance, after birth, in neonatal tissues, a rapid reprogramming of cell metabolism is necessary, and autophagy is activated soon after the transplacental nutrient supply is suddenly interrupted. However, autophagosome formation after birth is completely prevented, suggesting that neonates use the amino acids produced by autophagy for energy homeostasis (Schiaffino et al., 2008).

Displaying a negative control mechanism will thus help cells avoid overactivation of autophagy, enabling them to calibrate autophagy to an optimal level and ensuring that they can survive prolonged starvation. In fact, this study supports a mechanism of cross-regulation of *ULK1* mRNA transcription, protein translation, and degradation in response to the oscillatory activation of mTOR that regulates autophagy induction (see our model in Fig. 9). It is well known that the mTOR pathway activity is also regulated by oscillation in other contexts, such as in regulatory T cell proliferation, where another proautophagic

(D) Densitometric analysis of ULK1+MG132/ULK1 control over TUBULIN bands is also shown. Data are expressed as the mean \pm SEM ($n = 3$). (F) HeLa cells were transfected with a vector encoding a 6xHIS-tag ubiquitin together with ULK1^{WT}, ULK1^{K925R} and ULK1^{K933R} HA-tagged proteins in the presence of NEDD4L. Protein extracts were prepared in a denaturing urea buffer and subjected to Ni-NTA purification. The amount of ubiquitylated ULK1 copurified with 6xHIS-ubiquitin was evaluated by WB. The intensity of ULK1 bands is shown. Data are the mean \pm SEM ($n = 3$). (G) HeLa cells were transfected with a vector encoding a 6xHIS-tag ubiquitin together with ULK1^{WT} and ULK1^{K925R+K933R} mCherry-tagged proteins in the presence of NEDD4L. Protein extracts were prepared in a denaturing urea buffer and subjected to Ni-NTA purification. The amount of ubiquitylated ULK1 copurified with 6xHIS-ubiquitin was evaluated by WB. (H) Endogenous ULK1 was silenced by RNAi; cells were then transfected with ULK1^{WT} or ULK1^{K925R+K933R} mCherry-tagged plasmids. Cells were nutrient-starved for the indicated time periods, fixed and labeled with anti-ATG16L antibody (green puncta), and visualized by confocal microscopy. Analysis of the number of ATG16L occurrence per cell is shown in the graph. Data are expressed as the mean value \pm SEM ($n = 3$). Representative images are shown. Bars, 20 μ m (>50 cells analyzed per sample). In A, B, D, and F, data were analyzed by one-way ANOVA followed by Tukey post hoc test. *, $P < 0.05$; ****, $P < 0.0001$. In H, data were analyzed by two-way ANOVA followed by Bonferroni's multiple comparison post test. **, $P < 0.01$; ****, $P < 0.0001$. For all ULK1 mutant constructs the same amount of DNA is used for the transfection; the differences are caused by the increased stability of these mutants.

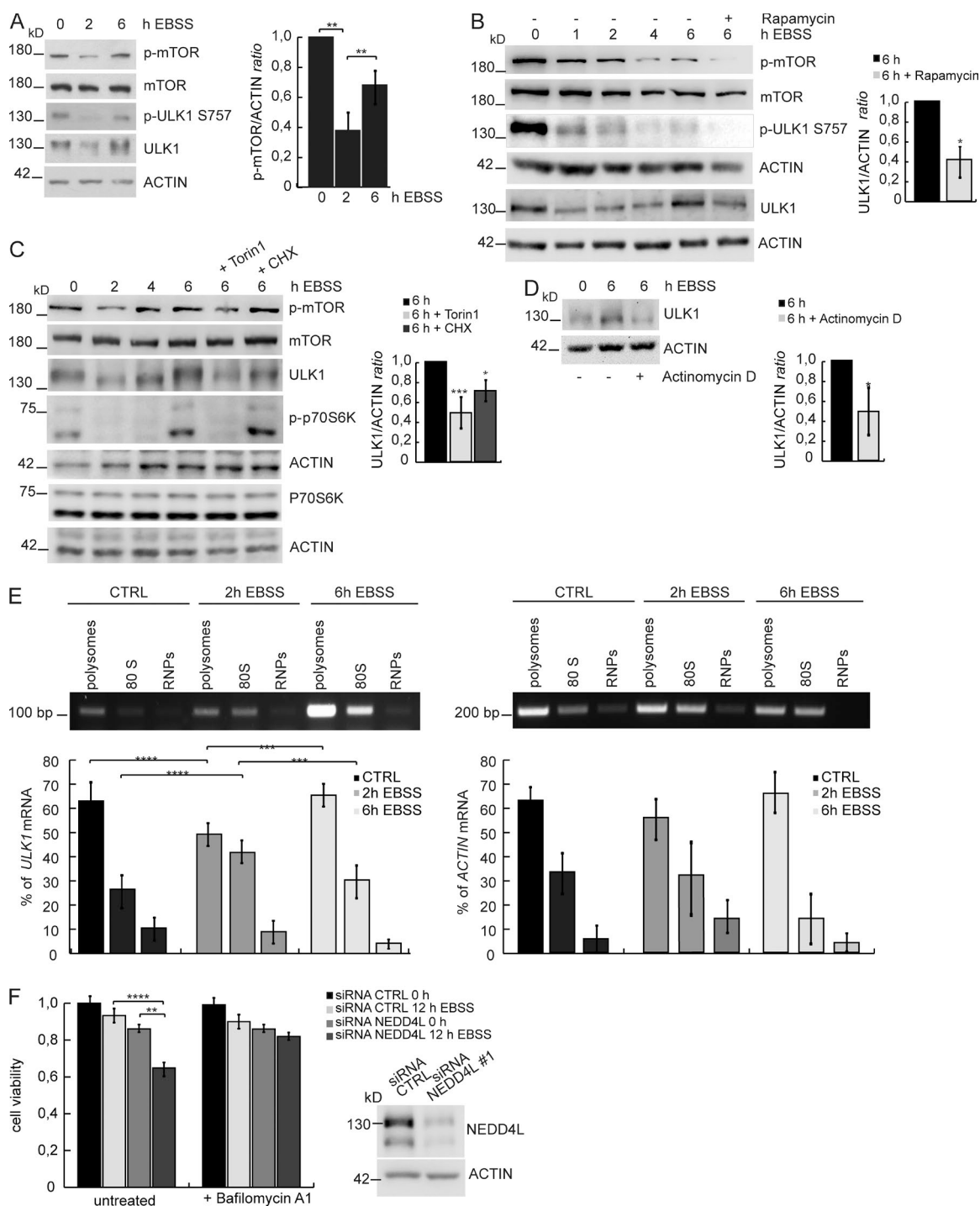


Figure 7. ULK1 restoration requires de novo mTOR-dependent protein synthesis. (A) HeLa cells were treated with EBSS for the indicated time periods. The levels of p-mTOR, mTOR, ULK1, p-ULK1 S757, ULK1, and ACTIN were detected by WB. Densitometric analysis of p-mTOR over ACTIN is also shown (right graph). Data are expressed as the mean \pm SEM ($n = 4$). (B) HeLa cells were treated with EBSS for the indicated time periods; at 4 h of starvation, rapamycin (100 nM) was added. Levels of p-mTOR, mTOR, ULK1, p-ULK1 S757, and ACTIN were detected by WB. Densitometric analysis of ULK1 over ACTIN is also shown (right graph). Data are expressed as the mean \pm SD ($n = 3$), and statistical analysis was performed using unpaired Student's *t* test. *, $P < 0.05$. (C) HeLa cells were treated with EBSS for the indicated time periods and at 4 h of starvation, 250 nM Torin1 or 50 μ M CHX was added. Levels of p-mTOR, mTOR, p-p70S6K, ULK1, and ACTIN were detected by WB. (D) HeLa cells were treated with EBSS for 6 h in the presence or not of Act D. Levels of ULK1 and ACTIN were detected by WB. Densitometric analysis of ULK1 over ACTIN is also shown (right graph). Data are expressed as the mean \pm SD ($n = 3$) and statistical analysis was performed using unpaired Student's *t* test. *, $P < 0.05$. (E) qPCR analysis of polysomal recruitment of ULK1 and ACTIN mRNAs in control (CTRL) and EBSS-starved (2 h EBSS and 6 h EBSS) HeLa cells. Densitometric analysis of the signal in each fraction was performed, and the results were represented as the percentage of total signal in all fractions. Data represent mean \pm SEM ($n = 3$). (F) NEDD4L expression was down-regulated by RNAi. Cells were nutrient-starved for 12 h in the presence or not of Baf A1 and analyzed by MTS assay. NEDD4L down-regulation was detected by WB. In A and C, data were analyzed by one-way ANOVA followed by Tukey post hoc test. *, $P < 0.05$; **, $P < 0.01$; ***, $P < 0.001$. In E and F, data were analyzed by two-way ANOVA followed by Bonferroni's multiple comparison post test. ***, $P < 0.001$; ****, $P < 0.0001$.

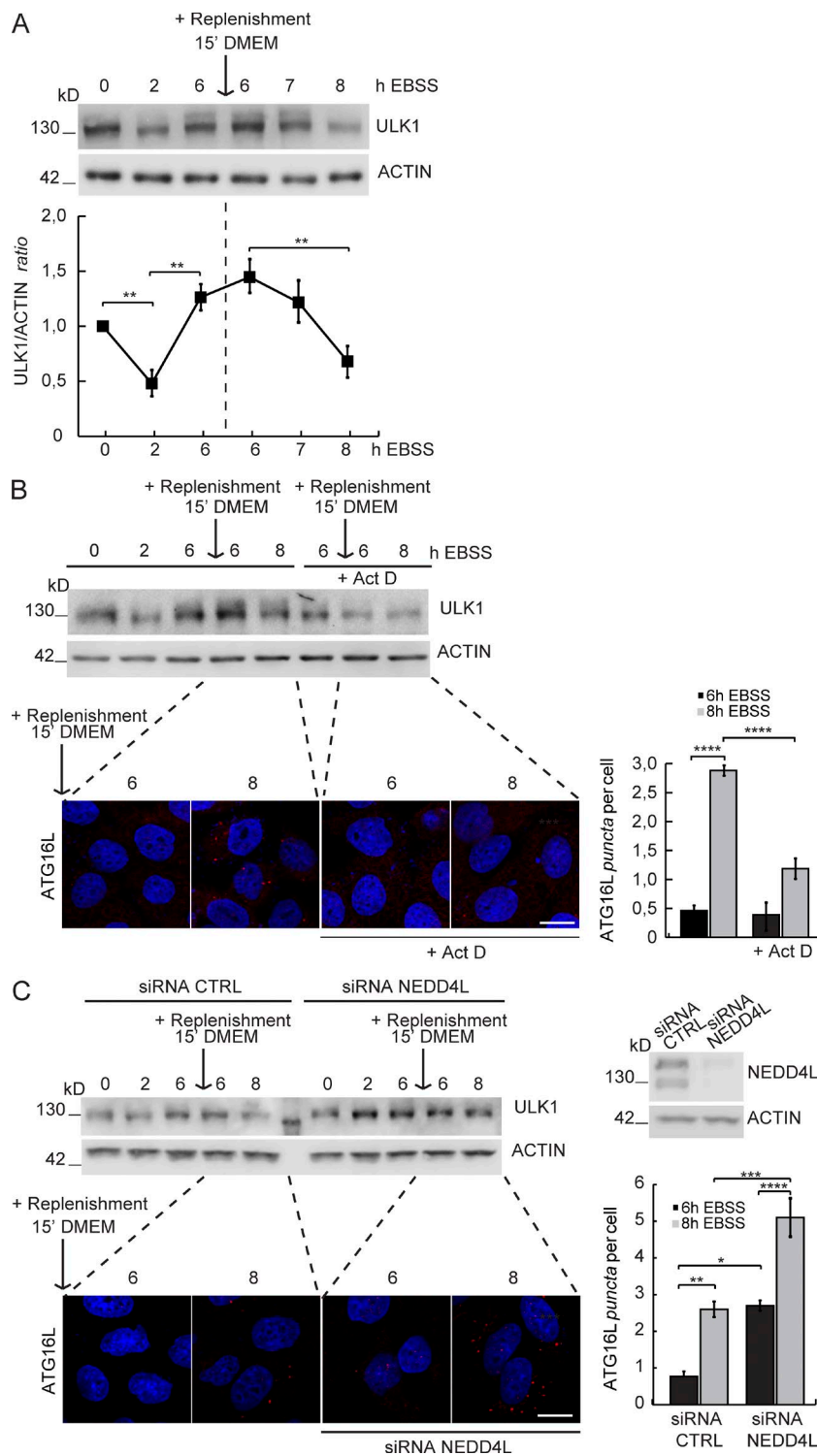


Figure 8. Autophagy restimulation requires mRNA preaccumulation and is amplified by NEDD4L down-regulation. (A) HeLa cells were treated with EBSS for the indicated time periods. After 6 h, in some samples, full medium was added for 15 min, and then cells were starved again for 1 and 2 h, respectively. Protein levels of ULK1 and ACTIN were detected by WB. Densitometric analysis of ULK1 over ACTIN is also shown (below graph). Data are expressed as the mean \pm SEM ($n = 3$). (B) HeLa cells were treated with EBSS as in A. In some samples, Act D was added for the first 4 h of starvation. Then, cells were analyzed both by WB and by immunofluorescence. Protein levels of ULK1 and ACTIN were detected by WB. ATG16L puncta occurrence (red puncta) was visualized by confocal microscopy. Analysis of the number of ATG16L puncta per cell is shown in the graph. Data are expressed as the mean \pm SEM ($n = 3$); representative images are shown. Bar, 20 μ m (>50 cells analyzed per sample). Data represent mean \pm SEM ($n = 3$). In A, data were analyzed by one-way ANOVA followed by Tukey post hoc test. **, $P < 0.01$. In B and C, data were analyzed by two-way ANOVA followed by Bonferroni's multiple comparison post hoc test. *, $P < 0.05$; **, $P < 0.01$; ***, $P < 0.001$; ****, $P < 0.0001$.

stimulus, the mTOR inhibitor rapamycin, might differentially affect regulatory T cells reactivity depending on their metabolic state (Procaccini et al., 2010). Moreover, the *ULK1* gene has been found to be a target of C/EBP β protein, a transcription factor that links autophagy to the circadian pacemaker and maintains nutrient homeostasis throughout light/dark cycles; this is consistent with the fact that autophagy is highly sensitive to nutritional status (Ma et al., 2011). In sum, ULK1 complex regulation may represent a hinge point in a cell response to stress, and its oscillatory nature, intended as the key to the remitting and

relapsing nature of autophagy, can be considered as an essential element of the cell's struggle between death and survival.

NEDD4L is a ubiquitin ligase implicated in several cellular or physiological processes (Goel et al., 2015). It is known that two members of the NEDD4 family, NEDD4 and SMURF1 (SMAD-specific E3 ubiquitin protein ligase 1), are involved in autophagy. NEDD4 has been found to promote BECLIN 1 degradation by the proteasome (Platta et al., 2012). Further, RNAi analyses revealed that NEDD4 down-regulation leads to an autophagy increase (Behrends et al., 2010). SMURF1

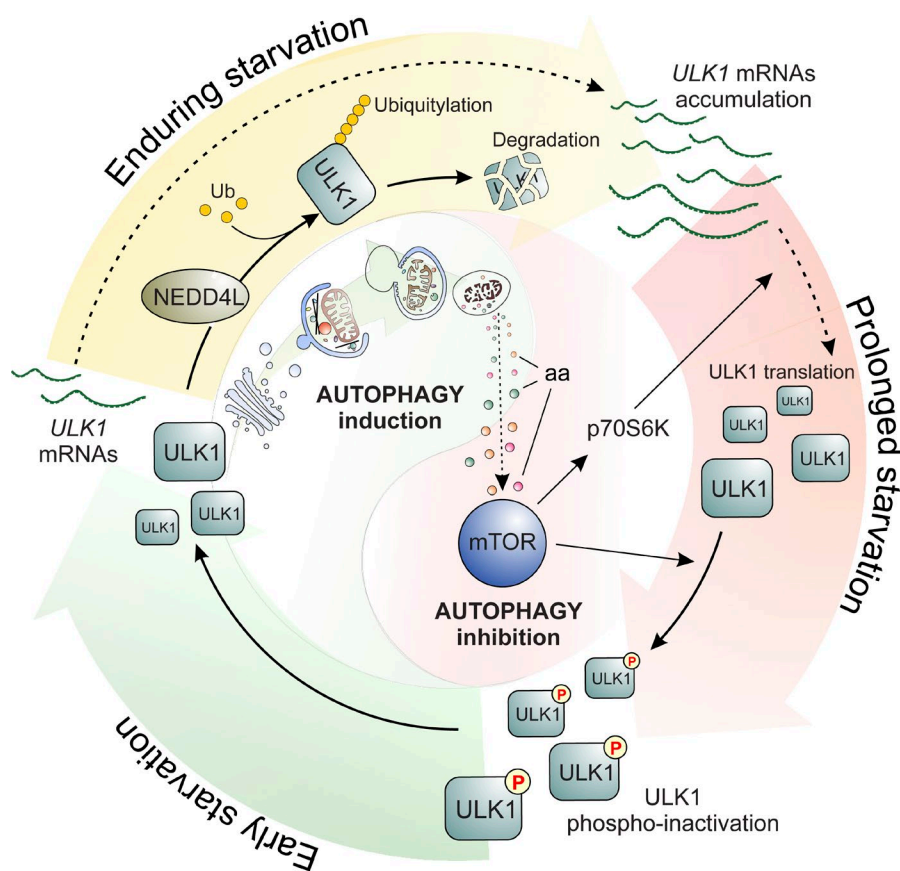


Figure 9. **A cyclic scheme representing autophagy oscillatory regulation.** (A) In enduring starvation, NEDD4L promotes ULK1 degradation while *ULK1* mRNA is actively transcribed. When the autophagy recycling activity makes more nutrients available for protein synthesis, mTOR is reactivated (in conditions of prolonged starvation), and *ULK1* mRNA is actively translated upon p70S6K phosphorylation. Then the mTOR kinase function inhibits again the ULK1 protein by phosphorylation, thus making the system ready to respond a putative new stimulus (early starvation), capable to reactivate autophagy. This regulation allows oscillatory autophagy behavior, both preventing excessive autophagy and preparing the cell for a prompt autophagy response upon its reinduction.

plays multiple physiological functions through targeting a variety of substrates acting in both viral autophagy and mitophagy (Orvedahl et al., 2011).

We previously described ubiquitylation of ULK1 by a K63-linked chain mediated by the TRAF6–AMBRA1 complex during short-term starvation and at early time points (30 min), an event stabilizing the active ULK1 complex (Nazio et al., 2013). In a recent paper, we found that the other autophagy activator and ULK1 regulator AMBRA1 is degraded by the Cullin4–DDB1 complex during prolonged starvation and that AMBRA1–TRAF6 binding to ULK1 decreases during prolonged autophagy (Antonioli et al., 2014). An obvious hypothesis is that when the AMBRA1–TRAF6 complex dissociates from ULK1, the ULK1 carboxy-terminal domain becomes unmasked and available for NEDD4L-dependent ubiquitylation.

Moreover, the NEDD4L-mediated ULK1 ubiquitylation is reminiscent of another target of TRAF6 and NEDD4L ligases, TrkA; TRAF6-dependent ubiquitylation is supposed to function nonproteolytically, whereas NEDD4L-mediated ubiquitylation results in the degradation of this plasma membrane receptor (Geetha et al., 2005; Georgieva et al., 2011). We can thus speculate that, similarly to TrkA, ULK1 can be alternatively regulated by these two ligases with two opposite effects, implicating the existence of an ULK1-targeting E3 ligase network regulating cell fate. Last, the recent finding that Cullin3–KHLH20 can also degrade ULK1, Beclin 1, and Vps34 during prolonged autophagy may reflect the need for the cell to possess alternative backup systems for autophagy termination, highlighting the absolute need for a tight control of this event in the general cellular homeostasis (Liu et al., 2016).

As a matter of fact, E3 ligases can promote the formation of polyubiquitin chains on substrates through any of the seven lysines present on ubiquitin molecules. Interestingly, the NEDD4L-mediated ubiquitylation of ULK1 is K27- and K29-linked, but not typical K48-linked, ubiquitylation. Our finding adds to the recent and relatively small amount of existing data on this type of posttranslational modification.

A final issue of interest is the fact that NEDD4L is able to regulate autophagy also in basal conditions. Although basal autophagy has been shown to be independent of ULK1 in a few instances (Petherick et al., 2015; Joo et al., 2016), this does not seem to be the case in cancer cell lines that are characterized by a strong basal autophagy, including HeLa cells (Mizushima, 2010; Wong et al., 2015). Indeed, we found that NEDD4L interacts with ULK1 also in basal conditions and also when the ULK1 kinase domain is disrupted. However, NEDD4L is able to degrade only activated ULK1. Several general principles apply to the degradation of activated protein kinases or their regulators for ubiquitylation and degradation (Lu and Hunter, 2009). Autophosphorylation of ULK1 could change its conformation for NEDD4L-mediated ubiquitylation or, alternatively, the NEDD4L pool binding ULK1 in the absence of autophagy induction is in an inactive form. The trans-phosphorylation of a protein kinase could, indeed, create a phosphodegron that is necessary for ubiquitylation by a phospho-dependent ligase, such as NEDD4L. In addition, because phosphorylation on S342 of NEDD4L is necessary for its subsequent ubiquitylation activity (Lee et al., 2007; Gao et al., 2009), ULK1 could also be involved in regulating other kinases (such as SGK1, Akt, and PKA) known to phosphorylate the NEDD4L residue S342.

A comprehensive analysis of the autophagy-related posttranslational modifications is therefore of the high importance in biomedicine and may represent the forefront of autophagy research.

Materials and methods

Cell culture and autophagy assays

HeLa and HEK293 cells were cultured in DMEM (Sigma-Aldrich) supplemented with 10% FBS (Sigma-Aldrich), 2 mM L-glutamine, and 1% penicillin/streptomycin solution at 37°C under 5% CO₂.

The induction of autophagy by nutrients starvation was obtained washing the cells with PBS and incubating them with Earle's balanced salt solution (EBSS; Sigma-Aldrich). Proteasome activity was inhibited for indicated time points with 5 μM MG132 (Sigma-Aldrich) and 20 μM lactacystin; lysosome activity was inhibited for 1 h with 20 μM Clq (added for the last hour of the treatment; Sigma-Aldrich), 10 μM leupeptin (Sigma-Aldrich), or 10 nM Baf A1, and autophagy was induced with 100 nM rapamycin (Sigma-Aldrich) or 250 nM Torin1 (Tocris Bioscience). Transcription was inhibited with 0.5 μM Act D (Sigma-Aldrich). HeLa cells were transiently transfected with Lipofectamine 2000 (Thermo Fisher Scientific) as provided by the supplier.

Ni-NTA assay

For detection of whole-cell ubiquitylation, HeLa cells were transfected with a 6×HIS-ubiquitin expression plasmid along with equal amounts of the indicated plasmids. Thereafter, cells were collected in PBS, resuspended in 1 ml lysis buffer (8 M urea, 0.1 M NaH₂PO₄, 0.05 M Tris, pH 8.0, 40 mM imidazole, 0.5% CHAPS, and 50 mM 2-chloroacetamide), sonicated, and centrifuged. To lysates containing equal amounts of whole-cell protein, 30 μl nickel-nitrilotriacetic acid (Ni-NTA) beads (QIAGEN) were added, and the mixture was incubated at room temperature for 4 h with rotation. Subsequently, the beads were washed for 5 min at room temperature with 800 μl lysis buffer containing 40 mM imidazole. Ubiquitylated proteins were eluted by incubating the beads in 30 μl buffer containing 400 mM imidazole and 2× Laemmli buffer and resolved by SDS-PAGE followed by immunoblotting with the indicated antibodies.

In vitro ubiquitylation assays

HeLa cells were independently transfected with plasmids encoding NEDD4L-HA and Myc-ULK1. 24 h later, cells were lysed in buffer (20 mM Hepes, pH 7.4, 2 mM EGTA, 50 mM M glycerophosphate, 0.5% Triton X-100, 0.5% CHAPS, and 10% glycerol) containing protease inhibitors. Lysates were cleared by centrifugation and subjected to IP using agarose-coupled antibodies against HA or Myc tags. After lysis and before IP, 1% SDS was added and the lysates were incubated for 5 min at 90° to dissociate protein–protein interactions. The samples were diluted 10-fold with the same buffer and the IP assay was performed as previously described. NEDD4L-HA was eluted using 300 mg/ml HA peptide (Sigma-Aldrich). The assays were performed in a 20-μl reaction volume combining the immunopurified proteins and the following recombinant components: 0.2 μg Ube1 (Boston Biochem), 0.5 μg UbcH5b (Boston Biochem), and 100 μM HIS-ubiquitin (Boston Biochem). The reaction was performed at 30°C for 1 h with agitation. The incorporation of ubiquitin was analyzed by WB using an antibody against the ubiquitin.

Plasmids

Plasmids encoding for wild-type ULK1-Myc, ULK1-K46I, and wild-type ULK1-HA were provided by S.A. Tooze (The Francis Crick Institute,

Lincoln's Inn Fields Laboratories, London, England, UK). NEDD4L-HA^{WT} and NEDD4L-HA^{CA} plasmids were from Addgene. J. Massaguè (Memorial Sloan Kettering Cancer Center, New York, NY) provided NEDD4L deletion constructs. ULK1 mutant constructs were generated by using the site-directed mutagenesis kit (Agilent Technologies). The sequences used are as follows: K925R, 5'-GACCAGATCCGGGCCGGCAGGCTCTGC CTGTGCTCCACTGTG-3'; K933E, 5'-CTGCCTGTGCTCCACTGT GAGGCAGGTGGTGCAGGCTGAATG-3'; S1047A, 5'-GACTCT CGGCCCTGCTGGCTGGTGTCTATGCCTGA-3'.

Antibodies

The primary antibodies used in this study were: mouse and rabbit anti-HA tag antibody (Sigma-Aldrich), mouse anti-Myc (Santa Cruz Biotechnology, Inc.), rabbit anti-BECLIN 1 (Santa Cruz Biotechnology, Inc.), rabbit anti-LC3 (Cell Signaling Technology), rabbit anti-human AMBRA1 (Novus Biologicals), mouse anti-multiubiquitin (MBL), rabbit anti-ULK1 (Santa Cruz Biotechnology, Inc.), goat anti-ULK1 (Santa Cruz Biotechnology, Inc.), rabbit anti-pS757 ULK1 (Cell Signaling Technology), mouse anti-ULK2 (Abcam), rabbit anti-NEDD4L (Cell Signaling Technology), mouse anti-NEDD4L (Santa Cruz Biotechnology, Inc.), rabbit anti-pS342 NEDD4L (Cell Signaling Technology), rabbit anti-mTOR (Cell Signaling Technology), rabbit p-S2448 mTOR (Cell Signaling Technology), rabbit anti-p62 (Santa Cruz Biotechnology, Inc.), rabbit anti-ATG13, rabbit p-S318 ATG13 (Rockland), rabbit anti-Actin (Sigma-Aldrich), mouse anti-Tubulin (Sigma-Aldrich), rabbit cleaved-PARP (Cell Signaling Technology), rabbit anti-Atg16L (Cell Signaling Technology), and rabbit p-p70S6K and p70S6K (Cell Signaling).

Immunoprecipitation and WB

HeLa cells were rinsed with ice PBS and lysed in CHAPS lysis buffer (40 mM Hepes, pH 7.4, 2 mM EDTA, 0.3% CHAPS, and protease and phosphatase inhibitor cocktail; Sigma-Aldrich). 0.5 mg lysates for co-IP in overexpression and 2 mg lysates for co-IP in endogenous conditions were then incubated with 2 μg primary antibody for ULK1 and NEDD4L or 1 μg primary antibody for MYC at 4°C with rotation overnight before addition of 30 μl protein A agarose beads (Roche) and then incubated at 4°C for 1 h.

For the co-IP of HA-tagged proteins, lysates were incubated with 20 μl agarose-coupled antibodies against HA at 4°C for 2 h.

To detect ubiquitin, after lysis and before immunoprecipitation, 1% SDS was added, and the lysates were incubated for 5 min at 90° to dissociate protein–protein interactions. The samples were diluted 10-fold with the same buffer, and the immunoprecipitation assay was performed as described above in this paragraph.

Immunoprecipitates were then washed 5 × 5 min with lysis buffer (40 mM Hepes, pH 7.4, 2 mM EDTA, 0.3% CHAPS, and NaCl 150 mM) and then denatured by adding 1 vol of 4× Laemmli SDS sample buffer with β-mercaptoethanol and incubated at 95° for 10 min.

Proteins were separated on acrylamide gels (Bio-Rad Laboratories) and electroblotted onto nitrocellulose (Protran; Schleicher & Schuell) or polyvinylidene difluoride (EMD Millipore) membranes. Blots were incubated with primary antibodies in 5% nonfat dry milk or 5% BSA in TBS plus 0.1% Tween-20 overnight at 4°C. Detection was achieved using horseradish peroxidase-conjugated secondary antibody (Bio-Rad Laboratories) and visualized with ECL (EMD Millipore).

Of note, in some cases, Western blots were captured using a digital camera (Fluor Chem SP; Alpha Innotec; see Fig. 1, A and E, bottom panels; Fig. 2 C; Fig. 3 E, HA, bottom panel; Fig. 3 F, bottom panels; Fig. 4, B and D; Fig. 5 A, bottom panels; Fig. 6 G; Fig. 7, B–E; and Fig. 8, A–C), whereas in others, they were captured on film (Aurogene). Backgrounds in Western blot images from different

experimental approaches were then equalized by changing their exposition postacquisition.

RNAi

RNAi was performed using the following RNA oligonucleotide (oligo) duplex from Thermo Fisher Scientific: NEDD4L#1 HSS118597, 5'-CCCAAGACUGCAGAACCCAGCUAAU-3' (10620318); 5'-AAUAGCUGGGUUCUGCAGUCUUGGG-3' (10620319); NEDD4L#2 ID: 22855 (3' UTR), 5'-GGCAUUUAUGUACUACAU-3'; 5'-AUGUAGUACAUAAAGUGCC-3'; ULK1 HSS140824, 5'-GAGAACGUCACC AAGUGCAAGCUGU-3' (127303D05); 5'-ACAGCUUGCAGUUGGUGACGUUCUC-3' (127303D06); ULK1 (3'UTR) ID: 118261, 5'-CCC AAGCACUUUAUGCAU-3'; 5'-UAUGCAUAAAGUGCUUGGG-3'.

2.5 × 10⁵ cells per well were transfected with 100 pmol siRNA oligos in six-well plates using Lipofectamine 2000 (Thermo Fisher Scientific) following the manufacturer's instructions.

qPCR

Total RNA was isolated by using the RNeasy mini kit (QIAGEN). 2 µg RNA was retrotranscribed using M-MLV enzyme and oligodT (Promega). qPCR was then performed using SYBR Green Mix (Roche) with the LC480 qPCR system (Roche). The following oligos primers were used: *ULK1*, 5'-CAGACAGCCTGATGTGCAGT-3'; 5'-CAGGGTGGGGATGGAGAT-3'; *β-ACTIN*: 5'-CCAACCGCGAGAAGATGA-3'; 5'-CCAGAGGCGTACAGGGATAG-3'; *NEDD4L*: 5'-AGCCCAATGGGTCAGAAATAA-3'; 5'-TCTGGACCCTGTTCACAAATC-3'. Melting curve analysis was used to confirm primer specificity. To ensure linearity of the standard curve, reaction efficiencies over the appropriate dynamic range were calculated. Using the ddCt method, we calculated fold-increases in the mRNA expression of the gene of interest normalized to *β-Actin* expression. We then normalized the mRNA levels to the control condition. Reported values are the means of three independent biological replicates with technical triplicates that were averaged for each experiment. Error bars represent SD of the mean.

Immunocytochemistry

Cells were washed in PBS and fixed with 4% paraformaldehyde in PBS for 15 min. After permeabilization with 0.4% Triton X-100 in PBS for 5 min, cells were blocked in 3% horse serum in PBS and incubated overnight at 4°C with primary antibodies. Cells were then washed and incubated for 1 h with labeled anti-mouse (Alexa Fluor 488; Molecular Probes) or anti-rabbit (FITC; Jackson ImmunoResearch Laboratories, Inc.; Alexa Fluor 647 donkey anti-rabbit) secondary antibodies. Images were examined under a confocal laser scanning microscope (FV1000; Olympus) interfaced with 1 × 81 inverted microscope equipped with a 60× (NA 1.35) oil-immersion objective. A 405-nm diode laser was used for the blue channel, a 488-nm argon laser was used for the green channel, and a 543-nm HeNe laser was used for the red channel.

Polysome fractionation

Polysome separation was performed as previously described (Paronetto et al., 2006). In brief, HeLa cells were grown overnight to 60–70% confluence and incubated for the indicated time period (2 and 6 h) in EBSS or control medium. After extensive washing in cold PBS, cells were scraped in lysis buffer (100 mM NaCl, 10 mM MgCl₂, 30 mM Tris-HCl, pH 7.5, 1% Triton X-100, 1 mM DTT, 0.5 mM Na₂VO₃, and 25 U/ml RNasin [Promega]) supplemented with protease inhibitor cocktail (Sigma-Aldrich) and lysed by 10-min incubation in ice. Cell lysates were centrifuged for 10 min at 12,000 g at 4°C, and the supernatants were collected (cell extracts). 1 mg cell extracts was loaded on a 15–50% (wt/vol) sucrose gradients (10 ml) and sedimented by ultracentrifugation for 2 h at

37,000 rpm in a rotor (SW41; Beckman Coulter). UV-absorption (A₂₆₀) profiles of polysome gradients were measured by UV detector (UVis-920; GE Healthcare), and each gradient was collected in 10 fractions of 1 ml each. For RT-PCR analysis, 500 µl of fractions 1–5, 6 and 7, and 8–10 were pooled to generate polysomal, 80S, and RNP samples, respectively, and RNA was isolated with RNeasy Mini kit (QIAGEN). Proteins were isolated from the remaining 500 µl of each gradient fraction by adding 50 µl of 72% trichloroacetic acid. Suspensions were mixed, incubated for 15 min in ice, and centrifuged at 12,000 g for 10 min at 4°C. Protein pellets were washed with –20°C chilled acetone and resuspended in Laemmli buffer for Western blot analysis.

MTS assay

For the MTS (3-(4,5-dimethylthiazol-2-yl)-5-(3-carboxymethoxyphenyl)-2-(4-sulphophenyl)-2H-tetrazolium) assay, cells were knocked-down for NEDD4L or with control as indicated in the RNAi section. After 48 h of transfection, cells were seeded in 96-well plates (5,000 cells in each well), exposed to full medium or EBSS alone or in combination with Baf A1 for 12 h. During the last hour, MTS was added to the medium. Each combination of cells was analyzed in triplicate wells and analyzed at least three times. The MTS assay was analyzed spectrophotometrically at 490 nm using a 96-well plate reader, as indicated by the supplier (Promega).

Background absorbance were calculated on set of control wells (without cells) containing the same volumes of medium and Baf A1.

MS analysis

Protein elution from ULK1 co-IP was denatured 5 min at 90°C and incubated for 30 min at 56°C with 10 mM DTT for cysteine reduction and 20 min at room temperature with 55 mM iodoacetamide for cysteine alkylation.

Proteins were precipitated by adding five volumes of ethanol 100% (overnight at 4°C) and then centrifuged at 4,000 g (40 min at 10°C), resuspended in a buffer containing 2 M urea in 50 mM ammonium bicarbonate, and digested with 0.2 µg trypsin overnight at 37°C.

Tryptic peptides were concentrated with ZipTip mC18 pipette tips (EMD Millipore) and eluted in 80% acetonitrile, 0.1% trifluoroacetic acid. Samples were dried in a vacuum centrifuge and resuspended in 7 µl 2.5%, 0.1% trifluoroacetic acid for the liquid chromatography fractionation and matrix-assisted laser desorption/ionization time-of-flight/time-of-flight (MALDI-TOF/TOF) analysis as described previously (Perdomo et al., 2012; Montaldo et al., 2014). The interpretation of both the MS and MS/MS data was performed with GPS Explorer software (version 3.6; Applied Biosystems) MS peptide fingerprint and MS/MS peptide-sequencing searches were performed against the NCBI nonredundant database using the MASCOT search algorithm. These searches specified trypsin as the digestion enzyme (allowing for one missed trypsin cleavage); carbamidomethylation of cysteine as fixed modification; partial oxidation of methionine; phosphorylation of serine, threonine, and tyrosine; and ubiquitination (glycine-glycine dipeptide) as variable modifications.

Statistical analysis

For all experiments shown, *n* is indicated in the figure legends.

Densitometric analysis was performed using ImageJ software; the mean of the values from different experiments (as indicated) related to the control ratio was arbitrarily defined as 1.00. Each point value represents the mean ± SD or mean ± SEM (as indicated in the figure legends) from three independent experiments unless specified otherwise. Comparison between control and sample in the WB intensity measurement was made from the same Western blot.

Statistical significance was measured using an unpaired Student's *t* test, one-way and two-way analysis of variance (ANOVA) followed by Tukey's post hoc test or Bonferroni's multiple comparison posttest using GraphPad Prism program (version 6) as indicated in the figure legends.

Online supplemental material

Fig. S1 show that ULK1 protein levels are finely regulated upon starvation, but not its interacting proteins, supporting the data shown in Fig. 1. Fig. S2 shows that ULK2 is degraded during autophagy, supporting the data shown in Fig. 3. Fig. S3 shows that NEDD4L is able to bind the kinase-dead ULK1, supporting the data shown in Fig. 4. Fig. S4 shows that the overexpression of ULK1 mutant constructs impairs autophagy dynamics, supporting data shown in Fig. 6. Fig. S5 shows that NEDD4L down-regulation influences cell death, supporting the data shown in Fig. 7. Table S1 shows the identification of ubiquitylation sites of ULK1 protein by MALDI-TOF/TOF analysis.

Acknowledgments

We thank Giuseppe Filomeni for assistance with the preparation of the model in Fig. 9. We thank M. Acuna Villa and M.W. Bennett for editorial and secretarial work.

F. Cecconi's laboratory is supported by grants from the Kræftens Bekæmpelse (KBVU R72-A4408), the Lundbeckfonden (R167-2013-16100), the Novo Nordisk UK Research Foundation (7559), the Associazione Italiana per la Ricerca sul Cancro (IG2013), Fondazione Roma, and in part by Associazione Italiana Sclerosi Multipla (2013), Fondazione Telethon (GGP14202 to F. Cecconi and P. Bonaldo), the Ministero dell'Istruzione dell'Università e della Ricerca (Fondo per gli Investimenti della Ricerca di Base Accordi di Programma 2011 to F. Cecconi and P. Bonaldo), and the Ministero della Salute (GR2011 to F. Strappazzon and GR-2011-02351643 to S. Campello). This work was also supported by the European Union's Horizon 2020 research and innovation program (Marie Skłodowska-Curie grant agreement 642295 [MEL-PLEX]) F. Cecconi's lab in Copenhagen is part of the newly established Center of Excellence in Autophagy, Recycling and Disease, funded by the Danmarks Grundforskningsfond.

The authors declare no competing financial interests.

Author contributions: F. Nazio designed and performed most experiments with crucial help from M. Carinci (immunoprecipitation), C. Valacca (qPCR), P. Bielli (polysome gradient), F. Strappazzon and S. Campello (confocal analysis), M. Antonoli (ubiquitin assays), and F. Ciccossanti and G.M. Fimia (mass spectrometry and critical reagents). F. Nazio and F. Cecconi wrote the manuscript with the help and suggestions of C. Sette and P. Bonaldo. F. Cecconi conceived the research. All authors discussed the results and commented on the manuscript.

Submitted: 23 May 2016

Revised: 19 September 2016

Accepted: 23 November 2016

References

Alers, S., A.S. Löffler, S. Wesselborg, and B. Stork. 2012. The incredible ULKs. *Cell Commun. Signal.* 10:7. <http://dx.doi.org/10.1186/1478-811X-10-7>

An, H., D.T. Krist, and A.V. Statsyuk. 2014. Crosstalk between kinases and Nedd4 family ubiquitin ligases. *Mol. Biosyst.* 10:1643–1657. <http://dx.doi.org/10.1039/c3mb70572b>

Antonoli, M., F. Albiero, F. Nazio, T. Vescovo, A.B. Perdomo, M. Corazzari, C. Marsella, P. Piselli, C. Gretzmeier, J. Dengjel, et al. 2014. AMBRA1 interplay with cullin E3 ubiquitin ligases regulates autophagy dynamics. *Dev. Cell.* 31:734–746. <http://dx.doi.org/10.1016/j.devcel.2014.11.013>

Behrends, C., M.E. Sowa, S.P. Gygi, and J.W. Harper. 2010. Network organization of the human autophagy system. *Nature.* 466:68–76. <http://dx.doi.org/10.1038/nature09204>

Bianchini, A., M. Loiarro, P. Bielli, R. Busà, M.P. Paronetto, F. Loreni, R. Geremia, and C. Sette. 2008. Phosphorylation of eIF4E by MNKs supports protein synthesis, cell cycle progression and proliferation in prostate cancer cells. *Carcinogenesis.* 29:2279–2288. <http://dx.doi.org/10.1093/carcin/bgn221>

Bruce, M.C., V. Kanelis, F. Fouladkou, A. Debonneville, O. Staub, and D. Rotin. 2008. Regulation of Nedd4-2 self-ubiquitination and stability by a PY motif located within its HECT-domain. *Biochem. J.* 415:155–163. <http://dx.doi.org/10.1042/BJ20071708>

Choi, A.M., S.W. Ryter, and B. Levine. 2013. Autophagy in human health and disease. *N. Engl. J. Med.* 368:651–662. <http://dx.doi.org/10.1056/NEJMr1205406>

Ding, Y., Y. Zhang, C. Xu, Q.H. Tao, and Y.G. Chen. 2013. HECT domain-containing E3 ubiquitin ligase NEDD4L negatively regulates Wnt signaling by targeting dishevelled for proteasomal degradation. *J. Biol. Chem.* 288:8289–8298. <http://dx.doi.org/10.1074/jbc.M112.433185>

Dorsey, F.C., K.L. Rose, S. Coenen, S.M. Prater, V. Cavett, J.L. Cleveland, and J. Caldwell-Busby. 2009. Mapping the phosphorylation sites of Ulk1. *J. Proteome Res.* 8:5253–5263. <http://dx.doi.org/10.1021/pr900583m>

Fotia, A.B., D.I. Cook, and S. Kumar. 2006. The ubiquitin-protein ligases Nedd4 and Nedd4-2 show similar ubiquitin-conjugating enzyme specificities. *Int. J. Biochem. Cell Biol.* 38:472–479. <http://dx.doi.org/10.1016/j.biocel.2005.11.006>

Füllgrabe, J., M.A. Lynch-Day, N. Heldring, W. Li, R.B. Struijk, Q. Ma, O. Hermanson, M.G. Rosenfeld, D.J. Klionsky, and B. Joseph. 2013. The histone H4 lysine 16 acetyltransferase hMOF regulates the outcome of autophagy. *Nature.* 500:468–471. <http://dx.doi.org/10.1038/nature12313>

Gao, S., C. Alarcón, G. Sapkota, S. Rahman, P.Y. Chen, N. Goerner, M.J. Macias, H. Erdjument-Bromage, P. Tempst, and J. Massagué. 2009. Ubiquitin ligase Nedd4L targets activated Smad2/3 to limit TGF-beta signaling. *Mol. Cell.* 36:457–468. <http://dx.doi.org/10.1016/j.molcel.2009.09.043>

Geetha, T., J. Jiang, and M.W. Wooten. 2005. Lysine 63 polyubiquitination of the nerve growth factor receptor TrkA directs internalization and signaling. *Mol. Cell.* 20:301–312. <http://dx.doi.org/10.1016/j.molcel.2005.09.014>

Georgieva, M.V., Y. de Pablo, D. Sanchis, J.X. Comella, and M. Llovera. 2011. Ubiquitination of TrkA by Nedd4-2 regulates receptor lysosomal targeting and mediates receptor signaling. *J. Neurochem.* 117:479–493. <http://dx.doi.org/10.1111/j.1471-4159.2011.07218.x>

Goel, P., J.A. Manning, and S. Kumar. 2015. NEDD4-2 (NEDD4L): the ubiquitin ligase for multiple membrane proteins. *Gene.* 557:1–10. <http://dx.doi.org/10.1016/j.gene.2014.11.051>

Harvey, K.F., A. Dinudom, P. Komwatana, C.N. Jolliffe, M.L. Day, G. Parasivam, D.I. Cook, and S. Kumar. 1999. All three WW domains of murine Nedd4 are involved in the regulation of epithelial sodium channels by intracellular Na+. *J. Biol. Chem.* 274:12525–12530. <http://dx.doi.org/10.1074/jbc.274.18.12525>

Jiao, H., G.Q. Su, W. Dong, L. Zhang, W. Xie, L.M. Yao, P. Chen, Z.X. Wang, Y.C. Liou, and H. You. 2015. Chaperone-like protein p32 regulates ULK1 stability and autophagy. *Cell Death Differ.* 22:1812–1823. <http://dx.doi.org/10.1038/cdd.2015.34>

Joo, J.H., F.C. Dorsey, A. Joshi, K.M. Hennessy-Walters, K.L. Rose, K. McCastlain, J. Zhang, R. Iyengar, C.H. Jung, D.F. Suen, et al. 2011. Hsp90-Cdc37 chaperone complex regulates Ulk1- and Atg13-mediated mitophagy. *Mol. Cell.* 43:572–585. <http://dx.doi.org/10.1016/j.molcel.2011.06.018>

Joo, J.H., B. Wang, E. Frankel, L. Ge, L. Xu, R. Iyengar, X. Li-Harms, C. Wright, T.I. Shaw, T. Lindsten, et al. 2016. The noncanonical role of ULK/ATG1 in ER-to-Golgi trafficking is essential for cellular homeostasis. *Mol. Cell.* 62:491–506. <http://dx.doi.org/10.1016/j.molcel.2016.04.020>

Jung, C.H., C.B. Jun, S.H. Ro, Y.M. Kim, N.M. Otto, J. Cao, M. Kundu, and D.H. Kim. 2009. ULK-Atg13-FIP200 complexes mediate mTOR signaling to the autophagy machinery. *Mol. Biol. Cell.* 20:1992–2003. <http://dx.doi.org/10.1091/mbc.E08-12-1249>

Kim, H.C., and J.M. Huibregtse. 2009. Polyubiquitination by HECT E3s and the determinants of chain type specificity. *Mol. Cell Biol.* 29:3307–3318. <http://dx.doi.org/10.1128/MCB.00240-09>

Kim, J., M. Kundu, B. Viollet, and K.L. Guan. 2011. AMPK and mTOR regulate autophagy through direct phosphorylation of Ulk1. *Nat. Cell Biol.* 13:132–141. <http://dx.doi.org/10.1038/ncb2152>

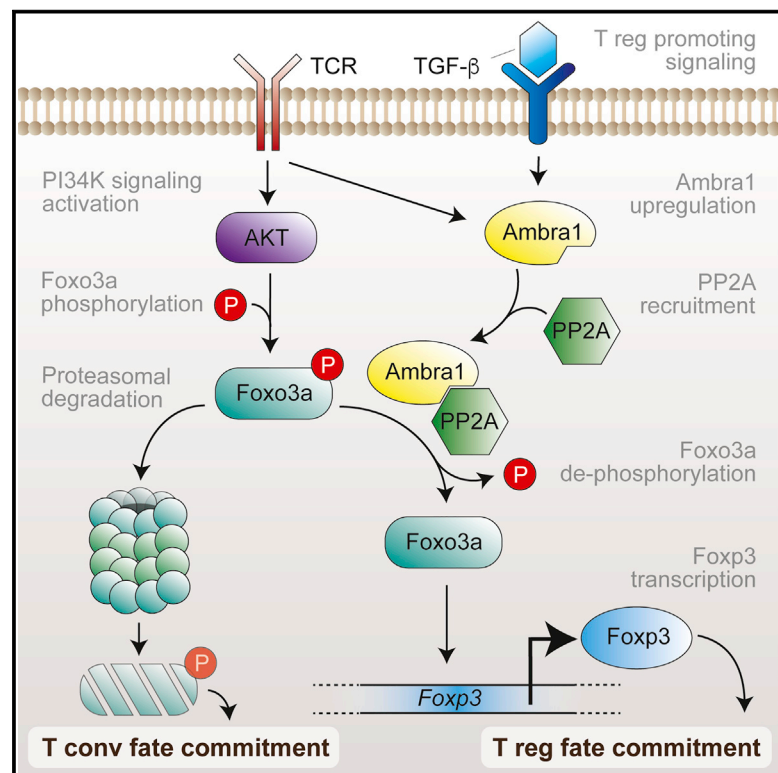
Kuang, E., J. Qi, and Z. Ronai. 2013. Emerging roles of E3 ubiquitin ligases in autophagy. *Trends Biochem. Sci.* 38:453–460. <http://dx.doi.org/10.1016/j.tubs.2013.06.008>

- Lee, I.H., A. Dinudom, A. Sanchez-Perez, S. Kumar, and D.I. Cook. 2007. Akt mediates the effect of insulin on epithelial sodium channels by inhibiting Nedd4-2. *J. Biol. Chem.* 282:29866–29873. <http://dx.doi.org/10.1074/jbc.M701923200>
- Léon, S., and R. Haguenauer-Tsapis. 2009. Ubiquitin ligase adaptors: regulators of ubiquitylation and endocytosis of plasma membrane proteins. *Exp. Cell Res.* 315:1574–1583. <http://dx.doi.org/10.1016/j.yexcr.2008.11.014>
- Li, J., W. Qi, G. Chen, D. Feng, J. Liu, B. Ma, C. Zhou, C. Mu, W. Zhang, Q. Chen, and Y. Zhu. 2015. Mitochondrial outer-membrane E3 ligase MUL1 ubiquitinates ULK1 and regulates selenite-induced mitophagy. *Autophagy*. 11:1216–1229. <http://dx.doi.org/10.1080/15548627.2015.1017180>
- Lin, S.Y., T.Y. Li, Q. Liu, C. Zhang, X. Li, Y. Chen, S.M. Zhang, G. Lian, Q. Liu, K. Ruan, et al. 2012. GSK3-TIP60-ULK1 signaling pathway links growth factor deprivation to autophagy. *Science*. 336:477–481. <http://dx.doi.org/10.1126/science.1217032>
- Liu, C.C., Y.C. Lin, Y.H. Chen, C.M. Chen, L.Y. Pang, H.A. Chen, P.R. Wu, M.Y. Lin, S.T. Jiang, T.F. Tsai, and R.H. Chen. 2016. Cul3-KLHL20 ubiquitin ligase governs the turnover of ULK1 and VPS34 complexes to control autophagy termination. *Mol. Cell*. 61:84–97. <http://dx.doi.org/10.1016/j.molcel.2015.11.001>
- Lu, Z., and T. Hunter. 2009. Degradation of activated protein kinases by ubiquitination. *Annu. Rev. Biochem.* 78:435–475. <http://dx.doi.org/10.1146/annurev.biochem.013008.092711>
- Lu, P.J., X.Z. Zhou, M. Shen, and K.P. Lu. 1999. Function of WW domains as phosphoserine- or phosphothreonine-binding modules. *Science*. 283:1325–1328. <http://dx.doi.org/10.1126/science.283.5406.1325>
- Ma, D., S. Panda, and J.D. Lin. 2011. Temporal orchestration of circadian autophagy rhythm by C/EBP β . *EMBO J.* 30:4642–4651. <http://dx.doi.org/10.1038/emboj.2011.322>
- Maspero, E., E. Valentini, S. Mari, V. Cecatiello, P. Soffientini, S. Pasqualato, and S. Polo. 2013. Structure of a ubiquitin-loaded HECT ligase reveals the molecular basis for catalytic priming. *Nat. Struct. Mol. Biol.* 20:696–701. <http://dx.doi.org/10.1038/nsmb.2566>
- Mizushima, N. 2010. The role of the Atg1/ULK1 complex in autophagy regulation. *Curr. Opin. Cell Biol.* 22:132–139. <http://dx.doi.org/10.1016/j.ccb.2009.12.004>
- Montaldo, C., C. Mancone, A. Conigliaro, A.M. Cozzolino, V. de Nonno, and M. Tripodi. 2014. SILAC labeling coupled to shotgun proteomics analysis of membrane proteins of liver stem/hepatocyte allows to candidate the inhibition of TGF-beta pathway as causal to differentiation. *Proteome Sci.* 12:15. <http://dx.doi.org/10.1186/1477-5956-12-15>
- Nazio, F., F. Strappazzon, M. Antonioli, P. Bielli, V. Cianfanelli, M. Bordi, C. Gretzmeier, J. Dengjel, M. Piacentini, G.M. Fimia, and F. Cecconi. 2013. mTOR inhibits autophagy by controlling ULK1 ubiquitylation, self-association and function through AMBRA1 and TRAF6. *Nat. Cell Biol.* 15:406–416. <http://dx.doi.org/10.1038/ncb2708>
- Noda, N.N., and Y. Fujioka. 2015. Atg1 family kinases in autophagy initiation. *Cell. Mol. Life Sci.* 72:3083–3096. <http://dx.doi.org/10.1007/s00018-015-1917-z>
- Orvedahl, A., R. Sumpter Jr., G. Xiao, A. Ng, Z. Zou, Y. Tang, M. Narimatsu, C. Gilpin, Q. Sun, M. Roth, et al. 2011. Image-based genome-wide siRNA screen identifies selective autophagy factors. *Nature*. 480:113–117. <http://dx.doi.org/10.1038/nature10546>
- Paronetto, M.P., F. Zalfa, F. Botti, R. Geremia, C. Bagni, and C. Sette. 2006. The nuclear RNA-binding protein Sam68 translocates to the cytoplasm and associates with the polysomes in mouse spermatocytes. *Mol. Biol. Cell*. 17:14–24. <http://dx.doi.org/10.1091/mbc.E05-06-0548>
- Perdomo, A.B., F. Ciccocanti, O.L. Iacono, C. Angeletti, M. Corazzari, N. Daniele, A. Testa, R. Pisa, G. Ippolito, G. Antonucci, et al. 2012. Liver protein profiling in chronic hepatitis C: identification of potential predictive markers for interferon therapy outcome. *J. Proteome Res.* 11:717–727. <http://dx.doi.org/10.1021/pr2006445>
- Petherick, K.J., O.J.L. Conway, C. Mpamhanga, S.A. Osborne, A. Kamal, B. Saxty, and I.G. Ganley. 2015. Pharmacological inhibition of ULK1 kinase blocks mammalian target of rapamycin (mTOR)-dependent autophagy. *J. Biol. Chem.* 290:11376–11383. <http://dx.doi.org/10.1074/jbc.C114.627778>
- Platta, H.W., H. Abrahamsen, S.B. Thoresen, and H. Stenmark. 2012. Nedd4-dependent lysine-11-linked polyubiquitination of the tumour suppressor Beclin 1. *Biochem. J.* 441:399–406. <http://dx.doi.org/10.1042/BJ20111424>
- Procaccini, C., V. De Rosa, M. Galgani, L. Abanni, G. Cali, A. Porcellini, F. Carbone, S. Fontana, T.L. Horvath, A. La Cava, and G. Matarese. 2010. An oscillatory switch in mTOR kinase activity sets regulatory T cell responsiveness. *Immunity*. 33:929–941. <http://dx.doi.org/10.1016/j.immuni.2010.11.024>
- Sahani, M.H., E. Itakura, and N. Mizushima. 2014. Expression of the autophagy substrate SQSTM1/p62 is restored during prolonged starvation depending on transcriptional upregulation and autophagy-derived amino acids. *Autophagy*. 10:431–441. <http://dx.doi.org/10.4161/auto.27344>
- Schiaffino, S., C. Mammucari, and M. Sandri. 2008. The role of autophagy in neonatal tissues: just a response to amino acid starvation? *Autophagy*. 4:727–730. <http://dx.doi.org/10.4161/auto.6143>
- Shearwin-Whyatt, L., H.E. Dalton, N. Foot, and S. Kumar. 2006. Regulation of functional diversity within the Nedd4 family by accessory and adaptor proteins. *BioEssays*. 28:617–628. <http://dx.doi.org/10.1002/bies.20422>
- Wirth, M., J. Joachim, and S.A. Tooze. 2013. Autophagosome formation—the role of ULK1 and Beclin1-PI3KC3 complexes in setting the stage. *Semin. Cancer Biol.* 23:301–309. <http://dx.doi.org/10.1016/j.semcancer.2013.05.007>
- Wong, P.M., Y. Feng, J. Wang, R. Shi, and X. Jiang. 2015. Regulation of autophagy by coordinated action of mTORC1 and protein phosphatase 2A. *Nat. Commun.* 6:8048. <http://dx.doi.org/10.1038/ncomms9048>
- Xia, P., S. Wang, G. Huang, Y. Du, P. Zhu, M. Li, and Z. Fan. 2014. RNF2 is recruited by WASH to ubiquitinate AMBRA1 leading to downregulation of autophagy. *Cell Res.* 24:943–958. <http://dx.doi.org/10.1038/cr.2014.85>
- Yang, B., and S. Kumar. 2010. Nedd4 and Nedd4-2: closely related ubiquitin-protein ligases with distinct physiological functions. *Cell Death Differ.* 17:68–77. <http://dx.doi.org/10.1038/cdd.2009.84>
- Yu, L., C.K. McPhee, L. Zheng, G.A. Mardones, Y. Rong, J. Peng, N. Mi, Y. Zhao, Z. Liu, F. Wan, et al. 2010. Termination of autophagy and reformation of lysosomes regulated by mTOR. *Nature*. 465:942–946. <http://dx.doi.org/10.1038/nature09076>
- Zhou, X., J.R. Babu, S. da Silva, Q. Shu, I.A. Graef, T. Oliver, T. Tomoda, T. Tani, M.W. Wooten, and F. Wang. 2007. Unc-51-like kinase 1/2-mediated endocytic processes regulate filopodia extension and branching of sensory axons. *Proc. Natl. Acad. Sci. USA*. 104:5842–5847. <http://dx.doi.org/10.1073/pnas.0701402104>

Developmental Cell

AMBRA1 Controls Regulatory T-Cell Differentiation and Homeostasis Upstream of the FOXO3-FOXP3 Axis

Graphical Abstract



Authors

Juliane Becher, Luca Simula, Elisabetta Volpe, ..., Franco Locatelli, Luca Battistini, Francesco Cecconi

Correspondence

cecconi@cancer.dk

In Brief

Regulatory T cells (T_{reg}) maintain immunological tolerance and help control autoimmune disease susceptibility. Becher et al. show pro-autophagy factor AMBRA1 regulates human and mouse T_{reg} differentiation and maintenance. AMBRA1 is upregulated in stimulated T cells to stabilize FOXO3 and has a protective effect in a mouse model of multiple sclerosis.

Highlights

- AMBRA1 is upregulated in stimulated T cells and correlates with FOXP3 expression
- AMBRA1 favors FOXP3 gene expression through positively regulating FOXO3
- Interaction of AMBRA1 with PP2A is required for stable FOXO3 protein expression
- Ambra1 depletion worsens disease pathogenesis in a mouse model of multiple sclerosis



AMBRA1 Controls Regulatory T-Cell Differentiation and Homeostasis Upstream of the FOXO3-FOXP3 Axis

Juliane Becher,^{1,17} Luca Simula,^{2,17} Elisabetta Volpe,¹ Claudio Procaccini,^{1,3} Claudia La Rocca,³ Pasquale D'Acunzo,² Valentina Cianfanelli,⁴ Flavie Strappazzon,^{1,5} Ignazio Caruana,² Francesca Nazio,² Gerrit Weber,² Vincenzo Gigantino,⁶ Gerardo Botti,⁶ Fabiola Ciccocanti,⁷ Giovanna Borsellino,¹ Silvia Campello,^{1,5} Georgia Mandolesi,¹ Marco De Bardi,¹ Gian Maria Fimia,^{7,8} Marcello D'Amelio,^{1,9} Francesca Ruffini,¹⁰ Roberto Furlan,¹⁰ Diego Centonze,^{11,12} Gianvito Martino,¹⁰ Paola Braghetta,¹³ Martina Chrisam,¹³ Paolo Bonaldo,^{13,14} Giuseppe Matarese,^{3,15} Franco Locatelli,^{2,16} Luca Battistini,¹ and Francesco Cecconi^{1,4,5,18,*}

¹IRCCS Fondazione Santa Lucia, Rome 00143, Italy

²Department of Pediatric Hemato-Oncology and cell and gene therapy, IRCCS Bambino Gesù Children's Hospital, Rome 00143, Italy

³Istituto per l'Endocrinologia e l'Oncologia Sperimentale, Consiglio Nazionale delle Ricerche (IEOS-CNR), Naples 80131, Italy

⁴Unit of Cell Stress and Survival, Danish Cancer Society Research Center, Copenhagen 2100, Denmark

⁵Department of Biology, University of Rome Tor Vergata, Rome 00133, Italy

⁶Unità di Patologia, Istituto Nazionale Tumori Fondazione "G. Pascale", Naples, Italy

⁷National Institute for Infectious Diseases IRCCS "L. Spallanzani", Rome 00149, Italy

⁸Department of Biological and Environmental Sciences and Technologies (DiSTeBA), University of Salento, Lecce 73100, Italy

⁹University Campus Bio-Medico, Rome, Italy

¹⁰Dipartimento di Ricerca Biologica e Tecnologia, Istituto Scientifico San Raffaele, Milan, Italy

¹¹Department of Systems Medicine, University of Rome Tor Vergata, Rome 00133, Italy

¹²Unit of Neurology and of Neurorehabilitation, IRCCS Neuromed, Pozzilli 86077 (IS), Italy

¹³Department of Molecular Medicine, Università Degli Studi di Padova, Padova 35131, Italy

¹⁴CRIBI Biotechnology Center, Università Degli Studi di Padova, Padova 35131, Italy

¹⁵Dipartimento di Medicina Molecolare e Biotecnologie Mediche, Università di Napoli "Federico II", Naples, Italy

¹⁶Department of Gynecology/Obstetrics and Pediatrics, Sapienza University of Rome, Italy

¹⁷These authors contributed equally

¹⁸Lead Contact

*Correspondence: cecconi@cancer.dk

<https://doi.org/10.1016/j.devcel.2018.11.010>

SUMMARY

Regulatory T cells (T_{reg}) are necessary to maintain immunological tolerance and are key players in the control of autoimmune disease susceptibility. Expression of the transcription factor FOXP3 is essential for differentiation of T_{reg} cells and indispensable for their suppressive function. However, there is still a lack of knowledge about the mechanisms underlying its regulation. Here, we demonstrate that pro-autophagy protein AMBRA1 is also a key modulator of T cells, regulating the complex network that leads to human T_{reg} differentiation and maintenance. Indeed, through its ability to interact with the phosphatase PP2A, AMBRA1 promotes the stability of the transcriptional activator FOXO3, which, in turn, triggers FOXP3 transcription. Furthermore, we found that AMBRA1 plays a significant role *in vivo* by regulating T_{reg} cell induction in mouse models of both tumor growth and multiple sclerosis, thus highlighting the role of AMBRA1 in the control of immune homeostasis.

INTRODUCTION

T regulatory cells (T_{reg}) are a unique T cell subset capable of suppressing the functions of effector T cells, preserving peripheral tolerance. They are primary actors in preventing excessive inflammation and the onset of autoimmune diseases, but they can also limit beneficial immune responses and antitumor immunity (Vignali et al., 2008). T_{reg} cells are characterized by the expression of their master regulator Forkhead box P3 (FOXP3), and loss of this transcription factor is associated with the onset of the fatal immune dysregulation, polyendocrinopathy, enteropathy, and X-linked (IPEX) syndrome (Wildin et al., 2001). T_{reg} cells are commonly classified in two subsets, natural occurring thymus-derived T_{reg} (nT_{reg}) and induced T_{reg} (iT_{reg}), which arise in the periphery of naive T cells (Horwitz et al., 2008), depending on the environmental signals present during activation (O'Shea and Paul, 2010). Conventional T cell (T_{conv}) activation has been associated with the activation of molecular target of rapamycin (mTOR) pathway, which is a central mediator of naive T cell differentiation. Indeed, mTOR integrates different environmental cues that promote T_{conv} , but not T_{reg} , cell commitment (Shi et al., 2011; Delgoffe et al., 2009), for example, by phosphorylating AKT on Ser473, which inversely correlates with T_{reg} differentiation (Delgoffe et al., 2009). Moreover,



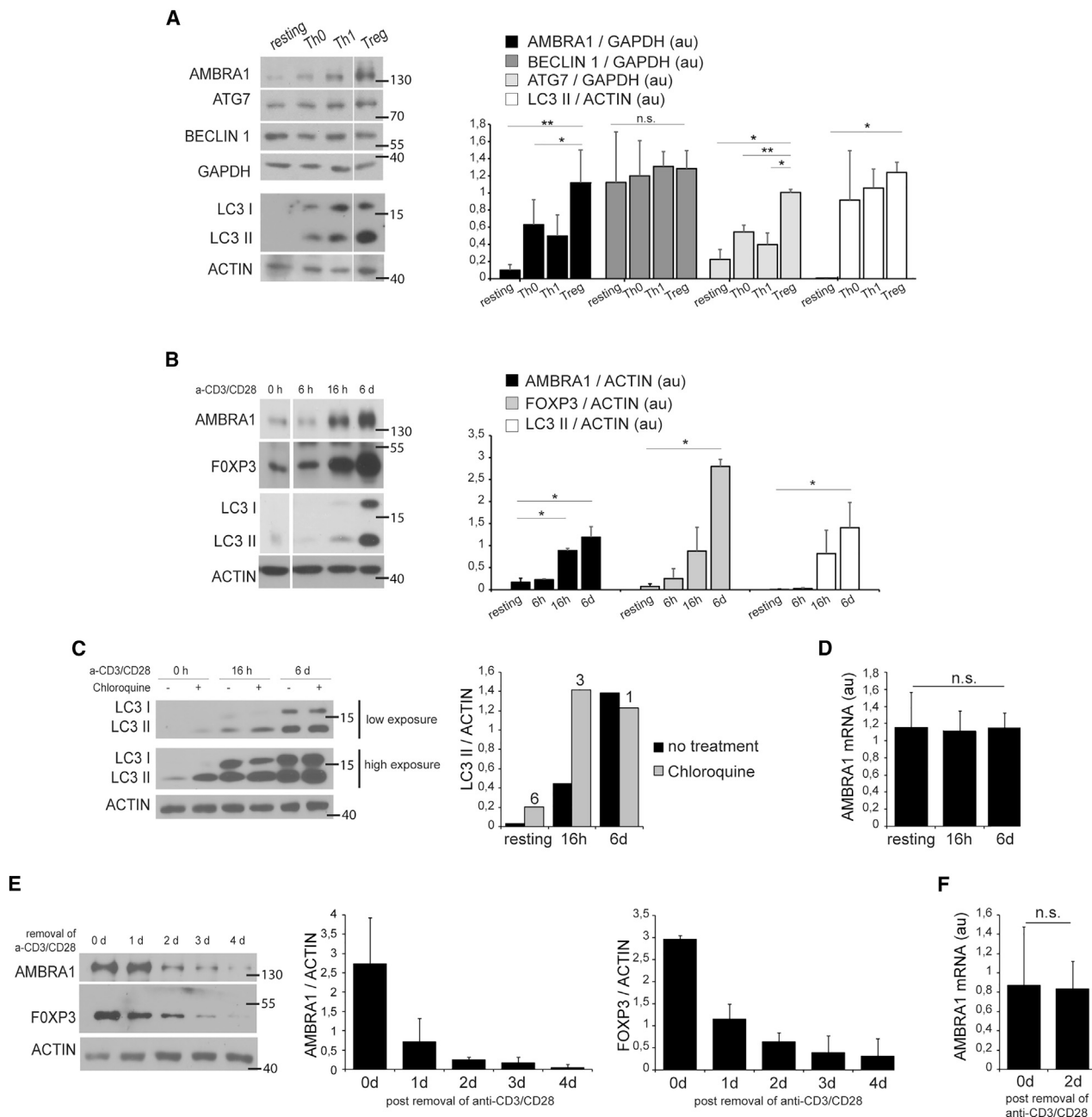


Figure 1. AMBRA1 Is Upregulated in Stimulated T Cells and Correlates with FOXP3 Expression in T_{reg}

(A) Resting *naïve* CD4⁺ T cells were stimulated by α -CD3/CD28 and polarized into T_{reg} and Th1 or in the absence of cytokines (Th0). Left panel: western blot of AMBRA1, ATG7, BECLIN 1, LC3, GAPDH, and Actin. Right panel: densitometry of AMBRA1 (n = 6), ATG7 (n = 3), BECLIN 1 (n = 6), and LC3 II (n = 4). Data are shown as mean \pm SEM. *p < 0.05; **p < 0.01.

(B) Left panel: AMBRA1, FOXP3, and LC3 were analyzed by western blot in resting *naïve* T cells, 6 hr, 16 hr, and 6 days after induction of T_{reg} polarization and normalized with actin. Right panel: densitometry of AMBRA1, FOXP3, and LC3 II (n = 3). Data are shown as mean \pm SEM. *p < 0.05.

(C) Resting *naïve* cells were stimulated for the indicated time with α -CD3/CD28 and either vehicle treated or treated with chloroquine for 1 hr. LC3 and ACTIN were analyzed by western blot. Right panel: densitometry of LC3 II over ACTIN. Numbers indicated above the columns show the fold increase of LC3 II upon chloroquine treatment. Results are representative of three independent experiments.

(D) AMBRA1 mRNA expression was analyzed by quantitative PCR in resting *naïve* T cells, 16 hr or 6 days after TCR stimulation under T_{reg} polarizing conditions. Cycling threshold values are normalized to those of mRNA encoding ribosomal protein L34. Results are representative of four independent experiments. Data are shown as mean \pm SEM. p > 0.05.

(E and F) *In vitro* polarized T_{reg} were depleted of α -CD3/CD28-coated beads to remove the TCR stimulus. AMBRA1 and FOXP3 were analyzed by western blot at 0, 1, 2, 3 and 4 days after anti-CD3/CD28 removal (E) (left panel). Densitometry of AMBRA1 and FOXP3 (right panels). Data are shown as mean \pm SEM. mRNA

(legend continued on next page)

mTOR has been associated with decreased T_{reg} proliferation, and its transient inhibition unlocks T_{reg} *in vitro* anergy and leads to their intensive proliferation (Procaccini et al., 2010).

Besides its role in controlling the cell cycle, mTOR is also the major inhibitor of autophagy, a lysosomal degradation pathway. Recently, T_{reg} -specific loss of either ATG5 or ATG7, two major players in autophagy, has been associated with breakdown of self-tolerance, facilitating tumor clearance (Wei et al., 2016). Consistently, ATG7 deficiency leads to decreased T_{reg} lineage stability, accompanied by upregulation of the mTOR pathway, as well as by increased c-Myc expression (Wei et al., 2016). Furthermore, autophagy has been shown to be involved in global T cell homeostasis. While autophagy is crucial to promote *naive* $CD4^+$ T cell survival by mitochondria quality control (Willinger and Flavell, 2012), $CD4^+$ T cells from *Atg7*- or *Beclin 1*-defective mice are characterized by failure of T cell activation, caused by impaired proliferation (*Atg7*^{-/-}) or increased cell death (*Beclin 1*^{-/-}) (Kovacs et al., 2012; Hubbard et al., 2010). Of note, we showed that, in the presence of excessive TCR stimulation igniting activation-induced cell death, a block of macroautophagy takes place (Corrado et al., 2016). However, little is known about the role of autophagy and autophagy-related genes in T cell commitment of *naive* $CD4^+$ T cells.

AMBRA1 (autophagy and beclin 1 regulator 1) is inhibited by mTOR (Nazio et al., 2013), and it promotes autophagy both by triggering the functional interaction of BECLIN 1 and VPS34 (Di Bartolomeo et al., 2010; Fimia et al., 2007) and by regulating the kinase ULK1 (Nazio et al., 2013), which plays a key role in auto-phagosome formation. Further, AMBRA1 regulates the cross-talk among autophagy, cell proliferation, and cell death (Strappazon et al., 2016; Cianfanelli et al., 2015; Strappazon et al., 2015; Yazdankhah et al., 2014; Strappazon et al., 2011). Indeed, its interaction with the phosphatase PP2A promotes oncogene c-Myc dephosphorylation, resulting in inhibition of cell proliferation (Cianfanelli et al., 2015).

Here, we identified AMBRA1 as a protein specifically upregulated in activated T cells due to a TCR-dependent mechanism. Indeed, when we induced *naive* T cells to differentiate, AMBRA1 was found to be crucial in inducing T_{reg} fate. By dissecting the molecular pathway behind this induction, we found AMBRA1 to be necessary for PP2A-dependent and stable *FOXP3* gene expression, through positive regulation of FOXO3. Interestingly, murine *Ambra1* is crucial for the proper induction of both nT_{reg} and iT_{reg} cells *in vivo* and their accumulation and function in mouse models of both tumor growth and inflammation. In addition, we demonstrated that *Ambra1* plays a protective role in murine experimental autoimmune encephalomyelitis (EAE) *in vivo*, further highlighting a key role for this molecule in anti-inflammatory responses.

RESULTS

AMBRA1 Is Strongly Upregulated during T_{reg} Differentiation

T_{reg} cells are characterized by a high rate of autophagy, which is necessary for their lineage stability (Wei et al., 2016). This evi-

dence prompted us to also investigate the role of key autophagy regulators during T_{reg} differentiation. With this aim, we stimulated *naive* human T cells *in vitro* through TCR in different polarizing conditions (Figure S1A) and monitored the expression of three different autophagy proteins (Figure 1A). We found BECLIN 1 to be invariably expressed at high levels in resting *naive* T cells and in T cells stimulated and differentiated *in vitro*. In contrast, AMBRA1 protein appeared to be expressed at low levels in resting T cells but to be strongly upregulated after *in vitro* stimulation and differentiation. Of note, stimulation in the absence of cytokines (Th0) was sufficient to induce AMBRA1 upregulation. Remarkably, when compared with cells polarized toward Th0 or Th1 phenotype, differentiation into T_{reg} triggered an even stronger induction of AMBRA1 (Figure 1A). Lastly, ATG7 was also upregulated after *in vitro* stimulation and differentiation, and this effect was stronger in T_{reg} rather than in Th1-polarizing conditions (Figure 1A). However, ATG7 underwent considerably less pronounced induction when compared to AMBRA1. In line with AMBRA1 expression, while resting T cells exhibited low levels of LC3, after *in vitro* stimulation and differentiation, a strong increase in LC3 expression (both LC3 I and LC3 II forms) has been observed (Figure 1A).

Based on these observations, we can conclude that autophagy is strongly regulated during T-cell stimulation and differentiation, with AMBRA1 being a good candidate to play a role in these processes.

AMBRA1 Regulation in T Cell Polarization Depends on TCR Signaling, while It Is Independent on Transcriptional Regulation

Since autophagy is necessary for T_{reg} lineage stability (Wei et al., 2016) and AMBRA1 expression increased after polarization into T_{reg} , we focused on its role during T_{reg} differentiation. We thus found that upregulation of AMBRA1 and LC3 (both LC3 I and LC3 II isoforms) occurred 16 hr after T cell stimulation in T_{reg} -polarizing conditions (Figure 1B). Notably, AMBRA1 upregulation correlated with the increased expression of the T_{reg} transcription factor FOXP3 and further enhanced after 6 days of stimulation, raising the question whether FOXP3 could be responsible for this event. Further, in order to ascertain whether autophagy signaling in FOXP3-positive cells was followed by autophagy progression and verify the on-rate/off-rate ratio of autophagy, we analyzed the autophagy flux by blocking the lysosomal function. Interestingly, while an active autophagy flux could be observed in resting *naive* T cells, autophagy slowed down 16 hr after stimulation and was blocked after 6 days in polarized T_{reg} cells, independent of the drugs we used (Figures 1C and S1B). This could be probably ascribed to an increase in cell proliferation, since it has been recently shown that autophagy is blocked rather than activated in proliferating T cells (Xu et al., 2014). Of note, the upregulation of AMBRA1 on T cell stimulation did not depend on such a block in the autophagy flux, since AMBRA1 was not degraded by the autophagic machinery in resting T cells (Figure S1C).

expression of AMBRA1 was analyzed in polarized T_{reg} and 2 days after the removal of anti-CD3/CD28 (F). Cycling threshold values are normalized to those of mRNA encoding ribosomal protein L34. Molecular weights are indicated at the right side of each western blot image. Results are representative of three independent experiments. Data are shown as mean \pm SEM. $p > 0.05$. See also Figure S1.

To understand the nature of *AMBRA1* upregulation, we next checked *AMBRA1* mRNA expression in resting *naive* T cells and after stimulation under T_{reg} -polarizing conditions. In contrast to the strong upregulation of its protein levels, *AMBRA1* mRNA levels appear to be unaffected by T cell stimulation (Figure 1D). This argues against a transcriptional role of FOXP3 in *AMBRA1* upregulation following T cell stimulation. To further validate the correlation between upregulation of *AMBRA1* protein levels, T cell stimulation, and FOXP3 expression, we removed the TCR stimulus from *in vitro* polarized T_{reg} cells and measured the levels of FOXP3 and *AMBRA1*. Interestingly, we found that removal of TCR stimulus was associated with a substantial decrease in FOXP3 and *AMBRA1* protein levels after 2 days of culture (Figure 1E). In line with our observations in stimulated T_{reg} cells, *AMBRA1* mRNA levels did not undergo any significant changes also upon removal of the T cell stimulus (Figure 1F). Lastly, *AMBRA1* is nearly absent in freshly isolated human T_{reg} cells (Figure S1D), and this finding further suggested that its expression requires direct TCR stimulation.

Taken together, these results strongly suggest that *AMBRA1* is associated with T_{reg} cell differentiation, with its protein levels being increased by TCR signaling, independent of its mRNA transcription.

AMBRA1 Positively Regulates FOXP3 Expression

Given the strong correlation between *AMBRA1* and FOXP3, we next chose to investigate whether *AMBRA1* could regulate the expression of FOXP3. With this aim, we downregulated *AMBRA1* during T_{reg} differentiation by lentiviral transduction of an *AMBRA1*-interfering short hairpin RNA (shRNA). Interestingly, we observed a strong decrease in T_{reg} differentiation in cells lacking *AMBRA1*, as testified by a significant decrease in FOXP3 protein levels (Figures 2A and 2B), suggesting a positive role of *AMBRA1* in T_{reg} differentiation. Moreover, confocal microscope analysis revealed co-expression of *AMBRA1* and FOXP3 in the same cells in control conditions (Figure 2C). Of note, *AMBRA1* expression was not restricted to cells expressing FOXP3. In contrast, in cells deficient in *AMBRA1*, we detected a neat decrease in FOXP3 positivity (Figure 2C).

Next, we investigated whether *AMBRA1* specifically acted on T_{reg} cells during differentiation or whether it impacted FOXP3 levels also in already differentiated T_{reg} cells. With this aim, we differentiated T_{reg} cells *in vitro* and then infected them, as described above, to downregulate *AMBRA1* expression. We then cultured T_{reg} cells in the presence of interleukin-2 (IL-2) alone, a cytokine crucial for their proliferation (Battaglia et al., 2005), or in combination with transforming growth factor β (TGF- β), which is necessary to maintain FOXP3 transcription in induced T_{reg} (Marie et al., 2005). Similar to what was observed during T_{reg} differentiation, *AMBRA1* was also necessary to maintain FOXP3 levels in differentiated T_{reg} cells, cultured in the presence of either IL-2 or IL-2 and TGF- β (Figure 2D). Subsequently, we checked whether the observed effect of *AMBRA1* on FOXP3 could be due to the regulation of FOXP3 transcriptional levels and found that *FOXP3* mRNA was, indeed, downregulated in *AMBRA1*-defective cells (Figure 2E). Furthermore, we were able to rule out that *AMBRA1* deficiency was associated with an unspecific downregulation of any differentiation factors. Indeed, under the same T_{reg} -polarizing conditions, *AMBRA1*-

interfered cells did not show decreased levels of T-BET (which is rather upregulated), another transcription factor recently described as having also a role in T_{reg} cells (Levine et al., 2017) (Figure S2A).

Further, we investigated whether *AMBRA1* deficiency was associated with an altered cytokine secretion profile in T cells. However, no significant increase in the production of the effector cytokines IL-17 and interferon (IFN)- γ could be detected (Figures S2B and S2C).

Thus, it can be concluded that *AMBRA1* plays a role in T_{reg} differentiation and maintenance by specifically and positively regulating FOXP3 transcription.

AMBRA1 Regulates FOXP3 through FOXO3

FOXP3 can be transcriptionally regulated by different factors, among which a key role is played by its prominent activator FOXO3 (Harada et al., 2010; Kerdales et al., 2010; Ouyang et al., 2010), whose transcriptional activity can be negatively regulated by post-translational phosphorylation events. In this context, one of its main negative regulators is AKT, which phosphorylates FOXO3 on at least two major sites, Ser253 (S253) and Thr32 (T32), leading to its degradation or cytosolic sequestration (Plas and Thompson, 2003; Brunet et al., 1999). Interestingly, T cells grown under T_{reg} -polarizing conditions, in which *AMBRA1* was downregulated, exhibit significantly decreased levels of total FOXO3 (Figure 3A), which cannot be ascribed to its transcriptional downregulation (Figure 3B).

Primed by this evidence, we checked whether, upon *AMBRA1* downregulation, FOXO3 decrease could be related to its phosphorylation on S253 and T32 (Plas and Thompson, 2003; Brunet et al., 1999). Indeed, we found that there was a significant increase in the ratio between phospho-S253 FOXO3 and total FOXO3 upon *AMBRA1* downregulation under T_{reg} -polarizing conditions (Figure 3A), while phospho-T32 FOXO3 was not altered (Figure 3C). Of note, AKT phosphorylation at T308, a hallmark of activation for this kinase (Alessi et al., 1997), also appeared to be unaffected by *AMBRA1* regulation (Figure 3A), raising the question whether the increase in phospho-S253 FOXO3, observed upon *AMBRA1* knockdown was due to a decreased phosphatase activity rather than to an increased AKT (or other kinases) activity.

Lastly, we checked, by confocal microscope analysis, *AMBRA1*-defective T_{reg} for total FOXO3 protein levels or intracellular distribution, both parameters being potentially altered by its phosphorylation at S253 (Plas and Thompson, 2003). Indeed, we detected a strong global decrease in FOXO3, associated with *AMBRA1* downregulation (Figure 3D).

Overall, our results establish *AMBRA1* as a positive regulator of FOXO3, acting by mediating the modulation of its phospho-S253 status.

AMBRA1 Controls FOXO3 through Its Interaction with PP2A

As mentioned above, our findings cannot rule out whether other kinases rather than AKT (as ERK [Yang et al., 2008] or others [Hu et al., 2004; Rena et al., 2002]) or dephosphorylation events could affect various FOXO3 residues. Such modifications would be associated with changes in its stability and thus, eventually, may account for the difference we detected in *AMBRA1*-deficient

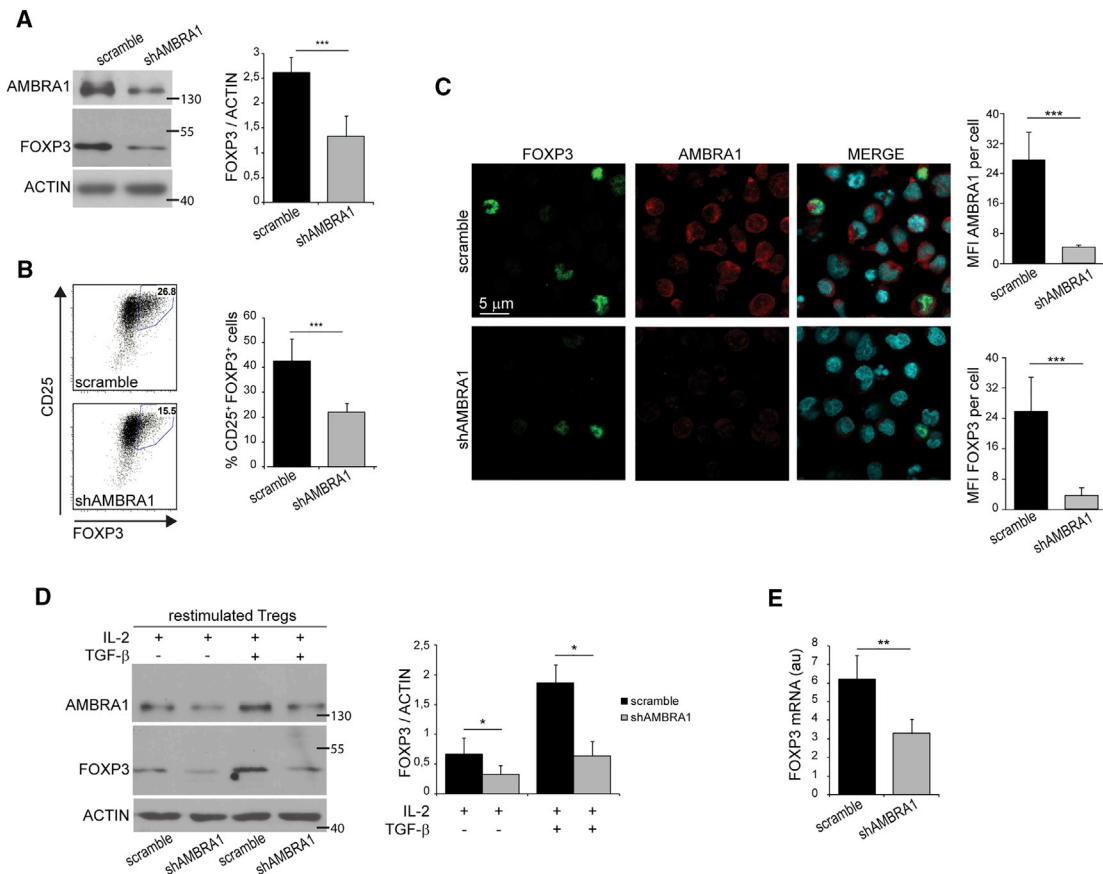


Figure 2. AMBRA1 Is Necessary for the Expression of FOXP3 in Regulatory T Cells Differentiated *In Vitro*

Naive CD4⁺ T cells were transduced with lentivirus-expressing shRNA against AMBRA1 or a scramble construct and cultured for 6 days under regulatory T cell-polarizing conditions.

(A) Western blot of AMBRA1, FOXP3, and ACTIN. Densitometry of FOXP3 is shown in the right panel (n = 9). Data are shown as mean ± SEM. ***p < 0.001.

(B) Percentage of CD25⁺ and FOXP3⁺ cells gated on live dead negative and CD4⁺ cells was analyzed by flow cytometry. Data are shown as mean ± SEM. ***p < 0.001, n = 6.

(C) AMBRA1 and FOXP3 were analyzed by confocal microscopy. FOXP3 is shown in green, AMBRA1 in red, and nuclei were stained with DAPI. Quantifications of the AMBRA1 and FOXP3 median fluorescence indexes (MFI) per cell are reported in the graphs on the right; ***p < 0.001; n = 3. Scale bar = 5 μm.

(D) Naive T cells were transduced and polarized as in (A). After 6 days, anti-CD3/CD28 was removed, and cells were re-stimulated for another 5 days with anti-CD3/CD28 in the presence of IL-2 only or IL-2 plus TGF-β. AMBRA1, FOXP3, and ACTIN were analyzed by western blot (left panel). Densitometry of FOXP3 (right panel). Data are shown as mean ± SEM. *p < 0.05, n = 3.

(E) FOXP3 mRNA expression of *in vitro* polarized T_{reg} transduced as in (A) was analyzed by qPCR. Cycling threshold values are normalized to those of mRNA encoding ribosomal protein L34. Molecular weights are indicated at the right side of each western blot image. Data are shown as mean ± SEM. **p < 0.01; n = 9. See also Figure S2.

versus -proficient conditions. In this context, interestingly, we have recently shown that AMBRA1 directly interacts with the protein phosphatase PP2A, negatively regulating cell proliferation (Cianfanelli et al., 2015). Indeed, PP2A can not only dephosphorylate and inactivate AKT (Kuo et al., 2008) but can also directly remove the S253 inhibitory phosphorylation of FOXO3, thereby restoring its activity (Singh et al., 2010). Due to the existing interplay between AMBRA1 and PP2A, we thus checked whether the impact of AMBRA1 on FOXO3 was due to its ability to bind and positively regulate PP2A. With this aim, we switched to HeLa cells, a cellular model in which multiple molecular manipulations can be performed simultaneously, with limited impact on cell viability. There, we (1) downregulated AMBRA1 using a small interfering RNA and subsequently (2) overexpressed a construct

carrying either AMBRA1-wild-type (AMBRA1^{WT}) or AMBRA1^{PXP}, a mutant form that has lost its ability to bind PP2A (Cianfanelli et al., 2015). In line with our previous results in primary T cells, downregulation of AMBRA1 in HeLa cells led to a significant decrease in FOXO3 levels and a relative increase in the phosphorylation of FOXO3 at S253 (Figure 3E). Strikingly, this effect could be abolished by overexpression of AMBRA1^{WT}, while overexpression of AMBRA1^{PXP} could not counteract the effect of AMBRA1 downregulation on FOXO3 levels and its relative phosphorylation status (Figure 3E).

We then checked whether the decrease in FOXO3 associated with AMBRA1 loss was a result of increased proteasomal degradation. FOXO3 half-life was thus examined using the protein synthesis inhibitor cycloheximide (CHX). Decrease in FOXO3 could

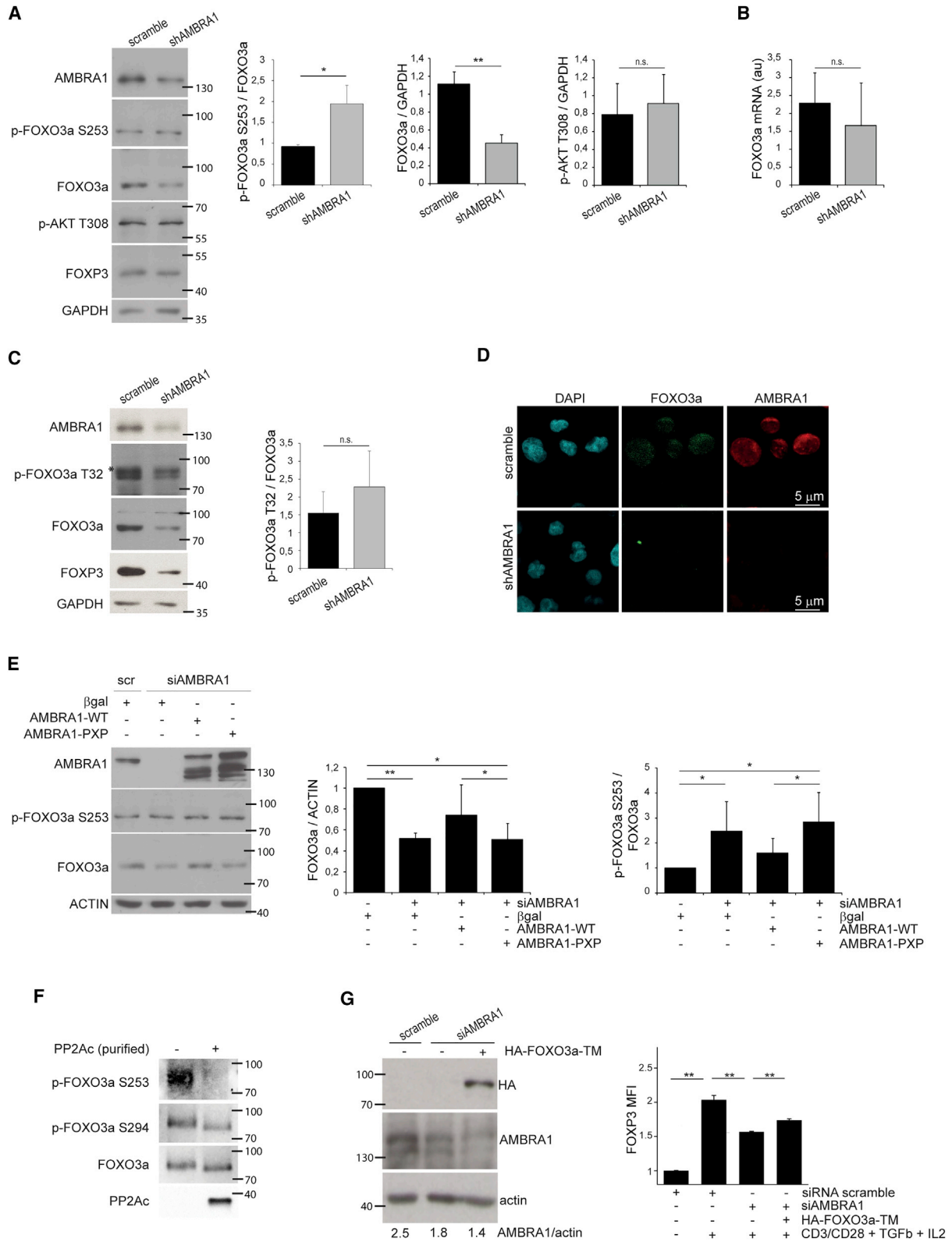


Figure 3. The FOXP3 Activating Transcription Factor FOXO3 Is Positively Regulated by AMBRA1

Naive CD4⁺ T cells were transduced with lentivirus expressing shRNA against AMBRA1 or a scramble construct and cultured for 6 days under regulatory T cell-polarizing conditions.

(legend continued on next page)

be observed in control cells following CHX treatment, and this was even more rapid in *AMBRA1*-deficient cells (Figure S3A). Additionally, treatment of *AMBRA1*-deficient cells with the proteasome inhibitor MG-132 led to a robust accumulation of FOXO3 (Figure S3B), suggesting that lack of *AMBRA1* results in proteasomal degradation of FOXO3.

Of note, an additional phosphorylation event on Ser294 (S294), triggered in this case by the kinase ERK, targets FOXO3 to the proteasome (Yang et al., 2008), even though little is known about the phosphatase that can remove this inhibitory phosphorylation. To investigate this issue, we evaluated primary T cells and assessed the phosphorylation of FOXO3 on S294 in *AMBRA1*-proficient or -deficient conditions. Indeed, we could detect neither a significant increase of phospho-S294 FOXO3 on total FOXO3 (Figure S3C) nor any significant difference in the phosphorylation of ERK1/2 between *AMBRA1*-deficient and control T_{reg} (Figure S3C). We therefore determined, by means of an *in vitro* phosphatase assay, whether PP2A could be responsible for dephosphorylating FOXO3 at S294. With this aim, we incubated FOXO3 immunoprecipitates with recombinant PP2A. While S253 was strongly dephosphorylated by PP2A (as in Singh et al. (2010)), S294 appears not to be a PP2A target site (Figure 3F), confirming that the latter site is not involved in FOXO3 regulation in our systems.

Interestingly, an increase in the known *AMBRA1*-PP2A target c-Myc (Cianfanelli et al., 2015) that can be observed on ATG7 ablation has been correlated to decreased T_{reg} lineage stability (Wei et al., 2016). In line with our previous results (Cianfanelli et al., 2015), we detected a significant increase in c-Myc in *AMBRA1*-deficient T cells polarized under T_{reg} conditions (Figure S3D). This may argue for opposite roles of c-Myc and FOXO3a in T_{reg} homeostasis.

Lastly, we demonstrated that, in T_{reg} cells, FOXO3 is the key mediator of the *AMBRA1*-mediated regulation of FOXP3 expression. Indeed, overexpression of an active form of FOXO3a (triple mutant [TM], in which all three previously mentioned phospho-residues were mutated into alanine) was able to rescue FOXP3 expression in *AMBRA1*-silenced cells (Figure 3G).

Altogether, our results let us conclude that *AMBRA1* regulates PP2A activity on S253 of FOXO3, protecting FOXO3 from intracellular degradation.

The Regulation on FOXP3 Expression Is *AMBRA1* Specific

To understand whether the observed effects on T_{reg} development and homeostasis were specific for *AMBRA1*, and not related to a global effect of the observed positive signaling of autophagy (see Figures 1A and 1B), we knocked down other autophagy genes in differentiating T cells. Indeed, lentiviral knockout (KO) of BECLIN 1 led to a slight but not significant decrease in FOXP3 protein expression after *in vitro* polarization under T_{reg}-polarizing conditions (Figure 4A). Furthermore, different from the effect of *AMBRA1* inhibition, we could not observe any change in the levels of T-BET and in the phosphorylation of FOXO3 (Figure 4C), suggesting that BECLIN 1 does not act on the same pathway of *AMBRA1* in this context. We next tested the impact of ATG7 knockdown on FOXP3; ATG7 is not part of the upstream VPS34 complex but is involved in autophagy progression and has been shown to be crucial for T_{reg} survival and stability (Wei et al., 2016). Even in this case, we found that differentiation of naive T cells under T_{reg}-polarizing conditions was not influenced by ATG7 (Figure 4B). This indicates a role of ATG7 during T_{reg} differentiation distinct to that previously described in maintaining lineage (Wei et al., 2016). Concomitantly, no significant changes were detected in either FOXO3 levels or phosphorylation of FOXO3 on Ser253 on ATG7 depletion (Figure 4D).

In brief, we can conclude that the observed positive impact on FOXO3/FOXP3 and T_{reg} differentiation seems to be specific for *AMBRA1*, among key pro-autophagy genes, and it does not depend on global autophagy regulation.

Ambra1 Deficiency Impacts T_{reg} Functionality Also *In Vivo*

Given the role of *AMBRA1* in sustaining T_{reg} differentiation via FOXP3 upregulation *in vitro*, we next asked whether this protein could regulate T_{reg} cell induction also *in vivo*. First, we analyzed the phenotype of *Ambra1* conditional KO mice (*Ambra1*^{fl/fl;cre+}), in which this protein is specifically removed only from the T cell lineage, thanks to the Cre recombinase expression controlled by the Lck promoter (Figure S4A). Although we observed a normal percentage of Foxp3⁺CD25⁺ T_{reg} cells in all lymphoid organs (Figure 5A), we found that Foxp3 expression was significantly downregulated on a per cell basis in *Ambra1*-deficient

(A) Western blot of *AMBRA1*, p-FOXO3 S253, FOXO3, p-AKT T308, FOXP3, and ACTIN (left panel) and quantification by densitometry (right panels). Data are shown as mean ± SEM. **p < 0.01, n = 4.

(B) mRNA expression of FOXO3 was analyzed by qPCR. Cycling threshold values are normalized to those of mRNA encoding ribosomal protein L34. Data are shown as mean ± SEM. p > 0.05, n = 9.

(C) Western blot of *AMBRA1*, p-FOXO3 T32, FOXO3, FOXP3, and GAPDH (left panel, asterisk indicates p-FOXO3 T32 band). Densitometry of p-FOXO3 T32/FOXO3 (right panel). Data are shown as mean ± SEM. p > 0.05, n = 4.

(D) Representative images of cells stained with anti-*AMBRA1* in red and anti-FOXO3 in green and analyzed at confocal microscope (number of cells analyzed: 99 scramble and 85 sh*AMBRA1*, n = 2; scale bar = 5 μm).

(E) HeLa cells were transfected with a control siRNA or a siRNA against *AMBRA1* and subsequently with a plasmid overexpressing β-Gal, *AMBRA1*-WT, or *AMBRA1*-PXP. Western blot of *AMBRA1*, p-FOXO3 S253, and ACTIN (left panel). Quantification of protein bands is shown in the right panel. *p < 0.05; **p < 0.01, n = 5.

(F) *In vitro* phosphatase assay of FOXO3 from Jurkat cells. Phosphatase activity of PP2A on FOXO3 was analyzed by western blot using antibodies against FOXO3, p-FOXO3 S253, p-FOXO3 S294, and PP2A-c. Results are representative of three independent experiments.

(G) Jurkat cells were electroporated with scramble siRNA or siRNA against *AMBRA1* and then, after 24 hr, electroporated again with either empty vector (-) or HA-FOXO3a-TM plasmid. Cells have been stimulated or not o.n. with α-CD3/CD28-coated beads in the presence of IL-2 and TGF-β and subsequently analyzed for *AMBRA1* and HA-tag expression (western blot, on the left) or FOXP3 median fluorescence index (cytofluorimetric analysis, on the right). Molecular weights are indicated at the right side of each western blot image. Data are shown as mean ± SEM. **p < 0.01; n = 3.

See also Figure S3.

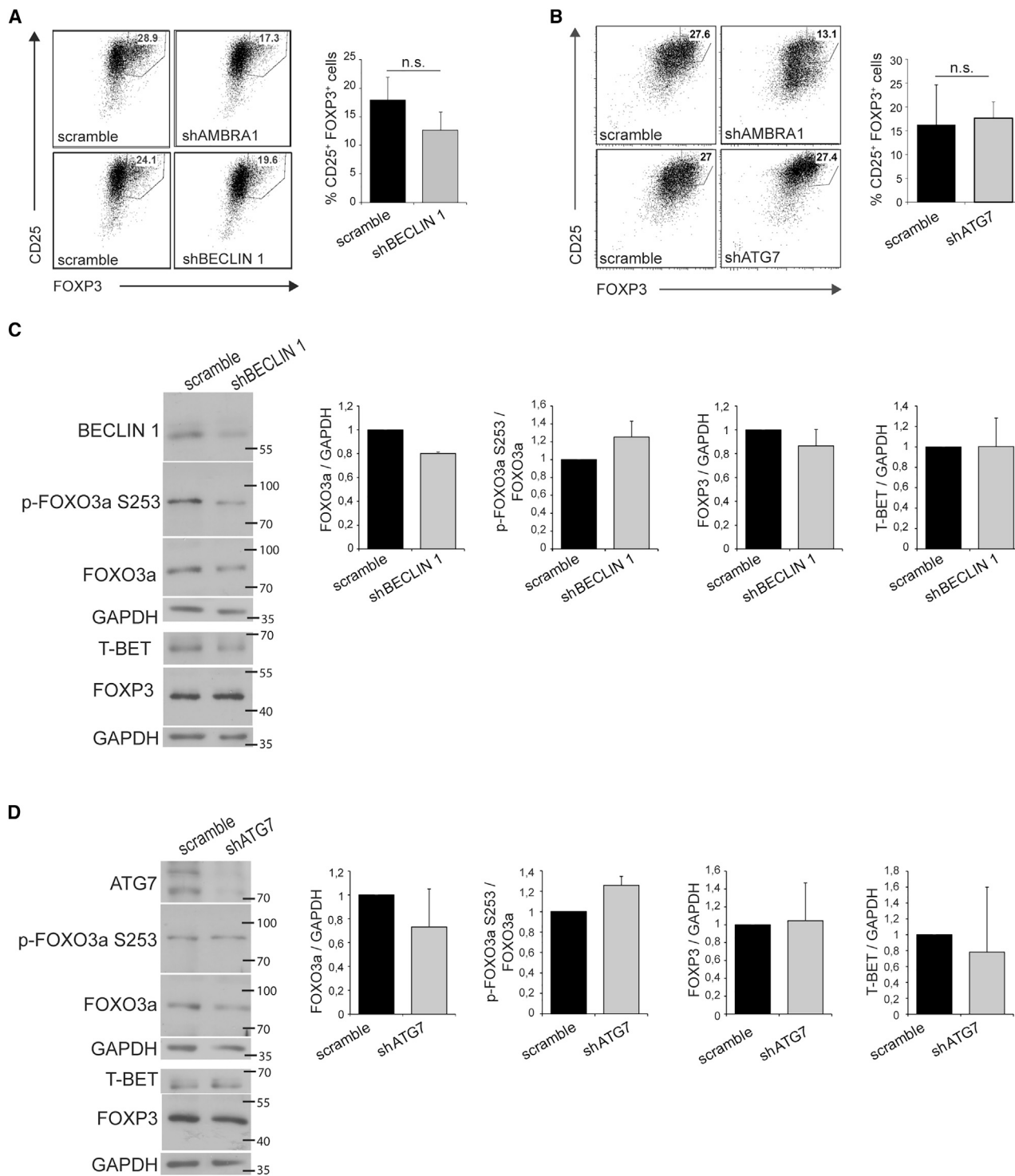


Figure 4. FOXP3 Expression Is Not Dependent on the Autophagic Proteins BECLIN 1 and ATG7

Naive T cells were infected with an shRNA expressing lentiviral construct specific for BECLIN 1 or ATG7, respectively, and cultured for 6 days under regulatory T cell-polarizing conditions. Infection with an shRNA expressing lentiviral construct against AMBRA1 served as a positive control.

(A and B) Percentage of CD25⁺ and FOXP3⁺ cells gated on live dead negative and CD4⁺ cells was analyzed by flow cytometry in BECLIN 1 (A) or ATG7 (B) defective cells. Data are shown as mean \pm SEM, $p > 0.05$; $n = 4$.

(C and D) BECLIN 1, ATG7, p-FOXO3 S253, FOXO3, FOXP3, T-BET, and GAPDH were analyzed by western blot of protein lysates from BECLIN 1 (C) or ATG7 (D) defective cells (left panel). Densitometric analysis is shown in the right panels. Molecular weights are indicated at the right side of each western blot image. Data are shown as mean \pm SEM. $p > 0.05$; $n = 4$.

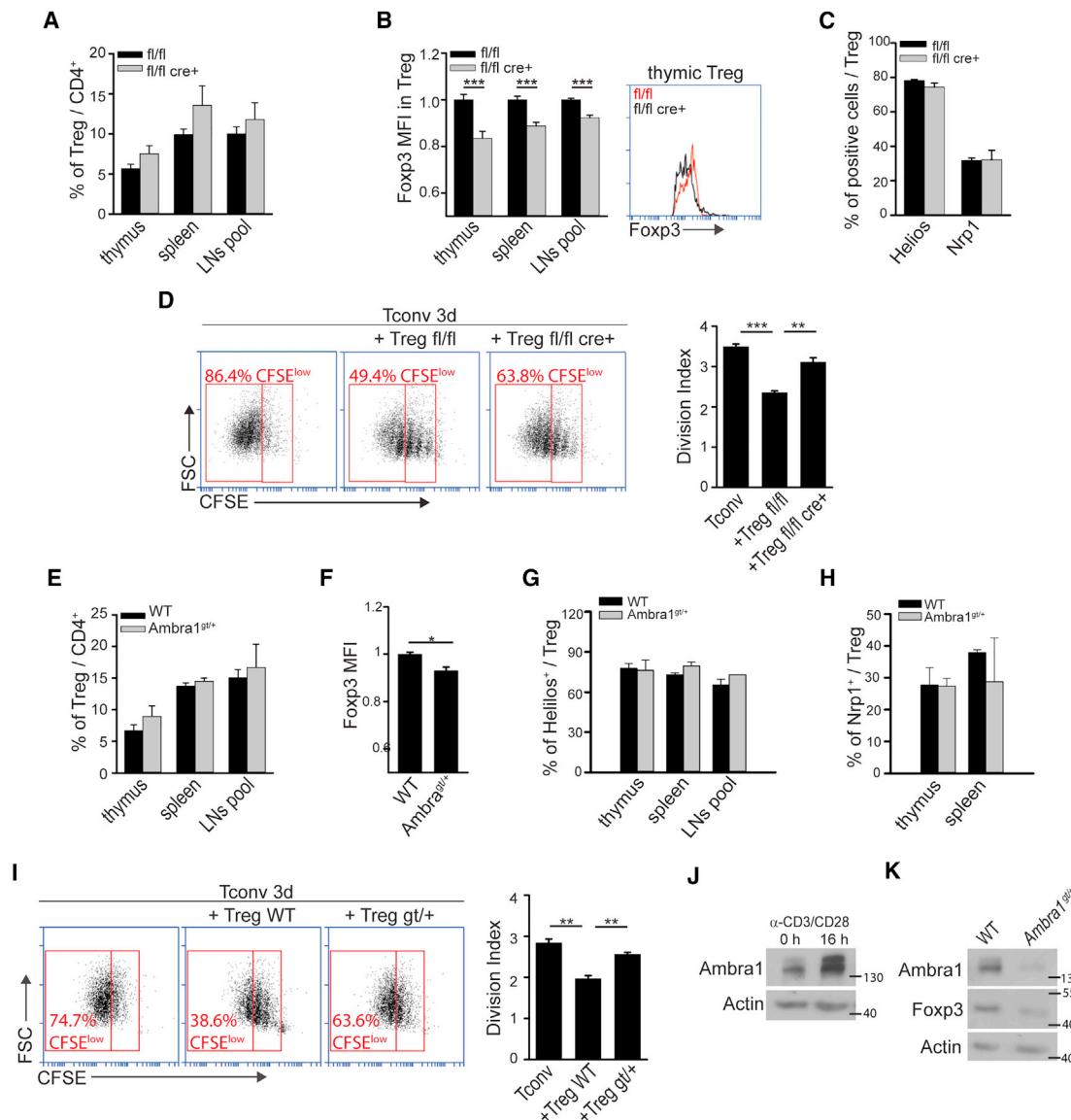


Figure 5. AMBRA1 Is Required for the Generation and Functionality of T_{reg} Cells *In Vivo*

(A and E) Cytofluorimetric analysis of the percentage of CD25⁺ Foxp3⁺ T_{regs} among CD4⁺ T cells from thymus, spleen, and lymph nodes (LNs pool) from *Ambra1*^{fl/fl;cre+} (n = 6) and *Ambra1*^{fl/fl} mice (n = 5) (A) or from *Ambra1*^{gt/+} (n = 7) and WT (n = 5) mice (E). (B and F) Foxp3 median fluorescence index (MFI) in CD4⁺ CD25⁺ Foxp3⁺ T_{regs} from thymus, spleen, and lymph nodes (LNs pool) from *Ambra1*^{fl/fl;cre+} (n = 7) and *Ambra1*^{fl/fl} mice (n = 6) (B) or from spleen of *Ambra1*^{gt/+} (n = 3) and WT (n = 2) mice (F). *p < 0.05; ***p < 0.001. (C) Percentage of thymic Foxp3⁺ T_{regs} from *Ambra1*^{fl/fl;cre+} and *Ambra1*^{fl/fl} mice positive for Helios (n = 4 ctrl, 6 KO) and Nrp1 (n = 3) expression. (D and I) WT CD4⁺ CD25⁺ T_{conv} cells have been stained with CFSE dye and then cultured with α-CD3/CD28-coated beads in presence or not of purified CD4⁺ CD25⁺ T_{reg} cells at 1:1 ratio. T_{reg} cells have been isolated from *Ambra1*^{fl/fl;cre+} (n = 3) and *Ambra1*^{fl/fl} mice (n = 3) (D) or from *Ambra1*^{gt/+} (n = 3) and WT (n = 3) mice (I). Cell division index (see STAR Methods text for details) is reported in the corresponding graphs on the right. **p < 0.01; ***p < 0.001. (G and H) Percentage of Foxp3⁺ T_{regs} positive for Helios (G) or Nrp1 (H) expression from thymi, spleen, or LNs pool of *Ambra1*^{gt/+} (n = 4) and WT (n = 3) mice. (J and K) Naive CD4⁺ T cells were sorted from either WT or *Ambra1*^{gt/+} mouse splenocytes. Ambra1 and Actin were analyzed in WT resting naive T cells and T cells following 16 hr of α-CD3/CD28 treatment by western blot (J). Ambra1, Foxp3, and Actin expression in naive T cells derived from either WT or *Ambra1*^{gt/+} mouse splenocytes *in vitro* differentiated under T_{reg}-polarizing conditions were analyzed by western blot (K). Results in (J) and (K) are representative of three independent experiments. Molecular weights are indicated at the right side of each western blot image. All data are shown as mean ± SEM. See also Figure S4.

T_{reg} cells (Figure 5B), as proven by the reduction of its median fluorescence intensity (MFI). Interestingly, most of these cells are thymic-derived nT_{reg}, as indicated by Helios expression, a much more reliable nT_{reg} marker than Nrp1 in our c57/BL6

mouse line (Figure 5C), as also suggested by a previous report (Singh et al., 2015). Consistent with their Foxp3 downregulation, we found that these *Ambra1* KO T_{reg} cells were unable to suppress *in vitro* T_{conv} cell proliferation at a rate similar to control

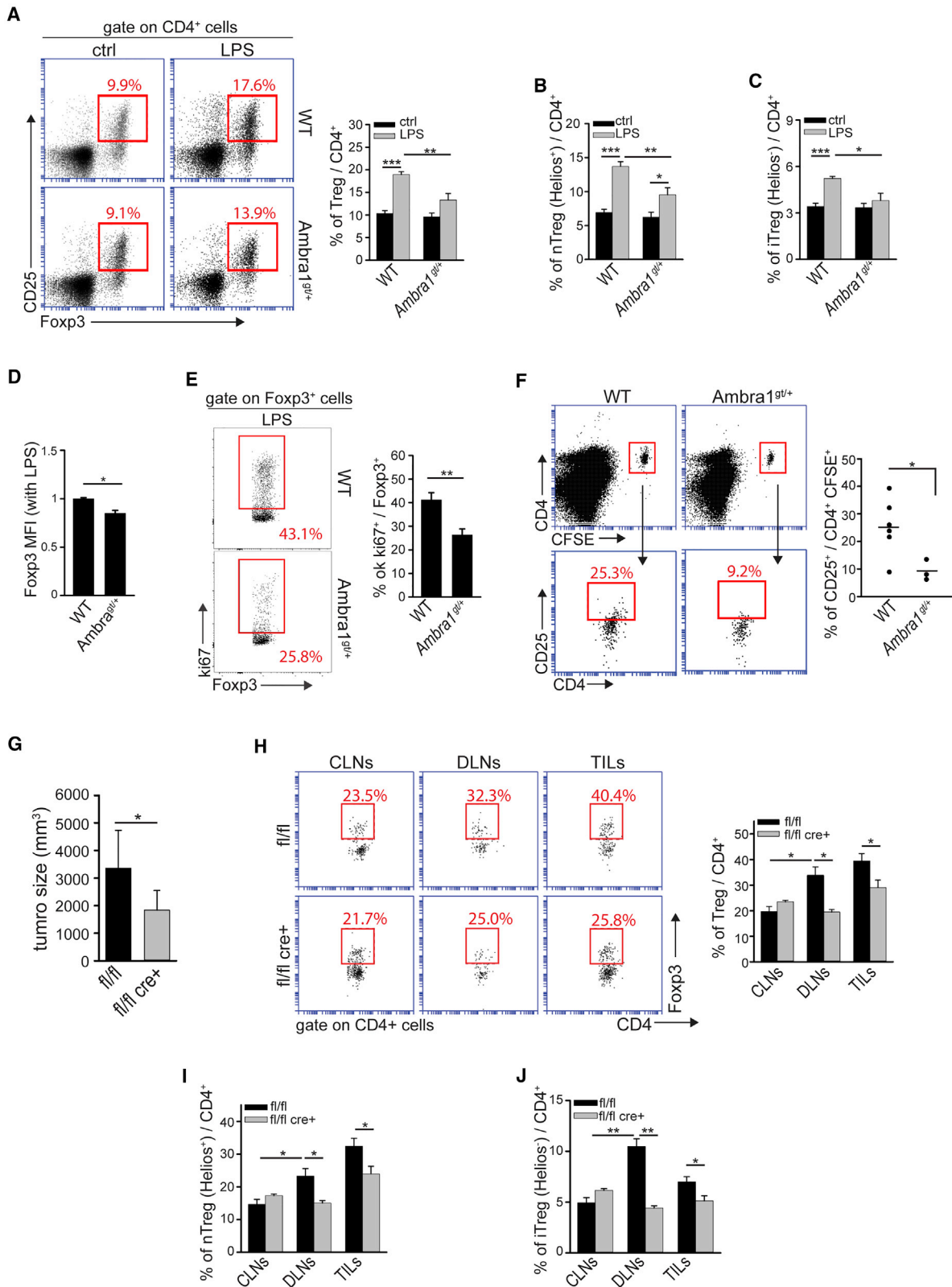


Figure 6. AMBRA1 Sustains the Increase in nTreg and iTreg Cell Number on Different Immune System Challenges

(A–E) Flow cytometric profile of CD25⁺ Foxp3⁺ T_{reg} cells among CD4⁺ T cells from spleen of *Ambr1^{glt/+}* (n = 5 unstimulated and n = 6 LPS) and WT (n = 4 unstimulated and n = 6 LPS) mice after 4 days from i.p. LPS injection. The percentage of CD25⁺ Foxp3⁺ T_{reg} cells among CD4⁺ T cells is reported in the graph on the

(legend continued on next page)

T_{reg} ($Ambra1^{fl/fl}$) (Figure 5D); however, this does not depend on differential expression of CD39 and CD73 enzymes (Figure S4B). We also confirmed similar results with $Ambra1$ haploinsufficient ($Ambra1^{gt/+}$) mice (Cianfanelli et al., 2015), in terms of Foxp3 downregulation in T_{reg} cells (Figures 5E and 5F), Helios, Nrp1, CD73 and CD39 expression, and defective suppressive ability (Figures 5G–5I, S4C, and S4D). Altogether, this indicates that $Ambra1$ haploinsufficiency is also sufficient to impair T_{reg} functionality *in vivo*. Lastly, we investigated whether the *de novo* conversion of naive T cells into iTreg is also affected in $Ambra1^{gt/+}$ murine T cells, similar to what we reported for human T cells. First, we found that resting naive murine T cells expressed low level of $Ambra1$, which was strongly upregulated following TCR stimulation (Figure 5J). Second, *in vitro* T_{reg} polarization of naive T cells isolated from $Ambra1^{gt/+}$ heterozygous mice resulted in decreased Foxp3 expression compared to T cells isolated from wild-type mice (Figure 5K).

Taken together, our data indicate that $Ambra1$ is required to sustain Foxp3 expression also *in vivo* in both n T_{reg} and iT T_{reg} populations.

Ambra1 Is Required for a T_{reg} Response to Immune System Challenges

We next asked whether $Ambra1$ deficiency could impact T_{reg} response in immune system challenges. With this aim, we first infected WT and $Ambra1^{gt/+}$ mice with lipopolysaccharide (LPS), which promotes both T cell activation (Figure S5A) and T_{reg} induction (Okeke et al., 2013). Interestingly, we found that $Ambra1$ haploinsufficiency impairs T_{reg} accumulation in the spleen of LPS-infected mice (Figure 6A). Although most of these cells are bona fide Helios⁺ n T_{reg} cells, by distinguishing n T_{reg} and iT T_{reg} according to Helios expression, we found that both n T_{reg} and iT T_{reg} $Ambra1^{gt/+}$ populations accumulated less than WT cells in the spleen of LPS-infected mice (Figures 6B and 6C). Further, we confirmed that $Ambra1^{gt/+}$ T_{reg} cells show reduced Foxp3 expression on a per cell basis, when compared to control WT T_{reg} cells upon LPS stimulation (Figure 6D). Interestingly, such a defective increase in the n T_{reg} cells inside the LPS-infected spleens is associated with an impaired T_{reg} proliferation rate, as indicated by reduced Ki67 staining (Figure 6E) in the absence of $Ambra1$, and not with an altered T_{reg} recruitment, as indicated by a similar migration rate in response to chemokine gradient and the correct expression of CCR7 and CXCR4 receptors by thymic $Ambra1$ KO T_{reg} cells (Figures S5B and S5C). Regarding iT T_{reg} cells, to better investigate their generation from T_{conv} cells in this model, we injected LPS-infected WT

mice with either WT or $Ambra1^{gt/+}$ purified CFSE-labeled CD4⁺ CD25⁻ T_{conv} cells. In line with the previous results (Figure 6C), in the absence of $Ambra1$, we found on LPS a defective *de novo* conversion of conventional CD25⁺ CD4⁺ T cells into CD25⁺ CD4⁺ T_{reg} cells (Figure 6F). Moreover, we confirmed that these cells are bona fide iT T_{reg} by looking directly at their Foxp3, whose expression was reduced in $Ambra1^{gt/+}$ cells (Figure S5D).

Lastly, we asked whether $Ambra1$ deficiency could also impact immune surveillance against tumors, a well-known context, in which T_{reg} cells play a fundamental role. Indeed, as expected, we found that MC38-derived tumors were smaller in $Ambra1^{fl/fl;cre+}$ mice than those in $Ambra1^{fl/fl}$ controls (Figure 6G), and this phenomenon correlated with a reduced amount of T_{regs} within both DLNs and tumor masses of KO mice (Figure 6H). By distinguishing n T_{reg} and iT T_{reg} according to Helios expression, we further confirmed that, in this context, both populations from $Ambra1$ -deficient mice did not increase their number into DLNs and tumor masses at the same rate than WT n T_{reg} and iT T_{reg} cells (Figures 6I and 6J). Interestingly, it seems that the strongest effect of $Ambra1$ deficiency is the defective generation of iT T_{reg} cells in the DLNs of tumor-bearing mice. Since in this tumor model most T_{reg} cells infiltrating tumor mass are n T_{reg} cells (Figure S5E), as previously indicated (Waight et al., 2015), our results suggest that the absence of $Ambra1$ from the T cell lineage could affect, at an even greater rate, the growth of tumors in which infiltrating T_{regs} have mainly an iT T_{reg} phenotype (Valzasina et al., 2006).

Altogether, our results indicate that $Ambra1$ deficiency impacts T_{reg} formation/induction and functionality *in vivo*, during both LPS-mediated stimulation and tumor response.

Ambra1 Insufficiency *In Vivo* Worsens the Clinical Scenario of a Mouse Model of Multiple Sclerosis

The strong impact of $Ambra1$ on T_{reg} fate decision prompted us to study a putative involvement of this factor in protecting against autoimmune diseases. We chose the experimental autoimmune EAE, induced through MOG_(35–55) peptide injection into female mice, as a mouse model for multiple sclerosis. Interestingly, $Ambra1^{gt/+}$ mice were characterized by a more severe clinical score, when compared to control mice (Figure 7A). On day 18 post immunization, the animals were sacrificed, and spinal cords were analyzed by immunohistochemistry to reveal the progress of central nervous system infiltration (H&E staining), demyelination (Kluver-Barrera staining), and axonal loss (Biecholsky staining). Again, slices from $Ambra1^{gt/+}$ mice showed

right (A). In addition, CD25⁺ Foxp3⁺ T_{reg} cells have been distinguished according to Helios expression into Helios⁺ nTreg cells (B) and Helios⁻ iTreg cells (C), and their frequency among CD4⁺ T cells quantified in all conditions. The Foxp3 median fluorescence index (MFI) in CD25⁺ Foxp3⁺ T_{reg} cells upon LPS injection into $Ambra1^{gt/+}$ (n = 11) and WT (n = 3) mice is also reported (D). Further, ki67 positive cells among CD25⁺ Foxp3⁺ T_{reg} cells upon LPS injection into $Ambra1^{gt/+}$ (n = 12) and WT (n = 5) mice have been quantified (E, representative dot plot on the left and quantification in the graph on the right). *p < 0.05; **p < 0.01; ***p < 0.001. (F) Conventional CD4⁺ CD25⁻ T cells stained with CFSE dye from $Ambra1^{gt/+}$ (n = 3) and WT (n = 6) mice have been injected i.v. into WT recipient mice, subsequently injected i.p. with LPS. After 4 days, mice have been sacrificed and the percentage of CD25⁺ cells among exogenous CD4⁺ CFSE⁺ cells have been analyzed by flow cytometry. Quantification is reported on the graph below. *p < 0.05.

(G–J) $Ambra1^{fl/fl;cre+}$ (n = 4) and $Ambra1^{fl/fl}$ mice (n = 4) have been injected subcutaneously with 5 × 10⁵ MC38 tumor cells. After 18 days, mice were sacrificed and tumor's size was assessed (G). In (H), the representative dot plots of the percentages of Foxp3⁺ T_{reg} cells among CD4⁺ T cells from contralateral and draining lymph nodes (CLNs and DLNs) and tumor masses (TILs, tumor infiltrating lymphocytes) are reported on the left and the relative quantification in the graph on the right. Further, CD25⁺ Foxp3⁺ T_{reg} cells have been distinguished according to Helios expression into Helios⁺ nTreg cells (I) and Helios⁻ iTreg cells (J), and their frequency among CD4⁺ T cells quantified in all conditions. *p < 0.05; **p < 0.01. All data are shown as mean ± SEM.

See also Figure S5.

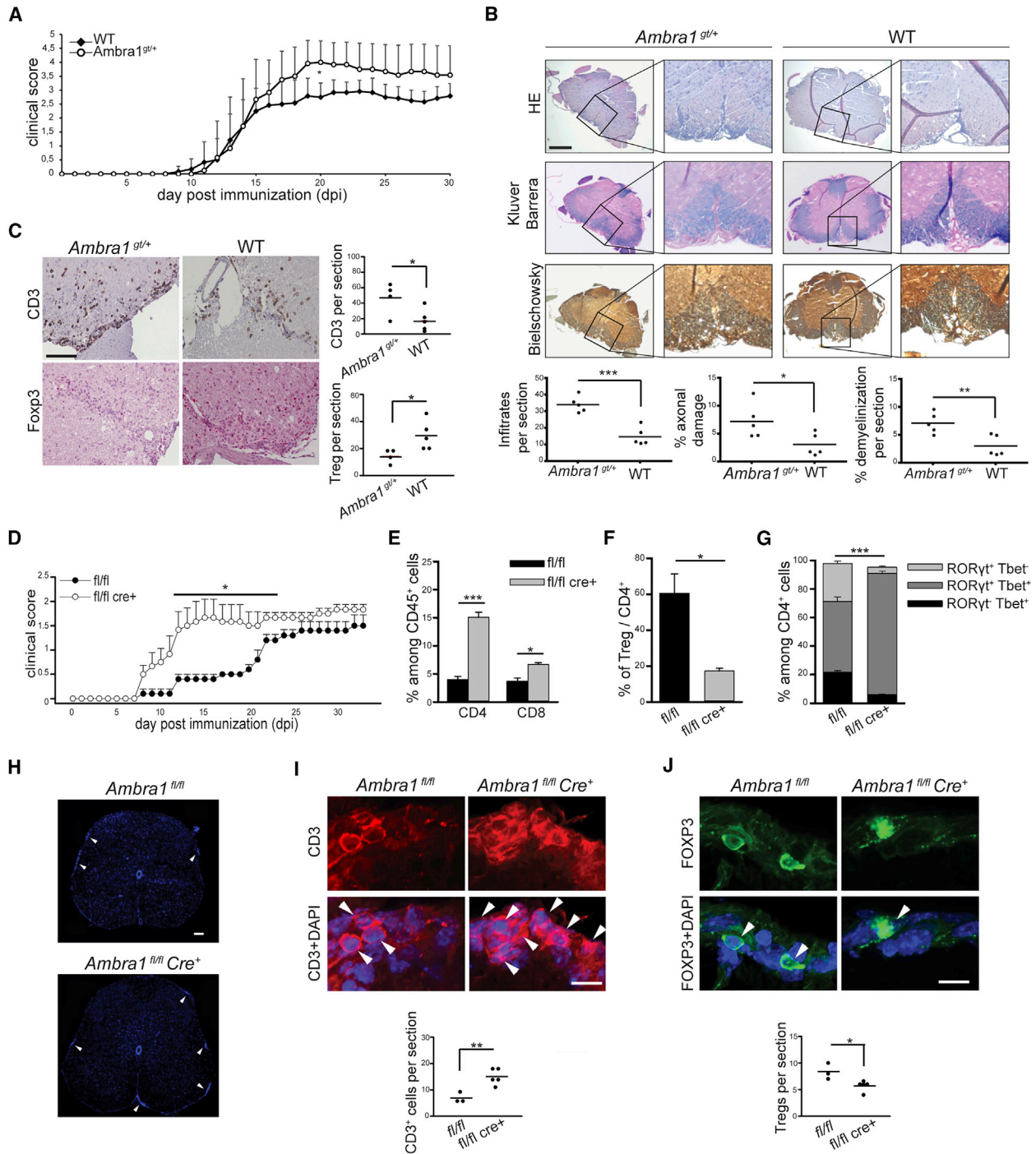


Figure 7. *Ambra1* Downregulation Worsens the Clinical Readout in Experimental Autoimmune encephalomyelitis (EAE)

Chronic progressive EAE was induced by immunization with MOG₃₅₋₅₅.

(A) Mean clinical score of C57BL/6J *Ambra1*^{gt/+} mice (gray line and circles, n = 5) and C57BL/6J wild-type controls (black line and triangles, n = 5) after immunization with MOG₃₅₋₅₅. *p < 0.05.

(B and C) Immunohistochemical analysis of spinal cord slices from mice sacrificed at 18 dpi. Central nervous system infiltrating cells were analyzed by hematoxylin/eosin (HE) staining; demyelination was assessed by Kluver-Barrera staining and axonal damage by Bielschowsky silver staining (B, scale bar = 500 μm) or with antibodies against CD3 and Foxp3 proteins (C, scale bar = 60 μm). Quantifications of the data are reported in the corresponding graphs. *p < 0.05, ***p < 0.001.

(D) Mean clinical score of C57BL/6J *Ambra1*^{fl/fl;cre+} mice (white, n = 6) and C57BL/6J *Ambra1*^{fl/fl} controls (black, n = 5) after immunization with MOG₃₅₋₅₅. *p < 0.05.

(E–G) Cytofluorimetric analysis of the percentage of CD4⁺ and CD8⁺ T cells among CD45⁺ infiltrates (E), of CD25⁺ Foxp3⁺ T_{regs} (F) and RORγt⁺Tbet⁻, RORγt⁺Tbet⁺ and RORγt⁻Tbet⁺ cells (G) among CD4⁺ T cells. *p < 0.05; ***p < 0.001; n = 3.

(legend continued on next page)

significantly stronger pathogenic signs than those from wild-type littermates (Figure 7B). In addition, we found that *Ambra1*^{9V/+} mice showed increased levels of CD3⁺ T cells infiltrates in the spinal cord, but reduced levels of T_{reg} cells (Figure 7C), in agreement with impaired differentiation of this cell type in the absence of *Ambra1* and with a more aggressive EAE.

We further confirmed that the more severe EAE progression in *Ambra1*^{9V/+} mice was due to the specific absence of *Ambra1* in the T cell compartment, by finding that EAE onset and progression were faster also in *Ambra1*^{fl/fl;cre+} mice compared to *Ambra1*^{fl/fl} controls (Figure 7D). Moreover, cytofluorimetric analyses indicate that conditional KO mice showed increased levels of both CD4⁺ and CD8⁺ T cells infiltrating in the central nervous system (Figure 7E) and a strong reduction in CD4⁺ T_{reg} cell percentage among CD4⁺ cells (Figure 7F), with a concomitant increased proportion of pro-inflammatory CD4⁺ Th17 cells (ROR γ t⁺) (Figure 7G); of note, this finding was consistent with the reduced amount of infiltrating T_{reg} cells. Immunofluorescence on spinal cord sections confirmed the increased amount of CD3⁺ infiltrates and the reduction of Foxp3⁺ infiltrates per slice (Figures 7H–7J).

Altogether, these results strongly indicate AMBRA1 as a bona fide anti-inflammatory protein, crucial to trigger differentiation and expansion of T_{reg}, thus protecting against severe autoimmune disorders, such as multiple sclerosis.

DISCUSSION

Here, we found pro-autophagic AMBRA1 to be upregulated in CD4⁺ T cells 16 hr after T cell receptor engagement. This strongly correlates with the expression kinetics of FOXP3, which is not only upregulated in T_{reg} cells but is transiently expressed also in T_{eff} cells, with its peak in the latter coinciding with AMBRA1 induction. Strikingly, we found that AMBRA1 is required to ensure FOXP3 expression and development or maintenance of functional T_{reg} cells both *in vitro* and *in vivo*. The fact that AMBRA1 is induced during T cell stimulation when negative modulators of T_{reg} cells, including c-Myc and mTOR, are hyperactivated (Wang et al., 2011) led us to hypothesize that AMBRA1 assumes a crucial role in counteracting this event, thus allowing T_{reg} cell differentiation. Of note, several pathways merge together to induce the expression of FOXP3. The PI3K/AKT/mTOR pathway has been shown to negatively affect TGF- β -driven FOXP3 expression (Shen et al., 2011; Haxhinasto et al., 2008), while inhibition of this pathway favors differentiation into T_{reg} cells through activation of the transcription factor FOXO3 (Harada et al., 2010; Kerdiles et al., 2010; Ouyang et al., 2010). Both AKT and FOXO3 are targets of PP2A, and dephosphorylation of either PP2A substrates results in enhanced FOXO3 activity (Singh et al., 2010; Kuo et al., 2008; Yang et al., 2008; Hu et al., 2004; Rena et al., 2002). Here, we found that AMBRA1 targets S253 phosphorylation of FOXO3 via PP2A independent of AKT, resulting in increased FOXO3 levels associated with effective FOXP3 transcription.

Interestingly, ablation of PP2A in T_{reg} cells leads to a severe, multi-organ lymphoproliferative autoimmune disorder (Apostolidis et al., 2016). In more detail, PP2A controls the activity of mTOR complex 1 in T_{reg} cells, ensuring the maintenance of their metabolic and cytokine profile, essential for their suppressive capacity.

Besides regulating PP2A-dependent FOXO3 dephosphorylation, we previously demonstrated that AMBRA1 can also promote PP2A-mediated degradation of cMyc (Cianfanelli et al., 2015), which is a major factor regulating T_{eff} cell differentiation through metabolic reprogramming (Wang et al., 2011). Therefore, we hypothesize that the axis AMBRA1-PP2A may favor T_{reg} differentiation by regulating at the same time c-Myc and FOXO3, but in opposite ways, thereby forcing a “T_{reg} fate” decision. Taken together, results of this study not only point to AMBRA1 as a novel protein triggering anti-inflammatory processes and thus contrasting autoimmune diseases (such as multiple sclerosis) but also opening new interesting scenarios that may involve AMBRA1 in FOXO3-mediated transcriptional regulation of a series of processes. In fact, besides its role in T_{reg} cells, FOXO3 has been shown to regulate autophagy and mitophagy in skeletal muscles (Mammucari et al., 2007; Romanello et al., 2010); promote cell-cycle arrest, apoptosis, stress resistance (Chiacchiera and Simone, 2010); and inhibit glycolysis by downregulating cMyc (Khatri et al., 2010). In sum, AMBRA1 can be defined as a mediator of this FOXO3/cMyc antagonism, favoring the FOXO3 rather than c-Myc transcriptional program that culminates in induction of autophagy, inhibition of cell cycle, and, specifically in T cells, promotion of T_{reg} instead of T_{eff} commitment.

When we moved to murine models, our data indicated that *Ambra1* is a crucial regulator of T_{reg} commitment and function also *in vivo*. Indeed, we first confirmed that iT_{reg} induction from T_{conv} cell precursors is defective in the absence of *Ambra1*. This was not only observed for iT_{reg} cells generated *in vitro* from purified murine T_{conv} cells but also directly *in vivo* on both LPS injection (mimicking an inflamed state) and in a subcutaneous murine tumor model, in which the accumulation of iT_{reg} cells into lymphoid organs and tumor mass was strongly reduced. In addition, we found that *Ambra1* deficiency reduces Foxp3 expression in nT_{reg} cells. Although the mechanism regulating nT_{reg} formation is less understood compared to iT_{reg}, our data suggest that *Ambra1* may represent a general regulator of Foxp3 expression in T_{reg} cells upon TCR stimulation, a finding not only limited to cytokine-mediated T_{reg} induction in periphery but also extended to T_{reg} cells originating in the thymus upon TCR stimulation. Interestingly, *Foxp3*-deficient T_{reg} cells are reported to show defective suppressive function and reduced expansion (Kuczma et al., 2009). Consistent with this, we found that *Ambra1*-deficient nT_{reg} cells, which express low levels of Foxp3, show defective *in vitro* suppressive function and an impaired *in vivo* proliferation, as indicated by reduced ki67 staining upon LPS injection and reduced accumulation in DLNs and

(H–J) Immunofluorescence analysis of lumbosacral spinal cord section from EAE-infected *Ambra1*^{fl/fl;cre+} (n = 5) and *Ambra1*^{fl/fl} mice (n = 3). DAPI staining on whole sections has been used to identify the localization of immune cell infiltrates (H, white arrows, scale bar, 100 μ m), which were further analyzed at single-cell level for the expression of CD3⁺ (I, in red, indicated by white arrows, scale bar, 15 μ m) and Foxp3⁺ (J, in green, indicated by white arrows, scale bar, 15 μ m). Quantification of the number of CD3⁺ T cells and Foxp3⁺ T_{reg} cell infiltrates per section is reported in the corresponding graphs below each panel. *p < 0.05; **p < 0.01. All data are shown as mean \pm SEM or as dot density plot (mean value indicated with a black bar).

tumor mass of a murine tumor model. Although we cannot exclude *per se* additional *Ambra1*-dependent and *Foxp3*-independent roles in regulating nT_{reg} functionality, our data strongly suggest that *Ambra1* regulates nT_{reg} activity mainly through the modulation of *Foxp3* levels. Therefore, *Ambra1* should be considered as a general regulator of T_{reg} fate commitment both *in vivo* and *in vitro*.

Of note, since *Ambra1* was depleted from all T cell lineages in our murine system, we could not rule out in principle that our results *in vivo* were due to a general gain of function of T_{conv} cells in the absence of *Ambra1*, rather than to a specific defect in T_{reg} generation. However, the deletion of several other autophagic proteins in the T cell lineage, such as Beclin1 or ATG7, has always resulted so far in a loss of function of the T_{conv} cell response, in terms of reduced proliferation and increased cell death (Kovacs et al., 2012; Hubbard et al., 2010). Moreover, upon LPS injection, we found that *Ambra1* haplodeficient T_{conv} cells are activated at a similar rate compared to controls.

Therefore, the effect of *Ambra1* depletion on T_{reg} cells seems to be the driving force in the observed phenotypes.

Lastly, *Ambra1* haplodeficiency and homozygous deficiency also restrains the number of T_{reg} cells infiltrating the central nervous system in a mouse model of multiple sclerosis, exacerbating the progression of the disease. Therefore, *Ambra1* is a positive regulator of the T_{reg} response in different pathological conditions, such as inflammation, tumor response, and auto-immunity, and could represent a novel target for future therapeutic approaches, aimed at modulating the induction and function of immunosuppressive T_{reg} cells in all these different pathological settings.

STAR★METHODS

Detailed methods are provided in the online version of this paper and include the following:

- KEY RESOURCES TABLE
- CONTACT FOR REAGENT AND RESOURCE SHARING
- EXPERIMENTAL MODEL AND SUBJECT DETAILS
- METHOD DETAILS
 - Cell Isolations
 - Cell Culture, Lentiviral Infection and Transfection
 - Flow Cytometry
 - Transwell Assay
 - Western Blot and *In Vitro* Phosphatase Assay
 - Immunocytochemistry
 - Real-Time PCR
 - Suppression Assay
 - LPS Infection
 - Tumor Model
 - Mice and EAE Induction
 - Evaluation of Neuropathology in EAE Mice
 - Immunohistochemistry and Immunofluorescence
- QUANTIFICATION AND STATISTICAL ANALYSIS
- DATA AND SOFTWARE AVAILABILITY

SUPPLEMENTAL INFORMATION

Supplemental Information includes five figures and can be found with this article online at <https://doi.org/10.1016/j.devcel.2018.11.010>.

ACKNOWLEDGMENTS

We thank M.C. (Chicca) Riviello and A. Wirz for the mouse work; M. Acuña Villa for the secretarial work; and V. Benedetti, R. Angelini, and C. Marsella for the research assistance. This work was supported mainly by FISM (2009, 2013) and Fondazione Roma to F. Cecconi and in part by the Italian Ministry of University and Research (Accordi di Programma, 2011) and the Italian Ministry of Health (Progetto Giovani Ricercatori GR2011-2012 to F.S. and S.C.) and “Associazione Italiana per la Ricerca sul Cancro” (AIRC-15180 to F.Cecconi and AIRC-IG-2017-19826 to S.C. and AIRC 5x1000 “Immunity in Cancer and Spreading Metastasis” to F.L.). C.P. was supported by the Italian Ministry of Health, GR-2016-02363749. G. Matarese was supported by grants from European Research Council “mentORingTregs” n. 310496, Fondazione Italiana Sclerosi Multipla (FISM) n. 2016/R/18, and Telethon n. GGP17086. L.B. was supported by grants from FISM-Fondazione Italiana Sclerosi Multipla (cod.2013/R/2) and by Italian Ministry of Health, Italy (RF-2011- 02346771 and RF-2011-02347228) and by Roche (award 2016). V.C. is supported by the Lundbeck Foundation (R209-2015-3505 and R233-2016-3360). We are also grateful to the Lundbeck Foundation (R167-2013-16100) and the Novo Nordisk Foundation (7559). Further, F. Cecconi lab in Copenhagen is part of the Center of Excellence in Autophagy, Recycling and Disease (CARD), funded by the Danish National Research Foundation.

AUTHOR CONTRIBUTIONS

J.B. and L.S. designed and performed most experiments with crucial help from E.V., G. Borsellino, and L.B. (cytofluorimetry analysis); P.D. (immunostaining); I.C., G.W., and F.N. (real time); V.C. (phosphatase assay); F.S. (imaging); F. Cicciosanti (preparation of lentivirus); C.P., C.L.R., D.C., and G. Matarese (EAE induction); M.D.B. (cell sorting); M.D. (*in vivo* experiments); and F.R., R.F., G. Mandolesi, V.G., and G. Botti (immunohistochemistry). S.C. and G.M.F. provided critical reagents and critical help. P. Braghetta, M.C., and P. Bonaldo generated the *Ambra1* floxed mouse line. E.V., F.L., and G. Matarese discussed the results, commented, and wrote the manuscript. J.B., L.S., and F. Cecconi wrote the manuscript. F. Cecconi conceived and coordinated the research and wrote the manuscript.

DECLARATION OF INTERESTS

The authors declare no competing interests.

Received: May 25, 2018

Revised: September 3, 2018

Accepted: November 1, 2018

Published: December 3, 2018

REFERENCES

- Alessi, D.R., James, S.R., Downes, C.P., Holmes, A.B., Gaffney, P.R., Reese, C.B., and Cohen, P. (1997). Characterization of a 3-phosphoinositide-dependent protein kinase which phosphorylates and activates protein kinase B α . *Curr. Biol.* 7, 261–269.
- Apostolidis, S.A., Rodríguez-Rodríguez, N., Suárez-Fueyo, A., Dioufa, N., Ozcan, E., Crispin, J.C., Tsokos, M.G., and Tsokos, G.C. (2016). Phosphatase PP2A is requisite for the function of regulatory T cells. *Nat. Immunol.* 17, 556–564.
- Battaglia, M., Stabellini, A., and Roncarolo, M.G. (2005). Rapamycin selectively expands CD4+CD25+FoxP3+ regulatory T cells. *Blood* 105, 4743–4748.
- Brunet, A., Bonni, A., Zigmond, M.J., Lin, M.Z., Juo, P., Hu, L.S., Anderson, M.J., Arden, K.C., Blenis, J., and Greenberg, M.E. (1999). Akt promotes cell survival by phosphorylating and inhibiting a Forkhead transcription factor. *Cell* 96, 857–868.
- Cencioni, M.T., Santini, S., Ruocco, G., Borsellino, G., De Bardi, M., Grasso, M.G., Ruggieri, S., Gasperini, C., Centonze, D., Barilá, D., et al. (2015). FAS-ligand regulates differential activation-induced cell death of human T-helper 1 and 17 cells in healthy donors and multiple sclerosis patients. *Cell Death Dis.* 6, e1785.

- Chiacchiera, F., and Simone, C. (2010). The AMPK-FoxO3a axis as a target for cancer treatment. *Cell Cycle* 9, 1091–1096.
- Cianfanelli, V., Fuoco, C., Lorente, M., Salazar, M., Quondamatteo, F., Gherardini, P.F., De Zio, D., Nazio, F., Antonioli, M., D'Orazio, M., et al. (2015). AMBRA1 links autophagy to cell proliferation and tumorigenesis by promoting c-Myc dephosphorylation and degradation. *Nat. Cell Biol.* 17, 20–30.
- Corrado, M., Mariotti, F.R., Trapani, L., Taraborrelli, L., Nazio, F., Cianfanelli, V., Soriano, M.E., Schrepfer, E., Cecconi, F., Scorrano, L., et al. (2016). Macroautophagy inhibition maintains fragmented mitochondria to foster T cell receptor-dependent apoptosis. *EMBO J.* 35, 1793–1809.
- Delgoffe, G.M., Kole, T.P., Zheng, Y., Zarek, P.E., Matthews, K.L., Xiao, B., Worley, P.F., Kozma, S.C., and Powell, J.D. (2009). The mTOR kinase differentially regulates effector and regulatory T cell lineage commitment. *Immunity* 30, 832–844.
- Di Bartolomeo, S., Corazzari, M., Nazio, F., Oliverio, S., Lisi, G., Antonioli, M., Pagliarini, V., Matteoni, S., Fuoco, C., Giunta, L., et al. (2010). The dynamic interaction of AMBRA1 with the dynein motor complex regulates mammalian autophagy. *J. Cell Biol.* 191, 155–168.
- Fimia, G.M., Stoykova, A., Romagnoli, A., Giunta, L., Di Bartolomeo, S., Nardacci, R., Corazzari, M., Fuoco, C., Ucar, A., Schwartz, P., et al. (2007). Ambra1 regulates autophagy and development of the nervous system. *Nature* 447, 1121–1125.
- Harada, Y., Harada, Y., Elly, C., Ying, G., Paik, J.H., DePinho, R.A., and Liu, Y.C. (2010). Transcription factors Foxo3a and FoxO1 couple the E3 ligase Cbl-b to the induction of Foxp3 expression in induced regulatory T cells. *J. Exp. Med.* 207, 1381–1391.
- Haxhinasto, S., Mathis, D., and Benoist, C. (2008). The AKT-mTOR axis regulates de novo differentiation of CD4+Foxp3+ cells. *J. Exp. Med.* 205, 565–574.
- Horwitz, D.A., Zheng, S.G., and Gray, J.D. (2008). Natural and TGF-beta-induced Foxp3(+)CD4(+) CD25(+) regulatory T cells are not mirror images of each other. *Trends Immunol.* 29, 429–435.
- Hu, M.C., Lee, D.F., Xia, W., Golfman, L.S., Ou-Yang, F., Yang, J.Y., Zou, Y., Bao, S., Hanada, N., Saso, H., et al. (2004). IkkappaB kinase promotes tumorigenesis through inhibition of forkhead FOXO3a. *Cell* 117, 225–237.
- Hubbard, V.M., Valdor, R., Patel, B., Singh, R., Cuervo, A.M., and Macian, F. (2010). Macroautophagy regulates energy metabolism during effector T cell activation. *J. Immunol.* 185, 7349–7357.
- Kerdiles, Y.M., Stone, E.L., Beisner, D.R., McGargill, M.A., Ch'en, I.L., Stockmann, C., Katayama, C.D., and Hedrick, S.M. (2010). Foxo transcription factors control regulatory T cell development and function. *Immunity* 33, 890–904.
- Khatiri, S., Yepiskoposyan, H., Gallo, C.A., Tandon, P., and Plas, D.R. (2010). FOXO3a regulates glycolysis via transcriptional control of tumor suppressor TSC1. *J. Biol. Chem.* 285, 15960–15965.
- Kovacs, J.R., Li, C., Yang, Q., Li, G., Garcia, I.G., Ju, S., Roodman, D.G., Windle, J.J., Zhang, X., and Lu, B. (2012). Autophagy promotes T-cell survival through degradation of proteins of the cell death machinery. *Cell Death Differ.* 19, 144–152.
- Kuczma, M., Podolsky, R., Garge, N., Daniely, D., Pacholczyk, R., Ignatowicz, L., and Kraj, P. (2009). Foxp3-deficient regulatory T cells do not revert into conventional effector CD4+ T cells but constitute a unique cell subset. *J. Immunol.* 183, 3731–3741.
- Kuo, Y.C., Huang, K.Y., Yang, C.H., Yang, Y.S., Lee, W.Y., and Chiang, C.W. (2008). Regulation of phosphorylation of Thr-308 of Akt, cell proliferation, and survival by the B55alpha regulatory subunit targeting of the protein phosphatase 2A holoenzyme to Akt. *J. Biol. Chem.* 283, 1882–1892.
- Levine, A.G., Mendoza, A., Hemmers, S., Moltedo, B., Niec, R.E., Schizas, M., Hoyos, B.E., Putintseva, E.V., Chaudhry, A., Dikiy, S., et al. (2017). Stability and function of regulatory T cells expressing the transcription factor T-bet. *Nature* 546, 421–425.
- Mammucari, C., Milan, G., Romanello, V., Masiero, E., Rudolf, R., Del Piccolo, P., Burden, S.J., Di Lisi, R., Sandri, C., Zhao, J., et al. (2007). FoxO3 controls autophagy in skeletal muscle in vivo. *Cell Metab.* 6, 458–471.
- Mandolesi, G., Grasselli, G., Musella, A., Gentile, A., Musumeci, G., Sepman, H., Haji, N., Fresegna, D., Bernardi, G., and Centonze, D. (2012). GABAergic signaling and connectivity on Purkinje cells are impaired in experimental autoimmune encephalomyelitis. *Neurobiol. Dis.* 46, 414–424.
- Marie, J.C., Letterio, J.J., Gavin, M., and Rudensky, A.Y. (2005). TGF-beta1 maintains suppressor function and Foxp3 expression in CD4+CD25+ regulatory T cells. *J. Exp. Med.* 201, 1061–1067.
- Nazio, F., Strappazzon, F., Antonioli, M., Bielli, P., Cianfanelli, V., Bordi, M., Gretzmeier, C., Dengjel, J., Piacentini, M., Fimia, G.M., et al. (2013). mTOR inhibits autophagy by controlling ULK1 ubiquitylation, self-association and function through AMBRA1 and TRAF6. *Nat. Cell Biol.* 15, 406–416.
- O'Shea, J.J., and Paul, W.E. (2010). Mechanisms underlying lineage commitment and plasticity of helper CD4+ T cells. *Science* 327, 1098–1102.
- Okeke, E.B., Okwor, I., Mou, Z., Jia, P., and Uzonna, J.E. (2013). CD4+CD25+ regulatory T cells attenuate lipopolysaccharide-induced systemic inflammatory responses and promotes survival in murine *Escherichia coli* infection. *Shock* 40, 65–73.
- Ouyang, W., Beckett, O., Ma, Q., Paik, J.H., DePinho, R.A., and Li, M.O. (2010). Foxo proteins cooperatively control the differentiation of Foxp3+ regulatory T cells. *Nat. Immunol.* 11, 618–627.
- Plas, D.R., and Thompson, C.B. (2003). Akt activation promotes degradation of tuberlin and FOXO3a via the proteasome. *J. Biol. Chem.* 278, 12361–12366.
- Procaccini, C., De Rosa, V., Galgani, M., Abanni, L., Cali, G., Porcellini, A., Carbone, F., Fontana, S., Horvath, T.L., La Cava, A., et al. (2010). An oscillatory switch in mTOR kinase activity sets regulatory T cell responsiveness. *Immunity* 33, 929–941.
- Rena, G., Woods, Y.L., Prescott, A.R., Peggie, M., Unterman, T.G., Williams, M.R., and Cohen, P. (2002). Two novel phosphorylation sites on FKHR that are critical for its nuclear exclusion. *EMBO J.* 21, 2263–2271.
- Romanello, V., Guadagnin, E., Gomes, L., Roder, I., Sandri, C., Petersen, Y., Milan, G., Masiero, E., Del Piccolo, P., Foretz, M., et al. (2010). Mitochondrial fission and remodelling contributes to muscle atrophy. *EMBO J.* 29, 1774–1785.
- Shen, E., Zhao, K., Wu, C., and Yang, B. (2011). The suppressive effect of CD25+Treg cells on Th1 differentiation requires cell-cell contact partially via TGF-beta production. *Cell Biol. Int.* 35, 705–712.
- Shi, L.Z., Wang, R., Huang, G., Vogel, P., Neale, G., Green, D.R., and Chi, H. (2011). HIF1alpha-dependent glycolytic pathway orchestrates a metabolic checkpoint for the differentiation of TH17 and Treg cells. *J. Exp. Med.* 208, 1367–1376.
- Singh, A., Ye, M., Bucur, O., Zhu, S., Tanya Santos, M., Rabinovitz, I., Wei, W., Gao, D., Hahn, W.C., and Khosravi-Far, R. (2010). Protein phosphatase 2A reactivates FOXO3a through a dynamic interplay with 14-3-3 and AKT. *Mol. Biol. Cell* 21, 1140–1152.
- Singh, K., Hjort, M., Thorvaldson, L., and Sandler, S. (2015). Concomitant analysis of Helios and Neuropilin-1 as a marker to detect thymic derived regulatory T cells in naïve mice. *Sci. Rep.* 5, 7767.
- Strappazzon, F., Di Rita, A., Cianfanelli, V., D'Orazio, M., Nazio, F., Fimia, G.M., and Cecconi, F. (2016). Prosurvival AMBRA1 turns into a proapoptotic BH3-like protein during mitochondrial apoptosis. *Autophagy* 12, 963–975.
- Strappazzon, F., Nazio, F., Corrado, M., Cianfanelli, V., Romagnoli, A., Fimia, G.M., Campello, S., Nardacci, R., Piacentini, M., Campanella, M., et al. (2015). AMBRA1 is able to induce mitophagy via LC3 binding, regardless of Parkin and p62/SQSTM1. *Cell Death Differ.* 22, 419–432.
- Strappazzon, F., Vietri-Rudan, M., Campello, S., Nazio, F., Florenzano, F., Fimia, G.M., Piacentini, M., Levine, B., and Cecconi, F. (2011). Mitochondrial BCL-2 inhibits AMBRA1-induced autophagy. *EMBO J.* 30, 1195–1208.
- Valzasina, B., Piconese, S., Guiducci, C., and Colombo, M.P. (2006). Tumor-induced expansion of regulatory T cells by conversion of CD4+CD25- lymphocytes is thymus and proliferation independent. *Cancer Res.* 66, 4488–4495.
- Vignali, D.A., Collison, L.W., and Workman, C.J. (2008). How regulatory T cells work. *Nat. Rev. Immunol.* 8, 523–532.

- Waight, J.D., Takai, S., Marelli, B., Qin, G., Hance, K.W., Zhang, D., Tighe, R., Lan, Y., Lo, K.M., Sabzevari, H., et al. (2015). Cutting edge: epigenetic regulation of Foxp3 defines a stable population of CD4+ regulatory T cells in tumors from mice and humans. *J. Immunol.* *194*, 878–882.
- Wang, R., Dillon, C.P., Shi, L.Z., Milasta, S., Carter, R., Finkelstein, D., McCormick, L.L., Fitzgerald, P., Chi, H., Munger, J., et al. (2011). The transcription factor Myc controls metabolic reprogramming upon T lymphocyte activation. *Immunity* *35*, 871–882.
- Wei, J., Long, L., Yang, K., Guy, C., Shrestha, S., Chen, Z., Wu, C., Vogel, P., Neale, G., Green, D.R., et al. (2016). Autophagy enforces functional integrity of regulatory T cells by coupling environmental cues and metabolic homeostasis. *Nat. Immunol.* *17*, 277–285.
- Wildin, R.S., Ramsdell, F., Peake, J., Faravelli, F., Casanova, J.L., Buist, N., Levy-Lahad, E., Mazzella, M., Goulet, O., Perroni, L., et al. (2001). X-linked neonatal diabetes mellitus, enteropathy and endocrinopathy syndrome is the human equivalent of mouse scurfy. *Nat. Genet.* *27*, 18–20.
- Willinger, T., and Flavell, R.A. (2012). Canonical autophagy dependent on the class III phosphoinositide-3 kinase Vps34 is required for naive T-cell homeostasis. *Proc. Natl. Acad. Sci. USA* *109*, 8670–8675.
- Xu, X., Araki, K., Li, S., Han, J.H., Ye, L., Tan, W.G., Konieczny, B.T., Bruinsma, M.W., Martinez, J., Pearce, E.L., et al. (2014). Autophagy is essential for effector CD8(+) T cell survival and memory formation. *Nat. Immunol.* *15*, 1152–1161.
- Yang, J.Y., Zong, C.S., Xia, W., Yamaguchi, H., Ding, Q., Xie, X., Lang, J.Y., Lai, C.C., Chang, C.J., Huang, W.C., et al. (2008). ERK promotes tumorigenesis by inhibiting FOXO3a via MDM2-mediated degradation. *Nat. Cell Biol.* *10*, 138–148.
- Yazdankhah, M., Farioli-Vecchioli, S., Tonchev, A.B., Stoykova, A., and Cecconi, F. (2014). The autophagy regulators Ambra1 and Beclin 1 are required for adult neurogenesis in the brain subventricular zone. *Cell Death Dis.* *5*, e1403.

STAR★METHODS

KEY RESOURCES TABLE

REAGENT or RESOURCE	SOURCE	IDENTIFIER
Antibodies		
anti-human CD4-FITC	Miltenyi	130-114-531; RRID: AB_2726690
anti-human CD45RA-PE	Miltenyi	130-092-248; RRID: AB_615094
anti-human CD27-APC	Miltenyi	130-093-186; RRID: AB_1036201
anti-mouse CD4-FITC	eBioscience	11-0041-82; RRID: AB_464892
anti-mouse CD62L-PE	eBioscience	12-0629-42; RRID: AB_10804144
anti-mouse CD44 APC	eBioscience	17-0441-82; RRID: AB_469390
anti-mouse/rat Foxp3-FITC	Biolegend	320012; RRID: AB_439748
anti-Ambra1	Millipore	ABC131; RRID: AB_2636939
anti-HA	Thermo Fisher	26183; RRID: AB_2533050
anti-human CD3	eBioscience	16-0037-85; RRID: AB_468855
anti-human CD28	eBioscience	16-0289-85; RRID: AB_468927
anti-human CD25-PE	Miltenyi	130-091-024; RRID: AB_244320
anti-human FOXP3-APC	Miltenyi	130-093-013; RRID: AB_871547
anti-human Interferon- γ -PEVio770	Miltenyi	130-096-752; RRID: AB_2661063
anti-human Interleukine-17-FITC	Miltenyi	130-105-262; RRID: AB_2652369
anti-mouse CD4-PECy7	Biolegend	100422; RRID: AB_312707
anti-mouse-CD69-PECy7	Biolegend	104512; RRID: AB_493564
anti-mouse CD8a-PE	Biolegend	100708; RRID: AB_312747
anti-mouse CD25-PE	Biolegend	102008; RRID: AB_312857
anti-mouse/human Helios-Alexa647	Biolegend	137218; RRID: AB_10660750
anti-mouse CD39-PE	Biolegend	143804; RRID: AB_11218603
anti-mouse CD73-APC	Biolegend	127210; RRID: AB_11218786
anti-mouse Nrp1-APC	Biolegend	145206; RRID: AB_2562032
anti-mouse CCR7-PE-Cy7	eBioscience	25-1971-82; RRID: AB_469652
anti-mouse CXCR4-APC	eBioscience	17-9991-82; RRID: AB_10670878
anti-human/mouse Ki67-Alexa647	BD Pharmingen	558615; RRID: AB_647130
anti-mouse ROR γ t-APC	eBioscience	17-6988-82; RRID: AB_10609207
anti-mouse/human Tbet-PE	eBioscience	12-5825-82; RRID: AB_925761
anti-Foxp3 (for WB)	eBioscience	14-4774-80; RRID: AB_467551
anti-ATG7 (for WB)	Cell Signalling	2631; RRID: AB_2227783
anti-Beclin1 (for WB)	Cell Signalling	4122; RRID: AB_11178656
anti-Tbet (for WB)	eBioscience	14-5824-82; RRID: AB_763637
anti-FOXO3 (for WB and IP)	Cell Signalling	2497; RRID: AB_836876
anti-phospho-FOXO3 S253 (for WB)	Cell Signalling	9466; RRID: AB_2106674
anti-phospho-FOXO3 T32 (for WB)	Cell Signalling	9464; RRID: AB_329842
anti-ERK (for WB)	Cell Signalling	4695; RRID: AB_390779
anti.phospho-ERK T202/204 (for WB)	Cell Signalling	4370; RRID: AB_2315112
anti-LC3 (for WB)	Cell Signalling	3868; RRID: AB_2137707
anti-phospho-AKT T308 (for WB)	Cell Signalling	4056; RRID: AB_331163
polyclonal anti-Ambra1 (for IF)	Covalab	0224
monoclonal anti-FOXO3 (for IF)	Sigma	WH0002309M3; RRID: AB_1841675
monoclonal anti-FOXP3 (for IF) (FJK-16s)	eBioscience	14-5773-82; RRID: AB_467576
Alexa Fluor 488 anti-mouse	Molecular Probes	R37120; RRID: AB_2556548
Alexa Fluor 555 anti-mouse	Molecular Probes	A21422; RRID: AB_141822

(Continued on next page)

Continued

REAGENT or RESOURCE	SOURCE	IDENTIFIER
Cy3 anti-rabbit	Jackson IR	111-165-144; RRID: AB_2338006
anti-Foxp3 rabbit polyclonal (for IHC)	Abcam	54501
anti-CD3 rabbit monoclonal SP7 (for IHC)	Abcam	ab16669; RRID: AB_443425
HRP-Goat Anti-Rabbit antibody	Perkin Elmer	NEF812001EA
HRP-Biotinylated Secondary Antibody	Novocastra (Leica)	RE7103; RRID: AB_876940
biotin-conjugated goat anti-mouse secondary antibody	Perkin Elmer	NEF823001EA
Biological Samples		
Human Peripheral Blood Mononuclear Cells (from Buffy Coat)	Human Donors Volunteers	N/A
Chemicals, Peptides, and Recombinant Proteins		
anti-CD3/anti-CD28 coated Dynabeads	Life Technologies	11131D
Human IL2	Roche	11-147-528-001
Human TGF- β	R&D System	240-B
Lipofectamine 2000	Thermo Fisher	11668019
MG-132	Sigma	M7449
CCL19	R&D System	440-M3-025/CF
CCL21	R&D System	457-6C-025/CF
Cycloheximide	Sigma	C4859
chloroquine	Sigma	C6628
Bafilomycin	Sigma	SML1661
sulfate latex beads	Thermo Fisher	S-37227
Protein G dynabeads	Thermo Fisher	10004D
PP2Ac recombinant protein	Cayman Chemical	10011237
SuperScript II Reverse Transcriptase	Thermo Fisher	18064014
CFSE	eBioscience	65-0850-84
eFluor670 Cell Proliferation Dye	eBioscience	65-0840-85
Lipopolysaccharide	Sigma	L4005
Percoll	GE Healthcare	GE17-0891-01
myelin oligodendrocyte glycoprotein p35–55	Epsikem	EPK1
pertussin toxin	Sigma	P7208
Vulcan Fast Red	Biocare Medical	FR805
DAB chromogen	Biocare Medical	DB801
HRP-streptavidin	Perkin Elmer	NEL750001EA
TSA Cyanine 3 Tyramide Reagent Pack	Perkin Elmer	SAT704A001EA
Critical Commercial Assays		
Foxp3 Transcription Factor Staining Buffer Kit	eBioscience	A25866A
RNeasy Micro Kit	Qiagen	74004
CD4+ T cell Isolation Kit	Miltenyi	130-104-454
CD25+ Microbeads	Miltenyi	130-091-072
RosetteSep Human T cell enrichment cocktail	Stemcell	15061
Experimental Models: Cell Lines		
Jurkat cell line	Laboratory stock	N/A
HeLa cell line	Laboratory stock	N/A
MC38 cell line	A kind gift from Dr. Silvia Piconese (Dipartimento di Medicina Interna e Specialità Mediche, University of Rome La Sapienza, Italy)	N/A
Experimental Models: Organisms/Strains		
c57BL/6 Ambra1 fl/fl Lck:cre	This paper	N/A
c57BL/6 Ambra1 gt/+	Cianfanelli et al. (2015)	N/A

(Continued on next page)

Continued

REAGENT or RESOURCE	SOURCE	IDENTIFIER
Oligonucleotides		
shRNA against Ambra1	Sigma	SHCLNV-NM_017749
shRNA against Atg7	Sigma	SHCLNV-NM_006395
shRNA against Beclin 1	Sigma	SHCLNV-NM_003766
shRNA scramble	Sigma	SHC202V
siRNA Ambra1 5'-GGCCUAUGGUACUAACAAAUU-3' 5'-UUUGUUAGUACCAUAGGCCUU-3'	This paper	N/A
Foxp3 Taqman probe	Applied Biosystems	Hs01085834_m1
Tbet Taqman Probe	Applied Biosystems	Hs00203436_m1
RORc Taqman Probe	Applied Biosystems	Hs01076112_m1
Foxo3 Taqman Probe	Applied Biosystems	Hs00921424_m1
ribosomal protein L34 Taqman Probe	Applied Biosystems	Hs00241560_m1
primers for Ambra1 amplification RT-PCR Fw: 5'-AACCTCCACTGCGAGTTGA-3' Rw: 5'-TCTACCTGTTCCGTGGTTCTCC-3'	This paper	N/A
Recombinant DNA		
pLPCX- β -Gal	Cianfanelli et al. (2015)	N/A
pLPCX-AMBRA1-WT	Cianfanelli et al. (2015)	N/A
pLPCX-AMBRA1-PXP	Cianfanelli et al. (2015)	N/A
pCDNA3-FOXO3a-TM-HA	This paper	N/A
Software and Algorithms		
Adobe Illustrator CS6	Adobe System	www.adobe.com
ImageJ2	NIH	https://imagej.nih.gov/ij/
ZEN 2009 Light edition software	Zeiss	www.zeiss.com
FlowJo vX.0.7	FlowJo, LLC	www.flowjo.com
Other		
High Performance Cell Sorting (MoFlo)	Beckman Coulter	N/A
Neon Transfection System	Thermo Fisher	N/A
Zeiss LSM 700	Zeiss	N/A
BD Accuri C6 Flow Cytometer	BD Bioscience	N/A
BD FACSCanto II Flow Cytometer	BD Bioscience	N/A
LightCycler 480	Roche	N/A
Transwell Assay 24-well Multiwell 3 μ m-pores	Corning Costar	3415

CONTACT FOR REAGENT AND RESOURCE SHARING

Further information and requests for resources and reagents should be directed to and will be fulfilled by the Lead Contact, Francesco Cecconi (cecconi@cancer.dk).

EXPERIMENTAL MODEL AND SUBJECT DETAILS

Peripheral blood samples were purified from buffy coats of healthy adult (range 20–65 years of age) volunteer blood donors (independently of sex) under procedures approved by ethical committee from Policlinico Tor Vergata (Rome), including informed consensus for research purpose, by density gradient over Ficoll-Hypaque (Amersham Pharmacia Biotech, Uppsala, Sweden) according to standard procedures, as previously described ([Cencioni et al., 2015](#)). Briefly, blood cells were incubated with RosetteSep Human T cell enrichment cocktail antibody mix (StemCell) and unlabeled T cells were isolated by density gradient over Ficoll-Hypaque, with centrifugation for 20min at 1200rcf. Then T cells have been collected, washed and further processed by Cell Sorting to isolate naïve cells (as detailed below).

C57BL/6 Lck:Cre transgenic mice purchased from Jackson Laboratory were crossed with C57BL/6 Ambra1 floxed mice, a new line generated in our laboratory, to generate KO Ambra1 fl/fl Lck:Cre mice (indicated as fl/fl cre+ in the Figures) and control Ambra1 fl/fl mice (fl/fl). Ambra1 gt/+ line was already present in our animal facility (see "[Cianfanelli et al., 2015](#)"). All mice were bred and

maintained under conventional conditions at Plaisant Srl (Castel Romano) and IRCCS Fondazione Santa Lucia Animal Facilities. They were kept in cages of no more than 5-6 mice each, divided by sex, under 12h/12h light/dark cycle, with standard temperature, humidity and pressure conditions according to FELASA guidelines. Small red squared mice house and paper were used for cage enrichment. From breeding until weaning a specific food (richer in fat and protein than the standard one used for maintenance) were used in all cages. Mice health were monitored daily by veterinary staff and health analysis for pathogens were performed every three months according to FELASA guidelines. Weaning was performed not earlier than 28 post-natal days. For all the experiments, mice were sacrificed by neck dislocation at 2-3 months of age. Male mice have been used for studies with tumors, while female mice for EAE experiments. All other experiments were performed on mice independently of sex. Blood has been collected from heart ventricles by syringe needle or from submandibular plexus. All efforts were made to minimize animal suffering and to reduce the number of mice used, in accordance with the European Communities Council Directive of 24 November 1986 (86/609/EEC). The mice protocols have been approved by the IRCCS Fondazione Santa Lucia and the Plaisant Srl Ethical Committees as well as by the Italian Ministry of Health (Authorizations #459/2015-PR and #84/2014-B). They have been written following both the ARRIVE Guidelines, and the numeric details have been chosen following the criteria described in The National Centre for the Replacement, Refinement and Reduction of Animals in Research (NC3Rs) (<http://www.nc3rs.org.uk/>).

Jurkat cell line has been cultured in complete RPMI 1640 medium (Gibco) supplemented with 10% Fetal Bovine Serum (Gibco), 2mM L-glutamine, 100U/ml penicillin/streptomycin, 1x Gibco MEM Non-essential amino-acids and 1mM Sodium pyruvate (Thermo Fisher).

HeLa cell line has been cultured in complete DMEM medium (Gibco) supplemented with 10% Fetal Bovine Serum (Gibco) and 100U/ml penicillin/streptomycin solution.

Murine T cells have been cultured in complete RPMI 1640 medium (Gibco) supplemented with 10% Fetal Bovine Serum (Gibco), 2mM L-glutamine, 100U/ml penicillin/streptomycin, 1x Gibco MEM Non-essential amino-acids, 1mM Sodium pyruvate, 100µg/ml Gentamycin and 55µM beta-mercaptoethanol (Thermo Fisher).

MC38 tumor cells have been cultured in complete DMEM medium (Gibco) supplemented with 10% Fetal Bovine Serum (Gibco), 2mM L-glutamine, 100U/ml penicillin/streptomycin, 1x Gibco MEM Non-essential amino-acids, 1mM Sodium pyruvate and 55µM beta-mercaptoethanol (Thermo Fisher).

METHOD DETAILS

Cell Isolations

Human or murine naive CD4⁺ T cells were isolated by high performance cell sorting (MoFlo) from human peripheral blood mononuclear cells (PBMC) or mouse spleens, respectively. The human CD4⁺ CD45RA⁺ CD27⁺ fraction was sorted using anti-human CD4-FITC, anti-human CD45RA-PE and anti-human CD27-APC (all Miltenyi). The murine CD4⁺ CD62L^{high} CD44^{low} fraction was sorted using anti-mouse CD4-FITC, anti-mouse CD62L PE and anti-mouse CD44 APC (eBioscience).

Cell Culture, Lentiviral Infection and Transfection

Human naive CD4⁺ T cells were cultured in X-VIVO and stimulated in the presence of anti-CD3/anti-CD28 coated Dynabeads (Life Technologies) and 10 ng/ml IL-12 (Th1); 10 ng/ml IL-2 and 2 ng/ml TGF- β (T_{reg}) or in the absence of cytokines (Th0) for 5 days. AMBRA1 was downregulated by infection with a lentiviral construct expressing a shRNA against AMBRA1 (Sigma) and polarized as described. Mouse CD4⁺ T cells were cultured in RPMI and stimulated in the presence of anti-CD3/anti-CD28 coated Dynabeads (Life Technologies) and 2,5 ng/ml human-TGF- β .

HeLa cells were transfected with Lipofectamin2000 (Life Technologies) according to the manufactures' protocol with a siRNA against AMBRA1 or with the following vectors: pLPCX- β -Gal, pLPCX-AMBRA1-WT; pLPCX-AMBRA1-PXP.

HeLa cells were treated with the proteasome inhibitor MG-132 (5 μ M) or the ribosomal inhibitor Cycloheximide for the indicated time periods.

Human peripheral blood T cells have been polarized under T_{reg} conditions and treated or not with lysosomal inhibitor 50nM chloroquine or 50nM Bafilomycin for 1 hour before protein extraction for western blot analysis.

Jurkat cells have been electroporated with a specific siRNA against Ambra1 and with pCDNA3-FOXO3a-TM-HA plasmid (after 24 hours) using Neon Transfection System (Thermo Fisher), following manufacturer instructions. After 6 hours, Jurkat cells were stimulated at 1:1:1 ratio with anti-CD3/CD28 (eBioscience)-coated latex beads (Invitrogen) for 16 hours and then processed for FOXP3 expression (flow cytometry) and AMBRA1 and HA levels (western blot).

Flow Cytometry

All plots shown are on populations gated on lymphocytes by forward and side scatter. For intracellular staining the FOXP3 staining kit (eBioscience) was used. Cells were stained with the following antibodies: anti-human CD4, anti-human CD25, anti-human FOXP3, anti-human Interferon- γ , anti-human Interleukine-17 (Miltenyi), anti-mouse CD4, anti-mouse CD8, anti-mouse Foxp3, anti-mouse CD25, anti-mouse Helios, anti-mouse Nrp1, anti-mouse CD39, anti-mouse CD73, anti-mouse CCR7, anti-mouse CXCR4, anti-mouse ROR γ t and anti-mouse Tbet (Biolegend) and anti-human/mouse ki67 (BD Pharmingen). Samples were analysed using BD Accuri C6 or FACSCanto II cytometers (BD Bioscience) and analysed using FlowJo vX.0.7 software.

Transwell Assay

5×10^5 thymocytes have been starved from serum for 2 hours in Basal Medium (RPMI complete medium without FBS, BSA added at final 0.1% concentration) and then plated in 100 μ l of Basal Medium in the upper chamber of 3 μ m-pore transwell assay chambers (Corning). The lower chamber has been filled with 600 μ l of Basal Medium containing CCL19 and CCL21 chemokines at 50nM (R&D System). Cells have been allowed to migrate for 2 hours and then quantified with BD Accuri C6 cytometer (gating on CD8⁻CD4⁺CD25⁺ cells). Migration index indicates the number of migrated cells (corrected for initial cell number) relative to the amount of control (fl/fl) migrated ones.

Western Blot and *In Vitro* Phosphatase Assay

Total cell lysates and western blots were performed as previously described (Cianfanelli et al., 2015). Briefly, cells were lysed with RIPA buffer (10 mM Tris-Cl pH 8.0; 1 mM EDTA; 1% Triton X-100; 0.1% sodium deoxycholate; 0.1% SDS; 140 mM NaCl; including protease and phosphatase inhibitor cocktail from Thermo Scientific), denatured using NuPage LDS Sample Buffer (Thermo Scientific) and heated at 95°C for 5min. The following primary antibodies were used: anti-AMBRA1 (SDIX, Millipore), anti-FOXP3, anti T-BET (both e-Bioscience), anti-FOXO3, anti-phospho-FOXO3 S253, anti-LC3, anti-phospho-AKT T308 (all Cell Signaling), anti-HA (Thermo Fisher), anti-ACTIN.

Endogenous FOXO3 substrate was isolated from a mammalian system (Jurkat cells) to ensure proper phosphorylation status. Cells were lysed in phosphatase assay buffer (50mM Hepes, pH 7.5, 100 mM NaCl, 2 mM MgCl₂, 1 mM dithiothreitol (DTT) and 0.5% NP-40) supplemented with protease and phosphatase inhibitors. FOXO3a was immunoprecipitated with Anti-FOXO3 antibody (cat num 2497, Cell Signaling) and then incubated with Protein G dynabeads (Thermo Fisher Scientific), subsequently PP2Ac recombinant protein (Cayman chemical) was added.

Immunocytochemistry

Cells were washed in PBS and fixed with 4% formaldehyde in PBS for 15 min, permeabilized with 0.4% Triton X-100 for 10 min, blocked in 3% Normal goat serum and incubated over-night at 4 degrees using the following primary antibodies: polyclonal anti-AMBRA1 (Covalab 0224), monoclonal anti-FOXO3 (Sigma) and monoclonal anti-FOXP3 (eBioscience) and finally labelled with anti-mouse (Alexa Fluor 488, Molecular Probes, Eugene, OR) or anti-rabbit (Cy3, Jackson ImmunoResearch, West Grove, PA) secondary antibodies. Nuclei were stained with DAPI and examined under a Zeiss LSM 700 100x oil-immersion objective. We used "ZEN 2009 Light edition" software and ImageJ for image analysis. All analyses were performed in non-saturated single z-confocal planes.

Real-Time PCR

RNA was extracted using the RNeasy Micro Kit (Qiagen) according to the manufactures protocol. A mixture containing random hexamers, oligo(dT) (Promega) and SuperScript II Reverse Transcriptase (Invitrogen) was used for cDNA synthesis. Transcripts were quantified by real-time quantitative PCR on a LightCycler 480 (Roche) with Applied Biosystems predesigned TaqMan Gene Expression Assays and Absolute QPCR ROX mix (Thermo Fisher Scientific). The following probes were used (Applied Biosystems assay identification numbers in parentheses): FOXP3 (Hs01085834_m1), T-bet (Hs00203436_m1), RORc (Hs01076112_m1), FOXO3 (Hs00921424_m1). For each sample, mRNA abundance was normalized to the amount of ribosomal protein L34 (Hs00241560_m1).

Suppression Assay

Murine T cells have been isolated from spleen and purified using Miltenyi CD4⁺ T cell Isolation Kit and Miltenyi CD25⁺ Microbeads to isolate CD4⁺ CD25⁻ T cells (T_{conv}) and CD4⁺ CD25⁺ T cells (T_{reg} cells). T_{conv} have been pre-treated with CFSE (eBioscience) for 30min and T_{reg} cells with eFluor670 Cell Proliferation Dye (eBioscience). Then T_{conv} have been cultured for up to 3 days in 96w plate at 1:1 ratio with anti-CD3/CD28 coated latex beads (Invitrogen) plus IL2 and in presence or not of T_{reg} cells at 1:1 ratio. CFSE fluorescence have been analysed at 1 and 3 days from initial stimulation. The Cell Division Index (i.e. the mean number of cell divisions in each condition) has been calculated according to FlowJo Software procedure.

LPS Infection

2 months-old mice have been injected i.p. with 200 μ g of lipopolysaccharide (LPS). Then after 4 days mice have been sacrificed and cells isolated from spleen for cytofluorimetric analysis. When indicated, WT mice have been previously injected i.v. with 2×10^6 purified naive CD4⁺ CD25⁻ T cells (Miltenyi CD25⁺ Microbeads) labelled with either CFSE or eFluor670 Cell Proliferation dyes (eBioscience) and then immediately injected i.p. with LPS.

Tumor Model

5×10^5 MCA38 cells were injected subcutaneously into the right flank of two-month old c57BL6 male mice. After 18 days, mice were sacrificed and tumors, together with inguinal lymph nodes were collected. Tumor size was recorded as longest diameter \times (shortest diameter)² (in cubic millimeters). Tumor tissue were mechanically dissociated over 70 μ m-cell strainers, and mononuclear cells were enriched from tumor-derived cell suspensions by 40% - 80% Percoll (GE Healthcare) density gradient, by collecting cells at the interface between 40% and 80% Percoll solution. T cells were extracted from lymph nodes as previously described.

Mice and EAE Induction

8 weeks old mice were sacrificed by neck dislocation and T cells have been isolated from spleen, inguinal lymph nodes and thymus for cytofluorimetric analyses.

EAE was induced in 8 weeks old female c57BL6 *Ambra1*^{9t/+} or c57BL6 wild-type mice or in 12 weeks old female c57BL6 *Ambra1*^{fl/fl:cre} or control c57BL6 *Ambra1*^{fl/fl} mice by active immunization with myelin oligodendrocyte glycoprotein p35–55 (MOG_(35–55)) as previously described (Mandolesi et al., 2012). Animals were scored daily for clinical symptoms of EAE, according to the following scale: 0, no clinical signs; 1, flaccid tail; 2, hind limb weakness; 3, hind limb paresis; 4, complete bilateral hind limb paralysis; 5, death.

For cytofluorimetric analysis, immune infiltrates have been isolated from brain and spinal cord of EAE mice by centrifugation on a Percoll 35% - 70% gradient.

Evaluation of Neuropathology in EAE Mice

At the time of sacrifice, mice were transcardially perfused with 4% paraformaldehyde. Spinal cords were removed and post-fixed in the same fixative for 2–4 h, washed in PBS, and then embedded in paraffin or post-fixed o.n. in the same fixative, cryopreserved in sucrose 30% for 24 hours and then included in OCT solution. Tissue sections were cut at 4 μm on a microtome or at 12 μm with the cryostat and stained for histological examination. Haematoxylin and eosin staining were used to reveal perivascular inflammatory infiltrates, Kluver Barrera staining was used to reveal demyelinated areas, and Bielschowsky staining was used to detect axonal loss.

Immunohistochemistry and Immunofluorescence

Immunohistochemical staining was performed on spinal cord slides, in order to evaluate FoxP3 (anti-Foxp3 rabbit polyclonal ab, 54501, Abcam) and CD3 (anti-CD3 rabbit monoclonal ab, clone SP7, Abcam) expression. Paraffin slides have been deparaffinized in xylene and rehydrated through graded alcohols. Antigen retrieval has been performed with slides heated in 0.01 M citrate buffer (pH 6.0) in a bath for 20 min at 97°C. After antigen retrieval, the slides were allowed to cool, rinsed with TBS and the endogenous peroxidase was inactivated with 3% hydrogen peroxide. After protein block (BSA 5% in PBS 1x), every slide has been incubated with specific primary antibody. The sections have been rinsed in TBS and incubated for 1 hour with respectively Goat Anti-Rabbit antibody (Alkaline Phosphatase-conjugated) for FoxP3 and Novocastra Biotinylated Secondary Antibody (HRP-conjugated) for CD3 and visualized with Vulcan Fast Red and DAB chromogen respectively. Finally, the sections were counterstained with haematoxylin and mounted. For each sample, positive cells were counted evaluating at least five fields at 400x magnification in each sample.

For FOXP3 immunofluorescence, spinal cord slices were washed, permeabilized in 0.4% Triton/PBS for 30 minutes, blocked in 0.5% BSA/0.5% Casein in TN Buffer (hereafter “blocking buffer”) for 1h and incubated overnight at 4°C with a mouse anti-FOXP3 antibody (eBioscience) 1:100 in blocking buffer. Immunodetection was performed with a goat anti-mouse AlexaFluor488 antibody 1:1000 in blocking buffer (2h room temperature). Nuclei were counterstained in DAPI 0.5 μg/ml.

CD3 required an amplification step to be properly detected by immunofluorescence. Briefly, slides were treated with 0,3% H2O2 in TN buffer for 1 h, blocked for 1h in blocking buffer then incubated overnight at 4°C with a mouse anti-CD3 antibody (Biolegend) 1:50 in blocking buffer. Slides were subsequently incubated 1h with a biotin-conjugated goat anti-mouse secondary antibody (Perkin Elmer) 1:1000 in blocking buffer, treated for 30 min with HRP-streptavidin (1:250 in blocking buffer, Perkin Elmer) and processed with a Cy3 tyramide solution (Perkin Elmer) for 10 min. Nuclei were counterstained as indicated above.

QUANTIFICATION AND STATISTICAL ANALYSIS

Statistical analysis has been performed using paired or unpaired student T-test (two groups) or with one-way and two-way ANOVA (multiple groups). Wilcoxon Signed Rank Test have been used for qPCR data. Data are shown as mean ± SEM or SD or as dot density plot (mean value indicated by black horizontal bar).

DATA AND SOFTWARE AVAILABILITY

No datasets or software have been generated in this study.

ATM kinase sustains breast cancer stem-like cells by promoting ATG4C expression and autophagy

Martina Antonelli^{1,2}, Flavie Strappazon¹, Ivan Arisi³, Rossella Brandi³, Mara D'Onofrio³, Manolo Sambucci⁴, Gwenola Manic², Ilio Vitale^{2,5}, Daniela Barilà^{1,2}, Venturina Stagni¹

¹Instituto di Ricovero e Cura a Carattere Scientifico (IRCCS) Fondazione Santa Lucia, Rome, Italy

²Department of Biology, University of Rome 'Tor Vergata', Rome, Italy

³Genomics Facility, European Brain Research Institute (EBRI) 'Rita Levi-Montalcini', Rome, Italy

⁴Neuroimmunology Unit, Fondazione Santa Lucia, IRCCS, Rome, Italy

⁵Regina Elena National Cancer Center Institute, Rome, Italy

Correspondence to: Venturina Stagni, **email:** venturina.stagni@gmail.com
Daniela Barilà, **email:** daniela.barila@uniroma2.it

Keywords: ATM kinase, breast cancer stem cells (BCSCs), mammospheres, autophagy, ATG4

Received: July 05, 2016

Accepted: January 23, 2017

Published: February 20, 2017

ABSTRACT

The efficacy of Ataxia-Telangiectasia Mutated (ATM) kinase signalling inhibition in cancer therapy is tempered by the identification of new emerging functions of ATM, which suggests that the role of this protein in cancer progression is complex. We recently demonstrated that this tumor suppressor gene could act as tumor promoting factor in HER2 (Human Epidermal Growth Factor Receptor 2) positive breast cancer. Herein we put in evidence that ATM expression sustains the proportion of cells with a stem-like phenotype, measured as the capability to form mammospheres, independently of HER2 expression levels. Transcriptomic analyses revealed that, in mammospheres, ATM modulates the expression of cell cycle-, DNA repair- and autophagy-related genes. Among these, the silencing of the autophagic gene, autophagy related 4C cysteine peptidase (ATG4C), impairs mammosphere formation similarly to ATM depletion. Conversely, ATG4C ectopic expression in cells silenced for ATM expression, rescues mammospheres growth. Finally, tumor array analyses, performed using public data, identify a significant correlation between ATM and ATG4C expression levels in all human breast cancer subtypes, except for the basal-like one.

Overall, we uncover a new connection between ATM kinase and autophagy regulation in breast cancer. We demonstrate that, in breast cancer cells, ATM and ATG4C are essential drivers of mammosphere formation, suggesting that their targeting may improve current approaches to eradicate breast cancer cells with a stem-like phenotype.

INTRODUCTION

The cancer stem cell hypothesis proposes that cancers arise from and are maintained by a small population of cancer-initiating cells residing within tumor mass. These cells are characterized by the re-expression of stem cell markers and self-renewal potential, and have therefore been named cancer stem cells (CSCs) or more exactly cancer stem-like cells. [1]. In recent years, CSCs have been identified in multiple cancers, including

breast cancer, and they were shown to be particularly resistant to conventional anticancer therapy, which may contribute to treatment failure and tumor relapse [2]. The fate of cancer stem cells is determined by the "stem cell niche" in the tumor, which comprises stromal cells, cytokines, and growth factors. Moreover this niche is characterized by starvation and hypoxic conditions that are considered critical niche factors to promote invasive growth of tumors. The observation that CSCs have a specific regulation by the microenvironment suggests the

presence of a peculiar metabolic demand and a specific response to environmental stresses in these cells compared to the bulk tumor [3]. Molecular mechanisms involved in their regulation, maintenance and resistance to therapies are peculiar and specific for this subpopulation of cells in the tumor and so targeting strategies for the destruction of CSCs specific signalling pathways provides a novel opportunity for cancer research [3].

Ataxia-Telangiectasia Mutated (ATM) is a multifunctional kinase that plays complex and controversial roles in cancer. ATM is historically considered a tumor suppressor gene for its central role in the DNA damage response (DDR) [4, 5]. Indeed, this kinase is considered as a good target for cancer therapies and, consistently with its DDR function, also drives the therapeutic resistance of CSCs [6-8]. We have recently identified ATM as a promoter of HER2 tumorigenicity in breast cancer [9], suggesting a dual function of ATM in cancer. In particular, we showed that abrogating ATM function significantly impaired HER2-dependent tumorigenicity *in vitro* and *in vivo* also uncovering a novel cancer-related function of ATM as regulator of HER2 receptor stability [9]. Importantly, ATM plays non-nuclear functions in addition to the DDR signalling that may contribute to its dual, opposing role in cancer [6-8]. The emerging role of ATM in the regulation of autophagy is intriguing [10-12], although its impact on cancer progression has been poorly investigated so far. Interestingly, by using *Atm*^{-/-}*Becn1*^{+/-} mice model, it was demonstrated that the genetic inactivation of the autophagic gene Beclin 1 results in a significant delay of lymphoma and leukaemia onset normally occurring in *Atm*-deficient mice, due to the rescue of mitochondrial abnormalities and not of the DDR [13]. This observation supports the hypothesis that ATM kinase and autophagy could talk each other in the regulation of cancer progression.

The role of autophagy in carcinogenesis remains elusive. Autophagy may promote or counteract tumor initiation and progression depending on the specific context [14]. Recent evidence support the idea that autophagy could act as a cytoprotective process to augment CSC survival under conditions of nutrient or growth factor starvation, metabolic stress, and hypoxia within the “stem cell niche” in the tumor [15, 16]. Consistently, autophagy is an important driver of stem-like phenotype in breast cancer [17-19] and autophagic genes such as ATG4A and Beclin 1 play a role in breast (B)CSC maintenance, further supporting the idea that BCSCs employ autophagy for promoting their survival and growth [18, 19].

Overall these evidences led us to investigate the role of ATM kinase in the regulation of the stem-like phenotype in breast cancer. Herein, we utilised the preparation of 3D spheroid cultures, also known as “mammospheres” [20], as functional assay to enrich for a population of cells with a stem-like phenotype to investigate the role of ATM in the regulation of Breast Cancer Stem-like cells. Our results give

novel insights into the molecular mechanisms underlying mammosphere formation attributing a previously unrecognised role in this process to the crosstalk between ATM kinase and ATG4C autophagic gene in breast cancer progression.

RESULTS

ATM expression determines the ability to form mammospheres and promotes breast cancer-stem like phenotype

Recent works suggest that HER2 is a driver of cancer stem-like phenotype in luminal estrogen receptor-positive (ERp) breast cancers, in the absence of HER2 gene amplification, and in breast cancers with amplification of HER2 receptor [21, 22]. In order to analyse the impact of ATM kinase on formation of cells with a stem-like phenotype in breast cancer, we choose as cancer model system: 1) mammospheres derived from luminal estrogen receptor-positive HER2-low breast cancer cell line (MCF7); 2) mammospheres derived from luminal estrogen receptor-positive HER2-overexpressing breast cancer cell line (MCF7-HER2). To avoid off-target effects, ATM expression was genetically downregulated by two specific shRNA interference in both cell lines, using lentiviral vectors, (Figure 1A) and *in vitro* mammospheres formation was assayed by measuring the ability to grow in low serum and anchorage independent conditions [20] (Figure 1B). In these experiments, we observed that the downregulation of ATM led to a decrease in mammospheres number and size in both MCF7 cell lines with the two ATM target sequences (Figure 1B). On average, 200 mammospheres formed from 8000 MCF7 cells (~2,5% of Sphere Forming Efficiency, SFE) seeded under serum-free suspension conditions and 400 mammospheres formed from 8000 MCF7-HER2 cells (~5 %, SFE) (Figure 1B), which is in accordance with the crucial role of HER2 receptor as promoter of mammospheres formation. Interestingly, the silencing of ATM caused a ~50% reduction in mammospheres number and diameter in both cell lines (Figure 1B). In addition to sphere formation, the colony formation capacity of dissociated mammospheres seeded in 2D adherent plate was analysed. As shown in Figure 1C, silencing of ATM expression significantly reduced the number of colonies grown in both cell lines. It is well established that, cells grown as mammospheres, compared to cells grown in adherent conditions, significantly upregulate the expression of genes driving the stem like phenotype [23]. In line with this observation, we could show that the expression of HER2 and of several stem cell markers such as SRY-box 2 (SOX2), POU class 5 homeobox 1 (POU5F1; best known as OCT4) and Nanog homeobox (NANOG) was elevated in mammospheres, derived from both cell lines, compared to adherent cells (Figure 2A).

Similarly, the level of ATM mRNA was upregulated in mammospheres, when compared to adherently cultured cells (Figure 2A). However, the selective silencing of ATM expression, with both target sequences using lentiviral vectors, resulted in the impairment of SOX2, but not of OCT4 and NANOG mRNA expression in mammospheres (Figure 2B).

To further investigate the role of ATM expression in driving the stem-like phenotype in breast cancer, we evaluated, by flow cytometry, the percentage of aldehyde dehydrogenase (ALDH) activity-positive cell population in our cell lines; indeed ALDH activity is validated as a well-known marker of the sub-population of cells with stem-like characteristics [24]. Consistently with previous reports [10], HER2 overexpression enhanced ALDH activity (Figure 2C) [10]. More interestingly, we could show that the genetic downregulation of ATM expression, with both shRNA sequences, resulted in the reduction of ALDH activity in both cell lines (Figure 2C and Supplementary Table 1). Overall, while these data indicate a role of ATM expression in the modulation of mammospheres formation, probably this is independent of HER2 expression levels. They also suggest that ATM exerts a mild effect on the expression of stemness markers.

Identification of ATM-dependent regulated gene set in mammospheres

To further uncover the molecular mechanism involved in ATM-mediated regulation of mammospheres formation, we performed a gene expression analysis. We used two different RNA interference sequences targeting ATM and we performed the experiment as biological triplicate: three independent lentiviral infections were carried out on both cell lines (MCF7 and MCF7-HER2) silenced or not for ATM, grown as mammospheres. Microarray based expression profiling, pooling all the experiments, revealed that 550 probes for MCF7 and 196 probes for MCF7-HER2 were significantly expressed in mammospheres derived from cells silenced for ATM in a differential fashion compared to those obtained from control cell lines, interfered with shGFP (Figure 3A). As ATM impairs mammospheres formation independently of HER2 expression (Figure 1), we focused our analysis on the differential expression of 115 genes intersected in MCF7 and MCF7-HER2, which are downregulated or upregulated upon ATM expression silencing (Figure 3A). We hypothesized that these genes could be responsible for ATM-dependent reduction of mammospheres formation irrespective of HER2 expression levels. Functional annotation of these 115 genes using DAVID (Database for Annotation, Visualization and Integrated Discovery) revealed that they are mainly associated to mitosis, regulation of protein kinase, cell cycle, DNA repair and cell death (Figure 3B). In Supplementary Table 2, we selected the first 10 upregulated and first 10 downregulated

genes in mammospheres shATM versus shCTR, involved in these pathways (Supplementary Table 2). Validation of the expression pattern of 9 genes (4 upregulated and 5 downregulated), from our 20 selected genes, obtained by microarray analysis was performed by qRT-PCR (Figure 3C and Supplementary Figure 1A-1B). In all cases, the trend of fold change of expression identified in the microarrays studies was confirmed by qRT-PCR experiments (Figure 3C). Interestingly, when we compared the expression of our selected genes in mammospheres with respective adherent parental cell lines, we observed that silencing ATM in mammospheres resulted in an expression profile more similar to that of adherent parental cells, supporting the idea that ATM expression could modulate essential genes involved in mammospheres formation (Supplementary Figure 1A-1B) [19].

Autophagic gene ATG4C promotes mammospheres formation

It was recently reported that some autophagic regulator genes, such as Beclin-1 and ATG4A, modulated the autophagic flux in mammospheres derived from MCF7 cells, and that the deregulation of this feature impaired mammospheres forming capacity [18, 19]. By analyzing our microarray and qRT-PCR expression data, we observed that the expression of the autophagic gene ATG4C was significantly downregulated in mammospheres interfered for ATM expression, compared to control ones (Supplementary Table 2 and Figure 3C). Moreover, ATG4C mRNA expression was upregulated in cells grown as mammosphere compared to the ones grown in adherent conditions (Supplementary Figure 1A). Overall, these data suggest that ATG4C may promote mammospheres formation.

To further validate our hypothesis we downregulated ATG4C expression by specific RNA interference selective for this isoform (Figure 4A and Supplementary Figure 2C). Remarkably, we could show that the downregulation of ATG4C expression impairs mammospheres forming ability (Figure 4B), similarly to what previously observed upon ATM expression silencing (Figure 1A-1B). ATG4C is one of the four members of ATG4s protease family (including ATG4A, B, C and D); the family members share similar structure but have very well established different functions [25]. Recently, ATG4A has been identified as a modulator of mammospheres formation [18]. Accordingly, we could show that the expression of all ATG4 family members is enhanced, although to different extent, in mammospheres compared to adherent cells. Importantly ATG4A was the ATG4 family members most strongly up regulated in our models (Figure 5A). More interestingly, ATM does not affect the mRNA levels of ATG4A, B and D neither in MCF7 nor in MCF7-HER2 cells (Figure 5B) driving the conclusion that ATM selectively impinges on ATG4C expression.

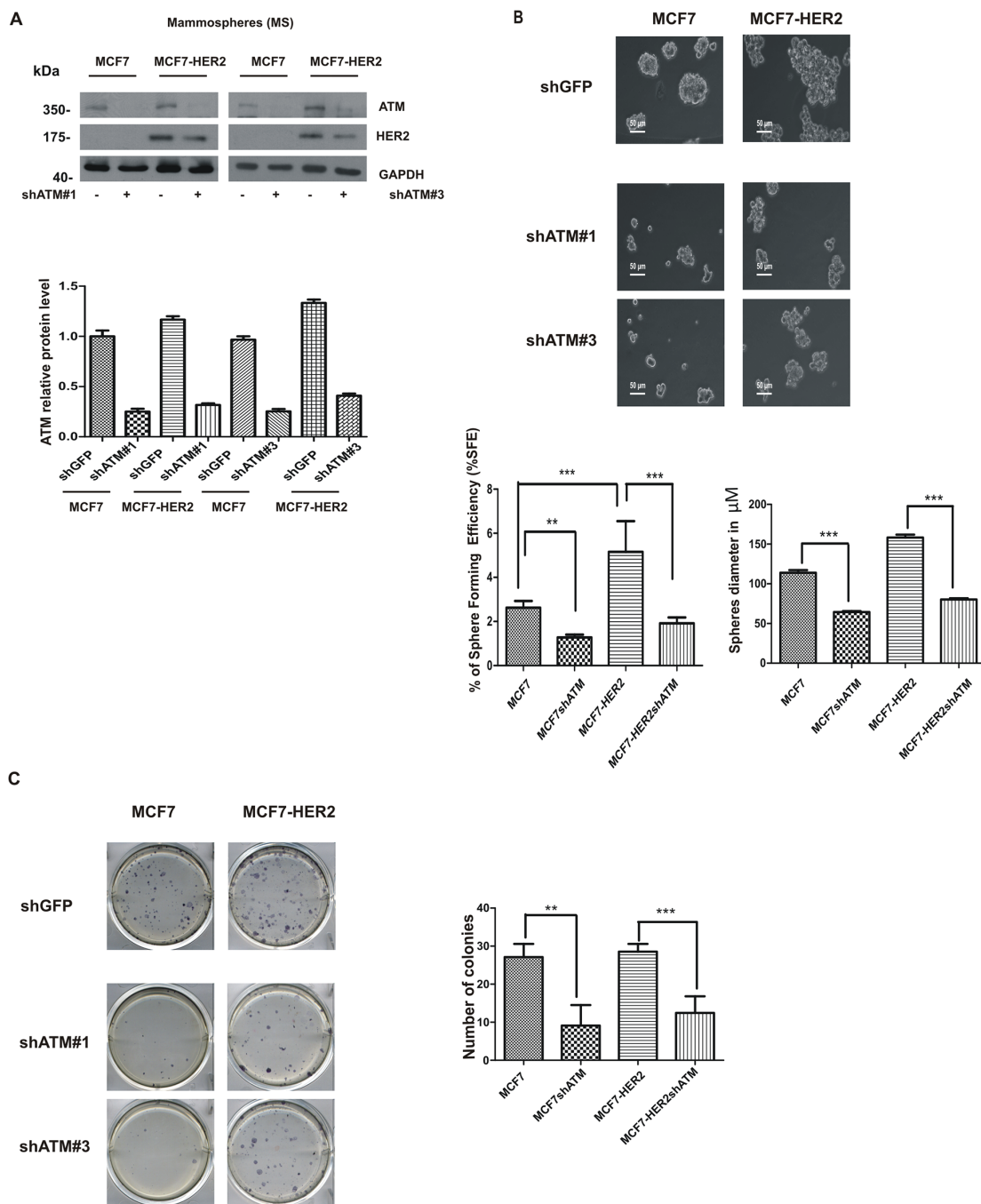


Figure 1: ATM expression promotes mammospheres formation. MCF7 and MCF7-HER2 breast cancer cell lines were infected with lentivirus expressing two different RNA interference for ATM (shATM #1 and shATM #3) or a control sequence (shGFP). **A.** Representative Western Blot analysis of ATM and HER2 protein levels in mammospheres (MS); GAPDH was used as loading control (upper panel). The graph represent quantification of ATM protein levels and it was determined using the ImageJ software. Results are indicated as mean±s.d. for three independent experiments **B.** Single cells were plated in ultralow attachment plates as described in Materials and methods section, so that cells with stem cell properties were allowed to grow as non-adherent spheroids (mammospheres). Images of the mammospheres were captured on day 7. Representative phase-contrast images of mammospheres are shown. Bars denote 50 μm. Numbers of the mammospheres (diameter>50 μm) were counted, and the % of Sphere Forming Efficiency (%SFE) was calculated based on the numbers of cells that were initially seeded as mean±s.d. for three independent experiments performed with both targeting sequences for ATM (shATM#1 and shATM#3). The diameter of mammosphere (in μm) was quantified using I.A.S software (Delta Sistemi, Italy). **C.** Mammospheres were dissociated by trypsin digestion and 600 cells/well were seeded in 6-well plates in differentiating media (mammospheres medium + 5% FBS serum). Colony formation was assessed 7 days later and stained with MTT (left panel). The number of colonies are expressed as mean±s.d. for three independent experiments performed with both targeting sequences for ATM (shATM #1 and shATM #3). Student's t-test **P<0.01, ***P<0.001 (right panel).

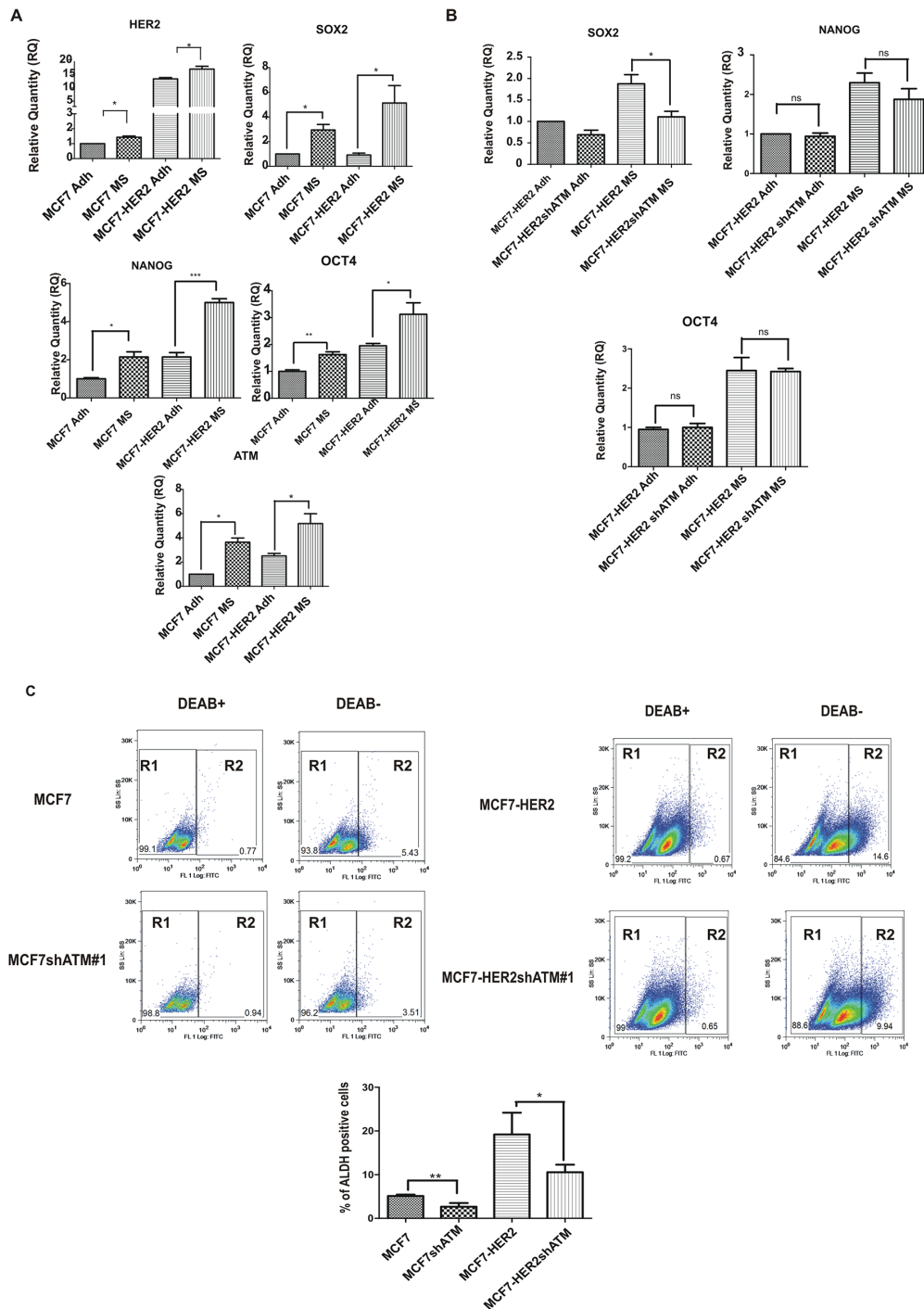


Figure 2: ATM expression promotes stem-like phenotype. **A.** The expression of HER2, ATM and SOX2, OCT4 and NANOG mRNA levels in non-infected Mammospheres (MS) and Adherent (Adh) cells was investigated using by quantitative Real-Time PCR. Relative quantities (RQ) were calculated to TBP (TATA-box Binding Protein) and are relative to MCF7 adherent parental cells (Adh). Results are expressed as the mean±s.d. for at least three independent experiments and analyzed using Student's t-test (*P<0.05, ***P<0.001). **B.** The expression of SOX2, OCT4 and NANOG mRNA levels was investigated as in infected Mammospheres (MS) with lentivirus expressing control interference (shGFP) or shATM. **C.** Indicated cells were assayed for ALDH activity utilizing the ALDEFLUOR™ assay (STEMCELL™ TECHNOLOGIES). Cells incubated with ALDEFLUOR substrate (BAAA) and the specific inhibitor of ALDH, diethylaminobenzaldehyde (DEAB), were used to establish the baseline fluorescence of these cells (R1) and to define the ALDEFLUOR-positive region (R2). Incubation of cells with ALDEFLUOR substrate in the absence of DEAB (DEAB-) induces a shift in BAAA fluorescence defining the ALDEFLUOR-positive population (R2). The quantification of ALDH-positive cells in each breast cancer cell line is shown (lower panel). Error bars indicate the s.d. from three independent experiments with both targeting sequences for ATM (shATM#1 and shATM#3).

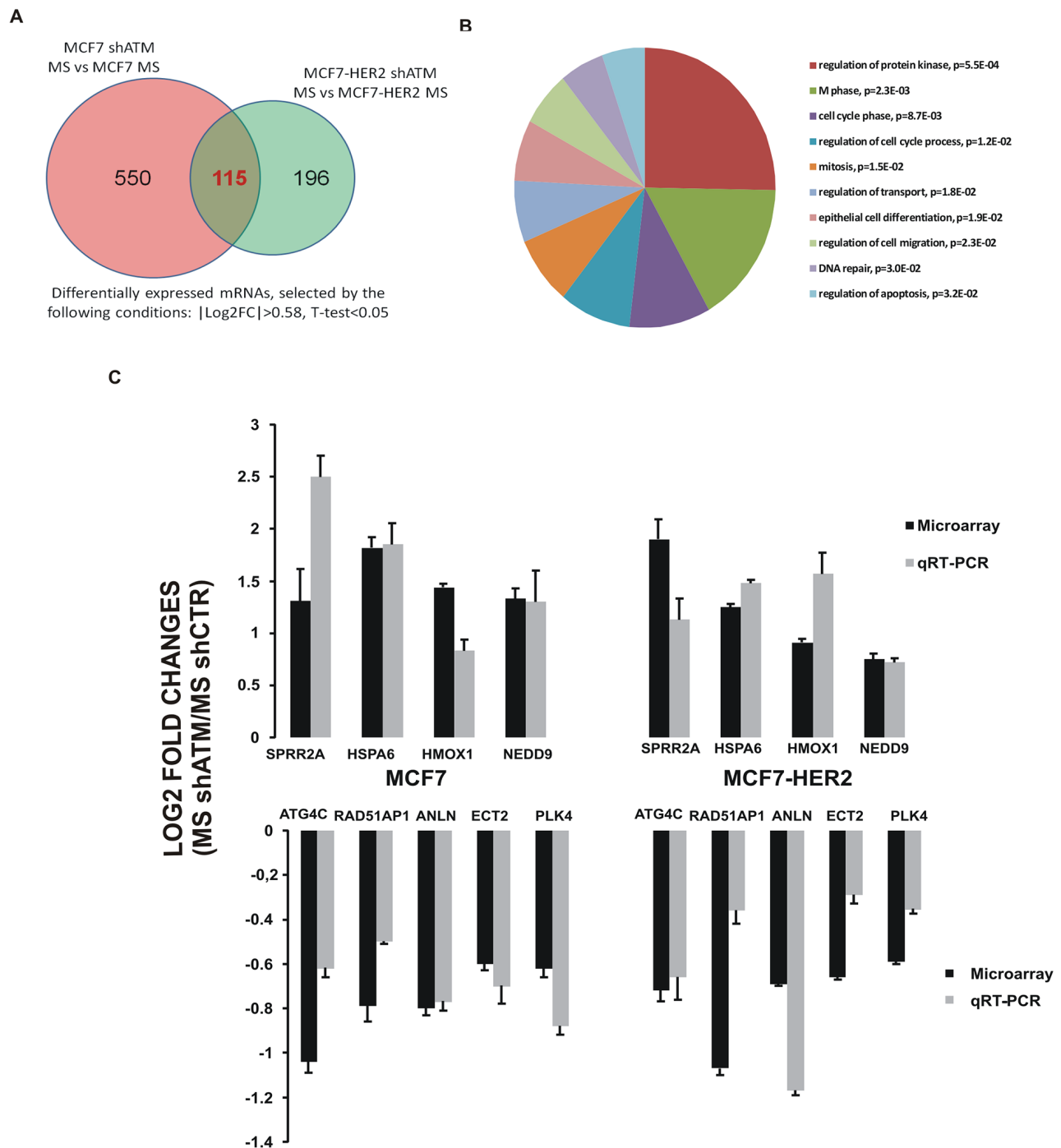


Figure 3: Gene expression profiling of mammospheres with or without interfering ATM expression. **A.** Number of differentially expressed mRNAs between mammospheres silenced for ATM and control mammospheres, obtained from three independent experiment performed with both targeting sequences for ATM (shATM#1 and shATM#3) and selected by the following conditions: $|\text{Log}_2\text{FC}| > 0.58$, T-test < 0.05 . In the Figure are shown the number of differentially expressed genes in mammospheres derived from MCF7 and from MCF7-HER2 cells. The intersection area encloses 115 common genes between mammospheres derived from both cell lines. **B.** Gene Ontology analysis of intersection set (115 mRNAs), obtained by the DAVID online tool. **C.** Microarray and qRT-PCR comparison. Log₂ Fold Change of 9 genes between mammospheres shATM vs shCTR detected by microarray (black lines) were compared with those measured by qRT-PCR (grey lines). Positive values represent gene expression upregulation and negative values downregulation in mammospheres silenced for ATM gene (shATM) compared to control cells (shCTR). qRT-PCR results were normalized with TBP. Error bars indicate standard deviations of at least three independently performed experiments.

ATM modulates ATG4C levels and sustains autophagic flux in mammospheres

ATG4C is a member of ATG4s proteases that are responsible for the cleavage of Microtubule-associated protein 1A/1B-light chain 3 (LC3-I) into LC3-II protein, which is then lipidated and recruited to autophagosomal membranes [25]. Tracking the conversion of LC3-I to LC3-II is indicative of ATG4s activity and thus of autophagic activity [26]. We therefore investigated whether the loss of ATM-dependent regulation of ATG4C expression level may result in a defect in autophagosome formation in mammospheres upon ATM silencing. To quantify autophagosome formation we analysed the expression and the processing of LC3 protein, a well-known marker of autophagy [27]. Western blot analysis

showed that the downregulation of ATM expression in mammospheres triggers the reduction of ATG4C protein levels (Figure 6A), and the impairment of LC3-I conversion into LC3-II monitored through quantification of LC3-II/LC3-I ratio (Figure 6A).

To further assess the effect of ATM-dependent regulation of ATG4C on autophagic response we checked the levels of the autophagic receptor p62/SQSTM1, an indicator of the autophagic flux which is known to be degraded following autophagy induction [28, 29]. Interestingly the downregulation of ATM expression in mammospheres, resulted in the accumulation of p62 compared to control cells (Figure 6A). Since autophagosome formation can result either from increased *de novo* autophagosome biosynthesis or from the inhibition of the autophagic flux, we distinguished between

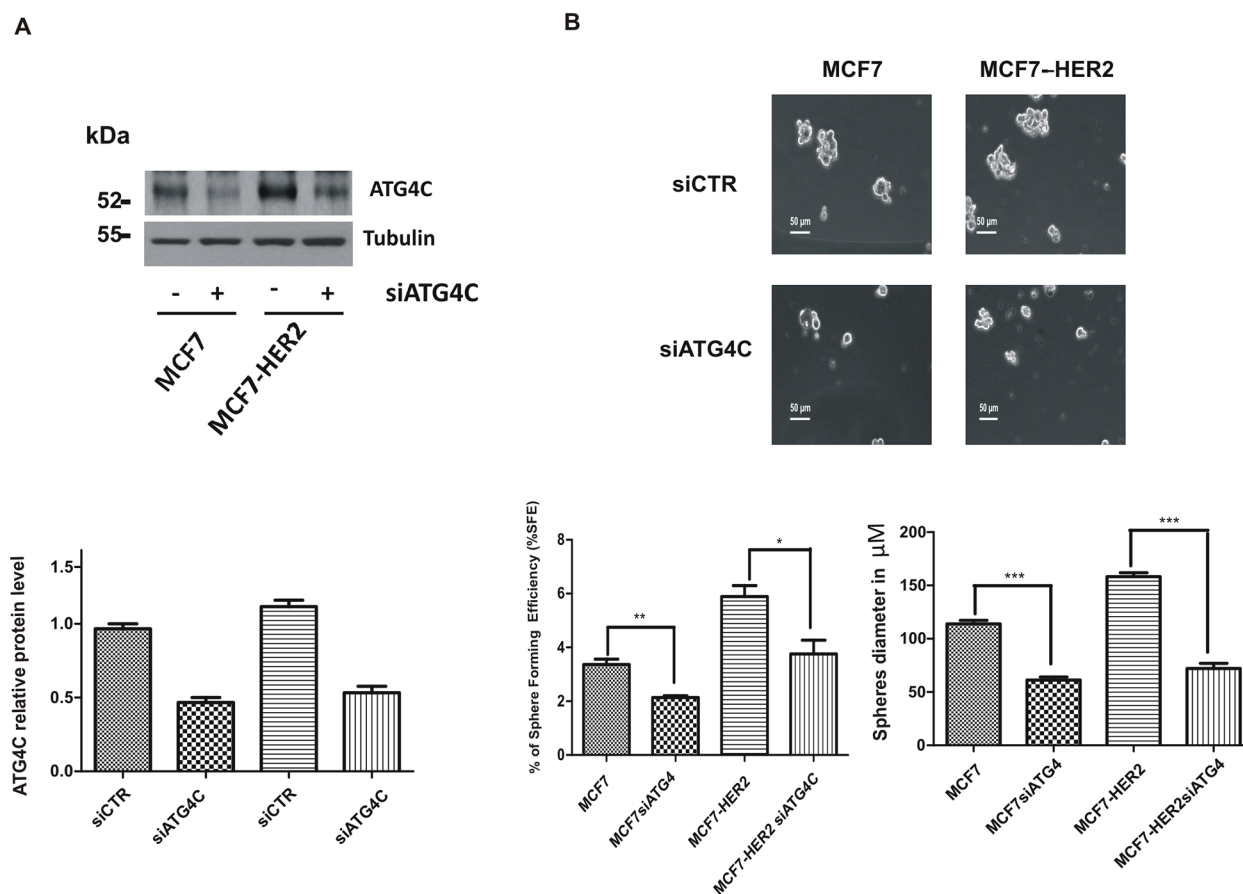


Figure 4: ATG4C expression promotes mammospheres formation. MCF7 and MCF7-HER2 breast cancer cell lines were transfected with ATG4C siRNA or a control sequence (SignalSilence®, Cell Signaling) using Lipofectamine® 3000 Reagent (Life Technologies). **A.** Representative Western Blot analysis of ATG4C protein levels in mammospheres (MS); Tubulin was used as loading control (upper panel). **B.** Single cells were plated in ultralow attachment plates as described in Materials and Methods section, so that cells with stem cell properties were allowed to grow as mammospheres. Images of the mammospheres were captured on day 7. Representative phase-contrast images of mammospheres are shown (upper). Bars denote 50 μm . Numbers of the mammospheres (diameter > 50 μm) were counted, and the %SFE was calculated based on the numbers of cells that were initially seeded (Bottom). mean \pm s.d. for three independent experiments and analysed using Student's t-test (* $P < 0.05$, ** $P < 0.01$, *** $P < 0.001$). The diameter of mammosphere (in μm) was quantified using I.A.S software (Delta sistemi, Italy).

these two possibilities using the lysosomal inhibitor chloroquine (CQ). Interestingly, in control condition, as expected, the CQ treatment blocks autophagic flux after LC3-II formation and before p62 degradation, resulting in an increased in LC3-II and p62 levels, (Figure 6B). Conversely, CQ treatment failed to induce an increase in LC3-II and p62 levels in ATM silenced mammospheres (Figure 6B) suggesting a block in the autophagic flux in shATM cells.

We confirmed these results by performing a confocal microscopy analysis of LC3 protein in mammospheres downregulated or not for ATM. In normal condition LC3 protein is cytosolic whereas it appears as “puncta” when autophagy is induced (LC3-II form). We could show a marked increase of LC3 dots in mammospheres compared to adherent cells in basal condition (Supplementary Figure 2A). Interestingly, consistently with western blot analysis (Figure 6A-6B), silencing of ATM expression drives a dramatic reduction in the formation of LC3-II dots in mammospheres (Figure 6C). To further investigate whether the reduction in the number of LC3 dots may be due to differences in the autophagic flux, MCF7 cells and

derived mammospheres, were treated with Chloroquine (CQ). Efficacy of this treatment was confirmed by an increase in LC3-II dots number/cells in response to CQ in control adherent cells and control mammospheres (Figure 6C and Supplementary Figure 2A). Conversely, shATM did not increase LC3 dots formation after chloroquine treatment in mammospheres, indicating that the downregulation of ATM expression induces a decrease in the autophagic flux in this context (Figure 6C), which confirmed data obtained with western blot analysis.

We next decided to check for autophagosome degradation. To this end, we quantified LC3-II dots co-localized with the lysosomal protease Cathepsin D, following CQ treatment. As expected, we found a significant reduction of LC3-II dots fused with lysosomes in shATM cells compare to control cells (Figure 6D). Of note, ATG4A, ATG7 and ATG5-12 are stable following shATM or siATG4C treatments (Supplementary Figure 2B-2C). These data indicate a specific and unique effect of ATM on ATG4C protein. Overall these results suggest that ATM expression sustains ATG4C levels and thus the autophagic response in mammosphere context.

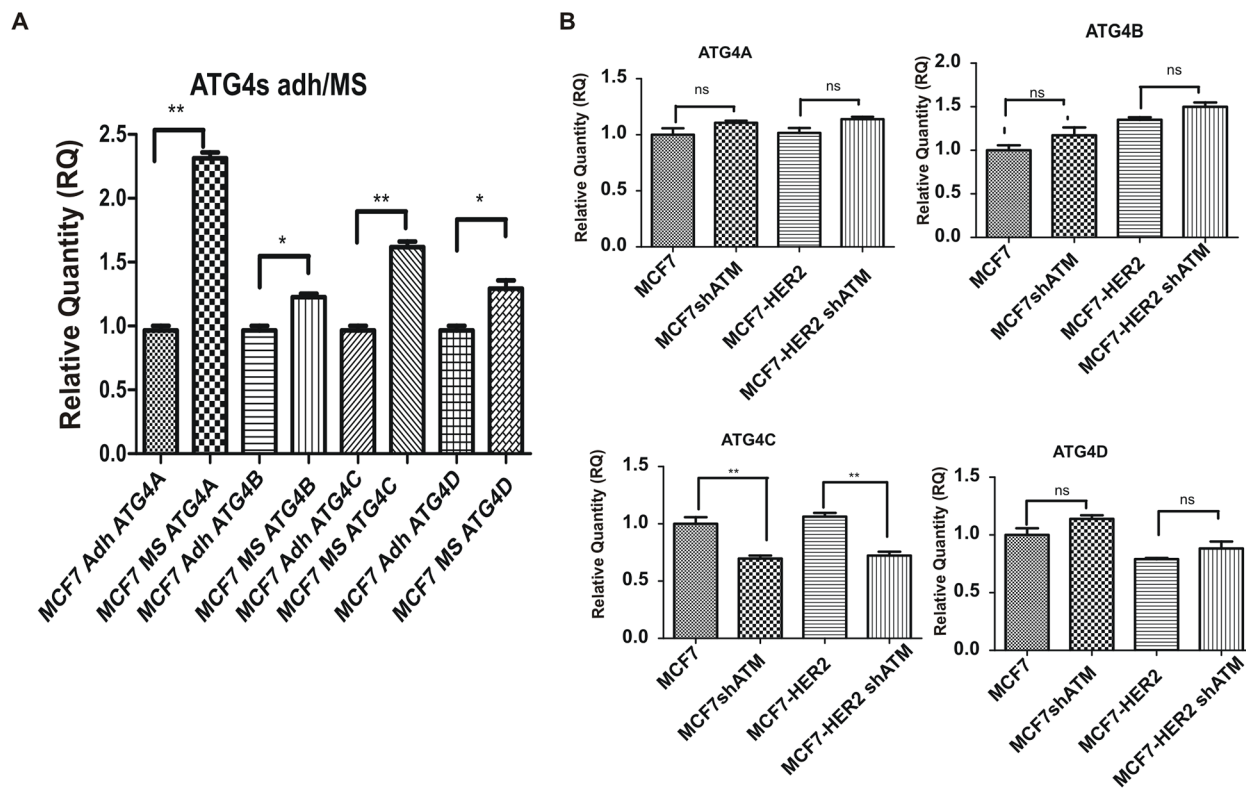


Figure 5: Downregulation of ATM expression selectively impinges on ATG4C expression. A. The expression of ATG4A, B, C and D mRNA levels in non-infected Mammospheres (MS) and Adherent (Adh) cells was investigated using by quantitative Real-Time PCR. Relative quantities (RQ) were calculated to TBP (TATA-box Binding Protein) and are relative to MCF7 adherent parental cells (Adh). Results are expressed as the mean±s.d. for at least three independent experiments and analyzed using Student's t-test (*P<0.05, **P<0.01). B. The expression of ATG4A, B, C and D mRNA levels was investigated as in (A) in infected Mammospheres (MS) with lentivirus expressing control interference (shGFP) or shATM.

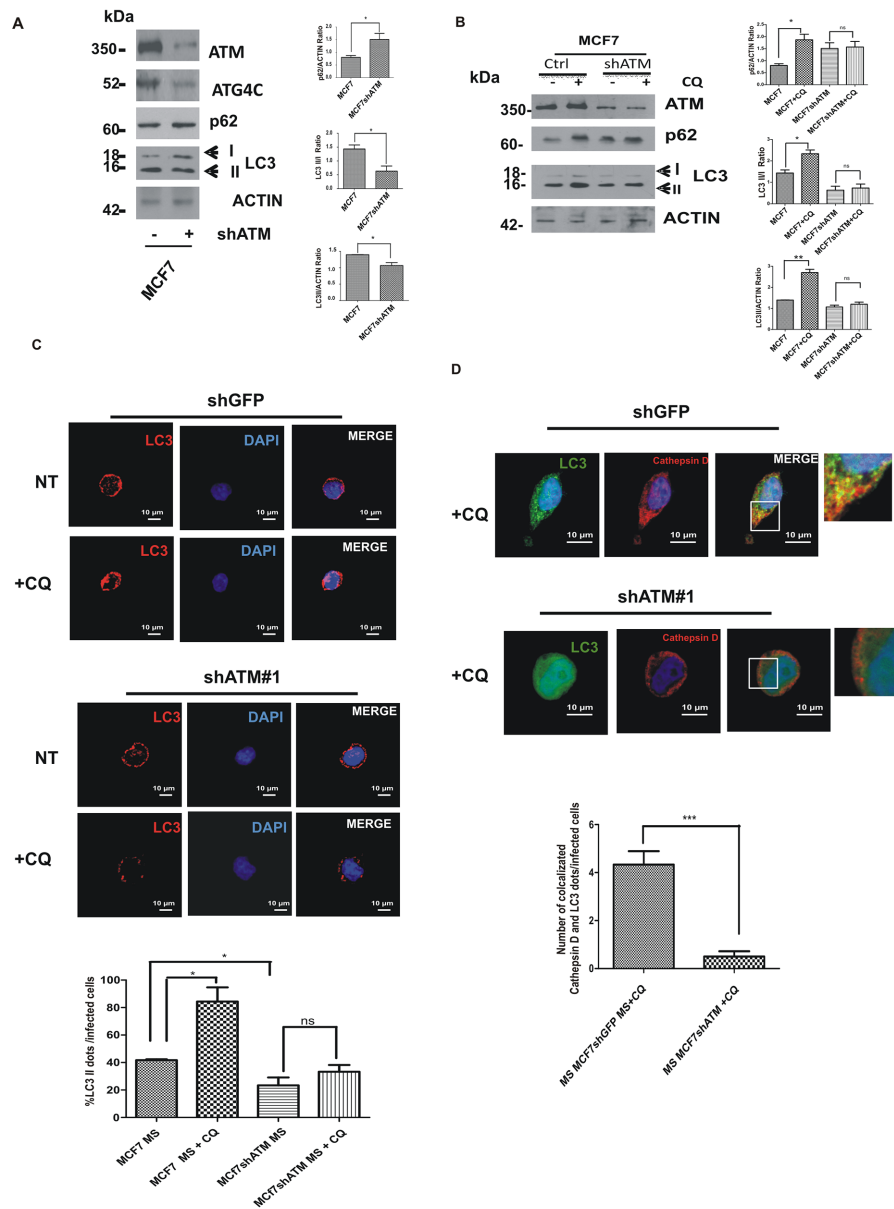


Figure 6: ATM expression regulates ATG4C levels and autophagic flux in mammospheres (MS). **A.** Representative Western Blot analysis of ATM, ATG4C, p62 and LC3 protein levels in mammospheres (MS) derived from MCF7 cell lines, with or without shATM. Actin was used as loading control. The graphs represented quantification of LC3 II/I ratio, LC3II/actin and p62/actin ratio was determined using the ImageJ software. Results are indicated as mean±s.d. for three independent experiments performed with both targeting sequences for ATM (shATM#1 and shATM#3) and analysed using Student's t-test (* $P < 0.05$, ** $P < 0.01$, *** $P < 0.001$). **B.** Representative Western Blot analysis of p62 and LC3 proteins in mammospheres (MS) with or without shATM and treated with CQ (20 μ M, 30 min). Actin was used as loading control. The graphs represented quantification of LC3 II/I ratio, LC3II/actin and p62/actin ratio was determined using the ImageJ software. Results are indicated as mean±s.d. for three independent experiments performed with both targeting sequences for ATM (shATM#1 and shATM#3) and analysed using Student's t-test (* $P < 0.05$). **C.** Representative image, using confocal microscopy, of the formation of autophagosome assayed by immunofluorescence for endogenous LC3 protein in MCF7 cells seeded from dissociated mammospheres. Mammospheres were treated or not with chloroquine CQ (20 μ M, 30 min) for analysing autophagic flux. The graph show the accumulation of LC3 dots per infected cells. Results are expressed as the mean±s.d. for at least three independent experiments performed with both targeting sequences for ATM (shATM#1 and shATM#3) and analysed using Student's t-test (* $P < 0.05$). **D.** Representative image, using confocal microscopy, of the lysosomal degradation of autophagosomes assayed by immunofluorescence for endogenous LC3 and Cathepsin D proteins in MCF7 cells seeded from dissociated mammospheres. Mammospheres were treated with chloroquine CQ (20 μ M, 30 min) in order to visualize the autophagosome degradation (co-localization LC3-II dots with Cathepsin D). The graph indicates a clear reduction of LC3-II dots co-localizing with Cathepsin D in ShATM infected cells. Results are expressed as the mean±S.D of at least three independent experiments performed with both targeting sequences for ATM (shATM#1 and shATM#3) and analysed using Student's t-test (*** $P < 0.001$).

Restoration of ATG4C expression rescues ATM ability to form mammospheres

To further validate the functional link between ATM and ATG4C expression in the modulation of autophagy and mammospheres formation, we overexpressed ATG4C in mammospheres previously silenced for ATM expression. In Figure 7A we confirmed by RT-PCR the overexpression of ATG4C in MCF7 and MCF7-HER2 cell lines interfered with shCTR and shATM constructs (Figure 7A). Importantly, the overexpression of ATG4C in cells silenced for ATM expression, significantly rescued the percentage of spheres formation (%SFE) of shATM cells which turn to be comparable to the one of shCTR cells (Figure 7B). This result demonstrated that there is a strong correlation between ATM-dependent regulation of ATG4C expression level and ATM-dependent regulation of mammospheres formation. This connection was independent of HER2 receptor expression levels as it can be observed in both cell lines. We cannot exclude that other proteins could be directly or indirectly involved in this regulation. Interestingly, re-expression of ATMwt in shATM mammospheres rescues ATG4C levels and mammosphere formation (Supplementary Figure 3A and 3B) further confirming the correlation between mammosphere formation and expression levels of ATM and ATG4C mRNA.

ATM and ATG4C gene expression correlation in breast cancer human samples

To further evaluate the clinical significance of our findings, we asked whether we could identify a significant correlation between ATM and ATG4C expression in breast cancer human samples. To this aim we took advantage of The Cancer Genome Atlas (TCGA) microarray data on of breast cancer samples. To quantify the correlation, we downloaded normalized genes microarray data from the TCGA Data Coordination Center [30] and computed the Pearson correlation coefficients and corresponding *P* values (Table 1). Highlighting ATM expression showed a significant positive correlation with the expression of autophagic gene ATG4C among microarray data derived from 511 breast cancer samples (Table 1). This observation suggests that the functional correlation between ATM and ATG4C genes in mammospheres could have also a significant relevance in breast cancer patients.

Breast cancer is a very heterogeneous disease. To further explore the relationship between ATM and ATG4C genes we calculated the correlations between ATM and ATG4 genes in all four subtypes of breast cancer based on published classifications [30]: two estrogen receptor (ER)-positive subtypes separated mainly by relatively low (luminal A) and high (luminal B) expression of proliferation-related genes, a subtype enriched for HER2-amplified tumors [human epidermal growth factor receptor 2 (HER2)-enriched], a subtype associated with triple-

negative [lacking expression of ER, progesterone receptor (PR), and HER2] tumors (basal-like). Positive correlation between ATM and ATG4C expression was statistically significant in all subtypes, except for the basal like subtype, suggesting that the functional link between ATM and ATG4C genes could have a clinical significance (Table 1).

DISCUSSION

Although our knowledge concerning new functions of ATM kinase has greatly increased during the last decade, their exact role in carcinogenesis and cancer therapies remains elusive. We previously demonstrated that ATM promotes HER2-dependent tumorigenesis in breast cancer, reporting also a context-dependent role of ATM targeting in cancer [9]. In this study, we described for the first time a mechanism through which ATM regulates autophagy in a fashion independent on HER2, which has crucial implications in breast cancer progression. In particular, we showed that: (1) ATM expression is induced in mammospheres culture as compared to parental adherent breast cancer cell lines, and (2) ATM depletion with a small interfering RNA leads to impaired mammospheres formation. Interestingly, we put in evidence that ATM expression sustains SOX2 expression and ALDH activity without significantly impinging on other stemness markers such as NANOG and OCT4 (Figure 2) suggesting the existence of mechanisms of modulation of mammosphere formation by ATM other than the regulation of the stemness genes. To clarify this issue, we performed microarray experiments revealing that, in mammospheres, ATM regulates the expression of genes involved in the control of DNA repair and cell division, which is consistent with the central role of ATM as guardian of the genome [4]. Moreover, in this experiment we showed that other ATM-dependent function could be involved in the regulation of Breast cancer stem-like phenotype. In particular, we focused our attention on the autophagic gene ATG4C. Indeed, autophagy is a well-established pro-survival mechanism for BCSCs maintenance [17] [18, 19] suggesting the hypothesis that ATM may modulate BCSCs via ATG4C. Accordingly, we observed by western blot and real time PCR that the depletion of ATM leads to the decrease in mRNA and protein levels of ATG4C. The ATM-dependent downregulation of ATG4C expression correlates very well with an impairment of the autophagic flux in mammospheres silenced for ATM. Consistently, we showed that silencing of ATG4C impairs mammospheres formation similarly to the silencing of ATM. More interestingly, ATG4C overexpression rescues mammospheres defects induced by ATM down regulation. These findings provide the first evidence on a link between the expression of ATM and the autophagic gene ATG4C. In previous studies, ATM and ATG4C were reported to have a tumor-suppressive

role [31, 32]. Here, we demonstrated that these proteins promote stem-like phenotype in breast cancer, suggesting that ATM kinase and autophagy could play also a tumorigenic role in breast cancer.

In addition, in this study, we demonstrated that ATM specifically regulates ATG4C isoform in mammospheres,

without affecting other members of ATG4 family, even though the precise molecular mechanism deserves further investigation. Little information is reported about the transcriptional regulation of the ATG4 proteases. Some observations indicated that ATG4C could be transcriptionally regulated by p53 upon DNA damage

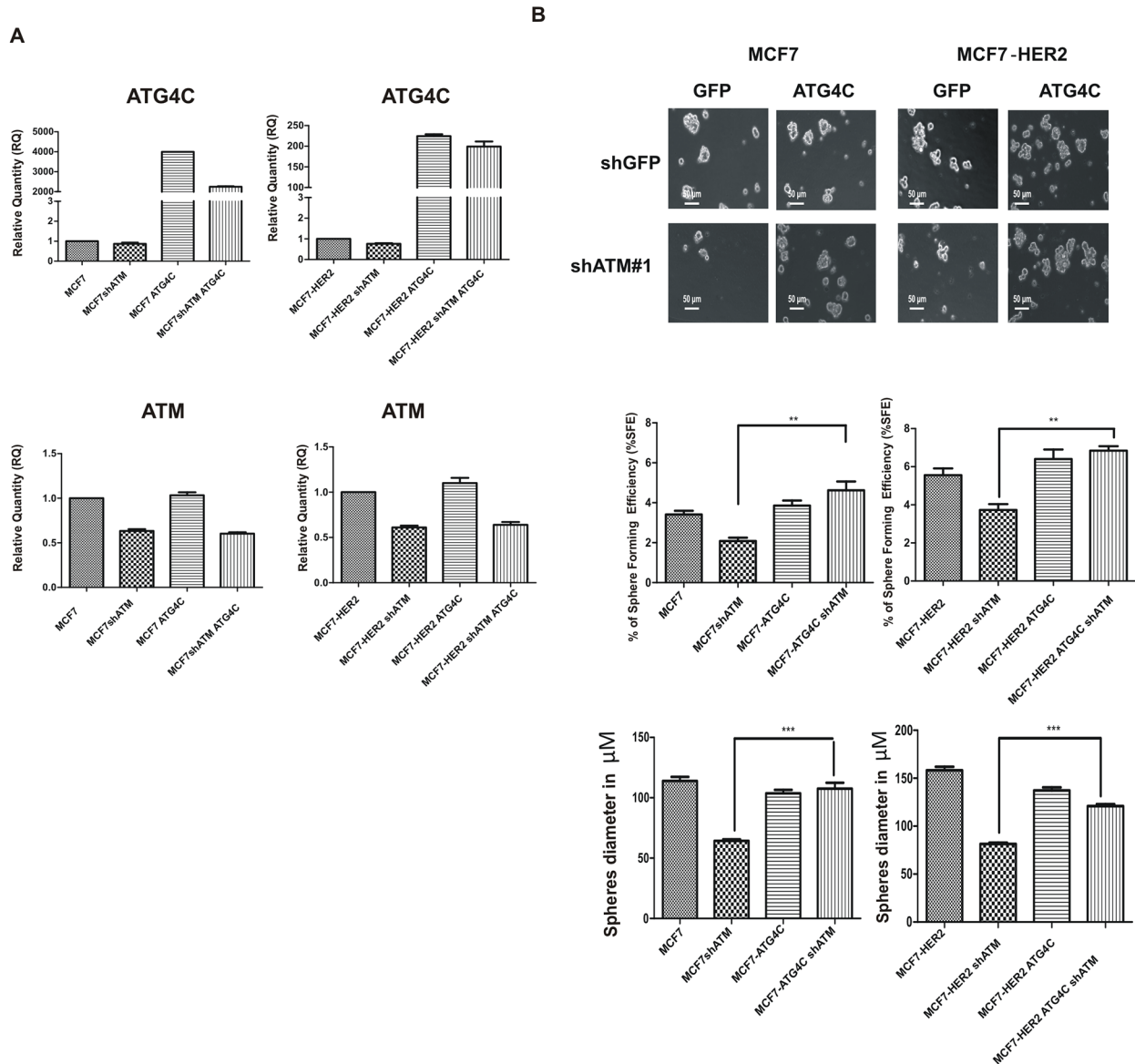


Figure 7: ATG4C expression rescues mammospheres formation ability in ATM interfered cells. MCF7 and MCF7-HER2 breast cancer cell lines transfected with construct overexpressing human pCMV3-hATG4C-HA (ATG4C) and control GFP overexpressing construct, using Lipofectamine® 3000 Reagent (Life Technologies) **A.** The expression of ATG4C mRNA levels in Mammospheres (MS), was investigated by quantitative Real-time PCR. Relative quantities (RQ) were calculated to TBP and are relative to control MCF7 mammospheres. Results are expressed as the mean±s.d. for at least three independent experiments. **B.** Single cells were plated in ultralow attachment plates as described in Materials and methods section, so that cells with stem cell properties were allowed to grow as non-adherent spheroids (mammospheres). Images of the mammospheres were captured on day 7. Representative phase-contrast images of mammospheres are shown (upper). Bars denote 50 μm . Numbers of the mammospheres (diameter>50 μm) were counted, and the %SFE was calculated based on the numbers of cells that were initially seeded (Bottom). Mean±s.d. for three independent experiments performed with both targeting sequences for ATM (shATM#1 and shATM#3) and analysed using Student's t-test (**P<0.01, ***P<0.001). The diameter of mammosphere (in μm) was quantified using I.A.S software (Delta sistemi, Italy).

Table 1: Correlation of ATM with ATG4C gene in BRCA samples from TCGA cancer atlas data

TCGA sample group (n)	Pearson correlation	P-value	Bonferroni corrected P-value
All BRCA (511)	0.26	2.70E-09	1.35E-08
Basal (95)	0.15	1.26E-01	6.30E-01
HER2 (58)	0.37	3.55E-03	1.78E-02
Luminal A (231)	0.17	9.60E-03	4.80E-02
Luminal B (127)	0.3	3.29E-04	1.65E-03

We computed the Pearson correlation coefficients and corresponding uncorrected and Bonferroni corrected P-values between ATM and ATG4C genes in expression data from 511 breast cancer samples extracted from the TCGA Cancer Atlas. Statistically significant results shown in bold font ($P < 0.05$).

activation, and that ATG4C mRNA is modulated by miR-376b upon starvation and rapamycin-induced autophagy [33, 34]. Future experiment will be launched to clarify whether ATM regulates ATG4C expression through p53 or via the modulation of miR-376b.

Moreover, we cannot rule out that ATM may regulate also ATG4 protein levels and activity. Interestingly, ATG4s proteins are reported to be regulated by ROS during starvation [35]. According to this study, the Cys81 residue near the catalytic site of ATG4 is a direct oxidation target by H₂O₂ and the oxidation of this residue inhibits ATG4 protease activity. This, in turn, prevents the delipidation of LC3 without affecting the C-Terminal processing of LC3 by ATG4, thus leading to increased autophagosome formation [35]. It was proposed that cytosolic ATM regulates autophagy via its activation upon ROS rather than DNA damage induction [36-39]. This evidence prompts us to speculate that the selective ATM-dependent regulation of ATG4C and autophagy in mammospheres may be ascribed to differences in ROS regulation between cells grown in adherent conditions or as mammospheres. Interestingly, ATM dependent regulation of ROS plays a critical role in hematopoietic stem cell (HSC) maintenance [40]. In this study, the treatment of *Atm*^{-/-} mice with antioxidant N-acetylcystine (NAC) restored the HSC pool, confirming the critical role of ROS regulation by ATM for stemness [40]. So, we could speculate that ATM could act as a ROS sensor modulating the autophagic flux according to ROS levels in different populations of cells within the tumor. Further experiments are required to clarify whether ATM activity is involved in the regulation of the stem-like phenotype, and whether ROS- and/or DNA damage-mediated ATM activation are essential for the regulation of this phenotype. Finally, we showed that ATG4A, ATG7 and ATG5-ATG12 protein levels are unaffected by shATM treatment (Supplementary Figure 2B), supporting the idea that defects in autophagic flux

mainly rely on ATG4C, even though the elucidation of the molecular mechanism requires further experimental investigations.

Interestingly, the findings reported in this study suggest that ATM may represent a novel candidate target to impair the autophagic activity in Breast Cancer Stem-like cells independently of HER2. Indeed, our results suggest that ATM targeting severely impinges not only on the DDR, as previously reported [41-43], but also on autophagy functionality, which is required for the homeostasis of the specific subset of breast cancer cells. Along similar lines, we surmise that ATG4C could also represent a valuable molecular target, as demonstrated by a large set of evidences suggesting that anti-autophagy compounds are effective in suppressing tumor growth and countering tumor resistance to chemotherapies [44][45][46]. Moreover, the inhibition of autophagy is reported to sensitize CSCs to several anticancer treatment [47]. Unfortunately, the relevance of autophagy inhibition in cancer treatment remains controversial because of the limited availability of chemical modulators. ATG4s are the only cysteine proteases among ATG genes proposed as an attractive candidate to efficiently achieve autophagy inhibition in cancer so far [48]. As an example, ATG4B has been recently proposed has a novel target for leukemic stem cells, supporting the idea that ATG4s proteases are good target for CSCs eradication [49].

Remarkably, we were able to show a correlation between ATM and ATG4C expression in all breast cancer subtypes except for the basal-like one (Table 1) underscoring a clinical impact of our findings. This evidence suggests also that the elucidation of the molecular mechanism whereby ATM regulates ATG4C and autophagy in breast cancer can be relevant as it may pave the way for the development of new biomarkers for diagnostic and/or prognostic evaluation and for the design of novel therapeutic strategies.

MATERIALS AND METHODS

DNA constructs, antibodies and reagents

The shATM construct, generously provided by Y Lerenthal and Y Shiloh, had the following sequence: shATM construct (#1 position 912 5'-GACTTTGGCTGTCAACTTTTCG-3') and shATM (#3 position 8538 5' GGA GCG CAC CAT CTT CTT C 3') shRNA and control shGFP 5'- GGAGCGC ACCATCTTCTTC-3' [50]. The ATG4C siRNA was from Signaling Silence®, Cell Signaling. ATG4C expression construct pCMV3-C-HA was from Sino Biological Inc (HG16060-CY). pEGFP-C3 (Clontech). The following antibodies and reagents were used: anti-ATM (2C1; Santa Cruz Biotechnology), anti-tubulin (Sigma, St. Louis, MO, USA), Mouse anti-c-ErbB-2 protein monoclonal antibodies, clone 3B5 (Ab-3, Oncogene Science, Uniondale, NY), anti-ATG4C (Cell Signaling, Beverly, MA, USA), anti-Hsp90 (F8, Santa Cruz Biotechnology), anti-LC3 (Cell Signaling, Beverly, MA, USA), anti-p62 (Santa Cruz Biotechnology), anti-Actin (Sigma, St. Louis, MO, USA), anti-GAPDH (Chemicon). Chloroquine (Sigma, St. Louis, MO, USA), anti-ATG4A (Biorbyt United Kingdom), anti-ATG7 (Cell Signaling, Beverly, MA, USA), Anti-ATG5 (Cell Signaling, Beverly, MA, USA), anti-Cathepsin D (Scripps laboratories, San Diego CA).

Cell cultures, transfection and infection

Human breast cancer cell lines MCF-7 and MCF-7HER2, described in Stagni et al 2015 [6], were cultured in RPMI-1640 containing 2 mM L-glutamine and supplemented with 10% HyClone* Fetal Bovine Serum (Invitrogen) at 37°C in a CO₂ incubator (5%). ATM was silenced in MCF7 and MCF7-HER2 cells by lentivirus mediated expression of short-hairpin RNA using lentivirus produced in HEK 293T cells by cotransfecting pSIN18.cPPT.RNAi. p.EGFP.WPRE lentiviral vector with targeting sequences together with respective plasmids encoding for gag-pol and VSV-G proteins. Viral supernatant was collected 48 h post-transfection, filtered through a 0.45 µm pore size filter and added to the cells (MCF7 and MCF7-HER2 breast cancer cell lines) in the presence of 2 µg/ml polybrene [8]. Cells were transiently transfected using Lipofectamine 3000 (Life Technologies) essentially following the manufacturer's instruction.

Mammosphere culture

Single cell suspensions of breast cancer cell lines, MCF7 and MCF7-HER2, were grown in ultralow attachment 6-well plates (Corning) at a density of 4000 cell/mL in mammosphere medium [Dulbecco's modified Eagle's medium/F- 12, containing 5 µg/mL

insulin (Sigma), B27 (Invitrogen), 20 ng/ml epidermal growth factor (GIBCO), 10 ng/ml basic fibroblast growth factor (GIBCO) and 0,4% Bovine Serum Albumine (Sigma)] as described in Dontu *et al.* 2003 [20]. After 7 days, the diameter of mammospheres were measured in phase contrast pictures using the I.A.S. software (Delta Sistemi, Rome, Italy). Numbers of the mammospheres (diameter>50 µM) were counted and the efficiency of mammosphere formation was evaluated (%SFE= number of mammospheres / number of plated cells * 100). Mammospheres pellet was collected by gentle centrifugation (900 rpm, 5 min) to further analysis or dissociated into single cell by trypsin addition (5 min 37°C) and mechanical pipetting. Single cells were plated at a density of 600 cell/well in mammosphere medium supplemented with 5% Fetal Bovine Serum (HyClone, Invitrogen) to test the clonogenic activity. After 10 days the cells were stained with 3-[4,5-Dimethylthiazol-2-yl]-2,5-Diphenyltetrazolium Bromide (MTT Vitality Stain, promega) 5 mg/ml for 16 hours and the colony number enumerated. Mammospheres diameter was measured using I.A.S. software (Delta Sistemi, Rome, Italy).

ALDH activity assay

To measure and isolate cells with high ALDH activity, the Aldefluor assay was performed according to manufacturer's (Stemcell Technologies, Durham, NC) guidelines. Dissociated single cells were suspended in Aldefluor assay buffer containing the ALDH substrate, Bodipyaminoacetaldehyde (BAAA) at 1,5 µM and incubated for 40 minutes at 37 °C. To distinguish between ALDH-positive and -negative cells, a fraction of cells was incubated under identical condition in the presence of a 10-fold molar excess of the ALDH inhibitor, diethylamino benzaldehyde (DEAB). This results in a significant decrease in the fluorescence intensity of ALDH-positive cells and was used to compensate the flow cytometer (FACScan, Becton Dickinson).

RNA extraction and analysis

Total RNA was extracted from breast cancer cell lines MCF7 and MCF7-HER2 and derived mammospheres with TRIzol (Invitrogen) according to the manufacturer's instructions. RNA quantitation was performed via quantitative real-time PCR (RT-PCR). The total RNA was reverse-transcribed with SuperScript III reverse transcriptase (Invitrogen), and amplified by using the Power SYBR Green PCR Master Mix (Applied Biosystems) and the 7900HT Fast Real-Time PCR System (Applied Biosystems). Primers were designed from the Roche Universal Probe Library and were as follows:

Gene name	Primer sequence 5' - 3'
hsa-ANL For	TCCCTAGAAGAAGCTGAAGCAG
hsa-ANL Rev	TTCAATTCATCAATCAAAAAGTGTTCC
hsa-ATG4A For	ACAGATGAGCTGGTATGGATCCTT
hsa-ATG4A Rev	AGACGAGCACTTATATCAGACAACA
hsa-ATG4B For	ATTGGTGCCAGCAAGTCAA
hsa-ATG4B Rev	GCAGGCCAGATGTGAAGG
hsa-ATG4C For	GCATAAAGGATTTCCCTCTTGA
hsa-ATG4C Rev	GCTGGGATCCATTTTTTCG
hsa-ATG4D For	ACGTTTCTCAGGACTGCACA
hsa-ATG4D Rev	ACAGACTTCCACTCGGCTGT
hsa-ATM For	TTGTTGTCCCTACTATGGAAATTAAG
hsa-ATM Rev	AGCGAAATTCTGCTTTAAATGAC
hsa-ECT2 For	AGTAAAAGATCTTCCCTTTGAACCT
hsa-ECT2 Rev	CTCGGGCATCCATTTGAA
hsa-HER2 For	TCCTGTGTGGACCTGGATGAC
hsa-HER2 Rev	CCAAAGACCACCCCAAGA
hsa-HMOX1 For	GGCAGAGGGTGATAGAAGAGG
hsa-HMOX1 Rev	AGCTCCTGCAACTCCTCAAA
hsa-HSPA6 For	CCGCCTATTTCAATGACTCG
hsa-HSPA6 Rev	ATTGATGATCCGCAACACG
hsa-NEDD9 For	GAGCTGGATGGATGACTACGA
hsa-NEDD9 Rev	AGCTCTTTCTGTTGCCTCTCA
hsa-SPRR2A For	TCAACAGCAGCAGTGCAAG
hsa-SPRR2A Rev	CTGTGGACACTTTGGTGGTG
hsa-PLK4 For	GAAAACCAAAAAGGCTGTGGT
hsa-PLK4 Rev	TGAGATGCATACTCCTTTACAAGC
hsa-RAD51 For	AATCCAAATGTAATGCTTTGGTG
hsa-RAD51 Rev	AGGACTGAGATTCTGATTTGACG
hsa-SOX2 For	GGCAGCTACAGCATGATGCAGGAGC
hsa-SOX2 Rev	CTGGTCATGGAGTTGTACTGCAGG
hsa-TBP For	TGCCCGAAACGCCGAATATAATC
hsa-TBP Rev	TGGTTCGTGGCTCTCTTATCCTC
hsa-NANOG For	CAGCTGTGTGTACTCAATGATAGATT
hsa-NANOG Rev	ACACCATTGCTATTCTTCGGCCAGTTG
hsa-OCT4 For	GACAACAATGAAAATCTTCAGGAG
hsa-OCT4 Rev	CTGGCGCCGGTTACAGAACCA

Relative changes in gene expression were quantified by applying the comparative threshold method, also called $2^{-\Delta\Delta C_t}$ method, after determining the C_t values for the

reference gene (TBP, the endogenous control) and the target genes in each sample set. All reactions were performed in triplicate. Numerical data were expressed as mean \pm s.d.

Protein extraction and western blot analysis

Cells pellet were incubated in RIPA buffer (50 mM Tris-Hcl pH 7.4, 1% NP-40, 0.5% Sodium Deoxycholate, 0.1% SDS, 150mM NaCl, 2mM EDTA, 1mM phenylmethylsulfonyl fluoride, 25mM NaF, 1mM orthovanadate, 40 mM beta-glycerophosphate, 10 mg/ml TPCK, 5 mg/ml TLCK) 30' on ice and centrifugated at 12000 rpm 10' a 4°C. For immunoblotting, 20 µg of protein extract were separated by SDS–polyacrylamide gel electrophoresis, blotted onto nitrocellulose membrane and detected with specific antibodies. All immunoblots were revealed by enhanced chemiluminescence (Amersham). Quantification of western blot were determined using ImageJ software. All statistical analyses were performed with GraphPad Prism 5 software (GraphPad Software, San Diego, CA, USA), using the Student's t-test, $P < 0.05$ being considered significant.

Immunofluorescence

Cells were washed in PBS and fixed with 4% paraformaldehyde in PBS for 30 min. After permeabilization with 0.4% TritonX-100 in PBS for 5 min or with Digitonin 50µg/ml (in the case of Cathepsin D staining) for 5 min, cells were blocked in 3% normal goat serum in PBS and incubated overnight at 4°C with primary antibodies. We used the antibodies directed against LC3. Cells were then washed in blockingbuffer and incubated for 1 h with labelled anti-rabbit (FITC or Cy3, Jackson ImmunoResearch, West Grove, PA, USA) secondary antibody. Nuclei were stained with 1 mg/ml DAPI and examined under a Zeiss LSM 700100 oil-immersion objective (Zeiss, Oberkoechen, Germany). We used 'ZEN2009 Light edition' software for image analysis. All measurements in this work were performed by a blind approach. All analyses were performed in non-saturated single z-confocal planes.

Microarray hybridization and data analysis

The microarray assay was conducted using a biological triplicate and two different target sequence for ATM to avoid off targets effects. In particular three independent experiments were performed as follow:

1 Mammospheres MCF7 and MCF7-HER2 infected by lentivirus mediated expression of shGFP as shRNA control or shATM#1.

2 Mammospheres MCF7 and MCF7-HER2 infected by lentivirus mediated expression of pSin18 empty vector as shRNA control or shATM#1.

3 Mammospheres MCF7 and MCF7-HER2 infected by lentivirus mediated expression of shGFP as shRNA control; or shATM#3 .

Mammospheres pellet were collected after 7 days of culture. Total RNA was extracted with TRIzol (Invitrogen)

according to the manufacturer's instructions. RNA quality was assessed with an Agilent Bioanalyzer RNA 6000 Nano kit; 200 ng of RNA was labeled with Low Input Quick Amp Labeling Kit, One-Color (Agilent Technologies), purified and hybridized overnight onto, the Agilent 8X60K whole human genome oligonucleotide microarrays (Grid ID 039494) according to the manufacturer's instructions for one-color protocol. The Agilent DNA microarray scanner (model G2505C) was used for slide acquisition and spot analysis was performed with Feature Extraction software ver 10.7 (Agilent Technologies).

Data analysis

Data filtering and analysis were performed using Microsoft Excel and R-Bioconductor. All the features with the flag $gIsWellAboveBG=0$ (too close to background) were filtered out and excluded from the following analysis. Filtered data were normalized by aligning samples to the 75th percentile. Differentially expressed genes were selected by a combination of fold change and 1-tail T-test thresholds (p -value < 0.05 ; fold-change ratio > 1.5 or $< 1/1.5$ in linear scale and FCR is > 0.58 in logarithmic scale). The analysis of over- and under- represented functional annotations was performed using the DAVID web tool [51]. Hierarchical sample clustering and heatmaps were obtained by TM4 MultiexperimentViewer [52]. Updated microarray probe annotations were downloaded from the official Agilent website (<https://earray.chem.agilent.com>). Array data are deposited in private status on Gene Expression Omnibus database <https://www.ncbi.nlm.nih.gov/geo>, record GSE81360.

Comparative analysis with cancer genome atlas

From the TCGA data portal (<http://cancergenome.nih.gov>) we downloaded all breast cancer expression data files (in the aggregated gene symbol format, for 17814 genes in total) , including all metadata [30]. The whole dataset includes 511 primary tumours samples (metastatic and normal tissue samples were excluded), grouped into subtypes according to the Pam50 signature [29] : basal-like $n=95$, HER2-enriched $n=58$, luminal A $n=231$, luminal B, $n=127$). Within this dataset, we computed the Pearson correlation index, using R-Bioconductor, between ATG4C and ATM genes and all expression TCGA data divided into tumours subtypes.

Statistical analysis

All statistical analyses and graphs were performed with GraphPad Prism 5 software (GraphPad Software, San Diego, CA, USA). All data are represented as mean \pm SD. Mean values and standard deviation were generated from at least three biological replicates. For comparison between two groups the Student's t-test was used, $P < 0.05$ being considered significant.

ACKNOWLEDGMENTS

We thank Dr. Luca Battistini and Prof. Francesco Ceconi for critical reading of the manuscript, Dr. Maria Paola Paronetto for supporting M.A. fellowship and data discussion, Dr. Cinzia Rinaldo and Dr. Giulia Guarguaglini for helpful discussion of the data and Dr. Francesca Pacini for technical support. This work has been supported by research grants from Giovani Ricercatori-Ministero della Salute (GR2010-2312868) to V.S. and M.A., from PRIN 2010M4NEFY_005 and AIRC (IG8706) and PRIN_2015LZE9944_005 to D.B., from the FP7 Collaborative Project PAINCAGE (number 603191) to I.A., R.B., M.D., from GR2011-02351433 to F.S.. All authors concur with the submission and the material submitted for publication has not been previously reported and is not under consideration for publication elsewhere. The authors do not have competing commercial interests and no other conflict of interests in relation to the submitted work.

CONFLICTS OF INTEREST

The authors declare no conflicts of interest.

REFERENCES

1. Visvader JE. Cells of origin in cancer. *Nature*. 2011; 469:314-22. doi: 10.1038/nature09781.
2. Luo M, Clouthier SG, Deol Y, Liu S, Nagrath S, Azizi E and Wicha MS. Breast cancer stem cells: current advances and clinical implications. *Methods Mol Biol*. 2015; 1293:1-49. doi: 10.1007/978-1-4939-2519-3_1.
3. Plaks V, Kong N and Werb Z. The cancer stem cell niche: how essential is the niche in regulating stemness of tumor cells? *Cell Stem Cell*. 2015; 16:225-38. doi: 10.1016/j.stem.2015.02.015.
4. Shiloh Y and Ziv Y. The ATM protein kinase: regulating the cellular response to genotoxic stress, and more. *Nat Rev Mol Cell Biol*. 2013; 14:197-210. doi: 10.1038/nrm3546.
5. Cremona CA and Behrens A. ATM signalling and cancer. *Oncogene*. 2014; 33:3351-60. doi: 10.1038/onc.2013.275.
6. Stagni V, Oropallo V, Fianco G, Antonelli M, Cinà I and Barilà D. Tug of war between survival and death: exploring ATM function in cancer. *Int J Mol Sci*. 2014; 15: 5388-409. doi: 10.3390/ijms15045388.
7. Carruthers R, Ahmed SU, Strathdee K, Gomez-Roman N, Amoah-Buahin E, Watts C and Chalmers AJ. Abrogation of radioresistance in glioblastoma stem-like cells by inhibition of ATM kinase. *Mol Oncol*. 2015; 9:192-203. doi: 10.1016/j.molonc.2014.08.003.
8. Maugeri-Saccà M, Bartucci M and De Maria R. DNA damage repair pathways in cancer stem cells. *Mol Cancer Ther*. 2012; 11:1627-36. doi: 10.1158/1535-7163.MCT-11-1040.
9. Stagni V, Manni I, Oropallo V, Mottotese M, Di Benedetto A, Piaggio G, Falcioni R, Giaccari D, Di Carlo S, Sperati F, Cencioni MT and Barilà D. ATM kinase sustains HER2 tumorigenicity in breast cancer. *Nat Commun*. 2015; 6:6886. doi: 10.1038/ncomms7886.
10. Tripathi DN, Zhang J, Jing J, Dere R and Walker CL. A new role for ATM in selective autophagy of peroxisomes (pexophagy). *Autophagy*. 2016; 12: 711-2. doi: 10.1080/15548627.2015.1123375.
11. Valentin-Vega YA and Kastan MB. A new role for ATM: regulating mitochondrial function and mitophagy. *Autophagy*. 2012; 8: 840-1. doi: 10.4161/auto.19693.
12. Alexander A, Kim J and Walker CL. ATM engages the TSC2/mTORC1 signaling node to regulate autophagy. *Autophagy*. 2010; 6: 672-3. doi: 10.4161/auto.6.5.12509.
13. Valentin-Vega YA, Maclean KH, Tait-Mulder J, Milasta S, Steeves M, Dorsey FC, Cleveland JL, Green DR and Kastan MB. Mitochondrial dysfunction in ataxia-telangiectasia. *Blood*. 2012; 119:1490-500. doi: 10.1182/blood-2011-08-373639.
14. Galluzzi L, Pietrocola F, Bravo-San Pedro JM, Amaravadi RK, Baehrecke EH, Ceconi F, Codogno P, Debnath J, Gewirtz DA, Karantza V, Kimmelman A, Kumar S, Levine B, et al. Autophagy in malignant transformation and cancer progression. *EMBO J*. 2015; 34:856-80. doi: 10.15252/emboj.201490784.
15. Vitale I, Manic G, Dandrea V and De Maria R. Role of autophagy in the maintenance and function of cancer stem cells. *Int J Dev Biol*. 2015; 59: 95-108. doi: 10.1387/ijdb.150082iv.
16. Rodolfo C, Di Bartolomeo S and Ceconi F. Autophagy in stem and progenitor cells. *Cell Mol Life Sci*. 2016; 73: 475-96. doi: 10.1007/s00018-015-2071-3.
17. Maycotte P, Jones KL, Goodall ML, Thorburn J and Thorburn A. Autophagy Supports Breast Cancer Stem Cell Maintenance by Regulating IL6 Secretion. *Mol Cancer Res*. 2015; 13: 651-8. doi: 10.1158/1541-7786.MCR-14-0487.
18. Wolf J, Dewi DL, Fredebohm J, Müller-Decker K, Flechtenmacher C, Hoheisel JD and Boettcher M. A mammosphere formation RNAi screen reveals that ATG4A promotes a breast cancer stem-like phenotype. *Breast Cancer Res*. 2013; 15: R109. doi: 10.1186/bcr3576.
19. Gong C, Bauvy C, Tonelli G, Yue W, Delomélie C, Nicolas V, Zhu Y, Domergue V, Marin-Esteban V, Tharinger H, Delbos L, Gary-Gouy H, Morel AP, et al. Beclin 1 and autophagy are required for the tumorigenicity of breast cancer stem-like/progenitor cells. *Oncogene*. 2013; 32: 2261-72. doi: 10.1038/onc.2012.252.
20. Dontu G, Abdallah WM, Foley JM, Jackson KW, Clarke MF, Kawamura MJ and Wicha MS. In vitro propagation and transcriptional profiling of human mammary stem/progenitor cells. *Genes Dev*. 2003; 17: 1253-70. doi: 10.1101/gad.1061803.

21. Korkaya H, Paulson A, Iovino F and Wicha MS. HER2 regulates the mammary stem/progenitor cell population driving tumorigenesis and invasion. *Oncogene*. 2008; 27: 6120-30. doi: 10.1038/onc.2008.207.
22. Ithimakin S, Day KC, Malik F, Zen Q, Dawsey SJ, Bersano-Begey TF, Quraishi AA and Ignatoski KW, Daignault S, Davis A, Hall CL, Palanisamy N, Heath AN, et al. HER2 drives luminal breast cancer stem cells in the absence of HER2 amplification: implications for efficacy of adjuvant trastuzumab. *Cancer Res*. 2013; 73:1635-46. doi: 10.1158/0008-5472.CAN-12-3349.
23. Leis O, Eguiara A, Lopez-Arribillaga E, Alberdi MJ, Hernandez-Garcia S, Elorriaga K, Pandiella A, Rezola R, Martin AG. Sox2 expression in breast tumours and activation in breast cancer stem cells. *Oncogene*. 2012; 31: 1354-65. doi: 10.1038/onc.2011.338.
24. Ginestier C, Hur MH, Charafe-Jauffret E, Monville F, Dutcher J, Brown M, Jacquemier J, Viens P, Kleer CG, Liu S, Schott A, Hayes D, Birnbaum D, et al. ALDH1 is a marker of normal and malignant human mammary stem cells and a predictor of poor clinical outcome. *Cell Stem Cell*. 2007; 1: 555-67. doi: 10.1016/j.stem.2007.08.014.
25. Fernández ÁF, López-Otín C. The functional and pathologic relevance of autophagy proteases. *J Clin Invest*. 2015; 125: 33-41. doi: 10.1172/JCI73940.
26. Satoo K, Noda NN, Kumeta H, Fujioka Y, Mizushima N, Ohsumi Y and Inagaki F. The structure of Atg4B-LC3 complex reveals the mechanism of LC3 processing and delipidation during autophagy. *EMBO J*. 2009; 28: 1341-50. doi: 10.1038/emboj.2009.80.
27. Mizushima N. Methods for monitoring autophagy using GFP-LC3 transgenic mice. *Methods Enzymol*. 2009; 452:13-23. doi: 10.1016/S0076-6879(08)03602-1.
28. Bjørkøy G, Lamark T and Johansen T. p62/SQSTM1: a missing link between protein aggregates and the autophagy machinery. *Autophagy*. 2006; 2: 138-9.
29. Ichimura Y, Kominami E, Tanaka K and Komatsu M. Selective turnover of p62/A170/SQSTM1 by autophagy. *Autophagy*. 2008; 4: 1063-6.
30. Cancer Genome Atlas Network. Comprehensive molecular portraits of human breast tumours. *Nature*. 2012; 490: 61-70. doi: 10.1038/nature11412.
31. Mariño G, Salvador-Montoliu N, Fueyo A, Knecht E, Mizushima N and López-Otín C. Tissue-specific autophagy alterations and increased tumorigenesis in mice deficient in Atg4C/autophagin-3. *J Biol Chem*. 2007; 282: 18573-83. doi: 10.1074/jbc.M701194200.
32. Boultonwood J. Ataxia telangiectasia gene mutations in leukaemia and lymphoma. *J Clin Pathol*. 2001; 54: 512-6.
33. Kenzelmann Broz D, Spano Mello S, Biegging KT, Jiang D, Dusek RL, Brady CA, Sidow A and Attardi LD. Global genomic profiling reveals an extensive p53-regulated autophagy program contributing to key p53 responses. *Genes Dev*. 2013; 27: 1016-31. doi: 10.1101/gad.212282.112.
34. Korkmaz G, le Sage C, Tekirdag KA, Agami R and Gozuacik D. miR-376b controls starvation and mTOR inhibition-related autophagy by targeting ATG4C and BECN1. *Autophagy*. 2012; 8:165-76. doi: 10.4161/auto.8.2.18351.
35. Scherz-Shouval R, Shvets E, Fass E, Shorer H, Gil L and Elazar Z. Reactive oxygen species are essential for autophagy and specifically regulate the activity of Atg4. *EMBO J*. 2007; 26:1749-60. doi: 10.1038/sj.emboj.7601623.
36. Zhang J, Tripathi DN, Jing J, Alexander A, Kim J, Powell RT, Dere R, Tait-Mulder J, Lee JH, Paull TT, Pandita RK, Charaka VK, Pandita TK, et al. ATM functions at the peroxisome to induce pexophagy in response to ROS. *Nat Cell Biol*. 2015; 17:1259-69. doi: 10.1038/ncb3230.
37. Valentin-Vega YA and Kastan MB. A new role for ATM: regulating mitochondrial function and mitophagy. *Autophagy*. 2012; 8:840-1. doi: 10.4161/auto.19693.
38. Alexander A, Kim J and Walker CL. ATM engages the TSC2/mTORC1 signaling node to regulate autophagy. *Autophagy*. 2010; 6:672-3. doi: 10.4161/auto.6.5.12509.
39. Valentin-Vega YA, Maclean KH, Tait-Mulder J, Milasta S, Steeves M, Dorsey FC, Cleveland JL, Green DR and Kastan MB. Mitochondrial dysfunction in ataxia-telangiectasia. *Blood*. 2012; 119:1490-500. doi: 10.1182/blood-2011-08-373639.
40. Ito K, Hirao A, Arai F, Matsuoka S, Takubo K, Hamaguchi I, Nomiyama K, Hosokawa K, Sakurada K, Nakagata N, Ikeda Y, Mak TW and Suda T. Regulation of oxidative stress by ATM is required for self-renewal of haematopoietic stem cells. *Nature*. 2004; 431:997-1002. doi: 10.1038/nature02989.
41. Bao S, Wu Q, McLendon RE, Hao Y, Shi Q, Hjelmeland AB, Dewhirst MW, Bigner DD and Rich JN. Glioma stem cells promote radioresistance by preferential activation of the DNA damage response. *Nature*. 2006; 444: 756-760. doi: 10.1038/nature05236.
42. Raso A, Vecchio D, Cappelli E, Ropolo M, Poggi A, Nozza P, Biassoni R, Mascelli S, Capra V, Kalfas F, Severi P and Frosina G. Characterization of glioma stem cells through multiple stem cell markers and their specific sensitization to double-strand break-inducing agents by pharmacological inhibition of ataxia-telangiectasia mutated protein. *Brain Pathol*. 2012; 22: 677-688. doi: 10.1111/j.1750-3639.2012.00566.x.
43. Yin H and Glass J. The phenotypic radiation resistance of CD44+/CD24-/low breast cancer cells is mediated through the enhanced activation of ATM signaling. *PLoS One*. 2011; 6:e24080. doi: 10.1371/journal.pone.0024080.
44. Gammoh N, Fraser J, Puente C, Syred HM, Kang H, Ozawa T, Lam D, Acosta JC, Finch AJ, Holland E and Jiang X. Suppression of autophagy impedes glioblastoma development and induces senescence. *Autophagy*. 2016; 12: 1431-9. doi: 10.1080/15548627.2016.1190053.

45. Mancias JD and Kimmelman AC. Mechanisms of Selective Autophagy in Normal Physiology and Cancer. *J Mol Biol.* 2016; 428: 1659-80. doi: 10.1016/j.jmb.2016.02.027.
46. Manic G, Obrist F, Kroemer G, Vitale I and Galluzzi L. Chloroquine and hydroxychloroquine for cancer therapy. *Mol Cell Oncol.* 2014; 1: e29911. doi: 10.4161/mco.29911.
47. Ojha R, Bhattacharyya S and Singh SK. Autophagy in Cancer Stem Cells: A Potential Link Between Chemoresistance, Recurrence, and Metastasis. *Biores Open Access.* 2015; 4:97-108. doi: 10.1089/biores.2014.0035.
48. Akin D, Wang SK, Habibzadegah-Tari P, Law B, Ostrov D, Li M, Yin XM, Kim JS, Horenstein N and Dunn WA Jr. A novel ATG4B antagonist inhibits autophagy and has a negative impact on osteosarcoma tumors. *Autophagy.* 2014; 10: 2021-35. doi: 10.4161/auto.32229.
49. Rothe K, Lin H, Lin KB, Leung A, Wang HM, Malekesmaeili M, Brinkman RR, Forrest DL, Gorski SM and Jiang X. The core autophagy protein ATG4B is a potential biomarker and therapeutic target in CML stem/progenitor cells. *Blood.* 2014; 123: 3622-34. doi: 10.1182/blood-2013-07-516807.
50. Biton S, Dar I, Mittelman L, Pereg Y, Barzilai A and Shiloh Y. Nuclear ataxia-telangiectasia mutated (ATM) mediates the cellular response to DNA double strand breaks in human neuron-like cells. *J Biol Chem.* 2006; 281: 17482-91. doi: 10.1074/jbc.M601895200.
51. Huang da W, Sherman BT and Lempicki RA. Systematic and integrative analysis of large gene lists using DAVID bioinformatics resources. *Nat Protoc.* 2009; 4:44-57. doi: 10.1038/nprot.2008.211.
52. Saeed AI, Bhagabati NK, Braisted JC, Liang W, Sharov V, Howe EA, Li J, Thiagarajan M, White JA and Quackenbush J. TM4 microarray software suite. *Methods Enzymol.* 2006; 411:134-93. doi: 10.1016/S0076-6879(06)11009-5.

AMBRA1-induced mitophagy: A new mechanism to cope with cancer?

Flavie Strappazon^{1,2,*} and Francesco Cecconi^{1,2,3,*}

¹IRCCS Fondazione Santa Lucia; Rome, Italy; ²Department of Biology; University of Rome Tor Vergata; Rome, Italy; ³Unit of Cell Stress and Survival; Danish Cancer Society Research Center; Copenhagen, Denmark

Keywords: AMBRA1, mitophagy, cancer

Dysfunctions in mitophagy, the process by which mitochondria are eliminated, are associated with cancer. We found that the proautophagic protein AMBRA1 (activating molecule in beclin 1 regulated autophagy) binds the autophagosome adapter LC3, and that this interaction is crucial for mitochondrial clearance with or without involvement of the E3-ligase PARKIN. The discovery of a novel mitophagy pathway has the potential to promote new anticancer strategies.

Considering that mitochondria represent the cellular powerhouses, it is not a surprise that dysfunctional mitochondria are detrimental to the cell. Accumulation of damaged mitochondria is a feature of aging and multiple types of disease, including cancer. Fortunately, mammalian cells have developed a way to remove damaged mitochondria through a form of selective autophagy called mitophagy.

Mitophagy is induced after the loss of mitochondrial membrane potential ($\Delta\Psi_m$) and mitochondrial depolarization. PTEN-induced putative kinase 1 (PINK1) is stabilized at the mitochondria, where it recruits the E3 ubiquitin ligase PARKIN. In this context, activating molecule in beclin 1 regulated autophagy (AMBRA1) interacts with PARKIN to enhance mitochondrial clearance.¹ In our study,² we identified AMBRA1 as a LIR (LC3-interacting region)-containing protein and found that this motif is essential for the binding between AMBRA1 and LC3 only following mitophagy induction. In line with the findings of Van Humbeeck et al.¹ we provide molecular evidence that this interaction is crucial for the promotion of PARKIN-mediated mitochondrial clearance.

In addition to the PINK1/PARKIN pathway, the so-called mitophagy

receptors can also regulate mitophagy. These receptors are localized at the outer membrane of mitochondria and possess a consensus sequence (LIR motif: W/F/YxxL/I) that allows binding with LC3 for selective autophagy. To date, 2 types of mitophagy receptors have been identified: BCL2/adenovirus interacting protein 3 (best known as NIX/BNIP3L-BNIP3), which is involved in mitophagy during red blood cells maturation, and FUN14 domain containing 1 protein (best known as FUNDC1), which is involved in mitophagy induced by hypoxia or mitochondrial membrane depolarization. Our results suggest that AMBRA1 represents a third type of mitophagy receptor. We previously demonstrated that a pool of AMBRA1 could be found associated with BCL2 at the outer mitochondrial membrane.³ We now show that AMBRA1 possesses a LIR domain that allows it to bind to LC3 upon mitophagy induction. We further demonstrate that targeting AMBRA1 to mitochondria (AMBRA1-ActA) is sufficient to induce massive mitochondrial clearance in both PARKIN-dependent and -independent systems. Interestingly, it has recently been demonstrated that BECLIN 1 (best known as BECN1) interacts with PARKIN and

regulates translocation of PARKIN to the mitochondria.⁴ Since we showed that downregulation of BECN1 reduces AMBRA1-ActA-induced mitophagy, it would be interesting to investigate the role of BECN1 in this process. In principle, we can hypothesize that BECN1 delivers a putative E3 ubiquitin ligase in order to ubiquitylate mitochondria in AMBRA1-ActA-induced mitophagy.

Until now it was not clear whether the major pathways of mitophagy were dependent on or independent of each other. Our work indicates that a parallel pathway for mitophagy may exist when PARKIN is not present. It should be noted that lack of PARKIN is not particularly unusual; the *PARK2* (best known as *PARKIN*) gene is silenced in a number of common cell lines, such as HeLa or mouse embryonic fibroblasts. Of note, all known mitophagy receptors are regulated by specific kinases^{5,6} and it would be important to investigate whether the mitochondrial pool of AMBRA1 is subjected to post-translational modifications under mitochondrial stress.

A common feature of all mitophagic proteins is their deregulation in cancer. PARKIN-deficient mice are susceptible to hepatocarcinogenesis. In addition, the *PARK2* gene is often targeted in malignant

© Flavie Strappazon and Francesco Cecconi

*Correspondence to: Flavie Strappazon; E-mail: f.strappazon@hsantalucia.it; Francesco Cecconi; E-mail: cecconi@cancer.dk

Submitted: 10/04/2014; Revised: 10/07/2014; Accepted: 10/07/2014

<http://dx.doi.org/10.4161/23723556.2014.975647>

This is an Open Access article distributed under the terms of the Creative Commons Attribution-Non-Commercial License (<http://creativecommons.org/licenses/by-nc/3.0/>), which permits unrestricted non-commercial use, distribution, and reproduction in any medium, provided the original work is properly cited. The moral rights of the named author(s) have been asserted.

tumors.⁷ Together, these data define *PARK2* as a tumor suppressor gene (TSG). BNIP3 expression is lost in several cancers such as breast and pancreatic cancers⁸ and NIX expression is deregulated in ductal carcinoma of the breast.⁹

In line with these data, we recently discovered that *AMBRA1* mutant mice develop spontaneous tumors. Mutations of *AMBRA1* can also be found in a number of human cancers.¹⁰ In principle, inactivation of *AMBRA1*-induced mitophagy may be an aspect of the *AMBRA1*-deficient phenotype in tumorigenesis and warrants more detailed study as a potential prognostic indicator in cancer.

When we forced *AMBRA1* to the mitochondria surface using the *AMBRA1*-ActA construct, we observed that all mitochondria were ubiquitinated, as also observed in *PARKIN*-deficient cells. Thus, we can conclude that *AMBRA1*-ActA most likely serves as an adaptor for E3 ligases. This would not be an unusual job for this protein. Indeed, we demonstrated that the kinase *ULK1*, which is important in upstream regulation of autophagy, is ubiquitinated by the E3-ligase TNF receptor associated factor 6 (*TRAF6*) in a manner mediated by *AMBRA1*.¹¹ It is now crucial to identify which kind of E3 ubiquitin ligase is involved in *AMBRA1*-induced mitophagy. To better understand the

molecular mechanisms underlying the TSG function of *AMBRA1*, it would be interesting to identify new substrates of this unrevealed E3 ubiquitin ligase that might be related to controlling apoptosis or cell proliferation.

Another common feature of all mitophagic proteins is the negative regulation by *BCL2* family members; *BCL2* inhibits *PARKIN*-mediated mitophagy, whereas *BCL2L1* inhibits *FUNDC1*-mediated mitophagy. We demonstrated that *BCL2* could inhibit the proautophagic activity of *AMBRA1*³ and it will therefore be very important to explore whether *BCL2* can also control *AMBRA1*-induced mitophagy. Overexpression of *BCL2* family members is often associated with unfavorable pathogenesis in cancer, and this might at least in part be related to their role in inhibiting the different pathways of mitophagy. In **Figure 1** we summarize our model of the role of *AMBRA1* in mitophagy in mammalian cells.

In conclusion, the loss of mitophagy proteins appears to promote tumorigenesis, underlying a tumor suppressor function of mitophagy. Despite the complex nature of the role of autophagy/mitophagy in cancer, it thus appears that stimulation of mitophagy may play a pivotal role in fighting cancer. Our discovery of a new *AMBRA1*-induced mitophagy pathway, and in particular the identification of a new E3 ubiquitin ligase and its substrates in this context, could open new avenues of research in cancer therapy.

Disclosure of Potential Conflicts of Interest

No potential conflicts of interest were disclosed.

Acknowledgments

We are grateful to Dr. Giuseppe Filomeni for his help with **Figure 1**.

Funding

Our research is supported in part by grants from the Telethon Foundation (GGP10225), AIRC (IG2010 to FC), the Italian Ministry of University and Research (PRIN 2009 and FIRB Accordi di Programma 2011), the Italian Ministry

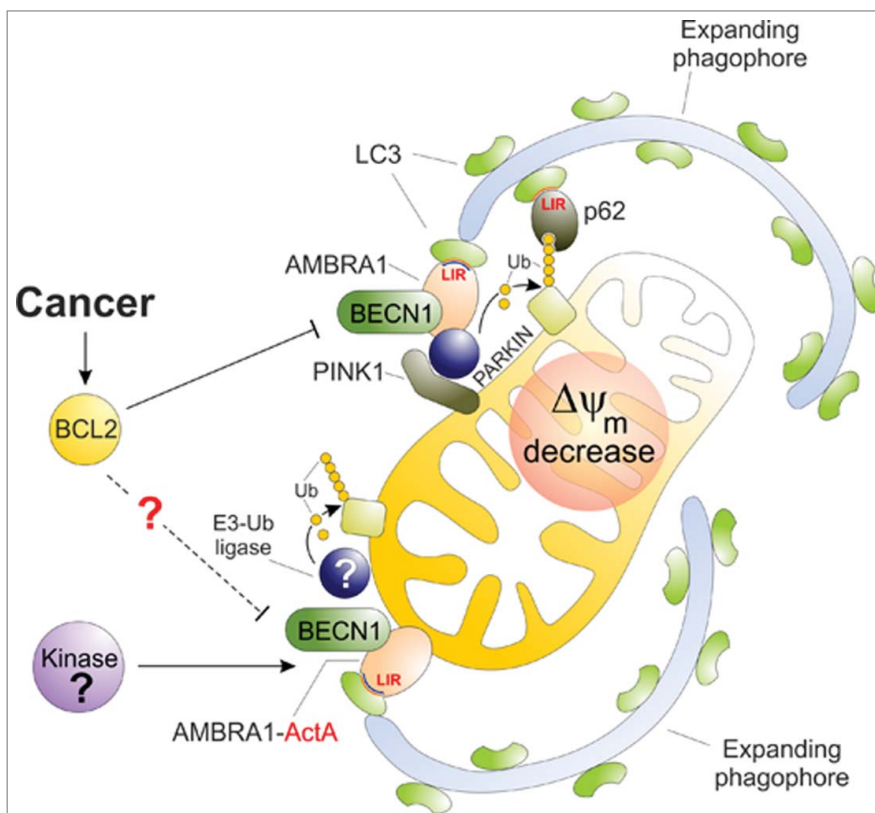


Figure 1. *AMBRA1*, a novel mitophagy receptor. The *PINK1*/*PARKIN* pathway is induced after mitochondrial membrane depolarization (indicated as $\Delta\psi_m$ decrease in the figure). *PINK1* (PTEN-induced putative kinase1) is stabilized on the mitochondria and allows mitochondrial recruitment of *PARKIN*. *PARKIN* ubiquitinates mitochondria (ubiquitin molecules are indicated as "Ub" in the figure), which can then be recognized by the cargo protein p62. *AMBRA1* (activating molecule in beclin 1 regulated autophagy) plays a crucial role in triggering mitochondria degradation by interacting with LC3 through its LIR (LC3-interacting region) motif. Furthermore, high levels of *AMBRA1*-ActA at the mitochondria are able to induce massive mitophagy in both *PARKIN*-dependent and -independent context. It is likely that an E3 ubiquitin ligase is involved in mitochondria ubiquitylation following *AMBRA1*-ActA expression. Based on our knowledge of other mitophagy receptors, a kinase is probably involved in the post-translational regulation of *AMBRA1* under mitochondrial stress. Finally, in cancer, an increase in *BCL2* expression leads to inhibition of *PARKIN*-mediated mitophagy and, most likely, *AMBRA1*-mediated mitophagy.

of Health (Ricerca Finalizzata and Ricerca Corrente to FC, Ricerca Finalizzata). FC Unit in Copenhagen is supported by

grants from the Danish Cancer Society (KBVU R72-A4408 to FC and KBVU R72-A4647 to GF); Lundbeck

Foundation (n. R167-2013-16100) and NovoNordisk (n. 7559).

References

1. Van Humbeek C, Cornelissen T, Hofkens H, Mandemakers W, Gevaert K, De Strooper Vandenberghe W. Parkin interacts with ambra1 to induce mitophagy. *J Neurosci* 2011; 28:10249-61; PMID:21753002; <http://dx.doi.org/10.1523/JNEUROSCI.1917-11.2011>
2. Strappazon F, Nazio F, Corrado M, Cianfanelli V, Romagnoli A, Fimia GM, Campello S, Nardacci R, Piacentini M, Campanella M, et al. AMBRA1 is able to induce mitophagy via LC3 binding, regardless of PARKIN and p62/SQSTM1. *Cell Death Diff* 2014; Sept 12; PMID:25215947; <http://dx.doi.org/10.1038/cdd.2014.139>
3. Strappazon F, Vietri-Rudan M, Campello S, Nazio F, Florenzano F, Fimia GM Piacentini M, Levine B, Ceccconi F. Mitochondrial BCL2 inhibits AMBRA1-induced autophagy. *EMBO J* 2011; 30:1195-208; PMID:21358617; <http://dx.doi.org/10.1038/emboj.2011.49>
4. Choubey V, Cagalinec M, Liiv J, Safiulina D, Hockey M, Kuum M Liiv M, Anwar T, Eskelinen EL, Kaasik A. BECN1 is involved in the initiation of mitophagy. It facilitates PARK2 translocation to mitochondria. *Autophagy* 2014; 10:1092-1106; PMID:24879156; <http://dx.doi.org/10.4161/auto.28615>
5. Zhu Y, Massen S, Terenzio M, Lang V, Chen-Lindner S, Eils R, Novak I, Dikic I, Hamacher-Brady A, Brady NR. Modulation of serines 17 and 24 in the LC3-interacting region of Bnip3 determines pro-survival mitophagy versus apoptosis. *J Biol Chem* 2013;2:1099-113; PMID:23209295; <http://dx.doi.org/10.1074/jbc.M112.399345>
6. Wu W, Tian W, Hu Z, Chen G, Huang L, Li W, Zhang X, Xue P, Zhou C, Liu L, et al. ULK1 translocates to mitochondria and phosphorylates FUNDC1 to regulate mitophagy. *EMBO Rep* 2014;5:566-75; PMID:24671035; <http://dx.doi.org/10.1002/embr.201438501>
7. Cesari R, Martin E, Calin GA, Pentimalli F, Bichi R, McAdams H, Trapasso F, Drusco A, Shimizu M, Masciullo V., Parkin, a gene implicated in autosomal recessive juvenile parkinsonism, is a candidate tumor suppressor gene on chromosome 6q25-q27. *PNAS* 2003; 100:5956-5961; PMID:12719539
8. Koop EA, Van Laar T, Van Wichen D, Weger RA, Van der Wall E Diest PJ. Expression of BNIP3 in invasive breast cancer: correlations with the hypoxic response and clinicopathological features. *BMC Cancer* 2009; 9:175; PMID:19505343; <http://dx.doi.org/10.1186/1471-2407-9-175>
9. Sowter HM, Ferguson M, Pym C, Watson P, Fox SB, Han C Harris AL. Expression of the cell death genes BNip3 and nix in ductal carcinoma in situ of the breast; correlation of BNip3 levels with necrosis and grade. *J Pathol* 2003; 201:573-80; PMID:14648660
10. Cianfanelli V, Fuoco C, Lorente M, Salazar M, Quondamatteo F, Gherardini PF, De Zio D, Nazio F, Antonioli M, D'Orazio M, Skobo T, Bordi M, Rohde M, Dalla Valle L, Helmer-Citterich M, Gretzmeier C, Dengjel J, Fimia GM, Piacentini M, Di Bartolomeo S, Velasco G, Ceccconi F. AMBRA1 links autophagy to cell proliferation and tumorigenesis by promoting c-Myc dephosphorylation and degradation. *Nat Cell Biol*. 2015 Jan;17(1):20-30.
11. Nazio F, Strappazon F, Antonioli M, Bielli P, Cianfanelli V, Bordi M Gretzmeier C, Dengjel J, Piacentini M, Fimia GM, mTOR inhibits autophagy by controlling ULK1 ubiquitination, self-association and function via AMBRA1 and TRAF6. *Nat Cell Biol* 2013; 4: 406-16; PMID:23524951; <http://dx.doi.org/10.1038/ncb2708>



The multifaceted mitochondrion: An attractive candidate for therapeutic strategies



Flavie Strappazzon^{a,b,*}, Francesco Cecconi^{a,b,c}

^a IRCCS Fondazione Santa Lucia, 00143 Rome, Italy

^b Department of Biology, University of Rome Tor Vergata, 00133 Rome, Italy

^c Unit of Cell Stress and Survival, Danish Cancer Society Research Center, 2100 Copenhagen, Denmark

ARTICLE INFO

Article history:

Received 18 November 2014

Received in revised form 7 March 2015

Accepted 13 March 2015

Available online 24 March 2015

Keywords:

Mitochondrial biogenesis

Mitochondrial quality control

Mitochondrial plasticity

ABSTRACT

Mitochondria are considered the powerhouse of the cell and disturbances in mitochondrial functions are involved in several disorders such as neurodegeneration and mitochondrial diseases. This review summarizes pharmacological strategies that aim at modifying the number of mitochondria, their dynamics or the mitochondrial quality-control mechanisms, in several pathological instances in which any of these mechanisms are impaired or abnormal. The interplay between different cellular pathways that involve mitochondria in order to respond to stress is highlighted. Such a high mitochondrial plasticity could be exploited for new treatments.

© 2015 Published by Elsevier Ltd.

1. Introduction

In mitochondria, energy obtained by nutrients is converted, thanks to the oxidative phosphorylation system (OXPHOS) – located in the inner-membrane of the mitochondria, into ATP. Mitochondria plays many other roles, such as regulating signals through mitochondrial reactive oxygen species (ROS) [1] that they produce, in regulating the membrane potential [2] and cell death processes [3], and in modulating calcium signalling [4] and steroid production [5]. According to the endosymbiotic hypothesis, mitochondria were previously considered to be prokaryotic cells (derived from alphaproteobacteria) and able to carry out oxidative functions that were not possible for eukaryotic cells. Mitochondria next went on to be considered as endosymbionts inside the eukaryotes. This specificity renders the mitochondria a unique organelle with its own mitochondrial DNA (mtDNA). However, mtDNA encodes only a few crucial proteins (13 proteins). Consequently, a controlled importation of nuclear DNA (nuDNA)-encoded proteins is required to allow a proper mitochondria functionality [6].

Mitochondrial shape is also crucial for their function, this being regulated through an association with the cytoskeleton [7]. Moreover, mitochondria are highly dynamic organelles, undergoing

continuous fusion and fission in order to react to extra cellular stressors [8].

When the organelle is excessively damaged, it becomes dangerous for the cell, initiating the apoptotic pathway [9]. Fortunately, cells have developed a mitochondrial quality control system that can selectively degrade damaged mitochondria, through a selective autophagic process, called mitophagy [10]. Healthy and damaged mitochondria are illustrated in a simplified way in Fig. 1.

Considering that mitochondria, the principal source of energy for the cell, coordinate metabolism, and coordinate a subtle balance between mtDNA and nuDNA transcription and translation, it is not surprising that defects in these functions are involved in several diseases requiring therapy [11,12].

In particular, ageing-related diseases, such as neurodegenerative diseases and cancer are linked to mitochondrial disturbances. For instance, mitochondrial dysfunction and increased oxidative damage (high production of ROS that can in turn damage mtDNA) are often associated with Alzheimer disease (AD), and Parkinson disease (PD), suggesting that oxidative stress may play an important role in the pathophysiology of these diseases [13]. Moreover, mtDNA mutations could contribute to cancer progression by increasing mitochondrial oxidative damage and changing the energy capacities of the cell (reviewed in [14]). Finally, metabolic disorders such as obesity and type 2 diabetes, are also directly linked to mitochondrial dysfunction. A number of mitochondrial therapeutic interventions aimed at improving these metabolic disorders have been favourably reviewed [15].

* Corresponding author at: IRCCS Fondazione Santa Lucia, 00143 Rome, Italy.
Tel.: +39 6501703093.

E-mail address: f.strappazzon@hsantalucia.it (F. Strappazzon).

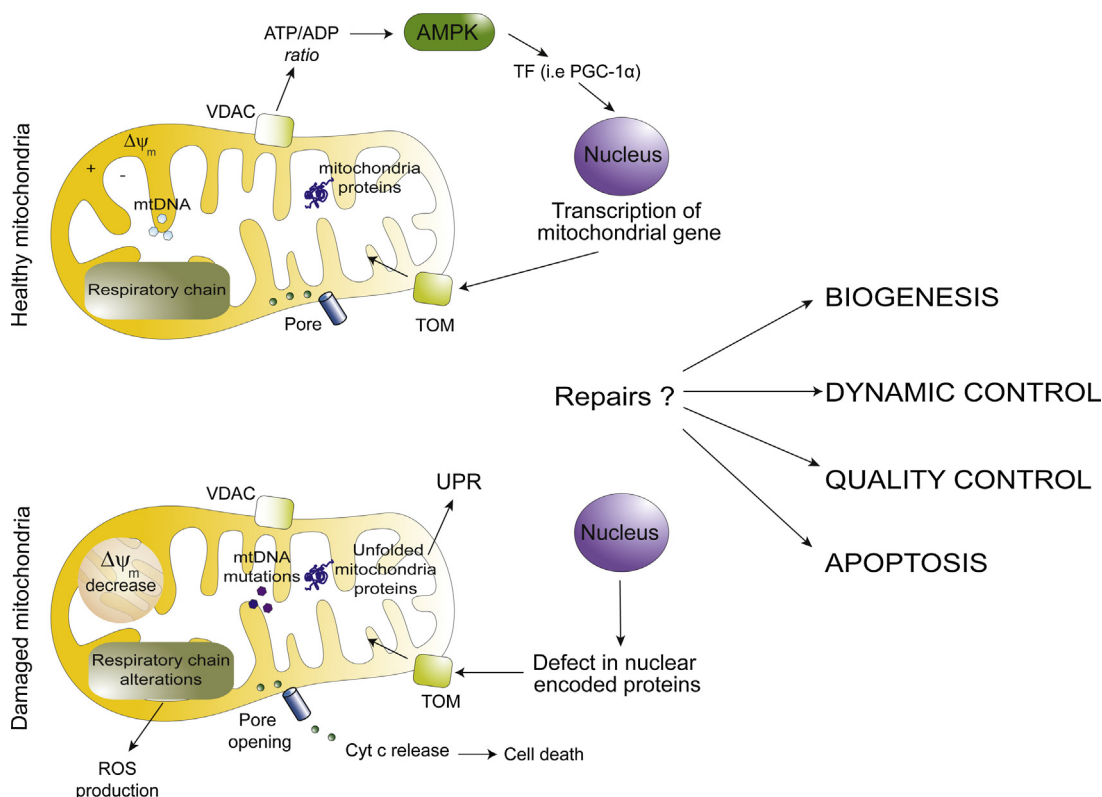


Fig. 1. Mitochondrial physiology and its major dysfunctions: principal pathways that can be manipulated to restore the organelle functions. Mitochondria produce ATP through the oxidative phosphorylation system (OXPHOS). When the cytosolic ATP/ADP ratio becomes too low, the AMP-dependent kinase (AMPK) is activated and acts principally on the transcriptional co-activator PGC-1 α . Mitochondrial DNA (mtDNA) encodes 13 key proteins responsible for respiratory chain synthesis and ATP synthase. The other mitochondrial proteins are imported from the cytosol after transcription of nuclear DNA (nuDNA). Mutations of the mitochondrial or nuclear DNA lead to alterations in the respiratory chain that, in turn, induce an increase in ROS production. Following apoptotic stimuli, the mitochondrial outer membrane becomes permeable (pore-opening) and cytochrome c (Cyt c) is released into the cytosol, where it can activate the apoptotic pathway.

Here are discussed the strategies aimed at repairing mitochondria functions in diseases in which they are damaged, such as PD, AD, Charcot–Marie–Tooth type 2A, the dominant optic atrophy and mitochondrial diseases such as the mitochondrial encephalopathy lactic acidosis. Thanks to the growing understanding of mitochondrial functions, we are now able to act, by using therapeutic compounds, on several functional aspects of the organelle. In this review, we present pharmacological strategies that affect mitochondria biogenesis, mitochondrial dynamics and mitochondria quality control, and we try to highlight the high plasticity that offers mitochondria a mechanism for coping with stress.

2. Strategies that affect mitochondrial biogenesis

Mitochondrial diseases are characterized by mutations on genes mtDNA- or nuDNA-encoded. For example, mitochondrial encephalopathy lactic acidosis is a disease due to a mutation in the mitochondrial tRNA gene that leads to defective assembly of oxidative phosphorylation complexes and defects in energy metabolism in the neuromuscular system [16]. Mutations on nuclear-encoded mitochondrial genes can also lead to defects in mitochondrial metabolic functions [17,18]. Cellular energy deficit is also a feature of several diseases, such as neurodegeneration, cancer, and metabolic diseases as obesity and type 2 diabetes [19]. Consequently, boosting mitochondria biogenesis, and thus the number of mitochondria, has considerable therapeutic potential since it may enhance ATP synthesis.

Physiologically, mitochondria number is stimulated following a workload or a reduction in nutrients. Indeed, caloric restriction is the well-known physiological intervention that can increase

lifespan [20]. A well-known way to stimulate mitochondrial biogenesis is to exert pressure on PGC-1 α (peroxisome proliferator-activated receptor gamma coactivator 1 alpha), a key player in mitochondrial biogenesis. PGC-1 α stimulates the activity of transcription factors such as nuclear respiratory factor (NRF-1), which, in turn, modulates the expression of other factors important for mtDNA replication and transcription [21]. More recently, synthetic chemicals that mimic the effects of a low-calorie intake have been identified and very well reviewed in Andreux et al. [22]. Here we summarize these principal components.

The Sirtuin family of histone deacetylase [23] is a good target to promote mitochondria biogenesis. In fact, these proteins depend on the metabolic co-factor NAD⁺ [24]; moreover, Sirtuin 1 (SIRT-1) is able to activate transcription factors such as PGC1 α [25]. The first compound discovered to act on Sirtuins was resveratrol, which by acting on AMPK (AMP-activated protein kinase), is responsible for an increase in NAD⁺ production that leads indirectly to Sirtuin activation [26,27]. Following this discovery, other SIRT-1-activating compounds have been identified, i.e., SRT1720 and SRT2014. The latest study describes a role for SRT1720 in extending the lifespan of mice by about 9% [28]. Again in order to activate sirtuins, researchers have developed a dietary supplemented with the NAD⁺ precursors nicotinamide mononucleotide (NMN) or nicotinamide riboside. In fact, NMN ameliorates glucose intolerance by restoring NAD⁺ levels in a type 2 diabetic mouse model [29].

The activation of AMPK is another way to increase mitochondrial biogenesis. AMPK is responsible of the enhancement of energy production which follows an increase of the AMP/ATP ratio [30]. AICAR (the AMPK agonist 5-aminoimidazole-4-carboxamide riboside) is responsible for AMPK activation and can then rescue

mitochondrial dysfunction [31]. The mTOR inhibitor Rapamycin can also act on AMPK activation, this action leading to a lifespan increase in mice and other organisms [32,33].

Other small molecules can trigger mitochondrial biogenesis by acting on downstream effectors, such as the nuclear receptors NRF-1 (nuclear respiratory factor 1) and TFAM (mitochondrial transcription factor A). Among them, we can mention compounds acting on the three peroxisome proliferator-activated receptors PPARs (agonists), such as L-16501L, GW501516, bezafibrate and rosiglitazone. Also compounds acting on oestrogen-related receptor- α can stimulate mitochondrial biogenesis, similarly to compounds acting more downstream on co-factors [22].

3. Strategies that affect mitochondrial dynamics

Mitochondria undergo a continuous fission and fusion. This dynamic process is very important for a normal morphology of the organelle, and to allow correct mitochondrial functions [34,35]. Key proteins regulate fusion events: MFN1 and MFN2 (Mitofusin 1 and 2), two GTPases anchored to the outer mitochondrial membrane [36] and another GTPase, OPA1 (optic atrophy 1), localized in the intermembrane space and the inner membrane of mitochondria [37,38]. A disturbance in the activity of these three proteins leads to excessive mitochondria fragmentation that in turn, impacts mitochondrial functions (depolarization of mitochondrial membrane, loss of mtDNA, respiratory chain alterations) [39]. Of note, these fusion factors are crucial for early development, as demonstrated by the fact that all mice lacking MFN1, MFN2 or OPA1 die at an early embryonic stage [39,40]. Mitochondrial fission is regulated by another GTPase, the dynamin-related protein 1 (DRP1) [41]. Drp1 is recruited to mitochondria through mitochondrial fission factor or MiD49/51 [41–43]. Cells lacking Drp1 present deficiency in mitochondrial fission with elongated mitochondria [44]. Most importantly, point mutations in *Mfn2* or *OPA1* lead to neurodegenerative diseases, such as Charcot–Marie–Tooth type 2A and the dominant optic atrophy [45,46].

As a result, in recent years, Drp1 has become an obvious target for these neurodegenerative diseases. One of the primary phenotypes associated with loss of fusion in mammalian cells is a severe defect in mitochondrial respiratory functions, caused in part by loss of mtDNA within a subset of mitochondria, this being due to excessive mitochondria division (an important factor contributing to the aetiology of these neurodegenerative diseases) [47,48]. Indeed, one of the fundamental roles of mitochondrial fusion is to provide an exchange mechanism that allows mtDNA maintenance [49].

Several chemical compounds have been reported to induce mitochondrial elongation through the inhibition of mitochondrial fission mediated by Drp1. In 2008, Cassidy-Stone et al. [50] identified mdivi-1 (mitochondrial division inhibitor 1) as the first selective inhibitor of mitochondrial division dynamins. The mechanism of mdivi-1 inhibition is distinct from the more general DRP inhibitor, dynasore, which was discovered in a chemical screen for inhibitors of dynamin-1 GTPase activity [51]. Dynasore inhibits the GTP hydrolysis of dynamin-1, dynamin-2 and Drp1 in a non-competitive manner, by binding to the GTPase domain in both assembled and unassembled states. Mdivi-1 selectively inhibits the activity of mitochondrial division DRPs by binding to an allosteric site, which does not exclusively act through the GTPase domain. Upon binding, mdivi-1 creates or stabilizes a conformational form of unassembled, and probably dimeric Dnm1 that can bind GTP, but at a significantly lower affinity. In addition, Mdivi-1 only partially blocks apoptosis by acting early in the pathway to inhibit mitochondrial outer membrane permeabilization (MOMP). Drp1 activity is regulated by covalent phosphorylation, ubiquitylation and sumoylation [52,53]. By attenuating mitochondrial division and increasing

mitochondrial connectivity, mdivi-1 is a selective inhibitor of mitochondrial division and apoptosis; this is highly beneficial in some of the many heteroplasmic mtDNA-linked diseases in humans.

Wang et al. [54] identified in 2012, from a phenotype image-based screen, the “M1 Hydrazone”, a small molecule that also promotes the fusion of fragmented mitochondria and protects cells from mitochondrial fragmentation associated cell death (M1 pre-treated cells showed decrease in Cytochrome c (Cyt c) release and higher survival rate). M1 regulates protein levels of the subunits of mitochondrial adenosine triphosphate (ATP5A and 5B). It is now considered as another approach to the treatment of diseases associated with mitochondrial dysfunction.

More recently, Yue et al. discovered a small natural compound, 15-oxospiramylactone (S3) derived from spiramine A of *Spiraea japonica* (rose family plant) which potently induces mitochondrial fusion. S3-induced inhibition of USP30, a mitochondrial-localized deubiquitinase, increased the ubiquitylation of MFN1 and MFN2 without affecting their protein levels. This non-degradative ubiquitylation of MFNs is involved in regulation of mitochondrial fusion [55]. S3 can restore the normal distribution of mtDNA and recover membrane depolarization; furthermore, it increases ATP levels and OXPHOS capacity. S3 has promising therapeutic implications in the treatment of diseases such as Charcot–Marie–Tooth type 2A and autosomal dominant optic atrophy. Hitherto, S3 is the first identified naturally derived small molecule from plants to activate mitochondrial fusion and facilitate restoration of the mitochondrial network.

The function of pharmacological compounds created to act on mitochondrial dynamics are illustrated in Fig. 2.

4. Strategies that could affect mitochondrial quality control

4.1. Mitophagy

Given the important mitochondria roles described above, damaged mitochondria could be detrimental to the cell. In fact, accumulation of dysfunctional mitochondria is a characteristic of many types of diseases, including Alzheimer's disease (AD), Parkinson's disease (PD), ageing and cancer [56,57]. AD is the most common age-associated neurodegenerative disorder, characterized by cognitive dysfunction and loss of memory, caused by neuronal death in cerebral cortex. Neurofibrillary tangles and extracellular amyloid plaques composed of beta-amyloid derived from amyloid precursor protein (APP) are observed in AD human brains. Mitochondrial damage has been implicated in the development of the disease: abnormalities in mitochondrial structure and accumulation of beta-amyloid fragment in mitochondria have been observed in AD patients [58,59]. PD is caused by loss of dopaminergic neurons in the *substantia nigra*, a region important for motor control and coordination. An increase of mutations and/or deletions of the mtDNA is observed in patients with PD [60,61]. Consistently, mitochondrial damage accumulation is observed in dopaminergic neurons of PD patients. Mitochondrial dysfunction has also been correlated with ageing. Indeed, mitochondria are the primary source of ROS [62]. Ageing particularly affects mitochondrial homeostasis with mtDNA mutations accumulating due to ROS generation in mitochondria, an event that has been correlated with age-related decreased autophagic activity [63,64].

Fortunately, cells have developed a mechanism to remove damaged mitochondria through a selective autophagy process called mitophagy. Stimulation of mitophagy may have a pivotal role in combating AD and PD development through the elimination of defective mitochondria. Autophagy (from ancient Greek, meaning *self-eating*) is a catabolic process occurring in all eukaryotic cells, by which cytoplasmic material (e.g., proteins, lipids and organelles)

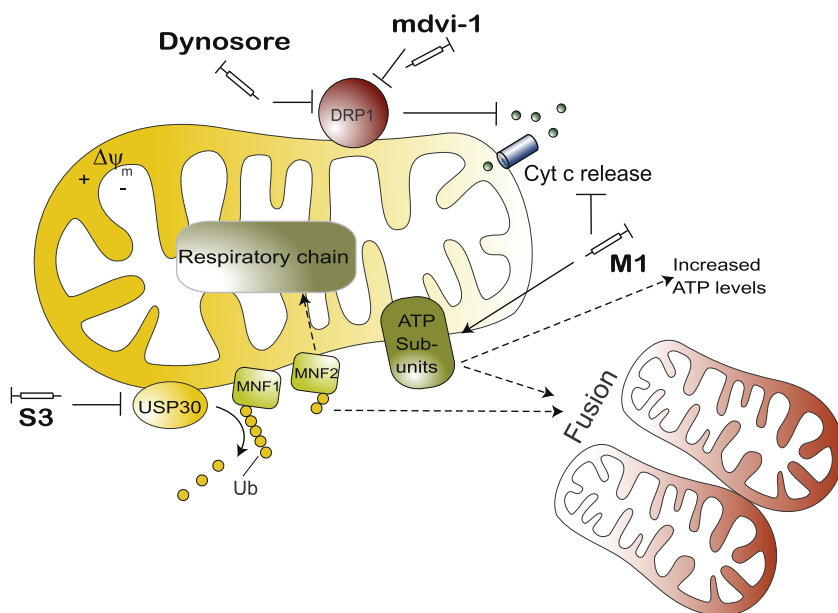


Fig. 2. Overview of the compounds acting on mitochondrial dynamics. Dynosore acts in a non-specific manner on DRP1 (inhibitor of dynamin-1, 2 and DRP1). By contrast, mdvi-1 inhibits DRP1 selectively and thus decreases division events that lead to a reduction of apoptosis by blocking Cyt c release. M1 Hydrazone is a small molecule that, by regulating levels of the subunits of mitochondrial adenosine phosphatase, promotes fusion of fragmented mitochondria and protects also cells from mitochondria-fragmentation-associated cell death. S3 induces mitochondrial fusion through inhibition of the deubiquitinase USP30. Consequently, USP30 cannot remove regulative ubiquitins on MFN1 and MFN2 which in turn increase their activity, promoting fusion events.

is degraded through the lysosome machinery. This process involves de novo formation of double-membraned vesicles, termed autophagosomes, which sequester the cytoplasm-derived materials and transport them to the lysosomes for degradation. There are three types of autophagy: microautophagy, chaperone-mediated autophagy (CMA), and macroautophagy. Macroautophagy is well conserved from yeast to mammals, and is the predominant pathway of autophagy. Non-selective autophagy (bulk autophagy) is induced by starvation, whilst selective autophagy is induced when organelles (such as mitochondria, and in this case the process is called mitophagy) are damaged or unwanted in the cell.

Fragmentation of the mitochondria is a critical step prior to engulfment of mitochondria into autophagosomes. Mitochondria damaged by the uncoupler CCCP (carbonyl cyanide *m*-chloro phenyl hydrazone) – due to a loss of their mitochondrial membrane potential ($\Delta\Psi_m$), are subjected to mitophagy [65,66]. During this process, the protein kinase PINK1 is stabilized to the outer membrane of the mitochondria, where it can recruit the E3 ubiquitin ligase PARKIN. These two proteins are found to be mutated in autosomal recessive forms of PD [65]. The mitochondrial quality control, driven by PINK1/PARKIN proteins, has been more effectively characterized by RNAi screens [67]. New proteins such as HSPA1L (Heat shock 70 kDa protein 1-like), BAG4 (BAG family molecular chaperone regulator 4), and SIAH3 (siah E3 ubiquitin protein ligase family member 3) have been found to modulate translocation of PARKIN to damaged mitochondria, whereas TOMM7 (translocase of outer mitochondrial membrane 7 homolog) stabilizes PINK1 on the mitochondria. Interestingly, it has been demonstrated that after mitochondrial depolarization, the cytosolic pool of AMBRA1 interacts with PARKIN to enhance mitochondrial clearance [68]. We recently investigated the molecular mechanism responsible for the AMBRA1-dependent enhancement of PARKIN-mediated mitophagy. AMBRA1 was found to be a LIR-containing protein; as we have demonstrated, this motif is essential for the binding between AMBRA1 and LC3, following mitophagy induction. Furthermore, we have shown that this interaction is crucial in order to amplify PARKIN-mediated mitochondrial clearance [69].

In this system, it has recently been demonstrated that the other pro-autophagic factor BECLIN 1 also interacts with PARKIN and regulates PARKIN translocation to mitochondria [70].

In mammalian cells, mitophagy receptors are localized at the outer membrane of mitochondria and possess a consensus sequence (W/F/YxxL/I) that allows their binding with LC3 for selective autophagy. Until today, 2 types of mitophagy receptors have been identified: The group including NIX/BNIP3L and BNIP3 (BCL-2/adenovirus E1B 19 kDa protein-interacting protein 3-like) [71–73] and FUNDC1 (FUN14 domain-containing protein 1) [75].

NIX/BNIP3L and BNIP3 contain LIR motifs that can recruit LC3 to the mitochondria during red blood cell maturation [74]. Phosphorylation of BNIP3 on serine 17 and 24 are required to promote the binding with LC3 and thus needed for a correct mitophagy [76].

FUNDC1 is a mitochondrial outer membrane factor possessing three TM domains. The N-terminal region of FUNDC1 contains a LIR motif; it is exposed into the cytosol, where it can binds LC3 under hypoxia or after mitochondrial membrane depolarization. The activity of FUNDC1-mediated mitophagy is also regulated at a post-translational level. After membrane depolarization, FUNDC1 is phosphorylated on Serine 17 by the ULK1 kinase [75], whereas Liu et al. demonstrated that FUNDC1 required a dephosphorylation on tyrosine 18 and serine 13 to be active in the mitophagic pathway [76].

In addition to NIX and FUNDC1, AMBRA1 has been recently described as a novel regulator of mitophagy [69]. AMBRA1 has long been known to be a key mediator of autophagy, regulating positively the PI3K complex [77]. In 2011, a pool of AMBRA1 was demonstrated to be associated to BCL-2, in the outer mitochondrial membrane [78]. In addition, AMBRA1 possesses a LIR domain in its C-terminal part that allows its binding with LC3 upon mitophagy induction (after mitochondrial membrane depolarization). Furthermore, high levels of AMBRA1 at the mitochondria (obtained by overexpressing a mitochondria-targeted AMBRA1, also known as AMBRA1-ActA) are able to trigger massive mitophagy in both PARKIN-dependent or independent systems in mammalian cells. AMBRA1-ActA can thus be considered a novel inducer of mitophagy

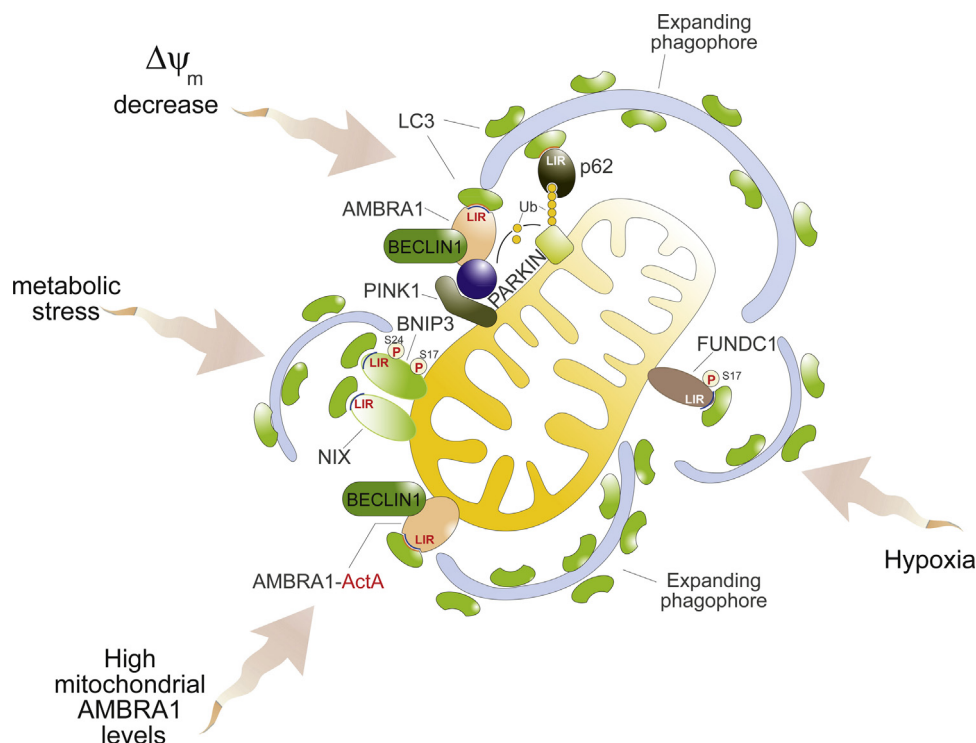


Fig. 3. Key players of mitophagy in mammalian cells. The PINK1/PARKIN pathway is induced after mitochondrial membrane depolarization. PINK1 is stabilized to mitochondria and allows mitochondrial recruitment of PARKIN. PARKIN ubiquitylates mitochondria that can subsequently be recognized by the scaffold protein p62. In this context, AMBRA1 is crucial to bring damaged mitochondria to degradation, by interacting with LC3 through its LIR motif. High levels of AMBRA1 at the mitochondria can induce massive mitophagy in a PARKIN-dependent or -independent context. AMBRA1 can thus be considered as a mitophagy receptor that binds LC3 through its LIR motif. FUNDC1, NIX/BNIP3L and BNIP also interact with LC3 through LIRs. Basically, FUNDC1 is phosphorylated on Tyr18 and Ser13. Hypoxia or mitochondrial depolarization induce dephosphorylation of the protein, leading to a stronger binding with LC3. By contrast, phosphorylation of BNIP3 on ser17 is necessary to favour its binding with LC3.

in the absence of any treatments with CCCP (a mitochondrial uncoupler known as the master mitophagy inducer), a finding which could herald new therapies to fight important human disorders, including age-associated pathologies such as PD, in which the PINK1/PARKIN pathway is mutated. Related to this, a pharmacological tool, named PMI (P62-mediated mitophagy) has been recently discovered to induce mitophagy in mammalian cells. This compound increases the expression and signalling of the autophagic adaptor molecule p62/SQSTM and induces mitochondrial removal. Even more interesting, this compound retains activity in cells devoid of a fully functional PINK1/PARKIN pathway [79]. This finding is of great interest in order to facilitate dissection of the molecular mechanisms underlying mitophagy. The mitophagy pathways described above are illustrated in Fig. 3.

4.1.1. Interplay between mitophagy and calcium

Gomez-Sanchez et al. [80] demonstrated that calcium overload is important in PINK1/PARKIN-mediated mitophagy. In fact, they found that increase of full-length PINK1 levels observed upon CCCP treatment is not due only to the stabilization of the protein but also to de novo PINK1 synthesis in a calcium dependent pathway. Since calcium chelators are able to inhibit mitochondrial removal following CCCP treatment, it will be interesting to test whether these kind of agents can directly decrease PINK1 transcription and thus act on mitophagy. Connected to this, Parkin mitochondrial localization increases the ER-mitochondrial crosstalk, favouring calcium transfer [81]. Since ER transfers calcium towards the mitochondria is fundamental for cell metabolism, it is not a surprise that disruption of proteins involved in ER/mitochondria connection induce calcium defects. Also, intracellular calcium has been shown to influence mitochondrial mobility [82]. In conclusion, all compounds that improve ER/mitochondria junction could be

opportune for the development of new therapies. Interestingly, the mitochondria-initiated calcium-mediated inter-organelle stress response is involved in cell death resistance in cancer cells [83]. In this review, we do not discuss apoptosis, which is another crucial feature of mitochondrial function, but this aspect has been extensively reviewed in [84].

4.2. Mitochondrial UPR

In addition to mitophagy, mammalian cells possess another quality control mechanism that involves the mitochondria-specific chaperones and proteases against misfolded proteins. Cancer cells, for example, survive in a highly oxidative environment. High levels of ROS induce oxidative damage to DNA, lipids and proteins, leading to their misfolding and aggregation in the mitochondria. Following an increase of misfolded and aggregated proteins into mitochondria, the cells triggers the mitochondrial unfolded protein response (UPR^{mt}), in order to decrease the proteotoxic stress and reach a good homeostasis. The UPR^{mt} is analogous to the UPR of the endoplasmic reticulum [85] but it was discovered more recently [86,87]. This signalling is controlled by 3 key proteins: (1) the transcription factor CHOP, which activates transcription of the mitochondrial chaperones and proteases [88]; there are two major mitochondrial chaperone systems that allow protein folding in the mitochondrial matrix: mtHSP70 and the HSP60-HSP10 machinery [89]; (2) the oestrogen receptor alpha (ER α), which exerts a cytoprotective action on the cell by acting on the proteasome and the protease Omi [90], and (3) SirT3, a novel major coordinator of the UPR^{mt} that orchestrates both the antioxidant machinery and mitophagy [91].

The UPR^{mt} is crucial for overcoming mitochondrial stress. Interestingly, Jin and Youle [92], demonstrated that a connection

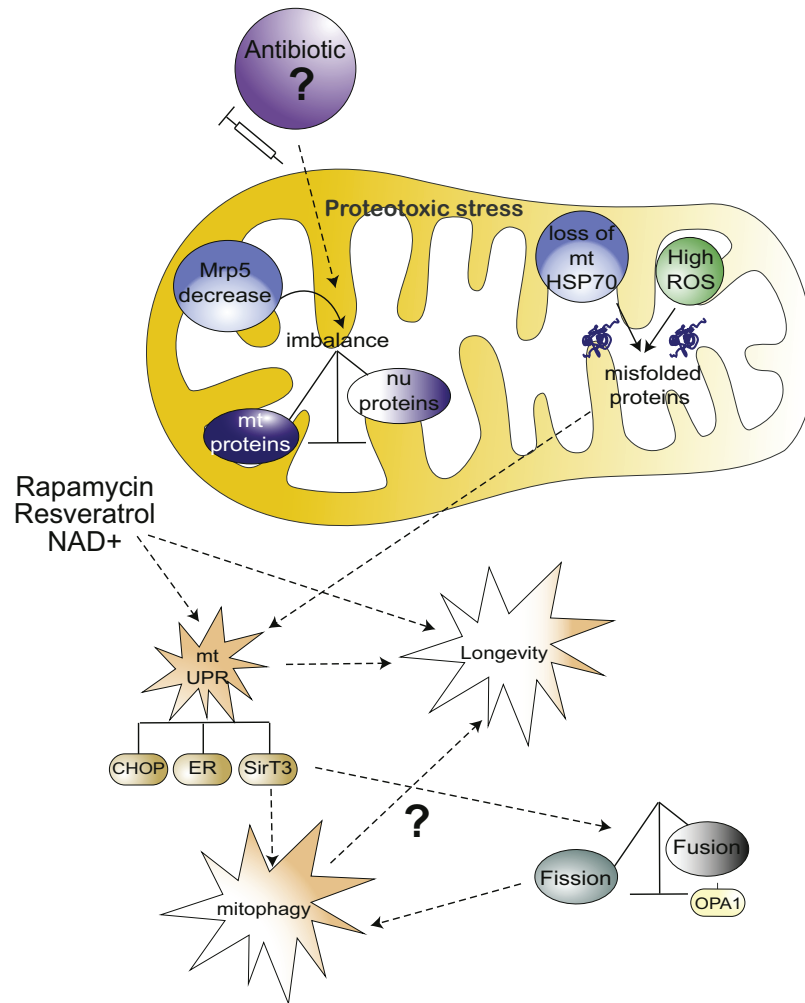


Fig. 4. UPR^{mt} signalling, as a target to develop therapeutic strategies in mammals. High levels of ROS induce oxidative damage to DNA, lipids and proteins, leading to their misfolding and aggregation. Following an increase of misfolded and aggregated proteins (mitochondrial proteotoxic stress) into mitochondria, the cells trigger the mitochondrial unfolded protein response (UPR^{mt}). UPR^{mt} can be activated after a loss of mtHSP70 that occurs in cells of PD patients, after a decrease of Mrps5 that triggers an imbalance between mitochondrial proteins and nuclear-encoded mitochondrial proteins. Three key proteins are involved in the UPR^{mt} signalling: CHOP, a transcription factor that activates transcription of chaperones and proteases; the oestrogen receptor alpha (ER α), that regulates proteasome activity, and the SirT3 protein that orchestrates both the antioxidant machinery and mitophagy. UPR^{mt} could thus be a novel target for therapeutic approaches. In fact, antibiotics seem to mimic, at least in *C. elegans*, Mrps5 decrease and then lead to longevity. Interconnection between UPR^{mt}, mitochondrial biogenesis, mitophagy, longevity and dynamics-related events are illustrated.

between the two quality control levels do, indeed, exist: expression of unfolded proteins in the matrix induces PINK1/PARKIN-mediated mitophagy and thus a reduction of unfolded protein load. Moreover, Papa et al. [91] recently demonstrated that if proteotoxic stress cannot be resolved, a mitophagic pathway, dependent of the protein SirT3, is triggered. SirT3 favours the activity of magnesium superoxide dismutase (MnSOD), a protein involved in the transformation of toxic superoxide into hydrogen peroxide and diatomic oxygen [93–95]. Consequently, a reduction of SirT3 is linked to an increase in ROS production [96]. Although the mechanism by which SirT3 coordinates the selection of damaged mitochondria has not been fully elucidated, it nevertheless shows mitochondria's remarkable plasticity in responding to stress.

Another study by Burbulla et al. illustrates the connection between UPR^{mt} and mitophagy: they showed that impaired intramitochondrial quality control, in PD, mediated by loss of mtHSP70 (also called Mortalin), can be compensated by PINK1/PARKIN-mediated mitophagy [97].

Of note, a gradual decrease of mitochondrial function occurs during ageing, as demonstrated by numerous studies, performed by using simple organisms as well as mammalian models [98]. Jovaisaite et al. [99] recently showed that activation of UPR^{mt} correlates

with longevity both in *Caenorhabditis elegans* and in mice [100]. The expression of mitochondrial ribosomal protein S5 (Mrps5) correlated with longevity. Knockdown of *mrps-5* expression decreases the translation of mtDNA-encoded components that leads to an imbalance between mtDNA and nuDNA-encoded OXPHOS complex components. This imbalance acts similarly to a proteotoxic stress for the host cell that – in turn, activates UPR^{mt} and prolongs lifespan. To pharmacologically mimic the reduction of *mrps-5*, Houtkooper et al. used antibiotics (doxycycline and chloramphenicol) that specifically targeted bacterial translation and thus also inhibited mitochondrial translation. They have obtained satisfactory results both in *C. elegans* and mouse hepatocyte cell cultures: Indeed, antibiotics are able to induce mito-nuclear imbalance leading to an UPR^{mt} and an increased of lifespan in *C. elegans*. Notably, exposition of worms or cells to mitochondrial biogenesis inducers, such as rapamycin and resveratrol (the well-known longevity agent described before) or NAD⁺ boosters (stimulator of the sirtuin 1 pathway), induce UPR^{mt} [100,101]. The next step is to better understand the physiological role of UPR^{mt} in mammals, although it seems that innovative therapeutic strategies can be developed, based on this process. In fact, given the studies performed in *C. elegans*, it is expected that pharmacological approaches that can mimic

UPR^{mt} could improve lifespan and health in age-related diseases such as AD or PD.

5. Discussion/conclusion

Mitochondria exhibit an ample range of stress responses in order to preserve the host cell. This feature underlines the fact that mitochondria are organelles with a high malleability. Therapeutic agents developed to restore mitochondrial function act principally on mitochondrial biogenesis and fusion/fission mechanisms. By gathering all information concerning possible ways to repair mitochondrial functions, it emerges that all pathways intended to save mitochondrial functions are interconnected. Biogenesis figures seem to be closely linked to the UPR^{mt} pathway, which is also linked to longevity. In addition, mitophagy, which is linked to mitochondrial dynamics (preceded by an increase in fission events), can be triggered if the UPR^{mt} pathway is not sufficient to help the cell. Finally, a recent study demonstrated that UPR^{mt} is directly linked to mitochondrial dynamics: SIRT3 binds and activates OPA1 to regulate mitochondrial dynamics during stress [102]. The interconnection between all mitochondrial pathways is illustrated in Fig. 4.

In conclusion, all therapies aimed at stimulating biogenesis can indirectly increase longevity, most likely by exerting pressure on the UPR^{mt} pathway. Further work should help to better understand whether mitophagy is important in increasing lifespan following caloric restriction. Finally, since novel molecules have been recently defined as novel mitophagy regulators (e.g., AMBRA1), efforts are now required to find new therapeutic approaches to exploit or target directly these novel mitophagic players. The same kind of studies are also required to find new compounds that can directly mimic UPR^{mt}, such as the antibiotics used in nematodes (that can create an imbalance between mtDNA and nuDNA).

Ideally, following from all the findings outlined here, the next step would be to identify a compound that acts on one of the pathways described before. This in turn would enhance the three other ways for restoring complete mitochondrial function under stresses.

Acknowledgements

We thank Mrs. M. Acuna Villa, Dr. M. Bennett and J. and D. Hodder for secretarial and proofreading work. The work performed by the author has been supported in part by from the Telethon Foundation (GGP14202), AIRC (IG2013 to FC), the Italian Ministry of University and Research (FIRB Accordi di Programma 2011), the Italian Ministry of Health (Ricerca Finalizzata and Ricerca Corrente to FC; GR2011-2012 to FS).

References

- [1] X. Li, P. Fang, J. Mai, E.T. Choi, H. Wang, X.F. Yang, Targeting mitochondrial reactive oxygen species as novel therapy for inflammatory diseases and cancers, *J. Hematol. Oncol.* 25 (2013) 6–19.
- [2] D. Voet, G. Judith, C. Voet, W. Pratt, *Fundamentals of Biochemistry*, 2nd ed., John Wiley and Sons, 2006, pp. 547.
- [3] D.R. Green, Apoptotic pathways: the roads to ruin, *Cell* 6 (1998) 695–698.
- [4] G. Hajnóczky, G. Csordás, S. Das, C. Garcia-Perez, M. Saotome, S. Sinha Roy, M. Yi, Mitochondrial calcium signalling and cell death: approaches for assessing the role of mitochondrial Ca²⁺ uptake in apoptosis, *Cell Calcium* 40 (5–6) (2006) 553–560.
- [5] M.F. Rossier, T channels and steroid biosynthesis: in search of a link with mitochondria, *Cell Calcium* 40 (2) (2006) 155–164.
- [6] M.T. Ryan, N.J. Hoogenraad, Mitochondrial nuclear communications, *Annu. Rev. Biochem.* 76 (2007) 701–722.
- [7] L. Rappaport, P. Oliviero, J.L. Samuel, Cytoskeleton and mitochondrial morphology and function, *Mol. Cell. Biochem.* 84 (1998) 101–105.
- [8] B. Westermann, Mitochondrial fusion and fission in cell life and death, *Nat. Rev. Mol. Cell Biol.* 11 (2010) 872–884.
- [9] J. Nunnari, A. Suomalainen, Mitochondria in sickness and in health, *Cell* 6 (2012) 1145–1159.
- [10] R. Youle, P. Narendra, Mechanism of mitophagy, *Nat. Rev. Mol. Cell Biol.* 12 (2011) 9–14.
- [11] D.C. Wallace, W. Fan, V. Procaccio, Mitochondrial energetics and therapeutics, *Annu. Rev. Pathol.* 5 (2010) 297–348.
- [12] M.R. Duchen, G. Szabadkai, Roles of mitochondria in human disease, *Essays Biochem.* 47 (2010) 115–137.
- [13] M.T. Lin, M.F. Beal, Mitochondrial dysfunction and oxidative stress in neurodegenerative diseases, *Nature* 7113 (2006) 787–795.
- [14] C. Hang, K. Yahui, Z. Hong, Oxidative stress mitochondrial dysfunction, and aging, *J. Signal Transduct. (Mol. Cell Biol.)* 646354.
- [15] J. Szendroedi, E. Phielix, M. Roden, The role of mitochondria in insulin resistance and type 2 diabetes mellitus, *Nat. Rev. Endocrinol.* 8 (2012) 92–103.
- [16] K. Goto, M. Nagasawa, O. Yanagisawa, T. Kizuka, N. Ishii, K. Takamatsu, Muscular adaptations to combinations of high- and low-intensity resistance exercises, *J. Strength Cond. Res.* 4 (2004) 730–737.
- [17] J.A. Smeitink, O. Elpeleg, H. Antonicka, H. Diepstra, A. Saada, P. Smits, F. Sasarman, G. Vriend, J. Jacob-Hirsch, A. Shaag, G. Rechavi, B. Welling, J. Horst, R.J. Rodenburg, B. van den Heuvel, E.A. Shoubridge, Distinct clinical phenotypes associated with a mutation in the mitochondrial translation elongation factor EFTs, *Am. J. Hum. Genet.* 5 (2006) 869–877.
- [18] C. Angelini, L. Bello, M. Spinazzi, C. Ferrati, Mitochondrial disorders of the nuclear genome, *Acta Myol.* 1 (2009) 16–23.
- [19] T.M. Wallace, D.R. Matthews, Poor glycemic control in type 2 diabetes: a conspiracy of disease suboptimal therapy and attitude, *QJM* 6(2000)369–374.
- [20] L. Fontana, L. Partridge, V.D. Longo, Extending healthy life span – from yeast to humans, *Science* 5976 (2010) 321–326.
- [21] R. Ventura-Clapier, Potentiating exercise training with resveratrol, *J. Physiol.* 590 (2012) 3215–3216.
- [22] P. Andreux, R.H. Houtkooper, J. Auwerx, Pharmacological approaches to restore mitochondrial function, *Nat. Rev. Drug Discov.* 12 (2013) 465–483.
- [23] R.H. Houtkooper, E. Pirinen, J. Auwerx, Sirtuins as regulators of metabolism and healthspan, *Nat. Rev. Mol. Cell Biol.* 4 (2012) 225–238.
- [24] S. Imai, C.M. Armstrong, M. Kaeberlein, L. Guarente, Transcriptional silencing and longevity protein Sir2 is an NAD-dependent histone deacetylase, *Nature* 6771 (2000) 795–800.
- [25] J.T. Rodgers, C. Lerin, W. Haas, S.P. Gygi, B.M. Spiegelman, P. Puigserver, Nutrient control of glucose homeostasis through a complex of PGC-1 α and SIRT1, *Nature* 7029 (2005) 113–118.
- [26] D. Beher, J. Wu, S. Cumine, K.W. Kim, S.C. Lu, L. Atangan, M. Wang, Resveratrol is not a direct activator of SIRT1 enzyme activity, *Chem. Biol. Drug Des.* 6 (2009) 619–624.
- [27] C. Cantó, L.Q. Jiang, A.S. Deshmukh, C. Matak, A. Coste, M. Lagouge, J.R. Zierath, J. Auwerx, Interdependence of AMPK and SIRT1 for metabolic adaptation to fasting and exercise in skeletal muscle, *Cell Metab.* 3 (2010) 213–219.
- [28] S.J. Mitchell, A. Martin-Montalvo, E.M. Mercken, H.H. Palacios, T.M. Ward, G. Abulwerdi, R.K. Minor, G.P. Vlasuk, J.L. Ellis, D.A. Sinclair, J. Dawson, D.B. Allison, Y. Zhang, K.G. Becker, M. Bernier, R. de Cabo, The SIRT1 activator SRT1720 extends lifespan and improves health of mice fed a standard diet, *Cell Rep.* 5 (2014) 836–843.
- [29] J. Yoshino, K.F. Mills, M.J. Yoon, S. Imai, Nicotinamide mononucleotide, a key NAD(+) intermediate, treats the pathophysiology of diet- and age-induced diabetes in mice, *Cell Metab.* 4 (2011) 528–536.
- [30] C. Cantó, J. Auwerx, NAD⁺ as a signaling molecule modulating metabolism, *Cold Spring Harb. Symp. Quant. Biol.* 76 (2011) 291–298.
- [31] C. Visconti, E. Bottani, G. Civiletto, R. Cerutti, M. Moggioli, E.A. Schon, C. Lamperti, M. Zeviani, In vivo correction of COX deficiency by activation of the AMPK/PGC-1 α axis, *Cell Metab.* 1 (2011) 80–90.
- [32] D.E. Harrison, R. Strong, Z.D. Sharp, J.F. Nelson, C.M. Astle, K. Flurkey, N.L. Nadon, J.E. Wilkinson, K. Frenkel, C.S. Carter, M. Pahor, M.A. Javors, E. Fernandez, R.A. Miller, Rapamycin fed late in life extends lifespan in genetically heterogeneous mice, *Nature* 7253 (2009) 392–395.
- [33] S. Robida-Stubbs, K. Glover-Cutter, D.W. Lamming, M. Mizunuma, S.D. Narasimhan, E. Neumann-Haefelin, D.M. Sabatini, T.K. Blackwell, TOR signaling and rapamycin influence longevity by regulating SKN-1/Nrf and DAF-16/FoxO, *Cell Metab.* 5 (2012) 713–724.
- [34] D.C. Chan, Mitochondria: dynamic organelles in diseases, aging, and development, *Cell* 7 (2006) 1241–1252.
- [35] S. Hoppins, L. Lackner, J. Nunnari, The machines that divide and fuse mitochondria, *Annu. Rev. Biochem.* 76 (2007) 751–780.
- [36] T. Koshiba, S.A. Detmer, J.T. Kaiser, H. Chen, J.M. McCaffery, D.C. Chan, Structural basis of mitochondrial tethering by mitofusin complexes, *Science* 305 (2004) 858–862.
- [37] S. Hiromi, M. Sheryl, M.P. Yaffe, R.E. Jensen, Mgm1p, a dynamin-related GTPase, is essential for fusion of the mitochondrial outer membrane, *Mol. Biol. Cell* 14 (2003) 2342–2356.
- [38] S. Cipolat, O. Martins de Brito, B. Dal Zilio, L. Scorrano, OPA1 requires mitofusin 1 to promote mitochondrial fusion, *Proc. Natl. Acad. Sci. U. S. A.* 101 (2004) 15927–15932.
- [39] H. Chen, S.A. Detmer, A.J. Ewald, E.E. Griffin, S.E. Fraser, D.C. Chan, Mitofusins Mfn1 and Mfn2 coordinately regulate mitochondrial fusion and are essential for embryonic, *J. Cell Biol.* 106 (2003) 189–200.
- [40] S. Cipolat, T. Rudka, D. Hartmann, V. Costa, L. Serneels, K. Craessaerts, K. Metzger, C. Frezza, W. Annaert, L. D'Adamio, C. Derks, T. Dejaegere, L. Pellegrini, R. D'Hooge, L. Scorrano, B. De Strooper, Mitochondrial rhomboid PARL regulates cytochrome c release during apoptosis via OPA1-dependent cristae remodeling, *Cell* 14 (2006) 163–175.

- [41] E. Smirnova, L. Griparic, D.L. Shurland, A.M. Van der Bliek, Dynamin-related protein Drp1 is required for mitochondrial division in mammalian cells, *Mol. Biol. Cell* 12 (2001) 2245–2256.
- [42] E. Ingerman, E.M. Perkins, M. Marino, J.A. Mears, J.M. McCaffery, J.E. Hinshaw, J. Nunnari, Dnm1 forms spirals that are structurally tailored to fit mitochondria, *J. Cell Biol.* 7 (2005) 1021–1027.
- [43] C.S. Palmer, L.D. Osellame, D. Laine, O.S. Koutsopoulos, A.E. Frazier, M.T. Ryan, Mid49 and Mid51, new components of the mitochondrial fission machinery, *EMBO Rep.* 6 (2011) 565.
- [44] N. Ishihara, M. Nomura, A. Jofuku, H. Kato, S.O. Suzuki, K. Masuda, H. Otera, Y. Nakanishi, I. Nonaka, Y. Goto, N. Taguchi, H. Morinaga, M. Maeda, R. Takayanagi, S. Yokota, K. Mihara, Mitochondrial fission factor Drp1 is essential for embryonic development and synapse formation in mice, *Nat. Cell Biol.* 8 (2009) 958–966.
- [45] S. Züchner, I.V. Mersianova, M. Muglia, N. Bissar-Tadmouri, J. Rochelle, E.L. Dadaei, M. Zappia, E. Nelis, A. Paticucci, J. Senderek, Y. Parman, O. Evgrafov, P.D. Jonghe, Y. Takahashi, S. Tsuji, M.A. Pericak-Vance, A. Quattrone, E. Battaloglu, A.V. Polyakov, V. Timmerman, J.M. Schröder, J.M. Vance, Mutations in the mitochondrial GTPase mitofusin 2 cause Charcot-Marie-Tooth neuropathy type 2A, *Nat. Genet.* 5 (2004) 449–451.
- [46] C. Alexander, M. Votruba, U.E. Pesch, D.L. Thiselton, S. Mayer, A. Moore, M. Rodriguez, U. Kellner, B. Leo-Kottler, G. Auburger, S.S. Bhattacharya, B. Wissinger, OPA1, encoding a dynamin-related GTPase, is mutated in autosomal dominant optic atrophy linked to chromosome 3q28, *Nat. Genet.* 2 (2000) 211–215.
- [47] A. Olichon, T. Landes, L. Arnauné-Pelloquin, L.J. Emorine, V. Mils, A. Guichet, C. Delettre, C. Hamel, P. Amati-Bonneau, D. Bonneau, P. Reynier, G. Lenaers, P. Belenguer, Effects of OPA1 mutations on mitochondrial morphology and apoptosis: relevance to ADOA pathogenesis, *J. Cell. Physiol.* 2 (2007) 423–430.
- [48] P.A. Parone, D.I. James, S. Da Cruz, Y. Mattenberger, O. Donzé, F. Barja, J.C. Martinou, Inhibiting the mitochondrial fission machinery does not prevent Bax/Bak-dependent apoptosis, *Mol. Cell. Biol.* 20 (2006) 7397–7408.
- [49] S. Hoppins, The regulation of mitochondrial dynamics, *Curr. Opin. Cell Biol.* 29C (August) (2014) 46–52.
- [50] A. Cassidy-Stone, J.E. Chipuk, E. Ingerman, C. Song, C. Yoo, T. Kuwana, M.J. Kurth, J.T. Shaw, J.E. Hinshaw, D.R. Green, J. Nunnari, Chemical inhibition of the mitochondrial division dynamin reveals its role in Bax/Bak-dependent mitochondrial outer membrane permeabilization, *Dev. Cell* 2 (2008) 193–204.
- [51] E. Macia, M. Ehrlich, R. Massol, E. Boucrot, C. Brunner, T. Kirchhausen, Dynasore, a cell-permeable inhibitor of dynamin, *Dev. Cell* 6 (2006) 839–850.
- [52] N. Nakamura, Y. Kimura, M. Tokuda, S. Honda, S. Hirose, MARCH-V is a novel mitofusin 2- and Drp1-binding protein able to change mitochondrial morphology, *EMBO Rep.* 10 (2006) 1019–1022.
- [53] N. Taguchi, N. Ishihara, A. Jofuku, T. Oka, K. Mihara, Mitotic phosphorylation of dynamin-related GTPase Drp1 participates in mitochondrial fission, *J. Biol. Chem.* 15 (2007) 11521–11529.
- [54] D. Wang, J. Wang, G.M. Bonamy, S. Meeusen, R.G. Bruschi, C. Turk, P. Yang, P.G. Schultz, A small molecule promotes mitochondrial fusion in mammalian cells, *Angew. Chem. Int. Ed. Engl.* 37 (2012) 9302–9305.
- [55] W. Yue, Z. Chen, H. Liu, C. Yan, M. Chen, D. Feng, C. Yan, H. Wu, L. Du, Y. Wang, J. Liu, X. Huang, L. Xia, L. Liu, X. Wang, H. Jin, J. Wang, Z. Song, X. Hao, Q. Chen, A small natural molecule promotes mitochondrial fusion through inhibition of the deubiquitinase USP30, *Cell Res.* 4 (2014) 482–496.
- [56] K. Palikaras, N. Tavernarakis, Mitophagy in neurodegeneration and aging, *Front Genet.* 3 (2012) 297.
- [57] S.J. Goldman, R. Taylor, Y. Zhang, S. Jin, Autophagy and the degradation of mitochondria, *Mitochondrion* 4 (2010) 309–315.
- [58] J.W. Lustbader, M. Cirilli, C. Lin, H.W. Xu, K. Takuma, N. Wang, C. Caspersen, X. Chen, S. Pollak, M. Chaney, F. Trinchese, S. Liu, F. Gunn-Moore, L.F. Lue, D.G. Walker, P. Kuppasamy, Z.L. Zewier, O. Arancio, D. Stern, S.S. Yan, H. Wu, AβAD directly links Aβeta to mitochondrial toxicity in Alzheimer's disease, *Science* 306 (2004) 448–452.
- [59] C.S. Casley, J.M. Land, M.A. Sharpe, J.B. Clark, M.R. Duchon, L. Canevari, Beta-amyloid fragment 25–35 causes mitochondrial dysfunction in primary cortical neurons, *Neurobiol. Dis.* 10 (2012) 258–267.
- [60] K. Bender, J. Krishnan, C.M. Morris, G.A. Taylor, A.K. Reeve, R.H. Perry, E. Jaros, J.S. Hersheson, J. Betts, T. Klopstock, R.W. Taylor, D.M. Turnbull, High levels of mitochondrial DNA deletions in substantia nigra neurons in aging and Parkinson disease, *Nat. Genet.* 38 (5) (2006) 515–517.
- [61] S.J. Baloyannis, V. Costa, I.S. Baloyannis, Morphological alterations of the synapses in the locus coeruleus in Parkinson's disease, *J. Neurol. Sci.* (1–2) (2006) 35–41.
- [62] L.A. Sena, N.S. Chandel, Physiological roles of mitochondrial reactive oxygen species, *Mol. Cell* 2 (2012) 158–167.
- [63] A.M. Cuervo, Autophagy and aging: keeping that old broom working, *Trends Genet.* 24 (2008) 604–612.
- [64] V.M. Hubbard, R. Valdor, F. Macian, A.M. Cuervo, Selective autophagy in the maintenance of cellular homeostasis in aging organisms, *Biogerontology* 13 (2012) 21–35.
- [65] N. Narendra, A. Tanaka, D.F. Suen, R.J. Youle, Parkin is recruited selectively to impaired mitochondria and promotes their autophagy, *J. Cell Biol.* 183 (2008) 795–803.
- [66] S.M. Jin, A. Tanaka, D.F. Suen, C.A. Gautier, S. Shen, et al., PINK1 is selectively stabilized on impaired mitochondria to activate Parkin, *PLoS Biol.* 8 (2010) 1000298.
- [67] S. Hasson, L.A. Kane, K. Yamano, C.H. Huang, D.A. Sliter, E. Buehler, et al., High-content genome-wide RNAi screens identify regulators of parkin upstream of mitophagy, *Nat. Lett.* 504 (2013) 291–295.
- [68] C. Van Humbeeck, T. Cornelissen, H. Hofkens, W. Mandemakers, K. Gevaert, De Strooper, et al., Parkin interacts with Ambra1 to induce mitophagy, *J. Neurosci.* 28 (2011) 10249–10261.
- [69] F. Strappazzon, F. Nazio, M. Corrado, V. Cianfanelli, A. Romagnoli, G.M. Fimia, S. Campello, R. Nardacci, M. Piacentini, M. Campanella, F. Ceconi, AMBRA1 is able to induce mitophagy via LC3 binding, regardless of PARKIN and p62/SQSTM1, *Cell Death Differ.* (2014), <http://dx.doi.org/10.1038/cdd.2014.139>.
- [70] V. Choubey, M. Cagalinec, J. Liiv, D. Safulina, M. Hockey, M. Kuum, et al., BECN1 is involved in the initiation of mitophagy. It facilitates PARK2 translocation to mitochondria, *Autophagy* 10 (2014) 1092–1106.
- [71] H. Sandoval, P. Thiagarajan, S.K. Dasgupta, A. Schumacher, J.T. Prchal, M. Chen, et al., Essential role for Nix in autophagic maturation of erythroid cells, *Nature* 454 (2008) 232–235.
- [72] I. Novak, V. Kirkin, D.G. McEwan, J. Zhang, P. Wild, A. Rozenknop, V. Rogov, F. Löhr, D. Popovic, A. Öchpinti, A.S. Reichert, J. Terzic, C.X. Deng, P.A. Ney, I. Dikic, Nix is a selective autophagy receptor for mitochondrial clearance, *EMBO Rep.* 1 (2010) 45–51.
- [73] I. Novak, I. Dikic, Autophagy receptors in developmental clearance of mitochondria, *Autophagy* 3 (2011) 301–303.
- [74] Y. Zhu, S. Massen, M. Terenzio, V. Lang, S. Chen-Lindner, R. Eils, I. Novak, I. Dikic, A. Hamacher-Brady, N.R. Brady, Modulation of serines 17 and 24 in the LC3-interacting region of Bnip3 determines pro-survival mitophagy versus apoptosis, *J. Biol. Chem.* 2 (2013) 1099–1113.
- [75] W. Wu, W. Tian, Z. Hu, G. Chen, L. Huang, W. Li, X. Zhang, P. Xue, C. Zhou, L. Liu, Y. Zhu, X. Zhang, L. Li, L. Zhang, S. Sui, B. Zhao, D. Feng, ULK1 translocates to mitochondria and phosphorylates FUNDC1 to regulate mitophagy, *EMBO Rep.* 5 (2014) 566–575.
- [76] L. Liu, D. Feng, G. Chen, M. Chen, Q. Zheng, P. Song, Q. Ma, C. Zhu, R. Wang, W. Qi, L. Huang, P. Xue, B. Li, X. Wang, H. Jin, J. Wang, F. Yang, P. Liu, Y. Zhu, S. Sui, Q. Chen, Mitochondrial outer-membrane protein FUNDC1 mediates hypoxia-induced mitophagy in mammalian cells, *Nat. Cell Biol.* 2 (2012) 177–185.
- [77] G.M. Fimia, A. Stoykova, A. Romagnoli, L. Giunta, R. Nardacci, M. Corazzari, et al., Ambra1 regulates autophagy and development of the nervous system, *Nature* 447 (2007) 1121–1125.
- [78] F. Strappazzon, M. Vietri-Rudan, S. Campello, F. Nazio, F. Florenzano, G.M. Fimia, et al., Mitochondrial BCL-2 inhibits AMBRA1-induced autophagy, *EMBO J.* 30 (2011) 1195–1208.
- [79] D.A. East, F. Fagiani, J. Crosby, N.D. Georgakopoulos, H. Bertrand, M. Schaap, A. Fowkes, G. Wells, Campanella PMI: a $\Delta\Psi_m$ independent pharmacological regulator of mitophagy, *Mol. Cell. Biol.* 11 (2014) 1585–1596.
- [80] R. Gómez-Sánchez, M.E. Gegg, J.M. Bravo-San Pedro, M. Niso-Santano, L. Alvarez-Erviti, E. Pizarro-Estrella, Y. Gutiérrez-Martín, A. Alvarez-Barrientos, J.M. Fuentes, R.A. González-Polo, A.H. Schapira, Mitochondrial impairment increases FL-PINK1 levels by calcium-dependent gene expression, *Neurobiol. Dis.* 62 (2014) 426–440.
- [81] T. Cali, D. Ottolini, A. Negro, M. Brini, Enhanced parkin levels favor ER-mitochondria crosstalk and guarantee Ca²⁺ transfer to sustain cell bioenergetics, *Biochim. Biophys. Acta* 4 (2013) 495–508.
- [82] Z.H. Sheng, Mitochondrial trafficking and anchoring in neurons: new insight and implications, *J. Cell Biol.* 7 (2014) 1087–1098.
- [83] H.K. Park, J.E. Lee, J. Lim, B.H. Kang, Mitochondrial Hsp90s suppress calcium-mediated stress signals propagating from mitochondria to the ER in cancer cells, *Mol. Cancer* 13 (2014) 148.
- [84] D.R. Green, L. Galluzzi, G. Kroemer, Mitochondria and the autophagy-inflammation-cell death axis in organismal aging, *Science* 6046 (2011) 1109–1112.
- [85] D.T. Rutkowski, R.J. Kaufman, A trip to the ER: coping with stress, *Trends Cell Biol.* 1 (2004) 20–28.
- [86] Q. Zhao, J. Wang, I.V. Levichkin, S. Stasinopoulos, M.T. Ryan, N.J. Hoogenraad, A mitochondrial specific stress response in mammalian cells, *EMBO J.* 17 (2002) 4411–4419.
- [87] J.E. Aldrige, T. Horibe, N.J. Hoogenraad, Discovery of genes activated by the mitochondrial unfolded protein response and cognate promoter elements, *PLoS ONE* 9 (2007) e874.
- [88] M.J. Backer, T. Tatsuda, T. Langer, Quality control of mitochondrial proteostasis, *Cold Spring Harb. Perspect. Biol.* 3 (7) (2011).
- [89] A. Chacinska, C.M. Koehler, D. Milenkovic, T. Lithgow, N. Pfanner, Importing mitochondrial proteins: machineries and mechanisms, *Cell* 4 (2009) 628–644.
- [90] S. Radke, H. Chander, P. Schäfer, G. Meiss, R. Krüger, J.B. Schulz, D. Germain, Mitochondrial protein quality control by the proteasome involves ubiquitination and the protease Omi, *J. Biol. Chem.* 19 (2008) 12681–12685.
- [91] L. Papa, D. Germain, SirT3 regulates the mitochondrial unfolded protein response, *Mol. Cell. Biol.* 4 (2014) 699–710.
- [92] S.M. Jin, R.J. Youle, PINK1- and Parkin-mediated mitophagy at a glance, *J. Cell Sci.* 125 (Pt 4) (2012) 795–799.
- [93] H.S. Kim, K. Patel, K. Muldoon-Jacobs, K.S. Bisht, N. Aykin-Burns, J.D. Pennington, R. van der Meer, P. Nguyen, J. Savage, K.M. Owens, A. Vassilopoulos, O. Ozden, S.H. Park, K.K. Singh, S.A. Abdulkadir, D.R. Spitz, C.X. Deng, D. Gius, SIRT3 is a mitochondria-localized tumor suppressor required for maintenance of mitochondrial integrity and metabolism during stress, *Cancer Cell* 1 (2010) 41–52.

- [94] N.R. Sundaresan, S.A. Samant, V.B. Pillai, S.B. Rajamohan, M.P. Gupta, SIRT3 is a stress-responsive deacetylase in cardiomyocytes that protects cells from stress-mediated cell death by deacetylation of Ku70, *Mol. Cell. Biol.* 20 (2008) 6384–6401.
- [95] R. Tao, M.C. Coleman, J.D. Pennington, O. Ozden, S.H. Park, H. Jiang, H.S. Kim, C.R. Flynn, S. Hill, W. Hayes McDonald, A.K. Olivier, D.R. Spitz, D. Gius, Sirt3-mediated deacetylation of evolutionarily conserved lysine 122 regulates MnSOD activity in response to stress, *Mol. Cell* 6 (2010) 893–904.
- [96] L.W. Finley, A. Carracedo, J. Lee, A. Souza, A. Egia, J. Zhang, J. Teruya-Feldstein, P.I. Moreira, S.M. Cardoso, C.B. Clish, P.P. Pandolfi, M.C. Haigis, SIRT3 opposes reprogramming of cancer cell metabolism through HIF1 α destabilization, *Cancer Cell* 3 (2011) 416–428.
- [97] L.F. Burbulla, J.C. Fitzgerald, K. Stegen, J. Westermeier, A.K. Thost, H. Kato, D. Mokranjac, J. Sauerwald, L.M. Martins, D. Voitalla, D. Rapaport, O. Riess, T. Proikas-Cezanne, T.M. Rasse, R. Krüger, Mitochondrial proteolytic stress induced by loss of mortalin function is rescued by Parkin and PINK1, *Cell Death Dis.* 5 (2014) e1180.
- [98] D.A. Pulliam, A. Bhattacharya, H. Van Remmen, Mitochondrial dysfunction in aging and longevity: a causal or protective role? *Antioxid. Redox Signal.* 12 (2013) 1373–1387.
- [99] V. Jovaisaite, L. Mouchiroud, J. Auwerx, The mitochondrial unfolded protein response, a conserved stress response pathway with implications in health and disease, *J. Exp. Biol.* 217 (Pt 1) (2014) 137–143.
- [100] R.H. Houtkooper, L. Mouchiroud, D. Ryu, N. Moullan, E. Katsyuba, G. Knott, R.W. Williams, J. Auwerx, Mitonuclear protein imbalance as a conserved longevity mechanism, *Nature* 497 (2013) 451–457.
- [101] L. Mouchiroud, R.H. Houtkooper, N. Moullan, E. Katsyuba, D. Ryu, C. Cantó, A. Mottis, Y.S. Jo, M. Viswanathan, K. Schoonjans, L. Guarente, J. Auwerx, The NAD(+)/Sirtuin pathway modulates longevity through activation of mitochondrial UPR and FOXO signaling, *Cell* 2 (2013) 430–441.
- [102] S.A. Samant, H.J. Zhang, Z. Hong, V.B. Pillai, N.R. Sundaresan, D. Wolfgeher, S.L. Archer, D.C. Chan, M.P. Gupta, SIRT3 deacetylates and activates OPA1 to regulate mitochondrial dynamics during stress, *Mol. Cell. Biol.* 5 (2014) 807–819.

 Should you have **institutional access?** [Here's how to get it ...](#)



€ EUR

EN

 0

Log in

[SUBJECTS](#)[SERVICES](#)[PUBLICATIONS](#)[ABOUT](#)

 **Publicly Available** Published by [De Gruyter](#) March 6, 2019

Mitophagy could fight Parkinson's disease through antioxidant action

Anthea Di Rita and Flavie Strappazzon

From the journal [Reviews in the Neurosciences](#)

<https://doi.org/10.1515/revneuro-2018-0095>

[Cite this](#)

Citations

5

Abstract

During aging, the process of mitophagy, a system that allows the removal of dysfunctional mitochondria through lysosomal degradation, starts to malfunction. Because of this defect, damaged mitochondria are not removed correctly, and their decomposing components accumulate inside the cells. Dysfunctional mitochondria that are not removed by mitophagy produce high amounts of reactive oxygen species (ROS) and, thus, cause oxidative stress. Oxidative stress, in turn, is very harmful for the cells, neuronal cells, in particular. Consequently, the process of mitophagy plays a crucial role in mitochondria-related disease. Mitochondrial dysfunctions and oxidative stress are well-established factors contributing to Parkinson's disease (PD), one of the most common neurodegenerative disorders. In this review, we

report various known antioxidants for PD treatments and describe the stimulation of mitophagy process as a novel and exciting method for reducing oxidative stress in PD patients. We describe the different mechanisms responsible for mitochondria removal through the mitophagy process. In addition, we review the functional connection between mitophagy induction and reduction of oxidative stress in several *in vitro* models of PD and also agents (drugs and natural compounds) already known to be antioxidants and to be able to activate mitophagy. Finally, we propose that there is an urgent need to test the use of mitophagy-inducing antioxidants in order to fight PD.

Keywords: [mitochondrial selective degradation](#); [neurodegeneration](#); [oxidative stress](#); [Parkinsonism](#)

Parkinson's disease and mitochondrial oxidative stress

Parkinson's disease (PD) is a severe and widespread neurodegenerative disorder characterized by a progressive reduction of neurons in the substantia nigra pars compacta leading to dopamine deficiency and α -synuclein aggregate formation. This pathology is associated with motor and non-motor symptoms, including bradykinesia, rigidity, dystonia, anxiety, dementia, and sexual dysfunction. The disease stems from the impairment of several molecular pathways, including α -synuclein proteostasis, mitochondrial function, oxidative stress, calcium homeostasis, axonal transport, and neuroinflammation ([Poewe et al., 2017](#)).

Although the etiology of PD is still elusive, mitochondrial dysfunctions and related oxidative stress are crucial contributing

factors ([Figure 1](#)). Several findings suggest that mitochondria are the primary source of reactive oxygen species (ROS) that are possibly contributing to intracellular oxidative stress ([Starkov, 2008](#); [Murphy, 2009](#)). Various groups observed a reduction in mitochondrial complex I protein level or activity in the nigral neurons of PD patients ([Schapira et al., 1990](#); [Bose and Beal 2016](#)). Inclusions of α -synuclein protein aggregates in the mitochondria induce an impairment in the mitochondrial complex I activity leading to oxidative stress ([Devi et al., 2008](#)). Moreover, it was demonstrated that the downregulation in dopaminergic neurons of the mitochondrial transcription factor A (TFAM), essential for mitochondrial DNA expression, leads to a defect in the electron transport chain, thus, promoting neuronal degeneration in adulthood ([Ekstrand et al., 2007](#)). In addition, some mitochondria-related genes, i.e. phosphatase and tensin homolog-induced kinase 1 (PINK1), parkin RING-in-between-RING E3 ubiquitin protein ligase (PARK2/PRKN), Parkinsonism-associated deglycase (DJ-1/PARK7), and F-box protein 7 (Fbxo7), prove to be mutated in the familial form of PD. These variations compromise mitochondria functioning and contribute to oxidative stress production. Furthermore, PD patients show high levels (40–60%) of mtDNA deletions, associated with a cytochrome c oxidase deficiency in the substantia nigra ([Bender et al., 2006](#); [Kraytsberg et al., 2006](#)). Isobe and colleagues showed that the levels of oxidized coenzyme Q-10 (CoQ10) in PD patients' cerebrospinal fluid were significantly increased ([Isobe et al., 2010](#)). Other pathologies, such as Alzheimer's disease (AD), multiple sclerosis (MS), or amyotrophic lateral sclerosis (ALS) are related to damaged mitochondria and

oxidative stress production ([Dutta et al., 2006](#); [Sau et al., 2007](#); [Campbell et al., 2011](#); [Swerdlow et al., 2014](#)). To date, pharmacological substitution of striatal dopamine, and more recently, therapies for cellular transport of α -synuclein remain the principal treatment for PD.

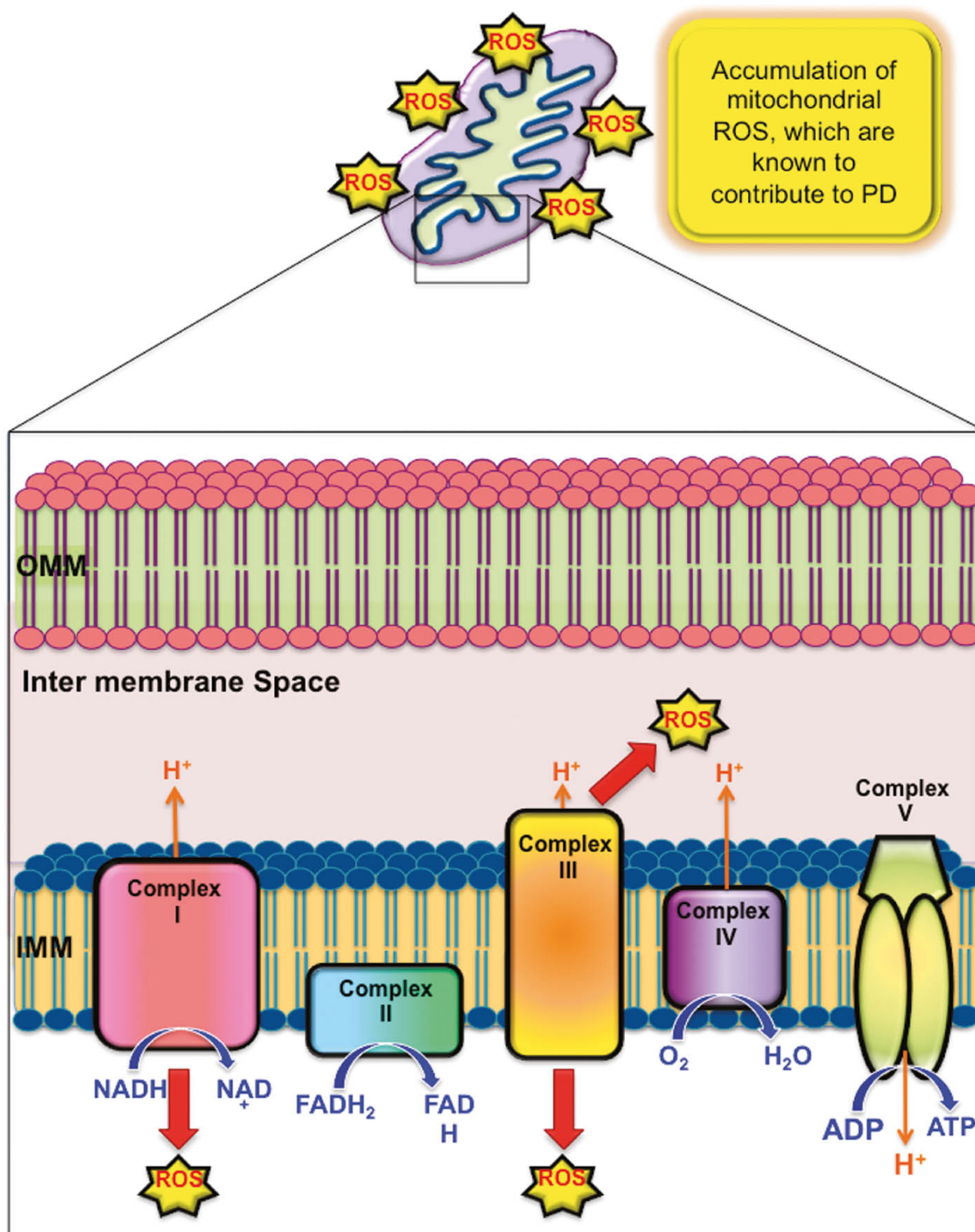


Figure 1:

Generation of mitochondrial ROS contributes to PD.

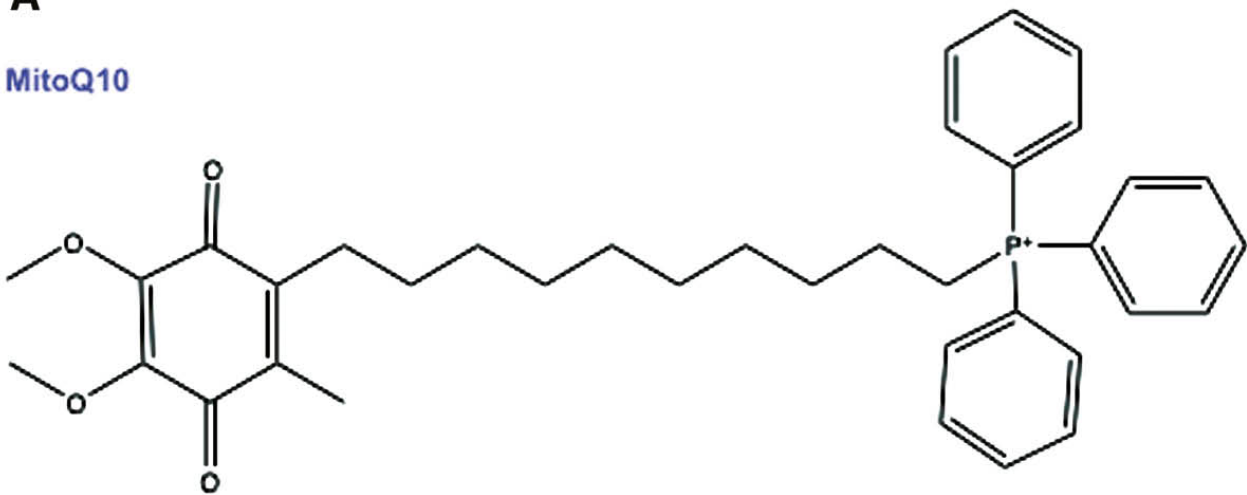
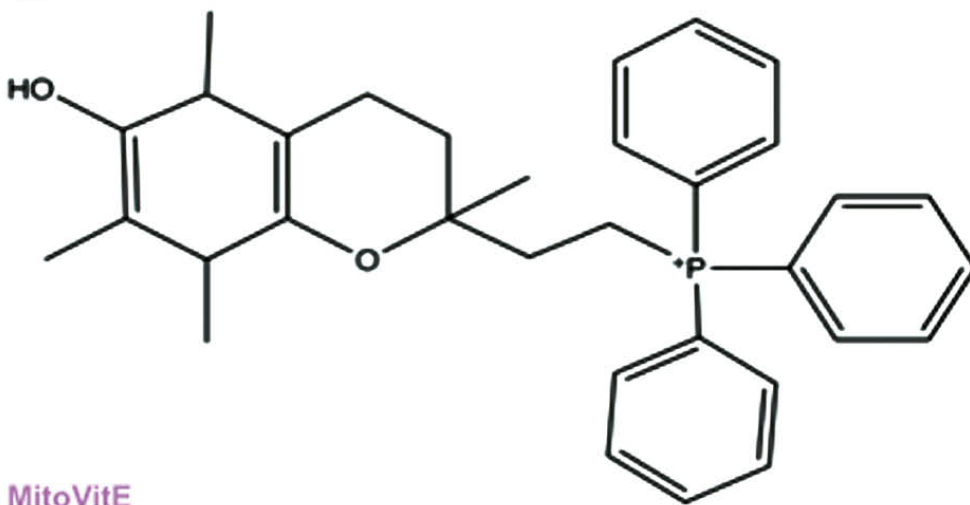
A defect in the complex I or complex III of mitochondrial respiratory chain promotes the accumulation of reactive radicals, leading to oxidative stress.

Given the link between mitochondrial dysfunctions and ROS

production in PD, clinical approaches that counteract the oxidative stress may be beneficial for patients. We review below some of the main promising antioxidants for improving PD patient health. In addition, we propose, as a novel and more effective strategy for combating PD, the adoption of a combined approach through the activation of both endogenous or exogenous antioxidants and the clearance system that eliminates ROS-produced damaged mitochondria (known as mitophagy).

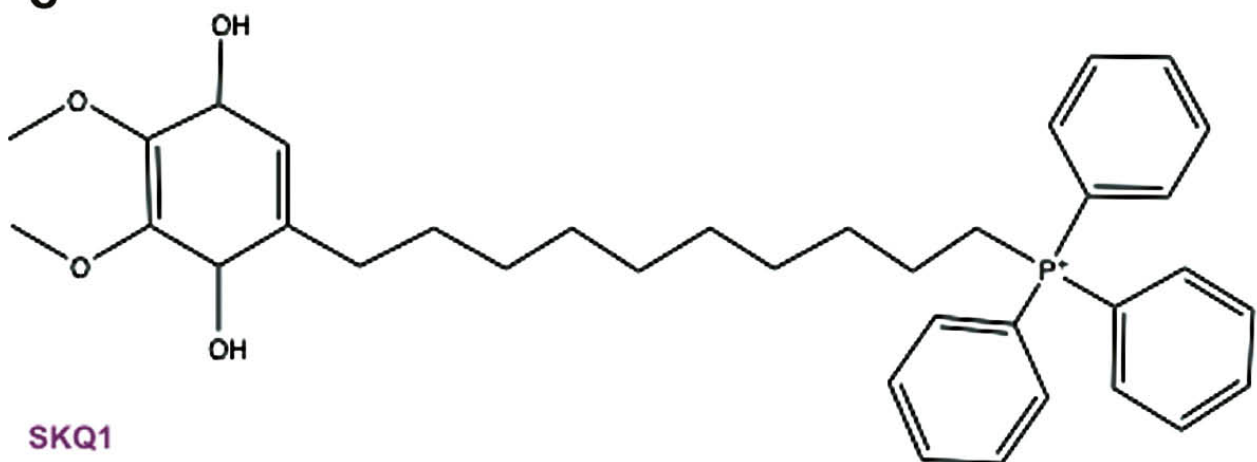
Antioxidants: preclinical and clinical studies in PD

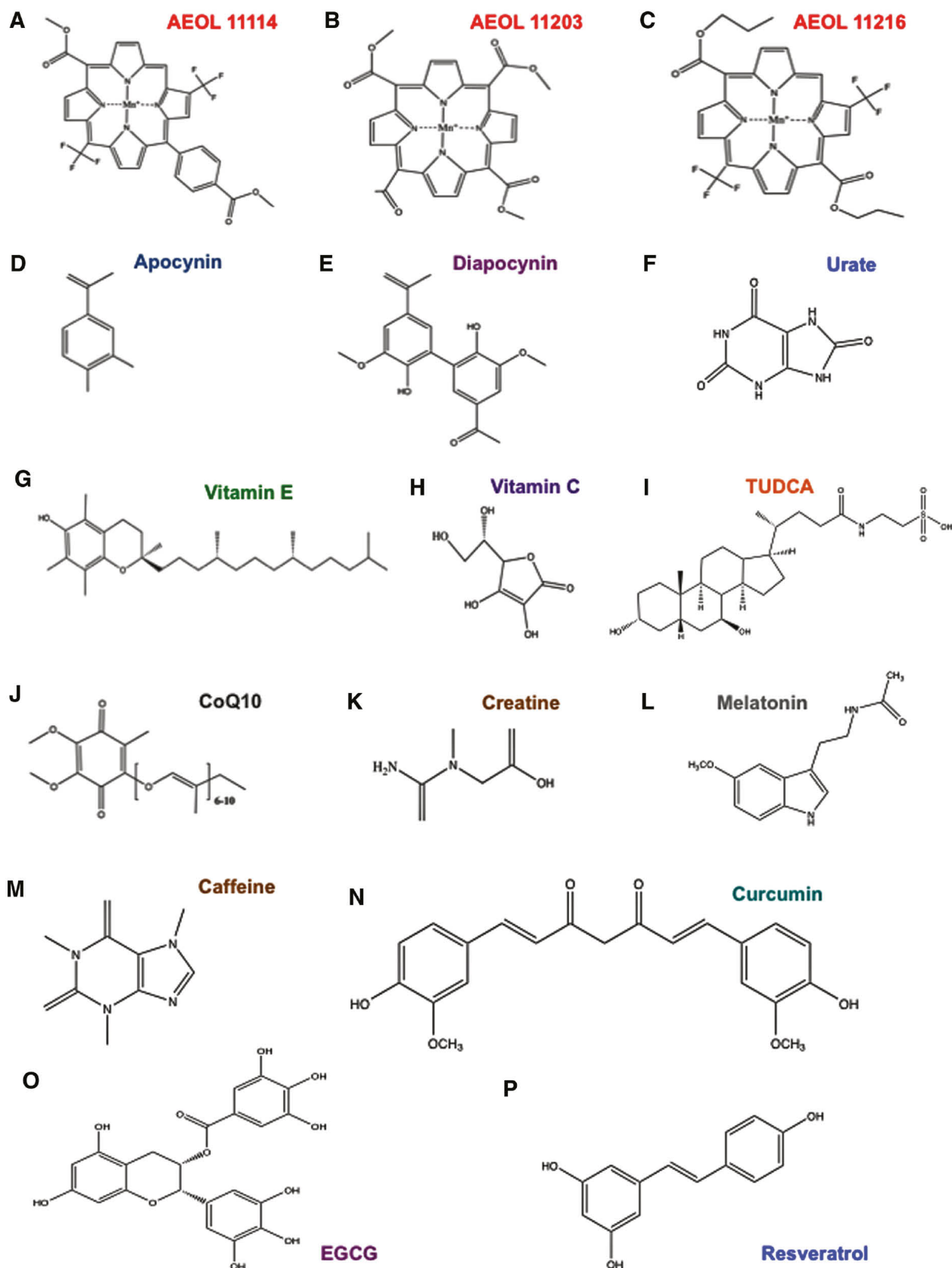
As nigrostriatal dopaminergic neuron degeneration in PD patients is related to oxidative stress and mitochondrial dysfunctions, general antioxidants or mitochondrial-targeted antioxidants (MTAs) may be a fruitful therapy for counteracting PD. Unlike the ubiquitous antioxidant, a common feature of MTAs is the presence of a positive charge in the lipophilic cation, known as triphenylphosphonium (TPP), necessary for crossing the mitochondrial membranes ([Murphy and Smith, 2007](#)). In this section, we list the most promising MTAs and general antioxidants in treating PD, their structures being reported in [Figures 2 and 3](#).

A**MitoQ10****B****MitoVitE****C****SKQ1****Figure 2:**

MTAs.

Structures of TPP⁺-containing molecules that seem to be able to fight PD, such as MitoQ10 (A), MitoVitE (B), and SkQ1 (C).



**Figure 3:**

Main general antioxidants.

Structures of a series of antioxidants that counteract Parkinsonism, such as AEOL11114 (A), AEOL11203 (B), AEOL11216 (C), apocynin (D), diapocynin (E), urate (F), vitamin E (G), vitamin C (H), TUDCA (I), CoQ10 (J), creatine (K) and melatonin (L), caffeine (M), curcumin (N), EGCG

MTAs

MitoQ

Mitoquinone (MitoQ) constitutes a 10-carbon aliphatic carbon chain necessary for TPP covalent binding to the endogenous antioxidant CoQ10 ([Figure 2A](#)). MitoQ is able to scavenge peroxy, peroxy nitrite, and superoxide and, after completing its function, is reduced to the active form ubiquinol by the complex II of the respiratory chain ([Smith and Murphy, 2011](#)). As *in vitro* and *in vivo* studies demonstrated the beneficial effects of MitoQ, it underwent phase I and then phase II clinical trials ([Gane et al., 2010](#); [Snow et al., 2010](#)). Despite its promising role, no neuroprotective benefits were detected in PD patients after MitoQ oral intake ([Snow et al., 2010](#)). Further studies are, thus, necessary to better analyze the therapeutic effect of MitoQ in PD patients.

MitoVitE

MitoVitE is the first MTA to be discovered and consists of TPP linked to the α -tocopherol of vitamin E through a two-carbon chain ([Figure 2B](#)). Despite its fast intake in the mitochondria of cell culture or mice tissue subjected to oxidative damage, the use of MitoVitE in patients is still being debated. In fact, although MitoVitE has a protective effect in both cellular and animal models ([Jauslin et al., 2003](#); [Zhang et al., 2012](#)), no beneficial effects were observed *in vivo* in striatal neurons. Moreover, high doses of MitoVitE are neurotoxic ([Convey et al., 2006](#)).

SkQ1

SkQ1 constitutes the TPP attached to plastoquinone ([Figure 2C](#)). This structure allows the incorporation of SkQ1 into the inner

mitochondrial membrane (IMM) where it protects from ROS-induced oxidation ([Skulachev et al., 2011](#)). It was observed that SkQ1 treatment reduces degeneration of dopaminergic neurons of the substantia nigra and ventral tegmental area (VTA) in PD mouse models ([Pavshintsev et al., 2017](#)).

General antioxidants

Metalloporphyrins

Synthetic catalytic antioxidants known as AEOL 11114, AEOL 11203, and AEOL 11216 metalloporphyrins show promising effects for PD treatment due to their ability to penetrate the blood brain barrier together with their oral bioavailability and longer plasma elimination half-lives ([Liang et al., 2017](#)) ([Figure 3A–C](#)).

Apocynin and diapocynin

Apocynin (4-hydroxy-3-methoxyacetophenone) and its derivate diapocynin are plant antioxidants that function as NADPH oxidase inhibitors. Their protective role in PD model systems was evaluated *in vivo* ([Vejrazka et al., 2005](#); [Luchtefeld et al., 2008](#)) ([Figure 3D, E](#)).

Urate

Acid uric or urate is a scavenger of superoxide, hydroxyl radical, single oxygen, and also an iron chelator ([Cohen et al., 1984](#)) ([Figure 3F](#)). Although over the year it was shown to improve the condition of PD patients, the treatment is limited as urate in high levels causes gout ([Choi et al., 2004](#)).

Vitamins

The antioxidant function of vitamins in counteracting oxidative stress was discovered in 1992 ([Sies et al., 1992](#)). In particular, vitamin E efficacy to prevent PD progression was demonstrated by

several groups (Zhang et al., 2002). By contrast, the role of vitamin C is still controversial (Zhang et al., 2002; Etminan et al., 2005) (Figure 3G, H).

TUDCA

Tauroursodeoxycholic acid (TUDCA) is a derivate from tauroine conjugated to the endogenous bile acid ursodeoxycholic acid (UDCA) (Figure 3I). It was observed that TUDCA improves mitochondrial functions in PD patient-derived fibroblasts (Mortiboys et al., 2015) and has a neuroprotective role in the nematode-PD model (Ved et al., 2005). Moreover TUDCA acts as an antioxidant in several neurodegenerative diseases, including ALS, AD, and HD (Keene et al., 2002; Nunes et al., 2012; Elia et al., 2016). Recently, Rosa and co-workers demonstrated that TUDCA has a neuroprotective effect by stimulating mitophagy in *in vitro* and *in vivo* models of PD (see the “Pharmacological inducers of mitophagy” section below) (Zheng et al., 2017).

CoQ₁₀

In vitro and *in vivo* studies demonstrated the beneficial role of coenzyme Q₁₀ (CoQ₁₀) in PD (Beal et al., 1998; Horvath et al., 2003; Moon et al., 2005). At high doses (1200 mg daily), CoQ₁₀ shows beneficial results in PD rating (Shults et al., 2002) and is currently in the clinical trial phase III (Figure 3J).

Creatine

Creatine is a nitrogenous derivative of the guanidinium cation necessary for supplying energy in vertebrate muscle and nerve cells (Figure 3K). In addition, its antioxidant function was well established in PD mice models (Matthews et al., 1999). Clinical

studies demonstrate that creatine has a neuroprotective role in PD patients. At present, creatine is still in the phase III clinical trial, in a long-term study on 1720 patients with PD ([Bloom, 2007](#); [Couzin, 2007](#)).

Melatonin

Melatonin is a pineal hormone with an antioxidant function that was demonstrated in different animal models of PD ([Saravanan et al., 2007](#); [Borah and Mohanakumar, 2009](#)). Melatonin was shown to block the pro-oxidant effect of both dopamine and L-dopa in an *in vitro* study ([Miller et al., 1996](#)). Moreover, it preserves the activity of tyrosine hydroxylase (TH) in MPP⁺-treated rats ([Jin et al., 1998](#)). Additionally, melatonin is used to reduce REM sleep behavior disorder (RBD), which is a typical feature of parkinsonism and other forms of dementia ([Aurora et al., 2010](#)) ([Figure 3L](#)).

Caffeine

As caffeine is in coffee and other beverages, it is the most widely consumed psychoactive drug. Different groups found that caffeine has a neuroprotective effect, attenuating the reduction in striatal dopamine, 3,4-dihydroxyphenylacetic acid (DOPAC) and DAT-binding sites ([Chen et al., 2001](#); [Joghataie et al., 2004](#)). More recently, Negida and colleagues revealed that caffeine reduces oxidative stress in PD through its antioxidant function, at the mitochondria. In addition, they found that caffeine binds α -synuclein proteins preventing their aggregation in Lewy's bodies and enhances the number of dopamine receptors ([Negida et al., 2017](#)) ([Figure 3M](#)).

Curcumin

Curcumin is a plant diarylheptanoid with a bright yellow color. It is widely used in cooking for its anti-inflammatory and antioxidant properties. Curcumin was shown to alleviate motor deficits and neuronal damage in 6-OHDA (6-hydroxydopamine)-treated rats. In fact, it inhibits the conversion of MPTP to MPP⁺ toxic metabolite (Rajeswari and Sabesan, 2008) (Figure 3N).

Epigallocatechin gallate

Epigallocatechin gallate (EGCG) is a plant catechin typical of the green tea. EGCG has a neuroprotective effect in the MPTP (1-metil 4-fenil 1,2,3,6-tetraidro-piridina) *in vivo* model of PD. In particular, EGCG controls ferroportin, which is the iron-export protein in the substantia nigra, and alleviates oxidative stress, thus, conferring a rescue effect against MPTP toxicity (Xu et al., 2017) (Figure 3O).

Resveratrol

Resveratrol, which is a polyphenol of red grapes, was shown to reduce mitochondria dysfunction of 6-OHDA dopaminergic neurons of rat (Jin et al., 2008). Moreover, a diet rich in resveratrol combats MPTP neurotoxicity (Blanchet et al., 2008). This polyphenol stimulates SIRTUIN-1 activity, thus, controlling various transcription factors and co-activators, including PGC1- α that regulates mitochondria biogenesis (Peng et al., 2016) (Figure 3P).

Iron chelators

As iron accumulation was found in the nervous system of patients, different iron chelators were used in preclinical studies of PD (Weinreb et al., 2013). Among them, desferrioxamine (DFO) preserves striatal dopamine degeneration induced by 6-OHDA

treatment, thus, partially restoring the normal behavior ([Ben-Shachar et al., 1992](#)). Despite its functional role, DFO is a large molecule, and its size limits the blood brain barrier crossing ([Zheng et al., 2005](#)). Novel iron chelators were tested in the *in vitro* model of PD ([Shachar et al., 2004](#)).

Besides these general antioxidants, the combination of R- α -lipoic acid and acetyl-L-carnitine has also beneficial effects in the *in vitro* model of PD, stimulating mitochondria biogenesis and reducing oxidative stress ([Zhang et al., 2010](#)).

Mitophagy

Antioxidant administration in combination with new approaches focused on the reduction of ROS could be more effective in halting neurodegeneration in PD.

Mitochondria are the main source of ROS production during oxidative phosphorylation for ATP production ([Lenaz, 2001](#)). Functional mitochondria maintenance is fundamental for cellular behavior, in particular, for neuronal cells. Despite its low mass, the brain consumes 20% of the body's oxygen for the production of ATP ([Attwell and Laughlin, 2011](#)). The majority of ATP production comes from the mitochondrial respiration chain, although glycolysis contributes to ATP generation ([Rangaraju et al., 2014](#)). Correct mitochondria functioning is, thus, crucial in order to regulate, in each region of the neuron, the balance between energy supply and energy demand. Therefore, some mitochondria remain in the soma, while others are carried along axons and dendrites in order to form energy sites in the presynaptic terminals and in

proximity of the nodes of Ranvier ([Berthold et al., 1993](#); [Shepherd and Harris, 1998](#)).

A selective elimination of damaged mitochondria through mitophagy and the maintenance of healthy mitochondria are, thus, both mandatory for cellular viability ([Palikaras and Tavernarakis, 2014](#)). Mitophagy is the most characterized selective autophagy pathway, and it is regulated by the outer mitochondrial membrane (OMM), IMM, or cytosolic proteins named mitophagy receptors ([Hamacher-Brady and Brady, 2016](#)).

Mitophagy receptors

Upon mitophagy induction, mitophagy receptors are recruited to damaged mitochondria. The engulfment of undesired mitochondria into the autophagy machinery needs a direct interaction between mitophagy receptors (see [Table 1](#)) and the autophagosome markers microtubule-associated proteins 1 light chain 3 (LC3s) or GABA type A receptor-associated proteins (GABARAPs). The binding is mediated by a particular sequence on mitophagy receptors, known as the LC3-interacting region (LIR) motif. Moreover, two crucial posttranslational modifications occur during mitophagy: phosphorylation and ubiquitylation. The former can be a positive or negative change that allows or inhibits the mitophagy receptor-autophagosome marker binding ([Hamacher-Brady and Brady, 2016](#)). The latter, takes place on the OMM proteins and is a signal for cytosolic mitophagy receptor recruitment and, therefore, for mitochondria elimination ([Yamano et al., 2016](#)). This pathway is able to selectively eliminate damaged mitochondria in order to maintain cellular homeostasis and to preserve mitochondria

vitality.

Table 1:

Overview of the known mitophagy pathways.

PINK1/PARK2-dependent pathway

PINK1 is a mitochondria kinase that functions as a sensor of mitochondria status. Upon mitophagy induction, PINK1 phosphorylates the OMM protein FUNDC1: is an OMM protein whose role in mitophagy was clarified since 2012 ([Wu et al., 2014](#))

PINK1/PARK2-independent pathway

BNIP3L: this OMM protein is the mammalian homolog of *NIX*, and it regulates mitophagy upon mitophagy induction

BCL2-L13: the mammalian homolog of Atg32 interacts with LC3B and regulates mitophagy upon mitophagy induction

FKBP8/FKBP38: is a member of the FK 506-binding protein family, and it interacts preferentially with LC3B

PINK1/PARK2-dependent/independent pathway

AMBRA1: is a cytosolic protein localized also on the OMM ([Strappazzon et al., 2011](#)) that interacts with LC3B

Cardiolipin

Cardiolipin or 1,3-bis(*sn*-3'-phosphatidyl)-*sn*-glycerol is a lipid of the IMM that functions as a sensor of mitochondrial stress. In detail, upon mitophagy induction, cardiolipin is externalized on the mitochondria where it interacts with the autophagosome marker LC3-II in order to mediate the engulfment into the autophagosome machinery ([Chu et al., 2013](#)).

Mitophagy receptors as therapeutic targets for PD

Neurodegenerative diseases, including PD, AD, and HD, are characterized by the accumulation of damaged mitochondria that produces critical effects on neuron functionality ([Johri and Beal, 2012](#)). Recent evidence shows that the selective mitochondria autophagy contributes to improving mitochondrial status and cellular homeostasis of neurons. In particular, two mitophagy receptors, Nix and AMBRA1, show a central role in delaying cell death in PD models through an antioxidant action. In particular, Koentjoro and colleagues demonstrated that when the main

mitophagy process (PINK1/PARK2-mediated mitophagy) is abrogated in PD dopaminergic neurons, Nix is able to stimulate a damaged mitochondria selective removal that preserves dopaminergic neurons. Moreover, phorbol 12-myristate 13-acetate (PMA) was reported to induce Nix expression, leading to a reduction in ROS production in PD dopaminergic neurons (Koentjoro et al., 2017).

In a similar manner, AMBRA1-mediated mitophagy is able to rescue mitophagy in fibroblasts of PD patients in which PINK1 or PARK2 are mutated (Strappazzon et al., 2015). In addition, a particular form of AMBRA1, localized at the OMM (AMBRA1^{ActA}) is able to stimulate mitophagy in an *in vitro* model of PD and reduces cell death induced by rotenone or 6-OHDA treatments, by limiting selectively the source of oxidative stress (Di Rita et al., 2018). In line with such evidence, both Nix and AMBRA1 could be considered as attractive therapeutic targets in drug development and human application.

Moreover, Chu and colleagues demonstrated that cardiolipin drives mitophagy in response to low doses of rotenone or 6-OHDA through a direct interaction with LC3. Despite the fact that, at present, cardiolipin has no antioxidant functions, in line with AMBRA1 and NIX, it possesses phosphorylation sites in the offset of its LIR motif that could control mitophagy in a fine-tuned system. These analogies could suggest that these three mitophagy regulators could control mitochondria degradation through the autophagy machinery in PD and that their synergic action could be useful in reducing PD progression by limiting the accumulation of

damaged mitochondria in neurons.

To date, scientists are able to induce mitophagy *in vitro* and *in vivo*, mainly using pharmacological compounds, i.e. antimycin A, or oligomycin or carbonyl cyanide-4-(trifluoromethoxy) phenylhydrazone (FCCP), and simulating hypoxic/ischemic conditions. However, in the near future, the generation of a drug that could specifically stimulate both AMBRA1- and NIX-mediated mitophagy presents an attractive challenge for counteracting PD by strongly reducing oxidative stress and preserving mitochondria health in dopaminergic neurons.

Inducers of mitophagy

As maintaining mitophagy is crucial in age-related diseases, several inducers of mitophagy were developed and can be classified in pharmacological or natural compounds.

Pharmacological inducers of mitophagy

NRF2 induction through PMI

NRF2 (nuclear factor erythroid 2-related factor 2) is a transcription factor that controls the expression of several genes, such as PINK1, nuclear dot protein 52 (NDP52) and sequestosome 1 (P62) by linking the antioxidant response element (ARE) in their promoter regions. It is, thus, considered the master regulator of the cellular redox homeostasis. NRF2 activity is able to defend cells against mitochondrial toxins; indeed, its function is suppressed in mitochondrial disorders such as PD ([Georgakopoulos et al., 2017](#)). PMI/HB229 is an inducer of NRF2 and stimulates P62 production by reversibly inhibiting the activity of Kelch-like ECH-associated

protein 1 (KEAP1), which is important for NRF2 degradation by the proteasome.

Mechanistically, PMI interferes protein-protein interaction (PPI) between NRF2 and KEAP1, blocking the NRF2 ubiquitylation and favoring its nuclear accumulation. Consequently, NRF2 activates gene production; among the genes activated, P62 becomes upregulated, and mitophagy is activated. Of note, this effect of NRF2 is independent of the PINK1/PARK2 pathway.

Interestingly, the mitophagic activity of PMI is related to the redox status of mitochondria as selective scavenging of mitochondrial superoxides (i.e. NAC, Mito-TEMPOL) inhibits the PMI-induced mitophagy. In this context, the inhibition of mitophagy by Mito-TEMPOL is intriguing, suggesting that ROS is necessary for inducing PMI-dependent mitophagy.

As PMI has an antioxidant action and induces mitophagy independent of PINK1/PARK2, its action has considerable potential in the case of PD patients, and as such, merits further study.

MitoQ

Mitoquinone was originally used to suppress ROS production and lipid peroxidation as explained above in the “Antioxidants: preclinical and clinical studies in PD” section. Interestingly, MitoQ was shown to reduce oxidative stress through mitophagy induction in an *in vivo* model of diabetic kidney disease (DKD). In fact, Xiao and collaborators demonstrated that MitoQ activates mitochondria-selective removal controlling the NRF2 expression, activity, and translocation, which, in turn, cooperates with PINK1

mitophagy induction (Xiao et al., 2017). Moreover, MitoQ was shown to support mitophagy by increasing mitochondrial membrane depolarization ($\Delta\Psi_m$) in aggressive cancer cells (Biel and Rao, 2018).

Phorbol 12-myristate 13-acetate (PMA)

Phorbol 12-myristate 13-acetate (PMA) was shown to favor *Nix* transcriptional activation *in vitro* through the stimulation of protein kinase C α (PRKCA) activity and by promoting the binding of the transcription factor SP1 to GC-rich elements in the *Nix* promoter in cultured neonatal rat cardiac myocytes (Galvez et al., 2006). More recently, PMA was found to stimulate mitophagy in PD models by increasing *Nix* expression (Koentjoro et al., 2017). This pharmacological induction of *Nix* promotes CCCP-induced mitophagy in the PARK2- and PINK1-related PD patient cell lines. Drugs targeting *Nix* are, thus, expected to provide neuroprotective action in PD patients.

TUDCA

TUDCA strongly prevents CCCP-induced cell death, ROS generation, and mitochondrial damage in neuroblastoma cell line. The neuroprotective role of TUDCA in this cell model is mediated by PARK2-dependent mitophagy. The demonstration that pharmacological upregulation of mitophagy by TUDCA prevents neurodegeneration provides new insights into the use of TUDCA in order to favor mitochondrial quality control in PD context.

Natural compound inducers of mitophagy

Melanoidin

Melanoidin derives from aged vinegar or pomegranate extract (PE)

and is a well-known antioxidant ([Delgado-Andrade et al., 2005](#)). Yang and colleagues found that melanoidins from Shanxi aged vinegar-induced mitophagy ([Yang et al., 2014](#)). In particular, they reported that melanoidins reduce ROS in normal human liver cells and mouse livers through a mitophagy-dependent pathway. These results support the fact that melanoidins are able to reduce ROS levels through mitophagy activation, by degrading damaged mitochondria, the source of oxidative stress. In addition, to be direct free radical scavengers, melanoidins are, thus, mitophagy inducers in the context of injury-induced hepatocytes and cardiomyocytes ([Yang et al., 2016](#)).

Melanoidins appears, thus, as new therapeutic target to be tested in the context of PD.

Of note, during the roasting process of coffee, melanoidins are formed ([Moreira et al., 2012](#)). As coffee could be one of the main sources of melanoidins in the human diet, their health implications are of great interest. Interestingly, epidemiologic links exist between caffeine and lower PD risk ([Ross et al., 2000](#); [Hernán et al., 2002](#)). However, the potential of coffee diet on health of PD patients were tested, but caffeine did not show improvement of PD symptomatic effects ([Postuma et al., 2017](#)). It should be interesting to test the effect of melanoidins directly on PD patients instead of caffeine.

Urolithin A

Urolithin A is a microflora human metabolite originating from the digestion by intestinal bacteria. Its precursor is the ellagic acid (ellagitannin family). When this acid is consumed by diet, the

bacterial microflora is able to transform it into urolithin A. Some foods are rich in ellagic acid (e.g., blackberries, cranberries, grapes, pecans raspberries, etc.); however, among these foods, it appears that pomegranates have the highest potential for producing the urolithin A.

This metabolite was shown to prevent accumulation of damaged mitochondria and improve lifespan in nematode and exercise capacity in mice ([Ryu et al., 2016](#)).

Again, it is expected that urolithin A may favor health of PD patients by causing mitophagy and reducing oxidative stress.

Spermidine

Spermidine is a small organic molecule of the polyamine family and controls several physiological processes such as cell growth, proliferation, and survival ([Gevrekci, 2017](#)). Interestingly, spermidine levels decline with age in some tissues such as the heart and kidneys ([Nishimura et al., 2006](#)). A diet enriched with spermidine was found to improve lifespans of yeast, nematodes flies, and mice ([Eisenberg et al., 2009](#)). Moreover, spermidine activates mitophagy in aged cardiomyocytes, thus, repairing mitochondrial activity ([Eisenberg et al., 2016](#)). Qi and colleagues demonstrated that spermidine-induced mitophagy is dependent on ATM (ataxia-telangiectasia-mutated kinase) ([Qi et al., 2016](#)). Administration of spermidine delays PD-related degenerative processes in the fruit fly *Drosophila melanogaster* and in the nematode *Caenorhabditis elegans*, two established model systems for PD pathology ([Büttner et al., 2014](#)). Spermidine-dietary supplementation, thus, has the potential for improving the health

of PD patients.

Resveratrol and other GSE components

Different studies demonstrated that resveratrol alleviates symptoms and is beneficial against cancers, heart disorders, and Alzheimer's disease. Recently, Wu and colleagues reported that daily assumption of GSE (grape skin extracts) alleviates mitochondrial dysfunctions in a *D. melanogaster* model of PD. In particular, besides resveratrol, GSE contains quercetin, myricetin, catechins, tannins, anthocyanidins, and ferulic acid. This work reported that there is a link between mitophagy stimulation and resveratrol beneficial effects necessary for improving lifespan ([Wu et al., 2018](#)).

Conclusion/perspectives

PMA, MitoQ, TUDCA, PMI, or GSE administration in mice models of PD, and eventually in PD patients, could, thus, offer an effective method of combating PD stimulating both antioxidant responses and mitophagy.

Another exciting issue is the proposal to increase the mitophagy process in PD patients through melanoidin, urolithin A, or spermidine consumption. Thus, there is a need to generate and test specialized diet to fit the PD context (see the proposed model in [Figure 4](#)).

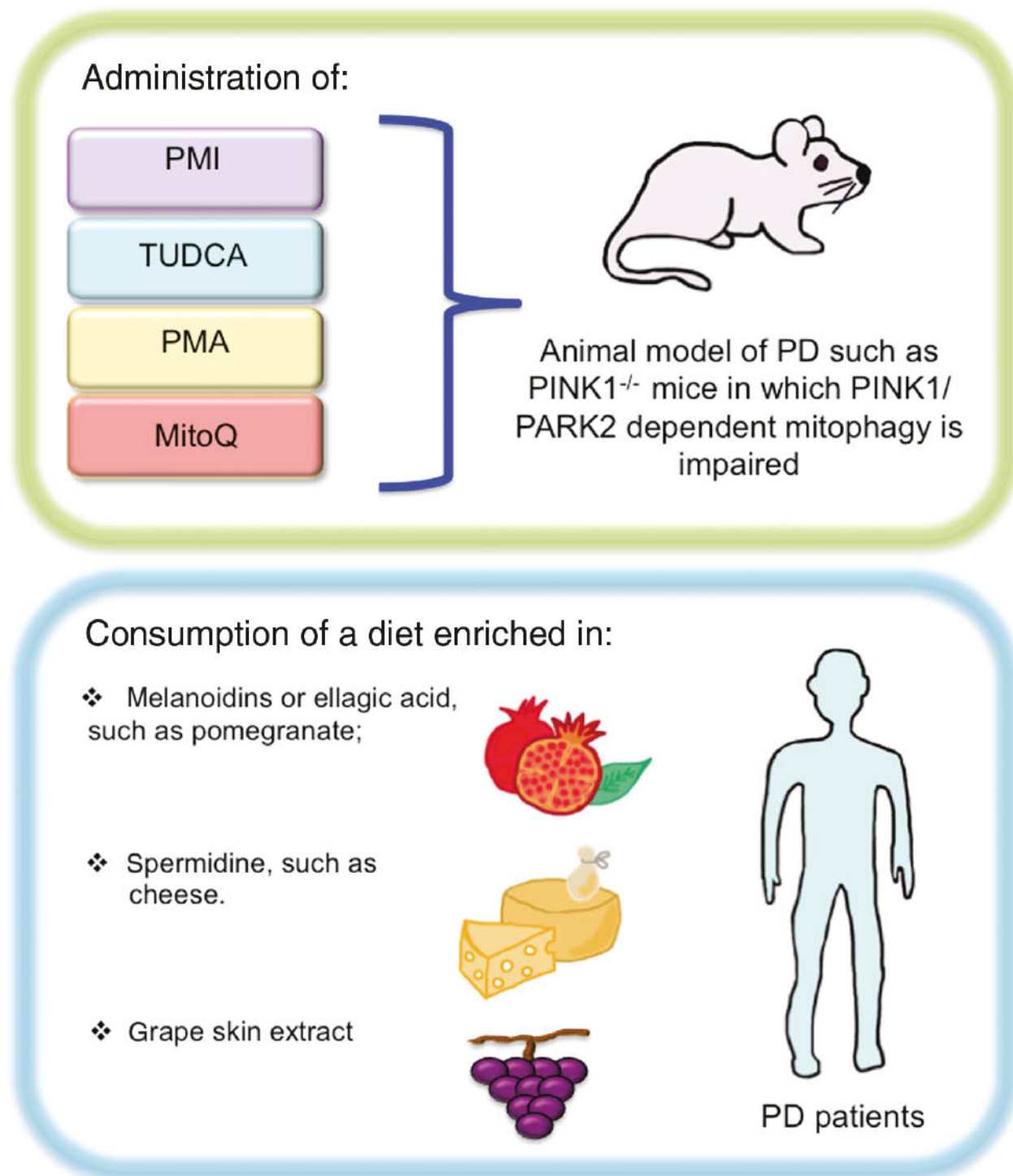


Figure 4:

Antioxidants and/or mitophagy inducer administration in order to counteract PD. The use of pharmacological compounds able to activate both mitophagy and antioxidant responses could be a promising strategy in PD mice models in order to delay neurodegeneration. In addition, it could be worth testing a diet enriched in natural mitophagy inducers and/or antioxidants, such as pomegranate or cheese, as a method of limiting oxidative stress and, thus, neurodegeneration in PD patients.

Acknowledgments

We wish to thank Roche Company who supports F.S. (Grant “Roche per la ricerca 2017”). We thank Dr. M. Bennett for proofreading the work.

References

Attwell, D. and Laughlin, S.B. (2011). An energy budget for signaling in the grey matter of the brain. *J. Cereb. Blood Flow Metab.* *21*, 1133–1145.

[10.1097/00004647-200110000-00001](https://doi.org/10.1097/00004647-200110000-00001)

[Search in Google Scholar](#)

Aurora, R.N., Zak, R.S., Maganti, R.K., Auerbach, S.H., Casey, K.R., Chowdhuri, S., Karippot, A., Ramar, K., Kristo, D.A., and Morgenthaler, T.I. (2010). Best practice guide for the treatment of REM sleep behavior disorder (RBD). *J. Clin. Sleep Med.* *6*, 85–95.

[10.5664/jcsm.27717](https://doi.org/10.5664/jcsm.27717)

[Search in Google Scholar](#)

Beal, M.F., Matthews, R.T., Tieleman, A., and Shults, C.W. (1998). Coenzyme Q10 attenuates the 1-methyl-4-phenyl-1,2,3,4-tetrahydropyridine (MPTP) induced loss of striatal dopamine and dopaminergic axons in aged mice. *Brain Res.* *783*, 109–114.

[10.1016/S0006-8993\(97\)01192-X](https://doi.org/10.1016/S0006-8993(97)01192-X)

[Search in Google Scholar](#)

Bender, A., Krishnan, K.J., Morris, C.M., Taylor, G.A., Reeve, A.K., Perry, R.H., Jaros, E., Hersheson, J.S., Betts, J., Klopstock, T., et al. (2006). High levels of mitochondrial DNA deletions in substantia nigra neurons in aging and Parkinson disease. *Nat. Genet.* *38*, 515–517.

[10.1038/ng1769](#)

[Search in Google Scholar](#)

[PubMed](#)

Ben-Shachar, D., Eshel, G., Riederer, P., and Youdim, M.B. (1992). Role of iron and iron chelation in dopaminergic-induced neurodegeneration: implication for Parkinson's disease. *Ann. Neurol.* 1992, 32.

[10.1002/ana.410320718](#)

[Search in Google Scholar](#)

[PubMed](#)

Berthold, C.H., Fabricius, C., Rydmark, M., and Andersén, B. (1993). Axoplasmic organelles at nodes of Ranvier. I. Occurrence and distribution in large myelinated spinal root axons of the adult cat. *J. Neurocytol.* 22, 925–940.

[10.1007/BF01218351](#)

[Search in Google Scholar](#)

[PubMed](#)

Biel, T.G. and Rao, V.A. (2018). Mitochondrial dysfunction activates lysosomal-dependent mitophagy selectively in cancer cells. *Oncotarget* 9, 995–1011.

[10.18632/oncotarget.23171](#)

[Search in Google Scholar](#)

[PubMed](#)

[PubMed Central](#)

Blanchet, J., Longpré, F., Bureau, G., Morissette, M., DiPaolo, T., Bronchti, G., and Martinoli, M.G. (2008). Resveratrol, a red wine

polyphenol, protects dopaminergic neurons in MPTP-treated mice. *Prog. Neuropsychopharmacol. Biol. Psychiatry* 32, 1243–1250.

[10.1016/j.pnpbp.2008.03.024](https://doi.org/10.1016/j.pnpbp.2008.03.024)

[Search in Google Scholar](#)

[PubMed](#)

Bloom, M.Z. (2007). NIH announces phase III clinical trial of creatine for Parkinson's disease. *Consult. Pharm.* 22, 378.

[Search in Google Scholar](#)

Bose, A. and Beal, M.F. (2016). Mitochondrial dysfunction in Parkinson's disease. *J. Neurochem.* 139, 216–231.

[10.1111/jnc.13731](https://doi.org/10.1111/jnc.13731)

[Search in Google Scholar](#)

[PubMed](#)

Bhujabal, Z., Birgisdottir, Å.B., Sjøttem, E., Brenne, H.B., Øvervatn, A., Habisov, S., Kirkin, V., Lamark, T., and Johansen, T. (2017).

FKBP8 recruits LC3A to mediate Parkin-independent mitophagy.

EMBO Rep. 18, 947–961.

[10.15252/embr.201643147](https://doi.org/10.15252/embr.201643147)

[Search in Google Scholar](#)

[PubMed](#)

[PubMed Central](#)

Borah, A. and Mohanakumar, K.P. (2009). Melatonin inhibits 6-hydroxydopamine production in the brain to protect against experimental Parkinsonism in rodents. *J. Pineal Res.* 47, 293–300.

[10.1111/j.1600-079X.2009.00713.x](https://doi.org/10.1111/j.1600-079X.2009.00713.x)

[Search in Google Scholar](#)

Büttner, S., Broeskamp, F., Sommer, C., Markaki, M., Habernig, L., Alavian-Ghavanini, A., Carmona-Gutierrez, D., Eisenberg, T., Michael, E., Kroemer, G., et al. (2014). Spermidine protects against α -synuclein neurotoxicity. *Cell Cycle* 13, 3903–3908.

[10.4161/15384101.2014.973309](https://doi.org/10.4161/15384101.2014.973309)

[Search in Google Scholar](#)

Campbell, G.R., Ziabreva, I., Reeve, A.K., Krishnan, K.J., Reynolds, R., Howell, O., Lassmann, H., Turnbull, D.M., and Mahad, D.J. (2011). Mitochondrial DNA deletions and neurodegeneration in multiple sclerosis. *Ann. Neurol.* 69, 481–492.

[10.1002/ana.22109](https://doi.org/10.1002/ana.22109)

[Search in Google Scholar](#)

Chen, J.F., Xu, K., Petzer, J.P., Staal, R., Xu, Y.J., Beilstein, M., Sonsalla, P.K., Castagnoli, K., Castagnoli, N., and Schwarzschild, M.A. (2001). Neuroprotection by caffeine and A(2A) adenosine receptor inactivation in a model of Parkinson's disease. *J. Neurosci.* 21, RC143.

[10.1523/JNEUROSCI.21-10-j0001.2001](https://doi.org/10.1523/JNEUROSCI.21-10-j0001.2001)

[Search in Google Scholar](#)

Choi, H.K., Atkinson, K., Karlson, E.W., Willett, W., and Curhan, G. (2004). Alcohol intake and risk of incident gout in men: a prospective study. *Lancet* 363, 1277–1281.

[10.1016/S0140-6736\(04\)16000-5](https://doi.org/10.1016/S0140-6736(04)16000-5)

[Search in Google Scholar](#)

Cohen, A.M., Aberdroth, R.E., and Hochstein, P. (1984). Inhibition of free radical-induced DNA damage by uric acid. *FEBS Lett.* 174,

147–150.

[10.1016/0014-5793\(84\)81094-7](https://doi.org/10.1016/0014-5793(84)81094-7)

[Search in Google Scholar](#)

Couzin, J. (2007). Clinical research. Testing a novel strategy against Parkinson's disease. *Science* 315, 1778.

[10.1126/science.315.5820.1778](https://doi.org/10.1126/science.315.5820.1778)

[Search in Google Scholar](#)

[PubMed](#)

Covey, M.V., Murphy, M.P., Hobbs, C.E., Smith, R.A., and Oorschot, D.E. (2006). Effect of the mitochondrial antioxidant, Mito Vitamin E, on hypoxic-ischemic striatal injury in neonatal rats: a dose-response and stereological study. *Exp. Neurol.* 199, 513–519.

[10.1016/j.expneurol.2005.12.026](https://doi.org/10.1016/j.expneurol.2005.12.026)

[Search in Google Scholar](#)

[PubMed](#)

Chu, C.T., Ji, J., Dagda, R.K., Jiang, J.F., Tyurina, Y.Y., Kapralov, A.A., Tyurin, V.A., Yanamala, N., Shrivastava, I.H., Mohammadyani, D., et al. (2013). Cardiolipin externalization to the outer mitochondrial membrane acts as an elimination signal for mitophagy in neuronal cells. *Nat. Cell Biol.* 15, 1197–1205.

[10.1038/ncb2837](https://doi.org/10.1038/ncb2837)

[Search in Google Scholar](#)

[PubMed](#)

[PubMed Central](#)

Delgado-Andrade, C., Rufián-Henares, J.A., and Morales, F.J. (2005). Assessing the antioxidant activity of melanoidins from

coffee brews by different antioxidant methods. *J. Agric. Food Chem.* *53*, 7832–7836.

[10.1021/jf0512353](https://doi.org/10.1021/jf0512353)

[Search in Google Scholar](#)

[PubMed](#)

Devi, L., Raghavendran, V., Prabhu, B.M., Avadhani, N.G., and Anandatheerthavarada, H.K. (2008). Mitochondrial import and accumulation of alpha-synuclein impair complex I in human dopaminergic neuronal cultures and Parkinson disease brain. *J. Biol. Chem.* *283*, 9089–9100.

[10.1074/jbc.M710012200](https://doi.org/10.1074/jbc.M710012200)

[Search in Google Scholar](#)

Di Rita, A., D'Acunzo, P., Simula, L., Campello, S., Strappazzon, F., and Cecconi, F. (2018). AMBRA1-mediated mitophagy counteracts oxidative stress and apoptosis induced by neurotoxicity in human neuroblastoma SH-SY5Y cells. *Front. Cell Neurosci.* *12*, 92.

[10.3389/fncel.2018.00092](https://doi.org/10.3389/fncel.2018.00092)

[Search in Google Scholar](#)

Dutta, R., McDonough, J., Yin, X., Peterson, J., Chang, A., Torres, T., Gudz, T., Macklin, W.B., Lewis, D.A., Fox, R.J., et al. (2006).

Mitochondrial dysfunction as a cause of axonal degeneration in multiple sclerosis patients. *Ann. Neurol.* *59*, 478–489.

[10.1002/ana.20736](https://doi.org/10.1002/ana.20736)

[Search in Google Scholar](#)

Eisenberg, T., Knauer, H., Schauer, A., Büttner, S., Ruckenstein, C., Carmona-Gutierrez, D., Ring, J., Schroeder, S., Magnes, C.,

Antonacci, L., et al. (2009). Induction of autophagy by spermidine promotes longevity. *Nat. Cell Biol.* *11*, 1305–1314.

[10.1038/ncb1975](https://doi.org/10.1038/ncb1975)

[Search in Google Scholar](#)

Eisenberg, T., Abdellatif, M., Schroeder, S., Primessnig, U., Stekovic, S., Pendl, T., Harger, A., Schipke, J., Zimmermann, A., Schmidt, A., et al. (2016). Cardioprotection and lifespan extension by the natural polyamine spermidine. *Nat. Med.* *22*, 1428–1438.

[10.1038/nm.4222](https://doi.org/10.1038/nm.4222)

[Search in Google Scholar](#)

Ekstrand, M.I., Terzioglu, M., Galter, D., Zhu, S., Hofstetter, C., Lindqvist, E., Thams, S., Bergstrand, A., Hansson, F.S., Trifunovic, A., et al. (2007). Progressive parkinsonism in mice with respiratory-chain-deficient dopamine neurons. *Proc. Natl. Acad. Sci. USA* *104*, 1325–1330.

[10.1073/pnas.0605208103](https://doi.org/10.1073/pnas.0605208103)

[Search in Google Scholar](#)

Elia, A.E., Lalli, S., Monsurrò, M.R., Sagnelli, A., Taiello, A.C., Reggiori, B., La Bella, V., Tedeschi, G., and Albanese, A. (2016). Tauroursodeoxycholic acid in the treatment of patients with amyotrophic lateral sclerosis. *Eur. J. Neurol.* *23*, 45–52.

[10.1111/ene.12664](https://doi.org/10.1111/ene.12664)

[Search in Google Scholar](#)

Etminan, M., Gill, S.S., and Samii, A. (2005). Intake of vitamin E, vitamin C, and carotenoids and the risk of Parkinson's disease: a meta-analysis. *Lancet Neurol.* *4*, 362–365.

[10.1016/S1474-4422\(05\)70097-1](https://doi.org/10.1016/S1474-4422(05)70097-1)

[Search in Google Scholar](#)

Gálvez, A.S., Brunskill, E.W., Marreez, Y., Benner, B.J., Regula, K.M., Kirschenbaum, L.A., and Dorn, G.W. (2006). Distinct pathways regulate proapoptotic Nix and BNip3 in cardiac stress. *J. Biol. Chem.* *281*, 1442–1448.

[10.1074/jbc.M509056200](https://doi.org/10.1074/jbc.M509056200)

[Search in Google Scholar](#)

[PubMed](#)

Gane, E.J., Weilert, F., Orr, D.W., Keogh, G.F., Gibson, M., Lockhart, M.M., Frampton, C.M., Taylor, K.M., Smith, R.A., and Murphy, M.P. (2010). The mitochondria-targeted anti-oxidant mitoquinone decreases liver damage in a phase II study of hepatitis C patients. *Liver Int.* *30*, 1019–1026.

[10.1111/j.1478-3231.2010.02250.x](https://doi.org/10.1111/j.1478-3231.2010.02250.x)

[Search in Google Scholar](#)

[PubMed](#)

Georgakopoulos, N.D., Frison, M., Alvarez, M.S., Bertrand, H., Wells, G., and Campanella, M. (2017). Reversible Keap1 inhibitors are preferential pharmacological tools to modulate cellular mitophagy. *Sci. Rep.* *7*, 10303.

[10.1038/s41598-017-07679-7](https://doi.org/10.1038/s41598-017-07679-7)

[Search in Google Scholar](#)

Gevrekci, A.Ö. (2017). The roles of polyamines in microorganisms. *World J. Microbiol. Biotechnol.* *33*, 204.

[10.1007/s11274-017-2370-y](https://doi.org/10.1007/s11274-017-2370-y)

[Search in Google Scholar](#)

Hamacher-Brady, A. and Brady, N.R. (2016). Mitophagy programs: mechanisms and physiological implications of mitochondrial targeting by autophagy. *Cell Mol. Life Sci.* 73, 775–795.

[10.1007/s00018-015-2087-8](https://doi.org/10.1007/s00018-015-2087-8)

[Search in Google Scholar](#)

Hernán, M.A., Takkouche, B., Caamaño-Isorna, F., and Gestal-Otero, J.J. A meta-analysis of coffee drinking, cigarette smoking, and the risk of Parkinson's disease. *Ann. Neurol.* 52, 276–284.

[10.1002/ana.10277](https://doi.org/10.1002/ana.10277)

[Search in Google Scholar](#)

Horvath, T.L., Diano, S., Leranth, C., Garcia-Segura, L.M., Cowley, M.A., Shanabrough, M., Elsworth, J.D., Sotonyi, P., Roth, R.H., Dietrich, E.H., et al. (2003). Coenzyme Q induces nigral mitochondrial uncoupling and prevents dopamine cell loss in a primate model of Parkinson's disease. *Endocrinology* 144, 2757–2760.

[10.1210/en.2003-0163](https://doi.org/10.1210/en.2003-0163)

[Search in Google Scholar](#)

Isobe, C., Abe, T., and Terayama, Y. (2010). Levels of reduced and oxidized coenzyme Q-10 and 8-hydroxy-2'-deoxyguanosine in the cerebrospinal fluid of patients with living Parkinson's disease demonstrate that mitochondrial oxidative damage and/or oxidative DNA damage contributes to the neurodegenerative process. *Neurosci. Lett.* 469, 159–163.

[10.1016/j.neulet.2009.11.065](https://doi.org/10.1016/j.neulet.2009.11.065)

[Search in Google Scholar](#)

Jauslin, M.L., Meier, T., Smith, R.A., and Murphy, M.P. (2003). Mitochondria-targeted antioxidants protect Friedreich ataxia fibroblasts from endogenous oxidative stress more effectively than untargeted antioxidants. *FASEB J.* 17, 1972–1974.

[10.1096/fj.03-0240fje](https://doi.org/10.1096/fj.03-0240fje)

[Search in Google Scholar](#)

Jin, B.K., Shin, D.Y., Jeong, M.Y., Gwag, M.R., Baik, H.W., Yoon, K.S., Cho, Y.H., Joo, W.S., Kim, Y.S., and Baik, H.H. (1998). Melatonin protects nigral dopaminergic neurons from 1-methyl-4-phenylpyridinium (MPP+) neurotoxicity in rats. *Neurosci. Lett.* 245, 61–64.

[10.1016/S0304-3940\(98\)00170-0](https://doi.org/10.1016/S0304-3940(98)00170-0)

[Search in Google Scholar](#)

Jin, F., Wu, Q., Lu, Y.F., Gong, Q.H., and Shi, J.S. (2008). Neuroprotective effect of resveratrol on 6-OHDA-induced Parkinson's disease in rats. *Eur. J. Pharmacol.* 600, 78–82.

[10.1016/j.ejphar.2008.10.005](https://doi.org/10.1016/j.ejphar.2008.10.005)

[Search in Google Scholar](#)

[PubMed](#)

Joghataie, M.T., Roghani, M., Negahdar, F., and Hashemi, L. (2004). Protective effect of caffeine against neurodegeneration in a model of Parkinson's disease in rat: behavioral and histochemical evidence. *Parkinsonism Relat. Disord.* 10, 657–661.

[10.1016/j.parkreldis.2004.06.004](https://doi.org/10.1016/j.parkreldis.2004.06.004)

[Search in Google Scholar](#)

PubMed

Johri, A. and Beal, M.F. (2012). Mitochondrial dysfunction in neurodegenerative diseases. *J. Pharmacol. Exp. Ther.* 342, 619–630.

[10.1124/jpet.112.192138](https://doi.org/10.1124/jpet.112.192138)

[Search in Google Scholar](#)

Keene, C.D., Rodrigues, C.M.P., Eich, T., Chhabra, M.S., Steer, C.J., and Low, W.C. (2002). Tauroursodeoxycholic acid, a bile acid, is neuroprotective in a transgenic animal model of Huntington's disease. *Proc. Natl. Acad. Sci. USA* 99, 10671–10676.

[10.1073/pnas.162362299](https://doi.org/10.1073/pnas.162362299)

[Search in Google Scholar](#)

Koentjoro, B., Park, J.S., and Suea, C.M. (2017). Nix restores mitophagy and mitochondrial function to protect against PINK1/Parkin-related Parkinson's disease. *Sci. Rep.* 7, 44373.

[10.1038/srep44373](https://doi.org/10.1038/srep44373)

[Search in Google Scholar](#)

Kraytsberg, Y., Kudryavtseva, E., McKee, A.C., Geula, C., Kowall, N.W., and Khrapko, K. (2006). Mitochondrial DNA deletions are abundant and cause functional impairment in aged human substantia nigra neurons. *Nat. Genet.* 38, 518–520.

[10.1038/ng1778](https://doi.org/10.1038/ng1778)

[Search in Google Scholar](#)

Lazarou, M., Sliter, D.A., Kane, L.A., Sarraf, S.A., Wang, C., Burman, J.L., Sideris, D.P., Fogel, A.I., and Youle, R.J. (2015). The ubiquitin kinase PINK1 recruits autophagy receptors to induce mitophagy. *Nature* 524, 309–314.

[10.1038/nature14893](https://doi.org/10.1038/nature14893)

[Search in Google Scholar](#)

Lenaz, G. (2001). The mitochondrial production of reactive oxygen species: mechanisms and implications in human pathology. *IUBMB Life* 52, 159–164.

[10.1080/15216540152845957](https://doi.org/10.1080/15216540152845957)

[Search in Google Scholar](#)

Liang, L.P., Huang, J., Fulton, R., Pearson-Smith, J.N., Day, B.J., and Patel, M. (2017). Pre-clinical therapeutic development of a series of metalloporphyrins for Parkinson's disease. *Toxicol. Appl. Pharmacol.* 326, 34–42.

Pharmacol. 326, 34–42.

[10.1016/j.taap.2017.04.004](https://doi.org/10.1016/j.taap.2017.04.004)

[Search in Google Scholar](#)

Luchtefeld, R., Luo, R., Stine, K., Alt, M.L., Chernovitz, P.A., and Smith, R.E. (2008). Dose formulation and analysis of diapocynin. *J. Agric. Food Chem.* 56, 301–306.

[10.1021/jf072792n](https://doi.org/10.1021/jf072792n)

[Search in Google Scholar](#)

Matthews, R.T., Ferrante, R.J., Klivenyi, P., Yang, L., Klein, A.M., Mueller, G., Kaddurah-Daouk, R., and Beal, M.F. (1999). Creatine and cyclocreatine attenuate MPTP neurotoxicity. *Exp. Neurol.* 157, 142–149.

[10.1006/exnr.1999.7049](https://doi.org/10.1006/exnr.1999.7049)

[Search in Google Scholar](#)

Miller, J.W., Selhub, J., and Joseph, J.A. (1996). Oxidative damage caused by free radicals produced during catecholamine

autoxidation: protective effects of O-methylation and melatonin.

Free Radic. Biol. Med. 21, 241–249.

[10.1016/0891-5849\(96\)00033-0](https://doi.org/10.1016/0891-5849(96)00033-0)

[Search in Google Scholar](#)

Moon, Y., Lee, K.H., Park, J.H., Geum, D., and Kim, K. (2005).

Mitochondrial membrane depolarization and the selective death of dopaminergic neurons by rotenone: protective effect of coenzyme Q10. J. Neurochem. 93, 1199–1208.

[10.1111/j.1471-4159.2005.03112.x](https://doi.org/10.1111/j.1471-4159.2005.03112.x)

[Search in Google Scholar](#)

[PubMed](#)

Moreira, A.S., Nunes, F.M., Domingues, M.R., and Coimbra, M.A. (2012). Coffee melanoidins: structures, mechanisms of formation and potential health impacts. Food Funct. 3, 903–915.

[10.1039/c2fo30048f](https://doi.org/10.1039/c2fo30048f)

[Search in Google Scholar](#)

[PubMed](#)

Mortiboys, H., Furmston, R., Bronstad, G., Aasly, J., Elliott, C., and Bandmann, O. (2015). UDCA exerts beneficial effect on mitochondrial dysfunction in LRRK2 (G2019S) carriers and *in vivo*. Neurology 85, 846–852.

[10.1212/WNL.0000000000001905](https://doi.org/10.1212/WNL.0000000000001905)

[Search in Google Scholar](#)

[PubMed](#)

[PubMed Central](#)

Murakawa, T., Yamaguchi, O., Hashimoto, A., Hikoso, S., Takeda,

T., Oka, T., Yasui, H., Ueda, H., Akazawa, Y., Nakayama, H., et al. (2015). Bcl-2-like protein 13 is a mammalian Atg32 homologue that mediates mitophagy and mitochondrial fragmentation. *Nat. Commun.* *6*, 7527.

[10.1038/ncomms8527](https://doi.org/10.1038/ncomms8527)

[Search in Google Scholar](#)

[PubMed](#)

[PubMed Central](#)

Murphy, M.P. (2009). How mitochondria produce reactive oxygen species. *Biochem. J.* *417*, 1–13.

[10.1042/BJ20081386](https://doi.org/10.1042/BJ20081386)

[Search in Google Scholar](#)

[PubMed](#)

[PubMed Central](#)

Murphy, M.P. and Smith, R.A. (2007). Targeting antioxidants to mitochondria by conjugation to lipophilic cations. *Annu. Rev. Pharmacol. Toxicol.* *47*, 629–656.

[10.1002/9780470372531.ch25](https://doi.org/10.1002/9780470372531.ch25)

[Search in Google Scholar](#)

Negida, A., Elfil, M., Attia, Farahat, E., Gabr, M., Essam, A., Attia, D., and Ahmed, H. (2017). Caffeine; the forgotten potential for Parkinson's disease. *CNS Neurol. Disord. Drug Targets* *16*, 652–657.

[10.2174/1871527315666161107091149](https://doi.org/10.2174/1871527315666161107091149)

[Search in Google Scholar](#)

[PubMed](#)

Nishimura, K., Shiina, R., Kashiwagi, K., and Igarashi, K. (2006).

Decrease in polyamines with aging and their ingestion from food and drink. *J. Biochem.* *139*, 81–90.

[10.1093/jb/mvj003](https://doi.org/10.1093/jb/mvj003)

[Search in Google Scholar](#)

[PubMed](#)

Novak, I., Kirkin, V., McEwan, D.G., Zhang, J., Wild, P., Rozenknop, A., Rogov, V., Lohr, F., Popovic, D., Occhipinti, A., et al. (2010). Nix is a selective autophagy receptor for mitochondrial clearance. *EMBO Rep.* *11*, 45–51.

[10.1038/embor.2009.256](https://doi.org/10.1038/embor.2009.256)

[Search in Google Scholar](#)

[PubMed](#)

[PubMed Central](#)

Nunes, A.F., Amaral, J.D., Lo, A.C., Fonseca, M.B., Viana, R.S.J., Callaerts-Vegh, Z., D'Hooge, R., and Rodrigues, C.M.P. (2012). TUDCA, a bile acid, attenuates amyloid precursor protein processing and amyloid beta deposition in APP/PS1 mice, *Mol. Neurobiol.* *45*, 440–454.

[Search in Google Scholar](#)

Palikaras, K. and Tavernarakis, N. (2014). Mitochondrial homeostasis: the interplay between mitophagy and mitochondrial biogenesis. *Exp. Gerontol.* *56*, 182–188.

[10.1016/j.exger.2014.01.021](https://doi.org/10.1016/j.exger.2014.01.021)

[Search in Google Scholar](#)

[PubMed](#)

Pavshintsev, V.V., Podshivalova, L.S., Frolova, O.Y., Belopolskaya,

M.V., Averina, O.A., Kushnir, E.A., Marmiy, N.V., and Lovat, M.L. (2017). Effects of mitochondrial antioxidant SkQ1 on biochemical and behavioral parameters in a parkinsonism model in mice. *Biochemistry (Mosc)*. 82, 1513–1520.

[10.1134/S0006297917120100](https://doi.org/10.1134/S0006297917120100)

[Search in Google Scholar](#)

[PubMed](#)

Peng, K., Tao, Y., Zhang, J., Wang, J., Ye, F., Dan, G., Zhao, Y., Cai, Y., Zhao, J., Wu, Q., et al. (2016). Resveratrol regulates mitochondrial biogenesis and fission/fusion to attenuate rotenone-induced neurotoxicity. *Oxid. Med. Cell Longev*. 2016, 6705621.

[10.1155/2016/6705621](https://doi.org/10.1155/2016/6705621)

[Search in Google Scholar](#)

[PubMed](#)

[PubMed Central](#)

Poewe, W., Seppi, K., Tanner, C.M., Halliday, G.M., Brundin, P., Volkman, J., Schrag, A.E., and Lang, A.E. (2017). Parkinson disease. *Nat. Rev. Dis. Primers* 3, 17013.

[10.1038/nrdp.2017.13](https://doi.org/10.1038/nrdp.2017.13)

[Search in Google Scholar](#)

[PubMed](#)

Postuma, R.B., Anang, J., Pelletier, A., Joseph, L., Moscovich, M., Grimes, D., Furtado, S., Munhoz, R.P., Appel-Cresswell, S., Moro, A., et al. (2017). Caffeine as symptomatic treatment for Parkinson disease (Café-PD): A randomized trial. *Neurology* 89, 1795–1803.

[10.1212/WNL.0000000000004568](https://doi.org/10.1212/WNL.0000000000004568)

[Search in Google Scholar](#)

[PubMed](#)

[PubMed Central](#)

Qi, Y., Qiu, Q., Gu, X., Tian, Y. and Zhanga, Y. (2016). ATM mediates spermidine-induced mitophagy via PINK1 and Parkin regulation in human fibroblasts. *Sci Rep.* 6, 24700.

[10.1038/srep24700](https://doi.org/10.1038/srep24700)

[Search in Google Scholar](#)

[PubMed](#)

[PubMed Central](#)

Rajeswari, A. and Sabesan, M. (2008). Inhibition of monoamine oxidase-B by the polyphenolic compound, curcumin and its metabolite tetrahydrocurcumin, in a model of Parkinson's disease induced by MPTP neurodegeneration in mice.

Inflammopharmacology 16, 96–99.

[10.1007/s10787-007-1614-0](https://doi.org/10.1007/s10787-007-1614-0)

[Search in Google Scholar](#)

[PubMed](#)

Rangaraju, V., Calloway, N., and Ryan, T.A. (2014). Activity-driven local ATP synthesis is required for synaptic function. *Cell* 156, 825–835.

[10.1016/j.cell.2013.12.042](https://doi.org/10.1016/j.cell.2013.12.042)

[Search in Google Scholar](#)

[PubMed](#)

[PubMed Central](#)

Ross, G.W., Abbott, R.D., Petrovitch, H., Morens, D.M., Grandinetti, A., Tung, K.H., Tanner, C.M., Masaki, K.H., Blanchette, P.L., Curb,

J.D., et al. (2000). Association of coffee and caffeine intake with the risk of Parkinson disease. *JAMA* 283, 2674–2679.

[10.1001/jama.283.20.2674](https://doi.org/10.1001/jama.283.20.2674)

[Search in Google Scholar](#)

[PubMed](#)

Ryu, D., Mouchiroud, L., Andreux, P.A., Katsyuba, E., Moullan, N., Nicolet-Dit-Félix, A.A., Williams, E.G., Jha, P., Lo Sasso, G., Huzard, D., et al. (2016). Urolithin A induces mitophagy and prolongs lifespan in *C. elegans* and increases muscle function in rodents. *Nat. Med.* 22, 879–888.

[10.1038/nm.4132](https://doi.org/10.1038/nm.4132)

[Search in Google Scholar](#)

[PubMed](#)

Saravanan, K.S., Sindhu, K.M., and Mohanakumar, K.P. (2007). Melatonin protects against rotenone-induced oxidative stress in a hemiparkinsonian rat model, *J. Pineal Res.* 42, 247–253.

[10.1111/j.1600-079X.2006.00412.x](https://doi.org/10.1111/j.1600-079X.2006.00412.x)

[Search in Google Scholar](#)

[PubMed](#)

Sau, D., De Biasi, S., Vitellaro-Zuccarello, L., Riso, P., Guarnieri, S., Porrini, M., Simeoni, S., Crippa, V., Onesto, E., Palazzolo, I., et al. (2007). Mutation of SOD1 in ALS: a gain of a loss of function. *Hum. Mol. Genet.* 16, 1604–1618.

[10.1093/hmg/ddm110](https://doi.org/10.1093/hmg/ddm110)

[Search in Google Scholar](#)

[PubMed](#)

Shachar, D.B., Kahana, N., Kampel, V., Warshawsky, A., and Youdim, M.B. (2004). Neuroprotection by a novel brain permeable iron chelator, VK-28, against 6-hydroxydopamine lesion in rats. *Neuropharmacology* 46, 254–263.

[10.1016/j.neuropharm.2003.09.005](https://doi.org/10.1016/j.neuropharm.2003.09.005)

[Search in Google Scholar](#)

[PubMed](#)

Schapira, A.H., Cooper, J.M., Dexter, D., Clark, J.B., Jenner, P., and Marsden, C.D. (1990). Mitochondrial complex I deficiency in Parkinson's disease. *J. Neurochem.* 54, 823–827.

[10.1111/j.1471-4159.1990.tb02325.x](https://doi.org/10.1111/j.1471-4159.1990.tb02325.x)

[Search in Google Scholar](#)

[PubMed](#)

Shepherd, G.M. and Harris, K.M. (1998). Three-dimensional structure and composition of CA3-CA1 axons in rat hippocampal slices: implications for presynaptic connectivity and compartmentalization. *J. Neurosci.* 18, 8300–8310.

[10.1523/JNEUROSCI.18-20-08300.1998](https://doi.org/10.1523/JNEUROSCI.18-20-08300.1998)

[Search in Google Scholar](#)

Shults, C.W., Oakes, D., Kieburtz, K., Beal, M.F., Haas, R., Plumb, S., Juncos, J.L., Nutt, J., Shoulson, I., Carter, J., et al. (2002). Effects of coenzyme Q10 in early Parkinson disease: evidence of slowing of the functional decline. *Arch. Neurol.* 59, 1541–1550.

[10.1001/archneur.59.10.1541](https://doi.org/10.1001/archneur.59.10.1541)

[Search in Google Scholar](#)

[PubMed](#)

Sies, H., Stahl, W., and Sundquist, A.R. (1992). Antioxidant functions of vitamins. Vitamins E and C, beta-carotene, and other carotenoids. *Ann. NY Acad. Sci.* *669*, 7–20.

[10.1111/j.1749-6632.1992.tb17085.x](https://doi.org/10.1111/j.1749-6632.1992.tb17085.x)

[Search in Google Scholar](#)

[PubMed](#)

Skulachev, M.V., Antonenko, Y.N., Anisimov, V.N., Chernyak, B.V., Cherepanov, D.A., Chistyakov, V.A., Egorov, M.V., Kolosova, N.G., Korshunova, G.A., Lyamzaev, K.G., et al. (2011). Mitochondrial-targeted plastoquinone derivatives. Effect on senescence and acute age-related pathologies. *Curr. Drug Targets* *12*, 800–826.

[10.2174/138945011795528859](https://doi.org/10.2174/138945011795528859)

[Search in Google Scholar](#)

[PubMed](#)

Smith, R.A. and Murphy, M.P. (2011). Mitochondria-targeted antioxidants as therapies. *Discov. Med.* *11*, 106–114.

[Search in Google Scholar](#)

Snow, B.J., Rolfe, F.L., Lockhart, M.M., Frampton, C.M., O'Sullivan, J.D., Fung, V., Smith, R.A., Murphy, M.P., and Taylor, K.M. (2010). A double-blind, placebo-controlled study to assess the mitochondria-targeted antioxidant MitoQ as a disease-modifying therapy in Parkinson's disease. *Mov. Disord.* *25*, 1670–1674.

[10.1002/mds.23148](https://doi.org/10.1002/mds.23148)

[Search in Google Scholar](#)

[PubMed](#)

Starkov, A.A. (2008). The role of mitochondria in reactive oxygen

species metabolism and signaling. *Ann. NY Acad. Sci.* 1147, 37–52.

[10.1196/annals.1427.015](https://doi.org/10.1196/annals.1427.015)

[Search in Google Scholar](#)

[PubMed](#)

[PubMed Central](#)

Strappazzon, F., Vietri-Rudan, M., Campello, S., Nazio, F., Florenzano, F., Fimia, G.M., Piacentini, M., Levine, B., and Cecconi, F. (2011). Mitochondrial BCL-2 inhibits AMBRA1-induced autophagy. *EMBO J.* 30, 1195–1208.

[10.1038/emboj.2011.49](https://doi.org/10.1038/emboj.2011.49)

[Search in Google Scholar](#)

[PubMed](#)

[PubMed Central](#)

Strappazzon, F., Nazio, F., Corrado, M., Cianfanelli, V., Romagnoli, A., Fimia, G.M., Campello, S., Nardacci, R., Piacentini, M., Campanella, M., et al. (2015). AMBRA1 is able to induce mitophagy via LC3 binding, regardless of PARKIN and p62/SQSTM1. *Cell Death Differ.* 22, 517.

[10.1038/cdd.2014.190](https://doi.org/10.1038/cdd.2014.190)

[Search in Google Scholar](#)

[PubMed](#)

[PubMed Central](#)

Swerdlow, R.H., Burns, J.M., and Khan, S.M. (2014). The Alzheimer's disease mitochondrial cascade hypothesis: progress and perspectives. *Biochim. Biophys. Acta* 1842, 1219–1231.

[10.1016/j.bbadis.2013.09.010](https://doi.org/10.1016/j.bbadis.2013.09.010)

[Search in Google Scholar](#)

[PubMed](#)

[PubMed Central](#)

Van Humbeeck, C., Cornelissen, T., Hofkens, H., Mandemakers, W., Gevaert, K., De Strooper, B., and Vandenberghe, W. (2011). Parkin interacts with Ambra1 to induce mitophagy. *J. Neurosci.* *31*, 10249–10261.

[10.1523/JNEUROSCI.1917-11.2011](https://doi.org/10.1523/JNEUROSCI.1917-11.2011)

[Search in Google Scholar](#)

[PubMed](#)

[PubMed Central](#)

Ved, R., Saha, S., Westlund, B., Perier, C., Burnam, L., Sluder, A., Hoener, M., Rodrigues, C.M., Alfonso, A., Steer, C., et al. (2005). Similar patterns of mitochondrial vulnerability and rescue induced by genetic modification of α -synuclein, parkin, and DJ-1 in *Caenorhabditis elegans*. *J. Biol. Chem.* *280*, 42655–42668.

[10.1074/jbc.M505910200](https://doi.org/10.1074/jbc.M505910200)

[Search in Google Scholar](#)

[PubMed](#)

[PubMed Central](#)

Vejrazka, M., Micek, R., and Stipek, S. (2005). Apocynin inhibits NADPH oxidase in phagocytes but stimulates ROS production in non-phagocytic cells. *Biochim. Biophys. Acta* *1722*, 143–147.

[10.1016/j.bbagen.2004.12.008](https://doi.org/10.1016/j.bbagen.2004.12.008)

[Search in Google Scholar](#)

[PubMed](#)

Wei, Y., Chiang, W.C., Sumpter, R., Jr., Mishra, P., and Levine, B.

(2017). Prohibitin 2 is an inner mitochondrial membrane mitophagy receptor. *Cell* 168, 224–238 e210.

[10.1016/j.cell.2016.11.042](https://doi.org/10.1016/j.cell.2016.11.042)

[Search in Google Scholar](#)

[PubMed](#)

[PubMed Central](#)

Weinreb, O., Mandel, S., Youdim, M.B.H., and Amit, T. (2013). Targeting dysregulation of brain iron homeostasis in Parkinson's disease by iron chelators. *Free Radic. Biol. Med.* 62, 52–64.

[10.1016/j.freeradbiomed.2013.01.017](https://doi.org/10.1016/j.freeradbiomed.2013.01.017)

[Search in Google Scholar](#)

[PubMed](#)

Wu, W., Tian, W., Hu, Z., Chen, G., Huang, L., Li, W., Zhang, X., Xue, P., Zhou, C., Liu, L., et al. (2014). ULK1 translocates to mitochondria and phosphorylates FUNDC1 to regulate mitophagy. *EMBO Rep.* 15, 566–575.

[10.1002/embr.201438501](https://doi.org/10.1002/embr.201438501)

[Search in Google Scholar](#)

[PubMed](#)

[PubMed Central](#)

Wu, Z., Wu, A., Dong, J., Sigears, A., and Lu, B. (2018). Grape skin extract improves muscle function and extends lifespan of a *Drosophila* model of Parkinson's disease through activation of mitophagy. *Exp. Gerontol.* 113, 10–17.

[10.1016/j.exger.2018.09.014](https://doi.org/10.1016/j.exger.2018.09.014)

[Search in Google Scholar](#)

[PubMed](#)

Xiao, L., Xu, X., Zhang, F., Wang, M., Xu, Y., Tang, D., Wang, J., Qin, Y., Liu, Y., Tang, C., et al. (2017). The mitochondria-targeted antioxidant MitoQ ameliorated tubular injury mediated by mitophagy in diabetic kidney disease via Nrf2/PINK1. *Redox Biol.* *11*, 297–311.

[10.1016/j.redox.2016.12.022](https://doi.org/10.1016/j.redox.2016.12.022)

[Search in Google Scholar](#)

[PubMed](#)

[PubMed Central](#)

Xu, Q., Langley, M., Kanthasamy, A.G., and Reddy, M.B. (2017). Epigallocatechin gallate has a neurorescue effect in a mouse model of Parkinson disease. *J. Nutr.* *147*, 1926–1931.

[10.3945/jn.117.255034](https://doi.org/10.3945/jn.117.255034)

[Search in Google Scholar](#)

[PubMed](#)

[PubMed Central](#)

Yamano, K., Matsuda, N., and Tanaka, K. (2016). The ubiquitin signal and autophagy: an orchestrated dance leading to mitochondrial degradation. *EMBO Rep.* *17*, 300–316.

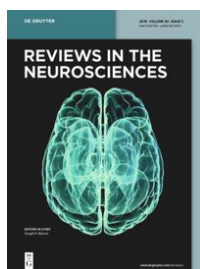
[10.15252/embr.201541486](https://doi.org/10.15252/embr.201541486)

[Search in Google Scholar](#)

[PubMed](#)

[PubMed Central](#)

Yang, L., Wang, X., and Yang, X. (2014). Possible antioxidant mechanism of melanoidins extract from Shanxi aged vinegar in mitophagy-dependent and mitophagy-independent pathways. *J.*

From the journal**Reviews in the Neurosciences**

Volume 30 Issue 7

Journal and Issue

Search journal

 This issue All issues**Articles in the same Issue**[Frontmatter](#)[Evidence for nucleolar dysfunction in Alzheimer's disease](#)[National Institutes of Health Stroke Scale, modified Rankin Scale, and modified Thrombolysis in Cerebral Infarction as autonomy predictive tools for stroke patients](#)[Immune system and new avenues in Parkinson's disease research and treatment](#)[Mitophagy could fight Parkinson's disease through antioxidant action](#)[Metabolic pattern analysis of ¹⁸F-FDG PET as a marker for Parkinson's disease: a systematic review and meta-analysis](#)[Pathological and cognitive changes in patients with type 2 diabetes mellitus and comorbid MCI and protective hypoglycemic therapies: a narrative review](#)[Pain in cervical dystonia and the antinociceptive effects of botulinum toxin: what is currently known?](#)[N2 amplitude modulation across the antisocial spectrum: a meta-analysis](#)**Subjects**[Architecture and Design](#)[Geosciences](#)[Materials Sciences](#)

[Arts](#)[Asian and Pacific Studies](#)[Business and Economics](#)[Chemistry](#)[Classical and Ancient Near Eastern Studies](#)[Computer Sciences](#)[Cultural Studies](#)[Engineering](#)[General Interest](#)[History](#)[Industrial Chemistry](#)[Islamic and Middle Eastern Studies](#)[Jewish Studies](#)[Law](#)[Library and Information Science, Book Studies](#)[Life Sciences](#)[Linguistics and Semiotics](#)[Literary Studies](#)[Mathematics](#)[Medicine](#)[Music](#)[Pharmacy](#)[Philosophy](#)[Physics](#)[Social Sciences](#)[Sports and Recreation](#)[Theology and Religion](#)

Services

[For journal authors](#)[For book authors](#)[For librarians](#)[Rights & Permissions](#)

Publications

[Publication types](#)[Open Access](#)

About

[Contact](#)[Career](#)[About De Gruyter](#)[Partnerships](#)[Press](#)[New website FAQs](#)

Social

[!\[\]\(add754807a27cbf5e63930370ca2e8dc_img.jpg\) Facebook](#)[!\[\]\(ded64129de9a6a4d13a98cdbcdcf895f_img.jpg\) Twitter](#)[!\[\]\(102b5d74094c76021cc1eb5c235af37d_img.jpg\) Instagram](#)[!\[\]\(99774c1e3ffb5b86126095a1269b11a0_img.jpg\) YouTube](#)[!\[\]\(fd1cf9fc5378387e738fae669a454182_img.jpg\) LinkedIn](#)

Winner of the OpenAthens
Best Publisher UX Award 2022

[Help/FAQ](#) [Privacy policy](#) [Cookie Policy](#) [Accessibility](#) [Terms & Conditions](#) [Legal Notice](#)

© Walter de Gruyter GmbH 2022

CHAPTER 5

Neuroblastoma and oxidative stress: From pathogenesis to in vitro models of neurodegeneration

Anthea Di Rita^{a,b}, Flavie Strappazon^b

^aUniversity of Rome “Tor Vergata”, Rome, Italy

^bIRCCS Santa Lucia Foundation, Rome, Italy

Abbreviations

6-OHDA	6-hydroxidopamine
AD	Alzheimer diseases
ALK	anaplastic lymphoma kinase
AMBRA1	activated molecule in BECLIN-1 regulation
Bcl-2	apoptosis regulator Bcl-2
BNIP3	BCL2/adenovirus E1B 19 kDa protein-interacting protein 3
CCH	chronic cerebral hypoperfusion
CNS	central nervous system
DMF	dimethyl fumarate
DβH	dopamine-β-hydroxylase
FoxO3a	forkhead box protein O3
GCL	glutamate cysteine ligase
GSH	glutathione
IDPm	mitochondrial isocitrate dehydrogenase
MYC	myc proto-oncogene protein
NADP(+)	nicotinamide adenine dinucleotide phosphate oxidated
NADPH	nicotinamide adenine dinucleotide phosphate reduced
NB	neuroblastoma
NO	nitric oxide
PCA	protocatechuic aldehyde
PD	Parkinson's disease
PHOX2B	paired-like homeobox 2b
Q3G	quercetin 3-glucoside
RNS	nitrogen species
ROS	reactive oxygen species
SIRT1	sirtuin 1
SOD2	superoxide dismutase [Mn], mitochondrial
SREBP-2	sterol regulatory element-binding protein-2
TH	tyrosine hydroxylase
TXA2R	thromboxane A2 receptor
Tyr	tyrosinase
VA	vanillic acid

Neuroblastoma

Neuroblastoma (NB) is a tumor that originates from the cells of the autonomic nervous system. “Neuro” indicates that the tumor develops in the nerves; “blastoma” indicates, on the other hand, that the cells involved are immature or developing.

Among the various solid tumors of infants NB is, after those affecting the central nervous system (CNS), the most widespread (8%) in patients under the age of 1.¹ Indeed, 15% of deaths linked to childhood neoplasia are due to NB. Unfortunately, in major and serious cases, after the diagnosis, NB is already at the step metastasis stage and children are refractory to chemotherapy.

NB is a cancer that occurs at all ages, but as said before, the majority of patients affected by NB are children. In some rare cases, it is possible to perform a prenatal diagnosis using ultrasound; however, the average age of young patients at diagnosis varies between 1 and 2 years and almost all tumors (about 95%) are discovered by the age of 5 years. Its cause remains unknown, but it often occurs in children born to parents who are alcoholics, smokers, who suffer from hypertension, or in children with mothers younger than 20.²

This said, basically, NB is due to genetic disturbances, which are linked to mutations in genes such as oncogenes (which promote tumor formation) or tumor suppressors (which block the cancer) that occur during childhood. These kinds of gene mutations deregulate proliferation of immature nerve cells (neuroblasts), which cause cancer.

Several genes are known to be involved in the onset of NB such as MYCN oncogene and ALK, PHOX2B genes. In particular, the amplification of MYCN (25% of NB cases) is correlated with a high risk of disease and poor prognosis.

Contribution of oxidative stress in cancer pathogenesis

Free radicals and reactive oxygen species (ROS) take part in the so-called *reactive species*. These species are generated following metabolic reactions inside the mitochondria of eukaryotic cells. At a low concentration (normal condition), they play a crucial role in the signal transduction pathways and in particular in the redox signaling, acting as second messengers. A correct regulation of reactive species production is thus vital for cell function.

Oxidative stress occurs when the prooxidant/antioxidant balance is lost, altering and damaging many intracellular molecules, including DNA, RNA, lipids, and proteins.³ The mechanisms and pathways involved in oxidative stress are conserved in mammalian cells.

Cancer cells, which are known to possess an increased metabolism, require high concentrations of ROS in order to be able to proliferate at a higher rate than normal cells. In addition, ROS favor other aspects of tumor development and progression, such as evasion of apoptosis or anoikis, tissue invasion and metastasis, and angiogenesis.

For this reason in the field of cancer therapy, several radio and chemotherapeutic drugs are used to modulate tumor behavior by directly modulating ROS production.

Contribution of oxidative stress in neuroblastoma pathogenesis

Oxidative stress associated with NB growth

Solid tumors, such as NB, exhibit regions of acute/chronic hypoxia that may be predisposed to develop an oxidative tumor environment. An oxidative and antioxidant imbalance exists in the blood circulation system of children with liquid and solid cancers.⁴ However, oxidation status of tumor has not clearly been defined as an indicator of the severity of the NB.

One study of Novotny et al. indicates that a deregulation in the redox status occurs in NB.⁵ These authors investigated whether plasma measurements of oxidants/antioxidants in an animal model of human NB were correlated with tumor growth. Although they found no clear response in plasma antioxidant activity, they did find an increase of oxidative stress in the animal model of human NB at the beginning of the growth, thus suggesting a link between oxidative stress and NB formation (Fig. 1).

MYCN amplification provides resistance of NB cells to oxidative stress

MYCN amplification correlates with high-risk disease and poor prognosis. Overexpression of MYCN in whole mice or cells is able to induce NB and tumor progression.⁶⁻⁸ In addition, cells with MYCN amplification show resistance to apoptosis. By contrast, MYCN downregulation promotes proliferation arrest,⁹ differentiation, and apoptosis in human NB cells.^{10,11} Since resistance and the degree of malignancy of NB correlate with the amplification of the oncogene MYCN, MYC appears to be a crucial factor in promoting cell survival in NB.

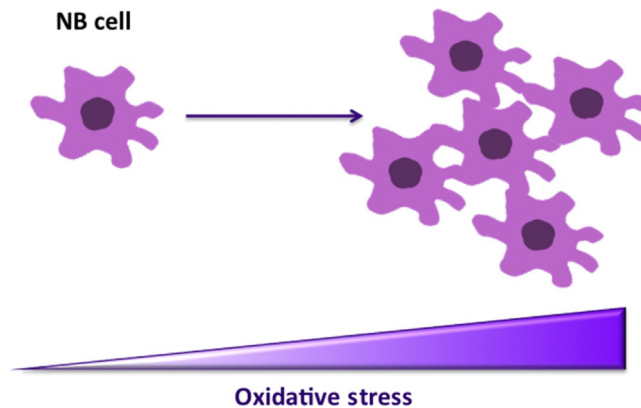


Fig. 1 Oxidative stress contributes to cancer progression. Reactive oxygen species production increases oxidative stress and induces cancer cells proliferation.

For this reason, identification of the relationship between MYCN amplification and cancer resistance to apoptosis presents an interesting challenge. A crucial link is emerging between pro-survival activity of NB and the efficiency of its antioxidant system. In line with this, in 2008, Marengo and collaborators demonstrated that high levels of glutathione (GSH) preserve cells following irradiation and chemotherapy.¹² In particular, they showed that cells with amplified MYCN possess higher levels of glutathione, this conferring an increased ability to dispose of reactive oxygen species, such as H₂O₂. By contrast, neuroblastoma cells with low levels of MYCN are more sensitive to oxidative stress due to a decrease in GCL (responsible for GSH biosynthesis), leading to the reduction of glutathione production. Because GSH is the most abundant low-molecular thiol involved in cellular detoxification against reactive oxygen species,¹³ the authors cited highlight a link between the resistance of NB cells to apoptosis and their antioxidant function. They demonstrated that MYCN transcriptionally upregulates the catalytic subunit of GCL in MYCN-amplified NB cells, but not in NB cells without MYCN amplification, thus conferring resistance to oxidative damage. In addition, they found that inhibition of GCL favors apoptosis of NB cells.¹² Such results underline GCL as a potential therapeutic target for the treatment of NB with MYCN amplified.

Recently, it has been demonstrated that a forced overexpression of MYCN, in neural crest progenitor cells, enhances glutaminolysis, a hallmark of cancer metabolism, which contributes, in part, to ROS production. Glutaminolysis by inducing oxidative stress renders NB cells sensitive to ROS augmentation. To corroborate this, Wang and colleagues found that dimethyl fumarate (DMF), a Food and Drug Administration, approved drug for multiple sclerosis, blocks proliferation of NB cells in vitro and tumor growth in vivo. Mechanistically, the authors demonstrated that DMF stops NB cell proliferation by increasing ROS levels, which, in turn, suppresses MYCN expression.¹⁴ These recent data indicate that manipulation of the metabolism and the increase of ROS could be a novel way for combatting NB (Fig. 2).

Nitro-oxidative stress contributes to NB cell death

Nitrogen species (RNS) are reactive species derived from nitrogen and cellular metabolism. In analogy with ROS production, they are mainly generated from mitochondria.¹⁵ They are classified as ions (peroxynitrite) or nonions (nitric oxide). Also like ROS, RNS are involved in several physiological processes, such as cellular response to stress, mitochondrial network, signaling, and apoptosis.^{16,17} However, the imbalance between oxidants-nitrosants and their elimination are associated with nitro-oxidative stress production. In this latter case, RNS are harmful for the cell, leading to cellular dysfunctions by acting on proteins, lipids, DNA, and sugars.^{18,19} The potentially deleterious effects of RNS can be neutralized by the antioxidative defense systems.^{20,21}

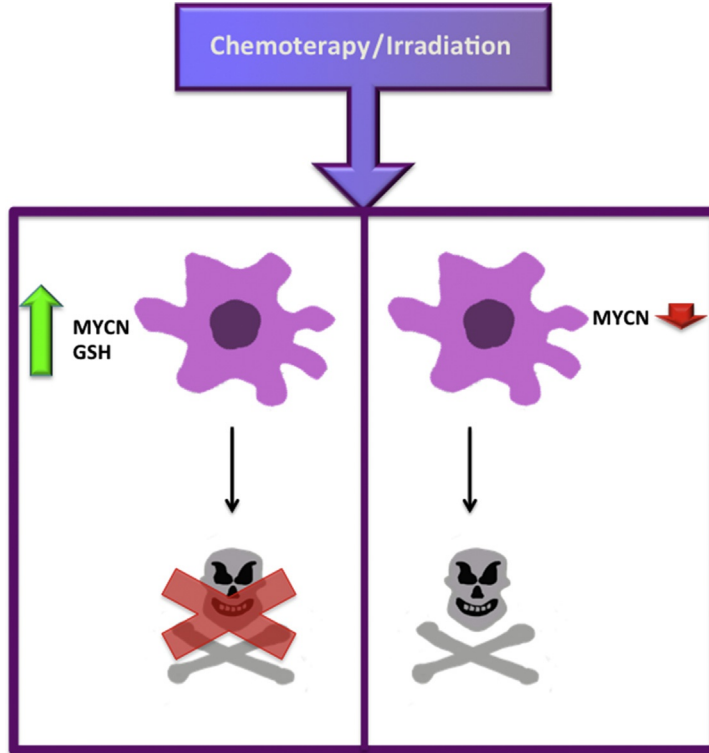


Fig. 2 Correlation between glutathione and MYC levels and cancer cells resistance. High levels of MYC and GSH contribute to tumor cell proliferation, thus allowing irradiation- and chemo-resistance. Low levels of the oncogene MYC are associated with the death of cancer cells.

A recent work by Gorska and colleagues indicates that favoring the imbalance between production and elimination of RNS could expose NB cells to apoptosis.²² In particular, the same authors tested the effect of 2-methoxyestradiol on NB SH-SY5Y cells. 2-methoxyestradiol is an agent already known to be efficient for breast and prostate cancer treatment. They discovered that at pharmacologically relevant concentrations, 2-methoxyestradiol induces apoptosis of neuroblastoma SH-SY5Y cells via nitric oxide generation and reduction of mitochondrial membrane potential. The same work confirms the efficiency of 2-methoxyestradiol in the treatment of cancer and in this case NB. In addition, it proposes the hypothesis that favoring an imbalance of the redox status in NB cells could favor apoptosis of these cells (Fig. 3).

In vitro uses of neuroblastoma cell line

A common hallmark of neuroblastoma cell lines is the ability to proliferate in an unlimited manner, constituting the most diffuse in vitro model system for generating neuronal cells

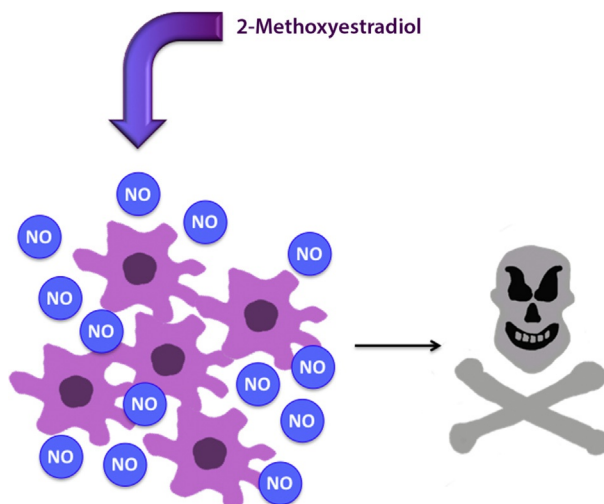


Fig. 3 NO accumulation causes a reduction of neuroblastoma cells. 2-methoxyestradiol induces nitric oxide generation, so contributing to a reduction of mitochondrial membrane potential and apoptosis.

upon several differentiation-inducing treatments. In recent years, NB cell lines were widely used for various purposes: (a) to analyze anticancer effects of antimalarial drugs²³ or (b) to understand the relationship between proliferation, differentiation, and apoptosis,²⁴ or (c) to unravel the virus-host cell relationship²⁵ or (d) to better understand the molecular mechanisms at the basis of pediatric cancer neuroblastoma.²⁶

To date, there are three different morphological variants of neuroblastoma cells that favor the heterogeneity among these cells: neuroblastic (N), substrate adherent (S), and intermediate (I).^{27–29} These variants can be distinguished by using different biochemical markers, such as tyrosine hydroxylase (TH), dopamine- β -hydroxylase (D β H), and tyrosinase (Tyr) (Table 1).

Among these cells, SH-SY5Y is the elective model system in neuronal differentiation *in vitro*. In particular, SH-SY5Y cells can be both adherent and floating cells with neuroblast- and epithelial-like phenotypes. In contrast to epithelial-like cells, neuroblast-like SH-SY5Y cells are positive for tyrosine hydroxylase and dopamine- β -hydroxylase, typical markers of catecholaminergic neurons, thus mimicking neuronal cells.³⁰ In addition, SH-SY5Y cells can be differentiated to a more mature neuron-like phenotype by using an easy *in vitro* method allowing a more consistent comparison with neurons. Differentiated SH-SY5Y cells present several neuritic projections and are positive for differentiation markers.³¹ We summarize the differentiation protocol in Fig. 4.

In the last 10 years, SH-SY5Y cells have been used in several studies in order to understand the causes/effects of oxidative stress in neuronal cells and to find molecular mechanisms that could reduce it, thus counteracting neurodegeneration.^{32,33}

Table 1 Overview of neuroblastoma cell lines and their classification.

Parental cell line	Subtypes	Morphologic variant	Protein marker
SKNSH	SH-SY5Y	N	TH, D β H
	SH-EP	S	
	SH-EPI	S	Tyr
	SH-EPIE	S	
	SH-IN	I	TH, D β H
SK-N-BE(1)	SK-N-BE(1) _n	N	
	SK-N-BE(1) _s	S	
SK-N-BE(2)	BE(2)-M17	N	TH
	BE(2)-M17V	N	TH
	BE(2)-M17F	S	THTH
	BE(2)-M17M	I	
	BE(2)-7S	S	Tyr
	BE(2)-C	I	D β H, TH
LA-N-I	LAI-15 _n	N	TH
	LAI-19 _n	N	TH
	LAI-21 _n	N	TH
	LAI-5 _s	S	Tyr
	LAI-6 _s	S	
	LAI-22 _n /i	N/I	D β H
NAP	NAP(H) _n	N	TH
	NAP(H) _s	S	
NBL-W	NBL-W-N	N	D β H, TH
	NBL-W-S	S	
RT-BMV	RT-BMV-I	N	
	RT-BMV-C6	I	
SMS-KCN	KCN-62 _n	N	TH
	KCN-65 _n	N	TH
	KCN-71 _n	N	TH
	KCN-83 _n	N	TH
	KCN-9 _s	S	Tyr

The neuroblastoma cell line presents three different phenotypes: neuroblastic (N), substrate adherent (S), and intermediate (I). Each cell line has several subtypes expressing typical markers including tyrosine hydroxylase (TH), dopamine- β -hydroxylase (D β H), and tyrosinase (Tyr).

Overview of the main mechanisms that reduce oxidative stress in neuroblastoma cells

During the last 10 years, many studies have described molecules that are able to counteract oxidative stress in neuroblastoma cells used as an in vitro model of neurodegenerative pathologies, including Parkinson (PD) and Alzheimer diseases (AD).

In the following section, we focus on the most characterized processes for combatting oxidation events and ameliorating neurotoxicity thus preserving cell viability in neuroblastoma cells.

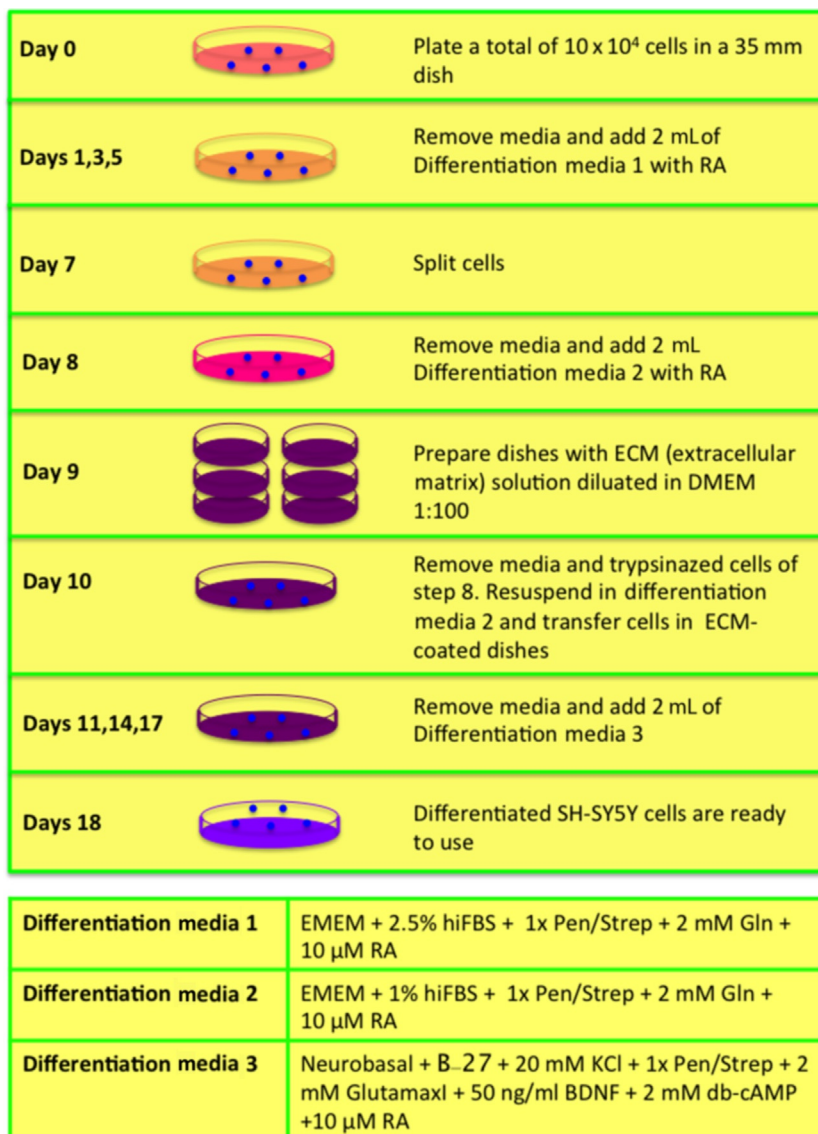


Fig. 4 In vitro differentiation of SH-SY5Y cells to neuronal cells. Schematic representation of the 18 days long differentiation methods used to obtain SH-SY5Y cells with a neuronal-like phenotype. The protocol is articulated in eight phases in which SH-SY5Y cells are cultured in three different media, specific for their differentiation.

Autophagy/mitophagy

Autophagy is a cyto-protective auto-degradation process that operates through lysosome enzymatic digestion. To date, specific forms of autophagy are known to selectively remove organelles. In particular, mitophagy is a selective autophagy pathway

for dysfunctional or undesired mitochondrial clearance.³⁴ Since mitochondria are fundamental for cells, especially for neurons, there is a body of evidence to underline the role of mitophagy process in combatting ROS production thus restricting oxidative stress and preserving cellular homeostasis, especially in the in vitro model of neurodegenerative disease. For instance, the mitophagy receptor AMBRA1 is able to stimulate mitophagy in PD model systems, in which SH-SY5Y cells were treated with two mitochondrial toxins, 6-hydroxidopamine (6-OHDA) and rotenone. The AMBRA1-mediated mitophagy pathway also preserves SH-SY5Y cell viability by reducing ROS production and death induction through its antioxidant function.³² In line with these data, Song and colleagues have recently demonstrated that the aberrant mitochondria accumulation related to a precursor phase of AD, known as chronic cerebral hypoperfusion (CCH), is due to impairment in BNIP3-mediated mitophagy. In particular, they observed that low levels of BNIP3 gene in murine Neuro2A cells, as in the ex vivo model of CCH, are related to damaged mitochondria accumulation and oxidative stress production, contributing to neuronal cell damage during hypoxia. This evidence suggests a beneficial role of BNIP3-induced mitophagy for neurons³⁵ (Fig. 5).

Mitohormesis

A mild mitochondrial stress rapidly activates a broad range of cytosolic and nuclear responses able to restrict subsequent perturbations.³⁶ In particular, H₂ pretreatment in NB cells prevents H₂O₂-induced cell death in its capacity as a mitohormetic factor counteracting oxidative stress.³⁷

Combined treatment of vitamin E, folate, and acetyl-L-carnitine

Dhitavat and colleagues demonstrated that administration of vitamin E, folate, and acetyl-L-carnitine, which all prevent de novo oxidative damage, preserve levels of the *endogenous* glutathione, and limit mitochondrial damage and ATP depletion, respectively. This combined treatment has been useful for preventing ROS accumulation and neurodegeneration in neuroblastoma SH-SY5Y cells, an in vitro model of Alzheimer's disease.³⁸

Phenolic compounds

Phenolic compounds, known as protocatechuic aldehyde (PCA) elements of *Hydnophytum formicarum* Jack., attenuate ROS-induced cell death, so counteracting hydrogen peroxide (H₂O₂)-induced depletion of SIRT1 and FoxO3a in human neuroblastoma SH-SY5Y cells. This induces an increase in SOD2, catalase, and Bcl-2 protein levels, leading to beneficial effects for cellular homeostasis.³⁹

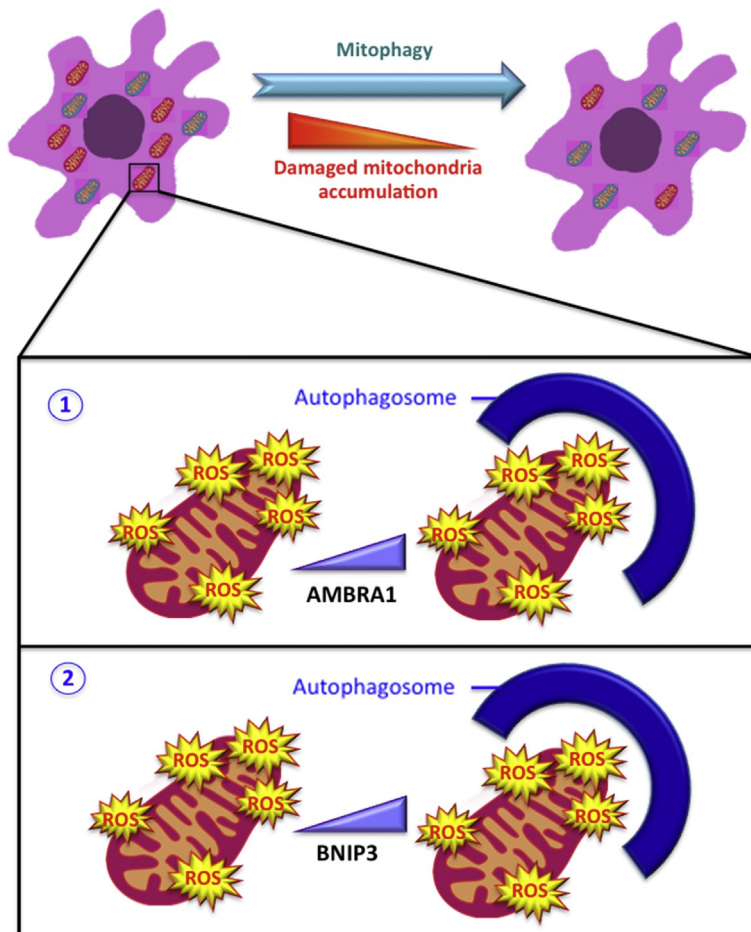


Fig. 5 Mitophagy counteracts oxidative stress in neurodegeneration. Neuroblastoma cells are used as an *in vitro* model of neurodegenerative diseases. In particular, the accumulation of dysfunctional mitochondria (*red* mitochondria) in respect to healthy mitochondria (*blue* mitochondria) is a typical feature of neurodegeneration. As shown in ① the AMBRA1 protein allows mitochondrial ROS reduction through mitophagy in the NB model system. In addition, BNIP3 could contribute to dysfunctional mitochondria clearance by inducing their selective recruitment into the autophagosome ②.

SQ29548 treatment

SQ29548 is an antagonist of thromboxane A2 receptor (TXA2R), which is responsible of the regulation of oxidative stress.⁴⁰ SQ29548 treatment not only ameliorates intracellular ROS levels and enhances the expression of SOD2 and catalase; but also it restricts apoptosis and favors viability in NB cells.⁴¹

Flavonoid-induced cytoprotection

The flavonoid quercetin 3-glucoside (Q3G) is known to counteract H₂O₂-induced oxidative stress by activating the sterol regulatory element-binding protein-2 (SREBP-2) in SH-SY5Y cells. In turn, SREBP-2 mediates sterol synthesis that attenuates lipid peroxidation preserving membrane integrity during oxidative stress.⁴² In addition, Proxison (7-decyl-3-hydroxy-2-(3,4,5-trihydroxyphenyl)-4-chromenone) is a synthetic flavonoid that consists of a lipophilic hydrocarbon tail with a modified polyphenolic head group. This structure allows an efficient cellular uptake and favors Proxison radical scavenging function.⁴³

Mitochondrial isocitrate dehydrogenase

Mitochondrial isocitrate dehydrogenase (IDPm) is involved in the enzymatic reduction of NADP(+) to NADPH and in glutathione (GSH) supply. Kim and colleagues observed that IDPm transfected SH-SY5Y cells were more resistant than the control cells to staurosporine (apoptosis inducer). In fact, they demonstrated that IDPm mediates an increase in NADPH and GSH levels that, in turn, inhibits mitochondrial ROS production, thus attenuating cellular apoptosis.³³

Conclusion

Neuroblastoma cells are widely used for studying cancer progression and neurodegeneration. In particular, some features of these cells, including their high proliferation rate and their accumulation of reactive species, make them a helpful system for evaluating oxidative stress and its correlation with pathologies. Reactive species production is beneficial for both cancer and neurodegenerative diseases, in that it confers chemoresistance on cancer cells and limits cellular homeostasis maintenance in neuronal cells. Accordingly, using neuroblastoma cells is a helpful strategy: it provides cellular in vitro models for investigating the molecular mechanisms responsible for oxidative stress production, opening the way for new therapies for the patients with cancer and neurodegenerative diseases.

Summary points

- This chapter focuses on oxidative stress in neuroblastoma.
- Oxidative stress is critical for cancer progression and metastatization.
- Reactive oxygen species accumulation is a common hallmark of tumor and neurodegenerative diseases.
- Neuroblastoma cells are an in vitro model of neuronal differentiation.
- Neuroblastoma can be used as in vitro model in the search for molecular mechanisms counteracting oxidative stress and thus ameliorating neuronal viability.

References

1. Brodeur GM. Neuroblastoma: biological insights into a clinical enigma. *Nat Rev Cancer* 2003;**3**:203–16.
2. Yang Q, Olshan AF, Bondy ML, Shah NR, Pollock BH, Seeger RC, et al. Parental smoking and alcohol consumption and risk of neuroblastoma. *Cancer Epidemiol Biomark Prev* 2000;**9**:967–72.
3. Veskoukis AS, Tsatsakis AM, Kouretas D. Dietary oxidative stress and antioxidant defense with an emphasis on plant extract administration. *Cell Stress Chaperones* 2012;**17**:11–21.
4. Drabko K, Kowalczyk J. Imbalance between pro-oxidative and anti-oxidative processes in children with neoplastic disease. *Med Wieku Rozwoj* 2004;**8**:217–23.
5. Novotny NM, Grosfeld JL, Turner KE, Rescorla FJ, Pu X, Klaunig JE, et al. Oxidative status in neuroblastoma: a source of stress? *J Pediatr Surg* 2008;**43**:330–4.
6. Schwab M, Varmus HE, Bishop JM. Human N-myc gene contributes to neoplastic transformation of mammalian cells in culture. *Nature* 1985;**316**:160–2.
7. Yancopoulos GD, Nisen PD, Tesfaye A, Kohl NE, Goldfarb MP, Alt FW. N-myc can cooperate with ras to transform normal cells in culture. *Proc Natl Acad Sci USA* 1985;**82**:5455–9.
8. Cavalieri F, Goldfarb M. N-myc proto-oncogene expression can induce DNA replication in Balb/c 3T3 fibroblasts. *Oncogene* 1988;**2**:289–91.
9. Goldsmith KC, Hogarty MD. Targeting programmed cell death pathways with experimental therapeutics: opportunities in high-risk neuroblastoma. *Cancer Lett* 2005;**228**:133–41.
10. Kang JH, Rychahou PG, Ishola TA, Qiao J, Evers BM, Chung DH. MYCN silencing induces differentiation and apoptosis in human neuroblastoma cells. *Biochem Biophys Res Commun* 2006;**351**:192–7.
11. Nara K, Kusafuka T, Yoneda A, Oue T, Sangkhathat S, Fukuzawa M. Silencing of MYCN by RNA interference induces growth inhibition, apoptotic activity and cell differentiation in a neuroblastoma cell line with MYCN amplification. *Int J Oncol* 2007;**30**:1189–96.
12. Marengo B, De Ciucis C, Verzola D, Pistoia V, Raffaghello L, Patriarca S, et al. Mechanisms of BSO (l-buthionine-S,R-sulfoximine)-induced cytotoxic effects in neuroblastoma. *Free Radic Biol Med* 2008;**44**:474–82.
13. Forman HJ, Zhang H, Rinna A. Glutathione: overview of its protective roles, measurement, and biosynthesis. *Mol Aspects Med* 2008;**30**:1–12.
14. Wang T, Liu L, Chen X, Shen Y, Lian G, Shah N, et al. MYCN drives glutaminolysis in neuroblastoma and confers sensitivity to an ROS augmenting agent. *Cell Death Dis* 2018;**9**:220.
15. Thannickal VJ, Fanburg BL. Reactive oxygen species in cell signaling. *Am J Physiol Lung Cell Mol Physiol* 2000;**279**:L1005–28.
16. Bolisetty S, Jaimes EA. Mitochondria and reactive oxygen species: physiology and pathophysiology. *Int J Mol Sci* 2013;**14**:6306–44.
17. Baran CP, Zeigler MM, Tridandapani S, Marsh CB. The role of ROS and RNS in regulating life and death of blood monocytes. *Curr Pharm Des* 2004;**10**:855–66.
18. Gella A, Durany N. Oxidative stress in Alzheimer disease. *Cell Adhes Migr* 2009;**3**:88–93.
19. Ogino K, Wang DH. Biomarkers of oxidative/nitrosative stress: an approach to disease prevention. *Acta Med Okayama* 2007;**61**:181–9.
20. Klandorf H, Van Dyke K. Oxidative and nitrosative stresses: their role in health and disease in man and birds. In: Lushchak V, editor. [chapter 3] *Oxidative Stress-Molecular Mechanisms and Biological Effects*. Rijeka, Croatia: InTech; 2012.
21. Khassaf M, McArdle A, Esanu C, et al. Effect of vitamin C supplements on antioxidant defence and stress proteins in human lymphocytes and skeletal muscle. *J Physiol* 2003;**549**:645–52.
22. Gorska M, Kuban-Jankowska A, Milczarek R, Wozniak M. Nitro-oxidative stress is involved in anti-cancer activity of 17 β -estradiol derivative in neuroblastoma cells. *Anticancer Res* 2016;**36**:1693–8.
23. Meshnick SR, Taylor TE, Kamchonwongpaisan S. Artemisinin and the antimalarial endoperoxides: from herbal remedy to targeted chemotherapy. *Microbiol Rev* 1996;**60**:301–15.
24. Mazar J, Rosado A, Shelley J, Marchica J, Westmoreland TJ. The long non-coding RNA GAS5 differentially regulates cell cycle arrest and apoptosis through activation of BRCA1 and p53 in human neuroblastoma. *Oncotarget* 2017;**8**:6589–607.
25. Abdullah H, Heaney LG, Cosby SL, McGarvey LP. Rhinovirus upregulates transient receptor potential channels in a human neuronal cell line: implications for respiratory virus-induced cough reflex sensitivity. *Thorax* 2014;**69**:46–54.

26. Ham J, Costa C, Sano R, Lochmann TL, Sennott EM, Patel NU, et al. Exploitation of the apoptosis-primed state of MYCN-amplified neuroblastoma to develop a potent and specific targeted therapy combination. *Cancer Cell* 2016;**29**:159–72.
27. Ciccarone V, Spengler BA, Meyers MB, Biedler JL, Ross RA. Phenotypic diversification in human neuroblastoma cells: expression of distinct neural crest lineages. *Cancer Res* 1989;**49**:219–25.
28. Ross R, Spengler B, Domenech C, Porubcin M, Rettig W, Biedler J. Human neuroblastoma I-type cells are malignant neural crest stem cells. *Cell Growth Differ* 1995;**6**:449–56.
29. Ross RA, Spengler BA, Rettig WJ, Biedler JL. Differentiation-inducing agents stably convert human neuroblastoma I-type cells to neuroblastic (N) or nonneuronal (S) neural crest cells. *Prog Clin Biol Res* 1994;**385**:253–9.
30. Ross RA, Spengler BA, Biedler JL. Coordinate morphological and biochemical interconversion of human neuroblastoma cells. *J Natl Cancer Inst* 1983;**71**:741–7.
31. Shipley MM, Mangold CA, Szpara ML. Differentiation of the SH-SY5Y human neuroblastoma cell line. *J Vis Exp* 2016;**17**:53193.
32. Di Rita A, D'Acunzo P, Simula L, Campello S, Strappazzon F, Cecconi F. AMBRA1-mediated mitophagy counteracts oxidative stress and apoptosis induced by neurotoxicity in human neuroblastoma SH-SY5Y cells. *Front Cell Neurosci* 2018;**12**:92.
33. Kim SJ, Yune TY, Han CT, Kim YC, Oh YJ, Markelonis GJ, et al. Mitochondrial isocitrate dehydrogenase protects human neuroblastoma SH-SY5Y cells against oxidative stress. *J Neurosci Res* 2007;**85**:139–52.
34. Lemasters JJ. Selective mitochondrial autophagy, or mitophagy, as a targeted defense against oxidative stress, mitochondrial dysfunction, and aging. *Rejuvenation Res* 2005;**8**:3–5.
35. Song Y, Du Y, Zou W, Luo Y, Zhang X, Fu J. Involvement of impaired autophagy and mitophagy in Neuro-2a cell damage under hypoxic and/or high-glucose conditions. *Sci Rep* 2018;**8**:3301.
36. Yun J, Finkel T. Mitohormesis. *Cell Metab* 2014;**19**:757–66.
37. Murakami Y, Ito M, Ohsawa I. Molecular hydrogen protects against oxidative stress-induced SH-SY5Y neuroblastoma cell death through the process of mitohormesis. *PLoS One* 2017;**12**:e0176992.
38. Dhitavat S, Ortiz D, Rogers E, Rivera E, Shea TB. Folate, vitamin E, and acetyl-L-carnitine provide synergistic protection against oxidative stress resulting from exposure of human neuroblastoma cells to amyloid-beta. *Brain Res* 2005;**1061**:114–7.
39. Gay NH, Phopin K, Suwanjang W, Songtawee N, Ruankham W, Wongchitrat P, et al. Neuroprotective effects of phenolic and carboxylic acids on oxidative stress-induced toxicity in human neuroblastoma SH-SY5Y cells. *Neurochem Res* 2018;**43**:619–36.
40. Valentin F, Field MC, Tippins JR. The mechanism of oxidative stress stabilization of the thromboxane receptor in COS-7 cells. *J Biol Chem* 2004;**279**:8316–24.
41. Cai G, Yan A, Fu N, Fu Y. Thromboxane A2 receptor antagonist SQ29548 attenuates SH-SY5Y neuroblastoma cell impairments induced by oxidative stress. *Int J Mol Med* 2018;**42**:479–88.
42. Soundararajan R, Wishart AD, Rupasinghe HP, Arcellana-Panlilio M, Nelson CM, Mayne M, et al. Quercetin 3-glucoside protects neuroblastoma (SH-SY5Y) cells in vitro against oxidative damage by inducing sterol regulatory element-binding protein-2-mediated cholesterol biosynthesis. *J Biol Chem* 2008;**283**:2231–45.
43. Drummond NJ, Davies NO, Lovett JE, Miller MR, Cook G, Becker T, et al. A synthetic cell permeable antioxidant protects neurons against acute oxidative stress. *Sci Rep* 2017;**7**:11857.